ADVANCED OPTIMIZATION AND CONTROL FOR SMART GRIDS WITH HIGH PENETRATION OF RENEWABLE ENERGY SYSTEMS

EDITED BY: Bo Yang, Dongran Song, Xing He, Xiaoshun Zhang, Sungyun Choi, Chao Duan and Yaxing Ren

PUBLISHED IN: Frontiers in Energy Research



frontiers Research Topics



frontiers

Frontiers eBook Copyright Statement

The copyright in the text of individual articles in this eBook is the property of their respective authors or their respective institutions or funders. The copyright in graphics and images within each article may be subject to copyright of other parties. In both cases this is subject to a license granted to Frontiers.

The compilation of articles constituting this eBook is the property of Frontiers.

Each article within this eBook, and the eBook itself, are published under the most recent version of the Creative Commons CC-BY licence. The version current at the date of publication of this eBook is CC-BY 4.0. If the CC-BY licence is updated, the licence granted by Frontiers is automatically updated to the new version.

When exercising any right under the CC-BY licence, Frontiers must be attributed as the original publisher of the article or eBook, as applicable.

Authors have the responsibility of ensuring that any graphics or other materials which are the property of others may be included in the CC-BY licence, but this should be checked before relying on the CC-BY licence to reproduce those materials. Any copyright notices relating to those materials must be complied with.

Copyright and source acknowledgement notices may not be removed and must be displayed in any copy, derivative work or partial copy which includes the elements in question.

All copyright, and all rights therein, are protected by national and international copyright laws. The above represents a summary only. For further information please read Frontiers' Conditions for Website Use and Copyright Statement, and the applicable CC-BY licence.

ISSN 1664-8714
ISBN 978-2-88974-389-6
DOI 10.3389/978-2-88974-389-6

About Frontiers

Frontiers is more than just an open-access publisher of scholarly articles: it is a pioneering approach to the world of academia, radically improving the way scholarly research is managed. The grand vision of Frontiers is a world where all people have an equal opportunity to seek, share and generate knowledge. Frontiers provides immediate and permanent online open access to all its publications, but this alone is not enough to realize our grand goals.

Frontiers Journal Series

The Frontiers Journal Series is a multi-tier and interdisciplinary set of open-access, online journals, promising a paradigm shift from the current review, selection and dissemination processes in academic publishing. All Frontiers journals are driven by researchers for researchers; therefore, they constitute a service to the scholarly community. At the same time, the Frontiers Journal Series operates on a revolutionary invention, the tiered publishing system, initially addressing specific communities of scholars, and gradually climbing up to broader public understanding, thus serving the interests of the lay society, too.

Dedication to Quality

Each Frontiers article is a landmark of the highest quality, thanks to genuinely collaborative interactions between authors and review editors, who include some of the world's best academicians. Research must be certified by peers before entering a stream of knowledge that may eventually reach the public - and shape society; therefore, Frontiers only applies the most rigorous and unbiased reviews.
Frontiers revolutionizes research publishing by freely delivering the most outstanding research, evaluated with no bias from both the academic and social point of view. By applying the most advanced information technologies, Frontiers is catapulting scholarly publishing into a new generation.

What are Frontiers Research Topics?

Frontiers Research Topics are very popular trademarks of the Frontiers Journals Series: they are collections of at least ten articles, all centered on a particular subject. With their unique mix of varied contributions from Original Research to Review Articles, Frontiers Research Topics unify the most influential researchers, the latest key findings and historical advances in a hot research area! Find out more on how to host your own Frontiers Research Topic or contribute to one as an author by contacting the Frontiers Editorial Office: frontiersin.org/about/contact

ADVANCED OPTIMIZATION AND CONTROL FOR SMART GRIDS WITH HIGH PENETRATION OF RENEWABLE ENERGY SYSTEMS

Topic Editors:
Bo Yang, Kunming University of Science and Technology, China
Dongran Song, Central South University, China
Xing He, Shanghai Jiao Tong University, China
Xiaoshun Zhang, Shantou University, China
Sungyun Choi, Korea University, South Korea
Chao Duan, Northwestern University, United States
Yaxing Ren, University of Warwick, United Kingdom

Citation: Yang, B., Song, D., He, X., Zhang, X., Choi, S., Duan, C., Ren, Y., eds. (2022). Advanced Optimization and Control for Smart Grids With High Penetration of Renewable Energy Systems. Lausanne: Frontiers Media SA.
doi: 10.3389/978-2-88974-389-6

Table of Contents

07 ***Editorial: Advanced Optimization and Control for Smart Grids With High Penetration of Renewable Energy Systems***
Bo Yang, Dongran Song, Xing He, Xiaoshun Zhang, Sungyun Choi, Chao Duan and Yaxing Ren

10 ***Optimal Placement and Sizing of Distributed Generators Based on Swarm Moth Flame Optimization***
Zhukui Tan, Ming Zeng and Liming Sun

18 ***A Powerful Bio-Inspired Optimization Algorithm Based PV Cells Diode Models Parameter Estimation***
Liming Sun, Jingbo Wang and Lan Tang

33 ***Full Life Cycle Management of Power System Integrated With Renewable Energy: Concepts, Developments and Perspectives***
Kang Wang, Yikai Li, Xiaojun Wang, Zengtao Zhao, Ning Yang, Shengcan Yu, Yi Wang, Zhanhong Huang and Tao Yu

46 ***Impedance Modeling and Analysis of Medium-Frequency Oscillation Caused by VSC-HVDC Connected to Local Weak Grid and DFIG-Based Wind Farms***
Kun Sun, Wei Yao, Cai Yan and Jinyu Wen

61 ***Hybrid Simulation for Large-Scale AC/DC Power System by Serial Interaction Process***
Song Zhang, Guoqing Li, Shuguang Li and Xintong Liu

71 ***Cost-Sensitive Extremely Randomized Trees Algorithm for Online Fault Detection of Wind Turbine Generators***
Mingzhu Tang, Yutao Chen, Huawei Wu, Qi Zhao, Wen Long, Victor S. Sheng and Jiabiao Yi

85 ***Accurate Solar Cell Modeling via Genetic Neural Network-Based Meta-Heuristic Algorithms***
Long Wang, Zhuo Chen, Yinyuan Guo, Weidong Hu, Xucheng Chang, Peng Wu, Cong Han and Jianwei Li

99 ***PV Cell Parameter Extraction Using Data Prediction–Based Meta-Heuristic Algorithm via Extreme Learning Machine***
Bing Li, Huang Chen and Tian Tan

114 ***Concepts, Structure and Developments of High-Reliability Cyber-Physical Fusion Based Coordinated Planning for Distribution System***
Chong Gao, Tianlin Wang, Huazhen Cao, Ziyao Wang, Tao Yu and Ran Cheng

125 ***Autonomous Control Method of Rotor UAVs for Power Inspection With Renewable Energy Based on Swarm Intelligence***
Yao Yao, Cao Jun-hua, Guo Yi, Fan Zhun, Zou An-Min, Xu Biao and gLi Ke

134 ***A Random Forest and Current Fault Texture Feature–Based Method for Current Sensor Fault Diagnosis in Three-Phase PWM VSR***
Lei Kou, Xiao-dong Gong, Yi Zheng, Xiu-hui Ni, Yang Li, Quan-de Yuan and Ya-nan Dong

146 ***Non-Intrusive Power Load Identification for High-Penetration Renewable Energy Grids***
Bin Liu, Zhukui Tan and Xiao Su

158 ***Unmanned Aerial Vehicle for Transmission Line Inspection: Status, Standardization, and Perspectives***
Xin Li, Zijian Li, Haizhi Wang and Wanlin Li

171 ***Optimal Array Reconfiguration of a PV Power Plant for Frequency Regulation of Power Systems***
Tingyi He, Shengnan Li, Yiping Chen, Shuijun Wu and Chuangzhi Li

182 ***Power Configuration Scheme for Battery Energy Storage Systems Considering the Renewable Energy Penetration Level***
Qing Chen, Rui Xie, Yuyan Chen, Heyu Liu, Shengqi Zhang, Fei Wang, Zhaohui Shi and Bin Lin

195 ***Fault Location Scheme for Abnormal Grounding Point in Isolated Ground Wire of Large-Scale Clean Energy Transmission***
Yunlong Wang, Nuo Chen, Xiangnan Ma and Zongzhang Yang

203 ***Convex Approximation Algorithm for AC/DC Distribution Network With Energy Router***
Tao Zhang, Yunfei Mu, Xiaoyu Wang, Youjun Deng, Yi Song, Kai Yuan and Hongjie Jia

212 ***Photovoltaic Power Station Electromagnetic Environment Complexity Evaluation Utilizing Logarithmic Morphological Gradient Spectrum***
Hua-chen Xi, Bing Li, Wen-hui Mai, Xiong Xu and Ya Wang

221 ***Optimal Locating and Sizing of BESSs in Distribution Network Based on Multi-Objective Memetic Salp Swarm Algorithm***
Sui Peng, Xianfu Gong, Xinmiao Liu, Xun Lu and Xiaomeng Ai

233 ***A Comprehensive Study on Maximum Power Point Tracking Techniques Based on Fuzzy Logic Control for Solar Photovoltaic Systems***
Tongsen Zhu, Jiayi Dong, Xingshuo Li and Shuye Ding

240 ***Deep Learning-Based Prediction of Wind Power for Multi-turbines in a Wind Farm***
Xiaojiao Chen, Xiuqing Zhang, Mi Dong, Liansheng Huang, Yan Guo and Shiying He

246 ***A Critical Survey on Renewable Energy Applications in the Philippines and China: Present Challenges and Perspectives***
Xin Li, Haizhi Wang, Yuanru Lu and Wanlin Li

255 ***Robust Stability Control for Electric Vehicles Connected to DC Distribution Systems***
Wei Teng, Yuejiao Wang, Shumin Sun, Yan Cheng, Peng Yu and Shibo Wang

263 ***Cost-Sensitive LightGBM-Based Online Fault Detection Method for Wind Turbine Gearboxes***
Mingzhu Tang, Qi Zhao, Huawei Wu and Zimin Wang

275 ***Optimal Sizing of a Grid Independent Renewable Heating System for Building Decarbonisation***
Si Chen, Daniel Friedrich and Zhibin Yu

289 ***Medium—And Long-Term Load Forecasting Method for Group Objects Based on the Image Representation Learning***
Daolu Zhang, Weiling Guan, Jiajun Yang, Huang Yu, WenCong Xiao and Tao Yu

304 ***Power Management of AC/DC Hybrid Distribution Network With Multi-Port PET Considering Reliability of Power Supply System***
Xinxing Xu, Wentao Huang, Yan Hu, Nengling Tai, Yaming Ji and Ning Xie

319 ***Research on Efficient Soft Switching Based on MPPT of PV Power Generation System***
Peng Tao, Yan Cui and Jiayuan Liang

329 ***Single-Ended Fast Protection for Transient Power of Multi-Terminal Flexible and Direct Power Grids Containing Renewable Energy***
Jieshan Shan, Xincui Tian, Yue Dai, Hongchun Shu, Yong Chang and Jian Song

337 ***Design of Control Strategy and Effect Evaluation for Primary Frequency Regulation of Wind Storage System***
Cuiping Li, Zheshen Zhang, Junhui Li, Yunbao Ma and Jiajun Zou

349 ***Nonlinear Maximum Power Point Tracking Control of Wind Turbine Based on Two-Mass Model Without Anemometer***
Jian Chen, Qun Lu, Libing Chen, Xiaohui Duan, Boping Yang, Wenyong Duan and Lanhong Zhang

355 ***Temperature Control of Proton Exchange Membrane Fuel Cell Based on Machine Learning***
Jiawen Li, Yaping Li and Tao Yu

361 ***Coordinated Frequency Regulation of Smart Grid by Demand Side Response and Variable Speed Wind Turbines***
Qi Zhu, Yingjie Wang, Jiuxu Song, L. Jiang and Yingliang Li

369 ***Control Method for PEMFC Using Improved Deep Deterministic Policy Gradient Algorithm***
Jiawen Li, Yaping Li and Tao Yu

374 ***Data-Driven Control for Proton Exchange Membrane Fuel Cells: Method and Application***
Jiawen Li, Kedong Zhu and Tao Yu

380 ***An Inductor Current Sensorless Control Strategy Based on Modified VSG Method for Single-Phase Microgrid Application With Seamless Transfer Capability***
Zhi Zhang, Junkai Wu, Liupeng Zheng, Di Xie and Xiao Tang

393 ***Distributed Imitation-Orientated Deep Reinforcement Learning Method for Optimal PEMFC Output Voltage Control***
Jiawen Li, Yaping Li and Tao Yu

400 ***Robust Optimal Dispatching of Wind Fire Energy Storage System Based on Equilibrium Optimization Algorithm***
Xiaojiao Chen, Liansheng Huang, Xiuqing Zhang, Shiying He, Zhicai Sheng, Zhenshang Wang, Tao Chen and Sheng Dou

407 ***Power Decoupling Control of MMC and Small-Signal Stability Analysis of AC/DC Distribution Network With Renewable Energy***
Zhang Xianyong, Guo Zijuan, Huang Yaohong, Li Li, Peng Weikuan and Cen Jian

421 ***PMSM Wind Farm Aggregation Algorithm Based on Power Equivalence Principle***
Haoshu Shao, Xu Cai, Heming Yan, Jiapei Zhou, Yao Qin and Zhixiang Zhang

430 ***A Learning-Based Bidding Approach for PV-Attached BESS Power Plants***
Xiang Gao, Haomin Ma, Ka Wing Chan, Shiwei Xia and Ziqing Zhu

439 ***Customer Load Forecasting Method Based on the Industry Electricity Consumption Behavior Portrait***
Weiling Guan, Daolu Zhang, Huang Yu, Binggang Peng, Yufeng Wu, Tao Yu and Keying Wang

451 ***Optimization and H∞ Performance Analysis for Load Frequency Control of Power Systems With Time-Varying Delays***
Kangyou Su, Yan Li, Jian Chen and Wenyong Duan

463 ***Coordinated Control Strategy of DC Fault Ride-through for the WF Connected to the Grid Through the MMC-HVDC***
Bo Zhu, Hongying Li, Panteng Xu, Shi Jiao, Lin Zhang and Yechun Xin

471 ***Delay-Dependent Stability Analysis of Load Frequency Control for Power System With EV Aggregator***
Zhe-Li Yuan, Da Xu, Li Jin and Hong-Zhang Wang

479 ***Optimal Operation and Control Design of DC Arrester for Renewable Energy Transmission***
Yue Feng, Kaiping Li, Min Gao, Yaozhang Liu, Xiaojun Li and Jiawei Zhu

486 ***Feedback Linearization Control Design for Battery/SMES Hybrid Energy Storage Systems Used in Distribution Network***
Chengye Tang and Yonghong Huang

497 ***Practical Method for Data-Driven User Phase Identification in Low-Voltage Distribution Networks***
Huang Yu, Yufeng Wu, Weiling Guan, Daolu Zhang, Tao Yu and Qianjin Liu

frontiers in Energy Research

EDITORIAL
published: 05 January 2022
doi: 10.3389/fenrg.2021.792249

Editorial: Advanced Optimization and Control for Smart Grids With High Penetration of Renewable Energy Systems

Bo Yang[1], Dongran Song[2], Xing He[3], Xiaoshun Zhang[4], Sungyun Choi[5], Chao Duan[6] and Yaxing Ren[7]*

[1]Faculty of Electric Power Engineering, Kunming University of Science and Technology, Kunming, China, [2]School of Automation, Central South University, Changsha, China, [3]School of Electronic Information and Electrical Engineering, Shanghai Jiao Tong University, Shanghai, China, [4]College of Engineering, Shantou University, Shantou, China, [5]School of Electrical Engineering, Korea University, Sejong, South Korea, [6]Department of Physics and Astronomy, Northwestern University, Evanston, IL, United States, [7]WMG, University of Warwick, Coventry, United Kingdom

Keywords: editorial, optimal control, optimal operation, smart grid, artificial intelligence

Editorial on the Research Topic

Advanced Optimization and Control for Smart Grids with High Penetration of Renewable Energy Systems

INTRODUCTION

This Research Topic aims to collect and encourage research related to the exploitation and implementation of various advanced optimization and control techniques, which aims to solve a series of strong inherent randomness and uncertainty problems in current power grids with large-scale renewable energy integration. Fortunately and Surprisingly, this research topic has received widespread interests and submissions from the researchers and engineers globally, which published 48 articles in total until its close date. These works are all in line with the original purpose and potential topics of this Research Topic, which significantly promotes up-to-date research and share promising ideas in the related fields. Basically, the topics in the energy research areas include optimal operation and optimal control.

OPTIMAL OPERATION

Hence, as for the work related to optimal operation, here are the basic summarization: Tan et al. propose an objective function considering integrated power losses, voltage profile and pollution emission, and swarm moth flame optimization algorithm (SMFO) is used to optimize the location and sizing of distributed generators. Tao et al. develop basic soft-switching technology based on hard switching, and an improved soft-switching technology is proposed to improve the conversion efficiency by reducing the switching loss, which can effectively optimize the dynamic and steady-state performance of MPPT and average tracking time. Tang et al. present a cost-sensitive extremely randomized trees (CS-ERT) algorithm to solve the problem of imbalanced classification in wind turbine generator fault detection, in which the cost-sensitive learning method is introduced into an extremely randomized trees (ERT) algorithm. Sun et al. design a novel bio-inspired grouped beetle antennae search (GBAS) algorithm is devised to effectively identify unknown parameters of different

OPEN ACCESS

Edited and reviewed by:
Hussein T. Mouftah, University of Ottawa, Canada

****Correspondence:***
Bo Yang
yangbo_ac@outlook.com

Specialty section:
This article was submitted to Smart Grids, a section of the journal Frontiers in Energy Research

Received: *10 October 2021*
Accepted: *15 December 2021*
Published: *05 January 2022*

Citation:
Yang B, Song D, He X, Zhang X, Choi S, Duan C and Ren Y (2022) Editorial: Advanced Optimization and Control for Smart Grids With High Penetration of Renewable Energy Systems. Front. Energy Res. 9:792249. doi: 10.3389/fenrg.2021.792249

PV models, which owns high optimization precision and stability. Chen et al. propose a deep learning approach for the power prediction of multiple wind turbines, in which a deep neural network combines spatiotemporal correlation to simultaneously predict the power of multiple wind turbines. Li et al. develop a novel parameter extraction strategy by data prediction-based meta-heuristic algorithm (DPMhA). Thus, PV cell parameters can be obtained with high accuracy and convergence rate. Chen et al. develop a BESS power configuration scheme (PCS) considering the renewable energy penetration (REP) constraint to configure the proper power of battery energy storage systems (BESSs) in system frequency regulation. He et al. establish a novel optimal array reconfiguration (OAR) of a PV power plant for secondary frequency control of automatic generation control (AGC), in which the battery energy storage system is used to balance the power deviation between the AGC signals and the PV power outputs. Kou et al. propose a random forest (RF) and current fault texture feature–based method for current sensor fault diagnosis in three-phase PWM VSR systems, and fault texture features are adopted to train the random forest current sensor fault detection and diagnosis (CSFDD) classifier. Wang et al.develop a novel genetic neural network (GNN)-based parameter estimation strategy for solar cells, based on measured *I-V* data, GNN accomplishes the training of the neural network via genetic algorithm. Gao et al. summarize a series of challenges brought by the highly coupled cyber-physical system, such as the primary and secondary collaborated planning models and solution algorithms. Tang et al. devise a new framework through combining the Spearman rank correlation feature extraction and cost-sensitive LightGBM algorithm for WT gearbox's fault detection, in which the feature selection is employed by using the expert experience and Spearman rank correlation coefficient. Peng et al. establish a multi-objective optimization model for the optimal locating and sizing of BESSs, which aims at minimizing the total investment cost of BESSs, the power loss cost of DN and the power fluctuation of the grid connection point. Chen et al. investigate a complete renewable heating system (RHS) framework and sizing the components to decarbonise building heating, which uses the particle swarm optimization algorithm for optimal sizing of each component in the RHS to find a solution to minimize CO_2 emissions. Liu et al. propose and constructs a Gaussian mixture model-binary parameter hidden Markov model (GMM-BPHMM) which takes into account the randomness of new energy power supply, clusters the load status based on active power and steady-state current to reduce the possibility of volatile clustering results from the new energy grid under a high penetration rate. Li et al. undertake a survey to design feasible schemes to ensure the sufficient utilization of renewable energy and the construction of integrated power grid systems to meet shortages of electricity supply especially in the isolated small islands in the Philippines through cooperation with China, meanwhile, Li et al. design feasible schemes to boost the international promotion of China's unmanned aerial vehicle (UAV) transmission line inspection standardization and further development of international UAV inspection technology. Zhu et al. review four FLC methods for comparative analysis. Furthermore, the design details and experimental result will also be given to help choose and measure these methods, which presents a clear image of the technology of FLC based MPPT to readers. Chen et al. propose a solution framework is to achieve the optimal robustness and economical operation of the system, which provides a new way for the application of the intelligent algorithm in the robust optimal dispatching. Xi et al. present feature extraction method for evaluating the complexity of the Electromagnetic Environment (EME) of the photovoltaic power station by using logarithmic morphological gradient spectrum (LMGS) based on the mathematical morphological theory. Zhang et al. propose a convex approximation algorithm to improve the feasibility of solving the model, and the steady-state model is developed with considering the loss characteristics and multiport coordinated control strategy. Zhang et al. takes distribution transformer as the research object and proposes a medium-and long-term load forecasting method for group objects based on Image Representation Learning (IRL). Shan et al. propose a single-ended protection principle based on the analysis method of transient power change for the "mesh structure" ring-shaped flexible direct current (DC) grid. Guan et al. propose a method for identifying the electricity consumption pattern of the customer based on the BB-Stacking model fusion framework, which yields the preliminary forecast results of customer load based on the actual load accounting results of the customers. Gao et al. propose a bidding model for PV-integrated BESS Power Plants in a pool-based day-ahead (DA) electricity market, in which the uncertainty of PV generation output is considered. Shao et al. propose a novel aggregation algorithm that considers the power loss of offshore submarine cable, which is different from the traditional wind farm modeling method that adopts amplifying transformer as aggregation medium. Yu et al. devise a novel data-driven phase identification algorithm based on advanced measurement infrastructure (AMI) in development of smart gird.

OPTIMAL CONTROL

Research aiming at optimal control can be outlined as: Wang et al. introduces the concepts, developments and perspectives of life cycle cost (LCC) management of equipment assets in high-penetrated renewable energy power grid, and probes into cost collection and estimation scheme in the process of equipment asset management. Xu et al. propose a three-layer and multi-time scale control mode of integrated automation system, PET cluster and PET controller based on the idea of hierarchical and partitioned control. Zhang et al. selects the bus as the hybrid simulation interface bus in the AC system near the DC system, which can effectively improve the simulation accuracy of the AC/DC system interaction. Li et al. propose a data-driven optimal control method for an air supply system in proton exchange membrane fuel cells (PEMFCs) with the aim of improving the PEMFC net output power and operational efficiency. Besides, to improve the proton exchange membrane fuel cell (PEMFC) working efficiency, a deep-reinforcement-learning based PID controller is proposed by Li et al. for realizing optimal

PEMFC stack temperature. Furthermore, Li et al. develop a data-driven PEMFC output voltage control method, moreover, an improved deep deterministic policy gradient algorithm is proposed for this method. Li et al. also propose a data-driven output voltage control strategy based on regulation of the duty cycle of the DC-DC converter to improve the stability of proton exchange membrane fuel cell (PEMFC) output voltage. Wang et al. apply the output power of different poles for the abnormal grounding point fault location based on the analysis of the output power of de-icing devices. Zhu et al. propose coordination rotor speed control (RSC), pitch angle control (PAC) and inertial control (IC) to control wind turbines, together with demand side response (DSR) participating in frequency regulation to balance active power in the power system. Yao et al. study and propose an optimization algorithm of automatic inspection of Unmanned Aerial Vehicles (UAVs) to improve the efficiency and cost of the inspection and maintenance work of renewable energy power grids. Sun et al. derive the sequence impedance model of the sending-end converter (SEC) of voltage source converter-based HVDC (VSC-HVDC) with the PQ-control outer loop and PLL with the explicit analytic expression. Teng et al. devise a robust control method based on H_{∞} loop shaping method to suppress the effect of uncertain integration on voltage stability of DC distribution system. Zhang et al. propose an inductor current sensorless control strategy based on modified virtual synchronous generator (VSG) method for single-phase inverter-interfaced microgrid application. Li et al. analyzes in detail the traditional control method, parallel control strategy and serial control strategy of the wind storage system, and combines the advantages of the two to propose an optimal control strategy. Zhang et al. adopt the direct modulation based on the virtual resistor and the reference value of dc-bus voltage, and instantaneous-value model of three-phase half-bridge MMC is derived by introducing differential-mode and common-mode component representation. Chen et al. develop a nonlinear control based on feedback linearization control (FLC) to track the ORS. In the FLC, the WT is linearized firstly, then the rotor speed controller is designed via linear control technique. Feng et al. devise a set of on-site DC test system of transmission line arresters to complete DC reference voltage test. Li et al. design the control mode switching strategy of M-CT-MMC to improve the power transmission capability of the non-fault pole and make it absorb surplus power independently. Yuan et al. study the exponential stability of load frequency control (LFC) for time-delay power system with electric vehicles (EV) aggregator based on Lyapunov theory and linear matrix inequality. Su et al. considers the optimization and H{infty} performance problem for LFC of power systems with time-varying delays. Tang et al. adopt FLC to achieve smooth and fast-tracking performance, and a rule-based strategy (RBS) is applied for power demand allocation.

AUTHOR CONTRIBUTIONS

BY: Structure, Writing-Reviewing and Editing. DS: Writing-Original draft preparation, Investigation. XH: Writing-Reviewing and Editing. XZ: Supervision. SC: Supervision, Investigation. CD: Resources. YR: Writing-Reviewing and Editing, Investigation.

Conflict of Interest: The authors declare that the research was conducted in the absence of any commercial or financial relationships that could be construed as a potential conflict of interest.

Publisher's Note: All claims expressed in this article are solely those of the authors and do not necessarily represent those of their affiliated organizations, or those of the publisher, the editors and the reviewers. Any product that may be evaluated in this article, or claim that may be made by its manufacturer, is not guaranteed or endorsed by the publisher.

Copyright © 2022 Yang, Song, He, Zhang, Choi, Duan and Ren. This is an open-access article distributed under the terms of the Creative Commons Attribution License (CC BY). The use, distribution or reproduction in other forums is permitted, provided the original author(s) and the copyright owner(s) are credited and that the original publication in this journal is cited, in accordance with accepted academic practice. No use, distribution or reproduction is permitted which does not comply with these terms.

frontiers in Energy Research

ORIGINAL RESEARCH
published: 15 April 2021
doi: 10.3389/fenrg.2021.676305

Optimal Placement and Sizing of Distributed Generators Based on Swarm Moth Flame Optimization

*Zhukui Tan[1,2], Ming Zeng[1] and Liming Sun[3]**

[1] School of Economics and Management, North China Electric Power University, Beijing, China, [2] Guizhou Power Grid Co., Ltd., Electric Power Research Institute, Guiyang, China, [3] Guangzhou Shuimutech Co., Ltd., Guangzhou, China

In order to deal with the problem of environmental pollution and energy consumption, developing clean and renewable energy to maintain the sustainable development of society has become an urgent matter for human beings. Therefore, distributed generation (DG) is widely concerned by engineers. However, the output of DG is generally random and intermittent. When it is connected to different locations, different capacities and different types of power grids, the safe and stable operation of the power system will be affected to different degrees. When selecting the optimal DG access scheme, power grid planners must consider the influence of capacity, type and location to ensure a safer, more stable, more reliable and more efficient power grid operation. Therefore, this paper proposes an objective function considering integrated power losses, voltage profile and pollution emission, and swarm moth flame optimization algorithm (SMFO) is used to solve. Finally, based on IEEE-33 bus, the effectiveness of the proposed algorithm is verified.

Keywords: DG, optimal placement and sizing, renewable energy, IEEE 33 bus, SMFO

OPEN ACCESS

Edited by:
Yaxing Ren,
University of Warwick,
United Kingdom

Reviewed by:
Jiawen Li,
South China University of Technology, China
Yixuan Chen,
The University of Hong Kong, Hong Kong
Kai Shi,
University of Warwick, United Kingdom

****Correspondence:***
Liming Sun
89244785@qq.com

Specialty section:
This article was submitted to Smart Grids, a section of the journal Frontiers in Energy Research

Received: *05 March 2021*
Accepted: *22 March 2021*
Published: *15 April 2021*

Citation:
Tan Z, Zeng M and Sun L (2021) Optimal Placement and Sizing of Distributed Generators Based on Swarm Moth Flame Optimization. Front. Energy Res. 9:676305. doi: 10.3389/fenrg.2021.676305

INTRODUCTION

Unreasonable distributed generation (DG) installation will increase the power loss of the distribution network and even lead to system instability (Gandomkar et al., 2005; Lund, 2006; Wang et al., 2014), on the other hand, increase the economic cost of grid-connection (Moradi and Abedini, 2016; Ogunjuyigbe et al., 2016; Meena et al., 2017). According to statistics, more than 80% of power failure accidents are closely related to the distribution network, so it is extremely urgent to choose an appropriate DG access way to the distribution network (Devi and Subramanyam, 2007; Mehleri et al., 2012; Paterakis et al., 2015). Therefore, it is necessary to study the optimal location and sizing of DG.

Nowadays, DG connected to the distribution network is mainly the intermittent power source whose output is related to the natural environment, such as wind power (Kansal et al., 2013; Murty and Kumar, 2015; Liu et al., 2020). The randomness of its output adds greater uncertainty to the load prediction, planning and operation of the power network, and increases the difficulty of the planning and design of the distribution network with DG (El-Zonkoly, 2011; Ameli et al., 2014; Poornazaryan et al., 2016). The problem of location and capacity of distributed power supply access to distribution network is an optimization problem that needs to consider the cooperation of multiple factors (Afzalan et al., 2012; Song et al., 2018, 2020). Thus, it is necessary to comprehensively consider various technical indicators to obtain a practical and feasible solution in

line with the planning area (Mitra et al., 2013; Naik et al., 2013; Iqbal et al., 2017). Literature (Lin and Bie, 2018) constructed a distribution network expansion planning model aiming at economic and environmental benefits. Literature (Kaur et al., 2014) proposes a method considering the load characteristics and regenerated DG probability to improve the voltage stability margin. Literature (Hung et al., 2010) proposes a location selection method based on node pricing that takes profit, network losses reduction and voltage improvement of DG as optimization objectives.

In the research of DG planning, the solution of a large number of planning models is relatively complex, so the study and selection of solving algorithms directly affect the choice of planning schemes (Gayme and Topcu, 2013; Calderaro et al., 2014; El-Fergany, 2015). At present, there are mainly mathematical optimization and meta-heuristic algorithm to solve the objective function (Zhu et al., 2006; Hedayati et al., 2008; Acharya et al., 2016). However, the mathematical optimization has been abandoned by the majority of scholars due to its low computational efficiency and only applicable to small-scale distribution networks, and meta-heuristic algorithm has been developed rapidly (Das et al., 2016; Hamida et al., 2018; He et al., 2020). Literature (Abri et al., 2013) applied genetic algorithm (GA) to optimize this problem for newly added load nodes in the expansion planning of distribution network, and then simulated annealing algorithm was used to optimize individual schemes generated in the process of genetic algorithm, thus reducing the load sizing of DG access to distribution lines and the influence of power flow of distribution network. Literature (Varesi, 2011) proposed an improved particle swarm optimization algorithm based on hybrid simulated annealing method to optimize the location and volume of distributed power supply. However, the convergence speed of the above algorithm is relatively slow, the efficiency is low, and the result is easy to appear in the local optimal situation.

Therefore, an objective function considering power losses, voltage profile and pollution emission is proposed in this paper, and which is solved by swarm moth flame optimization (SMFO). Finally, the method is verified based on IEEE-33 bus, and the results verify the effectiveness of the method.

The remaining of this paper is organized as follows: section "Problem Formulation" develops the objective function. In section "Swarm Moth-Flame Optimizer Moth Flame Optimization," SMFO is described. Comprehensive case studies are undertaken in section "Case Studies." And section "Conclusion" summarizes the main contributions of the paper.

PROBLEM FORMULATION

Objective Function

DG planning is an optimization problem with multiple optimization objectives and multiple constraints. Through the study on the influence of the distribution network connected with DG, this paper takes the losses reduction index, environmental emission reduction index and voltage profile index as the optimization objectives, so as to minimize the power loss of the distribution network.

Power Losses

When DG planning is carried out in the distribution network, the corresponding network losses calculation formula should be selected according to the characteristics of load in the distribution network to be planned to calculate the active power losses of the distribution network. The connection of DG will change the power losses of the distribution network, and the change effect on the power losses is related to the grid-connected location and sizing, so the losses reduction index is established to measure the influence of DG grid-connected on the active power losses. The losses reduction index is expressed as (Home-Ortiz et al., 2019):

$$E_P = \frac{P_{\mathrm{DGloss}}}{P_{\mathrm{Ploss}}} \tag{1}$$

$$P_{\mathrm{ploss}} = \sum_{l=1}^{L} R_l I_l^2 \tag{2}$$

where E_P represents the power losses reduction index, $P_{\mathrm{Ploss}}$and P_{DGloss}represent the active power losses of the distribution network before installing DG and after installing DG, respectively. The larger the losses reduction index E_P is, the greater the role of DG in reducing the line losses of the distribution network after DG planning. R_l is the resistance on the lth line; I_l is the current on the lth line.

Environmental Emission Reduction Index

Since the vast majority of electric energy in the power grid is generated by thermal generators, power generation releases a variety of polluting gases into the atmosphere at the same time. The three gases that are more destructive to the environment are CO_2, NO_x, and SO_2. Because the three gases have great differences in their destructiveness to the environment, NO_x and SO_2 will cause acid rain and do more serious harm to the environment, so they cannot be treated equally. Therefore, the corresponding weight coefficient is introduced into the formula to distinguish their destructiveness. Thus, the environmental protection emission reduction index can be expressed as (Varesi, 2011):

$$E_{\mathrm{E}} = \frac{w_{\mathrm{C}} M_{\mathrm{DGC}} + w_{\mathrm{N}} M_{\mathrm{DGN}} + w_{\mathrm{S}} M_{\mathrm{DGS}}}{w_{\mathrm{C}} M_{\mathrm{PC}} + w_{\mathrm{N}} M_{\mathrm{PN}} + w_{\mathrm{S}} M_{\mathrm{PS}}} \tag{3}$$

where E_{E} is the environmental emission reduction index.w_{C}, w_{N}, and w_{S} represent the weight coefficients of environmental pollution of CO_2, NO_x, and SO_2, which are set as 0.5, 0.25, and 0.25, respectively.M_{DGC}, M_{DGN}, and M_{DGS} represent the quality of reducing CO_2, NO_x, and SO_2 emissions after DG planning, respectively. M_{PC}, M_{PN}, and M_{PS}, respectively, represent the quality of CO_2, NO_x, and SO_2 emitted by the distribution network before installation of DG. The higher the E_{E} is, the greater the role of DG in reducing the emission of polluting gases. In addition, **Table 1** lists the emissions of three types of DG and thermal power generation (Home-Ortiz et al., 2019).

TABLE 1 | Four types of power generation emissions.

Generator	Pollution emissions (lb/MWh)		
	CO_2	SO_2	NO_x
Wind turbine	0	0	0
PV station	0	0	0
Micro turbine	1,596	0.008	0.44
Conventional generator	621	6.465	2.875

Voltage Profile Index

The voltage profile index of each node in the distribution network is an important symbol to measure the power quality of the distribution network. The addition of DG will support the node voltage. The voltage profile index is established to measure the improvement effect of DG on the node voltage profile, and its expression is as follows (Home-Ortiz et al., 2019):

$$E_{\mathrm{V}} = \frac{1}{N-1}\sum_{i=1}^{N-1}\frac{|V_N - V_{Pi}| - |V_N - V_{\mathrm{DG}i}|}{V_N} \tag{4}$$

where, E_{V} is the node voltage profile index. N represents the total number of nodes in the planned distribution; V_{Pi} represents the voltage of the ith node in the distribution network before installing DG; V_N denotes the rated voltage of distribution network; $V_{\mathrm{DG}i}$ represents the voltage at the ith node after DG is incorporated into the distribution network. The greater the voltage profile index E_{V} is, the greater the effect of DG grid-connection on reducing the voltage offset of each node of the distribution network.

Objective Function

$$\min E_{\mathrm{sum}} = \omega_{\mathrm{P}}E_{\mathrm{P}} + \omega_{\mathrm{E}}E_{\mathrm{E}} + \omega_{\mathrm{V}}E_{\mathrm{V}} \tag{5}$$

where $\omega_{\mathrm{P}} = 0.5$ represents the weight coefficient of the losses reduction index, $\omega_{\mathrm{E}} = 0.25$ represents the weight coefficient of the environmental emission reduction index, $\omega_{\mathrm{V}} = 0.25$ represents the weight coefficient of the voltage profile index. Besides, the weight coefficient can be reselected by engineers based on the actual application.

Constraint

Power Balance

$$\begin{cases} P_{\mathrm{G}i} + P_{\mathrm{DG}i} = P_{\mathrm{L}i} + U_i\sum_{j=1}^{N}U_j\left(G_{ij}\cos\theta_{ij} + B_{ij}\sin\theta_{ij}\right) \\ Q_{\mathrm{G}i} + Q_{\mathrm{DG}i} = Q_{\mathrm{L}i} + U_i\sum_{j=1}^{N}U_j\left(G_{ij}\sin\theta_{ij} - B_{ij}\cos\theta_{ij}\right) \end{cases} \tag{6}$$

where $P_{\mathrm{G}i}$ and $Q_{\mathrm{G}i}$ respectively represent the active power output and reactive power output of the power supply at ith node in the distribution network. $P_{\mathrm{DG}i}$ and $Q_{\mathrm{DG}i}$ are, respectively, the active power and reactive power of DG output at ith node. U_i is the voltage of the ith node; G_{ij} and B_{ij} represent the admittance and susceptance between the ith node and the jth node; θ_{ij} is the power angle between ith node and the jth node; $P_{\mathrm{L}i}$ and $Q_{\mathrm{L}i}$, respectively, represent the active power and reactive power required by the load on ith node in the distribution network (Home-Ortiz et al., 2019).

DG Sizing

Due to the limitation of the working principle, structure and production model of the production DG, and the influence of environmental factors on the operation of the production DG, the power dispatching cannot be completely controlled, which will have a great impact on the power flow, relay protection, voltage and waveform of the original power grid. Therefore, the power allowed to access the power grid DG is limited (Home-Ortiz et al., 2019).

$$\begin{cases} P_{i\mathrm{DGmin}} \le P_{i\mathrm{DG}} \le P_{i\mathrm{DGmax}} (i = 1, 2, \ldots, N) \\ 0.7 * P_{i\mathrm{load}} = P_{i\mathrm{DGmax}} \end{cases} \tag{7}$$

where $P_{i\mathrm{DGmin}}$ represents the minimum sizing of the DG connected by the ith node; $P_{i\mathrm{DG}}$ represents the active power sent to the power grid by DG connected to the ith node; $P_{i\mathrm{DGmax}}$ represents the maximum sizing of the DG connected by the ith node. $P_{i\mathrm{load}}$ is the total load on the ith node.

SWARM MOTH-FLAME OPTIMIZER MOTH FLAME OPTIMIZATION

Inspiration

Moths, a close relative of butterflies, belong to the order Lepidoptera of the class Insects. There are many kinds of moths, but most of them are nocturnal and phototropic (Mirjalili, 2015). Therefore, there is a folk saying that "moths burn themselves in the fire," and the inspiration of the optimization algorithm of moths in the fire is also derived from the biological behavior of "moths in the fire."

However, according to biologists, "moth to the fire" is not a suicide behavior, but the moth itself has a navigation mechanism. While moths have compound eyes, they have poor vision. At night, when they cannot see the road clearly, they can only determine their current position and the next direction of flight by evaluating the relative position of themselves and the light source (usually moonlight). This Orientation method is called Transverse Orientation (Yıldız and Yıldız, 2017). However, if artificial light, such as streetlights, is considered, moths are always observed approaching light in a spiral shape due to such a short distance. As shown in **Figure 1**, SMFO has two main features:

A. Each flame is surrounded by multiple moths at the same time for greater utilization, and the flame with higher brightness (i.e., smaller fitness function) will attract more moths;
B. A ring network is constructed between the flames so that moths can be guided to look for brighter flames more effectively, which may lead to broader exploration, that is, there is a higher possibility to avoid local optima.

Mathematical Model

There are two important components in SMFO, namely moth and flame. Both essentially are the solution, the difference is that the moths in the main body of the actual search algorithms of spiral flight and the flame are moths to search the optimal

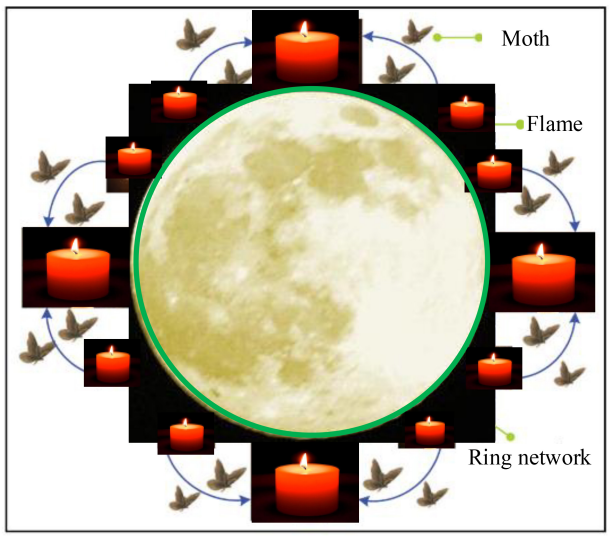


FIGURE 1 | Conceptual model figure of transverse orientation.

position so far, so better to search in moths to a flame position, will mark the fire, and of the surrounding spiral movement. When a moth spirals around a flame, it needs to meet three conditions: the initial position of the flight is the current position of the moth, the terminal position of the flight is the position of the flame, and the spiral flight follows a logarithmic spiral curve.

The SMFO can be regarded as a triplet approximate to the global optimal in the optimization problem, which can be represented by the following formula (Abd El Aziz et al., 2017):

$$MFO = (I, P, T) \tag{8}$$

where I represent a function that randomly generates the position of the moth and its corresponding fitness value, and its description is shown in Equation (9). M represents the set of moth positions and OM represents the set of moth fitness values.

$$I : \emptyset \rightarrow \{M, OM\} \tag{9}$$

P represents the main function that the moth follows when flying in the search space. When the moth flies to a new position, it updates its own position and returns to M, which is described in Equation (10). In Equation (10), the updated position set of moths is represented by $^*M$ to distinguish them (Yıldız and Yıldız, 2017).

$$P : M \rightarrow M^* \tag{10}$$

T is an end judge function that returns a Boolean value. When the return value is true, the algorithm stops running and prints the current global optimal value. When the return value is false, the function continues. Its description is shown in Equation (11):

$$T : M \rightarrow \{\text{true, false}\} \tag{11}$$

Meta-heuristic algorithm is usually initialized by random generation of population, and SMFO is no exception. Suppose M is an M by n matrix, as shown in Equation (12). Where M represents the number of individual moths and N represents the number of variables (dimensions) in the optimization problem (Abd El Aziz et al., 2017).

$$M = \begin{bmatrix} M_{11} & M_{12} & \cdots & M_{1n} \\ M_{21} & M_{22} & \cdots & M_{2n} \\ \vdots & \vdots & \ddots & \vdots \\ M_{m1} & M_{m2} & \cdots & M_{mn} \end{bmatrix} \tag{12}$$

Meanwhile, the array OM stores fitness values corresponding to individual moths, as shown in Equation (13). M is the number of moths.

$$OM = \begin{bmatrix} OM_1 \\ OM_2 \\ \vdots \\ OM_m \end{bmatrix} \tag{13}$$

The SMFO has another important component, the flame. It is also assumed that F is an m^*n matrix for storing the flame, as shown in Equation (14). Where M represents the number of individual moths and N represents the number of variables (dimensions) in the optimization problem.

$$F = \begin{bmatrix} F_{11} & F_{12} & \cdots & F_{1n} \\ F_{21} & F_{22} & \cdots & F_{2n} \\ \vdots & \vdots & \ddots & \vdots \\ F_{m1} & F_{m2} & \cdots & F_{mn} \end{bmatrix} \tag{14}$$

Similarly, an array OF stores the fitness value corresponding to flame F, as shown in Equation (15).

$$OF = \begin{bmatrix} OF_1 \\ OF_2 \\ \vdots \\ OF_m \end{bmatrix} \tag{15}$$

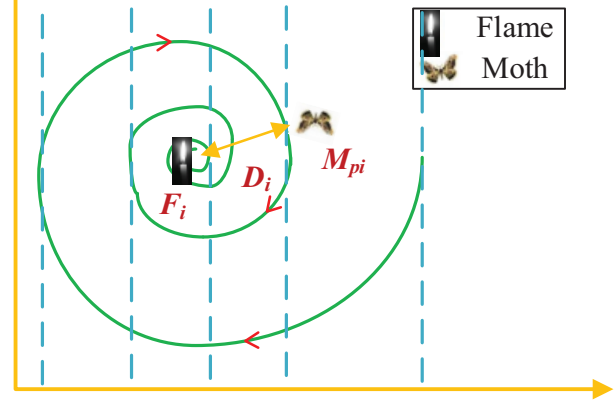


FIGURE 2 | Individual optimization track.

Hence, the brightness of each flame may be calculated based on the normalization of their fitness functions, as follows:

$$BF_i = \begin{cases} \frac{\max(OF)-OF_i}{\max(OF)-\min(OF)}, & \text{if } \max(OF) \neq \min(OF) \\ 1 \text{ otherwise} \end{cases} \quad (16)$$

where BF_i denotes the brightness of the ith flame, OF_i represents the fitness function of the ith flame.

In SMFO, a brighter flame (which has a smaller fitness function) will attract more moths than those of its adjacent flames via the ring network. The comparison of each flame's brightness and movement of moths to a brighter flame usually leads to a continuous variation of population size of each moth swarm to achieve a wider exploration. However, the participation of too many flames for moth swarm attraction may result in a local optimum. Based on the above, the brightness of a flame is compared with that of only two adjacent flames in SMFO, and thus a proper trade-off between a wider exploration and deeper exploitation may be obtained through construction of a ring network among all flames. For the pth individual of the ith moth swarm, it will immigrate to its adjacent moth swarm, i.e., the (i−1) moth swarm or the (i+1) moth swarm, according to their brightness.

A moth will gradually approach to the corresponding flame with a logarithmic spiral, which may be calculated as (Abd El Aziz et al., 2017):

In the process of SMFO search, moths individual M_i is a phototropism, will lock the flame F_j the flight movement of conforms to logarithmic spiral function, began to the location of the screw flight behavior is moths the current position, end position is the position of the fire, at the same time in the process of flight moths can't fly out of the specified area (the search space),

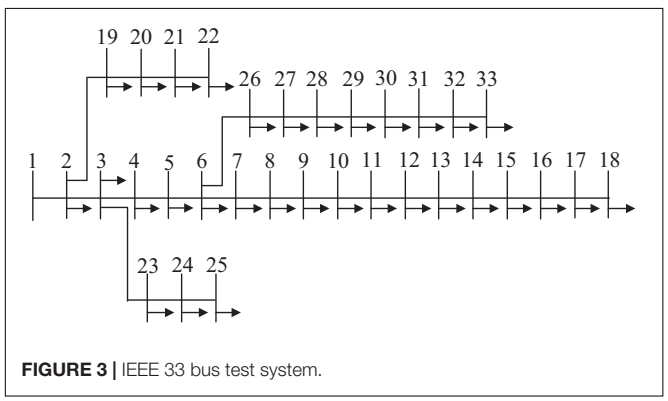


FIGURE 3 | IEEE 33 bus test system.

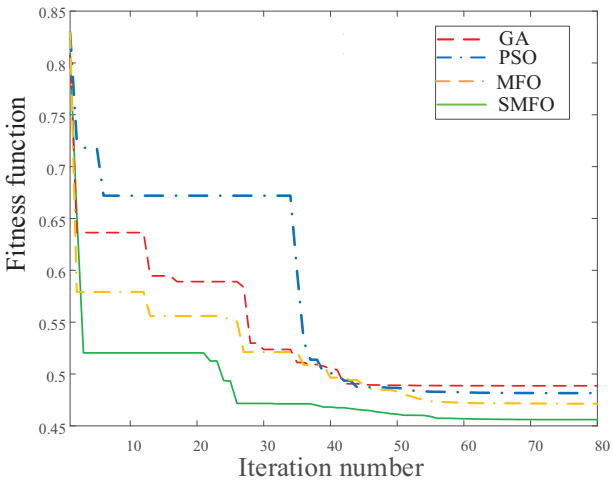


FIGURE 4 | Convergence curves.

TABLE 2 | Optimization results of two algorithms.

Approach	Generator	Bus location	DG sizing (kVA)	Losses function	Voltage function	Emission function	Fitness function
GA	The first PV	2	100	0.5037	0.3414	0.6424	0.4978
	The second PV	21	100				
	The first wind turbine	3	21.9006				
	The second wind turbine	23	58.5805				
	Micro turbine	11	18				
PSO	The first PV	3	99.3621	0.4864	0.3468	0.6123	0.4829
	The second PV	19	32.1545				
	The first wind turbine	21	49.5123				
	The second wind turbine	9	17.5684				
Moth flame optimization (MFO)	The first PV	18	99.6485	0.4759	0.3153	0.6425	0.4774
	The second PV	14	29.5142				
	The first wind turbine	23	69.3621				
	The second wind turbine	13	16.3254				
SMFO	Micro turbine	19	97.3607	0.4537	0.2931	'0.6322	0.4581
	The second PV station	16	31.1952				
	The first wind turbine	12	37.6497				
	The second wind turbine	20	23.3027				
	Micro turbine	11	18.3328				

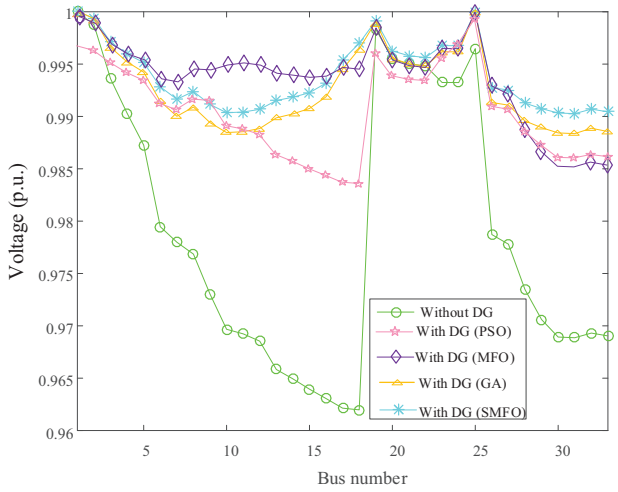


FIGURE 5 | Voltage profile improvement of the IEEE 33-bus.

description of the process is using a mathematical formula (Yıldız and Yıldız, 2017):

$$M_{pi}^{\text{new}} = D_{pi} \cdot e^{br} \cdot \cos(2\pi r) + F_i, p = 1, 2, \ldots, n_i \quad (17)$$

$$D_{pi} = \left|F_i - M_{pi}\right| \quad (18)$$

where M_i is the ith a moth individual, F_j is the jth flame. D_{pi} is the distance between the pth moth and the ith flame in the ith moth swarm. b is the spiral shape constant determining the shape of the logarithmic spiral, and distance coefficient r is a random number uniformly distributed in $[-1, 1]$. In addition, individual optimization track is shown in **Figure 2**.

CASE STUDIES

In this paper, IEEE-33 bus is selected to verify the effectiveness of the algorithm, and the topology structure of the system is shown in **Figure 3**. The system consists of 32 branches. In addition, the system voltage U_N = 12.66 kV, the base capacity S_b = 10 MW, the active load P_Σ = 715 kW, the reactive load Q_Σ = 450 kVar. Proposed project: three types of DG are connected in IEEE-33 bus, that is photovoltaic (PV) station, wind turbine and micro turbine. In addition, GA is used in this paper for comparison. In order to make a fair comparison, the population size of the two algorithms is set as 50 and the maximum number of iterations is 80. And the proposed method was coded in MATLAB 2017b.

Figure 4 shows the convergence curves of the four algorithms. It can be seen that SMFO has an excellent search mechanism and can converge to the minimum value with fewer iterations to avoid falling into the local optimum. **Table 2** for both algorithms after 100 iterations run results, as you can see, after installing DG, can reduce the power losses of system to some extent, the obtained high economic benefits, among them, SMFO to obtain the total power consumption of the prior to the introduction of DG decreased by 58.63%, and obtain the total power consumption of the GA was down 36.63% from before the installation of DG, thus, SMFO has strong search result, better quality can be acquired in less number of iterations of the solution. In addition, **Figure 5** shows the voltage profile curves of the two algorithms with and without DG installation, which effectively proves that DG has a significant optimization effect on improving the voltage profile of the distribution network, because DG is always installed near the load.

CONCLUSION

In this paper, SMFO is used to optimize the location and sizing of DG, and its contributions are as follows:

1. The objective function with three indexes of distribution network losses reduction index, voltage profile index and environmental emission reduction index is established to optimize the distribution network comprehensively;
2. Through IEEE-33 bus test, it is effectively verified that SMFO has a strong global search effect and convergence ability, and can avoid falling into local optimum under complex objective function;
3. After installing three types of DG, PV station, wind turbine and micro turbine, the connection of micro turbine can stabilize the instability of PV station and wind turbine. The results show that the power losses of the distribution network optimized by SMFO decreases by 50.37% and GA decreases by 45.37%, which effectively verifies the effectiveness of the algorithm. Besides, voltage profile is significantly improved.

In the future, a more advanced multi-objective decision making method will be used to solve this problem.

DATA AVAILABILITY STATEMENT

The original contributions presented in the study are included in the article/supplementary material, further inquiries can be directed to the corresponding author/s.

AUTHOR CONTRIBUTIONS

ZT: conceptualization, data curation, methodology, and writing—original draft. MZ: formal analysis, visualization, and resources. LS: writing—review and editing.

FUNDING

The authors gratefully acknowledge the project supported by Major Program of National Social Science Fund of China (19ZDA081).

REFERENCES

Abd El Aziz, M., Ewees, A. A., and Hassanien, A. E. (2017). Whale optimization algorithm and moth-flame optimization for multilevel thresholding image segmentation. *Expert Syst. Appl.* 83, 242–256. doi: 10.1016/j.eswa.2017.04.023

Abri, R. S. A., El-Saadany, E. F., and Atwa, Y. M. (2013). Optimal placement and sizing method to improve the voltage stability margin in a distribution system using distributed generation. *IEEE Trans. Power Syst.* 28, 326–334.

Acharya, N., Mahat, P., and Mithulananthan, N. (2016). An analytical approach for DG allocation in primary distribution network. *Int. J. Electr. Power Energy Syst.* 28, 669–678. doi: 10.1016/j.ijepes.2006.02.013

Afzalan, E., Taghikhani, M. A., and Sedighizadeh, M. (2012). Optimal placement and sizing of DG in radial distribution networks using SFLA. *Int. J. Energy Eng.* 2, 73–77. doi: 10.5923/j.ijee.20120203.03

Ameli, A., Bahrami, S., Khazaeli, F., and Haghifam, M. R. (2014). A multiobjective particle swarm optimization for sizing and placement of dgs from dg owner's and distribution company's viewpoints. *IEEE Trans. Power Deliv.* 29, 1831–1840. doi: 10.1109/tpwrd.2014.2300845

Calderaro, V., Conio, G., Galdi, V., Massa, G., and Piccolo, A. (2014). Optimal decentralized voltage control for distribution systems with inverter-based distributed generators. *IEEE Trans. Power Syst.* 29, 230–241. doi: 10.1109/tpwrs.2013.2280276

Das, B., Mukherjee, V., and Das, D. (2016). DG placement in radial distribution network by symbiotic organisms search algorithm for real power loss minimization. *Appl. Soft Comput.* 49, 920–936. doi: 10.1016/j.asoc.2016.09.015

Devi, A. L., and Subramanyam, B. (2007). Optimal DG unit placement for loss reduction in radial distribution system-a case study. *ARPN J. Eng. Appl. Sci.* 2, 57–61.

El-Fergany, A. (2015). Study impact of various load models on DG placement and sizing using backtracking search algorithm. *Appl. Soft Comput.* 30, 803–811. doi: 10.1016/j.asoc.2015.02.028

El-Zonkoly, A. M. (2011). Optimal placement of multi-distributed generation units including different load models using particle swarm optimisation. *IET Gener. Transm. Distrib.* 5, 760–771. doi: 10.1049/iet-gtd.2010.0676

Gandomkar, M., Vakilian, M., and Ehsan, M. J. E. P. C. (2005). A genetic–based tabu search algorithm for optimal DG allocation in distribution networks. *Electr. Power Compon. Syst.* 33, 1351–1362. doi: 10.1080/15325000590964254

Gayme, D., and Topcu, U. (2013). Optimal power flow with large-scale storage integration. *IEEE Trans. Power Syst.* 28, 709–717.

Hamida, I. B., Salah, S. B., Msahli, F., and Mimouni, M. F. (2018). Optimal network reconfiguration and renewable DG integration considering time sequence variation in load and DGs. *Renew. Energy.* 121, 66–80. doi: 10.1016/j.renene.2017.12.106

He, X., Chu, L., Qiu, R. C., Ai, Q., Ling, Z., and Zhang, J. (2020). Invisible units detection and estimation based on random matrix theory. *IEEE Trans. Power Syst.* 35, 1846–1855. doi: 10.1109/tpwrs.2019.2935739

Hedayati, H., Nabaviniaki, S. A., and Akbarimajd, A. A. (2008). Method for Placement of DG units in distribution networks. *IEEE Trans. Power Deliv.* 23, 1620–1628. doi: 10.1109/tpwrd.2007.916106

Home-Ortiz, J. M., Pourakbari-Kasmaei, M., Lehtonen, M., and Mantovani, J. R. S. (2019). Optimal location-allocation of storage devices and renewable-based DG in distribution systems. *Electr. Power Syst. Res.* 172, 11–21.

Hung, D. Q., Mithulananthan, N., and Bansal, R. C. (2010). Analytical expressions for DG allocation in primary distribution networks. *IEEE Trans. Energy Convers.* 25, 814–820. doi: 10.1109/tec.2010.2044414

Iqbal, F., Khan, M. T., and Siddiqui, A. S. (2017). Optimal placement of DG and DSTATCOM for loss reduction and voltage profile improvement. *Alex. Eng. J.* 57, 755–765. doi: 10.1016/j.aej.2017.03.002

Kansal, S., Kumar, V., and Tyagi, B. (2013). Optimal placement of different type of DG sources in distribution networks. *Int. J. Electr. Power Energy Syst.* 53, 752–760. doi: 10.1016/j.ijepes.2013.05.040

Kaur, S., Kumbhar, G., and Sharma, J. (2014). A MINLP technique for optimal placement of multiple DG units in distribution systems. *Int. J. Electr. Power Energy Syst.* 63, 609–617. doi: 10.1016/j.ijepes.2014.06.023

Lin, Y., and Bie, Z. (2018). Tri-level optimal hardening plan for a resilient distribution system considering reconfiguration and DG islanding. *Appl. Energy* 210, 1266–1279. doi: 10.1016/j.apenergy.2017.06.059

Liu, J., Yao, W., Wen, J. Y., Fang, J. K., Jiang, L., He, H. B., et al. (2020). Impact of power grid strength and PLL parameters on stability of grid-connected DFIG wind farm. *IEEE Trans. Sustain. Energy* 11, 545–557. doi: 10.1109/tste.2019.2897596

Lund, H. (2006). Large-scale integration of optimal combinations of PV, wind and wave power into the electricity supply. *Renew. Energy* 31, 503–515. doi: 10.1016/j.renene.2005.04.008

Meena, N. K., Swarnkar, A., Gupta, N., and Niazi, K. R. (2017). Multi-objective Taguchi approach for optimal DG integration in distribution systems. *IET Gener. Transm. Distrib.* 11, 2418–2428. doi: 10.1049/iet-gtd.2016.2126

Mehleri, E. D., Sarimveis, H., Markatos, N. C., and Papageorgiou, L. G. (2012). A mathematical programming approach for optimal design of distributed energy systems at the neighbourhood level. *Energy* 44, 96–104. doi: 10.1016/j.energy.2012.02.009

Mirjalili, S. (2015). Moth-flame optimization algorithm: a novel nature-inspired heuristic paradigm. *Knowl. Based Syst.* 89, 228–249. doi: 10.1016/j.knosys.2015.07.006

Mitra, S., Sun, L., and Grossmann, I. E. (2013). Optimal scheduling of industrial combined heat and power plants under time-sensitive electricity prices. *Energy* 54, 194–211. doi: 10.1016/j.energy.2013.02.030

Moradi, M. H., and Abedini, M. (2016). A novel method for optimal DG units capacity and location in microgrids. *Int. J. Electr. Power Energy Syst.* 75, 236–244. doi: 10.1016/j.ijepes.2015.09.013

Murty, V. V., and Kumar, A. (2015). Optimal placement of DG in radial distribution systems based on new voltage stability index under load growth. *Int. J. Electr. Power Energy Syst.* 69, 246–256. doi: 10.1016/j.ijepes.2014.12.080

Naik, S. G., Khatod, D. K., and Sharma, M. P. (2013). Optimal allocation of combined DG and capacitor for real power loss minimization in distribution networks. *Int. J. Electr. Power Energy Syst.* 53, 967–973. doi: 10.1016/j.ijepes.2013.06.008

Ogunjuyigbe, A. S. O., Ayodele, T. R., and Akinola, O. A. (2016). Optimal allocation and sizing of PV/wind/split-diesel/battery hybrid energy system for minimizing life cycle cost, carbon emission and dump energy of remote residential building. *Appl. Energy* 171, 153–171. doi: 10.1016/j.apenergy.2016.03.051

Paterakis, N. G., Erdinc, O., Bakirtzis, A. G., and Catalao, J. P. S. (2015). Optimal household appliances scheduling under day-ahead pricing and load-shaping demand response strategies. *IEEE Trans. Industr. Inform.* 11, 1509–1519. doi: 10.1109/tii.2015.2438534

Poornazaryan, B., Karimyan, P., Gharehpetian, G. B., and Abedi, M. (2016). Optimal allocation and sizing of DG units considering voltage stability, losses and load variations. *Int. J. Electr. Power Energy Syst.* 79, 42–52. doi: 10.1016/j.ijepes.2015.12.034

Song, D. R., Fan, X. Y., Yang, J., Liu, A. F., Chen, S. F., and Joo, H. Y. (2018). Power extraction efficiency optimization of horizontal-axis wind turbines through optimizing control parameters of yaw control systems using an intelligent method. *Appl. Energy* 224, 267–279. doi: 10.1016/j.apenergy.2018.04.114

Song, D. R., Zheng, S. Y., Yang, S., Yang, J., Dong, M., Su, M., et al. (2020). Annual energy production estimation for variable-speed wind turbine at high-altitude site. *J. Mod. Power Syst. Clean Energy* doi: 10.35833/MPCE.2019.000240

Varesi, K. (2011). Optimal allocation of dg units for power loss reduction and voltage profile improvement of distribution networks using PSO algorithm. *World Acad. Sci. Eng. Technol.* 60, 1938–1942.

Wang, Z., Chen, B., Wang, J., Kim, J., and Begovic, M. M. (2014). Robust optimization based optimal DG placement in microgrids. *IEEE Trans. Smart Grid* 5, 2173–2182. doi: 10.1109/tsg.2014.2321748

Yıldız, B. S., and Yıldız, A. R. (2017). Moth-flame optimization algorithm to determine optimal machining parameters in manufacturing processes. *Mater. Test.* 59, 425–429. doi: 10.3139/120.111024

Zhu, D., Broadwater, R. P., Tam, K.-S., Seguin, R., and Asgeirsson, H. (2006). Impact of DG placement on reliability and efficiency with time-varying loads. *IEEE Trans. Power Syst.* 21, 419–427. doi: 10.1109/tpwrs.2005.860943

Conflict of Interest: LS was employed by the company Guangzhou Shuimutech Co. ZT was employed by the Guizhou Power Grid Co., Ltd.

The remaining author declares that the research was conducted in the absence of any commercial or financial relationships that could be construed as a potential conflict of interest.

Copyright © 2021 Tan, Zeng and Sun. This is an open-access article distributed under the terms of the Creative Commons Attribution License (CC BY). The use, distribution or reproduction in other forums is permitted, provided the original author(s) and the copyright owner(s) are credited and that the original publication in this journal is cited, in accordance with accepted academic practice. No use, distribution or reproduction is permitted which does not comply with these terms.

NOMENCLATURE

E_P	power losses reduction index
P_{Ploss}	active power losses before installing DG
P_{DGloss}	active power losses after installing DG
R_l	resistance on the *l*th line
I_l	current on the *l*th line
E_{E}	environmental emission reduction index
E_{V}	voltage profile index
V_{Pi}	voltage of the *i*th node before installing DG
V_N	rated voltage
P_{Gi}	active power output at *i*th bus
Q_{Gi}	reactive power output at *i*th bus
$P_{i\text{DGmin}}$	minimum sizing of DG
$P_{i\text{DG}}$	active power sent to the power grid by DG connected to the *i*th bus
BF_i	brightness of the *i*th flame
$P_{i\text{DGmax}}$	maximum sizing of DG
OF_i	fitness function of the *i*th flame
M_i	the *i*th a moth individual
F_j	the *j*th flame.

frontiers in Energy Research

ORIGINAL RESEARCH
published: 28 April 2021
doi: 10.3389/fenrg.2021.675925

A Powerful Bio-Inspired Optimization Algorithm Based PV Cells Diode Models Parameter Estimation

*Liming Sun[1], Jingbo Wang[2] and Lan Tang[2]**

[1] Guangzhou Shuimuqinghua Technology Co., Ltd., Guangzhou, China, [2] Faculty of Electric Power Engineering, Kunming University of Science and Technology, Kunming, China

Accurate and reliable photovoltaic (PV) cell parameter identification is critical to simulation analysis, maximum output power harvest, and optimal control of PV systems. However, inherent high-nonlinear and multi-modal characteristics usually result in thorny obstacles to hinder conventional optimization methods to obtain a fast and satisfactory performance. In this study, a novel bio-inspired grouped beetle antennae search (GBAS) algorithm is devised to effectively identify unknown parameters of three different PV models, i.e., single diode model (SDM), double diode model (DDM), and triple diode model (TDM). Compared against beetle antennae search (BAS) algorithm, optimization efficiency of GBAS algorithm is markedly enhanced based on a cooperative searching group that consists of multiple individuals rather than a single beetle. Besides, a dynamic balance mechanism between local exploitation and global exploration is designed to increase the probability for a higher quality optimum. Comprehensive case studies demonstrate that GBAS algorithm can outperform other advanced meta-heuristic algorithms in both optimization precision and stability for estimating PV cell parameters, e.g., standard deviation (SD) of root mean square error (RMSE) obtained by GBAS algorithm is 64.34% smaller than the best value obtained by other algorithms in SDM, 61.86% smaller than that in DDM.

Keywords: parameter estimation, PV cell, grouped beetle antennae search, optimization strategy, metaheuristic algorithm

OPEN ACCESS

Edited by:
Xing He,
Shanghai Jiao Tong University, China

Reviewed by:
Xin Shi,
North China Electric Power University, China
Wentao Huang,
Shanghai Jiao Tong University, China

****Correspondence:***
Lan Tang
205545554@qq.com

Specialty section:
This article was submitted to Smart Grids, a section of the journal Frontiers in Energy Research

Received: *04 March 2021*
Accepted: *22 March 2021*
Published: *28 April 2021*

Citation:
Sun L, Wang J and Tang L (2021) A Powerful Bio-Inspired Optimization Algorithm Based PV Cells Diode Models Parameter Estimation. Front. Energy Res. 9:675925. doi: 10.3389/fenrg.2021.675925

INTRODUCTION

In the past few decades, excessive utilization of natural resources causes rapid fossil fuels depletion (Sun et al., 2020) and serious environmental degradation (Song et al., 2018), which inevitably accelerates ecological destruction and global energy crisis (Yang et al., 2018b). Hence, energy revolution and transformation have become essential and imperative for social and economic development (Peng et al., 2020), which is also in line with global sustainable development strategy (Song et al., 2020). Obviously, exploitation and utilization of new energy resources and renewable energy (Yang et al., 2018a), such as solar (Zhang et al., 2019) and wind (Li et al., 2019), are extremely critical which has aroused widespread attentions worldwide (Zhang et al., 2020). Particularly, solar energy is deemed as one of the most effective alternatives (Yang et al., 2016; He et al., 2017).

Photovoltaic (PV) system is widely used for solar energy applications which own elegant merits, e.g., inexhaustible in supply, wide distribution, and pollution-free. Particularly, measured

current-voltage (*I-V*) data based precise PV modeling is extremely critical to dynamic behavior analysis of PV system. Thus far, various PV models have been devised, among which two types of equivalent circuit models are most widely applied (Chin et al., 2015), i.e., single diode model (SDM) (Humada et al., 2016) and double diode model (DDM) (Abbassi et al., 2018). Meanwhile, other more complicated models, e.g., triple diode model (TDM) (Khanna et al., 2015) is barely investigated in recent reported literatures due to their huge computation burden resulted from a larger number of unknown parameters. However, more complicated physical behavior of PV systems is more likely to be more efficiently studied based on these models. Hence, three types of PV models, i.e., SDM, DDM, and TDM are all investigated in this study for a comprehensive evaluation of PV cell parameter identification.

Note that a reliable PV cell modeling mainly relies on an accurate identification of relevant model electrical parameters. In general, PV cell parameter identification is essential for performance analysis, optimal design (Youssef et al., 2017), real-time control, and maximum power point tracking (MPPT) of PV systems (Chaibi et al., 2019; Yang et al., 2019b). Nevertheless, the following two shortcomings make parameter identification difficult to achieve stable and satisfactory results in practical applications: (i) the parameters provided by manufacturer are unavailable and only tested under standard test condition (STC), while the practical operation condition is far from STC which might change the output characteristics of PV cells and (ii) these parameters are time-varying due to degradation and faults of PV cells (Gomes et al., 2017).

Until now, numerous methods have been developed to solve such high-nonlinear and multi-modal obstacle, which are categorized into three groups, i.e., analytical methods (Chan and Phang, 1987; Saleem and Karmalkar, 2009), deterministic techniques, and meta-heuristic algorithms. In general, analytical methods are based on some key points on *I-V* curves provided by manufacturer and a series of mathematical equations, which are characterized by simplicity and fast computation but relatively low accuracy (Wolf and Benda, 2013; Batzelis and Papathanassiou, 2016). Meanwhile, deterministic approaches and meta-heuristic algorithms can handle PV parameter estimation with some reference points of given *I-V* curves. However, deterministic techniques, such as least squares (Newton-based method) (Li et al., 2017) and iterative curve fitting (Villalva et al., 2009) are extremely strict with model characteristics. Moreover, they are highly sensitive to initial operation conditions, while inherent high-nonlinearity and multi-modality of PV systems always leads to premature convergence. Nevertheless, meta-heuristic algorithms can effectively avoid the shortcomings of the above two methods since they normally possess advantages of easy implementation (Zhang et al., 2021), high efficiency (Mahdavi et al., 2015), insensitivity to initial condition and gradient information (Roeva and Fidanova, 2018), etc. Hence, they are deemed as the most promising and efficient tools for PV cell parameter extraction.

Thus far, they have been widely adopted in PV cell parameter identification in recent years (Yang et al., 2020). For instance, genetic algorithm (GA) (Jervase et al., 2001), differential evolution (DE) (Ishaque and Salam, 2011), particle swarm optimization (PSO) (Ye et al., 2009), artificial bee colony (ABC) (Oliva et al., 2014; Yang et al., 2019a), bird mating optimizer (BMO) (Askarzadeh and Rezazadeh, 2013), whale optimization algorithm (WOA) (Elazab et al., 2018; Dasu et al., 2019), backtracking search algorithm (BSA) (Yu et al., 2018), month flame optimizer (MFO) (Allam et al., 2016), gray wolf optimization (GWO) (Yang et al., 2017; Nayak et al., 2019), biogeography-based optimization (BBO) (Niu et al., 2014), flower pollination algorithm (FPA) (Alam et al., 2015; Shang et al., 2018), harmony search (HS) (Askarzadeh and Rezazadeh, 2012), multiswarm spiral leader particle swarm optimization (MSLPSO) algorithm (Nunes et al., 2020), slime mold algorithm (SMA) (Mostafa et al., 2020) and so forth (Muangkote et al., 2019), along with their numerous hybrid/variants.

Inspiringly, beetle antennae search (BAS) algorithm is a recently developed biology-based meta-heuristic algorithm (Jiang and Li, 2018), which basically replicates the searching mechanism of long-horn beetles. Besides, the basic functioning mechanism of beetle's antennae and its random walking behavior are all considered in optimization principles of BAS. Note that such strategy owns the superiorities of simple structure and easy implementation, while its convergence and local minimum avoidance have been verified via two typical test functions. However, the effectiveness and accuracy of original BAS algorithm are still worthy to be further improved.

Hence, a powerful grouped BAS (GBAS) algorithm (Hao et al., 2020) is employed in this paper for PV cell parameter identification, whose contributions/novelties can be summarized as follows:

- GBAS algorithm can improve the optimization efficiency with a cooperative group of multiple beetles instead of a single beetle, while it also can acquire a high-quality optimum by a dynamic balance between local exploitation and global exploration;
- Practical performance of GBAS is comprehensively validated by SDM, DDM, and TDM, respectively;
- Comprehensive case studies verify that GBAS algorithm outperforms other meta-heuristic algorithms in both solution optimization accuracy and stability.

The rest of this paper is organized as follows: The problem formulation of PV cell models and applied objective function are illustrated in section "PV Cell Modeling and Problem Formulation." The main optimization principle of the proposed GBAS algorithm is elaborated in section "Grouped Beetle Antennae Search (GBAS) Algorithm." Case studies results and detailed statistical analysis on various PV cell models are shown and analyzed in section "Case Studies." Lastly, conclusions are given in section "Conclusion."

PV CELL MODELING AND PROBLEM FORMULATION

The first step to study the characteristics of PV cells, or to develop a more accurate prediction and optimization of PV systems

operation, is to establish an appropriate PV cell model. Then, PV cell parameters can be reliably extracted to more accurately depict the output *I-V* and power-voltage (*P-V*) characteristics for better analysis of PV cells. The most widely applied equivalent circuit models are SDM, DDM, and TDM.

Mathematical Modeling

In general, the main these structures of the three models are quite similar, thus a comprehensive summary is provided in **Table 1** for more detailed demonstration.

As demonstrated in **Table 1**, I_L and V_L represent PV cell output current and output voltage, respectively; I_{sh} means shunt resistor current R_{sh}; while thermal voltage V_T is defined as

$$V_T = \frac{KT}{q} \tag{1}$$

where T represents cell temperature; $K = 1.38 \times 10^{-23}$ J/K denotes Boltzmann constant; and $q = 1.6 \times 10^{-19}$C means electron charge, respectively.

Other variables can be referred in Nomenclature.

Objective Function

The main purpose of parameter identification is to find a group of proper parameters that can effectively minimize errors between experimental and simulated data, which can be quantitatively evaluated through objective functions. Here, RMSE is chosen as the objective function, as follows

$$\text{RMSE}(x) = \sqrt{\frac{1}{N}\sum_{k=1}^{N}(f(V_L, I_L, x))^2} \tag{2}$$

TABLE 1 | Summary on three photovoltaic (PV) cell models.

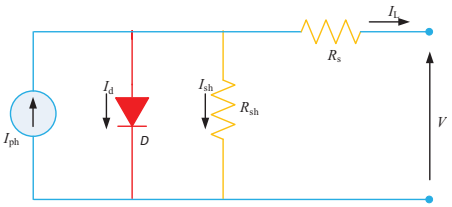
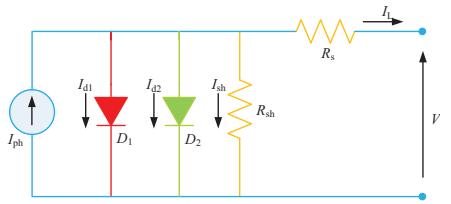
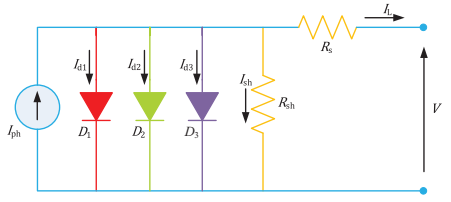
Diode model	Model drawing	Output *I-V* equation	Extracted parameters	Features
SDM (Zagrouba et al., 2010)		$I_L = I_{ph} - I_0\left[\exp\left(\frac{V_L + I_L R_s}{aV_T}\right) - 1\right] - \frac{V_L + I_L R_s}{R_{sh}}$	I_{ph}, I_0, R_s, R_{sh}, and a	(a) Simplest control structure and easy implementation (Chen and Yu, 2019); (b) Limited accuracy compared to DDM and TDM (Barukčić et al., 2015).
DDM (Ishaque et al., 2011)		$I_L = I_{ph} - I_{01}\left[\exp\left(\frac{q(V_L + I_L R_s)}{a_1 V_T}\right) - 1\right] - I_{02}\left[\exp\left(\frac{q(V_L + I_L R_s)}{a_2 V_T}\right) - 1\right] - \frac{V_L + I_L R_s}{R_{sh}}$	I_{ph}, I_{01}, I_{02}, R_s, R_{sh}, a_1, and a_2	(a) High accuracy under STC (Easwarakhanthan et al., 1986); (b) Simple implementation (Ram et al., 2018); (c) Medium complexity (Ram et al., 2018).
TDM (Khanna et al., 2015; Abbassi et al., 2018)		$I_L = I_{ph} - I_{01}\left[\exp\left(\frac{q(V_L + I_L R_s)}{a_1 V_T}\right) - 1\right] - I_{02}\left[\exp\left(\frac{q(V_L + I_L R_s)}{a_2 V_T}\right) - 1\right] - I_{03}\left[\exp\left(\frac{q(V_L + I_L R_s)}{a_3 V_T}\right) - 1\right] - \frac{V_L + I_L R_s}{R_{sh}}$	I_{ph}, I_{01}, I_{02}, I_{03}, R_s, R_{sh}, a_1, a_2, and a_3	(a) Highest accuracy and efficiency to investigate complicated PV systems behaviors (Khanna et al., 2015); (b) Slightly high complexity and implementation cost (Kamali et al., 2016).

TABLE 2 | Error functions of three different models.

Model	Error function	Solution vector
SDM	$f_{SDM}(V_L, I_L, x) = I_{ph} - I_0\left[\exp\left(\frac{V_L + I_L R_s}{aV_t}\right) - 1\right] - \frac{V_L + I_L R_s}{R_{sh}} - I_L$	$x = \{I_{ph}, I_0, R_s, \}R_{sh}, a$
DDM	$f_{DDM}(V_L, I_L, x) = I_{ph} - I_{01}\left[\exp\left(\frac{q(V_L + I_L R_s)}{a_1 V_t}\right) - 1\right] - I_{02}\left[\exp\left(\frac{q(V_L + I_L R_s)}{a_2 V_t}\right) - 1\right] - \frac{V_L + I_L R_s}{R_{sh}} - I_L$	$x = \{I_{ph}, I_{01}, I_{02}, R_s, R_{sh}, a_1, a_2\}$
TDM	$f_{TDM}(V_L, I_L, x) = I_{ph} - I_{01}\left[\exp\left(\frac{q(V_L + I_L R_s)}{a_1 V_t}\right) - 1\right] - I_{02}\left[\exp\left(\frac{q(V_L + I_L R_s)}{a_2 V_t}\right) - 1\right] - I_{03}\left[\exp\left(\frac{q(V_L + I_L R_s)}{a_3 V_t}\right) - 1\right] - \frac{V_L + I_L R_s}{R_{sh}} - I_L$	$x = \{I_{ph}, I_{01}, I_{02}, I_{03}, R_s, R_{sh}, a_1, a_2, a_3\}$

TABLE 3 | Parameters of grouped beetle antennae search (GBAS) for parameter identification of photovoltaic (PV) cell.

Parameters	Range	Value
C	$C > 0$	1.5
ω_{max}	$0.5 < \omega_{max} < 1$	0.95
ω_{min}	$0 < \omega_{min} < 0.5$	0.05
d_{max}	$d_{max} > 0$	5
δ_{max}	$0 < \delta_{max} < 1$	0.9
t_{max}	$t_{max} > 0$	5,000
n	$n > 0$	30

where x represents solution vector which contains the parameters need to be identified and N denotes number of experimental data, respectively.

For a more explicit and comprehensive illustration, the error functions $f(V_L, I_L, x)$ for different PV models are summarized in **Table 1**.

Based on **Table 2**, for the sake of minimizing the error between experimental data and simulated data, RMSE (x) needs to be minimized by optimizing solution vector x. Note that objective function value is inversely proportional to the solution quality.

GROUPED BEETLE ANTENNAE SEARCH (GBAS) ALGORITHM

This section presents the main inspiration, and the optimization principle of the proposed GBAS algorithm.

Optimization Mechanism

GBAS algorithm is mainly inspired by the special and efficient food searching mechanism of long-horn beetles that depends on their antennae to sense an odor from food sources. Compared with only one single searching agent based BAS algorithm, GBAS utilizes a searching group that consists many individuals to enlarge the searching extent and ensure more potential high quality solutions can be detected. The whole searching can be divided into two stages, i.e., searching and detecting, while the weights during the two process are adaptively adjusted to avoid local optimums. Thus, a proper trade-off between local exploitation and global exploration can be achieved, upon which the optimization efficiency and accuracy can be greatly achieved, while more details of this algorithm can be referred to literature (Hao et al., 2020) for interested readers.

Design of GBAS for PV Cell Parameter Identification

The detailed optimization structure of GBAS algorithm for PV cell parameter identification is illustrated in this section.

Optimization Variables

As shown in **Table 2**, optimization variables are different in various equivalent circuit models for PV cell. To achieve an efficient parameter identification of PV cell, optimization variables are limited within their lower and upper bounds, as follows:

$$x_j^{min} \le x_j \le x_j^{max},\ j = 1, 2, \ldots, J \tag{3}$$

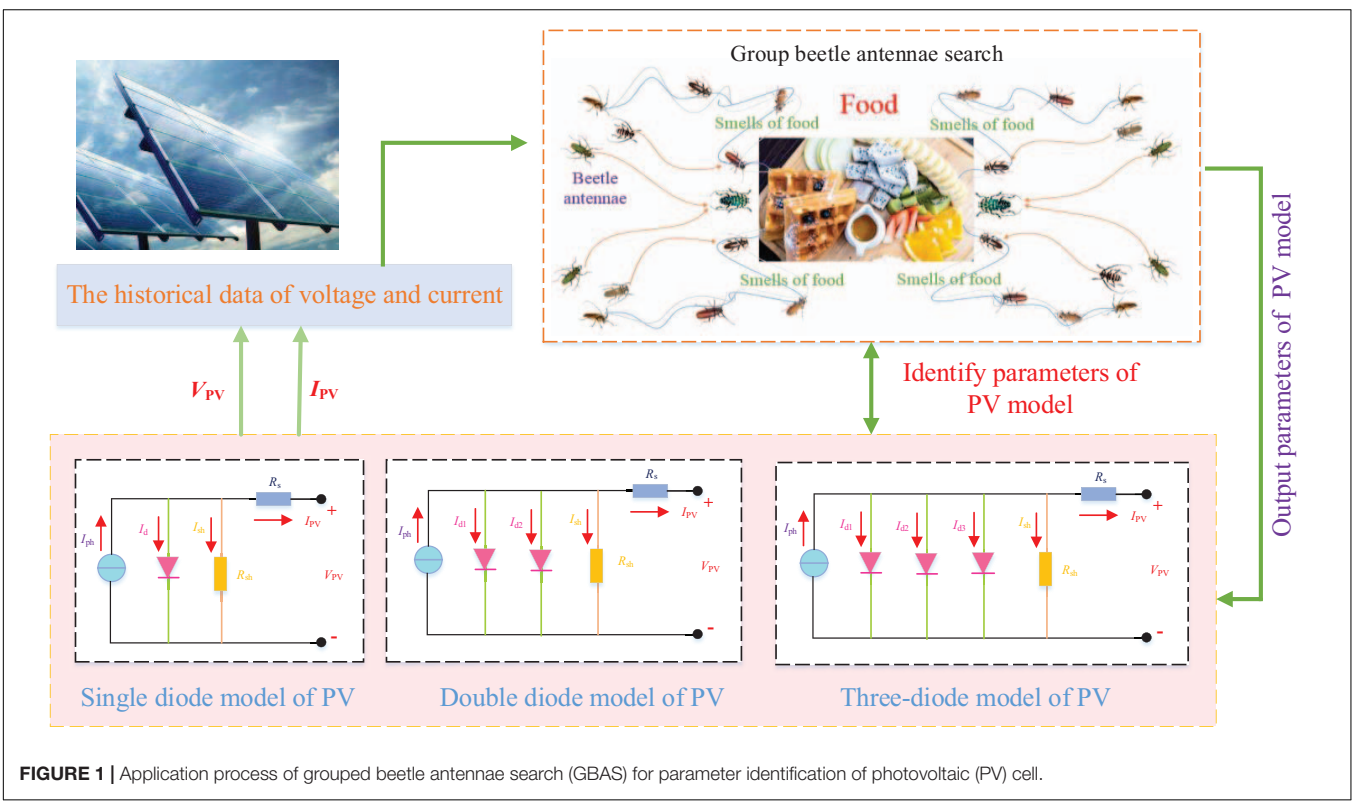


FIGURE 1 | Application process of grouped beetle antennae search (GBAS) for parameter identification of photovoltaic (PV) cell.

TABLE 4 | Benchmark experimental *I-V* dataset.

Item	1	2	3	4	5	6	7	8	9	10	11	12	13
V_L	−0.2057	−0.1291	−0.0588	0.0057	0.0646	0.1185	0.1678	0.2132	0.2545	0.2924	0.3269	0.3585	0.3873
I_L	0.7640	0.7620	0.7605	0.7605	0.7600	0.7590	0.7570	0.7570	0.7555	0.7540	0.7505	0.7465	0.7385
Item	14	15	16	17	18	19	20	21	22	23	24	25	26
V_L	0.4137	0.4373	0.4590	0.4784	0.4960	0.5119	0.5265	0.5398	0.5521	0.5633	0.5736	0.5833	0.5900
I_L	0.7280	0.7065	0.6755	0.6320	0.5730	0.4990	0.4130	0.3165	0.2120	0.1035	−0.010	−0.123	−0.210

TABLE 5 | Parameters bounds of different photovoltaic (PV) cell models.

Parameter	SDM/DDM/TDM	
	Lower bound	Upper bound
I_{ph}(A)	0	1
$I_0, I_{01}, I_{02}, I_{03}$(μA)	0	1
$R_s(\Omega)$	0	0.5
$R_{sh}(\Omega)$	0	100
a_1, a_2, a_3	0	2

where x_j denotes the jth optimization variable; $x_j^{\min}$ and $x_j^{\max}$ represents the lower and upper bounds of the jth optimization variable; while J is the number of optimization variables, respectively.

If a beetle violates constraint (3), its position will be reset randomly within their lower and upper bounds by

$$x_j = x_j^{\min} + r_2\left(x_j^{\max} - x_j^{\min}\right) \tag{4}$$

where r_2 means a random value ranging from 0 to 1.

Parameter Setting

Seven parameters of GBAS algorithm, including C, $\omega_{\max}$, $\omega_{\min}$, $d_{\max}$, $\delta_{\max}$, $t_{\max}$, and n, should be carefully set for parameter identification of PV cell. Note that maximum iteration number $t_{\max}$ and population size n are two most important parameters. Generally speaking, a larger $t_{\max}$ or n will increase the probability to acquire optimal solutions with higher quality, but also result in longer computation time. To ensure GBAS can locate a high-quality optimum in a high convergence rate, they are determined via trial-and-error, as tabulated in **Table 3**.

TABLE 7 | Model parameters identified by various algorithms for single diode model (SDM).

Algorithm	I_{ph}(A)	I_0(μA)	$R_s(\Omega)$	$R_{sh}(\Omega)$	a	RMSE	Rank
ABC	0.7599	0.4306	0.0351	70.7212	1.5106	1.1915E–03	7
BSA	0.7609	0.3155	0.0364	51.3636	1.4788	9.9292E–04	3
GWO	0.7609	0.3960	0.0356	57.7907	1.5019	1.0787E–03	6
MFO	0.7607	0.3615	0.0359	56.9751	1.4926	1.0092E–03	5
PSO	0.7607	0.3182	0.0364	53.5992	1.4796	9.8662E–04	2
WOA	0.7610	0.3240	0.0362	50.2320	1.4815	1.0070E–03	4
BAS	0.7700	0.5664	0.0375	67.0461	1.5390	8.3468E–03	8
GBAS	0.7607	0.3247	0.0363	53.7669	1.4817	9.861E–04	1

Application Process

The application process of GBAS algorithm for parameter identification of PV cell is illustrated in **Figure 1**. Historical data of output voltage and current determined from different PV cells will be regarded as the inputs of GBAS, which is converted into objective function by Eq. (2). Then, according to a specific equivalent circuit model, GBAS can execute optimization procedure based on **Table 3**. Finally, GBAS output the identified parameters of PV cell.

CASE STUDIES

In this section, three different kinds of PV models, i.e., SDM, DDM, and TDM are adopted for parameter identification based on GBAS algorithm. For this purpose, a total of 26 pairs of benchmark experimental *I-V* dataset are utilized for a fair simulation and comparison (Kamali et al., 2016), which are extracted from a 57 mm diameter R.T.C. France solar cell under

TABLE 6 | Statistical results of root mean square error (RMSE) obtained by various algorithms for single diode model (SDM).

Algorithm	RMSE					
	Min.	Median	Mean	Max.	SD	Sig.
ABC	1.1915E–03	1.5983E–03	1.5738E–03	1.8032E–03	1.5675E–04	+
BSA	9.9292E–04	2.2381E–03	6.3615E–03	3.8151E–02	9.6855E–03	+
GWO	1.0787E–03	2.5662E–03	8.5826E–03	3.8157E–02	1.3465E–02	+
MFO	1.0092E–03	2.2845E–03	6.6942E–03	3.8151E–02	1.2560E–02	+
PSO	9.8662E–04	2.1149E–03	1.9462E–03	2.5806E–03	5.0841E–04	+
WOA	1.0070E–03	4.9664E–03	2.2592E–02	2.2286E–01	5.2876E–02	+
BAS	8.3468E–03	3.4603E–02	3.5239E–02	6.7343E–02	1.2964E–02	+
GBAS	**9.8610E–04**	**1.0371E–03**	**1.0640E–03**	**1.2990E–03**	**7.5240E–05**	

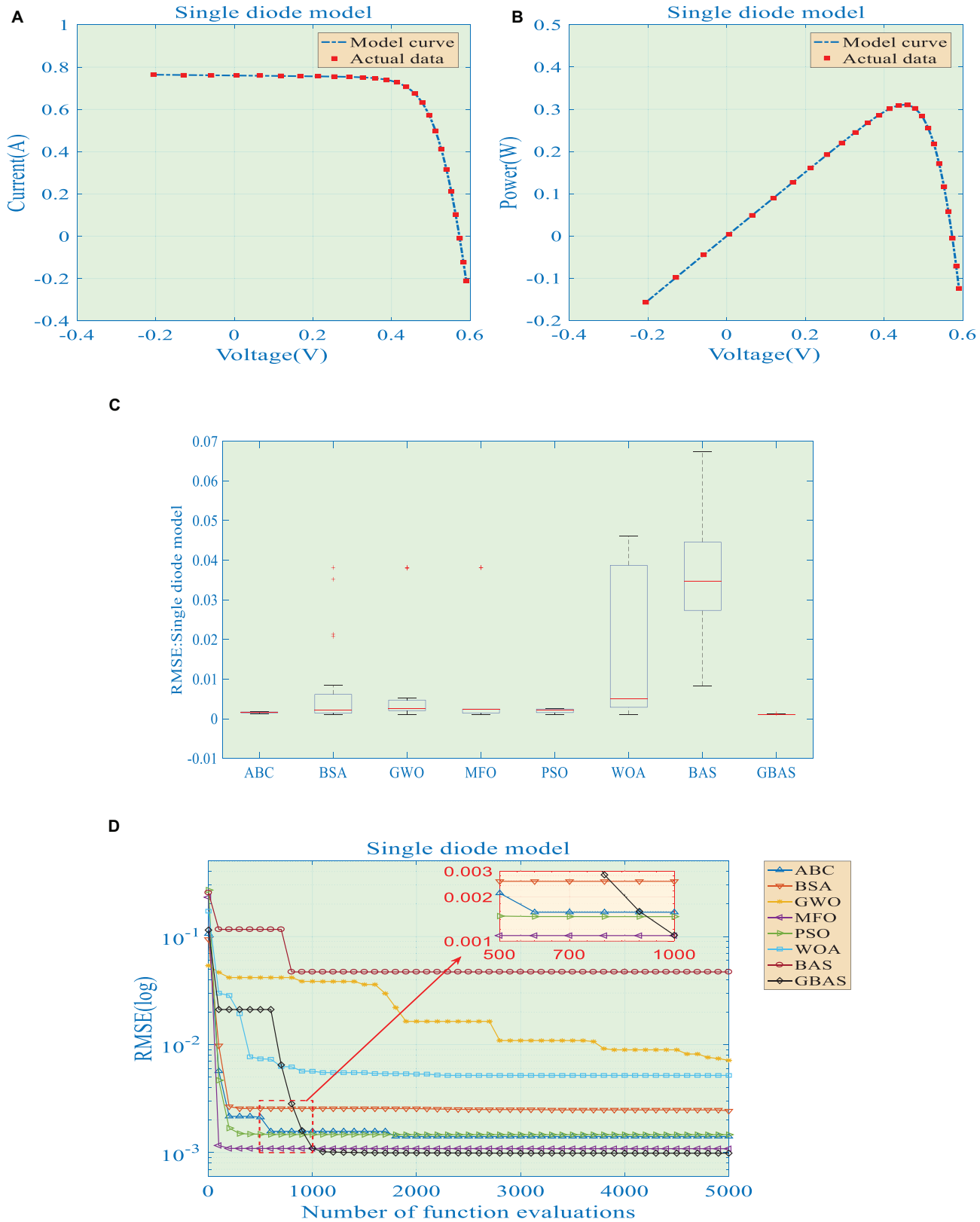


FIGURE 2 | Identification results obtained by grouped beetle antennae search (GBAS) algorithm for SDM: **(A)** *I-V* curve; **(B)** *P-V* curve; **(C)** boxplot of RMSE; **(D)** convergence graph.

TABLE 8 | Statistical results of root mean square error (RMSE) obtained by various algorithms for double diode model (DDM).

Algorithm	RMSE					
	Min.	**Median**	**Mean**	**Max.**	**SD**	**Sig.**
ABC	1.1773E–03	1.5708E–03	1.5912E–03	2.0258E–03	2.1602E–04	+
BSA	9.8592E–04	1.5191E–03	2.1906E–03	1.1525E–02	2.1542E–03	+
GWO	1.0031E–03	2.0547E–03	4.6647E–03	3.8152E–02	9.1613E–03	+
MFO	**9.8444E–04**	1.7950E–03	1.9188E–03	2.9249E–03	5.3192E–04	+
PSO	9.9333E–04	1.6163E–03	1.8196E–03	3.1263E–03	6.7792E–04	+
WOA	1.1342E–03	3.0642E–03	5.0451E–03	4.2018E–02	9.6293E–03	+
BAS	1.0665E–02	3.3901E–02	3.2488E–02	5.7557E–02	1.2245E–02	+
GBAS	9.8594E–04	**1.0448E–03**	**1.0720E–03**	**1.3229E–03**	**8.2371E–05**	

TABLE 9 | Model parameters identified by various algorithms for double diode model (DDM).

Algorithm	I_{ph} (A)	I_{01} (μA)	$R_{s(\Omega)}$	R_{sh} (Ω)	a_1	I_{02} (μA)	a_2	RMSE	Rank
ABC	0.7604	0.5450	0.0372	52.0978	1.8104	0.1511	1.4196	1.1915E–03	7
BSA	0.7607	0.1748	0.0365	53.6545	1.9999	0.2936	1.4728	9.8512E–04	2
GWO	0.7608	0.1106	0.0364	56.7057	1.4123	0.4655	1.6585	1.0031E–03	5
MFO	0.7607	0.2949	0.0364	54.3816	1.4735	0.2160	2.000	9.8444E–04	1
PSO	0.7608	0.3564	0.0368	52.4937	2.0000	0.2540	1.4597	9.9333E–04	4
WOA	0.7603	0.5333	0.0358	71.7116	1.6921	0.1502	1.4360	1.1342E–03	6
BAS	0.7745	0.3412	0.0382	55.7934	1.4911	0.5034	1.9143	1.0665E–02	8
GBAS	0.7608	0.2376	0.0366	53.4190	1.4570	0.2602	1.7954	9.8594E–04	3

conditions of $G = 1{,}000$ W/m^2 and $T = 33°$C ($T = 33°$C is the cell temperature), as shown in **Table 4**. This dataset is widely applied to validate algorithms for PV cell parameters identification in prior studies (El-Naggar et al., 2012; Gong and Cai, 2013; Oliva et al., 2017; Yu et al., 2017; Chen et al., 2018). Due to the benchmark *I-V* dataset used for case studies are only determined under conditions of $G = 1{,}000$ W/m^2 and $T = 33°$C, thus there is only one single fitted *I-V* curve.

GBAS algorithm is in comparison with other seven meta-heuristic algorithms, e.g., PSO (Oliva et al., 2014), ABC (Yang et al., 2019a), WOA (Elazab et al., 2018), BSA (Dasu et al., 2019), MFO (Yu et al., 2018), GWO (Yang et al., 2017), and BAS algorithm. Particularly, their maximum iteration number is designed to be the same, i.e., 50,000, while all approaches are executed in 30 independent runs to acquire statistical results. Besides, population size of each algorithm is designed to be 30, 50, and 70 for SDM, DDM, and TDM, respectively. Note that parameters bounds of different PV cell models is illustrated in **Table 5**.

In particular, the best simulation results of eight methods are highlighted in bold. All case studies are undertaken by MATLAB 2019a through a personal computer with IntelR CoreTMi7 CPU at 2.0 GHz and 32 GB of RAM.

Results Discussion on SDM

The statistical results acquired by each algorithm for SDM, such as minimum, median, mean, maximum, and standard deviation (SD) of RMSE are demonstrated in **Table 4**. Note that RMSE can explicitly quantify solution accuracy, while SD of RMSE indicates algorithm reliability. Symbols "+," "−," and "=" mean the experimental performance of GBAS algorithm is better than, worse than, or similar to that of its competitors, respectively.

Table 6 explicitly illustrates that simulation results of GBAS algorithm outperform other algorithms in terms of minimum, median, mean, maximum and SD of RMSE, upon which GBAS algorithm is verified to achieve the highest optimization accuracy. Particularly, median and SD values of RMSE obtained by GBAS algorithm are 97.00 and 99.42% lower than that of BAS algorithm, which verifies cooperative group can astonishingly improve searching efficiency and convergence stability of GBAS algorithm. Besides, the proper balance between local exploitation and global exploration can avoid low-quality optimum stagnation.

Moreover, optimal parameters identification results obtained by various algorithms, along with their RMSE are presented in **Table 7**, among which GBAS algorithm can acquire minimum RMSE, followed by PSO, BSA, WOA, MFO, GWO, ABC, and BAS algorithm.

The identification results are shown in **Figure 2**. The output *I-V* and *P-V* curves based on optimal parameters identified by GBAS algorithm are depicted in **Figures 2A,B**. Obviously, the model curves acquired by GBAS algorithm are highly consistent with actual data, which also reveals its superior performance for PV cell parameter identification.

Figure 2C presents boxplot of various algorithms for SDM, which demonstrates distribution of simulation results based on various algorithms in 30 runs. One can readily observe that RMSE obtained by GBAS algorithm can distribute within the smallest range with minimal lower and upper bounds among all algorithms. This verifies that GBAS algorithm can simultaneously

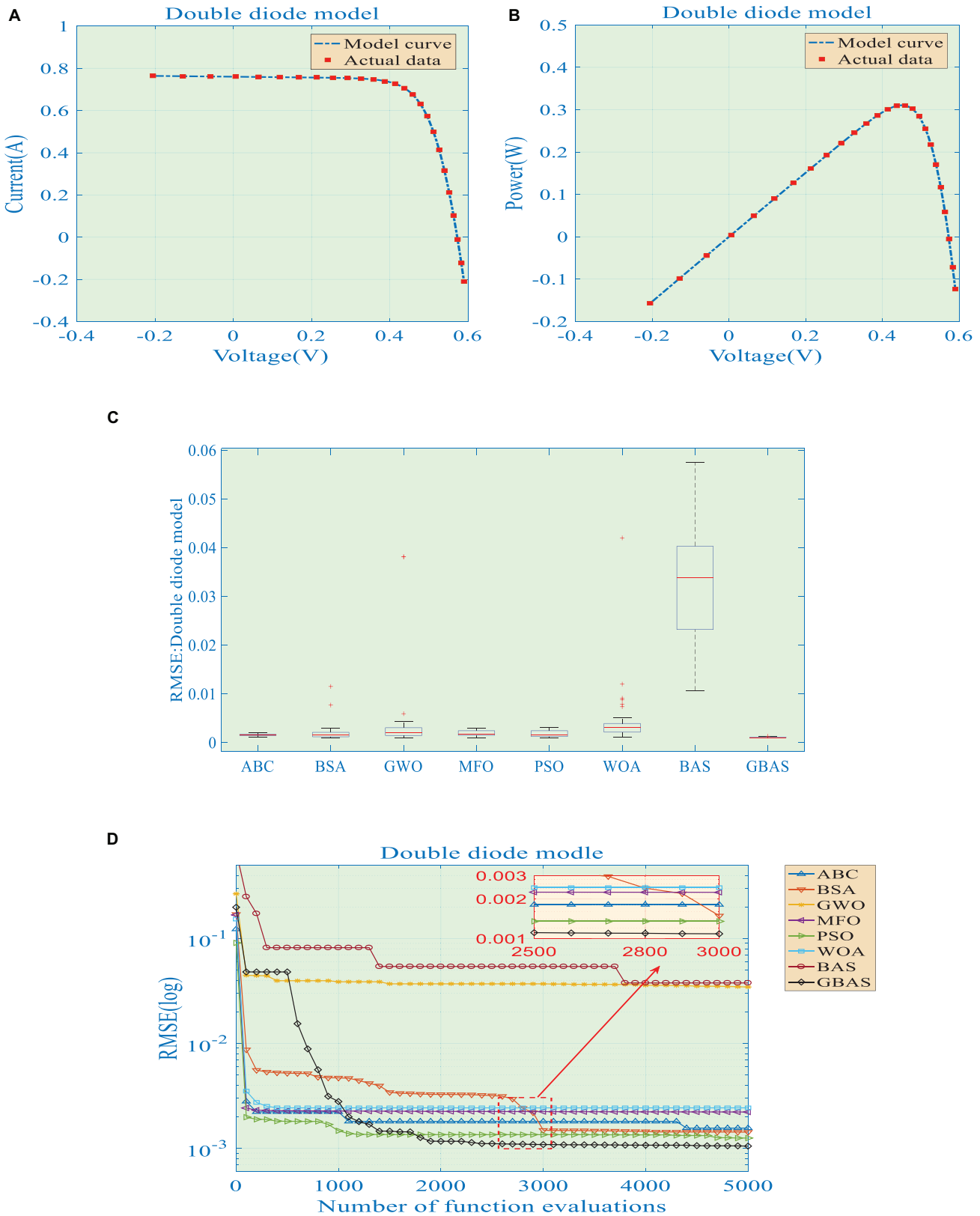


FIGURE 3 | Identification results obtained by grouped beetle antennae search (GBAS) algorithm for double diode model (DDM): **(A)** *I-V* curve; **(B)** *P-V* curve; **(C)** boxplot of RMSE; **(D)** convergence graph.

TABLE 10 | Statistical results of root mean square error (RMSE) obtained by various algorithms for triple diode model (TDM).

Algorithm	RMSE					
	Min.	Median	Mean	Max.	SD	Sig.
ABC	1.1656E–03	1.6491E–03	1.6164E–03	1.9484E–03	2.0904E–04	+
BSA	**9.8410E–04**	1.2671E–03	1.5012E–03	5.0039E–03	8.0729E–04	+
GWO	1.0125E–03	1.6959E–03	3.8259E–03	3.2771E–02	7.7960E–03	+
MFO	9.9054E–04	2.1265E–03	2.0886E–03	3.5509E–03	7.0063E–04	+
PSO	9.8634E–04	1.4949E–03	1.8829E–03	3.8209E–03	7.8566E–04	+
WOA	1.2060E–03	4.2454E–03	9.7443E–03	4.2789E–02	1.2459E–02	+
BAS	1.2146E–02	3.5046E–02	3.3053E–02	5.9392E–02	1.3223E–02	+
GBAS	9.8882E–04	**1.1237E–03**	**1.1232E–03**	**1.6124E–03**	**1.2964E–04**	

TABLE 11 | Model parameters identified by various algorithms for triple diode model (TDM).

Algorithm	I_{ph} (A)	I_{01} (μA)	R_s (Ω)	R_{sh} (Ω)	a_1	I_{02} (μA)	a_2	I_{03} (μA)	a_3	RMSE	Rank
ABC	0.7615	0.2446	0.0364	44.8763	1.4618	0.3504	1.5620	0.2663	1.9265	1.1656E–03	6
BSA	0.7607	0.0741	0.0365	54.1062	1.9999	0.2747	1.4673	0.2268	1.9691	9.8410E–04	1
GWO	0.7606	0.0442	0.0365	59.8501	1.4329	0.0189	1.3326	0.4895	1.6082	1.0125E–03	5
MFO	0.7607	0.0019	0.0363	54.9651	1.0000	0.3408	1.4873	0.0001	2.0000	9.9054E–04	4
PSO	0.7607	1.0000	0.0370	56.7914	2.0000	0.0564	1.4569	0.1374	1.4313	9.8634E–04	2
WOA	0.7598	0.3709	0.0364	76.7663	1.5757	0.0289	1.8577	0.0779	1.4071	1.2060E–03	7
BAS	0.7675	0.7381	0.0334	82.4121	1.7219	0.8315	1.6465	0.3362	1.7123	1.2146E–02	8
GBAS	0.7607	0.0231	0.0363	55.5354	1.9933	0.1729	1.7794	0.2746	1.4697	9.8882E–04	3

improve convergence stability and enhance searching ability. Besides, **Figure 2D** provides convergence graphs of various eight algorithms, among which BSA algorithm is difficult to acquire a high-quality optimal solution based on a single individual based global search. In contrast, GBAS algorithm can gradually find a better solution as it can properly balance local exploitation and global exploration via cooperative group.

Results Discussion on DDM

Statistical results of each algorithm for DDM are tabulated in **Table 8**, which illustrates that GBAS algorithm can obtain the optimal performance in median, mean, maximum and SD of RMSE. Although MFO can achieve minimum RMSE, minimum RMSE value obtained by MFO is only 0.15% lower than that of GBAS algorithm. Particularly, mean RMSE and SD obtained by GBAS algorithm are 44.13 and 84.51% lower than those obtained by MFO, respectively. Therefore, GBAS algorithm realizes the most desirable performance when both accuracy and reliability are taken into consideration for DDM.

Table 9 illustrates the best model parameters and RMSE obtained by various strategies for DDM. Among which MFO obtains the best RMSE, followed by BSA, GBAS, PSO, GWO, WOA, ABC, and BAS algorithm.

The identification results are shown in **Figure 3**. **Figures 3A,B** demonstrate the output *I-V* and *P-V* curves acquired by GBAS algorithm and actual data, upon which it can be seen that model curve obtained by GBAS algorithm highly matches actual data. Boxplot of different algorithms is depicted in **Figure 3C**, upon which one can easily find that RMSE obtained by GBAS algorithm has the smallest distribution range and upper/lower bounds compared with others, which indicates that GBAS algorithm has accurate searching ability in PV parameter identification and stable global searching ability.

In particular, **Figure 3D** provides convergence graphs of all algorithms. The results show that PSO can rapidly obtain an elegant solution in initial stage, but it is easy to produce premature convergence and difficult to find global optimum. In contrast, GBAS algorithm owns a high convergence rate and can avoid local optimum stagnation.

Results Discussion on TDM

For TDM, statistical results of each algorithm are tabulated in **Table 10**, upon which GBAS algorithm still performs quite satisfactory, which can obtain the best results in median, mean, maximum and SD of RMSE. Although BSA algorithm obtains the minimum RMSE, it performs worse than GBAS in other performance indices. For example, RMSE median and SD obtained by GBAS algorithm are 31.86 and 37.98% lower than those of ABC (second best), respectively. In addition, GBAS algorithm also performs well in the accuracy of PV cell parameter identification. Minimum RMSE obtained by GBAS algorithm is only 0.4% larger than that of BSA algorithm. Hence, GBAS algorithm owns the most satisfactory performance for TDM.

The best parameters identification results based on various algorithms for TDM is demonstrated in **Table 11**. Apparently, BSA algorithm achieves the best RMSE, followed by PSO, GBAS algorithm, MFO, GWO, ABC, and BAS.

The identification results are shown in **Figure 4**. **Figures 4A,B** demonstrate the output *I-V* and *P-V* curves acquired by GBAS algorithm and actual data, which can efficiently verify the

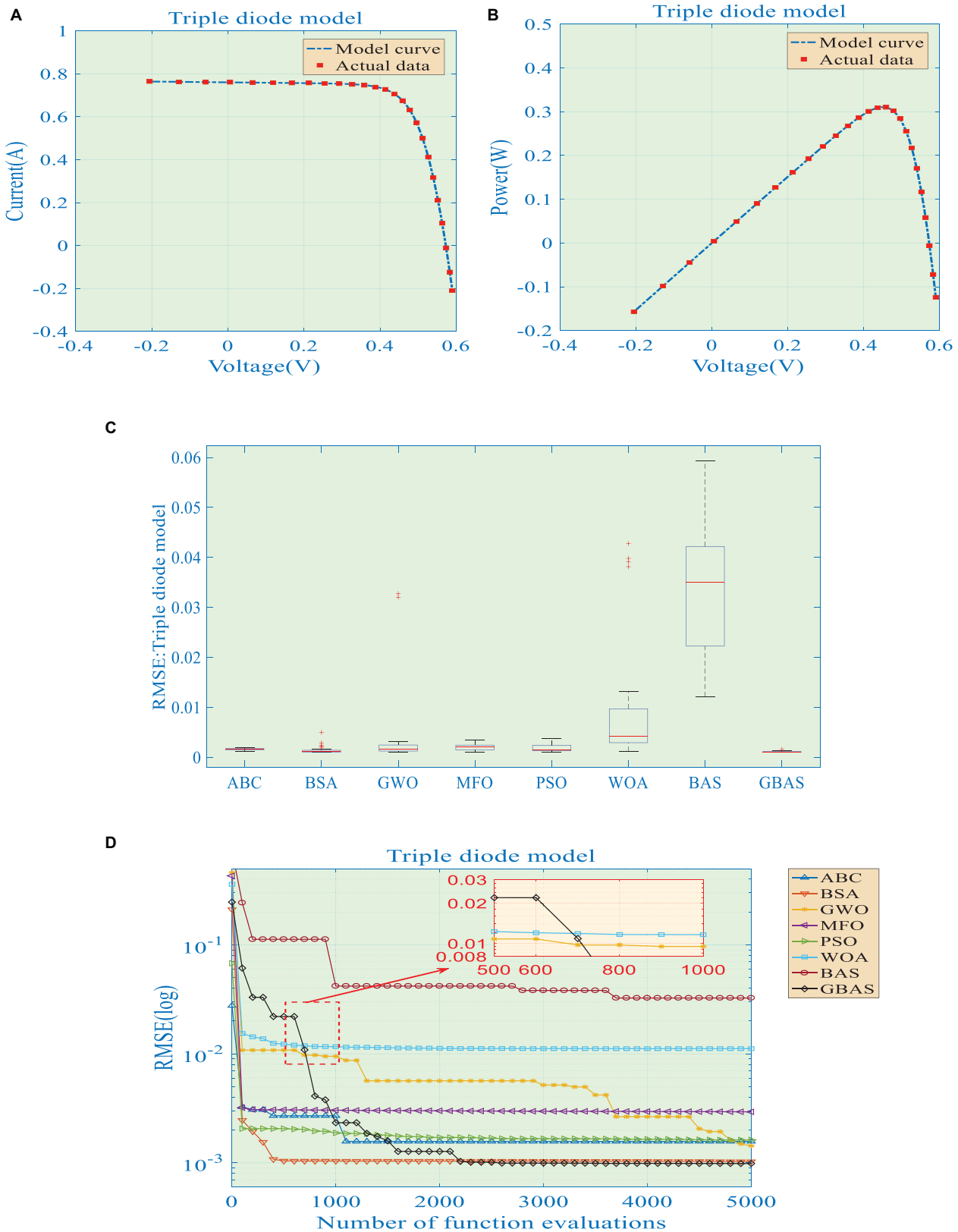


FIGURE 4 | Identification results obtained by grouped beetle antennae search (GBAS) algorithm for triple diode model (TDM): **(A)** *I-V* curve; **(B)** *P-V* curve; **(C)** boxplot of RMSE; **(D)** convergence graph.

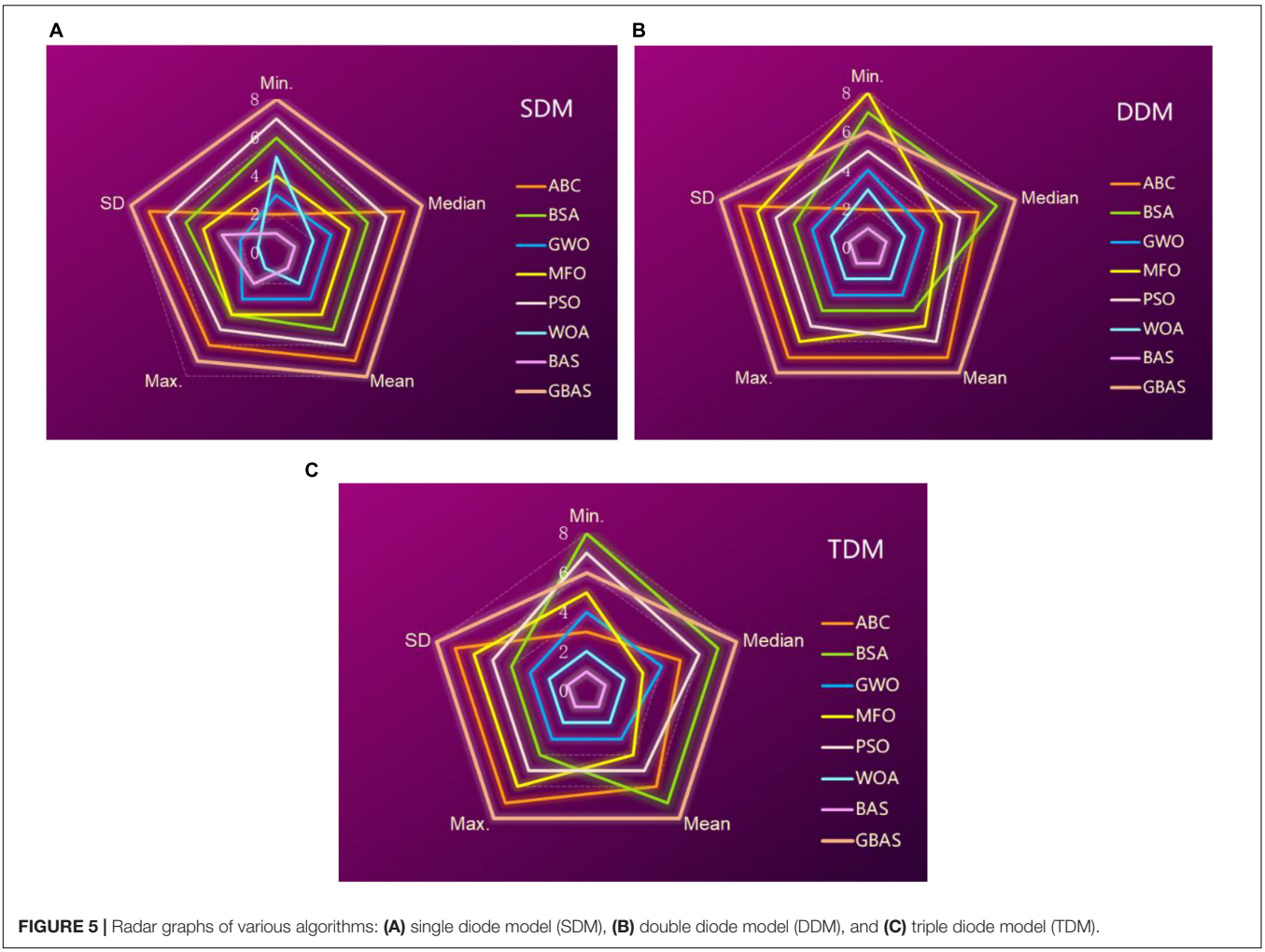


FIGURE 5 | Radar graphs of various algorithms: **(A)** single diode model (SDM), **(B)** double diode model (DDM), and **(C)** triple diode model (TDM).

precision of identified PV cell parameters. **Figure 4C** shows boxplot of different algorithms while. One can observe that GBAS algorithm is highly competitive in solution precision and stability compared with others.

At last, **Figure 4D** provides convergence graphs of all algorithms, which shows that GBAS algorithm can realize a proper trade-off between local exploitation and global exploration to find the best solution. In contrast, others are easily to fall into a local optimum.

Statistical Results and Analysis

Note that SD of RMSE indicates parameter identification reliability, upon which GBAS algorithm can achieve more desirable performance than other competitors for SDM, DDM, and TDM. Moreover, SD of RMSE obtained by GBAS algorithm is much smaller than others for all models, which can effectively verify the outstanding reliability of GBAS algorithm. For example, SD of RMSE obtained by GBAS algorithm is 64.34% smaller than the best value obtained by other algorithms in SDM, 61.86% smaller than that in DDM.

In addition, the distribution of results acquired by various methods over 30 independent runs for SDM, DDM, and TDM are clearly shown in **Figures 2–4**, respectively. In each model, RMSE obtained by GBAS algorithm has the minimum upper and lower limits and the smallest range. Moreover, solution distribution also illustrates the superior performance of GBAS algorithm. Besides, **Figure 5** provides radar charts of various algorithms, while the best ranking is assigned with 8 points and then decreased by 1 point in turn. Note that the marking and ranking basis of different algorithms is based on a comprehensive and overall comparison of their performance in PV cell parameter identification, i.e., optimization accuracy, optimization efficiency, convergence stability, and convergence speed. Based on the radar graphs, it can be explicitly and comprehensively illustrated that GBAS algorithm is much better than other algorithms.

CONCLUSION

A powerful bio-inspired GBAS algorithm is adopted in this paper for accurate and efficient parameter estimation of different PV cell diode models, which contains the following three contributions/novelties:

- Compared with BAS algorithm, GBAS algorithm can effectively enhance global optimum searching efficiency via a cooperative group of multiple beetles instead of a single beetle. Besides, it also can acquire a high-quality optimum via a dynamic and proper balance between local exploitation and global exploration;
- GBAS algorithm is utilized in parameter identification of SDM, DDM, and TDM, upon which its effectiveness and feasibility have been validated. The SD of RMSE obtained by GBAS for SDM is 52.00, 99.22, 99.44, 99.40, 85.20, 99.86, and 99.42% lower to that of ABC, BSA, GWO, MFO, PSO, WOA, and BAS, respectively. Besides, under the DDM, the SD of RMSE of GBAS is 61.87, 96.18, 99.10, 84.51, 87.85, 99.14, and 99.33% lower to that of ABC, BSA, GWO, MFO, PSO, WOA, and BAS, respectively;
- Case studies demonstrate that GBAS algorithm can effectively enhance optimization accuracy and stability compared with other meta-heuristic algorithms.

Future researches on the proposed algorithm can mainly focus on optimization accuracy and convergence speed enhancement due to these two indices of the proposed GBAS algorithm still can be further improved. Based on this, GBAS can be verified for online parameter estimation to validate its practical response speed and optimization ability, which is quite useful and necessary in practical engineering applications.

It is noteworthy that the PV cell parameters provided by manufacturers or experiments are usually tested under STC, while the practical operation conditions can barely maintain at STC. Hence, for the sake of verifying the practical performance of the proposed GBAS, the experiments require to be carried out under various operation conditions. Besides, GBAS can also be combined with corresponding reliable control strategies to achieve reliable PV cell fault diagnosis, which can considerably enhance operation stability and reliability of PV systems.

DATA AVAILABILITY STATEMENT

The original contributions presented in the study are included in the article/supplementary material, further inquiries can be directed to the corresponding author/s.

AUTHOR CONTRIBUTIONS

LS: conceptualization, writing – review and editing, and validation. JW: writing – original draft, formal analysis, data curation, and visualization. LT: methodology, software, and supervision. All authors contributed to the article and approved the submitted version.

REFERENCES

Abbassi, R., Abbassi, A., Jemli, M., and Chebbi, S. (2018). Identification of unknown parameters of solar cell models: a comprehensive overview of available approaches. *Renew. Sustain. Energy Rev.* 90, 453–474. doi: 10.1016/j.rser.2018.03.011

Alam, D. F., Yousri, D. A., and Eteiba, M. B. (2015). Flower pollination algorithm based solar PV parameter estimation. *Energy Convers. Manag.* 101, 410–422. doi: 10.1016/j.enconman.2015.05.074

Allam, D., Yousri, D. A., and Eteiba, M. B. (2016). Parameters extraction of the three diode model for the multi-crystalline solar cell/module using Moth-Flame optimization algorithm. *Energy Convers. Manag.* 123, 535–548. doi: 10.1016/j.enconman.2016.06.052

Askarzadeh, A., and Rezazadeh, A. (2012). Parameter identification for solar cell models using harmony search-based algorithms. *Solar Energy* 86, 3241–3249. doi: 10.1016/j.solener.2012.08.018

Askarzadeh, A., and Rezazadeh, A. (2013). Extraction of maximum power point in solar cells using bird mating optimizer-based parameters identification approach. *Solar Energy* 90, 123–133. doi: 10.1016/j.solener.2013.01.010

Barukčić, M., Ćorluka, V., and Miklošević, K. (2015). The irradiance and temperature dependent mathematical model for estimation of photovoltaic panel performances. *Energy Convers. Manag.* 101, 229–238. doi: 10.1016/j.enconman.2015.05.027

Batzelis, E. I., and Papathanassiou, S. A. (2016). A method for the analytical extraction of the single-diode PV model parameters. *IEEE Trans. Sustain. Energy* 7, 504–512. doi: 10.1109/tste.2015.2503435

Chaibi, Y., Allouhi, A., Salhi, M., and El-jouni, A. (2019). Annual performance analysis of different maximum power point tracking techniques used in photovoltaic systems. *Prot. Control Mod. Power Syst.* 4, 171–180.

Chan, D. S. H., and Phang, J. C. H. (1987). Analytical methods for the extraction of solar-cell single- and double-diode model parameters from *I-V* characteristics. *IEEE Trans. Electr. Dev.* 34, 286–293. doi: 10.1109/t-ed.1987.22920

Chen, X., Xu, B., Mei, C. L., Ding, Y. H., and Li, K. J. (2018). Teaching-learning-based artificial bee colony for solar photovoltaic parameter estimation. *Appl. Energy* 212, 1578–1588. doi: 10.1016/j.apenergy.2017.12.115

Chen, X., and Yu, K. J. (2019). Hybridizing cuckoo search algorithm with biogeography-based optimization for estimating photovoltaic model parameters. *Solar Energy* 180, 192–206. doi: 10.1016/j.solener.2019.01.025

Chin, V. J., Salam, Z., and Ishaque, K. (2015). Cell modelling and model parameters estimation techniques for photovoltaic simulator application: a review. *Appl. Energy* 154, 500–519. doi: 10.1016/j.apenergy.2015.05.035

Dasu, B., Sivakumar, M., and Srinivasarao, R. (2019). Interconnected multi-machine power system stabilizer design using whale optimization algorithm. *Prot. Control Mod. Power Syst.* 4, 13–23.

Easwarakhanthan, T., Bottin, J., Bouhouch, I., and Boutrit, C. (1986). Nonlinear minimization algorithm for determining the solar cell parameters with microcomputers. *Int. J. Solar Energy* 4, 1–12. doi: 10.1080/01425918608909835

Elazab, O. S., Hasanien, H. M., Elgendy, M. A., and Abdeen, A. M. (2018). Parameters estimation of single- and multiple-diode photovoltaic model using whale optimisation algorithm. *IET Renew. Power Gener.* 12, 1755–1761. doi: 10.1049/iet-rpg.2018.5317

El-Naggar, K. M., AlRashidi, M. R., AlHajri, M. F., and Al-Othman, A. K. (2012). Simulated annealing algorithm for photovoltaic parameters identification. *Solar Energy* 86, 266–274. doi: 10.1016/j.solener.2011.09.032

Gomes, R. C. M., Vitorino, M. A., Correa, M. B. R., Fernandes, D. A., and Wang, R. X. (2017). Shuffled complex evolution on photovoltaic parameter extraction: a comparative analysis. *IEEE Trans. Sustain. Energy* 8, 805–815. doi: 10.1109/tste.2016.2620941

Gong, W. Y., and Cai, Z. H. (2013). Parameter extraction of solar cell models using repaired adaptive differential evolution. *Solar Energy* 94, 209–220. doi: 10.1016/j.solener.2013.05.007

Hao, J. F., Huang, J. H., Zhang, A. L., Ai, H. J., Zhang, Q., and Yang, B. (2020). Correction: optimal coordinated control of hybrid AC/VSC-HVDC system integrated with DFIG via cooperative beetle antennae search algorithm. *PLoS One* 15:e0244757. doi: 10.1371/journal.pone.0242316

He, X., Ai, Q., Qiu, R. C. M., Huang, W. T., Piao, L. J., and Liu, H. C. (2017). A big data architecture design for smart grids based on random matrix theory. *IEEE Trans. Smart Grid* 8, 674–686.

Humada, A. M., Hojabri, M., Mekhilef, S., and Hamada, H. M. (2016). Solar cell parameters extraction based on single and double-diode models: a review. *Renew. Sustain. Energy Rev.* 56, 494–509. doi: 10.1016/j.rser.2015.11.051

Ishaque, K., and Salam, Z. (2011). An improved modeling method to determine the model parameters of photovoltaic (PV) modules using differential evolution (DE). *Solar Energy* 85, 2349–2359. doi: 10.1016/j.solener.2011.06.025

Ishaque, K., Salam, Z., Taheri, H., and Shamsudin, A. (2011). A critical evaluation of EA computational methods for photovoltaic cell parameter extraction based on two diode model. *Solar Energy* 85, 1768–1779. doi: 10.1016/j.solener.2011.04.015

Jervase, J. A., Bourdoucen, H., and Al-lawati, A. M. (2001). Solar cell parameter extraction using genetic algorithms. *Meas. Sci. Technol.* 12, 1922–1925. doi: 10.1088/0957-0233/12/11/322

Jiang, X. Y., and Li, S. B. A. S. (2018). Beetle antennae search algorithm for optimization problems. *Int. J. Robot. Control* 1, 1–5. doi: 10.5430/ijrc.v1n1p1

Kamali, S. K., Rahim, N. A., Mokhlis, H., and Tyagi, V. V. (2016). Photovoltaic electricity generator dynamic modeling methods for smart grid applications: a review. *Renew. Sustain. Energy Rev.* 57, 131–172. doi: 10.1016/j.rser.2015.12.137

Khanna, V., Das, B. K., Bisht, D., Vandana, P., and Singh, P. K. (2015). A three diode model for industrial solar cells and estimation of solar cell parameters using PSO algorithm. *Renew. Energy* 78, 105–113. doi: 10.1016/j.renene.2014.12.072

Li, G. D., Li, G. Y., and Zhou, M. (2019). Model and application of renewable energy accommodation capacity calculation considering utilization level of interprovincial tie-line. *Prot. Control Mod. Power Syst.* 4, 1–12.

Li, W., Paul, M. C., Rolley, M., Sweet, T., Gao, M., Siviter, J., et al. (2017). A scaling law for monocrystalline PV/T modules with CCPC and comparison with triple junction PV cells. *Appl. Energy* 202, 755–771. doi: 10.1016/j.apenergy.2017.05.182

Mahdavi, S., Shiri, M. E., and Rahnamayan, S. (2015). Metaheuristics in large-scale global continues optimization: a survey. *Inf. Sci.* 295, 407–428. doi: 10.1016/j.ins.2014.10.042

Mostafa, M., Rezk, H., Aly, M., and Ahmed, E. M. (2020). A new strategy based on slime mould algorithm to extract the optimal model parameters of solar PV panel. *Sustain. Energy Technol. Assess.* 42:100849. doi: 10.1016/j.seta.2020.100849

Muangkote, N., Sunat, K., Chiewchanwattana, S., and Kaiwinit, S. (2019). An advanced onlooker-ranking-based adaptive differential evolution to extract the parameters of solar cell models. *Renew. Energy* 134, 1129–1147. doi: 10.1016/j.renene.2018.09.017

Nayak, B., Mohapatra, A., and Mohanty, K. B. (2019). Parameter estimation of single diode PV module based on GWO algorithm. *Renew. Energy Focus* 30, 1–12. doi: 10.1016/j.ref.2019.04.003

Niu, Q., Zhang, L., and Li, K. (2014). A biogeography-based optimization algorithm with mutation strategies for model parameter estimation of solar and fuel cells. *Energy Convers. Manag.* 86, 1173–1185. doi: 10.1016/j.enconman.2014.06.026

Nunes, H. G. G., Silva, P. N. C., Pombo, J. A. N., Mariano, S. J. P. S., and Calado, M. R. A. (2020). Multiswarm spiral leader particle swarm optimisation algorithm for PV parameter identification. *Energy Convers. Manag.* 225:113388. doi: 10.1016/j.enconman.2020.113388

Oliva, D., Cuevas, E., and Pajares, G. (2014). Parameter identification of solar cells using artificial bee colony optimization. *Eenergy* 72, 93–102. doi: 10.1016/j.energy.2014.05.011

Oliva, D., Elaziz, M. A., and Hassanien, A. (2017). Parameter estimation of photovoltaic cells using an improved chaotic whale optimization algorithm. *Appl. Energy* 200, 141–154. doi: 10.1016/j.apenergy.2017.05.029

Peng, X. T., Yao, W., Yan, C., Wen, J. Y., and Cheng, S. J. (2020). Two-stage variable proportion coefficient based frequency support of grid-connected DFIG-WTs. *IEEE Trans. Power Syst.* 35, 962–974. doi: 10.1109/tpwrs.2019.2943520

Ram, J. P., Manghani, H., Pillai, D. S., Babu, T. S., Miyatake, M., and Rajasekara, N. (2018). Analysis on solar PV emulators: a review. *Renew. Sustain. Energy Rev.* 81, 149–160. doi: 10.1016/j.rser.2017.07.039

Roeva, O., and Fidanova, S. (2018). Comparison of different metaheuristic algorithms based on intercriteria analysis. *J. Comput. Appl. Math.* 340, 615–628. doi: 10.1016/j.cam.2017.07.028

Saleem, H., and Karmalkar, S. (2009). An analytical method to extract the physical parameters of a solar cell from four points on the illuminated J-V curve. *IEEE Electron Dev. Lett.* 30, 349–352. doi: 10.1109/led.2009.2013882

Shang, L. Q., Zhu, W. W., Li, P. W., and Guo, H. C. (2018). Maximum power point tracking of PV system under partial shading conditions through flower pollination algorithm. *Prot. Control Mod. Power Syst.* 3, 400–406.

Song, D. R., Fan, X. Y., Yang, J., Liu, A. F., Chen, S. F., and Joo, Y. H. (2018). Power extraction efficiency optimization of horizontal-axis wind turbines through optimizing control parameters of yaw control systems using an intelligent method. *Appl. Energy* 224, 267–279. doi: 10.1016/j.apenergy.2018.04.114

Song, D. R., Zheng, S. Y., Yang, S., Yang, J., Dong, M., Su, M., et al. (2020). Annual energy production estimation for variable-speed wind turbines at high-altitude sites. *J. Mod. Power Syst. Clean Energy* doi: 10.35833/MPCE.2019.000240

Sun, K., Yao, W., Fang, J. K., Ai, X. M., Wen, J. Y., and Cheng, S. J. (2020). Impedance modeling and stability analysis of grid-connected DFIG-based wind farm with a VSC-HVDC. *IEEE J. Emerg. Sel. Top. Power Electron.* 8, 1375–1390. doi: 10.1109/jestpe.2019.2901747

Villalva, M. G., Gazoli, J. R., and Filho, E. R. (2009). Comprehensive approach to modeling and simulation of photovoltaic arrays. *IEEE Trans. Power Electr.* 24, 1198–1208. doi: 10.1109/tpel.2009.2013862

Wolf, P., and Benda, V. (2013). Identification of PV solar cells and modules parameters by combining statistical and analytical methods. *Solar Energy* 93, 151–157. doi: 10.1016/j.solener.2013.03.018

Yang, B., Jiang, L., Wang, L., Yao, W., and Wu, Q. H. (2016). Nonlinear maximum power point tracking control and model analysis of DFIG based wind turbine. *Int. J. Electr. Power Energy Syst.* 74, 429–436. doi: 10.1016/j.ijepes.2015.07.036

Yang, B., Wang, J. B., Zhang, X. S., Yu, T., Yao, W., Shu, H. C., et al. (2020). Comprehensive overview of meta-heuristic algorithm applications on PV cell parameter identification. *Energy Convers. Manag.* 208:112595. doi: 10.1016/j.enconman.2020.112595

Yang, B., Yu, T., Shu, H. C., Dong, J., and Jiang, L. (2018a). Robust sliding-mode control of wind energy conversion systems for optimal power extraction via nonlinear perturbation observers. *Appl. Energy* 210, 711–723. doi: 10.1016/j.apenergy.2017.08.027

Yang, B., Yu, T., Shu, H. C., Zhang, Y. M., Chen, J., Sang, Y. Y., et al. (2018b). Passivity-based sliding-mode control design for optimal power extraction of a PMSG based variable speed wind turbine. *Renew. Energy* 119, 577–589. doi: 10.1016/j.renene.2017.12.047

Yang, B., Yu, T., Zhang, X. S., Li, H. F., Shu, H. C., Sang, Y. Y., et al. (2019a). Dynamic leader based collective intelligence for maximum power point tracking of PV systems affected by partial shading condition. *Energy Convers. Manag.* 179, 286–303. doi: 10.1016/j.enconman.2018.10.074

Yang, B., Zhang, X. S., Yu, T., Shu, H. C., and Fang, Z. H. (2017). Grouped grey wolf optimizer for maximum power point tracking of doubly-fed induction generator based wind turbine. *Energy Convers. Manag.* 133, 427–443. doi: 10.1016/j.enconman.2016.10.062

Yang, B., Zhong, L. E., Yu, T., Li, H. F., Zhang, X. S., Shu, H. C., et al. (2019b). Novel bio-inspired memetic salp swarm algorithm and application to MPPT for PV systems considering partial shading condition. *J. Clean. Prod.* 215, 1203–1222. doi: 10.1016/j.jclepro.2019.01.150

Ye, M. Y., Wang, X. D., and Xu, Y. S. (2009). Parameter extraction of solar cells using particle swarm optimization. *J. Appl. Phys.* 105, 094502–094502-8.

Youssef, A., El-Telbany, M., and Zekry, A. (2017). The role of artificial intelligence in photo-voltaic systems design and control: a review. *Renew. Sustain. Energy Rev.* 78, 72–79. doi: 10.1016/j.rser.2017.04.046

Yu, K. J., Liang, J. J., Qu, B. Y., Chen, X., and Wang, H. S. (2017). Parameters identification of photovoltaic models using an improved JAYA optimization algorithm. *Energy Convers. Manag.* 150, 742–753. doi: 10.1016/j.enconman.2017.08.063

Yu, K. J., Liang, J. J., Qu, B. Y., Cheng, Z. P., and Wang, H. S. (2018). Multiple learning backtracking search algorithm for estimating parameters of photovoltaic models. *Appl. Energy* 226, 408–422. doi: 10.1016/j.apenergy.2018.06.010

Zagrouba, M., Sellami, A., Bouaïcha, M., and Ksouri, M. (2010). Identification of PV solar cells and modules parameters using the genetic algorithms: application

to maximum power extraction. *Solar Energy* 84, 860–866. doi: 10.1016/j.solener.2010.02.012

Zhang, H. X., Lu, Z. X., Hu, W., Wang, Y. T., Dong, L., and Zhang, J. T. (2019). Coordinated optimal operation of hydro-wind-solar integrated systems. *Appl. Energy* 242, 883–896. doi: 10.1016/j.apenergy.2019.03.064

Zhang, X. S., Tan, T., Zhou, B., Yu, T., Yang, B., and Huang, X. (2021). Adaptive distributed auction-based algorithm for optimal mileage based AGC dispatch with high participation of renewable energy. *Int. J. Elect. Power Energy Syst.* 124:106371. doi: 10.1016/j.ijepes.2020.106371

Zhang, X. S., Xu, Z., Yu, T., Yang, B., and Wang, H. (2020). Optimal mileage based AGC dispatch of a GenCo. *IEEE Trans. Power Syst.* 35, 2516–2526. doi: 10.1109/tpwrs.2020.2966509

Conflict of Interest: LS was employed by company Guangzhou Shuimuqinghua Technology Co., Ltd.

The remaining authors declare that the research was conducted in the absence of any commercial or financial relationships that could be construed as a potential conflict of interest.

Copyright © 2021 Sun, Wang and Tang. This is an open-access article distributed under the terms of the Creative Commons Attribution License (CC BY). The use, distribution or reproduction in other forums is permitted, provided the original author(s) and the copyright owner(s) are credited and that the original publication in this journal is cited, in accordance with accepted academic practice. No use, distribution or reproduction is permitted which does not comply with these terms.

NOMENCLATURE

Variables		GBAS	Grouped beetle antennae search
a, a_1, a_2, a_3	Diode's ideality factors	GWO	Gray wolf optimization
I_d, I_{d1}, I_{d2},	Diode's currents (A)	HS	Harmony search
I_{ph}	Photocurrent (A)	*I-V*	Current-voltage
I_0, I_{01}, I_{02}, I_{03}	Diode's reverse saturation currents (A)	MDDM	Modified double diode model
R_s	Series resistor (Ω)	MFO	Month flame optimizer
R_{sh}	shunt resistor (Ω)	MPPT	Maximum power point tracking
Abbreviations		PSO	Particle swarm optimization
ABC	Artificial bee colony	PV	Photovoltaic
BAS	Beetle antennae search	*P-V*	Power-voltage
BBO	Biogeography based optimization	RMSE	Root mean square error
BMO	Bird mating optimization	SD	Standard deviation
BSA	Backtracking search algorithm	SDM	Single diode model
DDM	Double diode model	STC	Standard test condition
DE	Differential evolution	*T*	Temperature, °C
E.P.	Extracted parameters	TDM	Triple diode model
FPA	Flower pollination algorithm	TLBO	Teaching learning based optimization
G	Irradiation, W/m^2	WCA	Water cycle algorithm
GA	Genetic algorithm	WOA	Whale optimization algorithm

frontiers in Energy Research

REVIEW
published: 07 May 2021
doi: 10.3389/fenrg.2021.680355

Full Life Cycle Management of Power System Integrated With Renewable Energy: Concepts, Developments and Perspectives

*Kang Wang[1], Yikai Li[1], Xiaojun Wang[1], Zengtao Zhao[1], Ning Yang[2], Shengcan Yu[2], Yi Wang[1], Zhanhong Huang[2] and Tao Yu[2]**

[1] CSG POWER GENERATION CO., LTD., Guangzhou, China, [2] School of Electric Power Engineering, South China University of Technology, Guangzhou, China

Under high-penetration of renewable energy, power grid is facing with the development problems such as production delay, wind and solar power abandoning. With the continuous growth of renewable energy installation such as wind power, photovoltaic (PV), as well as the increase of power generation capacity, it is urgent to increase peak-load and frequency regulation capacity on a large scale to alleviate the consumption problems caused by large renewable energy integration, and then requires power generation enterprises of peak-load and frequency regulation to increase relevant equipment assets. As a result, peak-load and frequency regulation enterprises must carry out scientific cost management of equipment assets. This paper introduces the concepts, developments and perspectives of life cycle cost (LCC) management of equipment assets in high-penetrated renewable energy power grid, and probes into cost collection and estimation scheme in the process of equipment asset management.

Keywords: high-penetrated renewable energy power grid, peak-load and frequency regulation, asset full life cycle cost, cost collection and estimation, full life cycle management

OPEN ACCESS

Edited by:
Dongran Song,
Central South University, China

Reviewed by:
Jiawei Zhu,
Chang'an University, China
Jian Yang,
Central South University, China
Mingzhu Tang,
Changsha University of Science and Technology, China

****Correspondence:***
Tao Yu
taoyu1@scut.edu.cn

Specialty section:
This article was submitted to Smart Grids, a section of the journal Frontiers in Energy Research

Received: *14 March 2021*
Accepted: *30 March 2021*
Published: *07 May 2021*

Citation:
Wang K, Li Y, Wang X, Zhao Z, Yang N, Yu S, Wang Y, Huang Z and Yu T (2021) Full Life Cycle Management of Power System Integrated With Renewable Energy: Concepts, Developments and Perspectives. Front. Energy Res. 9:680355. doi: 10.3389/fenrg.2021.680355

INTRODUCTION

Development and Consumption of New Energy

With the continuous increase of environmental pressure and energy demand caused by energy development, the proportion of wind power, photovoltaic (PV) power generation and other renewable energy in the power grid is increasing year by year. Through policy guidance, preferential subsidies and other incentive policies, countries vigorously promote investment in wind power, PV and other renewable energy, develop advanced technology and architecture systems, so as to promote large-scale grid connection of renewable energy (Wen et al., 2008). According to statistics, by the end of 2020, the cumulative installed capacity of global offshore wind power has reached 32.5GW, and 162 offshore wind farms have been put into operation, an increase of 19.1% over the same period at the end of 2018, which indicates the promising prospect of renewable energy power development (Hu and Cheng, 2013; Feng et al., 2015). The variation of installed capacity of offshore wind power in the past decade is shown in **Figure 1**.

The rapid development of renewable energy leads to major changes in the investment scale and asset management mode of power system. In 2019, the annual investment in renewable

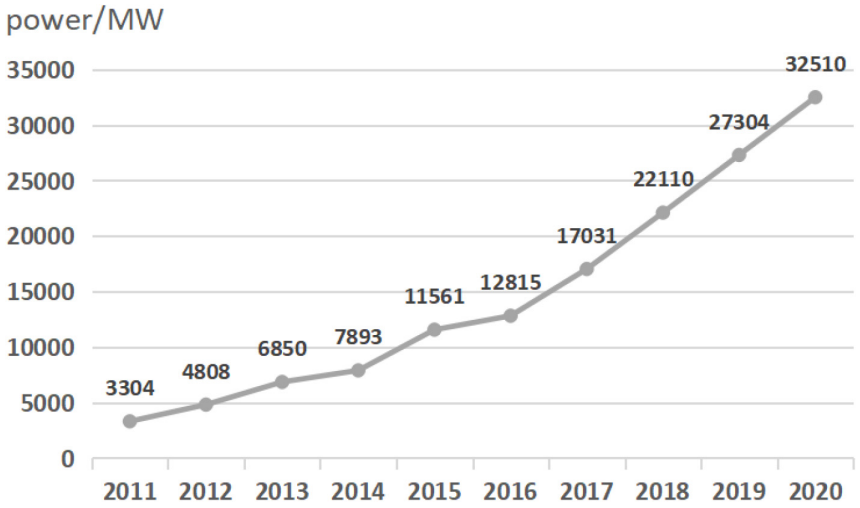


FIGURE 1 | The installed capacity of offshore wind power in the past decade.

energy power in the world reached 53.1 billion United States dollars, and the rapid growth of asset investment greatly promoted the research and development of related technologies and implementation of projects. However, in the process of rapid development of renewable energy, the problem of renewable energy accommodation, such as abandoned wind and solar, is becoming increasingly serious with the disharmony of the spatial and temporal distribution of capacity and load (Hu and Cheng, 2013).

Since 2012, China's installed PV capacity began to grow rapidly. In 2014, accommodation problem caused by this rapid growth began to appear, and the problem of abandoned solar aroused the attention of whole society. Therefore, the power grid needs to further improve the ability to absorb new energy (John, 2017). According to *Information Brief of PV Power Generation Construction from January to September 2015* released by National Energy Administration, cumulative PV power generation in China from January to September was 30.60 billion k·Wh, and PV power abandoning was about 3.03 billion k·Wh, with a solar abandoning rate of 10%. After wind power encountered wind abandoning dilemma, PV power generation also fell into the dilemma of capacity allocation redundancy (Bird et al., 2016). In the development of wind power in the past five years, two phenomena have been accompanied by: (1) the good news of the continuous increase in installed capacity of renewable energy; (2) the dilemma of "abandoned electricity" such as abandoned wind and solar due to insufficient accommodation capacity. The statistics of China's abandoned wind power from 2011 to 2015 are shown in **Figure 2**. From 2011 to the first half of 2015, China's total wind power on grid was 561.774 billion k·Wh, the total abandoned wind power was 80.191 billion k·Wh, and the average abandoned wind rate was 14.27%. In addition, large-scale integration of new energy power generation has made power frequency imbalances increasingly frequent (Basmadjian and Meer, 2018). In the context of China's economy entering the new normal of medium and high-speed growth, the problem of abandoned power has become increasingly prominent (Kasis et al., 2016).

Peak-load and frequency regulation power supplies can well alleviate accommodation problems caused by large-scale grid connection of renewable energy, and Improve system operation level (Chen et al., 2009). Fujian province of China increased the average utilization hours of nuclear power by more than 700 h year-on-year, and without abandoned wind, water, and solar phenomenon, which improve the utilization of electric power production equipment and increase the return on investment (Kasis et al., 2016). Renewable energy power generation investment rise needs to pay attention to equipment management and investment effectiveness (Kasis et al., 2016; Dui et al., 2018). Hence, under the guidance of renewable power investment mode and system, the investment planning for renewable energy industries such as wind power and PV and the asset management of power enterprises should take into account the economy and reliability in full life cycle, so that the huge renewable energy power construction can get a better return on investment (Yildiz and Kazimi, 2006; Spertino and Graditi, 2014). Combined with power equipment management and related technical characteristics in large-scale renewable energy grid connection, this paper explores a refined, multi-angle and strongly related asset cost management mode, which provides an important method channel for the environmental friendliness and green economic function of renewable energy power (Billinton and Huang, 2010; Dui et al., 2018).

Organization of the Paper

The rest of this article is arranged as follows: Section "Power Assets Full Life Cycle Cost Management" summarizes the development process and research status of the whole life cycle cost management of assets and power equipment at home and abroad. Section "LCC Cost Estimation Model" gives the estimation model of power equipment LCC by introducing the structure and estimation method of LCC in detail. Section

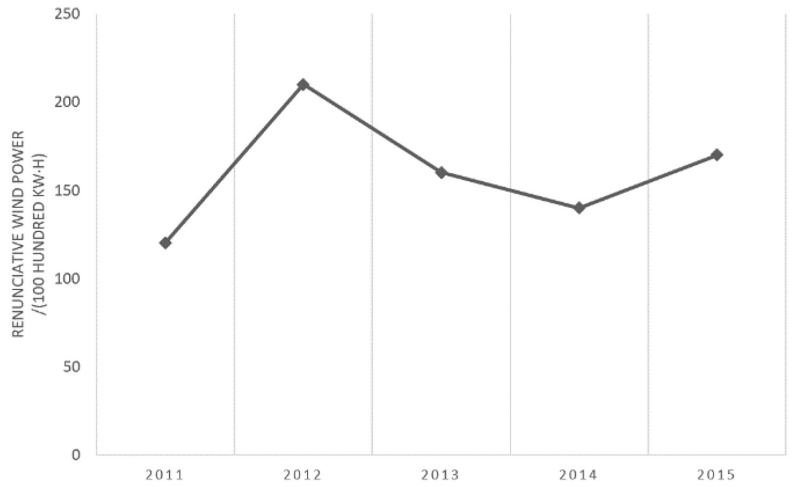


FIGURE 2 | The statistics on abandoned wind power nationwide between 2011 and 2015.

"Conclusion" summarizes the full text and gives the direction of the next stage of research.

POWER ASSETS FULL LIFE CYCLE COST MANAGEMENT

Asset Life-Cycle Cost Management

According to IEC60300-3-3 standard formulated by International Electrotechnical Commission, full life cycle refers to the life cycle stage of equipment, which can be divided into concept and definition stage (Hedley-Whyte, 2000), design and development stage (Arif and Khan, 2010), manufacturing stage (Lee et al., 2016), installation stage (Asiedu and Gu, 1998), operation and maintenance stage (Solomon et al., 2000), and decommissioning disposal stage. Therefore, full life cycle cost (LCC) is the sum of all costs incurred in the above stages. Full LCC occurs in different property rights, which can be seen from the perspective of society (Ozbay et al., 2004), producers and users (Kiritsis et al., 1999; Mascitelli, 2004). From the perspective of asset users, most of the research focuses on the estimation and modeling of product design phase (Park and Simpson, 2003; Liu et al., 2008).

The concept of LCC originated in the United States in 1927 and was proposed by Department of defense (White, 1976; Bajaj et al., 2004). In 1933, the general audit office of the United States formally proposed the concept of LCC for the first time (White, 1976). In the 1960s, this concept was successfully applied to F16 fighters (Yeung et al., 2013). In 1996, the United States Department of defense began to formally study LCC theory, which was first used in the army. Later, Britain, France, Germany and other countries gradually applied LCC theory in the army. With the successful application of LCC theory in the military neighborhood, it gradually gained attention in the civil field (Zhang and Wang, 2012). With the gradual expansion of the application field of the theory, scholars began to focus on engineering design, equipment selection, equipment maintenance, equipment decommissioning and other aspects of extensive and in-depth research.

Literature (Asiedu and Gu, 1998) described the complete steps of LCC theory and gives its reason, content and corresponding model of each step. Literature (Curry, 1989) summarized the life estimation of aerospace electronic equipment by the United States air force using LCC theory, and introduces a standardized evaluation procedure 'STEP.' Moreover, LCC technology is applied to the modernization of aircraft in-flight refueling and electronic system (Woodward, 1997; Seo et al., 2002). In literature (Furch, 2016), LCC theory is applied to establish the railway vehicle model, and the cost calculation formula of each stage is given. Besides, a prediction method for full life cycle scrap time of electronic components is established, a series of quantitative market or technical attributes were identified and obtained, and the scrap time of components was calculated by statistical method (Solomon et al., 2000). In addition, LCC analysis is carried out for the components of energy meter and resonant circuit in power system (Meyer and De Doncker, 2006; Cai et al., 2011). Literature (Nilsson and Bertling, 2007; Tian et al., 2011; Shafiee et al., 2016) applied LCC theory to wind power industry, and literature (Tian et al., 2011) established condition monitoring systems (CMS) based on LCC, which can reduce indirect damage in case of failure and provide favorable conditions for maintenance plans. Furthermore, it presents a LCC analysis strategy and employs CMS to improve the single wind turbine maintenance plan for onshore and offshore wind farms (Nilsson and Bertling, 2007). In literature (Shafiee et al., 2016), a wind farm investment cost regression model based on commodity price and seawater depth is proposed to estimate the accurate LCC.

In the fierce global competition environment, world-famous electric power enterprises have realized the importance of asset management for enterprise development, as well as electric power industry is also constantly exploring the full life cycle management and application of assets (Shahidehpour and Ferrero, 2005), so as to promote the maximum efficiency of

assets and serve the development of enterprises. Particularly, LCC theory has been gradually promoted and applied in the electric power industry.

National Grid Corporation of United Kingdom has integrated some intelligent management tools into daily management, established a complete set of asset management information sharing platform, among which project management, production operations, maintenance, and other fields are associated, finally achieve data integration, according to the need to generate various reports for reference of all kinds of managers.

In the late 1990s, Canada's Hydro One introduced the concept of asset full life cycle management and established a complete set of asset evaluation methods (Danish et al., 2014). In addition, it is worth noting that this company's asset management business has selected professional outsourcers to be responsible for the management of some assets, which not only saves the management workload of the main business personnel, but also improves the asset management level.

Ashburton Power Company of New Zealand makes a specific asset plan before making a clear investment objective, comprehensively considering all aspects of power grid planning, equipment transformation, maintenance and so on. Secondly, based on equipment condition and load forecast, the investment plan is optimized and analyzed. Finally, the information system is adopted to analyze how to achieve the optimal unit cost in the whole process of asset procurement, construction, operation and maintenance, transportation and scrapping.

Given the current situation of the power sector in Afghanistan, for improving the electricity environment in rural and remote areas, LCC theory is introduced to establish a cost-effective hybrid system. In 2004, International Power System Conference advocated that equipment manufacturers provide management reports for full life cycle of equipment and products (Lombardi, 2003; Joseph et al., 2018). As a result, world's major electrical equipment manufacturers, such as ABB Group and Siemens, began to study full life cycle management of their products (Zhang and Cai, 2014; Zakeri and Syri, 2015). In 2005, representatives of more than 50 countries and regions, including the United Kingdom and Norway, established international organizations of asset LCC (Steen, 2005).

The asset management of international advanced electric power enterprises is aimed at minimizing the life cost of assets and maximizing the investment value: (1) pay attention to the analysis of investment in the early stage and determine the investment strategy through the optimal rating; (2) determine the health condition of the assets by rating them and determine their disposal methods to achieve the highest utilization rate; (3) the employ of information means to achieve assets procurement, construction, operation and maintenance, return and scrap of full life cycle management.

Overview of Power Equipment Life Cycle Management

In literature (Shi et al., 2009), taking a 220 kV heavy load substation as an example, considering the loss of social output value, the comprehensive economy of full life cycle of substation construction is calculated and compared, which concludes that the scheme has the best reliability and economy is obtained.

Literature (Kim et al., 2010) establishes a two-dimensional model of power system LCC for the drawback that the application of power system LCC is traditionally limited to specific equipment or stage, in which research status of LCC technology is reviewed. The cost breakdown structure is described in detail from the device level and the system level. Besides, the maintenance cost of the combination of reliability-centered maintenance (RCM) and fault repair (overhaul) is also analyzed. On this basis, some studies have also proposed a component-cost-time 3D model (Luo et al., 2011).

Literature (Cai et al., 2011) analyzed the latest progress in LCC technology, problems that should be paid attention to and several suggestions for the management of LCC. A full LCC-benefit model for energy-saving transformation of distribution network is established in literature (Karamouz et al., 2017), in which a decision method considering financial and technical constraints is proposed. It is effective to apply the model and method to the actual distribution network transformation. Besides, in order to overcome the problem of neglecting the medium and long-term cost and underestimating the short-term investment in the current economic evaluation of power system, a three-dimensional LCC model of the whole power system is established from the perspective of component dimension, cost dimension and time dimension. Through the analysis of the structure of the device layer, a series of economic evaluation strategies based on LCC are proposed, and the transformation of devices with different lifetime is studied Change the cycle (Liu et al., 2012).

At present, the practice of asset LCC management mainly focuses on the following two forms:

The first is to seek a new breakthrough in asset management mode based on the cost management of full life cycle of assets. It mainly standardizes asset management through management means such as internal rules and regulations or norms of enterprises, and integrates cost management concepts into daily management, such as optimizing design schemes, equipment selection, cost schemes and other efforts to achieve the goal of the lowest asset cost of equipment or system.

Second, relying on the information system to achieve asset life cycle cost management. The labor of asset management is huge, which makes it cumbersome, time-consuming and prone to human errors. The establishment of a new information platform can break the departmental barriers, connect the processes of asset planning, design, construction, operation and maintenance, return and scrap, so that realize the cooperation of each module. The full life cycle management of assets is realized. Through the strict management of the full life cycle cost of equipment, the links of material procurement, equipment collection, financial settlement and payment are strictly controlled. The original mode of extensive management and information isolation is changed, and the equipment asset management information system of real-time dynamic and fine management is established. However, due to equipment defect state maintenance, risk assessment lacks support, which cannot provide decision-making basis for equipment overhaul and technical reform. At the same time, because of lack of effective assessment and assessment

means, as well as lack of quantitative assessment indicators for equipment and management, resulting in most of the current power enterprises still cannot solve the contradiction between low cost and high utilization of assets.

Asset management is no longer the management of a certain link, but the management of full life cycle of the equipment, which makes the asset management more scientific and makes the equipment achieve the optimal cost in full life cycle (Li et al., 2018; Orfanos et al., 2019). At present, the management mechanism of power grid companies has been difficult to meet the needs of the rapid development of power grid. It is urgent to transform and improve the asset management model, promote the information and digitization of asset management, and accelerate the construction of world-class power grid. Therefore, the research significance of asset life cycle management is as follows:

Firstly, it should not only implement the national strategy and enterprise strategy and continuously improve the sustainable development ability of power grid, but also vigorously promote the high-quality development of power grid and build a world-class energy internet enterprise. The concept of asset management is the source of exerting asset management efficiency and improving asset management capabilities. It plays an important role in improving the overall asset management performance of the enterprise. Enterprises must introduce advanced asset life cycle management concepts.

Secondly, enterprise asset life cycle management is not only a process of concept innovation, but also a process of technology application. By employing asset life cycle management technology, the asset life cycle resource value and asset utilization efficiency of power grid enterprises can be improved.

Thirdly, asset life cycle management concept determines the direction and content of asset management decision-making of power Grid Company, which has macro guiding significance.

Fourthly, the large scale, wide distribution and variety of assets of power grid companies increase the difficulty of life cycle management of assets of power grid companies. Power grid companies must innovate the concept of asset management, apply the full life cycle theory to asset management, take the full cost management of assets within the full life cycle as the basis for management decisions, and pay attention to the long-term nature and efficiency of asset management, which is an innovation of the traditional asset management concept (Liu et al., 2012).

LCC COST ESTIMATION MODEL

Since the concept of LCC is applied soon, there is no correlation between the historical data of relevant asset management systems of all enterprises, and the data of full life cycle is missing. Besides, the cost of equipment assets operation and maintenance can only be counted according to the management units, and cannot be collected into the equipment and the current situation of basic data cannot meet the requirements of efficient asset management (Xu and Wang, 2011). Therefore, it is necessary to estimate the assets of power system, and then estimate LCC (Liu et al., 2012; Lee et al., 2020). LCC estimation also estimates the possible LCC in the future, which is related to the establishment of budget (Savoretti et al., 2017), quotation generation (Govil, 1984) and development strategy (Govil, 1985), which is an indispensable part of the cost efficiency (reliability) evolution model in engineering (Yang et al., 2017).

The LCC estimation method is mainly established and implemented around the cost structure of the research target equipment. A reasonable estimate of the cost of the entire life cycle of the equipment is made in the form of engineering standards, and a targeted estimation method is used in conjunction with the composition of the entire life cycle of the equipment. Through the integration of various methods and cost components, a unified and comprehensive LCC estimation model is formed. In the process of establishing and revising the estimation model, the cost calculation of a single device is realized through accounting, statistics, and apportionment of various costs based on the current data situation. Taking into account the importance and value of the equipment, the LCC estimation work uses the method of setting the correction coefficient matrix to characterize the equipment difference, and the LCC estimation model is constantly revised and improved in the long-term work by mathematical checking and empirical judgment.

Structure Composition of LCC

Based on the full life cycle management requirements and operational characteristics of the research equipment, the cost structure of each part of the equipment LCC is decomposed. In terms of selecting equipment to be studied, this article takes important equipment such as transformers, generators, and circuit breakers in the power supply equipment of the power system as the main research objects. The above important equipment occupies an important position in the operation of the power grid and has a relatively comprehensive and highly targeted Cost management process. According to the equipment survey results, combined with the current status of equipment cost management in the power grid and advanced LCC theory, the cost structure based on the LCC management method mainly includes investment costs, operating costs, maintenance costs, failure costs, scrap costs, etc. Decompose the cost of each part of LCC, and its cost structure is shown in **Figure 3**.

Particularly, relevant cost breakdown of LCC can be computed by:

$$LCC = CI+CO+CM+CF+CD \tag{1}$$

where CI represents cost of investment; CO means operating cost; CM denotes maintenance cost; CF stands for fault cost; CD is abandon cost.

These costs can also be further broken down into sub costs, as mentioned above, LCC is related to future costs, and when the time value of funds is considered (Bastian, 2011), the cost incurred in the future shall be reduced and corrected multiply by $\left(\frac{1+r}{1+K_{cpi}}\right)^{year_i}$, where K_{cpi} represents CPI index, which reflects inflation; r denotes discount rate, and $year_i$ means service years.

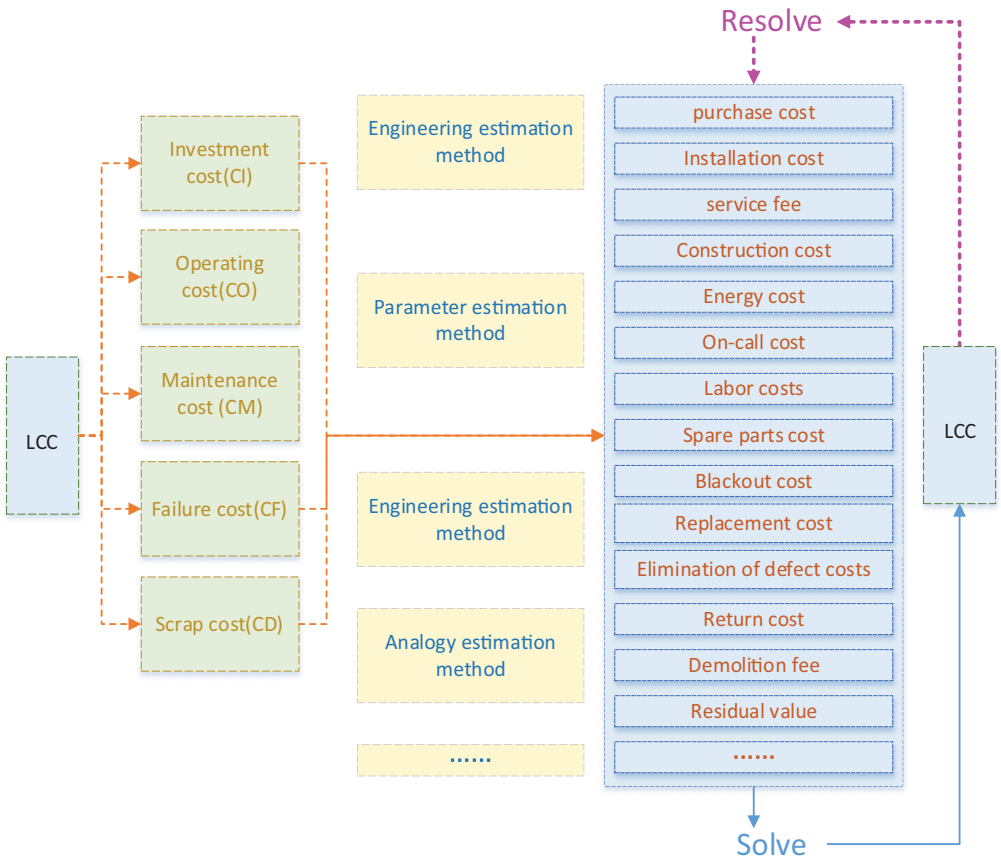


FIGURE 3 | Cost breakdown structure.

Some studies also put forward the environmental cost (Li et al., 2018), but for power supply of peak-load and frequency, it is relatively clean, so this item cannot be considered.

Estimation Method

The research object of LCC estimation is capital invested in the future (Lee et al., 2020). Through estimation of capital to be invested, it provides an important basis for economic judgment and final decision-making of the scheme (de Jong and Declercq, 2012). LCC estimation is the key content of LCC technology research and the basis of technology application.

Some studies believe that there are two main channels for data collection: professional manufacturers and suppliers, and historical data (Schneiderova-Heralova, 2018). The amount of data and information obtained determines the cost estimation method used. Besides, there are two kinds of estimation methods: certainty and uncertainty. For the former, there are more evaluation models (Cole and Sterner, 2000; Vahdat-Abouesshagh et al., 2014); for the latter, there are Monte Carlo method (Ammar et al., 2013; Goh and Sun, 2016), fuzzy set method (Shahata and Zayed, 2013; Plebankiewicz et al., 2020) and neural network (NN) (Ilg et al., 2017). For the existing asset estimation methods, the accuracy of LCC model depends on the choice of calculation method and the certainty of data. LCC of power system in estimation scheme at present is very diverse. In view of the different stages of development and enterprise data types can be estimated according to the advantages and disadvantages of the scheme selection. Defects of technological level is that the barriers to a large amount of data is temporarily unable to break in the process of cost separating, and partly by artificial decomposition cost reimbursement need to upload the data to the cloud, the time cost and the statistical labor costs rose, as a result, the unity of the intelligent data analysis big data platform construction is the core content of LCC technology, in combination with the discussion of data and analysis the process needed a big enterprise data platform construction. Therefore, the content of data application construction is not discussed. This paper only discusses the system framework and model application established by LCC asset management. The estimation methods applied in the big data analysis platform are introduced as follows:

Gray Fuzzy Estimation Method

Gray fuzzy estimation method (Chen and Ren, 2018) is that when some evaluation indexes cannot be accurately quantified, interval fuzzy method is usually used to evaluate the risk of contractor selection and installation construction unit selection. Fuzzy algorithm combines expert evaluation, fuzzy interval setting and other methods to integrate and calculate the evaluation opinions

given by multiple experts by the evaluation registration (Miah et al., 2017), so as to obtain the comprehensive evaluation of the risk of contractor or supplier selection, and formulate the cost quantification strategy based on the risk level.

Parameter Estimation Method

Parameter estimation, which is based on a lot of historical cost data of similar equipment, selection of sensitive to cost several main physical parameters and performance features, then employing the regression analysis, gray system and neural network data processing method to set up the mathematical relationship of cost between the parameters, so as to estimate LCC or estimate the cost of a main unit. The first task of establishing the cost parameter relationship is to determine which characteristic quantity the cost is related to. In this method, the most important link is the database (Wang et al., 2013). Database must meet some specific requirements, such as establishing related connections for similar power equipment, in which each similar data unit should be composed of similar components and be processed consistently in the same way, that is, to ensure comparability. Otherwise, it will lead to obvious deviations in the estimation relationship, or even unreliable.

With the continuous accumulation of data, the model can be modified, and the more the model is used, the higher the accuracy will be. Therefore, this method is most widely used in LCC estimation, in which full LCC can be approximately related to quality, yield, performance and other characteristic variables. Compared with analogy estimation method, parameter estimation method reflects the relationship between cost and attribute. Therefore, as long as get the value of some of attribute parameters of complex system, it only needs to input the characteristic quantity to calculate the cost of the equipment at this stage. Then according to equipment reliability, maintainability and other parameters calculate the cost of operation, maintenance and scrap recovery phase, so as to obtain LCC. This method is the most commonly used cost estimation method in the early stage of full LCC analysis, especially in the absence of detailed planning and design specifications. Another advantage of establishing this kind of cost parameter relation is that it can quickly estimate the influence of the change of power equipment performance or some characteristic parameters on cost, so as to evaluate the influence of cost when the scheme is chosen during the planning and design and when the scheme is changed.

The calculation equation of parameter estimation method can be expressed as follows:

$$C_2 = C_1\left(\frac{S_2}{S_1}\right)^n C_F \tag{2}$$

where C_1 represents actual engineering costs of similar projects; C_2 denotes costs required for the proposed project; S_1 means production scale of similar projects; S_2 stands for production scale of the proposed project; C_F represents price conversion index; and n denotes production scale index.

The value of n: the scale is enlarged, mainly with the increase of equipment capacity, n is 0.8∼0.9; for high-pressure equipment, n is 0.3∼0.5, and usually the average value of n is about 0.6. Therefore, this estimation method is also called 0.6 index method. However, there are obvious drawbacks to this approach. First of all, it needs a lot of historical data, which is almost impossible to obtain detailed historical data since the LCC management of power companies started late. Secondly, the model established by this method only represents the law of changes in the past costs. The period of power system engineering is large, and the geographical gap between regions is also large. These differences will lead to an increase in the error of estimation model and affect decision-making. Furthermore, comparing the various attribute parameters of a complex system, parameter estimation model only relies on limited and easily measurable parameters for cost estimation, and does not consider various situations in detail. It is generally used in the early development stage of complex system, when there are only system specifications but no detailed planning and design specifications, especially when the power equipment is not standardized. The reasonable degree of the model established by the parameter estimation method depends on the staff's understanding of the system and their modeling experience and skills. The prediction accuracy is highly subjective, and this method is no longer applicable when the new system adopts advanced development and production technology.

Engineering Estimation Method

Engineering estimation method is a traditional cost estimation method, also known as detailed estimation method or bottom-up method. It uses work breakdown structure to calculate each cost unit item by item from bottom to top, and then add item by item to get the total LCC (Ilg et al., 2017). Besides, engineering estimation method divides the research object into different sub-parts, and carries on the cost estimation, respectively, according to different characteristics of the parameters of each part. Finally, the estimated value of each part is summed up to obtain the total LCC. This estimation method is generally used in planning, development and production of research objects. With the accumulation of analysis, more and more data support for estimation, and the result of estimation becomes more and more accurate. It starts from the lowest level work unit, calculates LCC item by item from bottom to top by using work breakdown structure, sums up the cost of each work unit in the system, and then obtains the value of the upper-level cost unit item by item, and finally obtains LCC.

When applying engineering estimation method to calculate cost of each unit, it is necessary to collect detailed data information about the relevant costs. It is not difficult to observe that the advantages of this method are detailed and specific, with high estimation accuracy, but the disadvantages are cumbersome, time-consuming, heavy workload and complex calculation process. Therefore, this method can only be adopted after detailed design and mastering the relevant information of the equipment and the cost of its use and maintenance, which can be used to estimate the cost of some decision-making problems in the later stage.

Its mathematical model can be expressed as:

$$C = C_1 + C_2 + \cdots + C_n \tag{3}$$

where C represents LCC; and C_i denote cost of each unit at different stages.

The cost of each unit can be further divided into sub-units to form a complete cost breakdown structure diagram of the equipment, so as to obtain the estimated value of the total cost. This method is a detailed estimation method, its accuracy is directly related to the amount of information obtained, and is generally used in the later stage of the project.

Analogy Estimation Method

Analogy estimation method is a method to estimate LCC of equipment by referring to the known cost information and other data of similar equipment. Based on the existing data of similar equipment, the equipment to be built is compared with it, and the fixed coefficient value is taken according to the characteristics of the latter to estimate its cost. Analogical estimation method is generally used in the early stage of equipment life, and its accuracy depends on expert experience.

When the data of similar power equipment is relatively reliable and the database is complete, this method is a more suitable estimation method. In most cases, it is used in the early planning and design stage of LCC to preliminarily estimate full LCC of power equipment.

It is a method to estimate the cost of the target equipment by comparing known information of the same type of equipment. Particularly, the implementation steps are as follows: firstly, select the sampling equipment, and the key parameters of the sampling equipment shall be the same as the existing equipment, and then compare the existing equipment with the sampling equipment. During the comparison, the characteristic parameters of the existing equipment can be set according to the different points between the equipment. Finally, LCC is obtained through comparing the characteristic parameters with the historical values of the sampling equipment. As the key part of the analogy method, the characteristic parameters in the actual use, usually call some experts, comprehensive research and judgment after the value, so the analogy method is also known as the expert method. This method is mainly employed in the planning and feasibility study stage at the initial stage of engineering construction, which applies to the situation that the data of similar projects are more accurate and detailed.

Moreover, it is a method to estimate LCC by referring to the cost data of completed projects similar to construction projects (Angelis and Stamelos, 2000; Steinert, 2009). Employing the analogy method to calculate the cost is mainly to use the cost data of similar projects, and select the correlation coefficient to correct according to the specific situation, so as to accurately estimate the cost of the proposed project. The selection of correlation coefficient is very important, which is generally determined by consulting experts. Its mathematical model can be expressed as:

$$C = C_0 \sum_{i=1}^{n} a_i K_i \tag{4}$$

where C denotes cost of proposed project; C_0 represents cost of similar projects; a_i stands for the proportion of labor cost, material cost and procurement cost in the total cost of similar projects; K_i means the correlation coefficient of labor cost, material cost and purchase cost between the proposed project and similar project.

The analogy method estimates the cost based on the cost of similar products or technologies in the past. Besides, this method updates the historical data to reflect the impact of rising costs and technological progress, which is suitable for cost estimation with historical data and actual data reference.

Neural Network Method

Artificial neural network (ANN) has been studied since the early 1940s, which is an intelligent computing system that simulates a biological NN with a computer network system. Furthermore, ANN can simulate some unique behaviors of the human brain, such as learning, memory, and recall, through self-learning, self-organization, self-adaptation, and nonlinear dynamic processing. The main advantages of NN estimation method are as follows: because ANN owns self-learning function, through the network data training, it can quickly and accurately simulate the results, so it does not need to establish a specific mathematical model of the cost. There are many uncertain factors, such as different electrical parameters, equipment operating conditions, climate, policies, etc., in LCC estimation of power transformers, so it is more accurate and objective to use neural network to calculate.

However, NN estimation method also has certain shortcomings: a large amount of historical data of power transformers is required during model training, and this data is often lacking in practical applications; the choice of hidden layers does not have a very scientific basis, which can be determined after trial calculation; it is not easy to obtain the sensitivity of the key factors of LCC of power transformers.

Activity-Based Costing Method

Activity-based costing (ABC) is employed to calculate the cost of the equipment by summing up the activities related to the power equipment (Özbayrak et al., 2004; Karim et al., 2012). Based on historical information or estimated data, it first calculates the unit cost of each activity, and then calculates the activity consumed by new equipment, multiplying the two to get the total cost of power equipment (Waghmode and Sahasrabudhe, 2012; Bierer et al., 2015). It is mainly used in the later stage of LCC. The practical operation steps are as follows: ① select the main activity; ② collect the cost of resources to the homogeneous cost base; ③ select the cost driver; ④ calculate the allocation rate of each cost base; ⑤ allocate the collected cost in each cost base to power equipment according to allocation rate of cost base; ⑥ summarize and calculate the total cost of power equipment. The main problem of this method is that it is not easy to obtain unit activity cost (Ben-Arieh and Qian, 2003).

Case-Based Reasoning Method

In short, case-based reasoning method (CBR) adopts past problem-solving methods to deal with new problems (Ji et al., 2012). Its main spirit lies in how to systematically preserve and deal with the previous problem-solving knowledge and experience, in order to solve the new or repeated problems encountered, so as to reduce the mass of information, avoid

repeated process load. At the same time, CBR can accumulate experience. Each time a problem is solved, the new experience is saved. Nearest neighbor technique is probably the most widely used technique in CBR. For each case attribute, determine the similarity between the problem (target) case and the cases in the case base. This measure can be multiplied by a weighting factor. The similarity sum of all attributes is then calculated to provide a similarity measure between the case in the library and the target case.

The estimation range of LCC in CBR is limited by sample value and cannot be extrapolated, but its characteristic parameter quantity is independent of sample size. That is, the number of feature attributes can be increased a lot. Besides, it doesn't need to judge the number of feature coefficients by considering the number of samples. Moreover, CBR method is simple and can obtain superior estimation results.

Expert Estimation Method

Expert estimation method is the estimated value of full LCC of equipment based on expert experience judgment, which is the application of Delphi method in the prediction technology in cost estimation (Steinert, 2009). When using the expert estimation method, a certain number of experts independently estimate the corresponding equipment, and then synthesize them to obtain the estimated cost of equipment. Particularly, expert estimation method is generally adopted in the absence of data or the difficulty of collection, and the insufficient number of statistical samples, as well as employed as an auxiliary estimation of other estimation methods. Its mathematical model can be expressed as follows:

$$C = \frac{\sum_{i=1}^{n} C_i}{n} \tag{5}$$

where C denotes the estimated value of cost unit, here the average value is taken; C_i is the estimated value of the ith expert for cost unit; and n is the number of experts participating in the estimation.

Blind Number Theory Estimation Method

Blind number theory estimation method is to comprehensively consider the attributes and characteristics of various uncertain information from the initial purchase to the later decommissioning process, and make a reasonable evaluation of the uncertain information, so as to determine the blind number expression of full LCC (Liming and Bo, 2020).

Blind number expressions are expressed by the following equation:

$$f(x) = \begin{cases} a_k,\ x = x_k\ (k = 1, 2, \cdots, n) \\ 0,\ \text{otherwise} \end{cases} \tag{6}$$

where a_k indicates the reliability of a blind number; $x = x_k$ represents a possible value or range of possible values for a blind number.

Compared with traditional deterministic LCC calculation method, LCC method based on blind number theory can't only calculate the expected value of LCC, but also obtain possible distribution intervals of different costs and corresponding credibility information, so as to improve the rationality of estimation results.

Comparison of Various Estimation Methods

The purpose and precision of LCC estimation vary greatly in different stages due to variety and complexity of power equipment. Therefore, LCC estimation methods and models are not invariable, and different estimation algorithms are needed according to characteristics of collected historical data. Particularly, it concluded characteristics of different estimation methods, as shown in **Table 1**.

The focus of this part is to analyze and evaluate the most suitable and accurate LCC evaluation method according to different equipment categories, different equipment life stages and different data conditions.

In big data era, LCC estimated model at technical level can be combined with the deep learning framework to forecast, should not satisfy with the traditional estimation method, cyber-physical system and knowledge graph is the future of artificial intelligence in an important direction in big data analysis scenarios, the LCC estimation in the new method of artificial intelligence can be used on innovation breakthrough.

LCC Estimation Model of Power Assets

According to cost estimation model of different life cycle stages of power assets, LCC of power assets is estimated. The following is the detailed scheme of LCC cost structure separation to point out the data path and separation ideas, and the LCC cost reduction formula for a supplementary explanation. The cost mapping relationship of each cycle in cost collection and estimation is explained. As for the content of mutual diffraction in the cost of each life cycle, it is a reasonable method to establish the standard of cost calculation system within the stage to solve the superposition effect of cost. The content of LCC cost estimation standard is introduced as follows.

Investment Costs

The cost of investment and construction from start of planned construction to formal operation (excluding subsequent technical reform) mainly includes:

$$CI = C_{\text{purchase}} + C_{\text{installation}} + C_{\text{construction}} + C_{\text{field service}} \tag{7}$$

where C_{purchase} denotes purchase cost; $C_{\text{installation}}$ represents installation cost; $C_{\text{construction}}$ means construction cost; and $C_{\text{field service}}$ stands for field service cost.

Operating Costs

Operating costs can be expressed as follows:

$$CO = C_{\text{energy}} + C_{\text{duty}} \tag{8}$$

where C_{energy} represents energy cost; and C_{duty} denotes on-duty cost.

TABLE 1 | Summary of characteristics of different estimation methods.

Methods	Uncertainty	Application phase	Accuracy	Historical data
Parametric estimation method	Medium	Early stage	Medium	Many
Engineering estimation method	Low	Mid-late stage	High	Many
Analogy estimation method	High	Early stage	Low	Average
Neural Network method	medium	early stage	high	many
Expert estimation method	High	Early stage	Low	Few
Blind number theory estimation method	Medium	Early stage	Low	Fewer

Maintenance Costs

Maintenance costs can be computed by:

$$CM = C_{\text{labor(CM)}} + C_{\text{supply(CM)}} + C_{\text{spare(CM)}} \quad (9)$$

where C_{labor} represents labor costs; and C_{supply} denotes supply cost; and C_{spare} means spare cost.

Fault Costs

Fault costs can be expressed by:

$$CF = C_{\text{blackout}} + C_{\text{replace}} + C_{\text{deficiency}} + C_{\text{withdrawal}} \quad (10)$$

where C_{blackout} means power blackout cost; C_{replace} denotes equipment replace cost; $C_{\text{deficiency}}$ represents deficiency cost; and $C_{\text{withdrawal}}$ means withdrawal cost.

Discard Costs

Discard costs can be computed by:

$$CD = C_{\text{scrap}} + C_{\text{residual value}} \quad (11)$$

where C_{scrap} means scrap cost; and $C_{\text{residual value}}$ denotes residual value.

Recoverable costs can be estimated by parameter estimation: residual value is approximately equivalent to the product of the weight of steel and its price, or the original value of the equipment is added with a proportional coefficient.

Asset management system of project cost detail work, there are detailed classification is too rough form, it fails to meet the project cost to carry out the elaboration to the equipment and component levels of business requirements, therefore the present solutions for the project was obtained from the financial management system of financial course code and cost detail, after the model to further improve the account of the project cost, for the enterprise of the management system of data interface, after the export project cost detail, project data cleansing, obtain the LCC cost collects the required at all levels in different stages of the data.

Reliability Evaluation of LCC Estimation Method

In the construction of the theoretical model, must be based on historical data, using the total life cycle cost calculation model, calculation and analysis on specific historical node balance data, and combining with the investment cost is the subsequent comprehensive analysis comparison, the calculation model of correction methods, to ensure the effectiveness and reliability of the final model in the actual production. That is, with the application of the system, the model algorithm can be modified in real time by comparing the difference between the actual cost accounting and the data platform estimation model.

The model constructed by historical data predicts the situation of the plant or similar projects in the same area in the same period, and compares the actual data to verify whether the error between the calculation results of the model and the actual results is within a certain allowable range. If so, the model is accurate. On the contrary, it is necessary to consider revising or even changing the model, and study two ways of revising the model based on the revision method of years and the revision method based on economic parameters.

The cost structure split based on the whole life cycle management method basically includes the economic investment generated in equipment management. The LCC management method implemented around the cost structure needs to be adjusted in conjunction with the data foundation and the characteristics of the equipment object, and the cost structure is increased or decreased and optimized when necessary to ensure that the economic indicators of the equipment are comprehensively and systematically considered in the implementation of the LCC management.

CONCLUSION

Combined with LCC analysis of power assets, full LCC management method is adopted for peak-load and frequency regulation enterprises, which can't only be adopted for project cost budget, but also better guide a safe production and reliable operation, such as procurement, maintenance and scrap planning, as well as risk control.

In the application of full life cycle management, necessary data and information should be obtained to decompose each stage according to different costs, calculate appropriate estimation model, and collect from upper-level step by step to estimate final full LCC. Considering the time value of the capital, future-oriented full LCC needs to be converted into current-oriented value to facilitate the comparison and analysis of different schemes.

Since the transparency of data and information in different stages of full life cycle is different, various estimation algorithms should be carefully selected according to the characteristics of each period. At the same time, there are errors in estimation,

so the value of such uncertainty needs to be recognized. In the research, it is necessary to focus on the important systems and equipment, take the 20–80 principle as the analysis standard, and reasonably consider the research scope and precision of the equipment cost. The equipment content of asset management should be classified as primary and secondary in the classification of the equipment tree, and the importance level of the equipment should be divided. The equipment content with higher importance should focus on the evolution process of cost efficiency of LCC. The overall goal of power equipment cost model estimation is to have the lowest LCC of power equipment in the whole life cycle, and the goal of each stage is to have the lowest cost of each stage under the condition of meeting the total goal. Therefore, the target value of the consumption cost of each stage can be established to provide reference for the management mode of each stage of power equipment.

To sum up, the implementation of LCC needs to establish a complete database, a scientific decomposition mechanism, an appropriate estimation model and cooperation between various departments, which aims to improve accuracy of full LCC estimation and guide a satisfactory management of assets with a high assets efficiency.

Therefore, future research will focus more on improving the asset management level and the accuracy of the estimation model, and on this basis, consider a better combination of cost and efficiency. This is the next direction of work.

AUTHOR CONTRIBUTIONS

KW contributed to conceptualization. YL contributed to data curation and writing. XW contributed to formal analysis. NY contributed to funding acquisition. SY contributed to methodology. ZZ contributed to project administration. YW and TY contributed to resources. ZH contributed to visualization. All authors contributed to the article and approved the submitted version.

ACKNOWLEDGMENTS

The authors gratefully acknowledge the support of the analysis and research of power generation equipment management decision model based on LCC (STKJXM20190123).

REFERENCES

Ammar, M., Zayed, T., and Moselhi, O. (2013). Fuzzy-based life-cycle cost model for decision making under subjectivity. *J. Constr. Eng. Manag.* 139, 556–563. doi: 10.1061/(asce)co.1943-7862.0000576

Angelis, L., and Stamelos, I. (2000). A simulation tool for efficient analogy based cost estimation. *Empir. Softw. Eng.* 5, 35–68.

Arif, M., and Khan, M. E. (2010). Design and life cycle cost analysis of a SAPV system to electrify a rural area household in India. *Curr. World Environ.* 5, 101–106. doi: 10.12944/cwe.5.1.15

Asiedu, Y., and Gu, P. (1998). Product life cycle cost analysis: state of the art review. *Int. J. Prod. Res.* 36, 883–908. doi: 10.1080/002075498193444

Bajaj, A., Kekre, S., and Srinivasan, K. (2004). Cost and schedule performance in design and manufacturing management science. *Manag. Sci.* 50, 527–536. doi: 10.1287/mnsc.1030.0177

Basmadjian, R., and Meer, H. (2018). A heuristics-based policy to reduce the curtailment of solar-power generation empowered by energy-storage systems. *Electronics* 7, 349–370. doi: 10.3390/electronics7120349

Bastian, N. D. (2011). Optimizing army sustainability at fort bragg: a case study connecting life-cycle cost analysis with leadership in energy and environmental design for existing buildings. *Eng. Manag. J.* 23, 42–54. doi: 10.1080/10429247.2011.11431894

Ben-Arieh, D., and Qian, L. (2003). Activity-based cost management for design and development stage. *Int. J. Prod. Econ.* 83, 169–183. doi: 10.1016/s0925-5273(02)00323-7

Bierer, A., Götze, U., Meynerts, L., and Sygulla, R. (2015). Integrating life cycle costing and life cycle assessment using extended material flow cost accounting. *J. Clean. Prod.* 108, 1289–1301. doi: 10.1016/j.jclepro.2014.08.036

Billinton, R., and Huang, D. (2010). Wind power modelling and the determination of capacity credit in an electric power system. *Proc. Inst. Mech. Eng.* 224, 1–9. doi: 10.1243/1748006xjrr266

Bird, L., Lew, D., Milligan, M., Carlini, E. M., Estanqueiro, A., and Flynn, D. (2016). Wind and solar energy curtailment: a review of international experience. *Renew. Sustain. Energy Rev.* 65, 577–586.

Cai, Y. Z., Liu, L., Cheng, H. Z., Ma, Z. L., and Zhu, Z. L. (2011). Application review of life cycle cost (LCC) technology in power system. *Power Syst. Protect. Control* 39, 149–154.

Chen, H., Cong, T. N., Yang, Y., Tan, C., Li, Y., and Ding, Y. (2009). Progress in electrical energy storage system: a critical review. *Prog. Nat. Sci.* 19, 291–312. doi: 10.1016/j.pnsc.2008.07.014

Chen, L., and Ren, J. (2018). Multi-attribute sustainability evaluation of alternative aviation fuels based on fuzzy ANP and fuzzy grey relational analysis. *J. Air Trans. Manag.* 68, 176–186. doi: 10.1016/j.jairtraman.2017.10.005

Cole, R. J., and Sterner, E. (2000). Reconciling theory and practice of life-cycle costing. *Build. Res. Inform.* 28, 368–375. doi: 10.1080/096132100418519

Curry, E. E. (1989). STEP: a tool for estimating avionics life cycle costs. *Aerosp. Electron. Syst. Magazine IEEE.* 4, 30–32. doi: 10.1109/62.16986

Danish, M. S. S., Yona, A., and Senjyu, T. (2014). Pre-design and life cycle cost analysis of a hybrid power system for rural and remote communities in Afghanistan. *J. Eng.* 2014, 438–444. doi: 10.1049/joe.2014.0172

de Jong, M., and Declercq, K. (2012). Economic evaluation of urban track systems: integration of life cycle costs and socio-economic assessment. *Proc. Soc. Behav. Sci.* 48, 1264–1273. doi: 10.1016/j.sbspro.2012.06.1102

Dui, X., Zhu, G., and Yao, L. (2018). Two-stage optimization of battery energy storage capacity to decrease wind power curtailment in grid-connected wind farms. *IEEE Trans.Power Syst.* 33, 3296–3305. doi: 10.1109/tpwrs.2017.2779134

Feng, Y., Lin, H., Ho, S. L., Yanc, J., Dong, J., and Fang, S. (2015). Overview of wind power generation in China: status and development. *Renew. Sustain. Energy Rev.* 50, 847–858.

Furch, J. (2016). A model for predicting motor vehicle life cycle cost and its verification. *Trans. FAMENA*. 40, 15–26.

Goh, B. H., and Sun, Y. (2016). The development of life-cycle costing for buildings. *Build. Res. Inform.* 44, 319–333.

Govil, K. K. (1984). New analytical models for logistics support cost and life cycle cost vs reliability function. *Microelectron. Reliabil.* 24, 61–63. doi: 10.1016/0026-2714(84)90638-3

Govil, K. K. (1985). Optimum design of reliable systems for specified life cycle cost. *Microelectron. Reliabil.* 25, 239–241. doi: 10.1016/0026-2714(85)90007-1

Hedley-Whyte, J. (2000). Standardization of interface design for medical devices: international electrotechnical commission and international organization for standardization medical alarm systems. *Hum. Fact. Ergon. Soc. Annu. Meeting Proc.* 44, 215–218. doi: 10.1177/154193120004400158

Hu, Y., and Cheng, H. (2013). Development and bottlenecks of renewable electricity generation in China: a critical review. *Environ. Sci. Technol.* 47, 3044–3056. doi: 10.1021/es303146q

Ilg, P., Scope, C., Muench, S., and Guenther, E. (2017). Uncertainty in life cycle costing for long-range infrastructure. Part I: leveling the playing field to address uncertainties. *Int. J. Life Cycle Assess.* 22, 277–292. doi: 10.1007/s11367-016-1154-1

Ji, S. H., Park, M., and Lee, H. S. (2012). Case adaptation method of case-based reasoning for construction cost estimation in Korea. *J. Construct. Eng. Manag.* 138, 43–52. doi: 10.1061/(asce)co.1943-7862.0000409

John, E. (2017). Economic and technical challenges of flexible operations under large-scale variable renewable deployment. *Energy Econ.* 64, 363–372. doi: 10.1016/j.eneco.2017.04.012

Joseph, T., Ugalde-Loo, C. E., Liang, J., and Coventry, P. F. (2018). Asset management strategies for power electronic converters in transmission networks: application to HVDC and FACTS devices. *IEEE Access.* 6, 21084–21102. doi: 10.1109/access.2018.2826360

Karamouz, M., Yaseri, K., and Nazif, S. (2017). Reliability-based assessment of lifecycle cost of urban water distribution infrastructures. *J. Infrastruct. Syst.* 23:04016030. doi: 10.1061/(asce)is.1943-555x.0000324

Karim, H., Magnusson, R., and Natanaelsson, K. (2012). Life-cycle cost analyses for road barriers. *J. Trans. Eng.* 138, 830–851. doi: 10.1061/(asce)te.1943-5436.0000391

Kasis, A., Devane, E., Spanias, C., and Lestas, I. (2016). Primary frequency regulation with load-side participation part I: stability and optimality. *IEEE Trans. Power Syst.* 32, 3505–3518. doi: 10.1109/tpwrs.2016.2636286

Kim, G. T., Kim, K. T., Lee, D. H., Han, C. H., Kim, H. B., and Jun, J. T. (2010). Development of a life cycle cost estimate system for structures of light rail transit infrastructure. *Autom. Construct.* 19, 308–325. doi: 10.1016/j.autcon.2009.12.001

Kiritsis, D., Neuendorf, K. P., and Xirouchakis, P. (1999). Petri net techniques for process planning cost estimation. *Adv. Eng. Softw.* 30, 375–387. doi: 10.1016/s0965-9978(98)00126-4

Lee, J., Yang, H., Lim, J., Hong, T., Kim, J., and Jeong, K. (2020). BIM-based preliminary estimation method considering the life cycle cost for decision-making in the early design phase. *J. Asian Arch. Build. Eng.* 19, 384–399. doi: 10.1080/13467581.2020.1748635

Lee, S. Y., Jo, C., Bergan, P., Pettersen, B., and Chang, D. (2016). Life-cycle cost-based design procedure to determine the optimal environmental design load and target reliability in offshore installations. *Struct. Saf.* 59, 96–107. doi: 10.1016/j.strusafe.2015.12.002

Li, X., Chalvatzis, K. J., and Stephanides, P. (2018). Innovative energy islands: life-cycle cost-benefit analysis for battery energy storage. *Sustainability* 10, 1–19.

Liming, S., and Bo, Y. (2020). Nonlinear robust fractional-order control of battery/SMES hybrid energy storage systems. *Power Syst. Protect. Control* 48, 76–83.

Liu, H., Gopalkrishnan, V., Quynh, K. T. N., and Ng, W. (2008). Regression models for estimating product life cycle cost. *J. Intell. Manuf.* 20, 401–408. doi: 10.1007/s10845-008-0114-4

Liu, L., Wang, H., Cheng, H., and Liu, J. (2012). Economic evaluation of power systems based on life cycle cost. *Autom. Electr. Power Syst.* 36, 45–50. doi: 10.4324/9781315611730-12

Lombardi, L. (2003). Life cycle assessment comparison of technical solutions for CO2 emissions reduction in power generation. *Energy Convers. Manag.* 44, 93–108. doi: 10.1016/s0196-8904(02)00049-3

Luo, X., Li, L., and Wei, Z. (2011). Applications of life cycle cost theory in decision-making of investment for distribution transformers renovation. *Power Syst. Technol.* 35, 207–211.

Mascitelli, R. (2004). A simple cost evcluator for product design. *Mach. Des.* 76, 98–102.

Meyer, C., and De Doncker, R. W. (2006). LCC analysis of different resonant circuits and solid-state circuit breakers for medium-voltage grids. *IEEE Trans. Power Deliv.* 21, 1414–1420. doi: 10.1109/tpwrd.2005.861334

Miah, J. H., Koh, S. C. L., and Stone, D. (2017). A hybridised framework combining integrated methods for environmental life cycle assessment and life cycle costing. *J. Clean. Produ.* 168, 846–866. doi: 10.1016/j.jclepro.2017.08.187

Nilsson, J., and Bertling, L. (2007). Maintenance management of wind power systems using condition monitoring systems-life cycle cost analysis for two case studies. *IEEE Trans. Energy Convers.* 22, 223–229. doi: 10.1109/tec.2006.889623

Orfanos, N., Mitzelos, D., Sagani, A., and Dedoussis, V. (2019). Life-cycle environmental performance assessment of electricity generation and transmission systems in Greece. *Renew. Energy* 139, 1447–1462. doi: 10.1016/j.renene.2019.03.009

Ozbay, K., Jawad, D., Parker, N., and Hussain, S. (2004). Life-cycle cost analysis: state of the practice versus state of the art. *Trans. Res. Record J. Trans. Res. Board* 1864, 62–70. doi: 10.3141/1864-09

Özbayrak, M., Akgün, M., and Türker, A. K. (2004). Activity-based cost estimation in a push/pull advanced manufacturing system. *Int. J. Prod. Econ.* 87, 49–65. doi: 10.1016/s0925-5273(03)00067-7

Park, J., and Simpson, T. W. (2003). Production cost modeling to support product family design optimization. *Math. Problems Eng.* 2003, 165–174.

Plebankiewicz, E., Meszek, W., Zima, K., and Wieczorek, D. (2020). Probabilistic and fuzzy approaches for estimating the life cycle costs of buildings under conditions of exposure to risk. *Sustainability* 12, 226–236. doi: 10.3390/su12010226

Savoretti, A., Mandolini, M., Raffaeli, R., and Germani, M. (2017). Analysis of the requirements of an early life-cycle cost estimation tool: an industrial survey. *Procedia Manuf.* 11, 1675–1683. doi: 10.1016/j.promfg.2017.07.291

Schneiderova-Heralova, R. (2018). Importance of life cycle costing for construction projects. *Eng. Rural Dev.* 17, 1223–1227.

Seo, K. K., Park, J. H., Jang, D. S., and Wallace, D. (2002). Approximate estimation of the product life cycle cost using artificial neural networks in conceptual design. *Int. J. Adv. Manuf. Technol.* 19, 461–471. doi: 10.1007/s001700200049

Shafiee, M., Brennan, F., and Espinosa, I. A. (2016). A parametric whole life cost model for offshore wind farms. *Int. J. Life Cycle Assess.* 21, 961–975. doi: 10.1007/s11367-016-1075-z

Shahata, K., and Zayed, T. (2013). Simulation-based life cycle cost modeling and maintenance plan for water mains. *Struct. Infrastruct. Eng.* 9, 403–415. doi: 10.1080/15732479.2011.552509

Shahidehpour, M., and Ferrero, R. (2005). Time management for assets: chronological strategies for power system asset management. *IEEE Power Energy Magazine.* 3, 32–38. doi: 10.1109/mpae.2005.1436498

Shi, J. N., Han, H. L., and Xu, T. (2009). Application of life cycle costs analysis in planning design of power transformation projects. *Power Syst. Technol.* 9, 63–66.

Solomon, R., Sandborn, P. A., and Pecht, M. G. (2000). Electronic part life cycle concepts and obsolescence forecasting. *IEEE Trans. Compon. Packaging Technol.* 23, 707–717. doi: 10.1109/6144.888857

Spertino, F., and Graditi, G. (2014). Power conditioning units in grid-connected photovoltaic systems: a comparison with different technologies and wide range of power ratings. *Solar. Energy.* 108, 219–229.

Steen, B. (2005). Environmental costs and benefits in life cycle costing. *Manag. Environ. Qual. Int. J.* 16, 107–118. doi: 10.1108/14777830510583128

Steinert, M. (2009). A dissensus. *Technol. Forecast. Soc. Chang.* 76, 291–300.

Tian, Z., Jin, T., Wu, B., and Ding, F. (2011). Condition based maintenance optimization for wind power generation systems under continuous monitoring. *Renew. Energy.* 36, 1502–1509. doi: 10.1016/j.renene.2010.10.028

Vahdat-Aboueshagh, H., Nazif, S., and Shahghasemi, E. (2014). Development of an algorithm for sustainability based assessment of reservoir life cycle cost using fuzzy theory. *Water Resour. Manag.* 28, 5389–5409. doi: 10.1007/s11269-014-0808-7

Waghmode, L. Y., and Sahasrabudhe, A. D. (2012). Modelling maintenance and repair costs using stochastic point processes for life cycle costing of repairable systems. *Int. J. Comput. Integr. Manuf.* 25, 353–367. doi: 10.1080/0951192x.2010.551783

Wang, H. S., Wang, Y. N., and Wang, Y. C. (2013). Cost estimation of plastic injection molding parts through integration of PSO and BP neural network. *Exp. Syst. Appl.* 40, 418–428. doi: 10.1016/j.eswa.2012.01.166

Wen, F., Hua, D., Wang, Q., and Singh, S. N. (2008). Wind power generation in china: present status and future prospects. *Int. J. Energy Technol. Policy.* 6, 736–744.

White, G. (1976). The life cycle cost of an item is the sum of all funds expended in support of the item from its conception and fabrication through its operation to the end of its useful life. *Manag. Accounting* 57, 39–42.

Woodward, D. G. (1997). Life cycle costing-theory, information acquisition and application. *Int. J. Project Manag.* 15, 335–344. doi: 10.1016/s0263-7863(96)00089-0

Xu, W. R., and Wang, W. M. (2011). Summary and analysis of asset life cycle cost supported by the fixed grid asset operation and maintenance cost. *East China Electric Power*. 39, 1588–1591.

Yang, J., Liu, Q., Li, X., and Cui, X. (2017). Overview of wind power in China: status and future. *Sustainability* 9, 1–12. doi: 10.1002/9781118910054.ch1

Yeung, A. A., Yoho, K. D., and Arkes, J. (2013). Estimates of unit cost reductions of the F-16 fighter as a result of U.S. arms export production. *J. Cost Anal. Parametr.* 6, 3–22. doi: 10.1080/1941658x.2013.766547

Yildiz, B., and Kazimi, M. S. (2006). Efficiency of hydrogen production systems using alternative nuclear energy technologies. *Int. J. Hydrogen Energy.* 31, 77–92. doi: 10.1016/j.ijhydene.2005.02.009

Zakeri, B., and Syri, S. (2015). Electrical energy storage systems: a comparative life cycle cost analysis. *Renew. Sustain. Energy Rev.* 42, 569–596. doi: 10.1016/j.rser.2014.10.011

Zhang, G., and Wang, W. (2012). The research of comprehensive evaluation model for thermal power equipment based on life cycle cost. *Syst. Eng. Procedia* 4, 68–78. doi: 10.1016/j.sepro.2011.11.051

Zhang, Y., and Cai, M. (2014). Overall life cycle comprehensive assessment of pneumatic and electric actuator. *Chin. J. Mech. Eng.* 27, 584–594. doi: 10.3901/cjme.2014.03.584

Conflict of Interest: KW, YL, XW, ZZ, and YW were employed by the company CSG POWER GENERATION CO., LTD.

The remaining authors declare that the research was conducted in the absence of any commercial or financial relationships that could be construed as a potential conflict of interest.

Copyright © 2021 Wang, Li, Wang, Zhao, Yang, Yu, Wang, Huang and Yu. This is an open-access article distributed under the terms of the Creative Commons Attribution License (CC BY). The use, distribution or reproduction in other forums is permitted, provided the original author(s) and the copyright owner(s) are credited and that the original publication in this journal is cited, in accordance with accepted academic practice. No use, distribution or reproduction is permitted which does not comply with these terms.

frontiers in Energy Research

ORIGINAL RESEARCH
published: 12 May 2021
doi: 10.3389/fenrg.2021.693903

Impedance Modeling and Analysis of Medium-Frequency Oscillation Caused by VSC-HVDC Connected to Local Weak Grid and DFIG-Based Wind Farms

Kun Sun, Wei Yao, Cai Yan and Jinyu Wen*

State Key Laboratory of Advanced Electromagnetic Engineering and Technology, School of Electrical and Electronic Engineering, Huazhong University of Science and Technology, Wuhan, China

In the northwest of China, a strategy to transmit the wind-thermal–bundled power from the local grid and doubly fed induction generator (DFIG)–based wind farms through a voltage source converter–based HVDC (VSC-HVDC) can be widely applied. However, since the local grid is usually weak, a new type of electrical oscillation in the medium-frequency region may occur in the sending-end converter (SEC) of VSC-HVDC with PQ-control. The mechanism of this oscillation caused by the interaction between the DFIG, local grid, and SEC is not entirely understood. In this study, the sequence impedance model of the sending-end converter (SEC) of VSC-HVDC with the PQ-control outer loop and PLL is derived with the explicit analytic expression, and then, the oscillation mechanism is explored based on the intuitive analysis of the system impedance frequency characteristics. Compared with the subsynchronous oscillation (SSO) caused by the DFIG or power inverter, the theoretical analysis shows that this medium-frequency oscillation (MFO) mainly originates from the SEC due to its negative damping effect between about 100 and 200 Hz. In addition, the impact of the system controller parameters and operating conditions of the DFIG, local grid, and SEC on the oscillation characteristics is analyzed in detail. Finally, the correctness of the theoretical analysis is validated by time-domain simulation.

Keywords: sending-end converter, local weak grid, doubly fed induction generator, impedance model, stability analysis, medium-frequency oscillation

OPEN ACCESS

Edited by:
Bo Yang,
Kunming University of Science and Technology, China

Reviewed by:
Yang Liu,
South China University of Technology, China
Ping Zhao,
China Three Gorges University, China

****Correspondence:***
Wei Yao
w.yao@hust.edu.cn

Specialty section:
This article was submitted to Smart Grids, a section of the journal Frontiers in Energy Research

Received: *12 April 2021*
Accepted: *22 April 2021*
Published: *12 May 2021*

Citation:
Sun K, Yao W, Yan C and Wen J (2021) Impedance Modeling and Analysis of Medium-Frequency Oscillation Caused by VSC-HVDC Connected to Local Weak Grid and DFIG-Based Wind Farms. Front. Energy Res. 9:693903. doi: 10.3389/fenrg.2021.693903

1 INTRODUCTION

In Northwest China, large-scale wind power is generally bundled with local thermal power and then transmitted to the load centers in the eastern coast, as the wind power is fluctuant and intermittent while the thermal power is controllable (Sun et al., 2017; Gao et al., 2018). Recently, the VSC-HVDC technology is developing rapidly due to its advantage in the wind power integration (Flourentzou et al., 2009; Yang et al., 2018; Chen et al., 2020; Sun et al., 2020; Xiong et al., 2021). Therefore, the strategy to transmit the large-scale wind power through VSC-HVDC in the local grid will be widely applied. However, the proposed transmission mode may face potential stability issues induced by the power electrical converters, especially given that the local grid in Northwest China is usually weak.

Several oscillation incidents related to VSC-HVDC have occurred worldwide. In 2013, an SSO around 20 Hz occurred in the Nanao VSC-HVDC project in China and led to the outage of the integrated DFIG-based wind farms (Lyu et al., 2018). In addition, a 250–350 Hz current oscillation was observed in the North Sea VSC-HVDC project in Germany from the converter to the grid (Christoph et al., 2015; Zhou et al., 2019). Similarly, for the proposed system, the interaction between the DFIG-based wind farms, local grid, and VSC-HVDC may cause a new type of electrical oscillation issue, which is worthy of further study.

Currently, the impedance method is suitable for the stability issue caused by the grid-connected units due to its simple mathematical expression and stability criterion (Cespedes and Sun, 2014). There have been a lot of studies concentrating on the stability issue of the DFIG-based wind farms and VSC-HVDC based on the impedance method. For instance, the effect of the control parameters on the stability of the grid-connected converter is investigated in Wang et al. (2017), Wen et al. (2017), Xu et al. (2019), and Wang et al. (2020). However, in the above references, only the inner loop and PLL are considered in the modeling, while the influence of the outer loop is ignored. Thus, the accuracy of the stability analysis is doubtful. Recent references (Khazaei et al., 2018; Liu and Xie, 2019; Zhou et al., 2020) take the outer loop into account as well. However, the impedance model with the outer loop is normally given in matrix format instead of the explicit analytic expression, which is not clear and intuitive when it comes to illustrating the impedance characteristics. In addition, all of the above references only consider the outer loop of a power inverter instead of a converter. In Liu et al. (2021), Liu and Xie (2017), Miao (2012), Vieto and Sun (2018), Koralewicz et al. (2020), Yan et al. (2019), Yang et al. (2020), SSO existing in the DFIG-based wind farms interfaced with the series-compensated line or AC grid is investigated, and the impact of the various factors on SSO is analyzed. However, the influence of the integrated DFIG on the oscillation over the supersynchronous frequency region is not considered. Besides, few references consider the stability of the proposed system which transmits wind power in combination with thermal power through the SEC.

In particular, the interaction between the DFIG and VSC-HVDC is deeply analyzed in author's previous work (Sun et al., 2019). However, the system stability will be affected in a different way when the wind-thermal–bundled power is transmitted from the local grid and DFIG-based wind farms to the SEC with PQ-control instead of the amplitude–frequency control. Since the local grid is integrated and the control strategy of the SEC is changed, the interaction mechanism will be more complicated in the proposed transmission mode. The similar system of a VSC-HVDC connected to the DFIG-based wind farm or the thermal power plant has been preliminarily analyzed in Chen et al. (2018), Liu et al. (2018), and Zou et al. (2018). However, they mainly focus on SSO or high-frequency oscillation issues, while MFO is not considered. In addition, the control strategy of the SEC in the proposed transmission mode is different from that in the above studies since the output power of the wind-thermal–bundled system should be controlled by the SEC (Yogarathinam et al., 2017) and then transmitted to the power grid. Thus, the outer loop of the SEC cannot be ignored since it reflects the effect of the control strategy. In short, the stability of the proposed transmission mode is not yet systematically comprehended. Therefore, this work aims to explore the interaction between the DFIG, local grid, and SEC with PQ-control in the medium-frequency region.

The main contributions of this study are summarized as:

- The potential MFO risk of the SEC with PQ-control in the medium-frequency region is analyzed when it transmits the wind-thermal–bundled power from the local grid and DFIG-based wind farms.
- To analyze the interaction mechanism in the proposed transmission mode, the sequence impedance model of the SEC with the PQ-control outer loop and PLL is derived with the explicit analytic expression, which is clear and intuitive when it comes to illustrating the impedance characteristics.
- The coupling between the inner loop, outer loop, and PLL of the SEC is analyzed according to the derived impedance models, and their influence on the system stability can be intuitively found based on the analytic impedance expression and the corresponding impedance frequency characteristics. Compared with the power inverter, the mechanism and characteristics of MFO caused by the SEC are different.
- The impact of the local grid strength and the integration of DFIG-based wind farms on the system stability is analyzed as well. Compared with SSO caused by the DFIG, the controller parameters and operating conditions of the DFIG have a different influence on this MFO which mainly originates from the SEC.

The rest of this article is organized as follows. The structure and oscillation phenomenon of the system is investigated in **Section 2**. **Section 3** derives and validates the sequence impedance models of the SEC, the DFIG, and the local grid. In **Section 4**, the mechanism explanation of the oscillation is revealed based on the derived models, and the impact of various factors on the oscillation is analyzed. **Section 5** validates the correctness of the theoretical analysis by time-domain simulation. Finally, conclusions are drawn in **Section 6**.

2 STRUCTURE AND OSCILLATION PHENOMENON OF THE SYSTEM

The configuration of the investigated system is briefly introduced in this section. Then, time-domain simulation and spectrum analysis are conducted to analyze the potential electrical oscillation in the system.

2.1 System Configuration

The investigated system shown in **Figure 1** contains three parts: the local grid with a thermal power unit, the DFIG-based wind farms, and the VSC-HVDC system. Both the thermal power and wind power are stepped up to 110 kV and then transmitted to the main grid via VSC-HVDC. In order to keep

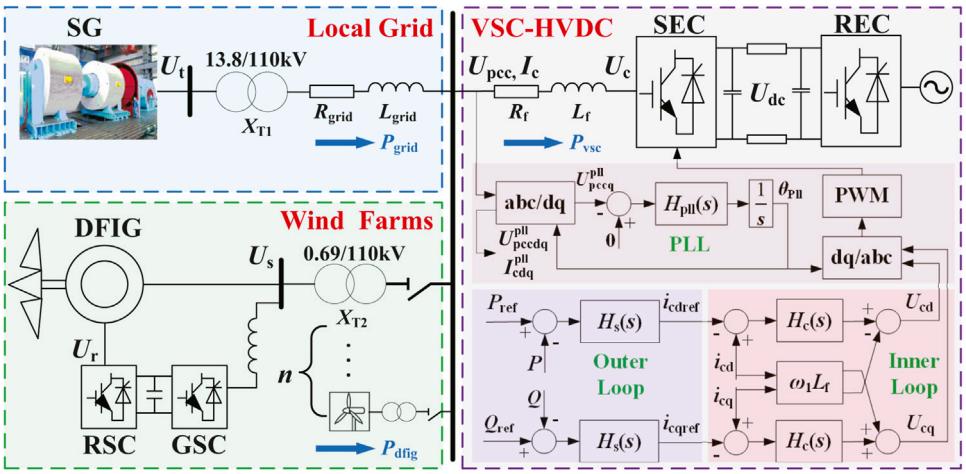


FIGURE 1 | VSC-HVDC connected to the local grid and DFIG-based wind farms.

TABLE 1 | Parameters of VSC-HVDC.

Parameter	Value	Parameter	Value
VSC capacity	500 MW	Base MVA	100 MW
Rated voltage	110 kV	K_{ps}/K_{is}	0.2/50 pu
DC voltage	200 kV	K_{pc}/K_{ic}	0.3/100 pu
DC capacitor	1,250 μF	K_{ppll}/K_{ipll}	60/1,400 pu
L_f	8 mH	P_{ref}/Q_{ref}	0.5/0 pu

TABLE 2 | Parameters of the DFIG.

Parameter	Value	Parameter	Value
Rated power	1.5 MW	r_s	0.0023 pu
Rated voltage	690 V	L_s	0.16 pu
Rated rotor speed	1.2 pu	r_r	0.0016 pu
DC capacitor	0.01 F	L_r	0.18 pu
DC voltage	1150 V	L_m	2.9 pu

the transmission power stable, the constant power control is used in the SEC, while the receiving-end converter (REC) regulates the DC voltage. Since the wind power is fluctuant while the thermal power is controllable, the local thermal power keeps the total output power constant by means of its self-regulation (Xiao et al., 2016; Yogarathinam et al., 2017; Shah et al., 2018). Besides, the thermal power unit also maintains the stable AC voltage and frequency on the point of common coupling (PCC).

Initially, the wind farms contain 200 DFIG wind turbines (WTs), which run in the maximum power point tracking mode (GE 1.5 MW). The capacity of the VSC-HVDC is 500 MW. Normally, it requires the thermal power unit to stabilize the fluctuation of full wind power with at least 40% rated loads. Therefore, the capacity of the local thermal power unit is set to 500 MW. To simplify the modeling, the equivalent aggregated model of the DFIG is adopted (Kunjumuhammed et al., 2017; Peng et al. 2020), since the impact of DFIG integration on the system is of concern instead of the internal action among the turbines.

2.2 Oscillation Phenomenon

A detailed simulation model of the system shown in **Figure 1** is established with a switching device model of the VSC-HVDC in MATLAB/Simulink, associated with the SimPowerSystems Blockset. To investigate the potential oscillation risk existing in the system, two scenarios are analyzed. The system parameters are listed in **Tables 1–3**.

TABLE 3 | Parameters of synchronous machine and AC line.

Parameter	Value	Parameter	Value
Rated capacity	500 MW	T'_d	8 s
Rated voltage	13.8 kV	T''_d	0.03 s
X_d	1.8 pu	T'_q	0.4 s
X_q	1.7 pu	T''_q	0.05 s
X'_d	0.3 pu	J_{sg}	6.5 s
X'_q	0.55 pu	AC line length	25 mile
X''_d	0.25 pu	R_{line}	0.1855 Ω/mile
X''_q	0.25 pu	L_{line}	1.685 mH/mile

2.2.1 Scenario 1: The Effect of the Outer Loop of the SEC

Initially, the wind farms are not integrated. The short circuit ratio (SCR) of the local grid is set to 6.8, and the output active power of VSC-HVDC is set to 0.5 pu. At t = 6 s, the SCR decreases to 5.1. To analyze the effect of the PQ-control outer loop of the SEC, the simulation models both with and without the outer loop are adopted. **Figure 2A** shows the active power response on the PCC. Since the local grid strength decreases, it can be found that the oscillation emerges with the outer loop considered, while the system is still stable with the outer loop ignored. Thus, the outer loop of the SEC influences the system stability.

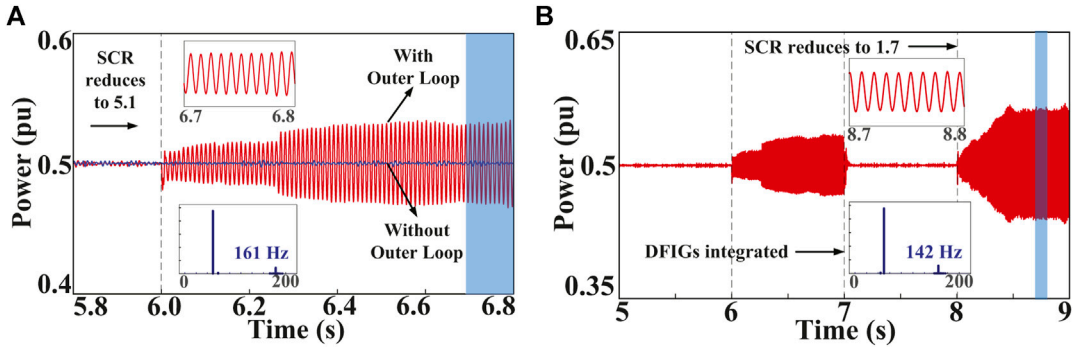


FIGURE 2 | Oscillation phenomenon. **(A)** The effect of the outer loop of the SEC. **(B)** The effect of the integration of the DFIG.

2.2.2 Scenario 2: The Effect of the Integration of the DFIG

The condition is the same as in scenario 1, and the outer loop of SEC is considered. At $t = 7$ s, the wind farms are integrated under the wind speed at 10 m/s. At $t = 8$ s, the SCR further decreases to 1.7. According to **Figure 2B**, the electrical oscillation can be suppressed due to the integration of the DFIG. However, the electrical oscillation emerges again when the local grid becomes even more weak. Discrete Fourier transform (DFT) is applied for the spectrum analysis of the current on the PCC. The current contains an oscillation component at 161 Hz in the abc frame before the integration and reduces to 142 Hz after the integration.

Therefore, the oscillatory behavior of the system can be influenced by the parameters' variation of the SEC, the DFIG, and the local grid. The frequency region of the electrical oscillation is about 100–200 Hz, which belongs to MFO.

3 SYSTEM MODELING AND STABILITY CRITERION

In this section, the sequence impedance model of the sending-end converter (SEC) with the power loop and PLL is derived in detail with the explicit analytic expression and validated. Then, the impedance models of the DFIG and the local AC grid are built as well.

3.1 Impedance Model of the SEC With PQ-Control

3.1.1 Model With PLL and Current Loop

The control method of the SEC and REC is discussed in **Section 2.1**, and the control structure of the SEC is depicted in **Figure 1**. Since the impact of the REC on the stability is small due to the isolation provided by the DC link, only the impedance model of the SEC needs to be built in detail. The control of the SEC is based on the dq reference frame, in which the d-axis is orientated to the PCC voltage U_{pcc} and the q-axis leading the d-axis by 90°.

The voltage equation of the SEC in the dq frame is expressed as

$$\begin{cases} U_{pccd} = U_{cd} - sL_f i_{cd} + \omega_1 L_f i_{cq} \\ U_{pccq} = U_{cq} - sL_f i_{cq} - \omega_1 L_f i_{cd} \end{cases}, \quad (1)$$

where U_c represent the output voltage and current of the SEC, the subscripts "d" and "q" denote the d-axis and q-axis components, s is the differential operator, ω_1 is the base frequency, and L_f is the filter inductance of the converter. Note that the influence of the filter capacitance is ignored since it only dominates in the middle–high frequency region.

The small-signal model of the current controller of the SEC can be described as

$$\begin{cases} \Delta U_{cdref} = H_c(s)\left(\Delta i_{cdref} - \Delta i_{cd}\right) + \Delta U_{pccd} - \omega_1 L_f \Delta i_{cq} \\ \Delta U_{cqref} = H_c(s)\left(\Delta i_{cqref} - \Delta i_{cq}\right) + \Delta U_{pccq} + \omega_1 L_f \Delta i_{cd} \end{cases}, \quad (2)$$

where the subscript "ref" denotes the reference, and K_{pc} and K_{ic} are the proportional and integral gains of the current controller $H_c(s)$ of the SEC. According to the control loop, $U_{cd} = U_{cdref}$ and $U_{cq} = U_{cqref}$ when the DC dynamics is not considered since it is normally stable.

Then, the influence of the PLL dynamics is taken into account. PLL is used for phase tracking of U_{pcc}. However, when the system is disturbed by a small-signal perturbation, the phase θ of U_{pcc} cannot be synchronized accurately and an angle deviation $\Delta\theta$ is introduced due to the PLL dynamics. Thus, the PLL output angle θ_{pll} can be expressed as $\theta_{pll} = \theta + \Delta\theta$. Therefore, the system has two dq frames during the transient process of PLL: one is the system dq frame defined by θ, while the other is the controller dq frame defined by θ_{pll}. Note that the variables in the controller dq frame are denoted with the superscript "pll." The small-signal disturbance relationship of the converter voltage and current between the two frames have been derived in detail in Wang et al. (2017), Wen et al. (2017), and Sun et al. (2019)

$$\begin{cases} \Delta U_{cdq}^{pll} = \Delta U_{cdq} + G_{pll}^{u}(s)\Delta U_{pccdq} \\ \Delta I_{cdq}^{pll} = \Delta I_{cdq} + G_{pll}^{i}(s)\Delta U_{pccdq} \end{cases}. \quad (3)$$

For simplicity, the voltage and current are expressed in matrix form: $U_{cdq} = [U_{cd}\, U_{cq}]^T$, $I_{cdq} = [i_{cd}\, i_{cq}]^T$. The transfer function matrices $G_{pll}^{u}(s)$ and $G_{pll}^{i}(s)$ in **Eq. 3** are defined as

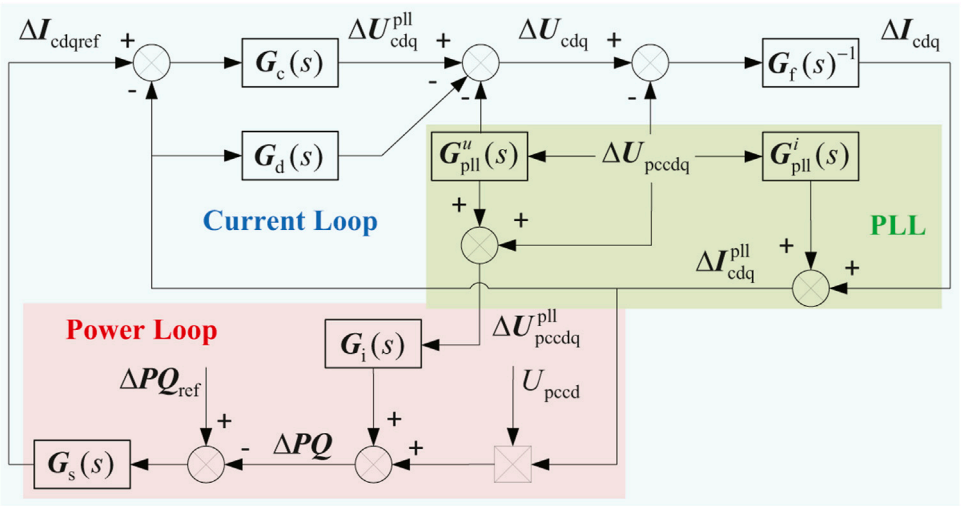


FIGURE 3 | Small-signal circuit model of the sending-end station of VSC-HVDC.

$$G_{pll}^{u}(s)=\begin{bmatrix}0 & U_{cq}T_{pll}(s)\\ 0 & -U_{cd}T_{pll}(s)\end{bmatrix},G_{pll}^{i}(s)=\begin{bmatrix}0 & i_{cq}T_{pll}(s)\\ 0 & -i_{cd}T_{pll}(s)\end{bmatrix}, \quad (4)$$

where $T_{pll}(s)=H_{pll}(s)/(s+U_{pccd}H_{pll}(s))$ and K_{ppll} and K_{ipll} are the proportional and integral gains of the PLL controller $H_{pll}(s)$ of the SEC.

According to **Figures 1–3**, the small-signal circuit model of the SEC with the current loop and PLL is obtained and shown in the blue and green blocks of **Figure 3**. $G_c(s)$ is the transfer function matrix of the current controller, $G_d(s)$ is the transfer function of the decoupling gain of the current controller, and $G_f(s)$ represents the impedance of the filter

$$G_c(s)=\begin{bmatrix}H_c(s) & 0\\ 0 & H_c(s)\end{bmatrix},G_d(s)=\begin{bmatrix}0 & \omega_1 L_f\\ -\omega_1 L_f & 0\end{bmatrix},G_f(s)=\begin{bmatrix}sL_f & -\omega_1 L_f\\ \omega_1 L_f & sL_f\end{bmatrix}. \quad (5)$$

According to **Figure 3**, the small-signal propagation path of the converter current in the current loop can be described as

$$\Delta I_{cdq}=\left[\Delta I_{cdqref}G_c(s)-\left(\Delta I_{cdq}+G_{pll}^{i}(s)\Delta U_{pccdq}\right)\cdot\left(G_c(s)+G_d(s)\right)-G_{pll}^{u}(s)\Delta U_{pccdq}-\Delta U_{pccdq}\right]G_f(s)^{-1}. \quad (6)$$

3.1.2 Model With Power Loop

Then, the influence of the outer loop with PQ-control is taken into account. The small-signal model of the power controller of the SEC can be described as

$$\begin{cases}\Delta i_{cdref}=H_s(s)\left(\Delta P_{ref}-\Delta P\right)\\ \Delta i_{cqref}=H_s(s)\left(\Delta Q_{ref}-\Delta Q\right)\end{cases}, \quad (7)$$

where K_{ps} and K_{is} are the proportional and integral gains of the power controller $H_s(s)$ of the SEC and ΔP_{ref} and ΔQ_{ref} are equal to zero in small-signal analysis since they are constant.

The small-signal analysis is applied to the measured power, which is defined as $P=U_{pccd}i_{cd}+U_{pccq}i_{cq}$, $Q=U_{pccd}i_{cq}-U_{pccq}i_{cd}$. Notice that the steady-state q-axis terminal voltage $U_{pccq}=0$. Then, the small-signal reference current of the converter can be obtained as follows

$$\begin{cases}\Delta P=U_{pccd}\Delta i_{cd}+\Delta U_{pccd}i_{cd}+\Delta U_{pccq}i_{cq}\\ \Delta Q=U_{pccd}\Delta i_{cq}+\Delta U_{pccd}i_{cq}-\Delta U_{pccq}i_{cd}\end{cases}, \quad (8)$$

$$\begin{cases}\Delta i_{cdref}=-H_s(s)\left(U_{pccd}\Delta i_{cd}+\Delta U_{pccd}i_{cd}+\Delta U_{pccq}i_{cq}\right)\\ \Delta i_{cdref}=-H_s(s)\left(U_{pccd}\Delta i_{cq}+\Delta U_{pccd}i_{cq}-\Delta U_{pccq}i_{cd}\right)\end{cases}. \quad (9)$$

In addition, the small-signal propagation path of the power loop is depicted in the red block of **Figure 3**, where the power is expressed in matrix form: $\Delta PQ=[\Delta P\,\Delta Q]^T$. In combination with **Eqs. 8, 9**, the reference current can be derived as

$$\Delta I_{cdqref}=-G_s(s)\left[U_{pccd}\left(\Delta I_{cdq}+G_{pll}^{i}(s)\Delta U_{pccdq}\right)+G_i(s)\left(\Delta U_{pccdq}+G_{pll}^{u}(s)\Delta U_{pccdq}\right)\right], \quad (10)$$

where $G_s(s)$ is the transfer function matrix of the power controller and $G_i(s)$ is the transfer function of the current

$$G_s(s)=\begin{bmatrix}H_s(s) & 0\\ 0 & H_s(s)\end{bmatrix},G_i(s)=\begin{bmatrix}i_{cd} & i_{cq}\\ i_{cq} & -i_{cd}\end{bmatrix}. \quad (11)$$

Then, the dq impedance of the SEC seen from the terminal is derived by combining **Eq. 6**

$$Z_{vsc}(s)=-\left[\left(1+U_{pccd}G_s(s)\right)\left(G_c(s)+G_d(s)+G_f(s)\right)\right]\cdot\left[1+G_s(s)G_c(s)G_i(s)+\left(1+G_s(s)G_c(s)G_i(s)\right)G_{pll}^{u}(s)+\left(\left(1+U_{pccd}G_s(s)\right)G_c(s)+G_d(s)\right)G_{pll}^{i}(s)\right]^{-1}. \quad (12)$$

However, the expression of the dq impedance model of the SEC is hard to understand since it has four components and each one does not contain an explicit physical meaning. Instead, to

analyze intuitively and conveniently, the dq impedance model of the SEC can be transformed into the sequence impedance model by combining **Eq. 12** and the following equation (Shah and Parsa, 2017)

$$Z_{pn}(s) = \begin{bmatrix} 1 & 1 \\ -j & j \end{bmatrix}^{-1} Z_{dq}(s) \begin{bmatrix} 1 & j \\ 1 & -j \end{bmatrix}, \tag{13}$$

where $Z_{pn}(s)$ and $Z_{dq}(s)$ represent the 2×2 impedance matrixes in the sequence-domain and dq-domain. The 2×2 sequence impedance of the SEC can be obtained by substituting $Z_{vsc}(s)$ in **Eq. 12** with $Z_{dq}(s)$. The off-diagonal elements of Z_{pn} represent the coupling between the positive and the negative components, and their influence on the stability is well analyzed in Zhang et al. (2019), which found that the model without off-diagonal elements is very close to the detailed model over the supersynchronous frequency range, whereas some overpessimistic conclusions are exhibited at the low-frequency range. Liu et al. (2021) also pointed out that the frequency coupling effect caused by the off-diagonal elements mainly influences the analysis of SSO. Therefore, the off-diagonal elements are not considered in this study since the investigated MFO region is much higher than the SSO range. In addition, since the system stability under the balanced condition is considered in this study, the positive sequence impedance model of the SEC is derived as

$$Z_{vsc}(s) = -\frac{\left(1 + U_{pccd} H_s(s - j\omega_1)\right) H_c(s - j\omega_1) + sL_f}{1 - \frac{1}{2}\left[\left(H_c(s - j\omega_1) - j\omega_1 L_f\right) I_c + U_{pccd}\right] T_{pll}(s - j\omega_1)}. \tag{14}$$

According to **Eq. 14**, the sequence impedance of the SEC has an explicit analytic expression, which is intuitive and convenient for further analysis. The denominator of **Eq. 14** mainly reflects the impact of the PLL dynamics. I_c is a negative value as a converter. Obviously, the current loop is directly coupled with the power loop in the numerator and directly coupled with PLL in the denominator. The power loop and PLL are decoupled in the denominator in the condition that $U_{pccq} = 0$, and thus, the measured power is the same in both the controller dq frame and the system dq frame.

3.2 Impedance Model of the DFIG

The control structure of the DFIG is depicted in **Figure 1**. The RSC regulates the power flowing between the stator and the grid, while the grid-side converter (GSC) regulates the DC voltage. Some simplifications are taken into account. For instance, the influence of the GSC and the excitation branch can be ignored since their magnitudes are sufficiently large in the investigated frequency region. Then, the positive sequence impedance model of the DFIG can be expressed as (Miao, 2012; Vieto and Sun, 2018; Sun et al., 2019; Liu et al., 2021)

$$Z_{dfig}(s) = \frac{\left(r_r + H_r(s - j\omega_1) - jK_{dr}\right) / S_{lip}(s) + sL_r + r_s + sL_s}{1 - \frac{1}{2}\left(i_{rd} H_r(s - j\omega_1) / S_{lip}(s) + U_{rd}\right) T_{pll-rsc}(s - j\omega_1)}, \tag{15}$$

where K_{pr} and K_{ir} are the proportional and integral gains of the RSC current controller $H_r(s)$. Besides, $T_{pll-rsc}(s) = H_{pll-rsc}(s)/(s + U_{rd} H_{pll-rsc}(s))$ and $K_{ppll-rsc}$ is the proportional gain of the PLL controller $H_{pll-rsc}(s)$ of the RSC. The slip of the rotor is expressed as $S_{lip}(s) = (s - j\omega_r)/s$ and ω_r is the rotor angular frequency. The rotor slip is a variable and can be expressed as a transfer function with the frequency. Besides, definitions of other parameters in the equation are explained in the above references.

3.3 Impedance Model of the Local Grid

The impedance of the local grid includes the internal impedance of the synchronous generator (SG) and the line impedance. The line impedance is expressed as $Z_{line}(s) = R_{line} + jX_{line}$. The impedance model of the SG has been well derived in Huang et al. (2021), which is expressed as

$$\begin{cases} Z_d(s) = \omega_{sg}\left[\left(X'_d - X''_d\right)\left(T'_d s + a_d\right) G(s) + X''_d\right] \\ Z_q(s) = \omega_{sg}\left[\left(X'_q - X''_q\right)\left(T'_q s + a_q\right) G(s) + X''_q\right] \end{cases}, \tag{16}$$

where $G(s) = 1/[T'_d T''_d s^2 + (T'_d + T''_d)s + 1]$, a_d $(X_d - X''d)/(X'_d - X''_d)$, and $a_q = (X_q - X''_q)/(X'_q - X''_q)$. ω_{sg} is the rotor speed and T'_d, T''_d and T'_q, T''_q are the transient and subtransient time constants in the dq frame. X_d, X'_d, X''_d and X_q, X'_q, X''_q are the stator, transient, and subtransient reactances in the dq frame. The positive sequence impedance of the SG is derived as $Z_{sg}(s) = j(Z_d(s) + Z_q(s))/2$. Therefore, $Z_{grid}(s) = Z_{line}(s) + Z_{sg}(s)$. However, according to the spectrum analysis in **Section 2**, the investigated MFO region of the system significantly exceeds the low-frequency oscillation, which refers to the dynamics of the generator sets (Baltas et al., 2021). Therefore, the influence of the generator on this new type of electrical oscillation can be ignored. In addition, $Z_{sg}(s)$ is relatively small compared with $Z_{line}(s)$ in the investigated MFO frequency region, especially when the local grid is weak (Wang et al., 2019). Therefore, only the impedance of the transmission line is considered in this study for the sake of simplified analysis. That is, $Z_{grid}(s) = Z_{line}$. This assumption is proved in the next part.

3.4 Validation and Stability Criterion

The verification and comparison of the impedance models are performed in **Figure 4**. The positive sequence impedance of the SEC is measured from 0 to 200 Hz with 40 points using the method of injecting current. A perturbation current (about 2% of rated current) at the measured frequency points is applied, and the related voltage is measured. The harmonic voltage and current in different frequency points are analyzed using the DFT tool. Thereby, the impedance is calculated by dividing the voltage by current at each frequency point. The operating condition for the measurement is given in **Tables 1–3**. As shown in **Figures 4A,B**, the impedance models of the SEC with or without PQ-control have been validated. It can be found that the PQ-control will influence the magnitude of $Z_{vsc}(s)$ and the frequency of the abrupt change in the phase angle. As shown in **Figure 4C**, compared with the impedance

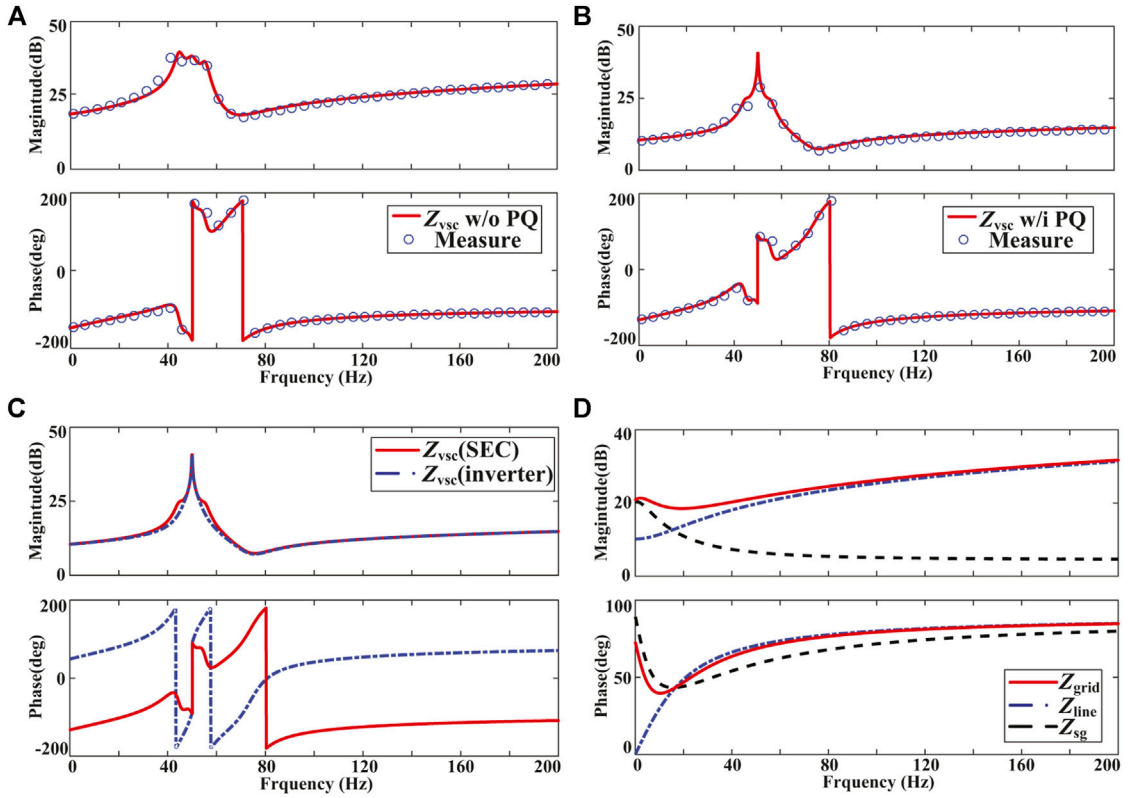


FIGURE 4 | Validation and comparison of the impedance models; **(A)** validation of $Z_{vsc}(s)$ without PQ-control; **(B)** validation of $Z_{vsc}(s)$ with PQ-control; **(C)** comparison of $Z_{vsc}(s)$ for the SEC and the inverter; and **(D)** comparison of $Z_{sg}(s)$, $Z_{line}(s)$ and $Z_{grid}(s)$.

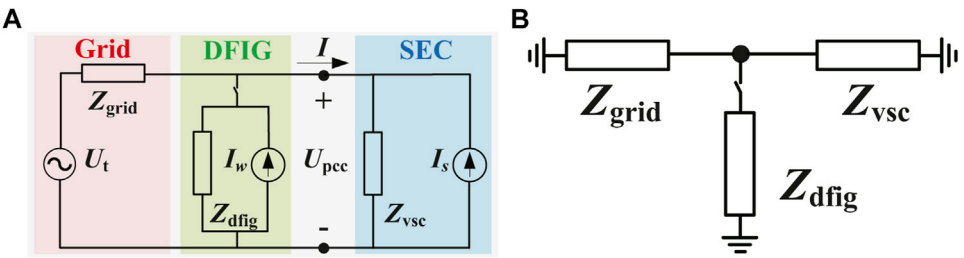


FIGURE 5 | (A) Equivalent circuit model of the whole system. **(B)** Equivalent impedance network model of the whole system.

model of the power inverter derived in Zhou et al. (2020), the risk region of the SEC is shifted from the supersynchronous frequency region to the MFO region. As shown in **Figure 4D**, the impedance of the SG can be ignored in the MFO region due to its magnitude being relatively small compared with $Z_{line}(s)$ with SCR = 5.1 in the MFO region.

Thereby, to investigate the interaction mechanism, the equivalent circuit model of the whole system is established by aggregating the impedance model of each part on the PCC, as shown in **Figure 5A**. In small-signal impedance analysis, the local grid is normally modeled as the Thevenin equivalent circuit, while the SEC and the wind farm are modeled as the Norton equivalent circuit. According to the impedance network model proposed in Liu et al. (2018), the system impedance can be aggregated by the parallel connection of wind farm impedance and AC grid impedance and then connected in series with SEC impedance. As shown in **Figure 5B**, the resistance and reactance of the whole system can be represented by the sum of each part.

The stability criterion based on the second-order RLC series resonance circuit has been widely applied in recent works (Miao, 2012; Liu and Xie, 2017) to assess the system stability. By combining with this criterion and the derived impedance models, the oscillation mechanism and characteristics can be

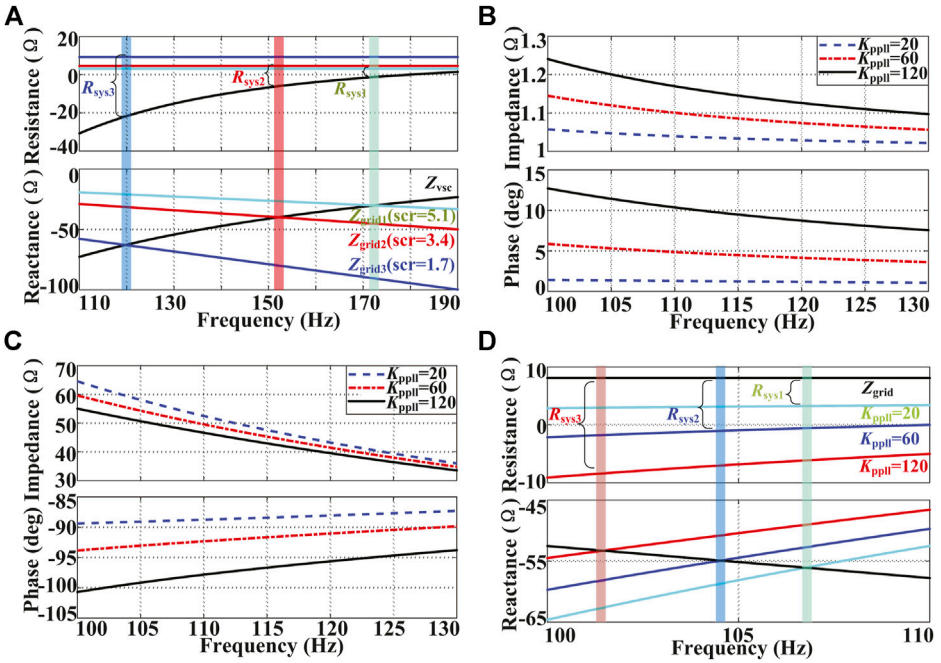


FIGURE 6 | Impact of SCR on the impedance-frequency curves. **(A)** $Z_{vsc}(s)$ and $Z_{grid}(s)$ and impact of K_{ppll} on the impedance-frequency curves. **(B)** $Z_{pll}(s)$; **(C)**$Z_{vsc}(s)$; and **(D)** $Z_{vsc}(s)$ and $Z_{grid}(s)$.

analyzed based on the impedance-frequency curves, which are more intuitive and convenient compared with the Nyquist plots

$$\begin{cases} R_{sys} = \mathrm{Re}\left(Z_{dfig}(s) \| Z_{grid}(s) + Z_{vsc}(s)\right) > 0 \\ X_{sys} = \mathrm{Im}\left(Z_{dfig}(s) \| Z_{grid}(s) + Z_{vsc}(s)\right) = 0 \end{cases}, \tag{17}$$

where R_{sys} and X_{sys} are the system resistance and reactance.

4 MECHANISM AND CHARACTERISTICS ANALYSIS

According to the equivalent impedance model of the system built in **Section 3**, the impact of local grid strength and SEC parameters on the system stability are analyzed in this section. Then, the effect of the integration of the DFIG-based wind farms on the oscillation is analyzed as well.

4.1 Local Grid Strength

To analyze the impact of local grid strength on the electrical oscillation, the variation of the SCR from 5.1 to 1.7 is analyzed under the same operating condition as Scenario 1 in **Section 2.2** without the SEC outer loop and the integrated DFIG. The impedance-frequency curves of the grid and the SEC are depicted in **Figure 6A**. It can be found that both the resistance and reactance of the SEC follow a parabolic trend increase with the negative value. Note that in **Figure 6A** and the following figures, the grid reactance is represented by its opposite number $-X_{grid}$ to better find out the frequency intersection point, while the grid resistance is still R_{grid}. According to **Eq. 17**, when the system equivalent reactance $X_{sys} = 0$ ($X_{vsc} = -X_{grid}$), the system will be stable when the system equivalent resistance $R_{sys} = R_{vsc} + R_{grid} > 0$. When reducing the SCR of the local grid, the grid resistance follows a small increase, while the grid reactance follows a significant increase and thus the intersection point for $X_{vsc} = -X_{grid}$ is shifted to the left, which means the resonant frequency of the system is reduced. Then, the system equivalent resistance ($R_{sys} = R_{vsc} + R_{grid}$) changes from positive to negative at the corresponding resonant frequency. In **Figure 6A**, the system equivalent resistance decreases from R_{sys1} to R_{sys3}. Therefore, the system stability is weakened with the reduction of the SCR. The fast uptrend of R_{vsc} and X_{vsc} in the investigated MFO region plays a key role in the oscillation, while the reduction of the SCR has an incentive effect.

4.2 Controller Parameters of the SEC

4.2.1 PLL Parameters of the SEC

According to **Eq. 14**, since the power loop is directly coupled with the current loop instead of PLL in the numerator, the term $(1 + H_s(s - j\omega_1))$ can be regarded as a disturbance term to the current loop and thus can be ignored in the analysis of the PLL parameters. Besides, the decoupling term can also be ignored for its small influence. Then, the impedance model of the SEC can be simplified as

$$Z_{vsc}(s) = -\frac{H_c(s - j\omega_1) + sL_f}{1 - \frac{1}{2}\left(I_c H_c(s - j\omega_1) + U_{pccd}\right)T_{pll}(s - j\omega_1)}. \tag{18}$$

The numerator of **Eq. 18** represents the impedance of the SEC without considering the influence of PLL. According to **Eq. 19**, it

can be found that the resistance of the SEC will be positive without the influence of PLL since $K_{pc} > 0$. The phase angle of $Z_{vsc,nopll}(s)$ will be less than −90° because of the existence of the resistance term K_{pc}

$$Z_{vsc,nopll}(s) = K_{pc} - j\left(\frac{K_{ic}}{\omega - \omega_1} - \omega L_f\right). \tag{19}$$

Then, the denominator of **Eq. 18** which represents the influence of PLL is analyzed. Since $K_{ppll} \gg K_{ipll}/(\omega - \omega_1)$ in the investigated MFO region, the integral gain of PLL can be ignored. Besides, $U_{pccd} = 1$ is considered in the further analysis. Thus, the denominator of **Eq. 18** can be simplified as

$$Z_{pll}(s) = \frac{1}{2}\frac{K_{ppll}^2\left(1 - I_cK_{pc}\right) + K_{ppll}I_cK_{ic} + 2(\omega - \omega_1)^2}{K_{ppll}^2 + (\omega - \omega_1)^2} + j\frac{1}{2}\frac{K_{ppll}^2I_cK_{ic} + K_{ppll}\left(1 + I_cK_{pc}\right)(\omega - \omega_1)^2}{(\omega - \omega_1)\left[K_{ppll}^2 + (\omega - \omega_1)^2\right]}, \tag{20}$$

$$\angle Z_{pll}(s) = arctan\frac{K_{ppll}^2I_cK_{ic} + K_{ppll}\left(1 + I_cK_{pc}\right)(\omega - \omega_1)^2}{(\omega - \omega_1)\left[K_{ppll}^2\left(1 - I_cK_{pc}\right) + K_{ppll}I_cK_{ic} + 2(\omega - \omega_1)^2\right]}. \tag{21}$$

According to **Eq. 20**, both $\mathrm{Re}(Z_{pll}(s))$ and $\mathrm{Im}(Z_{pll}(s))$ follow a parabolic trend increase with the increase of K_{ppll}. Therefore, the magnitude of $Z_{pll}(s)$ has a positive correlation with K_{ppll}. According to **Eq. 21**, since the coefficients of K_{ppll}^2 and K_{ppll} in the numerator are larger than the denominator, $\angle Z_{pll}(s)$ also has a positive correlation with K_{ppll}. By contrast, $\angle Z_{pll}^{-1}(s)$ has a decreasing trend and may cause the phase angle of $Z_{vsc}(s)$ to be over −90° in the investigated MFO region. Therefore, it can be found that the negative damping effect of the SEC is mainly caused by the influence of PLL.

The increase of K_{ppll} from 20 to 120 pu is analyzed under the same operating condition as in **Section 4.1**, with SCR = 1.7. The corresponding influence on the impedance-frequency curves of $Z_{pll}(s)$ and $Z_{vsc}(s)$ is illustrated in **Figures 6B,C**. Obviously, the variational tendency of the curves aligns with the above analysis. In addition, both the resistance and reactance-frequency curves of the SEC and the local grid are depicted in **Figure 6D**. With the increase of K_{ppll}, the resistance of the SEC changes from positive to negative, while the negative value of the reactance of the SEC becomes smaller. Thus, the system resonant frequency is reduced, and the system resistance at the corresponding resonant frequency decreases from R_{sys1} to R_{sys3}, which is changed from positive to negative. That means the larger the K_{ppll}, the more significant the negative effects of PLL on the system stability.

4.2.2 Current Loop Parameters of the SEC

According to **Eq. 18**, $Z_{vsc}(s)$ can be expressed as the quotient of $Z_{vsc,nopll}(s)$ and $Z_{pll}(s)$, and the influence of the SEC current loop is represented in both of them. First, the influence of K_{pc} is analyzed. According to **(19)**, with K_{pc} increases nearby the critical points of the oscillation, $\mathrm{Re}(Z_{vsc,nopll}(s))$ is increased and thus the strength of the system damping while $\mathrm{Im}(Z_{vsc,nopll}(s))$ remains unchanged. According to **Eq. 20** and **Eq. 21**, $\mathrm{Re}(Z_{pll}(s))$ decreases linearly while $\mathrm{Im}(Z_{pll}(s))$ increases linearly with the increase of K_{pc}, which means $\angle Z_{pll}(s)$ becomes more positive while $\angle Z_{pll}^{-1}(s)$ becomes more negative. Thus, the influence of K_{pc} on $Z_{vsc,nopll}(s)$ and $Z_{pll}(s)$ is opposite. However, the influence of K_{pc} on $Z_{pll}(s)$ is represented in the term $(I_cK_{pc} + 1)$ and thus the variation of K_{pc} has small influence on this term. Therefore, the influence of K_{pc} is mainly reflected in $Z_{vsc,nopll}(s)$ instead of $Z_{pll}(s)$.

The increase of K_{pc} from 0.25 to 0.35 pu is analyzed under the same operating condition as in **Section 4.1**, with SCR = 1.7 and K_{ppll} = 60 pu. The corresponding influence on the impedance-frequency curves of $Z_{vsc,nopll}(s)$, $Z_{pll}(s)$ and $Z_{vsc}(s)$ is illustrated in **Figures 7A–C**. In addition, both the resistance- and reactance-frequency curves of the SEC and the local grid are depicted in **Figure 7D**. According to **Figure 7C**, with K_{pc} increases nearby the critical points of the oscillation, $\angle Z_{vsc}(s)$ changes from more than −90° to less than −90°, which means that the resistance of the SEC changes from negative to positive. Correspondingly, the reactance of the SEC changes very little since the sine function is around the peak zone. Thus, the system resistance at the corresponding resonant frequency becomes positive. In **Figure 7D**, the system equivalent resistance increases from R_{sys1} to R_{sys3} due to the increase of SEC resistance with K_{pc}, which also validates the above analysis. Hence, the system stability has a positive correlation with K_{pc}.

In addition, the influence of K_{ic} is analyzed. According to **Eq. 19**, with K_{ic} increases, $\mathrm{Im}(Z_{vsc,nopll}(s))$ is decreased while $\mathrm{Re}(Z_{vsc,nopll}(s))$ remains unchanged. By comparison with that, the influence of K_{ic} on $Z_{pll}(s)$ can also be ignored and thus $Z_{pll}^{-1}(s)$ is regarded as constant. Note that $\mathrm{Re}(Z_{vsc,nopll}(s))$ remains unchanged during the variation of K_{ic}; thus, the resistance of the SEC is only determined by $Z_{pll}^{-1}(s)$ which can be expressed as $Z_{pll}^{-1}(s) = R_{pll} - jX_{pll}$, where $R_{pll}, X_{pll} > 0$. Therefore, $Z_{vsc}(s)$ can be expressed as

$$\begin{aligned} Z_{vsc}(s) &= \left[H_c(s - j\omega_1) + sL_f\right]\left(R_{pll} - jX_{pll}\right) \\ &= R_{pll}K_{pc} - X_{pll}\left(\frac{K_{ic}}{\omega - \omega_1} - \omega L_f\right) - j\left[X_{pll}K_{pc} + R_{pll}\left(\frac{K_{ic}}{\omega - \omega_1} - \omega L_f\right)\right]. \end{aligned} \tag{22}$$

According to **Eq. 22**, the increase of K_{ic} leads to the decrease of both the resistance and reactance of the SEC and thus causes the higher system resonant frequency. Then, the system resistance at the corresponding resonant frequency is reduced. Thus, the system stability has a negative correlation with K_{ic}.

4.2.3 Power Loop Parameters of the SEC

The term $(1 + H_s(s - j\omega_1))$ is reconsidered when focusing on the effect of the power loop of the SEC. As discussed before, only the influence of the power loop on $Z_{vsc,nopll}(s)$ needs to be analyzed since it has no effect on $Z_{pll}(s)$

$$\begin{aligned} Z_{vsc,nopll}(s) &= H_c(s - j\omega_1)\left(1 + H_s(s - j\omega_1)\right) + sL_f \\ &= K_{pc}\left(1 + K_{ps}\right) - \frac{K_{ic}K_{is}}{(\omega - \omega_1)^2} - j\left(\frac{K_{ic}\left(1 + K_{ps}\right) + K_{is}K_{pc}}{\omega - \omega_1} - \omega L_f\right). \end{aligned} \tag{23}$$

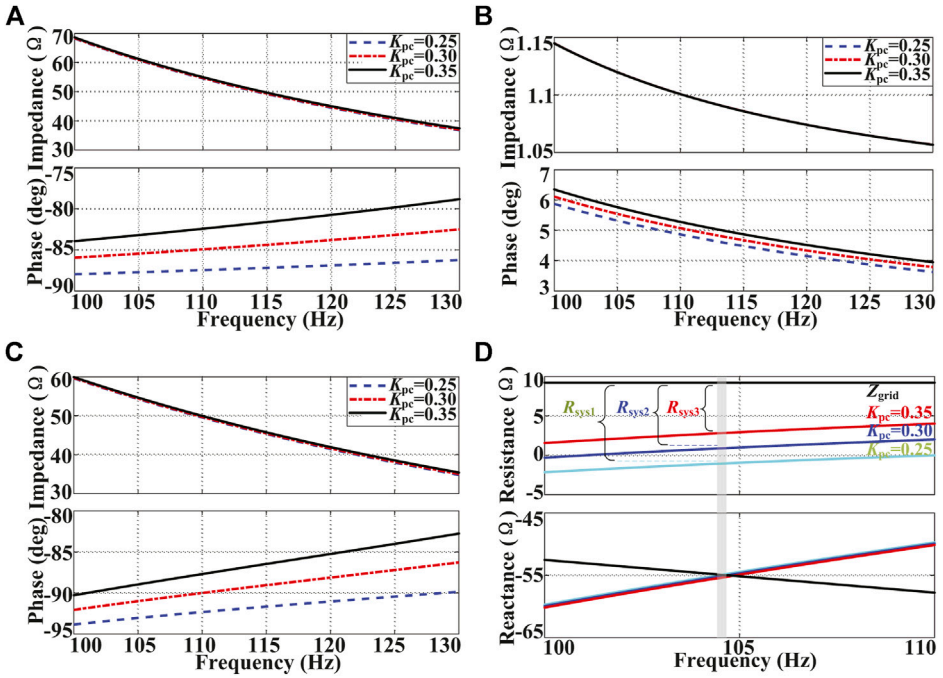


FIGURE 7 | Impact of K_{pc} on the impedance-frequency curves. **(A)** $Z_{vsc,nopll}(s)$; **(B)** $Z_{pll}(s)$; **(C)** $Z_{vsc}(s)$; and **(D)** $Z_{vsc}(s)$ and $Z_{grid}(s)$.

Obviously, the influence of the outer loop and inner loop on the impedance of the SEC is coupled directly. Considering $(\omega-\omega_1)^2 K_{pc}K_{ps} > K_{ic}K_{is}$ at the investigated MFO region, it can be found that the resistance of the SEC is improved slightly due to the consideration of the power loop at the same frequency. However, the reactance of the SEC becomes more negative and thus the resonant frequency point is shifted to the right, and the system resistance is reduced at the new resonant frequency. Then, further analysis of the interaction between the current loop and the power loop is provided. According to **Eq. 23**, when K_{pc} or K_{ps} increases, the resistance of the SEC becomes more positive while the reactance becomes more negative, and thus, the system stability is improved. K_{ps} increasing from 0.05 to 0.35 pu is analyzed under the same operating condition as in **Section 4.1**, with the SEC outer loop and SCR = 5.1. The corresponding influence on the resistance- and reactance-frequency curves of the SEC and the local grid is illustrated in **Figure 8A**. The system equivalent resistance increases from R_{sys1} to R_{sys3} due to the increase of SEC resistance with K_{ps}. The variational tendency of the curves aligns with the above analysis.

In addition, when K_{ic} or K_{is} increases, both the resistance and reactance of the SEC become more negative. Note that the reduction of the reactance is in favor of the system stability, while the reduction of the resistance has an opposite effect. Since $(\omega-\omega_1) > (1+K_{ps})K_{is}$, the variation of the resistance is larger than that of the reactance with K_{is} increases, which means that the system resistance at the corresponding resonant frequency becomes negative and thus weakens the system stability. Likewise, the influence of K_{ic} is similar to that of K_{is}. Besides, the coefficient of K_{pc} and K_{ic} in **Eq. 23** is $(1+K_{ps})$, while the coefficient of K_{ps} and K_{is} is K_{pc}. Thus, the influence of the power loop is lower than that of the current loop because $(1+K_{ps}) > K_{pc}$. This analysis is verified by comparing **Figures 8A,B**, which show that the influence of K_{pc} ranges from 0.2 to 0.3 pu, with $K_{ps} = 0.2$ pu.

4.3 Operating Condition and Controller Parameters of the DFIG

4.3.1 Number of Grid-Connected DFIG-WTs

The integration of the DFIG-based wind farms is not considered in the above subsections when focusing on the influence of the control parameters of the SEC. In this part, the effect of the number of grid-connected DFIG-WTs on the system stability is analyzed. According to **Eq. 15**, since the PLL dynamics of the DFIG mainly reflects the nearby fundamental frequency (Vieto and Sun, 2018; Sun et al., 2019), it can be neglected during the analysis in the investigated MFO region. Besides, K_{pr} is dominant in the RSC current control loop, while K_{ir} is less important and can be ignored in the following analysis. Thus, the equivalent resistance and reactance of the multiple DFIG-WTs can be simplified as (Sun et al., 2019)

$$R_{dfig} = \frac{r_r + K_{pr}}{nS_{lip}} + \frac{r_s}{n}, \quad X_{dfig} = \frac{\omega(L_r + L_s)}{n}, \tag{24}$$

where n represents the number of DFIG-WTs. According to **Eq. 24**, the DFIG represents as a resistance-inductance since the rotor slip $S_{lip} = (s - j\omega_r)/s$ is positive in the investigated MFO region. It is contrary to the SSO mechanism that the DFIG represents as an inductance in series with a negative resistance in the SSO

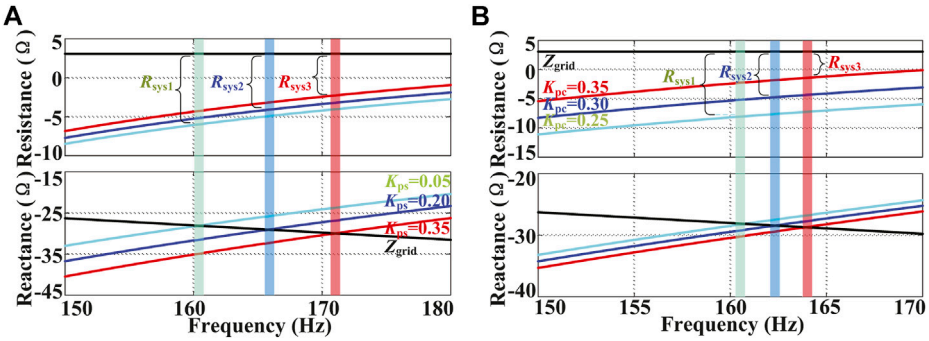


FIGURE 8 | Impact of different factors on $Z_{vsc}(s)$ and $Z_{grid}(s)$. **(A)** K_{ps}. **(B)** K_{pc}.

frequency region. Compared with SSO caused by the DFIG, the frequency of the electrical oscillation studied in this article is about 100–200 Hz, which is a kind of MFO. The negative damping of the system is induced by the SEC instead of the DFIG, which means that the mechanism of this electrical oscillation is totally different from that of SSO caused by the DFIG (Sun et al., 2019).

According to **Figure 5**, the integration of the DFIG is equivalent to inserting an impedance on the PCC, which is in parallel with the local grid. The parallel impedance is still resistive and inductive in the investigated MFO region, which can be expressed as

$$Z_{dfig}(s)||Z_{grid}(s) \approx \frac{-X_{grid}X_{dfig} + jX_{grid}R_{dfig}}{R_{dfig} + j\left(X_{grid} + X_{dfig}\right)} = \frac{X_{grid}\left[X_{grid}R_{dfig} + j\left(R_{dfig}^2 + X_{grid}R_{dfig} + X_{dfig}^2\right)\right]}{R_{dfig}^2 - \left(X_{grid} + X_{dfig}\right)^2}, \quad (25)$$

where R_{grid} is neglected due to its small value. According to **Eq. 25**, since $X_{dfig} \gg R_{dfig}$ in the investigated MFO region, the reduction of $\mathrm{Re}(Z_{dfig}(s)||Z_{grid}(s))$ is much larger than $\mathrm{Im}(Z_{dfig}(s)||Z_{grid}(s))$ with the increase of n. Thus, the resonant frequency point of the system shifts to the right, and the corresponding system resistance changes from negative to positive. The influence of n increasing from 180 to 220 is analyzed in **Figure 9A** under the same operating condition as Scenario 2 in **Section 2.2**, with SCR = 1.7. The system equivalent resistance increases from R_{sys1} to R_{sys3} due to the increase of SEC resistance with frequency. It can be concluded that the larger the n nearby the critical points of the oscillation, the more positive the effect of DFIG-WTs on the system stability. In addition, since R_{dfig} and X_{dfig} are the inverse proportional function of n, the influence of n on the system is significant when n is not large.

4.3.2 Wind Speed

According to **Eq. 24**, the resistance of the DFIG can be expressed as $(r_r + K_{pr})/nS_{lip} + r_s/n$. Contrary to the SSO mechanism of the DFIG, the rotor slip $S_{lip} = (s - j\omega_r)/s$ is positive in the investigated MFO region. With the increase of the wind speed, the rotor speed ω_r is increased while the rotor slip decreases. Thus, the rotor resistance $(r_r + K_{pr})/nS_{lip}$ is larger when the wind speed is high, which means that the DFIG will provide more positive damping for the whole system. The influence of wind speeds in the range of 9.5–10.5 m/s on the system impedance is analyzed in **Figure 9B**. The system equivalent resistance changes from R_{sys1} to R_{sys3}, which is increased slightly due to the increase of $\mathrm{Re}(Z_{dfig}(s)||Z_{grid}(s))$ with wind speed. Therefore, the increase of the wind speed leads to better system stability.

4.3.3 Current Loop Parameters of the RSC

With the increase of K_{pr}, the rotor resistance $(r_r + K_{pr})/nS_{lip}$ is increased directly since the rotor slip is positive in the investigated MFO region, which means that the DFIG will provide more positive damping for the whole system when K_{pr} is relatively large. The influence of K_{pr} in the range of 0.45–0.75 pu on the system impedance is analyzed in **Figure 9C**. The system equivalent resistance changes from R_{sys1} to R_{sys3}, which is increased slightly due to the increase of $\mathrm{Re}(Z_{dfig}(s)||Z_{grid}(s))$ with K_{pr}. Therefore, the influence of K_{pr} is similar to that of the wind speed, which is helpful for the system stability.

4.3.4 PLL Parameters of the DFIG

In this part, the influence of PLL parameters of the DFIG is reconsidered based on the impedance model in **Eq. 15**. The influence of $K_{ppll-rsc}$ increasing from 20 to 120 pu on the system impedance is illustrated in **Figure 9D**. Note that when the bandwidth of PLL increases with $K_{ppll-rsc}$, the equivalent resistance of the system increases slightly from R_{sys1} to R_{sys3}, while the reactance almost remains unchanged in the investigated MFO region. By combining **Figures 9A–D**, the change of the system impedance caused by the PLL parameters of the DFIG is much smaller than other factors. Thus, it is not an efficient method to improve the system stability by adjusting $K_{ppll-rsc}$ of the DFIG.

5 SIMULATION VERIFICATION

The impact of the controller parameters and the operating condition of the system on the oscillation are investigated in

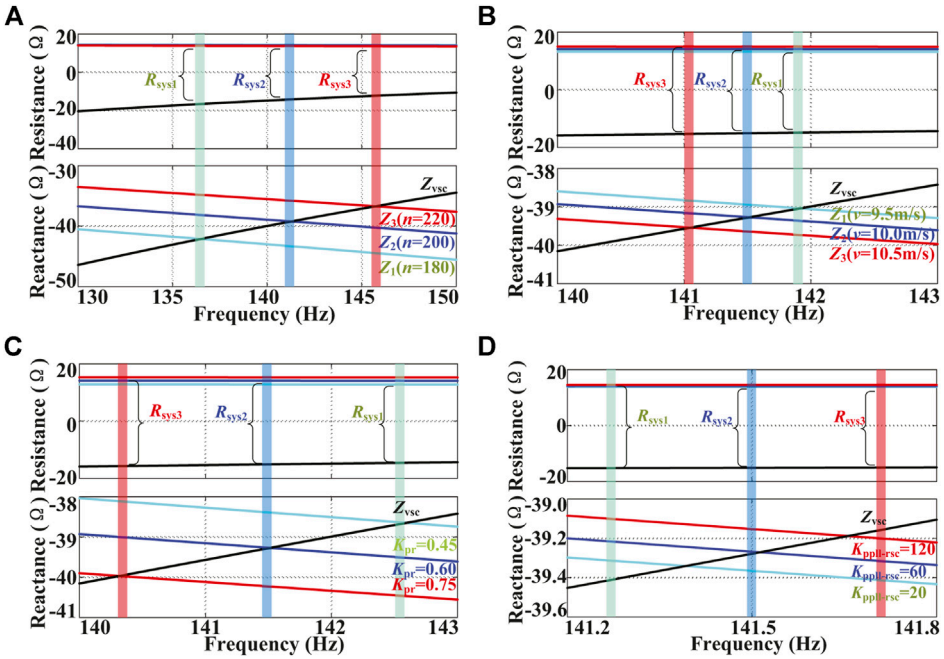


FIGURE 9 | Impact of different factors on $Z_{vsc}(s)$ and $Z_{grid}(s)$. **(A)** n; **(B)** wind speeds; **(C)** K_{pr}; and **(D)** $K_{ppll-rsc}$.

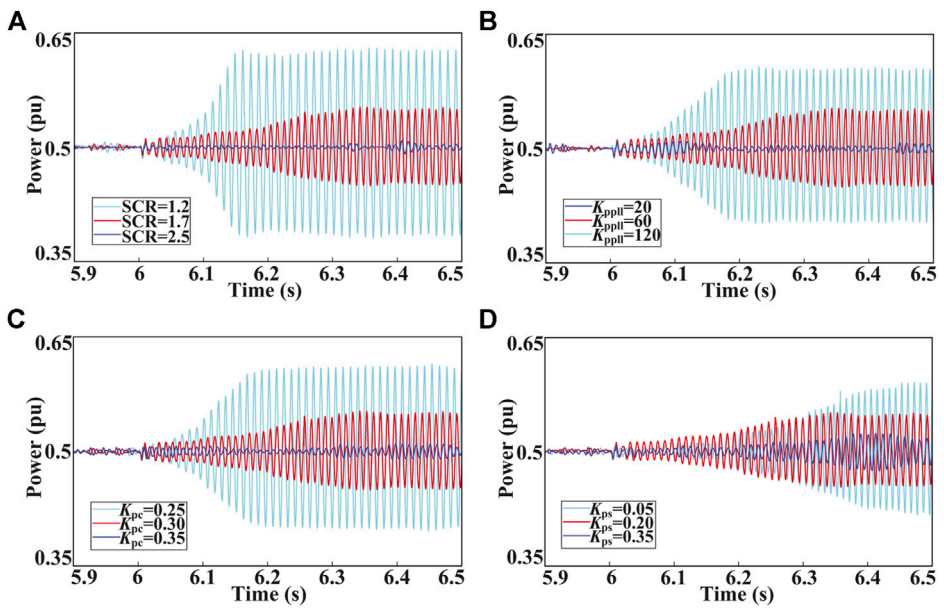


FIGURE 10 | Output power varies with **(A)** SCR, **(B)** K_{ppll}, **(C)** K_{pc}, and **(D)** K_{ps}.

Section 4. The time-domain simulations are conducted to validate the correctness of the theoretical analysis.

5.1 Local Grid Strength

The impact of the local grid strength is analyzed under the following operating condition: the number of grid-connected DFIG-WTs is 200, the wind speed is 10 m/s, SCR of the local grid is 3.4, and other system parameters are the same as in **Section 2.2**. **Figure 10A** shows the output active power responses on the PCC for a sudden change of the SCR from 1.2 to 2.5 at t = 6 s. Obviously, the oscillation state changes from convergent to divergent with the decrease of the SCR. Therefore, the system stability has a positive correlation with the local grid strength. The simulation results align with the analysis in **Section 4.1**.

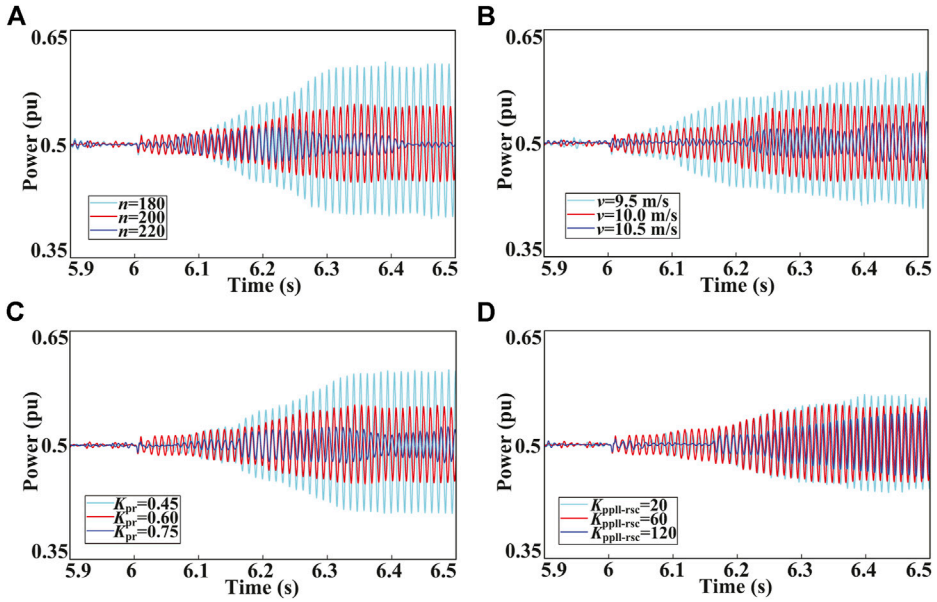


FIGURE 11 | Output power varies with **(A)** number of DFIG-WTs, **(B)** wind speed, **(C)** K_{pr}, and **(D)** $K_{ppll-rsc}$.

5.2 Control Parameters of the SEC

The impact of the PLL, current loop, and power loop of the SEC on the oscillation characteristics is analyzed under the same operating condition as in **Section 4.1**, with a sudden change of the SCR from 3.4 to 1.7 at t = 6 s. As shown in **Figure 10B**, the output active power responses on the PCC with K_{ppll} in the range of 20–120 pu are measured. With K_{ppll} increases, the oscillation state changes from convergent to invariable, which means that the oscillation is intensified when K_{ppll} is large. As can be seen in **Figure 10C**, the oscillation state changes from divergent to convergent when K_{pc} increases from 0.2 to 0.3 pu, which means that the system stability has a positive correlation with K_{pc}. **Figure 10D** illustrates the simulation results when K_{ps} changes from 0.05 to 0.35 pu. When K_{ps} increases, the divergence speed of the oscillation becomes slower, which means that the system stability has a positive correlation with K_{ps}. By comparing the waveforms in **Figure 10C**, it can be found that K_{ps} has less impact on the oscillation than K_{pc}. The above conclusions agree with the analysis in **Section 4.2**.

5.3 Operating Condition and Controller Parameters of the DFIG

The impact of n, wind speed, RSC current loop, and PLL of the DFIG on the oscillation characteristics is analyzed under the same operating condition as in **Section 5.2**, with other control parameters of the SEC kept unchanged. **Figure 11A** shows that the output active power responds to the number of grid-connected DFIG-WTs, which ranges from 180 to 220. Obviously, the oscillation is gradually suppressed while the n increases. As shown in **Figure 11B**, the simulation results with the wind speed changes from 9.5 to 10.5 m/s are depicted. It can be observed that the system stability has a positive correlation with the wind speed. The output active power responses on the PCC with K_{pr} from 0.45 to 0.75 pu are depicted in **Figure 11C**. As can be seen, the oscillation state changes from divergent to convergent when K_{pr} increases. **Figure 11D** illustrates the simulation results when $K_{ppll-rsc}$ changes from 20 to 120 pu. When $K_{ppll-rsc}$ increases, the divergence speed of the oscillation becomes slightly slower. It can be found that $K_{ppll-rsc}$ has little influence on the oscillation compared with other parameters. In conclusion, the above simulation results align with the analysis in **Section 4.3**.

6 CONCLUSION

A SEC with PQ-control faces the potential risk of a new type of electrical oscillation in the medium-frequency region when it transmits the wind-thermal–bundled power from the local grid and DFIG-based wind farms. In this study, the sequence impedance model of the SEC with the explicit analytic expression is derived to help understand the mechanism and characteristics of MFO. This oscillation mainly originates from the SEC, while the local AC grid strength and the integration of DFIG-based wind farms also have an influence on it. With regard to the SEC controllers, the system stability is weakened with the increased proportional gain of the PLL controller. In addition, system stability has a positive correlation with the proportional gains of both the current loop and the power loop. However, the influence of the power loop is not as large as that of the current loop. Regarding the influence of the local grid strength, the oscillation risk increases when the local grid is weak. Contrary to the SSO mechanism of the DFIG, the risk of this oscillation decreases when relatively more DFIG-WTs are integrated at a high wind speed. Besides, system stability has a positive correlation with the proportional gains of the RSC current loop, while the influence of PLL of the RSC is slight. In conclusion, these factors can influence the system resistance at the resonant frequency, and the oscillation may appear due to the negative damping under the undesired operating

conditions and controller parameters of the DFIG, local grid, and SEC. All the theoretical analyses are verified by time-domain simulation.

DATA AVAILABILITY STATEMENT

The original contributions presented in the study are included in the article/**Supplementary Material**; further inquiries can be directed to the corresponding author.

AUTHOR CONTRIBUTIONS

KS and WY contributed to the conception and design of the study. CY and JW organized case studies. KS wrote the first draft of the manuscript. All authors contributed to manuscript revision and read and approved the submitted version.

FUNDING

This work was supported by the National Key R&D Program of China (2019YFB1505400).

SUPPLEMENTARY MATERIAL

The Supplementary Material for this article can be found online at: https://www.frontiersin.org/articles/10.3389/fenrg.2021.693903/full#supplementary-material

REFERENCES

Baltas, G. N., Lai, N. B., Tarraso, A., Marin, L., Blaabjerg, F., and Rodriguez, P. (2021). Ai-based Damping of electromechanical oscillations by using grid-connected converter. *Front. Energ. Res.* 9, 598436. doi:10.3389/fenrg.2021.598436

Cespedes, M., and Jian Sun, J. (2014). Impedance Modeling and Analysis of Grid-Connected Voltage-Source Converters. *IEEE Trans. Power Electron.* 29, 1254–1261. doi:10.1109/TPEL.2013.2262473

Chen, C., Du, W., Du, W., Wang, H., and Littler, T. (2018). Sub-synchronous oscillations in power systems caused by grid-connected wind farms - a survey of mechanism studies. *Csee Jpes* 4, 495–503. doi:10.17775/CSEEJPES.2018.00560

Chen, J., Li, L., Dong, F., Wang, X., Sheng, H., Sun, C., et al. (2020). An improved coordination method of multi-terminal mmc-hvdc system suitable for wind farm clusters integration. *Int. J. Electr. Power Energ. Syst.* 117, 105652. doi:10.1016/j.ijepes.2019.105652

Christoph, B., Christian, R., Andreas, M., and Jochen, J. (2015). "Borwin1-first experiences with harmonic interactions in converter Dominated grids," in Proc. 2015 Int. ETG Congress, Bonn, Germany, November 17–18, 2015, 592–602.

Flourentzou, N., Agelidis, V. G., and Demetriades, G. D. (2009). Vsc-based hvdc power transmission systems: an overview. *IEEE Trans. Power Electron.* 24, 592–602. doi:10.1109/TPEL.2008.2008441

Gao, B., Hu, Y., Song, R., Li, R., Zhang, X., Yang, L., et al. (2018). Impact of DFIG-based wind farm integration on sub-synchronous torsional interaction between HVDC and thermal generators. *IET Generation, Transm. Distribution* 12, 3913–3923. doi:10.1049/iet-gtd.2018.0328

Huang, L., Xin, H., Yuan, H., Wang, G., and Ju, P. (2021). Damping effect of virtual synchronous machines provided by a Dynamical virtual impedance. *IEEE Trans. Energ. Convers.* 36, 570–573. doi:10.1109/TEC.2020.3040605

Khazaei, J., Beza, M., and Bongiorno, M. (2018). Impedance analysis of modular multi-level converters connected to weak ac grids. *IEEE Trans. Power Syst.* 33, 4015–4025. doi:10.1109/TPWRS.2017.2779403

Koralewicz, P., Shah, S., Gevorgian, V., Wallen, R., Jha, K., Mashtare, D., et al. (2020). Impedance analysis and phil Demonstration of reactive power oscillations in a wind power plant using a 4-mw wind turbine. *Front. Energ. Res.* 8, 156. doi:10.3389/fenrg.2020.00156

Kunjumuhammed, L. P., Pal, B. C., Oates, C., and Dyke, K. J. (2017). The adequacy of the present practice in Dynamic aggregated modeling of wind farm systems. *IEEE Trans. Sustain. Energ.* 8, 23–32. doi:10.1109/TSTE.2016.2563162

Liu, B., Li, Z., Wang, H., Dong, X., Su, W., Li, G., et al. (2021). Impedance modeling of Dfig wind farms with various rotor speeds and frequency coupling. *IEEE Trans. Circuits Syst.* 68, 406–410. doi:10.1109/TCSII.2020.2997927

Liu, H., and Xie, X. (2019). Comparative studies on the impedance models of vsc-based renewable generators for ssi stability analysis. *IEEE Trans. Energ. Convers.* 34, 1442–1453. doi:10.1109/TEC.2019.2913778

Liu, H., Xie, X., and Liu, W. (2018). An Oscillatory Stability Criterion Based on the Unified dq -Frame Impedance Network Model for Power Systems With High-Penetration Renewables. *IEEE Trans. Power Syst.* 33, 3472–3485. doi:10.1109/TPWRS.2018.2794067

Liu, H., Xie, X., Zhang, C., Li, Y., Liu, H., and Hu, Y. (2017). Quantitative ssr analysis of series-compensated Dfig-based wind farms using aggregated rlc circuit model. *IEEE Trans. Power Syst.* 32, 474–483. doi:10.1109/TPWRS.2016.2558840

Lyu, J., Cai, X., Amin, M., and Molinas, M. (2018). Sub-synchronous oscillation mechanism and its suppression in MMC-based HVDC connected wind farms. *IET Generation, Transm. Distribution* 12, 1021–1029. doi:10.1049/iet-gtd.2017.1066

Miao, Z. (2012). Impedance-model-based ssr analysis for type 3 wind generator and series-compensated network. *IEEE Trans. Energ. Convers.* 27, 984–991. doi:10.1109/TEC.2012.2211019

Peng, X., Yao, W., Yan, C., Wen, J., and Cheng, S. (2020). Two-stage variable proportion coefficient based frequency support of grid-connected Dfig-wts. *IEEE Trans. Power Syst.* 35, 962–974. doi:10.1109/TPWRS.2019.2943520

Shah, R., Sánchez, J. C., Preece, R., and Barnes, M. (2018). Stability and control of mixed AC-DC systems with VSC-HVDC: a review. *IET Generation, Transm. Distribution* 12, 2207–2219. doi:10.1049/iet-gtd.2017.1140

Shah, S., and Parsa, L. (2017). Impedance modeling of three-phase voltage source converters in Dq, sequence, and phasor Domains. *IEEE Trans. Energ. Convers.* 32, 1139–1150. doi:10.1109/TEC.2017.2698202

Sun, B., Yu, Y., and Qin, C. (2017). Should china focus on the Distributed Development of wind and solar photovoltaic power generation? a comparative study. *Appl. Energ.* 185, 421–439. doi:10.1016/j.apenergy.2016.11.004

Sun, K., Xiao, H., You, S., Li, H., Pan, J., Li, K.-J., et al. (2020). Frequency secure control strategy for power grid with large-scale wind farms through hvdc links. *Int. J. Electr. Power Energ. Syst.* 117, 105706. doi:10.1016/j.ijepes.2019.105706

Sun, K., Yao, W., Fang, J., Ai, X., Wen, J., and Cheng, S. (2020). Impedance modeling and stability analysis of grid-connected Dfig-based wind farm with a vsc-hvdc. *IEEE J. Emerg. Sel. Top. Power Electron.* 8, 1375–1390. doi:10.1109/JESTPE.2019.2901747

Vieto, I., and Sun, J. (2018). Sequence impedance modeling and analysis of type-iii wind turbines. *IEEE Trans. Energ. Convers.* 33, 537–545. doi:10.1109/TEC.2017.2763585

Wang, L., Peng, J., You, Y., and Ma, H. (2019). Iterative approach to impedance model for small-signal stability analysis. *IET Renew. Power Generation* 13, 78–85. doi:10.1049/iet-rpg.2018.5265

Wang, Q., Yao, W., Fang, J., Ai, X., Wen, J., Yang, X., et al. (2020). Dynamic modeling and small signal stability analysis of Distributed photovoltaic grid-connected system with large scale of panel level Dc optimizers. *Appl. Energ.* 259, 114132. doi:10.1016/j.apenergy.2019.114132

Wang, X., Harnefors, L., and Blaabjerg, F. (2018). Unified impedance model of grid-connected voltage-source converters. *IEEE Trans. Power Electron.* 33, 1775–1787. doi:10.1109/TPEL.2017.2684906

Wen, B., Boroyevich, D., Burgos, R., Mattavelli, P., and Shen, Z. (2017). Inverse nyquist stability criterion for grid-tied inverters. *IEEE Trans. Power Electron.* 32, 1548–1556. doi:10.1109/TPEL.2016.2545871

Xiao, H., Du, W., Song, Y., Wang, Q., Ding, J., Chen, D., et al. (2016). Wind-thermal-bundled power transmission by ac/dc system and coordinated control - a review. 12th IET International Conference on AC and DC Power Transmission (ACDC 2016), Beijing, China, January, 2016. doi:10.1049/cp.2016.0470

Xiong, Y., Yao, W., Wen, J., Lin, S., Ai, X., Fang, J., et al. (2020). Two-level combined control scheme of vsc-mtdc integrated offshore wind farms for onshore system frequency support. *IEEE Trans. Power Syst.* 36, 1. doi:10.1109/TPWRS.2020.2998579

Xu, J., Qian, Q., Zhang, B., and Xie, S. (2019). Harmonics and stability analysis of single-phase grid-connected inverters in Distributed power generation systems considering phase-locked loop impact. *IEEE Trans. Sustain. Energ.* 10, 1470–1480. doi:10.1109/TSTE.2019.2893679

Yan, C., Yao, W., Wen, J., Fang, J., Ai, X., and Wen, J. (2020). Modelling and comparison analysis of grid-connected DFIG-based wind farm in weak grid. *IET Renew. Power Generation* 14, 2406–2415. doi:10.1049/iet-rpg.2019.1382

Yan, C., Yao, W., Wen, J., Fang, J., Ai, X., and Wen, J. (2020). Optimal Design of probabilistic robust Damping controllers to suppress multiband oscillations of power systems integrated with wind farm. *Renew. Energ.* 158, 75–90. doi:10.1016/j.renene.2020.05.008

Yang, B., Jiang, L., Yu, T., Shu, H. C., Zhang, C.-K., Yao, W., et al. (2018). Passive control Design for multi-terminal vsc-hvdc systems via energy shaping. *Int. J. Electr. Power Energ. Syst.* 98, 496–508. doi:10.1016/j.ijepes.2017.12.028

Yogarathinam, A., Kaur, J., and Chaudhuri, N. R. (2017). Impact of inertia and effective short circuit ratio on control of frequency in weak grids interfacing lcc-hvdc and Dfig-based wind farms. *IEEE Trans. Power Deliv.* 32, 2040–2051. doi:10.1109/TPWRD.2016.2607205

Zhang, C., Cai, X., Molinas, M., and Rygg, A. (2019). Frequency-domain modelling and stability analysis of a DFIG-based wind energy conversion system under non-compensated AC grids: impedance modelling effects and consequences on stability. *IET Power Electro.* 12, 907–914. doi:10.1049/iet-pel.2018.5527

Zhou, Q., Ding, Y., Mai, K., Bian, X., and Zhou, B. (2019). Mitigation of subsynchronous oscillation in a vsc-hvdc connected offshore wind farm integrated to grid. *Int. J. Electr. Power Energ. Syst.* 109, 29–37. doi:10.1016/j.ijepes.2019.01.031

Zhou, W., Wang, Y., Torres-Olguin, R. E., and Chen, Z. (2020). Effect of reactive power characteristic of offshore wind power plant on low-frequency stability. *IEEE Trans. Energ. Convers.* 35, 837–853. doi:10.1109/TEC.2020.2965017

Zou, C., Rao, H., Xu, S., Li, Y., Li, W., Chen, J., et al. (2018). Analysis of resonance between a vsc-hvdc converter and the ac grid. *IEEE Trans. Power Electron.* 33, 10157–10168. doi:10.1109/TPEL.2018.2809705

Conflict of Interest: The authors declare that the research was conducted in the absence of any commercial or financial relationships that could be construed as a potential conflict of interest.

Copyright © 2021 Sun, Yao, Yan and Wen. This is an open-access article distributed under the terms of the Creative Commons Attribution License (CC BY). The use, distribution or reproduction in other forums is permitted, provided the original author(s) and the copyright owner(s) are credited and that the original publication in this journal is cited, in accordance with accepted academic practice. No use, distribution or reproduction is permitted which does not comply with these terms.

frontiers in Energy Research

ORIGINAL RESEARCH
published: 21 May 2021
doi: 10.3389/fenrg.2021.686566

Hybrid Simulation for Large-Scale AC/DC Power System by Serial Interaction Process

Song Zhang, Guoqing Li, Shuguang Li and Xintong Liu*

Department of Electrical Engineering, Northeast Electric Power University, Jilin, China

Electromechanical transient (EMT) and transient stability hybrid simulations can make full use of their fast-solving ability and high-precision computing ability to accurately simulate the dynamic characteristics of large-scale AC/DC systems. This paper selects the bus as the hybrid simulation interface bus in the AC system near the DC system, which can effectively improve the simulation accuracy of the AC/DC system interaction. At the interface bus, Norton equivalent and Thevenin equivalent are applied to the EMT simulation side and electromechanical transient simulation side, respectively. The three-phase simulation data and three-sequence component simulation data are extracted respectively, and the serial iteration method is used for hybrid simulation calculation. This paper takes Zhangbei multi terminal AC/DC system as an example, compares the hybrid simulation results with the EMT simulation results, and tries to verify the accuracy and effectiveness of the hybrid simulation method.

Keywords: hybrid simulation, HVDC, transient stability, Thevenin equivalent, electromagnetic transient

OPEN ACCESS

Edited by:
Bo Yang,
Kunming University of Science and Technology, China

Reviewed by:
SHi Peng,
Shanghai Jiao Tong University, China
Mingqiang Wang,
Shandong University, China

****Correspondence:***
Song Zhang
zhangsongneepu@aliyun.com

Specialty section:
This article was submitted to Smart Grids, a section of the journal Frontiers in Energy Research

Received: *27 March 2021*
Accepted: *12 April 2021*
Published: *21 May 2021*

Citation:
Zhang S, Li G, Li S and Liu X (2021) Hybrid Simulation for Large-Scale AC/DC Power System by Serial Interaction Process. Front. Energy Res. 9:686566. doi: 10.3389/fenrg.2021.686566

INTRODUCTION

With the proliferation of VSC-HVDC (Voltage Source Converter High Voltage Direct Current) based on power electronic devices, the influence of such fast responding devices on the AC/DC hybrid transmission system has become a research hotspot (Huang and Vittal, 2017a,b; Liming and Bo, 2020; Li et al., 2021). An EMT simulator is widely used in previous research on VSC-HVDC. The simulation results, which are in accordance with the principles of VSC-HVDC, correctly reflect the dynamic characters of the VSC-HVDC system in normal running conditions and fault conditions. However, an EMT simulator is limited in dealing with a bulk AC/DC hybrid transmission system (Venkatraman et al., 2019). This requires researchers and engineers to invest a lot of energy in modeling. Apart from that, the simulation scale is limited by computer resources, which often cannot accurately simulate the behavior characteristics of the whole system. It is necessary to combine the traditional EMT and electromechanical transient simulation methods to complement each other in the hybrid simulation technology, so as to realize the comprehensive analysis and practical engineering application of the large-scale AC/DC system transient process (Schneider et al., 2019).

At present, hybrid simulation technology has widely concerned experts and scholars at home and abroad. Meanwhile, a lot of research work has been done in this field. In reference

(Huang and Vittal, 2017b), a hybrid simulation method of transmission and distribution system is established by using a multi region Thevenin equivalent method. Moreover, the dynamic simulation of transmission and distribution network is carried out by using a partition modeling method, which effectively solves the interface hybrid problem of systems with different voltage level. In reference (Plumier et al., 2016), an iterative method of interface data between electromechanical transient simulation and EMT based on a variable vector is proposed, which effectively solves the problem of interface data distortion in hybrid simulation. In reference (Shu et al., 2018), the interface scheme of a hybrid simulation system for an AC/DC system is proposed based on a dynamic vector method, which effectively enhances the stability of the hybrid simulation interface for the AC/DC system. Although the above research focuses on solving the algorithm stability and smoothness of the hybrid simulation interface, there is not much research on the location selection of the hybrid simulation interface.

This paper proves that the dynamic characteristics of the AC/DC system can be accurately simulated by selecting the AC system bus near the DC system as the hybrid simulation interface. The construction method of hybrid simulation system with the AC bus as the interface bus is described in detail, and the serial iteration method is used as the operation flow of the hybrid simulation interface. Taking the Zhangbei multi terminal flexible HVDC transmission system as an example, this paper verifies the accuracy and effectiveness of the proposed hybrid simulation method.

A NEW HYBRID SIMULATION PLATFORM BASED ON MATLAB/SIMULINK AND MATDYN

Structure Design of the Hybrid Simulation Platform

The first task of building the hybrid simulation platform is to choose the simulation tools and design the main structure. These foundation works affect not only the applicability of the hybrid simulation but also its scalability. Indeed, a normal decoupled structure for combining an EMT and TS program has been proposed and completed in much of the literature (Zhang et al., 2013). A similar structure is employed in this paper, as shown in **Figure 1**. The TS and EMT program are under the parallel operation: when one subsystem is simulated, the other is replaced by a Thevenin equivalent system or NORTON equivalent system. The computing method of the equivalent system is introduced in detail in the following chapters.

Matlab/Simulink is adopted as the EMT simulator and MatDyn is used for TS simulation. MatDyn is a Matlab-based open-source toolbox for power system stability analysis (Zheng et al., 2019). The power flow solution of MatDyn is obtained from MATPOWER and a complete program of transient stability simulation for the power system is provided. It is noteworthy that users can flexibly add user-defined models, including generator models, governor models, exciter models, and different kinds of user-provided Ordinary Differential Equation (ODE) solvers. While it is used in the hybrid simulation as a TS simulation program, the versatility of script files and flexibility of user-defined function will be beneficial for the follow-up research work. With an appropriate adjustment of MatDyn, it is encapsulated in Matlab Function (MF) which is a user-defined function block in the Matlab/Simulink library. The EMT simulation results are specified as input data to the MF block. MatDyn will execute for simulation and generate code for a Simulink Coder target. Furthermore, the simulation results of MatDyn are specified as output data of MF blocks and input data of the EMT simulation system. The basic structure of the hybrid simulation is established, so that the EMT simulation and TS simulation operate in parallel in MATLAB/Simulink.

The EMT and TS simulation are combined by a user-defined function of MATLAB/Simulink in this hybrid simulation structure. Because of its sufficient flexibility and applicability, it could operate on one PC, a local area network through distributed communication or a real-time simulation machine like RT-LAB.

Network Partition Scheme

The common scheme of a hybrid simulation for an AC/DC system is selecting the converter bus as the interface to partition EMT and TS subsystem (van der Meer et al., 2015). The HVDC system and bulk AC power system are simulated in the EMT and TS program, respectively. A multi-interface hybrid simulation should be established while the simulation object is the VSC-MTDC system (see **Figure 1**).

T_S refers to the AC power system which is simulated in a TS simulation, T_{DC} refers to the VSC-MTDC system which is simulated in the EMT simulation, U_D refers to the vector of the converter bus voltage, I_D refers to the vector of the converter bus current.

In this scheme, the detailed model of the VSC-MTDC system (i.e., the fast responding device) is established in the EMT simulation. The dynamic characters of converter values, control, and protection system could be simulated accurately by a microsecond simulation step. The VSC-MTDC system and AC system are completely decoupled in the hybrid simulation. It is worth mentioning that the AC system fault has a great influence on the VSC-MTDC system, especially when its fault point is nearby to the converter bus. In this case, the common scheme for hybrid simulation could not simulate the dynamic characters of the AC/DC system before or after the fault happens accurately. An improved scheme of hybrid simulation is proposed in this paper. Beyond that, the AC buses and generators which are near the converter buses are simulated in the EMT simulation, as shown in **Figure 2**.

T_{AC1} refers to the near-region AC system which is simulated in the EMT simulation based on a detailed EMT model, T_{AC2} refers to the other AC system which is simulated in the TS simulation, U_B refers to the vector of multi-interface voltage, I_B refers to the vector of the multi-interface current.

Two-interface hybrid simulation is taken as an example to illustrate the difference between the two hybrid simulation schemes. On the EMT simulation side, the TS subsystem is

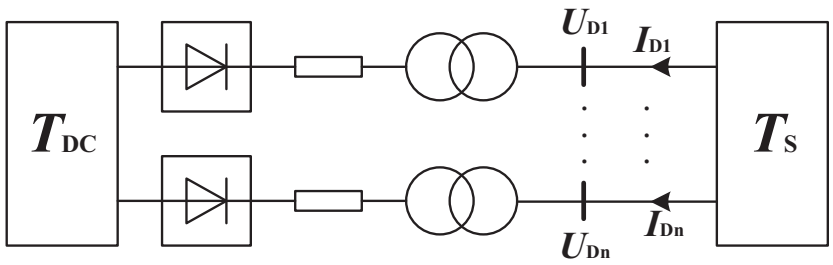


FIGURE 1 | Common scheme of the hybrid simulation.

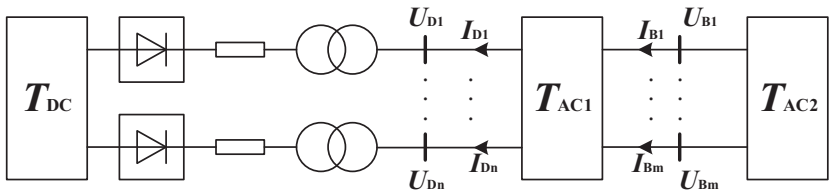


FIGURE 2 | Improved scheme of the hybrid simulation.

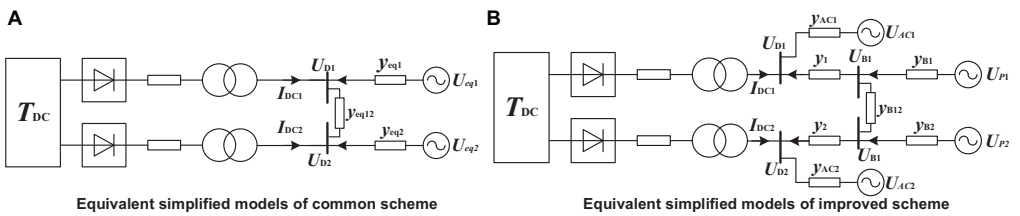


FIGURE 3 | Schematic diagram of the hybrid simulation scheme. **(A)** Equivalent simplified models of the common scheme. **(B)** Equivalent simplified models of the improved scheme.

replaced by the Thevenin equivalence method. For illustrative purposes, the equivalent model and the mathematics model of EMT simulation could be represented as **Figure 3**.

I_{DC1} and I_{DC2} refer to the currents of converter buses which are generated by the VSC-HVDC system, U_{D1} and U_{D2} refer to the voltages of converter buses, U_{eq1} and U_{eq2} refer to the voltages of Thevenin equivalent voltage source of T_S subsystem, U_{p1} and U_{p2} refer to the voltages of Thevenin equivalent voltage source of T_{AC2} subsystem, Y_{eq1}, Y_{eq2}, and Y_{eq12} refer to the Thevenin equivalent impedance of T_S subsystem, Y_{B1}, Y_{B2}, and Y_{B12} refer to the Thevenin equivalent impedance of T_{AC2} subsystem, Y_1 and Y_2 refer to the mutual impedance between the converter buses and interface buses, U_{AC1} and U_{AC2} refer to the voltages of Thevenin equivalent voltage source of active region in T_{AC1} subsystem, Y_{AC1} and Y_{AC2} refer to the Thevenin equivalent impedance of active region in T_{AC1} subsystem.

According to **Figure 3A**, the node voltage equation of the converter bus in the common scheme is established, which can be expressed as formula (1):

$$\begin{bmatrix} y_{eq1}+y_{eq12} & -y_{eq12} \\ -y_{eq12} & y_{eq2}+y_{eq12} \end{bmatrix} \begin{bmatrix} U_{D1} \\ U_{D2} \end{bmatrix} = \begin{bmatrix} y_{eq1}U_{eq1}+I_{DC1} \\ y_{eq2}U_{eq2}+I_{DC2} \end{bmatrix} \quad (1)$$

In **Figure 3B**, the structure is more complex, and the node voltage equations of converter buses and interface buses in the improved scheme are established, respectively, which can be expressed as formula (2) and (3):

$$\begin{bmatrix} y_1+y_{AC1} & \\ & Y_2+Y_{AC2} \end{bmatrix} \begin{bmatrix} U_{D1} \\ U_{D2} \end{bmatrix} = \begin{bmatrix} y_{AC1}U_{AC1}+y_1U_{B1}+I_{DC1} \\ y_{AC2}U_{AC2}+y_2U_{B2}+I_{DC2} \end{bmatrix} \quad (2)$$

$$\begin{bmatrix} y_{B1}+y_1+y_{B12} & -y_{B12} \\ -y_{B12} & y_{B2}+y_2+y_{B12} \end{bmatrix} \begin{bmatrix} U_{B1} \\ U_{B2} \end{bmatrix} = \begin{bmatrix} y_{B1}U_{P1}+y_1U_{D1} \\ y_{B2}U_{P2}+y_2U_{D2} \end{bmatrix} \quad (3)$$

From formula (3), the voltage of interface buses can be formulated as:

$$\begin{bmatrix} U_{B1} \\ U_{B2} \end{bmatrix} = Y_{BD} \begin{bmatrix} U_{D1} \\ U_{D2} \end{bmatrix} + Y_{BP} \begin{bmatrix} U_{P1} \\ U_{P2} \end{bmatrix} \quad (4)$$

where Y_{BD} and Y_{BP} are second order matrixes, which can be expressed as formula (5) and (6):

$$Y_{BD} = \begin{bmatrix} y_1\left(y_2 + y_{B2} + y_{B12}\right)/y_s & y_2 y_{B12}/y_s \\ y_1 y_{B12}/y_s & y_2\left(y_1 + y_{B1} + y_{B12}\right)/y_s \end{bmatrix} \tag{5}$$

$$Y_{BP} = \begin{bmatrix} y_{B1}\left(y_2 + y_{B2} + y_{B12}\right)/y_s & y_{B2} y_{B12}/y_s \\ y_{B1} y_{B12}/y_s & y_{B2}\left(y_1 + y_{B1} + y_{B12}\right)/y_s \end{bmatrix} \tag{6}$$

where y_s refers to the substitution value of multiple admittance calculations, and its specific expression is shown as follows:

$$y_s = \left(y_1 + y_{B1}\right)\left(y_2 + y_{B2} + y_{B12}\right) + y_{B12}\left(y_2 + y_{B2}\right)$$

Substituting (4) into (2), the voltage of converter buses in the improved scheme can be expressed as:

$$\begin{bmatrix} U_{D1} \\ U_{D2} \end{bmatrix} = Y_{DD}^{-1} Y_{DP} \begin{bmatrix} U_{P1} \\ U_{P2} \end{bmatrix} + Y_{DD}^{-1} Y_{DAC} \begin{bmatrix} U_{AC1} \\ U_{AC2} \end{bmatrix} + Y_{DD}^{-1} Y_{DI} \begin{bmatrix} I_{DC1} \\ I_{DC2} \end{bmatrix} \tag{7}$$

In order to analyze the influencing factors of the converter buses' voltages, the complex coefficient matrixes are replaced by different symbols, which can be expressed as follows:

$$Y_{DD} = \begin{bmatrix} 1 - \frac{y_1^2\left(y_2 + y_{B2} + y_{B12}\right)}{y_s\left(y_1 + y_{AC1}\right)} & -\frac{y_1 y_2 y_{B12}}{y_s\left(y_1 + y_{AC1}\right)} \\ -\frac{y_1 y_2 y_{B12}}{y_s\left(y_2 + y_{AC2}\right)} & 1 - \frac{y_2^2\left(y_1 + y_{B1} + y_{B12}\right)}{y_s\left(y_2 + y_{AC2}\right)} \end{bmatrix},$$

$$Y_{DP} = \begin{bmatrix} \frac{y_1 y_{B1}\left(y_2 + y_{B2} + y_{B12}\right)}{y_s\left(y_1 + y_{AC1}\right)} & \frac{y_1 y_{B2} y_{B12}}{y_s\left(y_1 + y_{AC1}\right)} \\ \frac{y_2 y_{B1} y_{B12}}{y_s\left(y_2 + y_{AC2}\right)} & \frac{y_2 y_{B2}\left(y_1 + y_{B1} + y_{B12}\right)}{y_s\left(y_2 + y_{AC2}\right)} \end{bmatrix}$$

$$Y_{DAC} = \begin{bmatrix} \frac{y_{AC1}}{y_1 + y_{AC1}} & 0 \\ 0 & \frac{y_{AC2}}{y_2 + y_{AC2}} \end{bmatrix},$$

$$Y_{DI} = \begin{bmatrix} 1/y_1 + y_{AC1} & 0 \\ 0 & 1/y_2 + y_{AC2} \end{bmatrix}$$

The voltage of converter buses in the common scheme can be deduced and expressed from (1) in the same way:

$$\begin{bmatrix} U_{D1} \\ U_{D2} \end{bmatrix} = Y_D^{-1} Y_{EQ} \begin{bmatrix} U_{eq1} \\ U_{eq2} \end{bmatrix} + Y_D^{-1} \begin{bmatrix} I_{DC1} \\ I_{DC2} \end{bmatrix} \tag{8}$$

where

$$Y_D = \begin{bmatrix} y_{eq1} + y_{eq12} & -y_{eq12} \\ -y_{eq12} & y_{eq2} + y_{eq12} \end{bmatrix}, Y_{EQ} = \begin{bmatrix} y_{eq1} & 0 \\ 0 & y_{eq2} \end{bmatrix}$$

The element admittance value of coefficient matrixes in formula (7) and (8) is obtained from actual system when it is established in the EMT simulation, and the equivalent admittance value of the TS subsystem is calculated by the multiport Thevenin equivalent method. In general, the simulation data interaction time is based on the TS simulation time step size, which is dozens or hundreds of the EMT simulation time step. According to the simulation theory of TS and EMT, the admittance of power system elements remains unchanged in one TS simulation time step. Hence, the elements of different coefficient matrixes are the fixed values.

Formula (7) and (8) can be, respectively, simplified as:

$$U_{Dim} = Y_{DD}^{-1} Y_{DP} U_P + Y_{DD}^{-1} Y_{DAC} U_{AC} + Y_{DD}^{-1} Y_{DI} I_{DC} \tag{9}$$

$$U_{Dcom} = Y_D^{-1} Y_{EQ} U_{eq} + Y_D^{-1} I_{DC} \tag{10}$$

The EMT simulation step and TS simulation time step are, respectively, set as Δt and ΔT. Besides, ΔT is N times of Δt. In the process of the hybrid simulation based on the improved scheme or common scheme, the change of the converter bus voltage at time $t+n\Delta t$ can be deduced as follows:

$$\begin{aligned} \Delta U_{Dim} &= U_{Dim}\left(t + n\Delta t\right) - U_{Dim}\left(t\right) \\ &= Y_{DD}^{-1} Y_{DAC}\left[U_{AC}\left(t + n\Delta t\right) - U_{AC}\left(t\right)\right] \\ &\quad + Y_{DD}^{-1} Y_{DI}\left[I_{DC}\left(t + n\Delta t\right) - I_{DC}\left(t\right)\right] \end{aligned} \tag{11}$$

$$\begin{aligned} \Delta U_{Dcom} &= U_{Dcom}\left(t + n\Delta t\right) - U_{Dcom}\left(t\right) \\ &= Y_D^{-1}\left[I_{DC}\left(t + n\Delta t\right) - I_{DC}\left(t\right)\right] \end{aligned} \tag{12}$$

where n refers to the number of EMT simulation time steps during t and $t+n\Delta t$, ΔU_{Dim} refers to the change of the converter bus voltage from time t to $t+n\Delta t$ when the hybrid simulation is based on the improved scheme, and ΔU_{Dcom} refers to the change of the converter bus voltage from time t to $t+n\Delta t$ when the hybrid simulation is based on the common scheme.

The change of the converter bus voltage is an important influence factor that determines the operation status of the VSC-HVDC system. In a TS simulation time step, the interface voltage of the hybrid simulation remains unchanged, and the simulation accuracy of the VSC-HVDC system in the EMT simulation depends on the precision of the converter bus voltage. From (11) and (12), it can be concluded that ΔU_{Dim} is influenced by I_{DC} and U_{AC}, and ΔU_{Dcom} is only influenced by I_{DC} in a TS simulation time step. While the improved scheme is adopted, the near-region AC system is simulated in the EMT simulation and its simulation step changes from ΔT to Δt. While a short-circuit fault or DC system fault happens on the power system, the improved scheme can effectively reduce the simulation error with the more accurate simulation results of a near-region AC system.

Interaction Process

A complete interaction process of hybrid simulation is related to the transmission mode of interface data between TS and EMT simulation. In previous research, there are two types of interaction processes used, namely the parallel and serial interaction process (Mugombozi et al., 2015). With the parallel interaction process, both simulator programs are running simultaneously, and the interface data is exchanged in each iteration by one TS simulation step. However, it could cause significant errors or singularities of the simulation system matrix when the large disturbance occurs in a large-scale power system. Additionally, with the serial interaction process, one simulator

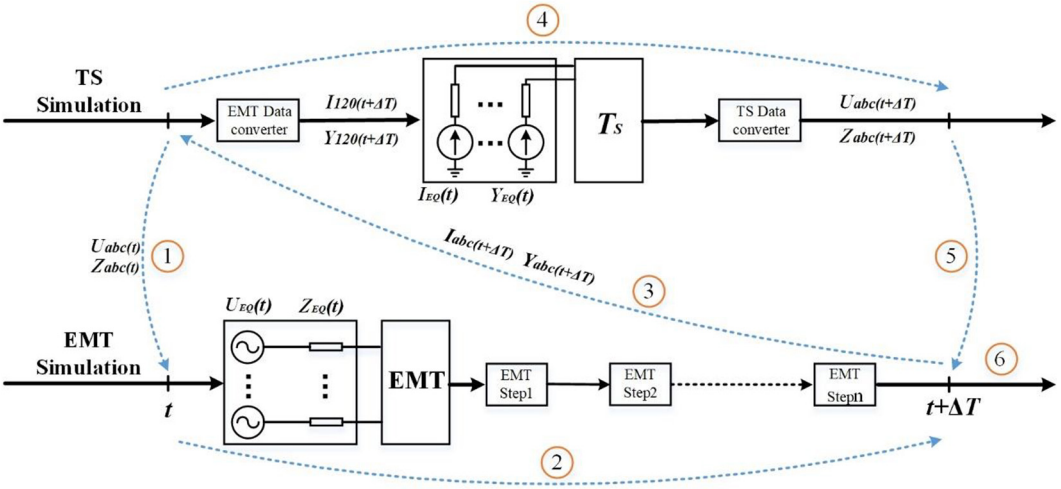


FIGURE 4 | Interaction process of the hybrid simulation.

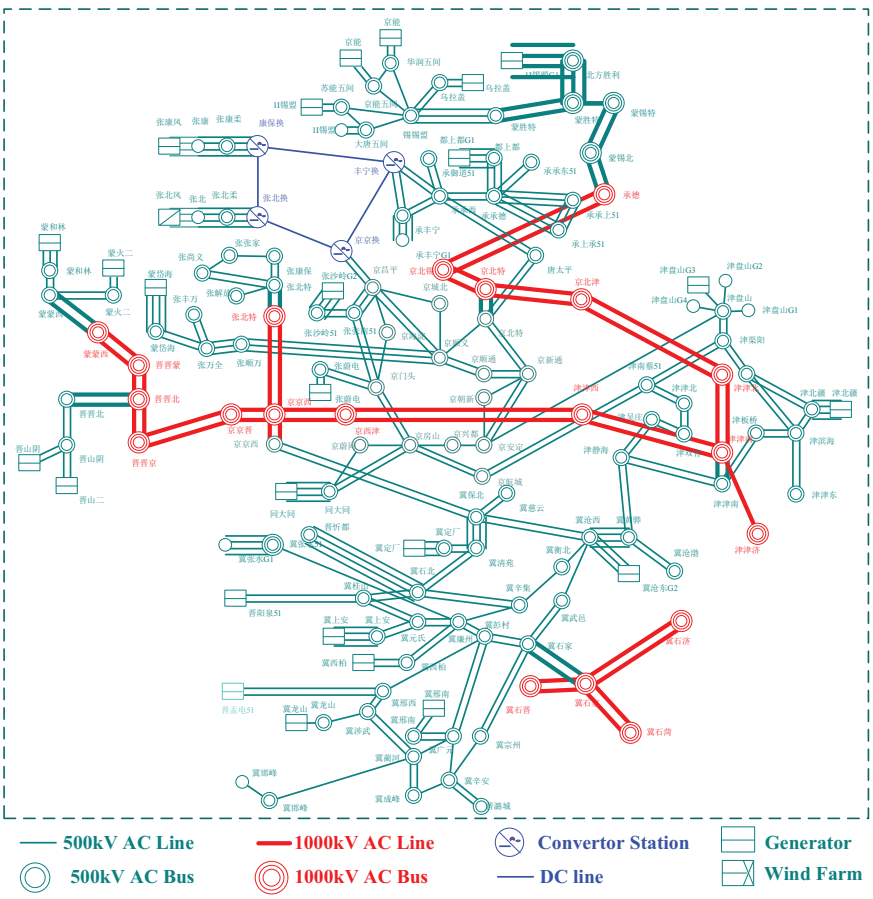


FIGURE 5 | Topology of the Zhangbei multi-terminal VSC-HVDC transmission system.

program must wait until the other completes the simulation of one interaction time step and transfers the interface data. The feature of the serial interaction process is not good for real-time simulation, but it could improve the convergence and accuracy of hybrid simulation when large disturbances occur in the simulation system. By comparing these two types of

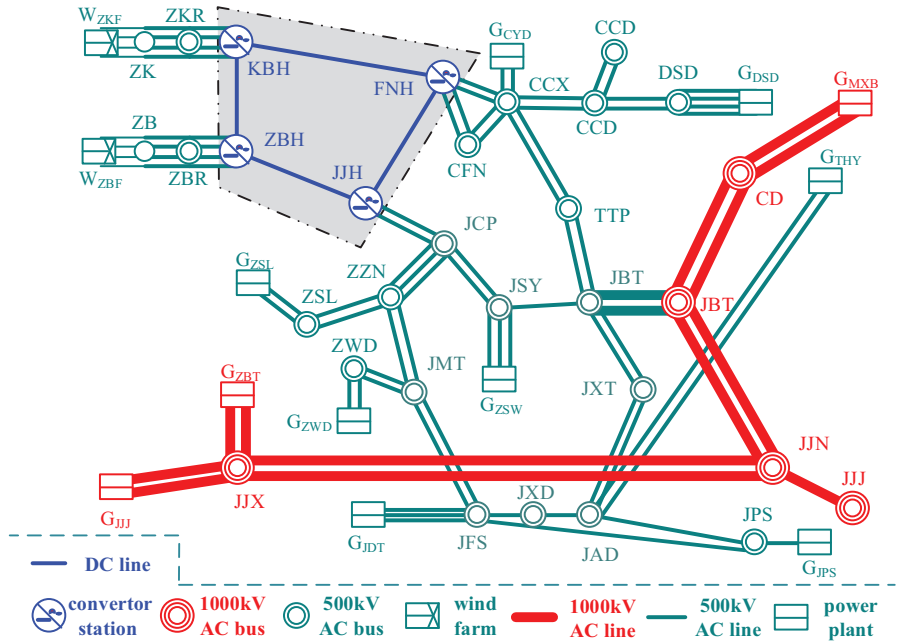


FIGURE 6 | Topology of the equivalent system.

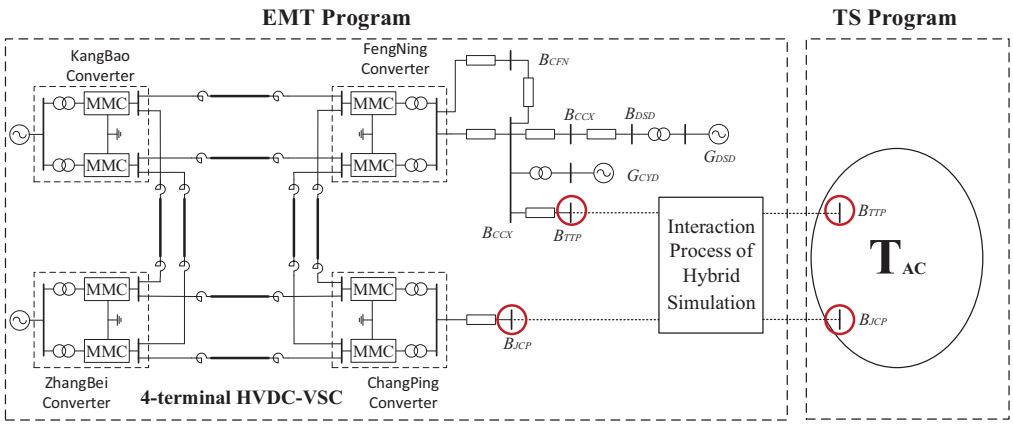


FIGURE 7 | Decomposition in the TS and EMT subsystems.

interaction processes, this paper finds that the serial interaction process is more suitable to be used in a hybrid simulation of a large-scale AC/DC power system.

The complicated data exchange process includes Thevenin equivalence, data conversion, data fitting, and boundary condition update.

The overall process from time t to time $t+\Delta T$ includes five main steps, as illustrated in **Figure 4**.

(1) Based on the simulation results of the electromechanical transient simulation at time t, the multi port Thevenin equivalent of the electromechanical transient side system is carried out with each interface bus, and the equivalent results of $U_{abc}(t)$ and $Z_{abc}(t)$ are transmitted to the EMT simulation side through the hybrid simulation interface.

(2) In the EMT simulation side, the parameters of the Thevenin equivalent circuit at the interface are updated, and the EMT calculation is carried out for N times until $t + \Delta T$.

(3) The EMT simulation results at the interface bus at $t+\Delta T$ time are transferred to the electromechanical transient side by $I_{abc}(t+\Delta T)$ and $Y_{abc}(t+\Delta T)$, and the interface data is converted in the interface program. The EMT calculation results based on ABC three-phase are converted into positive and negative zero three sequence interface data $I_{120}(t+\Delta T)$ and $Y_{120}(t+\Delta T)$ for electromechanical transient.

(4) The electromechanical transient simulation side updates the Norton equivalent circuit parameters at the interface, calculates the electromechanical transient once, and runs to t + Δ t time.
(5) At t + Δ t time, the data of the electromechanical transient simulation results $U_{120}(t+\Delta T)$ and $Z_{120}(t+\Delta T)$ at the interface bus are converted into the data of the ABC three-phase interface $U_{120}(t)$ and $Z_{120}(t)$, which are suitable for EMT. In addition, the data is transferred to the EMT side. Step (1) is repeated to start the next phase cycle until the hybrid simulation ends.

SIMULATION RESULTS

This section reports simulation results obtained with the Zhangbei multi-terminal VSC-HVDC transmission system which had been put into operation in 2020. The topology of the AC/DC system is shown in **Figure 5**.

It is essential to build the full electromagnetic simulation model and the electromechanical electromagnetic hybrid simulation model to verify the accuracy of the hybrid simulation. However, the huge network scale and complexity of the Sanhua power grid are not conducive to the construction of the full electromagnetic simulation model. Therefore, this paper uses the equivalent system of the Zhangbei four-terminal flexible DC power grid in reference (Chen et al., 2020) as the actual simulation example to build a hybrid simulation real platform. The Shanxi power grid connected by the Shanxi Beijing tie line is equivalent to two equivalent generators in Jinjing and Jindatong, the Inner Mongolia Chengde and Inner Mongolia Beijing tie line are equivalent to two equivalent generators in Mengxibei and Tuohunyuan, Zhangjiakou is equivalent to two equivalent generators in Zhangbeite and Zhangshunwan, and Chengde is equivalent to one equivalent generator in Chengyudao. The original system of Dushangdu, Zhangweidian, Zhangshaling, and Jinpanshan generators are retained, and Jinpanshan in the system is the reference generator node. The dynamic characteristics of the equivalent system of the Zhangbei DC power grid are verified in reference (Chen et al., 2020), which can fully characterize the dynamic characteristics of the original Zhangbei flexible DC power grid and its nearby AC system. **Figure 6** shows the equivalent system topology of the Zhangbei DC power grid.

According to the hybrid simulation method proposed in this paper, the AC system of the Zhangbei flexible DC power grid and its adjacent area which needs small step-length detailed simulation is divided into the EMT simulation side, and the EMT simulation modeling is conducted on the Simulink / Matlab platform. Among them, there are five generators at bdsd of Dushangdu bus, which is close to Fengning converter station, and one generator at bcyd of Chengyudao bus. All of them adopt five-order generator models for EMT modeling, while retaining detailed excitation and a speed control system. 500 kV AC bus Tangtaiping bttp and Jingchangping bjcp are selected as the hybrid simulation interface bus. The rest of the AC system is modeled in matdyn open-source software based on the MATLAB platform. **Figure 7** is the schematic diagram of the specific distribution scheme.

In the hybrid simulation, the Runge Kutta method is adopted to solve the stability of electromechanical transient simulation. The simulation step is Δt = 0.02 s, and the third-order dynamic model is used for the generator. The trapezoidal method is used to solve the EMT simulation in the Simulink platform. The fixed step mode is adopted, and the step size is $\Delta\ t$ = 50 μ s. In the hybrid simulation, the AC system parameters adopt the Fengda operation mode of the Sanhua power grid in 2018, and the parameters of the Zhangbei multi terminal DC system are shown in **Table 1**.

At the same time, the paper builds a full electromagnetic simulation model of the Zhangbei DC power grid equivalent system. Its system structure and parameters are identical with the hybrid simulation model of the Zhangbei DC power grid. Beyond that, the simulation results of the two models are compared to verify the accuracy and effectiveness of the hybrid simulation method proposed in this paper. A three-phase short circuit fault is set at the Jingxintong bus, with a fault duration of 0.1 s. The dynamic characteristics of AC and DC system at the electromechanical transient simulation side, EMT simulation side, and interface bus are compared, respectively, and the accuracy of the hybrid simulation method proposed in this paper is verified.

Figures 8, **9** compare the dynamic characteristics of GZWD and GDSD under different simulation conditions. Among them, the generator GDSD is located in the EMT simulation side of the hybrid simulation model. As shown in **Figure 10**, its dynamic characteristics in the hybrid simulation model are basically consistent with those in the full electromagnetic simulation condition. The generator GZWD is located in the electromechanical transient simulation side of the hybrid simulation model. As displayed in **Figure 9B**, the simulation results of its excitation voltage are slightly different under the two simulation conditions, which is due to different simulation algorithms. From the occurrence of the three-phase short-circuit fault to the first electromechanical transient step time, the generator and its excitation controller in the EMT are in a relatively continuous operation state, and the state of the generator changes with time and is synchronized with the whole

TABLE 1 | Parameters of the zhangbei multi terminal flexible dc system.

Parameters type	Kangbao	Zhangbei	Beijing	Fengning
Grid side voltage / kV	220	220	500	500
Valve side voltage / kV	255	255	255	255
Capacity / MVA	2 × 750	2 × 1,500	2 × 1,500	2 × 750
Connection mode	Yn/Δ-11	Yn/Δ-11	Yn/Δ-11	Yn/Δ-11
DC voltage / kV	500	500	500	500
Number of bridge arm sub modules	313	228	228	313
Sub module capacitance / MF	10	15	15	10
Bridge arm inductance / MH	150	100	100	150

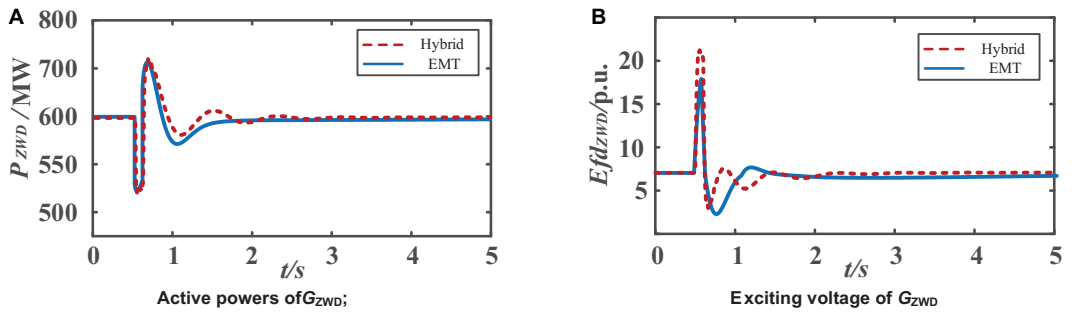


FIGURE 8 | Dynamic characteristics of generators in the TS simulation; **(A)** Active powers of G_{ZWD}; **(B)** Exciting voltage of G_{ZWD}.

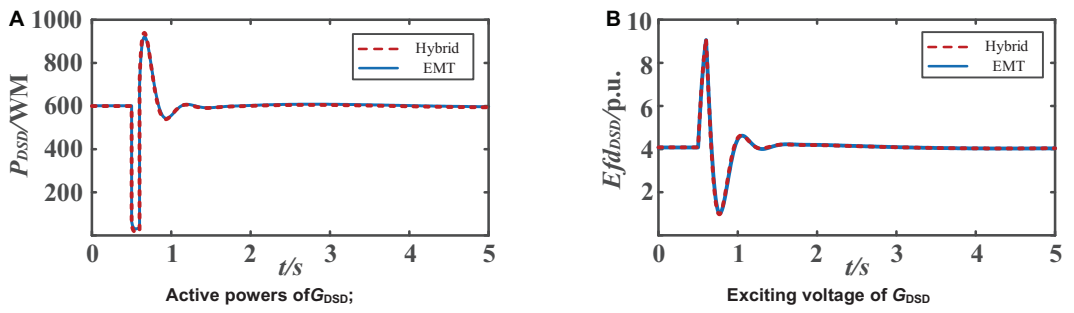


FIGURE 9 | Dynamic characteristics of generators in the EMT simulation; **(A)** Active powers of G_{DSD}; **(B)** Exciting voltage of G_{DSD}.

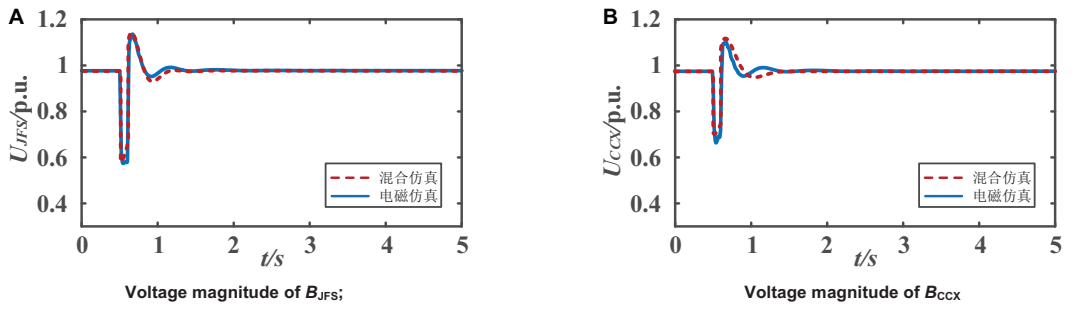


FIGURE 10 | Comparisons of voltage magnitude; **(A)** Voltage magnitude of B_{JFS}; **(B)** Voltage magnitude of B_{CCX}.

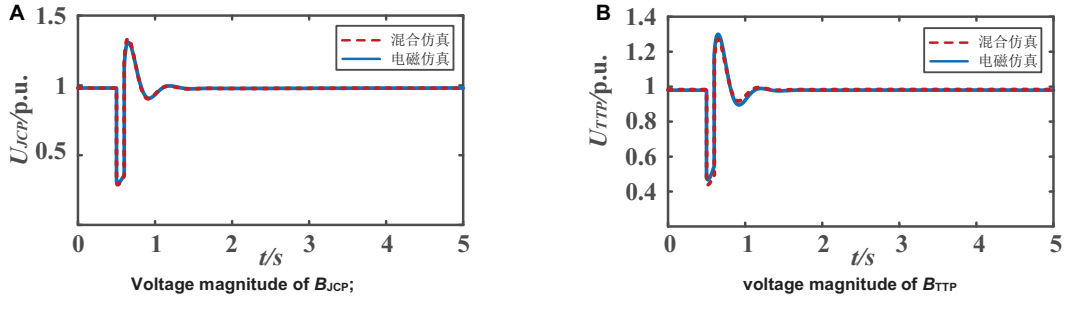


FIGURE 11 | Comparisons of voltage magnitude of interface buses; **(A)** Voltage magnitude of B_{JCP}; **(B)** Voltage magnitude of B_{TTP}.

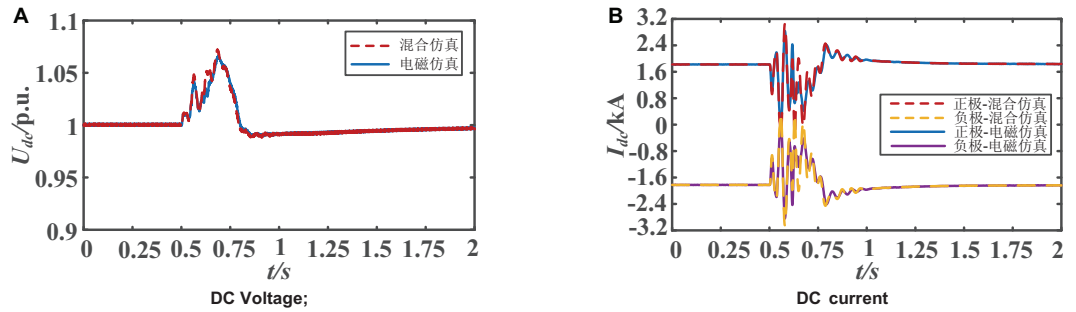


FIGURE 12 | Dynamic characteristics of Zhangbei station; **(A)** DC Voltage; **(B)** DC current.

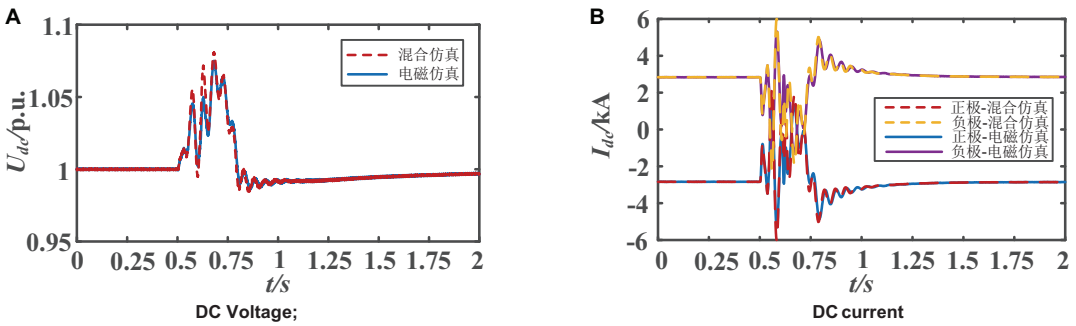


FIGURE 13 | Dynamic characteristics of Beijing station; **(A)** DC Voltage; **(B)** DC current.

simulation system. Hence, the excitation voltage increases to the maximum state in a diagonal line through the integral control link. In the electromechanical transient calculation environment, the generator directly calculates to an electromechanical transient step, the time span is large, and the controller in its exciter cannot play an integral role. Thus, the excitation voltage increases in a straight-line form after the fault, and the maximum values in this example are higher than the calculation results of EMT simulation. This further leads to the difference of simulation results of gzwd transient recovery process after fault removal, but the overall recovery time is basically the same. As displayed in **Figure 9A**, the difference between the simulation results of generator output power is small. Therefore, the hybrid simulation method proposed in this paper is basically accurate for the simulation of generator dynamic characteristics.

Figures 10A,B show the voltage amplitude dynamic characteristics of the electromechanical transient bus BJFS and the EMT bus BCCX, respectively. **Figure 11** shows the voltage amplitude dynamic characteristics of BJCP and BTTP. It can be seen that the simulation results of the AC system in the hybrid simulation model are basically consistent with all the EMT simulation models, and more accurate calculation results have been obtained.

Figures 12, **13** show the dynamic characteristics of the DC voltage and DC current of the Beijing converter station and Zhangbei converter station in the DC power grid, respectively. The calculation results of the hybrid simulation model are basically consistent with the total EMT model. For the simulation of the DC system, whether it is under mixed simulation or full EMT simulation, the real matter is to model the DC system in EMT software, without any difference in calculation method, step size, and underlying model. Whether the simulation results are accurate mainly depends on the dynamic characteristics of bus at the AC/DC interface, but the simulation of the dynamic characteristics of the whole AC system is accurate. The significance of the hybrid simulation is to save the huge workload and computing resources in order to build the full EMT simulation model. The detailed EMT modeling is carried out for the key research objects, and the complete system scale can be kept as much as possible.

In conclusion, the hybrid simulation model based on the equivalent system of the Zhangbei DC power grid can not only accurately simulate the dynamic characteristics of the AC system in the electromechanical transient side, EMT side, and hybrid simulation interface bus, but also fully and accurately simulate the dynamic characteristics of the Zhangbei DC system. Therefore, the accuracy and correctness of the proposed hybrid simulation method can be verified.

CONCLUSION

This paper has proposed a hybrid simulation method based on MATLAB/Simulink. Specifically, the user-defined function module provided by Simulink is used, and the matdyn toolkit is integrated into it. Furthermore, the electromechanical transient

simulation program is written to realize the parallel operation of the electromechanical transient simulation and EMT simulation on the same platform.

Aiming at the electromechanical electromagnetic hybrid simulation of the AC/DC hybrid system, this paper proposes that some AC power grids with a great influence on the DC system should be reserved in the EMT simulation side, which can more accurately simulate the interaction of the AC/DC system and improve the accuracy of the hybrid simulation. At the same time, the specific implementation method of electromechanical electromagnetic hybrid simulation is described in detail. In the interface program, the serial data iteration process is adopted, and the real-time update and conversion of equivalent circuit parameters are realized in the data interaction process, which ensures the stability and accuracy in the hybrid simulation calculation process. Finally, through the actual system of the Zhangbei DC power grid, this paper not only compares the results of the hybrid simulation model with those of all the electromagnetic simulation models, but also verifies the accuracy of the proposed hybrid simulation method and the practicability of applying it to a large-scale AC/DC system simulation.

The future research will focus on the following two aspects:

(1) Scientific Selection of the interface bus. In the hybrid simulation, the selection of the interface bus also depends on the manual selection of staff, which means that scientific planning scheme and calculation method should be established considering the interaction of the AC and DC system and the limitation of simulation resources.

(2) Adaptive problem of hybrid simulation. The hybrid simulation method proposed in this paper is mainly for an AC/DC power grid with VSC HVDC. If the hybrid simulation model is carried out for an AC/DC system including LCC HVDC or hybrid DC, it is essential to optimize the interface algorithm and implementation method so as to improve the applicability of the hybrid method, which deserves further research and discussion.

DATA AVAILABILITY STATEMENT

The original contributions presented in the study are included in the article/supplementary material, further inquiries can be directed to the corresponding author/s.

AUTHOR CONTRIBUTIONS

SZ and SL designed the model and the computational framework and analyzed the data. SZ and XL carried out the implementation. SL performed the calculations. SZ and GL wrote the manuscript with input from all authors. GL conceived the study and were in charge of overall direction and planning.

REFERENCES

Chen, H., Wang, W., Jiang, T., Wei, J., Zhang, S., and Li, G. (2020). Data-driven Dynamic Equivalence Method in Bulk Power Systems. *Power Syst. Tech* 44, 3047–3056.

Huang, Q., and Vittal, V. (2017b). Integrated Transmission and Distribution System Power Flow and Dynamic Simulation Using Mixed Three-Sequence/Three-Phase Modeling. *IEEE Trans. Power Syst.* 32, 3704–3714. doi: 10.1109/tpwrs.2016.2638910

Huang, Q., and Vittal, V. (2017a). Advanced EMT and phasor-domain hybrid simulation with simulation mode switching capability for transmission and distribution systems. *IEEE Trans. Power Syst.* 33, 6298–6308. doi: 10.1109/tpwrs.2018.2834561

Li, Y., Wang, C., Li, G., and Chen, C. (2021). Optimal scheduling of integrated demand response-enabled integrated energy systems with uncertain renewable generations: a Stackelberg game approach. *Energy Convers. Manag.* 235:113996. doi: 10.1016/j.enconman.2021.113996

Liming, S., and Bo, Y. (2020). Nonlinear robust fractional-order control of battery/SMES hybrid energy storage systems. *Power Syst. Prot. Control.* 48, 76–83.

Mugombozi, C. F., Mahseredjian, J., and Saad, O. (2015). Efficient computation of feedback-based control system equations for electromagnetic transients. *IEEE Trans. Power Deliv.* 30, 2501–2509. doi: 10.1109/tpwrd.2015.2446532

Plumier, F., Aristidou, P., Geuzaine, C., and Van Cutsem, T. (2016). Co-Simulation of Electromagnetic Transients and Phasor Models: a Relaxation Approach. *IEEE Trans. Power Deliv.* 31, 2360–2369. doi: 10.1109/tpwrd.2016.2537927

Schneider, K. P., Tuffner, F. K., Elizondo, M. A., Hansen, J., Fuller, J. C., and Chassin, D. P. (2019). Adaptive dynamic simulations for distribution systems using multi-state load models. *IEEE Trans. Smart Grid* 10, 2257–2266. doi: 10.1109/tsg.2018.2794180

Shu, D., Xie, X., Dinavahi, V., Zhang, C., Ye, X., and Jiang, Q. (2018). Dynamic Phasor Based Interface Model for EMT and Transient Stability Hybrid Simulations. *IEEE Trans. Power Syst.* 33, 3930–3939. doi: 10.1109/tpwrs.2017.2766269

van der Meer, A. A., Gibescu, M., van der Meijden, M. A. M. M., King, W. L., Ferreira, J. A., et al. (2015). Advanced hybrid transient stability and EMT simulation for VSC-HVDC systems. *IEEE Trans. Power Deliv.* 30, 1057–1066. doi: 10.1109/tpwrd.2014.2384499

Venkatraman, R., Khaitan, S. K., and Ajjarapu, V. (2019). Dynamic co-simulation methods for combined transmission-distribution system with integration time step impact on convergence. *IEEE Trans. Power Syst.* 34, 1171–1181. doi: 10.1109/tpwrs.2018.2874807

Zhang, Y., Gole, A. M., Wu, W., Zhang, B., and Sunet, H. (2013). Development and analysis of applicability of a hybrid transient simulation platform combining TSA and EMT elements. *IEEE Trans. Power Syst.* 28, 357–366. doi: 10.1109/tpwrs.2012.2196450

Zheng, A., Guo, C., Cui, P., Jiang, W., and Zhao, C. (2019). 'Comparative study on small-signal stability of LCC-HVDC system with different control strategies at the inverter station. *IEEE Access* 7, 34946–34953. doi: 10.1109/access.2019.2904395

Conflict of Interest: The authors declare that the research was conducted in the absence of any commercial or financial relationships that could be construed as a potential conflict of interest.

Copyright © 2021 Zhang, Li, Li and Liu. This is an open-access article distributed under the terms of the Creative Commons Attribution License (CC BY). The use, distribution or reproduction in other forums is permitted, provided the original author(s) and the copyright owner(s) are credited and that the original publication in this journal is cited, in accordance with accepted academic practice. No use, distribution or reproduction is permitted which does not comply with these terms.

frontiers in Energy Research

ORIGINAL RESEARCH
published: 25 May 2021
doi: 10.3389/fenrg.2021.686616

Cost-Sensitive Extremely Randomized Trees Algorithm for Online Fault Detection of Wind Turbine Generators

Mingzhu Tang[1], Yutao Chen[1], Huawei Wu[2], Qi Zhao[1], Wen Long[3], Victor S. Sheng[4]* and Jiabiao Yi[1]*

[1]School of Energy and Power Engineering, Changsha University of Science and Technology, Changsha, China, [2]Hubei Key Laboratory of Power System Design and Test for Electrical Vehicle, Hubei University of Arts and Science, Xiangyang, China, [3]Guizhou Key Laboratory of Economics System Simulation, Guizhou University of Finance and Economics, Guiyang, China, [4]Computer Science Department, Texas Tech University, Lubbock, TX, United States

The number of normal samples of wind turbine generators is much larger than the number of fault samples. To solve the problem of imbalanced classification in wind turbine generator fault detection, a cost-sensitive extremely randomized trees (CS-ERT) algorithm is proposed in this paper, in which the cost-sensitive learning method is introduced into an extremely randomized trees (ERT) algorithm. Based on the classification misclassification cost and class distribution, the misclassification cost gain (MCG) is proposed as the score measure of the CS-ERT model growth process to improve the classification accuracy of minority classes. The Hilbert-Schmidt independence criterion lasso (HSICLasso) feature selection method is used to select strongly correlated non-redundant features of doubly-fed wind turbine generators. The effectiveness of the method was verified by experiments on four different failure datasets of wind turbine generators. The experiment results show that average missing detection rate, average misclassification cost and gMean of the improved algorithm better than those of the ERT algorithm. In addition, compared with the CSForest, AdaCost and MetaCost methods, the proposed method has better real-time fault detection performance.

Keywords: fault detection, fault diagnosis, cost-sensitive learning, extremely randomized trees, class imbalance, wind turbine generator

OPEN ACCESS

Edited by:
Dongran Song,
Central South University, China

Reviewed by:
Jian Yang,
Central South University, China
Rizk Masoud,
University of Menoufia, Egypt
Lei Wang,
Chongqing University, China
Qiang Lin,
Northwest University for Nationalities, China

****Correspondence:***
Huawei Wu
whw_xy@hbuas.edu.cn
Victor S. Sheng
victor.sheng@ttu.edu

Specialty section:
This article was submitted to Smart Grids, a section of the journal Frontiers in Energy Research

Received: *27 March 2021*
Accepted: *05 May 2021*
Published: *25 May 2021*

Citation:
Tang M, Chen Y, Wu H, Zhao Q, Long W, Sheng VS and Yi J (2021) Cost-Sensitive Extremely Randomized Trees Algorithm for Online Fault Detection of Wind Turbine Generators. Front. Energy Res. 9:686616. doi: 10.3389/fenrg.2021.686616

INTRODUCTION

The global capacity of installed wind turbine generators in 2019 reached 60.4 GW, with an annual increment of 19% (Kandukuri et al., 2016). The operation and maintenance costs of wind turbine generators account for approximately 15–30% of their total cost (Artigao et al., 2018). Generator failures account for approximately 4% of total failures, and generator fault identification has attracted considerable attention in recent years (Chen et al., 2016; Quiroz et al., 2018; Lei et al., 2019). Failures in the generator may cause the whole mechanical system to stop functioning, reduce the operation efficiency of the wind turbine and even cause personnel casualties. Wind turbine generators, intermittent operating conditions, and severe weather pose challenges to the safe operation of wind turbines (Judge et al., 2019). Since the generator is the critical component of the wind turbine, wind turbine failure detection can greatly reduce the operation and maintenance costs by reducing unplanned failures (Willis et al., 2018; Yang et al., 2021).

Fault detection methods can be divided into two categories: model-based methods (Cho et al., 2018; Habibi et al., 2019) and data-based methods (Mingzhu et al., 2020; Liming and Bo, 2020; Song et al., 2021). Model-based fault detection methods include a parameter estimation method (Pan et al., 2017), state estimation methods (Shahriari et al., 2020; Ghahremani and Kamwa, 2016), and an equivalent space method (Bakri and Boumhidi, 2018). Bakri et al. proposed a model-based fault detection and isolation technology to solve the early fault detection problem of wind turbines (Bakri and Boumhidi, 2018).These methods can comprehensively examine the essence of dynamic systems for real-time fault detection. However, the structure of wind turbines is complex, with many characteristic parameters, and model-based methods have difficulty obtaining accurate models.

Data-based methods include signal-based methods, statistical analysis-based methods, and machine learning-based methods. Fernandez-Canti et al. proposed a wind turbine fault detection method based on the hybrid Bayesian set membership method (Fernandez-Canti et al., 2015). This method only uses the non-fault behavior model to generate the consistency index and the fault indicator, and detects whether the wind turbine fails by analyzing the noise of the equipment. It is difficult for methods based on statistical analysis to detect the fault of a combination of signal distortion and signal fading. Ibrahim et al. proposed a method based on an effective extended Kalman filter to iteratively estimate a fault signature component (FSC) and track its amplitude to realize fault detection in wind turbine generators (Ibrahim et al., 2018). The state characteristic signal is weak at the initial stage of the fault, which makes it difficult to accurately detect generator faults by the signal-based method.

Machine learning-based methods—for instance, artificial neural networks (ANNs) (Marugan et al., 2018; Hamidreza et al., 2014), support vector machines (Zeng et al., 2019; Li Z. M. et al., 2019), decision trees (Yu et al., 2018), bagging (Breiman, 1996), boosting (Cheki et al., 2016), and random forests (RFs) (Li et al., 2016; Joshuva and Sugumaran, 2017)—are often applied to solve binary classification problems. These methods can effectively predict the operating state of a wind turbine. Chun et al. used RF learning to evaluate the correlation between characteristic variables and target variables and then used a deep neural network (DNN) model to identify wind turbine permanent magnet drop failures. However, DNNs are computationally complex and easily overfit data (Teng et al., 2018). Gao et al. used the integrated extended load mean decomposition multiscale entropy method to extract features and then applied the least square support vector machine (LSSVM) method to perform wind turbine fault detection (Gao et al., 2018). The LSSVM method achieved strong fault detection performance but poor real-time performance when processing big data. Gopinath proposed a method for wind turbine fault detection that combines nuisance attribute projection and the classification and regression tree (CART) algorithm (Gopinath et al., 2016). Disturbance attribute projection was used to extract the frequency domain statistical characteristics of the current signal, and CART was used as a decision model to realize synchronous generator fault detection. Although a decision tree method has various advantages, such as a simple structure, strong real-time performance, and the ability to handle big data, a single decision tree is impractical. Li et al. adopted the short-term memory network of the residual generator and used an RF to build a detection model (Li M. et al., 2019). This method can effectively detect early faults of wind turbines in harsh environments. The RF model improves the generalization ability *via* integration.

In the actual operation of wind turbines, the number of fault samples is much smaller than the number of normal samples, which is characteristic of typical imbalanced classification problems (Malik and Mishra, 2016; Buda et al., 2018; Longting et al., 2019). Traditional fault detection methods perform poorly when applied to imbalanced data. For class-imbalanced problems, cost-sensitive learning combines misclassification costs and traditional fault detection methods. By introducing different types of cost functions to characterize the importance of a sample, the objective function is transformed from one designed to maximize the classification accuracy into one designed to minimize the misclassification cost. For example, the cost-sensitive decision tree algorithm has been widely used in industrial control processes and detection (Tan, 1993; Lomax and Vadera, 2013; Kim et al., 2018). Because the test cost and misclassification cost of cost-sensitive learning are often similar in scale, Zhang et al. presented a multiscale cost-sensitive decision tree algorithm that combines the misclassification cost and test cost. The approach solves the problem of integrating multiple costs together in cost-sensitive learning (Zhang, 2018). Qi et al. proposed a cost-sensitive decision tree algorithm that incorporates data cleaning algorithms to address poor-quality data, including the high cleaning cost (Qi et al., 2019). However, a single classifier easily leads to overfitting when considering complex industrial problems and the poor model generalization ability.

Ensemble learning combines multiple classifiers to obtain better performance than that achieved by a single classifier. Tree ensemble algorithms can be classified as either boosting or bagging. Masnadi-Shirazi et al. presented a cost-sensitive framework suitable for AdaBoost, RealBoost, and LogitBoost for class-imbalanced problems (Masnadi-Shirazi and Vasconcelos, 2011). Furthermore, Zelenkov et al. proposed a sample-based cost-sensitive adaptive boosting algorithm (Zelenkov, 2019) in which the misclassification cost and sample distributions are combined, and the cost matrix of the sample is corrected based on the training set to improve the overall performance. Because the boosting algorithm uses serial dependence, it is difficult to train data in parallel. The cost-sensitive RF algorithm uses a parallel approach and has strong generalization capabilities (Nami and Shajari, 2018; Siers and Islam, 2015). Siers et al. combined cost-sensitive parameters with an RF model, introduced misclassification costs when building models, and implemented a cost-sensitive forest (CSForest) algorithm based on a decision tree (Siers and Islam, 2015). Lu et al. embedded the cost of misclassification, test cost and rejection cost into a rotating forest algorithm (Lu et al., 2017), which was transformed into a cost-sensitive problem to effectively reduce the classification cost and improve the effectiveness of the algorithm. However, the computational

complexity of the cost-sensitive RF algorithm is high. Geurts et al. proposed an extremely randomized trees (ERT) algorithm based on the RF algorithm (Geurts et al., 2006). By adding random disturbances when nodes are split, the model achieves stronger generalization ability and reduced computational complexity. Moreover, each base classifier uses the complete training dataset for training, which reduces the variance of the ERT algorithm.

Although the ERT algorithm has faster calculation speed and smaller prediction variance (Geurts et al., 2006), the problem of low detection accuracy of failure samples still exists for unbalanced data. For the imbalance problem, many cost-sensitive fault detection methods based on tree ensemble algorithms have been proposed and have made certain achievements in the field of wind turbine generator fault detection. However, these methods make it difficult to meet both high performance and high real-time requirements. Therefore, this paper proposes a wind turbine generator fault detection method based on cost-sensitive extremely randomized trees (CS-ERT). The main contributions of this paper are as follows:

- To solve the class imbalance problem in the actual operation of wind turbine generators, cost sensitive learning was introduced into the ERT algorithm, and the CS-ERT algorithm was proposed to detect the fault of wind turbine generators. The objective function of the algorithm was transformed from minimizing classification error to minimizing misclassification cost. The proposed method was verified by the data of 1.5 MW doubly-fed wind turbine generators.
- The HSICLasso feature selection method was used to remove weak correlation features to address the high feature dimension problem of wind turbine generators. A feature subset composed of strongly correlated non-redundant variables was used to train the fault detection model.

EXTREMELY RANDOMIZED TREES

ERT (Geurts et al., 2006) is an ensemble algorithm with high randomness in which a set of nonpruned decision trees is established via a top-down process. In contrast to the RF algorithm, bagging is not used by the ERT model to train each basic classifier. Each tree of ERT uses the complete training samples for learning to minimize the deviation in the model. In the traditional ensemble method, the best feature and cut-point of a node are obtained by evaluating the Gini coefficient, Shannon entropy of each feature value of each feature, etc. ERT is different.

Given the dataset D (X, Y), the m-dimensional vector f_i represents the feature vector of the sample x_i. In the extreme decision tree splitting process, a value a_c^k is randomly selected from the maximum a_{max}^k to the minimum a_{min}^k for attribute k as the cut-point of this feature. Then, the score measure of feature k is calculated according to **Eq. 1**.

TABLE 1 | Cost matrix of two classification problems.

Predict class	Actual class	
	Normal	**Fault**
Normal	C_{TN}	C_{FN}
Fault	C_{FP}	C_{TP}

Note that C_{FN} is the cost of predicting the fault sample as a normal class, C_{FP} is the cost of predicting the normal sample as a fault class, and C_{TN} and C_{TP} represent the cost of correct detection. The larger the misclassification cost parameters, the more important the classification. For practical wind turbine generators, the economic losses caused by false negatives are far greater than those caused by missing detection. Therefore, the misclassification cost parameter C_{FN} of the fault class is greater than the misclassification cost parameter C_{FP} of the normal class ($C_{FN} > C_{FP}$).

$$\mathrm{Score}_c(k,S) = \frac{2I_c^k(S)}{H_k(S) + H_c(S)} \tag{1}$$

where $I_c^k(S)$ represents the mutual information of the two subsets with respect to the class after node S is split according to attribute k and cut-point a_c^k. $H_k(S)$ represents the split entropy of attribute k. $H_c(S)$ represents the information entropy of node S. Each candidate feature of the node is traversed according to the above method, and the feature and cut-point with the largest score measure $\mathrm{Score}_c(k,S)$ are selected to split the node. Then, the samples with a value of feature k less than the cut-point are placed in the left leaf node, and the remaining samples are placed in the right leaf node. The above steps are repeated recursively until the stop splitting condition is satisfied. The simplicity of the tree growth process makes the space complexity of ERT lower than that of other ensemble methods.

The final result of the ERT algorithm is determined by voting by all base classifiers, as follows.

$$P_{(c|f_i)} = \frac{1}{M}\sum_{t=1}^{M} P_t(c|f_i) \tag{2}$$

$$\hat{c} = \mathrm{argmax}_c\, P(c|f_i) \tag{3}$$

where M is the total number of trees, f_i is the feature vector of sample x_i, and P_t represents the conditional probability that the sample belongs to class c under the condition of vector f_i. For regression problems, **Eq. 2** defines the classification probability of the sample. For classification problems, the voting method is used to make decisions according to **Eq. 3**. In the fault detection method, **Eq. 3** is used to realize the fault detection of the sample.

COST-SENSITIVE EXTREMELY RANDOMIZED TREES

In this section, the CS-ERT algorithm is proposed, and the computational complexity of the algorithm is analyzed.

The Principle of Cost-Sensitive Extremely Randomized Trees

CS-ERT is a derivative of the ERT algorithm. CS-ERT combines cost-sensitive learning with the ERT algorithm, which solves the problem of low accuracy in the failure samples of traditional ERT

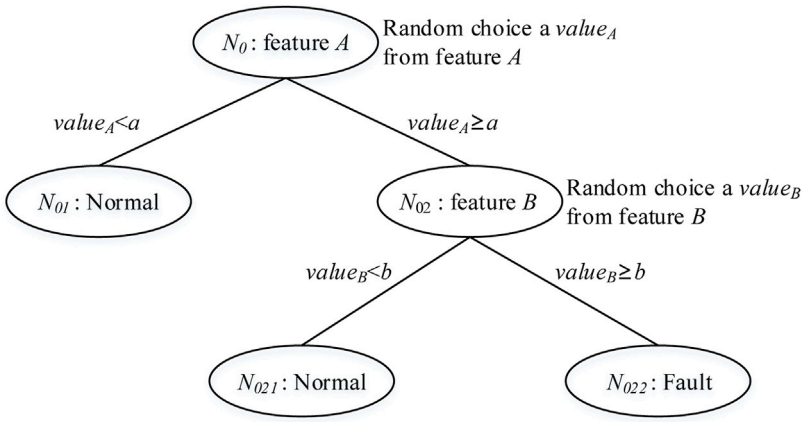


FIGURE 1 | Split rule of CS-ERT algorithm.

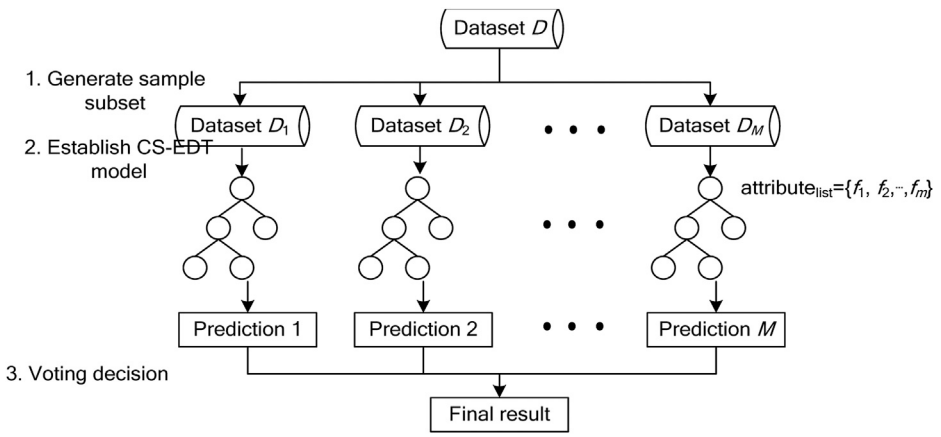


FIGURE 2 | Cost-sensitive extremely randomized trees algorithm.

algorithms in imbalanced data. The cost matrix is introduced to represent the misclassification cost in the fault detection field, as shown in **Table 1**.

The CS-ERT algorithm is composed of multiple cost-sensitive extreme decision trees (CS-EDT). Each CS-EDT model has a chain structure similar to a decision tree, which includes a finite set and edge set that constitute the root node, branch nodes and leaf nodes, as shown in **Figure 1**.

In **Figure 1**, Ni represents the *i*-th node. If Ni is a branch node, the cut-point is randomly selected for each feature of the node. To solve the problem of category imbalance, this paper proposes the MCG as the score measure of the branch node. The MCG G_k for attribute k is defined as follows:

$$G_k = C(parent_node) - \frac{N_L}{N_L + N_R} C(left_child_node) - \frac{N_R}{N_L + N_R} C(right_child_node) \quad (4)$$

where $C(parent_node)$ represents the misclassification cost of the parent node; $C(left_child_node)$ and $C(right_child_node)$ are the misclassification costs of the left and right child nodes, respectively; and N_L and N_R represent the numbers of the left and right child nodes, respectively. According to **Eq. 4**, the misclassification cost gain is calculated for each candidate feature. Then, the attribute and random value with the largest MCG is selected as the split feature and cut-point of the branch node.

The MCG is essentially the difference between the misclassification cost of the parent node and the weighted sum of the costs of all child nodes. The misclassification cost of the leaf *node* is defined as follows:

$$C(node) = C_P + C_N \quad (5)$$

where C_P is the cost of the fault class at *node*, and C_N is the cost of the normal class at *node*, as shown in **Eqs. 6**, **7**:

$$C_P = C_{FP} \cdot N_{FP} + C_{TP} \cdot N_{TP} \quad (6)$$

$$C_N = C_{FN} \cdot N_{FN} + C_{TN} \cdot N_{TN} \quad (7)$$

where N_{FP} is the number of false alarm samples, and N_{FN} is the number of missing detection samples. N_{TP} and N_{TN} are the numbers of samples correctly predicted as faults and normal, respectively. As shown in **Table 1**, C_{FN}, C_{FP}, C_{TN} and C_{TP} are the misclassification cost parameters.

The score measure of the branch node is affected by the sample distribution. Thus, to reduce the impact of class imbalance, the class distribution is added to the calculation of the misclassification cost function. In addition, C_{TP} and C_{TN} are usually regarded as zero in industry. The expression of the misclassification cost function is as follows:

$$C_P = p_P \cdot C_{FP} \cdot N_{FP} \quad (8)$$

$$C_N = p_N \cdot C_{FN} \cdot N_{FN} \quad (9)$$

where $p_P = N_P/(N_P + N_N)$ represents the proportion of faulty samples in the node, and $p_N = N_N/(N_P + N_N)$ is the proportion of normal samples in the node. N_P and N_N are the numbers of samples classified as faults and normal, respectively.

If N_i is a leaf node in **Figure 1**, according to Bayes' theorem, the classification with the minimized misclassification cost is selected as the category of the leaf node. The definition is as follows.

$$\hat{c} = \underset{i=0,1}{\arg\min} \left\{ \sum_j p(c_j|x) c_{ij} \right\} \quad (10)$$

where $p(c_j|x)$ represents the posterior probability that sample x belongs to class c_j, and c_{ij} represents the cost of a sample of class i being classified as belonging to class j.

The CS-ERT model is developed through generating sample subsets, establishing the CS-EDT method, and making decisions. A structure diagram of the CS-ERT method is shown in **Figure 2**.

D(X, Y) is the dataset, where $X = [x_1, x_2, \ldots, x_m]$ is the m-dimensional feature space, and $Y \in [0, 1]$ represents the target variables. First, **Figure 2** shows that one of the differences between ERT and a traditional random forest is that it generates M subsets that are the same as the original dataset D. Then, CS-EDT models $\{h(X, \theta_m), m = 1, \cdots, M\}$ are trained with these subsets, where M represents the number of CS-EDT models. Notably, the candidate features of the root node are all the features of the sample subset in the process of tree growth, and the leaf node is established recursively. Finally, the classification results of multiple CS-EDTs are integrated by means of the CS-ERT method, and the predicted category of the sample is determined according to majority voting, as shown in **Eq 11**:

$$H(x) = \underset{y}{\arg\max} \sum_{m=1}^{M} I[h(x, \theta_m) = y] \quad (11)$$

where $h(x, \theta_m)$ is a CS-EDT model, y is the classification result of the base classifier, and I(•) is an exponential function.

Pseudocode of CS-ERT is presented as follows.

Algorithm 1 CS-ERT approach.

Input: Training dataset D, Number of base classifiers M, Base classifier CS-EDT, Cost matrix $C = [C_{FP}, C_{FN}, C_{TP}, C_{TN}]$, Candidate attribute set attribute $_{\text{list}} = \{f_1, \cdots, f_m\}$

for m=1,2,. . .,M **do**
  Obtain the same dataset D_m as the train set D
  Create node N
  if the samples of node N have the same class c, **then**
    Return node N is a leaf node, node N classification is c;
  End if
  if attribute $_{\text{list}}$ is empty, **then**
  Calculate the misclassification cost of node N marked as normal or fault according to (5);
    Return node N is a leaf node, and node N is marked as a class with a low misclassification cost;
  End if
  Select the attribute A_{best} with the highest MCG in attribute $_{\text{list}}$;
  for each attribute A in attribute $_{\text{list}}$, **do**
    Randomly select a value of the attributeA_i as the cut-point a_i^c, and the MCG G_i is calculated according to (4);
    Return Select the attribute A_{best} with the largest G_i;
  End for
  attribute$_{\text{list}} \leftarrow$attribute$_{\text{list}} - A_{best}$
  Put the samples with $a_{best} < a_{best}^c$ into the left node N_L, and put the samples with $a_{best} \geq a_{best}^c$ into the right node N_R;
  Add node CS-ERT(N_L, C = [$C_{FP}, C_{FN}, C_{TP}, C_{TN}$], attribute$_{\text{list}} - A_{best}$) and CS-ERT($N_R$, C = [$C_{FP}, C_{FN}, C_{TP}, C_{TN}$], attribute$_{\text{list}} - A_{best}$);
  return $h(x, \theta_m)$ // Each base classifier is trained with a complete training set
End for
return $H(x) = \sum_m^M I[h(x, \theta_m) = y]$

Output: CS-ERT$H(x)$

The Computational Complexity of Cost-Sensitive Extremely Randomized Trees

The computational complexity of the RF algorithm is *O(M(mnlogn))*, where M represents the number of base classifiers, m represents the number of features, and n represents the number of samples. Compared with RFs, the CS-ERT algorithm introduces randomness in the process of tree growth. When a node selects a split feature, a random value for each feature is used as the cut-point for that attribute. Therefore, the computational complexity of CS-EDT is $O(mlogn)$, and the computational complexity of the CS-ERT algorithm is $O(M(mlogn))$, according to (11). The CS-ERT algorithm has better real-time performance.

WIND TURBINE GENERATOR FAULT DETECTION

In wind turbine generator fault detection, there are generally two types of erroneous predictions: 1) missed detection, where a

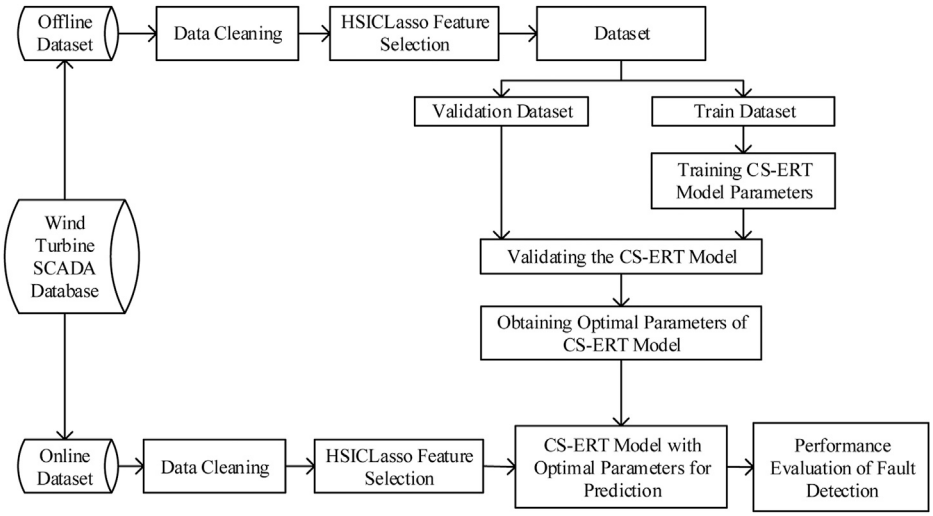


FIGURE 3 | Flowchart of wind turbine generator fault detection based on CS-ERT.

system in the fault state is predicted to be working normally, and 2) false alarm, where a system in the normal working state is predicted to be in a fault state. Clearly, the economic loss caused by missed detection is far greater than the loss caused by false alarms. CS-ERT can be used for fault detection of wind turbine generators to minimize the missing detection rate.

To provide a clearer structure, this section introduces three evaluation indicators for fault detection in advance. The missing detection rate, average misclassification cost, and gMean are abbreviated as MDR, AMC, and gMean, respectively. The evaluation index calculation equation is as follows.

$$\mathrm{MDR} = FN/(TP + FN) \tag{12}$$

$$\mathrm{AMC} = \frac{FN \cdot C_{FN} + FP \cdot C_{FP} + TP \cdot C_{TP} + TN \cdot C_{TN}}{FN + FP + TP + TN} \tag{13}$$

$$\mathrm{gMean} = \sqrt{Recall^{*}\mathrm{Specificity}} \tag{14}$$

Referring to **Eqs 12**, **13** TP represents true positives, FN represents false negatives, FP represents false positives, and TN represents true negatives. C_{FN}, C_{FP}, C_{TP}, and C_{TN} are the cost matrices. In **Eq 14**, $Recall = TP/(TP + FN)$ represents the probability of correct detection of fault samples, and $Specificity = TN/(TN + FP)$ represents the probability of correct detection of normal samples. The MDR refers to the ratio of the number of missed detection samples to the total number of samples when the wind turbine generator fails. The AMC considers not only the failure recognition rate but also the case where the misclassification cost is unequal. The gMean refers to the square root of the product of the failure detection rate and the normal detection rate, which is typically used as an evaluation of performance for class-imbalanced problems. The running time is closely related to the computational complexity of the algorithm. In this experiment, the running time is the mean value of the model's 10-fold cross-validation.

Figure 3 is a flowchart of a fault detection method based on the CS-ERT model. Offline wind turbine generator data are first collected from the SCADA database, and data cleaning is performed. Data cleaning includes normalization and removal of missing and null values. Expert experience and the HSICLasso method are used to select features and generate feature subsets to avoid the impact of weakly correlated features and redundant features on the fault detection performance. In addition, the offline data are divided into a train dataset and a validation dataset. The train set is used to train the CS-ERT model. The validation dataset is used to adjust the hyperparameters of the model and initially evaluate the performance of the model. The optimal hyperparameters of the CS-ERT model are obtained through offline data, and the CS-ERT model with optimal parameters is established according to the optimal hyperparameters. In the last step, wind turbine data is collected online, and data preprocessing is performed. The processed online data are then used as the input for the optimal CS-ERT model, which is used to predict the real-time working status of wind turbine generators. If a fault is predicted, an alarm is triggered. Finally, the performance of the fault detection model on online data is analyzed according to **Eqs 12–14**.

The pseudocode of the large-scale wind turbine generator fault detection method based on CS-ERT is described as follows. **Algorithm 2** represents the process of obtaining the optimal CS-ERT model on the offline dataset. **Algorithm 3** realizes online fault detection of wind turbine generators.

Algorithm 2 Offline implementation of the CS-ERT fault detection method.

Input: Wind turbine SCADA dataset D_{off};

1 Perform data cleaning on dataset D_{off}, and normalize it using **(15)**
2 Use HSICLasso method for feature selection, divide D_{off} into the train datasetD_{train} and the validation dataset D_{vali}
3 The CS-ERT model M was established by train dataset D_{train}

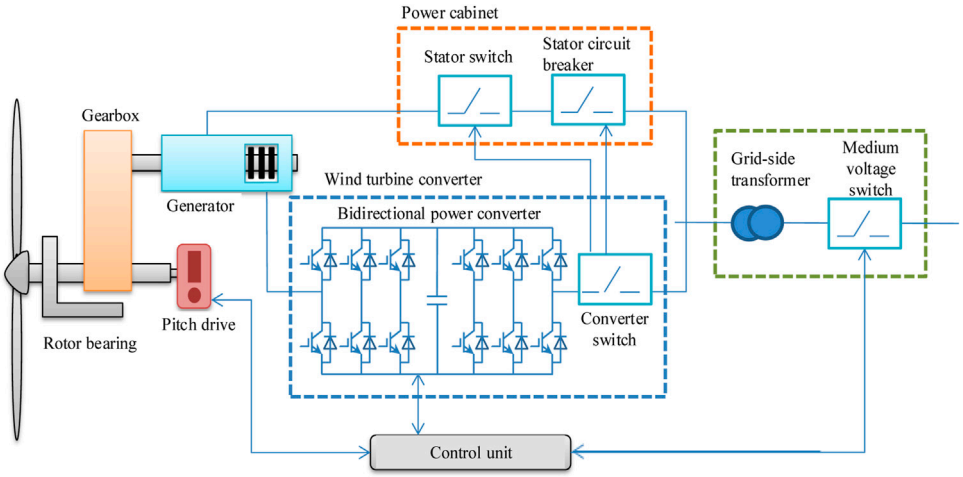


FIGURE 4 | Main structure of the doubly fed wind turbine.

TABLE 2 | Wind turbine generator fault type and sensitive parameters.

Dataset	Fault type	Failure mechanism	Sensitive parameters
Data 1	Generator winding temperature error	The winding temperature exceeds 165°C for 5 s	Winding temperature, bearing temperature, gearbox bearing temperature, cooling air temperature
Data 2	Generator bearing temperature error	The temperature of the front axle D-END of bearing a or the rear axle N-END of bearing b is greater than 95°C for 5 s	Bearing temperature, winding temperature, cooling air temperature
Data 3	Generator fan pump heater protection error	Protection switch of generator fan or heater trips	Cold wind temperature, wind speed, bearing temperature
Data 4	Generator brush error	The generator carbon brush is badly worn and lasts 5 s	Bearing temperature, engine room temperature, winding temperature

4 Taking AMC as the evaluation index, the hyperparameters of the model are adjusted by the validation datasetD_{vali} to obtain the optimal hyperparameters θ
5 the CS-ERT model M* with optimal parameters is established according to the optimal hyperparameters θ

Output: model M*

Algorithm 3 Online implementation of CS-ERT fault detection method.

Input: CS-ERT model M^*, Online data D_{on};

1 Perform data cleaning and feature selection on the online data D_{on} and normalize it using **(15)** to obtain D'_{on}
2 Begin timing
3 Obtain model M* from **Algorithm 1**, and use M^* and D'_{on} to predict the operating state of the wind turbine
4 **If** online data D_{on} is predicted to be a failure, **then**
5 Trigger alarms
6 **End if**
7 End timing
8 running time = Ending time - Beginning time
9 According to **(12)**–**(14)**, analyze the performance of the model M* on the online data D_{on}

Output: Trigger alarms, missing detection rate, gMean, AMC and running time

EXPERIMENTAL ANALYSIS

In this section, data preprocessing is first performed on the data in the SCADA database. Then, the HSICLasso feature selection method extracts the main features and verifies the effectiveness of the method. Finally, the operating data of a 1.5 MW wind turbine in a wind farm in Shandong is used as experimental data, the effectiveness of the proposed method in the wind turbine generator fault detection problem is verified, and its superiority is emphasized by comparison.

Data Description and Data Cleaning

A generator fault detection experiment was conducted on a 1.5 MW doubly fed wind turbine in a wind farm in Shandong, China, which proved the effectiveness of the method. The main structure diagram of the doubly fed wind turbine is shown in **Figure 4**. Wind turbines are mainly composed of generators, gearboxes, pitch systems, etc. Fan blades convert wind energy into

mechanical energy, and generators convert mechanical energy into electrical energy. The electrical energy generated by the generator is integrated into the power grid through components such as converters, power cabinets and transformers.

The research object of this paper is a doubly-fed wind turbine generator. The doubly-fed wind turbine generator is mainly composed of a generator and a cooling system. The generator is composed of a stator, a rotor, a bearing, etc. The stator winding of the generators is directly connected to the power grid, and the rotor winding is connected to the power grid through a frequency converter. The equipment realizes variable-speed and constant-frequency power generation, which meets the requirements of the grid connection. Due to the AC excitation characteristics, the doubly-fed wind turbine can accurately adjust the output voltage of the generator by adjusting the excitation current. However, the power factor of doubly-fed wind turbines is low and requires additional power compensation. Therefore, in order to ensure the normal operation of the wind turbine, it is very important to perform fault detection on the generator.

Four kinds of defects (i.e., generator winding temperature error (F1), generator bearing temperature error (F2), generator fan pump heater protection error (F3) and generator brush error (F4) are generated in the actual operation of the generator. **Table 2** shows the fault mechanism and sensitive parameters of the four types of faults of the generator. The failure mechanism indicates the cause of the failure. Sensitive parameters are features that have a greater impact on faults through manual analysis. Wind turbine generator data are obtained from the SCADA database. Each sample has 213 features. The starting sampling point is half an hour before the start of a fault. The ending sampling point is half an hour after the end of a fault, and the data sampling interval is 2 s.

Data cleaning methods include missing value processing outlier value processing, and commonly used methods such as the deletion method and data repair method. To solve this problem, this paper adopts the deletion method to clean the data. This experiment was conducted on the Python 3.6 platform. The multi-duplicated samples and the samples with missing and null values were removed from the dataset. This method can not only reduce the influence of noise on the model performance, but also reduce the data diversity. Furthermore, features that have all 0 values were removed to reduce the dimensionality of the feature space and the model. To ensure the comparability of each feature, z-score normalization was used to eliminate the dimensionality of each feature. The value of each feature was transformed into a dimensionless value in the interval [0, 1].

$$x_i^{'} = \frac{x_i - \mu}{\sigma} \tag{15}$$

where x_i represents an attribute variable, μ is the mean of attribute x_i, and σ is the variance of attribute x_i. Each dataset of Data 1-Data 4 contains only normal samples and designated failure samples. Each dataset is normalized using the z-score method.

Experimental Results and Analysis

In accordance with the procedure of **Figure 3**, the HSICLasso method is used to select the features of the wind turbine generators dataset. The HSICLasso feature selection method (Yamada et al., 2014) is a derived algorithm of the least absolute shrinkage and selection operator (lasso) (Tibshirani, 1996). We use non-negative constraints on α to improve the algorithm's ability to select effective features. In addition, the Gaussian kernel function and the triangular kernel function are used on the input vector and output vector of HSICLasso, respectively. We can incorporate structured outputs via kernels. Ren et al. (2020) proved that HSICLasso can effectively analyze the nonlinear relationship between multivariate time series. The F-norm replaces the L2-norm. The HSICLasso algorithm is defined as follows.

$$\min_{\alpha} \frac{1}{2}\left\|\overline{L} - \sum_{k=1}^{m} \alpha_k \overline{K}_{Frob}^{(k)}\right\|^2 + \lambda\|\alpha\|_1, \quad \text{s.t.} \quad \alpha_1, \cdots, \alpha_k \geq 0, \tag{16}$$

where $\overline{L} = \Gamma L \Gamma$ and $\overline{K}^{(k)} = \Gamma K^{(k)} \Gamma$ are centered Gram matrices, and L and $K^{(k)}$ are both Gram matrices. $\Gamma = I_n - \frac{1}{n} 1_n 1_n^T$ is the centering matrix. I_n represents the n-dimensional identity matrix. 1_n represents an n-dimensional matrix with all elements of 1. The first term in the above expression represents the linear set of the input kernel matrix K and the fitting output kernel matrix L, and the last part represents the regular term. The above formula is further expressed as:

$$\min_{\alpha}\left(\frac{1}{2}\mathrm{HSIC}(\mathrm{y},\mathrm{y}) - \sum_{k=1}^{d}\alpha_k \mathrm{HSIC}(u_k,\mathrm{y}) + \frac{1}{2}\sum_{k,l=1}^{d}\alpha_k\alpha_l \mathrm{HSIC}(u_k,u_l)\right) + \lambda\|\alpha\|_1, \tag{17}$$

where $\mathrm{HSIC}(\cdot)$ is the Hilbert-Schmidt independence criterion (HSIC). $\mathrm{HSIC}(u_k, \mathrm{y})$ represents a measure of independence based on the core. The higher the correlation between u_k and y is, the larger the value of $\mathrm{HSIC}(u_k, \mathrm{y})$ and the smaller the result of **Eq 16**. The strong correlation between the feature and the output vector is ensured. The lower the correlation between u_k and u_l is, the smaller the value of $\mathrm{HSIC}(u_k, u_l)$ and the smaller the result of **Eq 16**. Non-redundancy between features is guaranteed. In this way, the HSICLasso feature selection method is similar to a minimum redundancy maximum relevancy algorithm. The global optimal solution is effectively obtained by **Eq 17**. The method is extended to the high-dimensional feature selection problem. For massive high-dimensional data, the Gaussian kernel in HSIC Lasso is computationally expensive. Yamada et al. (2014) proposed a table lookup approach to reduce the computation time and memory size, reducing the computational complexity from $O(dn^2)$ to $O(dn + B)$, where d is the feature dimension, n is the number of samples, and B is the hyperparameter (we use $B = 20$ in our implementation).

The wind turbine generator dataset contains a large number of nonlinear and nonfunctional relationships. The high-dimensional feature space entails a large amount of calculation and low real-time performance for fault detection. The non-redundant features that have a strong correlation with the output vector are extracted based on expert experience and HSICLasso feature selection. Yamada et al. (2018) used the HSICLasso feature selection

TABLE 3 | HSICLasso feature selection results.

Feature	Tag	HSICLasso feature selection score			
		Data 1	Data 2	Data 3	Data 4
Generator winding temperature W	AW	0.009782277	**0.017599536**	**0.0615362**	0.025937422
Generator winding temperature V	AU	**0.66801703**	0.00001453	**0.10023695**	**0.010824516**
Generator bearing temperature B	BA	**0.033899892**	**0.2168639**	0.022490485	**0.36818618**
Generator cooling air temperature	BB	0.024351638	0.075802557	0.000024650	0.166879070
Gearbox shaft 1 temperature	AL	**0.063766375**	**0.069782838**	**0.037703969**	**0.052285645**
Gearbox shaft 2 temperature	AM	**0.017679539**	**0.062894136**	**0.029099241**	**0.14716054**
Gearbox inlet oil temperature	AN	**0.017236305**	**0.018463224**	**0.13771559**	**0.061054502**
30 s average wind speed	V	0.0052472115	0.00007895	**0.35092705**	0.0000784
Wind direction	H	**0.011375366**	0.00005421	**0.076073088**	0.0004825
Yaw deviation	AJ	**0.047915235**	**0.11275150**	0.0000251	0.0000854
Gearbox oil temperature	AO	0.0065203002	**0.004965703**	0.027400982	0.0001254
Nacelle temperature	BE	0.000003215	0.000695982	0.0027198601	**0.10510261**
Nacelle outdoor temperature	BD	0.022269854	0.00000234	0.0000154	**0.026983585**

The features corresponding to the bold values are selected for model construction.

TABLE 4 | Dataset description.

Dataset	Original feature number	Feature number after feature selection	Number of samples	Sample imbalance
Data 1	213	8	5,354	18.83
Data 2	213	8	3,554	24.48
Data 3	213	8	3,568	12.31
Data 4	213	8	3,585	8.98

TABLE 5 | Optimization of the cost parameters of CS-ERT for 4 datasets.

Dataset	C_{FP}	C_{FN}	C_{TP}	C_{TN}
Data 1	1	50	0	0
Data 2	1	74	0	0
Data 3	1	43	0	0
Data 4	1	40	0	0

method for ultrahigh-dimensional big data nonlinear feature selection and achieved good results. The features with the top 8 are selected as inputs for the wind turbine generator fault detection model. The feature selection results are as follows.

According to **Table 3**, the winding temperature, bearing temperature, and cooling air temperature are strongly correlated in the four fault datasets, consistent with the failure mechanism and sensitive parameters in **Table 2**. Therefore, the HSICLasso feature selection method can accurately extract attribute subsets from wind turbine generator data. The feature dimensions, fault types, and sample imbalance of the dataset after applying the HSICLasso feature selection method are shown in **Table 4**.

TheCS-ERT model has 4 hyperparameters: the number of decision trees M, the minimum number of leaf nodes n_{node}, and two misclassification cost parameters C_{FP} and C_{FN}. Because the model has many hyperparameters, the optimal hyperparameters are difficult to determine. Hyperparameter optimization methods include the gray wolf optimizer method (Long et al., 2018), butterfly optimization algorithm (Long et al., 2021; Long et al., 2021), and grid search method. We input the obtained low-dimensional feature set into the cost-sensitive extreme random forest classifier optimized by the grid optimization method to realize automatic fault identification of wind turbines. Four key parameters (n_{node}, M, C_{FN} and C_{FP}) of the CS-ERT classifier are selected through a grid search method using 10-fold cross-validation. To simplify the experimental process, C_{FN} is regarded as 1. The variation range of the parameter C_{FP} is [0, 200]. As shown in **Table 5**, the results of the cost parameters of the CS-ERT model are optimized for each dataset.

Comparison Among Different Methods

In this subsection, comparative studies among different methods are performed to verify the efficacy and superiority of the proposed algorithm. According to the procedure mentioned in *Experimental Results and Analysis* , different features are extracted to form four feature sets of four faults, and then these feature sets are input to the model to identify wind turbine generator faults. To evaluate the effectiveness of the CS-ERT fault detection method, three points should be emphasized. First, nonredundant features with strong correlation are selected via the HSICLasso method to reduce the feature dimensionality. Then, the parameters of different classifiers are selected based on grid optimization for each dataset. Finally, the experiment compares RF (Hsu et al., 2020; Jia et al., 2018) with XGBoost (Zhang et al., 2018), ERT (Janssens et al., 2016), CS-EDT (base classifier for CS-ERT), MetaCost (Kim et al., 2012), AdaCost (Yin et al., 2013), CSForest (Siers and Islam, 2015), and CS-ERT. To eliminate the contingency of the experiment, all methods use the 10-fold cross-validation method. During performance analysis, MDR, gMean, AMD and Time are used to evaluate the performance of the model.

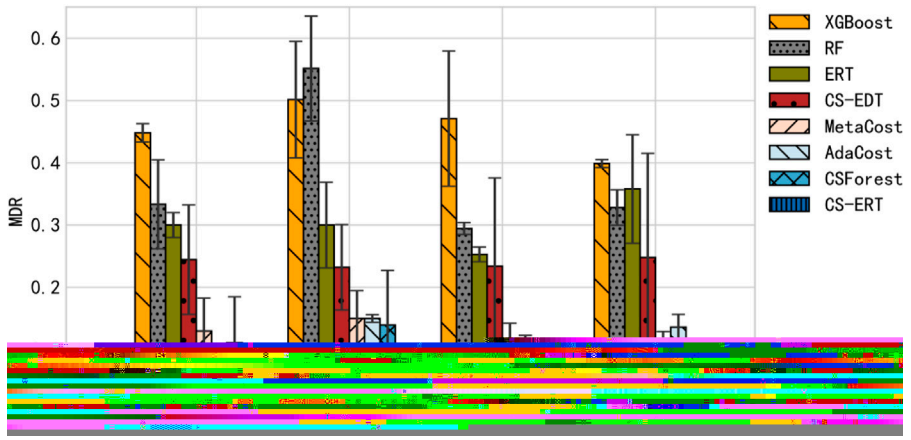


FIGURE 5 | Comparison of MDR for the eight algorithms on the four datasets.

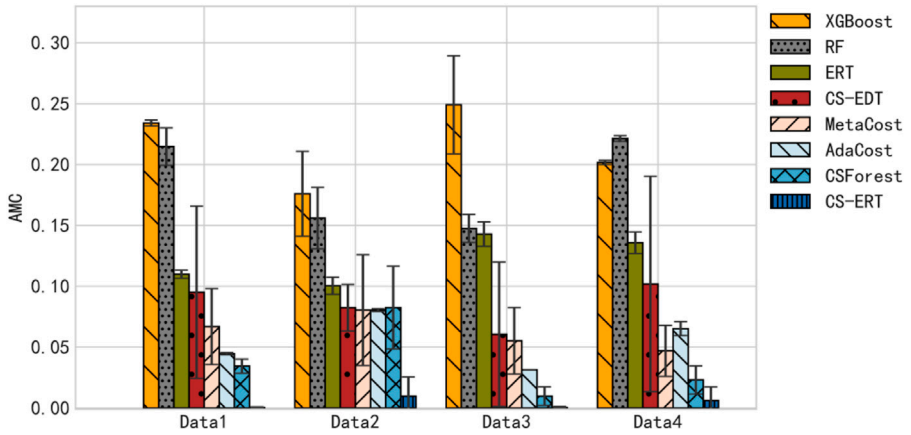


FIGURE 6 | Comparison of AMC for the eight algorithms on the four datasets.

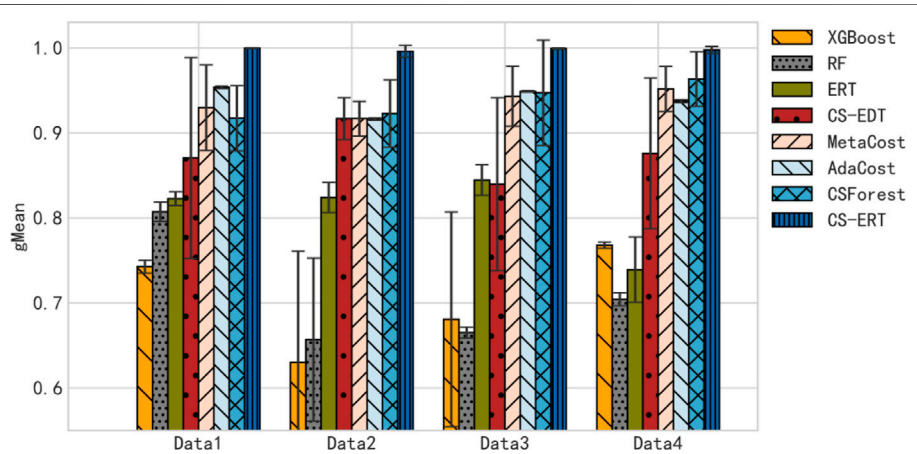


FIGURE 7 | Comparison of gMean for the eight algorithms on the four datasets.

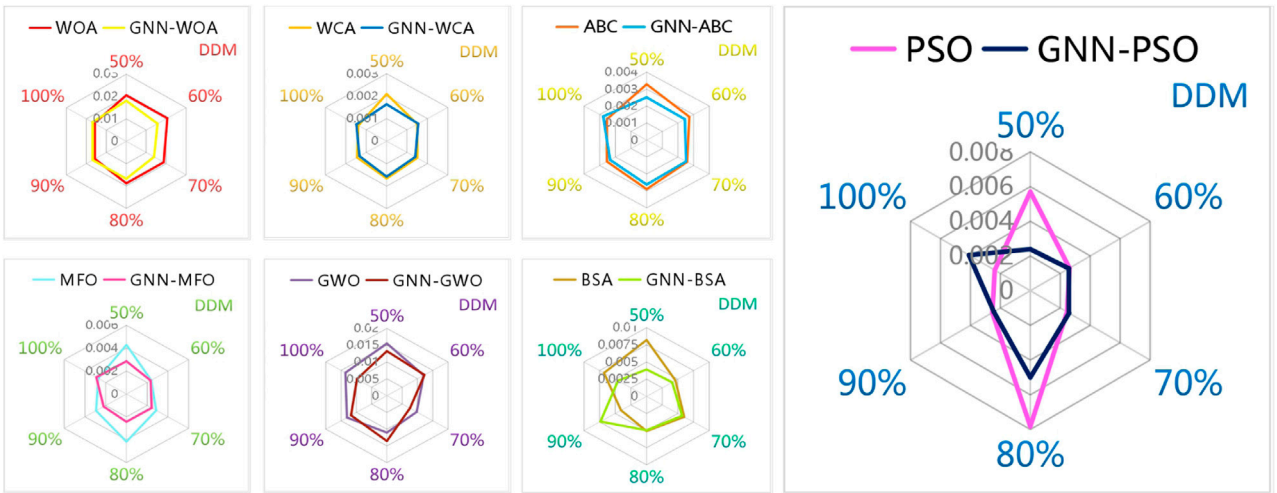


FIGURE 13 | Radar of average RMSE achieved by different algorithms for the DDM.

Statistical Results and Analysis

Radars of average RMSE achieved via each meta-heuristic algorithm with six groups of data at different scales are provided in **Figures 12**, **13**, which show that average RMSE acquired via all algorithms with GNN-based data prediction are smaller compared with that obtained without data prediction at different scales of data, especially under 50% data. In particular, the ranking basis of various methods is based on a comprehensive and systematic comparison of their performance in PV cell parameter extraction, e.g., extraction accuracy, convergence speed, and convergence stability. This effectively verifies the outstanding reliability of GNN-based meta-heuristic algorithms for accurate PV cell modeling.

CONCLUSION

This paper develops a novel hybrid of a GNN and advanced meta-heuristic algorithms for accurate modeling of different solar cells, and its main contributions are as follows:

- A GNN is applied to generate more virtual *I-V* data based on inadequate measured data, in which a GA is adopted to find optimal network parameters of an ANN, which can improve the accuracy of generated virtual *I-V* data. As a result, the GNN can significantly enrich the dataset, and provide a more reliable fitness function to the meta-heuristic algorithms for PV cell modeling;
- Two widely used PV cell models, i.e., the SDM and DDM, are adopted to verify the practical performance of the proposed strategy. For instance, the average RMSE obtained by the ABC, BSA, GWO, MFO, PSO, WCA, and WOA based on GNN prediction for the SDM is 72.29, 97.04, 79.72, 39.48, 43.74, 86.82, 100.96% to that of without GNN data prediction under 50% measured data, respectively;
- Case studies show that GNN-based meta-heuristic algorithms can comprehensively enhance optimization precision and convergence stability compared with original meta-heuristic algorithms utilizing untrained measured *I-V* data.

Future studies should focus on the improvement and optimization of the structure of the proposed GNN, e.g., data training process and relevant network parameters tuning can be further simplified to reduce the optimization burden. Besides, as all the experiments were carried out in a simulation environment which is different from real operation conditions, experiments combined with hardware platforms under practical working scenarios are imperative for future engineering applications.

DATA AVAILABILITY STATEMENT

The original contributions presented in the study are included in the article/Supplementary Material, further inquiries can be directed to the corresponding author.

AUTHOR CONTRIBUTIONS

LW: Conceptualization, Writing-Original Draft, Formal analysis; ZC: Project administration, Supervision, Writing-Review and Editing; YG: Visualization, Validation; WH: Data Curation, Visualization; XC: Formal analysis, Software; PW: Investigation, Validation; CH: Writing-Reviewing and Editing, Methodology; JL: Software, Data Curation.

ACKNOWLEDGMENTS

The authors gratefully acknowledge the support of the Key Technologies R and D Program of Henan Province (192102210306, 202102210335, 212102210254, 212102210026) and the Henan Province Science and Technology Enterprise Cultivation (Science and Technology Little Giant) Special Fund Project (KPJJ-201701).

REFERENCES

Abbassi, R., Abbassi, A., Jemli, M., and Chebbi, S. (2018). Identification of Unknown Parameters of Solar Cell Models: A Comprehensive Overview of Available Approaches. *Renew. Sustainable Energ. Rev.* 90, 453–474. doi:10.1016/j.rser.2018.03.011

Allam, D., Yousri, D. A., and Eteiba, M. B. (2016). Parameters Extraction of the Three Diode Model for the Multi-Crystalline Solar Cell/module Using Moth-Flame Optimization Algorithm. *Energ. Convers. Management*. 123, 535–548. doi:10.1016/j.enconman.2016.06.052

Awadallah, M. A. (2016). Variations of the Bacterial Foraging Algorithm for the Extraction of PV Module Parameters from Nameplate Data. *Energ. Convers. Management*. 113, 312–320. doi:10.1016/j.enconman.2016.01.071

Chang, K. Y. (2011). The Optimal Design for PEMFC Modeling Based on Taguchi Method and Genetic Algorithm Neural Networks. *Int. J. Hydrogen Energ.* 36 (21), 13683–13694. doi:10.1016/j.ijhydene.2011.07.094

Chin, V. J., Salam, Z., and Ishaque, K. (2015). Cell Modelling and Model Parameters Estimation Techniques for Photovoltaic Simulator Application: A Review. *Appl. Energ.* 154, 500–519. doi:10.1016/j.apenergy.2015.05.035

Fathy, A., and Rezk, H. (2017). Parameter Estimation of Photovoltaic System Using Imperialist Competitive Algorithm. *Renew. Energ.* 111, 307–320. doi:10.1016/j.renene.2017.04.014

Figueroa, O. R., Castellanos, M. Q., Montes, E. M., and Schütze, O. (2020). Metaheuristics to Solve Grouping Problems: A Review and a Case Study. *Swarm Evol. Comput.* 53, 100643. doi:10.1016/j.swevo.2019.100643

Gao, S. C., Wang, K. Y., Tao, S. C., Jin, T., Dai, H. W., and Cheng, J. J. (2021). A State-Of-The-Art Differential Evolution Algorithm for Parameter Estimation of Solar Photovoltaic Models. *Energ. Convers. Management* 230, 113784. doi:10.1016/j.enconman.2020.113784

Gao, X., Cui, Y., Hu, J., Xu, G., and Yu, Y. (2016). Lambert W-Function Based Exact Representation for Double Diode Model of Solar Cells: Comparison on Fitness and Parameter Extraction. *Energ. Convers. Management*. 127, 443–460. doi:10.1016/j.enconman.2016.09.005

Guchhait, P. K., and Banerjee, A. (2020). Stability Enhancement of Wind Energy Integrated Hybrid System with the Help of Static Synchronous Compensator and Symbiosis Organisms Search Algorithm. *Prot. Control. Mod. Power Syst.* 5 (2), 138–150. doi:10.1186/s41601-020-00158-8

He, X., Chu, L., Qiu, R. C., Ai, Q., Ling, Z., and Zhang, J. (2020). Invisible Units Detection and Estimation Based on Random Matrix Theory. *IEEE Trans. Power Syst.* 35 (3), 1846–1855. doi:10.1109/tpwrs.2019.2935739

Huang, Z., Fang, B. L., and Deng, J. (2020). Multi-objective Optimization Strategy for Distribution Network Considering V2G Enabled Electric Vehicles in Building Integrated Energy System. *Prot. Control. Mod. Power Syst.* 5 (5), 48–55. doi:10.1186/s41601-020-0154-0

Humada, A. M., Hojabri, M., Mekhilef, S., and Hamada, H. M. (2016). Solar Cell Parameters Extraction Based on Single and Double-Diode Models: A Review. *Renew. Sustainable Energ. Rev.* 56, 494–509. doi:10.1016/j.rser.2015.11.051

Ishaque, K., and Salam, Z. (2011). An Improved Modeling Method to Determine the Model Parameters of Photovoltaic (PV) Modules Using Differential Evolution (DE). *Solar Energy* 85 (9), 2349–2359. doi:10.1016/j.solener.2011.06.025

Ishaque, K., Salam, Z., Taheri, H., and Shamsudin, A. (2011). A Critical Evaluation of EA Computational Methods for Photovoltaic Cell Parameter Extraction Based on Two Diode Model. *Solar Energy*. 85 (9), 1768–1779. doi:10.1016/j.solener.2011.04.015

Jervase, J. A., Bourdoucen, H., and Al-lawati, A. M. (2001). Solar Cell Parameter Extraction Using Genetic Algorithms. *Meas. Sci. Technology* 12, 1922–1925. doi:10.1088/0957-0233/12/11/322

Jordehi, A. R. (2016). Parameter Estimation of Solar Photovoltaic (PV) Cells: a Review. *Renew. Sustainable Energ. Rev.* 61, 354–371. doi:10.1016/j.rser.2016.03.049

Khani, M. S., Baneshi, M., and Eslami, M. (2019). Bi-objective Optimization of Photovoltaic-thermal (PV/T) Solar Collectors According to Various Weather Conditions Using Genetic Algorithm: A Numerical Modeling. *Energy*. 185, 116223. doi:10.1016/j.energy.2019.116223

Khanna, V., Das, B. K., Bisht, D., Vandanaand Singh, P. K. (2015). A Three Diode Model for Industrial Solar Cells and Estimation of Solar Cell Parameters Using PSO Algorithm. *Renew. Energ.* 78, 105–113. doi:10.1016/j.renene.2014.12.072

Kler, D., Sharma, P., Banerjee, A., Rana, K. P. S., and Kumar, V. (2017). PV Cell and Module Efficient Parameters Estimation Using Evaporation Rate Based Water Cycle Algorithm. *Swarm Evol. Comput.* 35, 93–110. doi:10.1016/j.swevo.2017.02.005

Liu, J., Yao, W., Wen, J. Y., Fang, J. K., Jiang, L., He, H. B., et al. (2020). Impact of Power Grid Strength and PLL Parameters on Stability of Grid-Connected DFIG Wind Farm. *IEEE Trans. Sustainable Energ.* 11 (1), 545–557. doi:10.1109/tste.2019.2897596

Liu, K. L., Hu, X. S., Zhou, H. Y., Tong, L., Widanalage, D., and Marco, J. (2021). Feature Analyses and Modelling of Lithium-Ion Batteries Manufacturing Based on Random forest Classification. *IEEE/ASME Trans. Mechatronics,* 1. doi:10.1109/TMECH.2020.3049046

Mittal, M., Bora, B., Saxena, S., and Gaur, A. M. (2018). Performance Prediction of PV Module Using Electrical Equivalent Model and Artificial Neural Network. *Solar Energy*. 176, 104–117. doi:10.1016/j.solener.2018.10.018

Murty, V. V. S. N., and Kumar, A. (2020). Multi-objective Energy Management in Microgrids with Hybrid Energy Sources and Battery Energy Storage Systems. *Prot. Control. Mod. Power Syst.* 5 (1), 1–20. doi:10.1186/s41601-019-0147-z

Nayak, B., Mohapatra, A., and Mohanty, K. B. (2019). Parameter Estimation of Single Diode PV Module Based on GWO Algorithm. *Renew. Energ. Focus* 30, 1–12. doi:10.1016/j.ref.2019.04.003

Nesmachnow, S. (2014). An Overview of Metaheuristics: Accurate and Efficient Methods for Optimization. *Int. J. Metaheuristics* 3 (4), 320–347. doi:10.1504/ijmheur.2014.068914

Noriega, J. R., and Wang, H. (1998). A Direct Adaptive Neural-Network Control for Unknown Nonlinear Systems and its Application. *IEEE Trans. Neural Networks* 9 (1), 27–34. doi:10.1109/72.655026

Oliva, D., Cuevas, E., and Pajares, G. (2014). Parameter Identification of Solar Cells Using Artificial Bee colony Optimization. *Eenergy* 72, 93–102. doi:10.1016/j.energy.2014.05.011

Peng, X. T., Yao, W., Yan, C., Wen, J. Y., and Cheng, S. J. (2020). Two-stage Variable Proportion Coefficient Based Frequency Support of Grid-Connected DFIG-WTs. *IEEE Trans. Power Syst.* 35 (2), 962–974. doi:10.1109/tpwrs.2019.2943520

Pillai, D. S., and Rajasekar, N. (2018). Metaheuristic Algorithms for PV Parameter Identification: A Comprehensive Review with an Application to Threshold Setting for Fault Detection in PV Systems. *Renew. Sustainable Energ. Rev.* 82 (3), 3503–3525. doi:10.1016/j.rser.2017.10.107

Qais, M. H., Hasanien, H. M., Alghuwainem, S., and Nouh, A. S. (2019a). Coyote Optimization Algorithm for Parameters Extraction of Three-Diode Photovoltaic Models of Photovoltaic Modules. *Energy* 187, 116001. doi:10.1016/j.energy.2019.116001

Qais, M. H., Hasanien, H. M., and Alghuwainem, S. (2019b). Identification of Electrical Parameters for Three-Diode Photovoltaic Model Using Analytical and sunflower Optimization Algorithm. *Appl. Energ.* 250, 109–117. doi:10.1016/j.apenergy.2019.05.013

Ram, J. P., Manghani, H., Pillai, D. S., Babu, T. S., Miyatake, M., and Rajasekara, N. (2018). Analysis on Solar PV Emulators: A Review. *Renew. Sustainable Energ. Rev.* 81, 149–160. doi:10.1016/j.rser.2017.07.039

Rodriguez, J. D. B., Petrone, G., Paja, A. R., and Spagnuolo, G. (2017). A Genetic Algorithm for Identifying the Single Diode Model Parameters of a Photovoltaic Panel. *Mathematics Comput. Simulation*. 134, 38–54. doi:10.1016/j.matcom.2015.10.008

Roeva, O., and Fidanova, S. (2018). Comparison of Different Metaheuristic Algorithms Based on Intercriteria Analysis. *J. Comput. Appl. Mathematics*. 340, 615–628. doi:10.1016/j.cam.2017.07.028

Shangguan, X. C., He, Y., Zhang, C. K., Jiang, L., Spencer, J., and Wu, M. (2020a). Robust Load Frequency Control for Power System Considering Transmission Delay and Sampling Period. *IEEE Trans. Ind. Inform.* 17, 1. doi:10.1109/TII.2020.3026336

Shangguan, X. C., He, Y., Zhang, C. K., Jin, L., Yao, W., Jiang, L., et al. (2020b). Control Performance Standards Oriented Event-Triggered Load Frequency Control for Power Systems under Limited Communication Bandwidth. *IEEE Trans. Control. Syst. Technology.*, 1. doi:10.1109/TCST.2021.3070861

Soloway, D., and Haley, P. J. (1996). Neural Generalized Predictive Control. *Proc. 1996 IEEE Int. Symp. Intell. Control.* 277-282. doi:10.1109/ISIC.1996.556214

Song, D. R., Chang, Q., Zheng, S. Y., Yang, S., Yang, J., and Joo, Y. H. (2021). Adaptive Model Predictive Control for Yaw System of Variable-Speed Wind Turbines. *J. Mod. Power Syst. Clean Energ.* 9 (1), 219–224. doi:10.35833/mpce.2019.000467

Song, Y., Chen, Z. Q., and Yuan, Z. Z. (2007). New Chaotic PSO-Based Neural Network Predictive Control for Nonlinear Process. *IEEE Trans. Neural Networks*. 18 (2), 595–601. doi:10.1109/tnn.2006.890809

Sun, K., Yao, W., Fang, J. K., Ai, X. M., Wen, J. Y., and Cheng, S. J. (2019). Impedance Modeling and Stability Analysis of Grid-Connected DFIG-Based Wind Farm with a VSC-HVDC. *IEEE J. Emerging Selected Top. Power Electronics*. 8, 1375-1390. doi:10.1109/JESTPE.2019.2901747

Sun, L. M., and Yang, B. (2020). Nonlinear Robust Fractional-Order Control of Battery/SMES Hybrid Energy Storage Systems. *Power Syst. Prot. Control.* 48 (22), 76–83.

Torabi, K. E., Eddine, I. A., Obbadi, A., Errami, A., Rmaily, R., Sahnoun, S., et al. (2017). Parameters Estimation of the Single and Double Diode Photovoltaic Models Using a Gauss-Seidel Algorithm and Analytical Method: A Comparative Study. *Energ. Convers. Management* 148, 1041–1054. doi:10.1016/j.enconman.2017.06.064

Villalva, M. G., Gazoli, J. R., and Filho, E. R. (2009). Comprehensive Approach to Modeling and Simulation of Photovoltaic Arrays. *IEEE Trans. Power Electronics*. 24, 1198–1208. doi:10.1109/tpel.2009.2013862

Wolf, P., and Benda, V. (2013). Identification of PV Solar Cells and Modules Parameters by Combining Statistical and Analytical Methods. *Solar Energy*. 93, 151–157. doi:10.1016/j.solener.2013.03.018

Xiong, G. J., Zhang, J., Shi, D. Y., and He, Y. (2018). Parameter Extraction of Solar Photovoltaic Models Using an Improved Whale Optimization Algorithm. *Energ. Convers. Management*. 174, 388–405. doi:10.1016/j.enconman.2018.08.053

Yang, B., Jiang, L., Yao, W., and Wu, Q. H. (2015). Perturbation Estimation Based Coordinated Adaptive Passive Control for Multimachine Power Systems. *Control. Eng. Pract.* 44, 172–192. doi:10.1016/j.conengprac.2015.07.012

Yang, B., Wang, J. B., Zhang, X. S., Yu, T., Yao, W., Shu, H. C., et al. (2020). Comprehensive Overview of Meta-Heuristic Algorithm Applications on PV Cell Parameter Identification. *Energ. Convers. Management*. 208, 112595. doi:10.1016/j.enconman.2020.112595

Yang, J., Fang, L. Q., Song, D. R., Su, M., Yang, X. B., Huang, L. X., et al. (2021). Review of Control Strategy of Large Horizontal-axis Wind Turbines Yaw System. *Wind Energy*, 24 (2), 97–115. doi:10.1002/we.2564

Ye, M. Y., Wang, X. D., and Xu, Y. S. (2009). Parameter Extraction of Solar Cells Using Particle Swarm Optimization. *J. Appl. Phys.* 105 (9), 094502. doi:10.1063/1.3122082

Yu, K. J., Liang, J. J., Qu, B. Y., Cheng, Z. P., and Wang, H. S. (2018). Multiple Learning Backtracking Search Algorithm for Estimating Parameters of Photovoltaic Models. *Appl. Energ.* 226, 408–422. doi:10.1016/j.apenergy.2018.06.010

Zhang, H. X., Lu, Z. X., Hu, W., Wang, Y. T., Dong, L., and Zhang, J. T. (2019). Coordinated Optimal Operation of Hydro-Wind-Solar Integrated Systems. *Appl. Energ.* 242, 883–896. doi:10.1016/j.apenergy.2019.03.064

Zhang, X. S., Li, S. N., He, T. Y., Yang, B., Yu, T., Li, H. F., et al. (2019). Memetic Reinforcement Learning Based Maximum Power point Tracking Design for PV Systems under Partial Shading Condition. *Energy*. 174, 1079–1090. doi:10.1016/j.energy.2019.03.053

Zhou, Y. H., Romijnders, R., Romijnders, C., Campen, J., Maetzler, W., Hortobágyi, T., et al. (2020). The Detection of Age Groups by Dynamic Gait Outcomes Using Machine Learning Approaches. *Scientific Rep.* 10, 4426. doi:10.1038/s41598-020-61423-2

Conflict of Interest: Authors ZC, YG, WH, CH were employed by company Xuchang KETOP Testing Research Institute Co. Ltd. Author JL was employed by company XJ Group Corporation.

The remaining authors declare that the research was conducted in the absence of any commercial or financial relationships that could be construed as a potential conflict of interest.

Copyright © 2021 Wang, Chen, Guo, Hu, Chang, Wu, Han and Li. This is an open-access article distributed under the terms of the Creative Commons Attribution License (CC BY). The use, distribution or reproduction in other forums is permitted, provided the original author(s) and the copyright owner(s) are credited and that the original publication in this journal is cited, in accordance with accepted academic practice. No use, distribution or reproduction is permitted which does not comply with these terms.

frontiers in Energy Research

ORIGINAL RESEARCH
published: 08 June 2021
doi: 10.3389/fenrg.2021.693252

PV Cell Parameter Extraction Using Data Prediction–Based Meta-Heuristic Algorithm via Extreme Learning Machine

*Bing Li, Huang Chen and Tian Tan**

College of Engineering, Shantou University, Shantou, China

To reliably evaluate the practical performance and to undertake optimal control of PV systems, a precise PV cell parameter extraction–based accurate modeling of PV cells is extremely crucial. However, its inherent high nonlinear and multimodal characteristics usually hinder conventional optimization methods to obtain a fast and satisfactory performance. Besides, insufficient current–voltage *(I–V)* data provided by manufacturers cannot guarantee high accuracy and flexibility of PV cell parameter extraction under various operation scenarios. Hence, this article proposes a novel parameter extraction strategy by data prediction–based meta-heuristic algorithm (DPMhA). An extreme learning machine (ELM) is adopted to predict output *I–V* data from measured data, which can provide a more reliable fitness function to meta-heuristic algorithms (MhAs). Consequently, MhAs can undertake a more stable search for optimal solution through extended *I–V* data; thus, PV cell parameters can be obtained with high accuracy and convergence rate. Its effectiveness is validated via three typical PV cell models, that is, single diode model (SDM), double diode model (DDM), and three diode model (TDM). Last, comprehensive case studies illustrate that the DPMhA can considerably enhance the accuracy and effectiveness compared with those without data prediction.

Keywords: parameter extraction, PV cell, data prediction, meta-heuristic algorithm, extreme learning machine

OPEN ACCESS

Edited by:
Bo Yang,
Kunming University of Science and Technology, China

Reviewed by:
Feixiong Chen,
Fuzhou University, China
Zhe-Kang Dong,
Hangzhou Dianzi University, China
Linfei Yin,
Guangxi University, China

****Correspondence:***
Tian Tan
19ttan@stu.edu.cn

Specialty section:
This article was submitted to Smart Grids, a section of the journal Frontiers in Energy Research

Received: *10 April 2021*
Accepted: *26 April 2021*
Published: *08 June 2021*

Citation:
Li B, Chen H and Tan T (2021) PV Cell Parameter Extraction Using Data Prediction–Based Meta-Heuristic Algorithm via Extreme Learning Machine. Front. Energy Res. 9:693252. doi: 10.3389/fenrg.2021.693252

INTRODUCTION

With severe environmental deterioration (Peng et al., 2020), fossil fuel depletion (Yang et al., 2018), severe air pollution (Sun et al., 2020), and increasing concerns on global energy crisis over the past decade (Yang et al., 2018), energy reform and sustainable development have become essential for an environment-friendly society (Wang et al., 2020). Hence, environmental protection and energy conservation are paramount for all countries around the world (Shen et al., 2019), in which exploitation and utilization of various renewable energy technologies, for example, wind (Li et al., 2019; Zhang et al., 2019) and solar (Liu et al., 2020), have been broadly focused. In particular, solar energy is considered to be one of the most sustainable and viable energy sources of the future (Chaibi et al., 2019), such that photovoltaic (PV) system is widely used for solar energy applications thanks to its distinct merits, for example, abundant resources, low cost, and pollution-free (Yang et al., 2016).

Particularly, measured current–voltage (*I–V*) data–based reliable PV modeling is extremely critical to dynamic behavior analysis of PV systems. Thus far, a series of PV cell modeling

TABLE 1 | Error functions of three different models.

Model	Error function	Solution vector
SDM	$f_{SDM}(V_L, I_L, x) = I_{ph} - I_{sd}\left[\exp\left(\frac{V_L+I_L R_s}{aV_t}\right) - 1\right] - \frac{V_L+I_L R_s}{R_{sh}} - I_L$	$x = \{I_{ph}, I_{sd}, R_s, R_{sh}, a\}$
DDM	$f_{DDM}(V_L, I_L, x) = I_{ph} - I_{sd1}\left[\exp\left(\frac{q(V_L+I_L R_s)}{a_1 V_t}\right) - 1\right] - I_{sd2}\left[\exp\left(\frac{q(V_L+I_L R_s)}{a_2 V_t}\right) - 1\right] - \frac{V_L+I_L R_s}{R_{sh}} - I_L$	$x = \{I_{ph}, I_{sd1}, I_{sd2}, R_s, R_{sh}, a_1, a_2\}$
TDM	$f_{TDM}(V_L, I_L, x) = I_{ph} - I_{sd1}\left[\exp\left(\frac{q(V_L+I_L R_s)}{a_1 V_t}\right) - 1\right] - I_{sd2}\left[\exp\left(\frac{q(V_L+I_L R_s)}{a_2 V_t}\right) - 1\right] - I_{sd3}\left[\exp\left(\frac{q(V_L+I_L R_s)}{a_3 V_t}\right) - 1\right] - \frac{V_L+I_L R_s}{R_{sh}} - I_L$	$x = \{I_{ph}, I_{sd1}, I_{sd2}, I_{sd3}, R_s, R_{sh}, a_1, a_2, a_3\}$

methods have been proposed (Jordehi, 2016) to characterize the output of PV systems for better performance analysis and prediction (Youssef et al., 2017), maximum power point tracking (MPPT) (Yang et al., 2019; Yang et al., 2019), and fault diagnosis (Chen et al., 2018). Two equivalent circuit models, single diode model (SDM) (Nunes et al., 2018) and double diode model (DDM) (Abbassi et al., 2018), are extensively adopted for the sake of simplicity, while more complicated triple diode model (TDM) (Qais et al., 2019) is barely investigated because it might increase computation burden. Nevertheless, as the TDM allows a more efficient and accurate analysis of the complex output characteristics of PV systems, this article validates the performance of all three PV models mentioned above. In particular, the accurate extraction of several electrical parameters related to the model is the most basic and critical step of reliable modeling. However, they are unavailable and changeable as insufficient electrical parameters provided by manufacturers and are only experimentally obtained under standard test conditions (STCs) (Xiong et al., 2018). Besides, their values are also time-varying due to degradation and faults of PV cells, which further increases modeling uncertainties. Hence, the aforementioned two shortcomings render parameter extraction thorny to obtain satisfactory results in practical applications.

To tackle such obstacles, the design of numerous methods consists of three main categories, namely, analytical methods (Majdoul et al., 2015; Torabi et al., 2017), deterministic techniques, and meta-heuristic algorithms (MhAs). Analytical methods are based on a series of mathematical calculations and a number of key points on the I–V curve, which owns a high degree of simplicity, but lacks high accuracy in different operating scenarios. Meanwhile, deterministic techniques, including iterative curve fitting (Villalva et al., 2009) and Newtonian-based methods (Li et al., 2017), can yield more accurate results, while they are extremely demanding in terms of model properties. Moreover, they are highly sensitive to initial operation conditions; thus, the inherent high nonlinearity and multimodality of PV systems always make them easy to be trapped at a local optimum. Hence, the limitations of the aforementioned two methods hinder them to maintain a stable and satisfactory performance on PV cell parameter extraction. In contrast, MhAs can effectively avoid these shortcomings thanks to their outstanding merits, such as high flexibility on problem characteristics (Nesmachnow, 2014), easy implementation (Roeva and Fidanova, 2018), and insensitivity to gradient information (Figueroa et al., 2020). Until now, a large number of MhAs are adopted in PV cell parameter extraction (Yang et al., 2020), such as genetic algorithm (GA) (Jervase et al., 2001), differential evolution (DE) (Ishaque and Salam, 2011), particle swarm optimization (PSO) (Ye et al., 2009), artificial bee colony (ABC) (Oliva et al., 2014), whale optimization algorithm (WOA) (Amroune et al., 2019; Dasu et al., 2019), backtracking search algorithm (BSA) (Yu et al., 2018), moth flame optimizer (MFO) (Allam et al., 2016), grey wolf optimization (GWO) (Yang et al., 2017), bird mating optimizer (BMO) (Askarzadeh and Rezazadeh, 2013), water cycle algorithm (WCA) (Kler et al., 2017),wind-driven optimization (WDO) (Derick et al., 2017), fireworks algorithm (FWA) (Babu et al., 2016), and various hybrids.

Except for the improvements focusing on mechanism and structure of algorithms to enhance the optimization performance, one should realize that all modeling techniques heavily rely on the number and accuracy of measured data. However, in order to improve the simulation accuracy, some parameters in the PV system are not provided by the manufacturer and therefore need to be extracted based on the *I–V* curve. Such low-dimensional data provided by the manufacturer, while saving computational resources, may also cause important data information to be lost during the simulation. Hence, it is imperative to develop effective data processing methods to enrich data samples. Recently, artificial neural network (ANN) (Grondin-Perez et al., 2014; Zhao et al., 2019) and deep learning strategy (Schmidhuber, 2015) show their great effectiveness in data analysis and prediction. This article adopts a learning algorithm called extreme learning machine (ELM) with a single-hidden layer feedforward neural network (SLFN) for output *I–V* data prediction (Huang et al., 2006), which can provide a more reliable fitness function to MhAs. The main contributions of this article can be summarized as follows:

- The existing MhAs are directly adopted for PV cell parameter extraction via measured *I–V* data of PV systems, which are easy to be trapped at a low-quality optimum if measured *I–V* data are inadequate or distributed intensively. In contrast, the proposed data prediction–based MhA (DPMhA) can effectively solve this difficulty since measured *I–V* data can be extended via ELM-based data prediction.

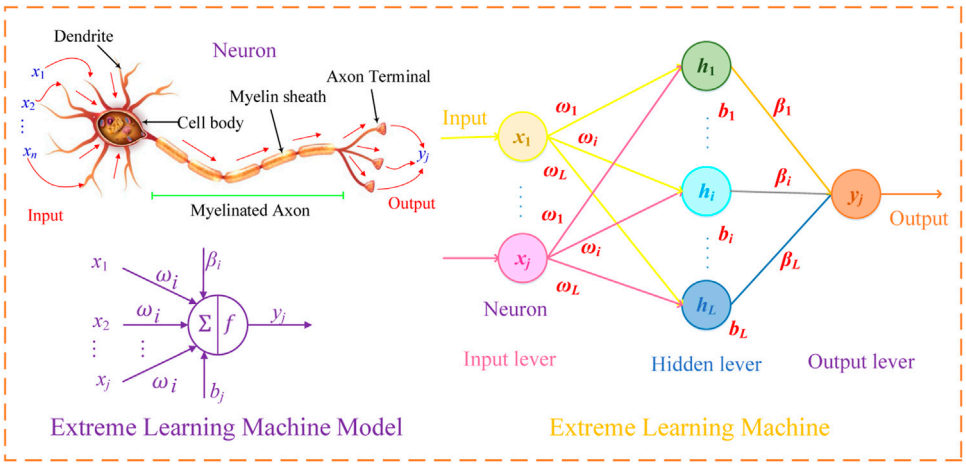


FIGURE 1 | Basic structure of ELM network.

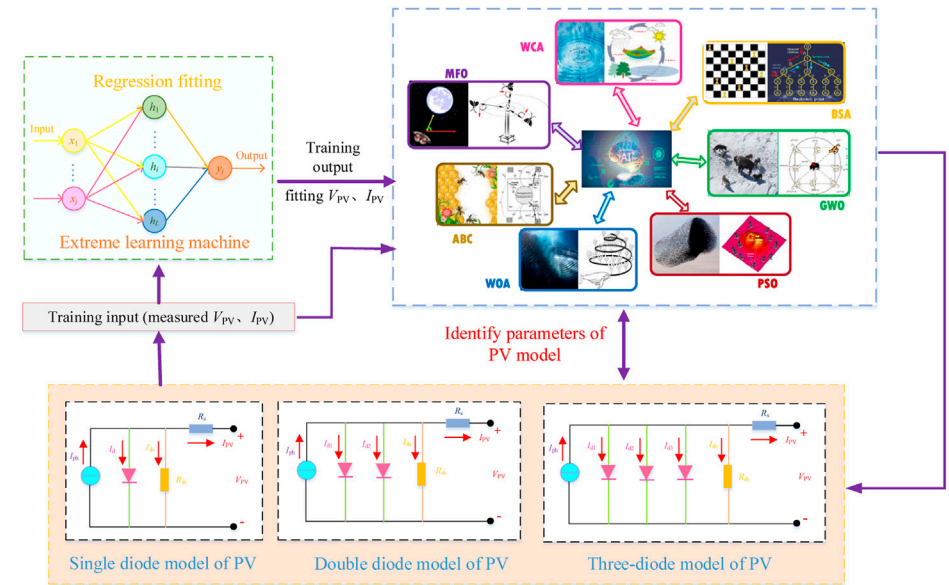


FIGURE 2 | Framework of ELM-based data-driven procedure for PV cell parameter identification.

- Several advanced MhAs with data prediction are applied for parameter extraction of PV cells, which are thoroughly validated via three different kinds of PV models.
- Four case studies show that DPMhA can achieve simulation results with higher precision and stability compared with those only based on measured data.

The rest of this article is organized as follows: *PV Cell Modeling and Problem Formulation* illustrates mathematical modeling of PV cell and objective function. The overall introduction of data prediction–based MhAs is elaborated in *Methodologies*. Case study results on different PV models are provided in *Case Studies*. Last, conclusions are given in *Conclusion*.

PV CELL MODELING AND PROBLEM FORMULATION

Shockley diode–based equivalent circuits are always deemed as standard PV models, among which three most widely used models, that is, SDM, DDM, and TDM are discussed in this section.

Design of Mathematical Modeling

In general, there are minor differences in the model structures of the three models mentioned above, which are also systematically summarized in **Supplementary Table S1** for a more detailed presentation.

As demonstrated in **Supplementary Table S1**, I_L and V_L represent the output current and output voltage of the PV cell respectively; I_{sh} refers to the current of the parallel resistor R_{sh}; and the thermal voltage V_T is calculated by

$$V_T = \frac{KT}{q}, \quad (1)$$

where T represents the surface temperature; K is the Boltzmann constant, which has a value of 1.38×10^{-23} J/K; and q means the electron charge, respectively, with a size of 1.6×10^{-19} C.

All the other variables are provided in Nomenclature.

Objective Function

The main objective of parameter identification for various PV models is to find suitable parameters so that the model can more accurately describe the output characteristics of the PV system and minimize the errors between the experimentally collected data and the simulation data, which can be evaluated quantitatively by means of an objective function. The root mean square error (RMSE) is chosen here as the objective function, which can be calculated as

$$\mathrm{RMSE}\ (x) = \sqrt{\frac{1}{N}\sum_{k=1}^{N}\left[f\left(V_L, I_L, x\right)\right]^2}, \quad (2)$$

where x represents the solution vector of the unknown parameters to be identified and N denotes the number of experimental data, respectively.

Error functions $f\left(V_L, I_L, x\right)$ for three PV models are tabulated in **Table 1**.

From **Table 1**, for the sake of minimizing the difference between experimental data and simulated data, objective function RMSE (x) needs to be minimized by optimizing solution vector x. Note that the objective function value is inversely proportional to the solution quality.

METHODOLOGIES

Data Prediction by Extreme Learning Machine

Principle of ELM

ELM is a simple learning strategy for SLFNs that mainly depends on generalized inverse matrix theory (Huang and Siew, 2005), which randomly initializes the input weight with no adjustment requirement in subsequent operations (Huang et al., 2000; Huang et al., 2006). Besides, output weight is analytically determined by generalized inverse, which only requires a one-step calculation. Hence, compared with other normal feedforward network learning strategies, for example, back-propagation (BP) algorithm, the ELM can significantly enhance robustness, generalization ability, learning speed, and training accuracy. The main operation structure of ELM is demonstrated in **Figure 1**.

For N different training samples $(x_i, y_i) \in R^n \times R^m$, $i = 1, 2, 3 \ldots, N$, network output of standard SLFNs with K hidden neurons and an activation function $g(\omega_i \cdot x_i + b_i)$ is calculated by (Huang et al., 2006)

$$y_i = \sum_{i=1}^{K}\beta_i g_i\left(x_j\right) = \sum_{i=1}^{K}\beta_i g\left(\omega_i \cdot x_i + b_i\right),\ j = 1,\ 2,\ 3,\ \ldots,\ N, \quad (3)$$

where ω_i represents the connecting weight vector between the ith hidden layer neuron and input neuron; b_i denotes threshold of the ith hidden layer of the network; β_i means the connection weight between the ith hidden layer neuron and output neuron, respectively.

Since SLFNs can approximate training samples with zero errors for any ω and b when the number of neurons in the hidden layer equals the number of training data samples (Huang et al., 2006), for example, $\sum_{i=1}^{N}\left\|y_i - t_i\right\| = 0$, which means there exist ω_i, b_i, and β_i that can satisfy the relationship, as follows:

$$t_j = \sum_{i=1}^{K}\beta_i g\left(\omega_i \cdot x_i + b_i\right),\ j = 1,\ 2,\ 3,\ \ldots,\ N. \quad (4)$$

Hence, the two equations above are rewritten more simply, as follows:

$$H\beta = T, \quad (5)$$

$$H = \begin{bmatrix} h(x_1) \\ \vdots \\ h(x_N) \end{bmatrix} = \begin{bmatrix} g(\omega_1 \cdot x_1 + b_1)\cdots g(\omega_K \cdot x_1 + b_K) \\ \vdots \\ g(\omega_1 \cdot x_N + b_1)\cdots g(\omega_K \cdot x_N + b_K) \end{bmatrix}, \quad (6)$$

$$\beta = \begin{bmatrix} \beta_1^{'} \\ \vdots \\ \beta_K^{'} \end{bmatrix}_{K\times m} \text{ and } T = \begin{bmatrix} T_1^{'} \\ \vdots \\ T_K^{'} \end{bmatrix}_{K\times m}, \quad (7)$$

where H represents the hidden layer output matrix; T denotes the expected output matrix; and β is determined by least square approach, as follows:

$$\left\|H\tilde{\beta} - T\right\| = \min_{\beta}\left\|H\beta - T\right\|, \quad (8)$$

When the hidden layer output matrix is column full rank, it yields

$$\tilde{\beta} = \mathrm{argmin}_{\beta}\left\|H\beta - T\right\| = H^{\dagger}T, \quad (9)$$

TABLE 2 | Execution procedure of DPMhA for PV cell parameter extraction.

1: Determine PV cell type
2: Initialize algorithms parameters and population
3: Set k: = 0
4: WHILE $k \le k_{max}$
5: FOR1 i = 1 : n
6: Calculate fitness function of the ith individual by **Eq. 10**
7: END FOR1
8: Determine roles of all individuals based on their fitness values
9: FOR2 i = 1 : n
10: Update solution of the ith individual according to its designated global exploration and local exploitation
11: END FOR2
12: Set k: = k+1
13: END WHILE
14: Output optimal parameters for PV cell

TABLE 3 | Average RMSE obtained by various algorithms for the SDM with six measured data.

Algorithm		Average RMSE					
		Number of measured data (%)					
	—	50%	60%	70%	80%	90%	100%
ABC	N	4.28×10^{-3}	3.60×10^{-3}	3.20×10^{-3}	3.47×10^{-3}	3.01×10^{-3}	3.04×10^{-3}
	Y	3.40×10^{-3}	3.13×10^{-3}	3.18×10^{-3}	3.21×10^{-3}	2.93×10^{-3}	3.12×10^{-3}
BSA	N	3.43×10^{-2}	3.40×10^{-2}	2.40×10^{-2}	3.16×10^{-2}	2.53×10^{-2}	2.41×10^{-2}
	Y	2.82×10^{-2}	2.55×10^{-2}	2.24×10^{-2}	2.54×10^{-2}	2.77×10^{-2}	2.63×10^{-2}
GWO	N	2.67×10^{-2}	2.09×10^{-2}	1.96×10^{-2}	1.99×10^{-2}	1.99×10^{-2}	2.17×10^{-2}
	Y	1.84×10^{-2}	1.79×10^{-2}	1.76×10^{-2}	1.81×10^{-2}	1.76×10^{-2}	2.03×10^{-2}
MFO	N	5.46×10^{-3}	3.65×10^{-3}	2.92×10^{-3}	5.39×10^{-3}	2.90×10^{-3}	3.74×10^{-3}
	Y	3.45×10^{-3}	2.94×10^{-3}	2.32×10^{-3}	3.66×10^{-3}	2.55×10^{-3}	3.54×10^{-3}
PSO	N	1.16×10^{-2}	9.39×10^{-3}	6.96×10^{-3}	1.09×10^{-2}	5.69×10^{-3}	2.72×10^{-3}
	Y	2.05×10^{-3}	6.30×10^{-3}	4.76×10^{-3}	6.55×10^{-3}	2.68×10^{-3}	5.11×10^{-3}
WCA	N	2.71×10^{-3}	1.98×10^{-3}	2.11×10^{-3}	2.35×10^{-3}	1.78×10^{-3}	1.87×10^{-3}
	Y	2.08×10^{-3}	1.84×10^{-3}	1.99×10^{-3}	1.96×10^{-3}	1.81×10^{-3}	1.75×10^{-3}
WOA	N	3.82×10^{-2}	3.70×10^{-2}	3.76×10^{-2}	4.45×10^{-2}	3.35×10^{-2}	3.40×10^{-2}
	Y	3.55×10^{-2}	3.44×10^{-2}	3.66×10^{-2}	3.41×10^{-2}	3.29×10^{-2}	3.52×10^{-2}

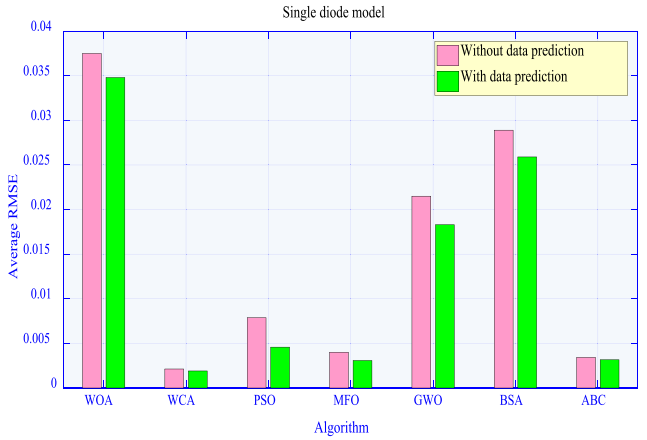


FIGURE 3 | Comparison of total average RMSE values with six different datasets for the SDM.

where $H^{\dagger}$ denotes Moore Penrose generalized inverse of the output matrix of hidden layer H.

Output *I–V* Data Prediction

For a PV cell, output current and voltage can be measured for parameter extraction, while the increase of measured data will lead to a high extraction accuracy. To employ ELM for output I–V data prediction, PV cell voltage and current are regarded as the input and output of ELM, respectively. Therefore, output I–V data prediction of a PV cell can be achieved by ELM with single input and single output, as described by **Eqs. 3–9**.

Data Prediction–Based MhAs

Data Prediction–Based Fitness Function

Based on prediction data, MhAs can implement a balance between global and local search with an updated fitness function. Due to all optimization, variables are limited within their lower and upper bounds; RMSE (2) is taken as the fitness function, which should also take the prediction data into account, as follows:

$$\mathrm{RMSE}\ (x) = \sqrt{\frac{1}{N+N_{\mathrm{p}}} \sum_{k=1}^{N+N_{\mathrm{p}}} \left[f\left(V_{\mathrm{L}}, I_{\mathrm{L}}, x\right)\right]^2}, \tag{10}$$

where N_{p} means the total count of the prediction data.

General Execution Procedure

The overall operation framework of DPMhA mainly consists of three parts, as illustrated in **Figure 2**. First, measured output I–V data of various PV cells are transferred to the ELM. Second, the ELM is trained by measured data to predict new data; thus, a more reliable fitness function can be established to evaluate the performance of various MhAs. Finally, MhAs implement relevant global exploration and local exploitation to find optimal PV parameters. Particularly, the detailed execution procedure of DPMhA is given in **Table 2**, in which the main differences between various algorithms are individual roles and searching mechanisms of global exploration and local exploitation.

CASE STUDIES

In this section, several well-established MhAs are utilized for parameter extraction of three PV cell models. In particular, a total of 26 pairs of measured I–V datasets utilized for simulation are acquired from Easwarakhanthan et al. (1986), which are measured on a 57 mm diameter commercial silicon R.T.C. France solar cell under weather condition (G = 1000 W/m^2 and T = 33°C). This dataset has been widely used to test the techniques developed for parameter extraction. Many existing studies (Ye et al., 2009)-(Yu et al., 2018) were tested based on these 26 pairs of measured data. To guarantee a fair comparison with them, the proposed GNN is also implemented based on these 26 pairs of measured data. For the sake of verifying the

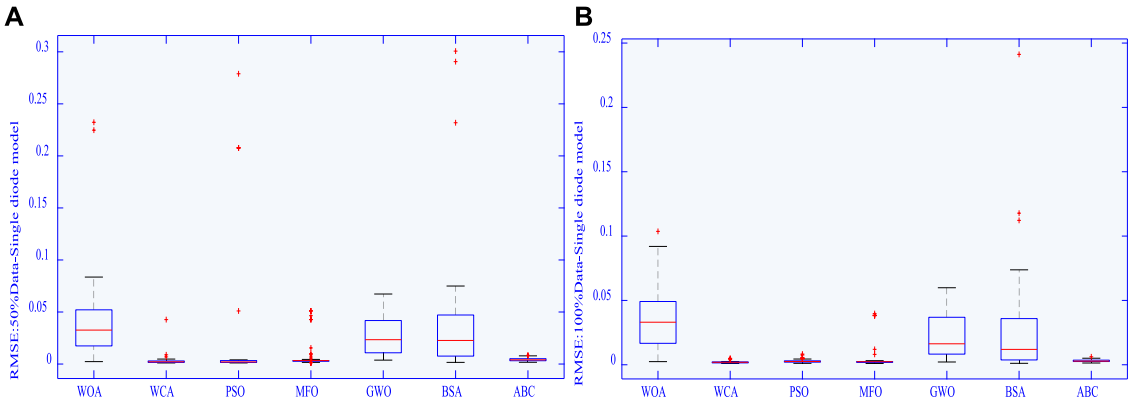


FIGURE 4 | Boxplot of RMSE obtained by various algorithms in different data for the SDM: **(A)** 50% data and **(B)** 100% data.

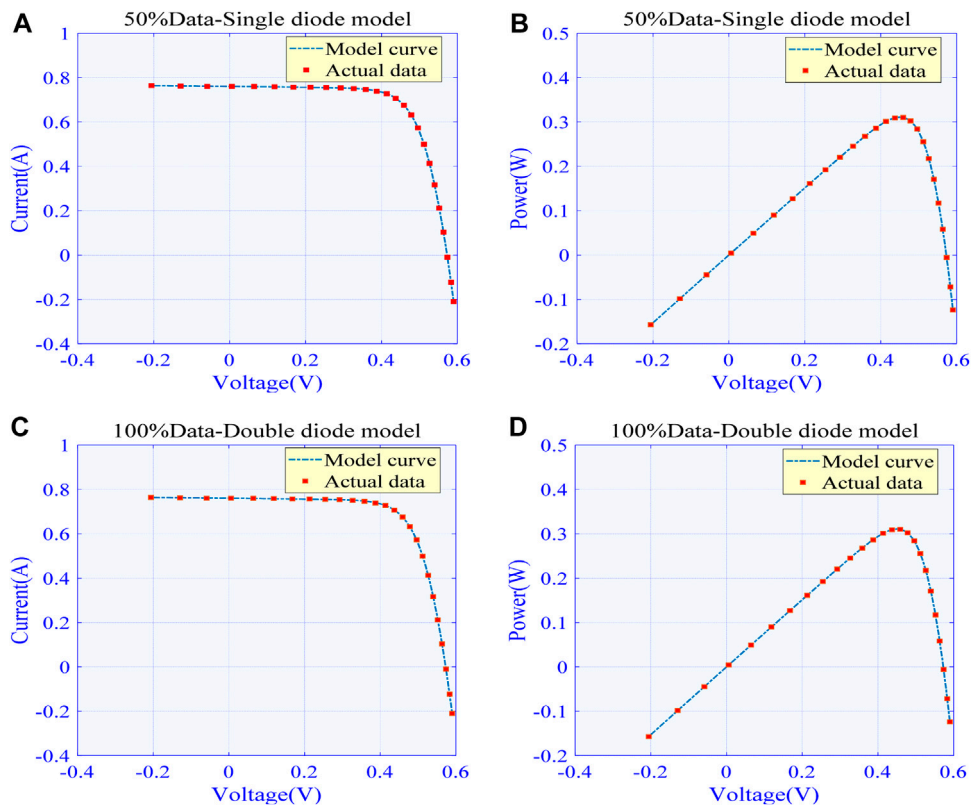


FIGURE 5 | Comparison between actual data and model curve obtained by the best algorithm in different training data for SDM: **(A)** *I-V* curve in 50% training data **(B)** *P-V* curve in 50% training data **(C)** *I-V* curve in 100% training data and **(D)** *I-V* curve in 100% training data.

optimization performance of MhAs based on insufficient measurement data, six sets of data were selected from 26 sets of measurement data in different ratios of 50, 60, 70, 80, 90, and 100% of the measurement data. The presented ELM is essentially a simple single-input and single-output network. Therefore, the pairs of measured data are adequate for training the ELM. To provide a reliable fitness function to MhAs, the total number of each dataset and the prediction data are set to be 50, for example, 24 prediction data for 100% dataset. In addition, each MhA is evaluated under two circumstances, that is, without data prediction (i.e., with only selected measured data) and with data prediction. Note that the measured *I–V*

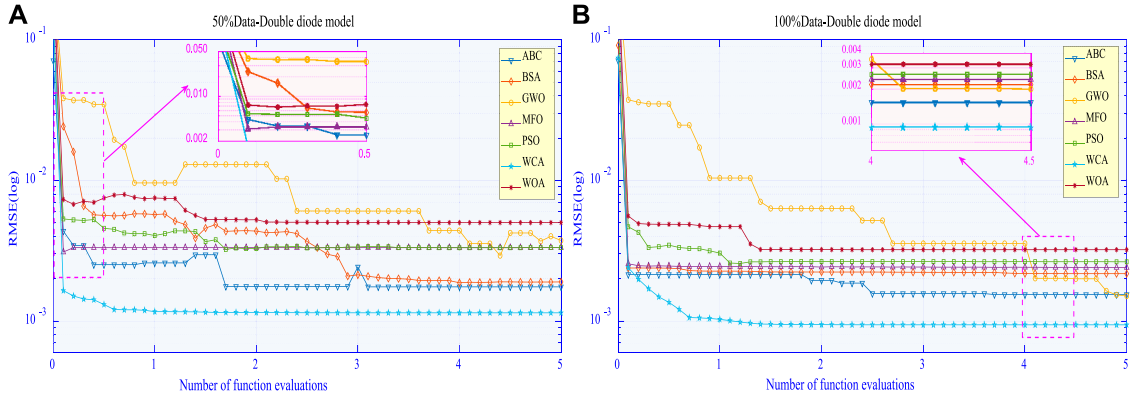


FIGURE 6 | Convergence of various algorithms for SDM: **(A)** 50% data and **(B)** 100% data.

TABLE 4 | Average RMSE obtained by various algorithms for the DDM with six measured data.

Algorithm	Average RMSE						
		Number of measured data (%)					
	—	50%	60%	70%	80%	90%	100%
ABC	N	4.16×10^{-3}	3.46×10^{-3}	3.25×10^{-3}	3.55×10^{-3}	3.26×10^{-3}	3.14×10^{-3}
	Y	3.48×10^{-3}	3.19×10^{-3}	3.16×10^{-3}	3.41×10^{-3}	3.12×10^{-3}	3.26×10^{-3}
BSA	N	1.30×10^{-2}	1.26×10^{-2}	1.01×10^{-2}	1.18×10^{-2}	1.19×10^{-2}	1.04×10^{-2}
	Y	8.97×10^{-3}	1.02×10^{-2}	8.48×10^{-3}	1.11×10^{-2}	7.29×10^{-3}	1.02×10^{-2}
GWO	N	2.22×10^{-2}	1.87×10^{-2}	1.53×10^{-2}	1.54×10^{-2}	1.70×10^{-2}	1.50×10^{-2}
	Y	1.15×10^{-2}	1.58×10^{-2}	1.46×10^{-2}	1.52×10^{-2}	1.26×10^{-2}	1.43×10^{-2}
MFO	N	4.88×10^{-3}	2.79×10^{-3}	2.78×10^{-3}	3.61×10^{-3}	2.43×10^{-3}	2.71×10^{-3}
	Y	3.64×10^{-3}	2.55×10^{-3}	2.46×10^{-3}	2.74×10^{-3}	2.43×10^{-3}	2.50×10^{-3}
PSO	N	5.92×10^{-3}	4.20×10^{-3}	2.99×10^{-3}	5.52×10^{-3}	2.71×10^{-3}	2.65×10^{-3}
	Y	3.14×10^{-3}	2.79×10^{-3}	2.91×10^{-3}	4.12×10^{-3}	2.88×10^{-3}	2.69×10^{-3}
WCA	N	2.38×10^{-3}	1.71×10^{-3}	1.75×10^{-3}	1.75×10^{-3}	1.51×10^{-3}	1.58×10^{-3}
	Y	1.89×10^{-3}	1.61×10^{-3}	1.71×10^{-3}	1.62×10^{-3}	1.60×10^{-3}	1.67×10^{-3}
WOA	N	2.56×10^{-2}	2.67×10^{-2}	2.30×10^{-2}	2.68×10^{-2}	2.43×10^{-2}	2.28×10^{-2}
	Y	2.25×10^{-2}	1.94×10^{-2}	2.16×10^{-2}	2.56×10^{-2}	1.90×10^{-2}	2.00×10^{-2}

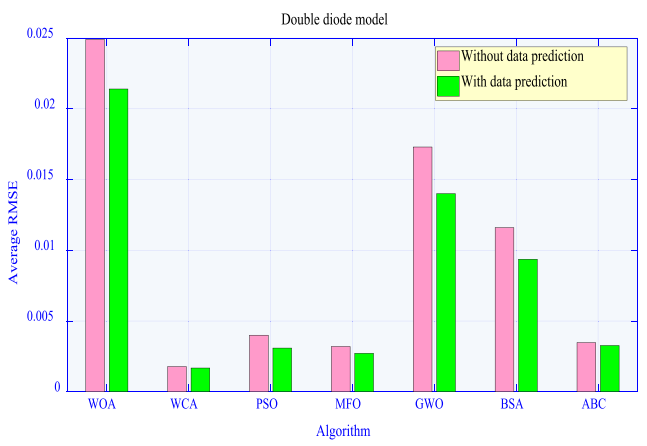


FIGURE 7 | Comparison of total average RMSE values with six different datasets for the TDM.

data are not hard to be acquired. But it is difficult to acquire adequate high-accuracy data with a general measuring instrument. Hence, the measured I–V data cannot completely represent the I–V output feature of the PV cell. Besides, the added prediction I–V data can provide a reliable fitness function; thus, the optimization accuracy and convergence stability of each meta-heuristic algorithm can be improved.

The main parameters of meta-heuristic algorithms are the population size and the maximum number of iterations. To guarantee a fair comparison, these two parameters are set to be the same values for all MhAs under each PV model that is designed to be identical, in which their specific parameters (e.g., the maximum velocity in PSO) are set to be the default values. In order to fairly compare the performance of each algorithm, the maximum number of iterations and the population size of each algorithm were set to be the same. Specifically, the maximum number of iterations for each model was 300, while the

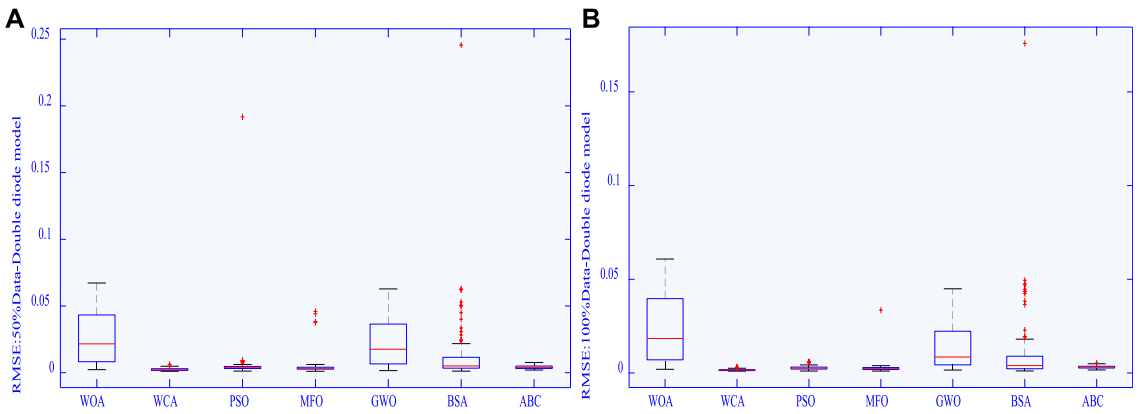


FIGURE 8 | Boxplot of RMSE obtained by various algorithms in different data for the DDM: **(A)** 50% data and **(B)** 100% data.

population sizes for SDM, DDM, and TDM were designed to be 30, 50, and 70, respectively. In addition, each algorithm was run 100 times independently in each PV cell model to obtain statistical results.

Results on SDM

Table 3 shows statistical results of the average RMSE obtained by each algorithm with six measured datasets, where symbol "Y" represents MhAs are applied with data prediction and "N" represents the condition that without data prediction. This shows the average RMSE obtained by each MhA with data prediction is significantly smaller than that with only measured data, especially under 50% measured data. For instance, the average RMSE obtained by PSO with data prediction is 82.32% smaller than that without data prediction under 50% measured data, which verifies such data prediction strategy can significantly enhance searching efficiency and optimization accuracy.

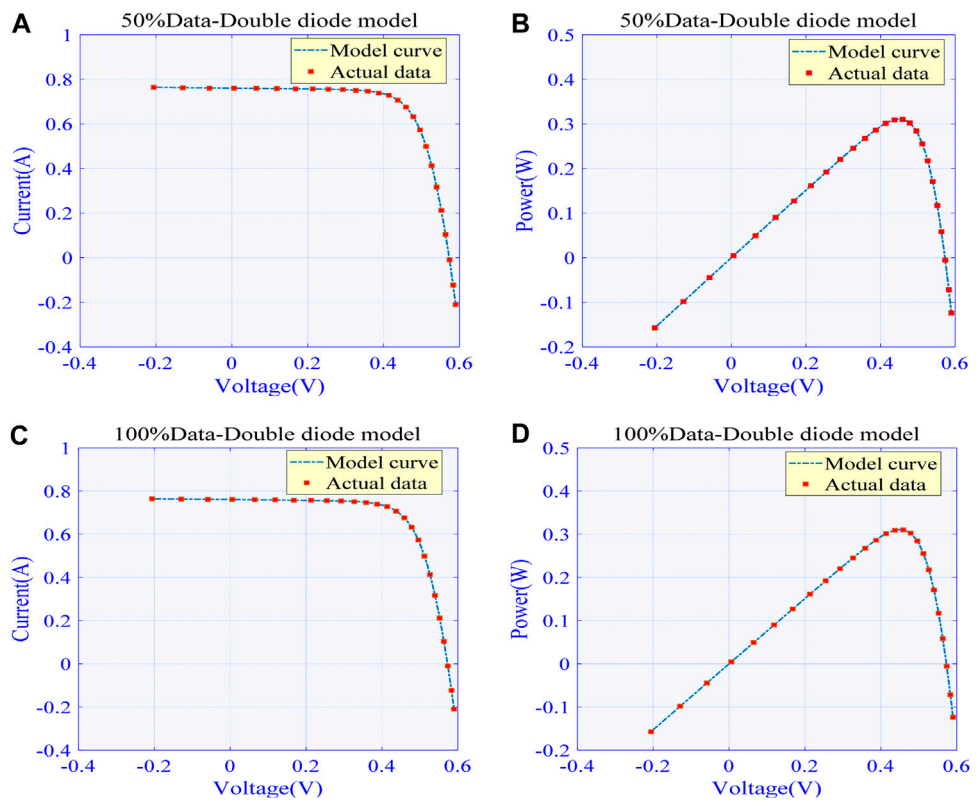


FIGURE 9 | Comparison between actual data and model curve acquired by the best algorithm in different training data for DDM: **(A)** *I-V* curve in 50% training data **(B)** *P-V* curve in 50% training data **(C)** *I-V* curve in 100% training data and (d) *I-V* curve in 100% training data.

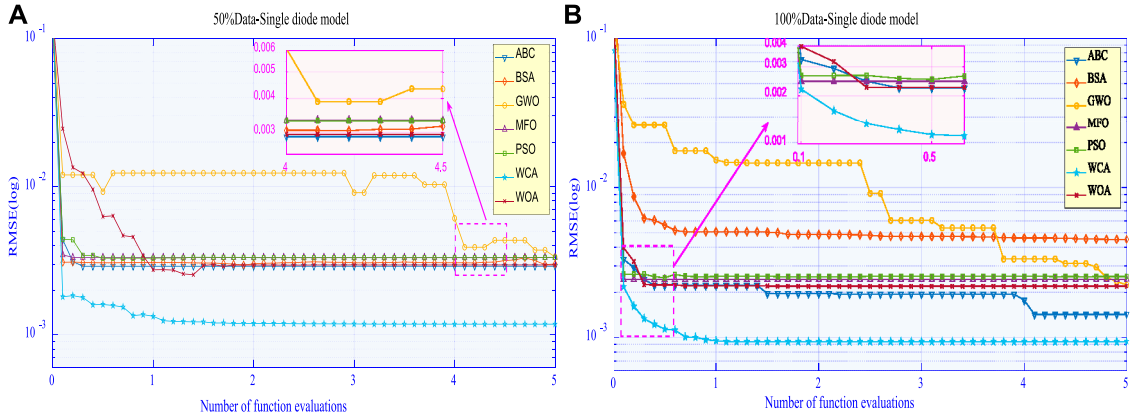


FIGURE 10 | Convergence of different algorithms for the DDM: **(A)** 50% data and **(B)** 100% data.

TABLE 5 | Average RMSE obtained by various algorithms for the TDM with six measured data.

Algorithm	Average RMSE						
		Number of measured data (%)					
	—	50%	60%	70%	80%	90%	100%
ABC	N	4.16×10^{-3}	3.49×10^{-3}	3.29×10^{-3}	3.47×10^{-3}	3.16×10^{-3}	3.13×10^{-3}
	Y	3.14×10^{-3}	3.19×10^{-3}	3.29×10^{-3}	3.24×10^{-3}	3.18×10^{-3}	3.17×10^{-3}
BSA	N	6.98×10^{-3}	7.56×10^{-3}	6.59×10^{-3}	9.55×10^{-3}	6.13×10^{-3}	5.22×10^{-3}
	Y	6.28×10^{-3}	6.03×10^{-3}	5.26×10^{-3}	6.17×10^{-3}	5.69×10^{-3}	5.90×10^{-3}
GWO	N	1.85×10^{-2}	1.57×10^{-2}	1.27×10^{-2}	1.21×10^{-2}	1.30×10^{-2}	1.44×10^{-2}
	Y	1.32×10^{-2}	1.22×10^{-2}	1.25×10^{-2}	1.06×10^{-2}	1.12×10^{-2}	1.24×10^{-2}
MFO	N	4.90×10^{-3}	3.06×10^{-3}	3.03×10^{-3}	3.20×10^{-3}	3.03×10^{-3}	2.63×10^{-3}
	Y	2.95×10^{-3}	2.69×10^{-3}	2.73×10^{-3}	2.56×10^{-3}	2.64×10^{-3}	2.72×10^{-3}
PSO	N	7.23×10^{-3}	4.20×10^{-3}	4.23×10^{-3}	7.32×10^{-3}	2.95×10^{-3}	2.97×10^{-3}
	Y	3.37×10^{-3}	2.87×10^{-3}	3.11×10^{-3}	2.85×10^{-3}	2.95×10^{-3}	2.87×10^{-3}
WCA	N	2.15×10^{-3}	1.54×10^{-3}	1.58×10^{-3}	1.62×10^{-3}	1.52×10^{-3}	1.47×10^{-3}
	Y	1.77×10^{-3}	1.47×10^{-3}	1.45×10^{-3}	1.48×10^{-3}	1.48×10^{-3}	1.47×10^{-3}
WOA	N	2.00×10^{-2}	2.06×10^{-2}	1.82×10^{-2}	2.07×10^{-2}	1.68×10^{-2}	1.89×10^{-2}
	Y	1.78×10^{-2}	1.55×10^{-2}	1.51×10^{-2}	1.38×10^{-2}	1.64×10^{-2}	1.37×10^{-2}

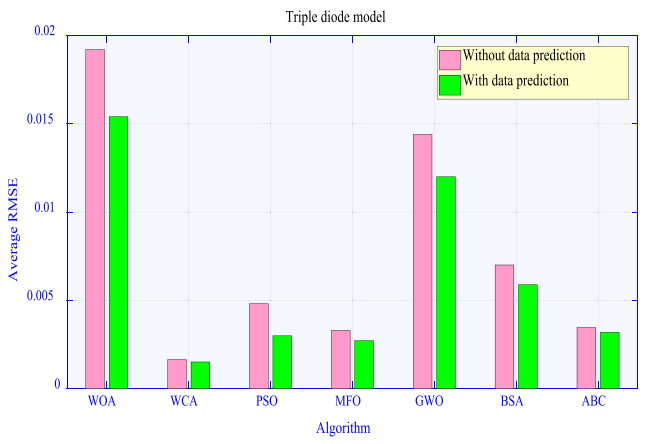


FIGURE 11 | Comparison of total average RMSE values with six different datasets for the TDM.

Besides, the average RMSE obtained by each algorithm with six inadequate measured datasets and six prediction datasets is demonstrated in **Figure 3**, which indicates prediction data–based PV parameter extraction for SDM can obtain higher accuracy and stability.

In addition, **Figure 4** shows the boxplots of RMSE obtained by various algorithms in the SDM. From **Figure 4**, it is clear that as the amount of data increases, the outliers of the RMSE obtained by each algorithm decrease. For instance, the RMSE of PSO exists as several outliers under 50% training data, while these outliers disappear as training data increase to 100%. Besides, the range and upper and lower limits of the distribution are smaller under the 100% data than that under the 50% data. This can effectively validate that MhA improves convergence stability and searching ability based on the increased amount of ELM data predicted.

Figure 5 plot I–V and P–V curves obtained by the best algorithm (i.e., algorithm can obtain the minimum RMSE)

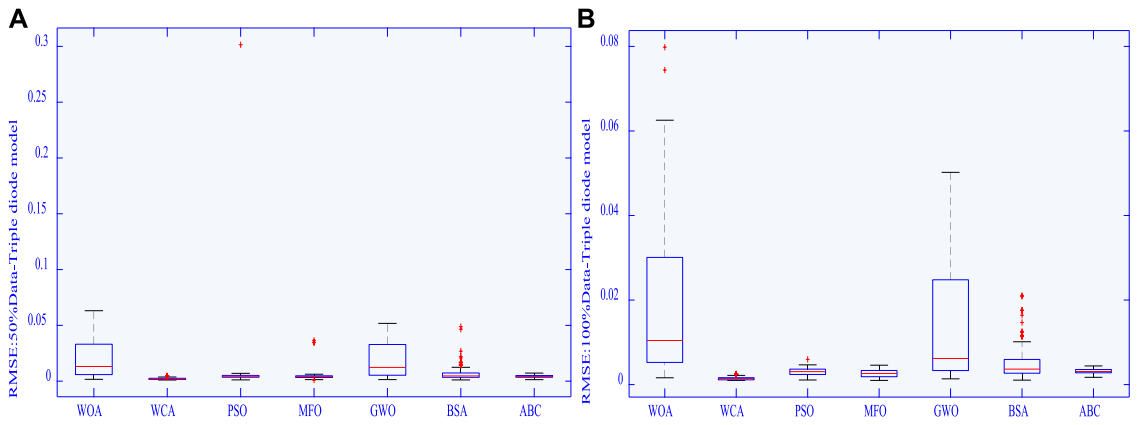


FIGURE 12 | Boxplot of RMSE obtained by various algorithms in different data for the TDM: **(A)** 50% data and **(B)** 100% data.

under 50% training data and 100% training data for the SDM, respectively. Note that WCA and MFO can achieve the minimum RMSE under 50% training data and 100% training data, respectively. It is not difficult to find that the model curves obtained from both WCA and MFO based on data prediction are in high agreement with the actual data, which can effectively demonstrate their superiority in PV cell parameter extraction.

Besides, **Figure 6** provides convergence of each algorithm under different training data. It can be seen that WOA tends to converge prematurely at the initial stage, and PSO has difficulty in obtaining high-quality optimal solutions with 50% of the training data. Besides, most algorithms can hardly achieve stable and efficient convergence due to inadequate data, along with unsatisfactory convergence accuracy. In contrast, the increase

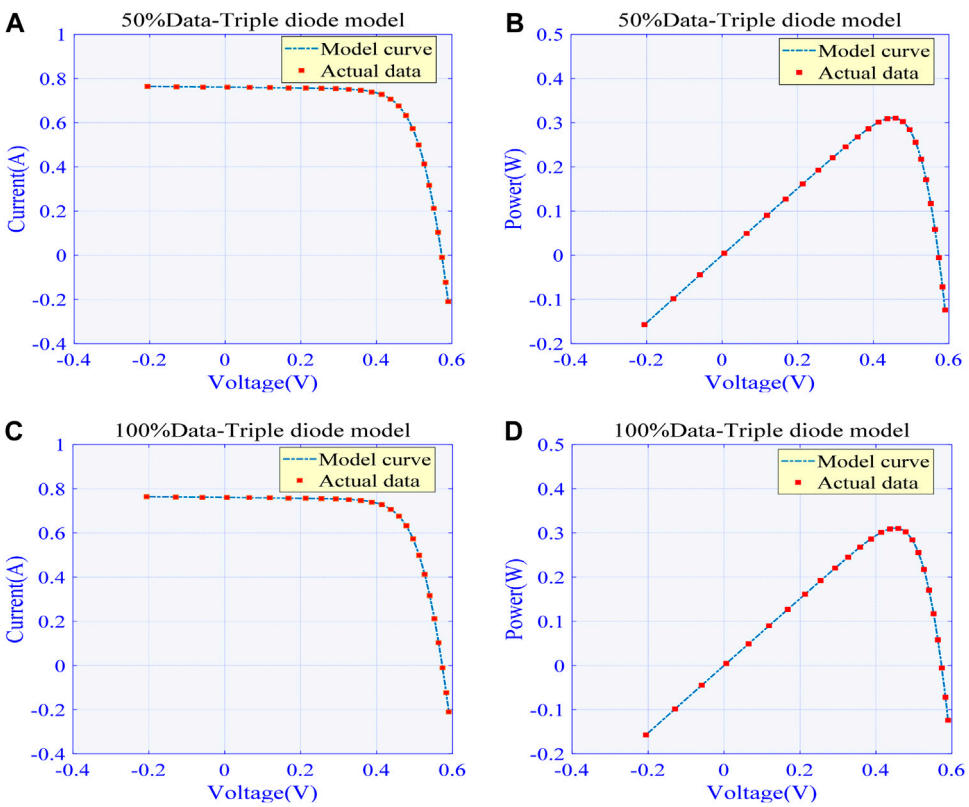


FIGURE 13 | Comparison between actual data and model curve obtained by the best algorithm in different training data for TDM: **(A)** *I-V* curve in 50% training data **(B)** *P-V* curve in 50% training data **(C)** *I-V* curve in 100% training data and **(D)** *I-V* curve in 100% training data.

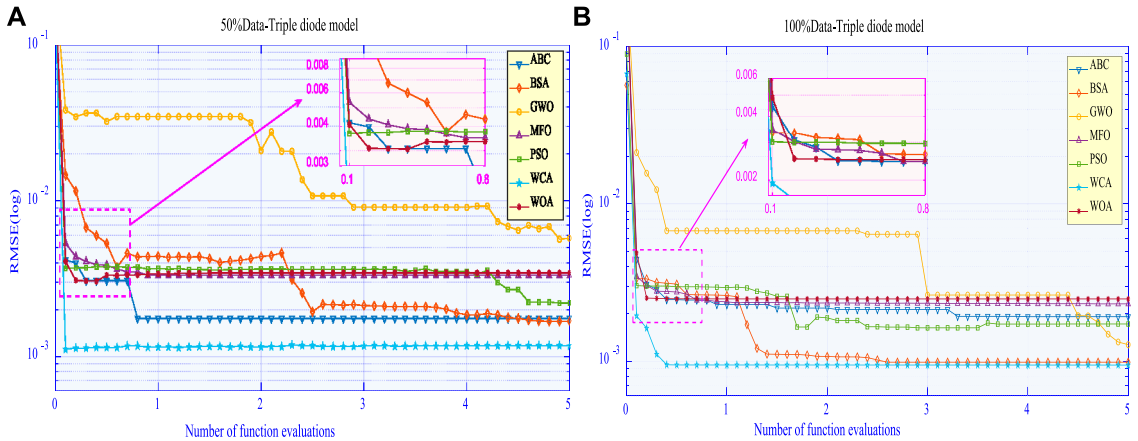


FIGURE 14 | Convergence of different algorithms for the TDM: **(A)** 50% data and **(B)** 100% data.

of training data helps them to gradually find high-quality solutions with higher convergence stability and searching efficiency as 100% data-based algorithms can better balance local exploitation and global exploration.

Results on DDM

The average RMSE of the DDM obtained over 100 runs by the different MhAs with six measurement datasets is shown in **Table 4**, which demonstrates that increased prediction data generated by the ELM can effectively improve calculation accuracy. For example, the average RMSE obtained by the GWO algorithm with data prediction is 48.19% lower than that without data prediction under 50% measured data scenario. This illustrates that the data prediction–based meta-algorithm can achieve highly increased stability in finding quality solution through increasing the amount of dataset with a desired solution accuracy; thus, such novel strategy can output desirable results when accuracy and reliability are both taken into consideration in the DDM.

Figure 7 compares the average RMSE obtained by each algorithm under six inadequately measured datasets with that obtained under six prediction datasets in the DDM. One can easily find that each algorithm can find the global optimum more easily when experimental data are expanded by prediction data, upon which optimal values of those unknown parameters can be determined in a more accurate and stable way.

Boxplot of various algorithms is shown in **Figure 8**, upon which one can easily find that algorithms under 100% training data have fewer outliers and smaller upper/lower bounds in RMSE compared with that under 50% data. This indicates that increase of training data from data-based prediction can effectively enhance the quality of solution and stabilize global searching ability in PV cell parameter extraction.

Figure 9 plot *I*–*V* and *P*–*V* curves acquired based on the best data prediction–based MhA (WCA) and actual data under 50% training data and 100% training data, respectively. This indicates that the model curves obtained by WCA are highly consistent with the actual data.

Moreover, **Figure 10** provides convergence of all algorithms with data prediction, which illustrates that convergence speed of WOA is low and GWO tends to fall into a local optimum with 50% of the training data. On the contrary, convergence under 100% training data verifies that they can more stably find a better solution, especially for GWO.

Results on TDM

Table 5 presents the average RMSE obtained by each algorithm with six different measured datasets, which reveals that data prediction–based algorithms still outperform those based on measured data. For example, the average RMSE obtained by PSO with data prediction is 61.06% lower than that without data prediction under 80% measured data. Hence, data prediction–based algorithms own the most satisfactory performance in terms of the accuracy of the solution for the TDM.

Figure 11 shows the comparison of the average RMSE of each algorithm under six inadequate measured datasets with that obtained under six prediction datasets in the TDM. It shows that the average RMSE obtained by WOA decreases by about 25% via data prediction, which verifies the effectiveness of data prediction in solution quality improvement.

Figure 12 presents the boxplot of different MhAs, while **Figure 13** show the best algorithm (WCA) and the I–V and P–V curves obtained with the actual data under different datasets, verifying the accuracy of the extracted PV cell parameters. **Figure 12** clearly shows that the increase in the volume of data can significantly reduce the RMSE outliers achieved by each algorithm, while lowering the upper/lower limits. Hence, solution precision and stability can be greatly enhanced by increasing the amount of experimental data.

Last, **Figure 14** provides convergence of all algorithms with data prediction, which shows that 100% training data–based algorithms can achieve a proper trade-off between local

exploitation and global exploration, while 50%-based algorithms are easy to be trapped at a local optimum.

Statistical Results and Analysis

The radars of the average RMSE obtained by each MhA with six groups of data at different scales are provided in **Supplementary Figure S1**, **Supplementary Figure S2**, and **Supplementary Figure S3**, where symbol "+" represents MhAs with data prediction, which provides a more explicit illustration of stability of each algorithm with data prediction for PV cell parameter extraction in each model. One can see that the average RMSE obtained by each algorithm with data prediction is smaller compared with that obtained without data prediction at different scales of data. This effectively verifies the outstanding reliability of DPMhA for PV cell parameter extraction.

CONCLUSION

This article proposes a novel PV cell parameter extraction strategy is developed for three different PV cell models. The main three contributions/innovations in this article can be summarized as follows:

- ELM-based data prediction allows MhAs to perform a more stable search for optimal solution for identification of PV cell parameter with inadequate measured output I–V data.
- Three different types of PV cell models are adopted to reliably verify the practical enhancements and general feasibility of the strategy of DPMhA for PV cell parameter extraction.
- Case studies demonstrate that DPMhAs can considerably improve the accuracy, robustness, and convergence rate of PV cell parameter extraction compared with those only based on original measured output I–V data.

Case studies show that ELM-based MhAs can effectively improve optimization accuracy and convergence stability compared with original MhAs utilizing untrained measured I–V data. Although the convergence stability of MhAs can be improved by extending the data through the ELM, the optimization accuracy of some MhAs still needs to be improved in some conditions due to the error between the generated artificial data and the real measurement data. Hence, the next work will aim to handle this issue by introducing some advanced neural networks with excellent generalization.

DATA AVAILABILITY STATEMENT

The original contributions presented in the study are included in the article/**Supplementary Material**; further inquiries can be directed to the corresponding author.

AUTHOR CONTRIBUTIONS

BL was responsible for the design and revision of the thesis proposal, HC was responsible for writing the introduction and model presentation, and TT was responsible for writing the simulation experiments and simulation analysis.

FUNDING

This work was jointly supported by the Research and Development Start-Up Foundation of Shantou University (NTF19016).

SUPPLEMENTARY MATERIAL

The Supplementary Material for this article can be found online at: https://www.frontiersin.org/articles/10.3389/fenrg.2021.693252/full#supplementary-material

REFERENCES

Abbassi, R., Abbassi, A., Jemli, M., and Chebbi, S. (2018). Identification of Unknown Parameters of Solar Cell Models: A Comprehensive Overview of Available Approaches. *Renew. Sust. Energ. Rev.* 90, 453–474. doi:10.1016/j.rser.2018.03.011

Allam, D., Yousri, D. A., and Eteiba, M. B. (2016). Parameters Extraction of the Three Diode Model for the Multi-Crystalline Solar Cell/module Using Moth-Flame Optimization Algorithm. *Energ. Convers. Manag.* 123, 535–548. doi:10.1016/j.enconman.2016.06.052

Amroune, M., Bouktir, T., and Musirin, I. (2019). Power System Voltage Instability Risk Mitigation via Emergency Demand Response-Based Whale Optimization Algorithm. *Prot. Control. Mod. Power Syst.* 4 (25). doi:10.1186/s41601-019-0142-4

Askarzadeh, A., and Rezazadeh, A. (2013). Extraction of Maximum Power Point in Solar Cells Using Bird Mating Optimizer-Based Parameters Identification Approach. *Solar Energy* 90, 123–133. doi:10.1016/j.solener.2013.01.010

Babu, T. S., Ram, J. P., Sangeetha, K., Laudani, A., and Rajasekar, N. (2016). Parameter Extraction of Two Diode Solar PV Model Using Fireworks Algorithm. *Solar Energy* 140, 265–286. doi:10.1016/j.solener.2016.10.044

Chaibi, Y., Allouhi, A., Salhil, M., and El-jouni, A. (2019). Annual Performance Analysis of Different Maximum Power Point Tracking Techniques Used in Photovoltaic Systems. *Prot. Control. Mod. Power Syst.* 4 (4), 171–180. doi:10.1186/s41601-019-0129-1

Chen, Z., Han, F., Wu, L., Yu, J., Cheng, S., Lin, P., et al. (2018). Random Forest Based Intelligent Fault Diagnosis for PV Arrays Using Array Voltage and String Currents. *Energ. Convers. Manag.* 178, 250–264. doi:10.1016/j.enconman.2018.10.040

Dasu, B., Sivakumar, M., and Srinivasarao, R. (2019). Interconnected Multi-Machine Power System Stabilizer Design Using Whale Optimization Algorithm. *Prot. Control. Mod. Power Syst.* 4 (4), 13–23. doi:10.1186/s41601-019-0116-6

Derick, M., Rani, C., Rajesh, M., Farrag, M. E., Wang, Y., and Busawon, K. (2017). An Improved Optimization Technique for Estimation of Solar Photovoltaic Parameters. *Solar Energy* 157, 116–124. doi:10.1016/j.solener.2017.08.006

Easwarakhanthan, T., Bottin, J., and Bouhouch, I. (1986). Nonlinear Minimization Algorithmfor Determining the Solar Cell Parameters with Microcomputers. *Int. J. Solar Energ.* 4 (1), 1–12. doi:10.1080/01425918608909835

Figueroa, O. R., Castellanos, M. Q., Montes, E. M., and Schütze, O. (2020). Metaheuristics to Solve Grouping Problems: A Review and a Case Study. *Swarm Evol. Comput.* 53, 100643. doi:10.1016/j.solener.2016.10.044

Grondin-Perez, B., Roche, S., Lebreton, C., Benne, M., Damour, C., and Kadjo, J.-J. A. (2014). Mechanistic Model versus Artificial Neural Network Model of a Single-Cell PEMFC. *Eng* 06 (8), 418–426. doi:10.4236/eng.2014.68044

Huang, G. B., Chen, Y. Q.., and Babri, H. A. (2000). Classification Ability of Single Hidden Layer Feedforward Neural Networks. *IEEE Trans. Neural Networks* 11 (3), 799–801. doi:10.1109/72.846750

Huang, G. B., and Siew, C. K. (2005). Extreme Learning Machine with Randomly Assigned RBF Kernels. *Int. J. Inf. Tech.* 11 (1), 1–8. doi:10.1109/ICARCV.2004.1468985

Huang, G. B., Zhu, Q. Y., and Siew, C. K. (2006). Extreme Learning Machine: Theory and Applications. *Neurocomputing* 70 (1-3), 489–501. doi:10.1016/j.neucom.2005.12.126

Humada, A. M., Hojabri, M., Mekhilef, S., and Hamada, H. M. (2016). Solar Cell Parameters Extraction Based on Single and Double-Diode Models: A Review. *Renew. Sust. Energ. Rev.* 56, 494–509. doi:10.1016/j.rser.2015.11.051

Ishaque, K., and Salam, Z. (2011). An Improved Modeling Method to Determine the Model Parameters of Photovoltaic (PV) Modules Using Differential Evolution (DE). *Solar Energy* 85 (9), 2349–2359. doi:10.1016/j.solener.2011.06.025

Ishaque, K., Salam, Z., Taheri, H., and Shamsudin, A. (2011). A Critical Evaluation of EA Computational Methods for Photovoltaic Cell Parameter Extraction Based on Two Diode Model. *Solar Energy* 85 (9), 1768–1779. doi:10.1016/j.solener.2011.04.015

Jervase, J. A., Bourdoucen, H., and Al-lawati, A. (2001). Solar Cell Parameter Extraction Using Genetic Algorithms. *Meas. Sci. Technol.* 12, 1922–1925. doi:10.1088/0957-0233/12/11/322

Jordehi, A. R. (2016). Parameter Estimation of Solar Photovoltaic (PV) Cells: a Review. *Renew. Sust. Energ. Rev.* 61, 354–371. doi:10.1016/j.rser.2016.03.049

Khanna, V., Das, B. K., Bisht, D., Vandana, and Singh, P. K. (2015). A Three Diode Model for Industrial Solar Cells and Estimation of Solar Cell Parameters Using PSO Algorithm. *Renew. Energ.* 78, 105–113. doi:10.1016/j.renene.2014.12.072

Kler, D., Sharma, P., Banerjee, A., Rana, K. P. S., and Kumar, V. (2017). PV Cell and Module Efficient Parameters Estimation Using Evaporation Rate Based Water Cycle Algorithm. *Swarm Evol. Comput.* 35, 93–110. doi:10.1016/j.swevo.2017.02.005

Li, G. D., Li, G. Y., and Zhou, M. (2019). Model and Application of Renewable Energy Accommodation Capacity Calculation Considering Utilization Level of Interprovincial Tie-Line. *Prot. Control. Mod. Power Syst.* 4 (4), 1–12. doi:10.1186/s41601-019-0115-7

Li, W., Paul, M. C., Rolley, M., Sweet, T., Gao, M., Siviter, J., et al. (2017). A Scaling Law for Monocrystalline PV/T Modules with CCPC and Comparison with Triple Junction PV Cells. *Appl. Energ.* 202, 755–771. doi:10.1016/j.apenergy.2017.05.182

Liu, J., Yao, W., Wen, J., Fang, J., Jiang, L., He, H., et al. (2020). Impact of Power Grid Strength and PLL Parameters on Stability of Grid-Connected DFIG Wind Farm. *IEEE Trans. Sustain. Energ.* 11 (1), 545–557. doi:10.1109/tste.2019.2897596

Majdoul, R., Abdelmounim, E., Aboulfatah, M., Touati, A. W., Moutabir, A., and Abouloifa, A. (2015). "Combined Analytical and Numerical Approach to Determine the Four Parameters of the Photovoltaic Cells Models," in International Conference on Electrical and InformationTechnologies (Marrakech, Morocco). 263–268.

Nesmachnow, S. (2014). An Overview of Metaheuristics: Accurate and Efficient Methods for Optimisation. *Ijmheur* 3 (4), 320–347. doi:10.1504/ijmheur.2014.068914

Nunes, H. G. G., Pombo, J. A. N., Mariano, S. J. P. S., Calado, M. R. A., and Felippe de Souza, J. A. M. (2018). A New High Performance Method for Determining the Parameters of PV Cells and Modules Based on Guaranteed Convergence Particle Swarm Optimization. *Appl. Energ.* 211, 774–791. doi:10.1016/j.apenergy.2017.11.078

Oliva, D., Cuevas, E., and Pajares, G. (2014). Parameter Identification of Solar Cells Using Artificial Bee Colony Optimization. *Energy* 72, 93–102. doi:10.1016/j.energy.2014.05.011

Peng, X., Yao, W., Yan, C., Wen, J., and Cheng, S. (2020). Two-stage Variable Proportion Coefficient Based Frequency Support of Grid-Connected DFIG-WTs. *IEEE Trans. Power Syst.* 35 (2), 962–974. doi:10.1109/tpwrs.2019.2943520

Qais, M. H., Hasanien, H. M., and Alghuwainem, S. (2019). Identification of Electrical Parameters for Three-Diode Photovoltaic Model Using Analytical and Sunflower Optimization Algorithm. *Appl. Energ.* 250, 109–117. doi:10.1016/j.apenergy.2019.05.013

Ram, J. P., Manghani, H., Manghani, D. S., Babu, T. S., Miyatake, M., Rajasekar, N., et al. (2018). Analysis on Solar PV Emulators: A Review. *Renew. Sust. Energ. Rev.* 81, 149–160. doi:10.1016/j.rser.2017.07.039

Roeva, O., and Fidanova, S. (2018). Comparison of Different Metaheuristic Algorithms Based on Intercriteria Analysis. *J. Comput. Appl. Math.* 340, 615–628. doi:10.1016/j.cam.2017.07.028

Schmidhuber, J. (2015). Deep Learning in Neural Networks: An Overview. *Neural Networks* 61, 85–117. doi:10.1016/j.neunet.2014.09.003

Shen, Y., Yao, W., Wen, J., He, H., and Jiang, L. (2019). Resilient Wide-Area Damping Control Using GrHDP to Tolerate Communication Failures. *IEEE Trans. Smart Grid* 10 (3), 2547–2557. doi:10.1109/tsg.2018.2803822

Sun, K., Yao, W., Fang, J., Ai, X., Wen, J., and Cheng, S. (2020). Impedance Modeling and Stability Analysis of Grid-Connected DFIG-Based Wind Farm with a VSC-HVDC. *IEEE J. Emerg. Sel. Top. Power Electron.* 8, 1375–1390. doi:10.1109/JESTPE.2019.2901747

Torabi, K. E., Eddine, I. A., Obbadi, A., Errami, A., Rmaily, R., Sahnoun, S., et al. (2017). Parameters Estimation of the Single and Double Diode Photovoltaic Models Using a Gauss-Seidel Algorithm and Analytical Method: A Comparative Study. *Energ. Convers. Manag.* 148, 1041–1054. doi:10.1016/j.solener.2016.10.044

Villalva, M. G., Gazoli, J. R., and Filho, E. R. (2009). Comprehensive Approach to Modeling and Simulation of Photovoltaic Arrays. *IEEE Trans. Power Electron.* 24, 1198–1208. doi:10.1109/tpel.2009.2013862

Wang, Q., Yao, W., Fang, J., Ai, X., Wen, J., Yang, X., et al. (2020). Dynamic Modeling and Small Signal Stability Analysis of Distributed Photovoltaic Grid-Connected System with Large Scale of Panel Level DC Optimizers. *Appl. Energ.* 259, 114132. doi:10.1016/j.apenergy.2019.114132

Xiong, G., Zhang, J., Shi, D., and He, Y. (2018). Parameter Extraction of Solar Photovoltaic Models Using an Improved Whale Optimization Algorithm. *Energ. Convers. Manag.* 174, 388–405. doi:10.1016/j.enconman.2018.08.053

Yang, B., Jiang, L., Wang, L., Yao, W., and Wu, Q. H. (2016). Nonlinear Maximum Power Point Tracking Control and Modal Analysis of DFIG Based Wind Turbine. *Int. J. Electr. Power Energ. Syst.* 74, 429–436. doi:10.1016/j.ijepes.2015.07.036

Yang, B., Wang, J., Zhang, X., Yu, T., Yao, W., Shu, H., et al. (2020). Comprehensive Overview of Meta-Heuristic Algorithm Applications on PV Cell Parameter Identification. *Energ. Convers. Manag.* 208, 112595. doi:10.1016/j.enconman.2020.112595

Yang, B., Yu, T., Shu, H., Dong, J., and Jiang, L. (2018). Robust Sliding-Mode Control of Wind Energy Conversion Systems for Optimal Power Extraction via Nonlinear Perturbation Observers. *Appl. Energ.* 210, 711–723. doi:10.1016/j.apenergy.2017.08.027

Yang, B., Yu, T., Shu, H., Zhang, Y., Chen, J., Sang, Y., et al. (2018). Passivity-based Sliding-Mode Control Design for Optimal Power Extraction of a PMSG Based Variable Speed Wind Turbine. *Renew. Energ.* 119, 577–589. doi:10.1016/j.renene.2017.12.047

Yang, B., Yu, T., Zhang, X., Li, H., Shu, H., Sang, Y., et al. (2019). Dynamic Leader Based Collective Intelligence for Maximum Power Point Tracking of PV Systems Affected by Partial Shading Condition. *Energ. Convers. Manag.* 179, 286–303. doi:10.1016/j.enconman.2018.10.074

Yang, B., Zhang, X., Yu, T., Shu, H., and Fang, Z. (2017). Grouped Grey Wolf Optimizer for Maximum Power Point Tracking of Doubly-Fed Induction Generator Based Wind Turbine. *Energ. Convers. Manag.* 133, 427–443. doi:10.1016/j.enconman.2016.10.062

Yang, B., Zhong, L., Zhang, X., Shu, H., Yu, T., Li, H., et al. (2019). Novel Bio-Inspired Memetic Salp Swarm Algorithm and Application to MPPT for PV Systems Considering Partial Shading Condition. *J. Clean. Prod.* 215, 1203–1222. doi:10.1016/j.jclepro.2019.01.150

Ye, M. Y., Wang, X. D., and Xu, Y. S. (2009). Parameter Extraction of Solar Cells Using Particle Swarm Optimization. *J. Appl. Phys.* 105 (9), 094502–094508. doi:10.1063/1.3122082

Youssef, A., El-Telbany, M., and Zekry, A. (2017). The Role of Artificial Intelligence in Photo-Voltaic Systems Design and Control: a Review. *Renew. Sust. Energ. Rev.* 78, 72–79. doi:10.1016/j.rser.2017.04.046

Yu, K., Liang, J. J., Qu, B. Y., Cheng, Z., and Wang, H. (2018). Multiple Learning Backtracking Search Algorithm for Estimating Parameters of Photovoltaic Models. *Appl. Energ.* 226, 408–422. doi:10.1016/j.apenergy.2018.06.010

Zhang, H., Lu, Z., Hu, W., Wang, Y., Dong, L., and Zhang, J. (2019). Coordinated Optimal Operation of Hydro-Wind-Solar Integrated Systems. *Appl. Energ.* 242, 883–896. doi:10.1016/j.apenergy.2019.03.064

Zhao, Y., Pei, J., and Chen, H. (2019). Multi-layer Radial Basis Function Neural Network Based on Multi-Scale Kernel Learning. *Appl. Soft Comput.* 82, 105541. doi:10.1016/j.asoc.2019.105541

Conflict of Interest: The authors declare that the research was conducted in the absence of any commercial or financial relationships that could be construed as a potential conflict of interest.

Copyright © 2021 Li, Chen and Tan. This is an open-access article distributed under the terms of the Creative Commons Attribution License (CC BY). The use, distribution or reproduction in other forums is permitted, provided the original author(s) and the copyright owner(s) are credited and that the original publication in this journal is cited, in accordance with accepted academic practice. No use, distribution or reproduction is permitted which does not comply with these terms.

GLOSSARY

Variables

I_{ph} photocurrent, A

I_d, I_{d1}, I_{d2}, diode's currents, A

I_{sd}, I_{sd1}, I_{sd2}, I_{sd3} diode's reverse saturation currents, A

R_s series resistor, Ω

R_{sh} shunt resistor, Ω

a, a_1, a_2, a_3 ideality factors of diode

Abbreviations

ABC artificial bee colony

AIS artificial immune system

ANN artificial neural network

BP back-propagation

BSA backtracking search algorithm

DDM double diode model

DE differential evolution

DPMhA data prediction–based meta-heuristic algorithm

ELM extreme learning machine

FWA fireworks algorithm

GA genetic algorithm

GWO grey wolf optimization

I–V current–voltage

MFO moth flame optimizer

MhA meta-heuristic algorithm

MPPT maximum power point tracking

PSO particle swarm optimization

PV photovoltaic

P-V power–voltage

RMSE root mean square error

SDM single diode model

SLFN single-hidden layer feedforward neural network

STC standard test condition

SSA salp swarm algorithm

TDM three diode model

WOA whale optimization algorithm

WCA water cycle algorithm

WDO wind-driven optimization

frontiers in Energy Research

ORIGINAL RESEARCH
published: 22 June 2021
doi: 10.3389/fenrg.2021.697959

Concepts, Structure and Developments of High-Reliability Cyber-Physical Fusion Based Coordinated Planning for Distribution System

Chong Gao[1], Tianlin Wang[1], Huazhen Cao[1], Ziyao Wang[2], Tao Yu[2] and Ran Cheng[1]*

[1]Grid Planning and Research Center, Guangdong Power Grid Co., Ltd., CSG, Guangzhou, China, [2]Electric Power College of South China University of Technology, Guangzhou, China

Coordinated control is imperative for the distribution network with the integration of wind power, photovoltaic system, and energy storage system. Meanwhile, the advanced automation terminal, intelligent control technology, and information communication technologies have greatly promoted the informatization of distribution networks which also increase the correlation between the physical system (primary system) and the cyber system (secondary system). Hence, it is critical to comprehensively coordinate the planning of the cyber-physical system for building a highly reliable power grid. This work summarizes a series of challenges brought by the highly coupled cyber-physical system, such as the primary and secondary collaborated planning models and solution algorithms. Then, the reliability assessment theories of cyber-physical systems and their application in distribution network planning models are introduced. Finally, three development directions of distribution network planning in the future are proposed, considering primary and secondary system coordinated planning.

Keywords: reliability, cyber-physical system, primary and secondary system, coordinated planning, distribution system

OPEN ACCESS

Edited by:
Bo Yang,
Kunming University of Science and Technology, China

Reviewed by:
Yang Li,
Northeast Electric Power University, China
Xuehan Zhang,
Korea University, South Korea

****Correspondence:***
Tao Yu
taoyu1@scut.edu.cn

Specialty section:
This article was submitted to Smart Grids, a section of the journal Frontiers in Energy Research

Received: *20 April 2021*
Accepted: *06 May 2021*
Published: *22 June 2021*

Citation:
Gao C, Wang T, Cao H, Wang Z, Yu T and Cheng R (2021) Concepts, Structure and Developments of High-Reliability Cyber-Physical Fusion Based Coordinated Planning for Distribution System. Front. Energy Res. 9:697959. doi: 10.3389/fenrg.2021.697959

INTRODUCTION

With the rapid development of information technology, communication technology, and electronic control technology, the cyber system has gradually become the core framework of power systems. As the coupling degree between the physical system (primary system) and cyber system (secondary system) increase, it is of great significance to realize coordinated planning of the distribution network, distribution automation (DA), and the communication network, etc (Cortes et al., 2017; Sun and Yang, 2020).

Primary system planning mainly includes distribution network structure determining, substation locating, and sizing. Particularly, the reliability evaluation for the primary system possesses huge challenges due to the renovation of microgrid (MG), DC distribution, and integrated energy system (IES), as well as the reformation of demand response (DR) and electric power system (Lotfi and Khodaei, 2017). The above factors further complicate the distribution network planning models, which result in lots of novel planning methods and solution algorithms in this field (Georgilakis and Hatziargyriou, 2015).

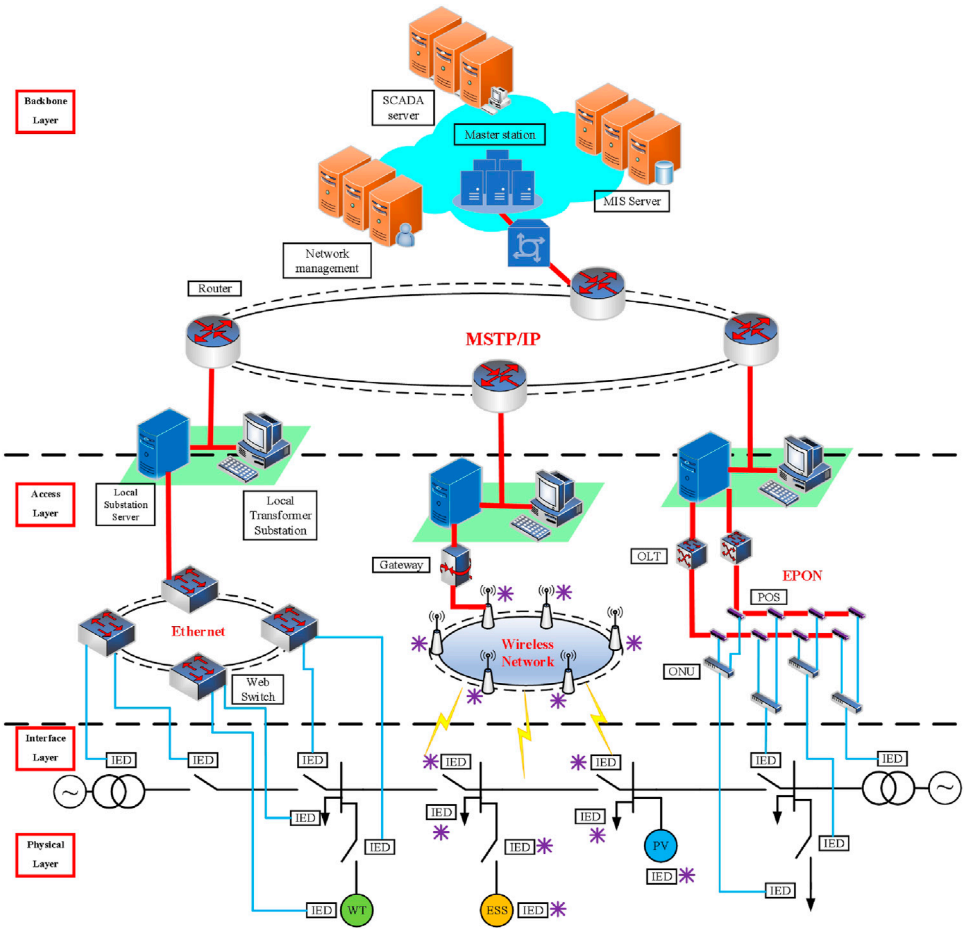


FIGURE 1 | Basic structure of CPS.

Secondary system planning is mainly composed of distribution automation system (DAS) planning and communication system planning. In the highly automated and information-based smart grid, a large amount of data information emerges along with data acquisition and control equipment that require a secondary system for synthetical management and analysis. Moreover, the stable operation of the power grid highly depends on the secondary system, which is the solid guarantee for building a strong power grid. However, in the process of promoting the automation and intelligence of the distribution network, the secondary system is a potential factor threatening the reliable operation of the primary system, for example, the well-known accidents at the Iran nuclear power plant blackout of 2010 (Farwell and Rohozinski, 2011) and Ukraine large blackout in 2015 (Liang et al., 2017). Secondary system failures directly or indirectly cause power grid performance deterioration and even load shedding, resulting in vast economic and social losses.

To improve the overall efficiency of the distribution network, it is necessary to implement the coordinated planning of primary and secondary systems from the perspective of global optimization (Gholizadeh et al., 2018). This paper introduces the basic contents of cyber-physical fusion based coordinated planning for the distribution network. The challenges of strongly coupled primary and secondary system planning are discussed from three aspects, i.e., secondary system reliability evaluation, coordinated planning models of the primary and secondary system, and solution algorithms. Besides, the current research status of high-reliability primary and secondary system planning from complex networks and optimization is also given. Lastly, this work summarizes the conclusions of primary and secondary coordinated planning for a highly reliable distribution network and proposes three future research directions from mathematical models, optimization algorithms, and engineering practices.

CYBER-PHYSICAL FUSION BASED COORDINATED PLANNING FOR DISTRIBUTION NETWORK

Basic Framework of the Primary and Secondary System

The primary system consists of a power supply, network frame, and switchgear coupled with a secondary system including an

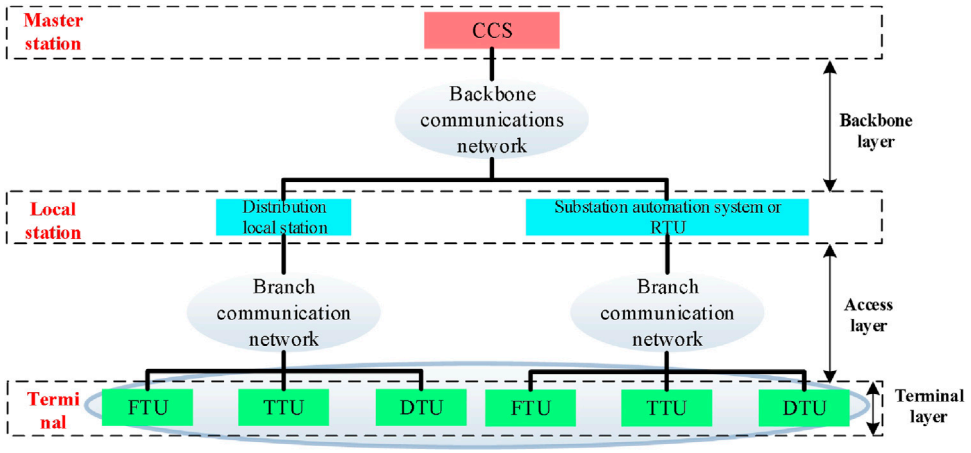


FIGURE 2 | Structure of DAS

automation system and communication system, which collaboratively establish the highly intelligent, strong, and inseparable distribution network. Note that the above definitions are different from the literature (Gholizadeh et al., 2018), in which primary system and secondary system refer to a high voltage network and low voltage network, respectively. The research and development of cyber-physical system (CPS) related theories (Humayed et al., 2017) explain the coupling relationship between the primary system and secondary system (Liu et al., 2018), and the basic structure of CPS is shown in **Figure 1**. The interface equipment connecting the primary system and secondary system in this figure is an intelligent electronic device (IED), which includes a data acquisition unit, data monitoring unit, relay protection unit, and control unit. In distribution network CPS, the primary system is composed of power supply, transformer, switch equipment, and line, while secondary system incorporates IED, communication line, switch, server, control decision master station, etc. Moreover, CPS can be divided into four layers, namely backbone network, access network, an interface layer, and physical layer.

Secondary System

Reasonable planning for the secondary system of the distribution network could greatly reduce the number of outage users and outage time, which is an effective way to improve the overall reliability of the distribution network (Popovic et al., 2019).

Distribution Automation System

According to the IEEE PES distribution automation team, DAS is defined as a system that enables power companies to realize remote monitor, manage, and operate distribution components in real-time. DAS is mainly composed of a central control system (CCS), distribution electronic station (optional), distribution terminal, and communication equipment, which is shown in **Figure 2**.

Feeder automation (FA) is one of the core contents of DA. When feeder failure occurs, FA can automatically or semi-automatically realize fault location, fault isolation, and power transfer to reduce the outage time for improving the reliability of the distribution network. If FA fails to work due to terminal failure or communication fault, it will weaken power reliability and even expand fault range. Therefore, the modeling and planning of FA are two key points in the coordinated planning of distribution networks considering reliability. Common distribution automation modes are shown in **Appendix A**.

The coverage of FTU and the selection of fault handling mode have a great impact on the reliability of the distribution network (Heidari and Fotuhi-Firuzabad, 2019). Especially, different automatic fault handling modes (e.g., local, centralized, and distributed), which rely on different FTU functions. FTU configuration based on primary equipment or collaborated planning of primary and secondary equipment has attracted the attention of scholars. For example, the "three remotes" terminals are equipped in most distribution network projects of China. This kind of mode improves the reliability of the distribution network, but blind allocation will reduce returns. In European countries, the investment subjects of DAS are distribution companies (DISCOs), which focus on both reliability and economy.

Distribution Communication System

The reliability of communication networks includes topology reliability and delay reliability. There are differences between different communication technologies. In general, optical fiber communication has strong reliability with expensive costs. The laying of optical cable often involves the restrictions of municipal construction. Wireless communication has the advantages of convenient maintenance and a small investment, but it will lead to communication delays due to information blocking. Furthermore, carrier communication and satellite communication are not widely used at present because of their inherent defects.

Different communication methods will affect the function realization of DAS and the reliability of the primary system. Thus, the communication mode planning and topology planning

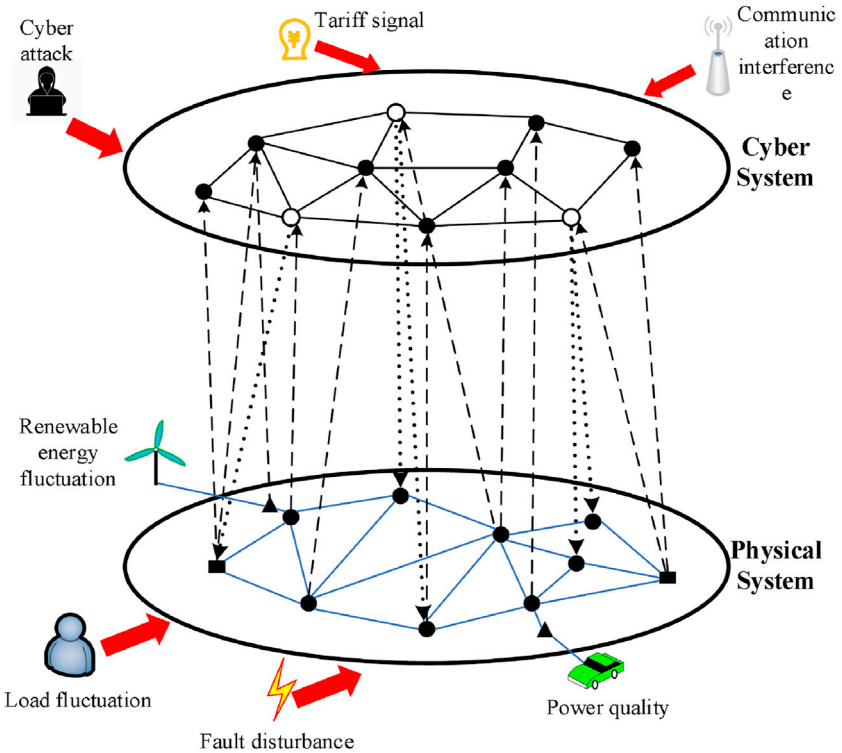


FIGURE 3 | Coupling relationship between the physical system and cyber system.

need to be simultaneously considered for high-reliability distribution network coordinated planning. Common distribution communication modes are shown in **Appendix B**.

CHALLENGES OF STRONG COUPLING PRIMARY AND SECONDARY SYSTEM PLANNING

There is a strong coupling between the primary and secondary systems, as shown in **Figure 3**. The primary system is easily affected by load fluctuation, fault disturbance, and renewable energy connection, while the secondary system is often influenced by electricity price, network attack, and communication interference. For deeply coupled CPS, these disturbances are potential threats that can reduce the reliability of the distribution network.

Influence of Secondary System on Reliability

In traditional high-reliability distribution network planning, N-1 Criterion (Lin et al., 2019) is often adopted to evaluate risk value (Esmaeeli et al., 2017). Besides, simulation methods and analytical algorithms are used to evaluate the reliability of the distribution network and locate the weak links in the primary system. The abnormality conditions of the secondary system are caused by data measuring instruments, automated terminal equipment, communication standard, and network topology, which can increase the operational risk of the primary system. The influence of these factors on the reliability of the distribution system mainly includes the following aspects:

(1) The automatic terminal equipment of the secondary system is key to realizing feeder automation;
(2) The communication topology of the secondary system is the premise of accurate fault location in the primary system (Harri et al., 2019);
(3) Communication mode and protocol affect the power supply reliability of primary system via DAS (Cai et al., 2019);
(4) The data collected by the secondary system contains valuable information for operation planning and decision (Colak et al., 2016; Tuballa and Abundo, 2016; Dileep, 2020).

Coordinated Planning Model

Power grid planning can be divided into two types: distribution network expansion planning (DSEP) and planning from scratch.

At present, research on primary system planning is relatively mature, but the study about connection modes, extreme environment, load uncertainties, and DG uncertainties still needs to be supplemented and improved. In particular, connection modes are diverse, including radial type, N-1 ring network, and composite structure, etc., which have a significant impact on the reliability of the primary system. The distribution network is highly sensitive to the climate condition and geographical location which may lead to grid fault. Moreover,

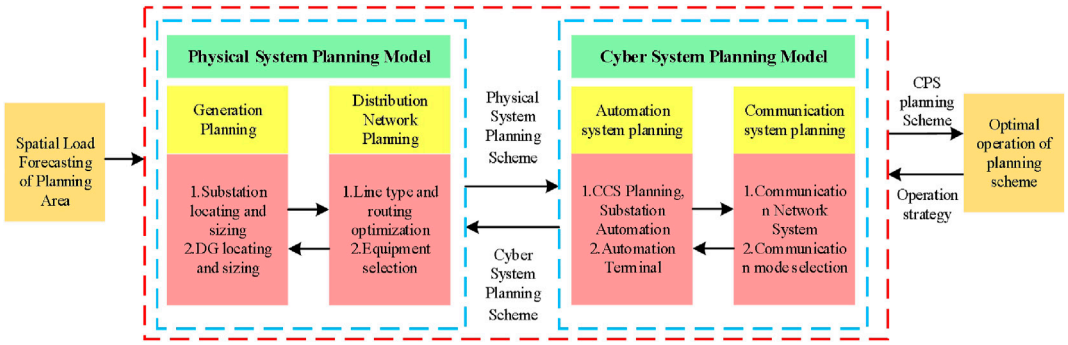


FIGURE 4 | Model solution block diagram.

the output of DGs (e.g., wind energy conversion system, photovoltaic system, etc.) in the power supply side also have uncertainties due to the randomness and intermittency of renewable energy. The operating characteristics of the load side have changed because of the implementation of demand response and power market reforms. Hence, the modeling and calculation of the above uncertain factors are crucial but thorny tasks for researchers.

The planning level of the secondary system mainly includes automation terminal layout planning and communication topology planning. The former is equipped with automatic terminals on switching elements (such as section switch, tie switch, circuit breaker, etc.) to locate, isolate, and recover faults in the distribution network. Research on communication topology planning mainly focuses on the access layer since the backbone layer is relatively simple, which only has a small optimization space. Access layer topology planning optimizes the connection relationship between the terminal nodes, the terminal, and the distribution station of a secondary system for improving the resistance against external interference and disturbances.

The planning of primary and secondary systems mentioned above involves not only the optimization of topological structure (e.g., power supply location, grid structure, communication structure, etc.) but also the selection of electrical and communication equipment, and power supply capacity optimization, etc. Furthermore, the operation conditions of various planning schemes need to be considered to evaluate a series of key indicators of the system, such as network loss, income, and renewable energy consumption rate, and then a double-layer optimization framework of operation planning can be obtained. The model solution block diagram is given in **Figure 4**.

Distribution network planning first needs to collect the load characteristics of the park and the diagram of the planning area, then implements spatial load forecasting. Primary system planning can be carried out including the location and capacity of substations and DG based on the results of spatial load forecasting. Then grid scheme planning is acquired by incorporating line equipment selection and path planning, which will be conveyed to power source planning for realizing further optimization. Lastly, source-network collaborated planning of the primary system is formed via iterating the above process in limited times.

It is crucial to install the automatic terminal on the switchgear of the primary system based on source-network planning. Then, the communication topology optimization between each terminal needs to be carried out to build a run-plan collaborated model for the secondary system. The planning indexes of the secondary system are obtained through determined communication and automation schemes which will return to primary system planning. Hence, a multi-level planning model of the primary and secondary systems is formed, and the common control variables, constraints, and objective functions of each sub-model are shown in **Table 1**. The general mathematical model of cyber-physical fusion-based coordinated planning model can be expressed as follows:

$$\min \quad c^I(x) + c^O(x,y) + c^R(z) \tag{1}$$

s.t.

$$x \in \{0,1\}^n \tag{2}$$

$$f(x,y) \le 0 \tag{3}$$

$$g(x,z) \le 0 \tag{4}$$

where x represents the binary investment variables; y is continuous operating variables; z is the vector relating to topology and reliability. c^I is the investment cost; c^O is the operating cost; c^R is the reliability cost. $f(x, y)$ represents the set of constrained functions used to model the operation and planning of distribution systems; and $g(x, z)$ is a new set of constrained functions relating to reliability constraint.

Solution Algorithms

In the field of operation control optimization, there is a high demand for the efficiency of algorithms. For example, unit commitment (UC) and automatic generation control (AGC) (Zhang et al., 2018) require algorithms' solution time within the hour level, minute level, or even second level. The distribution network planning pays more attention to the quality of solution, i.e., obtaining a high-quality global optimal solution planning scheme in the possible shortest time.

TABLE 1 | Basic characteristics of the distribution network planning model.

Planning model	Primary system		Secondary system	
	Power source planning	Grid scheme planning	Automation system planning	Communication system planning
Control variable	Power location; power capacity; construction time	Line model; equipment model, cable trench; topology structure; construction time	Automation terminal type; automation terminal location; main station type; construction time	Topology; communication protocol; communication mode; construction time
Constraint condition	Investment constraints; power flow constraints; DG constraints (PV/WT/ESS/EV capacity constraints); reliability index constraints (SAIDI, SAIFI, ASAI, ENS); safety constraints (N-1 verification, short-circuit current verification, node voltage constraint, branch current constraint, injection power constraint)	Investment constraints; power flow constraints; DG constraints (PV/WT/ESS/EV capacity constraints); reliability index constraints (SAIDI, SAIFI, ASAI, ENS); safety constraints (N-1 verification, short-circuit current verification, node voltage constraint, branch current constraint, injected power constraint); operating topology constraint; connection mode constraint; guideline/standard constraint	Investment constraints; reliability index constraints (SAIDI, SAIFI, ASAI, ENS); technical constraints (terminal configuration quantity constraints); power supply range; guidelines/standard constraints	Investment constraints; reliability index constraints (SAIDI, SAIFI, ASAI, ENS); topology constraints (ring network structure); guidelines/standard constraints
Objective function	Investment cost; maintenance cost; operating cost (network loss, curtailment of wind and solar); DISCOs' income; carbon emissions; renewable energy consumption rate; power outage loss cost	Investment cost; maintenance cost; operating cost (network loss, curtailment of wind and solar); DISCOs' income; carbon emissions; renewable energy consumption rate; power loss cost; life cycle cost	Investment cost; maintenance cost; power outage loss; the number of switching operations; DISCOs' income; guideline/standard constraints; life cycle cost	Investment cost; maintenance cost; power outage loss; topology indicators (network invulnerability, robustness, connectivity, node influence, topology potential); communication delay

Each level of decision-making in the multi-level planning model of the primary and secondary system has its objective function and constraint conditions. Regarding the decision variables from the upper layer as parameters, the lower layer could search the optimal solutions of this layer based on objective function and constraints which are finally returned to the upper layer. The upper layer can find the overall optimal solution within the possible range according to the feedback from the lower layer. Hence, the multi-level planning problem is complicated and it is difficult to obtain solutions. Even the simplest two-level planning problem is also an NP-hard problem (Jeroslow, 1985), as discussed in the literature on this subject (Blair, 1990; Bard, 1991).

Distribution network planning usually divides the planning cycle into several stages after considering load changes which increase the number of control variables and lead to dimensional disasters. Furthermore, the randomness of the DG and load side leads to vast uncertainties in the distribution system planning model. The uncertainty planning algorithms are then developed.

The main difficulty in high-reliability distribution network planning is that the reliability evaluation needs to consider topology search, which makes it difficult to acquire the explicit functional expression of the distribution network planning model and employ a convex optimization method to solve it. Therefore, it is necessary to simplify the reliability assessment appropriately according to the actual planning model.

Taking the primary grid scheme planning of the distribution network as an example, the number of feeders in the county can be reached by more than one hundred. Distribution network planning is a large-scale discrete and non-convex complex optimization problem in essence, and the commonly solved algorithms are classical mathematical methods and intelligent algorithms. After transforming the unsolved problem into the convex optimization problem, classical mathematical methods can be adopted to solve the global optimal solution. However, this method is hard to converge by high-dimensional non-convex problems. Intelligent algorithms have low dependence on models, but they generally have defects such as slow convergence speed, complex parameter settings, and falling into local optimum. In consequence, combining the above methods to form an effective hybrid algorithm is a valuable research direction.

COORDINATED PLANNING OF PRIMARY AND SECONDARY SYSTEM

The 24th International Power Supply Conference points out that the coordinated planning of the primary system and ICT system is key to improving the reliability of the distribution network which is worthy of attention.

Reliability Evaluation Algorithms

Although primary and secondary systems are coupled with each other, information equipment has an uninterrupted power supply that exerts little influence on the system. Hence, the reliability evaluation is mainly from the perspective of a physical system.

The factors that affect the reliability of the physical system by the cyber system include network equipment, network topology, communication mode, communication protocol, and communication distance, etc. Successful information transmission requires that the equipment components of the information link are in normal working conditions. A network component may exist in multiple information links at the same time, so failure will affect the

reliability of multiple information links. The transmission performance of communication links is influenced by the following aspects: the connectivity affected by a network node and transmission channel failure, the timeliness affected by message transmission delay, and the accuracy affected by transmission errors (Haghighat and Zeng, 2016).

The impact of a cyber system on the physical system is manifested as whether the physical element can correctly realize its function. Therefore, the reliability evaluation of the cyber-physical system can be described by the working state of physical elements. According to the failure type of cyber system, the interaction of cyber-physical system can be divided into direct impact and indirect impact. In detail, the former includes the direct impact of information components and cyber systems on physical components, while the indirect impact measures the influence on physical components such as power generation equipment via enumerating and merging the possible states of the cyber system (Falahati et al., 2012; Falahati and Fu, 2014). The components according to IEC 61850 standard in the cyber system have three levels, i.e., process layer, interval layer, and management layer. It is of great significance to analyze the random failure of information elements for improving the stability of the microgrid system (Lei et al., 2014; Liu et al., 2020).

With the development of information technologies and power markets, the influence of human factors such as cyber-attack should be considered. CPS carries out vulnerability assessment under the joint attack of man-made physical and information (Sridhar et al., 2011; Li et al., 2016), which extends the concept of operational reliability to the cyber system (Davis et al., 2015; Xin et al., 2015). It is valuable to analyze the reliability of the distribution network when the communication network fails, considering the influence of network communication facilities, as well as the arrangement of synchronous switches and fault monitors (Mohammadi et al., 2019).

Traditional reliability indicators are unable to describe the coupling relationship of cyber-physical systems. Hence, some novel indexes are presented. The concept of information entropy is introduced to the physical system based on the operational control of the cyber system. The disordered state of physical nodes is denoted through energy entropy to evaluate the reliability of the microgrid CPS (Munoz et al., 2018). In terms of system indicators, the generalized system average outage frequency index, the generalized system average outage duration index, the generalized power shortage expectation index, and the generalized power supply availability index are proposed, combining the influence of information components on system failure (Wang et al., 2019). To evaluate the impact of cyber-physical systems after cyber-attacks, a set of elastic index evaluation models are also established (Clark and Zonouz, 2019).

In recent years, some scholars have overcome the problem that the original reliability evaluation algorithms require topological search and cannot be expressed explicitly. Literature on this subject (Munoz et al., 2018) establishes an explicit calculation formula for the reliability evaluation of the distribution network that has successfully been applied to DSEP. However, this method is only suitable for specific grid frames. Furthermore, a study (Jooshaki et al., 2019) proposes a linearized explicit function expression, which can greatly improve the solution efficiency of distribution network planning with satisfactory accuracy. Recently, another study (Li et al., 2020a) proposes a mixed integer linearized programming formulation of mesh distribution networks and applied this model in the distribution network planning model successfully in Li et al. (2020b) and Li et al. (2021). Note that there are a few works that focus on establishing explicit functional expressions for evaluating the reliability of primary and secondary systems, a promising research field.

Coordinated Planning Methods

CPS often has four levels, namely backbone network, access network, an interface layer, and physical domain. The control instructions of the secondary system determine the operating status of the primary system. Moreover, the grid status will influence the input of the cyber system and provide an energy guarantee.

In another study Yang et al. (2017), a double-level planning model is used to optimize the capacity, communication terminal location, and communication topology of the energy storage system. Reference Harri et al. (2019) designs the collaborated optimization of DG, charging pile, and protection equipment in a smart grid, and an intelligent optimization algorithm is adopted to solve the complex collaborated planning model. Another work (Heidari et al., 2018) develops a reliability analysis algorithm, considering the influence of interaction between primary and secondary systems on the reliability of CPS. Meanwhile, the genetic algorithm (GA) is used to optimize the fault indicator and switch position in this paper. As outlined in other literature, a study Mohammadi et al. (2019) has employed GA to realize high-reliability planning for control equipment and protection equipment in the distribution network. Moreover, other studies Heidari et al. (2017) have built a collaborated planning model of the primary network and secondary terminal equipment based on the reliability index constraints from the perspective of DISCO, which are solved by GA.

CONCLUSION

This paper summarizes the key difficulties of high-reliability primary and secondary system coordinated planning, such as reliability evaluation algorithms, coordinated models, and solution algorithms, etc. Then, two hot research directions in distribution network modeling are classified, i.e., the complex network frame and its optimization. It also describes some achievements of primary and secondary system coordinated planning.

The essence of primary and secondary system coordinated planning is a large-scale non-convex and non-linear planning problem with multi-variable, multi-stages, and multi-objectives. Furthermore, there are still some obstacles in applying primary and secondary coordinated planning to practical engineering problems, which can be discussed as follows:

(1) Academician Xue in the Chinese Academy of Science first proposed the concept of CPSS in 2017, which is a power system considering market game mechanism, environmental science, economic policy, and other human factors (Yu and Xue, 2016; Xue and Yu, 2017). It is necessary to further study the influence of market mechanisms and environmental factors on distribution network models based on primary and secondary system coordinated planning. The introduction of market mechanisms will inevitably bring more uncertainties that increase the difficulty of modeling.
(2) The optimization methods in cyber-physical system planning are mainly classic mathematical optimization methods and intelligent optimization algorithms. The former converts a mathematical model into a convex optimization problem to obtain the global optimal solution. While the latter does not rely on a specific mathematical model, but easily traps at a local optimum. The actual distribution network planning model often includes large-scale nodes, as well as multi-variable, multi-time, and multi-stage optimization. It is an effective way to combine classical mathematical methods and intelligent optimization algorithms to establish a stronger hybrid algorithm for solving the aforementioned complicated planning model.
(3) The development of emerging technologies such as cloud computing, the ubiquitous internet of things (IoT), and big data has promoted the integration of primary and secondary systems. However, most of the above concepts and theories still stay at the level of simulation computing. The efficient smart grid CPS test platform needs to be further explored to test, evaluate, and verify the feasibility of these novel theories.

DATA AVAILABILITY STATEMENT

The original contributions presented in the study are included in the article/Supplementary Material, further inquiries can be directed to the corresponding author.

AUTHOR CONTRIBUTIONS

CG: conceptualization, methodology, and writing—original draft. TW, HC and RC: formal analysis, visualization, and resources. ZW and TY: writing—review, and editing.

FUNDING

The authors gratefully acknowledge the support of the Science and technology project of China Southern Power Grid Corporation (GDKJXM20173256)

REFERENCES

Bard, J. F. (1991). Some Properties of the Bilevel Programming Problem. *J. Optim Theor. Appl.* 68 (2), 371–378. doi:10.1007/bf00941574

Blair, B. A. E. (1990). Computational Difficulties of Bilevel Linear Programming. *Operations Res.* 38 (3), 556–560. doi:10.1287/opre.38.3.556

Cai, Z., Yu, M., Steurer, M., and Ng, J. (2019). A New Grouping Protocol for Smart Grids. *IEEE Trans. Smart Grid* 10 (1), 955–966. doi:10.1109/tsg.2017.2756863

Clark, A., and Zonouz, S. (2019). Cyber-physical Resilience: Definition and Assessment Metric. *IEEE Trans. Smart Grid* 10 (2), 1671–1684. doi:10.1109/tsg.2017.2776279

Colak, I., Sagiroglu, S., Fulli, G., Yesilbudak, M., and Covrig, C.-F. (2016). A Survey on the Critical Issues in Smart Grid Technologies. *Renew. Sustainable Energ. Rev.* 54, 396–405. doi:10.1016/j.rser.2015.10.036

Cortes, C. A., Contreras, S. F., and Shahidehpour, M. (2017). Microgrid Topology Planning for Enhancing the Reliability of Active Distribution Networks. *IEEE Trans. Smart Grid* 9 (6), 6369–6377. doi:10.1109/tsg.2017.2709699

Davis, K. R., Davis, C. M., Zonouz, S. A., Bobba, R. B., Berthier, R., Garcia, L., et al. (2015). A Cyber-Physical Modeling and Assessment Framework for Power Grid Infrastructures. *IEEE Trans. Smart Grid* 6 (5), 2464–2475. doi:10.1109/tsg.2015.2424155

Dileep, G. (2020). A Survey on Smart Grid Technologies and Applications. *Renew. Energ.* 146 (2), 2589–2625. doi:10.1016/j.renene.2019.08.092

Esmaeeli, M., Kazemi, A., Shayanfar, H., Chicco, G., and Siano, P. (2017). Risk-based Planning of the Distribution Network Structure Considering Uncertainties in Demand and Cost of Energy. *Energy* 119, 578–587. doi:10.1016/j.energy.2016.11.021

Falahati, B., and Fu, Y. (2014). Reliability Assessment of Smart Grids Considering Indirect Cyber-Power Interdependencies. *IEEE Trans. Smart Grid* 5 (4), 1677–1685. doi:10.1109/tsg.2014.2310742

Falahati, B., Fu, Y., and Wu, L. (2012). Reliability Assessment of Smart Grid Considering Direct Cyber-Power Interdependencies. *IEEE Trans. Smart Grid* 3 (3), 1515–1524. doi:10.1109/tsg.2012.2194520

Farwell, J. P., and Rohozinski, R. (2011). Stuxnet and the Future of Cyber War. *Survival* 53 (1), 23–40. doi:10.1080/00396338.2011.555586

Georgilakis, P. S., and Hatziargyriou, N. D. (2015). A Review of Power Distribution Planning in the Modern Power Systems Era: Models, Methods and Future Research. *Electric Power Syst. Res.* 121, 89–100. doi:10.1016/j.epsr.2014.12.010

Gholizadeh, R. R., Najafi, R. S., and Hosseinian, S. H. (2018). A Framework for Optimal Coordinated Primary-Secondary Planning of Distribution Systems Considering MV Distributed Generation. *IEEE Trans. Smart Grid* 9 (2), 1408–1415. doi:10.1109/tsg.2016.2590425

Haghighat, H., and Zeng, B. (2016). Distribution System Reconfiguration under Uncertain Load and Renewable Generation. *IEEE Trans. Power Syst.* 31 (4), 2666–2675. doi:10.1109/tpwrs.2015.2481508

Harri, A. M., Hejazi, M., and Hashemi, D. H. (2019). Reliability Optimization of Smart Grid Based on Optimal Allocation of Protective Devices, Distributed Energy Resources, and Electric Vehicle/plug-In Hybrid Electric Vehicle Charging Stations. *J. Power Sourc.* 436, 226824. doi:10.1016/j.jpowsour.2019.226824

Heidari, K. M., Sepehry, M., and Aravinthan, V. (2018). Fault Detector and Switch Placement in Cyber-Enabled Power Distribution Network. *IEEE Trans. Smart Grid* 9 (2), 980–992. doi:10.1109/tsg.2016.2573261

Heidari, S., and Fotuhi-Firuzabad, M. (2019). Integrated Planning for Distribution Automation and Network Capacity Expansion. *IEEE Trans. Smart Grid* 10 (4), 4279–4288. doi:10.1109/tsg.2018.2855218

Heidari, S., Fotuhi-Firuzabad, M., and Lehtonen, M. (2017). Planning to Equip the Power Distribution Networks with Automation System. *IEEE Trans. Power Syst.* 32 (5), 3451–3460. doi:10.1109/tpwrs.2017.2650210

Humayed, A., Lin, J., Li, F., and Luo, B. (2017). Cyber-physical Systems Security-A Survey. *IEEE Internet Things J.* 4 (6), 1802–1831. doi:10.1109/jiot.2017.2703172

Jeroslow, R. G. (1985). The Polynomial Hierarchy and a Simple Model for Competitive Analysis. *Math. Programming* 32 (2), 146–164. doi:10.1007/bf01586088

Jooshaki, M., Abbaspour, A., Fotuhi-Firuzabad, M., Farzin, H., Moeini-Aghtaie, M., and Lehtonen, M. (2019). A MILP Model for Incorporating Reliability Indices in Distribution System Expansion Planning. *IEEE Trans. Power Syst.* 34 (3), 2453–2456. doi:10.1109/tpwrs.2019.2892625

Lei, H., Singh, C., and Sprintson, A. (2014). Reliability Modeling and Analysis of IEC 61850 Based Substation protection Systems. *IEEE Trans. Smart Grid* 5 (5), 2194–2202. doi:10.1109/tsg.2014.2314616

Li, Z., Shahidehpour, M., Alabdulwahab, A., and Abusorrah, A. (2016). Bilevel Model for Analyzing Coordinated Cyber-Physical Attacks on Power Systems. *IEEE Trans. Smart Grid* 7 (5), 2260–2272. doi:10.1109/tsg.2015.2456107

Li, Z., Wu, W., Tai, X., and Zhang, B. (2021). A Reliability-Constrained Expansion Planning Model for Mesh Distribution Networks. *IEEE Trans. Power Syst.* 36 (2), 948–960. doi:10.1109/tpwrs.2020.3015061

Li, Z., Wu, W., Tai, X., and Zhang, B. (2020). Optimization Model-Based Reliability Assessment for Distribution Networks Considering Detailed Placement of Circuit Breakers and Switches. *IEEE Trans. Power Syst.*, 35 (9), 3991–4004. doi:10.1109/tpwrs.2020.29815085

Li, Z., Wu, W., Zhang, B., and Tai, X. (2020). Analytical Reliability Assessment Method for Complex Distribution Networks Considering post-fault Network Reconfiguration. *IEEE Trans. Power Syst.* 35 (2), 1457–1467. doi:10.1109/tpwrs.2019.2936543

Liang, G., Weller, S. R., Zhao, J., Luo, F., and Dong, Z. Y. (2017). The 2015 Ukraine Blackout: Implications for False Data Injection Attacks. *IEEE Trans. Power Syst.* 32 (4), 3317–3318. doi:10.1109/tpwrs.2016.2631891

Lin, Z., Hu, Z., and Song, Y. (2019). Distribution Network Expansion Planning Considering $N-1$ Criterion. *IEEE Trans. Power Syst.* 34 (3), 2476–2478. doi:10.1109/tpwrs.2019.2896841

Liu, W., Gong, Q., Han, H., Wang, Z., and Wang, L. (2018). Reliability Modeling and Evaluation of Active Cyber Physical Distribution System. *IEEE Trans. Power Syst.* 33 (6), 7096–7108. doi:10.1109/tpwrs.2018.2854642

Liu, W., Lin, Z., Wang, L., Wang, Z., Wang, H., and Gong, Q. (2020). Analytical Reliability Evaluation of Active Distribution Systems Considering Information Link Failures. *IEEE Trans. Power Syst.* 35 (6), 4167–4179. doi:10.1109/tpwrs.2020.2995180

Lotfi, H., and Khodaei, A. (2017). AC versus DC Microgrid Planning. *IEEE Trans. Smart Grid* 8 (1), 296–304. doi:10.1109/tsg.2015.2457910

Mohammadi, A., Soleymani, S., and Mozafari, B. (2019). A Stochastic Formulation for Distribution Automation Planning Incorporating Emergency Demand Response Programs. *Int. Trans. Electr. Energ. Syst.*, 29(12):e12138. doi:10.1002/2050-7038.12138

Munoz, D. G., Contreras, J., and Arroyo, J. (2018). Distribution Network Expansion Planning with an Explicit Formulation for Reliability Assessment. *IEEE Trans. Power Syst.* 33 (3), 2583–2596. doi:10.1109/tpwrs.2017.2764331

Popovic, Z. N., Knezevic, S. D., and Kerleta, V. D. (2019). Network Automation Planning in Distribution Networks with Distributed Generators Using a Risk-Based Approach. *Electr. Eng.* 101 (2), 659–673. doi:10.1007/s00202-019-00814-9

Sridhar, S., Hahn, A., and Govindarasu, M. (2011). Cyber–physical System Security for the Electric Power Grid. *Proc. IEEE* 100 (1), 210–224.

Sun, L. M., and Yang, B. (2020). Nonlinear Robust Fractional-Order Control of Battery/SMES Hybrid Energy Storage Systems. *Power Syst. Prot. Control.* 48 (22), 76–83. doi:10.19783/j.cnki.pspc.191598

Tuballa, M. L., and Abundo, M. L. (2016). A Review of the Development of Smart Grid Technologies. *Renew. Sustainable Energ. Rev.* 59, 710–725. doi:10.1016/j.rser.2016.01.011

Wang, Z. G., Chen, Y. R., and Ceng, J. (2019). Modeling and Reliability Assessment of Completely Distributed Microgrid Cyber Physical System. *Power Syst. Tech.* 43 (7), 2413–2421.

Xin, S., Guo, Q., Sun, H., Zhang, B., Wang, J., and Chen, C. (2015). Cyber-physical Modeling and Cyber-Contingency Assessment of Hierarchical Control Systems. *IEEE Trans. Smart Grid* 6 (5), 2375–2385. doi:10.1109/tsg.2014.2387381

Xue, Y., and Yu, X. (2017). Beyond Smart Grid-Cyber-Physical-Social System in Energy Future [point of View]. *Proc. IEEE* 105 (12), 2290–2292. doi:10.1109/jproc.2017.2768698

Yang, T., Huang, Z., Pen, H., and Zhang, Y. (2017). Optimal Planning of Communication System of CPS for Distribution Network. *J. Sensors* 2017, 1–10. doi:10.1155/2017/9303989

Yu, X., and Xue, Y. (2016). Smart Grids: A Cyber-Physical Systems Perspective. *Proc. IEEE* 104 (5), 1058–1070. doi:10.1109/jproc.2015.2503119

Zhang, X. S., Li, Q., and Yu, T. (2018). Consensus Transfer Q-Learning for Decentralized Generation Command Dispatch Based on Virtual Generation Tribe. *IEEE Trans. Smart Grid* 9 (3), 2152–2165. doi:10.1109/tsg.2016.2607801

Conflict of Interest: CG, TW, HC and RC were employed by the company Guangdong Power Grid Co., Ltd.

The remaining authors declare that the research was conducted in the absence of any commercial or financial relationships that could be construed as a potential conflict of interest.

Copyright © 2021 Gao, Wang, Cao, Wang, Yu and Cheng. This is an open-access article distributed under the terms of the Creative Commons Attribution License (CC BY). The use, distribution or reproduction in other forums is permitted, provided the original author(s) and the copyright owner(s) are credited and that the original publication in this journal is cited, in accordance with accepted academic practice. No use, distribution or reproduction is permitted which does not comply with these terms.

APPENDIX A

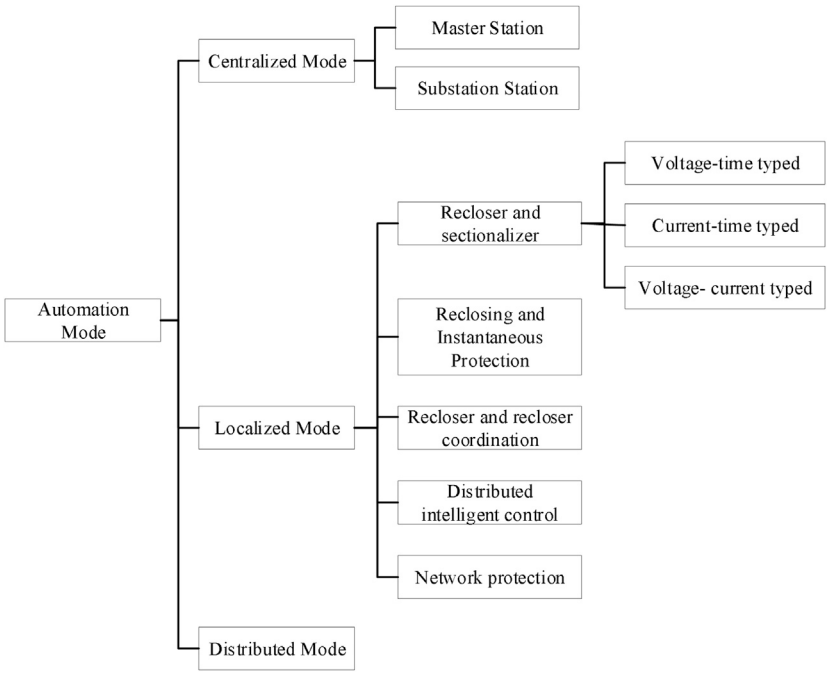


FIGURE A1 | Common Distribution Automation Mode

APPENDIX B

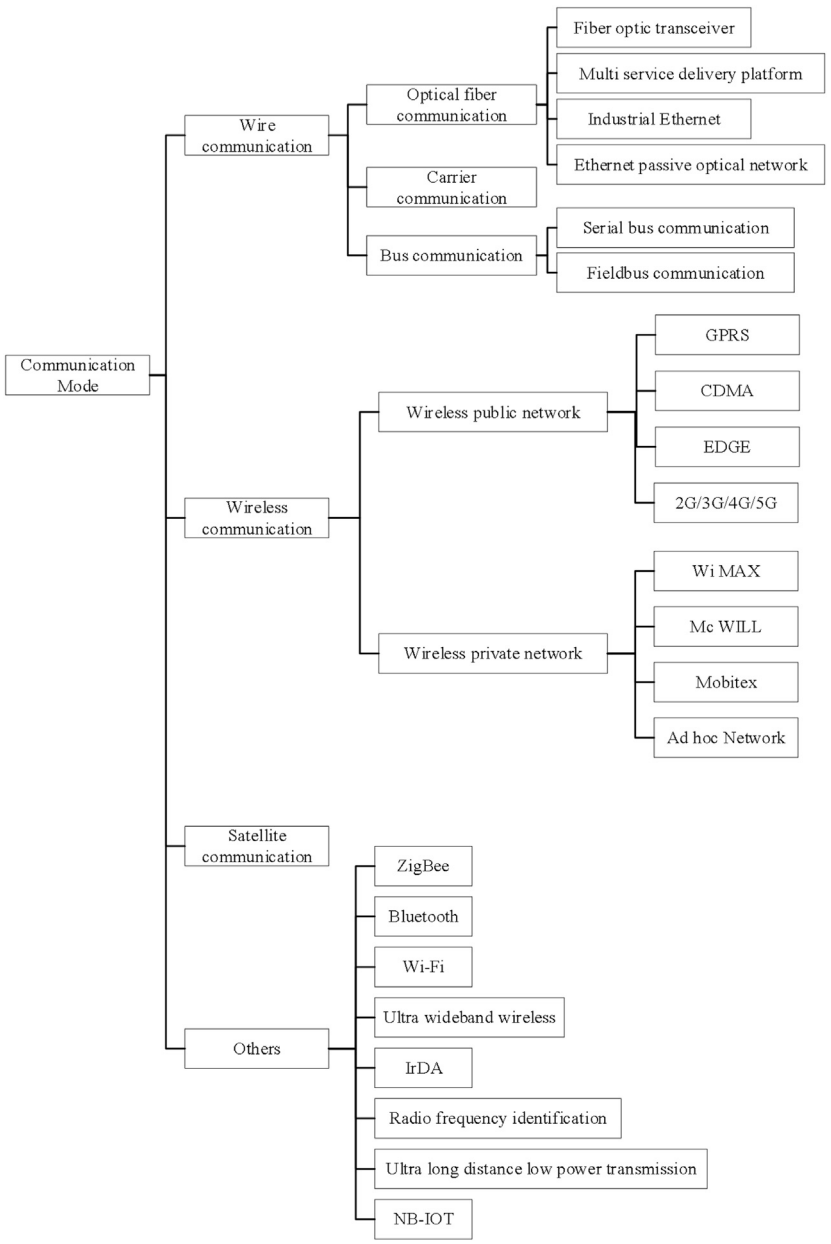


FIGURE B1 | Common Distribution Communication Mode

frontiers in Energy Research

METHODS
published: 22 June 2021
doi: 10.3389/fenrg.2021.697054

Autonomous Control Method of Rotor UAVs for Power Inspection With Renewable Energy Based on Swarm Intelligence

*Yao Yao[1,2], Cao Jun-hua[1], Guo Yi[3], Fan Zhun[1,2], Zou An-Min[1,2], Xu Biao[1,2] and Li Ke[1,2]**

[1]Department of Electronic Engineering, Shantou University, Shantou, China, [2]Key Lab of Digital Signal and Image Processing of Guangdong Province, Shantou, China, [3]Dalian Naval Academy, Dalian, China

With the rapid development of renewable energy, the scale of China's power grid with renewable energy has become much bigger than ever; as a result, we are facing severe challenges in the inspection and maintenance work of power grids that use renewable energy. Focusing on the shortcomings of the traditional manual inspection methods, this paper studies and proposes an optimization algorithm of automatic inspection of Unmanned Aerial Vehicles (UAVs) to improve the efficiency and cost of the inspection and maintenance work of renewable energy power grids. Firstly, the communication network of the swarm intelligence system has been established to transmit the local information sensed by each UAV in real time. Secondly, according to the sensing ability of UAVs, the segmentation model of UAVs overlapping sensing areas is established, which effectively reduces the probability of overlapping UAVs sensing areas. Thirdly, according to the difference between the coverage value and the effective coverage index of each point in the sensing area, the optimization function of the coverage index is given, which makes the UAV give priority to the inspection area with the lower coverage value. Finally, when a UAV completes a local coverage task, the traction speed is introduced to prevent the UAV from stopping, which ensures that the inspection task of the whole area can be completed in a limited time. The numerical simulation results show that the algorithm can effectively control the UAVs to complete the inspection task in the specified area, and compared with the single UAV inspection method, this algorithm can greatly improve the inspection efficiency and reduce the inspection cost.

Keywords: renewable energy, power grid, autonomous inspection, swarm intelligence, area coverage

OPEN ACCESS

Edited by:
Yaxing Ren,
University of Warwick,
United Kingdom

Reviewed by:
Xinxin Xie,
Sun Yat-sen University, China
Dandan Liu,
Yancheng Institute of Technology, China

****Correspondence:***
Li Ke
ericlee@stu.edu.cn

Specialty section:
This article was submitted to Smart Grids, a section of the journal Frontiers in Energy Research

Received: *18 April 2021*
Accepted: *03 May 2021*
Published: *22 June 2021*

Citation:
Yao Y, Jun-hua C, Yi G, Zhun F, An-Min Z, Biao X and Ke L (2021) Autonomous Control Method of Rotor UAVs for Power Inspection With Renewable Energy Based on Swarm Intelligence. Front. Energy Res. 9:697054. doi: 10.3389/fenrg.2021.697054

INTRODUCTION

Renewable energy refers to wind energy, solar energy, water energy, biomass energy, geothermal energy, and other non-fossil energy, and it is thus clean energy. Renewable energy is a type of green and low-carbon energy, which is an important part of China's multi-wheel drive energy supply system. It is of great significance to improve the energy structure, protect the ecological environment, cope with climate change, and achieve sustainable economic and social development (Dieter and Jennifer, 2008; Poonam et al., 2020). In 2020, China's renewable energy power generation will reach 2214.8 billion kilowatt-hours, with a year-on-year growth of about 8.4%. By the end of 2020, China's renewable energy power generation capacity will reach 934 million kilowatts, a year-on-year growth

of about 17.5% (Cai, 2020). With the continuous expansion of the scale of China's power grid with renewable energy, the area of inspection and maintenance work of power grids is now facing increasingly severe challenges. Traditional manual inspection methods are inefficient, and inspectors experience high work intensity and significant danger (Yin, 2016; Zhou et al., 2018). The current Unmanned Aerial Vehicle (UAV) inspection mainly relies on remote control by ground operators, which has high technical requirements for UAV operators. Due to the vast area of China's power grid that is to be inspected and the low efficiency of single UAV inspection, rotor UAVs for power inspection based on Swarm intelligence has become an inevitable trend.

Compared with the traditional single-UAV inspection method (Burciu, 2012; Stone et al., 2014; Jiang et al., 2020), the collaborative inspection of UAVs has the advantages of low cost and high efficiency, which can greatly improve the inspection speed and positioning accuracy. The key of UAVs autonomous inspection method is to realize the coverage control of the unknown area by UAVs. The essence of area coverage control is to design a UAV control method based on the relationship between the sensing model of the UAV and the distribution of information in the area so that the inspection task can be completed. Currently, the most commonly used UAV inspection method is sweeping inspection, that is, to control the formation of the UAVs to make them navigate along an appropriate track in a specific formation to complete the inspection task of the target area (Che et al., 2011; Wang et al., 2020). This method can complete the inspection task in a simple environment, but it has poor autonomy and low efficiency in a complex environment.

Aiming at the shortcomings of existing means, improving the autonomy and efficiency of the UAV system is the main purpose of our study. The advantage of the optimization algorithm of UAV autonomous inspection is that it can efficiently map the target area, and has the characteristics of high security and adaptability. The basic idea of the optimization algorithm is to build a swarm intelligence to make each UAV complete the task assignment of the sub-areas by communicating with the neighboring UAVs, which simplifies the original co-fixed area coverage problem (Cortés et al., 2005; Xiang et al., 2020; Zhang et al., 2020). This paper establishes an optimization algorithm model of UAV autonomous inspection and analyses the effects of the number of UAVs, effective coverage value, and other parameters on the efficiency of UAV autonomous inspection.

BASIC PRINCIPLE OF THE OPTIMIZATION ALGORITHM

The Communication Topology and Dynamic Description of UAVs System

Communication within the UAV system is an important part of the UAV's cooperative coverage problem. The communication topology of the coverage network composed of UAVs is given based on graph theory. $\boldsymbol{G} = (\mathrm{V}, \boldsymbol{E})$ is defined as the communication topological graph of the UAV overlay network. $\mathrm{V} = \{1, 2, \cdots, \mathrm{N}\}$ is the vertex, and the vertex set represents each UAV in the UAV system. The edge set $\boldsymbol{E} = \{\mathrm{e}_1, \mathrm{e}_2, \cdots, \mathrm{e}_l\} \subset \mathrm{V} \times \mathrm{V}$ indicates the edges in the communication topological graph, $e_i = \{\mathrm{j}, \mathrm{k}\}, j, k \in E$ indicates that the vertices j and k can communicate with each other, and $l \in \{1, \cdots, \mathrm{N}(\mathrm{N}-1)/2\}$ represents the number of edges $\boldsymbol{E}$. The neighbor set of vertex i defined in the overlay network communication topology diagram is

$$\mathrm{N}_i(\boldsymbol{E}) = \left\{ j \in \mathrm{V} \middle| (i,j) \in \boldsymbol{E} \right\} \tag{1}$$

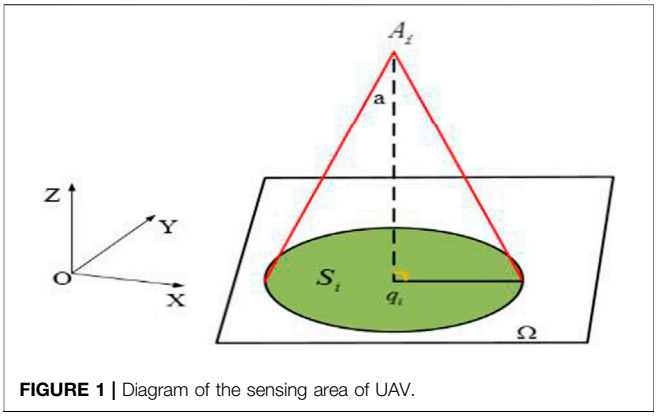


FIGURE 1 | Diagram of the sensing area of UAV.

In this paper, the problem of inspection in a fixed area under ideal conditions is studied. Therefore, the following assumptions are given:

Suppose 1. The communication network of the UAV system is always connected, and its communication topology is an undirected graph.

Suppose 2. The surface to be covered is smooth, and every UAV moves on a plane.

Firstly, the definition of the two-dimensional inertial coordinate system OXY is given in order to give the dynamic model of UAV: taking a certain point on the ground as the origin of the coordinate system OXY, OX, and OY point to the east and north, respectively.

Based on the coordinate system OXY, the dynamic model of UAV is established. For the convenience of describing the problem, we assume that the UAV is a particle. Define A_i to represent the ith UAV in the UAV system, where $i \in I_N, I_N = \{1, 2, \cdots, \mathrm{N}\}$ represents the subscript set of N UAVs. The location vector of UAV A_i is $\overrightarrow{P}_i = [x_i, y_i]^T$, the velocity vector of the UAV is $\overrightarrow{\mathrm{V}}_i = [v_{ix}, v_{iy}]^T$, If the acceleration of the UAV is $\overrightarrow{U}_i = [u_{ix}, u_{iy}]^T$ and $\overrightarrow{M}_i = [\overrightarrow{P}_i^T, \overrightarrow{V}_i^T]$, the dynamic model of the UAV is as follows:

$$\dot{\overrightarrow{M}}_i = A\overrightarrow{P}_i + B\overrightarrow{U}_i \tag{2}$$

where $A = \begin{pmatrix} \mathbf{0}_{2\times2} & I_{2\times2} \\ \mathbf{0}_{2\times2} & \mathbf{0}_{2\times2} \end{pmatrix}$, $B = \begin{pmatrix} \mathbf{0}_{2\times2} \\ I_{2\times2} \end{pmatrix}$.

The Sensing Area Model of UAV

When performing the inspection task, each UAV will be equipped with a vertically downward detection device.

Assuming that the divergence angle of each detection device is α, the sensing area of UAV A_i on the OXY plane is a circular area. Let $\boldsymbol{q}_i$ be the projection of UAV A_i on OXY plane. Therefore, the sensing area of UAV A_i is shown in **Figure 1**:

The sensing area model of UAV A_i can be specifically described as follows:

$$S_i(\overrightarrow{A}_i, \alpha) = \left\{q: \left\|\overrightarrow{q} - \overrightarrow{q}_i\right\| \le R\right\} \tag{3}$$

Where $\boldsymbol{q} \in \Omega$ represents the point within the detection range of UAV, and Ω represents the given area to be covered on OXY plane.

The Coverage Efficiency Optimization Index in the Fixed Area

The main task of inspection with UAVs system is to cover the task area Ω with the sensing areas of UAVs so that the detection degree of each point in Ω can reach an effective level, that is, effective coverage.

In order to give the coverage efficiency index of the UAVs inspection system, the definition of effective coverage of points in the fixed area is given first. This is because the information accumulation of points in the fixed area acquired by UAVs using sensors increases with time, that is, the effective coverage level of a point in the area increases with time, for the position $\boldsymbol{q} \in \Omega$ of any point in the area, the effective coverage of UAV A_i from the initial time t = 0 to t is defined as follows:

$$\gamma_i(q,t) = \int_0^t g(z,q)\mathrm{d}\tau \tag{4}$$

Where $g(z,q)$ is the sensing capacity function of each UAV. Assuming that $g(z,q)$ is proportional to z and $g(z,q)$ is dependent on z only, the sensing capacity of each UAV in the system is equal because the z of each UAV in the system is equal. Let C be the effective coverage of each point of Ω in the area, then the effective coverage of all points in the inspection area by UAVs is defined as follows:

Definition 1If all points in the region Ω are covered and meet $\gamma_{I_N}(q,t) = C$, that means all points in the region are effectively covered. The coverage efficiency index of the UAVs inspection system can be specifically described as follows:

$$J(t) = \int_\Omega h\left[C - \gamma_{I_N}(q,t)\right]\mathrm{d}q \tag{5}$$

where γ_{I_N} means the summation of the coverage of each USV. The total number of UAVs is N and $i \in I_N = \{1,2,3,\cdots,N\}$. $h(x)$ is a penalty function, which is positive definite, second-order differentiable, and strictly convex in the interval $(0,C]$, that is, $h(x) > 0, h'(x) > 0\, h''(x) > 0, \forall x \in (0,C]$, and when $x \le 0, h(x) = h'(x) = 0$ is satisfied. When $J(t) = 0$, the inspection task in the designated area is completed.

Undirected Sensing Set Segmentation

Reducing the overlap between sensing areas of adjacent UAVs is beneficial to improve the efficiency of marine coverage. Using the segmentation methods in references (Papatheodorou et al., 2016; Tian et al., 2020b), a sensing set segmentation method that can avoid overlapping sensing sets between adjacent UAVs is given below.

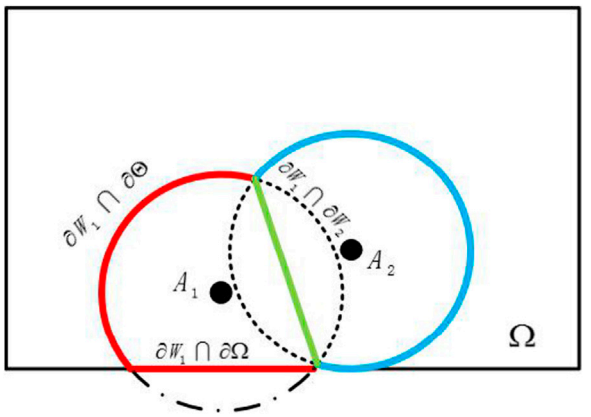


FIGURE 2 | The diagram of segmentation of undirected sensing area.

$$W_i = \{\boldsymbol{q} \in \Omega : g(z_i, \boldsymbol{q}) \ge g(z_j, \boldsymbol{q}), i, j\} \tag{6}$$

where z represents the distance between the UAV and the objective. With the increase of z, the sensing capability gradually decreased. So the sensing set segmentation depends on the z, the overlapping area belongs to the sensing area of UAV that z is smaller.

It can be known from **Eq. 6** that When $z_i = z_j$, their sensing ability is equal, so for the undirected sensing set, the sensing overlapping area is segmented according to its full symmetry and segmentation method (6), as shown in **Figure 2**.

As shown in **Figure 2**, ∂S_1 and ∂S_2 are the sensing areas of UAV A_1 and A_2, respectively. ∂S_1 is shown as the section surrounded by the red curve and green line segment. ∂S_2 is shown as the section surrounded by the blue curve and green line segment. When the sensing areas ∂S_1 and ∂S_2 intersect, the sensing set is divided into two equal parts according to the line segment between two intersection points on ∂S_1 and ∂S_2. The final sensing boundary ∂W_1 of UAV A_1 is composed of a circular arc and line segments. The solid line surrounded by red and green is the sensing boundary of UAV A_1 after segmentation.

The boundary ∂W_1 of UAV A_1 can be expressed as follows:

$$\partial W_1 = \{W_1 \cap \partial\Omega\} \cup \{\partial W_1 \cap \partial\Theta\} \cup \{\cup_{j \ne i}(\partial W_1 \cap \partial W_2)\} \tag{7}$$

In which $\partial W_1 \cap \partial\Omega$ represents the intersection of the boundary of the sensing area of UAV A_1 and given area boundary, $\partial W_1 \cap \partial\Theta$ represents the intersection of the boundary of the sensing area of UAV A_1 and undivided area boundary, and $\partial W_1 \cap \partial W_2$ represents the intersection of the boundary of the sensing area of UAV A_1 and that of UAV A_2. The boundary of the sensing area of UAV A_1 is indicated by solid lines.

Design of Motion Control Law of UAVs

According to the formula of coverage efficiency index (5) of the UAVs inspection system, the coverage efficiency index problem

of the UAVs inspection system can be described as the optimization problem (Fan et al., 2019; Zhang et al., 2021) for the minimum value of $J(t)$ in **Eq. 8**:

$$\text{Minimiz} \quad J(t) = \int_{\Omega} h(C - \gamma_{I_N}(q,t))\mathrm{d}q, \quad q_i \in \Omega \tag{8}$$

For the optimization problem described by **Eq. 8**, it is difficult to directly obtain the gradient information of $J(t)$ because the variable of $J(t)$ is not the variable to be optimized. Therefore, **Eq. 9** can be used to calculate the optimization index of $J(t)$,

$$H(t) = -\dot{J}(t) = \int_{\Omega} h_l\left(C - \gamma_{I_N}(\boldsymbol{q},t)\right) \underset{i \in I_N}{maxg}(z_i,\boldsymbol{q})\mathrm{d}\boldsymbol{q} \tag{9}$$

Because the points beyond the sensing area of UAV can not be sensed, that is, $g(z_i,q) = 0, \quad q \notin S_i$. Then, **Eq. 9** can be expressed as follows:

$$H(t) = \int_{\cup_i^N S_i} h_l\left(C - \gamma_{I_N}(\boldsymbol{q},t)\right) \underset{i \in I_N}{maxg}(z_i,\boldsymbol{q})\mathrm{d}\boldsymbol{q} \tag{10}$$

After dividing the sensing area of each UAV according to the dividing method of **Eqs 7**, **10** can be further expressed as follows:

$$H(t) = \sum_{i \in I_N} \int_{W_i} h_l\left[C - \gamma_{I_N}(\boldsymbol{q},t)\right] g(z_i,\boldsymbol{q})\mathrm{d}\boldsymbol{q} \tag{11}$$

To find the solution of the gradient of the variables to be optimized in the function $H(t)$ according to Leibniz's integral rule (Tian et al., 2020a), the process was described as follows:

$$\begin{aligned}
\frac{\partial H}{\partial \boldsymbol{q}_i} &= \sum_{i \in I_N}\left[\int_{\partial W_i} \Gamma_i^i \boldsymbol{n}_i h_l\left(C - \gamma_{I_N}(\boldsymbol{q},t)\right)\mathrm{g}(z_i,\boldsymbol{q})\mathrm{d}\boldsymbol{q}\right. \\
&\left.+\int_{W_i} h_l\left(C - \gamma_{I_N}(\boldsymbol{q},t)\right)\frac{\partial \mathrm{g}(z_i,\boldsymbol{q})}{\partial \boldsymbol{q}_i}\mathrm{d}\boldsymbol{q}\right] \\
&= \int_{\partial W_i} \Gamma_i^i \boldsymbol{n}_i h_l\left(C - \gamma_{I_N}(\boldsymbol{q},t)\right)\mathrm{g}(z_i,\boldsymbol{q})\mathrm{d}\boldsymbol{q} \\
&+\int_{W_i} h_l\left(C - \gamma_{I_N}(\boldsymbol{q},t)\right)\frac{\partial \mathrm{g}(z_i,\boldsymbol{q})}{\partial \boldsymbol{q}_i}\mathrm{d}\boldsymbol{q} \\
&+\sum_{j \neq i}\left[\int_{\partial W_j} \Gamma_j^i \boldsymbol{n}_j h_l\left(C - \gamma_{I_N}(\boldsymbol{q},t)\right)\mathrm{g}\left(z_j,\boldsymbol{q}\right)\mathrm{d}\boldsymbol{q}\right. \\
&\left.+\int_{W_j} h_l\left(C - \gamma_{I_N}(\boldsymbol{q},t)\right)\frac{\partial \mathrm{g}\left(z_j,\boldsymbol{q}\right)}{\partial \boldsymbol{q}_i}\mathrm{d}\boldsymbol{q}\right],
\end{aligned} \tag{12}$$

Where $\Gamma_j^i = \dfrac{\partial q}{\partial q_i}, \quad q \in \partial W_j$; Because the sensing function of UAVs has nothing to do with q_i, then $\frac{\partial \mathrm{g}(z_i,q)}{\partial q_i} = \frac{\partial \mathrm{g}(z_j,q)}{\partial q_i} = 0$. The result can be obtained as follows:

$$\begin{aligned}
\frac{\partial H}{\partial \boldsymbol{q}_i} &= \int_{\partial W_i} \Gamma_i^i \boldsymbol{n}_i h_l\left(C - \gamma_{I_N}(\boldsymbol{q},t)\right)\mathrm{g}(z_i,\boldsymbol{q})\mathrm{d}\boldsymbol{q} \\
&+\sum_{j \neq i}\int_{\partial W_j} \Gamma_j^i \boldsymbol{n}_j h_l\left(C - \gamma_{I_N}(\boldsymbol{q},t)\right)\mathrm{g}\left(z_j,\boldsymbol{q}\right)\mathrm{d}\boldsymbol{q}
\end{aligned} \tag{13}$$

For $\boldsymbol{q} \in \partial\Omega$, since the given area is static, $\Gamma_i^i = \mathbf{0}_{2\times 2}$. In addition, only the boundary $\partial W_i \cap \partial W_j$ shared by UAVs A_i and A_j will have an impact on the movement of UAVs. So $\frac{\partial H}{\partial \boldsymbol{q}_i}$ can be simplified as follows:

$$\begin{aligned}
\frac{\partial \boldsymbol{H}}{\partial \boldsymbol{q}_i} &= \int_{\partial W_i \cap \mathrm{O}} \Gamma_i^i \boldsymbol{n}_i h_l\left(C - \gamma_{I_N}(\boldsymbol{q},t)\right) g(z_i,\boldsymbol{q})d\boldsymbol{q} \\
&+\sum_{j \neq i}\int_{\partial W_j \cap \partial W_i} \Gamma_j^i \boldsymbol{n}_j h_l\left(C - \gamma_{I_N}(\boldsymbol{q},t)\right) g\left(z_j,\boldsymbol{q}\right)d\boldsymbol{q} \\
&+\sum_{j \neq i}\int_{\partial W_i \cap \partial W_j} \Gamma_i^i \boldsymbol{n}_i h_l\left(C - \gamma_{I_N}(\boldsymbol{q},t)\right) g(z_i,\boldsymbol{q})d\boldsymbol{q}
\end{aligned} \tag{14}$$

In **Equation 14**, $\partial W_i \cap \partial W_j$ is the common boundary of the sensing areas of UAV A_i and A_j,

$\Gamma_j^i = \Gamma_i^i = \frac{\partial q}{\partial q_i} = \begin{bmatrix} \frac{\partial x}{\partial x_i} & \frac{\partial x}{\partial y_i} \\ \frac{\partial y}{\partial x_i} & \frac{\partial y}{\partial y_i} \end{bmatrix} = \begin{bmatrix} 1 & 0 \\ 0 & 1 \end{bmatrix}$, and the external normal vector corresponding to the point on the boundary is $\overrightarrow{n}_i = -\overrightarrow{n}_j = \cos\beta \cdot \overrightarrow{x} + \sin\beta \cdot \overrightarrow{y}$. For $\boldsymbol{q} \in \partial\Omega$, the above formula can be simplified as follows:

$$\begin{aligned}
\frac{\partial \boldsymbol{H}}{\partial \boldsymbol{q}_i} &= \int_{\partial W_i \cap \mathrm{O}} \Gamma_i^i \boldsymbol{n}_i h_l\left(C - \gamma_{I_N}(\boldsymbol{q},t)\right) g(z_i,\boldsymbol{q})\mathrm{d}\boldsymbol{q} \\
&+\sum_{j \neq i}\int_{\partial W_j \cap \partial_{W_i}} \Gamma_i^i \boldsymbol{n}_i h_l\left(C - \gamma_{I_N}(\boldsymbol{q},t)\right)\left(g(z_i,\boldsymbol{q}) - g\left(z_j,\boldsymbol{q}\right)\right)\mathrm{d}\boldsymbol{q}
\end{aligned} \tag{15}$$

Where $\Gamma_i^i n_i = \begin{bmatrix} cos\beta \\ sin\beta \end{bmatrix}$.

Based on **Eq. 15**, the expected optimal speed of each UAV in the UAV system is designed as follows:

$$\begin{aligned}
\boldsymbol{v}_{i,q} &= -k_{\boldsymbol{q}_i}\int_{\partial W_i \cap \mathrm{O}} \Gamma_i^i \boldsymbol{n}_i h_l\left(C - \gamma_{I_N}(\boldsymbol{q},t)\right) g(z_i,\boldsymbol{q})\mathrm{d}\boldsymbol{q} \\
&= -k_{\boldsymbol{q}_i}\sum_{j \neq i}\int_{\partial W_j \cap \partial W_i} \Gamma_i^i \boldsymbol{n}_i h_l\left(C - \gamma_{I_N}(\boldsymbol{q},t)\right)\left(g(z_i,\boldsymbol{q}) - g\left(z_j,\boldsymbol{q}\right)\right)\mathrm{d}\boldsymbol{q}
\end{aligned} \tag{16}$$

The optimal speed of UAVs based on the gradient descent method of the variable q_i in the function $H(t)$ can only guarantee $H(t) = J_l(t) \to 0$, that is, $J(t)$ converges to a constant and $J(t) = 0$ cannot be guaranteed. It shows that when the points in the sensing area of the UAV are effectively covered, the UAV will tend to be stationary. However, the whole task area has not been covered completely. Therefore, in this instance, it is necessary to add a traction speed to the UAV to avoid the UAV falling into the local minimum.

TABLE 1 | Initial conditions of UAVs.

UAVs	Initial conditions (km)
A1	(1.2, 0.2)
A2	(2.4, 0.4)
A3	(3.6, 0.6)
A4	(4.8, 0.8)
A5	(6, 1)
A6	(7.2, 1.2)

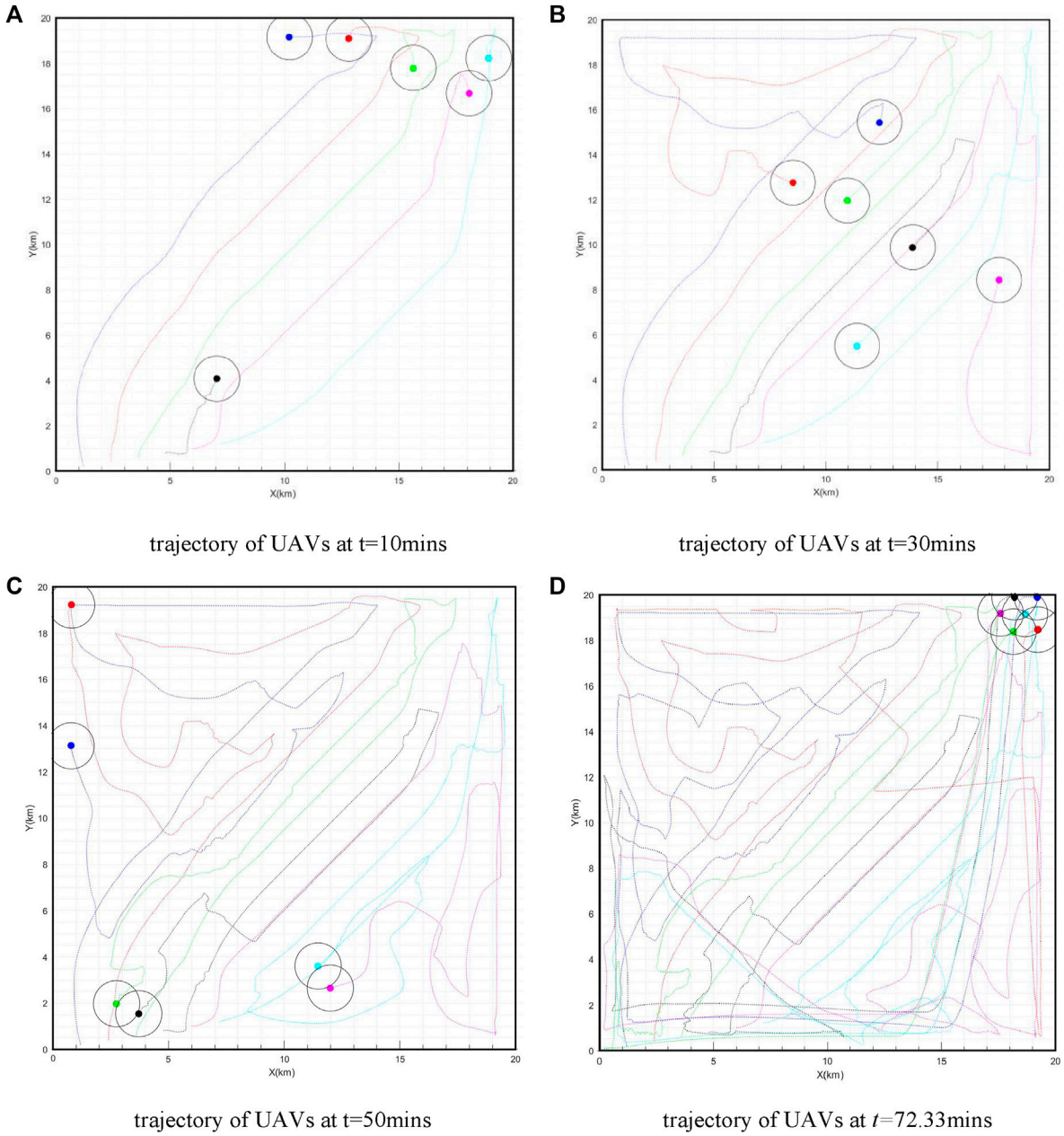


FIGURE 3 | Trajectory of UAVs at different time.

Firstly, the points that have not been effectively covered in the task area are defined as the following sets:

$$\Omega_e(t) = \{\boldsymbol{q} \in \Omega : 0 < \gamma_{\mathrm{I_N}}(\boldsymbol{q}, \mathrm{t}) < \mathrm{C}^*\} \tag{17}$$

Where $\Omega_e(t)$ represents a set of points that are not effectively covered in the area Ω at time t. Let $\overline{\Omega}_e(t)$ be the closure of set $\Omega_e(t)$. For UAV A_i, let $\widehat{\Omega}_e^i(t)$ represent the set of points with the shortest distance to $\boldsymbol{q}_i(t)$ in set $\Omega_e(t)$, that is, as follows:

$$\widehat{\Omega}_e^i(t) = \{\boldsymbol{q}^* \in \overline{\Omega}_e(\mathrm{t}) : \boldsymbol{q}^* = \mathrm{argmin}_{\mathrm{q} \in \overline{\Omega}_e(\mathrm{t})} ||\boldsymbol{q}_\mathrm{i} - \boldsymbol{q}||\} \tag{18}$$

A rule was set that a unique point q_m in the set can be chosen to calculate the UAV's speed at the next moment. At this time, according to the artificial potential field method (Zou and Li, 2019; Zou and Fan, 2020), the traction speed $\overrightarrow{v}_s$ of the UAV can be designed as follows:

$$\overrightarrow{v}_s = -k_1 \cdot (\overrightarrow{q}_i - \overrightarrow{q}_m), \quad k_1 > 0 \tag{19}$$

Where $k_1 > 0$ is the speed adjustment coefficient, $\overrightarrow{q}_i$ is the position vector of the projection of UAV on OXY plane, and $\overrightarrow{q}_m$ is the position vector of point q_m on OXY plane.

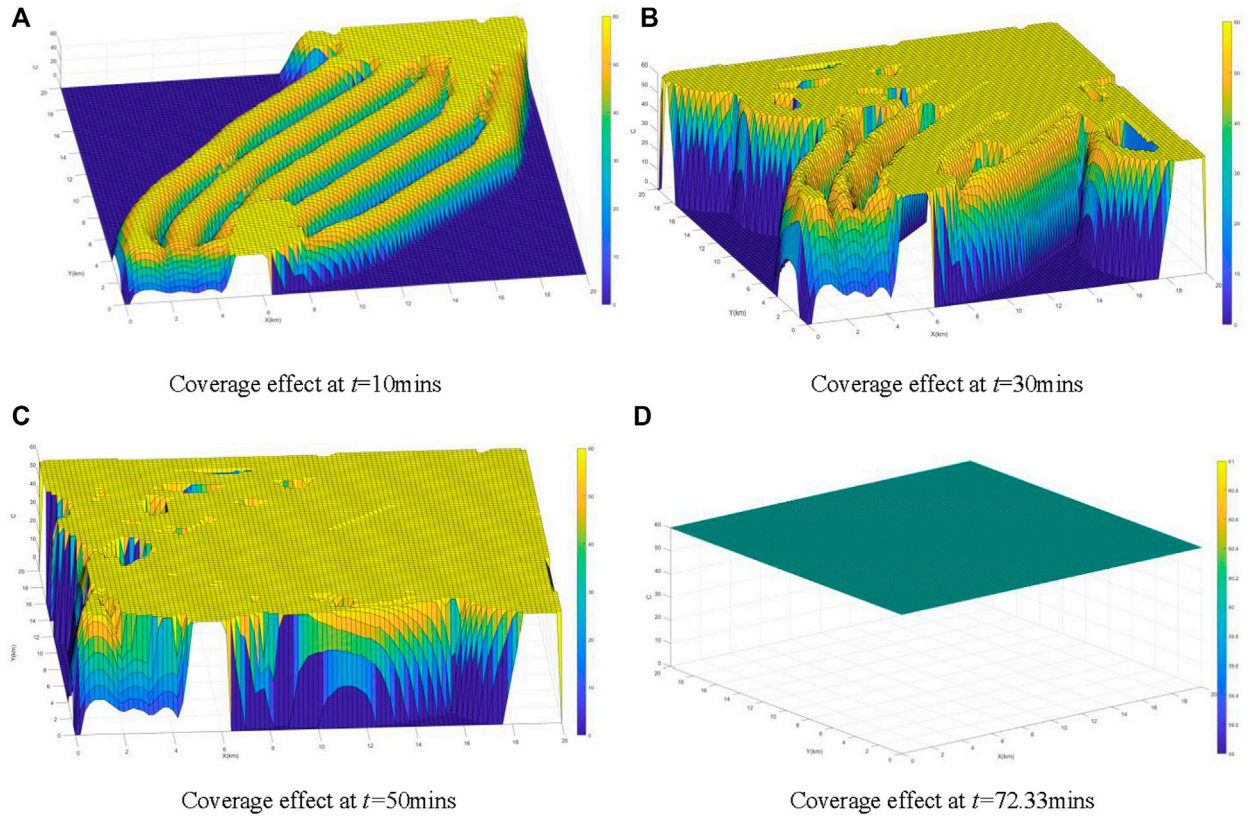


FIGURE 4 | Diagram of area coverage at different time.

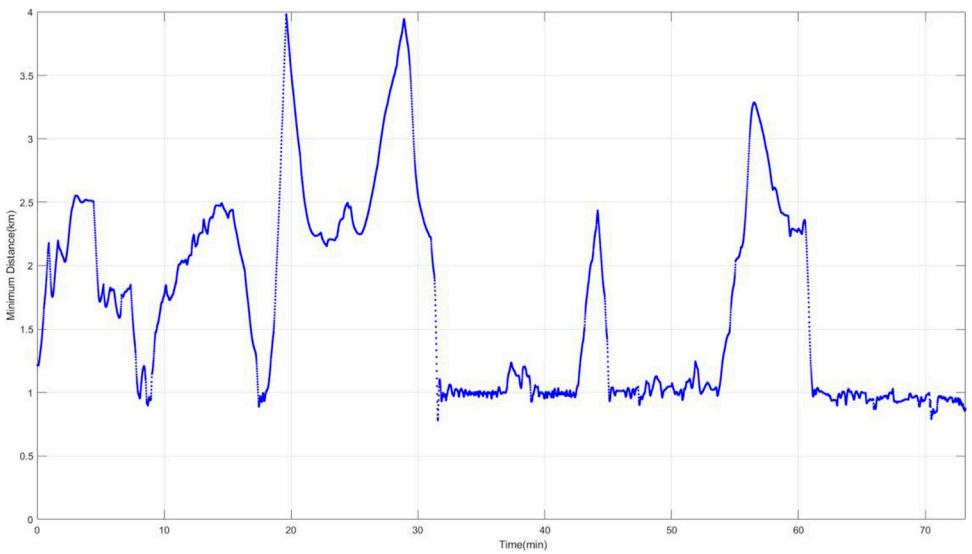


FIGURE 5 | The minimum distance between any two USVs at different time.

Above all, the expected optimal speed of each UAV $\overrightarrow{v}_i^*$ in the UAVs system can be described as the following:

$$\overrightarrow{v}_i^* = \begin{cases} -k_1 \cdot \dfrac{\partial H}{\partial q_i}, & H(t) \neq 0 \\ \overrightarrow{v}_s = -k_2 \cdot \left(\overrightarrow{q}_i - \overrightarrow{q}_m \right), & J(t) = C \neq 0 \end{cases} \tag{20}$$

The purpose of designing the acceleration of the UAV is to keep the current speed of the UAV consistent with the expected optimal speed. Therefore, if the acceleration $\overrightarrow{u}_i^*$ of the UAV A_i is defined as the function of the difference between the expected optimal speed $\overrightarrow{v}_i^*$ and the current speed $\overrightarrow{v}_i$, $\overrightarrow{u}_i^*$ can be expressed as (Zou and Li, 2019):

$$\overrightarrow{u}_i^* = k_3 (\overrightarrow{v}_i^* - v_i) \tag{21}$$

Where $k_3 > 0$ is the acceleration gain coefficient.

Simultaneous Cooperative Coverage Algorithm of Fixed Area Covered by UAVs

According to the above content, the pseudo-code of the optimization algorithm of the UAVs system is obtained as follows:

Algorithm 1: Simultaneous cooperative coverage algorithm of a fixed area covered by UAVs based on swarm intelligence.

Input: fixed area Ω, dynamic model of UAV, initial state of UAVs system, control gain parameter k_1,k_2,k_3;

Output: Output the optimal trajectory of each UAV;

1: Initialization: establishing an UAV object, and inputting initial position information and initial speed information of the UAV; Gain parameters of control rate, etc:

2: Build a task area model:

3: Calculating respectively the motion state information of each UAV A_i, $i \in I_N$, and setting the initial time $k = 1$;

4: while $J(t) > 0$ do

5: For each UAV do

6: If $H(t) \neq 0$;

7: Calculate the expected optimal speed of UAV A_i, $i \in I_N$ according to (16);

8: else

9: Calculate the expected optimal speed of UAV A_i, $i \in I_N$ according to (19);

10: End

11: Use (21) to calculate the acceleration U_i of UAV A_i;

12: Calculate the actual speed of UAV A_i at this time

13: According to the dynamic equation, calculating the position information $\boldsymbol{X_i}(k+1)$ of the UAV A_i at the next moment;

14: End

15: $k = k + 1$;

16: End

NUMERICAL SIMULATION

In order to verify the feasibility and effectiveness of the proposed method, a numerical calculation method is used to verify the method. Set the inspection area as a square area with a side length of 20 km. In total, six UAVs were used to cover the task area, and the initial position of each UAV is shown in the **Table 1**.

Assuming the effective coverage value $C = 60$ of each point in the area, the detection radius of a single UAV is 1 km, and the gains of the controllers in the algorithm are $k_1 = 0.8, k_2 = 0.5, k_3 = 1.2$, respectively, the trajectories of these UAVs at different times are shown in **Figure 3**.

The coverage of the whole task area at different times is shown in **Figure 4**.

It can be seen from the trajectory of UAVs at different times in **Figure 3** that all UAVs can perform inspection tasks in the task area, and there is no one crossed the border, which shows that the optimal motion direction obtained by the optimization algorithm can effectively restrain the behavior of UAVs and make them move in the direction with the lowest coverage in the sensing area. There are few overlapping areas among UAVs, which shows that the method based on undirected sensing set segmentation can effectively reduce the overlapping of sensing areas among UAVs. It can be seen from **Figure 4** that the algorithm can complete the inspection of the whole task area in a limited time, which shows that the algorithm is feasible and effective in controlling the UAVs to complete the inspection task of the designated area. To prove that the method of collision avoidance proposed in this paper is effective, we calculate the minimum distance between any two USVs in the system at any time, and the results are shown in **Figure 5**. It can be seen from **Figure 5** that the minimum distance between any two USVs is more than 0.5 km at any time. So it is obvious that there is no collision between any two USVs and the method proposed in this paper is effective and right.

When the number of UAVs is $N_a = 1, 2, 4, 6$, the time taken to complete the task area coverage is shown in **Table 2**.

Figure 6 shows the time-varying curve of the coverage rate of different numbers of UAVs to the mission area.

It can be seen from **Table 2** that the time spent by UAVs system is greatly reduced compared with single-UAV inspection, which shows that UAVs inspection system can greatly improve inspection efficiency compared with existing single-UAV inspection methods. It can be seen from **Figure 6** that with the increase of the number of UAVs, the area coverage efficiency of UAVs with different numbers increases obviously. This is mainly because the gradient operation of the penalty function is adopted in this algorithm, which makes the movement direction of the UAV choose the area with low coverage preferentially. Therefore, when the number of UAVs increases, the repeated paths of UAVs when performing inspection tasks can be effectively reduced.

TABLE 2 | Time to complete area coverage with different number of UAVs.

The number of UAVs	Time to complete area coverage *t* (mins)
1	362.04
2	194.52
4	120.35
6	72.33

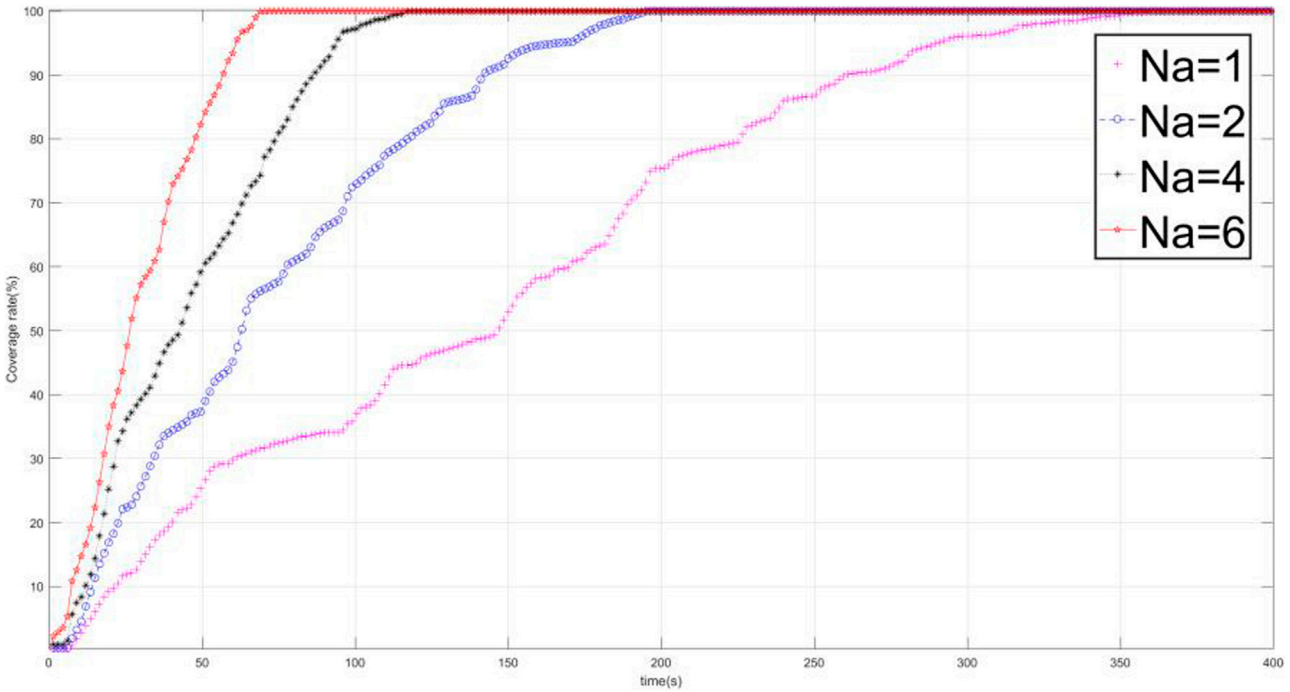


FIGURE 6 | The relation between the number of UAVs and the coverage rate of the area.

However, with the increase in the number of UAVs, the phenomenon of path repetition is inevitable. So the inspection efficiency of UAVs system would increase slowly with the increase of the number of UAVs.

CONCLUSION

Under ideal conditions, this paper studies how UAVs cooperate to improve the efficiency of the inspection task. An optimization algorithm for inspection with UAVs is given, and the feasibility and effectiveness of the algorithm are verified by numerical simulation. In this algorithm, firstly, the overlapping phenomenon of sensing areas of different UAVs is effectively reduced by dividing undirected sensing sets. Secondly, through the gradient operation of the penalty function, the area with the lowest coverage near the UAV is found and designated as the xxmoving direction of the UAV at the next moment, which reduces the repetition rate of the inspection path. The simulation results showed that the coverage efficiency of the UAVs system based on this algorithm increases with the number of UAVs.

To sum up, compared with the existing inspection methods, the UAV autonomous inspection optimization algorithm based on swarm intelligence can greatly improve the inspection efficiency and reduce the cost of inspections. UAV cooperative inspection will become the trend of development in the field of inspection in the future.

DATA AVAILABILITY STATEMENT

The raw data supporting the conclusion of this article will be made available by the authors, without undue reservation.

AUTHOR CONTRIBUTIONS

YY's main contribution is to design the algorithm. CJ-h's main contribution is to analyze the data and the results of experiments. GY's main contribution is to provide the application background. FZ's main contribution is to design the motion control law of UAVs. ZA-M's main contribution is to solve the problem of undirected sensing set segmentation. XB's main contribution is to obtain the coverage efficiency optimization index in the fixed area. LK's main contribution is to design the sensing area model of UAV and improve the algorithms.

FUNDING

This research were funded by the Scientific Research Staring Foundations of Shantou University (No: NTF19028) and (No: NTF20009) and supported by the Natural Science Foundation of Guangdong Province, China (Grant No.2021A1515011709).

REFERENCES

Burciu, Z. (2012). Reliability and Uncertainty in Determining Search Area during Search-And Rescue Action. *Polish Maritime Res.* 19 (1), 21–30. doi:10.2478/v10012-012-0003-9

Cai, Z. Q. (2020). *Research on Path Planning of 220k V Power Line Inspection UAV*. Shanxi, China: Taiyuan University of Science and Technology.

Che, M., Savkin, A. V., and Javed, F. (2011). Decentralized Control of a Group of mobile Robots for Deployment in Sweep Coverage. *Robotics nd A utonomous Syst.* 59 (7), 497–507. doi:10.1016/j.robot.2011.03.001

Cortés, J., Martínez, S., and Bullo, F. (2005). Spatially-distributed Coverage Optimization and Control with Limited-Range Interactions. *Esaim: Cocv* 11, 691–719. doi:10.1051/cocv:2005024

Dieter, H., and Jennifer, M. (2008). Renewable Energy-The Future for the Developing World. *Renew. Energ. Focus* 9 (1), 58–61. doi:10.1016/s1471-0846(08)70053-2

Fan, Z., Fang, Y., Li, W., Cai*, X., Wei, C., and Goodman, E. (2019). MOEA/D with Angle-Based Constrained Dominance Principle for Constrained Multi-Objective Optimization Problems. *Appl. Soft Comput.* 74 (1), 621–633. doi:10.1016/j.asoc.2018.10.027

Jiang, H., Liu, Z., Liu, C., Su, Y., and Zhang*, X. (2020). Community Detection in Complex Networks with an Ambiguous Structure Using central Node Based Link Prediction. *Knowledge-Based Syst.* 195, 1–13. doi:10.1016/j.knosys.2020.105626

Papatheodorou, S., Tzes, A., and Stergiopoulos, Y. (2016). Collaborative Visual Area Coverage Using Unmanned Aerial Vehicles. arXiv:1612.02065

Poonam, S., Manjaree, P., and Laxmi, S. (2020). Comparison of Traditional and Swarm Intelligence Based Techniques for Optimization of Hybrid Renewable Energy System. *Renew. Energ. Focus* 35 (12), 1–9. doi:10.1016/j.ref.2020.06.010

Stone, L. D., Keller, C. M., and Kratzke, T. M. (2014). Search for the Wreckage of Air France Flight AF 447. *Stat. Sci.* 29 (1), 69–80. doi:10.1214/13-sts420

Tian, Y., Lu, C., Zhang*, X., Tan, K. C., and Jin, Y. (2020a). Solving Large-Scale Multi-Objective Optimization Problems with Sparse Optimal Solutions via Unsupervised Neural Networks. *IEEE Trans. Cybernetics*. in press.

Tian, Y., Zhang, T., Xiao, J., Zhang*, X., and Jin, Y. (2020b). A Coevolutionary Framework for Constrained Multi-Objective Optimization Problems. *IEEE Trans. Evol. Comput.* in press.

Wang, C., Xu, R., Qiu, J., and Zhang, X. (2020). AdaBoost-inspired Multi-Operator Ensemble Strategy for Multi-Objective Evolutionary Algorithms. *Neurocomputing* 384, 243–255. doi:10.1016/j.neucom.2019.12.048

Xiang, X., Qiu, J., Xiao, J., and Zhang*, X. (2020). Demand Coverage Diversity Based Ant colony Optimization for Dynamic Vehicle Routing Problems. *Eng. Appl. Artif. Intelligence*. in press.

Yin, B. H. (2016). *High Voltage Distribution Network Visual Inspection System Based on Unmanned Aerial Vehicle (Uav) Research*. Guangzhou, China: Guangdong University of Technology.

Zhang, X., Tan, T., Zhou, B., Yu, T., Yang, B., and Huang, X. (2021). Adaptive Distributed Auction-Based Algorithm for Optimal Mileage Based AGC Dispatch with High Participation of Renewable Energy. *Int. J. Electr. Power Energ. Syst.* 124, 106371. doi:10.1016/j.ijepes.2020.106371

Zhang, X., Xu, Z., Yu, T., Yang, B., and Wang, H. (2020). Optimal Mileage Based AGC Dispatch of a GenCo. *IEEE Trans. Power Syst.* 35 (4), 2516–2526. doi:10.1109/tpwrs.2020.2966509

Zhou, Z. G., Zhou, H., Hu, B., et al. (2018). Application and Prospect of UAV in Power Line Inspection. *Scientific Technol. innovation* (23), 164–165. doi:10.3390/rs9080824

Zou, A. M., and Fan, Z. (2020). Distributed Fixed-time Attitude Coordination Control for Multiple Rigid Spacecraft. *Int. J. Robust Nonlinear Control.* 30 (1), 266–281. doi:10.1002/rnc.4763

Zou, A. M., and Li, W. (2019). Fixed-time Output-feedback Consensus Tracking Control for Second-order Multiagent Systems. *Int. J. Robust Nonlinear Control.* 29 (13), 4419–4434. doi:10.1002/rnc.4633

Conflict of Interest: The authors declare that the research was conducted in the absence of any commercial or financial relationships that could be construed as a potential conflict of interest.

Copyright © 2021 Yao, Jun-hua, Yi, Zhun, An-Min, Biao and Ke. This is an open-access article distributed under the terms of the Creative Commons Attribution License (CC BY). The use, distribution or reproduction in other forums is permitted, provided the original author(s) and the copyright owner(s) are credited and that the original publication in this journal is cited, in accordance with accepted academic practice. No use, distribution or reproduction is permitted which does not comply with these terms.

frontiers in Energy Research

ORIGINAL RESEARCH
published: 23 June 2021
doi: 10.3389/fenrg.2021.708456

A Random Forest and Current Fault Texture Feature–Based Method for Current Sensor Fault Diagnosis in Three-Phase PWM VSR

Lei Kou[1,2], Xiao-dong Gong[1,2,3], Yi Zheng[1,2], Xiu-hui Ni[1,2,3], Yang Li[4], Quan-de Yuan[5] and Ya-nan Dong[6]*

[1]Institute of Oceanographic Instrumentation, Qilu University of Technology (Shandong Academy of Sciences), Qingdao, China, [2]Joint China-Ukrainian Scientific and Innovation Laboratory for Hydroacoustics, Qingdao, China, [3]National Technical University of Ukraine "IgorSikorsky Kyiv Polytechnic Institute", Kyiv, Ukraine, [4]School of Electrical Engineering, Northeast Electric Power University, Jilin, China, [5]School of Computer Technology and Engineering, Changchun Institute of Technology, Changchun, China, [6]Qingdao Branch, China Merchants Bank, Qingdao, China

OPEN ACCESS

Edited by:
Bo Yang,
Kunming University of Science and Technology, China

Reviewed by:
Jun Yin,
North China University of Water Resources and Electric Power, China
Jia Cui,
Shenyang University of Technology, China

***Correspondence:**
Yi Zheng
zhengy@sdas.org

Specialty section:
This article was submitted to Smart Grids, a section of the journal Frontiers in Energy Research

Received: *12 May 2021*
Accepted: *25 May 2021*
Published: *23 June 2021*

Citation:
Kou L, Gong X, Zheng Y, Ni X, Li Y, Yuan Q and Dong Y (2021) A Random Forest and Current Fault Texture Feature–Based Method for Current Sensor Fault Diagnosis in Three-Phase PWM VSR. Front. Energy Res. 9:708456. doi: 10.3389/fenrg.2021.708456

Three-phase PWM voltage-source rectifier (VSR) systems have been widely used in various energy conversion systems, where current sensors are the key component for state monitoring and system control. The current sensor faults may bring hidden danger or damage to the whole system; therefore, this paper proposed a random forest (RF) and current fault texture feature–based method for current sensor fault diagnosis in three-phase PWM VSR systems. First, the three-phase alternating currents (ACs) of the three-phase PWM VSR are collected to extract the current fault texture features, and no additional hardware sensors are needed to avoid causing additional unstable factors. Then, the current fault texture features are adopted to train the random forest current sensor fault detection and diagnosis (CSFDD) classifier, which is a data-driven CSFDD classifier. Finally, the effectiveness of the proposed method is verified by simulation experiments. The result shows that the current sensor faults can be detected and located successfully and that it can effectively provide fault locations for maintenance personnel to keep the stable operation of the whole system.

Keywords: data-driven, random forests, current fault texture features, current sensors, fault diagnosis, three-phase PWM VSR

1 INTRODUCTION

Three-phase PWM VSR systems have been incrementally applied in the field of renewable energy systems, uninterruptible power supplies (UPSs), motor drivers, and so forth and have become an indispensable energy conversion device (Yang et al., 2016; Li and Yang, 2017; Bueno and Pomilio, 2018; Zhang et al., 2021). However, most of the renewable energy equipment is built in the mountains or remote areas away from the coast as the probability of sensor faults is very high under harsh climates or conditions (Bidadfar et al., 2021). Once the fault occurs in the key sensors related to the control system, it may cause the whole system to crash or run inefficiently (Peng et al., 2018). Therefore, the sensor fault diagnosis for three-phase PWM VSR systems is of great significance to ensure the reliability of the whole system.

According to the fault degree, the sensor fault types can be divided into hard faults and soft faults (Huang and Tan, 2008; Li et al., 2011; Darvishi et al., 2021). Hard faults are usually caused by sensor components' damage, or electrical system short circuit or open circuit, and the measured value will change greatly. Soft faults generally refer to the aging of sensor components. The harm of soft faults is not as great as that of hard faults, but long-term operation will reduce the efficiency and accelerate the aging of systems (Fravolini et al., 2019). For example, if the fault output signals of the current sensors are used as the input signals of the control system, it will affect the closed-loop feedback control, reduce the control performance, accelerate the aging of other equipment, and even lead to safety accidents. If the early soft fault features are monitored, the potential hazards can be found in time, the maintenance can be carried out in time, other health equipment can be protected, and the stability of the whole system can be ensured. Therefore, an accurate and effective fault diagnosis method for sensor faults is especially essential to enhance the reliability of the system, and it would be better if the fault locations can be detected.

Sensor fault detection and diagnosis (SFDD) methods can be broadly divided into data-driven and model-based methods (Reppa et al., 2015; Lee et al., 2021). The model-based methods are usually easy to integrate into control systems, but they also need to set complex thresholds, and the model-based methods are more difficult to apply in different fields, especially for a nonlinear system since the fault models are more difficult to establish (Kou et al., 2020; Wang et al., 2020). The data-driven methods can only use the historical data to establish a black-box model and use the mature black-box classifier to realize fault diagnosis and location, without the requirement of understanding the fault mathematical model about the sensor systems (Li F. et al., 2021; Shi et al., 2008). Therefore, the data-driven methods do not rely on mathematical models and have attracted attention of many scholars (Ojo et al., 2021). Lee et al. (2021) proposed a convolutional neural network (CNN)–based FDD method for battery energy storage systems to detect and classify false battery sensor data. Ojo et al. (2021) proposed a long short-term memory recurrent neural network (LSTM-RNN)–based thermal fault diagnosis method for lithium-ion batteries, which is an easy-to-implement way and does not need to pay attention to the complex mathematical modeling and parameters of battery physics. Chen et al. (2021a) proposed a hypergrid and statistical analysis–based FDD method, which can identify the sensor faults in wireless sensor networks. Jana et al. (2021) developed a distributed SFDD framework, in which a fuzzy deep neural network (FDNN) was adopted to detect and identify the sensor faults. Hajer and Okba (2020) proposed an interval-valued data-driven method, which was adopted to detect and locate the sensor faults in chemical industrial fields. Gao et al. (2020) proposed a CNN-based FDD method for micro-electromechanical system (MEMS) inertial sensors, in which the time-domain features of temperature-related sensor faults were adopted to train the data-driven FDD classifier. Haldimann et al. (2020) proposed a disentangled RNN and residual analysis–based SFDD method and developed a novel procedure to identify the fault sensors. Chen et al. (2021b) proposed an NN-based fault estimation method, which can obtain the accurate estimation of sensor faults. Li L. et al. (2021) proposed an LSTM-based CSFDD method, which can learn data features automatically and predict the acceleration responses from the measured data. According to the previous discussion, data-driven methods have been widely used for sensor fault diagnosis in various fields. Data-driven methods can effectively set up the nonlinear model between input features and fault modes, and the historical fault data under both normal and fault modes can be obtained from the simulation tools. However, the research on fault data extraction is very important, which is helpful to improve the fault diagnosis accuracy of the whole diagnosis system.

Many scholars have made good achievements in sensor fault diagnosis, which have given us many experiences. Although the artificial neural network (ANN) is a popular supervised learning algorithm, it is vulnerable to causing over-fitting and affecting the generalization ability and the diagnosis results. Therefore, the random forest (RF) algorithm is adopted to train the CSFDD classifier, which is not easy to fall into over-fitting due to the introduction of two randomness (random samples, random features) (Roy et al., 2020; Fezai et al., 2021). Meanwhile, the current fault texture features are proposed to train the RF CSFDD classifier, which can improve the feature diversity and the diagnosis accuracy. Hard faults can cause severe damage, and it usually takes a long time to change from soft faults to hard faults. Therefore, if soft faults can be detected and diagnosed in time, the equipment can be maintained in time and hard faults can be avoided.

As shown in **Figure 1**, the proposed method can be applied to the sensor fault diagnosis of power-electronics energy conversion systems in the photovoltaic system, the wind generation system, and so forth. Therefore, this paper mainly takes the soft faults and hard faults of current sensors in the three-phase PWM VSR as examples to verify the proposed CSFDD method. The detailed contributions of this study are summarized as follows:

(1) Only three-phase alternating currents (ACs) are selected as the input signals, additional sensors will not be introduced, and external interference can be avoided.
(2) It presents a current fault texture feature–based method, which can retain important fault features.
(3) A mature data-driven CSFDD classifier is trained by the RF algorithm and extracted current fault texture features, which can realize fault diagnosis and location for current sensors.

The remainder of this paper is organized as follows. **Section 2** describes the current sensor fault data and fault features. In **Section 3**, the current fault texture feature–based method is proposed and the mature RF CSFDD classifier is trained and compared with the classifier trained by original samples. In **Section 4**, the proposed method is verified by simulation experiments. Conclusions are drawn in **Section 5**.

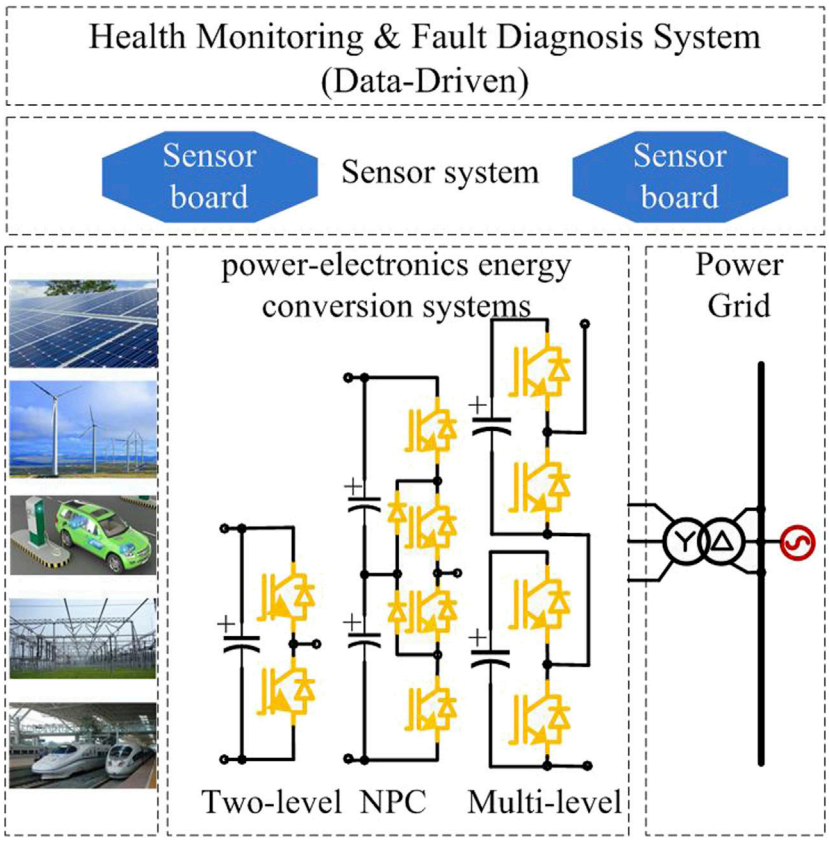


FIGURE 1 | Sensor fault diagnosis and health monitoring system.

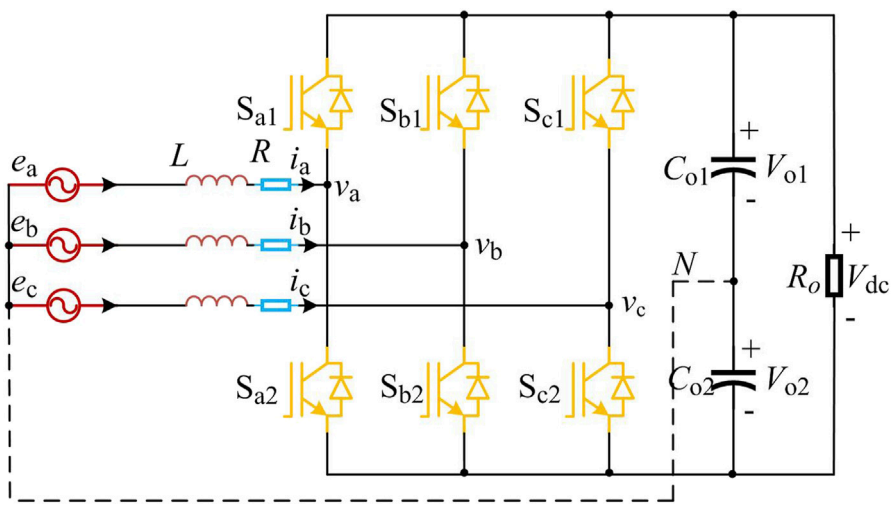


FIGURE 2 | Main circuit topology of the three-phase PWM VSR.

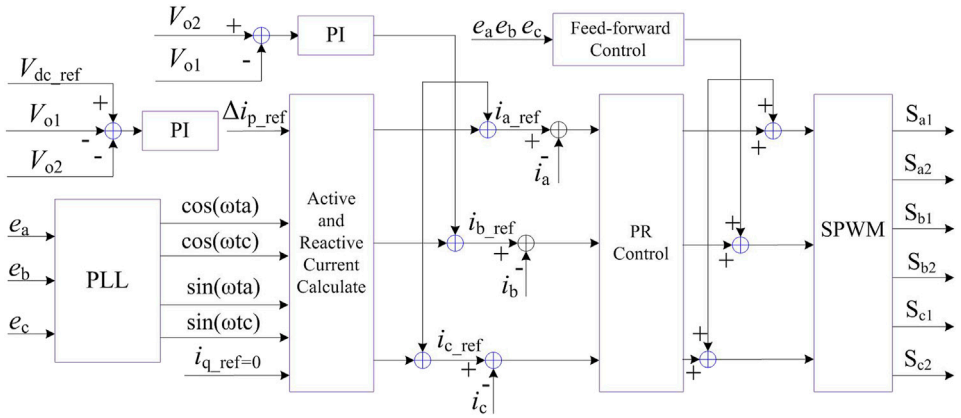


FIGURE 3 | Basic control block diagram.

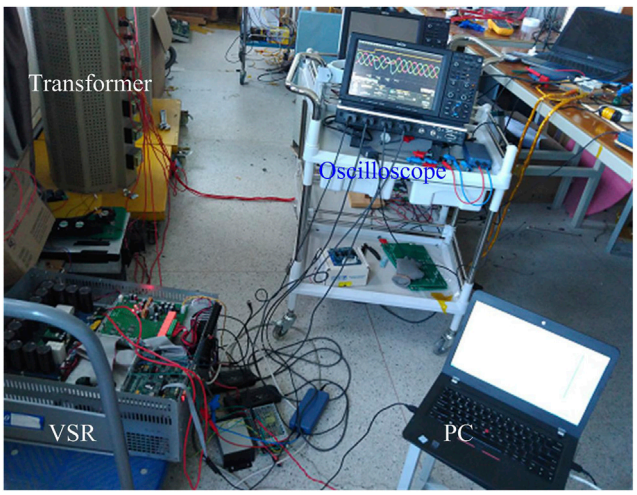


FIGURE 4 | Experimental platform.

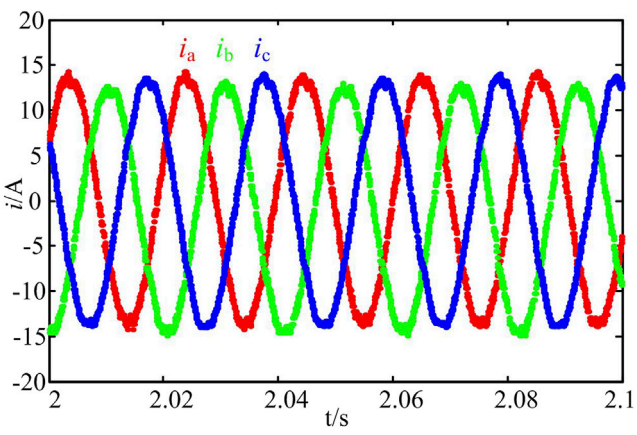


FIGURE 5 | Three-phase current data under normal conditions.

2 CURRENT SENSOR DATA OF THREE-PHASE PWM VSR

2.1 Structure of Three-Phase PWM VSR

The main circuit topology of the three-phase PWM VSR is depicted in **Figure 2**. As shown in **Figure 3**, the control strategy of the three-phase PWM VSR in this article is proportional resonance (PR), and it can be referred from Rocha et al. (2018).

Under ideal conditions, S_k stand for the switching functions, whose equation can be expressed as

$$S_k = \begin{cases} 1\,(S_{k1} = 1, S_{k2} = 0) \\ 0\,(S_{k1} = 0, S_{k2} = 1) \end{cases} (k = a, b, c) \tag{1}$$

where S_{k1} and S_{k2} stand for the upper and lower IGBTs' switching state of each phase, respectively.

The expression of v_k can be described as

$$\begin{cases} v_a = S_a V_{o1} - (1 - S_a) V_{o2}, \\ v_b = S_b V_{o1} - (1 - S_b) V_{o2}, \\ v_c = S_c V_{o1} - (1 - S_c) V_{o2}. \end{cases} \tag{2}$$

where the relational expressions of V_{o2} and the output voltage V_{dc} can be expressed as

$$V_{o1} = V_{o2} = \frac{1}{2} V_{dc}. \tag{3}$$

The dynamic model of the three-phase PWM rectifier can be expressed as follows:

$$\begin{cases} e_a = L\dfrac{di_a}{dt} + Ri_a + v_a, \\ e_b = L\dfrac{di_b}{dt} + Ri_b + v_b, \\ e_c = L\dfrac{di_c}{dt} + Ri_c + v_c. \end{cases} \tag{4}$$

According to **Eqs 1–4**, the mathematical models in the a–b–c frame for the three-phase PWM rectifier can be expressed as

$$\begin{cases} L\dfrac{di_a}{dt} = e_a - Ri_a - \dfrac{1}{2}V_{dc}(1-2S_a), \\ L\dfrac{di_b}{dt} = e_b - Ri_b - \dfrac{1}{2}V_{dc}(1-2S_b), \\ L\dfrac{di_c}{dt} = e_c - Ri_c - \dfrac{1}{2}V_{dc}(1-2S_c). \end{cases} \tag{5}$$

2.2 Current Sensor Fault Data

The three-phase currents of the three-phase PWM VSR are collected. **Figure 4** shows the experimental platform of the three-phase PWM VSR, where the input phase voltage is 40 V, the grid voltage frequency is 50 Hz, the load is 16Ω, the sampling frequency is 25.6 kHz, and the output voltage is 100 V. **Figure 5** shows the three-phase AC data under normal conditions.

Suppose the expression of normal three-phase currents is expressed as

$$\begin{cases} i_a = A\sin(\omega t), \\ i_b = A\sin\left(\omega t - \dfrac{2}{3}\pi\right), \\ i_c = A\sin\left(\omega t + \dfrac{2}{3}\pi\right), \end{cases} \tag{6}$$

where i_a, i_b, and i_c are the three-phase currents, A is the amplitude of three-phase currents, and $\omega = 100\pi$.

When the faults occur in the current sensors, the measured three-phase currents will be randomly increased by a number of different deviations. The measured three-phase currents can be expressed as

$$\begin{cases} i_a' = i_a + \sigma, \\ i_b' = i_b + \sigma, \\ i_c' = i_c + \sigma, \end{cases} \tag{7}$$

where $i_a^{'}$, $i_b^{'}$, and $i_c^{'}$ are the measured three-phase currents with different deviations and σ are the different deviations.

According to the research by Li et al. (2011) and Huang and Tan (2008), the soft faults and hard faults are simulated. Taking the soft fault and the hard fault of the A-phase current sensor as examples, the soft fault is simulated by reducing the measured A-phase current to 70% of the normal value (as shown in **Figure 6**) and the hard fault is simulated by reducing the measured value to 40% of the normal value (as shown in **Figure 7**). Meanwhile, the random noises are also superimposed. **Figure 8** shows the three-phase current data with multiple current sensor faults, **Figure 8A** shows the three-phase current data when soft faults occur in both A-phase and B-phase current sensors, and **Figure 8B** shows the three-phase current data when soft fault occurs in the A-phase current sensor and hard fault occurs in the B-phase current sensor. According to **Figures 6–8**, in some cases, when faults occur in multiple current sensors at the same time, the fault phase currents will have superposition effect of fault features. According to **Figures 6**, **7**, soft faults have little harm in a short time, but they will bring great harm when these faults develop into hard faults. Therefore, the soft faults of current sensors should be monitored in time to avoid hard faults.

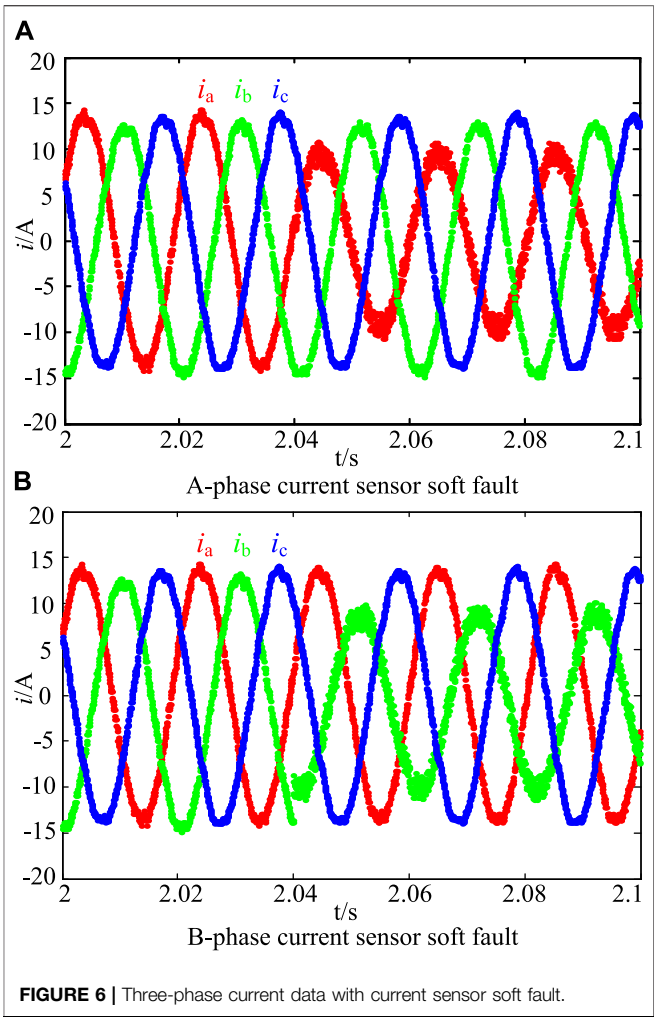


FIGURE 6 | Three-phase current data with current sensor soft fault.

3 CSFDD CLASSIFIER BASED ON RFS AND CURRENT FAULT TEXTURE FEATURES

In this section, the current fault texture features are proposed, and then the fault diagnosis method based on RFs and current fault texture features is described. And meanwhile compared with the CSFDD classifier trained with original samples, the CSFDD classifier trained with current fault texture feature samples obtained a higher accuracy.

3.1 Current Fault Texture Features

Current fault texture features are important attributes of three-phase ACs, which can reduce the data dimension, retain most of the main features, and improve the ability of anti-interference. The main current fault texture features include the mean value, standard deviation, smoothness, skewness, kurtosis, and root mean square value. The current fault texture features retain most of the important features of three-phase ACs in a cycle.

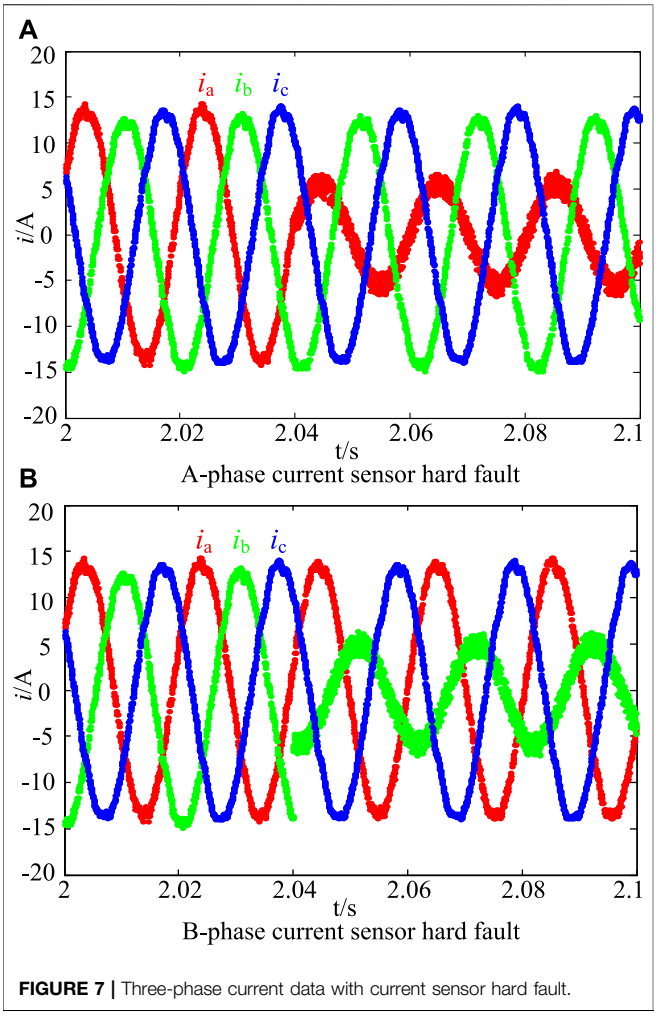


FIGURE 7 | Three-phase current data with current sensor hard fault.

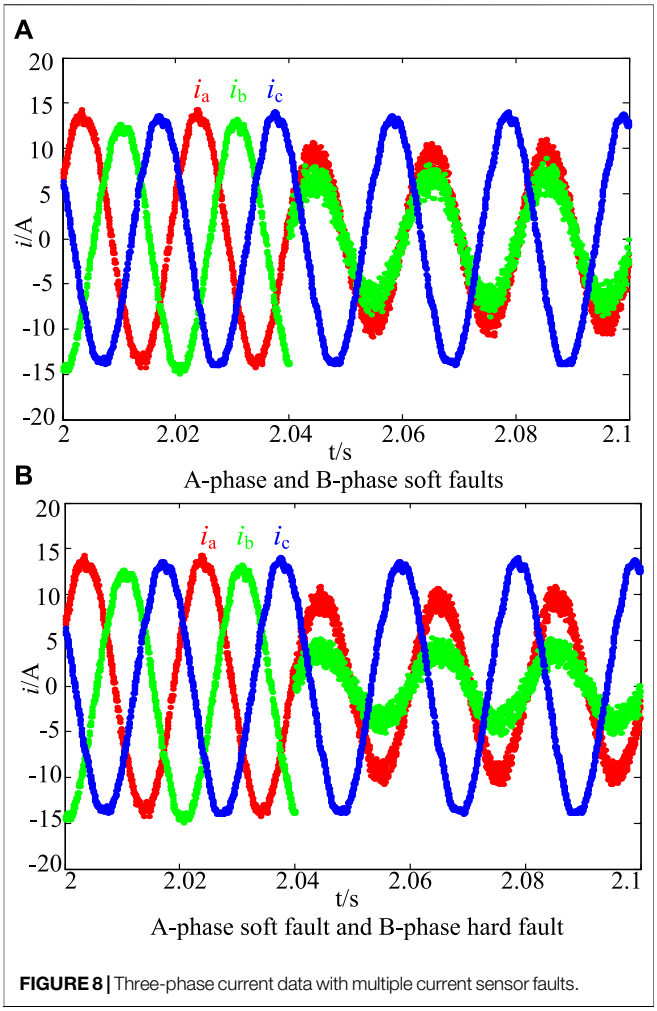


FIGURE 8 | Three-phase current data with multiple current sensor faults.

The expression of the mean value is

$$\bar{i} = \frac{1}{N}\sum_{j=0}^{N-1} i(j), \tag{8}$$

where N is the number of measured three-phase current values in a cycle and $i(j)$ is the j^{th} measured current value.

The expression of standard deviation is

$$\sigma_D = \sqrt{\frac{1}{N}\sum_{j=0}^{N-1}\left[i(j)-\bar{i}\right]^2}. \tag{9}$$

The expression of smoothness is

$$\sigma_P = 1 - \frac{1}{1+\sigma_D^2}. \tag{10}$$

The expression of skewness is

$$\sigma_S = \frac{1}{(N-1)\sigma_D^3}\sum_{j=0}^{N-1}\left[i(j)-\bar{i}\right]^3. \tag{11}$$

The expression of kurtosis is

$$\sigma_K = \frac{1}{(N-1)\sigma_D^4}\sum_{j=0}^{N-1}\left[i(j)-\bar{i}\right]^4. \tag{12}$$

The expression of the root mean square value is

$$\sigma_R = \sqrt{\frac{1}{N}\sum_{j=0}^{N-1} i(j)^2}. \tag{13}$$

Equations 8–13 are adopted to calculate the fault texture features of ABC three-phase currents, and the current fault texture features are used as the input signals of RFs. The input signals include ($\bar{i}_a$, σ_{aD}, σ_{aP}, σ_{aS}, σ_{aK}, σ_{aR}), ($\bar{i}_b$, σ_{bD}, σ_{bP}, σ_{bS}, σ_{bK}, σ_{bR}), and ($\bar{i}_c$,σ_{cD}, σ_{cP}, σ_{cS}, σ_{cK}, σ_{cR}). If 200 points are sampled in each cycle, the dimension of the original samples is 600 and the dimension of current fault texture feature samples will be reduced to 18. Through this method, the important features of the signal are extracted and the dimension of the training samples is reduced, which will be more conducive to improving the accuracy of the diagnosis classifier.

TABLE 1 | Process of the bagging classification algorithm.

(1) Input: Sample training set $S=(X^1, Y^1), (X^2, Y^2), \ldots, (X^N, Y^N)$,
X^N represents the feature attribute, Y^N represents the sample label;
The total number of training is M, ξ is the function of the weak classifier,
S_{sub-j} is the selected sample training set;
(2) for j = 1, 2, 3, …, M
(3) $h_j(X) = \xi(S, S_{sub-j})$;
(4) end
(5) Output: $H(X) = \text{argmax}\left(\sum_{j=1}^{M} \prod h_j(X) = Y\right)$

3.2 Training and Evaluation of the CSFDD Classifier

As a popular data-driven classifier design approach, RFs are applied to train the CSFDD classifier with the features ($\bar{i}_a$, σ_{aD}, σ_{aP}, σ_{aS}, σ_{aK}, σ_{aR}), ($\bar{i}_b$, σ_{bD}, σ_{bP}, σ_{bS}, σ_{bK}, σ_{bR}), and ($\bar{i}_c$,σ_{cD}, σ_{cP}, σ_{cS}, σ_{cK}, σ_{cR}). In general, over-fitting always is a troubled problem for most machine learning algorithms, but this problem does not easily occur in the RF classifier (Phan et al., 2020). That is because the RF algorithms can overcome the problem of over-fitting with the help of enough decision trees. The excellent performance of RFs in supervised machine learning is the reason why they are adopted to train the CSFDD classifier.

The RF algorithm is a widely used ensemble learning algorithm, which can make joint decision through multiple weak classification models to improve the accuracy of decision (Gu et al., 2020). In the training process of RFs, samples and features are randomly selected in order to increase the difference between each weak model; the tree model can be more diversified by this way. The bagging method is usually used in the RF algorithm (Song et al., 2016). In the bagging method, the independence of different models is improved by using different independent training datasets. Through random sampling with the replacement method, the training sample set is extracted from the original sample set, and n training samples sets are extracted from the original sample set each time.

TABLE 2 | Fault sensors and class labels.

Fault sensors	Class labels					
	S1	S2	S3	H1	H2	H3
Normal state	0	0	0	0	0	0
A-phase soft fault	1	0	0	0	0	0
A-phase hard fault	0	0	0	1	0	0
B-phase soft fault	0	1	0	0	0	0
B-phase hard fault	0	0	0	0	1	0
C-phase soft fault	0	0	1	0	0	0
C-phase hard fault	0	0	0	0	0	1
A–B–phase soft faults	1	1	0	0	0	0
A–B–phase hard faults	0	0	0	1	1	0
A-phase soft fault and B-phase hard fault	1	0	0	0	1	0

In the training sets, some samples may have been repeatedly extracted and some samples may have never been selected. Using n training sets to train n models, n models are independent of each other, and then the integration model is obtained by voting.

Suppose that the relationship between input samples X and output class labels Y is $Y = f(X)$. As shown in **Figures 10**, **11**, for the models $h_1(X), h_2(X), \ldots, h_N(X)$ of N different weak classifiers, the expected error of each model is

$$\begin{aligned} \text{err}(h_k) &= E_X\left[\left(h_k(X) - f(X)\right)^2\right] \\ &= E_X\left[\varepsilon_k^2(X)\right], \end{aligned} \tag{14}$$

where $\varepsilon_k(X) = h_k(X) - f(X)$ is the k^{th} error of the input samples X. And the average error of all weak models is

$$\begin{aligned} \overline{\text{err}}(h_k) &= \frac{1}{N}\sum_{k=1}^{N} E_X\left[\left(h_k(X) - f(X)\right)^2\right] \\ &= \frac{1}{N}\sum_{k=1}^{N} E_X\left[\varepsilon_k^2(X)\right]. \end{aligned} \tag{15}$$

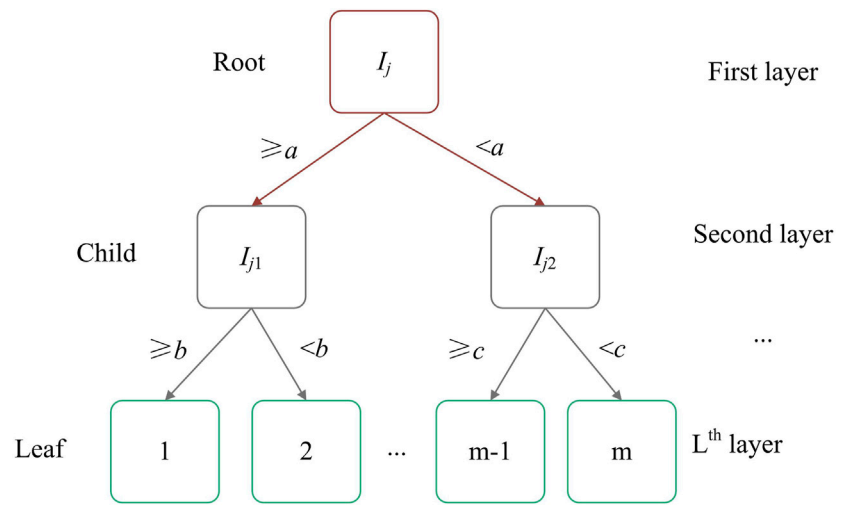


FIGURE 9 | CART structure.

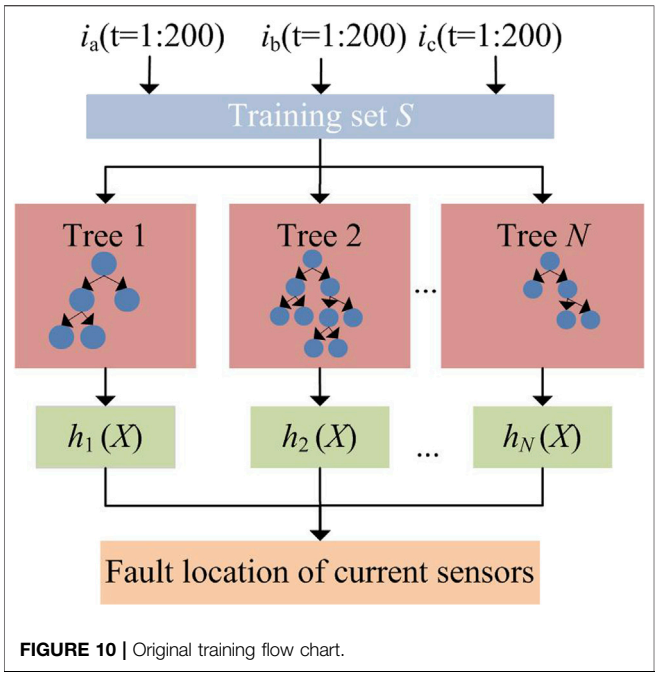


FIGURE 10 | Original training flow chart.

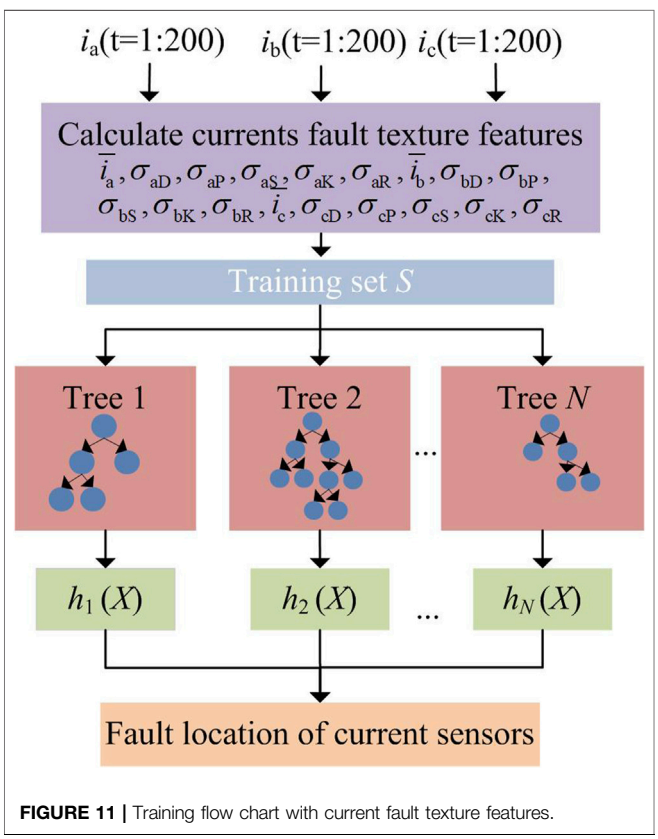


FIGURE 11 | Training flow chart with current fault texture features.

The direct average method is also adopted to integrate all weak classification models, and the expression of the integrated model is

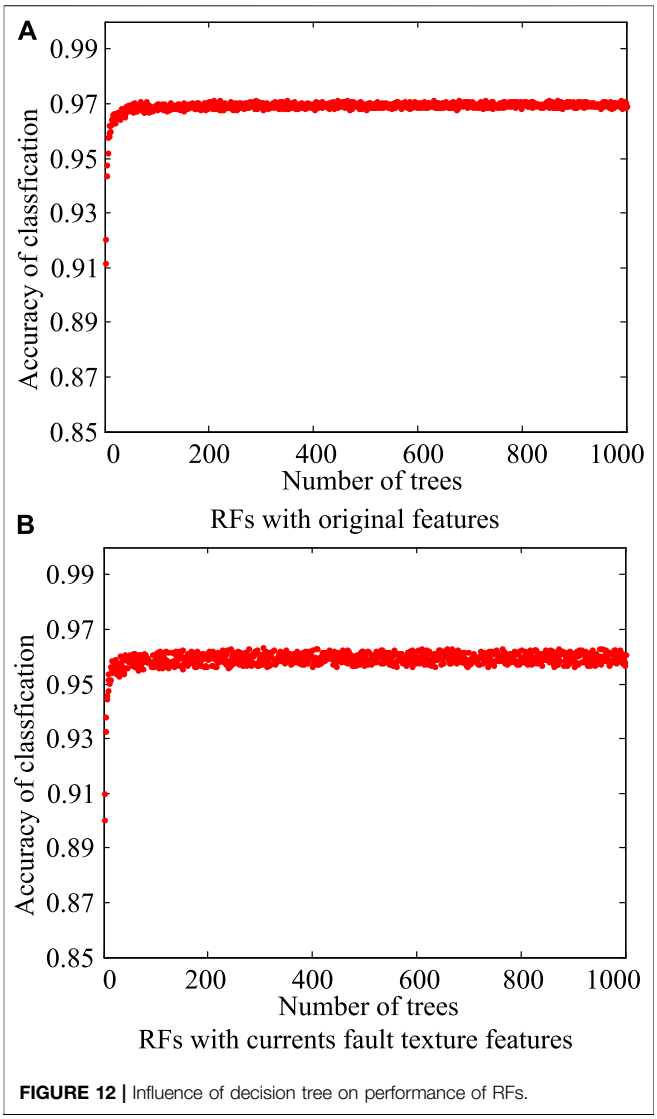


FIGURE 12 | Influence of decision tree on performance of RFs.

$$H(X) = \frac{1}{N}\sum_{k=1}^{N} h_k(X). \tag{16}$$

The expected error of the integrated model is

$$\begin{aligned} \mathrm{err}(H) &= E_X\left[\left(\frac{1}{N}\sum_{k=1}^{N} h_k(X) - f(X)\right)^2\right] \\ &= \frac{1}{N^2}E_X\left[\left(\sum_{k=1}^{N} \varepsilon_k(X)\right)^2\right] \\ &= \frac{1}{N^2}\sum_{k=1}^{N}\sum_{i=1}^{N} E_X[\varepsilon_k(X)\varepsilon_i(X)], \end{aligned} \tag{17}$$

where $E_X[\varepsilon_k(X)\varepsilon_i(X)]$ is the correlation of two different models' errors. When the error of each weak classification model is irrelevant, for any $n \neq i$, $E_X[\varepsilon_k(X)\varepsilon_i(X)] = 0$. When the error of each weak classification model is the same, for any $n \neq i$,

TABLE 3 | Accuracy of RFs with original features.

Fault sensors	Diagnosis accuracy	Misdiagnosis rate
Normal state	0.9671	0.0329
A-phase soft fault	0.9606	0.0394
A-phase hard fault	0.9652	0.0348
B-phase soft fault	0.9486	0.0514
B-phase hard fault	0.9673	0.0327
C-phase soft fault	0.9526	0.0474
C-phase hard fault	0.9611	0.0389
A–B–phase soft faults	0.9643	0.0357
A–B–phase hard faults	0.9606	0.0394
A-phase soft fault and B-phase hard fault	0.9666	0.0334

$\varepsilon_k(X) = \varepsilon_i(X)$. Because $\varepsilon_k(X) \geq 0$ for all weak classification models, the following relationships should be satisfied:

$$\overline{\mathrm{err}}(h) \geq \mathrm{err}(H) \geq \frac{1}{N}\overline{\mathrm{err}}(h). \tag{18}$$

According to the above derivation, the greater the difference between all weak models is, the better the performance of the integrated model will be. At the same time, the error will gradually decrease and tend to zero with the increase in the number of models.

The decision tree is a widely used classification model in the classification algorithm, where the classification and regression tree (CART) has the advantages of fast training speed, good stability, and supporting multiple segmentation of continuous data and feature data. Bagging algorithm plays a key role in the construction of random forest classifier, and its process is shown in **Table 1**. As shown in **Figure 9**, the CART is often used as the basic learning algorithm of RFs, whose structure is a binary classification tree.

As shown in **Table 2**, the class labels $S_k(k = 1–3)$ mean the case when the soft faults are in A-phase, B-phase, and C-phase current sensors, $H_k(k = 1–3)$ mean the case when the hard faults are in A-phase, B-phase, and C-phase current sensors, and $S_k = 1$ or $H_k = 1$ means the fault occurs in the current sensor. Each sample in the training datasets consists of several current fault texture features and one class label, for example, X=($\bar{i}_a$, σ_{aD}, σ_{aP}, σ_{aS}, σ_{aK}, σ_{aR}, $\bar{i}_b$, σ_{bD}, σ_{bP}, σ_{bS}, σ_{bK}, σ_{bR}, $\bar{i}_c$,σ_{cD}, σ_{cP}, σ_{cS}, σ_{cK}, σ_{cR}), Y=(S1, S2, S3, H1, H2, H3). The purpose of the RF classifier is adopted to make a useful model with better classification performance, and it will formulate some set of rules when inputting a training dataset with features X and labels Y into the RF algorithm (as shown in **Figure 10**). What is most mysterious is that it can correctly predict the target class label of the sample in the testing datasets, which are given only the features without class labels. **Figure 10** shows the original training flow chart of the RF algorithm with original features, and **Figure 11** shows the training flow chart of the RF algorithm with current fault texture features. The biggest difference between them is that the latter introduces the current fault texture feature–based method to transform the original data features, where the current fault texture features are obtained after the transform of three-phase currents. The current fault texture feature–based method is adopted to perform feature extraction, and the data-driven method is used to train the CSFDD classifier with the extracted features.

In the training process of the CSFDD classifier, the training set is formed by randomly selecting 16,800 samples from 24,000 samples under different operating conditions, and the rest samples are used as the test samples. Here, the repeated cross test method is adopted to train the RF classifier. **Figure 12A** shows the trend of diagnosis results varying with trees when the CSFDD classifier was trained with original features, and when the number of RF decision trees is set as 305, the highest accuracy is 0.9636. **Figure 12B** shows the trend of diagnosis results varying with trees when the CSFDD classifier was trained with current fault texture features, and when the RF trees' number is set as 209, the highest accuracy is 0.9715.

Table 3 shows the diagnosis accuracy of RFs with original features, in which the CSFDD classifier was trained with the original fault current samples (as shown in **Figure 10**).

TABLE 4 | Accuracy of RFs with current fault texture features.

Fault sensors	Diagnosis accuracy	Misdiagnosis rate
Normal state	0.9745	0.0255
A-phase soft fault	0.9743	0.0257
A-phase hard fault	0.9650	0.0350
B-phase soft fault	0.9663	0.0337
B-phase hard fault	0.9752	0.0248
C-phase soft fault	0.9715	0.0285
C-phase hard fault	0.9725	0.0275
A–B–phase soft faults	0.9735	0.0265
A–B–phase hard faults	0.9675	0.0325
A-phase soft fault and B-phase hard fault	0.9730	0.0270

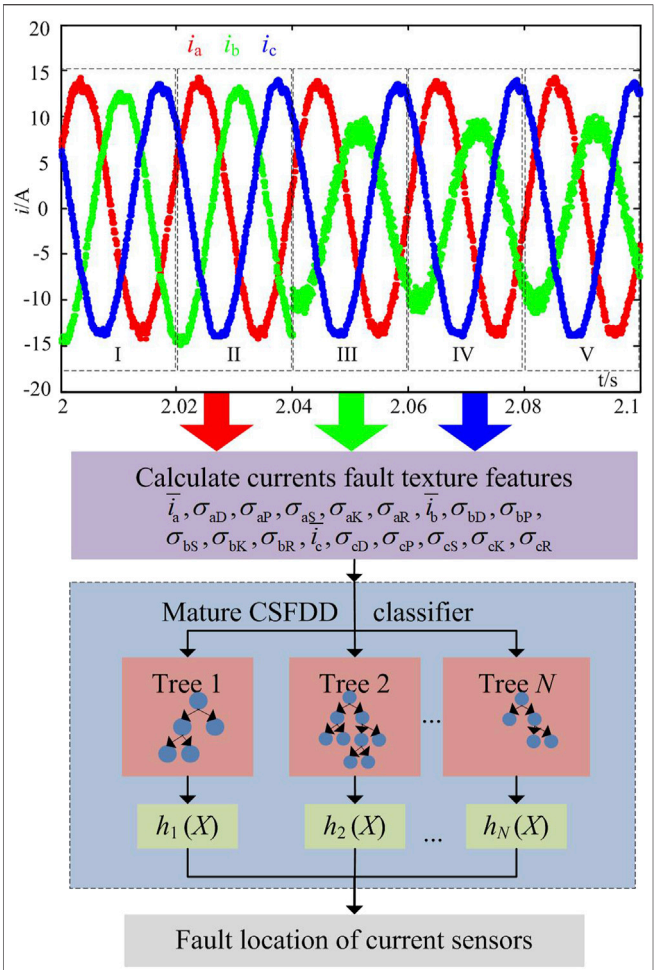


FIGURE 13 | Flow chart of sensor fault diagnosis.

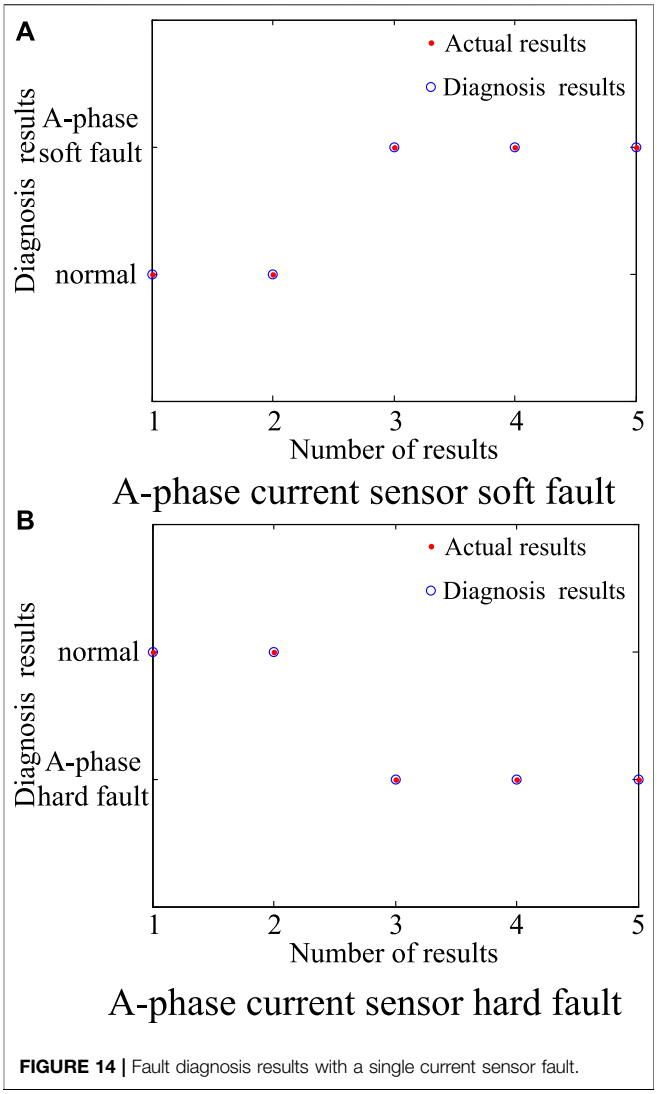


FIGURE 14 | Fault diagnosis results with a single current sensor fault.

Table 4 shows the diagnosis accuracy of the proposed method, in which the CSFDD classifier was trained with current fault texture features (as shown in **Figure 11**). According to **Tables 3**, **4**, since the original fault current samples contain more noise, and the current fault texture features retain a large number of important features and remove noise, the accuracies of the proposed method are higher than those of RFs with original features. The proposed method offers high accuracy even with a training dataset of 70% of total samples compared with the test/validation dataset, which gives more than 97.15% average accuracy for different types of faults.

4 SIMULATION EXPERIMENTS

To verify the validity of the CSFDD classifier based on RFs and current fault texture features, the simulation experiments of soft and hard faults are carried out, and the soft fault and hard fault of the A-phase current sensor and multiple current sensor faults are studied as examples. **Figure 13** shows the flow chart of sensor fault diagnosis, where the current samples are five cycles of fault samples, and it contains five sets of samples. When a set of fault samples are input each time, they will be processed by the current fault texture feature method and then input into the mature CSFDD classifier to get the final diagnosis results. The data of **Figures 6A**, **7A**, **8** are input into the mature CSFDD classifier (samples of one cycle are input at a time, as shown in **Figure 13**), and then the location and type of the fault sensor can be diagnosed.

Figure 14 shows the diagnosis results of five cycles. **Figure 14A** shows the diagnosis results of **Figure 6A**; at the beginning of diagnosis, the results are normal and the sensors work normally. When the soft fault occurs in the A-phase current sensor, the diagnosis results turn to A-phase soft faults, and the diagnosis results are consistent with the actual results. **Figure 14B** shows the diagnosis results of **Figure 7A**; the early diagnosis results are normal, the diagnosis results turn to A-phase hard faults when the hard fault occurs in the A-phase current sensor, and the diagnosis results are consistent with the actual results.

Figure 15 shows the fault diagnosis results with multiple current sensor faults. **Figure 15A** shows the diagnosis results

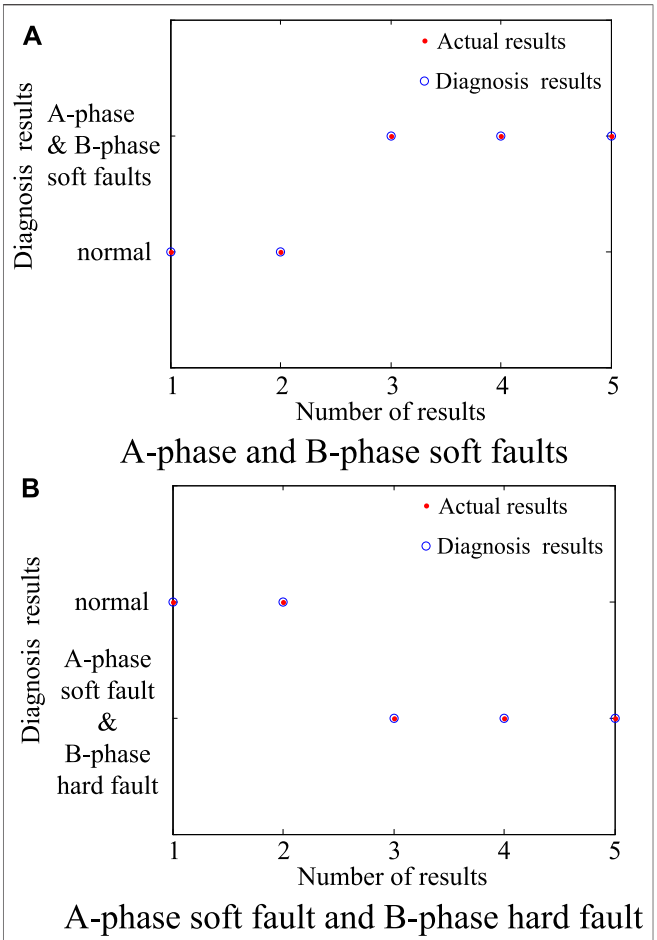


FIGURE 15 | Fault diagnosis results with multiple current sensor faults.

of **Figure 8A**, and **15B** shows the diagnosis results of **Figure 8B**. According to the diagnosis results, the proposed method can locate multiple faults and different types of faults.

According to the diagnosis results of **Figures 14**, **15**, the current sensor faults can be effectively diagnosed and located by the proposed method.

5 CONCLUSION

This paper proposed an RF and current fault texture feature–based method for current sensor fault diagnosis in three-phase PWM VSR systems. The proposed method employed only three-phase ACs without other additional hardware. Firstly, the current fault texture feature–based method is adopted for feature extraction, which can retain a large number of important features and remove noise. After that, the current fault texture features are used to train the CSFDD fault classifier by the RF algorithm, and the accuracy of the proposed method is higher than those of RFs with original features. Finally, the results of simulation experiments show that the current sensor faults can be effectively diagnosed and located by the proposed method, and the experimental results prove the effective and robust performance of the proposed method.

DATA AVAILABILITY STATEMENT

The raw data supporting the conclusions of this article will be made available by the authors, without undue reservation.

AUTHOR CONTRIBUTIONS

LK and X-DG involved in data curation and writing the original draft. LK, X-DG, and YL performed formal analysis. LK, X-HN, and Y-ND ran the software. LK, YZ, X-HN, YL, and Q-DY validated the data. LK, X-DG, YZ, X-HN, YL, Q-DY, and Y-ND reviewed and edited the paper. YZ administered the project and obtained the resources.

FUNDING

This research is funded by Special Program on Self-Innovation Ability Improvement (Smart Ocean Project) Central Infrastructure Investment Program 2020 under grant number Z135060000070.

REFERENCES

Bidadfar, A., Saborío-Romano, O., Cutululis, N. A., and Sorensen, P. E. (2021). Control of Offshore Wind Turbines Connected to Diode-Rectifier-Based Hvdc Systems. *IEEE Trans. Sustain. Energ.* 12, 514–523. doi:10.1109/TSTE.2020.3008606

Bueno, A. G., and Pomilio, J. A. (2018). "Balancing Voltage in the Dc Bus with Split Capacitors in Three-phase Four-Wire Pwm Boost Rectifier," in 2018 13th IEEE International Conference on Industry Applications (INDUSCON), 523–529. doi:10.1109/INDUSCON.2018.8627210

Chen, L., Li, G., and Huang, G. (2021a). A Hypergrid Based Adaptive Learning Method for Detecting Data Faults in Wireless Sensor Networks. *Inf. Sci.* 553, 49–65. doi:10.1016/j.ins.2020.12.011

Chen, L., Liu, M., Shi, Y., Zhang, H., and Zhao, E. (2021b). Adaptive Fault Estimation for Unmanned Surface Vessels with a Neural Network Observer Approach. *IEEE Trans. Circuits Syst.* 68, 416–425. doi:10.1109/TCSI.2020.3033803

Darvishi, H., Ciuonzo, D., Eide, E. R., and Rossi, P. S. (2021). Sensor-fault Detection, Isolation and Accommodation for Digital Twins via Modular Data-Driven Architecture. *IEEE Sensors J.* 21, 4827–4838. doi:10.1109/JSEN.2020.3029459

Fezai, R., Dhibi, K., Mansouri, M., Trabelsi, M., Hajji, M., Bouzrara, K., et al. (2021). Effective Random forest-based Fault Detection and Diagnosis for Wind Energy Conversion Systems. *IEEE Sensors J.* 21, 6914–6921. doi:10.1109/JSEN.2020.3037237

Fravolini, M. L., Del Core, G., Papa, U., Valigi, P., and Napolitano, M. R. (2019). Data-driven Schemes for Robust Fault Detection of Air Data System Sensors. *IEEE Trans. Contr. Syst. Technol.* 27, 234–248. doi:10.1109/TCST.2017.2758345

Gao, T., Sheng, W., Zhou, M., Fang, B., and Zheng, L. (2020). Mems Inertial Sensor Fault Diagnosis Using a Cnn-Based Data-Driven Method. *Int. J. Patt. Recogn. Artif. Intell.* 34, 2059048. doi:10.1142/S021800142059048X

Gu, K., Zhang, Y., and Qiao, J. (2020). Random forest Ensemble for River Turbidity Measurement from Space Remote Sensing Data. *IEEE Trans. Instrum. Meas.* 69, 9028–9036. doi:10.1109/TIM.2020.2998615

Lahdhiri, H., and Taouali, O. (2021). Interval Valued Data Driven Approach for Sensor Fault Detection of Nonlinear Uncertain Process. *Measurement* 171, 108776. doi:10.1016/j.measurement.2020.108776

Haldimann, D., Guerriero, M., Maret, Y., Bonavita, N., Ciarlo, G., and Sabbadin, M. (2020). A Scalable Algorithm for Identifying Multiple-Sensor Faults Using Disentangled Rnns. *IEEE Trans. Neural Netw. Learn. Syst.* 1, 1–14. doi:10.1109/TNNLS.2020.3040224

Huang, S. N., and Kok Kiang Tan, K. K. (2008). Fault Detection, Isolation, and Accommodation Control in Robotic Systems. *IEEE Trans. Automat. Sci. Eng.* 5, 480–489. doi:10.1109/TASE.2008.917009

Jan, S. U., Lee, Y. D., and Koo, I. S. (2021). A Distributed Sensor-Fault Detection and Diagnosis Framework Using Machine Learning. *Inf. Sci.* 547, 777–796. doi:10.1016/j.ins.2020.08.068

Kou, L., Liu, C., Cai, G.-w., Zhang, Z., Zhou, J.-n., and Wang, X.-m. (2020). Fault Diagnosis for Three-phase Pwm Rectifier Based on Deep Feedforward Network with Transient Synthetic Features. *ISA Trans.* 101, 399–407. doi:10.1016/j.isatra.2020.01.023

Lee, H., Kim, K., Park, J.-H., Bere, G., Ochoa, J. J., and Kim, T. (2021). Convolutional Neural Network-Based False Battery Data Detection and Classification for Battery Energy Storage Systems. *IEEE Trans. Energ. Convers.*, 1. doi:10.1109/TEC.2021.3061493

Li, Y., and Yang, Z. (2017). Application of Eos-Elm with Binary Jaya-Based Feature Selection to Real-Time Transient Stability Assessment Using Pmu Data. *IEEE Access* 5, 23092–23101. doi:10.1109/ACCESS.2017.2765626

Li, H., Zhao, M., Zhao, B., Tang, X., and Liu, Z. (2011). Fault Diagnosis Methods for Key Sensors of Doubly Fed Wind Turbine. *Proc. CSEE* 31, 73–78. doi:10.13334/j.0258-8013.pcsee.2011.06.011

Li, F., Li, Q., Zhang, J., Kou, J., Ye, J., Song, W., et al. (2021a). Detection and Diagnosis of Data Integrity Attacks in Solar Farms Based on Multilayer Long Short-Term Memory Network. *IEEE Trans. Power Electron.* 36, 2495–2498. doi:10.1109/TPEL.2020.3017935

Li, L., Liu, G., Zhang, L., and Li, Q. (2021b). Fs-lstm-based Sensor Fault and Structural Damage Isolation in Shm. *IEEE Sensors J.* 21, 3250–3259. doi:10.1109/JSEN.2020.3022099

Ojo, O., Lang, H., Kim, Y., Hu, X., Mu, B., and Lin, X. (2021). A Neural Network Based Method for thermal Fault Detection in Lithium-Ion Batteries. *IEEE Trans. Ind. Electron.* 68, 4068–4078. doi:10.1109/TIE.2020.2984980

Peng, Y., Qiao, W., Qu, L., and Wang, J. (2018). Sensor Fault Detection and Isolation for a Wireless Sensor Network-Based Remote Wind Turbine Condition Monitoring System. *IEEE Trans. Ind. Applicat.* 54, 1072–1079. doi:10.1109/TIA.2017.2777925

Phan, D., Nguyen, N., Pathirana, P. N., Horne, M., Power, L., and Szmulewicz, D. (2020). A Random forest Approach for Quantifying Gait Ataxia with Truncal and Peripheral Measurements Using Multiple Wearable Sensors. *IEEE Sensors J.* 20, 723–734. doi:10.1109/JSEN.2019.2943879

Reppa, V., Papadopoulos, P., Polycarpou, M. M., and Panayiotou, C. G. (2015). A Distributed Architecture for Hvac Sensor Fault Detection and Isolation. *IEEE Trans. Contr. Syst. Technol.* 23, 1323–1337. doi:10.1109/TCST.2014.2363629

Rocha, M. A., de Souza, W. G., Serni, P. J. A., Andreoli, A. L., Clerice, G. A. M., and da Silva, P. S. (2018). "Control of Three-phase Pwm Boost Rectifiers Using Proportional-Resonant Controllers," in 2018 Simposio Brasileiro de Sistemas Eletricos (SBSE), 1–6. doi:10.1109/SBSE.2018.8395803

Roy, S. S., Dey, S., and Chatterjee, S. (2020). Autocorrelation Aided Random forest Classifier-Based Bearing Fault Detection Framework. *IEEE Sensors J.* 20, 10792–10800. doi:10.1109/JSEN.2020.2995109

Shi, Z.-b., Yu, T., Zhao, Q., Li, Y., and Lan, Y.-b. (2008). Comparison of Algorithms for an Electronic Nose in Identifying Liquors. *J. Bionic Eng.* 5, 253–257. doi:10.1016/S1672-6529(08)60032-3

Song, H., Liu, Z., Xie, Y., Wu, L., and Huang, M. (2016). Rgbd Co-saliency Detection via Bagging-Based Clustering. *IEEE Signal. Process. Lett.* 23, 1722–1726. doi:10.1109/LSP.2016.2615293

Wang, B., Li, Z., Dai, Z., Lawrence, N., and Yan, X. (2020). Data-driven Mode Identification and Unsupervised Fault Detection for Nonlinear Multimode Processes. *IEEE Trans. Ind. Inf.* 16, 3651–3661. doi:10.1109/TII.2019.2942650

Yang, H., Zhang, Y., Zhang, N., Walker, P. D., and Gao, J. (2016). A Voltage Sensorless Finite Control Set-Model Predictive Control for Three-phase Voltage Source Pwm Rectifiers. *Chin. J. Electr. Eng.* 2, 52–59. doi:10.23919/CJEE.2016.7933126

Zhang, M., Li, J., Li, Y., and Xu, R. (2021). Deep Learning for Short-Term Voltage Stability Assessment of Power Systems. *IEEE Access* 9, 29711–29718. doi:10.1109/ACCESS.2021.3057659

Conflict of Interest: Y-ND is employed by Qingdao Branch, China Merchants Bank.

The remaining authors declare that the research was conducted in the absence of any commercial or financial relationships that could be construed as a potential conflict of interest.

Copyright © 2021 Kou, Gong, Zheng, Ni, Li, Yuan and Dong. This is an open-access article distributed under the terms of the Creative Commons Attribution License (CC BY). The use, distribution or reproduction in other forums is permitted, provided the original author(s) and the copyright owner(s) are credited and that the original publication in this journal is cited, in accordance with accepted academic practice. No use, distribution or reproduction is permitted which does not comply with these terms.

frontiers in Energy Research

ORIGINAL RESEARCH
published: 28 June 2021
doi: 10.3389/fenrg.2021.707706

Non-Intrusive Power Load Identification for High-Penetration Renewable Energy Grids

Bin Liu[1], *Zhukui Tan*[1] *and Xiao Su*[2]*

[1]Electric Power Research Institute of Guizhou Power Grid Co., Ltd, Guiyang, China, [2]Suzhou Huatian Power Technology Co., Ltd., Suzhou, China

With the popularity of new energy grids with high penetration rate, classic non-intrusive power load identification algorithms such as hidden Markov model (HMM) need to face the uncertainty caused by new energy generation. It will cause the load state like active power to continue to change, and new state transitions appear during operation, resulting in the lack of robustness of state identification and power decomposition. Aiming to solve this problem, this study proposes and constructs a Gaussian mixture model–binary parameter hidden Markov model (GMM-BPHMM) which takes into account the randomness of new energy power supply, clusters the load status based on active power and steady-state current to reduce the possibility of volatile clustering results from the new energy grid under a high penetration rate, improves the Viterbi algorithm to take into account the updating HMM parameters to achieve the optimal prediction of the load state, considers the random volatility of load power brought by new energy grids, constructs a power calculation optimization model, and realizes the power decomposition of the load based on the principle of maximum likelihood estimation. Finally, on the basis of the public data set AMPds2, the study generated simulation data based on the new energy generation model and verified the method, and the test case verified the effectiveness of the method.

Keywords: renewable energy, non-intrusive load monitor, hidden Markov model, Gaussian mixture model, maximum likelihood estimation

OPEN ACCESS

Edited by:
Bo Yang,
Kunming University of Science and Technology, China

Reviewed by:
Jiawei Zhu,
Chang'an University, China
Yiyan Sang,
Shanghai University of Electric Power, China

***Correspondence:**
Xiao Su
201530212486@mail.scut.edu.cn

Specialty section:
This article was submitted to Smart Grids, a section of the journal Frontiers in Energy Research

Received: *10 May 2021*
Accepted: *19 May 2021*
Published: *28 June 2021*

Citation:
Liu B, Tan Z and Su X (2021) Non-Intrusive Power Load Identification for High-Penetration Renewable Energy Grids. Front. Energy Res. 9:707706. doi: 10.3389/fenrg.2021.707706

INTRODUCTION

In order to cope with the shortage of traditional fossil energy and increasingly severe environmental pollution, China has been vigorously developing renewable energy in recent years. The installed capacity of wind power and photovoltaic and other renewable energy has ranked first in the world, and the installed capacity has been close to 20%. The main power source of the power system will continue to increase in the future, and it is expected to exceed 50% by 2040. At the same time, due to the strong volatility and randomness of wind and solar renewable energy output, issues such as the consumption of new energy have attracted great attention from government departments, academia, and industry. More importantly, as the installed scale of renewable energy continues to expand, the operation mode and system characteristics of the traditional power grid will undergo fundamental changes, and many technical problems need to be solved urgently, especially the power load identification technology under the background of high penetration rate of new energy.

Non-intrusive power load identification (NIPLI) was first proposed by Hart in the 1980s (Tongzhi, 2012), and as one of the most important components of the advanced measurement infrastructure (AMI) (Yu, 2009), this technology is only installed as monitoring equipment at the

user's electrical entrance, records the electricity consumption data, uses the monitoring algorithm to decompose the load, and obtains the electricity consumption status and energy consumption information of the internal load. Based on NIPLI, grid companies can optimize the allocation of power resources and support the construction of smart grids (Hart, 1992). At present, non-intrusive power load identification technology is developing rapidly, and scholars have proposed a variety of load identification algorithms. L et al. (2018) designed a normal distribution measurement function that comprehensively considered the steady-state harmonic current and power characteristics, and proposed a power load identification method based on an improved chicken flock algorithm. Li et al. (2016) constructed a harmonic-based current feature expression, combined power as the objective function of device switching status identification, and used the particle swarm algorithm to search for NIPLI. L et al. (2019) proposed a load identification method based on an associative recurrent neural network model, which memorizes historical input characteristics and improves the ability to identify load characteristics. W et al. (2019) proposed an NIPLI model based on sequence-to-sequence and attention mechanisms, which improved the ability to extract and utilize load information. Tongzhi (2017); X (2018); H (2016); H et al. (2019); Y (2019) all adopted an improved or expanded HMM, which greatly improved the algorithm calculation speed and the accuracy of electrical appliance status recognition.

Unlike the traditional application scenarios of NIPLI, the high-penetration new energy grid has the characteristics of diverse load types, random power generation, and greater voltage fluctuations. The aforementioned traditional NIPLI models have their own advantages in feature extraction or load identification, but none of them considered the unknown electrical characteristics of the high-penetration new energy grid, and lacked the adaptability for power load identification in this scenario. This lack of adaptability is particularly prominent in the HMM-based NIPLI model. The observation probability and transition probability of the HMM are calculated using historical data, but past data do not guarantee that all working states of the load are measured, and all transition information of each state is determined. The aforementioned HMM-based improvements are to make full use of the existing load information but fail to take into account the changes in load characteristics and model parameter updates caused by the high-penetration new energy grid, which makes it difficult to adapt to the power load identification under the high-penetration rate of new energy grid. This article believes that the improvement ideas of non-intrusive power load identification based on the HMM under high-penetration new energy grids mainly include the following three points: 1) reduce the impact of high-penetration new energy grid environment on the determination of load status; 2) take load into account unknown observation state and new state transition, that is, the model parameters of the HMM are considered to be constantly updated to predict and calculate the implicit state of the load; and 3) the random volatility of power is considered in the power decomposition calculation.

To this end, this article proposes a non-intrusive power load identification model based on the GMM-BPHMM. The model first establishes the hidden Markov model based on load active power and current and uses the Gaussian mixture model to accurately cluster load states; after the load, implicit state sequence is encoded and the Viterbi algorithm is improved to advance its adaptability to HMM parameter updates and then to achieve optimal prediction of the load state sequence; after the load state prediction, the sequence is obtained, the random volatility of power is taken into account, and the power decomposition optimization model is established based on the principle of maximum likelihood estimation, and the calculation of power decomposition is carried out according to the mean and variance of the cluster clusters of each working state of the load, and finally verified the accuracy of the method with a calculation example.

METHODS—ESTABLISHMENT OF NIPLI

This section first proposes and establishes the NIPLI model for a new energy grid mentioned in this article and then gives a detailed description of the performance improvement of power load identification in the next section, especially in the high-penetration new energy grid.

Establishment of New Energy Power Generation System

Introduction to New Energy Management System

The household new energy management system studied in this work is mainly composed of the energy storage system, photovoltaic power generation system, fan power generation system, household appliances, and smart meters, and its structure is shown in **Figure 1**. The aforementioned systems realize the interconnection of information and energy between devices using power electronic converters. The smart meter collects the information of power consumption and generation every day to realize non-invasive power load identification and

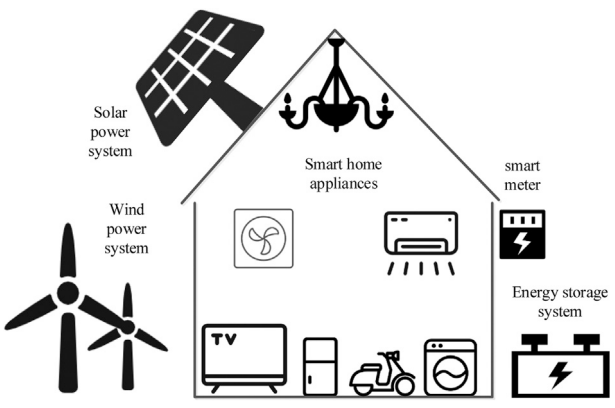


FIGURE 1 | Structure chart of the household new energy management system.

monitor the operation of corresponding equipment according to the demand.

Modeling of Wind Power Generation System

The power output prediction curve of the wind turbine can be obtained in advance using the wind speed prediction value in the weather forecast, and the power output value is given as follows (Marian and Fratia, 2018):

$$P_{\mathrm{vt},i} = \begin{cases} 0, v < v_{\mathrm{ci}} \\ a + bv, v_{\mathrm{ci}} \leqslant v < v_{\mathrm{r}} \\ P_{\mathrm{r}}, v_{\mathrm{r}} \leqslant v < v_{\mathrm{co}} \\ 0, v \geqslant v_{\mathrm{co}} \end{cases}, \quad (1)$$

where P_r is rated output power, v_{ci} is cut in wind speed, v_r is rated wind speed, v_{co} is cut out wind speed, constant coefficients a and b are related to wind speed and rated output power, and the calculation formula is $a = P_r v_{ci} / (v_{ci} - v_r)$, $b = - P_r / (v_{ci} - v_r)$, and units are kW and kW·s/m, respectively.

Modeling of Photovoltaic Power Generation System

The power of photovoltaic power generation is related to the ambient temperature and the actual solar radiation intensity. The specific calculation formula is as follows (Wang et al., 2016):

$$P_{\mathrm{v},i} = P_{\mathrm{s}} G_{\mathrm{a},i} \left\{ k_{\mathrm{s}} \left[T_{\mathrm{a},i} + \frac{G_{\mathrm{a},i}(T_{\mathrm{r}} - 20)}{800} - T_{\mathrm{r}} \right] + 1 \right\} \Big/ G_{\mathrm{s}}, \quad (2)$$

where G_a and G_s are the solar radiation intensity and the light intensity under standard test (1,000 W/m^2), T_r is the reference temperature of 25°C, T_a is the ambient temperature, P_v is the obtained photovoltaic power, P_s and k_s are the maximum power and power temperature coefficient under standard test, respectively, and k_s is 0.0036/°C.

Modeling of Energy Storage System

In the household energy management system, the energy storage system can store the surplus energy of renewable energy, store energy in the period of low electricity price, and supply energy for electrical equipment in the period of high electricity price so as to reduce the cost of household electricity and achieve the purpose of flexible economy. The energy storage system is composed of multiple storage batteries. The state of charge (SOC) represents the ratio of the existing capacity to the rated capacity as follows:

$$SOC_i = \begin{cases} SOC_{\mathrm{in}}, i = 0 \\ SOC_{i-1} + \dfrac{\left(P_{\mathrm{ESS}}^{\mathrm{ch}} \eta_{\mathrm{ch}} - \dfrac{P_{\mathrm{ESS}}^{\mathrm{deh}}}{\eta_{\mathrm{dech}}} \right) \Delta i}{C_{\mathrm{ESS}}^{\mathrm{rated}}}, 1 \leqslant i \leqslant T \end{cases}, \quad (3)$$

where SOC_{in} is the initial value of the charge ratio of the energy storage battery; $C_{\mathrm{ESS}}^{\mathrm{rated}}$ is the rated capacity; $P_{\mathrm{ESS}}^{\mathrm{ch}}$ and $P_{\mathrm{ESS}}^{\mathrm{deh}}$ are the charging power and discharge power of the energy storage system, respectively; η_{ch} and η_{dech} represents charging efficiency and discharging efficiency, respectively; and the value in this article is 0.96. A day is divided equally into T periods, and Δi is the duration of each period (h).

Establishment of BPHMM

Introduction to HMM

The hidden Markov model is a probability model about time series (G, 2018). In the hidden Markov model, there is a time series with unobservable values and an observable time series with values determined by the aforementioned time series. Time series with unobservable values are called implicit state series, and time series with observable values are called observation series. The model structure is shown in **Figure 2**.

An HMM can be described by the following parameters:

1) Implicit state set S:

$$\mathrm{S} = \{s_1, s_2, s_3, \cdots, s_N\}. \quad (4)$$

2) Observation state set V:

$$\mathrm{V} = \{v_1, v_2, v_3, \cdots, v_M\}. \quad (5)$$

3) State transition matrix:

$$\mathbf{A} = [a_{ii}]_{N \times N}. \quad (6)$$

Among them $a_{ij} = P(q_{t+1} = s_i | q_t = s_i)$

4) Output matrix:

$$\mathbf{B} = [b_{ik}]_{N \times M}. \quad (7)$$

Among them $b_{ik} = P(y_t = v_k | q_t = s_i)$

5) Initial probability matrix:

$$\boldsymbol{\pi} = [\pi_i]_{N \times 1}. \quad (8)$$

Among them $\pi_i = P(q_1 = s_i)$.

It can be seen from the aforementioned formulas that the state transition probability matrix **A** and the initial state probability vector $\boldsymbol{\pi}$ determine the hidden state sequence, and the observation probability matrix **B** determines how to generate the observation value from the hidden state. The number N and the number M of observation states are actually defined by the previous three matrices, so the hidden Markov model can be expressed by $\lambda = \{\mathbf{A}, \mathbf{B}, \boldsymbol{\pi}\}$.

The HMM is used to study the following three types of problems:

1) Probability calculation problem. Given the model $\lambda = \{\mathbf{A}, \mathbf{B}, \boldsymbol{\pi}\}$ and the observation sequence $O = \{O_1 O_2 \cdots O_T\}$, calculate $P = (O|\lambda)$.

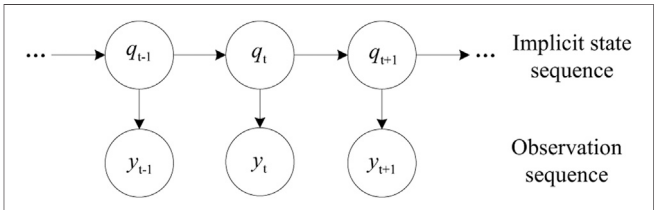


FIGURE 2 | Structure chart of hidden Markov model.

2) Learning problems. Given the observation sequence $O = \{O_1 O_2 \cdots O_T\}$, the model parameters $\lambda = \{\mathbf{A}, \mathbf{B}, \boldsymbol{\pi}\}$ are estimated, that is, to find the maximum value $P = (O|\lambda)$, the maximum likelihood estimation method is used to estimate the parameters.
3) Decoding problem. Knowing the model $\lambda = \{\mathbf{A}, \mathbf{B}, \boldsymbol{\pi}\}$ and the observation sequence $O = \{O_1 O_2 \cdots O_T\}$, the state sequence with the highest conditional probability $P = (I|O)$ for a given observation sequence $I = \{I_1 I_2 \cdots I_T\}$ is obtained, that is, the corresponding hidden state sequence is predicted according to the given observation sequence.

Problem Modeling and Parameter Calculation

In the NIPLI study, the physical meaning of the two time series in the HMM is very clear: the implicit state sequence corresponds to the operating state of each consumer, and the observation sequence corresponds to the measurable electrical quantity. Therefore, the NIPLI problem is transformed into a problem which is to obtain the most likely hidden state sequence corresponding to the observation sequence under the given HMM parameter and observation sequence, that is, the decoding problem.

Further, this study builds the NIPLI problem into the following the HMM and calculates its parameters:

1) Implicit state set S: In the NILD problem, S can be expressed as a set of combinations of operating states of each consumer, that is, a set of total states. The set is a complete arrangement of the operating states of each consumer, and the number of elements in the set is determined by the number of clusters of the status of each consumer, and its value is calculated using the state coding method introduced in **Section 3.1.3**.
2) Observation state set V: In the NILD problem, V represents the collection of specific electricity information data recorded by the user's electricity entrance. In particular, the element of the general HMM set V is the total active power, but the element in the set V of this article is a vector composed of the total active power and the total steady-state current, $v_i = [P_i^L, I_i^L]$,which is also the origin of the binary parameters in this article.
3) State transition matrix $\mathbf{A}$: a_{ij} refers to the probability of transition from the total state of each consumer at time t, $q_t = s_i$, to the total state at time $t + 1$, $q_{t+1} = s_j$. Calculation method is given as follows:

$$a_{ij} = \frac{h_{ij}}{\sum_{j=1}^{N} h_{ij}}, \tag{9}$$

where h_{ij} is the frequency of the total state transition from $q_t = s_i$ to $q_{t+1} = s_j$, and N is the total number of hidden states.

4) Output matrix $\mathbf{B}$: b_{ik} represents the probability that each consumer is in a general state $q_t = s_i$ at time t and the observed value is $y_t = v_k$. The calculation method is given as follows:

$$b_{ik} = \frac{o_{ik}}{\sum_{k=1}^{M} o_{ik}}, \tag{10}$$

where o_{ik} is the frequency of the total state $q_t = s_i$ at time t and the observed value is $y_t = v_k$, and M is the total number of observed values.

5) Initial probability matrix $\boldsymbol{\pi}$: π_i represents the probability that the overall state of each consumer is s_i at the initial moment. The calculation method is as follows:

$$\pi_i = \frac{d_i}{d}, \tag{11}$$

where d is the total amount of data in the training set and d_i represents the frequency of occurrence of hidden statess_i in the training set.

It should be pointed out that the factor hidden Markov model (FHMM) can be used for the modeling of multiple appliances. The FHMM contains multiple hidden state chains, which correspond to each appliance to be studied. However, related studies have shown that the state recognition accuracy of FHMM prediction is low (G, 2018). Therefore, this article improves on the basis of the classic HMM, cooperates with the state coding method described in **Section 3.1.3** to convert the combined vector of each consumer's state into a binary value, and solves the problem that the hidden state of the HMM is difficult to be represented by a vector, while not making each consumer state compared with the FHMM, the state transition matrix decoupling theoretically retains the correlation information between the state transitions of different appliances.

METHODS—IMPROVEMENT OF GMM-BPHMM FOR HIGH-PENETRATION NEW ENERGY GRIDS

Clustering and Encoding of Load Status Based on GMM

The selection of load characteristics determines the physical description of the load state, and clustering is the method of determining the load state. The selection of load characteristics and clustering methods is the first step of the method described in this article.

Selection of Load Feature

At present, the load characteristics selected by NIPLI's research can be roughly divided into two kinds: transient and steady states. Because the transient characteristics are generally synthetic data, they are not actually collected by the measurement device, and practicability is not strong. Therefore, this study selects the steady-state electrical quantity as the load characteristic.

The steady-state electrical quantities mainly include active power and steady-state current. Active power is an indicator of power decomposition calculation. NIPLI needs to give the decomposition value of load active power after state recognition

is completed, so active power is a characteristic adopted by most NIPLI research institutes. However, the steady-state power fluctuates slightly, the steady-state current is not affected by voltage fluctuations, and the calculated load recognition accuracy is higher (Z, 2016). Therefore, this study selects active power and steady-state current as load characteristics.

State Clustering

Various types of loads have different operating states during operation due to their own electrical characteristics or working conditions. From the perspective of power load identification, electrical appliances can be divided into three types of electrical appliances: switch-state electrical appliances, limited multistate electrical appliances, and continuously variable states according to their operating status (Hart, 1992). The number of operating states of the first two types of electrical appliances can be counted. In theory, all operating states can be obtained. However, the operating state of continuously variable electrical appliances changes continuously. To continue research into limited multistate electrical appliances, a clustering algorithm is required to cluster the operating states to make them discretized.

Considering that there are noisy points in the historical data, which will interfere with the hidden laws behind the model learning data so as to adversely affect the performance of the model, this study uses the GMM algorithm to extract and cluster the electrical load characteristics. The Gaussian mixture model is based on the assumption that the sample data points obtained are all independent and identically distributed, and the distribution is formed by the linear superposition of several Gaussian kernel functions (Berges, et al., 2009; Qiu, 2015). Therefore, compared with commonly used clustering algorithms such as K-means, the number of clusters in this algorithm does not need to be determined in advance, and it has multiple models, and the division is more refined. It is suitable for multi-category division and can be applied to complex object modeling and then smoothly to approximate the density distribution of any shape (Ap et al., 1977; Yu et al., 2013).

When estimating the parameters of the GMM, the expectation–maximization algorithm is generally used, so the entire GMM clustering algorithm process is as follows:

1) Let the data to be clustered be $\{y_1, y_2, ..., y_n\}$, establish a Gaussian mixture model and initialize the parameters:

$$P(y|\theta) = \sum_{k=1}^{K} \alpha_k \phi(y|\theta_k), \tag{12}$$

where α_k is the coefficient, $\sum_{k=1}^{K} \alpha_k = 1$, $\phi(y|\theta_k)$ is the Gaussian distribution density, $\theta_k = (\mu_k, \sigma_k^2)$, and

$$\phi(y|\theta_k) = \frac{1}{\sqrt{2\pi}\sigma_k} \exp\left(-\frac{(y-\mu_k)^2}{2\sigma_k^2} \right) \tag{13}$$

is called the k-th submodel;

2) Step E: according to the current model parameters, calculates the response of submodel k to data y_j:

$$\gamma_{jk} = \frac{\alpha_k \phi(y|\theta_k)}{\sum_{k=1}^{K} \alpha_k \phi(y|\theta_k)}, \tag{14}$$

where $j = 1,2...,N$, $k = 1,2...,K$;

3) Step M: calculate the model parameters of the new iteration as follows:

$$\mu_k = \frac{\sum_{j=1}^{N} \gamma_{jk} y_j}{\sum_{j=1}^{N} \gamma_{jk}}, k = 1, 2, ..., K \tag{15}$$

$$\sigma_k^2 = \frac{\sum_{j=1}^{N} \gamma_{jk} (y_j - \mu_k)^2}{\sum_{j=1}^{N} \gamma_{jk}}, k = 1, 2, ..., K \tag{16}$$

$$\alpha_k = \frac{\sum_{j=1}^{N} \gamma_{jk}}{N}, k = 1, 2, ..., K. \tag{17}$$

4) Repeat steps (2) and (3) until convergence.

State Encoding

In most studies, vectors are generally used to represent the current state of several electrical appliances at a time (hereinafter referred to as the total state for convenience). For example, assuming that the number of states of the three electrical appliances is 2, 3, and 8, respectively, and the state at that time is, respectively, is 0, 2, and 6, and then the total state can be expressed by the vector S = [0,2,6]. However, in HMM applications, the hidden state cannot be represented by a vector. To this end, this study proposes a binary-based state coding method, which encodes the hidden state vectors of multiple appliances into a binary state value. With the previous example, the specific steps are as follows:

1) Allocate digits: Determine the binary digits required for coding according to the number of electrical appliances. The number of states of the above three electrical appliances is 2, 3, and 8, respectively, and the binary digits allocated to each electrical appliance are 1, 2, and 3, respectively.
2) Determine the value. The binary status value is calculated according to the decimal status value of the electrical appliance at the current moment. The current three electrical appliances have decimal status values of 0, 2, and 6, respectively, and the binary status values are 0, 10, and 110, respectively.
3) Splicing representation. The obtained binary state values are spliced from high to low according to the sorting of electrical

TABLE 1 | State code of some electrical appliances.

Current moment	Display method	Appliance 1	Appliance 2	Appliance 3	Total state
1	Decimal binary	0	0	3	
		0	00	011	000011
2	Decimal binary	0	1	4	
		0	01	100	001100
3	Decimal binary	1	2	5	
		1	10	101	110101
4	Decimal binary	1	0	7	
		1	00	111	100111

appliances, and the final result is obtained. The state value of the state vector after splicing at the current time is 010110.

Table 1 shows other examples of the encoding method.

Implied State Prediction Taken Into Account the Unknown Observation State and the Transition of New State

The Viterbi algorithm was proposed by the American Italian scientist Andrew Viterbi in 1967. The Viterbi algorithm is a dynamic programming algorithm used to solve the shortest path problem and is widely used in decoding and natural language processing (Forney, 1973).

The basic idea of the Viterbi algorithm is to start at $t = 1$ and recursively calculate the maximum probability of transitioning to each state i at time t:

$$\delta[t,i] = \max_j\left(\mathbf{B}[i,y_t]\cdot\delta[t-1,j]\cdot\mathbf{A}[j,i]\right) \tag{18}$$

And record the state from time *t-1* to the state with the highest probability of state i at time t:

$$\psi[t,i] = \operatorname{argmax}_i\left(\delta[t-1,j]\cdot\mathbf{A}[j,i]\right) \tag{19}$$

After calculating the time T, find out the state $\max_i(\delta[T,i])$ which the probability belongs is the end point of the prediction sequence q_T^*. From this point, based on the prediction, point ψ is gradually obtained from back to front to obtain the optimal prediction sequence $Q^* = (q_1^*q_2^*,\cdots,q_T^*)$.

In the aforementioned classic Viterbi algorithm, the determination of HMM parameters is the prerequisite for the realization of the algorithm. However, in the scenario of a new energy grid with a high penetration rate, historical data cannot reflect the transfer relationship between all working states and states of the load, and the new measured data are not completely consistent with the measured electrical data. In other words, the model parameters of the HMM are not completely determined. Under this premise, the classical Viterbi algorithm that does not have the ability to adapt to unknown data is difficult to accurately solve the prediction problem of the optimal implicit sequence.

Based on the above ideas, this study proposes an improved Viterbi algorithm and makes the following improvements: 1) Considering that a new observation state will appear in electrical appliances and the observation state may correspond to the unknown operating state, this article uses the K-means algorithm to cluster into known measurement states for the new electrical data input; 2) considering that there may be new state transitions in electrical appliances, the calculation methods of δ and ψ are changed based on maximum likelihood estimation; 3) considering the sparsity of the state transition matrix and measurement matrix, for example, the sparse Viterbi algorithm proposed by (Makonin et al., 2016a), the algorithm only calculates the state transition probability and the measurement probability that are not zero.

For a given observation sequence $Y = \{y_0y_1,\cdots,y_T\}$ and implicit state sequence $Q = \{q_0q_1,\cdots,q_T\}$, the specific steps of the improved Viterbi algorithm proposed in this article are as follows:

1) Initialization:

$$\delta[0,i] = \pi[i]\cdot\mathbf{B}[i,y_0]. \tag{20}$$

2) Recursive calculation:

$$\delta[t,i] = \max_j\left(\mathbf{B}[i,y_t]\cdot\delta[t-1,j]\cdot\mathbf{A}[j,i]\right) \tag{21}$$

$$\psi[t,i] = \operatorname{argmax}_j\left(\delta[t-1,j]\cdot\mathbf{A}[j,i]\right). \tag{22}$$

In particular, let us set $y_t = k$ as the measurement state at time t. When this observation state occurs, according to the principle of maximum likelihood estimation, the hidden state with the greatest probability of occurrence should be the state i that satisfies $b_{ik} = \max(B[:,k])$.

When calculating $\delta[t,i]$ and $\psi[t,i]$, change the calculation of the above two formulas to the following:

$$\delta[t,i] = \max_j\left(\mathbf{B}[i,k]\cdot\delta[t-1,j]\right)\cdot\max(\mathbf{A}[:,:]) \tag{23}$$

$$\psi[t,i] = \max_j\left(\delta[t-1,j]\right)\cdot\max(\mathbf{A}[:,:]), \tag{24}$$

where $\mathbf{A}[:,:]$represents the element in $\mathbf{A}$.

Viterbi is a dynamic programming algorithm. It only pays attention to the optimal solution at each step. It is unnecessary to study the unknown but determined non-optimal solution. Therefore, this article only focuses on the new state transition of state i that meets $b_{ik} = \max(\mathbf{B}[:,k])$. The reason for the transition probability valued $\max(\mathbf{A}[:,:])$ is to prevent the path passing through this point from being abandoned by the algorithm. If the algorithm does not take other legal values, the model can still get the correct result, but it will make the value smaller, thereby

reducing the probability that the optimal path goes through the point in the future.

3) Calculation of termination status:

$$p_T^* = \max_i(\delta[T,i]) \tag{25}$$

$$q_T^* = \operatorname{argmax}_i(\delta[T,i]). \tag{26}$$

4) Optimal sequence backtracking:

$$q_t^* = \psi_{t+1}(q_{t+1}^*), t = T-1, T-2, \cdots, 0. \tag{27}$$

The sequence obtained at this time is the predicted optimal hidden state sequence $Q^* = (q_1^* q_2^*, \cdots, q_T^*)$.

Power Decomposition Considering the Random Volatility of New Energy Generation

Under the new energy generation, the power of electrical appliances in a certain stable operating state fluctuates, and this fluctuation can be regarded as a random observation under a certain probability distribution (Liang et al., 2010a; Liang et al., 2010b). In this study, the normal distribution is used to describe the randomness of generation fluctuations during stable operation of the appliance, and it is used to calculate the power decomposition of the appliance.

The power decomposition calculation steps in this study are as follows: 1) According to the average value and variance of the clusters of each electrical appliance sample, establish a normal distribution probability density function for each state of each electrical appliance. 2) Establish the objective function based on maximum likelihood estimation, that is, to obtain the maximum value of the joint probability, and note that the sum of the power decomposition values of the electrical appliances at the same time should be equal to the constraint condition of the total power. The power decomposition calculation model is constructed as follows:

$$\begin{cases} f_{[i,j]}(x) = \dfrac{1}{\sqrt{2\pi}\sigma_{[i,j]}} \exp\left(-\dfrac{\left(x-\mu_{[i,j]}\right)^2}{2\sigma_{[i,j]}^2} \right) \\ \max\limits_{P^{(1)},\ldots,P^N} \prod\limits_{i=1}^{N} f_{[i,j]}(P^{(i)}) \\ \text{s.t.} \quad \sum\limits_{i=1}^{N} P^i = P^L \end{cases} \tag{28}$$

In the formula, $\sigma_{[i,j]}$ and $\mu_{[i,j]}$ refer to the standard deviation and mean value of the j-th cluster of the i-th appliance, respectively; N is the number of appliances; $P^{(i)}$ refers to the decomposed active power of each appliance; and P^L refers to the active power of the total load. $f_{[i,j]}(P^{(i)})$ refers to the probability of $P^{(i)}$ when appliance i is in the j operating state. The a forementioned problem is a common convex quadratic programming problem after taking *ln()* on both sides of the objective function. The complete flow of the non-intrusive power load identification method proposed for high-penetration new energy grids in this study is shown in **Figure 3**.

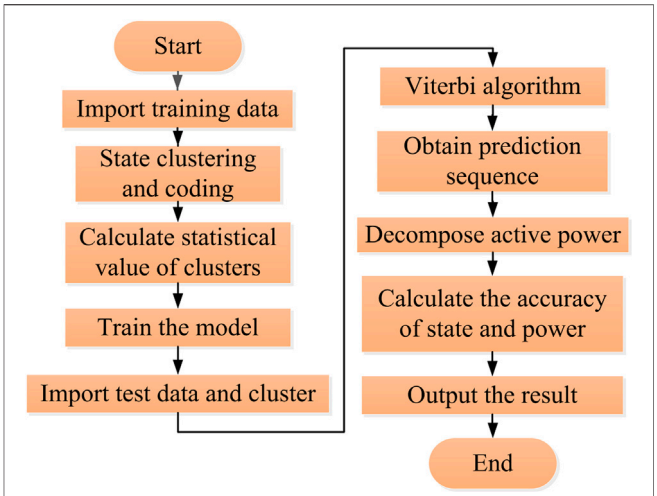


FIGURE 3 | Flow chart of NIPLI based on GMM-BPHMM.

RESULTS AND DISCUSSION

Experimental Method

Since there is no public data set containing new energy power generation equipment at present, the author will generate simulation data based on the power generation model described in **Section 2.1** on the basis of the public data set, for example, analysis.

This study selects the public data set AMPds2 established by a Canadian scholar Stephen Makonin and others to verify the method described in this article (Makonin et al., 2016b). AMPds2 collects real electrical data of electrical equipment in a household and records 11 electrical characteristics, including steady-state current and active power. The sampling frequency is 1/60 Hz, and the recording time is 2 yr. It is suitable as a data set for analysis.

From the data set, select six kinds of appliances, such as fireplace (WOE), clothes dryer (CDE), dishwasher (DWE), television (TVE), washing machine (CWE), and heat pump (HPE), for a total of 14,400 sampling points in 10 days The active power and steady-state current data are divided into 10 groups according to time, which are recorded as test1-test10, and 10-fold cross-validation is performed. In each experiment, nine groups of data are selected as training data, and one group is used as test data. Finally, the average is the result. The PC configuration used in this article is 16 GB RAM/Inter (R) Core (TM) i5-8300H@2.30 GHz, written in Python.

Decomposition Result

In this study, the basic accuracy rate ACC_{state} is used to evaluate the accuracy of load state recognition, and the root-mean-square

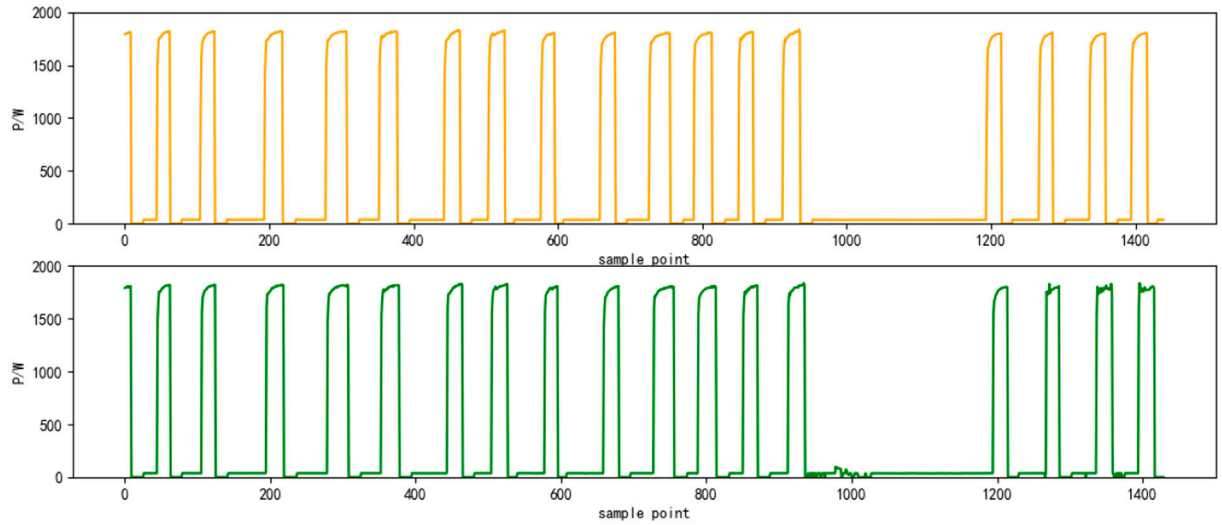


FIGURE 4 | Results of power decomposition (HPE).

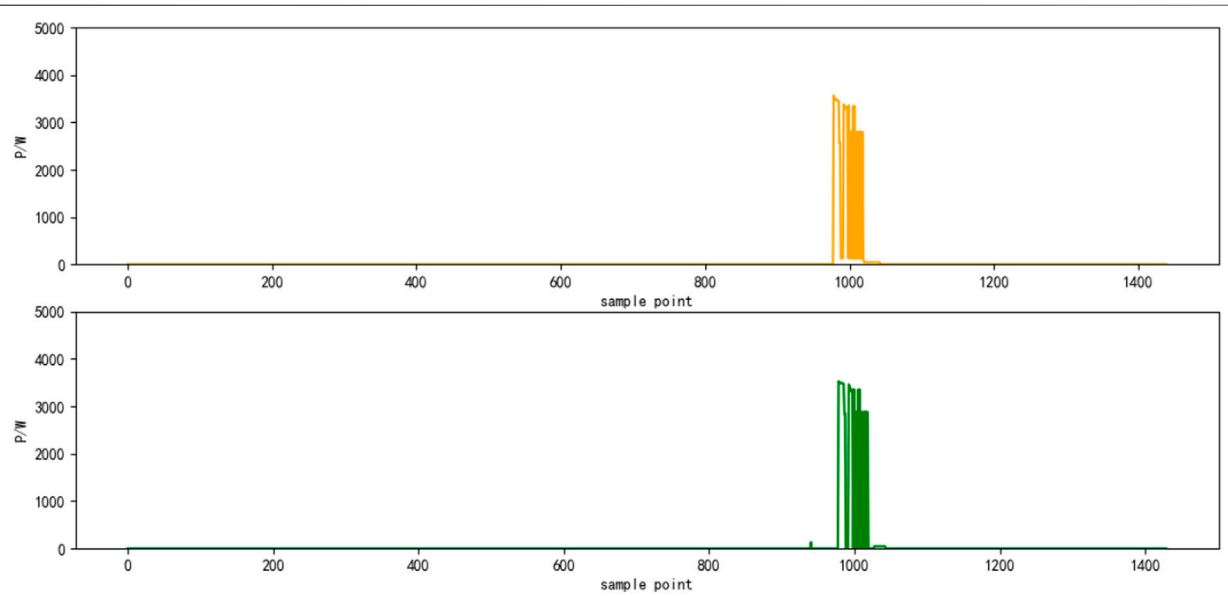


FIGURE 5 | Results of power decomposition (WOE).

errorACC_{power} is used to evaluate the accuracy of load power decomposition as follows:

$$ACC_{\text{state}} = \frac{\sum_{t=1}^{T} I\left(s_t = s_t^*\right)}{T} \tag{29}$$

$$ACC_{\text{power}} = \sqrt{\frac{1}{\mathrm{T}} \sum_{\mathrm{t}=1}^{T} \left(p_t - p_t^*\right)^2}. \tag{30}$$

In the formula, T is the length of the sampling period; $s_t$and $p_t$are the actual state and actual power value of the appliance at time t, respectively; $s_t^*$and $p_t^*$are the predicted state and decomposition power value, respectively; and I () is the indicator function.

Select the superposition value of active power of six electrical appliances on a certain day as the test set. The decomposition results are shown in **Figures 4–9**, respectively. The yellow line is the actual power, and the green line is the decomposition result.

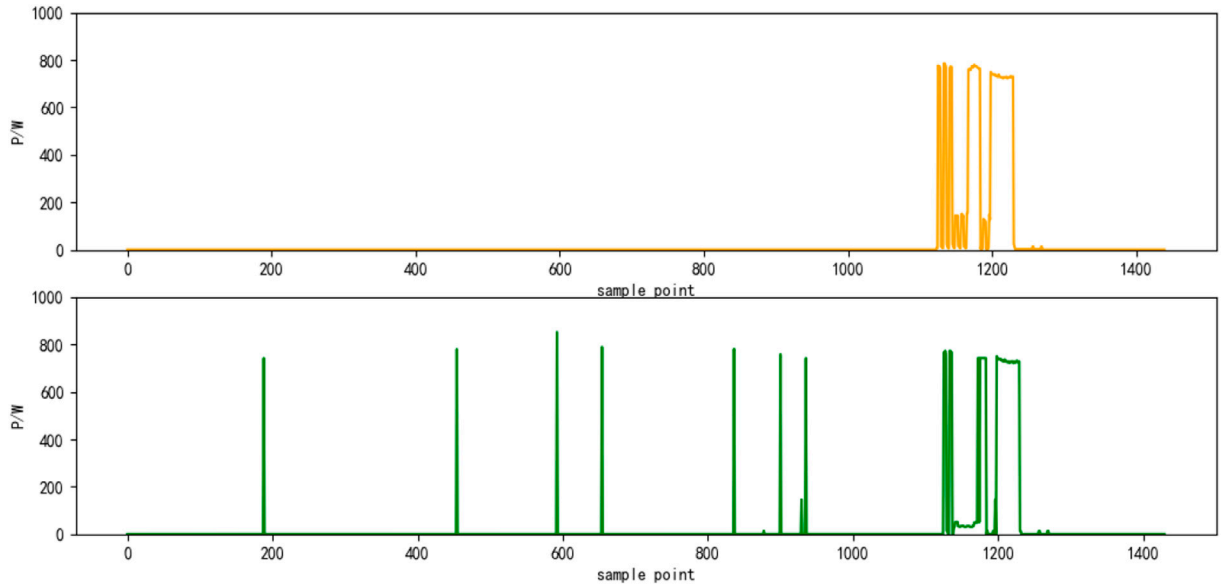


FIGURE 6 | Results of power decomposition (CDE).

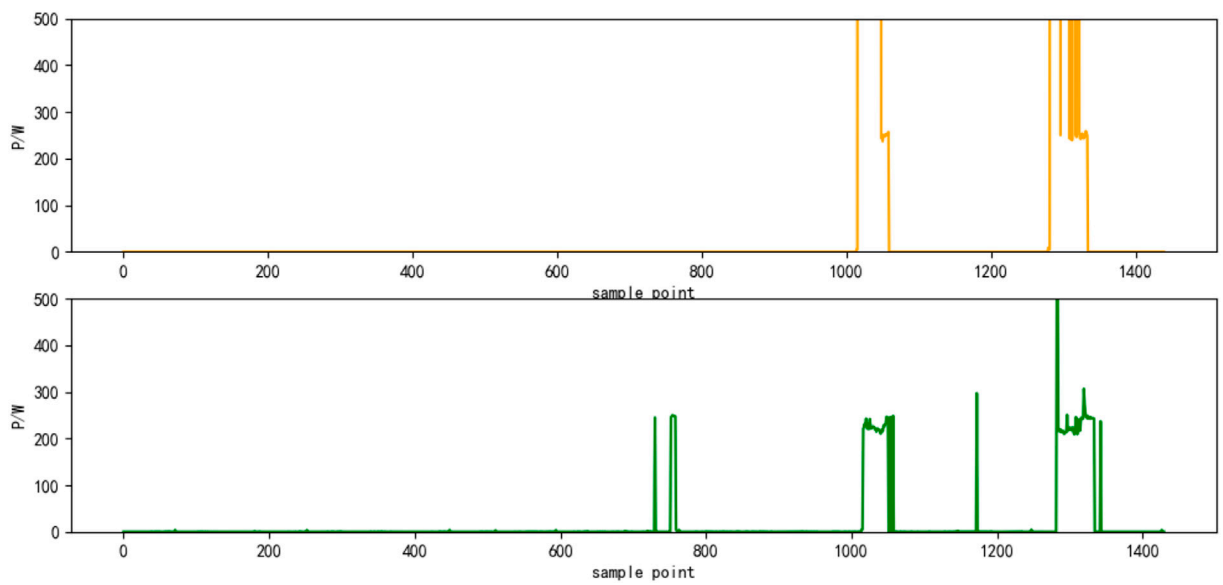


FIGURE 7 | Results of power decomposition (CWE).

This study selects the decomposition method based on the genetic algorithm (GA) proposed in Q et al. (2018), the decomposition method based on deep sequence translation model in W and G (2020) and the classic HMM (G, 2018) as comparison, and uses the same data to perform the 10-fold cross-validation calculation The average value, the average accuracy rate of load state identification by the four methods, and the average accuracy rate of power decomposition are shown in **Table 2** and **Figure 10**, respectively. It can be seen

TABLE 2 | Comparison of average accuracy of state recognition.

Appliance	GA/%	RNN/%	HMM/%	GMM-BPHMM/%
HPE	95.56	96.75	96.87	97.89
TVE	93.35	95.78	95.45	96.97
DWE	92.16	94.18	93.17	95.76
CWE	93.96	91.35	90.84	93.88
WOE	92.46	95.59	96.38	98.54
CDE	95.34	95.78	95.35	97.55

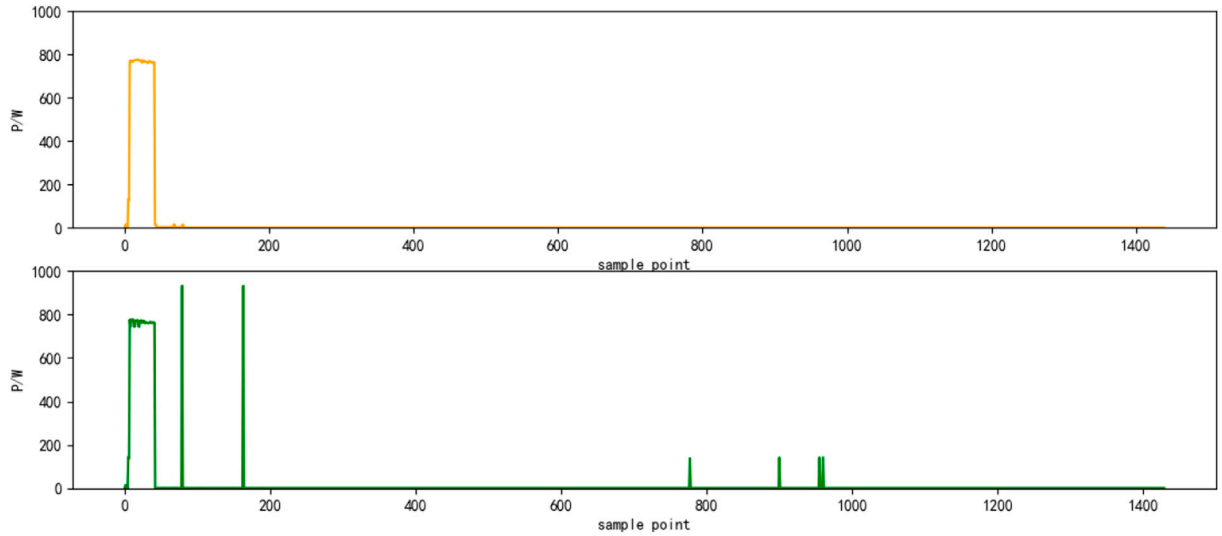


FIGURE 8 | Results of power decomposition (DWE).

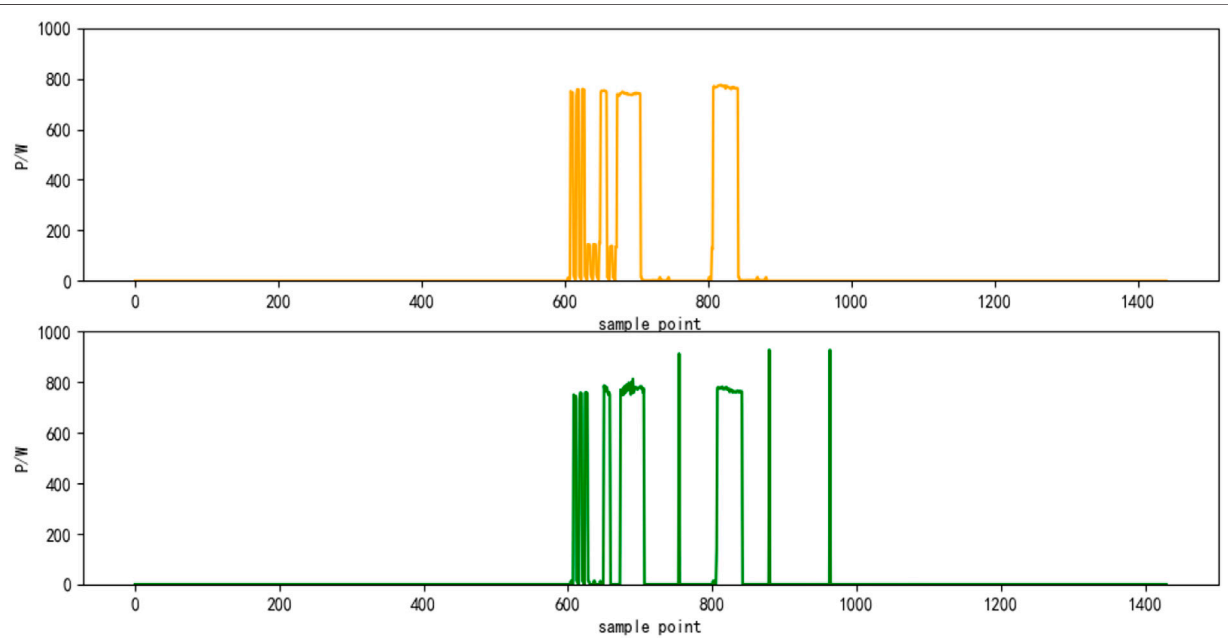


FIGURE 9 | Results of power decomposition (TVE).

that the load decomposition method based on the binary parameter HMM and the sparse Viterbi algorithm has a better effect on the state identification and power decomposition of the total load.

It can be seen from the aforementioned results that compared with the classic HMM algorithm, the use of the combined electrical characteristics of the method described in this article can enable the model to extract the operating state that better reflects the characteristics of the load, thereby improving the solution of the NIPLI problem in the high-permeability new energy grid performance. The power decomposition optimization model proposed in this study based on maximum likelihood estimation considers and learns the volatility behind the new energy generation to a

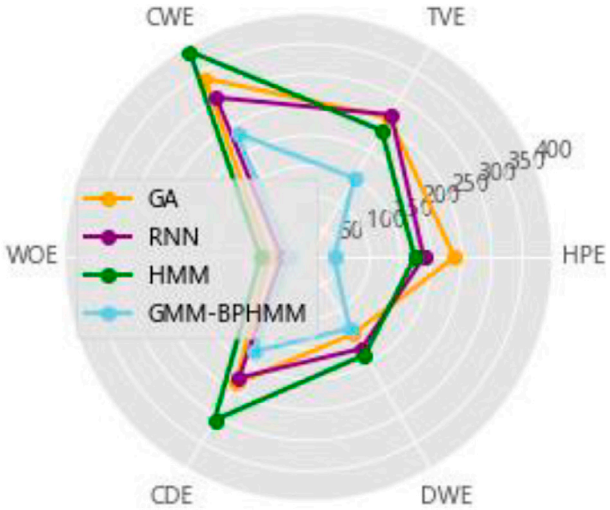


FIGURE 10 | Comparison of average accuracy of power decomposition.

certain extent, ensuring that the sum of the monitored power of each electrical appliance is equal to the total load power, making the power decomposition more accurate. For the more cutting-edge deep learning methods, the method described in this article is better than the deep learning–based solution in the accuracy of state recognition of multiple working state appliances, such as TVs and washing machines.

CONCLUSION

This article proposes non-intrusive power load identification under high-penetration new energy grids. This method proposes and constructs the binary parameter hidden Markov model BPHMM, uses the GMM algorithm to cluster the load characteristics, proposes a binary-based coding scheme to encode the load state combination, and improves the Viterbi algorithm to make it have the adaptability of the updating model parameter situation and then realize the optimal prediction of the load state. Finally, an optimization model that takes into account the random volatility of the new energy generation is established, and the power decomposition of the load is realized according to the mean and variance of the appliance cluster. The results of the calculation example show that in the high penetration rate new energy grid scenario, compared with the recognition scheme based on heuristic algorithms, deep learning methods, and classic HMM, the method proposed in this article has achieved higher load status recognition accuracy and lower power decomposition error. This article proposes various measures to improve the performance of the NIPLI model under high-penetration new energy grids, such as denoising data, improving traditional methods to increase its adaptability to unknown data, and enabling the model to learn the statistical characteristics behind data fluctuations. And other ideas, I also believe that it has reference value for the practicality of NIPLI.

The research on the high-penetration new energy grid in this work is still relatively preliminary, and the non-electrical characteristics of load operation are not considered. The next step of research will focus on how to use non-electrical characteristics, such as load working hours and user behavior habits, study the processing of new unknown electrical appliances, and propose a more practical non-intrusive power load identification method.

DATA AVAILABILITY STATEMENT

The original contributions presented in the study are included in the article/supplementary material; further inquiries can be directed to the corresponding author.

AUTHOR CONTRIBUTIONS

BL contributed to conceptualization, methodology. ZT contributed to project administration, funding acquisition, and formal analysis. XS contributed to data curation, visualization, and writing. All authors contributed to the article and approved the submitted version.

FUNDING

The paper is supported by Science and technology project of China Southern Power Grid Co., Ltd (Grant No. 066600KK52180051).

REFERENCES

Ap, D., Laird, N. M., and Rubin, D. B. (1977). Maximum Likelihood From Incomplete Data Via the EMAlgorithm. *J. R. Stat. Soc. Ser. B (Methodological)* 39 (1), 1–22. doi:10.1111/j.2517-6161.1977.tb01600.x

Berges, M., Goldman, E., Matthews, H. S., and Soibelman, L. (2009). *Learning Systems for Electric Consumption of Buildings [M]*, 1–10.

Forney, G. D. (1973). The Viterbi Algorithm. *Proc. IEEE* 61 (3), 268–278. doi:10.1109/proc.1973.9030

G, D. (2018). *Study on Non-intrusive Load Decomposition of Residential Electricity Based on HMM [D]*. Beijing: North China Electric Power University.

H, A. J., Yong-Sheng, W., Bo-Chuan, G. U., Xiao-Feng, L., and Yi, S. (2019). Non-intrusive Load Monitoring Method Based on Denoising Filtering and FHMM. *Automation & Instrumentation* 34 (11), 97–102. doi:10.19557/j.cnki.1001-9944.2019.11.023

H, C. (2016). *Study on Nonintrusive Load Monitoring Technology Based on HMM and its Variants[D]*. Tianjin: Tianjin University.

Hart, G. W. (1992). Nonintrusive Appliance Load Monitoring. *Proc. IEEE* 80 (12), 1870–1891. doi:10.1109/5.192069

L, H., Shuaibin, S., Xuhui, X. U., Dongguo, Z., Ruolin, M., and Wensha, H. (2019). A Non-intrusive Load Identification Method Based on RNN Model. *Power Syst. Prot. Control.* 47 (13), 162–170. doi:10.19783/j.cnki.pspc.180785

L, X., Meihan, C., and Yuejuan, X. U. (2018). Non-intrusive Load Monitoring Based on Improved Chicken Swarm Optimization Algorithm. *Electric Power Automation Equipment* 38 (5), 235–240. doi:10.16081/j.issn.1006-6047.2018.05.033

Li, R., Mingshan, H., Dongguo, Z., Hong, Z., and Wenshan, H. (2016). Optimized Nonintrusive Load Decomposition Method Using Particle Swarm Optimization Algorithm. *Power Syst. Prot. Control.* 44 (8), 30–36. doi:10.7667/PSPC160239

Liang, J., Ng, S. K. K., Kendall, G., and Cheng, J. W. M. (2010a). Load Signature Study—Part I: Basic Concept, Structure and Methodology. *IEEE Trans. Power Deliv.* 25 (2; 2), 551–560. doi:10.1109/TPWRD.2009.2033799

Liang, J., Ng, S. K. K., Kendall, G., and Cheng, J. W. M. (2010b). Load Signature Study-Part II: Disaggregation Framework, Simulation, and Applications. *IEEE Trans. Power Deliv.* 25 (2), 561–569. doi:10.1109/tpwrd.2009.2033800

Makonin, S., Ellert, B., Bajić, I. V., and Popowich, F. (2016b). Electricity, Water, and Natural Gas Consumption of a Residential House in Canada from 2012 to 2014. *Sci. Data* 3 (1), 160037. doi:10.1038/sdata.2016.37

Makonin, S., Popowich, F., Bajic, I. V., Gill, B., and Bartram, L. (2016a). Exploiting HMM Sparsity to Perform Online Real-Time Nonintrusive Load Monitoring. *IEEE Trans. Smart Grid* 7 (6), 2575–2585. doi:10.1109/tsg.2015.2494592

Marian, M., and Fratia, M. (2018). Photogrammetric Measurement of a Wooden Truss. *Slovak J. Civil Eng.* 26 (4), 1–10. doi:10.2478/sjce-2018-0022

Q, X., Lou, O., Zheng, A., and Liu, Y. (2018). A Non-intrusive Load Decomposition Method Based on Affinity Propagation and Genetic Algorithm Optimization. *Trans. China Electrotechnical Soc.* 33 (16), 3868–3878. doi:10.19595/j.cnki.1000-6753.tces.170894

Qiu, T. (2015). *EM Algorithm Based on Gaussian Mixture Model and its Application [D]*. Chengdu: University of Electronic Science and Technology.

Tongzhi, L. (2017). *Research on Event-Based HMM for Non-intrusive Electrical Load Monitoring Algorithm [D]*. Wuhan: Huazhong University of Science and Technology.

Tongzhi, L. (2012). Technical Implications and Development Trends of Flexible and Interactive Utilization of Intelligent Power. *Automation Electric Power Syst.* 36 (2), 11–17.

W, K., Haiwang, Z., Nanpeng, Y. U., and Qing, X. (2019). Nonintrusive Load Monitoring Based on Sequence-To-Sequence Model with Attention Mechanism. *Proc. CSEE* 39 (1), 75–83. doi:10.13334/j.0258-8013.pcsee.181123

W, R., and G, X. (2020). Non-intrusive Load Decomposition Method Based on Deep Sequence Translation Model. *Power Syst. Tech.* 44 (01), 27–37. doi:10.13335/j.1000-3673.pst.2019.0645

Wang, J., Wei, K., Zhang, J., Lin, T., and Bao, X. (2016). "Measurement Method for Vertical Tank Deformation Based on Laser Scanning Principle," in *2016 3rd International Conference on Systems and Informatics (ICSAI)*. (New York, NY: IEEE), 583–587.

X, S. (2018). *Research on Non-intrusive Load Decomposition Based on FHMM [D]*. Zhengzhou: Zhengzhou University.

Y, W. (2019). *Non-intrusive Load Decomposition Method Based on Factorial Hidden Markov Model [D]*. Beijing: North China Electric Power University.

Yu, Y., Bo, L., and Wenpeng, L. (2013). Nonintrusive Residential Load Monitoring and Decomposition Technology. *South. Power Syst. Tech.* 7 (4), 1–5. doi:10.13648/j.cnki.issn1674-0629.2013.04.004

Yu, Y. X. (2009). Technical Composition of Smart Grid and its Implementation Sequence. *South. Power Syst. Tech.* 3 (2), 1–5. doi:10.13648/j.cnki.issn1674-0629.2009.02.020

Conflict of Interest: BL and ZT were employed by the company Electric Power Research Institute of Guizhou Power Grid Co., Ltd. XS was employed by the company Suzhou Huatian Power Technology Co., Ltd.

Copyright © 2021 Liu, Tan and Su. This is an open-access article distributed under the terms of the Creative Commons Attribution License (CC BY). The use, distribution or reproduction in other forums is permitted, provided the original author(s) and the copyright owner(s) are credited and that the original publication in this journal is cited, in accordance with accepted academic practice. No use, distribution or reproduction is permitted which does not comply with these terms.

frontiers in Energy Research

ORIGINAL RESEARCH
published: 07 July 2021
doi: 10.3389/fenrg.2021.713634

Unmanned Aerial Vehicle for Transmission Line Inspection: Status, Standardization, and Perspectives

*Xin Li, Zijian Li, Haizhi Wang and Wanlin Li**

Law School, Kunming University of Science and Technology, Kunming, China

As the biggest country in power consumption and generation, China owns the largest scale of transmission line worldwide. The application of unmanned aerial vehicle (UAV) in inspection has been carried out for many years in China because of its strong adaptability and safety compared to the traditional manual way. For the further development of UAV application technology in transmission line inspection, China has accumulated rich experiences and greatly improved line inspection efficiency and formed a relatively complete UAV transmission line inspection standardization system including operation safety management, an equipment configuration method, and functional quality requirements. However, there still exist some obstacles that need to be tackled due to the fact that China's UAV transmission line inspection standardization and its international promotion have not been thoroughly and comprehensively studied at present. Based on an in-depth analysis of China's current UAV transmission line inspection standardization system, this study employs SWOT-PEST analysis to insightfully investigate international promotion opportunities/challenges under the current situation, upon which several constructive suggestions are proposed from four aspects of politics, economy, society, and technology. The ultimate purpose is to design feasible schemes to boost the international promotion of China's UAV transmission line inspection standardization and further development of international UAV inspection technology.

Keywords: UAV, transmission line inspection, standardization, promotion, SWOT analysis

OPEN ACCESS

Edited by:
Xiaoshun Zhang,
Shantou University, China

Reviewed by:
Borong Deng,
South China University of Technology, China
Zilin Li,
Hong Kong Polytechnic University, SAR China

****Correspondence:***
Wanlin Li
karen_lee_lx@126.com

Specialty section:
This article was submitted to Smart Grids, a section of the journal Frontiers in Energy Research

Received: *23 May 2021*
Accepted: *11 June 2021*
Published: *07 July 2021*

Citation:
Li X, Li Z, Wang H and Li W (2021) Unmanned Aerial Vehicle for Transmission Line Inspection: Status, Standardization, and Perspectives. Front. Energy Res. 9:713634. doi: 10.3389/fenrg.2021.713634

INTRODUCTION

As the traditional method of transmission line inspection (Liu et al., 2019a), manual inspection has some obvious disadvantages (Muniappan, 2021) when it comes to special terrain and meteorological conditions which frequently lead to low inspection efficiency (Padhy and Panda, 2021), and personnel safety is not always guaranteed (Kumar et al., 2021). Although the United States and European countries started to use helicopters to inspect transmission lines from the middle of the 20th century, the high risk and inefficiency of manual ways have not been fundamentally addressed (FU et al., 2017). With the development of UAV application technology, UAV inspection shows its irreplaceable advantages of safety and efficiency in transmission line inspection (Kumar Injeti and Kumar Thunuguntla, 2020; Miao et al., 2020), and it has little impact on transmission lines because it can undertake on-line inspection (He et al., 2020; Liang et al., 2020).

At present, research on UAV inspection tends to focus on technologies including defect monitoring, autonomous inspection, and so forth, which can be summarized as follows:

- Research on transmission line detection technology includes the use of deep learning target identification and navigation technology, which can effectively improve the monitoring ability and reduce the inspection cost (Gangolu and Sarangi, 2020; Sui and Ning, 2021)
- The endurance of line inspection UAV is based on the flight battery optimization, UAV nest and power supply, UAV radio power transmission technology, etc. (ZHAO et al., 2017)
- Autonomous line patrol of UAV includes intelligent image data processing and autonomous intelligent line inspection, as well as the ultimate goal of the complete autonomous inspection (Tavakoli and Nafar, 2020)

This study initially investigates the characteristics of line inspection UAV and concludes that different UAV types correspond to different line inspection tasks. The development status of UAV line inspection technology is analyzed combined with the current application situation of other countries. Then, this work deeply studies China's UAV line inspection standardization system, which aims to find the international promotion path of China's UAV inspection standardization through SWOT-PEST analysis. The points are summarized as follows:

- Relying on the advantages of UAV technology, China's UAV line inspection technology is widely used and has rich experience in line inspection, which can provide efficient line inspection solutions for other countries.
- China's UAV line inspection standard has a relatively perfect system, which can provide a valuable reference for other countries to use UAV line inspection.
- Strengths-weaknesses-opportunities-threats (SWOT) analysis and political-economical-social-technological (PEST) analysis are adopted to illustrate the strengths and weaknesses of international promotion, which also discuss the opportunities and challenges.
- The promotion of China's UAV line inspection standard may be limited by laws and regulations, but it can be changed according to the actual situation to adapt to the specific situation of corresponding countries. Generally, it has strong practicability for its promotion in the world.

OVERVIEW OF UAV

UAV refers to the unmanned aircraft operated by radio remote control equipment and a self-contained program control device or operated by using an onboard computer completely or intermittently (ICAO'scircularUAS, 2011). UAV was introduced for military investigation and attack in 1920s, as shown in **Figure 1**. Nowadays, it has been widely used in the civil fields including photography, security, inspection, and other industries where manual work cannot be accomplished easily. With the development of UAV technology, the range of its utilization will be much wider.

Classification of UAVs

UAV can be classified into different types according to its utilization, size, flight platform, and flight range, as shown in **Figure 2** (Hassanalian and Abdelkefi, 2017). Among them, flight platform of UAV is the most significant factor to the line inspection since it considerably affects the specific application of UAV. Moreover, different characteristics of flight platforms more or less affect the mode of line patrol. Therefore, investigation of different platforms of UAV is critical to optimize the line inspection method. Next, the classification of UAV is discussed from several main aspects of the flight platform.

- *Fixed-Wing UAV*. Fixed-wing UAVs are larger than rotary-wing UAVs under the same specifications and are more complex in taking off and landing. The fixed-wing UAV has faster speed, longer endurance, and higher flight altitude than the rotary-wing UAV (Yi et al., 2017). Fixed-wing UAVs can be used in various environments, including jungle, desert, city, ocean, and mountain areas, as shown in **Figure 3A**.
- *Rotary-Wing UAV*. Based on the rotor blade or propeller system, the rotary-wing UAVs is a smaller-size and higher-payload UAV. It has the flexibility and ability to hover in the air and go to places where fixed-wing UAVs cannot go. The rotary-wing UAV is also the cheapest compared with other types of UAV. However, its disadvantages include low endurance, instability in the wind, and limitation of flight range and altitude (Tang et al., 2018a), as shown in **Figure 3B**.
- *Flapping-Wing UAV*. Flapping-wing UAVs are based on bionics, and most of them have flexible and light wings which are important for their aerodynamic proficiency and flight stability (Chen et al., 2020), as shown in **Figure 3C**. Moreover, the flapping-wing UAV has strong adaptive wind resistance, but it is not widely used in the civil UAV field.
- *Unmanned Airship*. As an aircraft based on the principle of buoyancy, it has the fundamental characteristics of long dead time, heavy load, and stable flight, as shown in **Figure 3D**. It takes advantage of the lower stratospheric wind speed and other favorable conditions, carries the mission load, and lifts off by buoyancy, so as to realize the stable residence and controllable flight in the specific area (Fei, 2019). The technological development of unmanned airships varies from country to country, so it has not been popularized.
- *Parafoil UAV*. The parafoil UAV takes off using a powered parachute instead of wings or propellers, as shown in **Figure 3E**. It has the characteristics of strong endurance, vulgarity, low altitude, and stable flight (Guo et al., 2017). Also, it can be used in agriculture and forestry, aerial photography, aerial survey, weather modification operation, rescue, and relief.

Application of UAV

Nowadays, UAV has been widely used in various areas corresponding to its different characteristics (Tang et al., 2018b). Applications of UAV are listed in **Table 1**.

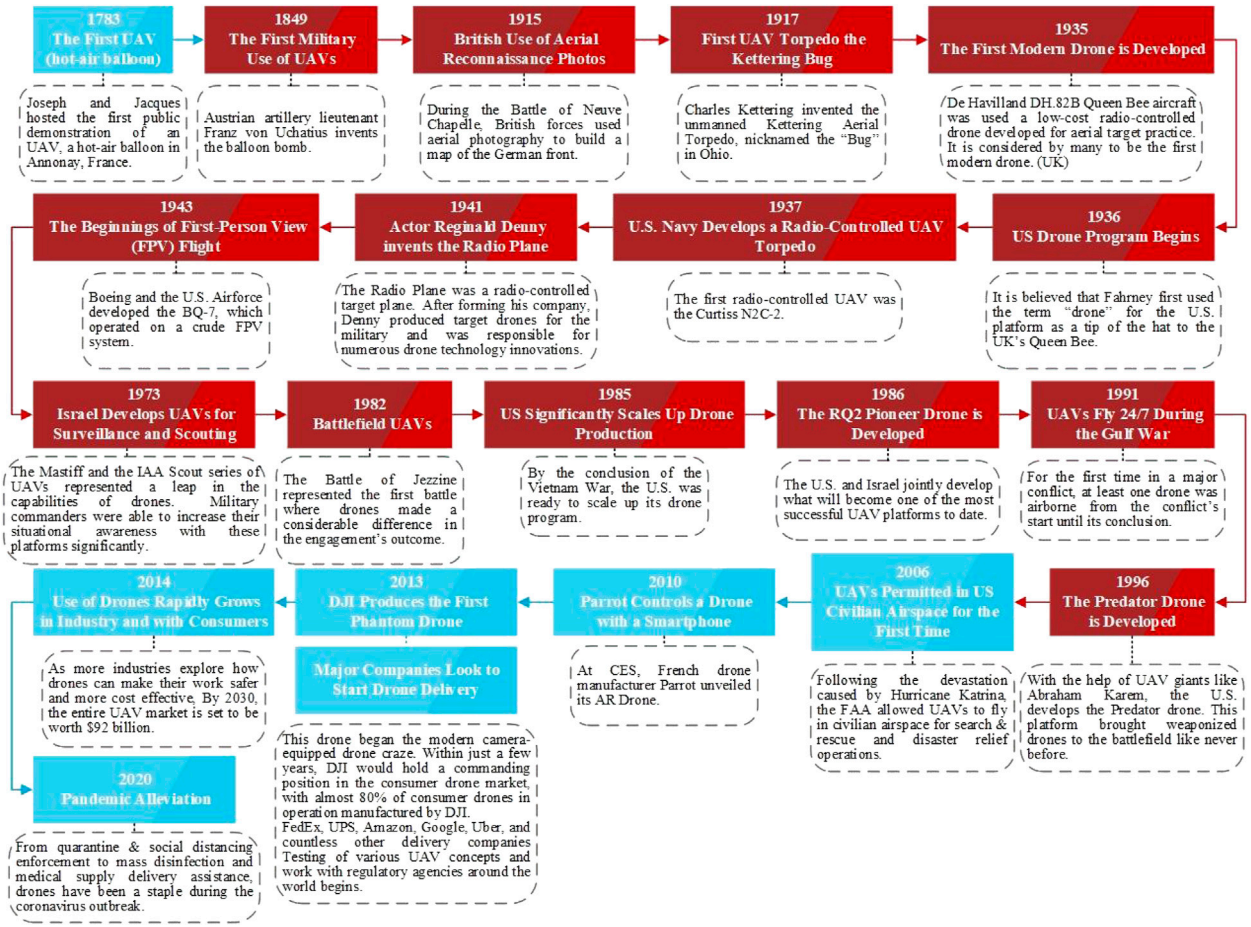


FIGURE 1 | History of UAV development.

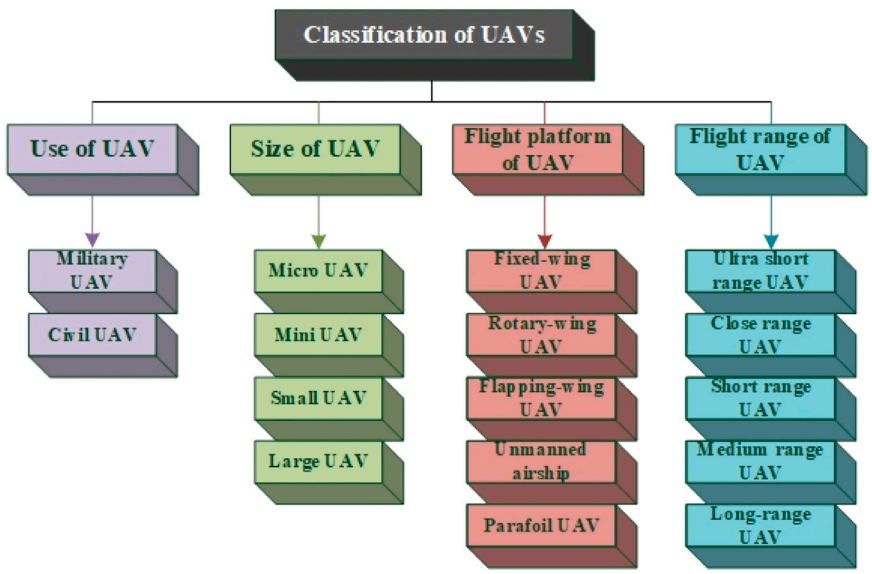


FIGURE 2 | Classification of UAVs.

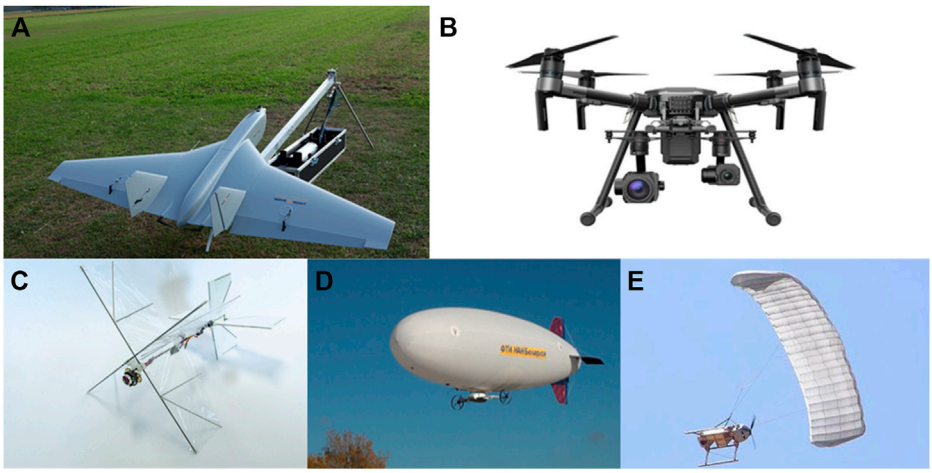


FIGURE 3 | Different types of UAVs: **(A)** fixed wing (Volt Aerial Robotics, 2016), **(B)** rotary wing (Geospatial Media and Communications, 2018), **(C)** flapping wing (Tzu-ti, 2020), **(D)** unmanned airship (Unmanned airship, 2014), and **(E)** parafoil UAV (Lanny Lin, 2021).

TABLE 1 | Application of UAV.

Application fields	Applicable UAV	Characteristics of demand
Aerial photography	Rotary-wing UAV	Easy to operate, good image transmission effect
Security	Rotary-wing UAV	Long endurance, strong adaptability to harsh environment, good image transmission effect
Inspection	Rotary-wing UAV, fixed-wing UAV	Long endurance, strong adaptability to harsh environment, good image transmission effect, stable signal, strong load capacity, easy maintenance
Others	Rotary-wing UAV, fixed-wing UAV	Long endurance, strong load capacity, strong anti-interference ability

- *Aerial Photography*. UAV can carry high-definition cameras with small volumes. Using the unique perspective of the air to record sports events, performing arts activities, and film and television shooting improves the efficiency and quality of shooting (Guo et al., 2017).
- *Security*. UAV has been more widely used in security, such as forest fire early warning, public security prevention and control, UAV security inspection, and monitoring (Volt Aerial Robotics, 2016), which can effectively supplement and strengthen the traditional security methods.
- *Inspection*. UAV inspection improves efficiency *via* the combination of visible light, thermal infrared, and lidar image fusion technology (Geospatial Media and Communications, 2018), as well as reduces the occurrence of safety accidents.
- *Others*. By improving the accuracy of mapping, UAV plays an important role in the protection of cultural relics, urban planning and water conservancy monitoring, and other applications (Unmanned airship, 2014).

APPLICATION OF UAV IN TRANSMISSION LINE INSPECTION

Economic development relies on the construction of power grid. Transmission lines are getting longer and more complex in many countries. In 2009, China's power grid length of more than 200 kV reached 375,000 km, which surpassed the United States and ranked first in the world. By 2018, the length of the grid over 35 kV reached 1,892,000 km. Failure or loss of power may bring direct economic losses and personnel casualty. Hence, the task of transmission line detection and maintenance is of great significance. However, due to high cost, inefficiency, and high safety risk, traditional methods for manual line inspection have many drawbacks in operation, which cannot meet the needs today. UAV inspection can make up for the deficiency of manual way and become the mainstream tool of the future of line inspection (Singhal et al., 2018).

Manual Vs. Unmanned Aerial Vehicle Transmission Line Inspection

The transmission line inspection task involves mapping and inspection of transmission line components, vegetation encroachment monitoring, icing detection and measurement, and disaster monitoring. Manual and UAV line inspection have their own advantages and disadvantages, respectively.

Manual line inspection has the disadvantages of large labor, long inspection cycle, and low efficiency. Since a lot of lines are located in the suburbs or even depopulated zones, manual line inspection requires a long trip to get there, and due to the height



FIGURE 4 | Manual transmission line inspection and UAV inspection (Manual transmission line Inspection, 2018) (UAV transmission line Inspection, 2020).

TABLE 2 | Comparison between manual line inspection and UAV line inspection.

Line inspection mode	Manual transmission line inspection	UAV transmission line inspection
Advantage	1. Can work in a severe weather environment 2. Maintenance at the same time 3. Low cost of manual training	1. High efficiency 2. Low cost of equipment 3. Ensure personnel safety 4. Live working
Disadvantage	1. Time consuming and inefficient 2. High safety risk	1. Restricted by harsh climate 2. High cost of training

of the power tower (the general tower is 30–50 m high and the ultra-high voltage tower is 100 m high), technicians need to climb up and inspect the defects under live working, as shown in **Figure 4**. However, manual inspection can operate in extremely low temperature and high-altitude areas when most UAVs cannot operate normally. In addition, manual line inspection can repair the equipment in the process of line inspection, but UAV cannot yet (Peng et al., 2016).

Compared with manual inspection, UAV has lower equipment cost and higher line inspection efficiency. In the process of line inspection, UAVs can not only ensure the safety of personnel but also ensure the normal operation of transmission lines because they can do the living work. With the development of technology, UAVs may operate more complex inspection with even simple maintenance. Therefore, UAV inspection has high performance and application potential (Liu et al., 2019a). Comparisons between manual line inspection and UAV line inspection are listed in **Table 2**.

Current Status of Unmanned Aerial Vehicle Transmission Line Inspection

With the development of UAV and airborne sensor technology, multisensor cooperation can be realized, which improves the accuracy and automation of equipment defect judgment. Through UAV equipped with some infrared, ultraviolet, camera, and other equipment, hidden trouble in the budding state can be located and found in time, and the fault can be eliminated to protect the safe operation of the transmission line (Hu et al., 2018). Then, the abnormal point of transmission line fault is inquired by the equipment carried, and then, the fault point is photographed in hover to obtain more obvious information, which is prepared for subsequent image processing and decision making.

According to the different working principles, the imaging loads applied in UAV inspection can be divided into three categories, namely, a visible imaging load, an infrared imaging load, and an ultraviolet imaging load, as shown in **Figure 5**. Infrared imaging load is mainly used for accurate and efficient detection and identification of abnormal heating defects of power transmission equipment in the process of power operation. The visible and infrared image fusion process is shown in **Figure 6**. Ultraviolet imaging technology is a kind of inspection technology for abnormal corona discharge and surface local pollution of transmission equipment.

Airborne lidar technology is the most representative technology for detecting the safe distance between line and ground objects. It can obtain reliable and accurate three-dimensional topography and feature information of the corridor, mainly including power towers, green trees, and tall buildings.

However, UAV line inspection technology has not been widely used in the world until now. From the early 20th century, some developed countries carried out UAV line inspection on transmission lines, including routine inspection, live maintenance, and other aspects. Nowadays, China's UAV application in transmission line inspection is at the top of the world.

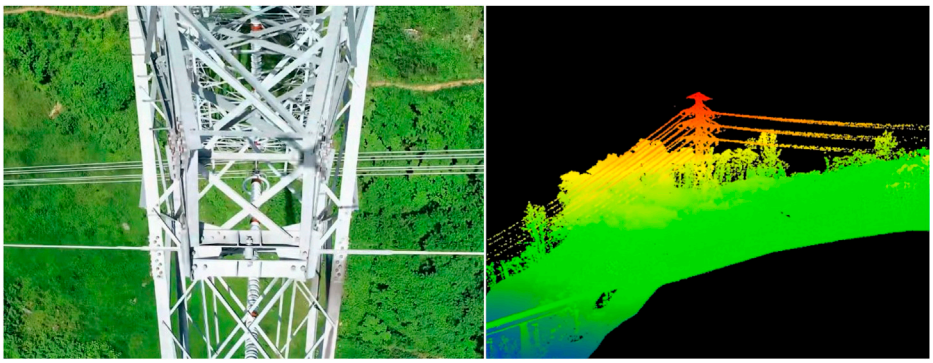


FIGURE 5 | Visible and infrared images.

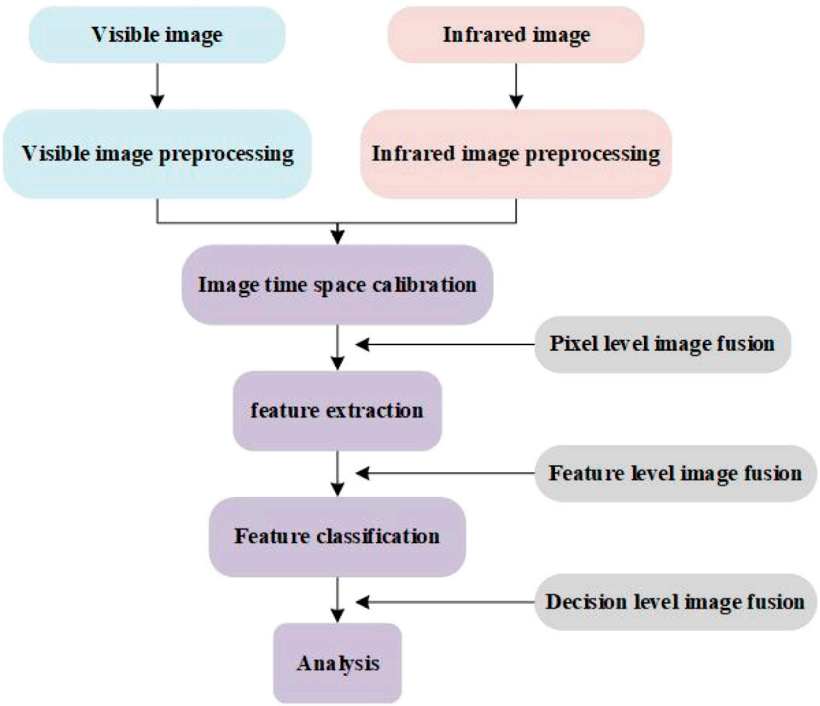


FIGURE 6 | Visible and infrared image fusion process.

Current Status of Unmanned Aerial Vehicle Transmission Line Inspection in China

From around 2010, China's electric companies have made achievements in UAV inspection and taken corresponding measures to promote the development of UAV application in line inspection. The Shandong Electric Power Research Institute and Luneng Company have jointly developed an unmanned helicopter for transmission line inspection with a high load, high-definition, and wide-angle camera; Shanghai Electric Power Company has used a small, fixed-wing UAV for transmission line inspection, which can detect high-voltage transmission lines in real-time. The State Grid also actively promotes the UAV line inspection work, sets up a UAV training center, conducts UAV flight technology training for power inspectors, and urges the formation of a UAV inspection team (Zhai et al., 2018).

In 2013, the China Southern Power Grid Corporation promoted the intelligent inspection mode of "machine inspection and manual inspection" for transmission lines and has fully realized the collaborative inspection mode of "machine inspection as the main and manual inspection as the auxiliary." In 2016, the large-scale unmanned helicopter line inspection system independently developed by Guangdong Power Grid Company was applied to electric power inspection. The UAV was equipped

with a visible light camera, infrared thermal imager, ultraviolet imager, 3D lidar, and other sensors and realized real-time analysis and processing of inspection data (Qian et al., 2016). After 2019, Guangdong Power Grid established the first formal UAV patrol management center in China, which has mastered technical difficulties such as night patrol, radar positioning, laser point cloud data splicing, and laser automatic modeling. UAV has been widely used in power inspection, with an annual operation volume of more than 210,000 times, accounting for 87.5% of the patrol work, ranking first in the country (China Electric Power Enterprise Federation, 2020). In 2020, the UHV company of Southern Power Grid used UAV to inspect the UHV converter station in the Kunming North Converter Station in Yunnan Province and realized the automatic flight inspection of UAV and real-time data management and analysis, which is another milestone of UAV application in China's power grid. In 2021, Longnan power grid of the State Grid began to scale and use UAV to conduct an independent inspection. The intelligence level of autonomous inspection of UAV is standardized comprehensively, and the autonomous cruise modeling and visible light modeling of key lines in the region are completed. The three-dimensional map database of transmission line patrol path is established, and the efficiency of line inspection can be improved by using new technological intelligent equipment. China's UAV inspection technology is more and more mature, diversifying the application.

Current Status of Unmanned Aerial Vehicle Transmission Line Inspection in Other Countries

Britain. In 1995, Wales University and EA power consulting company developed and tested the robot for transmission line inspection based on the unmanned helicopter of aerobatics (Chen et al., 2011). The UAV was equipped with a high-resolution CCD color visible light camera and a stability control system to enhance its antiwind ability and realize visual tracking and online detection.

Japan. In 2010, the Kansai Electric Power Company and Chiba University jointly developed a set of UAV systems for line inspection (Montambault et al., 2010). The system had a powerful image processing and recognition function, which can automatically identify common faults of transmission equipment, such as broken wire strand, abnormal heating, and welding cracks, and carry out large-scale line corridor inspection, as well as identify the growth of trees near the transmission line and tower.

Spain. In 2000, Campoy and Mejias of Madrid Polytechnic University in Spain were equipped with a visual navigation system in UAV (Mejias et al., 2007). Through machine vision navigation combined with GPS-aided positioning, the automatic navigation function of UAV line inspection was realized. The system included the helicopter airborne subsystem and ground control subsystem. The airborne subsystem gets the real-time image and its pose information. The ground control system analyzes the information returned by the airborne system and provides navigation and control information for UAV.

STANDARDIZATION OF UNMANNED AERIAL VEHICLE TRANSMISSION LINE INSPECTION

According to GB/T 20000.1:2014 Guidelines for Standardization, standardization is an activity of establishing provisions for common and repeated use regarding actual or potential problems, as well as activity of preparing, issuing, and implementing documents aimed at the achievement of the optimum order in a context and the promotion of common benefit.

The application of standardization in scientific research can avoid repetitive work in research and shorten the design cycle of products. Technical standardization is the most basic technical and competitive requirement for industrial competition in the development of global economic integration and the guarantee to ensure that the industry can be recognized in international competition.

Standardization of China's Unmanned Aerial Vehicle Transmission Line Inspection

China has formed a relatively complete set of UAV transmission line inspection standardization after many years' development of UAV transmission line inspection. Industry standards have laid a foundation for electric power enterprises to conduct UAV line inspection, and enterprise standard has also supplemented and improved industry standard. These standards, listed in **Table 3**, standardize UAV inspection operation from the aspects of operation safety management, equipment configuration method, functional quality requirements, etc., which improve the operation safety regulations, equipment and technical conditions, and personnel training.

China's standardizations apply to fixed-wing UAV and rotor UAV patrol overhead transmission lines. Through preparing UAV line inspection, the line inspection mode and method are specified and required (China's National Energy Administration, 1482). The UAV line inspection process is shown in **Figure 7**, and the basic inspection contents are listed in **Table 4**.

Patrol Mode. It is mainly divided into careful line inspection, channel line inspection, fault line inspection, and special line inspection. The rotary-wing UAV is used in careful line inspection for the first time, such as the line body equipment and ancillary facilities and the lines with defects or abnormalities that need a fine inspection. Fault line inspection and special line inspection are mainly to find and confirm the fault point and check the equipment damage and other abnormal conditions.

Preparation before Line Inspection. The preparation before line inspection includes personnel preparation and operation preparation. The personnel should be qualified to operate UAV and have corresponding health conditions and reasonably allocated according to the line inspection task and the type of aircraft used. Operation preparation is composed of airspace declaration, field investigation, and equipment inspection. Airspace declaration of UAV inspection should be

TABLE 3 | Standardization of China's UAV transmission line inspection.

Approved time	Standard number	Standard name	Standard issuing department
2015	DL/T 1482–2015	Technical guidelines for UAV inspection of overhead transmission lines	National energy administration
	Q/GDW 11383–2015	Configuration guide for UAV inspection system of overhead transmission line	State grid
	Q/GDW 11399–2015	Safety regulations for patrol inspection of electric UAV	
2016	DL/T 1578–2016	Unmanned helicopter inspection system for overhead transmission lines	National energy administration
2018	T/CEC 193–2018	Specification for training and assessment of UAV patrol operators in power industry	China Electricity Council

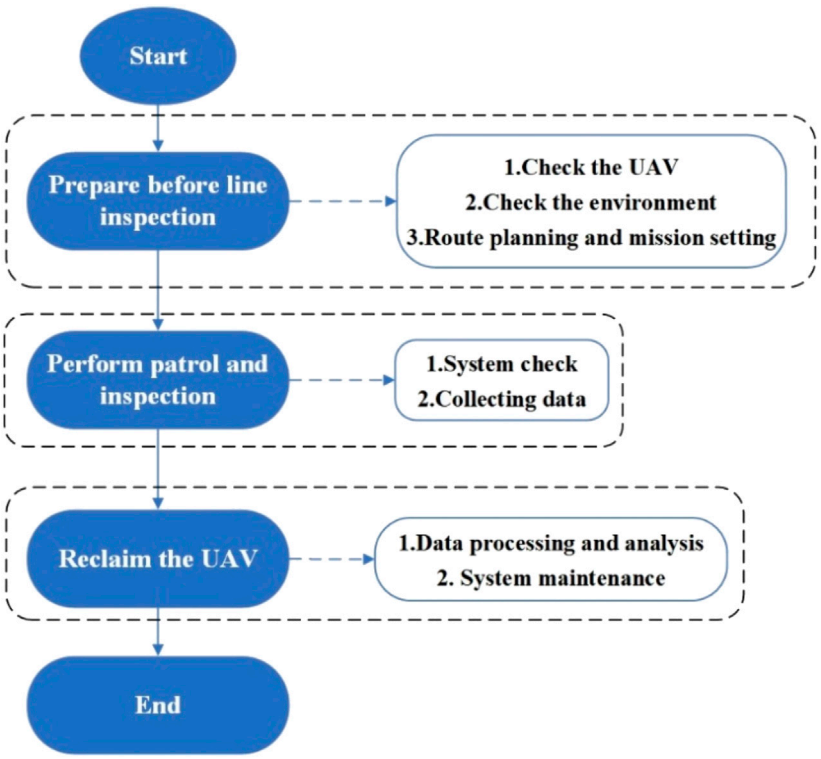


FIGURE 7 | UAV line inspection process.

TABLE 4 | Basic inspection contents.

Equipment	Visible light inspection	Infrared inspection
Conducting wire	Broken wire, obstacle, broken strand	Hot spot
Drainage line	Broken wire, obstacle, broken strand	Hot spot
Clamp	Loose	Contact hot spot
Coiled tubing	—	Heating
Tower	Damage, deformation, bolt looseness	—
Insulator	Scattered, self-exploding, obstacle	Thermal breakdown
Damper	Damage, displacement, defect	—
Accessory equipment	Defect	—
Line corridor	Geological disasters, vegetation growth, external destruction	—

carried out according to the inspection scope and relevant administrative management measures. Flight inspection requires operators to conduct field investigation in advance to verify the trajectory of the UAV inspection route and surrounding environment and find a suitable place as the take-off and landing point. It is necessary to check the line coordinates and altitude of each tower of the inspection line and whether lines are crossing. The equipment inspection mainly contains the visible light load debugging inspection and infrared temperature measurement load debugging inspection.

Line Inspection Method. The major methods of line inspection are tower line inspection and intermediate line inspection. Rotary-wing UAV should approach the tower at low speed and hover to collect data when necessary. During patrol inspection, the distance between UAV and line equipment shall not be less than 30 m, the horizontal distance shall not be less than 25 m, and the distance between UAV and surrounding obstacles shall not be less than 50 m. The direction of the line inspection should be parallel to the direction of the ground wire in the corresponding shift. It is not suitable for medium and large UAVs to fly, hover, and cross directly above the line.

Standardization of Other Countries

To meet the standardization needs of international UAV industry development, the International Organization for Standardization (ISO) established the ISO/TC20/SC16 UAV system standardization subtechnical committee in 2014. The American Society for Testing and Materials (ASTM) has issued 12 civil UAV standards, including eight airworthiness standards, three operational standards, and one training and certification standard. There are three standards for agricultural UAV operators and maintenance in Japan, which specify the safety requirements of UAV design, overhaul, operator qualification, operation, and maintenance (Zeng et al., 2016).

The U.S.A. In 2019, the United States proposed to establish a standardized system of UAV transmission line inspection. Specifically, with energy-related UAV inspections, the American Society of Mechanical Engineers (ASME) is drafting a document of what information need inspectors and UAV owner operators need to know for such missions. The energy industry often adopts a "wait and see" approach when it comes to drones in America. To make inspections of pipelines and transmission lines over long distances practical, flights that are beyond the visual line of sight (BVLOS) are needed. However, there are legal restrictions on the flight range of civil UAVs, so the UAV inspection needs special approval and its standardization process is also more difficult.

Japan. In April 2019, Japan established a research group on UAV line inspection technology and proposed to establish a standardized system of UAV line inspection (Application report of Japan's transmission, 2018). However, the technology of UAV line inspection still stays in the use of visual line inspection but not the radar, infrared, and other technologies. Due to the Japanese UAV laws and regulations, the problem of UAV line inspection in urban areas still needs to be solved. Japan has mature development in the usage of UAV in agriculture which can share experiences in line inspection standards setting.

European Union. Most EU standards refer to ISO and International Electrotechnical Commission (IEC) standards. Although the application of UAV in transmission line inspection is very extensive, the automatic line inspection of UAV is not mature and a standard system has not been planned yet. Legal regulations restrict the greater use of BVLOS UAVs. BVLOS UAVS need special granted permits for utilities to test.

SWOT-PEST ANALYSIS OF INTERNATIONAL PROMOTION OF CHINA'S UNMANNED AERIAL VEHICLE TRANSMISSION LINE INSPECTION STANDARDIZATION

SWOT analysis is a systematic and logical approach to investigate the internal and external factors of the studied subject, upon which the most suitable promotion mode under the current situation can be determined *via* the comprehensive analysis of related factors of the investigation subject. Meanwhile, PEST analysis refers to the specific and detailed analysis of the macroenvironment. This study combines SWOT and PEST to study the feasibility of international promotion of China's UAV transmission line inspection standardization.

Strengths

Political

In 2018, the standardization administration of China announced the "Belt and Road" (B&R) action plan (2018–2020 years) which further defined "promoting the internationalization of China's standards and promoting international cooperation in production and equipment manufacturing,". Moreover, through the standards information platform established by the Belt and Road (B&R) initiative, some of China's standards have been widely promoted around the world. Since the line inspection technology of B&R countries is not as advanced as that of China and the standard has not been formed yet, China can use its accumulated experience in this field to provide them with more services. Meanwhile, the standardization is a consequential technical basis and rule for economic and trade exchanges and industrial cooperation in promoting the B&R construction process (Shao et al., 2020).

Economical

Located in the east of Asia, China covers 9,600,000 square kilometers, with a population of 1.437 billion and GDP of 15.67 trillion US dollars in 2020 (Hu, 2021). At present, China has become the world's second-largest economy, the largest industrial, commodity trading, and foreign exchange reserve country. Unlike other economies, China has maintained economic growth despite COVID-19, and its GDP is projected to grow by 8.4% in 2021, according to the International Monetary Fund. The booming economy provides opportunities for the technology development and promotion of the standardization of UAV transmission line inspection.

Social

With the commercialization of civil UAV, people have a deeper understanding of UAV and a higher degree of acceptance. At the same time, UAV application reduces the risk and cost of line inspection, providing more options for power companies and creating new jobs. 5G technology and the application of artificial intelligence will further improve the efficiency of line inspection. China's line inspection UAV has more functions and more

reliable technology, and the key is low price and high-cost performance. These advantages add a greater attraction to the promotion of China's UAV line inspection standard.

Technological

China owns a variety of key technologies of UAV inspection and has rich experience in operation. In 2013, China Southern Power Grid Company (CSG) began to promote the mechanical patrol operation of transmission lines and established the mechanical patrol operation center in 2015. Focused on the development of power UAV application capability, this operation center issued the standard system and carried out the key technology research work.

At present, lidar technology and RTK technology are the main means of UAV autonomous inspection (DUAN, 2016). Using CW lidar, CSG realized the measurement of safe distance between the conductor and ground. With the help of Internet of Things technology, the State Grid Corporation of China and CSG upload UAV inspection data to the data cloud in real time and use the deep neural network algorithm, big data, and image recognition technology to automatically analyze inspection data and accurately find defects and generate inspection report. In the UAV line inspection, the defect intelligent recognition technology is adopted. Through the UAV inspection image intelligent recognition algorithm, the manual interpretation of inspection images is gradually reduced or even replaced, so as to realize the practicability of artificial intelligent recognition technology (Cui, 2016). These key technologies in inspection lay the foundation for the popularization of China's UAV inspection standards.

Weaknesses

Political

China lacks an effective platform for the application and promotion of standards abroad, and the communication channels among the government, industry, and enterprises are limited. For the internationalization achievements of key technical fields and helpful standards, there is insufficient cooperation and exchange between governments. Meanwhile, European and American standards are still dominant in many fields, so China's standards encounter great difficulties in the promotion and application.

Economical

COVID-19 has led to a global recession and severely hampered international economic cooperation, and most of the cooperation projects between China and other countries are blocked. Under the global environment of economic downturn, China's exported products may face high import taxes, which is not conducive to the promotion of China's UAV inspection standards.

Social

UAV application in transmission lines includes equipment maintenance and technical personnel training. UAV may encounter various technical obstacles and damages in the process of inspection. Simple faults may be solved on site, but for some complex problems of UAVs, they can only be returned to the manufacturer for maintenance, which increases the maintenance cost of line inspection UAVs. Furthermore, since the training of line inspection UAV operators is not common in the world, for countries with less-developed technology, the cost of training UAV operators will increase. This will hinder the promotion of China's UAV line inspection standards.

Technological

It is difficult to break through the technical level of UAV line inspection. Although China's enterprises have abundant funds and numerous technical personnel teams, the development of UAV is still facing a strong technical bottleneck, endurance and weather resistance, which greatly limits the application of civil UAV (Liu et al., 2019b). Besides, there are professional UAV line inspection operation training institutions in China, such as the UTC training center in DJI, which can provide training and issue flight certificates for UAV line inspection operators. However, the number of operators who meet the UAV flight qualification is still very limited, and a large number of UAV operators need to be trained to realize UAV line inspection widely.

Opportunities

Political

The B&R initiative has been promoted by the Chinese government, and foreign cooperation between the relevant enterprises was benefited from it. At the same time, China continues to improve the national innovation system, speed up the construction of a powerful country in science and technology, and strongly support the development of UAV and other new technologies.

Economical

In the 14th five-year plan (2021–2025), China clearly points out that it is necessary to improve the overseas production service network and circulation system, accelerate the international development of producer services such as finance, consulting, accounting, and law, and promote the going out of China's products, services, technology, brands, and standards. The Chinese government will improve the integrated regulatory system for domestic and foreign trade and promote the convergence of laws and regulations, regulatory system, business qualifications, quality standards, inspection and quarantine, certification, and accreditation. These measures provide a good business environment for China's economy in the future. Meanwhile, the international economy will usher in a great recovery with the increasing coverage of COVID-19 vaccine, which has laid an economic foundation for the international promotion of China's UAV line inspection standardization.

Social

Language is an important factor for the international promotion of Chinese UAV line inspection standards. At present, some translators do not understand UAV line inspection technology while the operators and engineers are not proficient in foreign languages. The shortage of professional translators may lead to the problems of incorrect or inconsistent expression of technological

terms. Translation should be faithful to the original, not only to meet the requirements of grammar and correct expression of content but also to reflect the professionalism and standardization, so as to avoid multiple foreign expressions in the same Chinese professional vocabulary, ambiguity, and misunderstanding (Chen and Zhang, 2020).

Technological

China's artificial intelligence development has achieved a desirable technical goal, and 5G network construction has basically reached the annual goal. With the steady development of these two technologies, artificial intelligence will further enhance the intelligent interaction, information processing, analysis, and decision-making capabilities of UAVs, while 5G will improve the communication and data transmission capabilities of UAVs. The two will jointly release more potential power in the international promotion of China's UAV line inspection standard.

Threats

Political

For developing countries or less-developed countries and regions, their national standards are missing or not perfect. For example, the technical indicators of most central Asian countries still follow the standards of the former Soviet Union from the 1960s to the 1970s (Ma and Ma, 2018). The lack of a top-level strategy, planning of related promotion work, professional promotion personnel, and institutions, especially the lack of systematic, mature, and effective application, creates challenges for the local application of China's UAV line inspection standard.

Economical

Since 2018, trade frictions between China and the United States have escalated to many fields such as trade, science and technology, finance, and international rules, which has led to a dramatic impact on the global economy. Although vaccination has brought hope to stimulate economic activity and expand investment, the continuous economic stimulus policies around the world, especially the unprecedented scale of the US stimulus plan, have also triggered concerns about economic overheating and rising inflation expectations.

Social

The projects invested in many countries are generally required to follow European or American standards, and the acceptance of China's standards is not very often. Usually, the standards of these projects have been clearly implemented in bidding documents. At the same time, it may be restricted by law in some countries, and the promotion of China's UAV line inspection standard may need to make corresponding changes.

Technological

The system of standards is distinctive in different countries. Relevant technical standards in the United States are prepared and adopted voluntarily by industry organizations, institutions, and enterprises according to the technical regulations issued by the government. EU standards which are formulated by government agencies are part of the regulations, and most of them are mandatory. China's technical regulations and standards are governed by the state and are divided into four levels: national standards, industry standards, local standards, and enterprise standards. At present, China implements a standard system that combines mandatory standards with recommended standards (Chen, 2021).

Information security and personal privacy are also problems of UAV line inspection applications. It is inevitable for UAV from taking photos of buildings and roads when it conducts the line inspection, which may involve personal privacy, especially in urban areas. Moreover, how to ensure the security of information and data collected during the analysis is also a crucial issue that should be paid attention to.

CONCLUSIONS AND EXPECTATIONS

Nowadays, UAV has gradually become the main tool of transmission line inspection. Meanwhile, the standardization of such industry further accelerates the promotion of line inspection technology. Based on the analysis of the promotion of UAV line inspection *via* the SWOT analysis method, the following conclusions can be summarized:

(a) China's civil UAV technology is at the leading level in the world, which has abundant experience and advanced technologies. Thus, China's UAV line inspection standard can be used as a reference standard for other countries, which can help them to promote such industry in a more reliable and fast way.
(b) China's UAV line inspection standards may be limited by laws and regulations in other countries, and the acceptance of Chinese standards in other countries is also relatively low. Therefore, China's standards can be correspondingly changed according to the actual situation of other countries, and China's UAV line inspection technology can also act as an important driving force for promotion.
(c) China is the main member of the Belt and Road Initiative and the global destiny community, which needs to take the responsibility to promote China's technology around the world. In this context, the promotion of China's UAV line inspection standard will be strongly supported, which will contribute to the development and popularization of international UAV line inspection technology.

The existing standards of UAV inspection enable electric power companies to use UAVs for routine patrol tasks, but for the future development and application of patrol technology, there still exists a lot of room for UAVs to exploit for more advancement. With the development of UAV technology, the merits of UAV such as high economy, strong flexibility, and not restricted by terrain make it a hot research topic in transmission line inspection. There are some prospects for future development of UAV inspection.

Autonomous inspection: Manually manipulated UAV inspection is extremely complicated and difficult for the flyer, and there is a great demand to develop an intelligent UAV for autonomous inspection. The inspection results of different manual operation modes may vary greatly, and the inspection of overhead transmission lines is mostly cyclic and repetitive work. Relying on the operators completely will cause the problems of high labor intensity and low inspection efficiency, which will make it difficult to adapt to the new needs of power operation and maintenance. Therefore, autonomous inspection has become one of the research directions.

Battery life improvement: On the other hand, the lack of UAV range is a bottleneck problem that limits the promotion of the mounted UAV power patrol mode, and the current stage of application in the field of power inspection of small- and medium-sized multirotor UAVs in the patrol grid technology inspection load after the endurance of the patrol to maintain 10–30 min inspectors need to frequently replace the battery, which seriously affects the efficiency of inspection. In the future, it is also possible to improve the endurance of UAVs by using nest power supply.

Auxiliary maintenance: UAV can carry out not only defect monitoring but also simple maintenance operations. In the field of UAV auxiliary maintenance, we need to actively explore new technologies, including developing live water flushing, emergency lighting, and equipment anomaly detection based on voiceprint recognition, in order to further expand the application of UAV in inspection.

The last is the maintenance of UAV. In the aspect of UAV maintenance, the maintenance manual is formulated for the whole cycle process of UAV inspection, and the routine maintenance and research work on key components of UAV is carried out. Therefore, in addition to the UAV transmission line inspection standards, it is also necessary to formulate corresponding standards for UAV maintenance.

DATA AVAILABILITY STATEMENT

The original contributions presented in the study are included in the article/Supplementary Material; further inquiries can be directed to the corresponding author.

AUTHOR CONTRIBUTIONS

XL: conceptualization and writing–reviewing and editing. ZL: writing–original draft preparation and investigation. HW: writing–reviewing and editing. WL: conceptualization, resources, and supervision.

ACKNOWLEDGMENTS

We appreciatively acknowledge the support of the program entrusted by the legislative Affairs Commission of the Standing Committee of the Yunnan Provincial People's Congress (648820140054) and the Talents Training Program of Kunming University of Science and Technology (KKZ3201524007).

REFERENCES

Application report of Japan's transmission (2018). Application Report of Japan's Transmission Line Inspection UAV. Available at: https://www.meti.go.jp/meti_lib/report/H30FY/000078.pdf.

Chen, C., Chen, B. M., and Lee, T. H. (2011). Special Issue on Development of Autonomous Unmanned Aerial Vehicles. *Mechatronics* 21, 763–764. doi:10.1016/j.mechatronics.2011.03.009

Chen, D., Geng, J., Zhang, W., and Guo, L. (2020). Dynamic Modeling and Simulation of Flapping wing UAV. *Computer Meas. Control* 28 (06), 202–206.

Chen, J., and Zhang, B. (2020). Research on Overseas Application and Promotion Mode of Chinese Standards. *China standardization* 1, 57–61.

Chen, L. (2021). One Dimensional " B&R " Background Standardization and Modern Circulation Industry Development. *Business Econ. Res.* 1, 18–21.

China Electric Power Enterprise Federation (2020). *Annual Development Report 2020 of China Electric Power Industry*, 6.

China's National Energy Administration *Technical Guidelines for UAV Inspection of Overhead Transmission Lines*, China: Beijing. DL/T 1482—2015.

Cui, M. (2016). *Parameter Test and Radiation Calibration of Solar Blind Ultraviolet Image Intensifier and ICCD*. Graduate School of Chinese Academy of Sciences.

Duan, M. (2016). 3D Power Lines Reconstruction from Airborne LiDAR point Cloud. *Acta Geodaetica et Cartographica Sinica* 45 (12), 1495.

Fei, L. (2019). Research on the Development Status of Stratospheric Airship. *Decis. making exploration* 05, 96.

Fu, J., Shao, G., and Wu, L. (2017). Defect Detection of Line Facility Using Hierarchical Model with Learning Algorithm. *High Voltage Eng.* 43 (1), 266–275.

Gangolu, S., and Sarangi, S. (2020). A Novel Complex Current Ratio-Based Technique for Transmission Line protection. *Prot. Control. Mod. Power Syst.* 5 (3), 239–247. doi:10.1186/s41601-020-00168-6

Geospatial Media and Communications (2018). Rotary-wing UAV. Available at: https://www.geospatialworld.net/news/dji-announces-drone-law-enforcement-partnership-with-axon.

Guo, H., he, W., and Sun, Y. (2017). "Development prospect and Prospect of Parafoil UAV," in Proceedings of the third China Aviation Science and technology conference.

Hassanalian, M., and Abdelkefi, A. (2017). Classifications, Applications, and Design Challenges of Drones: A Review. *Prog. Aerospace Sci.* 91, 99–131. doi:10.1016/j.paerosci.2017.04.003

He, J., Chen, K., Meng, L., Luo, Y., Liang, C., and Xu, Y. (2020). Review of protection and Fault Handling for a Flexible DC Grid. *Prot. Control. Mod. Power Syst.* 5 (2), 151–165. doi:10.1186/s41601-020-00157-9

Hu, A. (2021). The Year of Building a Moderately Prosperous Society in an All-Round Way in 2020 (An Evaluation of China's Economic and Social Development). *J. Beijing Univ. Technology*, 1–20.

Hu, M., Liu, W., Lu, J., Fu, R., Peng, K., Ma, X., et al. (2018). On the Joint Design of Routing and Scheduling for Vehicle-Assisted Multi-UAV Inspection. *Future Generation Computer Syst.* 94, 214–223.

Icao's circularUAS (2011). ICAO's Circular UAS. Available at: https://www.icao.int/Meetings/UAS/Documents/Circular%20328_en.pdf.

Kumar, A., Anwar, M. N., and Kumar, S. (2021). Sliding Mode Controller Design for Frequency Regulation in an Interconnected Power System. *Prot. Control. Mod. Power Syst.* 6 (1), 77–88. doi:10.1186/s41601-021-00183-1

Kumar Injeti, S., and Kumar Thunuguntla, V. (2020). Optimal Integration of DGs into Radial Distribution Network in the Presence of Plug-In Electric Vehicles to Minimize Daily Active Power Losses and to Improve the Voltage Profile of the System Using Bioinspired Optimization Algorithms. *Prot. Control. Mod. Power Syst.* 5 (1), 21–35. doi:10.1186/s41601-019-0149-x

Lanny Lin (2021). Parafoil UAV. Available at: http://lannyland.blogspot.com/2009/05/robot-of-day-cq-10-snowgoose-cargo.html.

Liang, W., Wu, D., and Gu, S. (2020). Route Optimization Method for fine Autonomous Inspection of Transmission Line Multi Rotor UAV. *High voltage Technol.* (9).

Liu, Z., DU, Y., and Chen, Y. (2019a). Simulation and experiment on the Safety Distance of Typical ±500 kV DC Transmission Lines and Towers for UAV Inspection. *High Voltage Eng.* 45 (2), 426–432.

Liu, Z., Wang, X., and Liu, Y. (2019b). *Application of Unmanned Aerial Vehicle Hangar in Transmission Tower Inspection Considering the Risk Probabilities of Steel Towers*. IEEE Access.

Ma, P., and Ma, J. (2018). Overview and Analysis of Standardization Development in Tajikistan. *Stand. Sci.* 9, 14–16.

Manual transmission line Inspection (2018). News Feature: Power Line Inspector under High Temperature. Available at: https://www.sohu.com/a/244982732_99923877.

Mejias, L., Correa, J. F., Mondragon, I., and Campoy, P. (2007). COLIBRI: A Vision-Guided UAV for Surveillance and Visual Inspection. *Proc. 2007 IEEE Int. Conf. Robotics Automation*. doi:10.1109/robot.2007.363883

Miao, X., Liu, Z., and Yan, Q. (2020). Overview of UAV Transmission Line Intelligent Inspection Technology. *J. Fuzhou Univ. Nat. Sci. Edition* (2), 198–209.

Montambault, S., Beaudry, J., Toussaint, K., and Pouliot, N. (2010). "On the Application of VTOL UAVs to the Inspection of Power Utility Assets," in 2010 1st International Conference on Applied Robotics for the Power Industry. doi:10.1109/carpi.2010.5624443

Muniappan, M. (2021). A Comprehensive Review of DC Fault protection Methods in HVDC Transmission Systems. *Prot. Control. Mod. Power Syst.* 6 (1), 1–20. doi:10.1186/s41601-020-00173-9

Padhy, S., and Panda, S. (2021). Application of a Simplified Grey Wolf Optimization Technique for Adaptive Fuzzy PID Controller Design for Frequency Regulation of a Distributed Power Generation System. *Prot. Control. Mod. Power Syst.* 6 (1), 21–36. doi:10.1186/s41601-021-00180-4

Peng, X., Qian, J., and Mai, X. (2016). Automatic Power Line Inspection Technology of Large Unmanned Helicopter and its Application. *South. Power Syst. Technology* 10 (2), 24–31.

Qian, J., Mai, X., and Wang, K. (2016). Application and Effect of Large Scale Patrol Inspection for Power Lines of Large Unmanned Helicopter in Guangdong Power Grid. *Guangdong electric power* 29 (005), 124–129.

Shao, G., Liu, Z., Fu, J., Tan, J., Yi, C., and Zhou, L. (2020). Research Progress of UAV Inspection Technology for Overhead Transmission Lines. *High voltage Technol.* 46 (01), 14–22.

Singhal, G., Bansod, B., and Mathew, L. (2018). *Unmanned Aerial Vehicle Classification, Applications and Challenges: A Review*. Basel, Switzerland: Preprints.

Sui, Y., and Ning, F. (2021). Review of Power Inspection Technology of UAV Mounted on Overhead Transmission Line. *Power grid Technol.* 1–15.

Tang, L., Yu, L., and Zhang, Y. (2018). Research and Application of Civil UAV System. *Machine tool and hydraulic* 46 (05), 127–133.

Tang, L., Yu, L., and Zhang, Y. (2018). Research and Application of Civil UAV System. *Machine tools and hydraulics*.

Tavakoli, M., and Nafar, M. (2020). Human Reliability Analysis in Maintenance Team of Power Transmission System protection. *Prot. Control. Mod. Power Syst.* 5 (4), 270–282. doi:10.1186/s41601-020-00176-6

Tzu-ti, H. (2020). Flapping-wing UAV. *Taiwan News*. 2020/07/23. https://www.taiwannews.com.tw/en/news/3972498.

Uav transmission line Inspection (2020). Professional UAV System Manufacturer AOPA Training Institutions. http://www.ttaviation.com.

Unmanned airship (2014). Russia Purchased from Belarus an Unmanned Airship "BAK EM". Available at: https://en.topwar.ru/61036-rossiya-priobrela-u-belorussii-bespilotnyy-dirizhabl-bak-em.html.

Volt Aerial Robotics (2016). Fixed-wing UAV. Available at: https://www.voltaerialrobotics.com/wavesight.

Yi, W., Liming, C., Lingyu, K., Jie, Z., and Miao, W. (2017). "Research on Application Mode of Large Fixed-wing UAV System on Overhead Transmission Line," in 2017 IEEE International Conference on Unmanned Systems (ICUS) in Beijing, 88–91.

Zeng, Q., Chen, G., and Yang, G. (2016). "UAV Standardization Research and Application Promotion," in Standardization helps supply side structural reform and Innovation: Proceedings of the 13th China Standardization Forum.

Zhai, Y., Zhao, H., Zhao, M., and Jiao, S. (2018). Design of Electric Patrol UAVs Based on a Dual Antenna System. *Energies* 11, 866. doi:10.3390/en11040866

Zhao, T., Pan, X., and He, Q. (2017). "Application of Dynamic Ant colony Algorithm in Route Planning for UAV," in Seventh International Conference on Information Science and Technology of IEEE, 433–437.

Conflict of Interest: The authors declare that the research was conducted in the absence of any commercial or financial relationships that could be construed as a potential conflict of interest.

Copyright © 2021 Li, Li, Wang and Li. This is an open-access article distributed under the terms of the Creative Commons Attribution License (CC BY). The use, distribution or reproduction in other forums is permitted, provided the original author(s) and the copyright owner(s) are credited and that the original publication in this journal is cited, in accordance with accepted academic practice. No use, distribution or reproduction is permitted which does not comply with these terms.

frontiers in Energy Research

ORIGINAL RESEARCH
published: 12 July 2021
doi: 10.3389/fenrg.2021.698003

Optimal Array Reconfiguration of a PV Power Plant for Frequency Regulation of Power Systems

*Tingyi He[1], Shengnan Li[1], Yiping Chen[2], Shuijun Wu[1] and Chuangzhi Li[3]**

[1]Yunnan Power Grid Co Ltd., Electric Power Research Institute, Kunming, China, [2]China Southern Power Dispatching and Control Center, Guangzhou, China, [3]College of Engineering, Shantou University, Shantou, China

This paper establishes a novel optimal array reconfiguration (OAR) of a PV power plant for secondary frequency control of automatic generation control (AGC). Compared with the existing studies, the proposed OAR can further take the AGC signal responding into account except the maximum power output, in which the battery energy storage system is used to balance the power deviation between the AGC signals and the PV power outputs. Based on these two conflicted objects, the OAR is formulated as a bi-objective optimization. To address this problem, the efficient non-dominated sorting genetic algorithm II (NSGA-II) is designed to rapidly obtain an optimal Pareto front due to its high optimization efficiency. The decision-making method called VIKOR is employed to determine the best compromise solution from the obtained Pareto front. To verify the effectiveness of the proposed bi-objective optimization of OAR, three case studies with fixed, step-increasing, and step-decreasing AGC signals are carried out on a 10 × 10 total-cross-tied PV arrays under partial shading conditions.

Keywords: optimal array reconfiguration, pv power plant, battery energy storage system, automatic generation control, bi-objective optimization

OPEN ACCESS

Edited by:
Xing He,
Shanghai Jiao Tong University, China

Reviewed by:
Yang Gao,
Shanghai Jiao Tong University, China
Songli Fan,
Suzhou University of Science and Technology, China

****Correspondence:***
Chuangzhi Li
20czli1@stu.edu.cn

Specialty section:
This article was submitted to Smart Grids, a section of the journal Frontiers in Energy Research

Received: *20 April 2021*
Accepted: *29 April 2021*
Published: *12 July 2021*

Citation:
He T, Li S, Chen Y, Wu S and Li C (2021) Optimal Array Reconfiguration of a PV Power Plant for Frequency Regulation of Power Systems. Front. Energy Res. 9:698003. doi: 10.3389/fenrg.2021.698003

INTRODUCTION

Recently, renewable energies are becoming increasingly welcomed and are gradually replacing most fossil fuels due to their inexhaustibility and eco-friendly nature. One of the most promising of these energies is solar energy (Sahu, 2015) since it can result in zero noise, less maintenance, and ready availability of source with abundant availability. However, the solar photovoltaic (PV) array faces some major challenges on dynamic environmental conditions, including insolation (Yousri et al., 2020a), temperature gradient and partial shading, etc. Among the parameters listed above, partial shading leads to a significant reduction in the PV array's energy output due to mismatch loss and power loss. The main reason for partial shading is cloud coverage, building shadows, and dropping dust (Koad et al., 2017).

Various PV array topologies like series-parallel (SP), total-cross-tied (TCT), and bridge linked (BL) have been designed to reduce the mismatch and power loss to address this issue (Fathy, 2020). It is verified that the power generated in TCT topology is the highest among the above topologies under partial shading conditions (PSC) (Winston et al., 2020). Three basic techniques for the reconfiguration process of the PV array, including physical relocation (Venkateswari and Rajasekar, 2020), electrical array reconfiguration (EAR) (Dhanalakshmi and Rajasekar, 2018), and electrical rewiring (Rao et al., 2014), were proposed based on the TCT topology. These techniques aimed to mitigate the mismatch loss via shade dispersion over the whole array.

In addition, the reconfiguration can be roughly divided into static (fixed) reconfiguration and dynamic reconfiguration according to whether the electrical interconnection changes after the array rearrangement. In the static reconfiguration group, the physical positions of all the modules are fixed under all shading conditions, which means that the electrical interconnection remains unchanged after array rearrangement, also known as one-time rearrangement (Potnuru et al, 2015). Various static reconfiguration utilized electrical rewiring techniques to improve the power output under PSC, including fixed electrical reconfiguration (Satpathy and Sharma, 2019), column index method (Pillai and Ram, 2018), unique connection method (Pareek and Dahiya, 2016), and Sudoku (Horoufiany and Ghandehari, 2018). Compared with the other three reconfigurations, Su Do Ku is found as one of the most effective ways to relocate PV modules (Rani et al., 2013), which was also proposed to reduce line losses (Potnuru et al., 2015) and to mitigate the mutual shadow (MSH) (Horoufiany and Ghandehari, 2018). In addition to electrical rewiring, many physical relocation techniques, such as Magic-square (MS) puzzle reconfiguration (Yadav et al., 2017), fixed electrical connection (PRM-FEC) (Sahu and Nayak, 2016), odd-even configuration (OEC) (Nasiruddin et al., 2019), were proposed to relocate modules without changing the electrical connection. It has been proved that physical migration based on MS reconstruction can avoid complex MPPT algorithms and provide superior performance (Horoufiany and Ghandehari, 2018; Rakesh and Madhavaram, 2016; Samikannu et al, 2016). On the other hand, OEC performed well compared with the other two technologies under the diagonal processing shadowing scenario (Yadav and Kumar, 2020). Unlike static reconfiguration, dynamic reconfiguration changes the electrical interconnection through a switching arrangement once the shade varies, which does not require massive labor and complex applications (Babu et al., 2018). Based on EAR technology, quite a few meta-heuristic algorithms have become novel techniques in recent years, including particle swarm optimization (PSO) (Babu et al., 2018), grasshopper optimization algorithm (GOA) (Fathy, 2018), multi-objective grey wolf algorithm (MOGWO) (Yousri et al., 2020d), standard genetic algorithm (SDGA) (Rajan et al., 2017), Marine predators algorithm (MPA) (Yousri et al., 2020b), artificial ecosystem-based optimization (AEO) (Yousri et al., 2020c), flow regime algorithm (FRA) (Babu et al., 2020), social mimic optimization algorithm (SMO) (Babu et al., 2020), Rao optimization (Babu et al., 2020).

Nevertheless, the existing studies of PV array reconfiguration did not consider the power response for automatic generation control (AGC) (Xi et al., 2018), while the battery energy storage system (BESS) (Jin et al., 2017) was not taken for the power fluctuation balance. Consequently, this paper establishes a novel optimal array reconfiguration (OAR) of a PV power plant with a BESS for AGC, which not only attempts to maximize the power output, but also aims to minimize the power deviation between the power outputs and the AGC signals. To solve OAR, the meta-heuristic based multi-objective optimization algorithms are suitable to find a high-quality Pareto front due to their flexible application and strong global searching ability. Hence, this work adopts the efficient non-dominated sorting genetic algorithm II (NSGA-II) for OAR, while a decision-making method called VIKOR is employed to determine the best compromise solution from the obtained Pareto front.

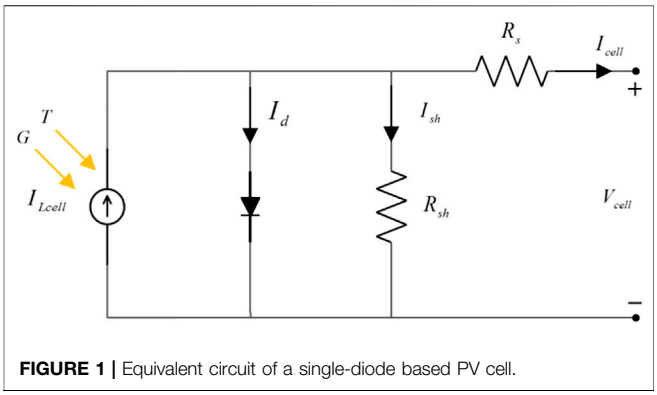


FIGURE 1 | Equivalent circuit of a single-diode based PV cell.

The remaining sections are organized as follows: The mathematical model of OAR is given in *Mathematical Model of Optimal Array Reconfiguration* Section. The solving process of NSGA-II and VIKOR for OAR is provided in *Design of NSGA-II and VIKOR for Optimal Array Reconfiguration* Section. *Case Studies* Section shows the simulation results. At last, the conclusion is given in *Conclusion* Section.

MATHEMATICAL MODEL OF OPTIMAL ARRAY RECONFIGURATION

Model of PV Array

The PV array can be formed by multiple PV modules in series and parallel, usually consisting of numerous series-parallel PV cells. For simplicity, the PV cells can be seen as a current generator. **Figure 1** shows the single-diode model (Rajasekar et al., 2013), which is a frequently used model, like the double diode model and triple diode model. Applying Kirchhoff's current law (KCL), the output current of a PV cell can be calculated by (Krishna and Moger, 2019):

$$I_{\text{cell}} = I_{\text{Lcell}} - I_{\text{d}} - I_{\text{sh}} \tag{1}$$

where I_{cell} is the output current of the PV cell; I_{Lcell} is the light generated current of the PV cell; I_{d} is the diode current; and I_{sh} is the current of the shunt resistance.

Further the PV cell's output current can be expressed as **Eq. 2** by expanding I_{d} and I_{sh} in **Eq. 1**:

$$I_{\text{cell}} = I_{\text{Lcell}} - I_{\text{o}}\left[exp\left(q\frac{V_{\text{cell}} + I_{\text{cell}}R_{\text{s}}}{b\sigma T_{\text{c}}} - 1\right)\right] - \frac{V_{\text{cell}} + I_{\text{cell}}R_{\text{s}}}{R_{\text{sh}}} \tag{2}$$

where I_o, q, V_{cell}, T_c, σ, b, R_s, and R_{sh} are the diode's saturation current, electron charge, PV cell's output voltage, operating temperature, ideality factor, Boltzmann's constant, PV cell's series and shunt resistance, respectively.

For a n_s series connected PV cells constructed PV module, its output current can be given as:

$$I_m = I_L - I_o\left[\exp\left(q\frac{V_m + I_m R_S}{n_s b\sigma T_c} - 1\right)\right] - \frac{V_m + I_m R_S}{R_{SH}} \quad (3)$$

where I_m is the output current of the PV module; q is the electron charge; V_m is output voltage of the PV module; R_S and R_{SH} are the series and shunt resistance of the PV module, respectively; and I_L is the light generated current of the PV module, which can be acquired as

$$I_L = \frac{G}{G_0}\left[I_{Lstc} + K_{sc}(T_c - T_0)\right] \quad (4)$$

where the actual and standard irradiation values are represented by G and G_0, respectively; I_{Lstc} is the light generated current of the PV module under the standard test condition; K_{sc} is the short-circuit current coefficient factor; and T_0 is the standard values of the operating temperature.

Applying **Eq. 3**, the output current equations for a PV array consisting of $N_s \times N_p$ modules, as shown in **Figure 2**, can then be rewritten in **Eq. 5** as (Krishna and Moger, 2019):

$$I_a = N_p I_L - N_p I_o\left[exp\left(q\frac{V_a + \frac{N_s}{N_p} I_a R_S}{N_s n_s b\sigma T_c} - 1\right)\right] - \frac{V_a + \frac{N_s}{N_p} I_a R_S}{\frac{N_s}{N_p} R_{SH}} \quad (5)$$

where I_a and V_a denote output current and output voltage of the PV array, respectively.

Total-Cross-Tied Connected Arrays in a PV Power Plant

Among conventional PV array topologies, TCT topology has been proved that the power generated is highest under PSC. It's clearly seen from **Figure 3** that the TCT interconnection scheme shows a 10 × 10 PV array's electrical connection where all the rows are connected in series connection, giving rise to 10 such series strings in parallel at each row.

Calculating the total output voltage and current of TCT connected PV arrays is of utmost importance. According to the circuit characteristics of TCT topology, the current of each column via PV array, which is in series connection, are equal. And the voltage of each row is also identical as each row via PV array is parallel. Applying Kirchhoff's voltage law (KVL) and KCL, we can get the overall PV power plant output voltage and current calculated as (Babu et al., 2018):

$$V_D = \sum_{p=0}^{9} V_{ap} \quad (6)$$

$$I_D = \sum_{q=0}^{9}\left(I_{pq} - I_{(p+1)q}\right) = 0, \quad p = 0, 1, 2, \ldots, 8 \quad (7)$$

where V_D is the overall output voltage, V_{ap} is the maximum voltage at the pth row, I_D is the overall output current, I_{pq} denotes the output current of the array at the pth row and the qth column.

Objective Function

In this work, two conflicted objectives are simultaneously considered, which aims to improve the generation benefit for the PV power plant while helping to balance the power disturbance for the power systems (Xi et al., 2018). The first objective is the maximization of power output for the PV power plant. It can be converted into a minimization of power deviation f_1 between the rated power output and the average power output. The second objective f_2 is the minimization of power deviation between the AGC signals and the power outputs, while the peak-valley difference of the power outputs is also taken into account. As a result, these two objectives can be calculated as follows:

$$\begin{cases} \min f_1 = P_{pv}^{rate} - \frac{1}{T}\sum_{t\in T} P_{pv}(t) \\ \min f_2 = \frac{1}{T}\sum_{t\in T}\left|P_{agc}(t) - \left[P_{pv}(t) - P_{bess}(t)\right]\right| + \max_{t\in T}\left[P_{pv}(t) - P_{bess}(t)\right] - \min_{t\in T}\left[P_{pv}(t) - P_{bess}(t)\right] \end{cases} \quad (8)$$

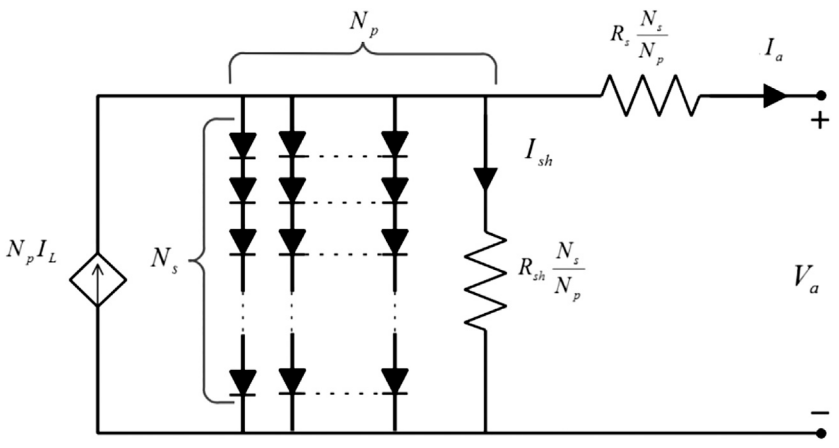


FIGURE 2 | Equivalent circuit of a PV array with $N_s \times N_p$ modules.

where P_{pv}^{rate} is the rated power output of the PV power plant; T is the time cycle of AGC ancillary services; $P_{pv}(t)$ is the power output of the PV power plant at the tth control time period; $P_{bess}(t)$ is the charging power of BESS at the tth control time period; and $P_{agc}(t)$ is the AGC signal at the tth control time period.

Note that many existing studies of PV array reconfiguration only focused on the maximum power output. In contrast, the presented objective functions in **Eq. 8** not only aims to maximize the power output of PV power plant, but also aims to response the AGC signal as close as possible. Hence, it can guarantee an economic and safe operation simultaneously.

Constraints

Firstly, OAR should satisfy the constraints of electrical switching states since each PV array can only exchange its row with another array from the same column, which can be described as follows (Zhang et al., 2021):

$$\begin{cases} s_{pq} \in \{0,1,\cdots,9\}, & p = 0,1,2,\ldots,9; \quad q = 0,1,2,\ldots,9 \\ \cup_{p=0}^{9} s_{pq} = \{0,1,\cdots,9\}, & q = 0,1,2,\ldots,9 \end{cases} \tag{9}$$

where s_{pq} denotes the electrical switching state of the array at the pth row and the qth column.

Secondly, the BESS should satisfy the power and energy capability constraints, as follows (Jin et al., 2017):

$$P_{bess}^{min} \le P_{bess}(t) \le P_{bess}^{max}, \quad t \in T \tag{10}$$

$$SOC_{bess}^{min} \le SOC_{bess}(t) \le SOC_{bess}^{max}, \quad t \in T \tag{11}$$

$$SOC_{bess}(t) = \begin{cases} SOC_{bess}(t-1) + P_{bess}(t) \cdot \Delta t \cdot \eta_{ch} / E_{bess}, & \text{if } P_{bess}(t) \ge 0 \\ SOC_{bess}(t-1) + P_{bess}(t) \cdot \Delta t / (\eta_{dis} \cdot E_{bess}), & \text{otherwise} \end{cases} \tag{12}$$

where P_{bess}^{min} and P_{bess}^{max} are the minimum and maximum charging power of BESS, respectively; SOC_{bess}^{min} and SOC_{bess}^{max} are the minimum and maximum state of charge (SOC) of BESS, respectively; η_{ch} is the charging efficiency; η_{dis} is the discharging efficiency; Δt is the control interval; and E_{bess} is the rated energy capability of BESS.

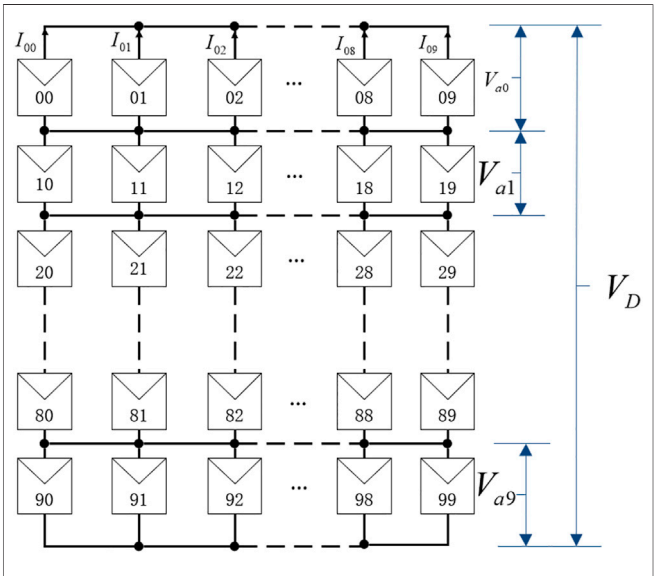


FIGURE 3 | 10 × 10 TCT connected arrays in a PV power plant.

DESIGN OF NSGA-II AND VIKOR FOR OPTIMAL ARRAY RECONFIGURATION

Design of NSGA-II

NSGA-II is suitable for OAR due to its high application flexibility and optimization efficiency. Since NSGA-II is a classical multi-objective optimization algorithm, the specific optimization operations (Deb et al., 2002) are not presented in this work. Here, we will focus on the design combination between NSGA-II and OAR.

Constraints Handling

To satisfy the electrical switching constraints in **Eq. 9**, all the PV arrays at each column can be assigned with different numbers from 0 to 9. In this work, these numbers will be re-assigned according to the sequence of the current solutions value. For the qth column, the numbers of all the PV arrays can be updated as follows:

$$s_{pq} = Rank\left(x_{pq}, \boldsymbol{x}_q\right) \tag{13}$$

where x_{pq} denotes the solution value for the array at the pth row and the qth column, which can be limited within a range; $\boldsymbol{x}_q$ denotes the solution vector of the arrays at the qth column; and $Rank(x_{pq}, \boldsymbol{x}_q)$ denotes the order of x_{pq} among all the solutions $\boldsymbol{x}_q$, which is set to be ascending order.

On the other hand, the solution for the charging power of BESS can be initialized and limited within its lower and upper bounds, as follows:

$$x_{bess} = P_{bess}^{min} + r \cdot \left(P_{bess}^{max} - P_{bess}^{min}\right) \tag{14}$$

where r is an uniform random number from 0 to 1.

Fitness Functions

Since the constraints in **Eqs 9**, **10** can be satisfied during the optimization, the fitness functions can be designed by considering the rest constraints in **Eqs 11**, **12**. Based on the penalty function method, the fitness functions of NSGA-II can be designed as follows:

$$\begin{cases} F_1 = f_1 + \sum_{t \in T} M(t) \\ F_2 = f_2 + \sum_{t \in T} M(t) \end{cases} \tag{15}$$

$$M(t) = \begin{cases} \chi \cdot \left[SOC_{bess}(t) - SOC_{bess}^{min}\right] \cdot \left[SOC_{bess}(t) - SOC_{bess}^{max}\right], & \textit{if violated} \\ 0, & \textit{otherwise} \end{cases} \tag{16}$$

where $M(t)$ is the penalty component for the constraints in **Eq. 11** at the tth control time period; and χ is the penalty factor, which is used to avoid an infeasible solution and commonly set to be a large positive value.

Design of Vikor

As an ideal solution based decision making method, VIKOR (Lin et al., 2021) can objectively select the best compromise solution according to the distribution of the obtained Pareto front without human intervention. For the OAR with two objective functions, the calculation process of VIKOR can be given as follows (Lin et al., 2021):

Step 1: Determine the positive and negative ideal solutions based on the obtained Pareto front, as

$$\begin{cases} \boldsymbol{y}^{+} = \{y_1^{+}, y_2^{+}\} \\ \boldsymbol{y}^{-} = \{y_1^{-}, y_2^{-}\} \end{cases} \tag{17}$$

$$\begin{cases} y_j^{+} = \min\limits_{i=1,2,\ldots,n} y_j^{i}, \quad j = 1, 2; \\ y_j^{-} = \max\limits_{i=1,2,\ldots,n} y_j^{i}, \quad j = 1, 2; \end{cases} \tag{18}$$

where $\boldsymbol{y}^{+}$ and $\boldsymbol{y}^{-}$ are the positive and negative ideal solutions, respectively; and y_j^i is the value of the jth objective function corresponding to the ith Pareto solution.

Step 2: Calculate the group utility and the regret of each alternative Pareto solution, as

$$GU_i = \sum_{j=1,2} \omega_j \frac{y_j^{+} - y_j^{i}}{y_j^{+} - y_j^{-}}, \quad i = 1, 2, \ldots, n \tag{19}$$

$$IR_i = \max_{j=1,2} \left(\omega_j \frac{y_j^{+} - y_j^{i}}{y_j^{+} - y_j^{-}} \right), \quad i = 1, 2, \ldots, n \tag{20}$$

where ω_j is the weight coefficient of the jth objective function; GU_i and IR_i are the group utility and the regret of the ith Pareto solution, respectively.

Step 3: Calculate the comprehensive evaluation value for each alternative Pareto solution, as

$$Q_i = \theta \cdot \frac{GU_i - GU^{+}}{GU^{-} - GU^{+}} + (1 - \theta) \cdot \frac{IR_i - IR^{+}}{IR^{-} - IR^{+}}, \quad i = 1, 2, \ldots, n \tag{21}$$

$$\begin{cases} GU^{+} = \min\limits_{i=1,2,\ldots,n} GU_i \\ GU^{-} = \max\limits_{i=1,2,\ldots,n} GU_i \end{cases} \tag{22}$$

$$\begin{cases} IR^{+} = \min\limits_{i=1,2,\ldots,n} IR_i \\ IR^{-} = \max\limits_{i=1,2,\ldots,n} IR_i \end{cases} \tag{23}$$

where Q_i is the comprehensive evaluation value of the ith Pareto solution; GU^{+} and GU^{-} are minimum and maximum group utilities, respectively; IR^{+} and IR^{-} are minimum and maximum regrets, respectively; and θ denotes the weight coefficient of the group utility.

Step 4: Determine the best compromise solution based on the comprehensive evaluation values, as

$$\boldsymbol{x}_{\text{best}} = \arg\min_{i=1,2,\ldots,n} Q_i(\boldsymbol{x}_i^{*}) \tag{24}$$

where $\boldsymbol{x}_i^{*}$ denotes the ith Pareto solution and $\boldsymbol{x}_{\text{best}}$ denotes the best compromise solution.

Execution Procedure

Taken together, the specific execution procedure of NSGA-II and VIKOR for OAR can be given in **Table 1**, where k denotes the kth iteration of NSGA-II and $k_{\max}$ is the maximum iteration number.

CASE STUDIES

In this work, a 30-MW PV power plant (Zhang et al., 2021) with 30 identical sub-systems is introduced to evaluate the performance of the proposed method, in which each sub-system is formed by the 10 × 10 TCT PV arrays. The specific parameters of the testing system can be found in Zhang et al. (2021). The operating temperature for all the PV arrays is set to be 25°C, while the irradiation distribution for each sub-system at different minutes are given in **Figure 4**. **Figure 5** provides the output features of each sub-systems at the 1st and 5th minutes. It is obvious that PSC at the 5th minute can directly lead to multiple peaks of P-V curves instead of a single peak at the 1st minute. Besides, the main parameters of the BESS is given in **Table 2**.

In NSGA-II, a larger population size or maximum iteration number will result in a high-quality Pareto front with a higher probability. However, it also easily leads to a long computation time. Hence, these two parameters can set to be as large as possible if the computation time of NSGA-II can satisfy the real-time optimization of OAR. In this work, they are set to be 200 and 100 respectively via trial-and-error based on this setting rule. Moreover, the penalty factor is set be 10^8. To guarantee a fair preference for each objective function, all weight coefficients of VIKOR are set to be 0.5. All the simulations are carried out in the platform of Matlab R2020a.

Study on a Constant Automatic Generation Control Signal

In this study, a constant AGC signal $P_{\text{agc}}(t) = 27$ MW is adopted to test the performance of the proposed method. **Figure 6** shows the optimal Pareto front by NSGA-II and the best compromise solution by VIKOR. It is apparent that the obtained Pareto front can distribute equably within a quite large range, while VIKOR can effectively achieve an impersonal decision without any preference on each objective function. **Figure 7** gives the irradiation distribution based on the compromise solution. It shows that the PSC of some arrays can be shared by other arrays.

Based on the reconfiguration scheme, **Figure 7** gives the comparison of theoretical output between the compromise solution and the initial distribution at the 5th minute. It can be found from **Table 3** that the proposed method can significantly increase the theoretical maximum power point, which is about 116.22% of that with the initial distribution in **Figure 4**.

TABLE 1 | The specific execution procedure of NSGA-II and VIKOR for OMAR.

1: Input the real-time predictive weather conditions;
2: Initialize the parameters of NSGA-II and VIKOR;
3: Initialize the population of NSGA-II by **Eqs 13**, **14**;
4: Set k: = 1;
5: **WHILE** k ≤ kmax
6: Calculate the fitness functions of all the searching individuals by **Eqs (1)–(8)** and **(15)–(16)**;
7: Select the non-dominated individuals;
8: Update the repository of the Pareto solutions;
9: Implement the optimization operators of NSGA-II;
10: Update the solutions of all the searching individuals;
11: Set k: = *k*+1;
12: **END WHILE**
13: Output the optimal Pareto front of OAR;
14: Select the best compromise solution by VIKOR with **Eqs 17–24**;
15: Re-execute the bi-objective optimization of OAR from step 1 to step 14 at the next time period.

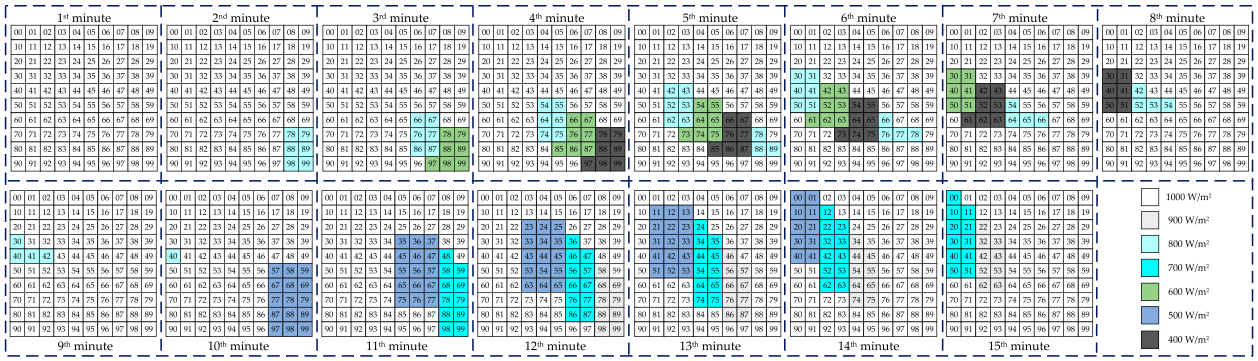


FIGURE 4 | The irradiation distribution for each sub-system of the PV power plant.

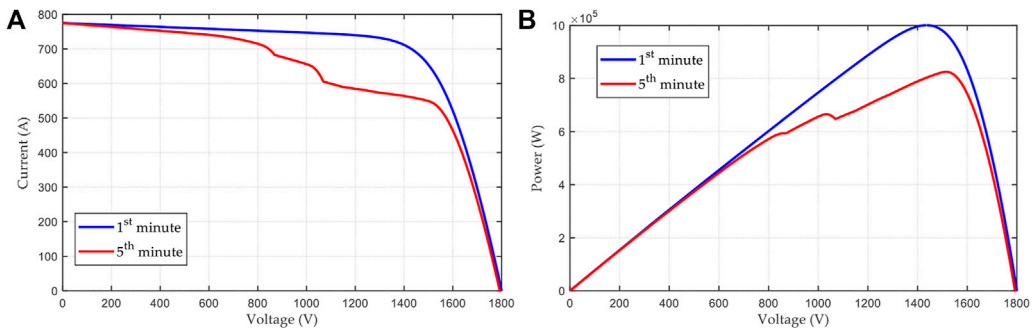


FIGURE 5 | Output feature of each sub-system at the 1st and 5th minutes. **(A)** *I–V* curve and **(B)** *P–V* curve.

Figure 8 shows the optimal power outputs of the proposed method and that without optimization on a constant AGC signal, where the power outputs of the proposed method is the results corresponding to the best compromise solution. Firstly, it can be seen from **Figure 8A** that the power outputs obtained by the proposed method can approximate the AGC signal closer than that without optimization. At the same time, the charging power of BESS obtained by the proposed method can effectively adapt to the power output of the PV power plant. Furthermore, it is clearly that the power output of the PV power plant obtained by the proposed method is much higher than that without optimization, as illustrated in **Figure 8B**.

Figure 9 provides the result comparison between proposed method and that without optimization on a constant AGC signal. Post hoc analysis reveals that the power deviations of the two objective functions obtained by the proposed method are much

TABLE 2 | Main parameters of BESS.

P_{bess}^{min} (MW)	P_{bess}^{max} (MW)	E_{bess}(MW·h)	SOC_{bess} (t = 0)	SOC_{bess}^{min}	SOC_{bess}^{max}	η_{ch}	η_{dis}
2	2	10	50%	10%	90%	0.95	0.95

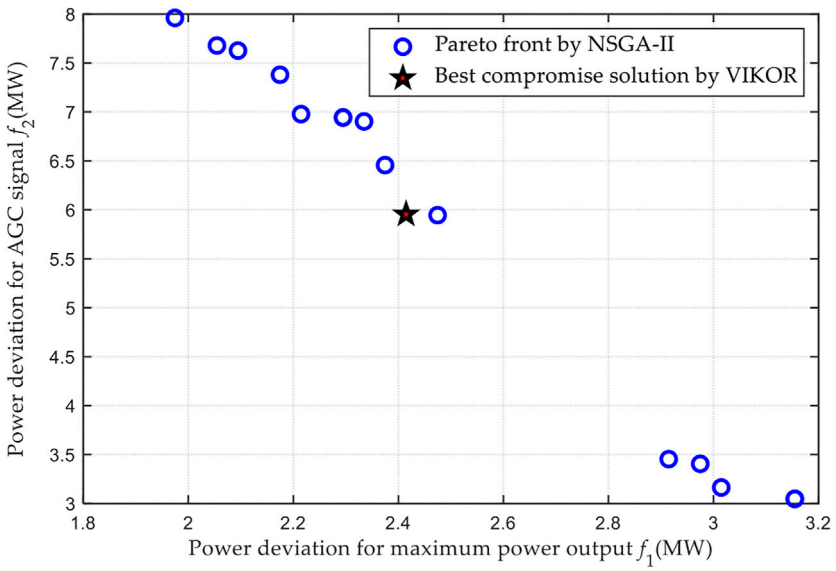


FIGURE 6 | Optimal Pareto front by NSGA-II and best compromise solution by VIKOR on a constant AGC signal.

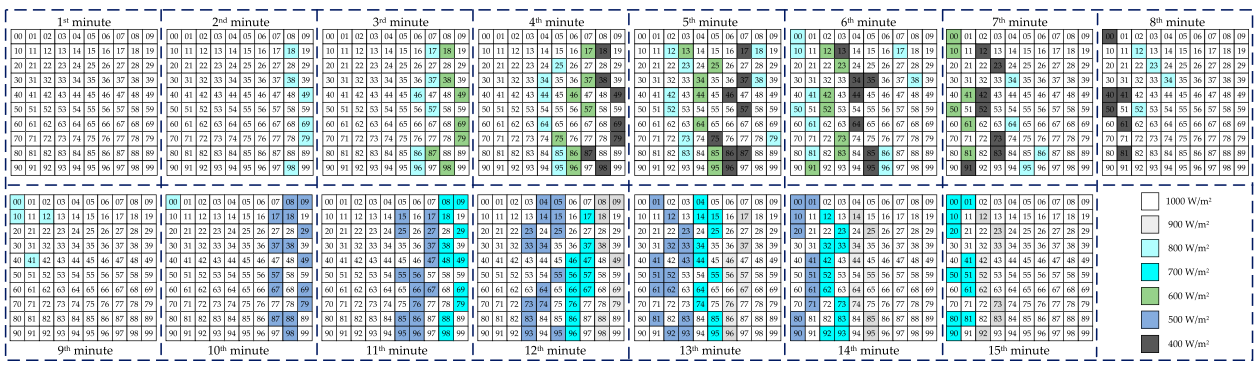


FIGURE 7 | The irradiation distribution for each sub-system based on the compromise solution.

smaller than that without optimization. Particularly, both of these two power deviations can be reduced 51.27 and 44.03% compared with that without optimization.

Study on the Varying Automatic Generation Control Signals

In this study, the varying AGC signals are design to evaluate the performance of the proposed method, where the AGC signals can be represented as follows:

$$P_{agc}(t) = \begin{cases} 28, & 0 \le t < 5 \\ 20, & 5 \le t < 10 \\ 26, & 10 \le t < 15 \end{cases} \tag{25}$$

Figure 10 shows the optimal Pareto front by NSGA-II and the best compromise solution by VIKOR for the varying AGC signals. Similarly, the Pareto front obtained by NSGA-II can effectively cover the large ranges for both of two objective functions. Besides, VIKOR can select an impersonal compromise solution from the Pareto front.

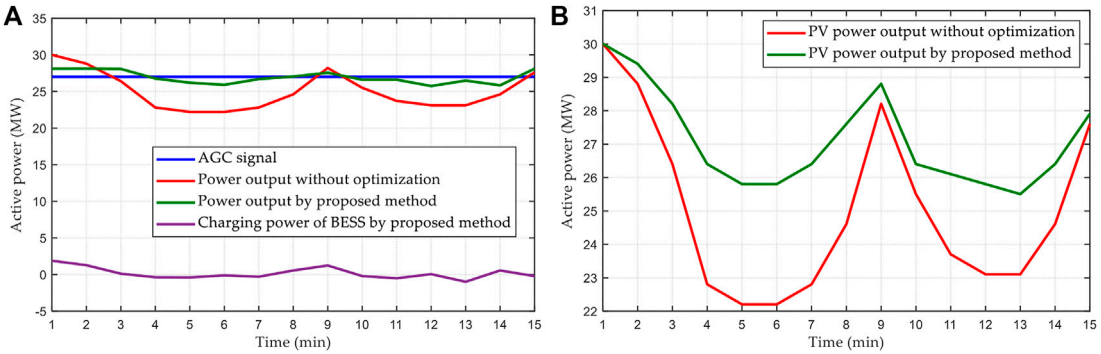


FIGURE 8 | Optimal power outputs of the proposed method and that without optimization on a constant AGC signal. **(A)** Total power output and **(B)** PV power output.

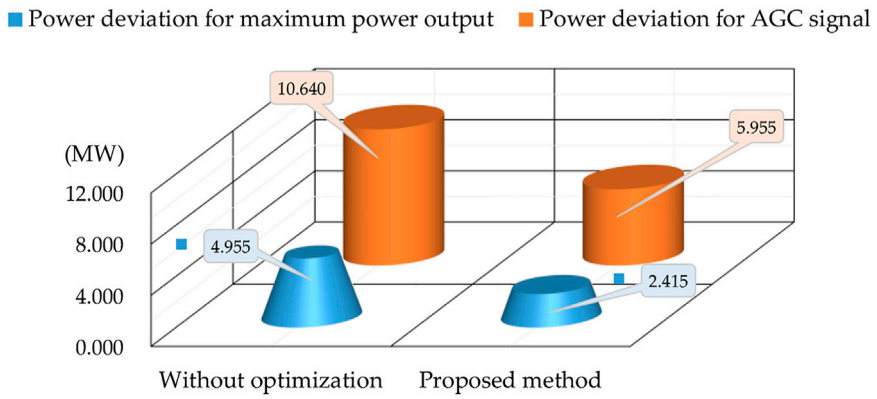


FIGURE 9 | Result comparison between proposed method and that without optimization on a constant AGC signal.

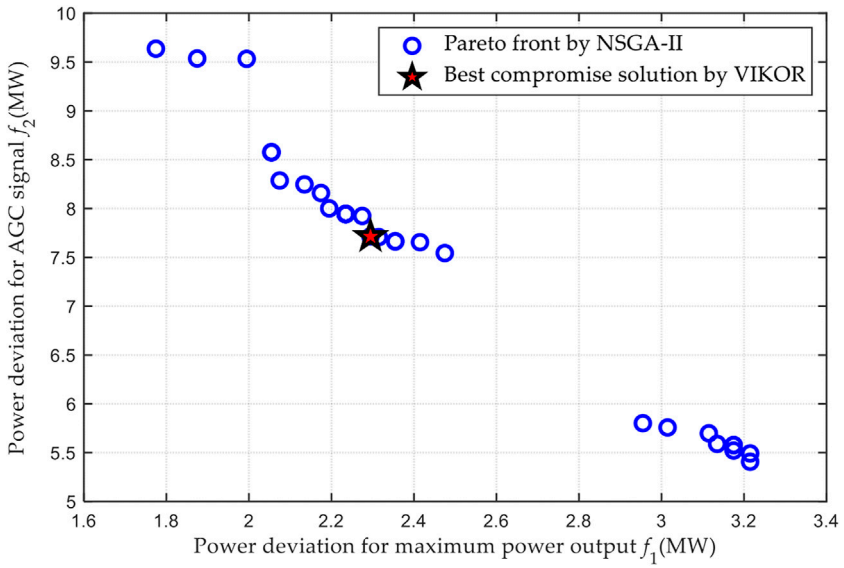


FIGURE 10 | Optimal Pareto front by NSGA-II and best compromise solution by VIKOR on the varying AGC signals.

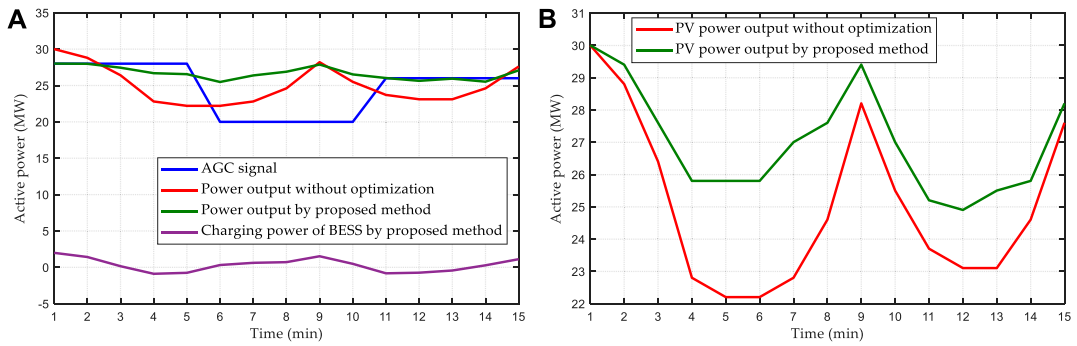


FIGURE 11 | Optimal power outputs of the proposed method and that without optimization on the varying AGC signals.

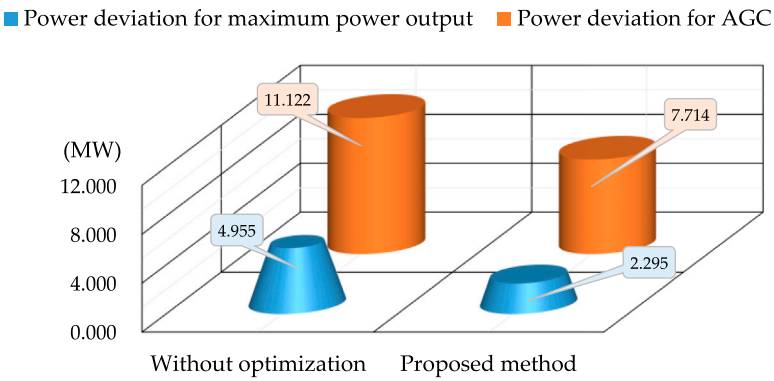


FIGURE 12 | Result comparison between proposed method and that without optimization on the varying AGC signals.

TABLE 3 | Comparison of theoretical output between the compromise solution and the initial distribution at the 5th minute

Row no	Initial distribution			Row no	Compromise solution		
	I_D	V_D	P^{max}		I_D	V_D	P^{max}
#7	$7.4I_{am}$	$10V_{am}$	74 V_{am} I_{am}	#1	$8.6I_{am}$	$10V_{am}$	86 V_{am} I_{am}
#6	$7.6I_{am}$	$9V_{am}$	68.4 V_{am} I_{am}	#3	$8.8I_{am}$	$9V_{am}$	79.2 V_{am} I_{am}
#8	$7.8I_{am}$	$8V_{am}$	62.4 V_{am} I_{am}	#4	—	—	—
#5	$8.8I_{am}$	$7V_{am}$	61.6 V_{am} I_{am}	#8	—	—	—
#4	$9.6I_{am}$	$6V_{am}$	57.6 V_{am} I_{am}	#7	$9I_{am}$	$6V_{am}$	$54V_{am}$ I_{am}
#0	$10I_{am}$	$5V_{am}$	50 V_{am} I_{am}	#9	—	—	—
#1	—	—	—	#5	$9.2I_{am}$	$4V_{am}$	$36.8V_{am}$ I_{am}
#2	—	—	—	#2	$9.4I_{am}$	$3V_{am}$	$28.2V_{am}$ I_{am}
#3	—	—	—	#6	$9.6I_{am}$	$2V_{am}$	$19.2V_{am}$ I_{am}
#9	—	—	—	#0	$10I_{am}$	$1V_{am}$	$10V_{am}$ I_{am}

Figure 11 gives the optimal power outputs of the proposed method and that without optimization on the varying AGC signals. Compared with the power output of that without optimization, the power outputs obtained by the proposed method is more closer to the varying AGC signals, especially in the periods of $0 \le t < 5$ and $10 \le t < 15$. Moreover, the PV power output obtained by the proposed method is much higher than that without optimization, in which the maximum increment is about 6 MW at the 5th minute.

Figure 12 gives the result comparison between proposed method and that without optimization on the varying AGC signals. It clearly shows that the proposed method can dramatically reduce the power deviations for both of two objective functions against to that without optimization. More specially, both of these two power deviations

obtained by the proposed method are only about 46 and 69% of that without optimization.

CONCLUSION

In this paper, a novel bi-objective optimization method is proposed for optimal array reconfiguration of a PV power plant with a battery energy storage system, in which the main contributions can be summarized as follows:

1) The constructed OAR not only can achieve a maximum power output of PV power plant via the array reconfiguration under various irradiations, but also can effectively respond to the AGC signal via the power scheduling with BESS. As a result, the operation economy of the PV power plant and the operation safety of the connected power grid can be significantly improved.
2) The design of NSGA-II can efficiently find a high-quality Pareto front for OAR, thus the dispatchers of the PV power plant can select different high-quality optimal dispatch schemes to satisfy the current operating requirement from the Pareto front.
3) The design of VIKOR can objectively make a decision to select the best compromise solution from the obtained Pareto front, which can guarantee a fair preference on each objective function. Hence, the operation economy and safety can be improved simultaneously.

In future works, the control cost of PV array reconfiguration can be considered as an added objective function in OAR, thus the service life of the switching devices can be extended. As the number of objective functions, a more efficient multi-objective optimization algorithms will be more suitable to obtain a high-quality Pareto front for OAR.

DATA AVAILABILITY STATEMENT

The original contributions presented in the study are included in the article/Supplementary Material, further inquiries can be directed to the corresponding author.

AUTHOR CONTRIBUTIONS

TH contributed to the conception of the study. TH and SL contributed significantly to analysis and manuscript preparation; YC and CL performed the data analyses and wrote the manuscript; SW helped perform the analysis with constructive discussions.

FUNDING

This work was jointly supported by Research on Regional Power Grid Frequency Regulation with Renewable Energy Participation (YNKJXM20191240), Research and Development Start-Up Foundation of Shantou University (NTF19001).

REFERENCES

Babu, T. S., Ram, J. P., Miyatake, T. M., Blaabjerg, F., and Rajasekar, N. (2018). Particle Swarm Optimization Based Solar PV Array Reconfiguration of the Maximum Power Extraction under Partial Shading Conditions. *IEEE Trans. Sustain. Energ.* 9 (1), 74–85. doi:10.1109/tste.2017.2714905

Babu, T. S., Yousri, D., and Balasubramanian, K. (2020). Photovoltaic Array Reconfiguration System for Maximizing the Harvested Power Using Population-Based Algorithms. *IEEE Access* 8, 2169–3536. doi:10.1109/access.2020.3000988

Deb, K., Pratap, A., and Agarwal, S. (2002). A Fast and Elitist Multiobjective Genetic Algorithm: NSGA-II. *IEEE Trans. Evol. Comput.* 6 (2), 182–197. doi:10.1109/4235.996017

Dhanalakshmi, B., and Rajasekar, N. (2018). A Novel Competence Square Based PV Array Reconfiguration Technique for Solar PV Maximum Power Extraction. *Energ. Convers. Manag.* 174, 897–912. doi:10.1016/j.enconman.2018.08.077

Fathy, A. (2020). Butterfly Optimization Algorithm Based Methodology for Enhancing the Shaded Photovoltaic Array Extracted Power via Reconfiguration Process. *Energ. Convers. Manag.* 220, 113115. doi:10.1016/j.enconman.2020.113115

Fathy, A. (2018). Recent Meta-Heuristic Grasshopper Optimization Algorithm for Optimal Reconfiguration of Partially Shaded PV Array. *Sol. Energ.* 171, 638–651. doi:10.1016/j.solener.2018.07.014

Horoufiany, M., and Ghandehari, R. (2018). Optimization of the Sudoku Based Reconfiguration Technique for PV Arrays Power Enhancement under Mutual Shading Conditions. *Sol. Energ.* 159, 1037–1046. doi:10.1016/j.solener.2017.05.059

Jin, X., Mu, Y., Wu, J., and Jia, H. (2017). Dynamic Economic Dispatch of a Hybrid Energy Microgrid Considering Building Based Virtual Energy Storage System. *Appl. Energ.* 194, 386–398. doi:10.1016/j.apenergy.2016.07.080

Koad, R. B. A., Zobaa, A. F., and El-Shahat, A. (2017). A Novel MPPT Algorithm Based on Particle Swarm Optimization for Photovoltaic Systems. *IEEE Trans. Sustain. Energ.* 8 (2), 468–476. doi:10.1109/tste.2016.2606421

Krishna, G. S., and Moger, T. (2019). Improved SuDoKu Reconfiguration Technique for Total-Cross-Tied PV Array to Enhance Maximum Power under Partial Shading Conditions. *Renew. Sustain. Energ. Rev.* 109, 333–348. doi:10.1016/j.rser.2019.04.037

Lin, M., Chen, Z., Gou, X., and Xu, Z. (2021). Score Function Based on Concentration Degree for Probabilistic Linguistic Term Sets: An Application to TOPSIS and VIKOR. *Inform. Sci.* 551, 270–290. doi:10.1016/j.ins.2020.10.061

Nasiruddin, I., Khatoon, S., Jalil, F., and Bansal, R. (2019). Shade Diffusion of Partial Shaded PV Array by Using Odd-Even Structure. *Sol. Energ.* 181, 519–529. doi:10.1016/j.solener.2019.01.076

Pareek, S., and Dahiya, R. (2016). Enhanced Power Generation of Partial Shaded Photovoltaic Fields by Forecasting the Interconnection of Modules. *Energy* 95, 561–572. doi:10.1016/j.energy.2015.12.036

Pillai, D. S., and Ram, J. P. (2018). Power and Mismatch Losses Mitigation by a Fixed Electrical Reconfiguration Technique for Partially Shaded Photovoltaic Arrays. *Energy Convers. Manage.* 172, 402–417. doi:10.1016/j.enconman.2018.07.016

Potnuru, S. R., Pattabiraman, D., and Ganesan, S. I. (2015). Positioning of PV Panels for Reduction in Line Losses and Mismatch Losses in PV Array. *Renew. Energ.* 78, 264–275. doi:10.1016/j.renene.2014.12.055

Rajan, N. A., Shrikant, K. D., Dhanalakshmi, B., and Natarajan, R. (2017). Solar PV Array Reconfiguration Using the Concept of Standard Deviation and Genetic Algorithm. *Energ. Proced.* 117, 1062–1069. doi:10.1016/j.egypro.2017.05.229

Rajasekar, N., Kumar, N. K., and Venugopalan, R. (2013). Bacteril Foraging Algorithm Based Solar PV Parameter Estimation. *Sol. Energ.* 97, 255–265. doi:10.1016/j.solener.2013.08.019

Rakesh, N., and Madhavaram, T. V. (2016). Performance Enhancement of Partially Shaded Solar PV Array Using Novel Shade Dispersion Technique. *Front. Energ.* 10, 227–239. doi:10.1007/s11708-016-0405-y

Rani, B. I., Ilango, G. S., and Nagamani, C. (2013). Enhanced Power Generation from PV Array under Partial Shading Conditions by Shade Dispersion Using Su Do Ku Configuration. *IEEE Trans. Sustain. Energ.* 4, 594–601. doi:10.1109/tste.2012.2230033

Rao, P. S., Ilango, G. S., and Nagamani, C. (2014). Maximum Power from PV Arrays Using a Fixed Configuration under Different Shading Conditions. *IEEE J. Photovolt.* 4 (2), 679–686. doi:10.1109/JPHOTOV.2014.2300239

Sahu, B. K. (2015). A Study on Global Solar PV Energy Developments and Policies with Special Focus on the Top Ten Solar PV Power Producing Countries. *Renew. Sustain. Energ. Rev.* 43, 621–634. doi:10.1016/j.rser.2014.11.058

Sahu, H. S., and Nayak, S. K. (2016). Extraction of Maximum Power from a PV Array under Nonuniform Irradiation Conditions. *IEEE Trans. Electron. Devices* 63 (12), 4825–4831. doi:10.1109/ted.2016.2616580

Samikannu, S. M., Namani, R., and Subramaniam, S. K. (2016). Power Enhancement of Partially Shaded PV Arrays through Shade Dispersion Using Magic Square Configuration. *J. Renew. Sust. Energ.* 8, 063503. doi:10.1063/1.4972285

Satpathy, P. R., and Sharma, R. (2019). Power and Mismatch Losses Mitigation by a Fixed Electrical Reconfiguration Technique for Partially Shaded Photovoltaic Arrays. *Energ. Convers. Manag.* 192, 52–70. doi:10.1016/j.enconman.2019.04.039

Venkateswari, R., and Rajasekar, N. (2020). Power Enhancement of PV System via Physical Array Reconfiguration Based Lo Shu Technique. *Energ. Convers. Manag.* 215, 112885. doi:10.1016/j.enconman.2020.112885

Winston, D. P., Kumaravel, S., and Kumar, B. P. (2020). Performance Improvement of Solar PV Array Topologies during Various Partial Shading Conditions. *Sol. Energ.* 196, 228–242. doi:10.1016/j.solener.2019.12.007

Xi, L., Chen, J., Xu, Y., and Huang, Y. (2018). Smart Generation Control Based on Multi-Agent Reinforcement Learning with the Idea of the Time Tunnel. *Energ.* 153, 977–987. doi:10.1016/j.energy.2018.04.042

Yadav, A. S., Pachauri, R. K., Chauhan, Y. K., Choudhury, S., and Singh, R. (2017). Performance Enhancement of Partially Shaded PV Array Using Novel Shade Dispersion Effect on Magic-Square Puzzle Configuration. *Sol. Energ.* 144, 780–797. doi:10.1016/j.solener.2017.01.011

Yadav, K., and Kumar, B. (2020). Mitigation of Mismatch Power Losses of PV Array under Partial Shading Condition Using Novel Odd Even Configuration. *Energ. Rep.* 6, 427–437. doi:10.1016/j.egyr.2020.01.012

Yousri, D., Allam, D., and Eteiba, M. B. (2020a). Optimal Photovoltaic Array Reconfiguration for Alleviating the Partial Shading Influence Based on a Modified Harris Hawks Optimizer. *Energ. Convers. Manag.* 206, 112470. doi:10.1016/j.enconman.2020.112470

Yousri, D., Babu, T. S., Balasubramanian, K., and Osama, A. (2020d). Multi-Objective Grey Wolf Optimizer for Optimal Design of Switching Matrix for Shaded PV Array Dynamic Reconfiguration. *IEEE Access* 8, 159931–159946. doi:10.1109/access.2020.3018722

Yousri, D., Babu, T. S., Beshr, E., and Eteiba, M. (2020b). A Robust Strategy Based on Marine Predators Algorithm for Large Scale Photovoltaic Array Reconfiguration to Mitigate the Partial Shading Effect on the Performance of PV System. *IEEE Access* 8, 112407–112426. doi:10.1109/access.2020.3000420

Yousri, D., Babu, T. S., Mirjalili, S., and Natarajan, R. (2020c). A Novel Objective Function with Artificial Ecosystem-Based Optimization for Relieving the Mismatching Power Loss of Large-Scale Photovoltaic Array. *Energ. Convers. Manage* 225, 113385. doi:10.1016/j.enconman.2020.113385

Zhang, X., Li, C., Li, Z., Yin, X., Yang, B., Gan, L., et al. (2021). Optimal Mileage-Based PV Array Reconfiguration Using Swarm Reinforcement Learning. *Energ. Convers. Manage.* 225, 113892. doi:10.1016/j.enconman.2021.113892

Conflict of Interest: TH, SL, and SW were employed by the company Yunnan Power Grid Co Ltd.

The remaining authors declare that the research was conducted in the absence of any commercial or financial relationships that could be construed as a potential conflict of interest.

Copyright © 2021 He, Li, Chen, Wu and Li. This is an open-access article distributed under the terms of the Creative Commons Attribution License (CC BY). The use, distribution or reproduction in other forums is permitted, provided the original author(s) and the copyright owner(s) are credited and that the original publication in this journal is cited, in accordance with accepted academic practice. No use, distribution or reproduction is permitted which does not comply with these terms.

frontiers in Energy Research

ORIGINAL RESEARCH
published: 16 July 2021
doi: 10.3389/fenrg.2021.718019

Power Configuration Scheme for Battery Energy Storage Systems Considering the Renewable Energy Penetration Level

Qing Chen[1], *Rui Xie*[1], *Yuyan Chen*[2], *Heyu Liu*[2], *Shengqi Zhang*[2]*, *Fei Wang*[2], *Zhaohui Shi*[1] *and Bin Lin*[1]

[1]*Key Laboratory of Far-shore Wind Power Technology of Zhejiang Province, Hangzhou, China,* [2]*Department of Mechatronic Engineering and Automation, Shanghai University, Shanghai, China*

With the increase of the renewable energy penetration (REP) level in the interconnected power grid, the proportion of the grid-connected conventional synchronous generators reduces continuously, resulting in the decrease of the system inertia. The insufficient system inertia brings challenges to the system frequency stability. Battery energy storage systems (BESSs), regarded as the high-quality frequency regulation resource, play an important role in maintaining the frequency stability of the system with the high REP level. To configure the proper power of BESSs in system frequency regulation, a BESS power configuration scheme (PCS) considering the REP constraint is proposed in this paper. In particular, the process to obtain the REP boundary of the interconnected grid on the premise of system frequency stability is included in the PCS, and the optimal power configuration of the BESS is further determined on the analysis of the BESS impact on the REP boundary. Furthermore, a simulation model of the Australian five-area interconnected power grid is built in MATLAB/Simulink, and the proposed REP-constrained PCS is verified and analyzed. At last, the promising results show that the PCS can take full advantages of the BESS in frequency regulation and meet the system requirement of the frequency stability at a particular REP level.

Keywords: renewable energy penetration, battery energy storage system, interconnected power grid, system frequency stability, system inertia

OPEN ACCESS

Edited by:
Xing He,
Shanghai Jiao Tong University, China

Reviewed by:
Zhendong Ji,
Nanjing University of Science and Technology, China
Wenchao Miao,
The University of Hong Kong, China

****Correspondence:***
Shengqi Zhang
shengqi_zhang8816@163.com

Specialty section:
This article was submitted to Smart Grids, a section of the journal Frontiers in Energy Research

Received: *31 May 2021*
Accepted: *14 June 2021*
Published: *16 July 2021*

Citation:
Chen Q, Xie R, Chen Y, Liu H, Zhang S, Wang F, Shi Z and Lin B (2021) Power Configuration Scheme for Battery Energy Storage Systems Considering the Renewable Energy Penetration Level. Front. Energy Res. 9:718019. doi: 10.3389/fenrg.2021.718019

INTRODUCTION

To reduce the greenhouse gas emission, replacing fossil energy generation by renewable energy generation (REG) has become an inevitable trend in the modern power grid. At the end of 2020, the capacity of the grid-connected REG including photovoltaic and wind generation reached 1300 GW, accounting for 9.4% of the total installed power generation capacity (Khan et al., 2021) all over the world. Unlike the conventional generators, REG connected to the power grid *via* power electronic converters cannot provide the system inertia and the frequency regulation support when a load disturbance occurs (De Carne et al., 2020). Meanwhile, the output of REG has high fluctuation and intermittency, which requires more active power reserves to maintain the system frequency stability. Also, the frequency stability issue becomes worse (Ortiz-Villalba et al., 2020; He et al., 2020), when REG is absorbed across control areas *via* the transmission lines in the interconnected power grid. Therefore, with the increase of the renewable energy penetration (REP) level, the frequency

instability caused by the insufficient system inertia and the active power reserve becomes a distinct threat of the interconnected power grid. In addition, the blackouts in the United Kingdom on August 9, 2019 (Li et al., 2021), and in South Australia on September 28, 2016 (Yan et al., 2018), and the DC bipolar block in the Jinsu-Jiangsu region of East China on September 19, 2015 (Rahman et al., 2017), result from the system frequency instability.

Obviously, to restrict the REP level is the most effective way to maintain the frequency stability of the low-inertia system, but a huge waste of energy is by Yan et al. (2017) and Yang et al. (2020), and the maximum power point operation is used by Ochoa and Martinez (2017), Kumar et al. (2018), and Kumar et al. (2019) to enable REG to provide frequency regulation. The photovoltaic generator and wind turbine are operated below the maximum power point with virtual inertia controllers, and the active power reserved by battery storages is applied to system frequency regulation (Kumar et al., 2018; Kumar et al., 2019). In a study by Ochoa and Martinez (2017), a neuro-fuzzy controller is utilized to adjust the output power of the photovoltaic generator for frequency regulation without energy storage. However, the regulation capacity of REG has high randomness. Recently, battery energy storage systems (BESSs) have been recognized as a high-quality frequency regulation resource by both the academics and the industrialists (Xu and Bishop, 2016; Dozein and Mancarella, 2019; Yoo et al., 2020). Therefore, to meet the frequency stability requirement of the interconnected power grid with high REP level, the research on the BESS power configuration scheme (PCS) becomes a topic of concern.

Many literature studies focus on the economy in the BESS PCS. For example, Mantar Gundogdu et al. (2018) and Zhang et al. (2019) introduced BESS profit models of the frequency regulation service in the ancillary service market of the United Kingdom and the United States. The PCS developed by Chen et al. (2018) combines the market mechanism with the probability distribution of the frequency regulation demand. BESSs are enabled to make more profit by participating in both frequency regulation and energy arbitrage (Cheng and Powell, 2018), and the corresponding PCS determines the optimal configuration by a Markov decision process according to the real-time electricity price. However, those PCSs give priority to BESS profit, and the actual demand of system frequency regulation is ignored. To sum up, the profit priority–based PCS can be hardly applied in countries without mature electricity market.

To make the best use of BESS in frequency regulation, the PCS comprehensively considers the economy and system stability as mentioned in the following references. Specifically, a configuration–operation collaborative optimization method based on the mixed integer linear programming is proposed by Quan et al. (2019), considering the overall economic optimization of equipment planning and system operation. Similarly, Pan et al. (2020) used KKT conditions to combine the economy and stability optimization problems as a single one. Also, an optimal PCS presented by He et al. (2016) considers the BESS frequency regulation performance and BESS life. An energy management and optimization method for the BESS based on the dynamic SoC limit setting is introduced by Byrne et al. (2017). Although the system frequency stability is considered a constraint in the process of those PCSs, the system frequency instability cannot be completely avoided, as the economy optimization still has high priority.

Up to now, the research on the BESS PCS from the perspective of the system frequency stability is still insufficient. Primarily, the impact of REP level on the power system frequency stability is discussed by Meegahapola and Flynn (2010), Miller et al. (2011), and Wang et al. (2019). For example, Wang et al. (2019) indicated that the wind and photovoltaic generation can reduce the power system inertia, which further affects the frequency stability. Also, Meegahapola and Flynn (2010) and Miller et al. (2011) pointed out that areas with low system inertia face the worse frequency stability issue than other areas in the interconnected power grid, which leads to the decrease of the frequency nadir and severer frequency fluctuations under the same active power disturbances. Meanwhile, the frequency deviations within a certain range are allowed, and the standards of some countries have been given by Sun et al. (2020). Therefore, it is valuable to further explore the influence factors of frequency stability and the REP boundary of the interconnected grid.

Furthermore, BESSs play a positive role in improving the frequency regulation performance of the system. For example, a control strategy is introduced by Wen et al. (2016) in that fast-response BESS devices are used to maintain the frequency dynamic safety. Also, an adaptive SoC feedback control is designed by Tan and Zhang (2017), and BESSs are able to be applied in the coordinate control of the multi-timescale frequency deviations of the wind power plant. However, BESSs have a certain power in those research studies, and the quantitative analysis of the impact of BESSs on frequency stability is not included.

Therefore, the BESS PCS considering the REP constraint for the interconnected power grid is proposed in this paper. In detail, an REP boundary calculation method is presented on the condition of the system frequency stability. Also, the influence of BESS on the system frequency stability is quantified. Finally, the optimal BESS power configuration is achieved to enable the system meeting a particular REP level. The proposed PCS for the BESS can improve the renewable energy absorbing consumption in the interconnected power grid effectively. Meanwhile, the PCS can configure BESS power according to the actual requirement of system frequency regulation, which is beneficial to improving the comprehensive utilization rate of the BESS.

The rest of this paper is organized as follows. The framework of the interconnected power grid including the BESS is introduced in *Framework of the Interconnected Power Grid Considering BESS*. In *Operation of the Penetration Level–Constrained PCS for BESS*, the details about the REP-constrained PCS for the BESS are presented, and the performance of the proposed PCS is simulated in the Australian five-area power grid in *Simulation and Discussion*. This paper is summarized in *Conclusion*.

FRAMEWORK OF THE INTERCONNECTED POWER GRID CONSIDERING BESS

The equivalent dynamic model of the control area as shown in **Figure 1** consists of several generators and BESSs. The model of

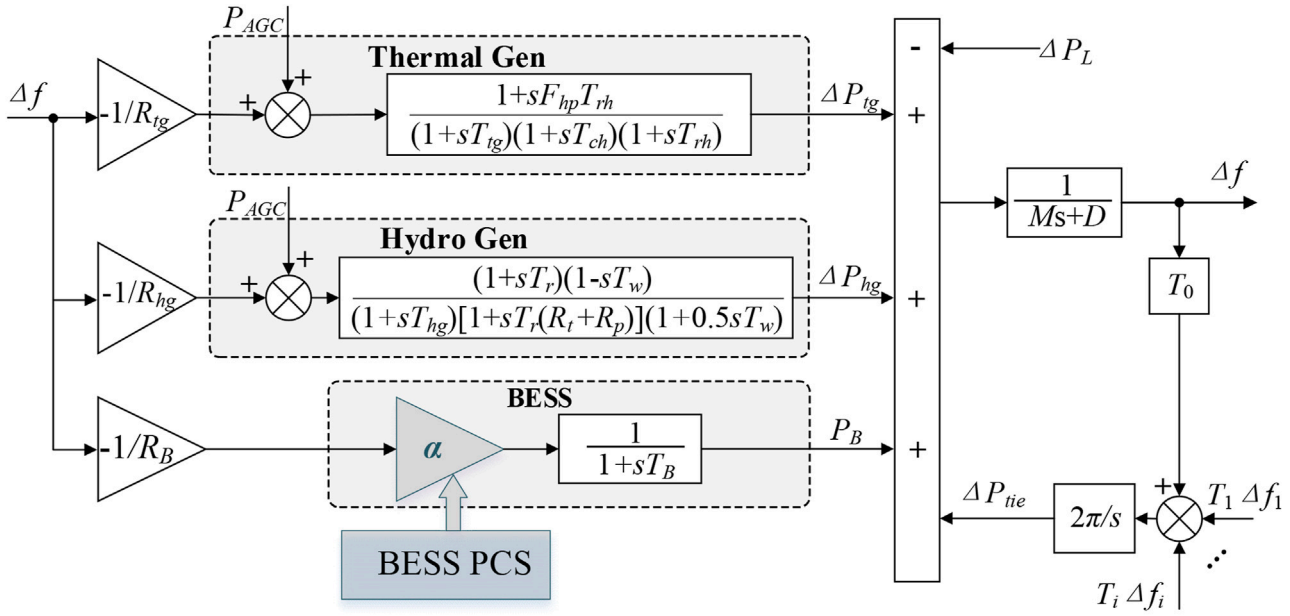


FIGURE 1 | Dynamic model of a control area belonging to the interconnected power grid including the BESS PCS.

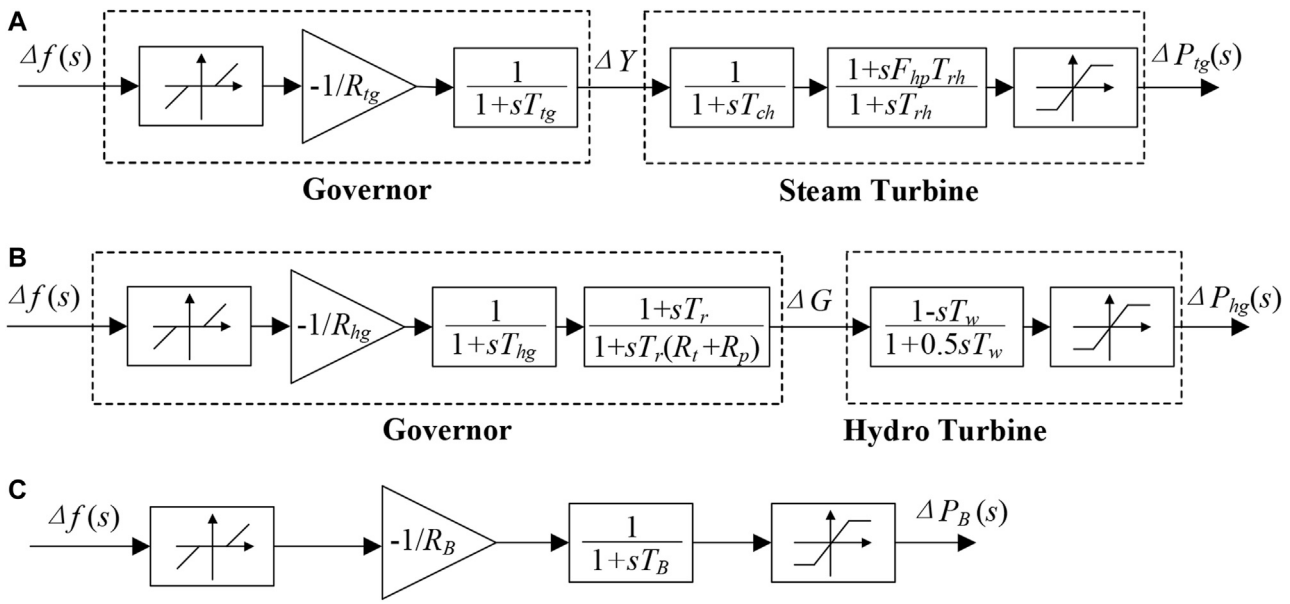


FIGURE 2 | Dynamic models of frequency regulation units. **(A)** Dynamic model of Thermal Gen. **(B)** Dynamic model of Hydro Gen. **(C)** Dynamic model of the BESS.

the BESS can be equivalent to a first-order inertia block, according to Ramalingam et al. (2018) and Calero et al. (2021), and the conventional generator is constructed referring to Liang et al. (2018). Also, the frequency deviations Δf caused by the system load fluctuations can be stabilized dynamically by the inertial response and frequency regulation from generators and BESSs. As a part of frequency regulation, the droop coefficients of Thermal Gen, Hydro Gen, and BESSs are denoted R_{tg}, R_{hg}, and R_B, respectively. Particularly, the participation of the BESS in frequency regulation is indicated by the configuration factor α, which can be deduced by the BESS PCS. In addition, P_{AGC} denotes the automatic generation control signal, M and D are the inertial constant and damping coefficient, and ΔP_L denotes the net load power fluctuations. ΔP_{tg}, ΔP_{tg}, and P_B denote the output power of Thermal Gen, Hydro Gen, and BESSs for frequency regulation. Note that P_B in **Figure 1** is under

constrains of the optimal power configuration for the BESS. More details of the control area model are shown below.

Dynamic Model of the Conventional Generators

The principles of Thermal Gen and Hydro Gen in frequency regulation are similar, but the dynamic models of those two Gens are different because of the different mechanical structures. The simplified dynamic model of Thermal Gen is shown in **Figure 2A** (Zhang et al., 2017), which consists of a governor and a steam turbine. In detail, the dynamic model of the governor consists of three parts: the frequency regulation dead zone, the droop coefficient, and the response delay, while the output is the opening change ΔY representing the steam valve of the steam turbine. The governor of Thermal Gen can determine whether the generator participates in frequency regulation by measuring the system frequency deviations, as long as Δf cross the frequency dead band. Also, the governor can determine the adjustment degree of the control valve by setting the droop coefficient R_{tg} and the primary frequency regulation range according to the droop characteristics of the generator. The response delay of the governor is simulated as a first-order inertia model, and T_{tg} is the time constant of the governor. Meanwhile, in the model of the steam turbine, T_{ch}, T_{rh}, and F_{hp} are the adjustment response time, the time constant, and the gain coefficient of the reheater, respectively. Finally, the output value of the frequency regulation power ΔP_{tg} is obtained considering the operation boundary of the generator.

Similarly, the dynamic model of Hydro Gen is composed of the governor and the hydro turbine, as shown in **Figure 2B**. Specifically, the governor consists of the frequency regulation dead zone, the droop coefficient, and the response delay. Referring to Alhejaj and Gonzalez-Longatt (2017), the transient parameters T_r and R_t are used to simulate the reverse variation of the mechanical power caused by the mechanical inertia of water. Also, T_w represents the required time for the water accelerating from standstill to velocity V_0 in the hydro turbine model. At last, according to the above analysis, the transfer functions G_{tg} and G_{hg} of Thermal Gen and Hydro Gen can be derived as follows:

$$G_{tg}(s) = \frac{\Delta P_{tg}(s)}{\Delta f(s)} = -\frac{1 + sF_{hp}T_{rh}}{R_{tg}\left(1 + sT_{tg}\right)(1 + sT_{ch})(1 + sT_{rh})}, \quad (1)$$

$$G_{hg}(s) = \frac{\Delta P_{hg}(s)}{\Delta f(s)} = -\frac{(1 + sT_r)(1 - sT_w)}{R_{hg}\left(1 + sT_{hg}\right)\left[1 + sT_r\left(R_t + R_p\right)\right](1 + 0.5sT_w)}. \quad (2)$$

Dynamic Model of BESS

To represent the external characteristics of the BESS participating in the load frequency control, the dynamic model of the BESS can be expressed as a first-order inertial control block in **Figure 2C**. In the model, T_B is the time constant used to describe the response time delay of the BESS (Kundur et al., 1994). Meanwhile, the droop coefficient $1/R_B$ represents the proportional relationship between the BESS frequency regulation power and the system frequency deviations. Also, the blocks describing the BESS charging and discharging power range and BESS capacity boundaries are added. At last, the transfer function of BESS G_B is shown as

$$G_B(s) = \frac{P_B(s)}{\Delta f(s)} = -\frac{1}{R_B(1 + sT_B)}. \quad (3)$$

OPERATION OF THE PENETRATION LEVEL–CONSTRAINED PCS FOR BESS

The REP level–constrained PCS can dynamically determine the BESS frequency regulation power configuration coefficient α, based on the REP level the power system is required to absorb and the frequency stability requirements. And the PCS can further realize the power configuration of the BESS participating in system frequency regulation. The process of the REP level–constrained PCS is shown in **Figure 3**. In general, the PCS for the BESS includes the system REP level calculation (RLC) block and BESS power configuration (BPC) block. More details about the proposed PCS are introduced below.

REP Level Calculation Block

In the interconnected power grid, the power mismatch between the generation and the load leads to the system frequency deviations, which is the key index of the system stability. The traditional generators can stop the frequency drop (Δf^{nadir}) and stabilize the frequency around the nominal value (50 or 60 Hz) after a short while, through their own inertia control and the frequency regulation control. To meet the severe active power unbalance of the power system, the under/overload-shedding mechanisms are triggered to maintain the system frequency stability.

Primarily, the conventional generators contribute to the system inertia, as their rotational speed is synchronous to the system frequency. Also, the relationship between the mechanical power, the electrical power, and the rotation speed of the synchronous generator is shown in **Eq. 4**. The expression of the system inertia is shown in **Eqs 5, 6**, which is a function of ω_r. The change of the generator's electric output power ΔP_E caused by the system load fluctuation is shown in **Eq. 7**. Also, the change of ΔP_E further results in the shift of the generator speed, which further causes the frequency fluctuation of the control area. Furthermore, the influence of load fluctuations and system inertia on the system frequency deviations can be deduced in **Eq. 8** from **Eqs 4, 7**. In summary, the synchronous generator can effectively smooth the system frequency drop (Δf^{nadir}) due to the rotational inertia generated by its own mechanical structure:

$$\Delta P(s) = \Delta P_G(s) - \Delta P_E(s) = Ms\Delta\omega(s), \quad (4)$$

$$M = 2H, \quad (5)$$

$$H = \frac{j\omega_r^2}{P_G}, \quad (6)$$

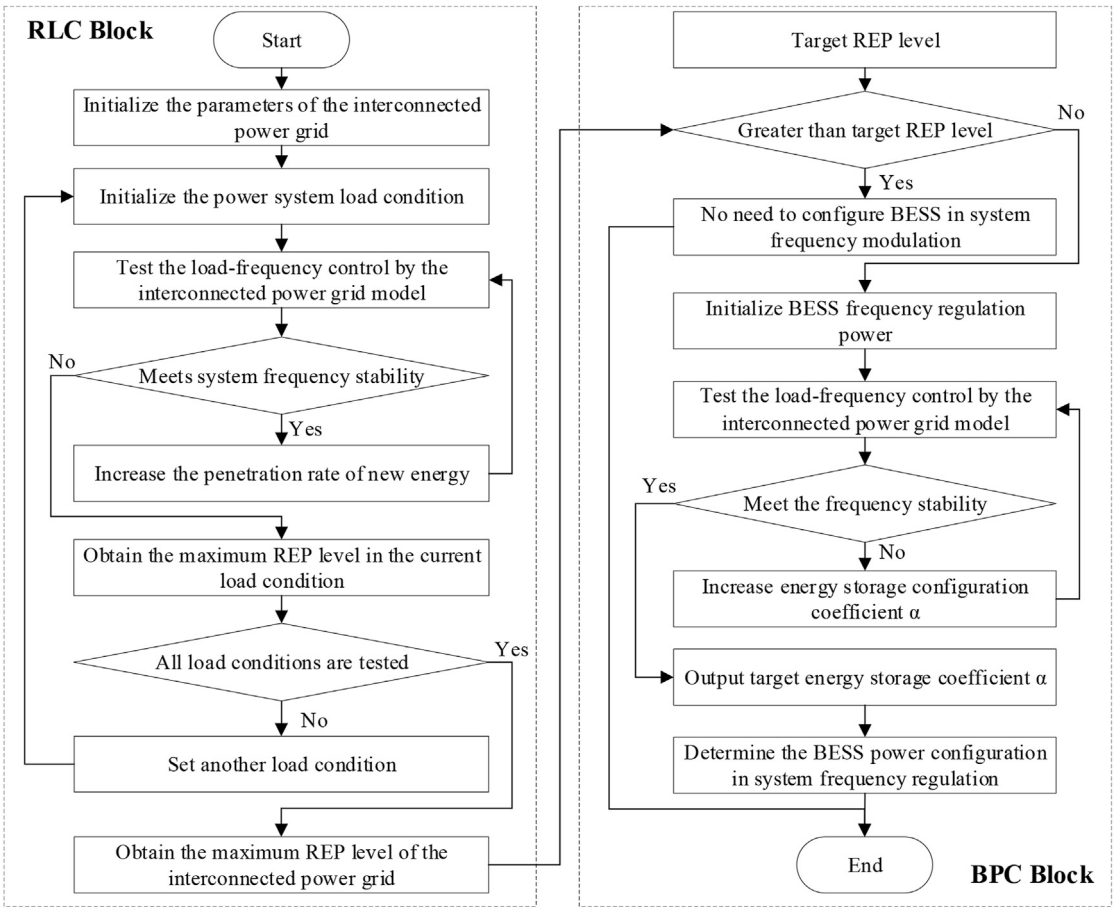


FIGURE 3 | Process of the penetration level–constrained PCS for the BESS.

$$\Delta P_E(s) = \Delta P_L(s) + \Delta P_{Lf}(s) = \Delta P_L(s) + D\Delta\omega(s), \tag{7}$$

$$\frac{\Delta\omega(s)}{\Delta P_G(s) - \Delta P_L(s)} = \frac{1}{D + sM}, \tag{8}$$

$$\Delta P_G(s) = \Delta P_{tg}(s) + \Delta P_{hg}(s), \tag{9}$$

where ΔP_G is the mechanical power change of the conventional generators and the corresponding ΔP_E is the electromagnetic power; $\Delta P_{tg}(s)$ and $\Delta P_{hg}(s)$ are the output values of frequency regulation power of Thermal Gen and Hydro Gen, respectively; M is the sum of generator inertia constants in the control area; $\Delta\omega$ is the angular frequency deviation of the generator; ΔP_L is the load fluctuation; $\Delta P_{Lf}(s)$ is the frequency-sensitive load change; and D is the system load damping constant.

Unlike the conventional generator, renewable energy generation is unable to participate in frequency regulation because renewable energy generation does not have the rotational inertia and usually operates on its maximum power point. Meanwhile, with the increase of the REP level, the proportion of the traditional generators decreases. In other words, a downward trend in the overall inertia level of the power system leads to the insufficient frequency regulation capabilities and the instability of the system frequency. Therefore, the interconnected power grid has a limitation of REP.

The RLC block is used to calculate the REP boundary that the interconnected grid can withstand under the premise of system frequency stability. As shown in **Figure 3**, the PLC block sets the load condition in advance according to the power system parameters and introduces a large load disturbance to test the frequency stability. To observe the REP boundary, a series of tests about whether the system frequency deviations exceed the limitation under the same load disturbance event are applied by increasing the REP level step by step. Thus, the maximum REP level in a certain load condition is obtained. Furthermore, several typical load conditions are introduced one by one, and the maximum REP level of each load condition is determined. At last, the minimum REP level of the interconnected power grid is obtained by comparing the maximum REP levels in different load conditions.

BESS Power Configuration

A virtual droop control strategy is usually adopted for the BESS in the primary frequency regulation. In other words, the BESS can imitate the droop characteristic of the generator in response to the system frequency deviation. The dynamic model of the BESS

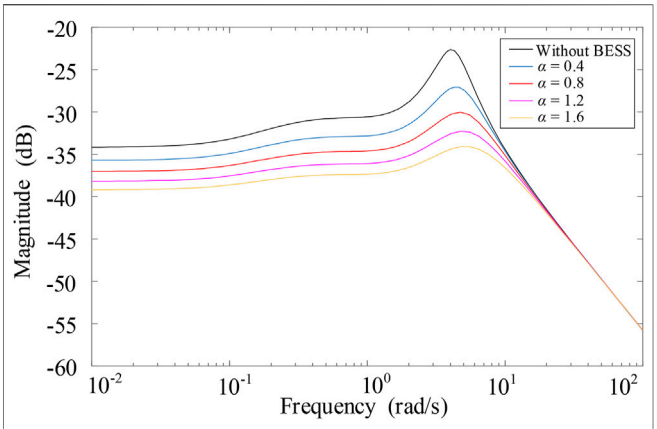


FIGURE 4 | Amplitude–frequency characteristic curve.

including the virtual droop control strategy is introduced in **Figure 2C**. For the same frequency deviation, the power from the BESS P_B can be adjusted by the BESS power configuration coefficient α, and the influence of BESS on the frequency stability can be deduced in **Eq. 10**. Furthermore, the system amplitude–frequency characteristic functions can be written in **Eqs 11, 12**, respectively, representing the system with and without BESS. The corresponding amplitude–frequency characteristic curves are shown in **Figure 4**. In detail, the amplitudes are very small or relatively close when the frequency deviations are caused by the low-frequency or high-frequency load fluctuations, no matter whether BESSs are involved. However, the amplitude of $H_B(s)$ is obviously smaller than that of $H_G(s)$ when the middle-frequency load fluctuations occur. Also, a larger α leads to a smaller amplitude of $H_B(s)$. Therefore, the frequency deviation suppression effect brought by load fluctuations in the middle-frequency band is stronger, with the increase of the configuration coefficient α:

$$\Delta f(s) = \frac{\Delta P_{tg}(s) + \Delta P_{hg}(s) + P_B(s) - \Delta P_L(s)}{D + sM} = \frac{-\Delta P_L(s)}{D + sM - G_{tg} - G_{hg} - \alpha G_B}, \tag{10}$$

$$H_B(s) = \frac{\Delta f(s)}{\Delta P_L(s)} = \frac{1}{D + sM - G_{tg} - G_{hg} - \alpha G_B}, \tag{11}$$

$$H_G(s) = \frac{\Delta f(s)}{\Delta P_L(s)} = \frac{1}{D + sM - G_{tg} - G_{hg}}. \tag{12}$$

Based on the above theoretical analysis, the BESS participating in the primary frequency regulation can improve the ability of the power system to cope with the load deviations effectively. In this way, the aim of the REP level of the interconnected power grid can be guaranteed, and the system frequency deviation can always meet the system stability requirement when the load disturbance occurs under a certain configuration coefficient α. Thus, the optimal power configuration of the BESS can be deduced according to the configuration coefficient α.

The BPC block is used to calculate the minimum BESS charge and discharge power that can enable the control area to meet the aim of the REP level and frequency stability. As shown in **Figure 3**, the necessity of involving the BESS in frequency regulation is determined in the first place, by comparing whether the maximum REP levels are larger than the aim of the REP level of the control area. The BESS power configuration coefficient α is gradually increased, when the aim of the REP level cannot be met. A series of tests are applied until the system frequency stability of the control area with the target REP level is satisfied. Finally, according to the proper power configuration coefficient α, the optimal BESS power configuration that meets the frequency stability of the region is obtained.

SIMULATION AND DISCUSSION

The Australian power grid is regarded as one of the longest interconnected power grids, as shown in **Figure 5**, and can be generally simplified as a 5-area 14-bus system. The maximum power generation capacity of the system is 25,430 MW, while the maximum load demand is 24,800 MW. According to the Australian state layout, Area #2 (New South Wales) and Area #3 (Victoria) are typical load centers and Area #4 (Queensland) and Area #5 (South Australia) are rich in solar energy and wind energy resources, respectively. Thus, the feasibility of the REP level–constrained PCS for the BESS is verified based on the Australian power grid, as it is a typical interconnected power grid with high REP.

The dynamic model of the Australian interconnected power grid in MATLAB/Simulink is shown in **Figure 6** based on the system data (Gibbard and Vowles, 2010) in **Table 1**, including the traditional generators, renewable generators, and BESSs in each area. To consider the actual operation of the Australian power grid, five typical load scenarios (Gibbard and Vowles, 2010) are formulated in **Table 2**, which are the peak scenario, heavy scenario, medium heavy scenario, medium scenario, and light scenario. Furthermore, a positive P_{42} means the active power flows from Area #4 to Area #2, and the negative one means the opposite power flow. P_{21}, P_{13}, and P_{35} follow the same rules. In addition, Area #2 and Area #4 are chosen as examples to configure the BESS verifying the influence of BESS on system frequency control in the load center and the renewable generation center.

Feasibility of RLC Block

Based on the former theoretical analysis, the inertia of the control area decreases with the increase of the REP level, which results in the system frequency instability. In the simulation, a fixed step load disturbance of ±5% p.u. occurred in the control area, and none of frequency deviations exceeding ±0.25 Hz is defined as the system frequency stability. Also, the frequency recovery time is neglected as the indication of the system frequency stability because the response time of the BESS is faster than that of the traditional generators. The REP boundary of the control area is calculated by increasing the REP level of Area #2 and Area #4 from 0 gradually, until the constraint of frequency stability is no longer satisfied. In the heavy load scenario, the frequency deviations of the load center Area #2 and the renewable generation center Area #4 are shown in **Figures 7A,B**, while the performance of the frequency fluctuations is indicated in **Tables 3, 4**.

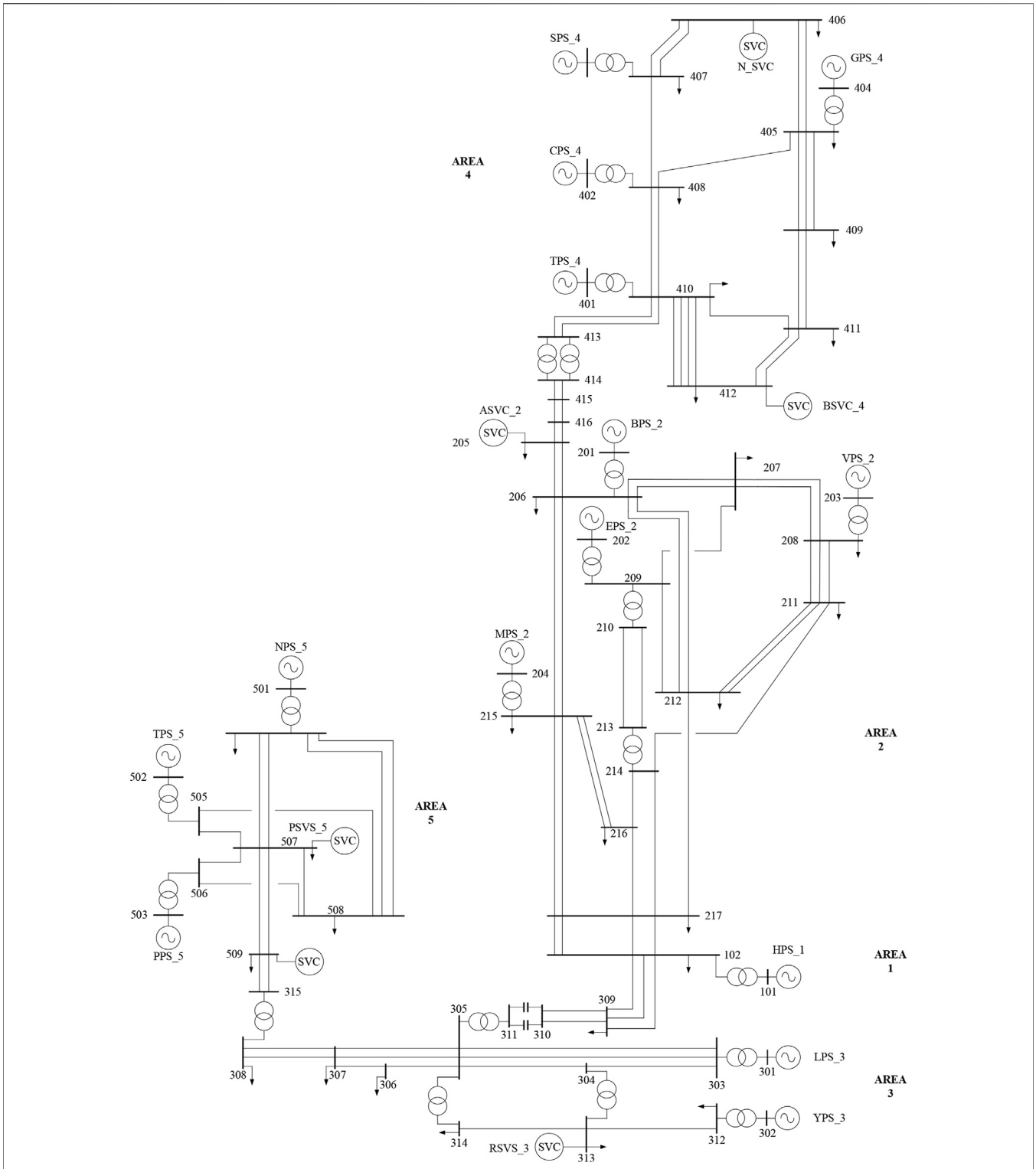


FIGURE 5 | Australian 5-area 14-bus power grid.

In detail, the system frequency of the load center Area #2 becomes unstable when the REP level reaches 5%, and the REP boundary of the area is 5%. Similarly, the renewable generation center Area #4 has an REP boundary of 9%. Thus, with the decrease of the system inertia, Δf^{nadir} continues to approach the system stability limit ±0.25 Hz. Also, the rate of change of frequency and the time to achieve the frequency recovery increase.

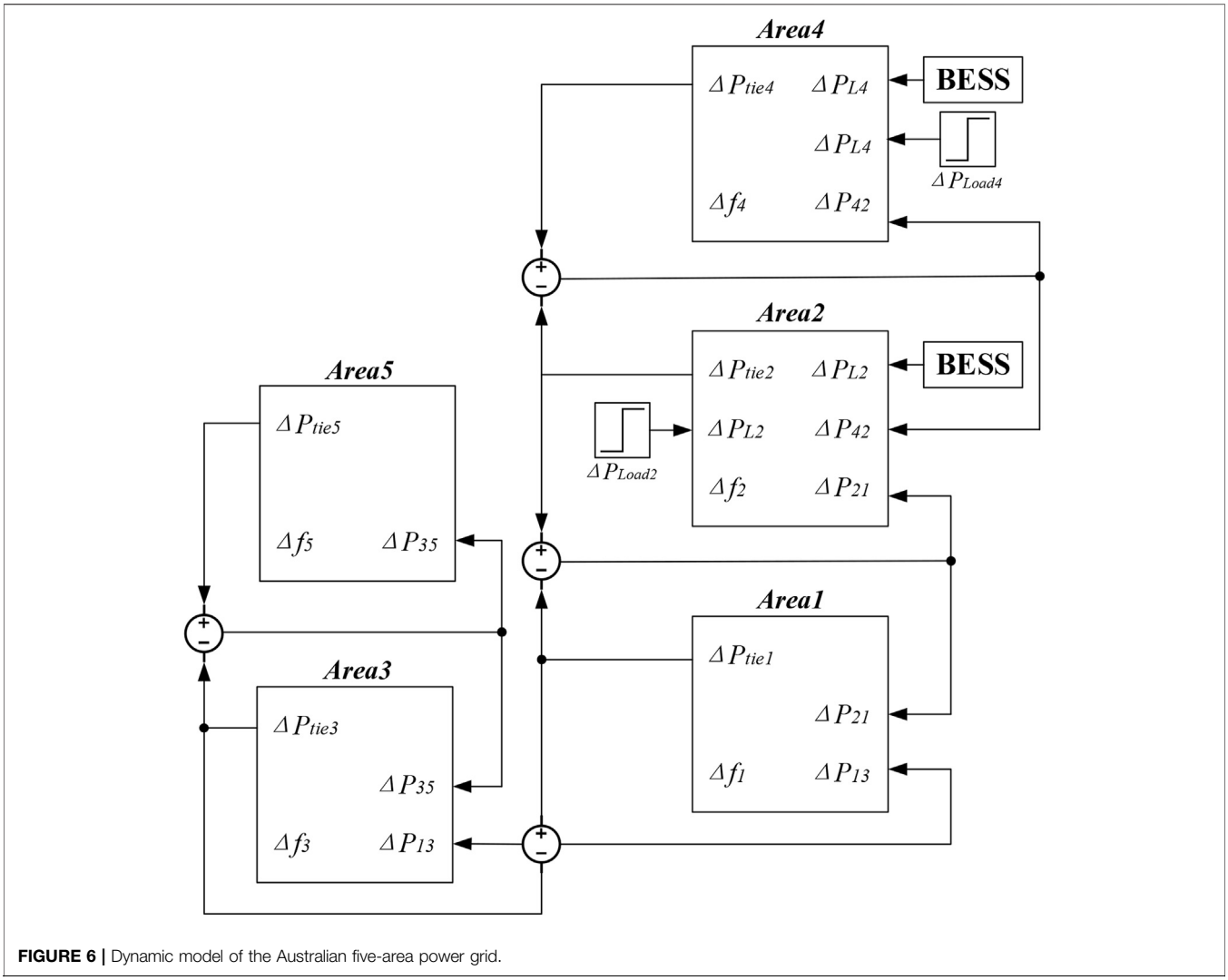


FIGURE 6 | Dynamic model of the Australian five-area power grid.

TABLE 1 | Characteristic parameters of the Australian five-area power grid.

	Area #1	Area #2	Area #3	Area #4	Area #5
V	1.0p.u.	1.0p.u.	1.0p.u.	1.0p.u.	1.0p.u.
D	1.0	1.0	1.0	1.0	1.0
R	4.0%	4.0%	4.0%	4.0%	4.0%
T_{tg}	0.2	0.2	0.2	0.2	0.2
T_{ch}	0.3	0.3	0.3	0.3	0.3
T_{rh}	7	7	7	7	7
F_{hp}	0.3	0.3	0.3	0.3	0.3
T_{hg}	0.2	0.2	0.2	0.2	0.2
T_w	1.0	1.0	1.0	1.0	1.0
T_r	5.0	5.0	5.0	5.0	5.0
R_p	4.0%	4.0%	4.0%	4.0%	4.0%
R_t	0.38	0.38	0.38	0.38	0.38
ACE	−0.3	−0.3	−0.3	−0.3	−0.3
G	25	25	25	25	25
B	26	26	26	26	26

Specifically, Area #4 and Area #2 are regarded as the renewable generation center and the load center, respectively, and the grid-connected traditional generators in the heavy load scenario provide more system inertia in the renewable generation center Area #4. Meanwhile, Area #2 transfers more power to the load center through the tie line, and part of the renewables is absorbed actually in the load center Area #2. Thus, the boundary of the REP level of the renewable generation center Area #4 is higher than that of the load center Area #2.

TABLE 2 | Power transmission under different load scenarios (p.u.).

	Peak	Heavy	Medium heavy	Medium	Light
P_{42}	−5.0	5.0	−5.0	3.0	−2.0
P_{21}	−15.2	11.34	−11.2	7.4	4.7
P_{13}	10.0	10.0	−10.0	−2.0	2.0
P_{35}	2.5	5.0	−5.0	2.5	2.0

Furthermore, as the REP level of the load center is set to 5%, Area #2 can meet the requirements of frequency stability in the heavy load scenario. Another four load scenarios from **Table 2** are tested, and the frequency fluctuations are shown in **Figure 8A**. The maximum Δf^{nadir} of Area #2 does not exceed ±0.25 Hz in

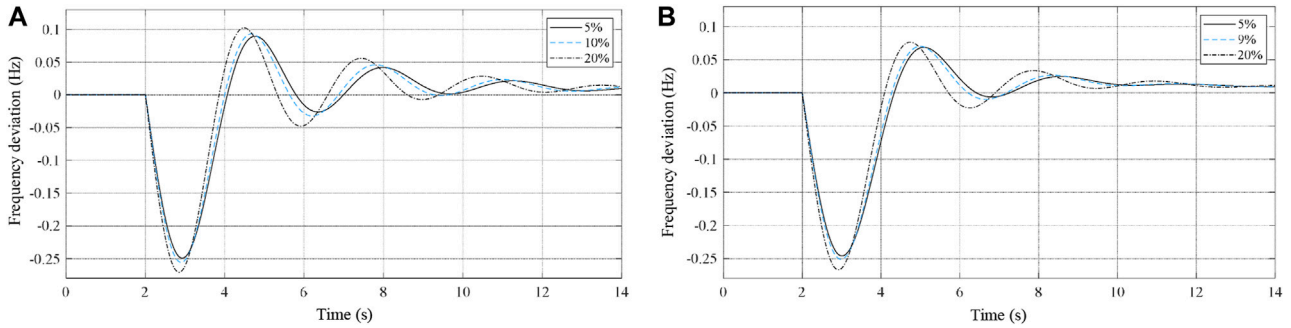


FIGURE 7 | Frequency fluctuations under different REP levels. **(A)** Frequency fluctuations of Area #2 under different REP levels. **(B)** Frequency fluctuations of Area #4 under different REP levels.

TABLE 3 | Frequency response performance of Area #2 under different REP levels.

Area #2	5% REP level	10% REP level	20% REP level
Inertia level	5.7228	5.4216	4.8192
Minimum frequency deviation (Hz)	−0.2492	−0.2558	−0.2708
Maximum frequency deviation (Hz)	0.08958	0.09307	0.1022
Peak frequency time (s)	2.928	2.901	2.847

TABLE 4 | Frequency response performance of Area #4 under different REP levels.

Area #4	5% REP level	9% REP level	20% REP level
Inertia level	5.8672	5.6202	4.9408
Minimum frequency deviation (Hz)	−0.2460	−0.2511	−0.2670
Maximum frequency deviation (Hz)	0.06855	0.07007	0.07638
Peak frequency time (s)	3.010	2.986	2.920

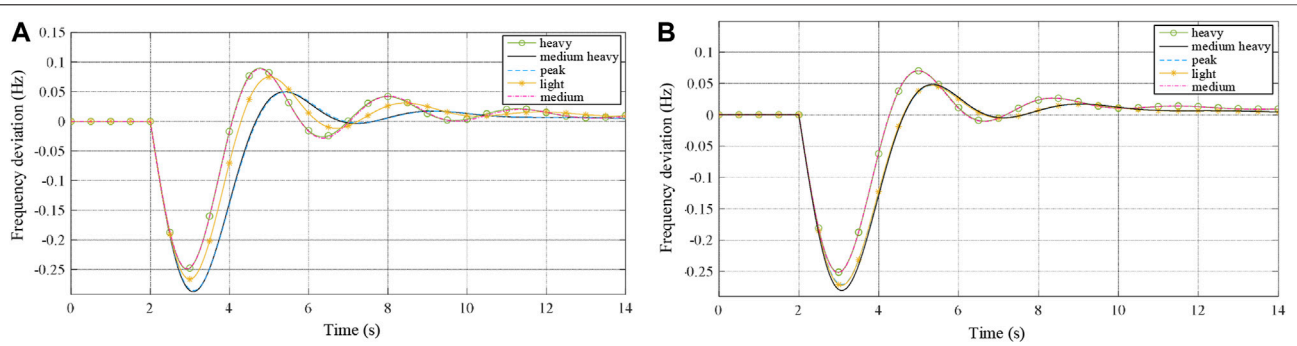


FIGURE 8 | Frequency fluctuations under different load scenarios. **(A)** Frequency fluctuations of Area #2 under different load scenarios. **(B)** Frequency fluctuations of Area #4 under different load scenarios.

heavy and medium load scenarios but goes across the limitation in peak, medium heavy, and light scenarios. Similarly, considering the REP level of the renewable generation center Area #4 as 9%, the simulation results of five different load scenarios are shown in **Figure 8B**. Similar simulation results are obtained such that the REP boundary of a control area changes according to the load scenarios.

At last, considering the comprehensive effectiveness of the system inertia and load scenarios on the system frequency stability, the REP boundaries of five control areas are shown in **Table 5**, according to the calculation process of the RLC block. Obviously, the REP level cannot be satisfied in both load centers and renewable generation centers, and it is necessary to configure the BESS to improve the REP level.

TABLE 5 | REP boundary of each control area.

	Peak (%)	Heavy (%)	Medium heavy (%)	Medium (%)	Light (%)	Penetration boundary (%)
Area #1	5	15	2	4	14	2
Area #2	1	5	1	6	3	1
Area #3	2	10	2	3	11	2
Area #4	2	9	2	7	3	2
Area #5	10	12	3	16	15	3

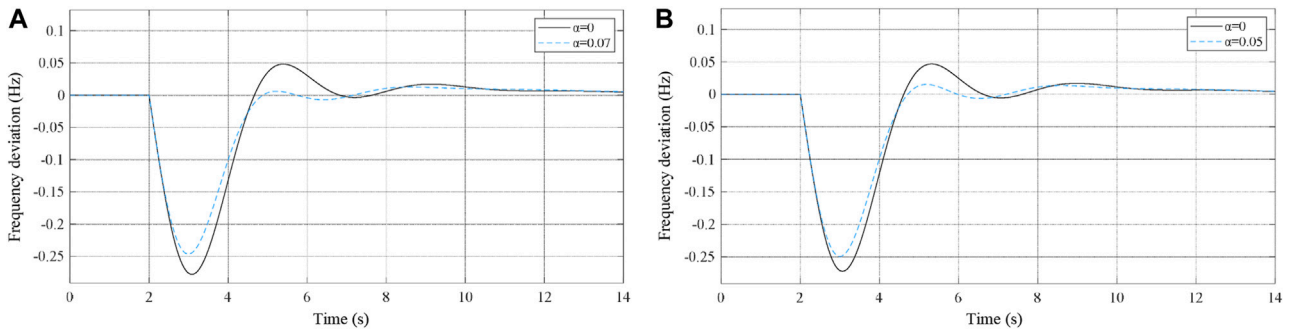


FIGURE 9 | Frequency fluctuations considering different BESS configuration coefficients. **(A)** Frequency fluctuations of Area #2 considering different BESS configuration coefficients. **(B)** Frequency fluctuations of Area #4 considering different BESS configuration coefficients.

TABLE 6 | Parameters of BESS power configuration for five control areas.

	Initial penetration boundary (%)	Target penetration (%)	Configuration coefficient	BESS power configuration (p.u.)
Area #1	2	5	0.04	±0.03012
Area #2	1	5	0.07	±0.04538
Area #3	2	5	0.06	±0.04558
Area #4	2	10	0.05	±0.03890
Area #5	3	10	0.04	±0.03716

Performance of BPC Block

Based on the former theoretical analysis, BESSs have high control accuracy and fast response speed, which can improve the system frequency stability by mitigating the frequency deviation quickly. To verify the effectiveness of the BPC block, optimal BESS power is configured in both the load center and the renewable energy generation center.

The target of the REP levels of load centers and renewable generation centers is set to 5 and 10%, respectively. According to the results in **Table 3**, the smallest REP levels of Area #2 and Area #4 occur under the medium heavy load scenario. Thus, to achieve the setting REP level, BPC block calculation is applied by increasing the configuration coefficient α gradually, and the simulation results of the frequency fluctuations are shown in **Figures 9A,B**.

In particular, the maximum Δf^{nadir} of Area #2 and Area #4 exceeds the frequency limitation, if BESSs are not equipped in areas. Meanwhile, the maximum Δf^{nadir} decreases gradually and reaches within ±0.25 Hz eventually with the increase of BESS configuration coefficients. The system frequency fluctuations are mitigated in a shorter period. Thus, the performance of system frequency regulation improves significantly with BESS involvement. Finally, the configuration parameters of BESSs are obtained based on the target REP levels, and the results are shown in **Table 6**. To sum up, the target REP levels are achieved by the proposed PCS for the BESS.

CONCLUSION

This paper proposes a BESS PCS considering the REP constraint on the premise of system frequency stability. At the beginning, the dynamic models of Thermal Gen, Hydro Gen, and BESSs are established. The REP-constrained PCS can dynamically determine the BESS power configuration by comparing the target REP levels and the REP boundaries of each control area in different load scenarios. A model of the Australian five-area interconnected power grid is established in

MATLAB/Simulink to verify the effectiveness of the PCS, and the suggested BESS power for each control area is obtained. Therefore, high REP level can be achieved in the future, as the BESS mitigates the system frequency fluctuations effectively, and the proposed PCS indicates the optimal BESS power. In addition, the implementation of the BESS is not only for frequency regulation but also for the way to configure BESS power in multiple purposes, which will be discussed in further work.

DATA AVAILABILITY STATEMENT

The original contributions presented in the study are included in the article/supplementary material, and further inquiries can be directed to the corresponding author.

AUTHOR CONTRIBUTIONS

QC proposed the concept of the project, and FW acted as the project administrator. YC and HL designed the system model and established the details of the power configuration scheme. ZS and BL analyzed the data and carried out the simulation. RX and SZ contributed to funding acquisition and writing the paper. All authors approved the submitted version.

FUNDING

This work was supported by the Key Laboratory Open Fund of Far-shore Wind Power Technology of Zhejiang Province (ZOE2020008) and the Jiangsu Natural Science Foundation (BK20180391).

REFERENCES

Alhejaj, S. M., and Gonzalez-Longatt, F. M. (2016). "Impact of Inertia Emulation Control of Grid-Scale BESS on Power System Frequency Response," in 2016 Int. Conf. Students Appl. Eng. ICSAE (IEEE), 254–258. doi:10.1109/ICSAE.2016.7810198

Byrne, R. H., Nguyen, T. A., Copp, D. A., Chalamala, B. R., and Gyuk, I. (2018). Energy Management and Optimization Methods for Grid Energy Storage Systems. *IEEE Access* 6, 13231–13260. doi:10.1109/ACCESS.2017.2741578

Calero, F., Canizares, C. A., and Bhattacharya, K. (2021). Dynamic Modeling of Battery Energy Storage and Applications in Transmission Systems. *IEEE Trans. Smart Grid* 12, 589–598. doi:10.1109/TSG.2020.3016298

Chen, P., Tao, S., Xiao, X., and Li, L. (2018). Uncertainty Level of Voltage in Distribution Network: An Analysis Model with Elastic Net and Application in Storage Configuration. *IEEE Trans. Smart Grid* 9, 2563–2573. doi:10.1109/TSG.2016.2614547

Cheng, B., and Powell, W. (20161997–2005). Co-Optimizing Battery Storage for the Frequency Regulation and Energy Arbitrage Using Multi-Scale Dynamic Programming. *IEEE Trans. Smart Grid* 9, 1. doi:10.1109/TSG.2016.2605141

De Carne, G., Buticchi, G., Liserre, M., and Vournas, C. (2020). "Real-Time Primary Frequency Regulation Using Load Power Control by Smart Transformers," in 2020 IEEE Power & Energy Society General Meeting (PESGM) (IEEE), 1. doi:10.1109/PESGM41954.2020.9281635

Dozein, M. G., and Mancarella, P. (2019). "Frequency Response Capabilities of Utility-Scale Battery Energy Storage Systems, with Application to the August 2018 Separation Event in Australia," in 2019 9th International Conference on Power and Energy Systems (ICPES) (IEEE), 1–6. doi:10.1109/ICPES47639.2019.9105646

Gibbard, M., and Vowles, D. (2010). *Simplyfied 14-generator Model of the SE Australian Power System*.

He, G., Chen, Q., Kang, C., Pinson, P., and Xia, Q. (2016). Optimal Bidding Strategy of Battery Storage in Power Markets Considering Performance-Based Regulation and Battery Cycle Life. *IEEE Trans. Smart Grid* 7, 2359–2367. doi:10.1109/TSG.2015.2424314

He, X., Chu, L., Qiu, R. C., Ai, Q., Ling, Z., and Zhang, J. (2020). Invisible Units Detection and Estimation Based on Random Matrix Theory. *IEEE Trans. Power Syst.* 35, 1846–1855. doi:10.1109/TPWRS.2019.2935739

Khan, F. H., Pal, T., Kundu, B., and Roy, R. (2021). "Wind Energy: A Practical Power Analysis Approach," in 2021 Innovations in Energy Management and Renewable Resources(52042) (IEEE), 1–6. doi:10.1109/IEMRE52042.2021.9386754

Kumar, N., Hussain, I., Singh, B., and Panigrahi, B. K. (2018). Self-Adaptive Incremental Conductance Algorithm for Swift and Ripple-free Maximum Power Harvesting from PV Array. *IEEE Trans. Ind. Inf.* 14, 2031–2041. doi:10.1109/TII.2017.2765083

Kumar, N., Singh, B., and Panigrahi, B. K. (2019). Integration of Solar PV with Low-Voltage Weak Grid System: Using Maximize-M Kalman Filter and Self-Tuned P&O Algorithm. *IEEE Trans. Ind. Electron.* 66, 9013–9022. doi:10.1109/TIE.2018.2889617

Kundur, P., Balu, N. J., and Lauby, M. G. (1994). *Power System Stability and Contol*. New York, NY, USA: McGraw-Hill Education.

Li, T., Li, Y., Li, S., and Zhang, W. (2021). Research on Current-Limiting Control Strategy Suitable for Ground Faults in AC Microgrid. *IEEE J. Emerg. Sel. Top. Power Electron.* 9, 1736–1750. doi:10.1109/JESTPE.2020.2983726

Liang, C., Wang, P., Han, X., Qin, W., Jia, Y., and Yuan, T. (2018). Battery Energy Storage Selection Based on a Novel Intermittent Wind Speed Model for Improving Power System Dynamic Reliability. *IEEE Trans. Smart Grid* 9, 6084–6094. doi:10.1109/TSG.2017.2703578

Mantar Gundogdu, B., Nejad, S., Gladwin, D. T., Foster, M. P., and Stone, D. A. (2018). A Battery Energy Management Strategy for U.K. Enhanced Frequency Response and Triad Avoidance. *IEEE Trans. Ind. Electron.* 65, 9509–9517. doi:10.1109/TIE.2018.2818642

Meegahapola, L., and Flynn, D. (2010). "Impact on Transient and Frequency Stability for a Power System at Very High Wind Penetration," in IEEE PES Gen. Meet. PES, Minneapolis, MN, USA (IEEE), 1–8. doi:10.1109/PES.2010.5589908

Miller, N. W., Clark, K., and Shao, M. (2011). "Frequency Responsive Wind Plant Controls: Impacts on Grid Performance," in 2011 IEEE Power and Energy Society General Meeting (IEEE), 1–8. doi:10.1109/PES.2011.6039137

Ochoa, D., and Martinez, S. (2017). Fast-Frequency Response provided by DFIG-Wind Turbines and its Impact on the Grid. *IEEE Trans. Power Syst.* 32, 4002–4011. doi:10.1109/TPWRS.2016.2636374

Ortiz-Villalba, D., Rahmann, C., Alvarez, R., Canizares, C. A., and Strunck, C. (2020). Practical Framework for Frequency Stability Studies in Power Systems with Renewable Energy Sources. *IEEE Access* 8, 202286–202297. doi:10.1109/ACCESS.2020.3036162

Pan, G., Gu, W., Lu, Y., Qiu, H., Lu, S., and Yao, S. (2020). Optimal Planning for Electricity-Hydrogen Integrated Energy System Considering Power to Hydrogen and Heat and Seasonal Storage. *IEEE Trans. Sustain. Energ.* 11, 2662–2676. doi:10.1109/TSTE.2020.2970078

Quan, R., Li, G., Jin, G., Liu, Z., and Chen, Q. (2019). "Multi-objective Optimal Dispatch Method Based on Source-Network-Load-Storage Interaction System for DC Distribution Network," in IET Conf. Publ, Shanghai, China (IET), 1–8. doi:10.1049/cp.2019.0363

Rahman, K. M. J., Munnee, M. M., and Khan, S. (2016). "Largest Blackouts Around the World: Trends and Data Analyses," in WIECON-ECE 2016 - 2016 IEEE Int. WIE Conf. Electr. Comput. Eng., Pune, India (IEEE), 155–159. doi:10.1109/WIECON-ECE.2016.8009108

Ramalingam, G., Choudhary, A. K., and Mikkili, S. (2018). "Modeling and Analysis of a PV-Based Shunt Active Filter with BESS for Power Quality Enhancement under Dynamic Load Conditions," in INDICON 2018 - 15th IEEE India Counc. Int. Conf. 0, Coimbatore, India (IEEE). doi:10.1109/INDICON45594.2018.8987181

Sun, M., Xie, G., Chen, L., Liu, Y., Li, X., and Min, Y. (2020). "Study on the Necessity and Role of Inertia in Power System Frequency Response," in 2020 IEEE 4th Conference on Energy Internet and Energy System Integration (EI2) (IEEE)), 155–159. doi:10.1109/EI250167.2020.9347330

Tan, J., and Zhang, Y. (2017). Coordinated Control Strategy of a Battery Energy Storage System to Support a Wind Power Plant Providing Multi-Timescale Frequency Ancillary Services. *IEEE Trans. Sustain. Energ.* 8, 1140–1153. doi:10.1109/TSTE.2017.2663334

Wang, D., Rueda Torres, J. L., Perilla, A., Rakhshani, E., Palensky, P., and Van Der Meijden, M. A. A. M. (2019). *Enhancement of Transient Stability in Power Systems with High Penetration Level of Wind Power Plants*. IEEE Milan PowerTech, 2–7. doi:10.1109/PTC.2019.8810696

Wen, Y., Li, W., Huang, G., and Liu, X. (2016). Frequency Dynamics Constrained Unit Commitment with Battery Energy Storage. *IEEE Trans. Power Syst.* 31, 5115–5125. doi:10.1109/TPWRS.2016.2521882

Xu, X., Bishop, M., Bishop, M., Donna G, O., and Chen, H. (2016). Application and Modeling of Battery Energy Storage in Power Systems. *Csee Jpes* 2, 82–90. doi:10.17775/cseejpes.2016.00039

Yan, B., Luh, P. B., Warner, G., Zhang, P., and Member, S. (2017). Operation and Design Optimization of Microgrids with Renewables. *IEEE Trans. Automat. Sci. Eng.* 14, 573–585. doi:10.1109/TASE.2016.2645761

Yan, R., -Masood, N.-A., Kumar Saha, T., Bai, F., and Gu, H. (2018). The Anatomy of the 2016 South Australia Blackout: A Catastrophic Event in a High Renewable Network. *IEEE Trans. Power Syst.* 33, 5374–5388. doi:10.1109/TPWRS.2018.2820150

Yang, B., Cao, X., Cai, Z., Yang, T., Chen, D., Gao, X., et al. (2020). Unit Commitment Comprehensive Optimal Model Considering the Cost of Wind Power Curtailment and Deep Peak Regulation of Thermal Unit. *IEEE Access* 8, 71318–71325. doi:10.1109/ACCESS.2020.2983183

Yoo, Y., Jung, S., and Jang, G. (2020). Dynamic Inertia Response Support by Energy Storage System with Renewable Energy Integration Substation. *J. Mod. Power Syst. Clean. Energ.* 8, 260–266. doi:10.35833/MPCE.2018.000760

Zhang, G., Ela, E., and Wang, Q. (2019). Market Scheduling and Pricing for Primary and Secondary Frequency Reserve. *IEEE Trans. Power Syst.* 34, 2914–2924. doi:10.1109/TPWRS.2018.2889067

Zhang, S., Mishra, Y., and Shahidehpour, M. (2017). Utilizing Distributed Energy Resources to Support Frequency Regulation Services. *Appl. Energ.* 206, 1484–1494. doi:10.1016/j.apenergy.2017.09.114

Conflict of Interest: The authors declare that the research was conducted in the absence of any commercial or financial relationships that could be construed as a potential conflict of interest.

Copyright © 2021 Chen, Xie, Chen, Liu, Zhang, Wang, Shi and Lin. This is an open-access article distributed under the terms of the Creative Commons Attribution License (CC BY). The use, distribution or reproduction in other forums is permitted, provided the original author(s) and the copyright owner(s) are credited and that the original publication in this journal is cited, in accordance with accepted academic practice. No use, distribution or reproduction is permitted which does not comply with these terms.

NOMENCLATURE

ACE Area control error

B Secondary frequency regulation coefficient

BESS Battery energy storage system

BPC BESS power configuration

D Load damping coefficient

Fhp Gain coefficient of the reheater

Δf^{nadir} Frequency drop

G Governor constant

GB Transfer function of the BESS

Ghg Transfer functions of Hydro Gen

Gtg Transfer functions of Thermal Gen

H Inertia constant of the synchronous generator

HB(s) Amplitude–frequency characteristic function with the BESS

HG(s) Amplitude–frequency characteristic function without BESS

M Generator inertia constant

PAGC Automatic generation control signal

PCS Power configuration scheme

R Speed regulation constant

RB Droop coefficients of the BESS

REG Renewable energy generation

REP Renewable energy penetration

Rhg Droop coefficients of Hydro Gen

RLC REP level calculation

Rt Transient parameters used to simulate the reverse variation of the mechanical power

Rtg Droop coefficients of Thermal Gen

TB Time constant used to describe the response time delay of the BESS

Tch Adjustment response time of the reheater

Thg Time constant of the hydro governor

Ti Synchronizing torque coefficient between adjacent areas

Tr Transient parameters used to simulate the mechanical inertia of water

Trh Time constant of the reheater

Ttg Time constant of the thermal governor

Tw Required time for the water accelerating from standstill to velocity V0 in the hydro turbine model

V Voltage magnitude

α Energy storage configuration factor

Δf Frequency deviations

Δfi Frequency deviations in the ith adjacent area

PB Output value of the frequency regulation power of the BESS

ΔPE Electrical power variation of the generator set

ΔPG Mechanical power variation of the generator set

ΔPhg Output value of the frequency regulation power of Hydro Gen

ΔPL Net load power fluctuations

ΔPL(s) Frequency-sensitive load change

ΔPtg Output value of the frequency regulation power of Thermal Gen

ΔPtie Power exchanged from other areas through the tie lines

ΔY Opening variation of the steam valve of the steam turbine

Δω Generator angular frequency deviation

ωr Generator rotor speed

frontiers in Energy Research

ORIGINAL RESEARCH
published: 16 July 2021
doi: 10.3389/fenrg.2021.702245

Fault Location Scheme for Abnormal Grounding Point in Isolated Ground Wire of Large-Scale Clean Energy Transmission

Yunlong Wang, Nuo Chen, Xiangnan Ma and Zongzhang Yang*

China Southern Power Grid EHV Transmission Company, Kunming, China

There is a large number of grounding switches along the isolated ground wire for the de-icing in the large-scale wind farm. If any of these grounding switches are left open by accident, this can create an unexpected abnormal grounding point in the isolated ground wire. Based on the analysis of the output power of de-icing devices, the output power of different poles can be applied for the abnormal grounding point fault location. Since the rise of output current to the rated current of de-icing devices requires a long time to build up, the protective relay may lock the de-icing device before the output current reaches the rated current. Thus, the ratio of output energy of two poles can be selected to locate the abnormal grounding point. This study verified this location method by conducting a large number of simulations.

Keywords: rising of current, de-icing, isolated ground wire, earthing switch, fault location

OPEN ACCESS

Edited by:
Xiaoshun Zhang,
Shantou University, China

Reviewed by:
Xia Fang,
Sichuan University, China
Rui Liang,
China University of Mining and Technology, China
Pulin Cao,
Kunming University of Science and Technology, China

****Correspondence:***
Yunlong Wang
2528462375@qq.com

Specialty section:
This article was submitted to Smart Grids, a section of the journal Frontiers in Energy Research

Received: *29 April 2021*
Accepted: *01 June 2021*
Published: *16 July 2021*

Citation:
Wang Y, Chen N, Ma X and Yang Z (2021) Fault Location Scheme for Abnormal Grounding Point in Isolated Ground Wire of Large-Scale Clean Energy Transmission. Front. Energy Res. 9:702245. doi: 10.3389/fenrg.2021.702245

INTRODUCTION

The wind farms of the northeast area of Yunnan province are a significantly important renewable energy base in China's Southern Power Grid (Miao et al., 2013). However, the cold rain in winter on the Yunnan-Guizhou Plateau freezes the ground wire of the transmission lines of the wind farms in this area (Juanjuan et al., 2012). To reduce the unfavorable harm induced by the freeze, a de-icing device that melts the ice in the ground wires, by injecting the direct current (DC) to ground wires to heat them (Sun et al., 2011; Zhu et al., 2019a), is widely applied in the China Southern Power Grid. Although the DC de-icing device can eliminate the ice in ground wires, studies on the fault location for ground wires are urgently needed. In addition, the ground wire, which connects the earth with the tower, needs to be isolated from the tower for the propagation of the DC current. Thus, any grounding points in the tower can block the de-icing for the whole line (Hao et al., 2015; Jiazheng et al., 2016; Zhu et al., 2019a; Zhu et al., 2019b; Guo et al., 2019; Haleem and Rajapakse, 2019; De Oliveira Neto et al., 2021). To maintain the lightning protection of ground wires, grounding switches are distributed along transmission lines. Normally, grounding switches are closed to connect ground wires to the earth, so ground wire keeps the potential with the earth. If the DC de-icing device is required to melt the ice, all grounding switches are open to propagate the current (Feng et al., 2016; Gao et al., 2020; Zasypkin and Shchurov, 2020; Chen et al., 2021; Wu et al., 2021).

The fault location for ground wires can be divided into two kinds: the traveling wave based method and the impedance based method (Zhi and Fangzong, 2011; Shukr et al., 2012; Kai et al., 2013; Lei et al., 2015; Yuansheng et al., 2015; Wangsheng et al., 2016; Yunke et al., 2017; Bin and Lin, 2020; Guang et al., 2020). Literature (Yunke et al., 2017) analyzes the fault characteristics of abnormal grounding points, then a fault location method based on the Bergeron model is proposed for DC de-

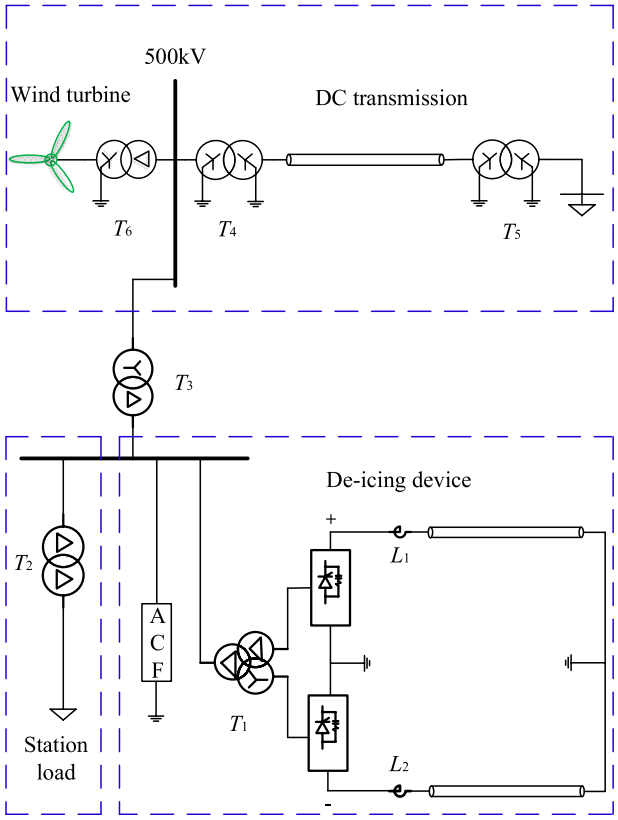


FIGURE 1 | DC de-icing diagram.

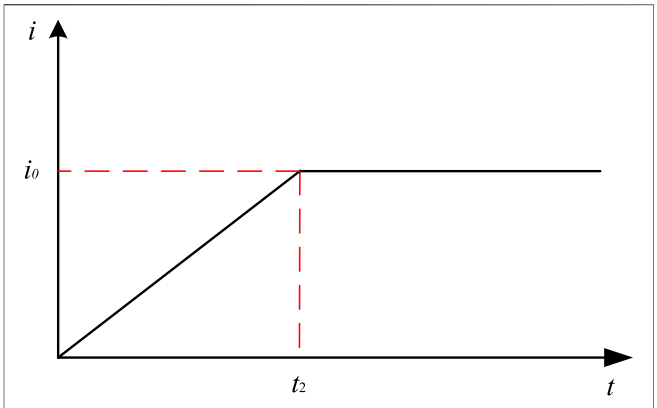


FIGURE 2 | The rising current.

icing devices. The traveling wave in the ground wire, a fault location based on the different distributed traveling waves, has also been presented in past studies (Lei et al., 2015; Wangsheng et al., 2016). The DC filter is usually the boundary of DC transmission lines, and the time-domain equation of the fault induced initial wave has been discussed in other studies (Yuansheng et al., 2015; Bin and Lin, 2020) for the accurate detection of traveling waves. In other works (Zhi and Fangzong, 2011; Shukr et al., 2012), transient impedance is calculated by the transient voltage and transient current to extract the capacitance for the fault location. To reduce the difficulty of the identification of the traveling wave, the spectrum of fault induced transients has also been analyzed (Kai et al., 2013) to obtain the natural frequency, which represents the distance between the fault point to the substation. In other literature (Guang et al., 2020), the time difference of the initial wave and the reflected wave was utilized to locate the fault point in transmission lines, which is a kind of single-ended fault location method.

Although the abnormal grounding point is a kind of fault for the ground wire, the abnormal grounding point always occurs before de-icing, which is different from faults in transmission lines. After starting the de-icing devices, the output current requires a long time to reach a steady state, hence transverse protection may be triggered if the voltage of both poles is extremely different due to the abnormal grounding point. Based on the operation characteristics of the DC de-icing device, this paper proposes an abnormal grounding point location method that utilizes the output power of the positive and negative poles. Furthermore, a large number of simulations is required to verify the robustness of the proposed location method.

OPERATION CHARACTERISTICS OF THE DC DE-ICING DEVICE

Structure of DC De-Icing Device

The schematic diagram of a classic DC de-icing device installed at the substation for the large-scale wind farm is demonstrated in **Figure 1**.

The top half of the schematic diagram shows the high voltage transmission of the large-scale wind farm. T_4 and T_5 are the transformers part of the high voltage transmission. The second part includes the DC de-icing device and the station power load of T_2, such as the cooling pump of the converter valve. The power for the de-icing device is supplied by the wind turbine and step-down transformer T_3. An alter current filter (ACF) and the transformer T_1 for the station load is connected to the bus which supplies power to the de-icing device. T_1 is the three-winding converter transformer of the DC de-icing device, which follows a twelve-pulse converter and smoothing reactors L_1 and L_2.

Current Rising Process of the DC De-Icing Device

Comparing with the substation load, the DC de-icing device has an enormous capacity load, which may even exceed the total power consumption of other loads at the substation. To reduce the adverse impact of starting the DC de-icing device, the DC de-icing device with large capacity has a current rising process time t after starting. This duration is related to the size of the rated current and the increasing speed of the control system which ranges from a few seconds to a few minutes. As shown in **Figure 2**, the current reaches the rated value i_0 and enters the steady-state operation process after a certain time t_2. If there is an abnormal grounding point on the insulated overhead ground wire, the transverse differential protection or overcurrent protection may detect the fault and block the converter valve during the power rising of the DC de-icing device.

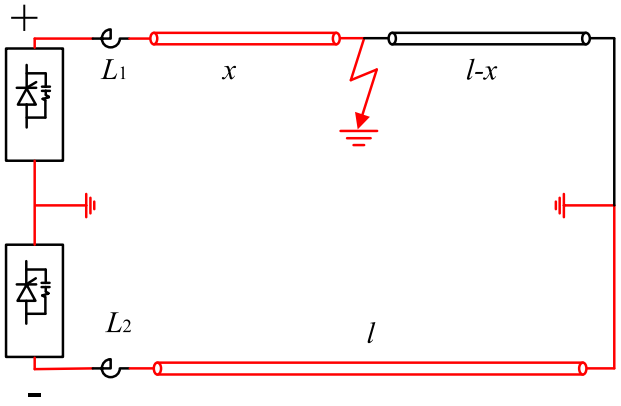


FIGURE 3 | An abnormal grounding point in the single insulated ground wire.

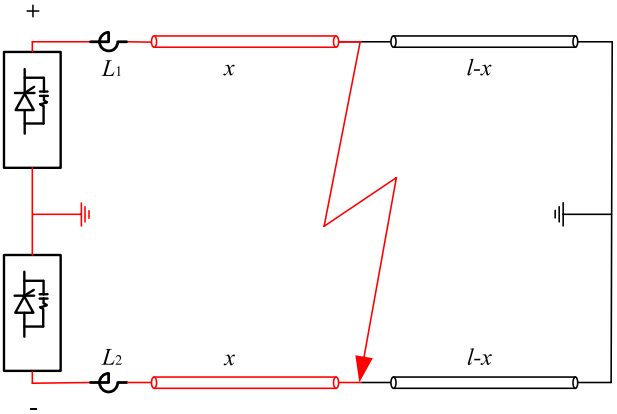


FIGURE 4 | Abnormal grounding of bipolar in the same position.

FAULT CHARACTERISTICS IN THE ISOLATED GROUND WIRE

To maintain the lightning protection of grounding wires for the isolated grounding wires, there is a large number of grounding switches on the towers of the transmission lines that need de-icing. If grounding wires require de-icing, all grounding switches are open, breaking the connection between the earth and ground wires. Grounding switches are closed if no de-icing is required, to equal the potential of ground wires to the earth. The abnormal grounding point may appear in the isolated ground wire if any grounding switches are not open. Furthermore, the abnormal grounding points of the isolated ground wires of EHV transmission lines during the de-icing can be divided into:

1) an abnormal grounding point in the single insulated ground wire.
2) Abnormal grounding points in both insulated ground wires on the same tower.
3) Abnormal grounding points in both insulated ground wires on the different towers.

Although the fault characteristics induced by abnormal grounding points are varied in different cases, all abnormal grounding points can cause de-icing devices to fail to connect to a part of ground wires, meaning the de-icing device is not able to melt the whole ground wire. The current of the DC de-icing device is under the control of the constant current control of the de-icing device, so the magnitude of the output current of both poles is very similar. The voltage magnitude of both poles may be different if the equivalent resistance of poles is various. Furthermore, the output power of each pole is proportional to the resistance of ground wires, which is the load of each pole. In other words, the abnormal grounding points on the isolated ground line may cause varied output power in different poles. Therefore, the distance from abnormal grounding points to the rectifier can be calculated by the different output energy by poles.

Unlike faults in normal transmission lines, the abnormal grounding point in the ground wires usually occurs before the operation of the DC de-icing device. Thus, fault characteristics can be detected during the rising of the output current.

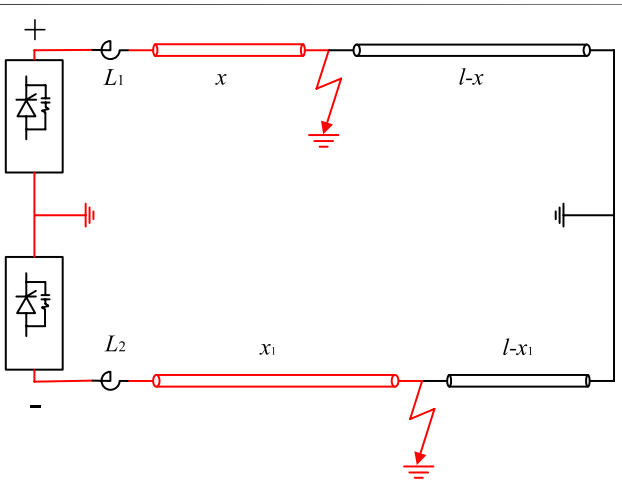


FIGURE 5 | Abnormal grounding at different bipolar positions.

TABLE 1 | Component parameters of ice melting model.

Element	Parameter
Ice melting power	35 kV
AC filter	20 MVar
Converter transformer	35/16.5/16.5 kV
Rated current of rectifier	4.5 kA
Smoothing reactor	0.025 H
Length of overhead ground wires	200 km
Resistivity of overhead ground wires	0.284 Ω/km

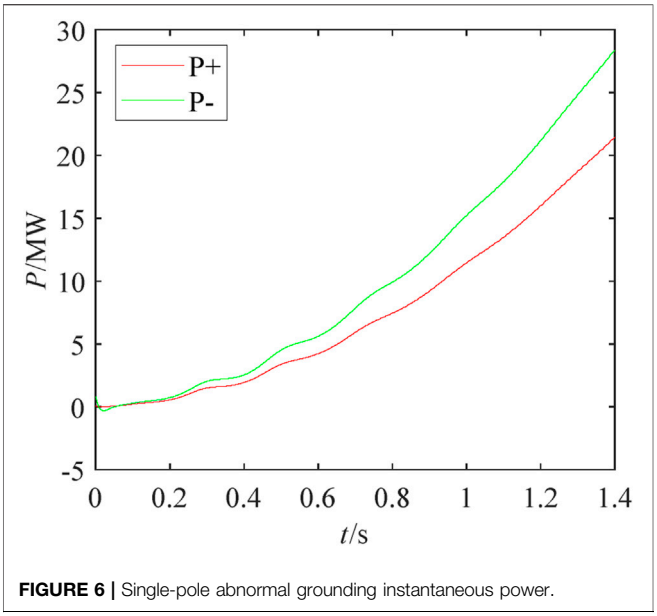


FIGURE 6 | Single-pole abnormal grounding instantaneous power.

An Abnormal Grounding Point in the Single Insulated Ground Wire

An abnormal grounding point occurs in the isolated ground wire which is connected to the positive pole as shown in **Figure 3**.

The equivalent resistance of the grounding switch is quite small, so the current of the positive pole transmits to the earth without propagating to the terminal of the grounding wire. There is only one abnormal grounding point in the positive isolated ground wire before the de-icing device works, hence the bipolar resistance can be written as

$$R_+ = \rho x \tag{1}$$

$$R_- = \rho l \tag{2}$$

where R_+ and R_- are the resistance of positive and negative poles; l stands for the length of the ground wire; x denotes the distance from the abnormal grounding point to the rectifier; ρ refers to the resistivity of the ice melting line.

The power of the de-icing device poles can be calculated by

$$\begin{cases} p_+ = i_+^2 R_x \\ p_- = i_-^2 R_l \end{cases} \tag{3}$$

where p_+ and p_- represents the output power of positive and negative poles, respectively; i_+ and i_- mean.n the direct current of the positive and negative poles, respectively.

Due to the influence of the current control of the DC de-icing device, the current of positive and negative poles keeps the same absolute value even though the loads of these two poles are different. As a result, the positive pole output voltage is less than the negative pole output voltage in **Figure 3**. The transverse differential protection can be triggered by detecting the voltage imbalance between two poles before the output power reaches a steady state.

The distance from the abnormal ground point in a single line to the de-icing device can be expressed by

$$W_{j1} = \int_{t_0}^{t_2} p_j dt \tag{4}$$

$$x = \frac{W_{j1}}{W_0} l \tag{5}$$

where W_{j1} represents the energy consumption of one pole (j = positive pole or negative pole); t_0 means the time of the de-icing device starting; t_2 means the time of transverse differential protection triggered; p_j denotes the outpower of the faulty pole; W_0 represents the rated power consumption. Due to the fixed length of the line, the current rising rate is also basically constant when the line is thawed. W_0 can be calculated according to the protection action time and starting time of the de-icing device.

Abnormal Grounding Points in Both Insulated Ground Wires on the Same Position

The schematic diagram of the fault circuit is shown in **Figure 4**, which indicates the situation of the abnormal grounding points of both poles in the same position.

TABLE 2 | Single-pole abnormal grounding distance measurement.

Power (MW)	Fault distance (km)	Energy ratio	Fault location distance (km)
164	50	0.2522	50.44
	80	0.4019	80.38
	100	0.5023	100.46
	150	0.7542	150.84
	180	0.8968	179.36
95	50	0.2513	50.65
	80	0.4032	80.64
	100	0.5044	100.88
	150	0.7530	150.60
	180	0.9022	180.44
24	50	0.2537	50.74
	80	0.4028	80.56
	100	0.5021	100.42
	150	0.7492	149.84
	180	0.8962	179.24

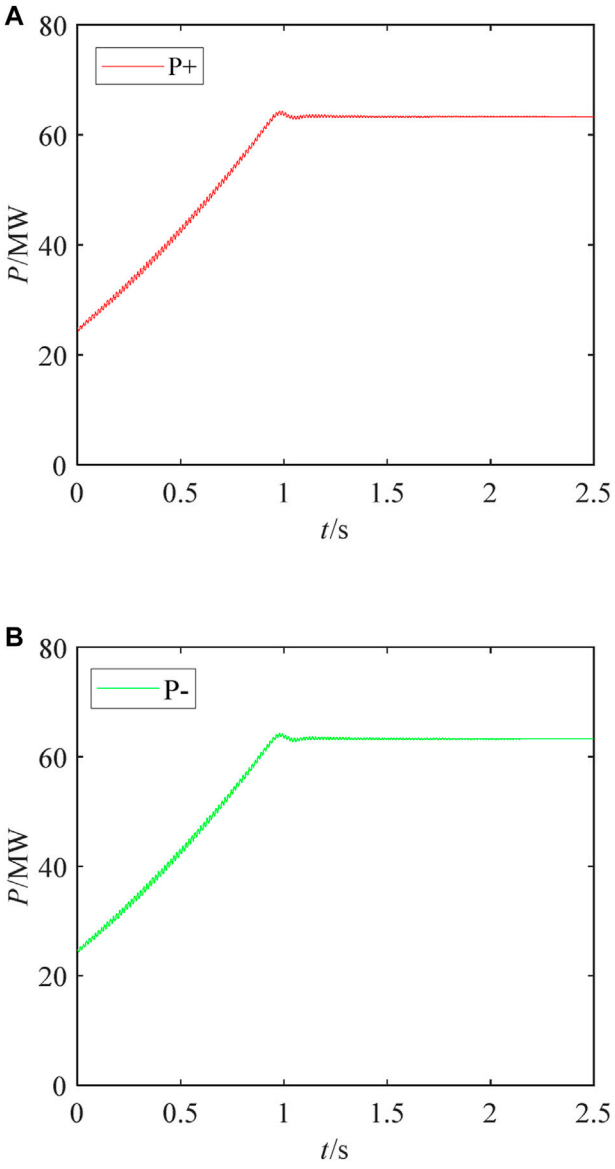


FIGURE 7 | Instantaneous power of abnormal grounding in the bipolar identical position.

As shown in **Figure 4**, the voltage amplitude and output power of the positive and negative poles are similar when the abnormal grounding points of both poles occur in the same position. The protection of the DC de-icing device cannot determine whether it has an abnormal grounding point on the ground wire since the output voltage of both poles is identical.

It is necessary to measure the rated value of the output power of the DC de-icing device to compare it with the actual output power of the DC de-icing device. The instantaneous power during the operation of the DC de-icing device can be expressed as follows:

$$\begin{cases} p_+ = i_+^2 R_x \\ p_- = i_-^2 R_x \end{cases} \tag{6}$$

The power of the two poles is the same in this case, so the transverse differential protection will not operate from the start of the DC de-icing device until the current reaches the set value. To identify whether abnormal grounding points occur, the output power of one pole can be selected and compared with the rated energy consumption of startup under normal conditions. The distance between the substation and abnormal grounding points can be calculated as

$$W_{j2} = \int_{t_0}^{t_2} p_j dt \tag{7}$$

$$x = \frac{W_{j2}}{W_0} l \tag{8}$$

where Wj_2 means start-up power consumption of any bipolar pole; t_2 denotes the time that the de-icing device reaches the steady state.

Abnormal Grounding Points in Both Insulated Ground Wires on the Different Position

The schematic diagram of abnormal grounding points in two insulated overhead ground wires with different positions is shown in **Figure 5**.

In **Figure 5**, although the output current amplitudes of the bipolar are the same, the voltage amplitudes and output power of the positive poles are both smaller than the negative pole, due to the smaller effective load of the positive pole than that of the negative pole. Furthermore, the output power of both poles is less than the normal state. The instantaneous output power of the DC de-icing device can be expressed as **Eq. 9**.

$$\begin{cases} p_+ = i_+^2 R_x \\ p_- = i_-^2 R_{x1} \end{cases} \tag{9}$$

The distance between abnormal grounding points is calculated by utilizing the ratio of the rated output power from the starting to the protection action and the actual output power.

$$W_{j3} = \int_{t_0}^{t2} p_j dt \tag{10}$$

$$x_j = \frac{W_{j3}}{W_0} l \tag{11}$$

where W_{j3} represents the start-up power consumption of the ground fault pole; x_j stands for the distance between the abnormal grounding point of the positive and negative poles and the outlet of the rectifier.

SIMULATION ANALYSIS

Simulation Modeling

The simulation model is built in PSCAD/EMTDC according to the structure diagram shown in **Figure 1**. The parameters are taken from the DC de-icing device of the converter station, as shown in **Table 1**.

TABLE 3 | Bipolar same position abnormal grounding distance measurement.

Power (MW)	Fault distance (km)	Energy ratio	Fault location distance (km)
164	50	0.2531	50.62
	80	0.4028	80.56
	100	0.5024	100.48
	150	0.7487	149.74
	180	0.8951	179.02
95	50	0.2536	50.72
	80	0.4019	80.38
	100	0.5027	100.54
	150	0.7535	150.70
	180	0.9013	180.26
24	50	0.2536	50.72
	80	0.4030	80.60
	100	0.5025	100.50
	150	0.7490	149.80
	180	0.8982	179.64

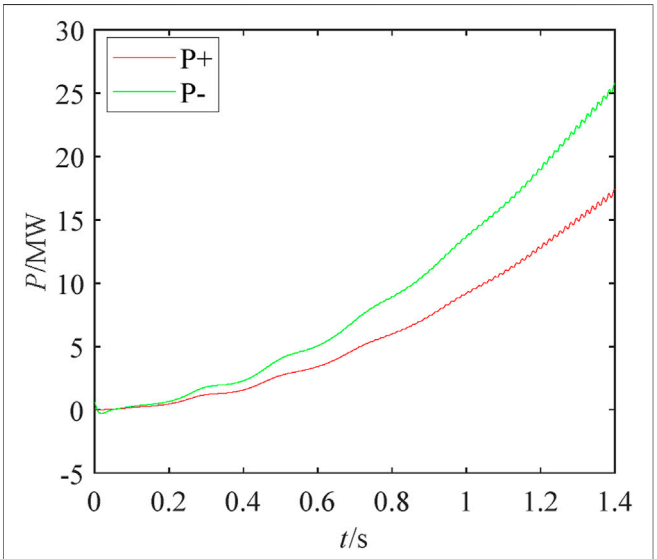


FIGURE 8 | Instantaneous power of abnormal grounding at different positions of bipolar.

An Abnormal Grounding Point in the Single Insulated Ground Wire

An abnormal grounding point is placed in the insulated overhead ground wire and connected, 150 km from the DC de-icing device. The output power of the positive and negative poles after the DC de-icing device is started, are shown in **Figure 6**.

Under the control of de-icing devices, the output current of both poles keeps rising with a constant speed, which also induces an improvement in the output power. Meanwhile, the equivalent resistance of the positive pole is smaller than the negative pole, since the isolated ground wire connected to the positive pole with an abnormal grounding point is shorter than the normal isolated grounding point connected to the negative pole. Furthermore, the output power is proportional to resistance due to the constant current of the de-icing devices, so the output power of the positive pole is smaller than that of the negative pole. The waveform in **Figure 6** presents the different rising speeds of the output power of both poles with an abnormal grounding point in the single insulated overhead ground wire.

Due to the imbalance of the output power of the two poles, the transverse differential protection of de-icing devices can be triggered to lock the converter and switch off the current. The distance between the abnormal grounding point and the deicing device is 150.84 km.

Table 2 was obtained by simulating abnormal grounding points in different positions to verify the accuracy of the proposed location method. It can be concluded that the location method is feasible for the abnormal grounding point in the single insulated ground wire since the location error is really small.

Abnormal Grounding Points in Both Insulated Ground Wires on the Same Tower

Both insulated ground wires are assumed to be abnormally grounded on the same tower, which is 150 km from the DC de-icing device. After the DC de-icing device is started, the power of the positive and negative poles is shown in **Figure 7A,B**. Combining **Eq 7** and **Eq 8**, can calculate the location of the abnormal grounding point, which is 149.74 km. Two abnormal grounding points on the same tower are not able to cause different output power of the poles of the DC de-icing device. Thus, the output power of the two poles is approximately the same after a long period of power rising, which cannot trigger the transverse differential protection.

Therefore, after reaching the constant power state, the comparation of the rated power should be applied to estimate the actual length of the two poles to prevent the incomplete de-icing of the ground wires due to abnormal grounding.

A large number of simulations were carried out to test the robustness of the proposed location method. Due to the page limit, some of them are illustrated in **Table 3**. The location method is suitable for the abnormal grounding point in the insulated ground wire due to the small number of errors of the location method.

TABLE 4 | Abnormal ranging at different bipolar positions.

Power (MW)	Fault distance (km)	Energy ratio	Fault location distance (km)	Energy ratio	Fault location distance (km)
164	(20,50)	0.1049	20.98	0.2546	50.92
	(50,80)	0.2538	50.76	0.4045	80.90
	(80,120)	0.4029	80.58	0.6020	120.40
	(100,150)	0.5025	100.50	0.7485	149.70
	(120,180)	0.6019	120.38	0.8980	179.60
95	(20,50)	0.1031	20.62	0.2524	20.48
	(50,80)	0.2523	50.46	0.4027	80.54
	(80,120)	0.4019	80.38	0.6026	120.52
	(100,150)	0.5032	100.64	0.7538	150.76
	(120,180)	0.6017	120.34	0.8996	179.92
24	(20,50)	0.1024	20.48	0.2537	20.74
	(50,80)	0.2537	20.74	0.4007	80.14
	(80,120)	0.4025	80.50	0.5989	119.78
	(100,150)	0.5019	100.38	0.7488	149.76
	(120,180)	0.6012	120.24	0.8986	179.72

Abnormal Grounding Points in Both Insulated Ground Wires on the Different Tower

Both insulated ground wires are assumed to be abnormally grounded on the different towers, which are 100 and 180 km away from the DC de-icing device, respectively. The power of the positive and negative poles after the DC de-icing device is started, is shown in **Figure 8**.

Two abnormal grounding points on various towers cause different equivalent resistance of the poles of the DC de-icing device, which further leads to the imbalance output power of poles. Therefore, the output power of the two poles is significantly different while the power is rising. The location of abnormal grounding points acquired by **Eq. 10** and **Eq. 11** are 120.38 and 179.60 km, respectively.

Table 4 is acquired by simulating abnormal grounding points in the different positions of two poles to verify the accuracy of the proposed location method. This location method is feasible for the abnormal grounding points in both insulated ground wires on the different towers. In **Table 4**, x1.

CONCLUSION

1) There is a long period of current rising for the reduction of the adverse impact of the DC de-icing device with large capacity, hence the abnormal grounding point may trigger the transverse protection of the de-icing device.
2) The resistance of transmission lines is fairly distributed, so the energy consumption of the positive and negative poles during the current rising can be applied to locate the abnormal grounding point.

DATA AVAILABILITY STATEMENT

The original contributions presented in the study are included in the article/supplementary material, further inquiries can be directed to the corresponding author.

AUTHOR CONTRIBUTIONS

YW: experiment design and article writting NC: simulation model design in PSCAD/EMTDC XM: fault location scheme verification ZY: article writting and reference searching.

FUNDING

This work is supported by China Southern Power Grid Project (No. 0109002021030103SJ00002).

REFERENCES

Bin, W., and Lin, Y. (2020). Error Analysis of Single Terminal Traveling Wave Fault Location for HVDC Transmission Lines. *Electrotechnical Appl.* 39 (10), 33–38.

Chen, Y., Yin, J., Li, Z., and Wei, R. (2021). Single-Line-to-Ground Fault Location in Resonant Grounded Systems Based on Fault Distortions. *IEEE Access* 9 (9), 34325–34337. doi:10.1109/access.2021.3061211

De Oliveira Neto, J. A., Sartori, C. A. F., and Junior, G. M. (2021). Fault Location in Overhead Transmission Lines Based on Magnetic Signatures and on the Extended Kalman Filter. *IEEE Access* 9 (9), 15259–15270. doi:10.1109/access.2021.3050211

Feng, X., Qi, L., and Pan, J. (2016). "A Novel Fault Location Method and Algorithm for DC Distribution protection," in 2016 IEEE Industry Applications Society Annual Meeting, Portland, October 2–6, 2016 (IEEE), 1–5.

Gao, X., Huang, W., and Tai, N. (2020). "Fault Location Method for MMC Multi-Terminal DC Distribution Network Using Transient DC Currents," in 2020 4th International Conference on HVDC (HVDC), Xi'an, China, November 6–9, 2020 (IEEE), 961–965.

Guang, S., Yang, W., and Feng, X. (2020). Research on an Improved Double-Terminal Traveling Wave Fault Location Method for UHVDC Project. *Power Syst. Prot. Control.* 48 (14), 113–120.

Guo, B., Song, G., Hou, J., Wu, L., and Han, W. (2019). A Single-Ended Fault Location Method for DC Line Based on Active Signal. 2019 IEEE 8th International Conference on Advanced Power System Automation and Protection (APAP), Xi'an, China, October 21–24, 2019 (IEEE), 1503–1507.

Haleem, N. M., and Rajapakse, A. D. (2019). "A Single Pole to Ground Fault Location Method for HVDC Transmission Lines Based on Coupling Characteristics," in 15th IET Int. Conf. AC DC Power Transm. (ACDC 2019), Coventry, UK, February 5–7, 2019 (Winnipeg, MB: IET), 1–6.

Hao, W., Peng, S., and Lu, J. (2015). Research on DC Ice-Melting Technologies for 500kV AC Transmission Lines. 2015 5th International Conference on Electric Utility Deregulation and Restructuring and Power Technologies. DRPT, Changsha, China, November 26–29, 2015 (IEEE), 1663–1666.

Jiazheng, L., Siguo, Z., Bo, L., Yanjun, T., Xiudong, Z., Qinjun, H., et al. (2016). Ice-melting Device with Function of Reactive Power Compensation and Active Filtering. *High Voltage Eng.* 42 (07), 2207–2214.

Juanjuan, W., Chuang, F., Yiping, C., Hong, R., Shukai, X., Tao, Y., et al. (2012). Research and Application of DC De–icing Technology in China Southern Power Grid. *IEEE Trans. Power Deliv.* 27 (3), 1234–1242. doi:10.1109/TPWRD.2012.2191576

Kai, L., Zhengyou, H., and Xiaopeng, L. (2013). Fault Location of HVDC Transmission Line Based on the Natural Frequency of Traveling Wave. *Automation Electric Power Syst.* 37 (03), 104–109.

Lei, A., Dong, X., Shi, S., and Wang, B. (2015). "A Novel Current Travelling Wave Based Single-Ended Fault Location Method for Locating Single-Phase-To-Ground Fault of Transmission Line," in 2015 50th International Universities Power Engineering Conference. (UPEC), Stoke on Trent, UK, September 1–4, 2015 (IEEE), 1–6.

Miao, L., Fang, J., Wen, J., and Luo, W. (2013). Transient Stability Risk Assessment of Power Systems Incorporating Wind Farms. *J. Mod. Power Syst. Clean. Energ.* 1 (2), 134–141. doi:10.1007/s40565-013-0022-2

Shukr, M., Thomas, D. W. P., and Zanchetta, P. (2012). "VSC-HVDC Transmission Line Faults Location Using Active Line Impedance Estimation," in 2012 IEEE International Energy Conference and Exhibition (ENERGYCON), Florence, Italy, September 9–12, 2012 (IEEE), 244–248.

Sun, P., Chen, S., and Zhang, S. (2011). "The Study of DC Melting Ice for Overhead Ground Wire," in 2011 International Conference on Electronics, Communications and Control (ICECC), Ningbo, China, September 9–11, 2011 (IEEE), 2960–2963.

Wangsheng, X., jiang, H., and Yongliang, Y. (2016). Study on Location Technology of Overhead Ground Wire Ice Melting Fault Based on Traveling Wave Method. *Mech. Electr. Inf.* 97 (15), 94–95.

Wu, J.-Y., Lan, S., Xiao, S.-J., and Yuan, Y.-B. (2021). Single Pole-to-Ground Fault Location System for MMC-HVDC Transmission Lines Based on Active Pulse and CEEMDAN. *IEEE Access* 9 (9), 42226–42235. doi:10.1109/access.2021.3062703

Yuansheng, L., Gang, W., and Haifeng, L. (2015). Time-Domain Fault-Location Method on HVDC Transmission Lines under Unsynchronized Two-End Measurement and Uncertain Line Parameters. *IEEE Trans. Power Deliv.* 30 (3), 1031–1038. doi:10.1109/tpwrd.2014.2335748

Yunke, Z., Botong, L., and Bin, L. (2017). Ground-fault Location Technology for Extra-high Voltage Transmission Lines during DC De-icing Process. *Automation Electric Power Syst.* 41 (20), 105–111.

Zasypkin, A., and Shchurov, A. (2020). "Capacitor Protection of Electromagnetic Voltage Transformers in DC Ice Melting Schemes on Overhead Transmission Lines," in 2020 International Multi-Conference on Industrial Engineering and Modern Technologies (FarEastCon), Vladivostok, Russia, October 6–9, 2020 (IEEE), 1–6.

Zhi, W., and Fangzong, W. (2011). A New Method of Earth Fault Detection in Distribution System. *Power Syst. Prot. Control.* 39 (20), 48–51.

Zhu, S., Li, B., Tan, Y., Han, Y., Ouyang, F., and Duan, X. (2019a). "Low Harmonic DC Ice Melting Device Capable of Reactive Power Compensation with SVG," in 2019 IEEE 3rd Conference on Energy Internet and Energy System Integration (EI2), Changsha, China, November 8–10, 2019 (IEEE), pp. 2460–2465.

Zhu, Y., Mao, X., Huang, Q., Feng, B., Zhu, S., and Tan, Y. (2019b). "Topology and Simulation of Charged Melting Ice on Transmission Lines," in 2019 IEEE 3rd Conference on Energy Internet and Energy System Integration (EI2), Changsha, China, November 8–10, 2019 (IEEE), pp. 2379–2381.

Conflict of Interest: YW, NC, XM and ZY were employed by China Southern Power Grid EHV Transmission Company.

The authors declare that the research was conducted in the absence of any commercial or financial relationships that could be construed as a potential conflict of interest.

Copyright © 2021 Wang, Chen, Ma and Yang. This is an open-access article distributed under the terms of the Creative Commons Attribution License (CC BY). The use, distribution or reproduction in other forums is permitted, provided the original author(s) and the copyright owner(s) are credited and that the original publication in this journal is cited, in accordance with accepted academic practice. No use, distribution or reproduction is permitted which does not comply with these terms.

frontiers in Energy Research

ORIGINAL RESEARCH
published: 23 July 2021
doi: 10.3389/fenrg.2021.731944

Convex Approximation Algorithm for AC/DC Distribution Network With Energy Router

Tao Zhang[1], *Yunfei Mu*[1]*, *Xiaoyu Wang*[1], *Youjun Deng*[1], *Yi Song*[2], *Kai Yuan*[2] *and Hongjie Jia*[1]

[1]*Key Laboratory of Smart Grid of Ministry of Education, Tianjin University, Tianjin, China,* [2]*State Grid Economic and Technological Research Institute Co., Ltd., Beijing, China*

The optimal operation model of AC/DC distribution network with energy router (ER) is essentially a nonconvex nonlinear programming (NLP) problem. In order to improve the feasibility of solving the model, a convex approximation algorithm is proposed in this work. The steady-state model of ER is developed with considering the loss characteristics and multiport coordinated control strategy. It is embedded in the optimization formulations of AC/DC network as basic operating equations. Then, using second-order cone relaxation technology, the power flow equations of AC and DC distribution networks are convexly relaxed. On this basis, the highly nonlinear operating model of ER is linearized by introducing a successive approximation approach. Therefore, the original NLP problem is transformed into the convex programming problem and the solution efficiency is improved. Meanwhile, an iterative solution algorithm is developed to ensure the accuracy of the convex approximation approach. Simulation results verify the feasibility and efficiency of the proposed algorithm.

Keywords: AC/DC distribution network, energy router, steady-state model, second-order cone relaxation, successive approximation

OPEN ACCESS

Edited by:
Bo Yang,
Kunming University of Science and Technology, China

Reviewed by:
Ke Peng,
Shandong University of Technology, China
Yingyun Sun,
North China Electric Power University, China

****Correspondence:***
Yunfei Mu
yunfeimu@tju.edu.cn

Specialty section:
This article was submitted to Smart Grids, a section of the journal Frontiers in Energy Research

Received: *28 June 2021*
Accepted: *12 July 2021*
Published: *23 July 2021*

Citation:
Zhang T, Mu Y, Wang X, Deng Y, Song Y, Yuan K and Jia H (2021) Convex Approximation Algorithm for AC/DC Distribution Network With Energy Router. Front. Energy Res. 9:731944. doi: 10.3389/fenrg.2021.731944

INTRODUCTION

The development of renewable energy technology poses new challenges for flexible access and effective regulation of the power system (Guo et al., 2019). Energy router (ER) is also known as power electronic transformer (PET), and solid-state transformer. It has the functions of voltage conversion and power flow routing (Chen et al., 2020; Li et al., 2021; Liu et al., 2018). The AC/DC hybrid distribution network with ER (ER-based AC/DC HDN) can interconnect networks with multiple voltage levels and frequencies. It is conducive to the flexible access and consumption of distributed generations (DGs), and has attracted extensive attention (Zhang et al., 2020). However, flexible device access, AC/DC hybrid connection, three-phase asymmetrical, and active and reactive power coupling make the analysis and solution of ER-based AC/DC HDN face great challenges (Meng et al., 2018; Tang et al., 2021; Zhang et al., 2021).

The existing literatures have carried out research on the establishment of the ER steady-state model and its application in the distribution network. In (Miao et al., 2016), each port of ER is equivalent to the voltage source converter. On this basis, taking into account the loss characteristics of the converter, a power flow model for ER has been proposed in (Dong et al., 2019). Then, in order to reduce network losses, operating costs, and improve the voltage distribution, a multi-objective optimization model for AC network with ER was developed in (Miao et al., 2018). To take advantage of flexible regulation capabilities of ER, an optimization method for voltage imbalanced suppression

is studied in (Dong et al., 2018). The above literatures have improved the operating performance of the ER based distribution networks from various aspects. However, the coordination control capability among multiport of ER needs to be further researched. Furthermore, the optimization model in the above literatures includes power flow constraints and highly nonlinear ER operation constraints. It is essentially a nonconvex nonlinear programming (NLP) problem, and obtaining the solution with an acceptable time is a great challenge (Deng et al., 2021)- (Soofi et al., 2021).

ER contains an intermediate DC/DC link. It isolates the distribution network into multiple AC and DC subnetworks with independent voltages and frequencies (Li et al., 2020). While operation, an appropriate coordinated control strategy is important to satisfy the power exchange demands of the ER and the subnetworks. For this issue, an optimal combination of operation strategy based on generalized droop control is introduced in (Rouzbehi et al., 2015). The switching of different operating modes (constant voltage control, constant power control, and droop control) of ER is determined by optimizing the droop coefficient. It is worth noting that the droop control strategy has been extensively studied in islanded system. In (Yu et al., 2018), a peer-to-peer control strategy for islanded networks is developed. In order to be apply to the asymmetric low voltage AC network, a three-phase droop control strategy has been studied in (Abdelaziz et al., 2013). On this basis, a secondary control strategy is introduced in (Allam et al., 2018) to improve the utilization efficiency of DGs. Applying these control methods to ER-based AC/DC HDN can improve the operating performance of the network, which has not been studied yet.

Generally, converting the original NLP problem into a convex programming problem can improve the efficiency of the solution. Using the second-order cone relaxation technology, an optimal operation model for AC distribution network is proposed in (Ji et al., 2017), which improves the feasibility of the solution. In (Gan and Low, 2014) a second-order cone programming (SOCP) model for DC network is introduced. These researches provide a basis for convex programming modeling of AC/DC network. However, several limitations can be found. 1) The highly nonlinear loss characteristic equation of ER is a quadratic function involving current. The existing SOCP approach cannot effectively deal with it. 2) The square of the voltage in SOCP model is the optimization variable. The droop control strategy involves the first-order term of voltage, which cannot be transformed in the form of SOCP manner.

In order to improve the feasibility of solving the optimization model of ER-based AC/DC HDN, a convex approximation algorithm is proposed in this work. The main contributions are summarized as follows.

1) An optimal operation model for ER-based AC/DC HDN is devolved in this paper. The multiport coordinated control strategy of ER is considered. Thus, the power balanced of ET and the system can be guaranteed. On this basis, a hierarchical droop control strategy is introduced, which improves the utilization efficiency of DGs.
2) The second-order cone relaxation method is adopted to handle the nonlinear power flow equations. Then, combined with the linear approximation approach, the operation constraints of ER are successfully linearized. The original NLP problem is converted into a convex programming problem, which improves the efficiency of the solution. Furthermore, the successive iteration algorithm is proposed to ensure the accuracy of the solution.

STEADY-STATE MODEL AND COORDINATED CONTROL STRATEGY OF ER

Steady-State Model of Multiport ER

The equivalent structure diagram of ER based on PET is shown in **Figure 1**. It includes M AC ports and N DC ports. Each port is composed of AC/DC or DC/DC converter, which is used to connect AC and DC networks, respectively.

While operation, the active power balanceed of ER should be satisfied, as described in **Eq. 1**.

$$\sum_{m=1}^{M} P_{\mathrm{ER.ac},i}^{\phi,t} + \sum_{n=1}^{N} P_{\mathrm{ER.dc},\,j}^{\phi,t} - P_{\mathrm{ER.loss}}^{t} = 0 \tag{1}$$

The power loss of each ER port $P_{loss,i}^{t}$ can be obtained by curve fitting. It is expressed as the quadratic function of the port current $I_{c,i}^{t}$ (Sun et al., 2019; Khan and Bhowmick, 2019).

$$P_{\mathrm{loss},i}^{t} = a_{c,i} + b_{c,i} I_{c,i}^{t} + c_{c,i}\left(I_{c,i}^{t}\right)^{2} \tag{2}$$

Then, the total loss of ER $P_{\mathrm{PET.loss}}^{t}$ is the sum of the power loss of all AC ports and DC ports, which is shown in **Eq. 3**.

$$P_{\mathrm{ER.loss}}^{t} = \sum_{m=1}^{M} \sum_{\phi=a}^{c} P_{\mathrm{loss.ac},i}^{\phi,t} + \sum_{n=1}^{N} P_{\mathrm{loss.dc},j}^{t} \tag{3}$$

Coo rdinated Control Strategy of Multiport ER

The AC and DC subnetworks are connected via ER coupling. Due to the intermediate DC/DC isolation link of ER, multiple AC subnetworks operate at different frequencies. To maintain the power balanced of ER, AC, and DC subnetworks, an appropriate coordinated control strategy is necessary. In (Rouzbehi et al., 2015), a generalized droop control strategy is proposed, which is the integration of constant voltage control, constant power control and droop control. The control mode is determined by the generalized droop coefficient. The simulation results show that the droop control strategy ($\alpha \neq 0, \beta \neq 0, \gamma \neq 0$) can effectively deal with the fluctuation of renewable energy. In this work, the secondary control layer is introduced. Then, the regulation performance of the controller can be improved, as shown in **Figure 2**. The droop control strategy is applied to the low voltage port of ER, as shown in **Eqs 4–6**. And the high voltage AC port of ER adopts constant voltage control mode to maintain the power balance.

$$P_{\mathrm{ER.ac},i}^{\phi,t} = \varsigma_{\mathrm{pet}}\left(\omega_0 + \delta\omega_{\mathrm{ER},i}^{\phi,t} - \omega^{t}\right) \tag{4}$$

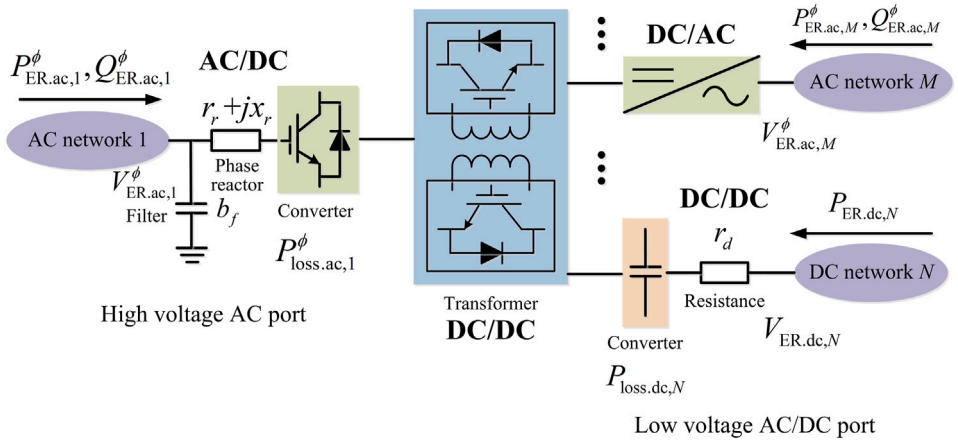


FIGURE 1 | Equivalent structure diagram of ER.

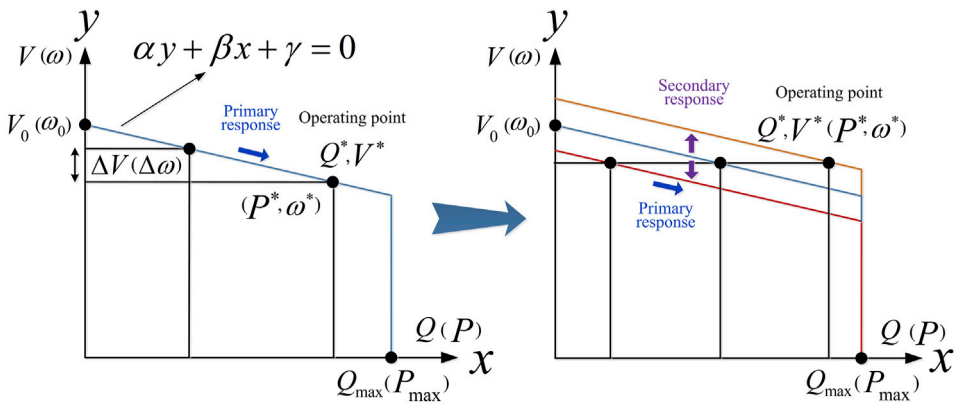


FIGURE 2 | Secondary coordinated control strategy.

$$Q^{\phi,t}_{\mathrm{ER.ac},i} = \xi_{\mathrm{er}}\left(V^{\mathrm{ac}}_{\mathrm{ER},0} + \delta V^{\phi,t}_{\mathrm{ER.ac},i} - V^{\phi,t}_{\mathrm{ER.ac},i}\right) \tag{5}$$

$$P^{t}_{\mathrm{ER.dc},i} = \zeta_{\mathrm{er}}\left(V^{\mathrm{dc}}_{\mathrm{ER},0} + \delta V^{t}_{\mathrm{ER.dc},i} - V^{t}_{\mathrm{ER.dc},i}\right) \tag{6}$$

The steady-state model of multiport ER is summarized by **Eqs 1–6**. It is embedded in the asymmetric AC/DC network optimization model as basic formulas in next section.

OPTIMAL OPERATION MODEL AND CONVEX APPROXIMATION CONVERSION

Optimal Operation Model for ER-Based AC/DC HDN

Objective Function

This work takes the minimum active power loss as the objective function, shown as follows:

$$\min f = \sum_{t=1}^{T}\left(\sum_{\phi=a}^{c}\sum_{ij\in\Psi_{\mathrm{AC}}} r^{\phi}_{ij.\mathrm{AC}}\widetilde{I}^{\phi,t}_{ij.AC}\Delta t + \sum_{ij\in\Psi_{\mathrm{DC}}} r_{ij.\mathrm{DC}}\widetilde{I}^{t}_{ij.\mathrm{DC}}\Delta t + P^{t}_{\mathrm{ER.loss}}\Delta t\right) \tag{7}$$

Constraints

The Distflow branch equations of AC/DC distribution networks include power flow constraints, branch voltage constraints, and current constraints (Zhang et al., 2018). It is relaxed by the cone relaxation technique, shown as follows:

$$\begin{cases} \sum_{ij\in\Psi_{\mathrm{AC}}}\left(P^{\phi,t}_{ij.\mathrm{AC}} - r^{\phi}_{ij.\mathrm{AC}}\widetilde{I}^{\phi,t}_{ij.\mathrm{AC}}\right) + P^{\phi,t}_{g.\mathrm{AC}} - P^{\phi,t}_{\mathrm{ER.ac}} - P^{\phi}_{l.\mathrm{AC}} = \sum_{jk\in\Psi_{\mathrm{AC}}} P^{\phi,t}_{jk.\mathrm{AC}} \\ \sum_{ij\in\Psi_{\mathrm{AC}}}\left(Q^{\phi,t}_{ij.\mathrm{AC}} - x^{\phi}_{ij.\mathrm{AC}}\widetilde{I}^{\phi,t}_{ij.\mathrm{AC}}\right) + Q^{\phi,t}_{g.\mathrm{AC}} - Q^{\phi,t}_{\mathrm{ER.ac}} - Q^{\phi}_{l.\mathrm{AC}} = \sum_{jk\in\Psi_{\mathrm{AC}}} Q^{\phi,t}_{jk.\mathrm{AC}} \\ \widehat{V}^{\phi,t}_{j.\mathrm{AC}} = \widehat{V}^{\phi,t}_{i.\mathrm{AC}} - 2\left(r^{\phi}_{ij.\mathrm{AC}}P^{\phi,t}_{ij.\mathrm{AC}} + x^{\phi}_{ij.\mathrm{AC}}Q^{\phi,t}_{ij.\mathrm{AC}}\right) + \left(\left(r^{\phi}_{ij.\mathrm{AC}}\right)^2 + \left(x^{\phi}_{ij.\mathrm{AC}}\right)^2\right)\widetilde{I}^{\phi,t}_{ij.\mathrm{AC}} \\ \left\|2P^{\phi,t}_{ij.\mathrm{AC}}2Q^{\phi,t}_{ij.\mathrm{AC}}\widetilde{I}^{\phi,t}_{ij.\mathrm{AC}} - \widehat{V}^{\phi,t}_{j.\mathrm{AC}}\right\|_2 \le \widetilde{I}^{\phi,t}_{ij.\mathrm{AC}} + \widehat{V}^{\phi,t}_{j.\mathrm{AC}} \end{cases} \tag{8}$$

$$\begin{cases} \sum_{ij\in\Psi_{\mathrm{DC}}}\left(P^{t}_{ij.\mathrm{DC}} - r_{ij.\mathrm{DC}}\widetilde{I}^{t}_{ij.\mathrm{DC}}\right) + P^{t}_{g.\mathrm{DC}} - P^{t}_{\mathrm{ER.dc}} - P_{l.\mathrm{DC}} = \sum_{jk\in\Psi_{\mathrm{DC}}} P^{t}_{jk.\mathrm{DC}} \\ \widehat{V}^{t}_{j.\mathrm{DC}} = \widehat{V}^{t}_{i.\mathrm{DC}} - 2r_{ij.\mathrm{DC}}P^{t}_{ij.\mathrm{DC}} + \left(r_{ij.\mathrm{DC}}\right)^2\widetilde{I}^{t}_{ij.\mathrm{DC}} \\ \left\|2P^{t}_{ij.\mathrm{DC}}\widetilde{I}^{t}_{ij.\mathrm{DC}} - \widehat{V}^{t}_{j.\mathrm{DC}}\right\|_2 \le \widetilde{I}^{t}_{ij.\mathrm{DC}} + \widehat{V}^{t}_{j.\mathrm{DC}} \end{cases} \tag{9}$$

Droop control characteristic constraints of DGs in the low voltage AC/DC networks are expressed as **Eqs 10–12**.

$$P^t_{g.\mathrm{AC},i} = \sum_{\phi=a}^{c} P^{\phi,t}_{g.\mathrm{AC},i} = \varsigma_{\mathrm{ac}}\left(\omega_0 + \delta\omega^{\phi,t}_{\mathrm{ac},i} - \omega^t\right) \tag{10}$$

$$Q^t_{g.\mathrm{AC},i} = \sum_{\phi=a}^{c} Q^{\phi,t}_{g.\mathrm{AC},i} = \xi_{\mathrm{ac}}\left(V^t_{i.\mathrm{AC},0} + \delta V^t_{i.\mathrm{AC}} - V^t_{i.\mathrm{AC}}\right) \tag{11}$$

$$P^t_{g.\mathrm{DC},i} = \zeta_{\mathrm{dc}}\left(V^t_{i.\mathrm{DC},0} + \delta V^t_{i.\mathrm{DC}} - V^t_{i.\mathrm{DC}}\right) \tag{12}$$

Operational constraints of the network are formulated as:

$$\underline{J}_i \le J^t_i \le \overline{J}_i \tag{13}$$

$$\underline{E}_{\mathrm{SOC}} \le E^t_{\mathrm{SOC}} \le \overline{E}_{\mathrm{SOC}} \tag{14}$$

$$\underline{P}_{\mathrm{stor}} \le P^t_{\mathrm{stor}} \le \overline{P}_{\mathrm{stor}} \tag{15}$$

$$\sum_{t=1}^{T} P^t_{\mathrm{stor}} = 0 \tag{16}$$

$$\left\| \widehat{P}^{\phi,t}_{\mathrm{ER.ac}} \ \widehat{Q}^{\phi,t}_{\mathrm{ER.ac}} \right\|_2 \le S^{\phi}_{\mathrm{ER.ac}} \tag{17}$$

The allowable range of variables is shown in **Eq. 13**, in which $J^t_i \in \{\widehat{V}^{\phi,t}_{i.\mathrm{AC}}, \widehat{V}^t_{i.\mathrm{DC}}, \omega^t, P^t_{g.\mathrm{AC},i}, Q^t_{g.\mathrm{AC},i}, P^t_{g.\mathrm{DC},i}, Q^{\phi,t}_{\mathrm{ER.ac},i}, P^t_{\mathrm{ER.dc},i}\}$. The amount of charge of energy storage system (ESS) E^t_{SOC} is represented in **Eq. 14**. The charge and discharge of ESS is expressed in **Eq. 15**. The sum of the charge and discharge power of ESS in a scheduling period is 0, as shown in **Eq. 16**. The capacity constraint of ER AC port is relaxed to the second-order cone form, as described in **Eq. 17**.

Eqs 7–17 together with the steady-state model of ER **Eqs 1–6** form the original optimal operation model F_0. It is worth noting that the highly nonlinear ER loss characteristic constraint is involved in F_0, which is essentially an NLP problem. Accurate and efficient solving algorithm is very necessary.

Successive Convex Approximation Conversion to NLP Problem

Linear Approximation

In section *Optimal Operation Model for ER-Based AC/DC HDN*, the second-order cone relaxation technique is adopted to linearize the Distflow branch equations, as shown in **Eqs 8**, **9**. The square of the branch current is introduced as the optimization variable. Thus, the constant term $a_{c,i}$ and second-order term $c_{c,i}\widehat{I}^t_{c,i}$ in **Eq. 2** are linear expressions. Given an initial value $I^{t,k-1}_{c,i}$, the first-order term $b_{c,i}I^t_{c,i}$ is approximately linearized by using Taylor expansion in this work.

$$b_{c,i}I^t_{c,i} \approx \frac{b_{c,i}}{2}\left(\sqrt{\left(I^{t,k-1}_{c,i}\right)^2} + \frac{\left(I^t_{c,i}\right)^2}{\sqrt{\left(I^{t,k-1}_{c,i}\right)^2}}\right) = \frac{b_{c,i}}{2}I^{t,k-1}_{c,i} + \frac{b_{c,i}}{2I^{t,k-1}_{c,i}}\widehat{I}^t_{c,i} \tag{18}$$

Using **Eq. 18**, the ER loss characteristic constraint in **Eq. 2** can be transformed into linear expression. Furthermore, the square of the node voltage is the optimization variable. The droop control constraints **Eqs 5**, **6**, **11**, **12** involve the first-order term of voltage, which are approximately linearized using **Eq. 19**.

$$V^t_i \approx \sqrt{\left(V^{t,k-1}_i\right)^2} + \frac{\left(V^t_i\right)^2}{\sqrt{\left(V^{t,k-1}_i\right)^2}} = \frac{V^{t,k-1}_i}{2} + \frac{\widehat{V}^t_i}{2V^{t,k-1}_i} \tag{19}$$

where, $V^t_i \in \{V^{\phi,t}_{\mathrm{ER.ac},i}, V^t_{\mathrm{ER.dc},i}, V^t_{i.\mathrm{AC}}, V^t_{i.\mathrm{DC}}\}$. After relaxation and linearization, the objective function is linear and the constraints are linear or second-order cone expression. The original NLP problem F_0 is converted into an approximate convex programming problem F_s, which can be efficiently solved.

Successive Convex Approximation Algorithm

The optimal values of branch current and node voltage $(I^t_{c,i}, V^t_i)$ in the original NLP problem F_0 cannot be obtained in advance. When the difference between the given initial values $(I^{t,k-1}_{c,i}, V^{t,k-1}_i)$ and the optimal values are large, high calculation error will occur in **Eqs 18**, **19**. To improve the accuracy between F_s and F_0, an iterative calculation process is necessary. The successive convex approximation model is defined as $\overrightarrow{F}_s$ in this work.

The diagram of the successive convex approximation algorithm is shown in **Figure 3**.

The solution process is as follows:

Step 1: Given initial values $(I^{t,k-1}_{c,i}, V^{t,k-1}_i)$ to formulate and solve F_s;
Step 2: The initial values are updated according to the current optimal values of F_s $(I^{t,k}_{c,i} = \sqrt{\widehat{I}^{s,t}_{c,i}}, V^{t,k}_i = \sqrt{\widehat{V}^{s,t}_i})$;
Step 3: If the difference between initial values in two adjacent iterations is less than the given threshold $\varepsilon = 0.001$, stop, and the convergence is obtained; otherwise, go back to step 1 based on the updated initial values $(I^{t,k}_{c,i}, V^{t,k}_i)$.

CASE STUDIES

In order to verify the effectiveness of the approach proposed in this work, the solver *Cplex* is used to solve the optimization program based on *Matlab-Yalmip* platform. The network topology of ER-based AC/DC HDN is shown in **Figure 4**. 10 kV high voltage AC network (Zhu, 2002), 380 V low voltage AC network, and 750 V low voltage DC network (Dong et al., 2019) are coupled through ER. The no load voltage in AC network is $V^t_{i.\mathrm{AC},0} = 1.05$p.u., and the allowable voltage range is set as [0.95, 1.05]p.u. The no load voltage in DC network is $V^t_{i.\mathrm{DC},0} = 1.02$p.u., and the allowable voltage range is set as [0.95, 1.02]p.u. The no load frequency is $\omega_0 = 1.004$p.u., and the allowable frequency range is set as [0.996, 1.004]p.u. Fitting coefficients of ER loss model are set as $a_{c,i} = 0.001$, $b_{c,i} = 0.005$, $c_{c,i} = 0.02$. The given initial values are $I^{t,k-1}_{c,i} = 0.01$, and $V^{t,k-1}_i = 1$.

Results of Optimal Power Flow

The original NLP problem F_0 and the successive convex approximation problem $\overrightarrow{F}_s$ are solved by the solver *Ipopt* and *Cplex*, respectively. The results of the optimal power flow in a period are shown as follows.

Table 1 shows the active power loss and solution time of model F_0 and $\overrightarrow{F}_s$. The active power loss in each network is

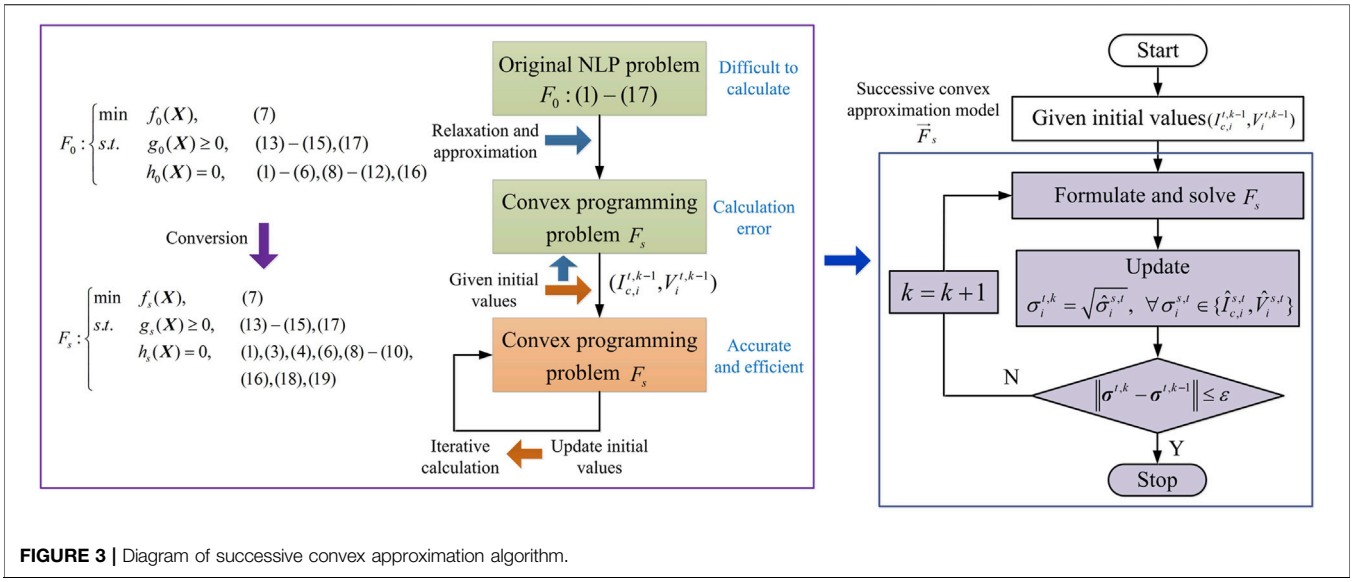


FIGURE 3 | Diagram of successive convex approximation algorithm.

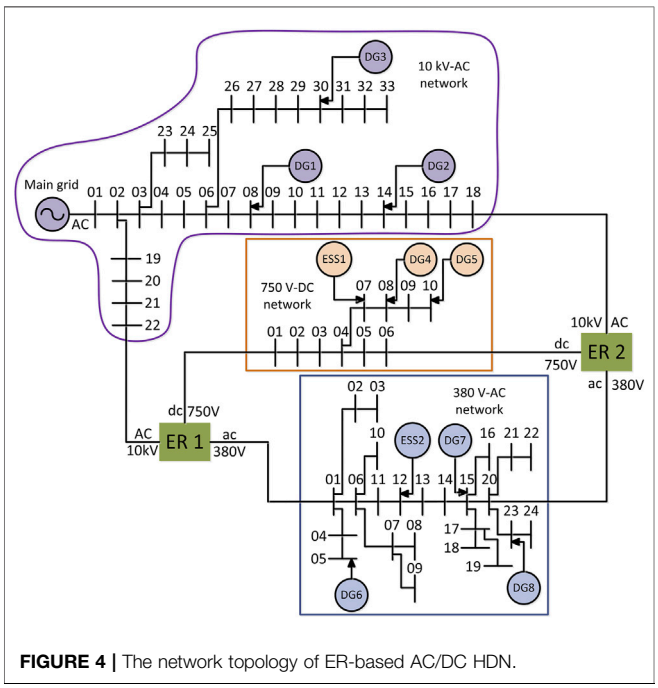


FIGURE 4 | The network topology of ER-based AC/DC HDN.

roughly the same, and the relative error of the total loss is only 0.67%. Thus, the accuracy of the proposed algorithm is verified. Furthermore, compared with the original NLP problem F_0 with solving time of 80.8 s, that is 17.3 s in the proposed model $\overrightarrow{F}_s$. Calculation efficiency increased by 78.6%.

To verify the effectiveness of the introduced secondary control strategy, three cases are studied here.

Case I: Droop control strategy without secondary layer is adopted by ER and DGs;
Case II: Droop control strategy without secondary layer is adopted by ER and secondary droop control strategy is adopted by DGs;
Case III: Secondary droop control strategy is adopted by ER and DGs.

Active power output by DGs and ER in the low voltage network and the total power loss are demonstrated in **Figure 5**. Droop control characteristic is shifted by introducing the secondary droop control layer. The regulation performance of the controller is improved. The active power output of DGs is increased, and the active power injected by ER is reduced. Thus, the utilization efficiency of DGs in Case III is 55.4 and 19.7% higher than Case I and Case II, respectively. Compared with Case I and Case II, the total power loss in Case III is reduced by 29.6 and 15.5%, respectively.

Results of Day-Ahead Optimal Scheduling

As demonstrated in **Figure 6**, the power output of DGs and main grid changes with the load curve. The ESS is charged at 1: 00–10:00 and 15:00–17:00 during the low load period, and discharged at 12:00–14:00 and 19:00–23:00 during the peak load period, as shown in **Figure 7**. Compared with before

TABLE 1 | Optimized results of active power loss and solution time.

Model	Active power loss in different networks (kW)				Total loss (kW)	Solution time (s)
	10 kV-AC	380 V-AC	750 V-DC	ER		
F_0	65.4	40.4	5.1	22.8	133.7	80.8
$\overrightarrow{F}_s$	64.6	41.4	5.1	21.7	132.8	17.3

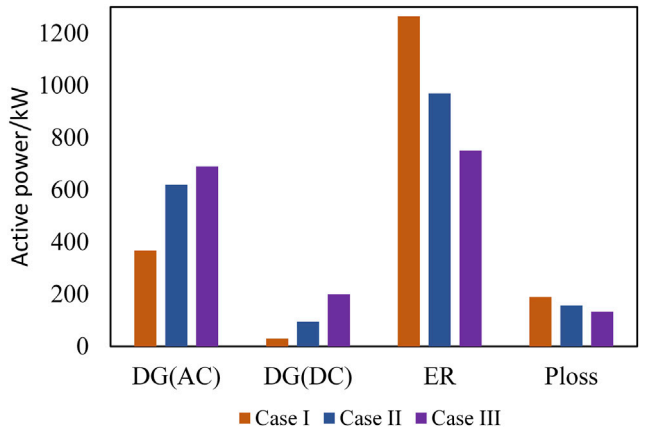


FIGURE 5 | Controllable unit active power output and the total power loss in three cases.

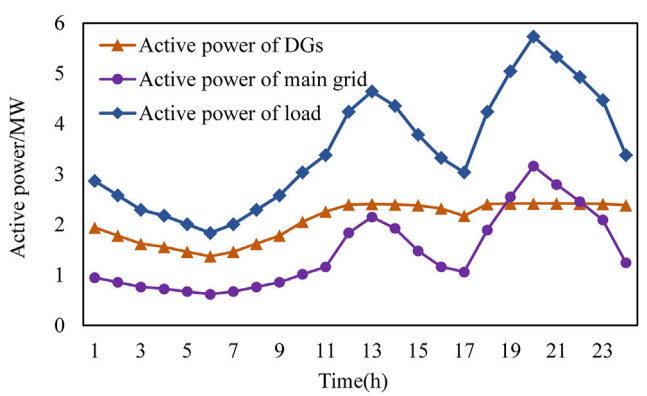


FIGURE 6 | Active power output of DGs and main grid.

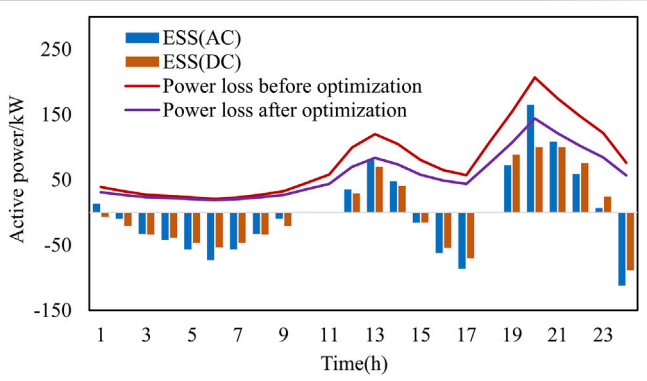


FIGURE 7 | Charging/discharging results of ESS and the power loss.

optimization, the total power loss after optimization has been reduced by 27.2%. Meanwhile, the active power loss of ER decreased from 331.9 to 300.3 kWh. The operating efficiency of the network is improved.

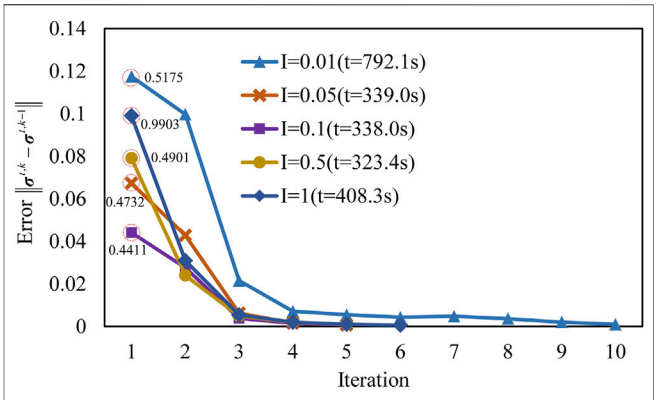


FIGURE 8 | Convergence error of initial values.

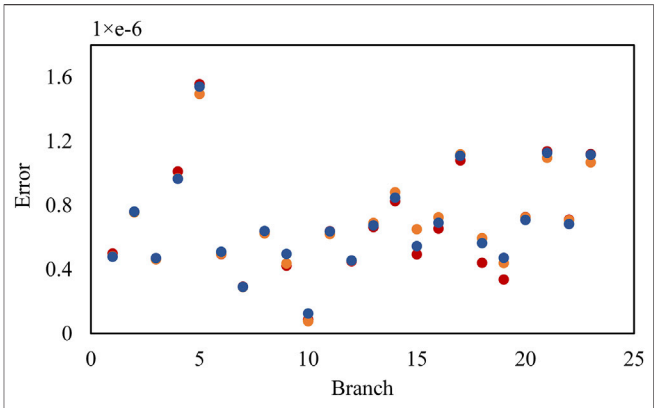


FIGURE 9 | Relaxation error of branch current in 380 V-AC network.

The node voltage is typically around 1p.u. To verify the convergence of the proposed successive convex approximation algorithm, various initial current values are analyzed here. As demonstrated in **Figure 8**, the convergence is obtained in all scenes. The solution time varies from 323.4 to 792.1 s, which is more than 5 h in the original NLP model. The number of iterations varies from 6 to 10. Furthermore, the relaxation error of branch current is 1e-6 order of magnitude, as depicted in **Figure 9**. These results reveal that the proposed approach in this work has good convergence and accuracy while improving the efficiency of the calculation.

CONCLUSION

The multi-period optimal operation model for ER-based AC/DC HDN is proposed in this work. The multiport coordinated control strategy of ER is considered in this paper. The introduction of a secondary droop control strategy improves the performance of the controller, which is conducive to enhance the utilization efficiency of DGs. On this basis, the operational efficiency of the network can be improved by coordinating and optimizing the active power output of DGs and ER. The second-order cone relaxation technique and

successive linear approximation approach are adopted to converter the original NLP problem into a convex programming model. The proposed successive convex approximation algorithm has good convergence and accuracy. Ensure that the optimal solution of ER-based AC/DC HDN is obtained within an acceptable time.

DATA AVAILABILITY STATEMENT

The original contributions presented in the study are included in the article/supplementary material, further inquiries can be directed to the corresponding authors.

AUTHOR CONTRIBUTIONS

TZ: conceptualization, writing-review and editing. YM: formal analysis, writing-review and editing. XW: data curation, and software. YD: data curation, and software. YS: writing-original draft, and review. KY: data curation, and review. HJ: methodology, software, and supervision.

FUNDING

The authors gratefully acknowledge the project supported by Science and Technology Project of State Grid Corporation (SGSDJY00GPJS1900058).

REFERENCES

Abdelaziz, M. M. A., Farag, H. E., El-Saadany, E. F., and Mohamed, Y. A.-R. I. (2013). A Novel and Generalized Three-Phase Power Flow Algorithm for Islanded Microgrids Using a newton Trust Region Method. *IEEE Trans. Power Syst.* 28, 190–201. doi:10.1109/tpwrs.2012.2195785

Allam, M. A., Hamad, A. A., Kazerani, M., and El-Saadany, E. F. (2018). A Novel Dynamic Power Routing Scheme to Maximize Loadability of Islanded Hybrid AC/DC Microgrids under Unbalanced AC Loading. *IEEE Trans. Smart Grid* 9, 5798–5809. doi:10.1109/tsg.2017.2697360

Chen, Y., Wang, P., Elasser, Y., and Chen, M. (2020). Multicell Reconfigurable Multi-Input Multi-Output Energy Router Architecture. *IEEE Trans. Power Electron.* 35, 13210–13224. doi:10.1109/tpel.2020.2996199

Deng, Y., Zhang, Y., Luo, F., and Mu, Y. (2021). Operational Planning of Centralized Charging Stations Utilizing Second-Life Battery Energy Storage Systems. *IEEE Trans. Sustain. Energ.* 12, 387–399. doi:10.1109/tste.2020.3001015

Dong, L., Zhang, T., Pu, T., Chen, N., and Sun, Y. (2019). A Decentralized Optimal Operation of AC/DC Hybrid Microgrids Equipped with Power Electronic Transformer. *IEEE Access* 7, 157946–157959. doi:10.1109/access.2019.2949378

Dong, L., Zhang, T., Pu, T. J., Chen, N. S., and Sun, Y. Y. (2018). "Optimal Scheduling of Asymmetrical AC/DC Micro-grid Based on PET," in International Conference on Power System Technology, Guangzhou, China, November 6-8, 2018, 1757–1763.

Gan, L., and Low, S. H. (2014). Optimal Power Flow in Direct Current Networks. *IEEE Trans. Power Syst.* 29, 2892–2904. doi:10.1109/tpwrs.2014.2313514

Guo, H., Wang, F., Zhang, L., and Luo, J. (2019). A Hierarchical Optimization Strategy of the Energy Router-Based Energy Internet. *IEEE Trans. Power Syst.* 34, 4177–4185. doi:10.1109/tpwrs.2019.2907323

Ji, H., Li, P., Wang, C., Song, G., Zhao, J., Su, H., et al. (2017). A Strengthened SOCP-Based Approach for Evaluating the Distributed Generation Hosting Capacity with Soft Open Points. *Energ. Proced.* 142, 1947–1952. doi:10.1016/j.egypro.2017.12.394

Khan, S., and Bhowmick, S. (2019). A Generalized Power-Flow Model of VSC-Based Hybrid AC-DC Systems Integrated with Offshore Wind Farms. *IEEE Trans. Sustain. Energ.* 10, 1775–1783. doi:10.1109/tste.2018.2870914

Li, K., Wen, W., Zhao, Z., Yuan, L., Cai, W., Mo, X., et al. (2021). Design and Implementation of Four-Port Megawatt-Level High-Frequency-Bus Based Power Electronic Transformer. *IEEE Trans. Power Electron.* 36, 6429–6442. doi:10.1109/tpel.2020.3036249

Li, P., Sheng, W., Duan, Q., Li, Z., Zhu, C., and Zhang, X. (2020). A Lyapunov Optimization-Based Energy Management Strategy for Energy Hub with Energy Router. *IEEE Trans. Smart Grid* 11, 4860–4870. doi:10.1109/tsg.2020.2968747

Liu, C., Li, X. J., Zhi, Y. M., and Cai, G. W. (2018). New Breed of Solid-State Transformer Mainly Combing Hybrid Cascaded Multilevel Converter with Resonant DC-DC Converters. *Appl. Energ.* 210, 724–736. doi:10.1016/j.apenergy.2017.08.052

Meng, F., Chowdhury, B., and Chamanamcha, M. (2018). Three-phase Optimal Power Flow for Market-Based Control and Optimization of Distributed Generations. *IEEE Trans. Smart Grid* 9, 3691–3700. doi:10.1109/tsg.2016.2638963

Miao, J. Q., Zhang, N., and Kang, C. Q. (2016). "Generalized Steady-State Model for Energy Router with Applications in Power Flow Calculation," in IEEE Power and Energy Society General Meeting, Boston, MA, USA, July 17-21, 2016, 1–5.

Miao, J., Zhang, N., Kang, C., Wang, J., Wang, Y., and Xia, Q. (2018). Steady-State Power Flow Model of Energy Router Embedded AC Network and its Application in Optimizing Power System Operation. *IEEE Trans. Smart Grid* 9, 4828–4837. doi:10.1109/tsg.2017.2672821

Rouzbehi, K., Miranian, A., Candela, J. I., Luna, A., and Rodriguez, P. (2015). A Generalized Voltage Droop Strategy for Control of Multiterminal DC Grids. *IEEE Trans. Ind. Applicat.* 51, 607–618. doi:10.1109/tia.2014.2332814

Soofi, A. F., Manshadi, S. D., Liu, G., and Dai, R. (2021). A SOCP Relaxation for Cycle Constraints in the Optimal Power Flow Problem. *IEEE Trans. Smart Grid* 12, 1663–1673. doi:10.1109/tsg.2020.3023890

Sun, Y., Hu, L., Malik, S. M., Chen, N., and Pu, T. (2019). Unified Method for Optimal Power Flow of AC/DC System with PET Based on Extended branch Model. *J. Eng.* 2019, 1942–1946. doi:10.1049/joe.2018.8707

Tang, K., Dong, S., Ma, X., Lv, L., and Song, Y. (2021). Chance-constrained Optimal Power Flow of Integrated Transmission and Distribution Networks with Limited Information Interaction. *IEEE Trans. Smart Grid* 12, 821–833. doi:10.1109/tsg.2020.3021829

Yu, M., Huang, W., Tai, N., Zheng, X., Wu, P., and Chen, W. (2018). Transient Stability Mechanism of Grid-Connected Inverter-Interfaced Distributed Generators Using Droop Control Strategy. *Appl. Energ.* 210, 737–747. doi:10.1016/j.apenergy.2017.08.104

Zhang, H., Moura, S. J., Hu, Z., Qi, W., and Song, Y. (2018). A Second-Order Cone Programming Model for Planning PEV Fast-Charging Stations. *IEEE Trans. Power Syst.* 33, 2763–2777. doi:10.1109/tpwrs.2017.2754940

Zhang, S., Pei, W., Xiao, H., Yang, Y., Ye, H., and Kong, L. (2020). Enhancing the Survival Time of Multiple Islanding Microgrids through Composable Modular Energy Router after Natural Disasters. *Appl. Energ.* 270, 115138. doi:10.1016/j.apenergy.2020.115138

Zhang, Y., Meng, X., Shotorbani, A. M., and Wang, L. (2021). Minimization of AC-DC Grid Transmission Loss and DC Voltage Deviation Using Adaptive Droop Control and Improved AC-DC Power Flow Algorithm. *IEEE Trans. Power Syst.* 36, 744–756. doi:10.1109/tpwrs.2020.3020039

Zhu, J. Z. (2002). Optimal Reconfiguration of Electrical Distribution Network Using the Refined Genetic Algorithm. *Electric Power Syst. Res.* 62, 37–42. doi:10.1016/s0378-7796(02)00041-x

Conflict of Interest: Authors YS and KY were employed by the company State Grid Economic and Technological Research Institute Co., Ltd.

The remaining authors declare that the research was conducted in the absence of any commercial or financial relationships that could be construed as a potential conflict of interest.

Publisher's Note: All claims expressed in this article are solely those of the authors and do not necessarily represent those of their affiliated organizations, or those of the publisher, the editors and the reviewers. Any product that may be evaluated in this article, or claim that may be made by its manufacturer, is not guaranteed or endorsed by the publisher.

Copyright © 2021 Zhang, Mu, Wang, Deng, Song, Yuan and Jia. This is an open-access article distributed under the terms of the Creative Commons Attribution License (CC BY). The use, distribution or reproduction in other forums is permitted, provided the original author(s) and the copyright owner(s) are credited and that the original publication in this journal is cited, in accordance with accepted academic practice. No use, distribution or reproduction is permitted which does not comply with these terms.

NOMENCLATURE

Sets

$\mathbf{\Psi_{AC}}$ Set of the branches in AC network

$\mathbf{\Psi_{DC}}$ Set of the branches in DC network

ϕ Three-phase system $\phi \in \{a, b, c\}$

Variables

$P^{\phi,t}_{\mathbf{PET.ac},\,i}$ Active power injected into the AC port of ER

$Q^{\phi,t}_{\mathbf{PET.ac},\,i}$ Reactive power injected into the AC port of ER

$P^{\phi,t}_{\mathbf{PET.dc},\,j}$ Active power injected into the DC port of ER

$P^{\phi,t}_{ij.\mathbf{AC}}$ Active power flow of branch in AC network

$Q^{\phi,t}_{ij.\mathbf{AC}}$ Reactive power flow of branch in AC network

$P^{\phi,t}_{g.\mathbf{AC}}$ Active power output of DG in AC network

$Q^{\phi,t}_{g.\mathbf{AC}}$ Reactive power output of DG in AC network

$\widehat{V}^{\phi,t}_{i.\mathbf{AC}}$ The square of the voltage in AC network

$\widehat{I}^{\phi,t}_{ij.\mathbf{AC}}$ The square of the current in AC network

$P^{t}_{ij.\mathbf{DC}}$ Active power flow of branch in DC network

$P^{t}_{g.\mathbf{DC}}$ Active power output of DG in DC network

$\widehat{V}^{t}_{i.\mathbf{DC}}$ The square of the voltage in DC network

$\widehat{I}^{t}_{ij.\mathbf{DC}}$ The square of the current in DC network

ω^t The frequency in low voltage AC network

δV Voltage bias of the secondary control

$\delta\omega$ Frequency bias of the secondary control

Parameters

a, b, c The fitting coefficient of ER loss model

$\boldsymbol{\varsigma}, \xi, \zeta$ The droop coefficient of the controller

$r^{\phi}_{ij.\mathbf{AC}}$ Resistance of branch in AC network

$x^{\phi}_{ij.\mathbf{AC}}$ Reactance of branch in AC network

$r_{ij.\mathbf{DC}}$ Resistance of branch in DC network

frontiers in Energy Research

ORIGINAL RESEARCH
published: 26 July 2021
doi: 10.3389/fenrg.2021.713501

Photovoltaic Power Station Electromagnetic Environment Complexity Evaluation Utilizing Logarithmic Morphological Gradient Spectrum

Hua-chen Xi[1,2], Bing Li[2], Wen-hui Mai[2], Xiong Xu[1] and Ya Wang[1]*

[1]State Key Laboratory of Complex Electromagnetic Environment Effects on Electronics and Information System (CEMEE), Luoyang, China, [2]College of Engineering, Shantou University, Shantou, China

In this paper, a feature extraction method for evaluating the complexity of the Electromagnetic Environment (EME) of the photovoltaic power station is presented by using logarithmic morphological gradient spectrum (LMGS) based on the mathematical morphological theory. We use LMGS to evaluate electromagnetic environment signals. We also explored the impact of structure element (SE) on the MS, MGS, and LMGS. Three types of SE, mean the line SE, square SE and diamond SE, are utilized and compared for computing the LMGS. EME signals with four complexity degrees are simulated to evaluate the effectiveness of the presented method. The experimental results have shown that the feature extraction scheme proposed in this paper is a reasonable method to classify the complexity of EME.

Keywords: electromagnetic environment, photovoltaic power station, mathematical morphological spectrum, evaluation, feature extraction

OPEN ACCESS

Edited by:
Yaxing Ren,
University of Warwick,
United Kingdom

Reviewed by:
Qintao Gan,
Army Engineering University of PLA, China
Z. Jn,
National University of Defense Technology, China

****Correspondence:***
Bing Li
rommandy@163.com

Specialty section:
This article was submitted to Smart Grids, a section of the journal Frontiers in Energy Research

Received: *23 May 2021*
Accepted: *23 June 2021*
Published: *26 July 2021*

Citation:
Xi H, Li B, Mai W, Xu X and Wang Y (2021) Photovoltaic Power Station Electromagnetic Environment Complexity Evaluation Utilizing Logarithmic Morphological Gradient Spectrum. Front. Energy Res. 9:713501. doi: 10.3389/fenrg.2021.713501

INTRODUCTION

With the rapid development of photovoltaic power generation technology and power electronics technology in the 21st century, photovoltaic power generation technology is becoming more and more mature. Human beings have built many large photovoltaic power stations on a large scale and use pollution-free green electric energy. On the other hand, the power of photovoltaic power stations is constantly expanding. Various electronic devices in photovoltaic power stations will produce electromagnetic radiation and form a complex and changeable electromagnetic environment. This will have an important impact on the efficiency of electronic equipment. Therefore, it is of great significance to study the complexity of the electromagnetic environment in photovoltaic power stations (Christoforidis et al., 2013; Wang et al., 2013; Salinas, 2018).

There are few related studies on the electromagnetic environment analysis of photovoltaic power stations, but there are many pieces of research on battlefield electromagnetic environment analysis, which can be used for reference to the electromagnetic environment analysis of photovoltaic power stations.

Tetley et al. proposed the analysis and prediction method of electromagnetic environment based on the mathematical model for the first time and gave the basic model of the electromagnetic environment from the point of view of mathematical analysis (Tetley, 1961). To classify the electromagnetic environment in different complexity degrees, feature extraction of

electromagnetic environment signal is a key step. In the past research, diverse features, such as spatial coverage, spectrum occupancy, time occupancy, energy domain average power density spectrum, and so on, have been developed and widely used to evaluate the electromagnetic environment in different complexity degrees (Chen et al., 2010; Zou et al., 2018; Liu et al., 2019; Fu, 2020). Dong and Li (2008) proposed a complexity assessment method of electromagnetic environment based on the Analytic Hierarchy Process (AHP), which refined the evaluation index, defined the evaluation standard parameters, and determined the scaling criterion. Wang and He (2008).introduced multivariate connection number to construct a comprehensive evaluation method of electromagnetic environment complexity, and the weight was set according to the principle of equal distribution. Li et al. (2017).provided a method to evaluate the complexity of electromagnetic environment based on generalized S-transform and probabilistic neural network (PNN), which used generalized S-transform to analyze the interfered sample signals in the electromagnetic environment, extracted signal parameters to train PNN, and classified them. (Li et al., 2013).proposed a new fractal dimension evaluation method based on morphological coverage to evaluate the complexity of the electromagnetic environment. (Li et al., 2019).proposed a method based on S-transform to simultaneously calculated timeshare, frequency share and energy share in the time-frequency domain and used the extreme learning machine to evaluate the environmental complexity. (Yin et al., 2019).proposed an electromagnetic environment assessment algorithm based on Fast S-transform and time-frequency space model. The time complex number, frequency complex number, and energy complex number were calculated at the same time, and F norm and root mean square were selected as evaluation indexes.

As a multi-scale analysis method based on mathematical morphology, mathematical morphological spectrum has been widely used in the field of image processing and feature extraction of mechanical vibration signals (Gao et al., 2015). The main idea is to filter the research object with structural elements of different scales and shapes to express the internal information of the research object.

Mathematical morphological spectrum is a very effective method to deal with image granularity and shape features proposed by Matheron (Matheron, 1975). Its vitality is strong, and it is widely used in image shape and texture feature description, image segmentation, image restoration, image denoising, and other fields. The main idea is to use sieves of different sizes and shapes to filter the image to understand its morphological characteristics. However, the traditional mathematical morphological spectrum is defined based on morphological open operation and difference operator, which is very effective in the analysis of binary images. In the past research, mathematical morphological spectrum has been applied to mechanical fault diagnosis, electronic device fault diagnosis and other fields (Song et al., 2018; Gao, 2019). (Zhao et al., 2018) proposed a method for Fault damage degree Identification based on high-order differential morphology gradient spectral entropy. (Zhao et al., 2020).proposed a performance degradation prediction (HMEPEM) method based on high-order differential mathematical morphology gradient spectral entropy, phase space reconstruction, and limit learning machine, and applied it to predict the performance degradation trend of rolling bearings. (Lv et al., 2014).applied the theory of multi-scale mathematical morphological spectrum and morphological spectral entropy to the vibration fault diagnosis of water pump, which could achieve the purpose of fault diagnosis.

However, previous studies have found that the traditional mathematical morphological spectrum is not very effective in analyzing complex electromagnetic environment signals.

Therefore, the purpose of this paper is to study the application of the mathematical morphological spectrum method in the extraction of characteristic parameters of complex electromagnetic environment signals and to improve the original calculation method of the mathematical morphological spectrum. In this work, we discussed the influence of different types of structural elements and methods on the representation ability of mathematical morphological spectrum, verified the method with a variety of standard signals and electromagnetic environment signals, and compared various morphological spectrums.

The paper is organized as follows. In *Logarithmic Morphological Gradient Spectrum*, we introduce the mathematical morphological spectrum feature extraction method and support vector machine classification method used in this paper. In *Experimental Results*, the electromagnetic environment information is simulated, and the signal is tested by the method in *Logarithmic Morphological Gradient Spectrum*. The experiments are described and commented on in *Conclusion*.

LOGARITHMIC MORPHOLOGICAL GRADIENT SPECTRUM

Mathematical Morphological Spectrum

The main idea of the mathematical morphological spectrum is to use structural elements of different scales and shapes to filter the research object, to represent the internal information of the research object. Mathematically, the mathematical morphological particle analysis is defined in the form of set $Y = \{\Psi_\lambda\}_{\lambda \geq 0}$, that is, a series of transformational Ψ_λ sets. $\Psi_\lambda$is defined as:

$$\Psi_\lambda(X) = X \circ \lambda g$$

Where "$\circ$" is the morphological operation symbol, λ is a scale parameter whose value is not less than 0, and g is a unit structural element, λg represents the structural element under a certain scale λ, and its expression is as follows:

$$\lambda g = \underbrace{g \oplus g \cdots \oplus g}_{\lambda}$$

In the formula, "$\oplus$" is the symbol of morphological dilation operation.

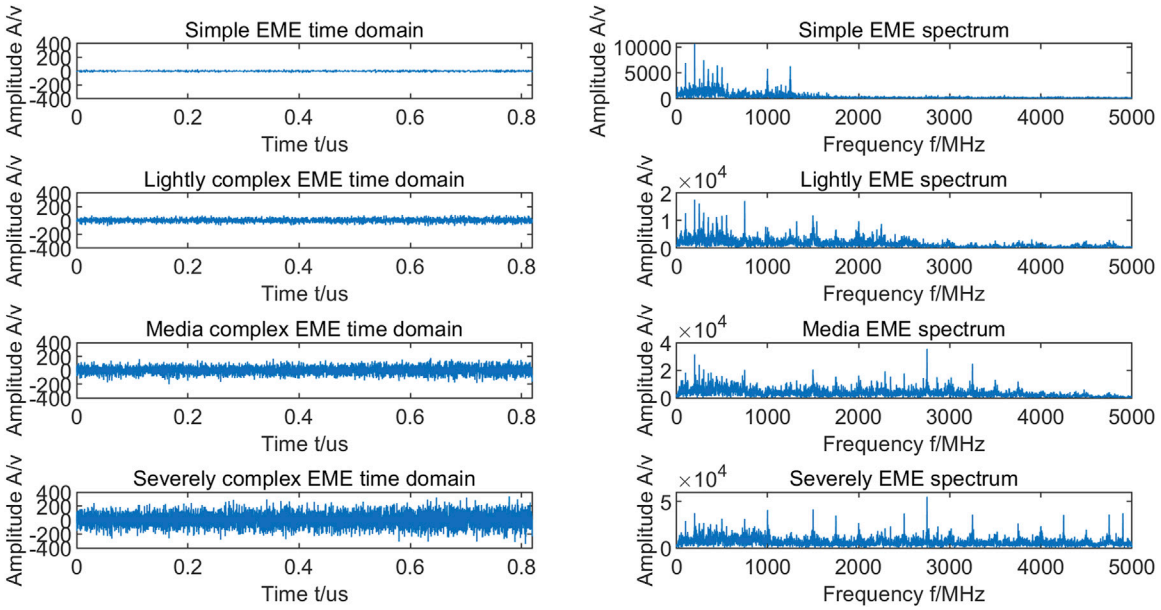


FIGURE 1 | Simulation for EME signal.

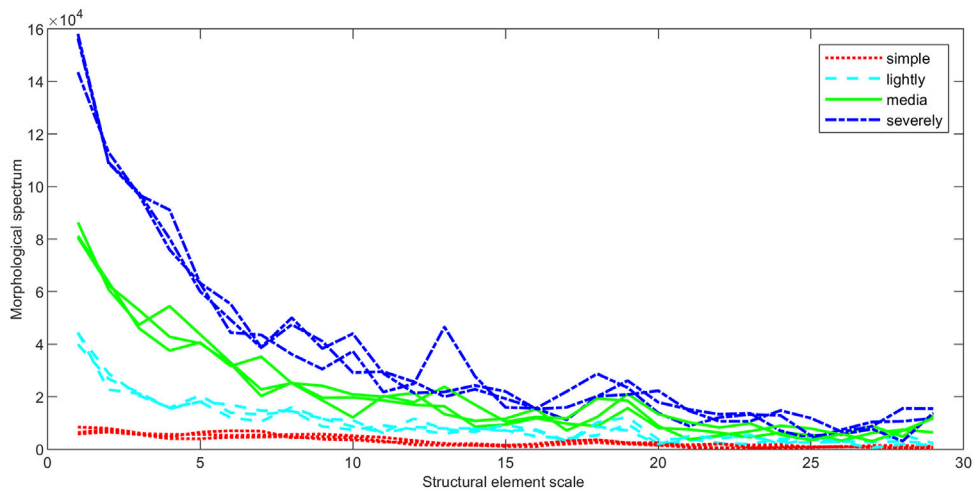


FIGURE 2 | MS analysis result of line SE.

Set a continuous-time domain function *f(n)*, structure-function *g(m)*, then the mathematical morphological spectrum expression of the function *f(n)* is as follows:

$$MS(f,\lambda,g)=\begin{cases}-\dfrac{dS(f\circ\lambda g)}{d\lambda} & \lambda\geq 0\\ -\dfrac{dS(f\cdot(-\lambda)g)}{d\lambda} & \lambda<0\end{cases}$$

In the formula, λ represents the scale of the structural element, $S=\int f(x)dx$ represents the measure of f(x) in the definition domain, and the umbra area of the gray value signal is taken. The scale of structural elements can be taken as a continuous integer value when analyzing the morphological particle distribution of the one-dimensional discrete signal. The morphological spectrum expression in the combination formula below simplifies the morphological spectrum of the open operation and closed operation of the one-dimensional discrete signal respectively:

$$MS_{+}(\lambda,g)=S[f\circ\lambda g-f\circ(\lambda+1)g],\quad 0\leq\lambda\leq\lambda_{max}$$
$$MS_{-}(\lambda,g)=S[f\cdot(-\lambda)g-f\cdot(-\lambda+1)g],\quad \lambda_{min}\leq\lambda<0$$

In the form, $S=\int f(x)dx$. The mathematical morphological spectrum reflects the distribution of signal morphological

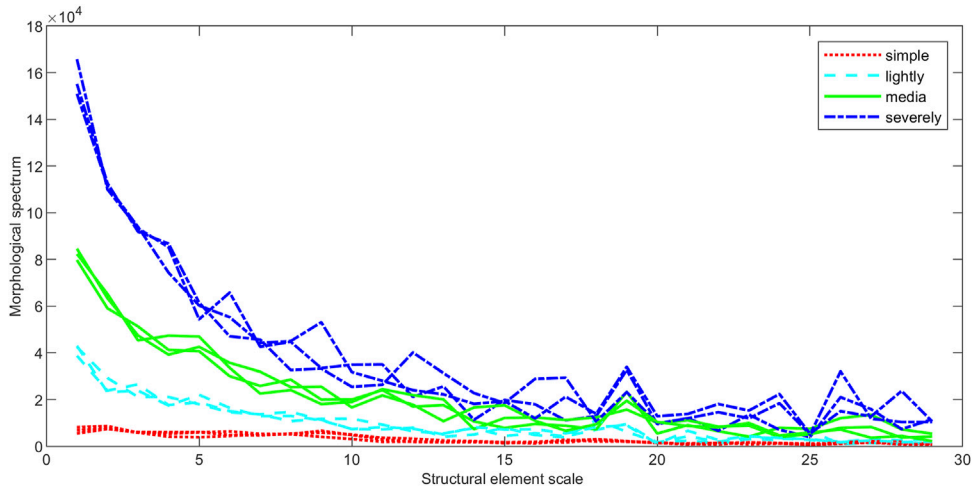


FIGURE 3 | MS analysis result of square SE.

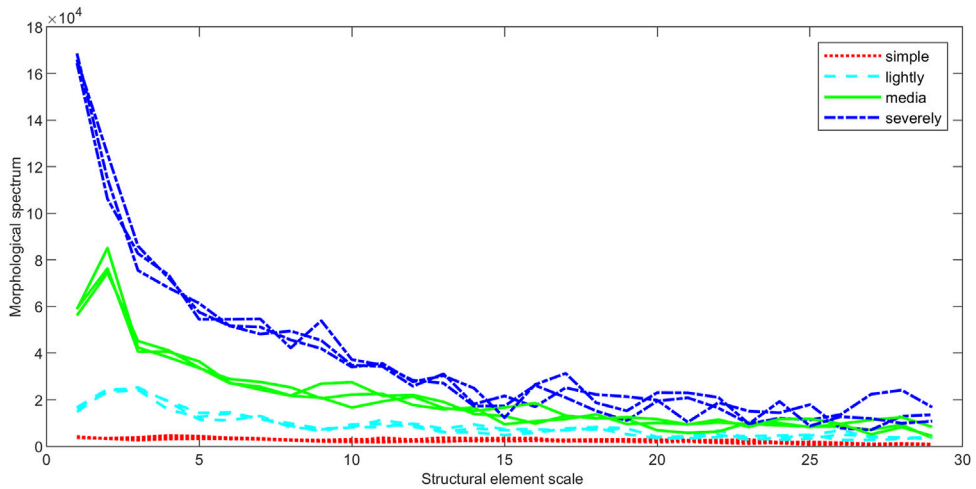


FIGURE 4 | MS analysis result of diamond SE.

characteristics at different structural element scales. For the structural element λg under a certain scale, the more morphological structural components corresponding to the signal, the larger the spectral line value in the signal mathematical morphological spectrum, on the contrary, the less the structural component, the smaller the corresponding spectral line value (Zhang et al., 2013).

The mathematical morphological spectrum can be simplified to the open operation morphological spectrum at scale $\lambda \geq 0$ and the closed operation morphological spectrum at scale $\lambda < 0$. The open operation morphological spectrum reflects the structural characteristic information of the signal itself, while the closed operation morphological spectrum reflects the corresponding background information (Li et al., 2015).

Mathematical Morphological Gradient Spectrum

The difference of the function f(n) after the expansion and erosion of the structural element g(m) forms the concept of the function morphological gradient. When processing the signal, the morphological gradient not only considers both the positive and negative pulse information of the signal but also can efficaciously extract the morphological features of the signal (Liu et al., 2016). The morphological gradient operator expression is as follows:

$$Gard(f) = f \oplus g(m) - f \Theta g(m)$$

Introducing the concept of morphological gradient into the mathematical morphological spectrum in formula above, the

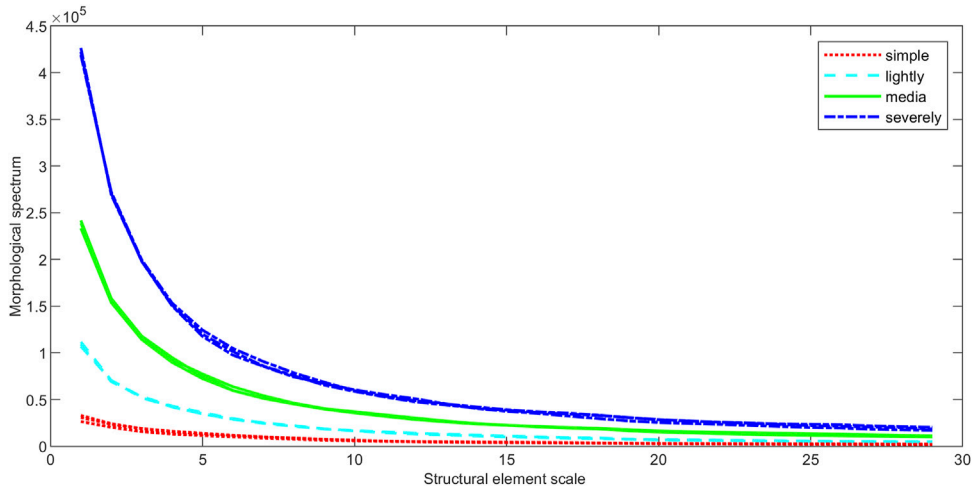


FIGURE 5 | MGS analysis result of line SE.

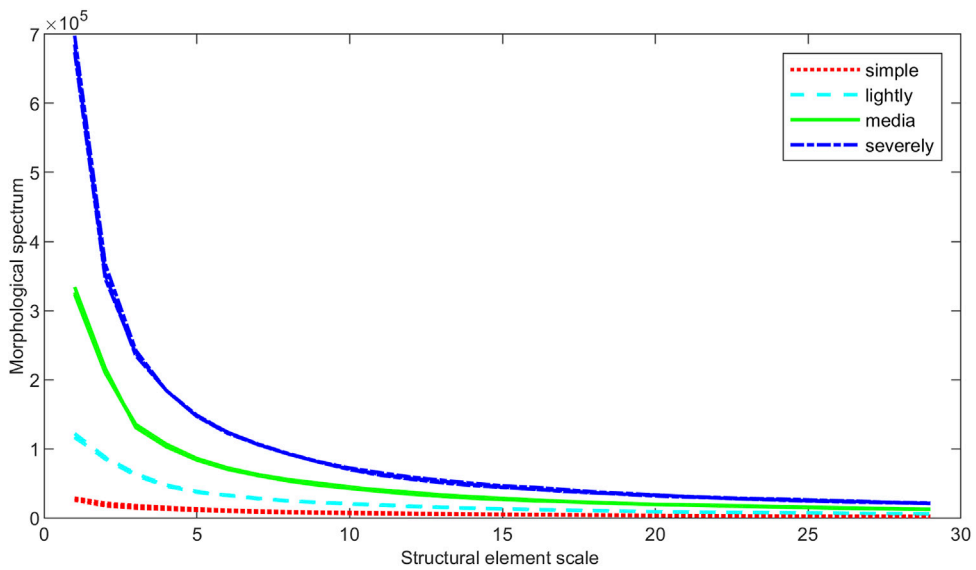


FIGURE 6 | MGS analysis result of square SE.

concept of mathematical gradient spectrum (MGS) is obtained (Zhang et al., 2013):

$$MGS(f,\lambda,g) = \begin{cases} -\dfrac{dS(f\oplus\lambda g - f\Theta\lambda g)}{d\lambda} & \lambda \geq 0 \\ -\dfrac{dS(f\Theta(-\lambda)g - f\oplus(-\lambda)g)}{d\lambda} & \lambda < 0 \end{cases}$$

For the one-dimensional discrete signal, considering the extension of the morphological gradient operator, the morphological gradient spectrum can be simplified as follows:

$$MGS_{+}(f,\lambda,g) = S[f\oplus(\lambda+1)g - f\Theta(\lambda+1)g - (f\oplus\lambda g - f\Theta\lambda g)]$$

$$MGS_{-}(f,\lambda,g) = S[f\Theta(-\lambda+1)g - f\oplus(-\lambda+1)g - (f\Theta(-\lambda)g - f\oplus(-\lambda)g)]$$

In the formula, the dilate and erode morphology gradient spectrum of $S(f) = \sum f(n)$, $MGS_{+}(f,\lambda,g)$, and $MGS_{-}(f,\lambda,g)$ respectively reflect the shape change law of the signal under different structural element scales in the positive and negative intervals. It can be seen from the duality of dilate and erode operations that these two kinds of morphological gradient spectrum are essentially the same structure when describing the morphological complexity of objects.

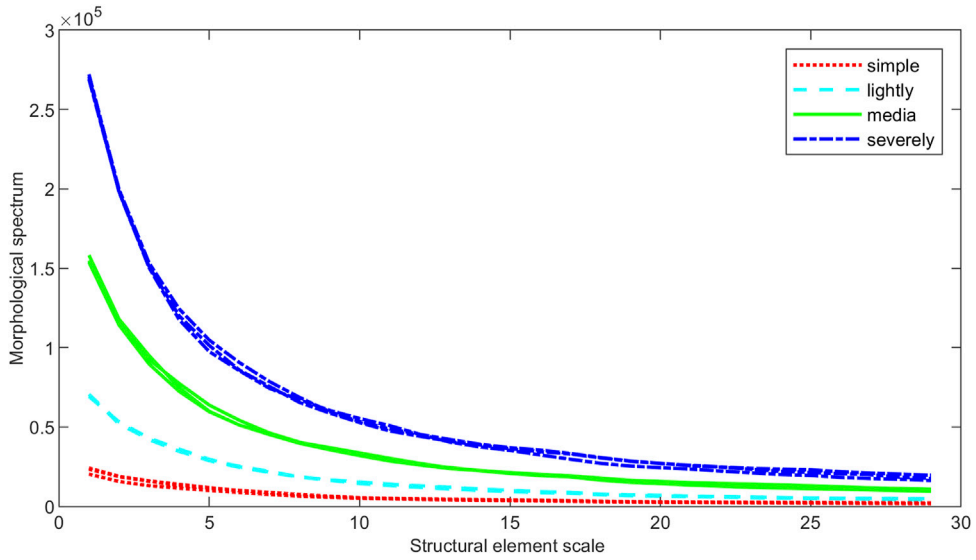


FIGURE 7 | MGS analysis result of diamond SE.

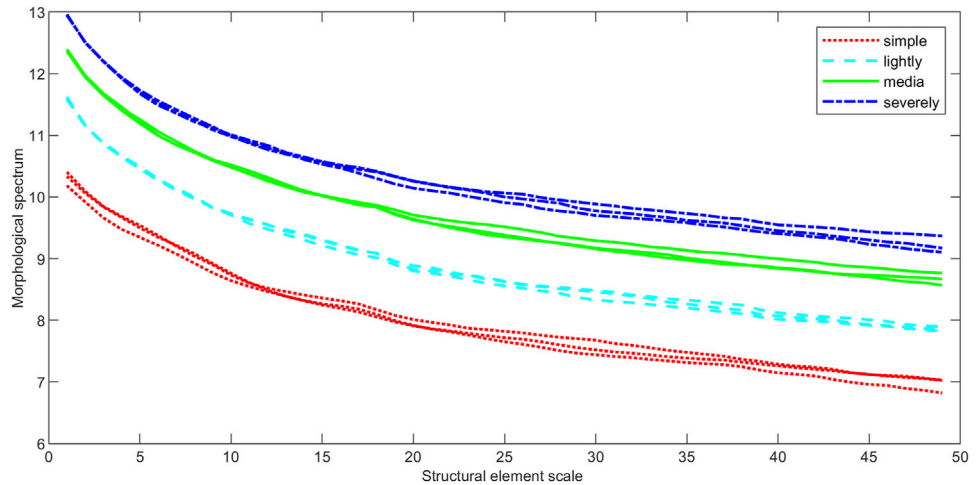


FIGURE 8 | LMGS analysis result of line SE.

Logarithmic Morphological Gradient Spectrum

Although both mathematical morphology spectrum and mathematical morphology gradient spectrum describe the change law of signal shape at different scales, it is found that the discrimination between EME signal spectral lines with different complexity is very poor by extracting the mathematical morphology spectrum characteristics of EME signal at different scales. The morphological gradient spectral curves calculated at different scales can distinguish EME signals with different complexity, but the distinguishing effect is poor. In this section, the morphological gradient spectrum is logarithmically processed, and the feature extraction method based on the logarithmic mathematical morphological gradient spectrum is adopted. Combined with the properties of logarithmic function and expansion corrosion morphology gradient spectrum, the expansion corrosion morphology gradient spectrum is processed logarithmically. The expression of the logarithmic morphological gradient spectrum on the positive interval is obtained.

$$LMGS_{+} = \log\left(MGS_{+}\left(f,\lambda,g\right)+1\right),\lambda \geq 0$$

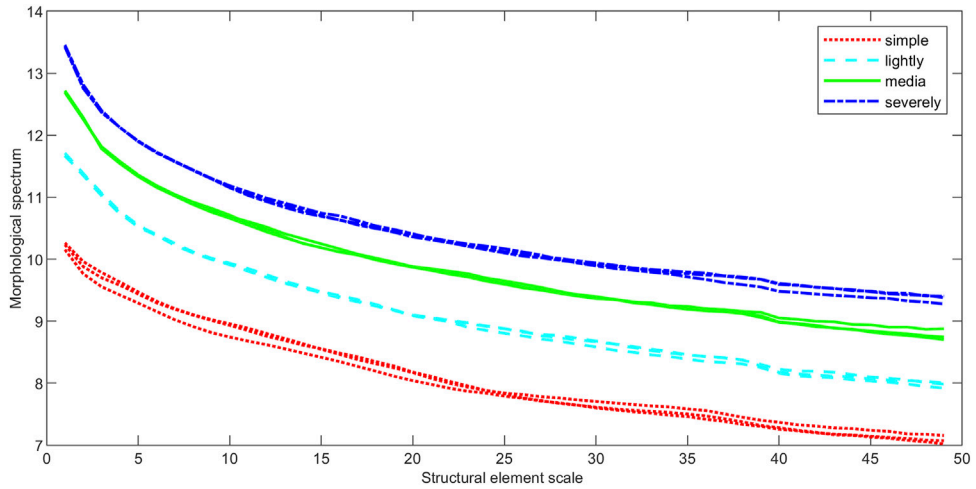


FIGURE 9 | LMGS analysis result of square SE.

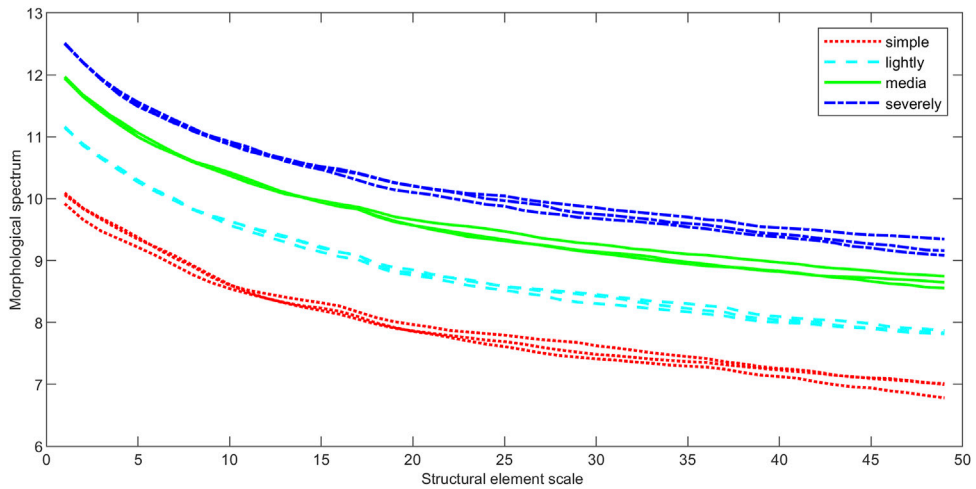


FIGURE 10 | LMGS analysis result of diamond SE.

TABLE 1 | Classification accuracy.

Accuracy	Line (%)	Square (%)	Diamond (%)
MS	84.5	83.6	85.2
MGS	90.3	89.8	92.1
LMGS	96.7	95.2	97.1

EXPERIMENTAL RESULTS

EME Simulation

Photovoltaic Power Station mainly consists of control devices and solar panel area (Wang et al., 2013). The control devices include the inverter cabinet, DC voltage regulator cabinet, DC control cabinet, AC control cabinet and so on. And there are lots of thin-film solar panels of different power in the solar panel area. These devices will produce a variety of electromagnetic signals with different frequencies and amplitudes when they are working, and these devices may not work at the same time, so the occurrence time of electromagnetic signals is not consistent. These various electromagnetic signals constitute the complex electromagnetic environment of photovoltaic power stations together.

Base on this, we simulate a variety of electromagnetic environment signals with different frequencies and apply these signals to construct the electromagnetic environment under the condition of random time and amplitude of the signals. According to the number of signals used, we construct four kinds of electromagnetic environment signals with simple, slight, moderate and severe complexity.

The generated electromagnetic environment signal is shown in **Figure 1**. The time-domain waveform and spectrum of simple, slightly

complex, moderately complex, and severely complex electromagnetic environment signals are arranged from top to bottom.

Feature Extraction

Mathematical Morphological Spectrum

Similar to the filter window in digital signal processing, the scale and shape of SE have an important influence on the calculation results. In this experiment, the line, square and diamond structure elements are used to verify the influence of different shape structure elements on the mathematical shape spectrum.

The mathematical morphological spectrum curves of different electromagnetic environment signals are calculated. The results are shown in **Figures 2–4**.

As the results show, the MS curve fluctuates up and down, and when the scale of the structural elements tends to 20, the curves are interlaced with each other. The morphological spectrum values calculated by the MS method cannot well distinguish the four kinds of EME signals when they are used as features.

Mathematical Morphological Gradient Spectrum

The mathematical morphological gradient spectrum curves of different electromagnetic environment signals are calculated. The structural elements are selected as line, square and diamond. The results are shown in **Figures 5–7**.

As the results show, the trend of the four MGS curves is the same, they all decrease monotonously, and the differentiation is certain when the scale is small, but with the increase of the scale, the differentiation of the four curves decreases.

Logarithmic Mathematical Morphological Gradient Spectrum Feature Extraction

The mathematical morphological gradient spectrum curves of different electromagnetic environment signals are calculated. The structural elements are selected as line, square and diamond. The results are shown in **Figures 8–10**.

The LMGS curves of four kinds of complexity EME signals are distinct and have the same trend, and their spectral values all decrease monotonously with the increase of the scale, they are well differentiated.

SVM Classification

The data samples used are all from the feature matrix extracted by mathematical morphological spectrum, mathematical morphological gradient spectrum, and logarithmic mathematical morphological gradient spectrum. After training the SVM through the training data, the test data is classified to obtain classification accuracy. The process is repeated 50 times, and the average classification accuracy of different types of support vector machines is shown in **Table 1**.

Through support vector machine classification, the classification effect obtained by LMGS is the best, and the classification effect obtained by MS and MGS is worse than LMGS. For line, square, and diamond structure elements, the results have shown that the diamond SE acquires the best performance on distinguishing the four EME complexity degrees.

CONCLUSION

This work has proposed an effective feature extraction method by using the logarithmic morphological gradient spectrum for evaluating the EME complexity degree of the photovoltaic power station. The EME signals with four complexity degrees are simulated to verify the effectiveness of the presented method. We use MS, MGS, and LMGS to evaluate electromagnetic environment signals. The experimental results have shown that LMGS can effectively distinguish the complexity of EME and show better performance than MS and MGS.

We also explored the effects of the structure elements, mean line, square, and diamond on t distinguishing the EME complexity degrees. Results have shown that the diamond SE acquires the best performance in distinguishing the four EME complexity degrees. Our research has shown that the feature extraction method of logarithmic morphological gradient spectrum is an ideal technique to evaluate the complexity of electromagnetic radiation of photovoltaic power stations.

DATA AVAILABILITY STATEMENT

The original contributions presented in the study are included in the article/supplementary material, further inquiries can be directed to the corresponding author.

AUTHOR CONTRIBUTIONS

HX contributed to conceptualization, data curation, methodology, and writing—original draft. BL contributed to formal analysis, visualization, and resources. WM, XX, and YW wrote sections of the manuscript. All authors contributed to manuscript revision, read, and approved the submitted version.

FUNDING

This research was funded by the Open Foundation of the State Key Laboratory of Complex Electromagnetic Environment Effects on Electronics and Information System (CEMEE 2020Z0101B) and the Start-up research projects of Shantou University (NTF19016).

REFERENCES

Chen, Y., Zhang, D., Qian, P., Wang, X., and Xiao, D. (2010). Review on Battlefield Electromagnetic Environment Quantitative Analysis. *Electron. Inf. Warfare Tech.* 25, 44–51.

Christoforidis, G. C., Papadopoulos, T. A., Parisses, C., and Mantzaras, G. E. (2013). Photovoltaic Power Plants as a Source of Electromagnetic Interference to Metallic Agricultural Pipelines. *Proced. Tech.* 8, 192–199. doi:10.1016/j.protcy.2013.11.027

Dong, Y., and Li, Q. (2008). Complexity Evaluation of Artificial Electromagnetism Environment Based on AHP. *Command Control & Simulation* 30, 106–110.

Fu, S. (2020). A Multi-Level Evaluation Method of Complex Electromagnetic Environment Based on Four-Domain Feature. *Telecommunication Eng.* 60, 1048–1054.

Gao, B. (2019). Feature Extraction of Performance Degradation of Mechanical Parts Based on Mathematical Morphological Spectral Entropy. *Mech. Electr. Inf.* 27, 115–116. doi:10.19514/j.cnki.cn32-1628/tm.2019.27.063

Gao, B., Liu, J., and Li, G. (2015). Fault Feature Extraction for Gearbox Bearing Using Improved Pattern Spectrum. *J. Vibration Eng.* 28, 831–838. doi:10.16385/j.cnki.issn.1004-4523.2015.05.019

Li, B., Jun, D., Cong, L., and Yuan, L. (2013). Evaluating the Complexity Degree of Electromagnetic Environment Utilizing Morphological Covering Based Fractal Dimension. IEEE 11th International Conference on Electronic Measurement & Instruments, 617–620. doi:10.1109/ICEMI.2013.6743181

Li, R., Wang, K., and Wang, B. (2015). The Method of Grey Markov Remaining Service Life Prediction Specific to Generalized Mathematical Morphological Particle. *J. Vibration Eng.* 28, 316–323. doi:10.16385/j.cnki.issn.1004-4523.2015.02.019

Li, Y., He, G., and Yin, Q. (2017). Electromagnetic Environment Complex Evaluation Based on S-Transform and PNN. *J. Hunan University(Natural Sciences)* 44, 123–129. doi:10.16339/j.cnki.hdxbzkb.2017.10.017

Li, Y., He, Y., and Yin, B. (2019). Evaluation Method for Complex Electromagnetic Environment. *Jaciii* 23, 891–897. doi:10.20965/jaciii.2019.p0891

Liu, H., Guo, J., and Liu, J. (2019). An Evaluation Method of Electromagnetic Environment Complexity Based on Two-Dimensional Entropy of Image. *Electron. Inf. Warfare Tech.* 34, 70–74+88.

Liu, P., Li, R., and Xu, H. (2016). A Performance Degradation Feature Extraction Method and its Application Based on Mathematical Morphological Gradient Spectrum Entropy. *J. Vibration Shock* 35, 86–90. doi:10.13465/j.cnki.jvs.2016.16.015

Lv, S., Lin, T., Liang, X., and Liu, X. (2014). Diagnostic Research on Vibration the Faults of Pumps Based on Mathematical Morphology. *China Rural Water and Hydropower* 2, 110–113.

Matheron, G. (1975). *Random Sets and Integral Geometry*. New York: Wiley.

Salinas, E. (2018). Some Aspects of Electromagnetic Interference, Electromagnetic Compatibility and Geomagnetic Induced Currents. *J. Phys. Conf. Ser.* 1143, 012030. doi:10.1088/1742-6596/1143/1/012030

Song, G., Zhang, W., Chen, H., Lin, T., and Zhou, B. (2018). Open-circuit Fault Diagnosis of Inverter Transistor Based on Mathematical Pattern Spectrum. *J. Power Supply* 16, 159–166. doi:10.13234/j.issn.2095-2805.2018.5.159

Tetley, W. (1961). Analytical Prediction of Electromagnetic Environments. *IEEE Trans. Commun.* 9, 175–185. doi:10.1109/TCOM.1961.1097669

Wang, F., Zhao, Z. B., and Zhang, H. (2013). Test Analysis on the Electromagnetic Environment of Photovoltaic Power Transmission System. *Amr* 805-806, 40–44. doi:10.4028/www.scientific.net/AMR.805-806.40

Wang, G., and He, J. (2008). Complexity Evaluation Method of Battlefield Electromagnetic Environment Based on Multivariate Connection Number Model. *Electron. Inf. Warfare Tech.* 23, 50–53.

Yin, B. Q., Wang, S. D., He, Y. G., Zuo, L., Li, B., and Cheng, Z. (2019). Electromagnetic Environment Complex Evaluation Algorithm Based on Fast S-Transform and Time-Frequency Space Model. *J. Electro. Inf. Tech.* 41, 195–201. doi:10.11999/JEIT180256

Zhang, K., Cheng, S., and Yang, Y. (2013). Rotating Machinery Fault Diagnosis Based on Local Mean Decomposition and Pattern Spectrum. *J. Vibration Shock* 32, 135–140. doi:10.13465/j.cnki.jvs.2013.09.016

Zhao, H., Liu, H., Xu, J., and Deng, W. (2020). Performance Prediction Using High-Order Differential Mathematical Morphology Gradient Spectrum Entropy and Extreme Learning Machine. *IEEE Trans. Instrum. Meas.* 69, 4165–4172. doi:10.1109/TIM.2019.2948414

Zhao, H., Yao, R., Xu, L., Yuan, Y., Li, G., and Deng, W. (2018). Study on a Novel Fault Damage Degree Identification Method Using High-Order Differential Mathematical Morphology Gradient Spectrum Entropy. *Entropy* 20, 682. doi:10.3390/e20090682

Zou, Z., Li, Y., and Li, L. (2018). Comprehensive Research on the Quantitative Methods of Electromagnetic Environment Complexity. *Electron. Inf. Warfare Tech.* 33, 63–66+75.

Conflict of Interest: The authors declare that the research was conducted in the absence of any commercial or financial relationships that could be construed as a potential conflict of interest.

Publisher's Note: All claims expressed in this article are solely those of the authors and do not necessarily represent those of their affiliated organizations, or those of the publisher, the editors and the reviewers. Any product that may be evaluated in this article, or claim that may be made by its manufacturer, is not guaranteed or endorsed by the publisher.

Copyright © 2021 Xi, Li, Mai, Xu and Wang. This is an open-access article distributed under the terms of the Creative Commons Attribution License (CC BY). The use, distribution or reproduction in other forums is permitted, provided the original author(s) and the copyright owner(s) are credited and that the original publication in this journal is cited, in accordance with accepted academic practice. No use, distribution or reproduction is permitted which does not comply with these terms.

frontiers in Energy Research

ORIGINAL RESEARCH
published: 27 July 2021
doi: 10.3389/fenrg.2021.707718

Optimal Locating and Sizing of BESSs in Distribution Network Based on Multi-Objective Memetic Salp Swarm Algorithm

Sui Peng[1], Xianfu Gong[1], Xinmiao Liu[2], Xun Lu[2] and Xiaomeng Ai[3]*

[1]Grid Planning and Research Center, Guangdong Power Grid Corporation, China Southern Power Grid Company Limited, Guangzhou, China, [2]Guangdong Power Grid Corporation, China Southern Power Grid Company Limited, Guangzhou, China, [3]State Key Laboratory of Advanced Electromagnetic Engineering and Technology, School of Electrical and Electronic Engineering, Huazhong University of Science and Technology, Wuhan, China

Battery energy storage systems (BESSs) are a key technology to accommodate the uncertainties of RESs and load demand. However, BESSs at an improper location and size may result in no-reasonable investment costs and even unsafe system operation. To realize the economic and reliable operation of BESSs in the distribution network (DN), this paper establishes a multi-objective optimization model for the optimal locating and sizing of BESSs, which aims at minimizing the total investment cost of BESSs, the power loss cost of DN and the power fluctuation of the grid connection point. Firstly, a multi-objective memetic salp swarm algorithm (MMSSA) was designed to derive a set of uniformly distributed non-dominated Pareto solutions of the BESSs allocation scheme, and accumulate them in a retention called a repository. Next, the best compromised Pareto solution was objectively selected from the repository via the ideal-point decision method (IPDM), where the best trade-off among different objectives was achieved. Finally, the effectiveness of the proposed algorithm was verified based on the extended IEEE 33-bus test system. Simulation results demonstrate that the proposed method not only effectively improves the economy of BESSs investment but also significantly reduces power loss and power fluctuation.

Keywords: distribution networks, battery energy storage systems, optimal locating and sizing, multi-objective memetic salp swarm algorithm, ideal-point decision method

OPEN ACCESS

Edited by:
Bo Yang,
Kunming University of Science and Technology, China

Reviewed by:
Yixuan Chen,
The University of Hong Kong, Hong Kong, SAR China
Yang Li,
Northeast Electric Power University, China

****Correspondence:***
Xinmiao Liu
lxm2021@foxmail.com

Specialty section:
This article was submitted to Smart Grids, a section of the journal Frontiers in Energy Research

Received: *10 May 2021*
Accepted: *07 June 2021*
Published: *27 July 2021*

Citation:
Peng S, Gong X, Liu X, Lu X and Ai X (2021) Optimal Locating and Sizing of BESSs in Distribution Network Based on Multi-Objective Memetic Salp Swarm Algorithm. Front. Energy Res. 9:707718. doi: 10.3389/fenrg.2021.707718

INTRODUCTION

In recent years, distributed generators (DGs) and controllable load in the distribution network (DN) have continued to increase, meaning that the traditional DN faces many challenges (Sepulveda Rangel et al., 2018; Liu et al., 2020; Peng et al., 2020). At present, one obvious tendency is that the rapid-developed photovoltaic (PV) and wind turbine (WT) power generation technologies make the permeability of distributed PV and WT in the DN higher. A series of problems ensue, such as voltage quality declination and power supply reliability reduction, etc (Wang et al., 2014; Yu et al., 2016; Sun et al., 2020). The active power through the line increases at the peak of power load, the loss increases, and a large voltage offset appears at the end of the line (Kerdphol et al., 2016a; Zhou et al., 2021).

Battery energy storage systems (BESSs) have the characteristics of flexibility and fast response and are an effective way to solve the above problems. The application of BESSs can greatly improve the

connection of renewable energy sources (RESs) (Kerdphol et al., 2016b; Gan et al., 2019; Hlal et al., 2019). BESSs can effectively solve the problems of enlarging the load peak and off-peak difference, delay in the power grid upgrading, alleviate the power supply capacity shortage in the transition phase of the power grid, improve the reliability and stability of the power grid, and optimize the power flow of the grid, as well as improving the economic benefits of system operation (Chong et al., 2016; Chong et al., 2018; Murty and Kumar., 2020). BESSs could provide a new direction for large-scale RESs integration, which is one of the most effective ways to solve renewable energy grid access (Trovão and Antunes, 2015; Liu et al., 2018; Wu et al., 2019).

However, prudent BESSs allocation and sizing in DN determine the satisfactory performance of BESSs applications. The optimal allocation and sizing of BESSs are crucial for the power quality improvement of DN and transmission system protection settings. Once BESSs are connected to the DN, the dispatching system of DN sends dispatching instructions to the BESSs according to the real-time running state of the system load, and then BESSs absorbs or sends power to the parallel network through its two-way energy flow (He et al., 2017; Jia et al., 2017; He et al., 2020). This two-way power regulation can save investment and improve the reliability and economy of BESSs. If the location and sizing of BESSs are not set reasonably, or the operation strategy adopted fails to efficiently play the role of BESSs, the voltage quality may deteriorate, and further increase investment and operation costs (Li et al., 2020). To enable us to take full advantage of distributed BESSs and make their access to the DN have a positive impact, it is important to select the appropriate location and sizing of BESSs based on the appropriate operation strategy (Li et al., 2018).

Recently, a large number of scholars have performed studies in this field (Yang et al., 2020). The literature (Oudalov et al., 2007) tends to optimize the location and power capacity of BESSs by calculating the sensitivity of network loss, and then reduce the power loss of DN. In one study (Pang et al., 2019), a semi-definite relaxation method was proposed to solve the optimal BESSs allocation problem. Another study (Wong et al., 2019) introduces a whale optimization algorithm for the optimal location and sizing of BESSs, while the optimization results do not achieve a significant breakthrough.

This paper devises a multi-objective optimization model considering total investment cost, power loss cost, and power fluctuation for optimal BESSs locating and sizing. For the sake of solving this model, a multi-objective memetic salp swarm algorithm (MMSSA) is proposed to search the non-dominated solutions of BESSs allocation strategy, which reach significant improvement and better balance on the global exploration and local exploitation abilities compared with the salp swarm algorithm (SSA). Furthermore, the ideal-point decision method (IPDM) is adapted to objectively determine the optimal weight coefficients of each objective function and then select the best compromised solution. To verify the effectiveness, the proposed model and algorithm are implemented in the extended IEEE-33 bus test system.

The rest of this paper is organized as follows: *Problem Formulation* develops the multi-objective optimization model. In *Multi-Objective Memetic Salp Swarm Algorithm Based on Pareto*, MMSSA based on IPDM is introduced. Case studies are undertaken in *Case Studies*. Finally, *Conclusion* summarizes the main contributions of this study.

TABLE 1 | The economic parameters of BESSs.

Parameters	Values
Installation cost	1470000 ($/per BESS)
Equipment cost	175,000 ($/MW)
	225,000 ($/MW h)
O&M cost	4,000 ($/MW year)
	2000 ($/(MW h) year)
Lifetime	20 (year)

PROBLEM FORMULATION

Objective Functions

The optimal allocation of BESSs is a multi-objective optimization problem with multiple variables and constraints. To realize the economic and reliable operation of BESSs in the DN, a multi-objective optimization model is established based on the Pareto principle, where minimizing the total investment cost of BESSs, power loss cost, and power fluctuation are the main objectives.

Total Investment Cost

This paper focuses on the DN that has been built and operated, so the investment and construction costs of DN other than BESSs are not included in the cost model. The economic parameters of BESSs are provided in **Table 1**, extracted from a previous study (Behnam and Sanna, 2015). The total investment cost is considered as the annual costs of BESSs, which can be mathematically formulated as follows

$$\mathrm{Min}\, F_1 = C_{ins} + C_{equ} + C_{om} \tag{1}$$

where F_1 is the annual total investment cost of BESSs; C_{ins}, C_{equ}, and C_{om} represent the annual installation cost, equipment cost, and operation and maintenance (O&M) cost, respectively.

The annual installation cost of BESSs is expressed as

$$C_{ins} = C_{\mathrm{cap}} \cdot N_{BESS} \cdot \mu_{CRF} \tag{2}$$

where C_{cap} means the cost of per BESS for installation; N_{BESS} is the number of BESSs deployed in DN; μ_{CRF} denotes the capital recovery factor (CRF) that is the knowing present worth. The CRF translates the costs throughout the useful life of BESSs to the initial moment of the investment, which is obtained by

$$\mu_{CRF} = \frac{r \cdot (1+r)^y}{(1+r)^y - 1} \tag{3}$$

where y is the economic life cycle of BESSs; r means the discount rate, which is calculated by the weighted average cost of capital as follows (Harvey, 2020)

$$r = f_{\mathrm{d}} \cdot i_{\mathrm{d}} + \left(1 - f_{\mathrm{d}}\right) \cdot i_{\mathrm{e}} \tag{4}$$

where f_d *and* i_e represent the debt ratio and the return on equity, is respectively, 80 and 50%; i_d denotes the interest rate of 4.165%.

The annual equipment cost of BESSs is calculated by

$$C_{equ} = \sum_{i=1}^{N_{BESS}} \left(\alpha \cdot P_{BESS,i} + \beta \cdot E_{BESS,i}\right) \cdot \mu_{CRF} \tag{5}$$

where α and β mean the costs per unit power and per unit capacity, respectively; $P_{BESS,i}$ and $E_{BESS,i}$ are the power capacity and energy capacity of the ith BESS.

The annual O&M cost of BESSs is expressed as

$$C_{OM} = \sum_{i=1}^{N_{BESS}} \left(\lambda \cdot P_{BESS,i} + \gamma \cdot E_{BESS,i}\right) \cdot \mu_{CRF} \tag{6}$$

where λ and γ are respectively the O&M cost of per unit power and per unit energy of BESSs. Note that the O&M costs of rectifier, inverter, and charge regulator are neglected.

Power Loss Cost

BESSs grid-connected will change the power flow of DN (Injeti and Thunuguntla, 2020). Furthermore, the different locations and sizes of BESSs will have different influences on power losses. For the sake of minimizing the total active power losses, the power losses index is established in the optimization model, as follows

$$\text{Min } F_2 = \sum_{t=1}^{T} \left(\rho_{loss}(t) \cdot P_{loss}(t)\right) \tag{7}$$

$$P_{loss}(t) = \sum_{j=1}^{L} \left(R_j I_j^2(t)\right) \tag{8}$$

where F_2 is the daily cost of power losses; $\rho_{loss}(t)$ and $P_{loss}(t)$ represent the time of use (TOU) electricity prices and power losses at time t; L is the total number of lines in the DN; R_j means the resistance on the jth line; $I_j(t)$ denotes the current on the jth line at time t. The lower F_2 is that the greater positive effect of BESSs deployment in reducing power loss.

Power Fluctuation

Owing to the intermittent nature of RESs, the integration of them into power grids poses significant power fluctuation in the grid connection point. However, BESSs can provide an effective supplement for RESs in smoothing power fluctuation to improve power quality. The power quality index can be expressed as

$$\text{Min } F_3 = \sqrt{\sum_{t=1}^{T} \left(P_{grid}(t) - \overline{P}_{grid}\right)^2} \tag{9}$$

where F_3 is the daily total power fluctuation of the grid connection point; $P_{grid}(t)$ represents the power fluctuation at time t; $\overline{P}_{grid}$ means the mean power fluctuation over a day.

Constraints

Power Balance

$$\begin{cases} P_i(t) = V_i(t) \sum_{j=1}^{N} V_j(t)\left(G_{ij}\cos\theta_{ij}(t) + B_{ij}\sin\theta_{ij}(t)\right) \\ Q_i(t) = V_i(t) \sum_{j=1}^{N} V_j(t)\left(G_{ij}\sin\theta_{ij}(t) - B_{ij}\cos\theta_{ij}(t)\right) \end{cases} \tag{10}$$

where $P_i(t)$ and $Q_i(t)$ represent the injected active power and reactive power at ith node in the DN at time t, respectively; $V_i(t)$ is the voltage of the ith node at time t; G_{ij} and B_{ij} represent the admittance and susceptance between the ith node and the jth node; $\theta_{ij}(t)$ is the power angle between the ith node and the jth node at time t.

Range of Node Voltages

$$V_i^{\min} < V_i < V_i^{\max} \tag{11}$$

where $V_i^{\min}$ and $V_i^{\max}$ represent the upper and lower limits of the voltages of the ith node.

Charging and Discharging Power Limits of BESSs

$$\begin{cases} 0 \le P_{cha,i}(t) \le P_{BESS,i} \cdot \eta_{cha} \\ -P_{BESS,i} \cdot \eta_{dis} \le P_{dis,i}(t) \le 0 \end{cases} \tag{12}$$

where $P_{cha,i}(t)$ and$P_{dis,i}(t)$ represent the charging and discharging power of BESSs at time t, respectively; η_{cha} and η_{dis} are respectively the charging and discharging efficiency of BESSs.

State of Charge Limits

$$SOC^{\min} < SOC(t) < SOC^{\max} \tag{13}$$

where $SOC^{\min}$ and $SOC^{\max}$, respectively, mean the upper and lower limits of SOC, is that 20 and 90%.

Multi-Objective Optimization Model

Establishment of the Optimization Model

In terms of multi-objective optimization problems such as BESSs allocation, all objectives generally conflict with each other, and optimizing one of the objectives leads to the deterioration of other objectives in most cases. It is difficult to objectively evaluate the superiority-inferiority of all solutions because there is no absolute optimal solution for the overall objective (Huang et al., 2020). Nevertheless, there exists an optimal solution set, elements of which are named Pareto optimal solutions, realizing the optimum matching among objectives (Fonseca and Fleming, 1993). In this paper, the multi-objective optimization model of BESSs locating and sizing is designed to simultaneously meet investment economy and operation reliability requirements, as follows

$$\begin{cases} \min \boldsymbol{F}(x) = [F_1(\boldsymbol{x}), F_2(\boldsymbol{x}), F_3(\boldsymbol{x})]^{\mathrm{T}} \\ \text{s.t.} E(\boldsymbol{x}) = 0 \\ I(\boldsymbol{x}) \le 0 \end{cases} \tag{14}$$

where $\boldsymbol{F}(\boldsymbol{x})$ represents the target space consists of all objective functions; $\boldsymbol{x}$ denotes the decision space that is constituted by all optimization variables; $E(\boldsymbol{x})$ and $I(\boldsymbol{x})$ are respectively, equality and inequality constraints that need to be satisfied in the multi-objective optimization model.

Design of Optimization Variables

Optimization variables include the installation locations, power, and energy capacities of two BESSs, all of which need to be constructed in a reasonable range, otherwise, some negative effects on the power flow, relay protection, voltage, and waveform of the original power grid raise. In this paper, nodes in the range of (Mirjalili et al., 2017; Liu et al., 2020) were selected as the installation locations, in which environmental and geographical factors need to be considered in engineering practice. The limits of power and energy capacities are determined to consider the topology of DN, the power limit of the interconnection point, especially the total load power. Therefore, the power capacity allowed to access the power grid of a BESS is determined as 90% of the total active power load of the power grid, and the numerical value of energy capacity limit is equal to power capacity limit, as follows

$$\begin{cases} P_{BESS,i} \le P_{BESS}^{\max} \\ E_{BESS,i} \le E_{BESS}^{\max} \end{cases} \tag{15}$$

where $P_{BESS,i}$ and $E_{BESS,i}$ are the power capacity and energy capacity of the ith BESS; $P_{BESS}^{\max}$ and $E_{BESS}^{\max}$ denote the upper limits of the energy capacity and power capacity of BESSs, are respectively, 3375 and 3375 kWh.

Note that the power and energy capacities of two BESSs are continuous, while installation locations are discrete. In this paper, continuous variables can converge to the optimal value in the iteration process while the optimal value of discrete variables needs to be rounded in continuous space (Zhang et al., 2017).

MULTI-OBJECTIVE MEMETIC SALP SWARM ALGORITHM BASED ON PARETO

Memetic Salp Swarm Algorithm

Optimization Framework

SSA is inspired by the swarming motility and foraging behavior of salps, which successfully solves varieties of optimization problems since it has a simple search mechanism and high optimization efficiency (Mirjalili et al., 2017). In recent years, the memetic algorithm has developed into a broad class of algorithms and can properly combine global search and local search mechanisms (Moscato, 1989; Neri and Cotta, 2012). In this paper, the memetic computing framework first proposed by Moscato (Moscato, 1989) is adopted in the memetic salp swarm algorithm (MSSA) to improve the searching ability of SSA. Then, multiple slap chains were employed to better balance global exploration and local exploitation abilities. Therefore, there are two important search mechanisms in MSSA, namely the local search in a single chain and the global coordination in the whole population. In MSSA, multiple salp chains are arranged in parallel, where each salp chain is regarded as a swarm of salps that independently perform local searches similar to SSA. Meanwhile, all salp chains are regrouped by information communication among all salps for the improvement of convergence stability. The optimization framework of MSSA is illustrated in **Figure 1**.

Mathematical Model

In the single chain, the salps can be divided into two roles, including the leaders and the followers. As illustrated in **Figure 1**, the leader is regarded as the salp at the front of each salp chain, while the rest of the salps are followers. In each iteration, the leading salp seeks the food source, while the follower salps follow each other in a row. Note that the best salp with the best fitness is considered to be the food source, and will be chased by the whole salp chain. The position of the leading salp and follower salps can be updated as follows (Mirjalili et al., 2017)

$$x_{m1}^{j} = \begin{cases} F_m^j + c_1\left(c_2\left(ub^j - lb^j\right) + lb^j\right), & if\ c_3 \ge 0 \\ F_m^j - c_1\left(c_2\left(ub^j - lb^j\right) + lb^j\right), & if\ c_3 < 0 \end{cases} \tag{16}$$

$$x_{mi}^{j} = \frac{1}{2}\left(x_{mi}^{j} + x_{m,i-1}^{j}\right), \quad i = 2, 3, \ldots, n;\ m = 1, 2, \ldots, M \tag{17}$$

where the j means the jth dimension of searching space; x_{m1}^{j} and x_{mi}^{j} respectively denote the positions of the leading salp and the ith follower salp in the mth salp chain; F_m^j is the position of a food source; ub^j and lb^j are respectively the upper and lower limits of the jth dimension variables; n and M represent the population size of a single salp chain and the number of salp chains, respectively; c_2, and c_3 are both the uniform random numbers from 0 to 1; c_1 is a random number that is related to the iteration number, as follows (Mirjalili et al., 2017)

$$c_1 = 2\mathrm{e}^{-\left(\frac{4k}{k_{\max}}\right)^2} \tag{18}$$

where k and $k_{\max}$ are the current iteration number and maximum iteration number, respectively.

In the salp population, each salp is taken as an individual of the virtual salp population. At each iteration, the population can be regrouped into multiple new salp chains based on the descending order of all salps' fitness values. In the regroup operation, the global coordination among different salp swarms is achieved, as shown in **Figure 2**. It can be seen that the best solution is assigned to salp chain #1, and then the second-best solution is assigned to salp chain #2, and so on. Therefore, the mth salp chain can be updated by (Eusuff and Lansey, 2015)

$$\begin{gathered} \boldsymbol{Y}^m = \left[\boldsymbol{x}_{mi}, f_{mi} | \boldsymbol{x}_{mi} = \boldsymbol{X}(m + M(i-1)),\right. \\ \left. f_{mi} = \boldsymbol{F}(m + M(i-1)),\ i = 1, 2, \cdots, n\right],\ \ m = 1, 2, \cdots, M \end{gathered} \tag{19}$$

where $\boldsymbol{x}_{mi}$ and f_{mi} are the position vector and fitness value of the ith salp in the mth chain, respectively; $\boldsymbol{X}$ and $\boldsymbol{F}$ denote a position vector set and a fitness value set of all the salps, respectively.

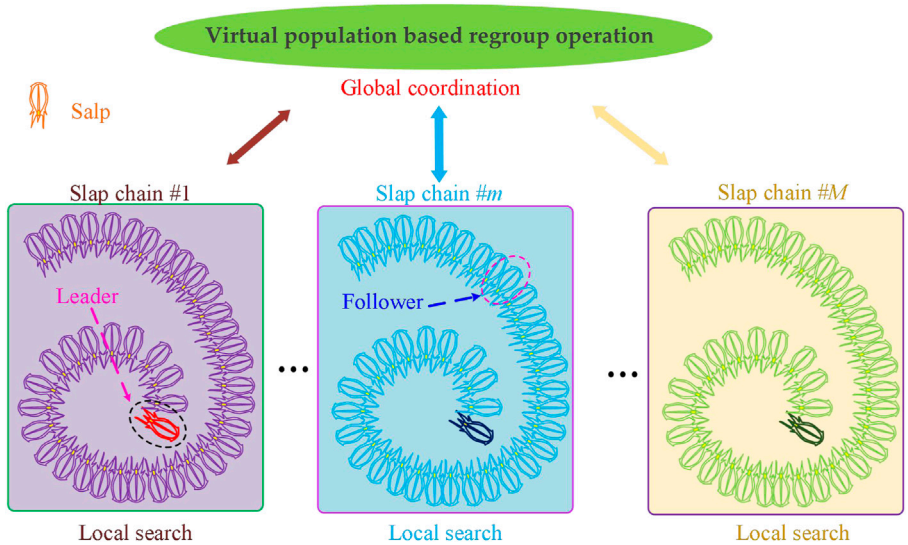


FIGURE 1 | Conceptual optimization framework of MSSA.

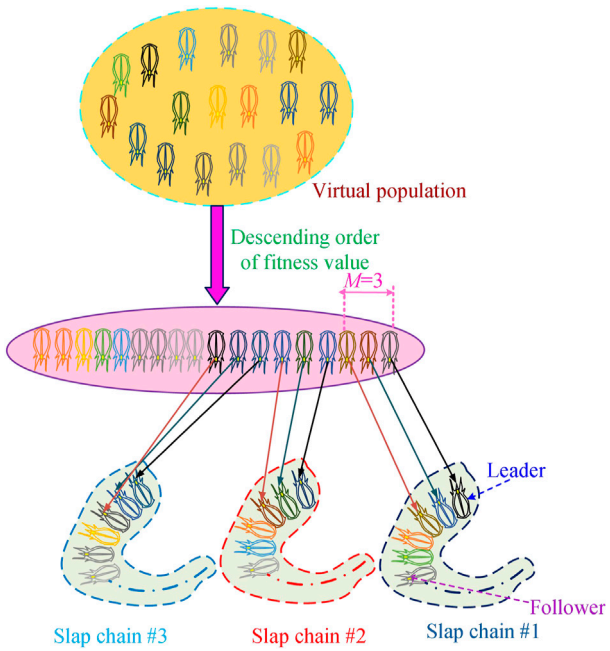


FIGURE 2 | Regroup operation of salp population for global coordination.

Multi-Objective Memetic Salp Swarm Algorithm

As discussed in *Problem Formulation*, the solutions for a multi-objective problem should be a set of Pareto optimal solutions. MSSA can drive salps towards the food source with the best solution for the optimization problem and update it at each iteration. The design of MMSSA is first to equip the food sources with a repository to restore the non-dominated solutions obtained by MSSA so far (Coello et al., 2004). In the optimization process, every new non-dominated solution needs to be compared against all residents in the repository using the Pareto dominance operators, as follows (Faramarzi et al., 2020).

- If a new solution dominates a set of solutions in the repository, they have to be swapped;
- If at least one of the solutions in the repository dominates the new solution, this new solution should be discarded straight away;
- If a new solution is non-dominated in comparison with all repository residents, this new solution will be added to the repository.

The repository can just store limited solutions. Therefore, a wise method adopted to remove the similar non-dominated solutions in the repository, is that the one in the populated region is identified as the best candidate to be removed from the repository to improve the distribution diversity of the Pareto optimal solution set. The solutions that are removed from the repository need to satisfy the following equation

$$\begin{cases} |F_h(x_m) - F_h(x_n) < D_h|,\ h = 1,\ 2,\ 3 \\ D_h = \dfrac{F_h^{\max} - F_h^{\min}}{N_r} \end{cases} \tag{20}$$

where $F_h(x_m)$ and $F_h(x_n)$ denote the hth fitness value of the mth salp and the nth salp, respectively; D_h is the distance threshold of the Pareto solution set; $F_h^{\max}$ and $F_h^{\min}$, respectively, represent the maximum and minimum of the hth objective function obtained as far; N_r is the maximum size of the repository to store the non-dominated solutions.

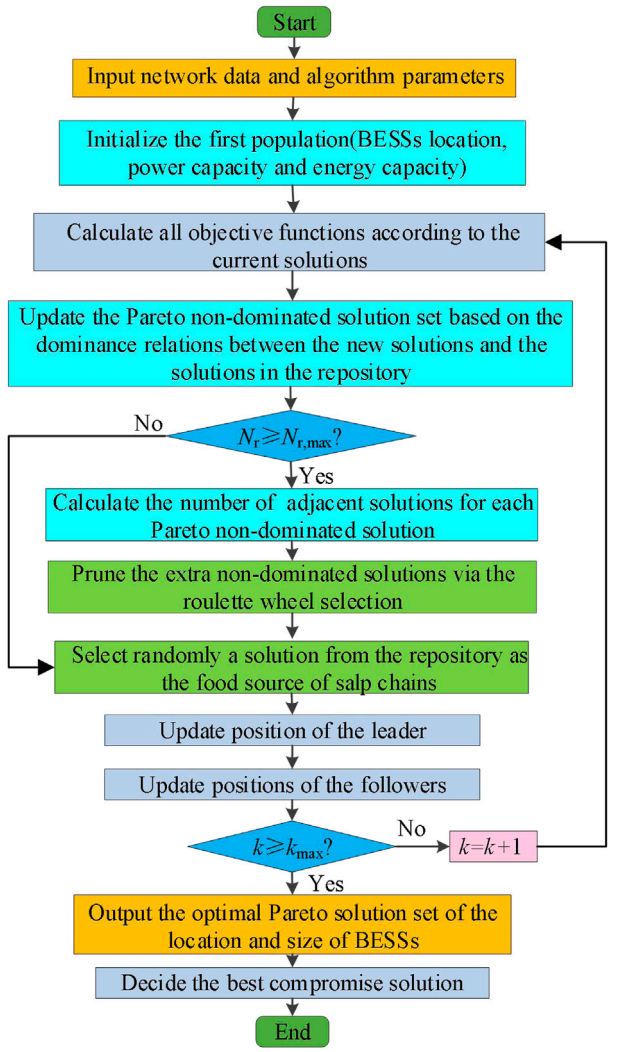


FIGURE 3 | The flowchart of MMSSA for the optimal locating and sizing of BESSs.

In this paper, the IPDM was adopted to filter out the best compromised solution of the Pareto non-dominated solution set, which is often used in multiple attribute decision making. Firstly, the objective functions of all Pareto non-dominated solutions obtained by MPOA are normalized as follows

$$f_h(x_m) = \frac{y_h(x_m) - y_h^{\min}}{y_h^{\max} - y_h^{\min}} \tag{21}$$

where $y_h(x_m)$ is the hth objective function value of the non-dominated solution x_m; $f_h(x_m)$ represents the normalized value of the hth objective function; $y_h^{\min}$ and $y_h^{\max}$ mean the maximum and minimum of the hth objective function.

Thus, an ideal point can be selected in the target decision-making region formed by all Pareto non-dominated solutions. It is worth mentioning that the objective functions of the ideal point can be normalized to be (0, 0, 0) in terms of the minimization problem. Crucially, the squared Euclidean distance between different solutions and the ideal point is taken as an important basis for ranking all non-dominated solutions and then decide the best compromised solution from them. The squared Euclidean distance can be calculated by

$$EU_i = \sum_{h=1}^{3} \left[f_h(x_m) - 0 \right]^2 \cdot \omega_h^2 \tag{22}$$

ω_h means the weights of the hth objective function, as follows

$$\omega_h = \frac{1}{\sum_{m=1}^{N_r} \left[f_h(x_m) - 0 \right]^2 \cdot \sum_{h=1}^{3} \frac{1}{\sum_{m=1}^{N_r} \left[f_h(x_m) - 0 \right]^2}} \tag{23}$$

Owing to the weights of each objective function obtained by IPDM, it does not rely on the evaluation and preference of experts so that the decision is credible. In the end, the best compromised solution is expressed as

$$x_{best} = \arg \min_{m=1,2,\ldots,N_r} \sum_{h=1}^{3} \left[f_h(x_m) - 0 \right]^2 \cdot \omega_h^2 \tag{24}$$

To sum up, the flowchart of MMSSA to solve the optimal locating and sizing of BESSs is shown in **Figure 3**.

CASE STUDIES

Test System

In this section, the optimal locating and sizing of BESSs based on MMSSA is implemented in the extended IEEE-33 bus system for verifying the effectiveness of the proposed algorithm. The topology structure of the test system with a total load of 3,715 + j2300 kVA is depicted in **Figure 4**. It is assumed that the resource units include one PV and three WT, where the maximum generation limits of PV and WT both are 0.2 MW. The typical daily curves of load, wind and PV power are demonstrated in **Figure 5**. In addition, multi-objective particle swarm optimization (MOPSO) (Hlal et al., 2019) is used for

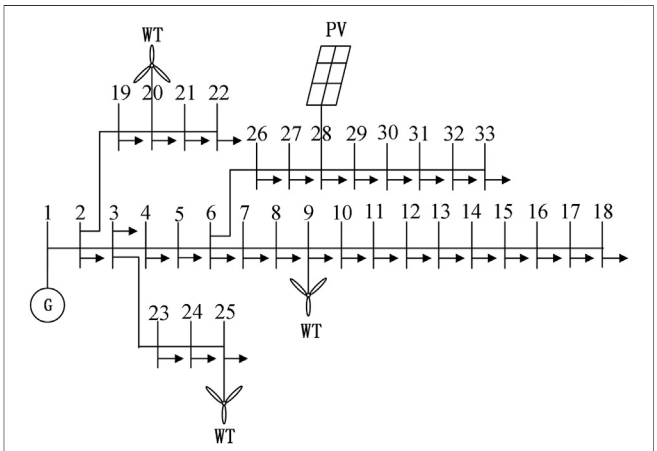


FIGURE 4 | Extended IEEE-33 bus test system.

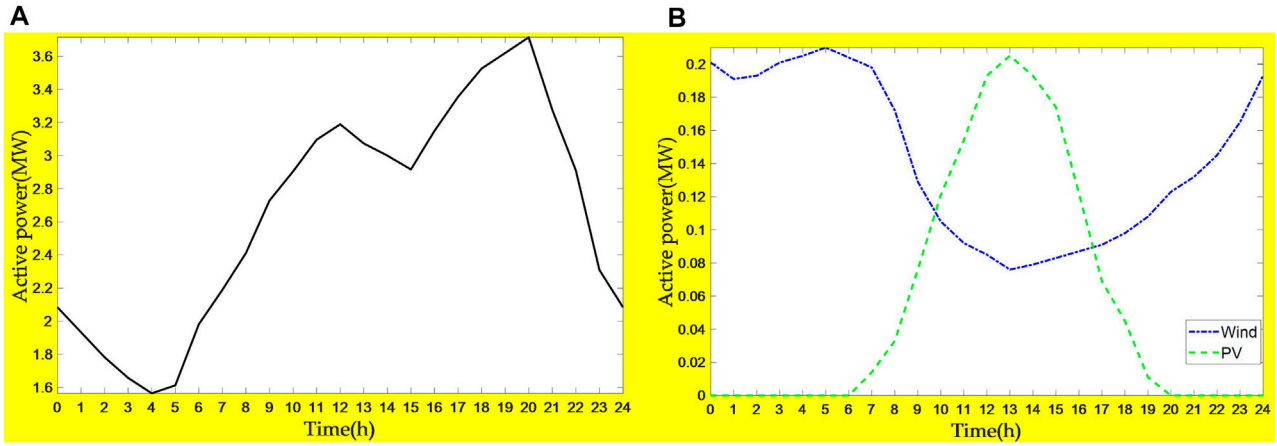


FIGURE 5 | Typical daily curves: **(A)** hourly load curves; **(B)** hourly wind and PV power curves.

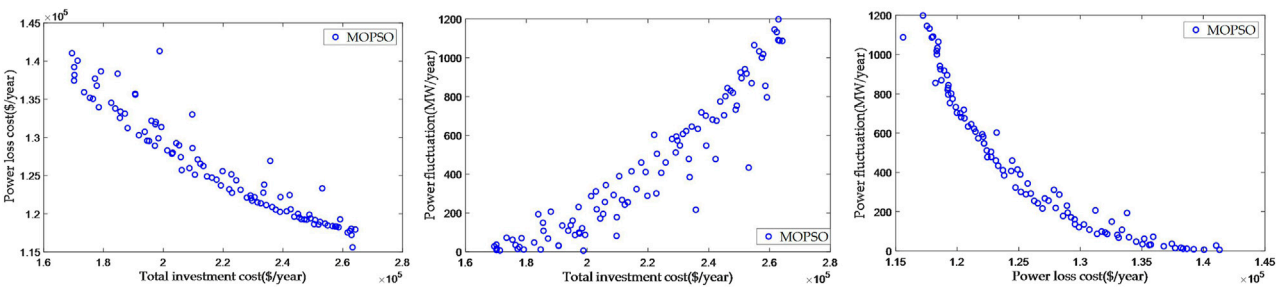


FIGURE 6 | Three-objective Pareto front results obtained by MOPSO.

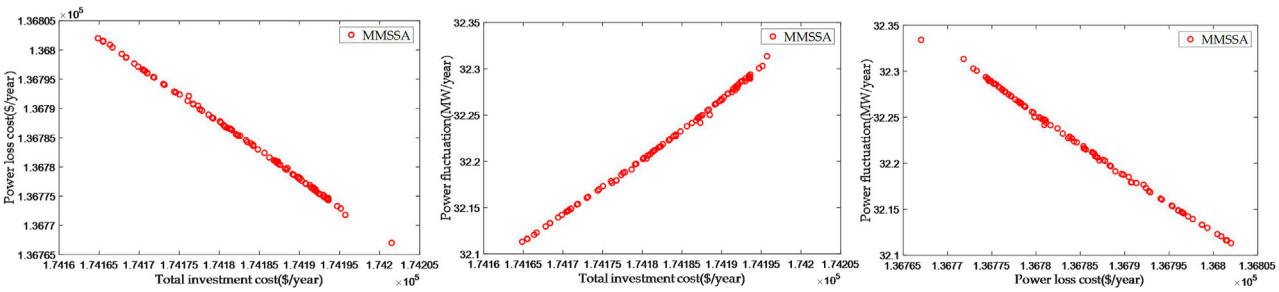


FIGURE 7 | Bi-objective Pareto front results obtained by MMSSA.

comparison. For the sake of a relatively fair comparison, the population size of MMSSA and other algorithms all are set to 100, and the maximum iterations are set to be 500. The size of the repository was chosen to equal 100 for multi-objective optimization. Some specific parameters of all comparison algorithms were set to the default values. If the parameters are not chosen properly, the convergence time will be too long or the local optimum will be trapped. It is worth mentioning that the key parameters in the MMSSA algorithm, such as $c1$, the most important parameter since they can directly influence the trade-off between exploration and exploitation. To achieve a proper balance, it was designed according to the iteration number.

Simulation Results

Figure 6 and **Figure 7**, respectively, exhibit the bi-objective Pareto front curves by two algorithms, including the total investment cost versus the power loss cost, the total investment cost versus the power fluctuation, as well as the power loss cost versus power fluctuation, which demonstrates these three bi-objective Pareto fronts obtained by MMSSA are

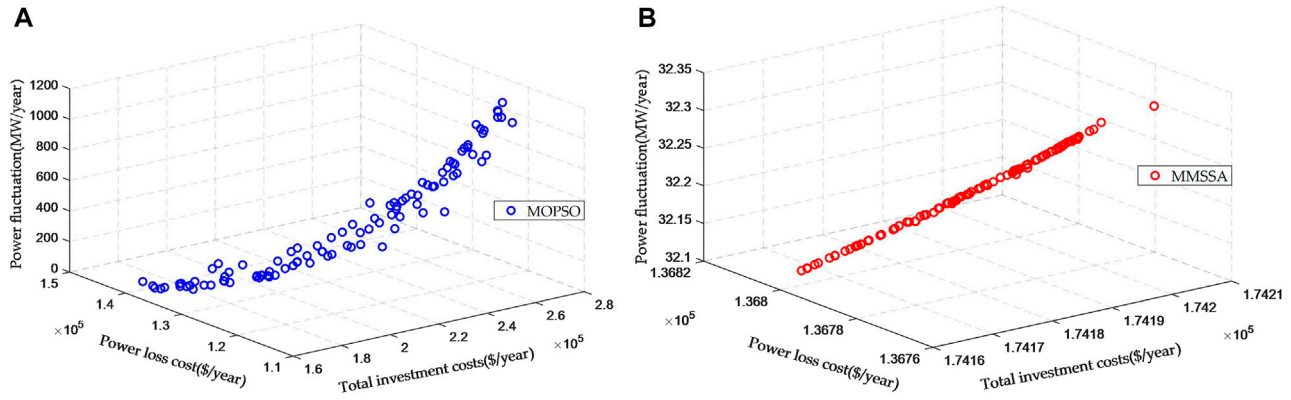


FIGURE 8 | Three-objective Pareto front results obtained by two algorithms: **(A)** MOPSO; **(B)** MMSSA.

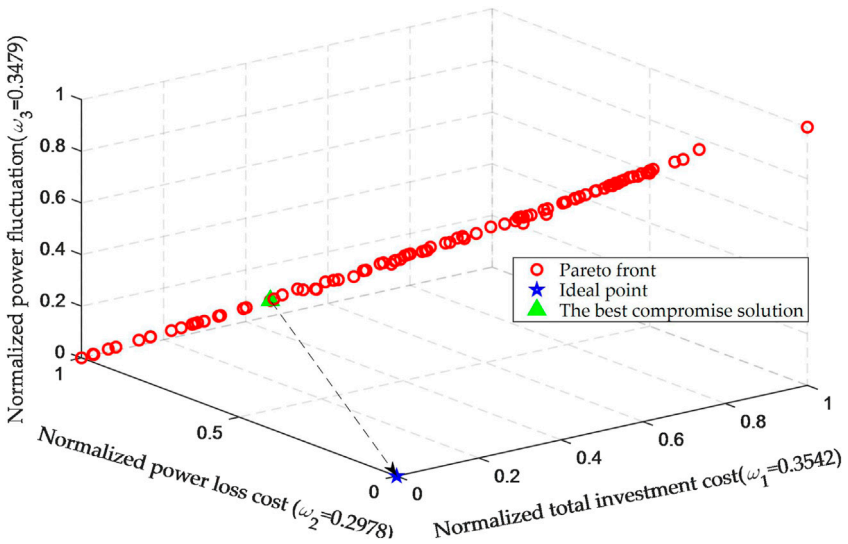


FIGURE 9 | The schematic diagram of IPDM based on MMSSA.

more uniform than MOPSO from the perspective of distribution. **Figure 8** shows the three-objective Pareto front obtained by two algorithms. As can be seen from **Figure 8**, MMSSA can acquire the Pareto solution set with higher quality compared with MOPSO. Moreover, the schematic diagram of the IPDM based on MMSSA is illustrated in **Figure 9**. **Figure 9** shows the normalized objective function curve based on MMSSA, as well as the decision-making schematic for the best compromise solution of BESSs allocation. IPDM based on MMSSA can obtain the objective weight coefficients and select the best compromise solution by means of the sum of squares of Euclidean distance.

To better compare the convergence and diversity of the Pareto solution set obtained by two algorithms, the performance indexes are evaluated in **Table 2**, including coverage over the Pareto front (CPF) (Tian et al., 2019), spread (Wang et al., 2010), spacing (Schott, 1995), and execution time. It is worth mentioning that CPF defines the diversity of Pareto solution set as its coverage over the Pareto front in an (M-1) dimensional hypercube (Wang et al., 2010), while spread and spacing respectively denote the diversity and the evenness of the Pareto solution set, which are all the negative indexes. In addition, **Table 3** shows the best compromise decision scheme of BESSs allocation from two algorithms, along with the objective function values. It is evident that the MMSSA outperforms the MOPSO in the multi-objective optimization model for optimal locating and sizing of BESSs:

TABLE 2 | Comparison of performance metrics of two algorithms.

Algorithm	Performance metric			
	CPF	Spread	Spacing	Time (s)
MOPSO	0.4996	0.4753	9,075.45	1.5428e+04
MMSSA	0.1636	0.4481	3.3858	1.4676e+04

TABLE 3 | Optimization results of two algorithms.

Algorithm	The best compromise allocation scheme of BESSs			Objective function values under the best compromise allocation scheme		
	Bus location	Power capacity (MW)	Energy capacity (MW·h)	Total investment cost ($/year)	Power loss cost ($/year)	Power fluctuation (MW/year)
MOPSO	Trovão and Antunes (2015); Mirjalili et al. (2017)	[0.1972, 0.2786]	[1.6203, 1.6204]	2.0873e+05	1.3698e+05	292.9054
MMSSA	Pang et al. (2019); Injeti and Thunuguntla (2020)	[0.0849, 0.0618]	[0.6535, 0.3943]	1.7417e+05	1.3679e+05	32.1682

- It has the smallest CPF value, indicating that MMSSA owns better diversity;
- It gains the smallest spread and spacing value, which indicates that the Pareto solutions obtained by MMSSA are evenly and widely distributed on the Pareto front;
- It also has the smallest execution time, which means that MMSSA can converge to the Pareto front much faster than conventional MOPSO;
- It has the least investment cost, meaning that MMSSA can improve the economy of BESSs investment;
- It slightly reduces power loss cost, and ensures a higher operation economy of DN;
- It significantly gains lower power fluctuation of the grid connection point, which means MMSSA can contribute to power supply reliability.

CONCLUSION

In this paper, a multi-objective optimization model based on the Pareto principle was established. This study proposes MMSSA as a method for solving the optimal location and size of BESSs in DN. The contributions of the proposed approach are as follows:

- The multi-objective optimization model takes the economic criteria, incorporates time value into cost, and the technical criteria relate to system reliability and take it into consideration, which aims to make BESSs more cost-effective and ensure the reliable operation of DN;
- The proposed MMSSA has a strong global search ability and convergence ability under complex multi-objective functions, which can quickly search high-quality non-dominated solutions, and then objectively select the best compromised solution with the help of IPDM;
- The simulation results based on the extended IEEE-33 bus test system effectively verify that the best-compromised solution of BESSs allocation scheme obtained by MMSSA owns the lowest investment cost, power loss cost, and power fluctuation, which is beneficial for DN to increase economic efficiency and improve system reliability.

However, there are several limitations to this work, including the inapplicability of the proposed MMSSA for the high-dimension optimization problem, and the limited scenario design in terms of validating its effectiveness. Therefore, the MMSSA can be further enhanced to improve the accuracy for high-dimensional objective optimization. Meanwhile, a multi-scenario design that combines different typical daily data in a year should be conducted to capture the time-variable nature and uncertainties related to RESs and load demand.

DATA AVAILABILITY STATEMENT

The original contributions presented in the study are included in the article/supplementary material, further inquiries can be directed to the corresponding author.

AUTHOR CONTRIBUTIONS

SP and XG contributed to conception and design of the study. XiL and XuL performed the case analysis. SP wrote the first draft of the manuscript. XG, XiL, XuL, and XA wrote sections of the article. All authors contributed to article revision, read, and approved the submitted version.

FUNDING

The paper is funded by the project supported by the China Southern Power Grid Science and Technology Project under Project 037700KK52190011 (GDKJXM20198273).

ACKNOWLEDGMENTS

The authors gratefully acknowledge that this project was supported by the China Southern Power Grid Science and Technology Project under Project 037700KK52190011 (GDKJXM20198273).

REFERENCES

Behnam, Z., and Sanna, S. (2015). Electrical Energy Storage Systems: A Comparative Life Cycle Cost Analysis. *Renew. Sust. Energ. Rev.* 42, 569–596. doi:10.1016/j.rser.2014.10.011

Chong, L. W., Wong, Y. W., Rajkumar, R. K., and Isa, D. (2018). An Adaptive Learning Control Strategy for Standalone PV System with Battery-Supercapacitor Hybrid Energy Storage System. *J. Power Sourc.* 394, 35–49. doi:10.1016/j.jpowsour.2018.05.041

Chong, L. W., Wong, Y. W., Rajkumar, R. K., and Isa, D. (2016). An Optimal Control Strategy for Standalone PV System with Battery-Supercapacitor Hybrid

Energy Storage System. *J. Power Sourc.* 331, 553–565. doi:10.1016/j.jpowsour.2016.09.061

Coello, C. A. C., Pulido, G. T., and Lechuga, M. S. (2004). Handling Multiple Objectives with Particle Swarm Optimization. *Evol. Comput. IEEE Trans.* 8, 256–279. doi:10.1109/tevc.2004.826067

Eusuff, M. M., and Lansey, K. E. (2015). Optimization of Water Distribution Network Design Using the Shuffled Frog Leaping Algorithm. *J. Water Resour. Plann. Manag.* 129 (3), 210–225. doi:10.1061/40569(2001)412

Faramarzi, A., Heidarinejad, M., and Stephens, b. (2020). Equilibrium Optimizer: a Novel Optimization Algorithm. *Knowledge Based Syst.* 191, 105190. doi:10.1016/j.knosys.2019.105190

Fonseca, C. M., and Fleming, P. J. (1993). Genetic Algorithms for Multiobjective Optimization: Formulation Discussion and Generalization. *Icga* 93, 416–423.

Gan, W., Ai, X., Fang, J., Yan, M., Yao, W., Zuo, W., et al. (2019). Security Constrained Co-planning of Transmission Expansion and Energy Storage. *Appl. Energ.* 239, 383–394. doi:10.1016/j.apenergy.2019.01.192

Harvey, H. L. D. (2020). Clarifications of and Improvements to the Equations Used to Calculate the Levelized Cost of Electricity (LCOE), and Comments on the Weighted Average Cost of Capital (WACC). *Energy* 207, 118340. doi:10.1016/j.energy.2020.118340

He, X., Ai, Q., Qiu, R. C., Huang, W. T., Piao, L. J., and Liu, H. C. (2017). A Big Data Architecture Design for Smart Grids Based on Random Matrix Theory. *IEEE Trans. Smart Grid.* 8 (2), 674–686.

He, X., Qiu, R. C., Ai, Q., and Zhu, T. Y. (2020). A Hybrid Framework for Topology Identification of Distribution Grid with Renewables Integration. *IEEE Trans. Power Syst.* 36 (2), 1493–1503. doi:10.1109/tpwrs.2020.3024955

Hlal, M. I., Ramachandaramurthya, V. K., Padmanaban, S., Kaboli, H. R., Pouryekta, A., and Tuan Abdullah, T. A. R. b. (2019). NSGA-II and MOPSO Based Optimization for Sizing of Hybrid PV/wind/battery Energy Storage System. *Ijpeds* 10 (1), 463–478. doi:10.11591/ijpeds.v10.i1.pp463-478

Huang, Z., Fang, B. L., and Deng, J. (2020). Multi-objective Optimization Strategy for Distribution Network Considering V2G Enabled Electric Vehicles in Building Integrated Energy System. *Prot. Control. Mod. Power Syst.* 5 (1), 48–55. doi:10.1186/s41601-020-0154-0

Injeti, S. K., and Thunuguntla, V. K. (2020). Optimal Integration of DGs into Radial Distribution Network in the Presence of Plug-In Electric Vehicles to Minimize Daily Active Power Losses and to Improve the Voltage Profile of the System Using Bioinspired Optimization Algorithms. *Prot. Control. Mod. Power Syst.* 5 (1), 21–35. doi:10.1186/s41601-019-0149-x

Jia, K., Chen, Y., Bi, T., Lin, Y., Thomas, D., and Sumner, M. (2017). Historical-data-based Energy Management in a Microgrid with a Hybrid Energy Storage System. *IEEE Trans. Ind. Inf.* 13 (5), 2597–2605. doi:10.1109/tii.2017.2700463

Kerdphol, T., Fuji, K., Mitani, Y., Watanabe, M., and Qudaih, Y. (2016). Optimization of a Battery Energy Storage System Using Particle Swarm Optimization for Stand-Alone Microgrids. *Int. J. Electr. Power Energ. Syst.* 81, 32–39. doi:10.1016/j.ijepes.2016.02.006

Kerdphol, T., Qudaih, Y., and Mitani, Y. (2016). Optimum Battery Energy Storage System Using PSO Considering Dynamic Demand Response for Microgrids. *Int. J. Electr. Power Energ. Syst.* 83, 58–66. doi:10.1016/j.ijepes.2016.03.064

Li, R., Wang, W., Chen, Z., and Wu, X. (2018). Optimal Planning of Energy Storage System in Active Distribution System Based on Fuzzy Multi-Objective Bi-level Optimization. *J. Mod. Power Syst. Clean. Energ.* 6 (2), 342–355. doi:10.1007/s40565-017-0332-x

Li, Y., Vilathgamuwa, M., Choi, S. S., Xiong, B., Tang, J., Su, Y., et al. (2020). Design of Minimum Cost Degradation-Conscious Lithium-Ion Battery Energy Storage System to Achieve Renewable Power Dispatchability. *Appl. Energ.* 260, 114282. doi:10.1016/j.apenergy.2019.114282

Liu, J., Yao, W., Wen, J., Fang, J., Jiang, L., He, H., et al. (2020). Impact of Power Grid Strength and PLL Parameters on Stability of Grid-Connected DFIG Wind Farm. *IEEE Trans. Sustain. Energ.* 11 (1), 545–557. doi:10.1109/tste.2019.2897596

Liu, Z., Chen, Y., Zhuo, R., and Jia, H. (2018). Energy Storage Capacity Optimization for Autonomy Microgrid Considering CHP and EV Scheduling. *Appl. Energ.* 210, 1113–1125. doi:10.1016/j.apenergy.2017.07.002

Mirjalili, S., Gandomi, A. H., Mirjalili, S. Z., Saremi, S., Faris, H., and Mirjalili, S. M. (2017). Salp Swarm Algorithm: A Bio-Inspired Optimizer for Engineering Design Problems. *Adv. Eng. Softw.* 114, 163–191. doi:10.1016/j.advengsoft.2017.07.002

Moscato, P. (1989). On Evolution, Search, Optimization, Genetic Algorithms and Martial Arts: Towards Memetic Algorithms. Caltech Concurrent Computation Program, Technical Reports 826.

Murty, V. V. S. N., and Kumar, A. (2020). Multi-objective Energy Management in Microgrids with Hybrid Energy Sources and Battery Energy Storage Systems. *Prot. Control. Mod. Power Syst.* 5 (1), 1–20. doi:10.1186/s41601-019-0147-z

Neri, F., and Cotta, C. (2012). Memetic Algorithms and Memetic Computing Optimization: A Literature Review. *Swarm Evol. Comput.* 2, 1–14. doi:10.1016/j.swevo.2011.11.003

Oudalov, A., Chartouni, D., and Ohler, C. (2007). Optimizing a Battery Energy Storage System for Primary Frequency Control. *IEEE Trans. Power Syst.* 22 (3), 1259–1266. doi:10.1109/tpwrs.2007.901459

Pang, M., Shi, Y., Wang, W., and Pang, S. (2019). Optimal Sizing and Control of Hybrid Energy Storage System for Wind Power Using Hybrid Parallel PSO-GA Algorithm. *Energy. explorat & exploitat.* 37 (1), 558–578. doi:10.1177/0144598718784036

Peng, X., Yao, W., Yan, C., Wen, J., and Cheng, S. (2020). Two-stage Variable Proportion Coefficient Based Frequency Support of Grid-Connected DFIG-WTs. *IEEE Trans. Power Syst.* 35 (2), 962–974. doi:10.1109/tpwrs.2019.2943520

Schott, J. R. (1995). *Fault Tolerant Design Using Single and Multicriteria Genetic Algorithm Optimization*. Cambridge, MA: Massachusetts Institute of Technology.

Sepulveda Rangel, C. A., Canha, L., Sperandio, M., and Severiano, R. (2018). Methodology for ESS-type Selection and Optimal Energy Management in Distribution System with DG Considering Reverse Flow Limitations and Cost Penalties. *IET Generation, Transm. Distribution.* 12 (5), 1164–1170. doi:10.1049/iet-gtd.2017.1027

Sun, K., Yao, W., Fang, J., Ai, X., Wen, J., and Cheng, S. (2020). Impedance Modeling and Stability Analysis of Grid-Connected DFIG-Based Wind Farm with a VSC-HVDC. *IEEE J. Emerg. Sel. Top. Power Electron.* 8 (2), 1375–1390. doi:10.1109/jestpe.2019.2901747

Tian, Y., Cheng, R., Zhang, X., Li, M., and Jin, Y. (2019). Diversity Assessment of Multi-Objective Evolutionary Algorithms: Performance Metric and Benchmark Problems. *IEEE Comput. Intelligence Mag.* 14 (3), 61–74. doi:10.1109/mci.2019.2919398

Trovão, J. P., and Antunes, C. H. (2015). A Comparative Analysis of Meta-Heuristic Methods for Power Management of a Dual Energy Storage System for Electric Vehicles. *Energ. Convers. Manag.* 95, 281–296. doi:10.1016/j.enconman.2015.02.030

Wang, B., Yang, Z., Lin, F., and Zhao, W. (2014). An Improved Genetic Algorithm for Optimal Stationary Energy Storage System Locating and Sizing. *Energies* 7 (10), 6434–6458. doi:10.3390/en7106434

Wang, Y., Wu, L., and Yuan, X. (2010). Multi-objective Self-Adaptive Differential Evolution with Elitist Archive and Crowding Entropy-Based Diversity Measure. *Soft Comput.* 14 (3), 193–209. doi:10.1007/s00500-008-0394-9

Wong, L. A., Ramachandaramurthy, V. K., Walker, S. L., Taylor, P., and Sanjari, M. J. (2019). Optimal Placement and Sizing of Battery Energy Storage System for Losses Reduction Using Whale Optimization Algorithm. *J. Energ. Storage.* 26, 100892. doi:10.1016/j.est.2019.100892

Wu, T., Shi, X., Liao, L., Zhou, C., Zhou, H., and Su, Y. (2019). A Capacity Configuration Control Strategy to Alleviate Power Fluctuation of Hybrid Energy Storage System Based on Improved Particle Swarm Optimization. *Energies* 12 (4), 642. doi:10.3390/en12040642

Yang, B., Wang, J., Chen, Y., Li, D., Zeng, C., Guo, Z., et al. (2020). Optimal Sizing and Placement of Energy Storage System in Power Grids: a State-Of-The-Art

One-Stop Handbook. *J. Energ. Storage.* 32, 101814. doi:10.1016/j.est.2020.101814

Yu, H., Tarsitano, D., Hu, X., and Cheli, F. (2016). Real Time Energy Management Strategy for a Fast Charging Electric Urban Bus Powered by Hybrid Energy Storage System. *Energy* 112, 322–331. doi:10.1016/j.energy.2016.06.084

Zhang, X. S., Yu, T., Yang, B., and Cheng, L. F. (2017). Accelerating Bio-Inspired Optimizer with Transfer Reinforcement Learning for Reactive Power Optimization. *Knowledge-Based Syst.* 116, 26–38. doi:10.1016/j.knosys.2016.10.024

Zhou, B., Fang, J. K., Ai, X. M., Yang, C. X., Yao, W., and Wen, J. Y. (2021). Dynamic Var Reserve-Constrained Coordinated Scheduling of LCC-HVDC Receiving-End System Considering Contingencies and Wind Uncertainties. *IEEE Trans. Sust. Energ.* 12 (01), 469–481. doi:10.1109/tste.2020.3006984

Conflict of Interest: Authors SP, XG, XiL, and XuL were employed by the company China Southern Power Grid Company Limited.

The remaining author declares that the research was conducted in the absence of any commercial or financial relationships that could be construed as a potential conflict of interest.

Publisher's Note: All claims expressed in this article are solely those of the authors and do not necessarily represent those of their affiliated organizations, or those of the publisher, the editors and the reviewers. Any product that may be evaluated in this article, or claim that may be made by its manufacturer, is not guaranteed or endorsed by the publisher.

Copyright © 2021 Peng, Gong, Liu, Lu and Ai. This is an open-access article distributed under the terms of the Creative Commons Attribution License (CC BY). The use, distribution or reproduction in other forums is permitted, provided the original author(s) and the copyright owner(s) are credited and that the original publication in this journal is cited, in accordance with accepted academic practice. No use, distribution or reproduction is permitted which does not comply with these terms.

GLOSSARY

BESSs battery energy storage systems

CRF capital recovery factor

DN distribution network

IPDM ideal-point decision method

MMSSA multi-objective memetic salp swarm algorithm

MOPSO multi-objective particle swarm optimization

O&M operation and maintenance

PV photovoltaic

RESs renewable energy sources

SOC state of charge

SSA salp swarm algorithm

TOU time of use

WT wind turbines

Variables

$P_{BESS,i}$ power capacity of the ith BESSs.

$E_{BESS,i}$ energy capacity of the ith BESSs.

$P_{cha,i}(t)$ charging power of the ith BESSs at time t

$P_{dis,i}(t)$ discharging power of the ith BESSs at time t

ρ_{loss} TOU electricity prices

$P_{loss}(t)$ power loss at time t

$P_{grid}(t)$ power fluctuation of the grid connection point at time t

x_{mi}^{j} positions of the ith follower salp in the mth salp chain

F_{m}^{j} position of food source

ω_{h} weights of the hth objective function

n population size of single salp chain

M the number of salp chains

$N_{\mathbf{r}}$ the maximum size of the repository

frontiers in Energy Research

ORIGINAL RESEARCH
published: 28 July 2021
doi: 10.3389/fenrg.2021.727949

A Comprehensive Study on Maximum Power Point Tracking Techniques Based on Fuzzy Logic Control for Solar Photovoltaic Systems

Tongsen Zhu, Jiayi Dong, Xingshuo Li and Shuye Ding*

School of Electrical and Automation Engineering, Nanjing Normal University, Nanjing, China

Maximum power point tracking (MPPT) methods based on fuzzy logic control (FLC) is a popular application in recent years. However, different kinds of fuzzy control methods lack comparative study, which led to confusion in practice. Hence, a comprehensive study on these methods is essential. Unfortunately, very few attempts have been made in this regard. In this paper, four FLC methods are selected for comparative analysis. Furthermore, the design details and experimental result will also be given to help choose and measure these methods, which presents a clear image of the technology of FLC based MPPT to readers.

Keywords: maximum power point tracking, fuzzy logic control, photovoltaic power system, control engineering, comparative study

OPEN ACCESS

Edited by:
Bo Yang,
Kunming University of Science and Technology, China

Reviewed by:
Xiaoyu Wang,
Xi'an Jiaotong University, China
Hongtao Tan,
Chongqing University, China

****Correspondence:***
Xingshuo Li
Xingshuo.Li@njnu.edu.cn

Specialty section:
This article was submitted to Smart Grids, a section of the journal Frontiers in Energy Research

Received: *20 June 2021*
Accepted: *01 July 2021*
Published: *28 July 2021*

Citation:
Zhu T, Dong J, Li X and Ding S (2021) A Comprehensive Study on Maximum Power Point Tracking Techniques Based on Fuzzy Logic Control for Solar Photovoltaic Systems. Front. Energy Res. 9:727949. doi: 10.3389/fenrg.2021.727949

1 INTRODUCTION

Due to the increasingly serious environmental problems, low carbon economy has received people's attention. Photovoltaic (PV) energy becomes a promising alternative as it is omnipresent, environment friendly, and has less operational and maintenance costs. An efficient maximum power point tracking (MPPT) technique is necessary that is expected to track the maximum power point (MPP) at all environmental conditions and then force the PV system to operate at that MPP (Sivakumar et al., 2015; Saravanan and Ramesh Babu, 2016; Kandemir et al., 2017; Al-Dhaifallah et al., 2018; Yang et al., 2018a; Yang et al., 2018b; Li X. et al., 2019a; Yang et al., 2019a; Li X. et al., 2019b; Yang et al., 2019b; Yang et al., 2019c; Li S. et al., 2020; Yang et al., 2020b; Eltamaly, 2021; Li F. et al., 2021).

In recent years, many advanced control techniques have been associated with the MPPT control such as fuzzy logic control (FLC) in order to increase the efficiency of solar panels. Several FLC methods are compared and reviewed in the literature (Dounis et al., 2013; Boukenoui et al., 2016; Kwan and Wu, 2016; Ouchen et al., 2016; Mohamed et al., 2017; Nabipour et al., 2017; Yilmaz et al., 2018; Youssef et al., 2018; Li X. et al., 2019c; Loukil et al., 2020; Verma et al., 2020; Jin et al., 2021; Rajesh et al., 2021; Tang et al., 2021). In this paper, four FLC methods are selected for comparative analysis. Then, comprehensive study has been made to compare the FLC methods regarding their features of input variables. Furthermore, the control effect has also been studied. Finally, the correctness of the conclusion is verified by simulation and experiment.

The paper is organized as follows. In **Section 2**, FLC MPPT techniques are extracted from a vast literature survey. Then, the comparative analysis of the four methods will be verified by experiments in **Section 3**. The concluding remarks are presented in **Section 4**.

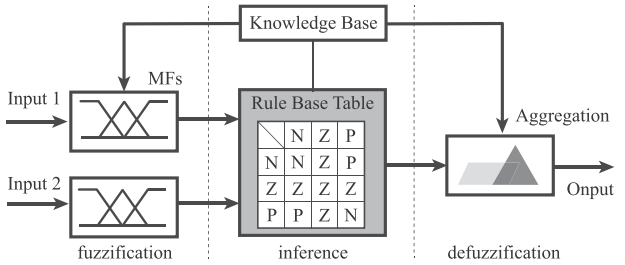


FIGURE 1 | The work progress of a FLC method.

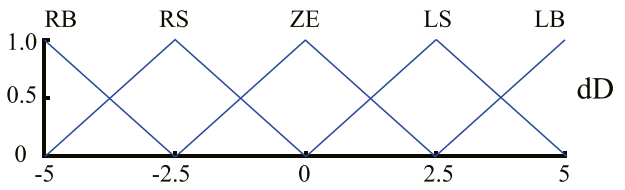


FIGURE 2 | The output of all FLC methods.

2 REVIEW OF MPPT ALGORITHMS BASED ON FUZZY LOGIC CONTROL

Generally, three stages can be identified in FLC MPPT's control **Figure 1**. In the first stage, the numerical input variables are converted into equivalent linguistic variables as input fuzzy sets. In the second stage, the input fuzzy sets are calculated into output fuzzy sets through the inference with the fuzzy rule base table. In the last stage, the output fuzzy sets are converted back to numerical variables as the output.

On the other hand, the design of FLC method is also divided into three stages. Firstly, the input variables should be selected to identify the position of work power point (WPP) related to MPP, and the output variable should be chosen to execute the command of the controller. After that, the rules of FLC methods should be set based on the study of PV characteristics. Finally, the parameters of FLC methods should be configured on the basis of the variable characteristic.

In FLC, the values of variable are expressed of linguistic variables such as PB (positive big), PS (positive small), ZE (zero), NS (negative small), and NB (negative big) using basic fuzzy subset. Each of these acronyms is defined by mathematical membership functions (MFs). Moreover, the setting of parameters involves two aspects: ranges and adjustments.

According to the consultation of other literature data and personal summary, four extant methods of fuzzy controls are compared. In addition, for ease of comparison, the output variable of the four methods should be consistent. The difference of duty cycle (dD) is the universal choice, and the range and parameters of dD are same in different methods (Rezk and Eltamaly, 2015). And boost circuit is chosen as the DC-DC converter. dD are expressed of linguistic variables such as LB (left big), LS (left small), ZE (zero), RS (right small), and RB (right big) using basic fuzzy subset, as shown in **Figure 2**.

TABLE 1 | The rules of dP&dV method.

		dP				
		NB	NS	ZE	PS	PB
dV	NB	RB	RS	ZE	LS	LB
	NS	RS	RS	ZE	LS	LS
	ZE	RS	ZE	ZE	ZE	LS
	PS	LS	LS	ZE	RS	RS
	PB	LB	LS	ZE	RS	RB

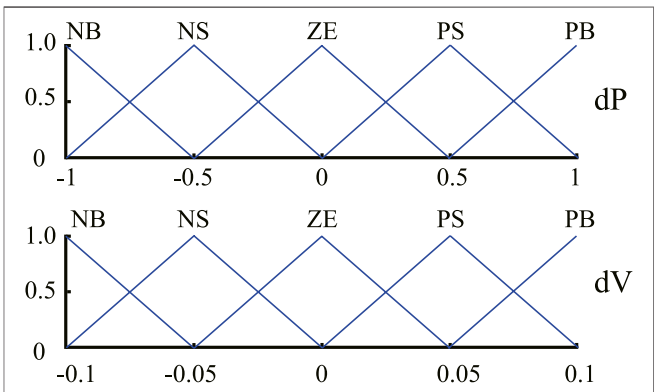


FIGURE 3 | The MFs of dP&dV method.

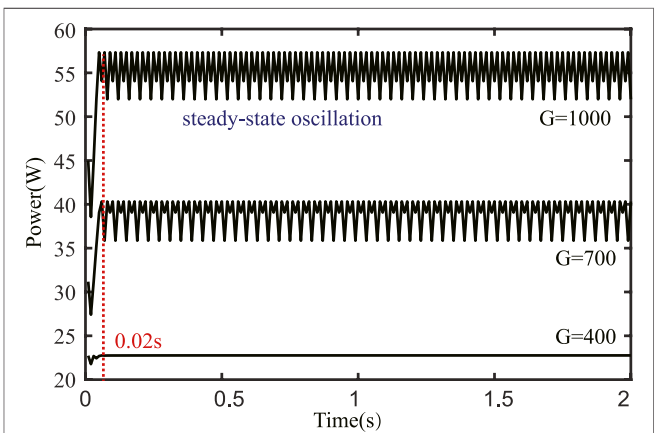


FIGURE 4 | The tracking effect of dP&dV method.

2.1 dP&dV Method and dP&dI Method

The dP&dV method is one of the most widely used in the industry (Boukenoui et al., 2017; Farajdadian and Hassan Hosseini, 2019). For the dP&dV method, the first and second inputs refer to **Eqs. 1**, **2**, respectively.

$$dP(k) = P(k) - P(k-1) \tag{1}$$

$$dV(k) = V(k) - V(k-1) \tag{2}$$

where $P(k)$ and $V(k)$ are PV output power and voltage, respectively at time k. According to the principle of dP&dV method, the basic operation principle can be expressed by:

TABLE 2 | The rules of dP&dI method.

		dP				
		NB	NS	ZE	PS	PB
dI	NB	LB	LS	ZE	RS	RB
	NS	LS	LS	ZE	RS	RS
	ZE	LS	ZE	ZE	ZE	RS
	PS	RS	RS	ZE	LS	LS
	PB	RB	RS	ZE	LS	LB

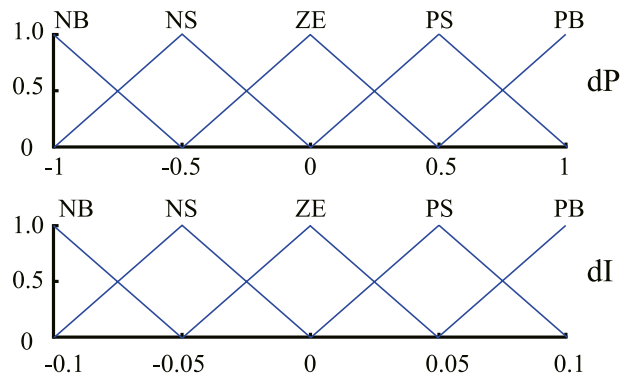


FIGURE 5 | The MFs of dP&dI method.

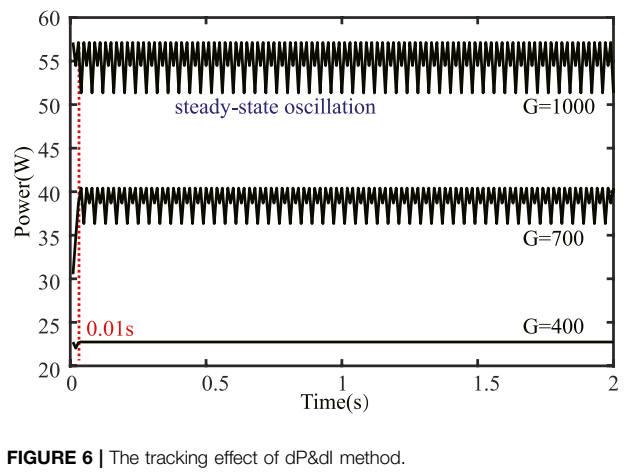


FIGURE 6 | The tracking effect of dP&dI method.

$$\begin{cases} dP > 0,\ dV > 0 \text{ or } dP < 0,\ dV < 0 & \text{Left of MPP} \\ dP > 0,\ dV < 0 \text{ or } dP < 0,\ dV > 0 & \text{Right of MPP} \end{cases} \tag{3}$$

Based on **Eqs. 1**–**3**, fuzzy rules are summarized in **Table 1**, and the MFs of dP and dV is shown as **Figure 3**.

As shown in **Figure 4**, the steady-state oscillation is significant when the irradiation is large. On the contrary, the steady-state oscillation disappears when the solar irradiance level is low. The tracking speed of this method is relatively fast, which helps to keep up with PV changes quickly.

The dP&dI method is another popular method, which is similar to the dP&dV method. For the dP&dV method, the first and second inputs refer to **Eqs. 4**, **5**, respectively.

TABLE 3 | The rules of E&dE method.

		E				
		NB	NS	ZE	PS	PB
dE	NB	ZE	ZE	ZE	ZE	ZE
	NS	LS	LS	ZE	RS	RS
	ZE	LB	LS	ZE	RS	RB
	PS	LS	LS	ZE	RS	RS
	PB	ZE	ZE	ZE	ZE	ZE

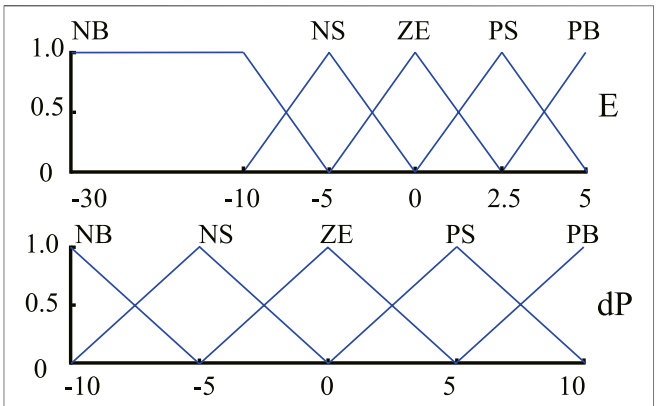


FIGURE 7 | The MFs of E&dE method.

$$dP(k) = P(k) - P(k-1) \tag{4}$$

$$dI(k) = I(k) - I(k-1) \tag{5}$$

where $P(k)$ and $I(k)$ are PV output power and voltage, respectively at time k. According to the principle of dP&dI method, the operation principle can be expressed by:

$$\begin{cases} dP > 0,\ dI < 0 \text{ or } dP < 0,\ dV > 0 & \text{Left of MPP} \\ dP > 0,\ dI > 0 \text{ or } dP < 0,\ dI < 0 & \text{Right of MPP} \end{cases} \tag{6}$$

Based on **Eqs 4**–**6**, fuzzy rules are summarized in **Table 2**, and the MFs of dP and dI is shown as **Figure 5**.

As shown in **Figure 6**, the steady-state oscillation is hard when the irradiation is large. On the contrary, the steady-state oscillation disappears when the irradiance decreases. The tracking speed of this method is relatively faster, which help to keep up with PV changes quickly.

The characteristics of the two methods can be summarized as follow:

- The control logic is simple and rules are easy to design.
- It is easy to produce steady-state oscillation.
- The tracking speed of the two methods is faster.

2.2 E&dE Method

For the E&dE method, the first and second inputs refer to **Eqs. 7**, **8**, respectively (Danandeh and Mousavi G, 2018; Bhukya and Nandiraju, 2020).

$$E(k) = \frac{dP}{dV} = \frac{P(k) - P(k-1)}{V(k) - V(k-1)} \tag{7}$$

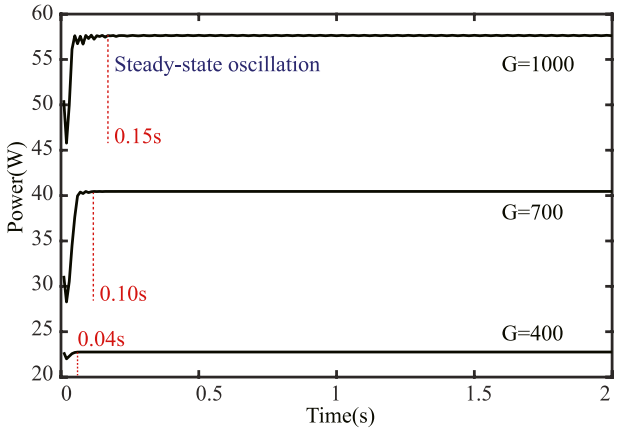


FIGURE 8 | The tracking effect of E&dE method.

$$dE(k) = E(k) - E(k-1) \tag{8}$$

where $P(k)$ and $V(k)$ are PV output power and voltage respectively at time k. According to the principle of E&dE method, the operation principle can be expressed by:

$$\begin{cases} E > 0 \text{ Left of MPP} \\ E < 0 \text{ Right of MPP} \end{cases} \tag{9}$$

Based on **Eqs. 7–9**, fuzzy rules are summarized in **Table 3**, and the MFs of E and dE is shown as **Figure 7**.

As shown in **Figure 8**, the steady-state oscillation still exists and is mainly decided by the solar exposure level. The tracking speed of this method is relatively slower, which is not suitable to cope with the rapid change of irradiation.

The characteristics of E&dE method can be summarized as follow:

- The tracking speed of the two methods is faster. The control logic is simple and rules are easy to design.
- The steady-state oscillation is slight.
- The tracking speed of E&dE method is slow.

2.3 G&F Method

For the G&F method, the first and second inputs refer to **Eq. 10** (Chen Y.-T. et al., 2016).

$$\begin{cases} G = 1 - \left|\frac{dI}{dV}\right| \Big/ \left|\frac{I}{V}\right| \\ F = 1 - \left|\frac{I}{V}\right| \Big/ \left|\frac{dI}{dV}\right| \end{cases} \tag{10}$$

According to the principle of G&F method, the operation principle can be expressed by:

$$\begin{cases} G > 0 \text{ and } F < 0 & \text{Left of MPP} \\ F > 0 \text{ and } G < 0 & \text{Right of MPP} \end{cases}$$

According to the above formulas, fuzzy rules can be designed, as shown in **Table 4**, and the MFs of G and F is shown as **Figure 9**.

TABLE 4 | The rules of G&F method.

		G				
		NB	NS	ZE	PS	PB
F	NB			ZE	RS	RB
	NS			ZE	RS	RS
	ZE	ZE	ZE	ZE	ZE	ZE
	PS	LS	LS	ZE		
	PB	LB	LS	ZE		

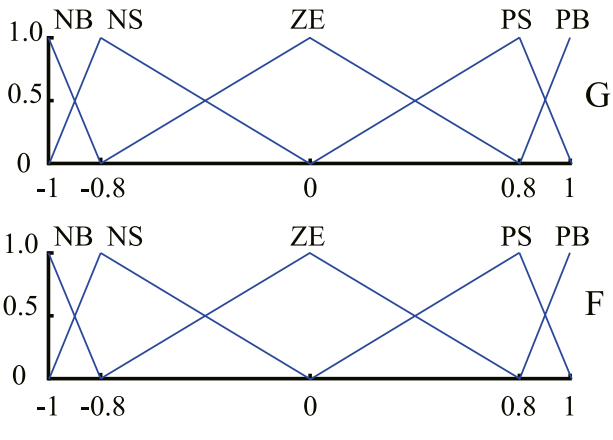


FIGURE 9 | The MFs of G&F method.

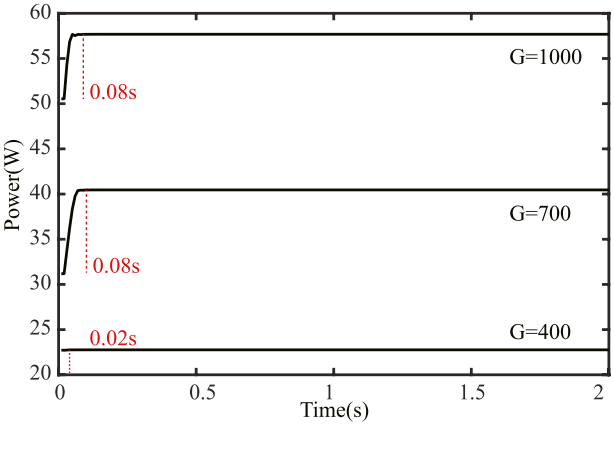


FIGURE 10 | The tracking effect of G&F method.

As shown in **Figure 10**, the steady-state oscillation is well canceled in this scheme. The tracking speed of this method is appropriate, which is enough to cope with the rapid change of irradiation.

The characteristics of E&dE method can be summarized as follow:

- The control logic is ingenious and rules are less.
- The steady-state oscillation is not found.
- The tracking speed of E&dE method is moderate.

TABLE 5 | The rules of β method.

β_{min}	PB			
β_{mid}	dP	dV		
β_{max}		NS	ZE	PS
	NS	NS	ZE	PS
	ZE	ZE	ZE	PS
	PS	PS	ZE	ZE
	NB			NS

2.4 The Composite Methods

After the combination of other control techniques, many FLC methods have been developed based on the above methods.

The beta-parameter based MPPT algorithm are derived from E&dE method (Li X. et al., 2019c). This method adds an input variable, β, to E&dE method, and changes the fuzzy rule based on the value of β, as shown in **Table 5**. The dilemma between the rules number and the universality for various operating conditions can be effectively solved with this new algorithm. In addition, it can simplify the Fuzzy rule membership functions since the number of fuzzy rules can be reduced.

The FLC-MPPT based on genetic algorithm and small-signal analysis are derived from dP&dV method (Mohamed et al., 2017). Then, proper FLC-MPPT control design was performed by means of combining genetic algorithm and the analytical design formulas. This method use the small-signal model with combination of a stochastic searching technique based on genetic algorithm to get the accurate design parameters of dP&dV method.

The FLC MPPT based on firefly algorithm are derived from dP&dV method (Farajdadian and Hassan Hosseini, 2019) This method utilize the firefly algorithm to design fuzzy controller membership functions for a better effectiveness. After optimizing the parameters by firefly algorithm, the MPPT method will have better dynamic performance and perform well at all irradiation levels.

Another MPPT method which is well adapted with microcontrollers is Neural networks (NN) method. Artificial neural network (ANN) emerged at the same time that fuzzy logic emerged and both are considered a part of soft computation. In complex neural networks, higher number of hidden layers are used. Number of layers and neurons of each layer and the functions employed in layers depend on user's knowledge. Input variables might be array parameters like V and I, weather information like temperature and solar irradiation or a combination of them. Output variable is usually duty cycle of the inverter.

3 SIMULATION RESULT AND EXPERIMENTAL EVALUATION

As shown in **Figure 11**, this experiment utilized Host PC, Real-Time Model Simulator (MT6016), Interface board, and Oscilloscope.

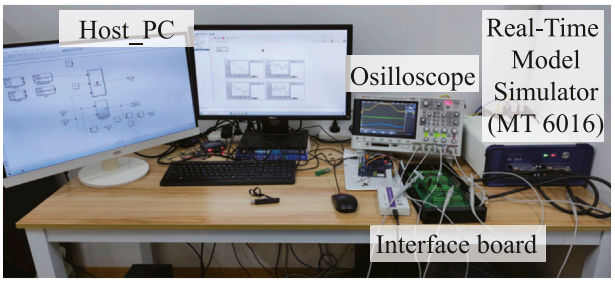


FIGURE 11 | Experimental platform.

TABLE 6 | Main parameters for EN50530 PV modules.

Parameter	Value
Maximum power, P_{mpp}	59.85 W
Voltage at MPP, V_{mpp}	17.1 V
Current at MPP, I_{mpp}	3.5 A
Open-circuit voltage, V_{oc}	21.1 V
Short-circuit current, I_{sc}	3.8 A
Temperature coefficient of V_{oc}	–80 mV/°C
Temperature coefficient of I_{sc}	0.065%/°C

TABLE 7 | Main parameters for the PV system.

Parameter	Value
Boost converter inductor, L	10^{-3} H
PV-side capacitor, C_{pv}	470^{-6} F
DC-link capacitor, C_{dc}	470^{-6} F
Load resistance, R_{load}	20 Ω
Switching frequency, f	20,000 Hz
Reference power, P_{limit}	40 W
Threshold power, dP_{th}	6 W
Simulation step size, $T_{control}$	10^{-4} s
Sampling step size, dT_{sample}	10^{-2} s

The PV model of EN50530 and boost converter are utilized in this experience (Chen P.-C. et al., 2015; Park and Choi, 2017; Ayop and Tan, 2018; Yang et al., 2020a; Li X. et al., 2021). **Table 6** lists main electrical parameters of the selected PV module in EN50530, and **Table 7** lists main electrical parameters of the PV system.

The results of the real-time simulation platform are consistent with the theoretical analysis. As shown in **Figure 12**, the tracking process of dP&dV method was successful in the whole process. However, with the irradiation intensifies, the oscillation becomes more obvious. This not only leads to the power loss, but also brings a large variation of voltage, which will seriously affect the power quality. Furthermore, the oscillation in E&dE and G&F methods is far smaller than the dP&dV method. The tracking speed of E&dE method is slower than that of the G&F method.

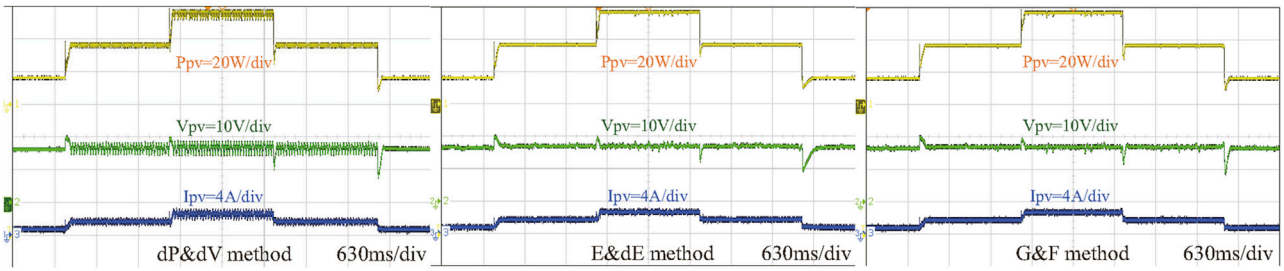


FIGURE 12 | The real-time experiences of all methods.

4 CONCLUSION

In this paper, four MPPT programs based FLC are compared. It can be concluded that, the selection of input variables determines the difficulty of the final control effects, based on the analysis of the design process and tracking effects. The correctness of the theoretical analysis is proved by simulation results and experiment evaluations.

However, this paper does not describes the MPPT progresses which combine FLC with other technologies in detail. Because, this paper focuses on the comparative analysis of the difference of basic FLC methods. The introduction of additional methods does not benefit comparative analysis.

DATA AVAILABILITY STATEMENT

The original contributions presented in the study are included in the article/Supplementary Material, further inquiries can be directed to the corresponding author.

AUTHOR CONTRIBUTIONS

TZ, JD, and XL contributed to conception and design of the study and wrote sections of the manuscript. TZ performed the statistical analysis and wrote the first draft of the manuscript. XL provides guidance. SD proof reading. All authors contributed to manuscript revision, read, and approved the submitted version.

REFERENCES

Al-Dhaifallah, M., Nassef, A. M., Rezk, H., Nisar, K. S., and Nisar, K. S. (2018). Optimal Parameter Design of Fractional Order Control Based INC-MPPT for PV System. *Solar Energy* 159, 650–664. doi:10.1016/j.solener.2017.11.040

Ayop, R., and Tan, C. W. (2018). Design of Boost Converter Based on Maximum Power Point Resistance for Photovoltaic Applications. *Solar Energy* 160, 322–335. doi:10.1016/j.solener.2017.12.016

Bhukya, L., and Nandiraju, S. (2020). A Novel Photovoltaic Maximum Power Point Tracking Technique Based on Grasshopper Optimized Fuzzy Logic Approach. *Int. J. Hydrogen Energy* 45 (16), 9416–9427. doi:10.1016/j.ijhydene.2020.01.219

Boukenoui, R., Ghanes, M., Barbot, J.-P., Bradai, R., Mellit, A., and Salhi, H. (2017). Experimental Assessment of Maximum Power Point Tracking Methods for Photovoltaic Systems. *Energy* 132, 324–340. doi:10.1016/j.energy.2017.05.087

Boukenoui, R., Salhi, H., Bradai, R., and Mellit, A. (2016). A New Intelligent MPPT Method for Stand-Alone Photovoltaic Systems Operating Under Fast Transient Variations of Shading Patterns. *Solar Energy* 124, 124–142. doi:10.1016/j.solener.2015.11.023

Chen, P.-C., Chen, P.-Y., Liu, Y.-H., Chen, J.-H., and Luo, Y.-F. (2015). A Comparative Study on Maximum Power Point Tracking Techniques for Photovoltaic Generation Systems Operating Under Fast Changing Environments. *Solar Energy* 119, 261–276. doi:10.1016/j.solener.2015.07.006

Chen, Y.-T., Jhang, Y.-C., and Liang, R.-H. (2016). A Fuzzy-Logic Based Auto-Scaling Variable Step-Size MPPT Method for PV Systems. *Solar Energy* 126, 53–63. doi:10.1016/j.solener.2016.01.007

Danandeh, M. A., and Mousavi G, S. M. (2018). A New Architecture of INC-Fuzzy Hybrid Method for Tracking Maximum Power Point in PV Cells. *Solar Energy* 171, 692–703. doi:10.1016/j.solener.2018.06.098

Dounis, A. I., Kofinas, P., Alafodimos, C., and Tseles, D. (2013). Adaptive Fuzzy Gain Scheduling PID Controller for Maximum Power Point Tracking of Photovoltaic System. *Renew. Energy* 60, 202–214. doi:10.1016/j.renene.2013.04.014

Eltamaly, A. M. (2021). A Novel Musical Chairs Algorithm Applied for MPPT of PV Systems. *Renew. Sustain. Energy Rev.* 146, 111135. doi:10.1016/j.rser.2021.111135

Farajdadian, S., and Hassan Hosseini, S. M. (2019). Design of an Optimal Fuzzy Controller to Obtain Maximum Power in Solar Power Generation System. *Solar Energy* 182, 161–178. doi:10.1016/j.solener.2019.02.051

Jin, J. X., Wang, J., Yang, R. H., Zhang, T. L., Mu, S., Fan, Y. J., et al. (2021). A Superconducting Magnetic Energy Storage With Dual Functions of Active Filtering and Power Fluctuation Suppression for Photovoltaic Microgrid. *J. Energy Storage* 38, 102508. doi:10.1016/j.est.2021.102508

Kandemir, E., Cetin, N. S., and Borekci, S. (2017). A Comprehensive Overview of Maximum Power Extraction Methods for PV Systems. *Renew. Sustain. Energy Rev.* 78, 93–112. doi:10.1016/j.rser.2017.04.090

Kwan, T. H., and Wu, X. (2016). Maximum Power Point Tracking Using a Variable Antecedent Fuzzy Logic Controller. *Solar Energy* 137, 189–200. doi:10.1016/j.solener.2016.08.008

Li, F., Lin, D., Tao, Y., Li, J., Wang, K., Zhang, X., et al. (2021). Adaptive Rapid Neural Optimization: A Data-Driven Approach to MPPT for Centralized TEG Systems. *Electr. Power Syst. Res.* 199, 107426. doi:10.1016/j.epsr.2021.107426

Li, S., Ping, A., Liu, Y., Ma, X., and Li, C. (2020). A Variable-Weather-Parameter MPPT Method Based on a Defined Characteristic Resistance of Photovoltaic Cell. *Solar Energy* 199, 673–684. doi:10.1016/j.solener.2020.02.065

Li, X., Wang, Q., Wen, H., and Xiao, W. (2019a). Comprehensive Studies on Operational Principles for Maximum Power Point Tracking in Photovoltaic Systems. *IEEE Access* 7, 121407–121420. doi:10.1109/access.2019.2937100

Li, X., Wen, H., Hu, Y., Du, Y., and Yang, Y. (2021). A Comparative Study on Photovoltaic MPPT Algorithms Under en50530 Dynamic Test Procedure. *IEEE Trans. Power Electron.* 36 (4), 4153–4168. doi:10.1109/tpel.2020.3024211

Li, X., Wen, H., Hu, Y., and Jiang, L. (2019b). A Novel Beta Parameter Based Fuzzy-Logic Controller for Photovoltaic MPPT Application. *Renew. Energy* 130, 416–427. doi:10.1016/j.renene.2018.06.071

Li, X., Wen, H., Hu, Y., and Jiang, L. (2019c). Drift-Free Current Sensorless MPPT Algorithm in Photovoltaic Systems. *Solar Energy* 177, 118–126. doi:10.1016/j.solener.2018.10.066

Loukil, K., Abbes, H., Abid, H., Abid, M., and Toumi, A. (2020). Design and Implementation of Reconfigurable MPPT Fuzzy Controller for Photovoltaic Systems. *Ain Shams Eng. J.* 11 (2), 319–328. doi:10.1016/j.asej.2019.10.002

Mohamed, A. A. S., Berzoy, A., and Mohammed, O. A. (2017). Design and Hardware Implementation of FL-MPPT Control of PV Systems Based on GA and Small-Signal Analysis. *IEEE Trans. Sustain. Energy* 8 (1), 279–290. doi:10.1109/tste.2016.2598240

Nabipour, M., Razaz, M., Seifossadat, S. G., and Mortazavi, S. S. (2017). A New MPPT Scheme Based on a Novel Fuzzy Approach. *Renew. Sustain. Energy Rev.* 74, 1147–1169. doi:10.1016/j.rser.2017.02.054

Ouchen, S., Betka, A., Abdeddaim, S., and Menadi, A. (2016). Fuzzy-Predictive Direct Power Control Implementation of a Grid Connected Photovoltaic System, Associated With an Active Power Filter. *Energy Convers. Manag.* 122, 515–525. doi:10.1016/j.enconman.2016.06.018

Park, J.-Y., and Choi, S.-J. (2017). A Novel Simulation Model for PV Panels Based on Datasheet Parameter Tuning. *Solar Energy* 145, 90–98. doi:10.1016/j.solener.2016.12.003

Rajesh, T., Gunapriya, B., Sabarimuthu, M., Karthikkumar, S., Raja, R., and Karthik, M. (2021). Frequency Control of PV-Connected Micro Grid System Using Fuzzy Logic Controller. *Mater. Today Proc.* 45, 2260–2264. International Conference on Advances in Materials Research - 2019. doi:10.1016/j.matpr.2020.10.255

Rezk, H., and Eltamaly, A. M. (2015). A Comprehensive Comparison of Different MPPT Techniques for Photovoltaic Systems. *Solar Energy* 112, 1–11. doi:10.1016/j.solener.2014.11.010

Saravanan, S., and Ramesh Babu, N. (2016). Maximum Power Point Tracking Algorithms for Photovoltaic System - A Review. *Renew. Sustain. Energy Rev.* 57, 192–204. doi:10.1016/j.rser.2015.12.105

Sivakumar, P., Abdul Kader, A., Kaliavaradhan, Y., and Arutchelvi, M. (2015). Analysis and Enhancement of PV Efficiency with Incremental Conductance MPPT Technique Under Non-Linear Loading Conditions. *Renew. Energy* 81, 543–550. doi:10.1016/j.renene.2015.03.062

Tang, L., Wang, X., Xu, W., Mu, C., and Zhao, B. (2021). Maximum Power Point Tracking Strategy for Photovoltaic System Based on Fuzzy Information Diffusion Under Partial Shading Conditions. *Solar Energy* 220, 523–534. doi:10.1016/j.solener.2021.03.047

Verma, P., Garg, R., and Mahajan, P. (2020). Asymmetrical Interval Type-2 Fuzzy Logic Control Based MPPT Tuning for PV System Under Partial Shading Condition. *ISA Trans.* 100, 251–263. doi:10.1016/j.isatra.2020.01.009

Yang, B., Wang, J., Zhang, X., Yu, T., Yao, W., Shu, H., et al. (2020a). Comprehensive Overview of Meta-Heuristic Algorithm Applications on PV Cell Parameter Identification. *Energy Convers. Manag.* 208, 112595. doi:10.1016/j.enconman.2020.112595

Yang, B., Wang, J., Zhang, X., Zhang, M., Shu, H., Li, S., et al. (2019a). MPPT Design of Centralized Thermoelectric Generation System Using Adaptive Compass Search Under Non-Uniform Temperature Distribution Condition. *Energy Convers. Manag.* 199, 111991. doi:10.1016/j.enconman.2019.111991

Yang, B., Yu, T., Shu, H., Zhu, D., An, N., Sang, Y., et al. (2018a). Energy Reshaping Based Passive Fractional-Order PID Control Design and Implementation of a Grid-Connected PV Inverter for MPPT Using Grouped Grey Wolf Optimizer. *Solar Energy* 170, 31–46. doi:10.1016/j.solener.2018.05.034

Yang, B., Yu, T., Shu, H., Zhu, D., An, N., Sang, Y., et al. (2018b). Perturbation Observer Based Fractional-Order Sliding-Mode Controller for MPPT of Grid-Connected PV Inverters: Design and Real-Time Implementation. *Control Eng. Pract.* 79, 105–125. doi:10.1016/j.conengprac.2018.07.007

Yang, B., Yu, T., Zhang, X., Li, H., Shu, H., Sang, Y., et al. (2019b). Dynamic Leader Based Collective Intelligence for Maximum Power Point Tracking of PV Systems Affected by Partial Shading Condition. *Energy Convers. Manag.* 179, 286–303. doi:10.1016/j.enconman.2018.10.074

Yang, B., Zhang, M., Zhang, X., Wang, J., Shu, H., Li, S., et al. (2020b). Fast Atom Search Optimization Based MPPT Design of Centralized Thermoelectric Generation System Under Heterogeneous Temperature Difference. *J. Clean. Prod.* 248, 119301. doi:10.1016/j.jclepro.2019.119301

Yang, B., Zhong, L., Zhang, X., Shu, H., Yu, T., Li, H., et al. (2019c). Novel Bio-Inspired Memetic Salp Swarm Algorithm and Application to MPPT for PV Systems Considering Partial Shading Condition. *J. Clean. Prod.* 215, 1203–1222. doi:10.1016/j.jclepro.2019.01.150

Yilmaz, U., Kircay, A., and Borekci, S. (2018). PV System Fuzzy Logic MPPT Method and PI Control as a Charge Controller. *Renew. Sustain. Energy Rev.* 81, 994–1001. doi:10.1016/j.rser.2017.08.048

Youssef, A., Telbany, M. E., and Zekry, A. (2018). Reconfigurable Generic FPGA Implementation of Fuzzy Logic Controller for MPPT of PV Systems. *Renew. Sustain. Energy Rev.* 82, 1313–1319. doi:10.1016/j.rser.2017.09.093

Conflict of Interest: The authors declare that the research was conducted in the absence of any commercial or financial relationships that could be construed as a potential conflict of interest.

Publisher's Note: All claims expressed in this article are solely those of the authors and do not necessarily represent those of their affiliated organizations, or those of the publisher, the editors and the reviewers. Any product that may be evaluated in this article, or claim that may be made by its manufacturer, is not guaranteed or endorsed by the publisher.

Copyright © 2021 Zhu, Dong, Li and Ding. This is an open-access article distributed under the terms of the Creative Commons Attribution License (CC BY). The use, distribution or reproduction in other forums is permitted, provided the original author(s) and the copyright owner(s) are credited and that the original publication in this journal is cited, in accordance with accepted academic practice. No use, distribution or reproduction is permitted which does not comply with these terms.

frontiers in Energy Research

BRIEF RESEARCH REPORT
published: 29 July 2021
doi: 10.3389/fenrg.2021.723775

Deep Learning-Based Prediction of Wind Power for Multi-turbines in a Wind Farm

Xiaojiao Chen[1], Xiuqing Zhang[1], Mi Dong[2], Liansheng Huang[1]*, Yan Guo[2] and Shiying He[1]*

[1]Institute of Plasma Physics, Chinese Academy of Sciences, Hefei, China, [2]School of Automation, Central South University, Changsha, China

The prediction of wind power plays an indispensable role in maintaining the stability of the entire power grid. In this paper, a deep learning approach is proposed for the power prediction of multiple wind turbines. Starting from the time series of wind power, it is present a two-stage modeling strategy, in which a deep neural network combines spatiotemporal correlation to simultaneously predict the power of multiple wind turbines. Specifically, the network is a joint model composed of Long Short-Term Memory Network (LSTM) and Convolutional Neural Network (CNN). Herein, the LSTM captures the temporal dependence of the historical power sequence, while the CNN extracts the spatial features among the data, thereby achieving the power prediction for multiple wind turbines. The proposed approach is validated by using the wind power data from an offshore wind farm in China, and the results in comparison with other approaches shows the high prediction preciseness achieved by the proposed approach.

Keywords: wind farm, wind turbine, convolutional neural network, long short-term memory network, spatiotemporal power prediction

OPEN ACCESS

Edited by:
Bo Yang,
Kunming University of Science and Technology, China

Reviewed by:
Zijian Wang,
Soochow University, China
Mingzhu Tang,
Changsha University of Science and Technology, China

****Correspondence:***
Mi Dong
mi.dong@csu.edu.cn
Liansheng Huang
huangls@ipp.ac.cn

Specialty section:
This article was submitted to Smart Grids, a section of the journal Frontiers in Energy Research

Received: *11 June 2021*
Accepted: *16 July 2021*
Published: *29 July 2021*

Citation:
Chen X, Zhang X, Dong M, Huang L, Guo Y and He S (2021) Deep Learning-Based Prediction of Wind Power for Multi-turbines in a Wind Farm. Front. Energy Res. 9:723775. doi: 10.3389/fenrg.2021.723775

INTRODUCTION

With the emphasis on environmental issues, developing clean energy represented by wind energy and solar energy (Yang et al., 2019a; Yang et al., 2020) is the direction of the energy revolution. In recent years, the solar energy has been rapidly developed (Yang et al., 2019b). The wind power has attracted much attention for its richer resources and efficient power generation technology (Liu et al., 2016). The Global Wind Energy Development Report 2019 shows that the newly installed capacity of global wind turbines in 2019 is 60.4 GW. Due to the randomness and uncertainty of the wind, the large-scale uncontrollable wind power could affect the stability of the power grid, when it is connected to the grid. The dispatch methods of wind farms are required to satisfy the power demand of the grid, which are mainly based on the average distribution method (Yang et al., 2021) and the proportional distribution method (Hazari et al., 2017) at present. However, the topographic effect, wake effect, turbulence intensity and other influencing factors in large wind farms make the wind captured by wind turbines vary at different locations (Song et al., 2021a). In order to avoid the instability of the power grid, for each wind turbine in a wind farm, its power distribution needs to be determined according to its own operating conditions, which requires the power prediction for each wind turbine (Song et al., 2021b).

In the past, there are two types of wind power prediction methods, including the physical method of analyzing the physical quantity to obtain the wind speed data and then converting it into the power data (Seo et al., 2019), and the statistical method for establishing wind power prediction models by collecting the historical data through the Supervisory Control and Data Acquisition system of wind

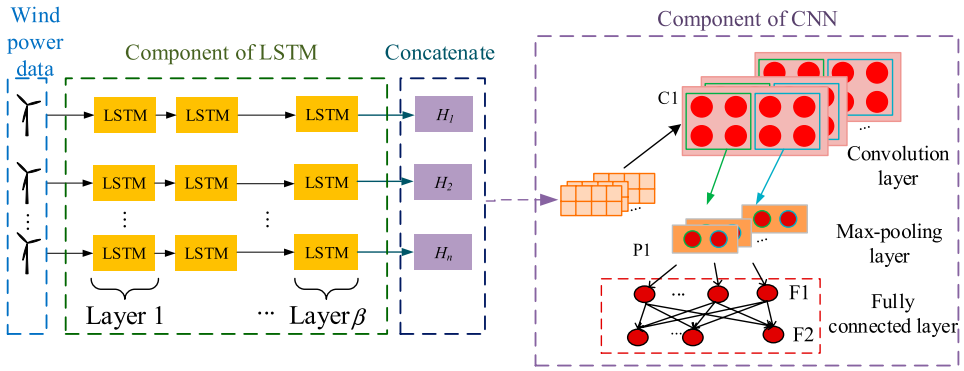


FIGURE 1 | The LSTM-CNN joint prediction model.

farms and then fitting curves. When most studies focus on predicting the total power of the wind farm or a single wind turbine, few studies aim at the prediction for the power of multiple wind turbines.

Making use of temporal correlation and spatial correlation (i.e., spatiotemporal correlation) in a wind farm could be helpful for multi-location wind power prediction (Jinfu et al., 2019). Since the wind faced by each wind turbine interacts in time and space, the power of a wind turbine is closely related to the wind at its location. In time, there is a certain correlation between the historical state of the wind at the same spatial point, that is, the temporal correlation; in space, winds in different spatial positions at the same time can also affect each other, that is, the spatial correlation. There could be a certain connection between the winds in different times and in different spaces, which is referred to as the spatiotemporal correlation. Nevertheless, it remains a challenge on how to combine the spatiotemporal correlation to solve the power prediction of multiple wind turbines in a wind farm.

In recent years, deep learning methods have been rapidly developed, and been recently used for the wind energy prediction. Compared with traditional machine learning methods, deep learning has better performance in terms of the feature extraction and model generalization. Among typical deep learning methods, Long Short-Term Memory Network (LSTM) shows the excellent performance when dealing with time series problems (Hochreiter and Schmidhuber, 1997), while Convolutional Neural Network (CNN) has an outstanding performance when processing data with spatial structure (Lecun et al., 2015). To take advantage of the spatiotemporal correlation, it is proposed a LSTM-CNN joint model for predicting the wind power of multiple wind turbines in this study. Specifically, LSTM captures the temporal dependence between the wind power data of each single wind turbine, and CNN extracts the spatial correlation between the wind power data of multiple wind turbines. In this way, the joint model learns the interaction between the winds in the wind farm and the wind dynamics with spatiotemporal properties, thus providing the precise prediction information for the wind turbines in the wind farm.

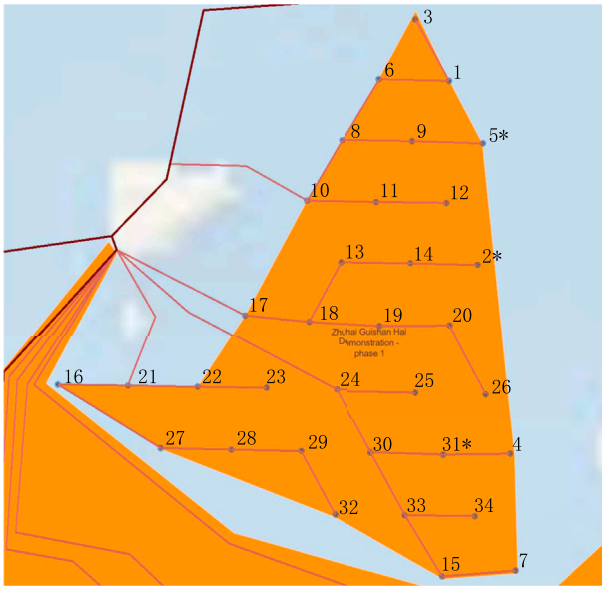


FIGURE 2 | Distribution map of Guishan offshore wind farm in Zhuhai.

The remainder of this paper is organized as follows. In **Section 2**, the LSTM-CNN power prediction model is explained. Experimental validation and result analysis are shown in the **Section 3**. Finally, **Section 4** concludes the paper.

THE PROPOSED LSTM-CNN JOINT PREDICTION MODEL

The difficulty of conducting the temporal-spatial sequence prediction, such as "wind turbine power prediction," is to simultaneously extract the time dependence and spatial features hidden in the data. After data preprocessing, the LSTM-CNN joint prediction model is proposed, which exploits a two-stage modeling strategy. In the first stage, the temporal features are extracted by the LSTM sub-model. In the

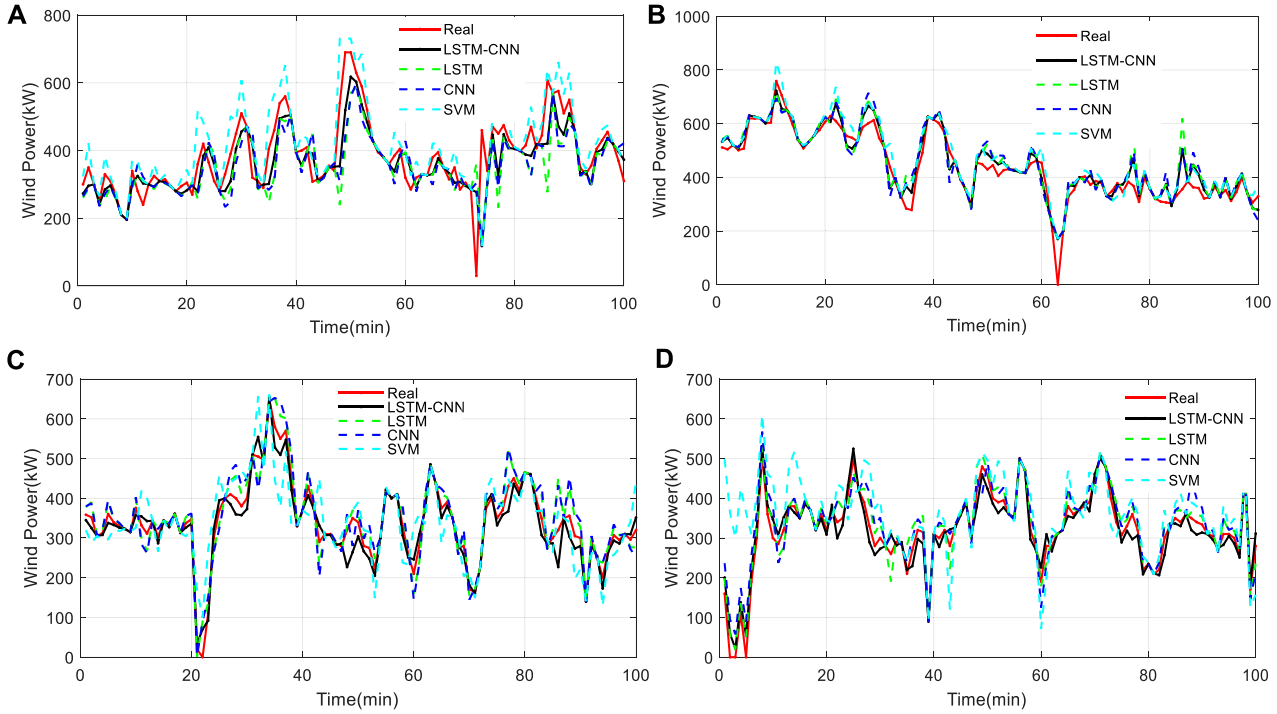


FIGURE 3 | Two-hour power prediction results for wind turbines: **(A)** #17; **(B)** #19; **(C)** #23; **(D)** #25.

second stage, the spatial correlation from the spatial matrix is determined by the CNN sub-model. On this basis, the algorithm training is explained.

Data Preprocessing

Giving that the neural network is very sensitive to the diversity of the input data, and that the uncertainty of the wind will cause outliers and noise in the power measurement data, the wind power data is preprocessed as follows:

$$S(x_i) = \frac{x_i - \mu}{\sigma} \tag{1}$$

Where, x_i represents the wind turbine power data at time i, the mean μ is calculated as:

$$\mu = \frac{1}{N}\sum_{i=1}^{N}(x_i) \tag{2}$$

And the standard deviation σ is calculated as:

$$\sigma = \sqrt{\frac{1}{N}\sum_{i=1}^{N}(x_i - \mu)^2} \tag{3}$$

Before establishing the model, the sets of input data and output data of the model are to be defined: assuming that $X_i = [x_{i1}, x_{i2}, x_{i3}, \ldots, x_{i(n-1)}, x_{in}]$ is the power measurement data of the ith wind turbine arranged in chronological order, taking α as the length of the sliding window, setting 1 as the step size of the sliding window, and using the sliding window sliding on the X_i to obtain the input data with the dimension of 1×α and compose the data set. Based on the sliding window length α, we take $S_{i1} = [x_{i1}, x_{i2}, x_{i3}, \ldots, x_{i\alpha}]$ as the first data in the input data set and $S_{i2} = [x_{i2}, x_{i3}, x_{i4}, \ldots, x_{i(\alpha+1)}]$ as the second data, and so on we get the processed historical power data of n wind turbines as the input set. Correspondingly, the output data set $Y_i = [x_{i(\alpha+1)}, x_{i(\alpha+2)}, x_{i(\alpha+3)}, \ldots\ldots, x_{in}]$ of each wind turbine can be obtained, and the values at the same moment of multiple turbines are formed a one-dimensional array $Y_p = [x_{1(\alpha+1)}, x_{2(\alpha+1)}, x_{3(\alpha+1)}, \ldots, x_{n(\alpha+1)}]$, which is the true value of the model output.

LSTM-CNN Joint Model

LSTM can effectively extract the data temporal dependence, has excellent performance in prediction on a variety of time scales, and can be trained by back-propagated through time algorithm. The CNN has the ability in processing the input in the form of two-dimensional images, and can meet the need to simultaneously predict the power of multiple wind turbines. As shown in **Figure 1**, the LSTM-CNN joint modelling is mainly divided into two stages, which are explained as follows.

In the first stage, the LSTM captures the temporal correlation in the data that has been preprocessed. Specifically, the processed power data of n wind turbines goes into n LSTM modules and each LSTM model is set to β layer. Each LSTM outputs a value. After concatenating and processing, the corresponding output values of each turbine are put into a two-dimensional matrix W_p according to the location of the wind turbines.

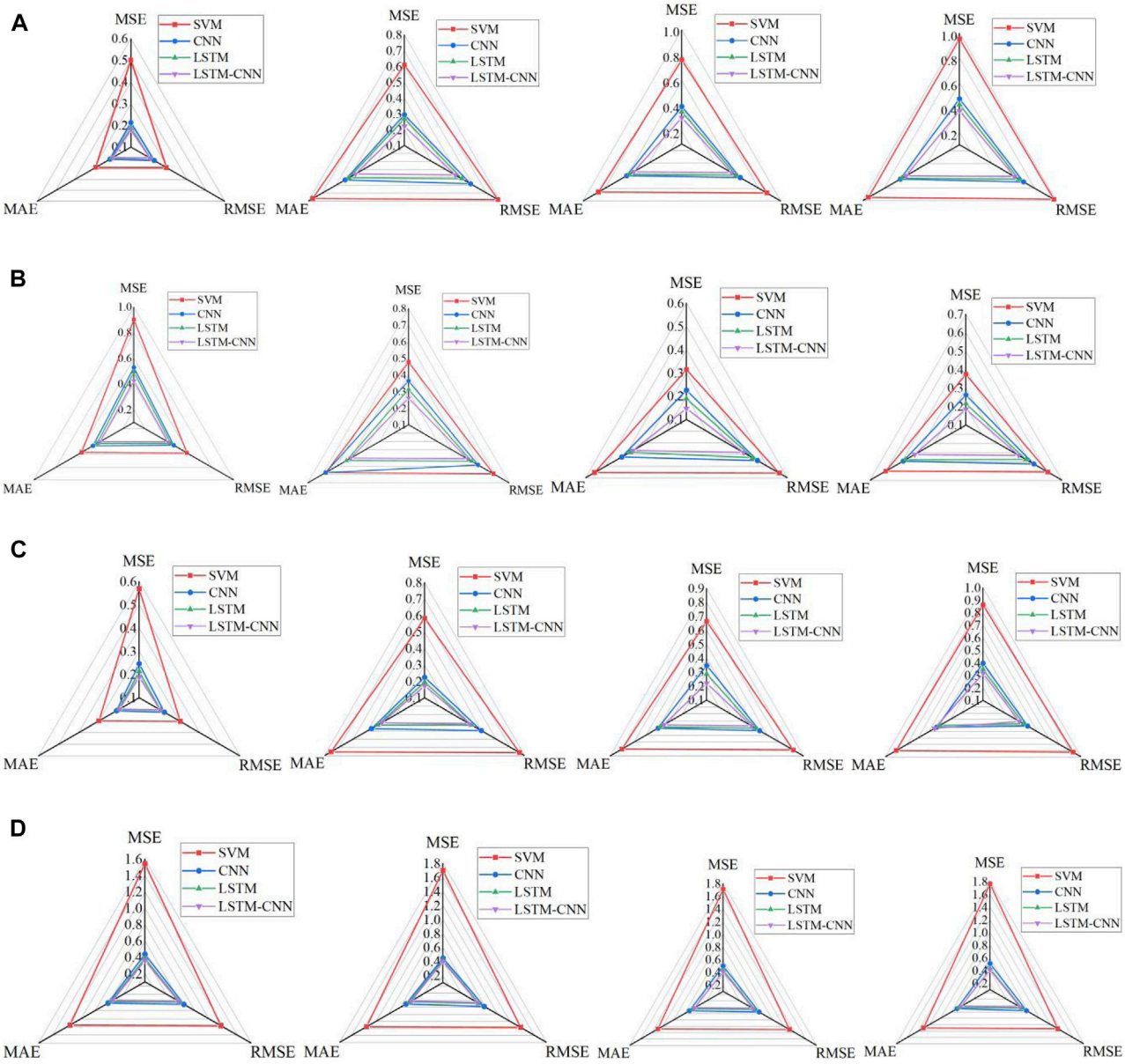


FIGURE 4 | Prediction results for the four wind turbines under different prediction steps: **(A)** step = 1; **(B)** step = 2; **(C)** step = 3; **(D)** step = 4.

In the second stage, the CNN is used to extract the spatial correlation stored in the matrix W_p. Starting from the input layer of CNN, the spatial features in the matrix W_p are captured by the convolution kernel to obtain a new feature map. The CNN will gradually extract the spatial information of the spatial power matrix after multiple convolution-pooling layer structures and output a one-dimensional vector in the final output layer as the actual output of the model. In this study, Rectified Linear Unit (ReLU) is selected as the activation function of the convolutional layer. As an unsaturated nonlinear function that can accelerate the convergence rate during training, ReLU can significantly improve the performance of CNN. The definition of ReLU is as follows:

$$g(x) = \begin{Bmatrix} x, x \geq 0 \\ 0, x < 0 \end{Bmatrix} \tag{4}$$

Algorithm Training

After establishing the joint model, a single loss function is used for end-to-end training. Because the power prediction can be regarded as a regression problem, the prediction goal is to minimize the error differentials between the model's output sequence and the true value. Therefore, the mean squared error (MSE) is selected as the loss function for model training, and its definition as follows:

$$L = \frac{1}{N}\sum_{i=1}^{N}\left(Y_p - \hat{Y}_p\right)^2 \quad (5)$$

Where, L is the loss function, N is the total number of samples, $\hat{Y}_p$ and Y_p are the predicted and true values, respectively.

The back-propagation rule and stochastic gradient descendant algorithm are adopted to train the entire network. The algorithms can automatically learn the rules of the network parameters to optimize the entire network, so that the output of the model can be closer to the true value. The error differential propagation starts from the last fully connected layer of the model through, i.e., propagating in the inverse time direction. Subsequently, the propagated error differentials pass through the entire CNN to the LSTM, and then backward propagate to the input layer of the entire model. In this way, the parameters of the model are iteratively updated according to the error differentials, and finally the optimal parameters are learned. In this process, the parameters of the entire model are supervised by the gradient-based training method. The prediction model integrates the learned spatiotemporal information and finally achieves the purpose of power prediction using the spatiotemporal correlation.

EXPERIMENTAL VALIDATIONS

Data Description

In this experiment, the SCADA data of 34 wind turbines at Guishan offshore wind farm in China within 1 wk of November 2019 was collected and used. The distribution of the wind farm is shown in **Figure 2**. All wind turbine models are exactly the same, and the time resolution of the data is 1 min. The single data set for the experiment contains a total of 20,160 frames. The data set is divided into three mutually exclusive subsets: training set, test set, and verification set. The training set and the test set account for the first 60 and 20% of the data set, respectively. The last 20% of the data set is used to evaluate the model's generalization ability. In order to achieve better results for the model, eight wind turbines with the closing distribution position in the wind farm are selected as the research objects, which are # 17, # 18, # 19, # 20, # 23, # 24, # 25, # 26, respectively.

Model Parameter Setting

First of all, a truncated normal distribution is used when initializing network parameters. Meanwhile, the Adam algorithm is selected as the optimization function of the model, of which the learning rate is set to 0.01, and the iteration is 100 times.

In the model, the length of the sliding window to obtain the input sequence (i.e., α) directly affects the effect of LSTM on the temporal correlation extraction of historical sequence data. If α is too small, the time features included in the input sequence are insufficient, which affect the prediction accuracy of the model. If α is too large, it makes the structure of the model complicated and training more difficult. Considering the above two aspects comprehensively, and through a large number of experimental tests, α is finally selected to be 20.

Then, the number of LSTM models is set to 8, which is the same as the quantity of the selected wind turbines. In order to extract the temporal features, the number of LSTM layers β is set to 2. In the merge processing module of the joint model, the output data of #17, #18, #19, #20 are put on the first row of W_p, and the output data of #23, #24, #25, #26 on the second row. By doing so, a two-dimensional spatial matrix W_p is obtained. Since W_p is just a matrix of (2, 4) shape, the contained features are not complicated, so only one convolution layer C1 is used in the CNN model.

Lastly, the convolution kernels' number of the convolutional layer is set to 32. Each convolution kernel is a two-dimensional matrix with a height and width of 2. The edge of the input image is filled with a size of 1, and the input is convolved with a step size of 1. The first layer of convolutional layer C1 outputs a convolutional image of size (2, 4, 32), which is used as the input of the pooling layer P1. In this study, the maximum pooling method is selected, that is, the P1 layer is the Max Pooling layer, the pooling core size of P1 is set to 2 × 2, and the step size is 2. When the output of C1 reaches P1, P1 outputs a result of shape (1, 2, 32). Subsequently, pass it to the fully connected layers F1 and F2. The F1 input dimension is set to 1 * 2 * 32 = 64, the output dimension is set to 100, and the F2 input dimension and output dimension are set to 100 and 8, respectively.

Experimental Results

In order to verify the comprehensive performance of the established model, three algorithms are selected and developed for comparison, including Support Vector Machine (SVM), LSTM and CNN. The three models have been trained separately, and the models having the best performance are saved. The data of four wind turbines, # 17, # 19, # 23 and # 25, are selected to discuss, and the predicted wind power of the four models are obtained.

The predicted value and the real values of the 2 h are plotted in **Figure 3**. As seen from **Figure 3**, the prediction curve of the LSTM-CNN joint model is closer to the true value than the other three prediction algorithms. To be specific, the LSTM effectively extracts the time correlation, and it also has good prediction performance. By comparison, the CNN and SVM perform poorly. The reason is that, when facing the problem of power prediction of multiple wind turbines, the CNN can effectively capture the spatial features of the data, but it does not take the temporal correlation into account. Similarly, the LSTM has excellent performance when facing timing prediction problems, but ignores the spatial features. Since the SVM only uses the global spatial and temporal information in the data, its prediction preciseness is noticeably lower than the three counterparts.

To further evaluate the performance of different prediction methods, the widely used performance indicators are used and calculated: root mean squared error (RMSE) and mean absolute error (MAE), and MSE. The data of the last 2 h in the prediction data obtained from the test set is selected and divided into four steps to evaluate the four models. That is, let k be the number of steps, and obtain 30-min prediction data at each step to compare with the comparison algorithm. The results of performance indicators are shown in **Figure 4**, from which the observations can be summarized as two aspects. On the one side, with the increase of the prediction step, the prediction effect of each model all decreases. Specifically, the SVM declines fastest, followed by CNN, LSTM, and the last comes the LSTM -CNN joint model.

On the other side, for the four prediction models, the MSE, RMSE, and MAE of the LSTM-CNN joint model are lower than the other three models, and the LSTM-CNN joint model has the best performance when facing the problem of prediction for power of multiple wind turbines at different locations.

To sum up, the proposed LSTM-CNN joint model making full use of high-level spatiotemporal features, is capable of simultaneously predicting the power of multiple wind turbines in terms of its two-stage structure. The input data of LSTM is a one-dimensional array of a specific length and multiple LSTMs are simultaneously operated to complete the extraction of the temporal features of the wind turbines in different locations, so that the temporal correlation in the time series can be fully extracted. After extracting time features by LSTM, a spatial power matrix is concatenated, in which the spatial features are captured by CNN, and thus the prediction task is successfully fulfilled.

CONCLUSION

The proposed prediction model is based on the modeling idea of "capturing temporal dependence first and then extracting spatial features." Composed of LSTM and CNN, the model was trained end-to-end by a unified loss function. The trained model can extract high-level spatiotemporal features from the historical power data of wind turbines, so as to achieve the purpose of simultaneously predicting the power of wind turbines at different locations. The measured data of an offshore wind farm in China was used for simulation experiments and the real values were compared with the predicted values of the model. The comparison results showed that the proposed method has more excellent performance than the existing prediction methods, such as LSTM, CNN, and SVM. With the proposed model, it is possible to precisely predict the wind power of multiple wind turbine within a wind farm with the regular layout. On this basis, it can be performed the accurate power scheduling, which is the future research direction.

DATA AVAILABILITY STATEMENT

The raw data supporting the conclusions of this article will be made available by the authors, without undue reservation.

AUTHOR CONTRIBUTIONS

XC: Methodology, Software, Validation, Writing- Original draft preparation, Writing- Reviewing and Editing. XZ: Methodology, Writing- Original draft preparation. MD: Methodology, Supervision. LH: Conceptualization, Supervision. YG: Test, Validation, Investigation. SH: Test, Writing-Reviewing and revise grammar and correct expression.

FUNDING

This work was supported in part by the Major Science and Technology Projects in Anhui Province under Grant 202003a05020019, and in part by the Comprehensive Research Facility for Fusion Technology under Grant 2018-000052-73-01-001228.

REFERENCES

Hazari, M., Mannan, M., Muyeen, S., Umemura, A., Takahashi, R., and Tamura, J. (2017). Stability Augmentation of a Grid-Connected Wind Farm by Fuzzy-Logic-Controlled DFIG-Based Wind Turbines. *Appl. Sci.* 8, 20. doi:10.3390/app8010020

Hochreiter, S., and Schmidhuber, J. (1997). Long Short-Term Memory. *Neural Comput.* 9 (8), 1735–1780. doi:10.1162/neco.1997.9.8.1735

Jinfu, C., Qiaomu, Z., Dongyuan, S., et al. (2019). A Multi-step Wind Speed Prediction Model for Multiple Sites Leveraging Spatio-Temporal Correlation. *Proc. CSEE* 39 (17), 2093–2105. doi:10.13334/j.0258-8013.pcsee.180897

Lecun, Y., Bengio, Y., and Hinton, G. (2015). Deep Learning. *Nature* 521 (7553), 436–444. doi:10.1038/nature14539

Liu, Bo., He, Zhijia., and Jin, Hao. (2016). Current Status and Development Trend of Wind Power Generation. *J. Northeast Dianli Univ.* 36 (02), 7–13. doi:10.19718/j.issn.1005-2992.2016.02.002

Seo, S., Oh, S.-D., and Kwak, H.-Y. (2019). Wind Turbine Power Curve Modeling Using Maximum Likelihood Estimation Method. *Renew. Energ.* 136 (JUN), 1164–1169. doi:10.1016/j.renene.2018.09.087

Song, D., Chang, Q., Zheng, S., Yang, S., Yang, J., and Hoon Joo, Y. (2021a). Adaptive Model Predictive Control for Yaw System of Variable-Speed Wind Turbines. *J. Mod. Power Syst. Clean. Energ.* 9 (1), 219–224. doi:10.35833/mpce.2019.000467

Song, D., Zheng, S., Yang, S., Yang, J., Dong, M., Su, M., et al. (2021b). Annual Energy Production Estimation for Variable-Speed Wind Turbine at High-Altitude Site. *J. Mod. Power Syst. Clean. Energ.* 9 (3), 684–687. doi:10.35833/MPCE.2019.000240

Yang, B., Wang, J., Zhang*, X., Yu, T., Yao, W., Shu, H., et al. (2020). Comprehensive Overview of Meta-Heuristic Algorithm Applications on Pv Cell Parameter Identification. *Energ. Convers. Manage.* 208, 112595. doi:10.1016/j.enconman.2020.112595

Yang, B., Yu, T., Zhang*, X., Li, H., Shu, H., Sang, Y., et al. (2019a). Dynamic Leader Based Collective Intelligence for Maximum Power point Tracking of PV Systems Affected by Partial Shading Condition. *Energ. Convers. Manage.* 179, 286–303. doi:10.1016/j.enconman.2018.10.074

Yang, B., Zhong, L., Zhang, X., Shu, H., Yu, T., Li, H., et al. (2019b). Novel Bio-Inspired Memetic Salp Swarm Algorithm and Application to MPPT for PV Systems Considering Partial Shading Condition. *J. Clean. Prod.* 215, 1203–1222. doi:10.1016/j.jclepro.2019.01.150

Yang, J., Fang, L., Song, D., Su, M., Yang, X., Huang, L., et al. (2021). Review of Control Strategy of Large Horizontal-axis Wind Turbines Yaw System. *Wind Energy* 24 (2), 97–115. doi:10.1002/we.2564

Conflict of Interest: The authors declare that the research was conducted in the absence of any commercial or financial relationships that could be construed as a potential conflict of interest.

Publisher's Note: All claims expressed in this article are solely those of the authors and do not necessarily represent those of their affiliated organizations, or those of the publisher, the editors and the reviewers. Any product that may be evaluated in this article, or claim that may be made by its manufacturer, is not guaranteed or endorsed by the publisher.

Copyright © 2021 Chen, Zhang, Dong, Huang, Guo and He. This is an open-access article distributed under the terms of the Creative Commons Attribution License (CC BY). The use, distribution or reproduction in other forums is permitted, provided the original author(s) and the copyright owner(s) are credited and that the original publication in this journal is cited, in accordance with accepted academic practice. No use, distribution or reproduction is permitted which does not comply with these terms.

frontiers in Energy Research

MINI REVIEW
published: 30 July 2021
doi: 10.3389/fenrg.2021.724892

A Critical Survey on Renewable Energy Applications in the Philippines and China: Present Challenges and Perspectives

*Xin Li, Haizhi Wang, Yuanru Lu and Wanlin Li**

Law School, Kunming University of Science and Technology, Kunming, China

China's Belt and Road (B&R) initiative provides new ideas and opportunities for international cooperation. Renewable energy plays a crucial role not only in the national sustainable development framework of China and the Philippines but also in bilateral cooperation between them. However, some obstacles still need to be addressed because renewable energy cooperation between China and the Philippines has not been thoroughly and comprehensively studied to date. Based on an in-depth analysis of current renewable energy cooperation between China and the Philippines, this paper employs PESTEL analysis to fully investigate the cooperative advantages and disadvantages by considering politics (P), economy (E), society (S), technology (T), environment (E), and legislation (L) and proposes several constructive suggestions. The ultimate purpose was to design feasible schemes to ensure the sufficient utilization of renewable energy and the construction of integrated power grid systems to meet shortages of electricity supply especially in the isolated small islands in the Philippines through cooperation with China. In particular, it offers valuable advice concerning the U.S.-China trade war and COVID- 19 pandemic, outlining how cooperation in the exploitation of potential renewable energy is vital.

Keywords: the belt and road, the Philippines-China cooperation, renewable energy, PESTEL analysis, renewable energy cooperation

OPEN ACCESS

Edited by:
Yaxing Ren,
University of Warwick,
United Kingdom

Reviewed by:
Si Chen,
University of Glasgow,
United Kingdom
Youcai Liang,
South China University of Technology,
China

****Correspondence:***
Wanlin Li
karen_lee_lx@126.com

Specialty section:
This article was submitted to Sustainable Energy Systems and Policies, a section of the journal Frontiers in Energy Research

Received: *15 June 2021*
Accepted: *19 July 2021*
Published: *30 July 2021*

Citation:
Li X, Wang H, Lu Y and Li W (2021) A Critical Survey on Renewable Energy Applications in the Philippines and China: Present Challenges and Perspectives. Front. Energy Res. 9:724892. doi: 10.3389/fenrg.2021.724892

INTRODUCTION

In response to the advantages of renewable energy (Gullberg et al., 2014), many countries and regional organizations have entered into cooperative targeted renewable energy initiatives (Anand et al., 2021; Mohan, 2021; Sasmita and Sidhartha, 2021). Existing research on renewable cooperation (Feng et al., 2020) is mainly focused on a comprehensive analysis of the renewable energy cooperative mechanism between two countries (Suryanarayana and Saumendra, 2020), a country and regional organizations (Mehdi and Mehdi, 2020), and regional organizations (Indeo, 2019), by forecasting the potentiality of cooperation and undertaking analysis *via* a mathematical model (Satish and Vinod, 2020). However, three existing gaps need to be overcome.

- Most previous studies fail to comprehensively analyze the advantages and disadvantages of renewable energy cooperation between specific countries under B & R.
- Specific suggestions based on the effective factors of cooperation such as politics, economy, society, technology, environment, and legislation have not been proposed.

TABLE 1 | The Philippine installed capacity mix (MW) (The Department of Energy, 2019).

Fuel type time	Coal	Oil based	Nature gas	Renewable energy (share)	Geothermal	Hydro	Win d	Biomass	Solar	Total
2017	8,049	4,153	3,447	7,079 (31.1%)	1,916	3,618	427	224	885	22,728
2018	8,844	4,292	3,453	7,227 (30.3%)	1,944	3,701	427	258	896	23,815
2019	10,417	4,262	3,453	7,399 (28.9%)	1,928	3,760	427	363	921	25,531

- The latest factors, including the COVID-19 pandemic and the United States-China trade war, have not been addressed.

This paper focuses on the exploitation of renewable energy cooperation between China and the Philippines, proposing a new perspective in response to this new context and undertakes a comprehensive investigation of a cooperative scheme between two countries. Based on a systematic overview of renewable energy systems in China and the Philippines, including the current situation, existing problems, policies, and plans, the basis and challenges for further cooperation between the two countries are explored (*Renewable Energy Development in the Philippines* and *Renewable Energy Development Status in China* Sections).

The background informing this topic and existing renewable energy cooperation projects between China and the Philippines are addressed, and a Political, Economic, Social, Technological, Environmental, and Legal (PESTEL) analysis is adopted to illustrate the advantages and disadvantages of those factors in cooperation (*The Philippines—China Renewable Energy Cooperation Under Political, Economic, Social, Technological, Environmental, and Legal Analysis* Section);

Finally, some feasible and promising suggestions are proposed to deal with emerging problems and opportunities in renewable cooperation between China and the Philippines under B&R (*Political, Economic, Social, Technological, Environmental, and Legal Recommendations* Section).

RENEWABLE ENERGY DEVELOPMENT IN THE PHILIPPINES

Current Status

The Philippines stores rich renewable energy which also plays an important role in the energy supply of the country. As **Table 1** shows, although the proportion of renewable energy in the total amount of installed capacity is only about 30% and there has been a slight downward trend in the last 3 years, the quantity produced is still steadily growing.

Geothermal Energy

The Philippines is located in a tropical low-latitude area at the junction of Asia, Europe, and the Pacific plate, which means the country has rich geothermal energy resources. After many years of development, the installed capacity of geothermal power reached 1,944 MW in 2018, accounting for 13% of the world's total, and ranking third after the United States and Indonesia (Ratio et al., 2020).

Hydropower Energy

The Philippines has 421 rivers, numerous mountains, rugged terrain, and a rainy climate, which create abundant hydropower resources that contribute the largest portion of installed capacity generated by renewable energy. Although the Philippines already has some large-scale hydropower plants and has made achievements in the development of hydropower infrastructure, there is still 13,097 MW of undeveloped hydropower generation capacity remaining, according to an assessment by the Philippine Department of Energy (The Department of Energy, 2019).

Solar Energy

With solar radiation of 4.0–6.0 kWh/m2/day, the Philippines has abundant solar energy resources which evenly distribute across the country and vary between 10 and 20% every month (Sharma and Kolhe, 2020). Due to the continuous improvement of technology and efficiency of solar photovoltaic (PV) modules, the solar energy industry has achieved scale development and significantly reduced the costs of solar power generation (Sharma and Kolhe, 2020). More and more residents and industrial sectors in the Philippines have started to use small-scale solar PV production.

Problem and Causes

The continuous economic expansion of the Philippines has brought serious problems in the form of insufficient energy supply (Mondal et al., 2018). The Philippines' GDP in 2018 grew by 6.2%, exceeding 6% for the seventh consecutive year (GPD, 2019). However, more than 11% of the population has no electricity, and a higher proportion suffers from unreliable electricity supply (Bertheau et al., 2020).

Huge reserves and the potential of renewable energy resources have not achieved a satisfying development in the Philippines.

The main reasons for the insufficient utilization of renewable energy, include the fact that the development of renewable energy requires high prepayment and technology costs (Zafar et al., 2019). Moreover, hydropower and geothermal energy, which generate the most electricity, have a very long development cycle (Barroco and Herrera, 2019). Moreover, the Philippines is unable to form an integrated power grid system, which impacts the sufficient transmission of electricity generated by renewable energy. The Philippine power supply system is also divided into "on-grid" and "off-grid" areas. The on-grid is supplied by two separate main power grids which lack a connection with each other. The off-grid covers these areas but suffers from insufficient power or even no power supply at all (Bertheau et al., 2020).

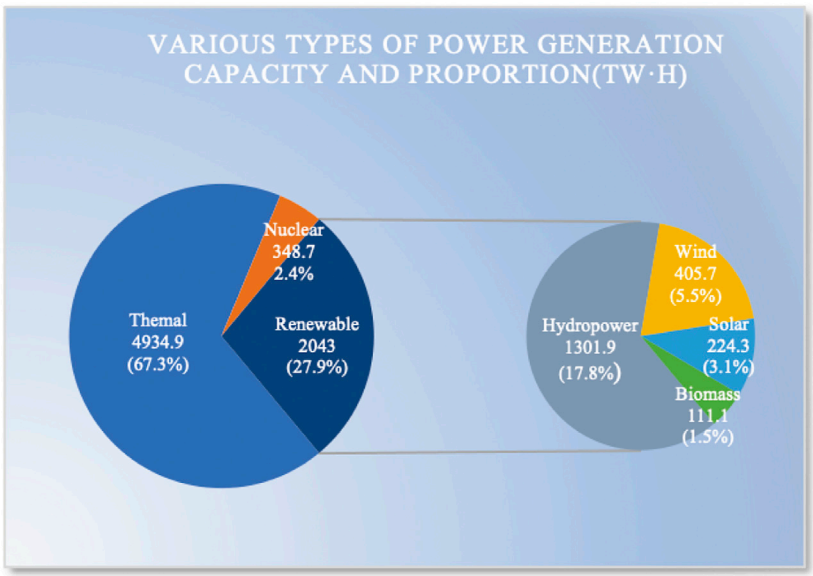


FIGURE 1 | Various types of power generation **(A)** installed capacity, and **(B)** proportion.

Policies and Plans

The Philippine government has realized the importance of developing renewable energy and has formulated several policies and plans based on the focuses: 1) ensuring energy security, 2) achieving optimal energy pricing, 3) diversifying fuel sources, and 4) developing sustainable energy systems (The Department of Energy, 2017). The National Renewable Energy Program (2011–2030) anticipates that the generation capacity of renewable energy will triple by 2030 (Wang et al., 2020) This has lead to the development of policies including carbon taxes, the improvement of energy efficiency in both generation and consumption, diversification of the energy supply-mix (Cabalu et al., 2015). Those policies and plans not only ensure energy security and reduced reliance on fossil energy they are also milestones in building a greener Philippines.

RENEWABLE ENERGY DEVELOPMENT STATUS IN CHINA

Current Status

As the second-largest economy in the world, China has abundant renewable energy storage. By the end of 2019, the installed capacity of renewable energy in China was as high as 794.88 GW and has increased by 8.7% since 2018 (Si et al., 2021). The current power generation capacity of each renewable energy source is shown in **Figure 1**, and the current situation of China's renewable energy is shown in **Table 2** (China Renewable Energy Engineering Institute, 2019). In 2013, China proposed the B&R initiative, which covers 65 countries in Asia, Africa, and Europe (Wang et al., 2020). More importantly, promoting the green and low-carbon transformation of the energy structure of countries along the B&R is a core content of green construction in the area and a significant measure in improving the ecological environment and supporting global sustainable development (Yang et al., 2021). As a key country along the Maritime Silk Road, the Philippines has also joined the Asian Infrastructure Investment Bank initiated by the Chinese government.

Advantages

After decades of efforts, China has developed innovative approaches to energy and shared these experiences with other countries through the green cooperation of B&R to eliminate dependence on high-carbon growth models.

The advantages of the Chinese approach stem from it being a strong financial power. China has promoted the vigorous development of renewable energy, and in 2018 China became the world's largest investor in renewable energy for the seventh consecutive year, an investment that accounts for almost one-third of the world's total, reaching US $91.2 billion (Si et al., 2021). Moreover, China's renewable energy technology, manufacturing level, and high-quality production capacity have significantly improved in recent years, and a complete industrial chain with international advanced levels has been constructed in the renewable energy sector. This huge renewable energy product market has also contributed to the development of renewable energy worldwide.

Policies and Plans

In 2005, China enacted the Renewable Energy Law, quickly followed by more than 100 policies, regulating grid subsidies and special fund management measures, including guidance on promoting renewable energy consumption and other aspects as shown in **Figure 2** (China Renewable Energy Engineering Institute, 2019). The most important renewable energy plan of China is the 14th Five-year Plan (2021–2025). The key tasks of which include giving priority to the development of renewable energy based on

TABLE 2 | Status of types of renewable energy in China.

Category	Status
Conventional	1. From 2016 to 2019, the newly added production reached 26.9 GW, and the newly started construction reached 34 GW, which was 68.1 and 56.7% of the planned target respectively 2. By the end of 2019, online monitoring data access for 273 hydropower stations had been completed, with a total installed capacity of 189 GW
Pumped	1. At present, the installed capacity of pumped storage sites included in the national plan is about 120 GW 2. From 2016 to 2019, 31.83 GW of new construction was started
Wind	1. The total grid- connected installed capacity reached 210 GW, accounting for 10.4% of the total installed capacity, of which onshore wind power was 204 GW and offshore wind power was 5.93 GW 2. The hoisting capacity increased by 27 GW. Among the world's top 10 onshore wind. Turbine manufacturers, the total share of Chinese enterprises accounted for 38%
Solar	1. New and cumulative installed capacity of PV generation ranks first in the world 2. In 2019, the electricity price of PV subsidy bidding projects dropped significantly
Biomass	China has put into operation 14 commercial biological natural gas projects, with an annual gas capacity of about 127.75 million m^3, an annual output of organic fertilizer of 1.056 million ton, and an annual output of 4 million ton of biological liquid fuel

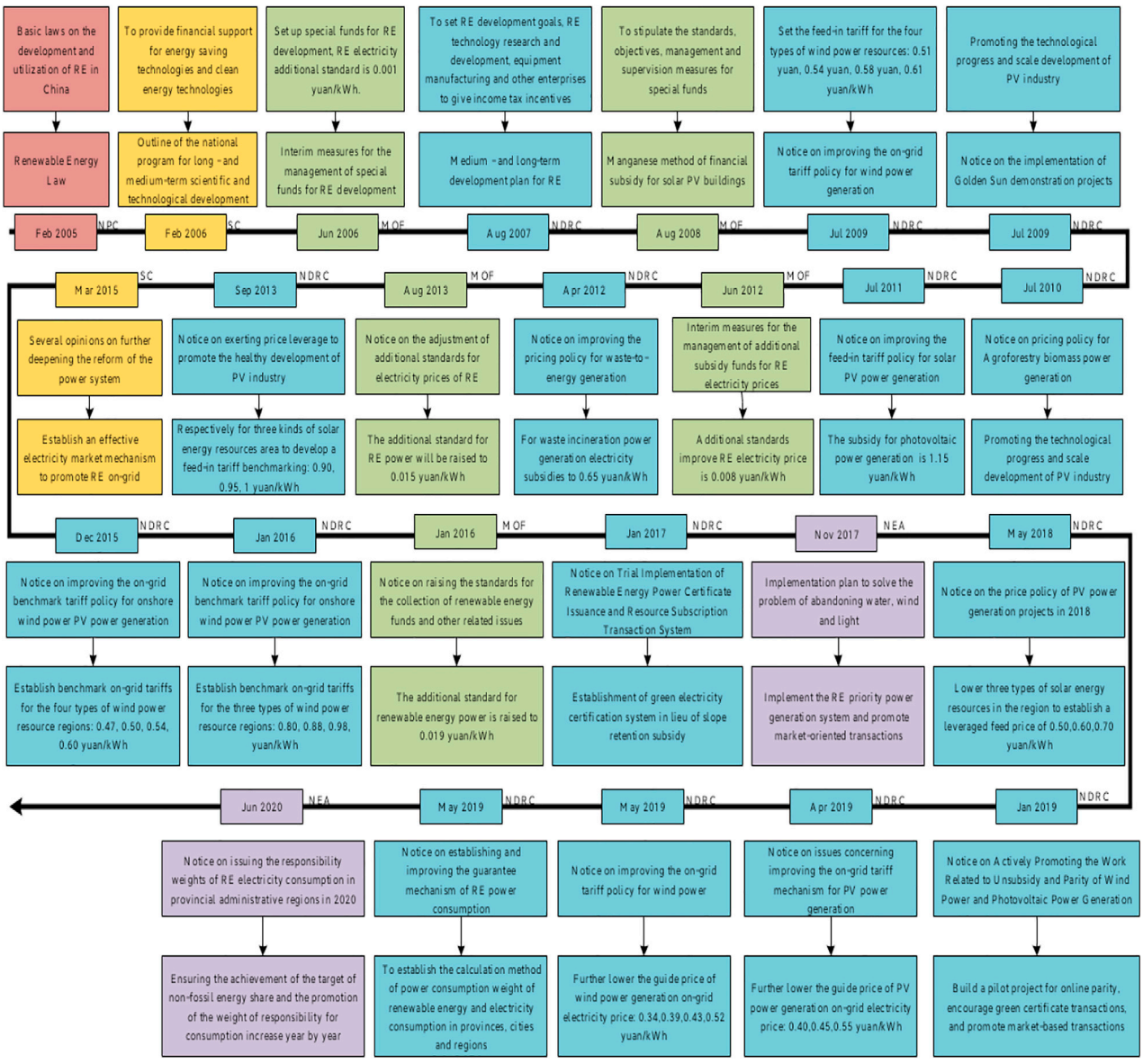


FIGURE 2 | Renewable energy policy roadmap in China (China Renewable Energy Engineering Institute, 2019). Abbreviations: National People's Congress (NPC); State Council (SC); Renewable Energy (RE); Ministry of Finance (MOF); National Development and Reform Commission (NDRC); National Energy Administration (NEA); Exchange rate: 100 (CNY) = 15.4400 (USD) (Date: January 22, 2021).

TABLE 3 | The Philippines—China renewable energy corporation projects.

No	Name of Power Station	Installed Capacity (MW)	Location	Type of Station	Date	Corporation Unit
1	Liangan	11.9	Bacolod	Hydropower	2016	China
2	Kapuan	60	Baguio	Hydropower	2016	China
3	Agus VI	69	Quezon	Hydropower	2017	China
4	Pulangi	250	Miandanao	Hydropower	2017	China
5	Sacasun	58.98	San Carlos	PV	2016	China
6	Garcia	20	Currimao	PV	2016	China
7	Leyte	30	Leyte	PV	2015	China

market forces and low costs, systematically evaluating the development conditions and goals of various renewable energy resources, promoting renewable energy technologies and equipment to develop a relative industrial system, etc., (Liu, 2019). In addition to the macro level, specific plans for different types of renewable energy exist that are international and jointly promote the construction of clean energy (Liu, 2019).

THE PHILIPPINES—CHINA RENEWABLE ENERGY COOPERATION UNDER POLITICAL, ECONOMIC, SOCIAL, TECHNOLOGICAL, ENVIRONMENTAL, AND LEGAL ANALYSIS

Existing Cooperation

China and the Philippines have a history of extensive cooperation in renewable energy, including hydropower, PV, biomass energy, and wind energy, as shown in **Table 3**. This includes both the supply of existing equipment and Engineering Procurement Construction (EPC). This has greatly improved the utilization of hydroelectric and PV in the Philippines, and has made up for power shortages in some areas.

Hydropower cooperation is the focus of the China-Philippines renewable energy cooperation agreement. Cooperative projects are mainly large-scale hydropower plants with an installed capacity of over 10 MW. Solar energy has now become the fastest-growing type of renewable energy in the Philippines, which has attracted many Chinese enterprises.

As one of the listed companies affiliated with the State Grid of China, the NARI Group owns several EPC projects of PV power stations in the Philippines. The Hengshun Group, a private company in China, signed an EPC contract of wind power and PV integration with Energy Logics Philippines, Inc. in 2016: the largest PV integration project to date in the Philippines.

Political, Economic, Social, Technological, Environmental, and Legal Analysis of Renewable Energy Cooperation

Under the intensifying forces of globalization and competition, PESTEL has recently evolved from PEST analysis, to consider the environmental and legal factors, with increased potential impact on businesses (Thakur, 2021). The PESTEL analysis model is an effective tool for macro-environmental analysis that can not only analyze the external environment but also identify all forces that have an impact on the organization. This analysis mode mainly analyzes the investment environment of enterprises.

Political

Advantage

China and the Philippines have established diplomatic relations for 45 years. A mutual friendship formed after the election of Roberto Duterte to President of the Philippines in 2016. Building upon this preexisting relationship, China's focus on green energy cooperation among countries means that it actively seeks energy cooperation partners in different regions. The Philippines is currently pursuing a green energy development model, implementing a large number of fiscal incentives to attract foreign investment in the renewable energy sector (Cabalu et al., 2015).

Disadvantage

The relevant disputes between China and the Philippines in the South China Sea once froze the bilateral relationship. The current highly friendly relationship benefits from Duterte's policy towards China, but this might change when Duterte's term in office ends in 2022. Besides, the Philippines has serious political corruption problems and bureaucracy that may also lead to the unfair treatment of Chinese companies.

Economic

Advantage

The Philippines is one of the most dynamic economies in the East Asia Pacific region. As a beneficiary of the power industry reform of the Philippines, the State Grid Corporation of China holds 40% of the National Grid Corporation of the Philippines. Meanwhile, Chinese energy enterprises have excellent brands and performance advantages. For example, as an active partner cooperating with the Philippines, China Energy Engineering Group Company has experience in power engineering projects and formed a complete industrial chain in international cooperation (Shang et al., 2020).

Disadvantage

In 2020, COVID- 19 pandemic caused a recession in the world economy and hindered international cooperation. In addition, the United States-China trade war has seriously affected the world market and greatly increased the trade barriers between economies. These international economic factors are detrimental to the cooperation between the two countries.

The overall economic level of the Philippines is not high, and the per capita GDP ranks 123rd in the world (International Monetary Fund Philippine GDP per capita, 2019). Moreover, the industrial development level of the Philippines is relatively low, and public facilities such as transportation, electricity, and hydropower lag behind other countries. An out-of-date economy and lesser developed technical facilities make cooperation between the Philippines and other countries difficult.

Social

Advantage

China and the Philippines belong to the East Asian cultural circle and have a long history of cultural exchange. A Cultural Exchange Forum and a series of public welfare activities between the two countries were also held recently (Sina News, 2018). After the COVID- 19 pandemic, China has repeatedly donated medical materials to the Philippines to jointly fight the epidemic.

The Philippines has an abundant labor force and a very young population structure in which the working-age population aged between 15 and 65 has reached 63.6%. In addition, English is the official language of the Philippines, and the literacy rate of Philippines residents is 96.4%, ranking among the highest in Asia (Ministry of Commerce of the People's Republic of China, 2019).

Disadvantage

The domestic security situation of the Philippines is not favorable. There were 8,826 murders and 16,100 robberies in 2017, with 8.40 per 100,000 people (Ministry of Commerce of the People's Republic of China, 2019). There are also several armed rebel terrors groups.

The price levels and costs in the Philippines are also extremely high. The prices of vegetables and fruits, electricity, and hotel accommodation and meals are 3–4 times, 2–3 times, and 1–2 times higher than that of China, respectively (Ministry of Commerce of the People's Republic of China, 2019).

Technological

Advantage

China and the Philippines are technically complementary in terms of energy development and power construction. China's power technology is in the front ranks of the world and could help power development in the Philippines. For example, the advanced UHVDC power transmission technology could realize a sufficient power supply in the offshore islands, which is highly conducive to the formation of the power grid system in the Philippines. Meanwhile, China's infrastructure construction, including 5G, the internet of things, and the industrial internet are also very advanced (Yang et al., 2021). The Philippines also attaches great importance to the development of science and technology through active cooperation with technology-developed countries in engineering and scientific projects *via* higher education.

Disadvantage

Due to the limitations of technology and financial resources, the level of large-scale projects independently constructed by the Philippines is very limited. Hence, many projects have been completed with capital and technologies from other countries. Chinese enterprises may lack the most advanced technology and experience in geothermal energy cooperation due to the lack of domestic geothermal resources.

The risks affecting electricity technical standards of design and construction cannot be ignored. The Philippines mainly adopts American standards which are different from those of China and lead to the extension of design and approval time.

Environment

Advantage

China is a maritime neighbor of the Philippines, and the local time of the Philippines is consistent with Beijing time, which is convenient for cooperation and communication.

Disadvantage

Due to its fragile climate and frequent geological disasters, the Philippines is frequently affected by natural disasters resulting in a great loss of human life and property (Bollettino et al., 2020). Besides, the construction of hydropower stations could adversely affect wildlife and plants and lead to geological disasters. Local people and environmental protection organizations are very opposed to the construction of hydropower stations and the development of geothermal energy, which may greatly impact energy cooperation.

Legal

Advantage

China and the Philippines issued the "Renewable Energy Law" in 2005 and 2008, respectively, to vigorously develop renewable energy and ensure energy security and the optimization of the ecological environment. Foreign investment in biomass and garbage power generation projects had a restriction of 40% lifted in November of 2019 after an announcement by the Philippine government. It is anticipated that other renewable energy projects will be further opened to foreign investment in the future (The Department of Energy Administrative Order, 2020).

Disadvantage

According to Philippine law, foreign investors are prohibited from buying land (The Department of Energy Administrative Order, 2020). In addition, the Philippines has strict controls over work visas for Chinese, which is not conducive to management and technical personnel traveling there from China. Furthermore, as the main form of contracted projects between Chinese enterprises and the Philippines, government projects can only be established after being approved by the Philippine National Economic Development Agency.

POLITICAL, ECONOMIC, SOCIAL, TECHNOLOGICAL, ENVIRONMENTAL, AND LEGAL RECOMMENDATIONS

Political

First, the Philippines and China should make the most of the existing mutual friendly diplomatic relationship to actively develop cooperation. The B&R and the China-ASEAN Free

Trade Area have brought more opportunities and favorable conditions for renewable energy cooperation between the two countries. In terms of disputes in the South China Sea, it is the consensus and commitment of China and the Philippines to settle through negotiation and properly manage their relevant dispute.

Secondly, the renewable energy development strategy could be deepened in the two countries respectively. China should consider renewable energy as a new orientation of developing export trade and investment outward, and actively guide and support overseas cooperation. The Philippines could absorb advanced foreign renewable energy technologies in grid construction while mobilizing domestic resources to develop renewable energy.

Economic

With the guidance of the B&R initiative and the help from the Asian Infrastructure Investment Bank, the Philippines could actively carry out infrastructure construction to improve the business environment. In terms of offshore islands, the construction of renewable energy power plants and grids would solve electricity shortages.

Hydropower and geothermal power generation are the main areas of international cooperation in the Philippines. The EPC mode could be an ideal choice in cooperation, which is relatively fixed, and the implementation period is not long. Chinese companies could integrate the upstream and downstream of the industrial chain systematically to achieve sufficient cooperation and expand the scale and benefits of collaboration.

Social

The two countries could continue to carry out cultural exchange under the background of B&R and promote non-government exchange. In addition, China and the Philippines always adhere to the coexistence of diversified culture, mutual learning, and cooperation for shared benefits. Therefore, Chinese companies participating in cooperation should pay attention to local cultural differences, and respect the local customs, religions, and living habits of the Philippines. Besides, the Philippine government needs to increase public security management through the reduction of crime rate, strictly control the possession of guns, and standardize its application administrative procedures.

Technological

Firstly, China is an advantageous partner in assisting the Philippines to form a complete power grid that especially aims to increase the power supply of offshore islands. To reduce the technical risk, research and exploitation in major technology should be strengthened. Making good use of a contract to constraint risk, promoting project supervision and construction quality should be the focus of project management.

Secondly, great attention should also be paid to the integration of power standards with international standards. Due to the different situations in each country, integration should not aim to achieve the unity of technical standards but to learn from the international advanced technical standards and increase public knowledge of China's working practices to continuously optimize and update standards.

Environment

Due to the frequent occurrence of natural disasters and tropical epidemic diseases in the Philippines, contractors should pay close attention to local news and take preventive measures to prevent personnel and property losses.

Actively fulfilling social responsibility and strengthening environmental awareness is of great significance, because they develop the local economy and improve local people's livelihoods. Through appropriate publicity in a local area, the public could be told more about the cooperative project, and gain an understanding of the fact that they will directly experience an improvement in quality of life quality from these projects. This would improve the enterprise's local popularity and form a positive corporate image.

Legal

On the governmental level, an agreement focused on the strategic cooperation of renewable energy and based on the national strategy and security of both two countries could be reached, which may include investment, technology cooperation, grid construction, and trade. Furthermore, governments of China and the Philippines could establish a unified and effective platform to share renewable cooperative information, corresponding policies, and administrative procedures to solve the difficulty of information collection and nontransparent policies faced by potential cooperators or contractors.

In terms of enterprises, Chinese organizations need to fully understand Philippine laws and regulations to ensure they operate legally, including visas, environmental protection, land, and localized employment regulations. Moreover, the restriction of the foreign investment ratio of renewable energy projects should be studied seriously to maximize the profit of the enterprises in accordance with the laws of the Philippines.

CONCLUSION

This paper is the first to undertake a systematic study of renewable energy cooperation between China and the Philippines under B&R, and draws the following crucial conclusions:

Firstly, the cooperation between China and the Philippines in renewable energy is a mthod of building a greener Philippines and protecting the environment. The coexistence of abundant but undeveloped renewable energy resources and the shortage of electricity supply, especially in the offshore islands, requires deep cooperation with China, as it has superior technological and extensive experience in grid construction. Among various renewable energy, hydropower and geothermal powers are major cooperative areas, in terms of the status of the Philippines. How to explore and utilize renewable energy more economically and efficiently, and realize a sufficient electricity supply are important factors in alleviating dependence on imported fossil fuel energy, a will form a top priority of any cooperative agreement. In addition, the two countries can use the opportunity of renewable energy cooperation to promote cooperation in other industries and achieve mutual benefit and win-win results between the two countries.

Secondly, renewable energy cooperation is the focus of energy cooperation in any B&R initiative. Moreover, a Regional Comprehensive Economic Partnership was established in 2020 and has eliminated trade barriers between Asia-Pacific countries and ASEAN countries. The combination of these initiatives and agreements presents an unprecedented opportunity for China and the Philippines to develop renewable energy cooperation. However, the outbreak of the United States-China trade war and the ongoing COVID- 19 pandemic have brought unprecedented challenges to such potential cooperation initiatives. In response to opportunities and challenges and to achieve a win-win situation, China and the Philippines need to strengthen political and economic cooperation and promote corresponding policies.

Thirdly, a cooperative agreement focused on strategic cooperation concerning renewable energy that is based on national strategy and the security of both two countries may include investment, technology cooperation, grid construction, and trade for renewable energy infrastructure. Furthermore, the Chinese and the Philippine governments could establish a unified and effective platform to share renewable cooperative information, corresponding policies, and administrative procedures to solve the difficulties of collecting information and nontransparent policies faced by potential cooperators or contractors.

Finally, although the disputes between China and the Philippines in the South China Sea once impacted this bilateral relationship seriously, the current friendly relationship has lasted 5 years, creating a positive and timely opportunity for cooperation between the two countries.

AUTHOR CONTRIBUTIONS

XL: Conceptualization, Writing- Reviewing and Editing. HW: Writing- Original draft preparation, Investigation. YL: Writing-Reviewing and Editing. WL: Supervision, Resources.

ACKNOWLEDGMENTS

The authors acknowledge the support of the Talents Training Program of Kunming University of Science and Technology (KKZ3201524007).

REFERENCES

Anand, K., Md Nishat, A., and Shekhar, K. (2021). Sliding Mode Controller Design for Frequency Regulation in an Interconnected Power System. *Prot. Control. Mod. Power Syst.* 6 (1), 77–88. doi:10.1186/s41601-021-00183-1

Barroco, J., and Herrera, M. (2019). Clearing Barriers to Project Finance for Renewable Energy in Developing Countries: A Philippines Case Study. *Energy Policy.* 135, 111008. doi:10.1016/j.enpol.2019.111008

Bertheau, P., Dionisio, J., Jütte, C., and Aquino, C. (2020). Challenges for Implementing Renewable Energy in a Cooperative Driven off- Grid System in the Philippines. *Environ. Innovation and Soci. Trans.* 35, 333–345. doi:10.1016/j.eist.2019.03.002

Bollettino, V., Alcayna-Stevens, T., Sharma, M., Dy, P., Pham, P., and Vinck, P. (2020). Public Perception of Climate Change and Disaster Preparedness: Evidence From the Philippines. *Clim. Risk Management.* 30, 100250. doi:10.1016/j.crm.2020.100250

Cabalu, H., Koshy, P., Corong, E., Rodriguez, U.-P. E., and Endriga, B. A. (2015). Modelling the Impact of Energy Policies on the Philippine Economy: Carbon Tax, Energy Efficiency, and Changes in the Energy Mix. *Econ. Anal. Pol.* 48, 222–237. doi:10.1016/j.eap.2015.11.014

China Renewable Energy Engineering Institute (2019). China Renewable Energy Development Report. Available at: http://www.creei.cn/portal/article/index/id/25365.html. 2020 (Accessed November 26, 2020).

Feng, T. T., Gong, X. L., Guo, Y. H., Yang, Y. S., Pan, B. B., Li, S. P., et al. (2020). Electricity Cooperation Strategy Between China and ASEAN Countries Under' the Belt and Road'. *Energy Strategy Reviews.* 30, 100512. doi:10.1016/j.esr.2020.100512

GPD (2019). *GDP (Current US$) – Philippine GDP*. World Development Indicators database. Available at: https://www.worldbank.org/cn/country/Philippine (Accessed November 19, 2020).

Gullberg, A. T., Ohlhorst, D., and Schreurs, M. (2014). Towards a Low Carbon Energy Future - Renewable Energy Cooperation between Germany and Norway. *Renew. Energ.* 68, 216–222. doi:10.1016/j.renene.2014.02.001

Indeo, F. (2019). ASEAN- EU Energy Cooperation: Sharing Best Practices to Implement Renewable Energy Sources in Regional Energy Grids. *Global Energy Interconnection.* 5 (2), 393–401.

International Monetary Fund Philippine GDP per capita (2019). International Monetary Fund Philippine GDP Per Capita. Available at: https://www.imf.org/external/index.htm (Accessed December 20, 2020).

Liu, J. (2019). China's Renewable Energy Law and Policy: A Critical Review. *Renew. Sustainable Energ. Rev.* 99, 212–219. doi:10.1016/j.rser.2018.10.007

Marquardt, J., and Delina, L. L. (2019). Reimagining Energy Futures: Contributions From Community Sustainable Energy Transitions in Thailand and the Philippines. *Energ. Res. Soc. Sci.* 49, 91–102. doi:10.1016/j.erss.2018.10.028

Mehdi, T., and Mehdi, N. (2020). Human Reliability Analysis in Maintenance Team of Power Transmission System protection. *Prot. Control. Mod. Power Syst.* 5 (4), 270–282.

Ministry of Commerce of the People's Republic of China (2019). Guide for Foreign Investment and Cooperation Countries (Regions)- Philippines. Available at: http://www.mofcom.gov.cn/mofcom/typt.shtml (Accessed December 25, 2020).

Mohan, M. (2021). A Comprehensive Review of DC Fault protection Methods in HVDC Transmission Systems. *Prot. Control. Mod. Power Syst.* 6 (1), 1–20.

Mondal, M. A. H., Rosegrant, M., Ringler, C., Pradesha, A., and Valmonte-Santos, R. (2018). The Philippines Energy Future and Low-Carbon Development Strategies. *Energy.* 147, 142–154. doi:10.1016/j.energy.2018.01.039

Ratio, M. A., Gabo- Ratio, J. A., and Fujimitsu, Y. (2020). Exploring Public Engagement and Social Acceptability of Geothermal Energy in the Philippines: A Case Study on the Makiling- Banahaw Geothermal Complex. *Geothermics.* 85, 101774. doi:10.1016/j.geothermics.2019.101774

Sasmita, P., and Sidhartha, P. (2021). Application of a Simplified Grey Wolf Optimization Technique for Adaptive Fuzzy PID Controller Design for Frequency Regulation of a Distributed Power Generation System. *Prot. Control. Mod. Power Syst.* 6 (1), 21–36.

Satish, K. I., and Vinod, K. T. (2020). Optimal Integration of DGs into Radial Distribution Network in the Presence of Plug- in Electric Vehicles to Minimize Daily Active Power Losses and to Improve the Voltage Profile of the System Using Bioinspired Optimization Algorithms. *Prot. Control Mod. Power Syst.* 5 (1), 21–35.

Shang, T., Liu, P., and Guo, J. (2020). How to Allocate Energy-Saving Benefit for Guaranteed Savings EPC Projects? A Case of China. *Energy.* 191, 116499. doi:10.1016/j.energy.2019.116499

Sharma, A., and Kolhe, M. (2020). Techno- Economic Evaluation of PV Based Institutional Smart Microgrid under Energy Pricing Dynamics. *J. Clean. Prod.* 264, 121486. doi:10.1016/j.jclepro.2020.121486

Si, S., Lyu, M., Lin Lawell, C.-Y. C., and Chen, S. (2021). The Effects of Environmental Policies in China on GDP, Output, and Profits. *Energ. Econ.* 94, 105082. doi:10.1016/j.eneco.2020.105082

Sina News (2018). The Largest Non- Governmental Cultural Exchange Event in the History of China and the Philippines Former Philippine President: Thank You China!. Available at: http://k.sina.com.cn/article_3974550866_ece6d55200100bv9g.html (Accessed December 22, 2020).

Suryanarayana, G., and Saumendra, S. (2020). A Novel Complex Current Ratio-Based Technique for Transmission Line protection. *Prot. Control. Mod. Power Syst.* 5 (3), 239–247.

Thakur, V. (2021). Framework for PESTEL Dimensions of Sustainable Healthcare Waste Management: Learnings From CO VID- 19 Outbreak. *J. Clean. Prod.* 287, 125562. doi:10.1016/j.jclepro.2020.125562

The Department of Energy Administrative Order (2020). The Department of Energy Administrative Order. Available at: https://www.doe.gov.ph/laws- and-issuances/administrative- order (Accessed November 05, 2020).

The Department of Energy (2017). Draft National Renewable Energy Program Overview. Available at: https://www.doe.gov.ph/presentations (Accessed November 05, 2020).

The Department of Energy (2019). Biomass Sector Roadmap. Available at: https://www.doe.gov.ph/presentations (Accessed November 05, 2020).

Wang, C., Wood, J., Geng, X. R., Wang, Y. L., Q iao, C. Y., and Long, X. L. (2020). Transportation CO2 Emission Decoupling: Empirical Evidence from Countries along the belt and Road. *J. Clean. Prod.* 263, 121450. doi:10.1016/j.jclepro.2020.121450

Yang, B., Swe, T., Chen, Y., Zeng, C., Shu, H., Li, X., et al. (2021). Energy Cooperation between Myanmar and China under One Belt One Road: Current State, Challenges and Perspectives. *Energy.* 215, 119130. doi:10.1016/j.energy.2020.119130

Zafar, M. W., Shahbaz, M., Hou, F., Sinha, A., and Sinha, A. (2019). From Nonrenewable to Renewable Energy and its Impact on Economic Growth: The Role of Research & Development Expenditures in Asia-Pacific Economic Cooperation Countries. *J. Clean. Prod.* 212, 1166–1178. doi:10.1016/j.jclepro.2018.12.081

Conflict of Interest: The authors declare that the research was conducted in the absence of any commercial or financial relationships that could be construed as a potential conflict of interest.

Publisher's Note: All claims expressed in this article are solely those of the authors and do not necessarily represent those of their affiliated organizations, or those of the publisher, the editors and the reviewers. Any product that may be evaluated in this article, or claim that may be made by its manufacturer, is not guaranteed or endorsed by the publisher.

Copyright © 2021 Li, Wang, Lu and Li. This is an open-access article distributed under the terms of the Creative Commons Attribution License (CC BY). The use, distribution or reproduction in other forums is permitted, provided the original author(s) and the copyright owner(s) are credited and that the original publication in this journal is cited, in accordance with accepted academic practice. No use, distribution or reproduction is permitted which does not comply with these terms.

frontiers in Energy Research

ORIGINAL RESEARCH
published: 02 August 2021
doi: 10.3389/fenrg.2021.740698

Robust Stability Control for Electric Vehicles Connected to DC Distribution Systems

Wei Teng, Yuejiao Wang, Shumin Sun, Yan Cheng, Peng Yu and Shibo Wang*

State Grid Shandong Electric Power Research Institute, Jinan, China

DC power distribution systems will play an important role in the future urban power distribution system, while the charging and discharging requirements of electric vehicles have a great impact on the voltage stability of the DC power distribution systems. A robust control method based on H_∞ loop shaping method is proposed to suppress the effect of uncertain integration on voltage stability of DC distribution system. The results of frequency domain analysis and time domain simulation show that the proposed robust controller can effectively suppress the DC bus voltage oscillation caused by the uncertain integration of electric vehicle, and the robustness is strong.

OPEN ACCESS

Edited by:
Yaxing Ren,
University of Warwick,
United Kingdom

Reviewed by:
Yan Li,
The Pennsylvania State University (PSU), United States
Xialin Li,
Tianjin University, China

***Correspondence:**
Wei Teng
1622725162@qq.com

Specialty section:
This article was submitted to Smart Grids, a section of the journal Frontiers in Energy Research

Received: *13 July 2021*
Accepted: *22 July 2021*
Published: *02 August 2021*

Citation:
Teng W, Wang Y, Sun S, Cheng Y, Yu P and Wang S (2021) Robust Stability Control for Electric Vehicles Connected to DC Distribution Systems. Front. Energy Res. 9:740698. doi: 10.3389/fenrg.2021.740698

Keywords: DC distribution system, electric vehicles, H∞ loop shaping, robust control, uncertainty

INTRODUCTION

Electric vehicles have become an important part of the low-carbon economy and the world is also in the stage of transformation from fuel vehicles to new energy vehicles (Needell et al., 2016; Wang et al., 2019; Ding et al., 2020; Connor et al., 2021; Zhang et al., 2021). Large-scale electric vehicles will be connected to the distribution network in the future. At present, the distribution network in the world is mainly in the form of AC power supply, and it is necessary to realize the charging of electric vehicles through AC/DC conversion links (Amamra and Marco, 2019; Li et al., 2019; Dong et al., 2021). So many electric energy conversion links will bring problems such as increased loss and reduced power efficiency (Rasheed et al., 2019). DC distribution systems has the advantages of low power loss, high power quality, and easy integration of DC distributed generations and loads (Rashad et al., 2018; Zhao et al., 2018; Dastgeer et al., 2019; Lin et al., 2019), which is gradually becoming the new direction of urban distribution system development in the future. However, the random charging of electric vehicles will cause uncertainty disturbance to the DC distribution system, which will easily lead to system oscillation and even instability (Staats et al., 1998; Tian et al., 2016).

Therefore, how to improve the stability of DC distribution system under the uncertain integration of electric vehicles has become a hot research topic at present. Scholars have put forward corresponding stability control methods from various points which can be summarized as follows:

1) Charging power adjustment method (Tabari and Yazdani, 2014; Tabari and Yazdanil, 2016). This strategy can effectively improve the system stability without changing system parameters or hardware, but it will have an impact on the charging rate of electric vehicles.
2) Virtual inertia control method. The first-order inertia compensation function is introduced into the outer loop of power control, which can improve the system damping and enhance the system stability after the electric vehicle is connected.

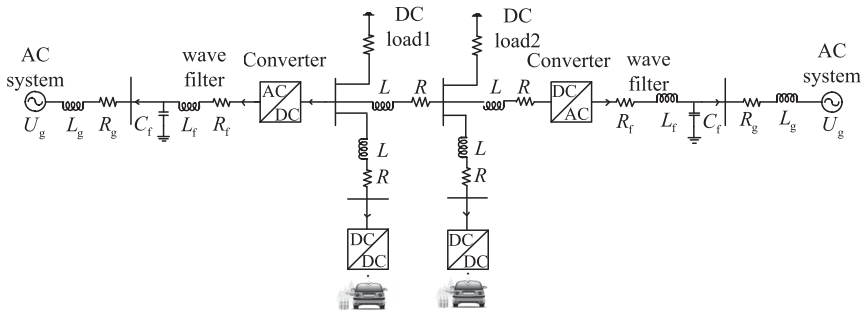


FIGURE 1 | Structure drawing of double-end DC distribution system with electric vehicle.

3) Virtual DC motor control method (Radwan and Mohamed, 2012; Alipoor et al., 2015). Based on the conventional double closed-loop control, the virtual DC motor is introduced to enhance the damping of the system by simulating the inertia of DC generator.
4) Nonlinear control (Tan et al., 2016; Tabari and Yazdani, 2014). Using nonlinear compensation function, fuzzy control, and other methods to improve system damping, but the control algorithm is more complex.

Most of the above studies do not consider the influence of uncertainty caused by random charging of electric vehicles. Therefore, this paper studies the robust stability control of electric vehicles connected to DC distribution system. In the manuscript, a model of the DC/DC converter control system is established and a robust stability controller based on H_∞ loop shaping method is designed to improve the stability of DC bus voltage and suppress system oscillation under uncertainty.

The major contributions of this paper are summarized as follows:

1) The uncertain integration of electric vehicles and the parameter perturbation of the controller affect the voltage stability of the DC distribution system. Therefore, H_∞ loop shaping method is introduced for DC/DC converters to improve the robust stability of the system.
2) A robust controller is designed for a DC distribution system with two EVs integration, and a high-order transfer function is obtained. For practical engineering application, the Hankel singular value algorithm is used to reduce the order. And the frequency domain analyses verify the control effect before and after order reduction.
3) A simulation model is established with DIgSILENT software, in which six scenarios are simulated. The simulation results show that the DC distribution system has good robustness to uncertain disturbances with the designed controller.

The remainder of this paper is organized as follows. In ***Topology of DC Distribution System with Electric Vehicle***, a model of the flexible DC distribution system with electric vehicle is established. ***H_∞ Loop Shaping Method*** introduces the H_∞ loop forming method, and the robust controller is designed for DC/DC converter. Frequency domain analysis is performed to verify the effectiveness of the robust controller in ***Frequency Domain Analysis***. In ***Simulation Verification and Analysis***, the effectiveness of the designed robust controller is verified by simulation. Finally, conclusions are summarized in ***Conclusion***.

TOPOLOGY OF DC DISTRIBUTION SYSTEM WITH ELECTRIC VEHICLE

The typical topology of DC distribution system is shown in **Figure 1**. Its main equipment includes interconnected AC/DC lines, interconnected AC/DC converters, DC distributed generations and DC loads, and DC/DC choppers, etc. The dynamic interaction among various equipment makes the stability of the system complex.

The AC/DC interconnected converter in **Figure 1** is based on the conventional three-phase bidirectional full-control rectifier bridge (Yazdani and Iravani, 2010), and its control mode adopts P-U_{dc} droop control, and the DC/DC chopper is based on the conventional Buck-Boost circuit.

Control Strategy of Electric Vehicle

Conventional control strategies of electric vehicle chopper are mainly divided into constant power, constant current and constant voltage control (Peng et al., 2021). In **Figure 1**, droop control is adopted for both sides of interconnected AC/DC converters to maintain the DC voltage stability in the system, while constant power control is adopted for electric vehicle chopper to realize the power balance in the system. When the electric vehicle is connected to the system for charging without certainty, the power of the system at the beginning will mutate and deviate from P_{ref}. According to the P-U_{dc} droop control curve of AC/DC converter, as shown in **Figure 2**, when the power is abrupt, the reference value of the direct current voltage $U_{dc,ref}$ in the system will also be abrupt, which will cause the fluctuation of the direct current voltage U_{dc} in the system.

However, when a robust controller is attached to the DC/DC converter, the power imbalance in the system caused by the uncertain connection of loads will be greatly reduced, and the fluctuation of DC voltage in the system will be reduced. In **Figure 2**, K_p is the droop coefficient. The constant power

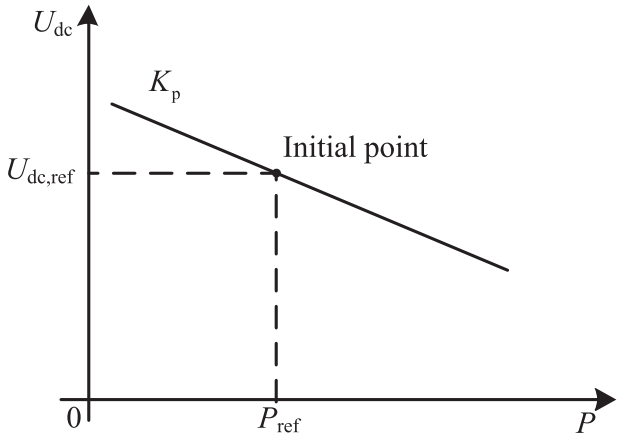


FIGURE 2 | P-U_{dc} droop control schematic diagram.

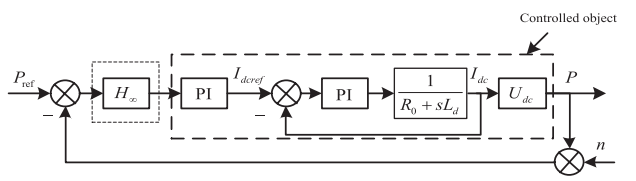


FIGURE 3 | Block diagram of constant power control of chopper.

control model of the chopper of electric vehicle is shown in the following **Eqs (1)** and **(2)**.

$$I_{\mathrm{dcref}} = \left(P_{\mathrm{dcref}} - P_{\mathrm{dc}}\right)G_{\mathrm{p}}(s) \tag{1}$$

$$\alpha = \left(I_{\mathrm{dcref}} - I_{\mathrm{dc}}\right)G_{\mathrm{i}}(s) \tag{2}$$

Where: α is the chopper switch control signal; I_{dc} and I_{dcref} respectively represent the DC current signal and its reference value of the current inner loop; $G_{\mathrm{i}}(s) = K_{\mathrm{ip}} + K_{\mathrm{ii}}/s$ is the current inner loop proportional integral (PI) controller, where K_{ip} and K_{ii} respectively represent the proportional and integral coefficients of the current inner loop PI controller; P_{dc} and P_{dcref} represent the active power signal and its reference value of the power outer loop respectively; $G_{\mathrm{p}}(s) = K_{\mathrm{pp}} + K_{\mathrm{pi}}/s$ is the power outer loop proportional integral (PI) controller, where K_{pp} and K_{pi} represent the proportional and integral coefficients of the power outer loop PI controller respectively.

Chopper constant power control strategy is based on the accurate mathematical model of the system to design the controller. However, due to the change of the operating environment, the change of the operating scene and the aging and damage of the equipment components, there will be some errors in the system model, so that the controller can not effectively control the system with errors. The robust control method based on H_∞ loop shaping method is to design the controller for the system perturbed model, and the additional robust controller can ensure the voltage stability of the system under certain load disturbance and parameter perturbation.

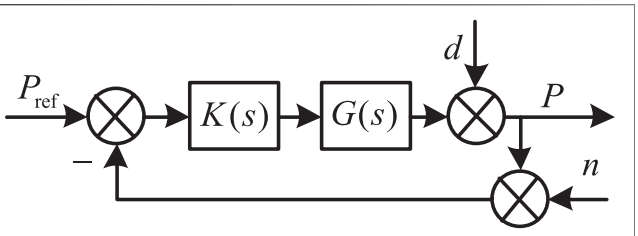


FIGURE 4 | Standard feedback structure diagram.

Controlled Object Model

According to the actual control system, the control object of current inner loop is $1/(R_0 + sL_{\mathrm{d}})$, the control object of power outer loop is U_{dc}, the double closed-loop control block diagram of constant power control is shown in **Figure 3**, where R_0 and L_{d} are the energy storage inductance and resistance of chopper, and n is the noise signal of voltage and current transformers during sampling. The left dotted line frame in the figure represents the robust stability controller designed, and the right dotted line box is the controlled object of the system.

Therefore, it can be seen from the black dotted box on the right side of **Figure 3** that the controlled object $G(s)$ is:

$$G(s) = \frac{U_{\mathrm{dc}}\left(K_{\mathrm{ip}}K_{\mathrm{pp}}s^2 + \left(K_{\mathrm{ip}}K_{\mathrm{pi}} + K_{\mathrm{pp}}K_{\mathrm{ii}}\right)s + K_{\mathrm{ii}}K_{\mathrm{pi}}\right)}{L_{\mathrm{d}}s^3 + \left(R_0 + K_{ip}\right)s^2 + K_{\mathrm{ii}}s} \tag{3}$$

The constant power control block diagram shown in **Figure 3** is transformed into the standard feedback structure diagram shown in **Figure 4**, Wherein, $K(s)$ represents the robust controller H_∞, and d represents the output disturbance. According to **Figure 4**, the relationship between the system output power P and the noise signal n can be obtained:

$$P = \frac{GK}{1+GK}\left(P_{ref} - n\right) + \frac{1}{1+GK}d \tag{4}$$

As can be seen from **Eq. 4**, in order to reduce the influence of output disturbance d on system stability, $\sigma\left(\frac{1}{1+GK}\right) \ll 1$, that is $\sigma(GK) \gg 1$ needs to be satisfied. In order to reduce the influence of transformer noise on system stability, it is required to satisfy $\sigma\left(\frac{GK}{1+GK}\right) \ll 1$, that is, $\sigma(GK) \ll 1$. Therefore, in the design of robust controller, anti-interference and noise reduction of transformer should be considered in a compromise. Considering that the output disturbance d mainly occurs in the low frequency domain, while the noise n of the transformer is significant in the high frequency domain, so the design of robust controller is considered in low frequency band $\sigma(GK) \gg 1$ and high frequency band $\sigma(GK) \ll 1$. $\sigma(\cdot)$ stands for finding the singular value.

H_∞ LOOP SHAPING METHOD

Design Steps of H_∞ Loop Shaping Method

H_∞ loop shaping method combines the advantages of H_∞ technology and loop shaping method. When using this

TABLE 1 | DC distribution system parameters.

Subsystem	Parameter name	Value
AC side grid 1/2	Input voltage U_g	220 V
	AC line R_g/L_g	0.018Ω/0.5 mH
	Filter circuit $R_f/L_f/C_f$	0.05Ω/ 2mH/45 μF
	Common bus voltage U_{dc}	800 V
DC side part	DC load 1/2	5,5/kW
	DC line R/L	7 mΩ/0.22mH
	Energy storage inductor of chopper L_d/R_0	5mH/0.1Ω

TABLE 2 | Converter control parameters.

	AC/DC converter 1/2	DC/DC converter 1/2
Droop coefficient K_p	1.5	
Inner loop scale factor K_{ip}	0.11	0.11
Integral coefficient of inner loop K_{ii}	11	11
Ratio coefficient of outer loop K_{pp}	0.205	0.1
Integral coefficient of outer loop K_{pi}	4.27	80

method to design robust controller, it can achieve the requirements of robust stability and robust performance at the same time. The design of robust controller is divided into the following three steps (Zhou et al., 1996):

1) Loop shaping. The requirements of the system for low, medium and high frequency are as follows: ① the low-frequency open-loop singular value is large, so as to improve the anti-disturbance ability of the system; ② the intermediate frequency curve transition is gentle, and its slope should be between (−40)dB/sec and (−20) dB/sec, so as to broaden the bandwidth of the system; ③ the high-frequency open-loop singular value is small, so as to improve the ability of the system to deal with unmodeled dynamics. According to the above requirements, the open-loop singular value shape $G_s(s)$ of the expected system is determined as (Shen, 2016):

$$G_s(s) = \frac{a}{bs^2 + cs + d},\ b \neq 0 \tag{5}$$

Among them, parameter a determines the low-frequency gain, b and c are used to adjust the cut-off frequency of the singular value curve, and d represents the steady-state error of the system.

2) Robust stabilization.

The maximum robust stability margin is calculated:

$$\varepsilon_{\max} = \left(\inf \left\| \begin{bmatrix} I \\ K \end{bmatrix} (I + G_s K)^{-1} M^{-1} \right\|_{\infty} \right)^{-1} = \sqrt{1 - \left\| N \quad M \right\|_H^2} < 1 \tag{6}$$

Where N(*s*) and M(*s*) are the normalized left coprime decomposition of the expected system $G_s(s)$, and $\varepsilon_{\max}$ represents the maximum allowable uncertainty disturbance of the system. When $\varepsilon_{\max}$ is 0.15–1, the system is considered to have good robust stability. If $\varepsilon_{\max} \ll 1$, it is considered that the robustness of the system is not enough, and the loop shaping must be carried out again in 1) Loop shaping to obtain the desired shape of open-loop singular value.

3) Select $\varepsilon \leq \varepsilon_{\max}$ and get the robust controller K(*s*) from loopsyn command in MATLAB.

Robust Controller Design

The structure diagram of double terminal DC distribution system is established as shown in **Figure 1**, in which the parameters of DC distribution system and the parameters of each converter are shown in **Tables 1**, **2** respectively.

From **Eq. 3**, the open-loop transfer function of the controlled object is obtained as follows:

$$G(s) = \frac{0.022s^2 + 19.8s + 1760}{0.005s^3 + 0.21s^2 + 11s} \tag{7}$$

According to the requirements of loop forming in 1) Loop shaping, the expected open-loop singular value curve is selected as follows:

$$G_s(s) = \frac{20000}{s^2 + 9.86s + 1.01} \tag{8}$$

$\varepsilon_{\max} = 0.3833$ can be obtained from **Eq. 6**, which meets the requirements of the system for robustness. The robust controller *K*(*s*) is obtained by loopsyn command, as shown in **Eq. 9**:

$$K(s) = \frac{4.441 \times 10^{-16} s^8 + 9.512 \times 10^{-12} s^7 + 4.338 \times 10^7 s^6 + 1.822 \times 10^{11} s^5 + \cdots}{s^8 + 9439 s^7 + 2.744 \times 10^7 s^6 + 2.447 \times 10^{10} s^5 + 7.098 \times 10^{12} s^4 + \cdots} \rightarrow \frac{1.876 \times 10^{13} s^4 + 8.627 \times 10^{14} s^3 + 2.44 \times 10^{16} s^2 + 1.087 \times 10^{13} s + 1.199 \times 10^{19}}{5.38 \times 10^{14} s^3 + 4.645 \times 10^{15} s^2 + 4.762 \times 10^{14} s + 1.16 \times 10^{11}} \tag{9}$$

Because the order of the controller is 8, which is not conducive to practical engineering application, Hankel singular value algorithm is used to reduce the order, as shown in **Eq. 10**:

$$K_h = \frac{0.0033233 s^5 + 4.338 \times 10^7 s^4 + 4.529 \times 10^9 s^3 + 2.092 \times 10^{11} s^2 + 5.956 \times 10^{12} s + 1.199 \times 10^9}{s^6 + 5343 s^5 + 5.558 \times 10^6 s^4 + 1.701 \times 10^9 s^3 + 1.311 \times 10^{11} s^2 + 1.134 \times 10^{12} s + 1.16 \times 10^{11}} \tag{10}$$

Comparing the frequency response curves of the robust controller before and after order reduction, as shown in **Figure 5**, it can be found that the control effect is basically the same before and after order reduction.

FREQUENCY DOMAIN ANALYSIS

The curves of open-loop singular value and closed-loop singular value of the system before and after the additional robust controller for EVs are compared, as shown in **Figures 6**, **7** respectively. It can be found that the low-frequency gain of the open-loop singular value is larger and the high-frequency value decays rapidly by adding the robust controller, and the low-frequency amplitude of the closed-loop singular value is 0 and the peak is smaller after adding the robust controller, which is conducive to the signal tracking and disturbance suppression.

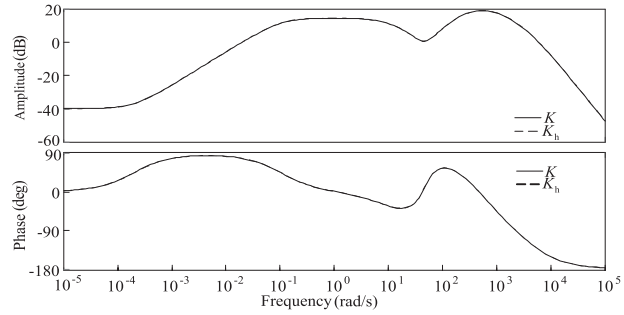


FIGURE 5 | The frequency response curves of the robust controller before order reduction and after order reduction.

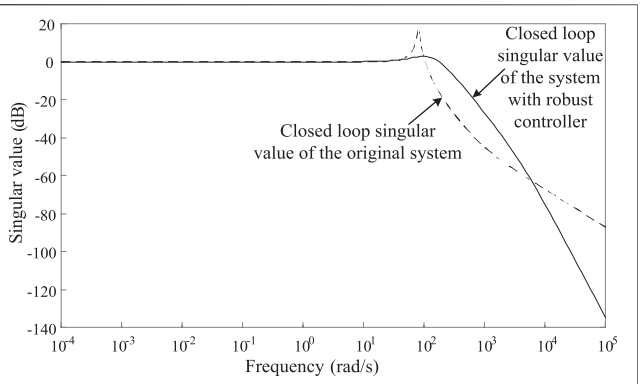


FIGURE 7 | The closed-loop singular value curves of the system before and after the addition of the robust controller.

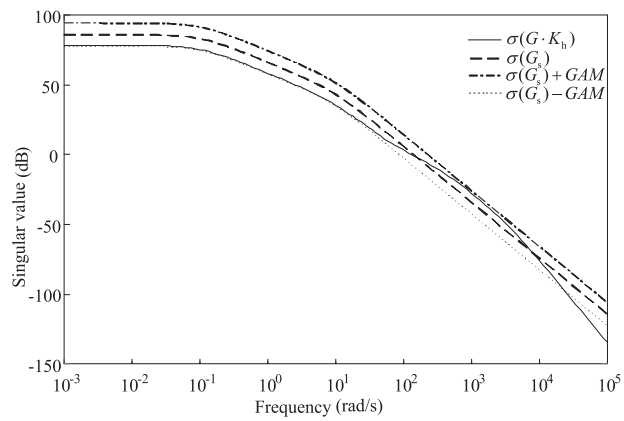


FIGURE 6 | Open-loop singular value curve after adding robust controller.

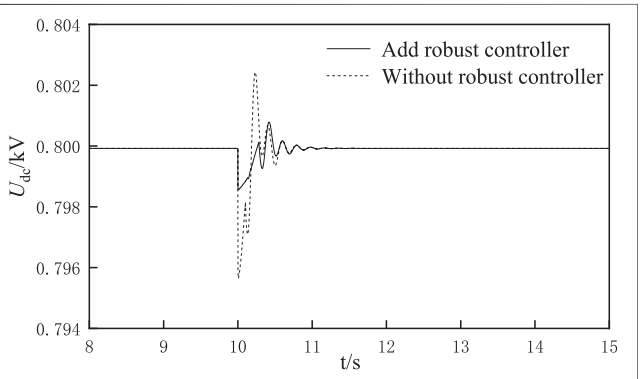


FIGURE 8 | DC bus voltage waveform when an electric vehicle is connected to the system.

SIMULATION VERIFICATION AND ANALYSIS

In order to verify the effectiveness of the designed robust controller, the system shown in **Figure 1** is built in DIgSILENT simulation software, in which two DC buses are used to simulate different integrated points of electric vehicles. Using the control variable method, only the analyzed parameters and load disturbance are variable. This paper analyzes the voltage fluctuation of DC distribution system before and after adding robust controller when one or two electric vehicles are connected with preset chopper parameters (**Table 2**) and the proportion and integral coefficient of chopper power outer loop and current inner loop change.

In this paper, the following six working conditions are simulated and analyzed.

Condition 1: when an electric vehicle is connected (Chopper operates with parameters in **Table 2**). The left DC bus is connected to the electric vehicle at 10 s, and the simulation ends at 15 s. The fluctuation of DC voltage of left DC bus before and after adding robust controller is shown in **Figure 8**.

It can be seen from **Figure 8** that when an electric vehicle is connected to the system, the DC bus voltage oscillates, and the oscillation amplitude is large, which makes the stability problem of the system decrease; while the oscillation amplitude of the system with a robust controller is small, and the adjustment time is short, because the system with a robust controller is less sensitive to the integration of the electric vehicle, and can still maintain the operation of the system in a better station.

Condition 2: when two electric vehicles are connected at the same time (Chopper operates with parameters in **Table 2**). The two DC buses are connected to the electric vehicle at 10 s, and the simulation ends at 15 s. The fluctuation of DC voltage of left DC bus before and after adding robust controller is shown in **Figure 9**.

It can be seen from **Figure 9** that when two electric vehicles are connected to the system, the DC bus voltage impulse system is larger and the oscillation time is longer than when one electric vehicle is connected to the system; similarly, adding a robust controller based on uncertainty modeling can reduce the oscillation amplitude and the regulation time of the system.

Condition 3: when an electric vehicle is connected, its chopper parameter K_{pp} is perturbed. The left DC bus connected to the electric vehicle at 10 s, and the simulation ends at 15 s. The chopper parameter K_{pp} becomes 0.4, and other parameters remain unchanged. The fluctuation of DC voltage of left DC

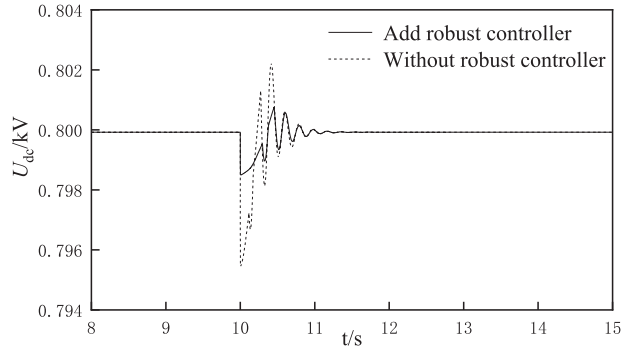


FIGURE 9 | DC bus voltage waveform when two electric vehicle is connected to the system.

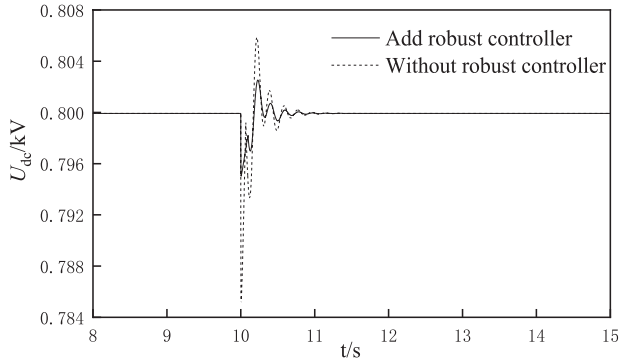


FIGURE 11 | DC bus voltage waveform when chopper K_{ip} is perturbed.

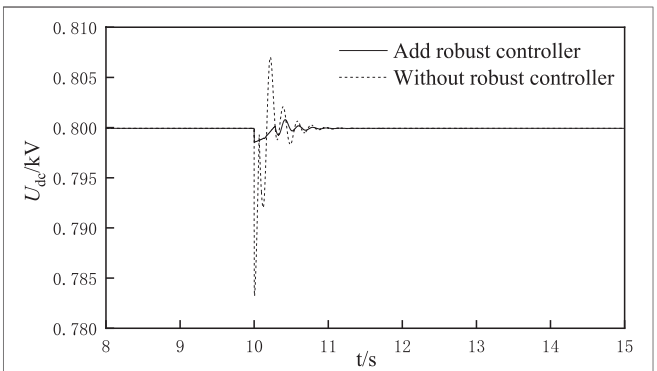


FIGURE 10 | DC bus voltage waveform when chopper K_{pp} is perturbed.

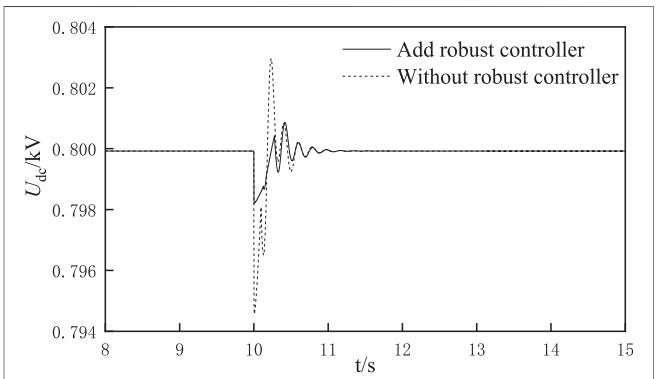


FIGURE 12 | DC bus voltage waveform when chopper K_{pi} is perturbed.

bus before and after adding robust controller is shown in **Figure 10**.

As can be seen from **Figure 10**, compared with the chopper operating with preset parameters (**Table. 2**), when the chopper parameter K_{pp} is perturbed, the DC bus voltage oscillation amplitude is larger and the oscillation time is longer; when the robust controller is added, the sensitivity to the perturbation change of control parameters is lower, the oscillation amplitude change is smaller and the adjustment time is shorter.

Condition 4: K_{ip} parameter perturbation of chopper when an electric vehicle is connected. Assuming the left DC bus is connected to the electric vehicle at 10 s and the simulation is finished at 15 s, the chopper parameter K_{ip} becomes 0.4. The fluctuation of DC voltage of left DC bus before and after adding robust controller is shown in **Figure 11**.

As can be seen from **Figure 11**, compared with the chopper operating with preset parameters (**Table 2**), the DC bus voltage oscillation amplitude is larger when the chopper parameter K_{ip} is perturbed, while the sensitivity to the perturbation change of control parameters is lower when the robust controller is added, and the oscillation amplitude changes less, and the adjustment time is shorter.

Condition 5: when an electric vehicle is connected, its chopper parameter K_{pi} is perturbed. The left DC bus is connected to the electric vehicle at 10 s, and the chopper parameter K_{pi} is changed to 100 at 15 s. The fluctuation of DC voltage of left DC bus before and after adding robust controller is shown in **Figure 12**.

As can be seen from **Figure 12**, compared with the chopper operating with preset parameters (**Table 2**), the DC bus voltage oscillation amplitude increases when the chopper parameter K_{pi} of electric vehicle is perturbed, while the sensitivity of the added robust controller to the perturbation changes of control parameters is lower, the oscillation amplitude changes less, and the regulation time is shorter.

Condition 6: when an electric vehicle is connected, its chopper parameter K_{ii} is perturbed. The left DC bus is connected to the electric vehicle at 10 s and the simulation is finished at 15 s, and the chopper parameter K_{ii} becomes 13.75. The fluctuation of DC voltage of left DC bus before and after adding robust controller is shown in **Figure 13**.

As can be seen from **Figure 13**, compared with the chopper operating with preset parameters (**Table 2**), when the chopper parameter K_{ii} is perturbed, the DC bus voltage oscillation amplitude increases, and the minimum oscillation amplitude reaches 0.794 kV; while the robust controller is added, the sensitivity to the perturbation changes of control parameters is lower, the oscillation amplitude changes less, and the adjustment time is shorter.

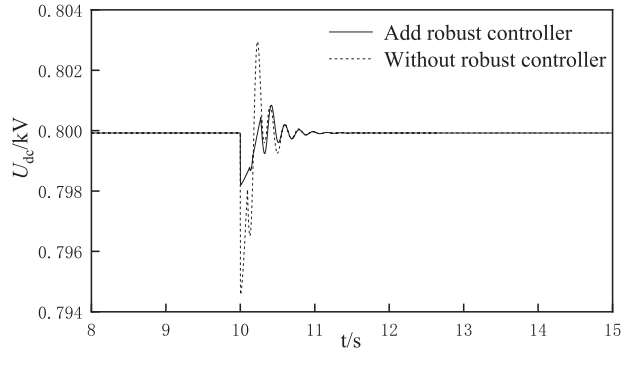


FIGURE 13 | DC bus voltage waveform when chopper K_{ii} is perturbed.

From the above simulation results, it can be seen that the robust controller based on H_∞ loop shaping method fully considers the influence of electric vehicle integration and chopper parameter perturbation on DC voltage stability, which can effectively improve the stability of the system and ensure the robustness.

CONCLUSION

In order to suppress the influence of uncertain integration of electric vehicles in DC distribution systems, a robust stability controller is designed based on loop shaping method in this paper, with the advantages of.

1) The robust controller can improve the voltage stability of the system effectively, without establishing the precise mathematical model of the system, and the sensitivity to load disturbance and parameter perturbation is weak.
2) When the order of robust controller is high and it is difficult to be used in engineering practice, Hankel singular value algorithm can be used to reduce the order, and the control effect before and after reduction is basically the same.

DATA AVAILABILITY STATEMENT

The original contributions presented in the study are included in the article/supplementary material, further inquiries can be directed to the corresponding author.

AUTHOR CONTRIBUTIONS

Conceptualization, WT, YW, SS, YC, PY, and SW; methodology, WT, YW, and SS; validation, WT, PY, YC, SW, and SS; formal analysis, WT, YW, and SW; writing-original draft preparation, WT, YW, and SW; writing-review and editing, WT, SS, and YW; All authors have read and agreed to the published version of the manuscript.

FUNDING

The Science and Technology Project of State Grid Shandong Electric Power Company, "Research on the Application of Flexible Direct Current Transmission Technology in Shandong Power Grid under the Framework of New Generation Power System" (grant number 52062618008J).

REFERENCES

Alipoor, J., Miura, Y., and Ise, T. (2015). Power System Stabilization Using Virtual Synchronous Generator with Alternating Moment of Inertia. *IEEE J. Emerg. Sel. Top. Power Electron.* 3 (2), 451–458. June. doi:10.1109/JESTPE.2014.2362530

Amamra, S.-A., and Marco, J. (2019). Vehicle-to-Grid Aggregator to Support Power Grid and Reduce Electric Vehicle Charging Cost. *IEEE Access* 7, 178528–178538. doi:10.1109/ACCESS.2019.2958664

Connor, W. D., Wang, Y., Malikopoulos, A. A., Advani, S. G., and Prasad, A. K. (2021). Impact of Connectivity on Energy Consumption and Battery Life for Electric Vehicles. *IEEE Trans. Intell. Veh.* 6 (1), 14–23. March 2021. doi:10.1109/TIV.2020.3032642

Dastgeer, F., Gelani, H. E., Anees, H. M., Paracha, Z. J., and Kalam, A. (2019). Analyses of Efficiency/energy-Savings of DC Power Distribution Systems/microgrids: Past, Present and Future. *Int. J. Electr. Power Energ. Syst.* 104, 89–100. doi:10.1016/j.ijepes.2018.06.05710.1016/j.ijepes.2018.06.057

Ding, X., Wang, Z., Zhang, L., and Wang, C. (2020). Longitudinal Vehicle Speed Estimation for Four-Wheel-Independently-Actuated Electric Vehicles Based on Multi-Sensor Fusion. *IEEE Trans. Veh. Technol.* 69 (11), 12797–12806. Nov. 2020. doi:10.1109/TVT.2020.3026106

Dong, L., Wang, C., Li, M., Sun, K., Chen, T., and Sun, Y. (2021). User Decision-Based Analysis of Urban Electric Vehicle Loads. *CSEE J. Power Energ. Syst.* 7 (1), 190–200. Jan. doi:10.17775/CSEEJPES.2020.00850

Tan, L., Wu, B., Rivera, S., Ise, T., et al. (2016). Comprehensive DC Power Balance Management in High-Power Three-Level DC–DC Converter for Electric Vehicle Fast Charging. *IEEE Trans. Power Electron.* 31 (1), 89–100.

Li, Y., Zhao, T., Liu, C., Zhao, Y., Wang, P., Gooi, H. B., et al. (2019). An Interactive Decision-Making Model Based on Energy and Reserve for Electric Vehicles and Power Grid Using Generalized Stackelberg Game. *IEEE Trans. Ind. Applicat.* 55 (4), 3301–3309. July-Aug. doi:10.1109/TIA.2018.2870834

Lin, G., Li, Y., Liu, J., and Li, C. (2019). Resonance Analysis and Active Damping Strategy for Shipboard DC Zonal Distribution Network. *Int. J. Electr. Power Energ. Syst.* 105, 612–621. doi:10.1016/j.ijepes.2018.08.038

Needell, Z. A., McNerney, J., Chang, M. T., and Trancik, J. E. (2016). Potential for Widespread Electrification of Personal Vehicle Travel in the united states. *Nat. Energ.* 1 (9), 16 112–116 118. Aug. doi:10.1038/nenergy.2016.112

Peng, K., Wei, Z., Chen, J., and Li, H. (2021). Hierarchical Virtual Inertia Control of DC Distribution System for Plug-And-Play Electric Vehicle Integration. *Int. J. Electr. Power Energ. Syst.* 128, 106769. doi:10.1016/j.ijepes.2021.106769

Radwan, A. A. A., and Mohamed, Y. A.-R. I. (2012). Assessment and Mitigation of Interaction Dynamics in Hybrid AC/DC Distribution Generation Systems. *IEEE Trans. Smart Grid* 3 (3), 1382–1393. doi:10.1109/TSG.2012.2201965

Rashad, M., Ashraf, M., Bhatti, A. I., and Minhas, D. M. (2018). Mathematical Modeling and Stability Analysis of DC Microgrid Using SM Hysteresis Controller. *Int. J. Electr. Power Energ. Syst.* 95, 507–522. doi:10.1016/j.ijepes.2017.09.001

Rasheed, A., Khan, S., Gelani, H. E., and Dastgeer, F. (2019). "AC vs. DC Home: An Efficiency Comparison," in International Symposium on Recent Advances in Electrical Engineering. Islamabad, Pakistan: (RAEE), 1–6. doi:10.1109/RAEE.2019.8887064

Shen, X. (2016). *Robust Control Based on Hinf Loop-Shaping of Variable-Speed Variable-Pitch Wind turbine[D]*. Harbin: Harbin University of Science and Technology. in chinese.

Staats, P. T., Grady, W. M., Arapostathis, A., and Thallam, R. S. (1998). A Statistical Analysis of the Effect of Electric Vehicle Battery Charging on Distribution

System Harmonic Voltages. *IEEE Trans. Power Deliv.* 13 (2), 640–646. doi:10.1109/61.660951

Tabari, M., and Yazdanil, A. (2016). *A Mathematical Model for a Stability-Enhanced DC Distribution System for Power System Integration of Plug-In Electric vehicles[C]//IEEE Power and Energy Society General Meeting*. Boston, USA: 5p. July 17-21. doi:10.1109/pesgm.2016.7741152

Tabari, M., and Yazdani, A. (2014). Stability of a Dc Distribution System for Power System Integration of Plug-In Hybrid Electric Vehicles. *IEEE Trans. Smart Grid* 5 (5), 2564–2573. doi:10.1109/TSG.2014.2331558

Tian, L. C., Wu, B., Rivera, S., and Yaramasu, V. (2016). Comprehensive DC Power Balance Management in High-Power Three-Level DC-DC Converter for Electric Vehicle Fast Charging. *IEEE Trans. Power Electron.* 34, 89–100. doi:10.1109/TPEL.2015.2397453

Wang, B., Dehghanian, P., Wang, S., and Mitolo, M. (2019). Electrical Safety Considerations in Large-Scale Electric Vehicle Charging Stations. *IEEE Trans. Ind. Applicat.* 55 (6), 6603–6612. Nov.-Dec. doi:10.1109/TIA.2019.2936474

Yazdani, A., and Iravani, R. (2010). *Voltage-sourced Converters in Power System: Modeling, Control, and Applications*. WileyIEEE Press. Voltage-Sourced Converters in Power Systems. doi:10.1002/9780470551578

Zhang, J., Salman, M., Zanardelli, W., Ballal, S., and Cao, B. (2021). An Integrated Fault Isolation and Prognosis Method for Electric Drive Systems of Battery Electric Vehicles. *IEEE Trans. Transp. Electrific.* 7 (1), 317–328. March 2021. doi:10.1109/TTE.2020.3025107

Zhao, X., Peng, K., Zhang, X., Liu, J., Zhao, Y., and Chen, J. (2018). Research on Influencing Factors and Improving Methods for DC Distribution System Stability. *J. Eng.* 2019 (16), 2147–2153. doi:10.1049/joe.2018.8557

Zhou, K., Doyle, J. C., and Glover, K. (1996). *Robust and Optimal Control*. Engle wood Cliffs, NJ: Prentice-Hall.

Conflict of Interest: The authors declare that the research was conducted in the absence of any commercial or financial relationships that could be construed as a potential conflict of interest.

Publisher's Note: All claims expressed in this article are solely those of the authors and do not necessarily represent those of their affiliated organizations, or those of the publisher, the editors and the reviewers. Any product that may be evaluated in this article, or claim that may be made by its manufacturer, is not guaranteed or endorsed by the publisher.

Copyright © 2021 Teng, Wang, Sun, Cheng, Yu and Wang. This is an open-access article distributed under the terms of the Creative Commons Attribution License (CC BY). The use, distribution or reproduction in other forums is permitted, provided the original author(s) and the copyright owner(s) are credited and that the original publication in this journal is cited, in accordance with accepted academic practice. No use, distribution or reproduction is permitted which does not comply with these terms.

frontiers in Energy Research

ORIGINAL RESEARCH
published: 06 August 2021
doi: 10.3389/fenrg.2021.701574

Cost-Sensitive LightGBM-Based Online Fault Detection Method for Wind Turbine Gearboxes

Mingzhu Tang[1†], *Qi Zhao*[1], *Huawei Wu*[2*] *and Zimin Wang*[3†]

[1]School of Energy and Power Engineering, Changsha University of Science and Technology, Changsha, China, [2]Hubei Key Laboratory of Power System Design and Test for Electrical Vehicle, Hubei University of Arts and Science, Xiangyang, China, [3]School of Computer Science and Information Security, Guilin University of Electronic Technology, Guilin, China

In practice, faulty samples of wind turbine (WT) gearboxes are far smaller than normal samples during operation, and most of the existing fault diagnosis methods for WT gearboxes only focus on the improvement of classification accuracy and ignore the decrease of missed alarms and the reduction of the average cost. To this end, a new framework is proposed through combining the Spearman rank correlation feature extraction and cost-sensitive LightGBM algorithm for WT gearbox's fault detection. In this article, features from wind turbine supervisory control and data acquisition (SCADA) systems are firstly extracted. Then, the feature selection is employed by using the expert experience and Spearman rank correlation coefficient to analyze the correlation between the big data of WT gearboxes. Moreover, the cost-sensitive LightGBM fault detection framework is established by optimizing the misclassification cost. The false alarm rate and the missed detection rate of the WT gearbox under different working conditions are finally obtained. Experiments have verified that the proposed method can significantly improve the fault detection accuracy. Meanwhile, the proposed method can consistently outperform traditional classifiers such as AdaCost, cost-sensitive GBDT, and cost-sensitive XGBoost in terms of low false alarm rate and missed detection rate. Owing to its high Matthews correlation coefficient scores and low average misclassification cost, the cost-sensitive LightGBM (CS LightGBM) method is preferred for imbalanced WT gearbox fault detection in practice.

Keywords: fault detection, Spearman rank correlation, cost-sensitive classification, lightGBM, wind turbine

OPEN ACCESS

Edited by:
Dongran Song,
Central South University, China

Reviewed by:
Rizk Masoud,
University of Menoufia, Egypt
Yunsong Xu,
Harbin Institute of Technology, China

***Correspondence:**
Huawei Wu
whw_xy@hbuas.edu.cn

†These authors have contributed equally to this work

Specialty section:
This article was submitted to Smart Grids, a section of the journal Frontiers in Energy Research

Received: *28 April 2021*
Accepted: *30 June 2021*
Published: *06 August 2021*

Citation:
Tang M, Zhao Q, Wu H and Wang Z (2021) Cost-Sensitive LightGBM-Based Online Fault Detection Method for Wind Turbine Gearboxes. Front. Energy Res. 9:701574. doi: 10.3389/fenrg.2021.701574

INTRODUCTION

With the increase in the capacity of wind turbine assembly machines, wind power generation brings economic benefits and also raised important crucial challenges related to reliability (Qiao and Lu, 2015; Wang et al., 2019). On the one hand, wind power generation technology has been developed rapidly, but wind turbine (WT) fault detection and condition monitoring technologies have not been improved accordingly, which results in frequent WT faults that cannot be timely maintained; on the other hand, WTs are often located in remote areas with rich wind resources and operated in harsh working environments for a long time, which can easily cause frequent WT faults (Yang et al., 2021). Gearboxes are often operating under tough circumstances, which will cause a high fault rate and irreversible damage to WT. The wind turbine gearbox faults will inevitably affect the performance of WT (Teng et al., 2016a). Therefore, fault detection of WT gearbox is of great significance for reducing

the operation and maintenance cost of WTs and improving the power generation efficiency of the entire wind farm (Chen et al., 2017).

WT is a typical complex system, and its operating status is complex and changeable, which brings difficulties to the fault detection and condition monitoring of WTs (Ra et al., 2021; Song et al., 2021). The fault mechanism is complicated, and the correlation characteristics between kinds of feature vectors under various fault types will be different (Liang et al., 2018). Data in the wind turbine SCADA system are usually high-dimensional data, so it is necessary to reduce the dimensionality of the big data in the SCADA system. For instance, Amirat et al. (2018) proposed an ensemble empirical mode decomposition fault diagnosis method. The Pearson correlation analysis method was implemented to select the closest intrinsic mode function and to analyse the data correlation. Yang et al. (2019) adopted the convolution neural network fault diagnosis method, in which the Spearman rank correlation analysis is used to sort the relevant image layers of the convolutional neural network and comprehensively extract data features (Long et al., 2018; Long et al., 2021a). This method effectively verifies the necessity of feature selection and improves the fault detection rate. Since data in the SCADA system are interrelated, feature selection and reducing the dimensionality of the big data of WTs will increase the availability of data samples and improve the accuracy of fault detection (Long et al., 2021b).

Many scholars and experts have carried out extensive and in-depth research on WT fault detection and diagnosis methods, including signal processing methods, multivariate statistical methods, and classification algorithms (Jiang et al., 2015). For example, Teng et al. (2016b) proposed a complex wavelet transform for multifault detection of the WT fault detection method. By analyzing the multiscale enveloping spectrogram, the fault characteristics of weak bearings can be detected and fault diagnosis of WTs can be realized. Due to the nonlinear and nonstationary characteristics of the gearbox, Han et al. (2020) considered the correlation between variables and used a quantitative diagnosis method for gearbox faults based on generalized canonical correlation analysis, which can effectively identify the severity of gearbox faults under various conditions. Gao et al. (2018) explained the drawbacks of the current support vector machine (SVM) algorithm and proposed the WT fault diagnosis method based on the least squares support vector machine. Zheng and Peng (2019) used an improved AdaBoost–SVM method for WT converter fault diagnosis, the wavelet transform is employed to reduce signal noise, and fault feature vectors are input into the improved AdaBoost–SVM classifier to achieve fault diagnosis. Zhang et al. (2018) proposed a wind turbine fault diagnosis method combining Random Forest (RF) and extreme gradient boosting (XGBoost) that were used to establish the data-driven WT fault detection framework. RF is used to rank the features of WTs by importance, and XGBoost trains the ensemble classifier for each specific fault. This method is able to protect against overfitting, and it achieves better wind turbine fault detection results than SVM when processing multidimensional data. Tang et al. (2020) adopted the WT gearbox fault detection method that combines correlation analysis and improved LightGBM. The maximum information coefficient analysis method is adopted to select features for the big data of WTs. The improved LightGBM is implemented by the Bayesian optimization for classification so as to diagnose the fault of WT gearbox. However, the fault diagnosis performance needs to be improved when the data are imbalanced.

To this end, the current fault diagnosis methods for WTs are generally based on machine learning (Stetco et al., 2019), that is, dealing with the existing data to train a fault diagnosis model and using this model to realize fault diagnosis. Machine learning algorithms have been employed to solve the problem of WT fault detection, in which samples are assumed based on a balanced distribution. Most of the current data-driven machine learning methods assume that the number of normal samples and fault samples are close. However, normal samples are specifically much greater than the number of fault samples in the real industrial field. This means that many machine learning methods fail in dealing with imbalanced data and the majority class has higher recognition rate while the minority class fails. During the operation of WTs, faults occur for a short period of time and most of the condition are in normal conditions; therefore, the fault sample is the minority class, and the normal sample is the majority class. However, traditional machine learning methods for WTs fault diagnosis do not consider the data imbalance problems and the losses caused by fault alarms and missing detection. The Gini coefficient and information gain rate are considered as the optimization target, in which the misclassification cost is not introduced in the base classifier evaluation function and the fault detection performance is not very well.

The contributions of this article are summarized as follows:

1) The fault diagnosis method takes misclassification costs into account, and the optimization objective aims to minimize average total cost, which will effectively improve the fault detection rate. The efficiency of the base classifier has been improved, especially in terms of their ability in WT fault detection.
2) Since the fault sample is the minority class and the normal sample is the majority class, a method based on cost-sensitive LightGBM WT fault detection is proposed to deal with the imbalance data distribution problem. Specifically, the cost function is introduced in the weight formula of the LightGBM algorithm to replace the information gain, so that the algorithm pays attention to the minority class in each iteration update, thereby improving the classification effect of imbalanced data.
3) Spearman rank correlation method is used for WT feature selection replacing the raw dataset studied with new attributes ranked in order of correlation; thus, it can help to reduce both the redundancy and the dimension between WT feature datasets and ensure to remove redundant and irrelevant information in the original feature space.
4) Experiment shows that the proposed method can quickly perform fault diagnosis of WTs. Compared with other cost-sensitive ensemble algorithms, the cost-sensitive

LightGBM is more suitable for highly imbalanced data and can achieve more accurate fault classification. The experiment verifies the effectiveness and validity of the proposed method.

RELATED WORK

The cost-learning methods aim to minimize total misclassification cost rather than total error. Cost-sensitive learning has attracted significant attention from researchers and scholars. Knoll et al. (1994) proposed misclassification costs to improve the classification accuracy of the decision tree. Domingos (1999) proposed MetaCost, which made use of the bagging algorithm to making the classifier cost sensitive by wrapping a cost-minimizing method. Many scholars attempted to adjust the classifier to be cost-sensitive by adding the cost function to train the algorithm. Among these works, Fan et al. (1999) presented the AdaCost method to reduce the cumulative misclassification cost more than AdaBoost. Fumera and Roli (2002) proposed cost-sensitive SVM under the framework of the structural risk minimization induction principle via minimizing the associate risk. Tremendous cost-sensitive learning has been conducted to improve the classifier performance. It is noteworthy that how to train LightGBM algorithm under an imbalanced fault diagnosis situation is still a problem for real WT fault diagnosis.

BACKGROUND

Spearman Rank Correlation Method for Feature Selection

Since data from WTs are big and the feature correlation between data has some problems such as low correlation and redundant features, it is necessary to use feature selection on the big data of WTs. The commonly used correlation coefficients include the Pearson linear correlation coefficient, Kendall rank correlation coefficient, Spearman rank correlation coefficient, and tail dependence coefficients (Bonett and Wright, 2000). Since the correlation analysis of characteristics of WTs showed nonlinear correlation between variables, while the Kendall rank correlation coefficient and Spearman rank correlation coefficient have similar properties, the Spearman rank correlation coefficient is used in this work (Croux and Dehon, 2010).

The Spearman rank correlation coefficient is designed to measure the linear or nonlinear relationship of variables. Given two discrete features of x and y and M data samples, the Spearman rank correlation coefficient can be calculated by the following formula:

$$r_s = \frac{\sum_i (x_i - \overline{x})(y_i - \overline{y})}{\sqrt{\sum_i (x_i - \overline{x})^2}\sqrt{\sum_i (y_i - \overline{y})^2}}. \quad (1)$$

Here, $\overline{x} = \frac{1}{M}\sum_{i=1}^{M} x_i$ and $\overline{y} = \frac{1}{M}\sum_{i=1}^{M} y_i$, which can also be rewritten as follows:

$$r_s = \frac{cov(x, y)}{\sigma x \sigma y}. \quad (2)$$

Here, cov represents the standard deviation, and σ is the covariance.

Spearman rank correlation coefficient r_s ranges from −1 to 1. When $r_s = 1$, it means that x and y are relatively positively correlated, $r_s = -1$, it means that x and y are strictly negatively correlated, and $r_s = 0$, it means that the two features are independent of each other.

The Spearman rank correlation coefficient is designed to measure the correlation between features. If the index with a higher correlation coefficient is directly deleted, some features may be missing. To ensure that the redundancy between fault features is reduced and the information of different features is retained, the feature with the highest Spearman rank correlation coefficient in the raw dataset is selected, while the other fault features and features with high linear correlation are classified into a set of feature sets according to the threshold, until fault features in the original data set are eliminated or selected. The feature selection method is shown in **Figure 1**.

Cost-Sensitive Learning

Since traditional classification algorithms are not suitable for imbalanced data, a cost-sensitive method was developed (Turney, 1994), that is, by introducing a misclassification cost in attribute splitting instead of information gain, Gini coefficient, and other indicators, which aims to minimize the average total cost and improve the prediction of the minority samples (Tang et al., 2019).

The misclassification costs are usually described as a cost matrix, as shown in **Table 1**.

In **Table 1**, C_F is the fault class, C_N is the normal class, $F(C_F,C_F)$ represents the cost of the fault class being correctly classified as the fault class, $F(C_F,C_N)$ represents the cost of the fault category being wrongly classified as the normal category, $F(C_N, C_F)$ represents the cost of the normal class being wrongly classified into the fault class, and $F(C_N, C_N)$ represents the cost of the normal class being correctly classified into the normal class.

Given the misclassification cost matrix C, if the actual class is j and the predicted category class is i, if $i = j$, the prediction is correct. The best prediction result of the sample x should be the class that minimizes the expected total sample:

$$R(C_I|x) = \sum P\left(C_j|x\right)F\left(C_j, C_i\right). \quad (3)$$

Here, $P(C_j|x)$ is the posterior probability of classifying sample x into C_j.

A training set S of N samples is given, where $S = \{(x_i, y_i)\}, i = 1, \ldots, N, x_i (x_i \in X)$ represents x in the k-dimensional vector space $X = \{x_1, x_2, \ldots, x_k\}, y_i \in Y = \{0, 1\}$ is the class label of x_i, and $y_i = 1$ indicates a small number of samples, namely, fault samples. Generally, $F(C_F,C_N) > F(C_F,C_F)$ and $F(C_N, C_F) > F(C_N, C_N)$. The essence of cost-sensitive classification is that even if the sample x is more likely to be

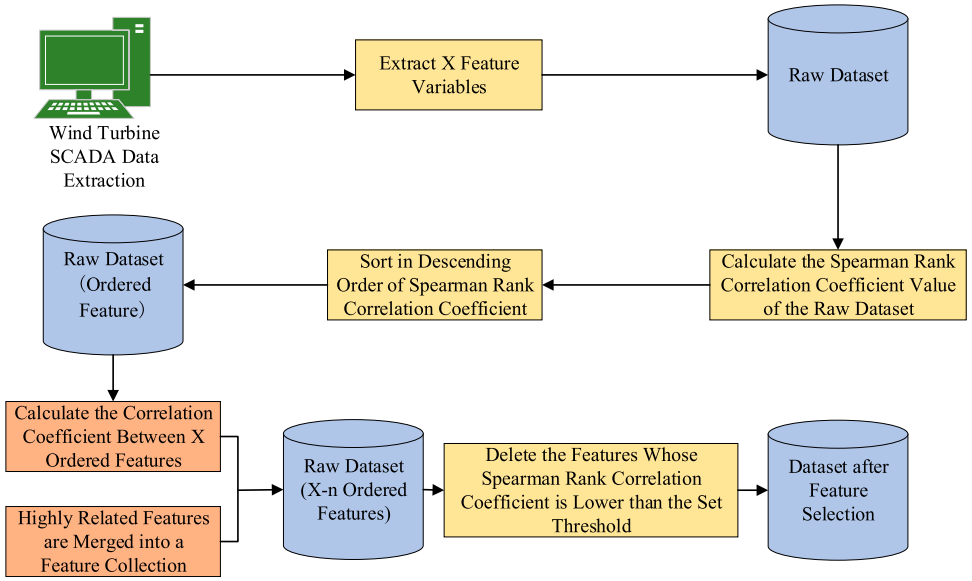


FIGURE 1 | Feature selection based on the Spearman rank correlation coefficient.

TABLE 1 | Cost matrix.

Type	C_F	C_N
C_F	$F(C_F, C_F)$	$F(C_F, C_N)$
C_N	$F(C_N, C_F)$	$F(C_N, C_N)$

assigned to a certain category, x needs to be classified into the class that minimizes the cost.

LightGBM Classifier

LightGBM is an improved variant gradient boosting decision tree (GBDT) framework based on the decision tree algorithm (Ke et al., 2017). Given the supervised learning dataset $X = \{(x_i, y_i)\}_{i=1}^{N}$, where x represents the samples data and y represents the class labels, the aims of LightGBM algorithm is to find a mapping relationship $\widehat{F}(x)$ to approximate the function $F(x)$, so as to minimize the loss function $\Psi\ (y, F(x))$,

$$\widehat{F} = \text{argmin}_F E_{y,x} \Psi(y,\ F(x)), \tag{4}$$

and the objective function $Obj^{(t)}$ can be expressed as follows:

$$Obj^{(t)} = \sum_{i=1}^{n} \Psi\left(y_i, F_{t-1}(x_i) + f_t(x_i)\right) + \sum_{k} \Omega(f_k). \tag{5}$$

Here, $\Omega(f_k)$ represents the regular term.

In LightGBM, Newton's method is used to quickly approximate the objective function.

$$Obj^{(t)} \cong \sum_{i=1}^{n} \left[g_i f_t(x_i) + \frac{1}{2} h_i f_t^2(x_i) \right] + \sum_{k} \Omega(f_k), \tag{6}$$

where g_i and h_i represent a first-order loss function and a second-order loss function, respectively.

$$g_i = \partial_{F_{t-1}(x_i)} \Psi\left(y_i, F_{t-1}(x_i)\right), \tag{7}$$

$$h_i = \partial^2_{F_{t-1}(x_i)} \Psi\left(y_i, F_{t-1}(x_i)\right). \tag{8}$$

The information gain in LightGBM is defined as follows:

$$G = \frac{1}{2}\left[\frac{\left(\sum_{i \in I_L} g_i\right)^2}{\sum_{i \in I_L} h_i + \lambda} + \frac{\left(\sum_{i \in I_R} g_i\right)^2}{\sum_{i \in I_R} h_i + \lambda} - \frac{\left(\sum_{i \in I} g_i\right)^2}{\sum_{i \in I} h_i + \lambda} \right]. \tag{9}$$

Compared to the GBM algorithm, the LightGBM algorithm is more efficient in processing high-dimensional big data. This is because of exclusive feature bundling (EFB) algorithm and gradient-based one-side sampling (GOSS) algorithm in LightGBM. The GOSS method introduces a data instance with a constant multiplier and a small gradient, which can sample the data from the big dataset that has the same distribution and characteristics as the raw data and ensuring the classification accuracy while improving the classification speed. In the high-dimensional space, the data are sparsely coded, while in the sparse feature space, nonzero values rarely appear at the same time. The EFB method is used for feature sampling to bundle two features to form a new feature which can decrease the data sample. Besides, the traditional gradient boosting method uses an exhaustive attack method to find segmentation features and thresholds, while LightGBM uses a histogram-based method to find suboptimal solution segmentation features and thresholds and reducing calculation time. Specifically, a certain feature of the data is discretized into a histogram algorithm and the discretized value is used as an index to accumulate statistics in the histogram. After data traversal, the histogram accumulates the required statistics and then according to the discrete value of the histogram, traverses to find the optimal split point. The tree of XGBoost is grown by the level-wise tree growth method (Mitchell and Frank, 2017; Chen and Guestrin 2016) and leaf-wise tree

growth in LightGBM; however, leaf-wise splits lead to an increase in complexity and may lead to overfitting, and a tree grown with leaf-wise growth will be deeper when the number of leaves is the same. **Figure 2** is a schematic presentation of two tree growth methods.

Because the minority fault samples and majority normal samples of WTs and the LightGBM algorithm are more focusing on the classification of the majority sample, the cost function is introduced to replace the information gain in the weight formula of the algorithm to form the cost-sensitive LightGBM algorithm (Elkan 2001). In each iteration update processing, the algorithm will pay much attention to the minority class which improves identification of the minority class.

Cost-Sensitive LightGBM Algorithm

For binary classification problems, the commonly used logistic loss function of LightGBM is the logistic loss function, and the expression is as follows:

$$logloss(\mathrm{x_i}, \mathrm{y_i}) = -\frac{1}{N}\sum_{i=1}^{N}[\mathrm{y_i} log P(\mathrm{x_i}) + (1-\mathrm{y_i}) log(1-P(\mathrm{x_i})] \tag{10}$$

where P represents the posterior probability. In the log loss function of the cost-sensitive LightGBM algorithm (Zheng and Peng, 2019), we replace $P(\mathrm{x_i})$with the following:

$$P(\mathrm{x_i}) = \frac{1}{1+e^{-2\delta(\mathrm{x_i})-2\eta}}, \tag{11}$$

where $\delta = \frac{F(C_F,C_N)+F(C_N,C_F)}{2}$,$\eta = \frac{1}{2} log \frac{F(C_N,C_F)}{F(C_F,C_N)}$, and the cost-sensitive logic loss function can be simplified asb follows:

$$CSlogloss(\mathrm{x_i}, \mathrm{y_i}) = \frac{1}{F(C_F,C_N)+F(C_N,C_F)} log\frac{P(c=F|\mathrm{x_i})F(C_N,C_F)}{P(c=N|\mathrm{x_i})F(C_F,C_N)}, \tag{12}$$

where $P(c=F|\mathrm{x_i})$ represents the posterior probability of dividing the sample x_i into the fault class and $P(c=N|\mathrm{x_i})$ represents the posterior probability of dividing the sample x_i into the normal class (Mitchell and Frank, 2017). Obviously, there is $P(c=F|\mathrm{x_i}) = 1-P(c=N|\mathrm{x_i})$.

According to **Eq. 5**, the objective function of CS LightGBM can be written as follows:

$$Obj^{(t)} = \sum_{i=1}^{n}\Psi(y_i, F_{t-1}(x_i)+f_t(x_i)) + \sum_k \Omega(f_k), \tag{13}$$

where Ψ is the loss function and Ω is the regular term. According to the second-order Taylor expansion, the objective function can be rewritten as

$$Obj^{(t)} \cong \sum_{i=1}^{n}\left[\Psi(y_i, F_{t-1}(x_i)) + g_i f_t(x_i) + \frac{1}{2}h_i f_t^2(x_i)\right] + \sum_k \Omega(f_k). \tag{14}$$

The first-order loss function g_i and the second-order loss function h_i of x_i are as follows:

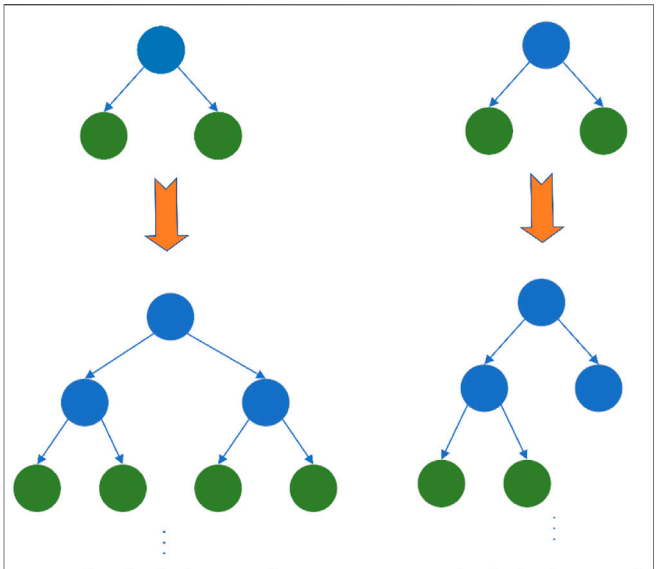


FIGURE 2 | Comparison of level-wise tree growth and leaf-wise tree growth.

$$g_i(x_i) = 2\delta[y - P(\mathrm{x_i})], \tag{15}$$

$$h_i(x_i) = -4\delta^2 P(\mathrm{x_i})[1-P(\mathrm{x_i})]. \tag{16}$$

Given the structure of the tree, the optimal weight w_j^* of each leaf node is obtained as follows:

$$w_j^* = -\frac{\sum_{i\in I_j} g_i}{\sum_{i\in I_j} h_i + \lambda}. \tag{17}$$

The algorithm of cost-sensitive LightGBM (CS LightGBM) is given as follows.

Algorithm1: Cost-sensitive LightGBM

Input: Wind turbines gearboxes SCADA dataset $D = \{(x_1,y_1),(x_2,y_2),\ldots(x_n,y_n)\}$,cost-sensitive loss function $\Psi(y,(F(x))$,regularization term Ω, δ, η,number of iteration T

1: Collecting normal wind turbines gearboxes operating dataset D

2: Initialize base learner F_0;

3: for t=1 to T do

4: Calculate the gradient on $\Psi: g_i(x_i) = 2\delta[y - P(\mathrm{x_i})]$

5: Calculate the Hessian on $\Psi: h_i(x_i) = -4\delta^2 P(\mathrm{x_i})[1-P(\mathrm{x_i})]$

6: Determine the tree structure q(x) by maximizing:

$$G = \frac{1}{2}\left[\frac{(\sum_{i\in I_L} g_i)^2}{\sum_{i\in I_L} h_i+\lambda} + \frac{(\sum_{i\in I_R} g_i)^2}{\sum_{i\in I_R} h_i+\lambda} - \frac{(\sum_{i\in I} g_i)^2}{\sum_{i\in I} h_i+\lambda}\right]$$

7: Determine the optimal leaf weight by:

$$w_j^* = argmin_{w_i}\{\sum_{i=1}^{n}\left[\Psi(y_i, F_{t-1}(x_i)) + g_i f_t(x_i) + \frac{1}{2}h_i f_t^2(x_i)\right] + \sum_k \Omega(f_k)\}$$

8: $w_j^* = -\frac{\sum_{i\in I_j} g_i}{\sum_{i\in I_j} h_i+\lambda}$

9: Calculate the optimal object function $Obj^{(t)}$(see the Eq.(13))

10: end for

Output: Cost-sensitive LightGBM Model $F_M(x)$

COST-SENSITIVE LIGHTGBM FAULT DETECTION MODEL

In order to minimize the loss caused by fault alarm and missed detection due to the imbalanced data of WTs, the CS LightGBM fault detection model is established. The WT fault detection process can be divided into two parts: offline modeling and online detection, as shown in

Figure 3. The main steps of offline modeling are given as follows.

Algorithm 2: Off-line modeling of cost-sensitive LightGBM fault detection method
Input: WTs gearboxes SCADA dataset $D = \{(x_1 y_1), (x_2, y_2), \ldots (x_n, y_n)\}$
1: Handing missing data , applying data normalization and dividing the raw data D into training set D_{train}, test set D_{test} and validation set D_{valid}, and normalize the training data 2: Perform feature selection on the normalized training data, using Spearman rank correlation coefficient to analyze the data 3: Using the training dataset D_{train} to train Cost-sensitive LightGBM fault detection model 4: Using the validation set D_{valid} to optimizing parameter of Cost-sensitive LightGBM 5: Repeat the training of the Cost-sensitive LightGBM fault detection model until output the optimized fault detection model.
Output: Cost-sensitive LightGBM WT fault detection Model M

The main steps of online fault detection are given as follows:

Algorithm 3: Online implementation of cost-sensitive LightGBM fault detection method
Input: Cost-sensitive LightGBM WT fault detection Model M, online data D_{test}
1: Use the test set D_{test} to verify the Cost-sensitive fault detection model 2: Obtain the output fault prediction value y according to the trained cost-sensitive LightGBM model M 3: If y=1, faults occurs, y=0, it is a normal operating condition 4: If the data is in fault, calculate the error between the model prediction y_p and the online test data y_0 5: Calculate the evaluation index
Output: False alarm rate, missing detection rate and Matthews correlation coefficient

Figure 3 gives out the basic framework of cost-sensitive LightGBM algorithm. The complete fault detection procedure including offline training and online detection is shown in **Figure 3**. Specifically, the procedure has gone through five phases, namely, data extraction, data preprocessing (normalization), feature selection (Spearman rank correlation), model optimization, and decision making.

EXPERIMENTAL CASE

The main structure of WT is shown in **Figure 4**. The main components of WT include a wind wheel, gearbox, generator, converter, yaw system, pitch system, and hydraulic system. Among these subsystems, the gearbox failure will cause a high fault rate and irreversible damage to WT. In order to verify the effectiveness of CS LightGBM compared with other cost-sensitive ensemble learning methods in the detection of WT gearbox faults, a comparative experiment was set up. The experimental steps are given as follows:

1) Collect raw data from the SCADA system and perform data preprocessing:

$$\overline{x}_i = \frac{x - x_{min}}{x_{max} - x_{min}} \tag{18}$$

2) Use Spearman rank correlation analysis methods to perform feature selection on the extracted features
3) Divide the training set, test set, and validation set into the existing dataset and establish the CS LightGBM offline model
4) Perform online detection based on the established CS LightGBM model
5) Evaluate the fault detection method of CS LightGBM and calculate the false alarm rate, missing detection rate, and Matthews correlation coefficient

Feature Extraction

In order to verify the performance of the gearbox fault detection model, the 1.5 MW WT in a wind farm was used as the research

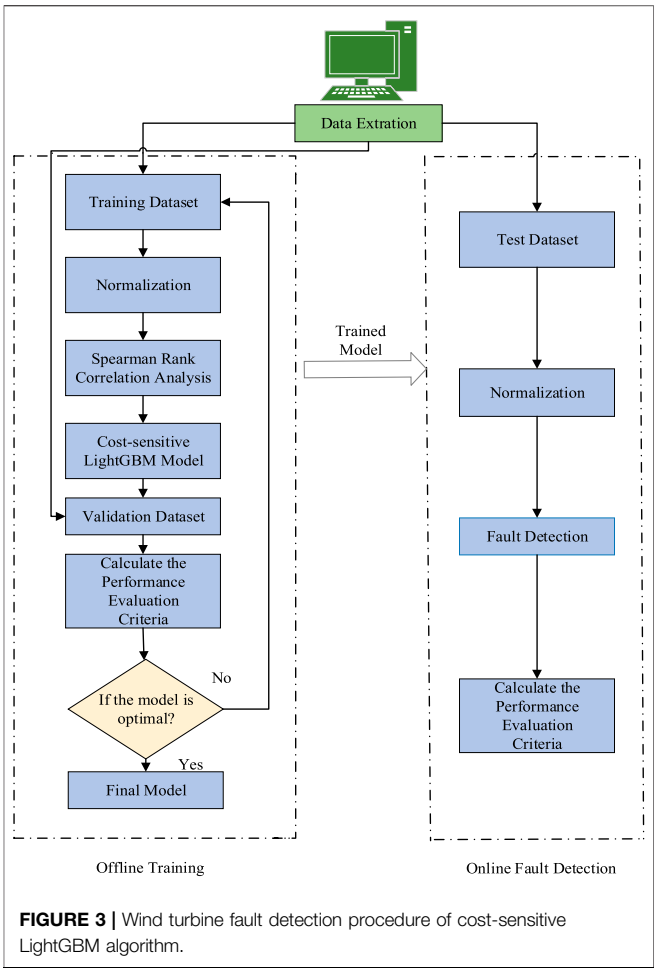


FIGURE 3 | Wind turbine fault detection procedure of cost-sensitive LightGBM algorithm.

object. A 3-year gearbox dataset is extracted from the SCADA data. The sampling interval is 2 s. Through the analysis of the WT gearbox mechanism and expert experience, the data within the period time from 30 min before the start of the fault to 30 min after the fault were selected as the experimental data. A part of the raw data is shown in **Table 2**.

We select the datasets containing gearbox oil temperature overrun fault, gearbox oil filter pressure fault, and gearbox lubrication oil level fault from the SCADA normal operating condition data and record them as Dataset 1, Dataset 2, and Dataset 3, as shown in **Table 3**.

Feature Selection

Dataset 1–Dataset 3 contain 3 types of gearbox faults, including the error gearbox oil temperature overrun, error gearbox oil filter pressure, and error gearbox lubrication oil level. To deal with the feature selection of WT, the fault mechanism and the correlated parameters of each fault are analyzed as shown in **Table 4**.

The gearbox bearing temperature information is used to evaluate the health of the gearbox. When selecting the state parameters, parameters that have a greater impact on parameters are mainly selected. According to the Spearman rank correlation coefficient analysis method, the correlation

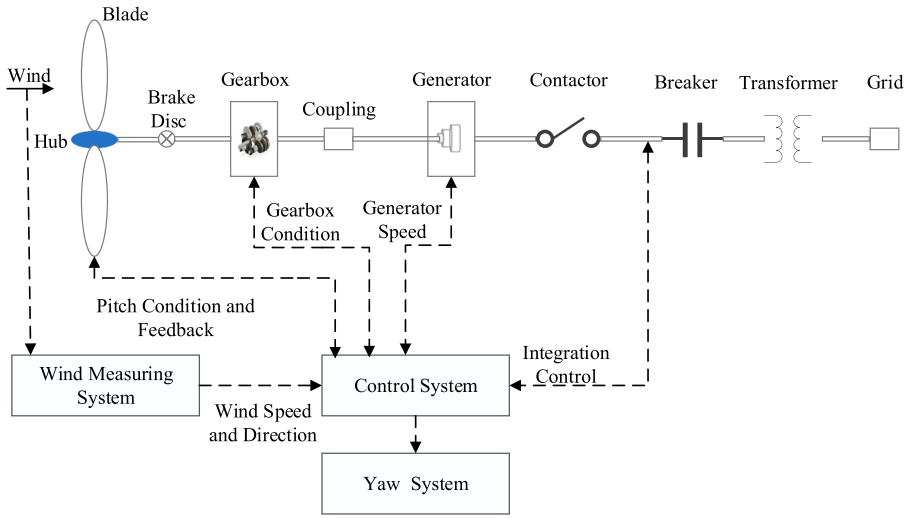


FIGURE 4 | Main structure of doubly fed WT.

TABLE 2 | Part of the raw data of wind turbines on February 27, 2018.

Feature	Time						
	11:03:22	11:03:24	11:03:26	–	12:59:44	12:59:46	12:59:48
30 s average wind speed	5.44	5.44	5.44	–	9.11	9.11	9.11
Gearbox shaft 1 temperature	84.2	84.2	84.3	–	87.7	87.7	87.7
Gearbox shaft 2 temperature	76.5	76.5	76.5	–	77.4	77.4	77.4
Gearbox inlet oil temperature	77.1	77.1	77.1	–	79.7	79.7	79.7
Gearbox oil temperature	69	69	68.9	–	77	77	77
Generator winding temperature U	69.1	69.1	69.1	–	77.1	77.1	77.1
–	–	–	–	–	–	–	–
Generator winding temperature V	69.4	69.4	69.3	–	77.1	77.1	77.1
Generator winding temperature W	57	57	57	–	56.5	56.5	56.5
Generator bearing temperature A	62.1	62.1	62.1	–	61.5	61.5	61.5
Generator bearing temperature B	45.7	45.7	45.7	–	45	45	45
Nacelle outdoor temperature	35.1	35.1	35.1	–	35.3	35.3	35.3
Main bearing rotor side temperature	38.9	38.9	38.9	–	38.9	38.9	38.9
Main bearing gearbox side temperature	50.1	50.1	50.1	–	50.3	50.3	50.3
Pitch position target	0	0	0		0.02	0.02	0.02
Converter motor speed	1,324.8	1,324.8	1,287.3	–	1735.7	1735.7	1735.7

TABLE 3 | Dataset description.

Dataset	Total number of samples	Total number of features	Fault-free	Faulty
Dataset 1	3,586	216	3,118	468
Dataset 2	5,172	216	3,670	1,502
Dataset 3	3,590	216	3,199	390

strength between each state parameter and the gearbox bearing temperature is calculated, as shown in **Table 5**.

From the correlation analysis results in **Table 5**, it can be seen that there is a large difference between features and the gearbox bearing temperature. In order to avoid the influence of irrelevant and weakly related features on the gearbox fault detection, the correlation coefficient is selected between ± 0.50 to ± 0.95, which are shown in bold in **Table 5**.

TABLE 4 | WT gearbox fault type and correlated parameters.

Fault type	Fault mechanism	Correlated parameters
Error gearbox oil temperature overrun	Oil temperature over 80°C and lasts 5 s	Gearbox oil temperature; bearing temperature; main bearing gearbox side temperature; gearbox shaft temperature; and 30 s average wind speed
Error gearbox oil filter pressure	Oil temperature over 55°C and lasts 12 s	Gearbox oil temperature; converter motor speed; converter power; and main loop rotor speed
Error gearbox lubrication oil level	No input high level (green light is off) and lasts 12 s	Gearbox oil temperature; bearing temperature; converter motor speed; and converter power

TABLE 5 | Gearbox features correlation analysis results.

Feature		Spearman rank coefficient correlation analysis		
Dataset	**Tag**	**1**	**2**	**3**
30 s average wind speed	W	–0.389262	0.014553	**0.800212**
Gearbox shaft 1 temperature	AL	1.000000	1.000000	1.000000
Gearbox shaft 2 temperature	AM	**0.749613**	**0.911267**	**0.990621**
Gearbox inlet oil temperature	AN	**0.593799**	**0.911752**	**0.947370**
Gearbox oil temperature	AO	**0.703876**	**0.923477**	**0.964006**
Generator winding temperature U	AT	**0.707279**	**0.532421**	**0.610418**
Generator winding temperature V	AV	**0.680785**	**0.627169**	**0.615225**
Generator winding temperature W	AX	**0.692507**	**0.642950**	**0.622792**
Generator bearing temperature A	AZ	**0.753099**	0.184554	**0.717485**
Generator bearing temperature B	BA	**0.775826**	**0.541165**	**0.798545**
Nacelle outdoor temperature	BD	**0.617450**	**0.599896**	**0.908760**
Nacelle temperature	BE	**0.871901**	**0.826202**	**0.671356**
Main bearing rotor side temperature	BS	**0.702117**	-0.036307	**0.649327**
Main bearing gearbox side temperature	BT	**0.780589**	0.214435	**0.745818**
Pitch position target	BU	**–0.543102**	–0.250650	**0.735036**
Converter motor speed	FD	–0.491465	–0.143006	0.261584
Converter power	FF	–0.472841	–0.251429	0.287380
Main loop rotor speed	FJ	–0.449845	–0.232728	0.323973

The bold values represents the correlation coefficient between ± 0.50 and ± 0.95.

Fault Detection Performance Evaluation Criteria

The four states including the normal state, gearbox oil temperature overrun fault, gearbox oil filter pressure fault, and gearbox oil level fault are, respectively, marked as Q = [0,1,2,3], and the dataset is divided into four parts. By combining the three types of faults with the normal state in turn, we perform WT fault detection through the CS LightGBM algorithm to obtain four sets of classification indicators. In order to measure the classification of imbalanced data, the Matthews correlation coefficient (MCC) is introduced to evaluate the fault detection model. At the same time, the false alarm rate (FAR) and missed detection rate (MDR) are used as fault detection evaluation indicators. The mixed matrix of two classification problems is shown in **Table 6**.

In this study, true positive (TP) is the number of samples correctly identified as faulty; false positive (FP) is the number of samples wrongly identified as fault free; true negative (TN) is the number of samples correctly identified as fault free; and false negative (FN) is the number of samples wrongly identified as faulty. The indicators under the binary classification are as follows:

TABLE 6 | Confusion matrix.

Actual class	Predictive class	
	Faulty	**Fault free**
Faulty	TP	FN
Fault free	FP	TN

$$\mathrm{FAR} = \frac{FP}{FP + TN,} \tag{19}$$

$$\mathrm{MDR} = \frac{FN}{TP + FN,} \tag{20}$$

$$MCC = \frac{TP{*}TN - FP{*}FN}{\sqrt{(TP + FP)(TP + FN)(TN + FP)(TN + FN)}}. \tag{21}$$

Results and Discussion

The experimental data are extracted from a 3-year SCADA dataset of a wind farm. The experiment verifies the effectiveness of the proposed cost-sensitive LightGBM for fault detection of WT gearboxes. In order to further verify the

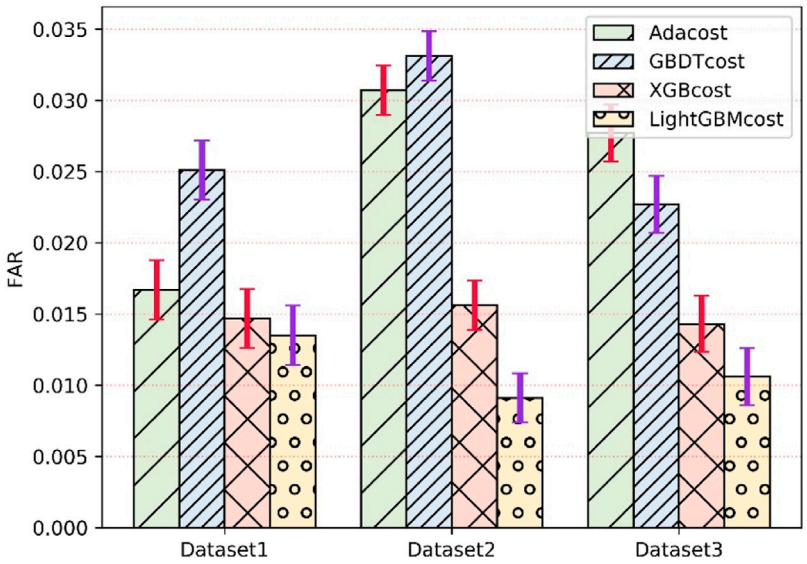


FIGURE 5 | False alarm rate of four algorithms for fault detection of wind turbines gearboxes.

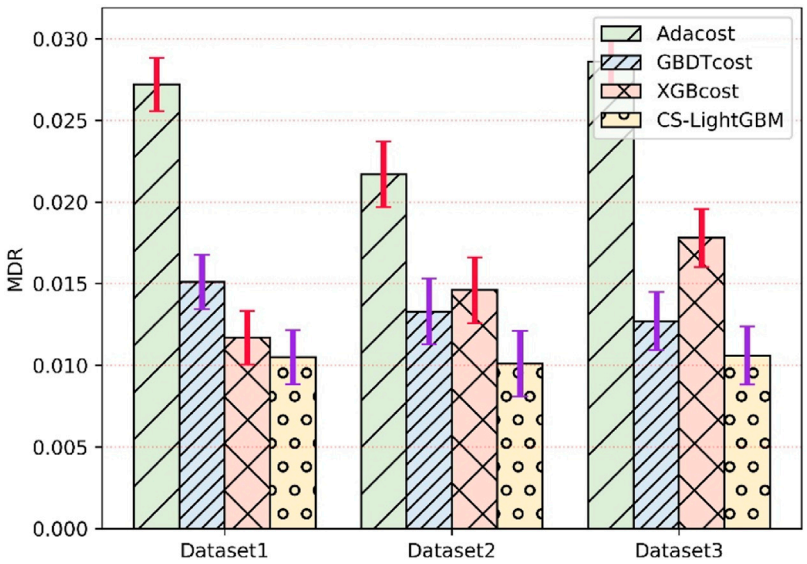


FIGURE 6 | Missing detection rate of four algorithms for fault detection of wind turbines gearboxes.

superiority of the method, three advanced fault diagnosis methods were compared, including cost-sensitive AdaBoost (AdaCost), cost-sensitive GBDT (GBDTcost), and cost-sensitive XGBoost (XGBcost). By using different evaluation criteria in three different datasets, **Figures 5**, **6** show FAR and MDR under different algorithms, respectively. In order to avoid overfitting in the model, a five-fold cross-validation method is used to evaluate the model. The smaller FAR and MDR mean better performance.

The comparison results of the proposed method and the AdaCost algorithm, GBDTcost algorithm, and XGBcost algorithm under different fault conditions are shown in **Figures 5**, **6**, respectively. It can be seen that the cost-sensitive LightGBM method is lower than the other three algorithms in terms of FAR and MDR, and the XGBcost criteria are generally better than the AdaCost and GBDTcost methods. When analyzing failure dataset 2, the FAR index of the CS LightGBM method is only 1.43% and the MDR index is only 1.01%. This method has good fault detection performance. The traditional cost-sensitive Boost method has high false positives and high false positives in the fault detection process, while the false negative and false positive

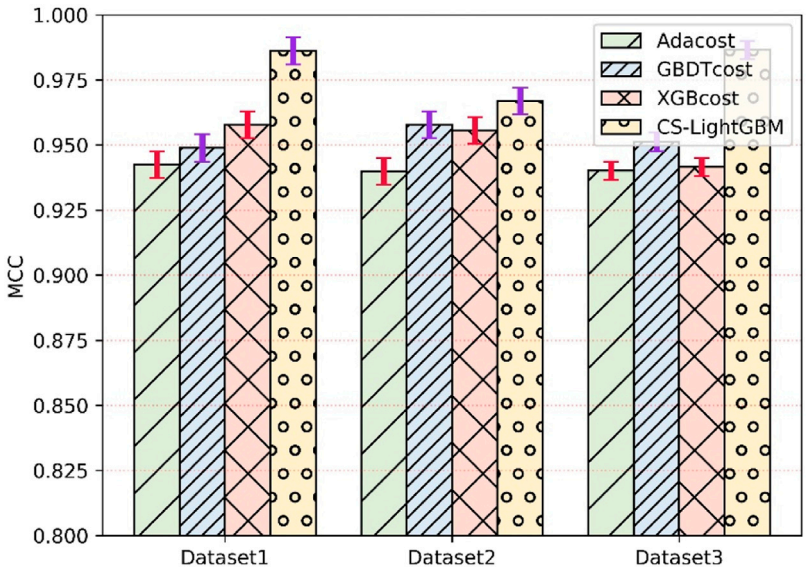


FIGURE 7 | Matthews correlation coefficient of four algorithms for fault detection of wind turbines gearboxes.

rates of the CS LightGBM method are lower than those of the other three methods.

Figure 7 shows the MCC of three different fault datasets. The MCC can also be used in the case of imbalanced samples. The closer the MCC is to 1, the better the performance of the method. It can be seen from **Figure 6** that the MCC of the cost-sensitive lightGBM method in dataset 2 is as high as 99.61% and the MCC of the remaining datasets is higher than that of the AdaCost, GBDTcost, and XGBcost.

CONCLUSION AND FUTURE WORK

WT gearboxes are operated in harsh conditions for a long time, the fault rate will increase, and it is extremely prone to faults. The accuracy of its diagnosis is often affected by many factors such as harsh environments and extreme weather. In order to improve the accuracy of fault diagnosis, the shortcomings of traditional algorithms are analyzed and compared, and a fault detection method based on CS LightGBM is proposed. The innovation is mainly reflected in the following two aspects:

1) The fault characteristics of the WT gearbox are analyzed, the fault features are extracted, and its fault feature indexes are obtained, by using the correlation between the feature correlation to improve the fault diagnosis performance
2) A method based on CS LightGBM is proposed and applied to the actual fault diagnosis of WTs and compared with the traditional cost-sensitive Boost methods

The experimental study demonstrated that existing algorithms had a low ability of wind turbine's fault detection. Two points that should be noticed are that the existing algorithm did not perform well just because it is not specially designed for wind turbine fault detection and it still has distinguished competences in industrial fault diagnosis and other fields. The cost-sensitive LightGBM is mainly suitable for imbalanced data, but its ability for other fault diagnosis remains unknown.

A single algorithm cannot detect all the faults in the WT, so the combined algorithm will become the research topic in the future. The comprehensive simulation of WT fault conditions will also be our research topic in the future. That is for all units of WT that are interconnected, and their features are strongly coupled. The occurrence of a fault in a particular component affects all the remaining units. Therefore, it is necessary to establish more compound fault models to conduct a comprehensive analysis of the WT system (Iranmehr et al., 2019).

DATA AVAILABILITY STATEMENT

The original contributions presented in the study are included in the article/supplementary material; further inquiries can be directed to the corresponding author.

AUTHOR CONTRIBUTIONS

All authors listed have made a substantial, direct, and intellectual contribution to the work and approved it for publication.

FUNDING

This work was supported in part by the National Natural Science Foundation of China (Grant No. 61403046), the Natural Science Foundation of Hunan Province, China (Grant No. 2019JJ40304), Changsha University of Science and Technology "The Double

First Class University Plan" International Cooperation and Development Project in Scientific Research in 2018 (Grant No. 2018IC14), the Research Foundation of the Education Bureau of Hunan Province (Grant No.19K007), Hunan Provincial Department of Transportation 2018 Science and Technology Progress and Innova-tion Plan Project (Grant No. 201843), the Key Laboratory of Renewable Energy Electric-Technology of Hunan Province, the Key Laboratory of Efficient and Clean Energy Utilization of Hunan Province, Innovative Team of Key Technologies of Energy Conservation, Emission Reduction and Intelligent Control for Power-Generating Equipment and System, CSUST, Hubei Superior and Distinctive Discipline Group of Mechatronics and Automobiles(XKQ2021003 and XKQ2021010), National Training Program of Innovation and Entrepreneurship for Undergraduates (Grant No. 202010536016), Major Fund Project of Technical Innovation in Hubei (Grant No. 2017AAA133), and Guangxi Key Laboratory of Trusted Software (No.201728).

REFERENCES

Amirat, Y., Benbouzid, M. E. H., Wang, T., Bacha, K., and Feld, G. (2018). EEMD-based Notch Filter for Induction Machine Bearing Faults Detection. *Appl. Acoust.* 133, 202–209. doi:10.1016/j.apacoust.2017.12.030

Bonett, D. G., and Wright, T. A. (2000). Sample Size Requirements for Estimating Pearson, Kendall and Spearman Correlations. *Psychometrika* 65, 23–28. doi:10.1007/bf02294183

Chen, T., and Guestrin, C. (2016). Xgboost: A Scalable Tree Boosting System. In Proceedings of the 22nd Acm Sigkdd International Conference on Knowledge Discovery and Data Mining, August 13-17, 2016, San Francisco, CA, USA, 785–794.

Chen, Z., Ding, S. X., Peng, T., Yang, C., and Gui, W. (2017). Fault Detection for Non-gaussian Processes Using Generalized Canonical Correlation Analysis and Randomized Algorithms. *IEEE Trans. Ind. Electro.* 65, 1559–1567. doi:10.1109/TIE.2017.2733501

Croux, C., and Dehon, C. (2010). Influence Functions of the Spearman and Kendall Correlation Measures. *Stat. Methods Appl.* 19, 497–515. doi:10.1007/s10260-010-0142-z

Domingos, P. M. (1999). A General Method for Making Classifiers Cost-Sensitive. InProceedings of the Fifth ACM SIGKDD International Conference on Knowledge Discovery and Data Mining, San Francisco, CA, USA, August 15-18, 1999; pp. 155–164.

Elkan, C. (2001). The Foundations of Cost-Sensitive Learning. In Proceedings of International Joint Conference on Artificial Intelligence 2, 973–978.

Fan, W., Stolfo, S. J., Zhang, J., and Chan, P. K. (1999). AdaCost: Misclassification Cost-Sensitive Boosting. *Proc. Icml*, 97–105.

Fumera, G., and Roli, F. J. V. C. A. I. p. L. I. A. (2002). Cost-sensitive Learning in Support Vector Machines. *Computer Science*.

Gao, Q. W., Liu, W. Y., Tang, B. P., and Li, G. J. (2018). A Novel Wind Turbine Fault Diagnosis Method Based on Intergral Extension Load Mean Decomposition Multiscale Entropy and Least Squares Support Vector Machine. *Renew. Energ.* 116, 169–175. doi:10.1016/j.renene.2017.09.061

Han, L., Wang, Q., Jiang, K., Wang, X., and Zhou, Y. (2020). Quantitative Diagnosis Method of Gearbox under Varying Conditions Based on ARX Model and Generalized Canonical Correlation Analysis. *IEEE Access* 8, 40629–40639. doi:10.1109/access.2020.2972381

Iranmehr, A., Masnadi-Shirazi, H., and Vasconcelos, N. (2019). Cost-sensitive Support Vector Machines. *Neurocomputing* 343, 50–64. doi:10.1016/j.neucom.2018.11.099

Jiang, Q., Yan, X., and Huang, B. (2015). Performance-driven Distributed PCA Process Monitoring Based on Fault-Relevant Variable Selection and Bayesian Inference. *IEEE Trans. Ind. Electro.* 63, 377–386. doi:10.1109/TIE.2015.2466557

Ke, G., Meng, Q., Finley, T., Wang, T., Chen, W., Ma, W., et al. (2017). Lightgbm: A Highly Efficient Gradient Boosting Decision Tree. *Proceedings of Advances in Neural Information Processing Systems* 30, 3146–3154. doi:10.5555/3294996.3295074

Knoll, U., Nakhaeizadeh, G., and Tausend, B. (1994). Cost-sensitive Pruning of Decision Trees. *Proceedings of European Conference on Machine Learning* 784, 383–386. doi:10.1007/3-540-57868-4_79

Liang, H., Chen, Y., Liang, S., and Wang, C. (2018). Fault Detection of Stator Inter-turn Short-Circuit in PMSM on Stator Current and Vibration Signal. *Appl. Sci.* 8, 1677. doi:10.3390/app8091677

Long, W., Jiao, J., Liang, X., and Tang, M. (2018). An Exploration-Enhanced Grey Wolf Optimizer to Solve High-Dimensional Numerical Optimization. *Eng. Appl. Artif. Intelligence* 68, 63–80. doi:10.1016/j.engappai.2017.10.024

Long, W., Jiao, J., Liang, X., Wu, T., Xu, M., and Cai, S. (2021a). Pinhole-imaging-based Learning Butterfly Optimization Algorithm for Global Optimization and Feature Selection. *Appl. Soft Comput.* 103, 107146. doi:10.1016/j.asoc.2021.107146

Long, W., Wu, T., Xu, M., Tang, M., and Cai, S. (2021b). Parameters Identification of Photovoltaic Models by Using an Enhanced Adaptive Butterfly Optimization Algorithm. *Energy* 229, 120750. doi:10.1016/j.energy.2021.120750

Mitchell, R., and Frank, E. J. (2017). Accelerating the XGBoost Algorithm Using GPU Computing. *PeerJ Comp. Sci.* 3, 127. doi:10.7717/peerj-cs.127

Qiao, W., and Lu, D. (2015). A Survey on Wind Turbine Condition Monitoring and Fault Diagnosis-Part I: Components and Subsystems. *IEEE Trans. Ind. Electron.* 62, 6536–6545. doi:10.1109/tie.2015.2422112

Ra, A ., Aeh, B., and Song, D. Chaos-opposition-enhanced Slime Mould Algorithm for Minimizing the Cost of Energy for the Wind Turbines on High-Altitude Sites. *ISA Trans.* 160, 2021. doi:10.1016/j.isatra.2021.04.011

Song, D., Chang, Q., Zheng, S., Yang, S., Yang, J., and Hoon Joo, Y. (2021). Adaptive Model Predictive Control for Yaw System of Variable-Speed Wind Turbines. *J. Mod. Power Syst. Clean Energ.* 9 (1), 219–224. doi:10.35833/mpce.2019.000467

Stetco, A., Dinmohammadi, F., Zhao, X., Robu, V., Flynn, D., Barnes, M., et al. (2019). Machine Learning Methods for Wind Turbine Condition Monitoring: A Review. *Renew. Energ.* 133, 620–635. doi:10.1016/j.renene.2018.10.047

Tang, M., Ding, S. X., Yang, C., Cheng, F., Shardt, Y. A. W., Long, W., et al. (2019). Cost-sensitive Large Margin Distribution Machine for Fault Detection of Wind Turbines. *Cluster Comput.* 22, 7525–7537. doi:10.1007/s10586-018-1854-3

Tang, M., Zhao, Q., Ding, S. X., Wu, H., Li, L., Long, W., et al. (2020). An Improved LightGBM Algorithm for Online Fault Detection of Wind Turbine Gearboxes. *Energies* 13, 807. doi:10.3390/en13040807

Teng, W., Ding, X., Zhang, X., Liu, Y., and Ma, Z. (2016). Multi-fault Detection and Failure Analysis of Wind Turbine Gearbox Using Complex Wavelet Transform. *Renew. Energ.* 93, 591–598. doi:10.1016/j.renene.2016.03.025

Turney, P. D. J. (1994). Cost-sensitive Classification: Empirical Evaluation of a Hybrid Genetic Decision Tree Induction Algorithm. *J. Artif. intelligence Res.* 2, 369–409. doi:10.1613/jair.120

Wang, T., Han, Q., Chu, F., and Feng, Z. (2019). Vibration Based Condition Monitoring and Fault Diagnosis of Wind Turbine Planetary Gearbox: A Review. *Mech. Syst. Signal Process.* 126, 662–685. doi:10.1016/j.ymssp.2019.02.051

Yang, D., Pang, Y., Zhou, B., and Li, K. (2019). Fault Diagnosis for Energy Internet Using Correlation Processing-Based Convolutional Neural Networks. *IEEE Trans. Syst. Man. Cybern, Syst.* 49, 1739–1748. doi:10.1109/tsmc.2019.2919940

Yang, J., Fang, L., Song, D., Su, M., Yang, X., Huang, L., et al. (2021). Review of Control Strategy of Large Horizontal-axis Wind Turbines Yaw System. *Wind Energy* 24 (2), 97–115. doi:10.1002/we.2564

Zhang, D., Qian, L., Mao, B., Huang, C., Huang, B., and Si, Y. (2018). A Data-Driven Design for Fault Detection of Wind Turbines Using Random Forests and XGboost. *IEEE Access* 6, 21020–21031. doi:10.1109/access.2018.2818678

Zheng, X.-X., and Peng, P. (2019). Fault Diagnosis of Wind Power Converters Based on Compressed Sensing Theory and Weight

Constrained Adaboost-SVM. *J. Power Electro.* 19, 443–453. doi:10.6113/JPE.2019.19.2.443

Conflict of Interest: The authors declare that the research was conducted in the absence of any commercial or financial relationships that could be construed as a potential conflict of interest.

Publisher's Note: All claims expressed in this article are solely those of the authors and do not necessarily represent those of their affiliated organizations, or those of the publisher, the editors and the reviewers. Any product that may be evaluated in this article, or claim that may be made by its manufacturer, is not guaranteed or endorsed by the publisher.

Copyright © 2021 Tang, Zhao, Wu and Wang. This is an open-access article distributed under the terms of the Creative Commons Attribution License (CC BY). The use, distribution or reproduction in other forums is permitted, provided the original author(s) and the copyright owner(s) are credited and that the original publication in this journal is cited, in accordance with accepted academic practice. No use, distribution or reproduction is permitted which does not comply with these terms.

frontiers in Energy Research

ORIGINAL RESEARCH
published: 17 August 2021
doi: 10.3389/fenrg.2021.746268

Optimal Sizing of a Grid Independent Renewable Heating System for Building Decarbonisation

Si Chen[1], *Daniel Friedrich*[2] *and Zhibin Yu*[1]*

[1]James Watt School of Engineering, The University of Glasgow, Glasgow, United Kingdom, [2]School of Engineering, The University of Edinburgh, Edinburgh, United Kingdom

As the use of fossil fuels has led to global climate change due to global warming, most countries are aiming to reduce greenhouse gas emissions through the application of renewable energies. Due to the distributed and seasonal heating demand, the decarbonisation of heating is more challenging, especially for countries that are cold in winters. Electrically powered heat pumps are considered as an attractive solution for decarbonising heating sector. Since grid-powered heat pumps may significantly increase the power demand of the grid, this paper considers using local renewable energy to provide power for heat pumps, which is known as the grid independent renewable heating system including photovoltaic, wind turbine, battery storage system and thermal energy storage. This paper investigates a complete renewable heating system (RHS) framework and sizing the components to decarbonise building heating. The relationship between the reduction of gas consumption and the requirement of battery storage system (BSS) under the corresponding installation capacity of renewable components is analysed with their technical requirements. Then, according to different investment plans, this paper uses the particle swarm optimisation algorithm for optimal sizing of each component in the RHS to find a solution to minimise CO_2 emissions. The results verify that the RHS with optimal sizing can minimise CO_2 emissions and reduce the operational cost of natural gas. This work provides a feasible solution of how to invest the RHS to replace the existing heating system based on gas boilers and CHPs.

Keywords: building heating decarbonisation, particle swarm optimisation, annual investment cost, renewable heating system, integrated energy network

OPEN ACCESS

Edited by:
Bo Yang,
Kunming University of Science and Technology, China

Reviewed by:
Xuehan Zhang,
Korea University, South Korea
Yixuan Chen,
The University of Hong Kong, Hong Kong, SAR China

***Correspondence:**
Zhibin Yu
zhibin.yu@glasgow.ac.uk

Specialty section:
This article was submitted to Smart Grids, a section of the journal Frontiers in Energy Research

Received: *23 July 2021*
Accepted: *03 August 2021*
Published: *17 August 2021*

Citation:
Chen S, Friedrich D and Yu Z (2021) Optimal Sizing of a Grid Independent Renewable Heating System for Building Decarbonisation. Front. Energy Res. 9:746268. doi: 10.3389/fenrg.2021.746268

INTRODUCTION

In recent decades, the rapid consumption of fossil fuels has greatly reduced global resource reserves and has led to global climate abnormalities (Ekren and Ekren, 2008; Luna-Rubio et al., 2012; Eltamaly et al., 2016). In order to reduce the risk of climate change caused by global warming, it is very important to reduce energy consumption and greenhouse gas (GHG) emissions (Ndwali et al., 2020; Rinaldi et al., 2021). As part of the European Green Agreement, the European Union (EU) has set a goal to reduce its GHG emissions by 55% by 2030 and become the world's first fully climate-neutral continent by 2050 (Maleki et al., 2016; Yue et al., 2020). Therefore, the EU has supported many energy projects in the past few years to enhance the role of renewable energy in the European energy plan (European Commission, 2016). To achieve these challenging goals, the energy structure of most countries needs to undergo major changes to reduce dependence on fossil fuels and the associated

GHG emissions (da Silva Lima et al., 2021). Increased use of renewable energy sources will make important contributions, such as wind energy, solar energy, hydropower, tides, waves, geothermal energy, environmental thermal energy, biofuels and municipal waste (Edenhofer et al., 2011). Due to the non-dispatchable nature of many renewables, energy storage is also required. In recent years, the integrated energy network (IEN) has developed rapidly in terms of energy efficiency improvement, carbon dioxide emission reduction, and renewable energy integration.

In countries with cold winters, heating accounts for a large part of energy consumption and is usually heavily dependent on the burning of fossil fuels such as natural gas and coal (Liang et al., 2018). The current energy demand in the building sector, such as space heating and domestic hot water, accounts for 40% of the total energy demand in the EU (Tulus et al., 2016). Nearly half of the total energy consumption in the United Kingdom is used for heating, and this proportion is even higher in Scotland (Renaldi et al., 2017). While it is crucial to decarbonise heating, it is challenging due to the distributed demand and large seasonal variations. In 2017, the GHG emission of United Kingdom equals to 460 million tons of CO_2, of which nearly 40% came from natural gas used for heating (Vanlint, 2018). In order to reduce GHG to net zero by 2050 as part of the government's carbon plan, the United Kingdom has pledged to establish more district heating networks and develop large-scale electrifying heating (Millar et al., 2021). Nearly 90% of the overall heat demand in the United Kingdom is provided by natural gas boilers and combined heat and power (CHP) (Millar et al., 2021). Since renewable energy can only generate electricity while CHP units have a strong interdependence between power generation and thermal power generation, CHPs are widely used to provide domestic hot water and space heating in district heating systems. However, CHP technology is entirely focused on efficiency improvement and cost optimisation and rarely considers carbon minimisation. In the past, the natural gas CHP was a good alternative to coal as it could significantly reduce carbon emissions. However, with the electricity grid carbon intensity dropping below 300 kg CO_2/MWh, natural gas CHP can only reduce carbon emissions in a few edge cases. In the United Kingdom, as the installation of renewable energy increases, the feasibility of fossil fuel cogeneration has gradually declined. It is estimated that by 2035, the carbon intensity of electricity will be lower than that of natural gas (Millar et al., 2021). This will encourage thermoelectricity, shifting from natural gas boilers to direct electric heating and electric heat pumps.

Heat pumps (HPs) are considered to be the key technology for decarbonization in the heating industry (Kim et al., 2014; Al-Tameemi et al., 2019). The HP uses a small amount of work energy to convert a low-grade heat source into a higher-grade heat source. The technical details of HP will not be discussed in this article since a lot of literature has previously discussed it (Cengel and Boles, 2007; Ozgener and Hepbasli, 2007; Trillat-Berdal et al., 2007; Self et al., 2013; Casasso and Sethi, 2014; Arat and Arslan, 2017; Grassi, 2017). If the heat source is outside air, the system is called an air source heat pump. If the heat source is underground soil or groundwater, it is called a geothermal heat pump. Geothermal heat pump is one of the fastest growing renewable energy sources in the world (Li et al., 2021). In the long-term, electrifying heating based on HPs is an attractive solution for the decarbonized heating sector. However, this will significantly increase the peak power demand in winter and will bring further challenges to the national grid in terms of creating additional power generation capacity and balancing power generation and demand. In addition, if electric power is generated from fossil fuels, the decarbonization effect will not be fully realized. Therefore, this paper considers using local renewable energy, which is grid-independent, to power the heat pump for building heating and reduce the usage of traditional gas boiler for decarbonisation.

The development of IEN is to integrate electricity, heat and gas systems into an integrated power distribution network. However, the further integration of heating and power networks has also expanded the opportunities for demand-side management to integrate more variable renewable energy generation into the energy system. Due to the rapid growth, the renewable power generation has been extensively studied in the past decades (O'Shaughnessy et al., 2018; Liu et al., 2017). In particular, solar energy and wind energy are used as sources to supply power to the grid (Dragicevic et al., 2014; Jamal et al., 2019; Khezri et al., 2020). However, the main disadvantage of most renewable energy sources is their intermittent nature, as they fluctuate on a daily, weekly, and seasonal basis. In order to filter these changes, battery energy storage systems have been widely accepted as one of the potential solutions to shift the electrical load from peak hours to off-peak hours (Yang et al., 2018a; Wali et al., 2021). The idea of combining power generation cycle and HP cycle has been extensively studied, such as solar collector - HP (Trillat-Berdal et al., 2007), PV—HP (Kavian et al., 2020), HP—thermal energy storage (TES) (Renaldi et al., 2017), organic Rankine cycle (ORC) - HP water heaters (Liang et al., 2018). However, due to the large differences in local weather conditions, occupancy, energy prices, government subsidies and building types, this optimisation must be done for each component (Renaldi et al., 2017). When different energy vectors are intertwined in future smart energy systems, optimal sizing of each component is especially important. In the research on the optimal sizing of renewable energy systems, many papers have considered WT, PV, ESS, and fuel cells (Yang et al., 2020; Yang et al., 2021). However, the previous published papers only considered the perspective of electrical power use, and do not consider both heat demand and electricity generation together as well as the impact of heating demand that increases the electrical energy use under the trend of electrified heating in the future. In addition, most of the literature considers sizing from the aspect of technical requirements and does not incorporate future technology and price trends. Therefore, within the author's knowledge, the past research has not done feasibility analysis and optimisation for different power generation, thermal systems and the investment allocation of each system.

This paper proposes a complete renewable heating system (RHS) framework, including PV, WT, BSS, HP, and TES, and

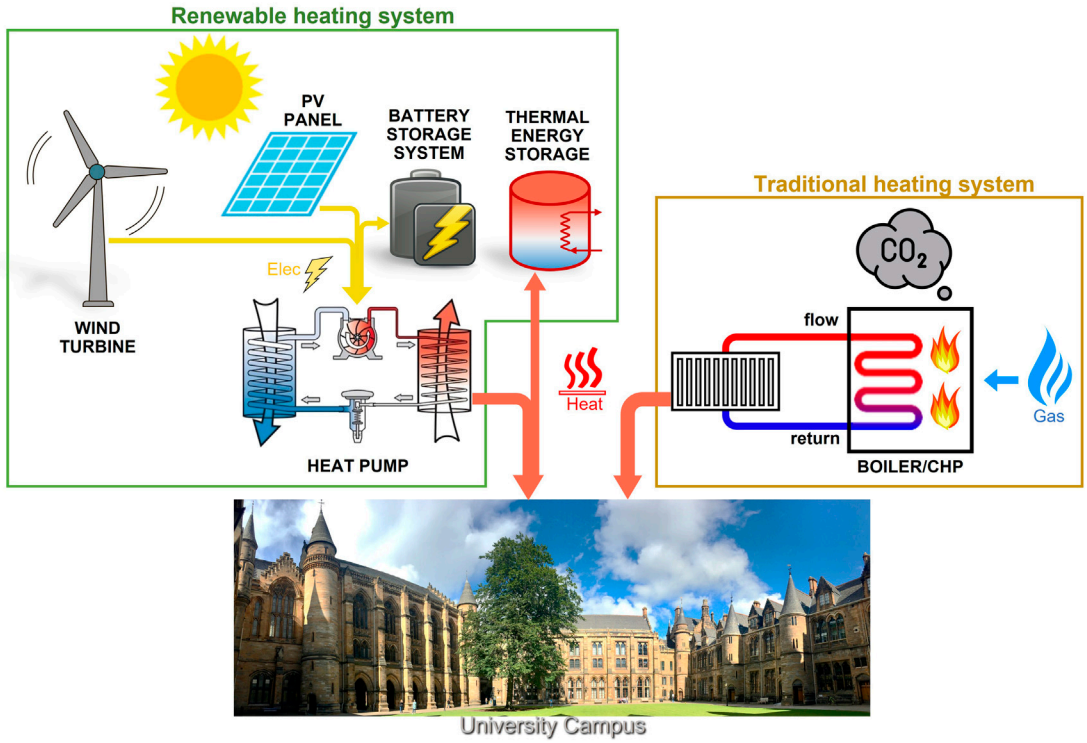


FIGURE 1 | Heating system of university campus.

provides a path to the decarbonisation with yearly investment decisions. In the context of British tariffs and government incentives, the size of each component in the system is optimised according to the annual investment cost (AIC) limit. Since there are many components in the RHS system that need to be optimised at the same time, the particle swarm optimisation (PSO) algorithm is selected for optimal sizing of the RHS. The optimisation goal is to obtain the least CO_2 emissions by adjusting the size of each component under the prescribed AIC. As a case study, this work provides a preliminary feasibility plan for how to invest in RHS to replace the traditional heating system in the university campus.

RENEWABLE HEATING SYSTEM MODELLING

Traditional heating systems use combined heat and power (CHP) and gas boilers to consume gas to generate heat for space heating of buildings. The use of gas can cause a large amount of CO_2 emissions. In order to reduce greenhouse gas emissions, one solution is to use electrically driven heat pumps to heat buildings. However, this will increase the cost in electricity and have an impact on the electricity grid, especially in winter when the heat demand is relatively high. This can lead to extra load to the power grid and affect its stability. To solve this problem, the usage of local renewable resources is considered as a substitute. Renewable resources mainly include wind and solar energy that both depend on weather conditions. Thus, the heating system requires battery storage systems and thermal energy storage to compensate the imbalance between generation and demand for electrical energy and thermal energy, respectively. The district heating network of the traditional heating system and the proposed renewable heating system (RHS) is shown in **Figure 1**.

Wind Turbine

The role of wind turbines (WT) is to convert wind energy, an environmentally friendly energy source, into a form of electrical energy. It is one of the most promising renewable energy sources and its global installed capacity is increasing year by year (Ren et al., 2021). According to the direction of their rotation axis, WTs can be classified into horizontal axis wind turbines (HAWT) and vertical axis wind turbines (VAWT). HAWT extracts wind energy on the horizontal axis and the blades rotate due to the lift provided by the aerodynamic force from wind. Because of it has higher efficiency than VAWT, the HAWT is more popular in research. However, HAWT needs to always point to the wind direction to work effectively. For unpredictable wind directions, the HAWT needs additional mechanisms to ensure that the blades are always facing the wind direction. The VAWT has its blades perpendicular to the ground and rotating around the

vertical axis. VAWT can receive wind power from any direction. Compared with HAWT, VAWT has several advantages, including no need to face to the wind flow, the ability of generating electricity at low wind speed, no need for additional control on yaw and pitch, less maintenance costs, and less noise (Eriksson et al., 2008; Johari et al., 2018). However, VAWT has much lower efficiency at high wind speeds than HAWT, its dynamic stability is relatively poor due to its light weight, and it is vulnerable to backtracking wind. For the above reasons, VAWT is often installed in slow and turbulent wind environments, such as roof top, for low-power generation (Bhutta et al., 2012), while HAWT is often used for high-power generation in isolated and remote areas, such as on-shore or off-shore wind farms (Johari et al., 2018). In recent years, some researchers have combined the two types of WT together to improve its operational capabilities (Govind, 2017).

Although HAWT and VAWT have lots of difference in structure, control strategy and power efficiency, the methods they use to capture power from wind energy are the same, and thus can be expressed by the same equation. The available power output of a WT is proportional to the cube of the wind speed. If the wind speed is too low, the output power of the WT can be ignored. When the wind speed increases, the output power of the WT increases rapidly. Therefore, in order to ensure the normal operation of a WT, three threshold wind speeds usually need to be considered, including the cut-in speed, the rated speed and the cut-out speed (Ren et al., 2016). When the wind speed is lower than the cut-in speed, the WT stops to avoid unnecessary mechanical wear and energy consumption; when the wind speed is higher than the cut-in speed and lower than the rated speed, the WT controls its rotating speed to track the maximum power point referring to the current wind speed; when the wind speed is higher than the rated speed and lower than the cut-out speed, the WT adjusts its pitch angle to limit the captured wind power not to exceed the limit of the generator; when the wind speed exceeds the cut-out speed, the WT shuts down to protect the rotor and the generator from the damage of strong wind.

The power output of WT captured from wind is presented as

$$P_{WT}(h) = \begin{cases} 0 & V_{ws}(h) < V_{cut-in} \text{ or } V_{ws}(h) \geq V_{cut-out} \\ \frac{1}{2}\rho A_r C_p V_{ws}^3(h) & V_{cut-in} \leq V_{ws}(h) < V_{rate} \\ P_{WT,rate} & V_{rate} \leq V_{ws}(h) < V_{cut-out} \end{cases} \quad (1)$$

where ρ is the air density, A_r is the swept area of WT that depends on the turbine radius or length of blades, $V_{ws}(h)$ is the hourly mean wind speed, and C_p is the power conversion coefficient that is determined by the aerodynamic structure of the WT. V_{cut-in}, V_{rate}, and $V_{cut-out}$ denote the cut-in wind speed, rated wind speed and cut-out wind speed.

When designing a renewable energy system, it is necessary to determine the suitable capacity of the WT according to the rated power of the WT and the local wind resources. During the operation, it is necessary to consider whether the current wind speed has reached the cut-in speed, rated speed and cut-out speed, and calculate the power that the WT can generate according to the wind speed.

Solar Photovoltaic

Solar energy is another well-known clean energy. Since most parts of the world have sufficient solar irradiance, solar power generation technology has attracted a large number of researchers. Photovoltaic (PV) is a device that uses the photoelectric effect to directly and conveniently convert solar energy into electricity (Liu et al., 2017). In recent years, with the development of PV technology and the rapid decline of PV costs, large-scale grid-connected solar PV power stations have been built all over the world (Mandal et al., 2012).

However, PV systems are highly dependent on solar radiation and weather characteristics. Due to the variability of solar radiation and ambient temperature, the power output of the PV system is uncertain and random (Mandal et al., 2012). The uncertainty is from the alternation of day and night, effect of seasonal changes, and random cloud movement (Jamal et al., 2017; Jamal et al., 2019). Compared with the distributed PV system, the power output of the relatively concentrated and single format PV power generation system in a small area can change very quickly. An isolated community can be completely or partially obscured by fast-moving clouds in the span of a few seconds to a few minutes (Schmidt et al., 2017). The movement of the cloud will affect the performance of the PV system, so prediction must be made to avoid undesirable technical problems and cost losses (Jamal et al., 2019). Predicting the power output of a PV system is a challenging task.

For a photovoltaic array composed of PV panels, the maximum power output can be expressed as (Tao et al., 2010)

$$P_{PV}(h) = \eta_{pv} A_{pv} S_T(h) \cdot [1 - 0.005(T_{air}(h) - 25)] \quad (2)$$

where η_{pv} is the photoelectric conversion efficiency of the PV array, A_{pv} is the total area of the PV array, S_T is the solar radiation incident on the panel, and T_{air} is the air temperature of the ambient in Celsius degree.

The power output of PV system mainly depends on the amount of solar radiation and the operating temperature of the installation location. In addition, as the equipment ages, the photoelectric conversion efficiency and power conversion efficiency will gradually decrease. But their changes in the system life cycle are very small, so they can be ignored. Therefore, as long as the solar radiation and panel temperature are known, the power output of the PV system can be predicted.

Battery Storage System

As the main renewable energy sources, solar and wind energy are intermittent and fluctuating weather resources. One of the possible solutions is to use a hybrid renewable energy system to integrate various renewable energy sources in the best combination (Yang et al., 2018a). A good example is the complementarity of solar and wind energy (Prasad et al., 2017). However, this approach still has large uncertainties. If the distributed resources cannot provide sufficient flexibility in power generation, network operators will have to limit the

penetration rate of renewable energy to a certain level, which will adversely affect the use of renewable energy systems (Jamal et al., 2019). For example, the power generation of the PV system usually exceeds the residential electricity load during the day but cannot meet the demand in the late afternoon and evening when the residential load tends to increase (O'Shaughnessy et al., 2018). Therefore, in order to highly integrate variable wind and solar energy and reduce the impact of weather changes on renewable power generation, energy storage systems have been widely accepted as one of the potential solutions (e Silva and Hendrick, 2017; Babacan et al., 2017; Zhang et al., 2018; Ren et al., 2020). The main function of energy storage system is to compensate the imbalance between power generation and demand, transfer energy from periods of high power generation to periods of low power generation, so that the system can maintain full functionality under various operating conditions (Dragicevic et al., 2014).

ESS includes a variety of technologies, such as pumped water storage, compressed air energy storage, hydrogen storage, flywheels, supercapacitors, and batteries (da Silva Lima et al., 2021). The batteries have higher energy density than supercapacitors, higher charging rate than pumped water storage and less power loss than flywheels. Therefore, the battery storage system (BSS) is the most suitable storage system to store the electricity energy for such localised small-scale applications due to its advantage of higher charging rate, higher energy density and shorter response time. The response time of BSS is between milliseconds and seconds, while that of PHS and CAES are from a few seconds to minutes (Castillo and Gayme, 2014). Due to their durability, low maintenance and low social environmental impact, it is expected that the development and use of BSS will increase significantly in the next decades (da Silva Lima et al., 2021). Among batteries, the most used are lithium-ion batteries (LIB) and vanadium redox flow batteries (VRB). The advantages of LIB are its high energy density, high efficiency, long lifecycle, and more environment friendly characteristics. However, due to these advantages of LIB, they are also widely used in a variety of other applications, including small electronic products and electric vehicles. VRB is a good substitute for LIB because of its safety, long service life, better scalability and high recyclability (da Silva Lima et al., 2021). However, the disadvantage of VRB is its low energy density (Castillo and Gayme, 2014). Therefore, a VRB requires more floor space than a LIB at the same capacity.

In the charging and discharging behaviour of a battery, the state of charge (SOC) is often used to reflect the ratio of the battery's remaining capacity to its rated capacity (Yang et al., 2018b). To protect battery lifecycle, it is necessary to limit the SOC within a certain range. During battery charging, the SOC can be given as (Zhang et al., 2018)

$$SOC_{BSS}(h) = SOC_{BSS}(h-1)\cdot(1-\sigma) + \frac{P_{BSS}(h)\cdot\Delta h}{E_{BSS,cap}}\cdot\eta_{ch} \quad (3)$$

and during battery discharging, the SOC can be given as

$$SOC_{BSS}(h) = SOC_{BSS}(h-1)\cdot(1-\sigma) + \frac{P_{BSS}(h)\cdot\Delta h}{E_{BSS,cap}}\Big/\eta_{dch} \quad (4)$$

where σ denotes the self-discharge rate, P_{BSS} denotes the power of BSS generated or absorbed, $E_{\mathrm{BSS,cap}}$ denotes the energy capacity of BSS, η_{ch} and η_{dch} denote the battery charge and discharge efficiency, respectively. Δh represents the time step, in this article, the time step is calculated in hours.

Heat Pump

Heat pumps are a group of energy systems that can extract heat energy from lower temperature sources such as ambient air, soil, water in lakes and rivers, and then upgrade and deliver it at a higher temperature for heating applications (Watzlaf and Ackman, 2006). If the heat source is outside air, the system is called an air source heat pump (ASHP). If the heat source is the ground, soil or groundwater, it is called a geothermal heat pump (GHP). GHP is one of the fastest growing renewable energy sources in the world (Arat and Arslan, 2017). Compared with traditional heating fuels, such as natural gas, heating oil and propane, the effectiveness of operational cost of GHPs is directly related to the cost of electricity that drives the HP (Self et al., 2013). But the installation costs of GHPs can be an order of magnitude higher compared to a gas boiler.

Heat energy delivered by the HP normally exceeds its electricity consumption. Coefficient of performance (COP) defined as the ratio of heat output to input power is used to describe the energy performance of heat pumps (Casasso and Sethi, 2014). The COP of heat pumps can reach 3–5 or more depending on temperature conditions (Renaldi et al., 2017), which means the heat pump can provide 3–5 kW of heat by consuming 1 kW of electricity. Furthermore, the smaller temperature difference between the heat source and the radiator, the greater the COP of the HP system. In cold weather, the COP of an ASHP is usually about 2 or lower. Therefore, GHP have higher efficiency than ASHP because the underground temperature is closer to the required indoor conditions than the outdoor air temperature in winter and the GHP usually use water which reduces the size of the evaporator heat exchanger due to the higher energy density compared to air. However, as GHP requires higher installation costs and larger spaces, ASHP is more suitable for heating smaller spaces.

In HP applications, its COP can be affected by different variables, such as external temperature, water supply temperature, inlet water temperature and load factor. Simplifications can be made to reduce this complexity. The COP can be calculated as (Ozgener and Hepbasli, 2007):

$$COP_{HP} = \frac{\dot{Q}_{HP}}{P_{HP,comp}} \quad (5)$$

where $\dot{Q}_{\mathrm{HP}}$ is the rate of heat transfer in condenser of HP, $P_{\mathrm{HP,comp}}$ is the input power to the compressor.

The rate of heat transfer from the condenser is obtained as

$$\dot{Q}_{HP} = \dot{m}_{ref}(T_{HP} - T_{return}) \quad (6)$$

In this study, the air source heat pump is considered. For simplification, the COP of the HP is modelled as a function of temperature lift, or the temperature lift is known as the difference between the supply water temperature T_{wat} and the external air temperature T_{temp} (Renaldi et al., 2017).

$$COP_{HP} = a \cdot \left(T_{wat} - T_{temp}\right) + b \tag{7}$$

where a and b are the parameters from the linear regression fits of manufacturer's data (Renaldi et al., 2017). However, the linear regression is just an initial fitting for the easy implementation of modelling. A nonlinear model can be more accurate. Since this paper aims to provide a feasible solution for investment of heat pump rather than operational control, the linear regression model is sufficient for estimating the COP of HP.

Thermal Energy Storage

The outdoor temperature changes between summer and winter during the year can produce huge changes of heat demand (Xu et al., 2018). In this case, a lot of heat will be wasted in the summer when the heating demand is minimal, and there will be insufficient heat in the winter. In addition, the mismatch between energy demand and supply is often observed. Among several storage technologies, thermal energy storage (TES) seems to be one of the most promising technologies that can compensate for the intermittent heat generation of new energy sources. The advantages of using TES in energy systems include improved overall efficiency, better reliability, bring better economy, reduced investment, and operating costs, and less pollution and CO_2 emission to the environment (Sarbu and Sebarchievici, 2018).

In recent decades, the TES technology has been widely studied. Considering the required storage time, the TES system can be divided into short-term storage and long-term storage. The short-term storage TES has a charging and discharging cycle of hours to several days, which is called diurnal thermal energy storage. The long-term storage TES can store heat for several months and is called seasonal TES (Dahash et al., 2019; Renaldi and Friedrich, 2019; Maximov et al., 2021). The principle of seasonal TES is to store heat energy through heating equipment in summer, and then discharge it for space heating in winter (Kubiński and Szabłowski, 2020). The use of TES can significantly increase the flexibility and self-consumption of renewable energy for end users (Waser et al., 2018). Therefore, this concept makes a significant contribution to the efficient use of renewable energy in district heating systems and the decarbonization of the building sector.

The most traditional TES design is provided in the form of a water tank. When there is excess thermal energy on the supply side, these tanks are charged (heated up), and when the demand for thermal energy exceeds the supply, these tanks are discharged (Abdelsalam et al., 2020). In the thermal system, the charging and discharging process of the storage tank can be carried out by direct heat exchange. The energy stored in the TES at time$h$ is expressed as (Renaldi et al., 2017)

$$Q_{TES,sto}(h) = Q_{TES,sto}(h-1) + \left[\dot{Q}_{TES,ch}(h) - \dot{Q}_{TES,dch}(h) - \dot{Q}_{loss}\right] \cdot \Delta h \tag{8}$$

where $Q_{\mathrm{TES,sto}}$ is the energy stored in TES, $\dot{Q}_{\mathrm{TES,ch}}$ and $\dot{Q}_{\mathrm{TES,dch}}$ denote the charge the discharge power, $\dot{Q}_{\mathrm{loss}}$ denotes the standing losses, which normally can be found from manufacturer's datasheet.

Among the performance indicators used to evaluate TES, the most common is TES efficiency, which is the ratio of the total heat energy recovered from the heat accumulator at the discharge temperature to the total heat input at the charging temperature as (Dahash et al., 2019)

$$\eta_{TES} = \frac{Q_{TES,dch}}{Q_{TES,ch}} \tag{9}$$

OPTIMAL SIZING OF RENEWABLE HEATING SYSTEM

Optimisation Problem

The purpose of this study is to find the most effective investment plan to reduce CO_2 emissions in building heating under a given financial budget. Therefore, the optimisation problem is transferred to minimising the total CO_2 emission in the period between 2020 and 2050. The objective function is expressed as

$$\min \sum_{y_i=2020}^{2050} S_{CO2}(y_i) \tag{10}$$

where $S_{\mathrm{CO2}}(y_i)$ denotes the annual CO_2 emission in year y_i, which is expressed as the product of specific CO_2 emission factor for nature gas, g_{gas}, and heat energy produced by gas boiler, Q_{gas}.

In this paper, the RHS uses the electricity from local renewable energy. Thus, it is assumed that electricity power generation has no CO_2 emissions in the RHS, and the CO_2 emissions are entirely generated by using the natural gas in the traditional heating system. This assumption can intuitively indicate the reduction in the use of traditional heating system and nature gas as well as the total CO_2 emission during operation. The factor of $S_{\mathrm{CO2}}(y_i)$ can be used as an indicator to quantify the decarbonization performance, which is defined as follows.

$$S_{CO2}(y_i) = g_{gas} \cdot Q_{gas}(y_i) \tag{11}$$

This equation only considers the CO_2 generated from gas and assumed that the electricity generation has no CO_2 emission in the RHS. This assumption is simple and directly react the CO_2 in operation. And use this factor as an index to justify the performance of decarbonisation.

And Q_{gas} can be presented as

$$Q_{gas}(y_i) = \sum_{h=1}^{8760} \left[\dot{Q}_{heat}(h) - \dot{Q}_{HP}(h) + \dot{Q}_{TES,ch}(h) - \dot{Q}_{TES,dch}(h)\right] \tag{12}$$

where $\dot{Q}_{\mathrm{heat}}(h)$ is the hourly heat demand of buildings and $\dot{Q}_{\mathrm{HP}}(h)$ is the hourly heat produced by heat pump, h is the time factor of hours in a whole year, which in total are 365 days times 24 h. The $\dot{Q}_{\mathrm{HP}}(h)$ is determined by both the electricity generated from PV, WT and BSS and its COP as

$$\dot{Q}_{HP}(h) = COP_{HP}(T_{air}(h)) \cdot (P_{PV}(h) + P_{WT}(h) - P_{BSS}(h)) \tag{13}$$

In practice, the output of power generator and heating equipment cannot exceed its rated value, and the energy stored by storage equipment cannot exceed its specified

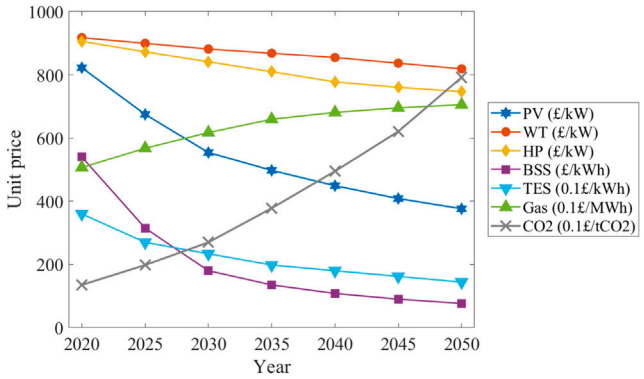


FIGURE 2 | Financial assumptions for components of future years.

capacity. In addition, the annual installed capacity cannot be negative, which means that the total capacity of each component cannot be lower than the previous year. The constraints of all types of components are given as

$$0 \le P_{PV} \le P_{PV,rate}(y_i) \tag{14}$$

$$0 \le P_{WT} \le P_{WT,rate}(y_i) \tag{15}$$

$$0 \le \dot{Q}_{HP} \le \dot{Q}_{HP,rate}(y_i) \tag{16}$$

$$SOC_{\min} < SOC_{BSS}(h) < SOC_{\max} \tag{17}$$

$$0 \le Q_{TES,sto} \le Q_{TES,cap}(y_i) \tag{18}$$

$$P_{PV,rate}(y_i) \ge P_{PV,rate}(y_i - 1) \tag{19}$$

$$P_{WT,rate}(y_i) \ge P_{WT,rate}(y_i - 1) \tag{20}$$

$$\dot{Q}_{HP,rate}(y_i) \ge \dot{Q}_{HP,rate}(y_i - 1) \tag{21}$$

$$E_{BSS,cap}(y_i) \ge E_{BSS,cap}(y_i - 1) \tag{22}$$

$$Q_{TES,cap}(y_i) \ge Q_{TES,cap}(y_i - 1) \tag{23}$$

In addition to the above technical constraints, another constraint is the financial budget. In this study, it is assumed that the investment plan has an Annual Investment Cost (AIC) limit. The investment cost in each year can be used to increase the capacity of any component, but the total cost cannot exceed AIC as

$$\begin{aligned} AIC \ge{}& \Delta P_{PV,rate}(y_i) \cdot U_{PV}(y_i) + \Delta P_{WT,rate}(y_i) \cdot U_{WT}(y_i) \\ &+ \Delta \dot{Q}_{HP,rate}(y_i) \cdot U_{HP}(y_i) + \Delta E_{BSS,cap}(y_i) \cdot U_{BSS}(y_i) \\ &+ \Delta Q_{TES,cap}(y_i) \cdot U_{TES}(y_i) \end{aligned} \tag{24}$$

where $\Delta P_{PV,cap}$, $\Delta P_{WT,cap}$, $\Delta \dot{Q}_{HP,rate}$, $\Delta E_{BSS,cap}$, and $\Delta Q_{TES,cap}$ denote the increased rated power of PV, WT and HP and capacity of BSS and TES of each year. $U_{\mathrm{PV}}(y_i)$, $U_{\mathrm{WT}}(y_i)$, $U_{\mathrm{HP}}(y_i)$, $U_{\mathrm{BSS}}(y_i)$, and $U_{\mathrm{TES}}(y_i)$ denote the unit cost of each component in year y_i.

The forecasted component unit price in future years is obtained based on different financial assumptions in recently published papers (Keiner et al., 2019; Yue et al., 2020; Rinaldi et al., 2021). In this study, the financial forecast for the unit cost of components for 2020–2050 is in British pounds, as shown in **Figure 2**. The prediction shows that the unit prices of PV, WT, HP, BSS, and TES will continue to fall in the next few decades, while the unit price of natural gas and CO_2 will increase rapidly in the coming decades.

Optimisation Approach

From the literature in the past decades, there are four main optimisation approaches that are commonly used, including the direct search, calculus-based optimisation, genetic algorithm (GA), and particle swarm optimisation (PSO). Direct search is a straightforward optimisation method that does not consider time delay and derivatives. Thus, the direct search method can be applied in optimising many nonlinear functions that have less dependence on its derivatives (Kolda et al., 2003). The most commonly used Calculus-based Optimisation method is to set the gradient of the objective function to zero (Kheiri, 2018). Another calculus-based optimisation method is Newton's method, which is similar to the Steepest Descent Method that uses an iterative process from an initial guessed starting point to finally converge to the optimum point. The GA is a population-based algorithm to search for the global-optimum solution. The iterative process of GA will converge to better solutions based on the breeding of the parents with higher performance (Elbeltagi et al., 2005; Kheiri, 2018). However, the GA has shortages that it requires a large amount of non-optimal data as the requirement of global search (Kheiri, 2018). The PSO is a population-based metaheuristic algorithm that attempts to find the global optimal solution of the optimisation problem by simulating the social gathering behaviour of animals (Eberhart and Kennedy, 1995; Kheiri, 2018). This paper chooses the PSO method to find the optimal sizing of RHS due to its strength in finding the global optimal solution and easy to implement.

PSO method uses a large number of the swarm to search the optimum point globally and share the information among all swarm for the next search step. In the PSO algorithm, each feasible solution is called a particle, which is specified by a vector containing problem variables (Maleki et al., 2016). Particles can remember their previous optimal position and share it with others (Shi, 2001). The motion of each particle is composed of two randomly weighted influences and an initial random velocity (Shi, 2001). The PSO algorithm simulates the

sociality of particle, combines the best position of the entire swarm and the trend of its own movement, effectively avoids the particles and swarm falling into the local optimal solutions (Baniasadi et al., 2020).

In the PSO algorithm, the state of each particle is represented by its position x_j and velocity v_j. The velocity update equation of the PSO algorithm has three key parameters, including the inertia constant w, the acceleration constant c_1 that controls the direction of the particles toward its best position in history, and the acceleration constant c_2 that attracts the particles to the best position of the swarm. The formula for updating the velocity and position of each particle in the space can be expressed as (Maleki et al., 2016; Mekontso et al., 2019)

$$v_j^{k+1} = w^k \cdot v_j^k + c_1 \cdot r_1^k \cdot \left(p_{best,j}^k - x_j^k\right) + c_2 \cdot r_2^k \cdot \left(g_{best}^k - x_j^k\right) \quad (25)$$

$$x_j^{k+1} = x_j^k + v_j^{k+1} \quad (26)$$

where v_j^k and x_j^k are the velocity and position of the jth particle in the kth iteration, $p_{\text{best},j}^k$ is the best position achieved by the jth particle and g_{best}^k is the best position of the swarm, r_1 and r_2 are the random factors between 0 and 1.

SIMULATION OF RENEWABLE HEATING SYSTEM

Heat demand is the most important input parameter for any heating system optimisation. It is essential to obtain good performance of the real system. A heat demand model needs to be established to predict the required heat through weather conditions such as ambient temperature. Modelling and simulation of energy systems are usually implemented using engineering models or data-driven models. The simulation test uses energy data from the Glasgow University campus as a case study. In our previous study, both the engineering modelling approach (Chen et al., 2019) and data-driven approach (Chen et al., 2020) have been used to predict the heat demand of campus buildings. The heat demand of the campus and the corresponding ambient temperature data are shown in **Figure 3**.

The hourly temperature obtained from the nearest weather station shows that the local annual temperature fluctuates between −10°C and 25°C. The heat demand data is recorded at the University Energy Centre, given as a blue line, varying from 0 kW to 8000 kW. From the data, the temperature is lower in winter and higher in summer, while the heat demand is the opposite. The parameters of each component in the RHS are given in **Table 1**.

Heat Pump Powered by Local Renewable Resources

In the previous simulation case, it can be found that the use of HP will bring additional power load to the grid. This shows that although the use of HP can greatly reduce CO_2 emissions, there is a potential risk of overloading or even fault occurring in the power grid. Therefore, the most promising alternative is to use local renewable resources to generate electricity to drive HP to heat buildings. This will reduce the impact of the large amount of electrical energy required by HP on the grid. In this case, it is assumed that the heating system is independent of the grid, and only uses renewable energy for power supply to the HP. The heating system combines the RHS based on local renewable resources and the traditional heating system using gas boiler. When renewable resources can generate enough power, the heat demand is completely supplied by HP, and the unconsumed power is stored in the BSS. When renewable resources driven HP cannot provide enough heat for the building, traditional gas boilers will be used to compensate for the remaining heat demand by consuming natural gas.

Figure 4 shows an example of monthly heat production when renewable generation capacity is 10 MW, where the rated power of PV and WT are both 5 MW. Since this case aims to consider the role of the BSS rather than its actual size, the capacity of the BSS is assumed to be large enough to store all unused energy from renewable energy sources. The blue part, the green part, and the yellow part in the bar chart represent the heat generated by the HP driven by power from PV, WT, and BSS, respectively. It can

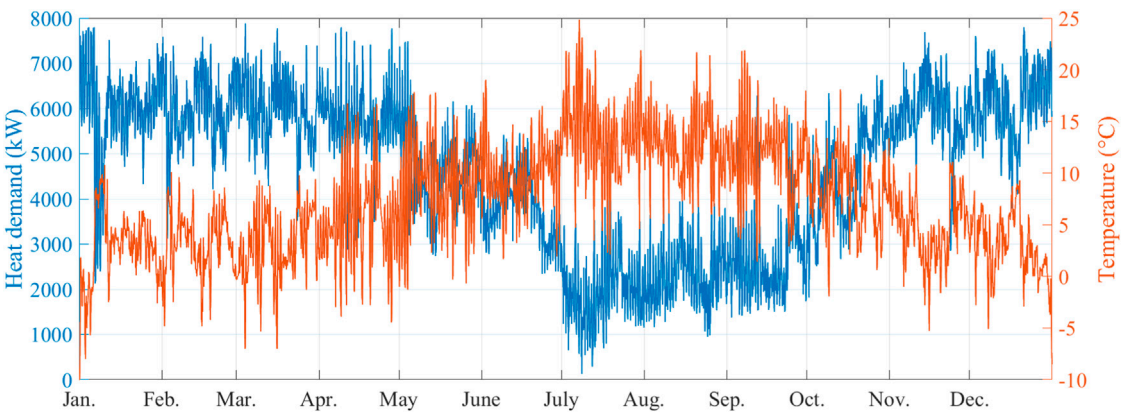


FIGURE 3 | Heat demand of university campus versus ambient temperature.

TABLE 1 | Model parameters of components in renewable heating system.

Parameters	Symbol	Value
WT—cut-in wind speed	V_{cut-in}	3.5 m/s
WT—rated wind speed	V_{rate}	14.5 m/s
WT—cut-out wind speed	$V_{cut-out}$	25 m/s
WT—air density	ρ	1.225 kg/m^3
WT—swept area	A_r	1735 m^2
WT—rated power	$P_{WT,rate}$	750 kW
PV—photoelectric conversion efficiency	η_{pv}	0.9
PV—area of unit array	A_{pv}	500 m^2
PV—rated power	$P_{PV,rate}$	350 W
BSS—self-discharge rate	σ	0.00005
BSS—charge efficiency	η_{ch}	0.95
BSS—discharge efficiency	η_{dch}	0.95
HP—linear regression parameter of COP	a	−0.066
HP—linear regression parameter of COP	b	5.7
HP—supply water temperature	T_{wat}	60°C
TES—efficiency	η_{TES}	0.9
CO_2—natural gas GHG emission	—	241 g/kWh

be seen from the results that, due to the large changes in the illumination time and the angle of solar radiation in high latitude areas such as Scotland, PV power generation is higher in summer and lower in winter. WT has the opposite trend as it will produce more power in winter and less power in summer. From the results of each month, the heat demand of the building in July, August, and September is less, so the heat demand can be fully supplied by HP. In addition, due to the low heat demand, the unconsumed power generated by renewable resources is stored in the BSS. Therefore, in October and November, most of the electricity is provided by the BSS that has stored electricity in the past few months. From December to April, the heat demand is high, but the power from renewable energy and BSS are low, so a large amount of heat is provided by gas boilers for building heating.

It can be seen from the above results that the natural gas consumption of gas boilers is related to the installed capacity of renewable energy. Therefore, the relationship between natural gas consumption and renewable energy installed capacity is shown in **Figure 5A**. Without the use of BSS, the gas consumption decreases slowly as the installed capacity of PV or WT increases, as shown by the dashed lines. Under the same installed capacity, WT-driven HP performs better than PV-driven HP in reduction of gas consumption. The reason is that WT's power generation is large in winter and small in summer, which is more in line with building heat demand. However, PV power generation has a small amount of power generation in winter, so the power generation of PV in winter is not enough to support HP consumption. However, after using BSS with installed capacity in **Figure 5B**, the time distribution of renewable resources has less impact, and the total power generation is more important. As the installed capacity of renewable energy increases, the consumption of natural gas decreases faster since unconsumed electricity is stored in the BSS and used to assist the renewable energy generation. With the same installed capacity, PV can generate more electricity than WT, and thus results in less gas consumption. In this case, HP driven by PV can reduce gas consumption faster than HP driven by WT. However, due to the time mismatch between heat demand and PV power generation, the BSS capacity required for PV is much higher than that of WT. The required capacity of BSS corresponding to different renewable energy installation capacity is shown in **Figure 5B**. When the PV installed capacity reaches 15 MW, the gas consumption can be reduced to zero. The corresponding required BSS is nearly 5 GWh, which is a very high capacity, while the same installation capacity of WT requires the BSS for just 1 GWh, which is still a massive capacity. Therefore, this result only considers the technical requirements and does not consider the financial feasibility.

The results in **Figure 5** are for cases with only a single renewable generation technology, i.e., either PV or WT but not at the same time. The result shows that PV driven HP is better in terms of total power generation but requires more BSS for energy storage. For this reason, another method is to install PV and WT at the same time to combine their advantages. The gas consumption and the required BSS corresponding to the PV and WT at different rated powers are shown in the 2D surfaces of **Figures 6A,B**. When the rated power of PV and WT is greater than 7 MW, only 2.5 GWh of BSS can reduce natural gas

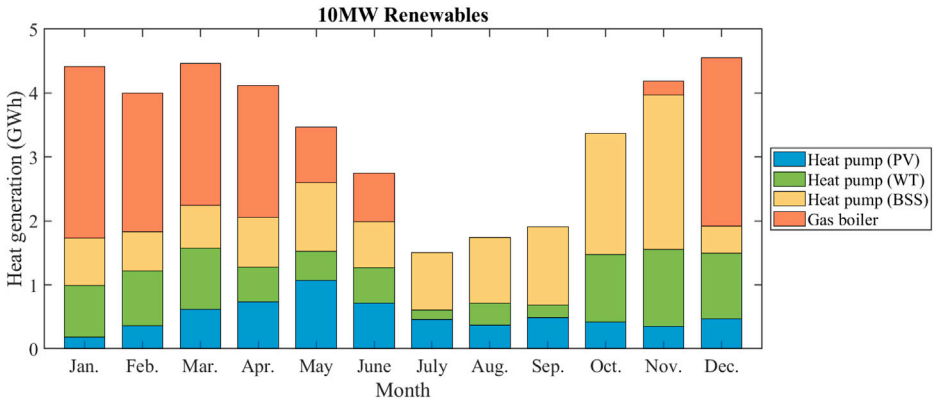


FIGURE 4 | Example of monthly heat generation from renewables and gas boiler.

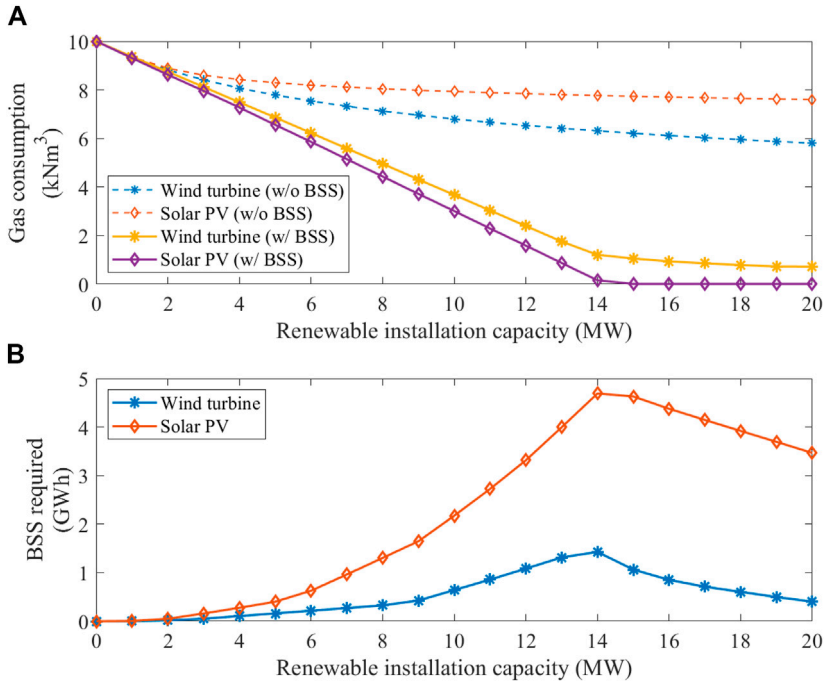


FIGURE 5 | Boiler gas consumption and required ESS capacity according to the installation capacity of renewable energy.

consumption to zero, which is only half the installed capacity of PV alone.

Optimal Sizing Considering CO_2 Emission and Financial Cost

The previous case only considered the technical requirements for the selection of components in RHS. This section considers the financial cost in reducing CO_2 emissions and optimises the investment capacity of each component for every year. The financial assumptions for the unit cost of each component in future years use the predictions given in **Figure 2**. Due to the limited AIC, more investment on one component means less investment on other components. Thus, its sizing needs to be optimised to find the optimal scheme to achieve the minimum CO_2 emission. The variables for optimisation include the capacity of PV, WT, BSS, HP, TES considering their constraints described in *Optimisation problem*. For this multi-parameter Optimisation problem, the optimisation method uses the PSO method described in *Optimisation approach* to find the most suitable component size to minimize the total CO_2 emissions. Since the financial assumption for the unit cost of each component in future years predicted in **Figure 2** is in every 5 years, the optimisation purpose is the total installed amount of each component in every 5 years. The indicator for the optimisation is the total amount of CO_2 emissions in 5 years. After that, the optimal size of each period is based on the installation amount of each component at the previous period and re-run the optimisation approach according to AIC. Therefore, the optimisation results of every 5 years are based on the optimal solution for the current period. It is ensured that the size of the components in the RHS will increase, and the CO_2 emissions will decrease year by year, and finally achieve the optimal result.

The optimisation result is shown in **Figure 7**, which shows the annual investment capacity of each component in the RHS based on different investment budgets. For example, if the university plans to spend 100,000 pounds per year, as shown by the blue line, the optimal capacity of PV, WT, HP, BSS, and TES for investment according to the optimisation results are given in **Figures 7A–E**. Using the optimal scheme, the least CO_2 emissions can be obtained, as shown in **Figure 7F**. In the blue line, the CO_2 emission will still not be reduced to zero by 2050 but will be reduced from 2.7 tons/year to 0.7 tons/year. If the university plans to use the grid independent RHS to completely eliminate CO_2 emissions by 2050, it will need at least 400,000 pounds per year. The optimisation results give a preliminary idea of how to construct the RHS. From the results, in the first 10 years, HP, as the main component of RHS, has the fastest growth in its investment capacity. At least after 2030, the investment of TES will have an effective impact on reducing CO_2 emissions. The investment capacity of PV, WT, and BSS is increased according to the local renewable energy resources and the unit cost of each component to achieve the optimal application of renewable energy.

Compared with different AIC, the more investment, the less CO_2 emissions are obtained, as shown in **Figure 8A**. Numerically, if RHS is not invested, the traditional heating system will generate at least 8×10^5 tons of CO_2 from 2020 to 2050. The higher the

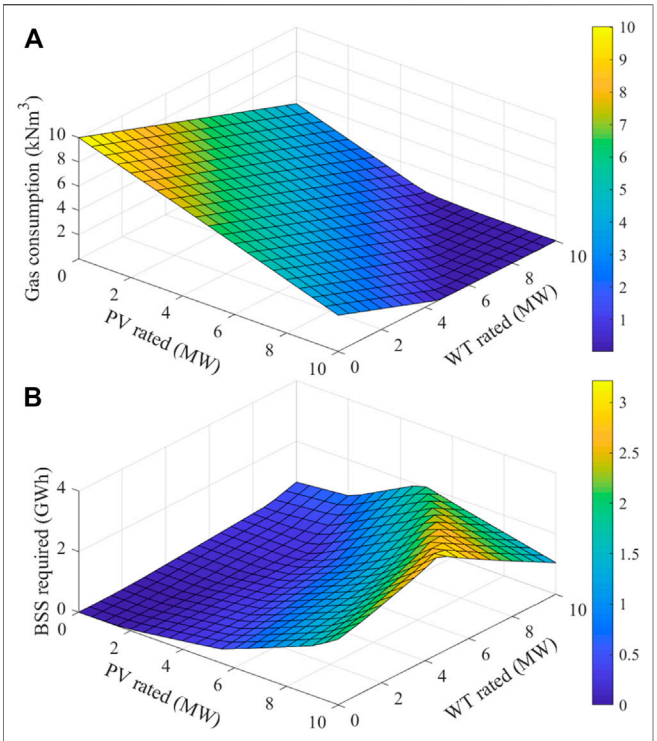


FIGURE 6 | Boiler gas consumption and required BSS capacity according to the rated power of PV and WT.

AIC of RHS, the less total CO_2 emissions are obtained. If the AIC reaches £300,000 per year, the total CO_2 emissions from 2020 to 2050 can be reduced to 1.6×10^5 tons, which is only 20% of continuous using the traditional heating system.

The estimated CO_2 emissions are based on the output of a district heating network model, which has been calibrated based on data from the past few years. The actual CO_2 emissions of the entire university are much more complicated and include commuting and business travel (Duncan and Haydon, 2019). Therefore, the estimated CO_2 emissions in this article are only for preliminary verification of the feasibility and effectiveness of RHS. In addition, the investment cost shown in this paper only considers the predicted unit price of devices. This makes the price and investment amount of the RHS system look much lower than expected. The actual cost will also include other cost, such as the installation fee, maintenance fee, ground rent, etc. These will greatly increase the complexity of prediction and optimisation, so this paper does not consider these factors.

In addition to the total CO_2 emissions, the operating cost of natural gas and CO_2 is another cost of the heating system, as shown in **Figure 8B**. If a traditional heating system is used, the total operating cost of natural gas and CO_2 is approximately 260 million pounds. And if the AIC of RHS reaches £300 k per annum for 30 years from 2020 to 2050, the total operating cost will be reduced to 36 million pounds, which is just 14% of the operating cost of the traditional heating system. This shows that

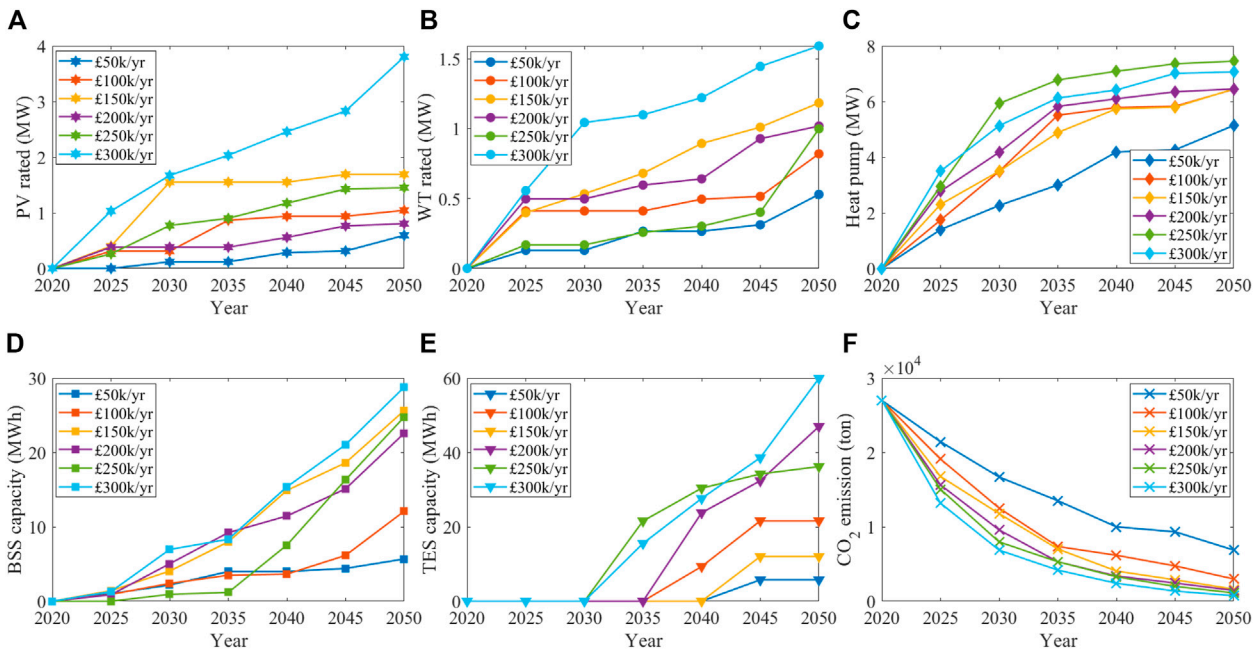


FIGURE 7 | Optimisation result of installing renewable energy, heat pump and BSS, and the reduction of CO_2 emission.

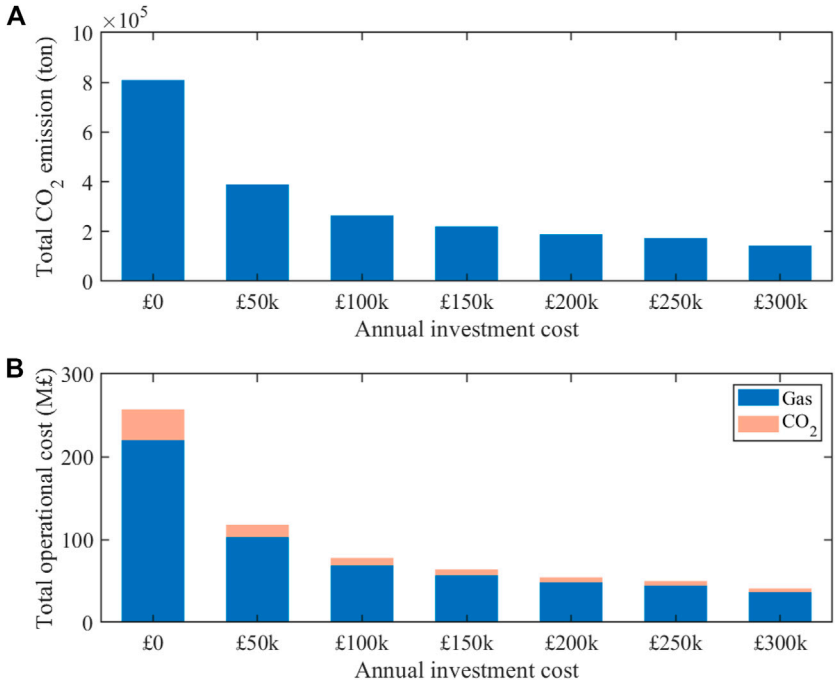


FIGURE 8 | Total CO_2 emission and total operational cost versus different annual investment cost until 2050.

the investment of RHS can reduce operating costs as well, which is a further benefit and profit for this investment.

CONCLUSION

This paper proposed a complete RHS framework, considering PV, WT, BSS, HP, and TES. In the RHS, it is analysed the reduction of gas consumption and the required BSS under the corresponding installed capacity of renewable components from their technical requirements. Meanwhile, in the context of British tariffs and government incentives, the size of each component in the system is optimised through the PSO algorithm according to different AICs. The results verify that the optimal size of RHS provided by this approach can minimise CO_2 emissions and reduce the operating cost of natural gas. This provides a preliminary feasibility plan for how to invest in RHS to replace the traditional heating system in the university campus. In the future work, we will design and analyse the operation scheme and control strategy of the RHS system as well as more detailed HP models. This aims to increase the efficiency and reduce the loss of the RHS system in order to further reduce the carbon emissions and help to alleviate the global warming issue.

DATA AVAILABILITY STATEMENT

The raw data supporting the conclusion of this article will be made available by the authors, without undue reservation.

AUTHOR CONTRIBUTIONS

SC, DF, and ZY contributed to conception and design of the study. SC performed the modelling and analysis and wrote the first draft of the manuscript. All authors contributed to manuscript revision, read, and approved the submitted version.

FUNDING

The research presented in this article was undertaken as part of a project joint founded by Energy Technology Partnership (ETP), SP Distribution PLC (Scottish Power), grant number 146.

ACKNOWLEDGMENTS

The authors would like to thank Gillian Brown for providing valuable information on the campus energy consumption.

REFERENCES

Abdelsalam, M. Y., Teamah, H. M., Lightstone, M. F., and Cotton, J. S. (2020). Hybrid thermal Energy Storage with Phase Change Materials for Solar Domestic Hot Water Applications: Direct versus Indirect Heat Exchange Systems. *Renew. Energ.* 147, 77–88. doi:10.1016/j.renene.2019.08.121

Al-Tameemi, M. R. J., Liang, Y., and Yu, Z. (2019). Design Strategies and Control Methods for a Thermally Driven Heat Pump System Based on Combined Cycles. *Front. Energ. Res.* 7, 131. doi:10.3389/fenrg.2019.00131

Arat, H., and Arslan, O. (2017). Optimization of District Heating System Aided by Geothermal Heat Pump: A Novel Multistage with Multilevel ANN Modelling. *Appl. Therm. Eng.* 111, 608–623. doi:10.1016/j.applthermaleng.2016.09.150

Babacan, O., Ratnam, E. L., Disfani, V. R., and Kleissl, J. (2017). Distributed Energy Storage System Scheduling Considering Tariff Structure, Energy Arbitrage and Solar PV Penetration. *Appl. Energ.* 205, 1384–1393. doi:10.1016/j.apenergy.2017.08.025

Baniasadi, A., Habibi, D., Al-Saedi, W., Masoum, M. A. S., Das, C. K., and Mousavi, N. (2020). Optimal Sizing Design and Operation of Electrical and thermal Energy Storage Systems in Smart Buildings. *J. Energ. Storage* 28, 101186. doi:10.1016/j.est.2019.101186

Bhutta, M. M. A., Hayat, N., Farooq, A. U., Ali, Z., Jamil, R., and Hussain, Z. (2012). Vertical axis Wind Turbine–A Review of Various Configurations and Design Techniques. *Renew. Sustain. Energ. Rev.* 16 (4), 1926–1939. doi:10.1016/j.rser.2011.12.004

Casasso, A., and Sethi, R. (2014). Efficiency of Closed Loop Geothermal Heat Pumps: A Sensitivity Analysis. *Renew. Energ.* 62, 737–746. doi:10.1016/j.renene.2013.08.019

Castillo, A., and Gayme, D. F. (2014). Grid-scale Energy Storage Applications in Renewable Energy Integration: A Survey. *Energ. Convers. Manag.* 87, 885–894. doi:10.1016/j.enconman.2014.07.063

Cengel, Y. A., and Boles, M. A. (2007). *Thermodynamics: An Engineering Approach 6th Editon (SI Units)*. New York: The McGraw-Hill Companies, Inc.

Chen, S., Friedrich, D., Yu, Z., and Yu, J. (2019). District Heating Network Demand Prediction Using a Physics-Based Energy Model with a Bayesian Approach for Parameter Calibration. *Energies* 12 (18), 3408. doi:10.3390/en12183408

Chen, S., Ren, Y., Friedrich, D., Yu, Z., and Yu, J. (2020). Sensitivity Analysis to Reduce Duplicated Features in ANN Training for District Heat Demand Prediction. *Energy and AI* 2, 100028. doi:10.1016/j.egyai.2020.100028

da Silva Lima, L., Quartier, M., Buchmayr, A., Sanjuan-Delmás, D., Laget, H., Corbisier, D., et al. (2021). Life Cycle Assessment of Lithium-Ion Batteries and Vanadium Redox Flow Batteries-Based Renewable Energy Storage Systems. *Sustain. Energ. Tech. Assess.* 46, 101286. doi:10.1016/j.seta.2021.101286

Dahash, A., Ochs, F., Janetti, M. B., and Streicher, W. (2019). Advances in Seasonal thermal Energy Storage for Solar District Heating Applications: A Critical Review on Large-Scale Hot-Water Tank and Pit thermal Energy Storage Systems. *Appl. Energ.* 239, 296–315. doi:10.1016/j.apenergy.2019.01.189

Dragicevic, T., Pandzic, H., Skrlec, D., Kuzle, I., Guerrero, J. M., and Kirschen, D. S. (2014). Capacity Optimization of Renewable Energy Sources and Battery Storage in an Autonomous Telecommunication Facility. *IEEE Trans. Sustain. Energ.* 5 (4), 1367–1378. doi:10.1109/tste.2014.2316480

Duncan, D., and Haydon, D. (2019). A Dear, Green Place": Towards A Climate Change Strategy and Action Plan for the University of Glasgow. Available at: https://www.gla.ac.uk/myglasgow/sustainability/climatechangestrategy/ (Accessed November 2019).

e Silva, G. d. O., and Hendrick, P. (2017). Photovoltaic Self-Sufficiency of Belgian Households Using Lithium-Ion Batteries, and its Impact on the Grid. *Appl. Energ.* 195, 786–799. doi:10.1016/j.apenergy.2017.03.112

Eberhart, R., and Kennedy, J. (1995). "A New Optimizer Using Particle Swarm Theory," in MHS'95. Proceedings of the Sixth International Symposium on Micro Machine and Human Science, Nagoya, Japan, 4–6 Oct 1995 (IEEE).

Edenhofer, O., Pichs-Madruga, R., Sokona, Y., Seyboth, K., Matschoss, P., Kadner, S., et al. (2011). *Renewable Energy Sources and Climate Change Mitigation: Special Report of the Intergovernmental Panel on Climate Change*. Cambridge University Press.

Ekren, O., and Ekren, B. Y. (2008). Size Optimization of a PV/wind Hybrid Energy Conversion System with Battery Storage Using Response Surface Methodology. *Appl. Energ.* 85 (11), 1086–1101. doi:10.1016/j.apenergy.2008.02.016

Elbeltagi, E., Hegazy, T., and Grierson, D. (2005). Comparison Among Five Evolutionary-Based Optimization Algorithms. *Adv. Eng. Inform.* 19 (1), 43–53. doi:10.1016/j.aei.2005.01.004

Eltamaly, A. M., Mohamed, M. A., and Alolah, A. I. (2016). A Novel Smart Grid Theory for Optimal Sizing of Hybrid Renewable Energy Systems. *Sol. Energ.* 124, 26–38. doi:10.1016/j.solener.2015.11.016

Eriksson, S., Bernhoff, H., and Leijon, M. (2008). Evaluation of Different Turbine Concepts for Wind Power. *Renew. Sustain. Energ. Rev.* 12 (5), 1419–1434. doi:10.1016/j.rser.2006.05.017

European Commission (2016). *An EU Strategy on Heating and Cooling*. Brussels, Belgium: European Commission, 51.

Govind, B. (2017). Increasing the Operational Capability of a Horizontal axis Wind Turbine by its Integration with a Vertical axis Wind Turbine. *Appl. Energ.* 199, 479–494. doi:10.1016/j.apenergy.2017.04.070

Grassi, W. (2017). *Heat Pumps: Fundamentals and Applications*. Springer.

Jamal, T., Carter, C., Schmidt, T., Shafiullah, G. M., Calais, M., and Urmee, T. (2019). An Energy Flow Simulation Tool for Incorporating Short-Term PV Forecasting in a Diesel-PV-Battery Off-Grid Power Supply System. *Appl. Energ.* 254, 113718. doi:10.1016/j.apenergy.2019.113718

Jamal, T., Urmee, T., Calais, M., Shafiullah, G., and Carter, C. (2017). Technical Challenges of PV Deployment into Remote Australian Electricity Networks: A Review. *Renew. Sustain. Energ. Rev.* 77, 1309–1325. doi:10.1016/j.rser.2017.02.080

Johari, M., Jalil, M., and Shariff, M. F. M. (2018). Comparison of Horizontal axis Wind Turbine (HAWT) and Vertical axis Wind Turbine (VAWT). *Int. J. Eng. Techn.* 7 (4), 74–80. doi:10.14419/ijet.v7i4.13.21333

Kavian, S., Aghanajafi, C., Jafari Mosleh, H., Nazari, A., and Nazari, A. (2020). Exergy, Economic and Environmental Evaluation of an Optimized Hybrid Photovoltaic-Geothermal Heat Pump System. *Appl. Energ.* 276, 115469. doi:10.1016/j.apenergy.2020.115469

Keiner, D., Ram, M., Barbosa, L. D. S. N. S., Bogdanov, D., and Breyer, C. (2019). Cost Optimal Self-Consumption of PV Prosumers with Stationary Batteries, Heat Pumps, thermal Energy Storage and Electric Vehicles across the World up to 2050. *Sol. Energ.* 185, 406–423. doi:10.1016/j.solener.2019.04.081

Kheiri, F. (2018). A Review on Optimization Methods Applied in Energy-Efficient Building Geometry and Envelope Design. *Renew. Sustain. Energ. Rev.* 92, 897–920. doi:10.1016/j.rser.2018.04.080

Khezri, R., Mahmoudi, A., and Haque, M. H. (2020). Optimal Capacity of Solar PV and Battery Storage for Australian Grid-Connected Households. *IEEE Trans. Ind. Applicat.* 56 (5), 5319–5329. doi:10.1109/tia.2020.2998668

Kim, Y. W., Ramousse, J., Fraisse, G., Dalicieux, P., and Baranek, P. (2014). Optimal Sizing of a Thermoelectric Heat Pump (THP) for Heating Energy-Efficient Buildings. *Energy Build.* 70, 106–116. doi:10.1016/j.enbuild.2013.11.021

Kolda, T. G., Lewis, R. M., and Torczon, V. (2003). Optimization by Direct Search: New Perspectives on Some Classical and Modern Methods. *SIAM Rev.* 45 (3), 385–482. doi:10.1137/s003614450242889

Kubiński, K., and Szabłowski, Ł. (2020). Dynamic Model of Solar Heating Plant with Seasonal thermal Energy Storage. *Renew. Energ.* 145, 2025–2033. doi:10.1016/j.renene.2019.07.120

Li, H., Rane, S., and Yu, Z. (2021). Investigation of the Performance and Flow Characteristics of Two-phase Reaction Turbines in Total Flow Geothermal Systems. *Renew. Energ.* 175, 345–372. doi:10.1016/j.renene.2021.05.022

Liang, Y., Al-Tameemi, M., and Yu, Z. (2018). Investigation of a Gas-Fuelled Water Heater Based on Combined Power and Heat Pump Cycles. *Appl. Energ.* 212, 1476–1488. doi:10.1016/j.apenergy.2017.12.117

Liu, D., Xu, Y., Wei, Q., and Liu, X. (2017). Residential Energy Scheduling for Variable Weather Solar Energy Based on Adaptive Dynamic Programming. *IEEE/CAA J. Autom. Sin.* 5 (1), 36–46. doi:10.1109/jas.2017.7510739

Luna-Rubio, R., Trejo-Perea, M., Vargas-Vázquez, D., and Ríos-Moreno, G. J. (2012). Optimal Sizing of Renewable Hybrids Energy Systems: A Review of Methodologies. *Sol. Energ.* 86 (4), 1077–1088. doi:10.1016/j.solener.2011.10.016

Maleki, A., Khajeh, M. G., and Ameri, M. (2016). Optimal Sizing of a Grid Independent Hybrid Renewable Energy System Incorporating Resource Uncertainty, and Load Uncertainty. *Int. J. Electr. Power Energ. Syst.* 83, 514–524. doi:10.1016/j.ijepes.2016.04.008

Mandal, P., Madhira, S. T. S., haque, A. U., Meng, J., and Pineda, R. L. (2012). Forecasting Power Output of Solar Photovoltaic System Using Wavelet Transform and Artificial Intelligence Techniques. *Proced. Comp. Sci.* 12, 332–337. doi:10.1016/j.procs.2012.09.080

Maximov, S. A., Mehmood, S., and Friedrich, D. (2021). Multi-objective Optimisation of a Solar District Heating Network with Seasonal Storage for Conditions in Cities of Southern Chile. *Sustain. Cities Soc.* 73, 103087. doi:10.1016/j.scs.2021.103087

Mekontso, C., Abubakar, A., Madugu, S., Ibrahim, O., and Adediran, Y. A. (2019). Review of Optimization Techniques for Sizing Renewable Energy Systems. *ComEngApp* 8 (1), 13–30. doi:10.18495/comengapp.v8i1.285

Millar, M.-A., Yu, Z., Burnside, N., Jones, G., and Elrick, B. (2021). Identification of Key Performance Indicators and Complimentary Load Profiles for 5th Generation District Energy Networks. *Appl. Energ.* 291, 116672. doi:10.1016/j.apenergy.2021.116672

Ndwali, K., Njiri, J. G., and Wanjiru, E. M. (2020). Multi-objective Optimal Sizing of Grid Connected Photovoltaic Batteryless System Minimizing the Total Life Cycle Cost and the Grid Energy. *Renew. Energ.* 148, 1256–1265. doi:10.1016/j.renene.2019.10.065

O'Shaughnessy, E., Cutler, D., Ardani, K., and Margolis, R. (2018). Solar Plus: Optimization of Distributed Solar PV through Battery Storage and Dispatchable Load in Residential Buildings. *Appl. Energ.* 213, 11–21. doi:10.1016/j.apenergy.2017.12.118

Ozgener, O., and Hepbasli, A. (2007). Modeling and Performance Evaluation of Ground Source (Geothermal) Heat Pump Systems. *Energy Build.* 39 (1), 66–75. doi:10.1016/j.enbuild.2006.04.019

Prasad, A. A., Taylor, R. A., and Kay, M. (2017). Assessment of Solar and Wind Resource Synergy in Australia. *Appl. Energ.* 190, 354–367. doi:10.1016/j.apenergy.2016.12.135

Ren, Y., Li, L., Brindley, J., and Jiang, L. (2016). Nonlinear PI Control for Variable Pitch Wind Turbine. *Control. Eng. Pract.* 50, 84–94. doi:10.1016/j.conengprac.2016.02.004

Ren, Y., Rind, S. J., and Jiang, L. (2020). A Coordinated Control Strategy for Battery/supercapacitor Hybrid Energy Storage System to Eliminate Unbalanced Voltage in a Standalone AC Microgrid. *J. Intell. Manufacturing Spec. Equipment* 1, 3. doi:10.1108/JIMSE-08-2020-0007

Ren, Z., Verma, A. S., Li, Y., Teuwen, J. J. E., and Jiang, Z. (2021). Offshore Wind Turbine Operations and Maintenance: A State-Of-The-Art Review. *Renew. Sustain. Energ. Rev.* 144, 110886. doi:10.1016/j.rser.2021.110886

Renaldi, R., and Friedrich, D. (2019). Techno-economic Analysis of a Solar District Heating System with Seasonal thermal Storage in the UK. *Appl. Energ.* 236, 388–400. doi:10.1016/j.apenergy.2018.11.030

Renaldi, R., Kiprakis, A., and Friedrich, D. (2017). An Optimisation Framework for thermal Energy Storage Integration in a Residential Heat Pump Heating System. *Appl. Energ.* 186, 520–529. doi:10.1016/j.apenergy.2016.02.067

Rinaldi, A., Soini, M. C., Streicher, K., Patel, M. K., and Parra, D. (2021). Decarbonising Heat with Optimal PV and Storage Investments: A Detailed Sector Coupling Modelling Framework with Flexible Heat Pump Operation. *Appl. Energ.* 282, 116110. doi:10.1016/j.apenergy.2020.116110

Sarbu, I., and Sebarchievici, C. (2018). A Comprehensive Review of thermal Energy Storage. *Sustainability* 10 (1), 191. doi:10.3390/su10010191

Schmidt, T., Calais, M., Roy, E., Burton, A., Heinemann, D., Kilper, T., et al. (2017). Short-term Solar Forecasting Based on Sky Images to Enable Higher PV Generation in Remote Electricity Networks. *Renew. Energ. Environ. Sustain.* 2, 23. doi:10.1051/rees/2017028

Self, S. J., Reddy, B. V., and Rosen, M. A. (2013). Geothermal Heat Pump Systems: Status Review and Comparison with Other Heating Options. *Appl. Energ.* 101, 341–348. doi:10.1016/j.apenergy.2012.01.048

Shi, Y. (2001). "Particle Swarm Optimization: Developments, Applications and Resources," in Proceedings of the 2001 congress on evolutionary computation (IEEE). IEEE Cat. No. 01TH8546.

Tao, C., Shanxu, D., and Changsong, C. (2010). "Forecasting Power Output for Grid-Connected Photovoltaic Power System without Using Solar Radiation Measurement," in The 2nd International Symposium on Power Electronics for Distributed Generation Systems (IEEE). doi:10.1109/pedg.2010.5545754

Trillat-Berdal, V., Souyri, B., and Achard, G. (2007). Coupling of Geothermal Heat Pumps with thermal Solar Collectors. *Appl. Therm. Eng.* 27 (10), 1750–1755. doi:10.1016/j.applthermaleng.2006.07.022

Tulus, V., Boer, D., Cabeza, L. F., Jiménez, L., and Guillén-Gosálbez, G. (2016). Enhanced thermal Energy Supply via central Solar Heating Plants with Seasonal Storage: A Multi-Objective Optimization Approach. *Appl. Energ.* 181, 549–561. doi:10.1016/j.apenergy.2016.08.037

Vanlint, K. (2018). *2017 UK Greenhouse Gas Emissions, Provisional Figures.* London: UK Department for Business, Energy and Industrial Strategy.

Wali, S. B., Hannan, M. A., Reza, M. S., Ker, P. J., Begum, R. A., Rahman, M. S. A., et al. (2021). Battery Storage Systems Integrated Renewable Energy Sources: A Biblio Metric Analysis towards Future Directions. *J. Energ. Storage* 35, 102296. doi:10.1016/j.est.2021.102296

Waser, R., Ghani, F., Maranda, S., O'Donovan, T. S., Schuetz, P., Zaglio, M., et al. (2018). Fast and Experimentally Validated Model of a Latent thermal Energy Storage Device for System Level Simulations. *Appl. Energ.* 231, 116–126. doi:10.1016/j.apenergy.2018.09.061

Watzlaf, G. R., and Ackman, T. E. (2006). Underground Mine Water for Heating and Cooling Using Geothermal Heat Pump Systems. *Mine Water Environ.* 25 (1), 1–14. doi:10.1007/s10230-006-0103-9

Xu, L., Torrens, J. I., Guo, F., Yang, X., and Hensen, J. L. M. (2018). Application of Large Underground Seasonal thermal Energy Storage in District Heating System: A Model-Based Energy Performance Assessment of a Pilot System in Chifeng, China. *Appl. Therm. Eng.* 137, 319–328. doi:10.1016/j.applthermaleng.2018.03.047

Yang, B., Wang, J., Chen, Y., Li, D., Zeng, C., Chen, Y., et al. (2020). Optimal Sizing and Placement of Energy Storage System in Power Grids: a State-Of-The-Art One-Stop Handbook. *J. Energ. Storage* 32, 101814. doi:10.1016/j.est.2020.101814

Yang, B., Yu, L., Chen, Y., Ye, H., Shao, R., Shu, H., et al. (2021). Modelling, Applications, and Evaluations of Optimal Sizing and Placement of Distributed Generations: A Critical State-of-the-art Survey. *Int. J. Energ. Res.* 45 (3), 3615–3642. doi:10.1002/er.6104

Yang, J., Liu, J., Fang, Z., and Liu, W. (2018). Electricity Scheduling Strategy for home Energy Management System with Renewable Energy and Battery Storage: a Case Study. *IET Renew. Power Gener.* 12 (6), 639–648. doi:10.1049/iet-rpg.2017.0330

Yang, Y., Bremner, S., Menictas, C., and Kay, M. (2018). Battery Energy Storage System Size Determination in Renewable Energy Systems: A Review. *Renew. Sustain. Energ. Rev.* 91, 109–125. doi:10.1016/j.rser.2018.03.047

Yue, X., Patankar, N., Decarolis, J., Chiodi, A., Rogan, F., Deane, J. P., et al. (2020). Least Cost Energy System Pathways towards 100% Renewable Energy in Ireland by 2050. *Energy (Oxf)* 207, 118264. doi:10.1016/j.energy.2020.118264

Zhang, W., Maleki, A., Rosen, M. A., and Liu, J. (2018). Optimization with a Simulated Annealing Algorithm of a Hybrid System for Renewable Energy Including Battery and Hydrogen Storage. *Energy* 163, 191–207. doi:10.1016/j.energy.2018.08.112

Conflict of Interest: The authors declare that the research was conducted in the absence of any commercial or financial relationships that could be construed as a potential conflict of interest.

Publisher's Note: All claims expressed in this article are solely those of the authors and do not necessarily represent those of their affiliated organizations, or those of the publisher, the editors and the reviewers. Any product that may be evaluated in this article, or claim that may be made by its manufacturer, is not guaranteed or endorsed by the publisher.

Copyright © 2021 Chen, Friedrich and Yu. This is an open-access article distributed under the terms of the Creative Commons Attribution License (CC BY). The use, distribution or reproduction in other forums is permitted, provided the original author(s) and the copyright owner(s) are credited and that the original publication in this journal is cited, in accordance with accepted academic practice. No use, distribution or reproduction is permitted which does not comply with these terms.

frontiers in Energy Research

METHODS
published: 26 August 2021
doi: 10.3389/fenrg.2021.739993

Medium—And Long-Term Load Forecasting Method for Group Objects Based on the Image Representation Learning

*Daolu Zhang [1,2], Weiling Guan [1,2], Jiajun Yang [1,2], Huang Yu [1,2], WenCong Xiao [1,2] and Tao Yu [1,2]**

[1]School of Electric Power Engineering South China University of Technology, Guangzhou, China, [2]Guangdong Provincial Key Laboratory of Intelligent Measurement and Advanced Metering of Power Grid, Guangzhou, China

Medium-and long-term load forecasting in the distribution network has important guiding significance for overload warning of distribution transformer, transformation of distribution network and other scenarios. However, there are many constraints in the forecasting process. For example, there are many predict objects, the data sample size of a single predict object is small, and the long term load trend is not obvious. The forecasting method based on neural network is difficult to model due to lack of data, and the forecasting method based on time sequence law commonly used in engineering is highly subjective, which is not effective. Aiming at the above problems, this paper takes distribution transformer as the research object and proposes a medium-and long-term load forecasting method for group objects based on Image Representation Learning (IRL). Firstly, the data of distribution transformer is preprocessed in order to restore the load variation in natural state. And then, the load forecasting process is decoupled into two parts: the load trend forecasting of the next year and numerical forecasting of the load change rate. Secondly, the load images covering annual and inter-annual data change information are constructed. Meanwhile, an Image Representation Learning forecasting model based on convolutional neural network, which will use to predict the load development trend, is obtained by using load images for training; And according to the data shape, the group classification of the data in different periods are carried out to train the corresponding group objects forecasting model of each group. Based on the forecasting data and the load trend forecasting result, the group forecasting model corresponding to the forecasting data can be selected to realize the numerical forecasting of load change rate. Due to the large number of predict objects, this paper introduces the evaluation index of group forecasting to measure the forecasting effect of different methods. Finally, the experimental results show that, compared with the existing distribution transformer forecasting methods, the method proposed in this paper has a better overall forecasting effect, and provides a new idea and solution for the medium-and long-term intelligent load forecasting of the distribution network.

Keywords: distribution network, medium-and long-term load forecasting, image representation learning, group objects, data shape

OPEN ACCESS

Edited by:
Bo Yang,
Kunming University of Science and Technology, China

Reviewed by:
Yiyan Sang,
Shanghai University of Electric Power, China
Yixuan Chen,
The University of Hong Kong, Hong Kong, SAR China

****Correspondence:***
Tao Yu
taoyu1@scut.edu.cn

Specialty section:
This article was submitted to Smart Grids, a section of the journal Frontiers in Energy Research

Received: *12 July 2021*
Accepted: *20 July 2021*
Published: *26 August 2021*

Citation:
Zhang D, Guan W, Yang J, Yu H, Xiao W and Yu T (2021) Medium—And Long-Term Load Forecasting Method for Group Objects Based on the Image Representation Learning. Front. Energy Res. 9:739993. doi: 10.3389/fenrg.2021.739993

INTRODUCTION

With the introduction of the concept of "Digital Power Grid" (Islam, 2016) and the development of measurement technology, power grid companies are constantly striving to promote the integration of multi-source heterogeneous data (Munshi and Mohamed, 2017), and many scholars are also constantly studying how to mine data implicit information to assist power grid decision-making (Chang and Huang, 2018). Load forecasting is the basis of generation control (Yang et al., 2015; Xi et al., 2016; Zhang et al., 2016), optimal dispatch (Zhang et al., 2015; Zhang et al., 2021), planning and construction in smart grid. As an important part of planning and construction, medium-and long-term load forecasting of distribution network plays an important role in network architecture optimization, selection of new energy access point, distribution transformer overload warning and other scenarios. Therefore, it is necessary to carry out in-depth research on medium-and long-term load forecasting of distribution network (Zhao et al., 2014).

The existing medium-and long-term load forecasting system is mainly divided into two categories: the methods based on the time sequence law of load and the methods based on the correlation between influencing factors and load (Kang et al., 2004; Li et al., 2018; Farrag and Elattar, 2021). The methods based on time sequence law requires the load sequence has certain trend law. Many literatures have applied these methods, such as time extrapolation method, exponential average method, dynamic average method, etc., (Kaytez, 2020); and the forecasting methods that take into account the influencing factors include the traditional unit consumption method and regression analysis method, as well as the emerging non-analytical artificial intelligence method (Alrashidi and El-Naggar, 2010; Kang and Zhao, 2012; Wen et al., 2020). Literature (Sun and Zhao, 2010) proposed a new continuous ant colony optimization algorithm called MG-CACO to optimize the parameters of SVM, and used 9 groups of historical load data to forecast the annual power load of Tianjin. Literature (Kazemzadeh et al., 2020) proposed a medium-and long-term load forecasting model based on PSO-SVR, and 6 groups of load data are used to predict the load peak of Iran's national grid in the next year.

The above methods are mainly applied to large power grid systems. Because the system-level load has the same trend of continuous growth and the range of growth is similar, better forecasting results can be obtained by using a small amount of historical data of predict object. However, when these methods are applied directly to the distribution network level with no obvious continuous trend, the forecasting effect is not ideal. At present, there are few literatures on the medium-and long-term forecasting of distribution network, it is mainly because of the following difficulties:

1) The continuous trend of distribution network load is not obvious, and it often presents a fluctuating state rather than a monotonic growth state. The error of using time sequence extrapolation method is large.
2) The data required for medium-and long-term forecasting of distribution network is annual dimension data, so the historical data of a single predict object is less, and it is difficult to obtain good forecasting effect through the establishment of neural network.
3) Distribution network has three levels: station, feeder and transformer. The smaller the level, the more predict objects. If we use the traditional idea to train and model each predict object separately, it will cost a lot of computation and it is not conducive to the implementation of engineering deployment.

However, in practical engineering applications, although the specific numerical changes of the peak load of the predict object can't be known, sometimes the load trend of the future year can be determined by relying on expert experience. Therefore, the forecasting problem of distribution network without obvious continuous trend is decomposed into two parts by taking advantage of the trend characteristics of predict object:

1) Judge whether the load of the predict object will increase or decrease in the future.
2) Forecast the load change amount of its increase or decrease.

The load data contains certain social information and load information, and the convolutional neural network (CNN) can extract representative features from the original load data and perform data representation learning. Literature (Dong et al., 2017) extracts seasonal cycle features from input data by using CNN model to carry out load forecasting. Literature (Wang et al., 2018a) uses a CNN model to extract features from historical load data, and establishes a nonlinear relationship between implicit features and users' social attributes for attribute recognition.

For the multi-object forecasting problem, the literature (Wang et al., 2018b; Gong et al., 2019) classifies users by clustering. After classification, each group is combined into a single predict object, and the historical data of the combined object is used for forecasting. But it only focuses on the overall load, so the load forecasting results of all the predict objects can't be obtained. Literature (Zhang and Li, 2020) connects the forecasting stage with the clustering stage through an additional feedback mechanism. The feedback mechanism returns the signal of model fitness and uses it as the clustering criterion to update the clustering members. Literature (Liu et al., 2018) divides the load trend into four categories by K-means algorithm, establishes classification rules between temperature and categories, and finally establishes XGBoost regression models for different classifications. Literature (Dong and Grumbach, 2019) takes the historical data of different predict objects as the input of the same LSTM forecasting model, and realizes the expansion of medium-and long-term forecasting data.

Therefore, this paper takes the smallest unit in the distribution network (distribution transformers) as the predict object, and

forecast its maximum load in the next year. First of all, the historical load data are restored to the data in the state of natural change through the identification of the transfer load. Then the load forecasting process of distribution transformer is decoupled into two parts: load trend forecasting (growth or decline) and load change rate numerical forecasting. Meanwhile, a group objects forecasting method based on Image Representation Learning is proposed. Among them, the load trend forecasting link constructs the load data into the power load image to reflect the annual and inter-annual load changes of each distribution transformer. Under the attention mechanism, the improved convolution neural network is used to automatically extract the hidden features and forecast the load trend; In the load change rate numerical forecasting link, a Multiple Objects-Group Forecasting model based on random forest regression is proposed. It is based on the data shape to make group classification forecasting, solve the problem that there are small amount of data and large number of predict objects when single object modeling and forecasting. For different forecasting links, different methods are selected for performance analysis and comparison, the best method combination is selected. The results of the method combination in this article are compared with the current engineering methods such as Linear regression forecasting method, Fixed growth rate forecasting method, Moving average forecasting method. Experiments have proved that the method proposed in this paper can improve the overall forecasting effect by using a few feature dimensions and short time length data.

DATA PREPROCESSING

Filling and Cleaning of Distribution Transformer Data

Since the complete daily load data is needed to construct the distribution transformer power load image, the data of the distribution transformer is filled and cleaned, such as vacancies and zero-value loads are filled and modified. For the data vacancy at the beginning and end, the trend proportion calculation method is used to complete the data. For the absence of intermediate data, methods such as Near-neighbor mean generation method, Linear interpolation non-neighbor mean generation method, Sequence and mean generation method, Cluster completion method can be used to fill the data, and outlier test and correction can be carried out. Refer to the literature (Kang et al., 2007) for specific treatment steps.

Classification of Distribution Transformer Development Stage

The classification of distribution transformer development stage determines which distribution transformers can be predicted by the method proposed in this paper. Although the distribution transformer load has no obvious continuous trend, the development stage can be roughly divided into rapid development period, fluctuating development period and mature and stable period by analyzing the information of distribution transformer operation time and load level.

The classification flow chart of distribution transformer development stage is shown in **Figure 1**. It is defined that the distribution transformer put into operation within the last 4 years is in rapid development period. Due to the commissioning and load release process, the maximum load of distribution transformer varies greatly in the rapid development period. It is defined that when the distribution transformer's maximum annual load change rate for four consecutive years does not exceed 10% and the absolute load value change is less than 50 kW, it is in a mature and stable period. According to the sample analysis, the load of most distribution transformers in the mature and stable period will also not change much in the next year. In this paper, we focus on the forecasting of distribution transformers in rapid development period, and the treatment methods of distribution transformers in the other two development stages will not be described in detail.

Identification and Restoration of Transfer Load

In the existing historical load data, there is a variation steep peak of load maximum in the partial distribution transformers, in which there is often a load transfer phenomenon, and the load transfer between different distribution transformers will destroy the original characteristics of the load variation. Therefore, identification and restoration of transfer load is required, the processing flow is as follows:

1) Identify distribution transformers where load transfer may present. Combined with the records of load transfer events, the distribution transformer whose annual peak load decreases by more than 40% is listed as the distribution transformer with possible load transfer, also called Bus-transformer (BT).
2) Establish an adjacent distribution transformer set of each Bus Transformer. Through the GISID and the topology information table, the distribution transformers near the Bus-transformer is included in its adjacent distribution transformer set.
3) Identify the distribution transformer that takes on the load. Distribution transformer with load growth change magnitude and load mutation date similar to the Bus Transformer are found from the adjacent distribution transformer set, and determine it as Sub-transformer (ST). In this paper, the variation of the load growth of the Sub-transformer should be within the 20% error range of the variation of the load decreases of the Bus-transformer. At the same time, the load mutation time interval between the Sub-transformer and the Bus-transformer is not more than 2 weeks.
4) Combine load. By superposing the daily load data of the Bus-transformer and the Sub-transformer, a virtual distribution transformer history data is obtained for forecasting.

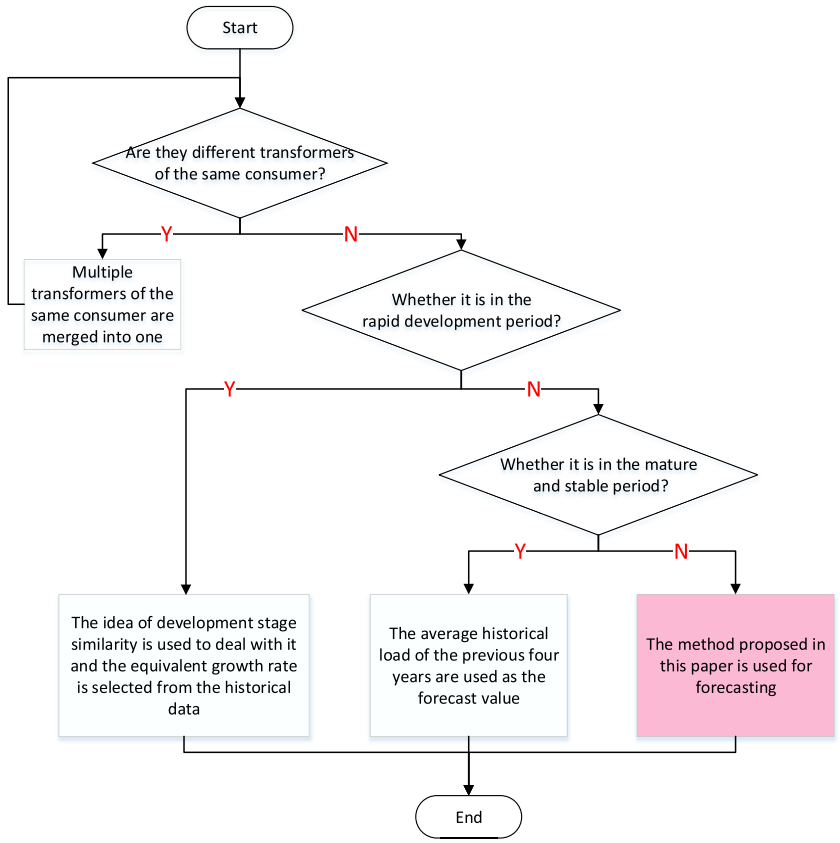


FIGURE 1 | Distribution transformer classification flow chart.

FORECASTING MODEL AND PRINCIPLE

Improved Convolutional Neural Network

Convolutional neural network (CNN) has translation invariance when extracting image features. Among them, the convolutional layer is used to extract different features of the input, and establish mapping through nonlinear activation function. The pooling layer takes the maximum or average value of the features of the convolutional layer to achieve dimensionality reduction of data features. The fully connected layer combines all local features into global features. Since the task of CNN in this article is actually a two-classification task, the network structure is improved. SVM is used to replace the Softmax layer in original CNN, and hidden features are extracted through the Dense layer, then input into the SVM layer for

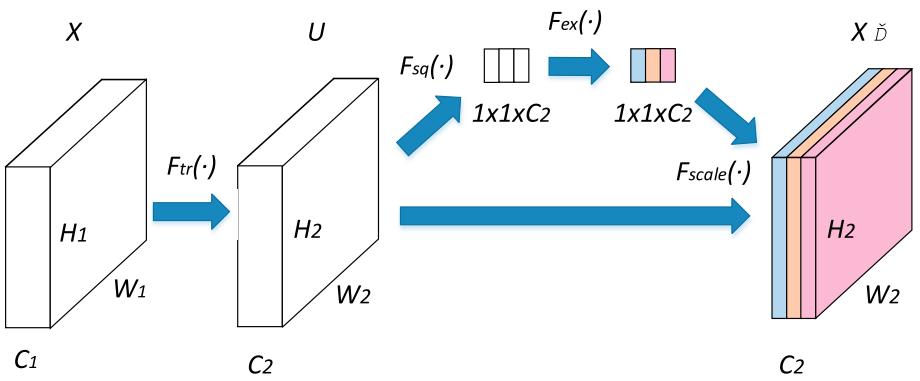


FIGURE 2 | Implementation process of Attention mechanism.

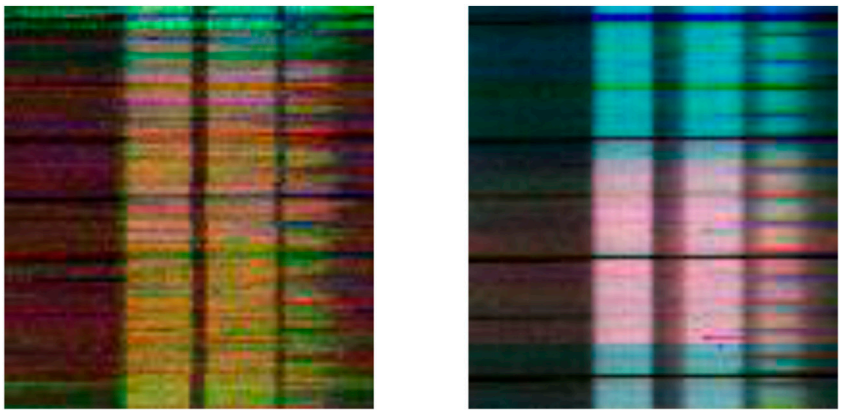


FIGURE 3 | Power load images.

load trend forecasting. **Figure 2** shows the implementation process of Attention mechanism.

Random Forest Regression

Random forest (Breiman, 2001) belongs to an ensemble learning method of Bagging. In the training stage, Bootstrap sampling is used to collect multiple different sub-training data sets from the input training data set to train multiple different decision trees in turn. By minimizing the impurity, the minimum segmentation variable and segmentation point are found. In the forecasting stage, random forest averages the forecasting results of multiple internal decision trees to get the final result.

Attention Mechanism

The Attention mechanism can simulate the human brain's attention distribution process. By means of probability distribution, the model can focus on the important information and fully learn it. This paper implements the channel attention mechanism through the Squeeze-and-Excitation module. For convolutional mapping F_{tr}: $X \rightarrow U, X \epsilon R^{H_1 \times W_1 \times C_1}, U \in R^{H_2 \times W_2 \times C_2}$, in order to learn the feature relationship between channels, the entire spatial feature on a channel is encoded as a global feature, and global average pooling is used to achieve:

$$Z_c = F_{sq}(u_c) = \frac{1}{H \times W} \sum_{i=1}^{H} \sum_{j=1}^{W} u_c(i,j), z \in R^c \quad (1)$$

The obtained global features are then fully connected in two levels, and finally limited to the range of (0, 1) with sigmoid:

$$s = F_{ex}(z, W) = \sigma(g(z, W)) = \sigma(W_2 ReLu(W_1 z)) \quad (2)$$

Multiply the obtained activation value by the original features on the C channels of the original output U, and the result is used as the input data of the next stage:

$$x_c = F_{scale}(u_c, s_c) = s_c \cdot u_c \quad (3)$$

The data of different channels have different degrees of influence on the target task. By introducing the channel attention mechanism, the weight coefficient of each channel can be automatically learned, the channel data with greater influence can be given greater attention, and the learning effect can be effectively improved.

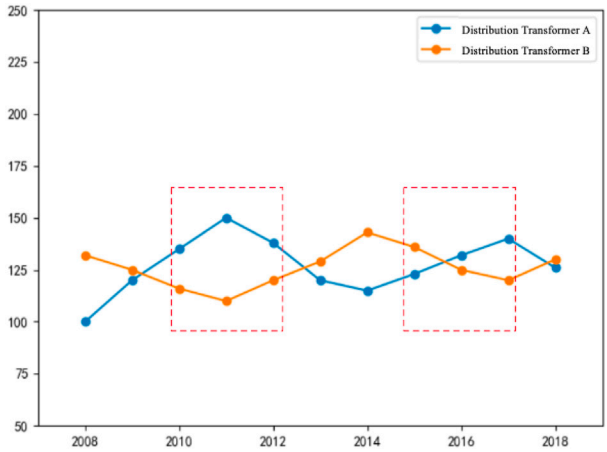


FIGURE 4 | Schematic diagram of Load Trend Shape.

FEATURE CONSTRUCTION OF PREDICTION METHODS

Input Feature Construction of Image Representation Learning

The annual load data of distribution transformer contains information of periodic and seasonal variation, and the load data between different years also reflects the change information of the inter-annual load level. Therefore, this paper constructs a power load image which can reflect the information of annual and inter-annual load changes. This paper needs to forecast the annual maximum load of the distribution transformer, so the construction of power load

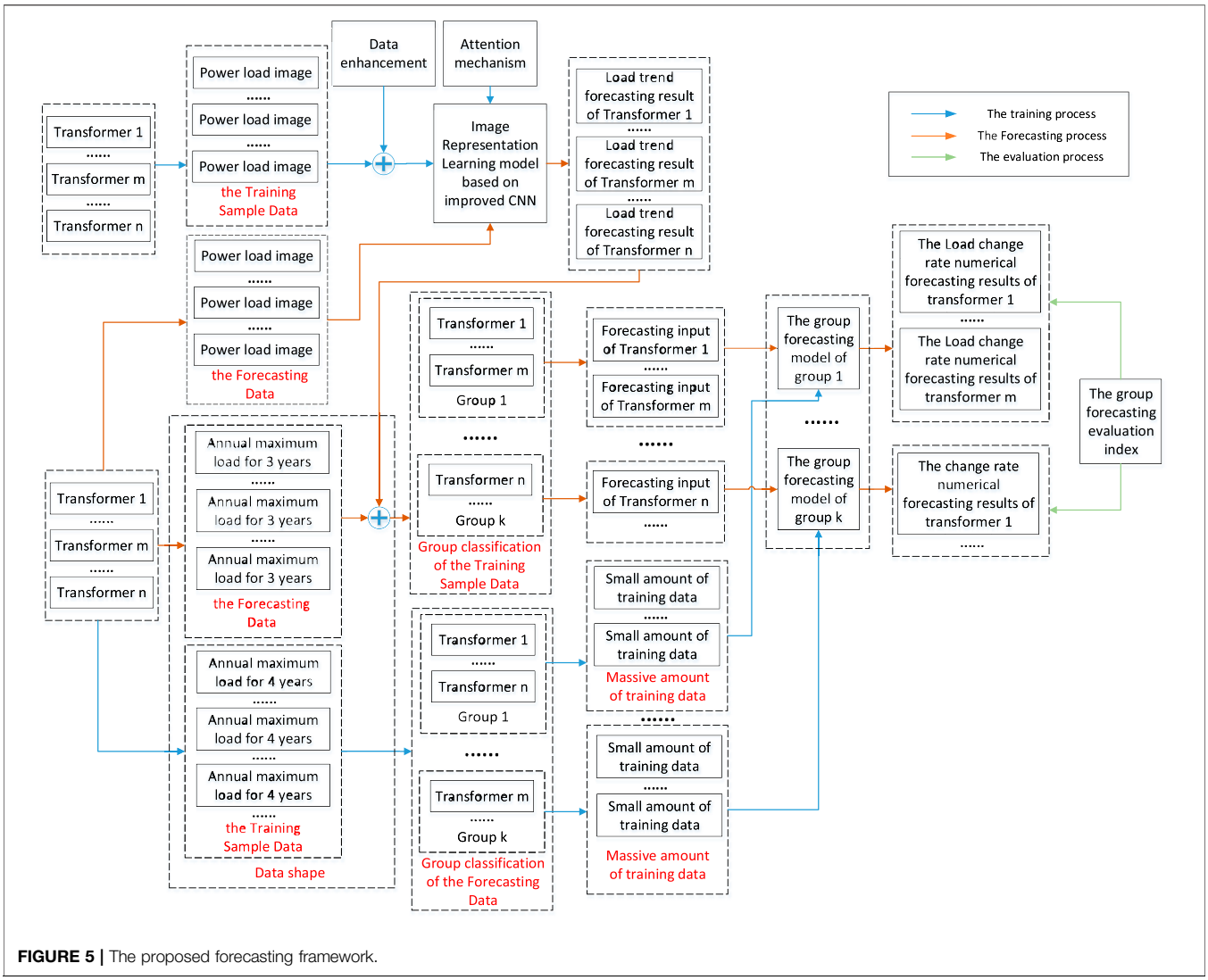


FIGURE 5 | The proposed forecasting framework.

image focuses on the moment when the annual maximum load appears.

Take the daily load data of a distribution transformer for 3 years, and daily load data of 105 days (i.e., 15 weeks) are continuously selected from the annual load data. The selected data should contain the data of the maximum load day of the distribution transformer each year. Since there are 96 load data measurement time points every day, three data matrices of 105*96 are formed. Each row of data represents the load at a different time on the same day, and each column of data represents the load at the same time on a different date. When the load levels of different distribution transformers differ too much, the training effect of the model will be disturbed, so the data is normalized, and the data distribution will not be changed after normalization. The formula used for normalization is as follows:

$$r' = \frac{r - r_{min}}{r_{max} - r_{min}} \tag{4}$$

In the formula, r_{max} is the maximum value in the input data of 3 years, r_{min} is the minimum value in the input data of 3 years, and r is the normalized data. The normalized data is in the interval of (0,1), and the load data for 3 years corresponds to the three color channels of the RGB image, so the power load image can be converted. The distribution transformer load data of every 3 years can be stored through one power load image and it is used as the input feature of the Image Representation Learning model. **Figure 3** shows the power load images formed by two different distribution transformers.

Feature Construction of Data Group Classification

A new concept "Load Trend Shape" (LTS) is introduced to describe the variation of annual maximum load, and define the time step for each LTS as 3 years. By comparing the relationship between the annual maximum load in each of the 3 years, the historical load data of any 3 years can be divided into the following four categories, corresponding to the four LTS:1. Continuous growth LTS; 2. Continuous decline LTS; 3. First rise and then fall LTS; 4. First fall and then rise LTS.

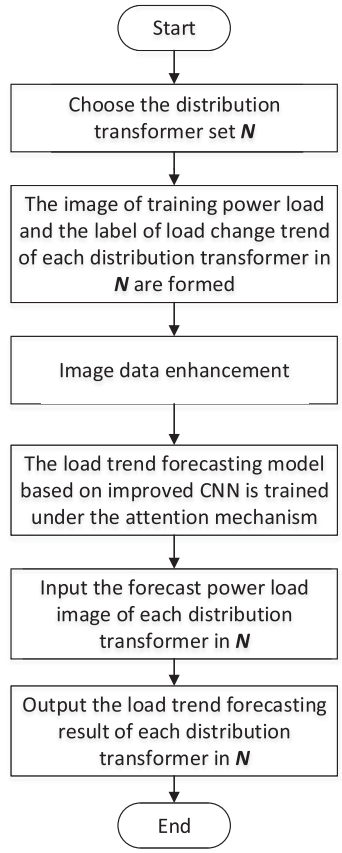


FIGURE 6 | The load trend forecasting link flow chart.

Figure 4 shows the annual maximum load curve of the two distribution transformers from 2008 to 2018. From 2010 to 2012, the maximum annual load of transformer A showed the first rise and then fall LTS, while that of transformer B showed the first fall and then rise LTS; From 2015 to 2017, the maximum annual load of transformer A showed the Continuous growth LTS, while that of transformer B showed Continuous decline LTS. For each LTS, there are only two load trends in the coming year: growth or decline. Therefore, the annual maximum load value in 4 years may present eight data shape, corresponding to 8 groups. Different from the aforementioned classification of distribution transformer development stage, the group classification feature is to classify the data of a certain time period, so the data of the same distribution transformer at different time periods may belong to different groups.

Due to the contingency of the annual maximum load, when extracting the annual maximum load, in order to truly reflect the maximum load level of the distribution transformer, the maximum daily load in the year of the distribution transformer was arranged in descending order, and the average value of the top five load values is selected as the annual maximum load used in the calculation of the change rate, which can effectively reduce the impact of abnormal accidents.

Input Feature Construction of Group Objects Forecasting

In the existing research on user pattern discrimination based on load data, some literature points out that there is a correlation between electricity load, population, and economic income (McLoughlin et al., 2011; Jin et al., 2014), but it is difficult to obtain the influencing factor data of the corresponding level of distribution transformer. Therefore, the economic growth rate and population growth rate of the district/county can be obtained from the statistical yearbook. Extract the maximum load of each substation under the jurisdiction of the district/county, then calculate the influence coefficient $\eta_{k,t}$ of each substation:

$$\eta_{k,t} = \frac{P_{k,t}}{P_{max,t}} \tag{5}$$

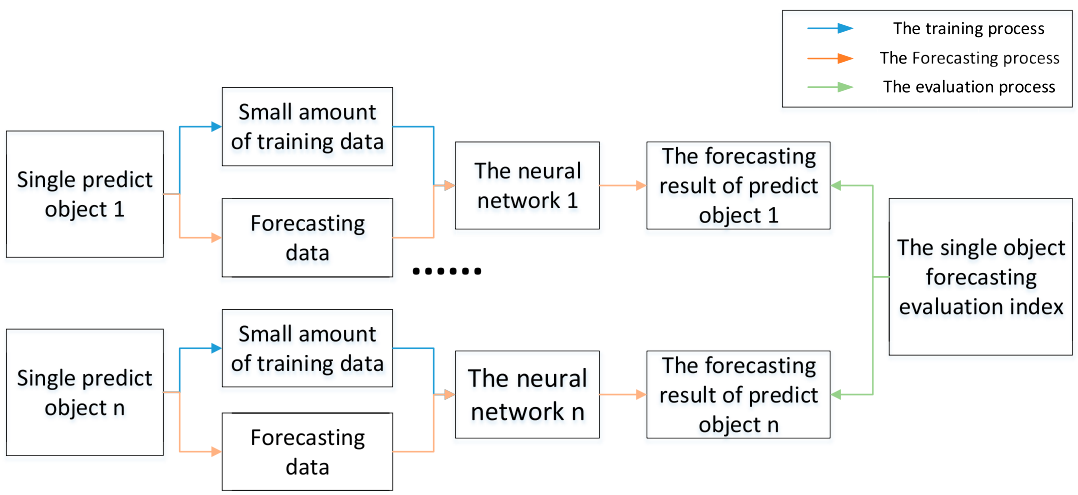


FIGURE 7 | Forecasting flow chart of Single Object—Single Forecasting model.

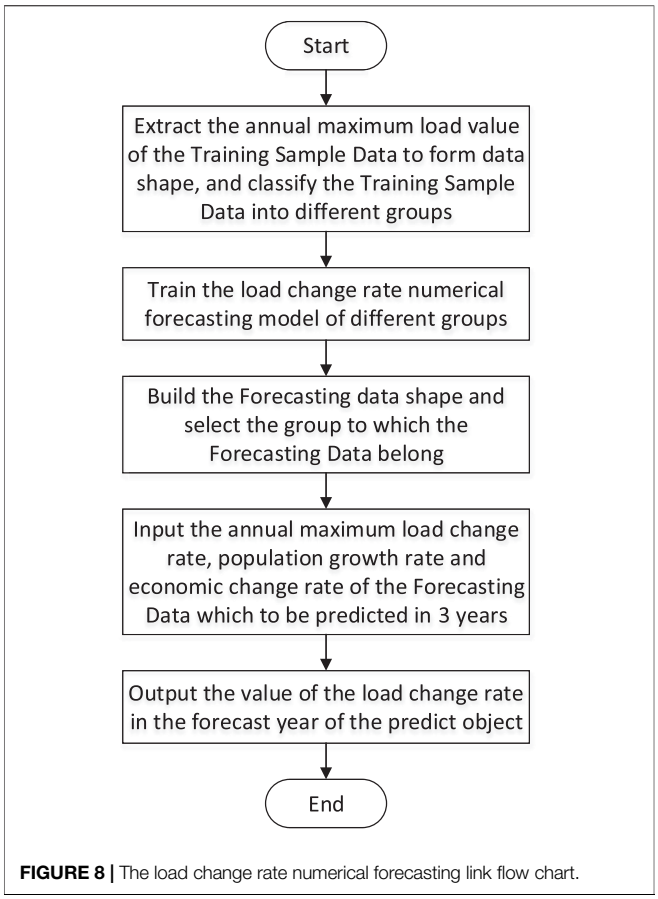


FIGURE 8 | The load change rate numerical forecasting link flow chart.

In the formula, $P_{k,t}$ is the annual maximum load value of the *kth* substation in year *t*, and $P_{max,t}$ is the largest annual load value of all substations in the administrative region in year *t*. The influence coefficient is multiplied by the economic growth rate and population growth rate of the district/county where the substation is located, so as to approximate the economic growth rate and population growth rate of the power supply region of the substation. The population change rate and economic change rate, as upper-level influencing factors, have good stability. When training and forecasting, the load change rate, population change rate, and economic change rate in the first 3 years of the forecast year are selected as the forecast input features. The population and economic change data of the distribution transformer can be approximated by the population and economic change data of the substation where it is located.

THE PROPOSED FORECASTING FRAMEWORK

Firstly, the load data of 4 years before the forecast year is defined as the Training Sample Data; the load data of 3 years before the forecast year is defined as the Forecasting Data. A large number of distribution transformers in the period of fluctuating development period are selected to form the distribution transformer set ***N***, taking T_0 as the forecast year and defining T_i year ($T_i = T_0 - i$), so the data of $T_4 - T_1$ is the Training Sample Data and the data of $T_3 - T_1$ is the Forecasting Data.

The framework of the medium-and long-term load forecasting method for group objects based on Image Representation Learning is shown in **Figure 5**. It can be divided into two forecasting links: load trend forecasting and load change rate numerical forecasting. The distribution transformer in the distribution transformer set N can be either a training sample object or a predict object. For the same distribution transformer, in the same forecasting link, the difference between the Training Sample Data and the Forecasting Data lies in the different time of data selection; in different forecasting links, the data dimensions of the Training Sample Data and the Forecasting Data are different.

Load Trend Forecasting Based on Image Representation Learning

The load trend forecasting link uses daily dimension data. The first 3 years of data in the Training Sample Data (i.e., $T_4 - T_2$ years) form a training power load image, and the annual maximum load of the third year and the fourth year (i.e., T_2 and T_1 years) are compared to obtain the load trend label (growth or decline). The load image and the label are paired to form *N* pieces of data, and *k*N* pieces of data ($k \geq 1$) can be obtained after data enhancement. Under the channel Attention mechanism, different learning weights are assigned to the data of different years in the load image. Based on the improved convolutional neural network training Image Representation Learning model, the nonlinear mapping relationship between the power load image and the load trend label can be established.

When the distribution transformer is taken as the predict object, the Forecasting Data of distribution transformer set ***N*** ($T_3 - T_1$ years) are formed into the forecast power load images, which will be input into the Image Representation Learning model, and the forecast load trend result of each distribution transformer of the distribution transformer set ***N*** in the forecast year (T_0 year) is output, which is applied to the next load change rate numerical forecasting link. **Figure 6** shows the process of The load trend forecasting link.

Load Change Rate Numerical Forecasting of Group Objects

The load change rate numerical forecasting link uses annual dimension data. The annual dimensional data of a single distribution transformer is small, and it is difficult to model for a single distribution transformer. Therefore, a Multiple Objects-Group Forecasting model which is different from the traditional Single Object-Single Forecasting model (As shown in **Figure 7**) is established. By integrating the annual dimension data of a large number of objects in a certain group, the training data can be expanded.

The annual maximum load value is extracted from the Training Sample Data of distribution transformer set *N*, and the inter-annual load change rate is calculated. Based on the data shape formed by the LTS of the previous 3 years (T_4–T_2 years) and the trends (growth or decline) of the fourth year (T_1 year), the Training Sample Data is divided into eight groups. From the Training Sample Data, the population change rate, economic

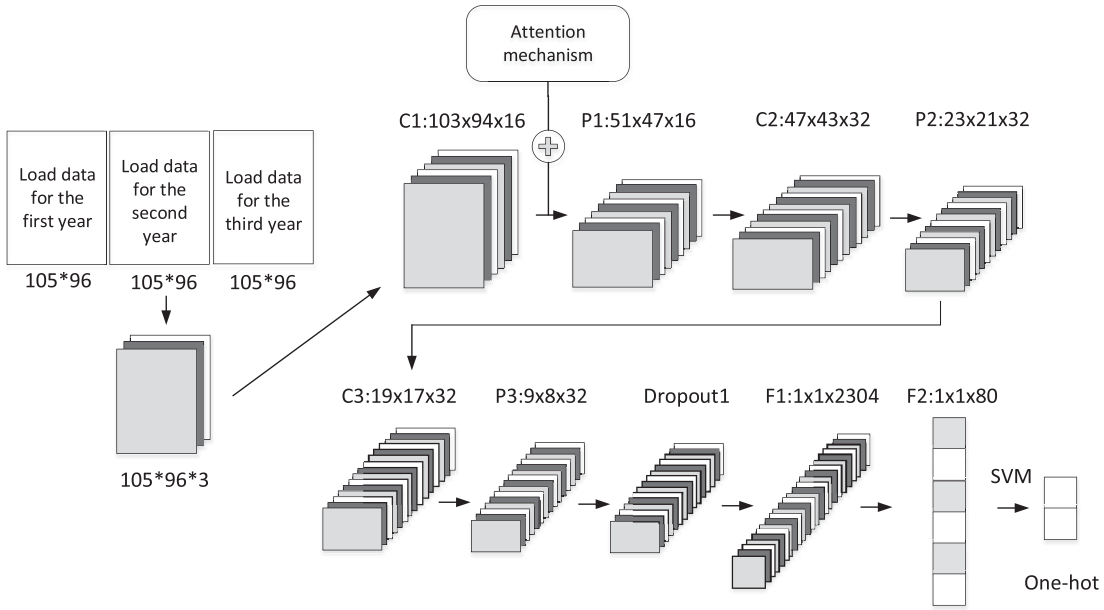


FIGURE 9 | The parameter structure of the improved CNN.

TABLE 1 | The load trend judgment accuracy of various methods.

Attention + improved CNN	Attention + CNN	CNN
67.46%	66.27%	62.23%
Linear regression forecasting method	Fixed growth rate forecasting method	Moving average forecasting method
50.12%	57.01%	54.63%

TABLE 2 | The median error of different numerical forecasting methods.

Improved CNN + RFR	Improved CNN + BP	Improved CNN + DTR	Improved CNN + SVR
9.65%	10.02%	11.09%	11.74%

TABLE 3 | The Mean Absolute Percentage Error of different numerical forecasting methods.

Improved CNN + RFR	Improved CNN + BP	Improved CNN + DTR	Improved CNN + SVR
13.68%	14.41%	15.03%	15.20%

growth rate and load change rate of the first 3 years in the power supply area where the distribution transformer is located are obtained as the input features of group objects forecasting model, and the load change rate in the fourth year is used as the training output label. Therefore, N training data can be divided into eight categories, and eight group forecasting models can be trained based on random forest regression.

When using the load change rate numerical forecasting model for group objects, we extracted the annual maximum load value from the Forecasting Data of the distribution transformer set $\boldsymbol{N}$ (T_3–T_1 years). Combined with the results obtained from the load trend forecasting link, the Forecasting Data shape is formed. According to the Forecasting Data shape, the corresponding group forecasting model is selected. Input the population change rate, economic growth rate and load change rate in the Forecasting Data, and output the load change rate of the distribution transformer in the forecast year. **Figure 8** shows the process of The load change rate numerical forecasting link.

For the same distribution transformer, as a training sample object, its Training Sample Data will present a data shape, which

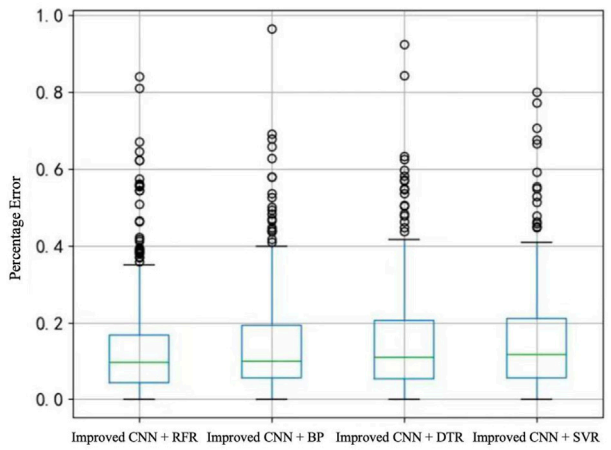


FIGURE 10 | Error box diagram of forecasting results by different numerical forecasting methods.

determines the group belonging of the Training Sample Data. As a forecasting object, its Forecasting Data and load trend forecasting results will present another data shape, which is often different from the former. The latter determines which group forecasting model should be selected for load change rate numerical forecasting.

EVALUATION INDEX

Evaluation Index of Load Trend Forecasting

Take the load trend judgment accuracy as the evaluation index of the load trend forecasting link, and the load trend judgment accuracy is defined as:

$$P_{ACCR} = \frac{n_1}{n_1 + n_2} \tag{6}$$

In the formula, n_1 represents the number of distribution transformers whose load trend judgment is correct, and n_2 represents the number of distribution transformers whose load trend judgment is incorrect.

Evaluation Index of Load Change Rate Numerical Forecasting

Due to the existence of multiple predict objects, the forecasting effect of different forecasting methods can be evaluated comprehensively from three aspects:

1) Error box diagram. Observe the overall distribution of the error of the forecasting results, compare the error aggregation interval and the median error of different methods.

TABLE 4 | The proportion of distribution transformer number in the error interval of 0–15%.

Improved CNN + RFR	Improved CNN + BP	Improved CNN + DTR	Improved CNN + SVR
69.83%	65.55%	59.14%	62.47%

TABLE 5 | The median error of different methods.

Improved CNN + RFR	Fixed growth rate forecasting method (%)	Linear regression forecasting method (%)	Moving average forecasting method (%)
9.65%	12.92	15.34	15.95

TABLE 6 | The Mean Absolute Percentage Error of different methods.

Improved CNN + RFR	Fixed growth rate forecasting method (%)	Linear regression forecasting method (%)	Moving average forecasting method (%)
13.68%	15.47	23.27	25.48

TABLE 7 | The proportion of distribution transformer number in the error interval of 0–15%.

Improved CNN + RFR	Linear regression forecasting method (%)	Fixed growth rate forecasting method (%)	Moving average forecasting method (%)
69.83%	58.19	48.93	48.69

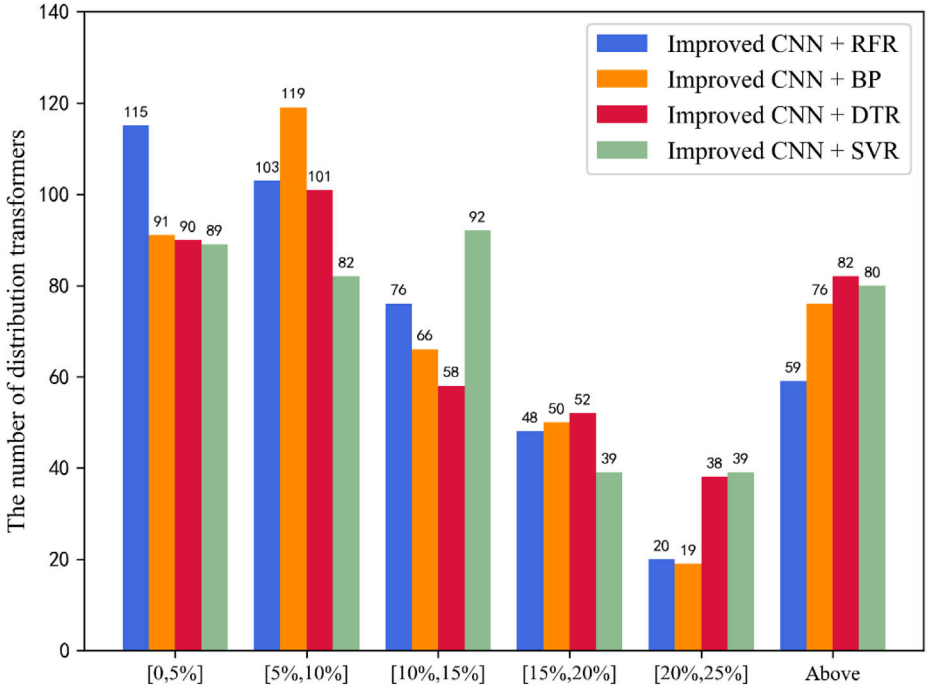


FIGURE 11 | The number of distribution transformer in different error interval.

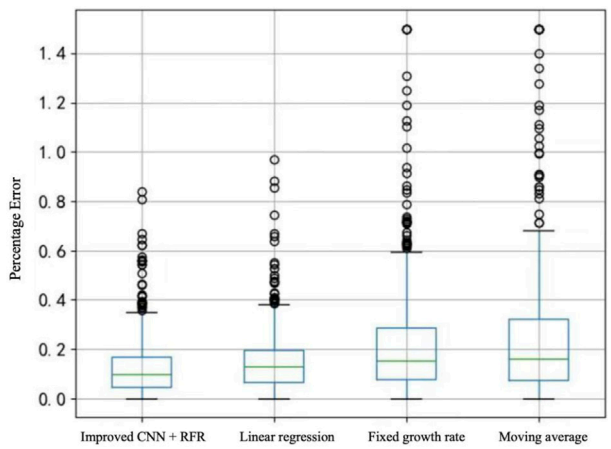


FIGURE 12 | Error box diagram of forecasting results by different methods.

2) Mean Absolute Percentage Error (MAPE). The calculation formula is:

$$MAPE = \frac{1}{n}\sum_{i=1}^{n}\frac{\left|y_{i,pre} - y_{i,real}\right|}{y_{i,real}} \tag{7}$$

In the formula, $y_{i,real}$ is the actual load value, and $y_{i,pre}$ is the load forecast value.

3) The number of transformers forecasting results Percentage Error falling within different error intervals. The more transformers forecasting results Percentage Error that fall in the small error interval, the better the overall forecasting effect of this method.

CASE STUDY

The data set of this paper is the load data of distribution transformers of an economically developed city in Guangdong Province from 2015 to 2019. One measurement point data is obtained in 15 min, with a total of 96 load data points per day. 5,360 distribution transformers in the fluctuating development period are randomly selected from the mature region as the training distribution transformer set $\boldsymbol{N}$. Among the 5,360 distribution transformers, 421 distribution substations belonging to a certain 110 kV substation are selected as the predict distribution transformer set $\boldsymbol{N}'$ for case study. The training distribution transformer set and the predict distribution transformer set of the Image Representation Learning model and the group forecasting model are the same. Taking 2019 as the forecast year, the load data from 2015 to 2018 is taken as the Training Sample Data, and the load data from 2016 to 2018 is taken as the Forecasting Data. According to the data statistics, although the load variation of a single distribution transformer is different, the distribution of annual maximum load change rate of the training distribution transformer set $\boldsymbol{N}$ is similar and relatively stable, showing an approximate normal distribution, indicating that the group objects' variation in the region has a certain degree of stability.

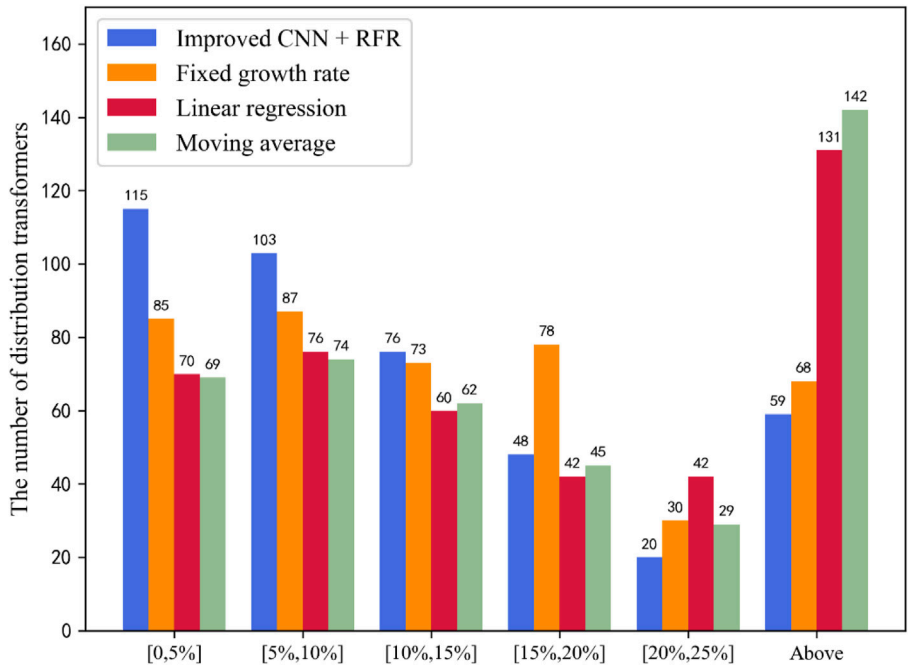


FIGURE 13 | The number of distribution transformer in different error interval.

Comparative Analysis of Load Trend Forecasting Results

Data cleaning is performed on the training distribution transformer set ***N***, 5,360 training power load images and corresponding load change trend labels can be obtained. Through data enhancement technology, the power load images are expanded. First, through the operation of cyclic shift (Zhang et al., 2020), with a cycle of 7 days a week, the data is expanded by 14 times. Secondly, by changing the data interception time window of the power load image, the vertical translation of the power load image is realized. Finally, small random perturbations are added to load data at different measuring times. Through data enhancement technology, 700,000 training sample power load images are obtained to train Image Representation Learning model. After the training is completed, input the power load image formed by the Forecasting Data of the predict distribution transformer set object in 2016–2018, and output the forecasting result of the load trend in 2018–2019.

In the training process, the Gaussian distribution matrix with mean value of 0 and standard deviation of 0.5 is selected for the training convolution kernel initialization of the improved CNN network, the Dropout layer discard rate is 0.3, The loss function is the cross entropy function, the error term penalty coefficient of SVM layer is 1.0, and the Gaussian kernel function is selected for the kernel function. The parameter structure of the improved CNN is shown in **Figure 9**.

In the load trend forecasting link, Attention + Improved CNN, Attention + CNN and CNN are used to build models respectively, and the load change trend judgment accuracy is compared with Linear regression forecasting method, Fixed growth rate forecasting method (3% annual growth rate), Moving average forecasting method. Among them, the last three methods calculate the load trend based on the predicted value and get the accuracy rate.

From the results in **Table 1**, it can be seen that the Linear regression forecasting method is affected by the overall data of the previous 3 years, and the ability to judge the load trend in the case of disorderly fluctuations is slightly weak, the accuracy rate is only 50.12%; Moving average forecasting method has the characteristic of following the load change, and its judgment of the load trend is greatly affected by the change of the previous year, and its judgment accuracy is slightly higher than the Linear regression forecasting method. The direction of load trend judgment for Fixed growth rate forecasting method is fixed, the larger the proportion of distribution transformers change in a growth state, the higher the accuracy of trend judgment accuracy, In this case, it is 57.01%. When using Image Representation Learning model, if only the original structure of CNN is used, the load trend judgment accuracy is 62.23%; Due to the establishment of power load images reflecting the annual and inter-annual load change information, its load trend judgment accuracy is slightly higher than that of the Fixed growth rate forecasting method. After adding the channel Attention mechanism, the load trend judgment accuracy increases to 66.27%; this article uses Attention + improved CNN, which can further effectively increase the load trend judgment accuracy to 67.46%, and the load trend judgment accuracy of the method proposed in this article is higher than that of other methods.

Comparative Analysis of Group Objects Numerical Forecasting Results

Based on the data shape of the Training Sample Data, the Training Sample Data is divided into eight categories. Input the annual maximum load value change rate, economic change rate and population change rate of the training distribution transformer set from 2015 to 2017, output the annual maximum load value change rate from 2017 to 2018. Therefore, eight numerical forecasting model for group objects are trained based on Random Forest Regression method. Combined with the load trend forecasting results of the distribution transformer set in 2018–2019 have been obtained, the numerical forecasting model for group objects corresponding to the data shape can be selected. Input the annual maximum load value change rate, economic change rate, and population change rate from 2016 to 2018, and output the annual maximum load change rate in 2018–2019. The experimental test shows that the model has a better forecasting effect when the number of trees in random forest is 300 and the splitting feature is 3.

When measuring the forecasting effect, the load change rate value predicted by numerical forecasting model for group objects is converted into the actual values of the annual maximum load, the absolute percentage error of each distribution transformer forecasting result can be calculated, and the error box diagram can be drawn. At the same time, calculate the Mean Absolute Percentage Error of the entire distribution transformer set, and count the number of distribution transformers in different error intervals.

Firstly, the load trend forecasting link adopts Attention + Improved CNN model to forecast, Random Forest Regression (RFR), BP neural network (BP) and Decision Tree (DTR), and Support Vector Regression (SVR) are respectively used to forecast the change rate in numerical forecasting link, and the forecasting results are compared.

It can be seen from **Figure 10** that when the RFR method is used in the numerical forecasting of load change rate, the error box of the group forecasting results is lower than that of other methods. As shown in **Table 2** and **Table 3**, the calculated Mean Absolute Percentage Error of the group forecasting results is 13.68%. In order to avoid the influence of individual large forecasting error on Mean Absolute Percentage Error, the median error of different methods are calculated. It can be seen that the median error of the RFR method is 9.65%, which is also lower than other methods.

The group forecasting results are obtained from the load change rate numerical forecasting link, and the number of distribution transformers whose forecasting results fall in each error interval can be obtained. As shown in **Table 4** and **Figure 11**, when RFR method is adopted, the number of forecasting errors in (0, 15%) is more than that of other methods, accounting for 69.83%. It shows that the forecasting error of most distribution transformers can be controlled in a small range. To sum up, when the performance of load trend forecasting link is consistent, the comprehensive performance of RFR method in the load change rate numerical forecasting link is better.

Comparative Analysis of the Overall Forecasting Results of Different Methods

After decoupled into two parts, the forecasting process can be flexibly combined with the methods which perform better under the current data distribution, so as to effectively improve the forecasting performance. Attention + Improved CNN and RFR methods are the best in their respective forecasting links, so they are combined and compared with Linear regression forecasting method, Fixed growth rate forecasting method and Moving average forecasting method applied in engineering.

As can be seen from the **Figure 12**, although the load trend judgment accuracy of Moving average forecasting method is higher than that of Linear regression forecasting method, the error box of the forecasting results of Moving average forecasting method is larger, indicating a larger error distribution range. The error box of Fixed growth rate forecasting method is narrower than that of Linear regression forecasting method and Moving average forecasting method, and the overall error is smaller. However, the overall error of the forecasting results of the method proposed in this paper is the smallest, and the error box is the narrowest, indicating that most of the forecasting errors are concentrated in a small error interval. From the calculation results in **Table 5** and **Table 6**, it can be seen that the Mean Absolute Percentage Error of the method proposed in this paper is smaller, and the median error is also the smallest.

The number of distribution transformers whose forecasting results fall in different error intervals is counted. It can be seen from **Figure 13** and **Table 7** that the number of forecasting results of this method in (0, 15%) small error interval is higher than other methods, accounting for 69.83%. The number of forecasting results of Fixed growth rate forecasting method in (0, 15%) accounted for 58.19%, while the number of Linear regression forecasting method and Moving average forecasting method results falling within each error interval is similar.

Therefore, the results show that the proposed method is superior to the existing distribution transformer forecasting methods.

CONCLUSION AND PROSPECT

The medium-and long-term load forecasting of distribution transformer level has guiding significance for heavy overload warning and grid risk assessment, but the corresponding research is almost blank. Therefore, this paper proposes a medium-and long-term forecasting method for group objects based on Image Representation Learning, and this method has been piloted in the Southern Power Grid project. The method in this paper has the following advantages:

1) A new idea of decoupling forecasting is proposed to realize the decomposition of forecasting task. We can improve the forecasting methods used in different links according to different forecasting objectives, or replace the existing methods with other methods that can achieve the same prediction objectives under different data conditions, so as to realize the flexible combination of forecasting methods and improve the forecasting effect.

2) It can fully integrate and utilize the load data of daily and annual dimensions, and use the Image Representation

Learning model to improve the forecasting ability of distribution transformer load trend.

3) Based on the stationarity of the overall change of group objects, the training data is expanded through data shape classification, The machine learning method of random forest regression is introduced to establish a Multiple Object-Population Forecasting model, which solves the data problem that restricts the application of machine learning method to the medium-and long-term forecasting of distribution network. At the same time, it can realizes the rapid forecasting of a large number of distribution transformation objects, and reduces the subjectivity of forecasting.
4) Compared with other medium-and long-term forecasting methods, the proposed method uses less data feature dimension and requires less recording time. By setting the forecasting process reasonably, the forecasting effect is better than the current engineering application methods.

After the group forecasting results of fine particle size are obtained, it is necessary to research on the method system of bottom-up superposition calculation, including how to reasonably solve the problem of simultaneous rate and error transfer, so as to obtain the load forecasting results of feeder, substation.

DATA AVAILABILITY STATEMENT

The raw data supporting the conclusion of this article will be made available by the authors, without undue reservation.

AUTHOR CONTRIBUTIONS

Conceptualization, DZ; Data curation, JY; Formal analysis, WG; Methodology, DZ; Project administration, DZ; Resources, TY; Visualization, WX; Writing, DZ.

ACKNOWLEDGMENTS

The authors gratefully acknowledge the support of The Natural Science Foundation of China- Smart Grid Joint Fund of State Grid Corporation of China (U2066212).

REFERENCES

Alrashidi, M. R., and El-Naggar, K. M. (2010). Long term electric load forecasting based on particle swarm optimization. *Appl. Energ.* 87 (1), 320–326. doi:10.1016/j.apenergy.2009.04.024

Breiman, L. (2001). Random forests. *MACH LEARN.* 45 (1), 5–32.

Chang, Y.-C., and Huang, T.-C. (2018). An interactive smart grid communication approach for big data traffic. *Comput. Electr. Eng.* 67, 170–181. doi:10.1016/j.compeleceng.2018.03.024

Dong, M., and Grumbach, L. (2019). A Hybrid Distribution Feeder Long-Term Load Forecasting Method Based on Sequence Prediction. *IEEE Trans. Smart Grid*, 97–108.

Dong, X., Qian, L., and Huang, L. (2017). *Short-term Load forecasting in smart grid: A combined CNN and K-means clustering approach.* IEEE International Conference on Big Data & Smart Computing. New Jersey, United States: IEEE, 119–125.

Farrag, T. A., and Elattar, E. E. (2021). Optimized Deep Stacked Long Short-Term Memory Network for Long-Term Load Forecasting. *IEEE Access* 9, 68511–68522. doi:10.1109/access.2021.3077275

Gong, X., Cardenas-Barrera, J. L., Castillo-Guerra, E., Cao, B., Saleh, S. A., and Chang, L. (2019). Bottom-Up Load Forecasting with Markov-Based Error Reduction Method for Aggregated Domestic Electric Water Heaters. *IEEE Trans. Ind. Applicat.* 55 (6), 6401–6413. doi:10.1109/tia.2019.2936330

Islam, S. (2016). *Digital applications in implementation of smart grid*, 2016, 3–7. International Conference on Accessibility to Digital World (ICADW), Guwahati, India: Institute of Electrical and Electronics Engineers.

Jin, N., Flach, P., Wilcox, T., Sellman, R., Thumim, J., and Knobbe, A. (2014). Subgroup Discovery in Smart Electricity Meter Data. *IEEE Trans. Ind. Inform.* 10 (2), 1327–1336.

Kang, C., Xia, Q., and Zhang, B. (2004). Review of power system load forecasting and its development. *Automation Electric Power Syst.* 28 (17), 1–11.

Kang, C., Xia, Q., and Mei, L. (2007). *Power System Load Forecasting*. Beijing: China Electric Power Press.

Kang, J., and Zhao, H. (2012). Application of Improved Grey Model in Long-term Load Forecasting of Power Engineering. *Syst. Eng. Proced.* 3, 85–91. doi:10.1016/j.sepro.2011.11.012

Kaytez, F. (2020). A hybrid approach based on autoregressive integrated moving average and least-square support vector machine for long-term forecasting of net electricity consumption. *Energy*, 197.

Kazemzadeh, M. R., Amjadian, A., and Amraee, T. (2020). A hybrid data mining driven algorithm for long term electric peak load and energy demand forecasting. *Energy*, 204.

Li, Y., Han, D., and Yan, Z. (2018). Long-term system load forecasting based on data-driven linear clustering method. *J. Mod. Power Syst. Clean. Energ.* 6 (2), 306–316. doi:10.1007/s40565-017-0288-x

Liu, Y., Luo, H., and Zhao, B. (2018). *Short-Term Power Load Forecasting Based on Clustering and XGBoost Method*. 2018 IEEE 9th International Conference on Software Engineering and Service Science. Beijing, China: ICSESS. doi:10.1109/icsess.2018.8663907

McLoughlin, F., Duffy, A., and Conlon, M. (2011). Characterising domestic electricity consumption patterns by dwelling and occupant socio-economic variables: An Irish case study. *Energy & Buildings* 43 (1), 240–248.

Munshi, A. A., and Mohamed, Y. A.-R. I. (2017). Big data framework for analytics in smart grids. *Electric Power Syst. Res.* 151, 369–380. doi:10.1016/j.epsr.2017.06.006

Sun, W., and Zhao, W. (2010). *Mid-long term power Load forecasting Based on MG-CACO and SVM method*. 2010 2nd International Conference on Future Computer and Communication, V1-118–V1-121.

Wang, Y., Chen, Q., Gan, D., Yang, J., Kirschen, D. S., and Kang, C. (2018). Deep Learning-Based Socio-demographic Information Identification from Smart Meter Data. *IEEE Trans. Smart Grid*, 1, 1.

Wang, Y., Chen, Q., Sun, M., Kang, C., and Xia, Q. (2018). An Ensemble Forecasting Method for the Aggregated Load with Subprofiles. *IEEE Trans. Smart Grid* 9 (4), 3906–3908. doi:10.1109/tsg.2018.2807985

Wen, Z., Xie, L., Fan, Q., and Feng, H. (2020). Long term electric load forecasting based on TS-type recurrent fuzzy neural network model. *Electric Power Syst. Res.* 179, 106106. doi:10.1016/j.epsr.2019.106106

Xi, L., Yu, T., Yang, B., Zhang, X., and Qiu, X. (2016). A wolf pack hunting strategy based virtual tribes control for automatic generation control of smart grid. *Appl. Energ.* 178, 198–211. doi:10.1016/j.apenergy.2016.06.041

Yang, B., Jiang, L., Yao, W., and Wu, Q. H. (2015). Perturbation estimation based coordinated adaptive passive control for multimachine power systems. *Control. Eng. Pract.* 44, 172–192. doi:10.1016/j.conengprac.2015.07.012

Zhang, C., and Li, R. (2020). A Novel Closed-Loop Clustering Method for Hierarchical Load Forecasting. *IEEE Trans. Smart Grid* (99), 1, 1.

Zhang, K., Cao, Z., and Wu, J. (2020). *Circular Shift: An Effective Data Augmentation Method For Convolutional Neural Network On Image*

Classification. IEEE International Conference on Image Processing. Ontario: ICIP. doi:10.1109/icip40778.2020.9191303

Zhang, X., Tan, T., Zhou, B., Yu, T., Yang, B., and Huang, X. (2021). Adaptive distributed auction-based algorithm for optimal mileage based AGC dispatch with high participation of renewable energy. *Int. J. Electr. Power Energ. Syst.* 124, 106371. doi:10.1016/j.ijepes.2020.106371

Zhang, X., Yu, T., Yang, B., and Li, L. (2016). Virtual generation tribe based robust collaborative consensus algorithm for dynamic generation command dispatch optimization of smart grid. *Energy* 101, 34–51. doi:10.1016/j.energy.2016.02.009

Zhang, X., Yu, T., Yang, B., Zheng, L., and Huang, L. (2015). Approximate ideal multi-objective solution Q(λ) learning for optimal carbon-energy combined-flow in multi-energy power systems. *Energ. Convers. Manag.* 106, 543–556. doi:10.1016/j.enconman.2015.09.049

Zhao, M., Liu, W., Su, J., Zhao, L., Dong, X., and Liu, W. (2014). *Medium and Long term Load forecasting method for Distribution Network with High penetration DGs*. 2014 China International Conference on Electricity Distribution (CICED), 442–444.

Conflict of Interest: The authors declare that the research was conducted in the absence of any commercial or financial relationships that could be construed as a potential conflict of interest.

Publisher's Note: All claims expressed in this article are solely those of the authors and do not necessarily represent those of their affiliated organizations, or those of the publisher, the editors and the reviewers. Any product that may be evaluated in this article, or claim that may be made by its manufacturer, is not guaranteed or endorsed by the publisher.

Copyright © 2021 Zhang, Guan, Yang, Yu, Xiao and Yu. This is an open-access article distributed under the terms of the Creative Commons Attribution License (CC BY). The use, distribution or reproduction in other forums is permitted, provided the original author(s) and the copyright owner(s) are credited and that the original publication in this journal is cited, in accordance with accepted academic practice. No use, distribution or reproduction is permitted which does not comply with these terms.

frontiers in Energy Research

ORIGINAL RESEARCH
published: 01 September 2021
doi: 10.3389/fenrg.2021.721385

Power Management of AC/DC Hybrid Distribution Network With Multi-Port PET Considering Reliability of Power Supply System

Xinxing Xu[1], Wentao Huang[1], Yan Hu[1], Nengling Tai[1], Yaming Ji[2] and Ning Xie[3]*

[1]Department of Electrical Engineering, School of Electronic Information and Electrical Engineering, Shanghai Jiao Tong University, Shanghai, China, [2]Beijing Sifang Jibao Automation Co., Ltd., Beijing, China, [3]Institute of Energy Storage, Electric Power Research Institute of Guangdong Power Grid Co., Ltd., Guangzhou, China

In the current distribution network, photovoltaic, wind power, energy storage, and other distributed energy are widely connected, and the proportion of generalized DC load is rapidly increasing. With the development of power electronics technology, using multi-port power electronic transformer (PET) to achieve high-efficiency access of large-capacity AC/DC source and load is the current research hotspot, and AC / DC hybrid power supply is inevitable. The introduction of a large number of power electronics and the flexible coordinated control and complementary fault-tolerant advantages of PET bring challenges to the operation and maintenance management of the AC/DC hybrid power system. In this paper, the structure of the AC/DC hybrid power system with the multi-port PET cluster is introduced. Based on the idea of hierarchical and partitioned control, a three-layer and multi-time scale control mode of integrated automation system, PET cluster and PET controller is proposed; Aiming at the problem of reliability evaluation, a sequential Monte Carlo simulation method is proposed to simulate the AC/DC hybrid power system with the multi-port PET cluster. The influence of multi-port PET parallel cluster mode and port capacity limitation on the reliability of the power system is analyzed, and the effectiveness of the model and algorithm is verified. Finally, an example is given to verify that the proposed structure is conducive to improving the utilization level of renewable energy in the distribution network.

Keywords: AC/DC hybrid, power electronic transformer, reliability, control, new energy access

OPEN ACCESS

Edited by:
Bo Yang,
Kunming University of Science and Technology, China

Reviewed by:
Haixiang Zang,
Hohai University, China
Fang Shi,
Shandong University, China

****Correspondence:***
Xinxing Xu
xuxinxing1128@sjtu.edu.cn

Specialty section:
This article was submitted to Smart Grids, a section of the journal Frontiers in Energy Research

Received: *06 June 2021*
Accepted: *16 July 2021*
Published: *01 September 2021*

Citation:
Xu X, Huang W, Hu Y, Tai N, Ji Y and Xie N (2021) Power Management of AC/DC Hybrid Distribution Network With Multi-Port PET Considering Reliability of Power Supply System. Front. Energy Res. 9:721385. doi: 10.3389/fenrg.2021.721385

INTRODUCTION

With the rapid increase of the proportion of generalized DC load, the long-term coexistence of AC load in a certain period in the future, and the increase of the proportion of new energy, the AC/DC hybrid power system may accept more types of source load and larger capacity in the future. The AC/DC hybrid system needs enough power supply capacity and power supply radius to meet the demand of rapid load growth and realize high-efficiency access of large-capacity AC/DC source and load. The integration of different AC/DC loads and distributed renewable energy makes the power flow direction of the whole system more complex and energy management more challenging. If the energy management of the system and the passive mode switching of the equipment are realized by the system level control, the calculation of the system control is large, the communication delay will

greatly affect the energy efficiency of the system, and the system will be paralyzed when the communication is interrupted. With the development of power electronics technology, which provides the hardware foundation for the integration of new energy and different types of loads into the distribution system. Considering the randomness and volatility of distributed generation and the diversity of user side load, it has become an important research direction to integrate AC, DC power, and load into AC/DC hybrid power system through multi-port PET with different voltage level ports.

The traditional operation mode of distribution network is dominated by the supplier and one-way radial power supply. It has a top-down one-way supply-demand relationship with the transmission network, and its function and structure are still relatively single. However, with the high proportion of new energy and electric vehicles with volatility and randomness, and all kinds of controllable AC and DC load access, the traditional distribution network fails to fully consider this factor in the configuration optimization and operation management stage, resulting in the actual operation of the traditional distribution network not being able to well adapt to the user's requirements for power supply reliability, environmental protection, and power quality of the distribution network (Huang et al., 2011; Pilo et al., 2011; Wang, 2014; Zha et al., 2014).

In order to solve a series of problems caused by distributed renewable energy access, improve the level of power quality, and improve the utilization efficiency of renewable energy, the concept of integrated energy subnet came into being. The integrated energy sub-network includes electricity, heat, cold, gas, and other energy forms, and the power collector constructed by flexible switchgear is used for unified management (Duan et al., 2016; Zhang et al., 2017; Dolatabodi et al., 2018; Miao et al., 2018). Distributed energy access, energy storage control, power quality management, power flow control, and other functions are managed by the power collector, which has the advantages of modularization and centralization. However, multiple energy sources are coupled and interact in the integrated energy sub network, which has different time scales, and its transient characteristics are more complex. Therefore, the integrated energy subnet is a new way to integrate distributed energy access, but the accompanying problems to be solved include optimal operation and fault protection (Dolatabodi et al., 2018).

In addition to the integrated energy sub-grid, it is also an effective method for distributed renewable energy to be connected to the distribution network through the microgrid (Funabashi and Yokoyama, 2006; Barnes et al., 2007; Hatziargyriou et al., 2007; Salonen et al., 2008; He et al., 2020). By integrating the distributed generation, energy storage unit, and local load, an independent microgrid that can be connected to the grid and operated off the grid has been widely studied, and it has been widely used in remote mountainous areas, independent islands, and other areas that are difficult to be covered by the large power grid.

AC distributed generation can be connected to a common coupling point through a grid connected inverter and transformer, and DC distributed generation and energy storage equipment can be connected to the AC/DC microgrid through DC line and rectifier. In Yin et al. (2012), the structure design of the AC/DC hybrid microgrid is studied, and its key technology and development direction are summarized. In Xiang et al. (2017), the influence of distributed generation, energy storage, load, and power converter on the stability of AC/DC microgrid is considered, and the method to improve the system stability is proposed. The control strategy of the AC/DC microgrid is studied in Dragicevic et al. (2014). Due to the existence of multi-level and various types of power conversion devices in AC/DC microgrid, on the one hand, it reduces the energy utilization efficiency of the system and, on the other hand, it makes the control system more complex and difficult to control the power quality, which is not conducive to the unified deployment of the system. Eghtedarpour and Farjah (2014) introduce a design scheme of AC/DC hybrid microgrid using PET and studies its operation mode and the switching strategy between each operation mode. Boroyevich et al. (2010) study the coordinated control strategy of PET and energy storage equipment, which improves the stability of the system.

At the same time, the research on structure design (Wang et al., 2015; Xiao, 2015), stability (Sanchez and Molinas, 2015; Pu et al., 2018; Wan et al., 2019), DC voltage control strategy (Dragicevic et al., 2014; Eghtedarpour and Farjah, 2014; Gao et al., 2017), and energy and power control strategy (Gao et al., 2017) has been widely carried out in the field of microgrid. AC/DC technology can improve the utilization efficiency of new energy to a certain extent but hesitates to limit the access capacity of microgrid. The access capacity of new energy is usually relatively small and does not support the power coordination optimization and adjustment control among multiple regions, which is limited by the popularization of this technology. At the same time, domestic and foreign scholars further proposed the AC/DC hybrid system based on PET (Huang et al., 2011), which can integrate a variety of distributed renewable energy in multiple voltage level systems of multiple AC/DC regions. In Yan et al. (2017), a hierarchical hybrid distribution system structure based on AC/DC converter is proposed. A construction scheme of AC/DC hybrid distribution network is proposed in Ma et al. (2015).

Through PET, a variety of new energy and AC/DC loads are connected to the distribution network to form a flexible and controllable new AC/DC hybrid distribution network, which makes the future distribution network develop into an information physical system with high integration of information and physical power grid for power and information integrated services (Pilo et al., 2011). At the same time, it can meet a variety of energy demands of users and allow new energy and power grid with random and fluctuation energy consumption platform with a high proportion of electric vehicle load and DC load controlled by users and stable operation (Zha et al., 2014).

Compared with the traditional distribution network, AC/DC hybrid distribution system has the advantages of reducing power supply cost, improving power supply reliability, improving power quality and reducing reactive power loss. The reliable operation of the distribution network is the basic guarantee for the stable supply of power.

However, up to now, with the rapid development of the national economy, China's power load is showing a trend of continuous growth, followed by the increasingly prominent contradiction between power supply and demand, It is very important to study the reliability of power system. In recent years, China has done a lot of research work on the optimal design and reasonable planning of the distribution network, and the reliability management is also carried out in an organized and planned way, in order to promote the development of distribution network reliability research (Liu, 2011; Peng, 2018).

In the reliability evaluation of the distribution network, the reliability analysis methods can be divided into analytical method and Monte Carlo method. The calculation amount of the analytical method will increase rapidly with the increase of system complexity or system accident dimension, so this method is generally only applicable to the reliability analysis of some simple systems. The commonly used reliability analytical methods are divided into the following categories (Zhang and Wang, 2004), such as failure mode and consequence analysis method, network equivalence method, minimum path method, Bayesian network-based evaluation algorithm, fault diagnosis method, fault diagnosis method and so on Vector method and analytic method are intuitive, easy to understand, and easy to solve by computer programming (Zhang and Alabdulwahab, 2017). For single fault or relatively small state space, the analytical method is very effective in most cases. When considering the multi-dimensional events or high failure rate, the computational complexity of the analytical method will be greatly improved. The analytic method can be used to evaluate the expected value and load point of the system reliability index. The main advantages of the analytical method are being easy to understand, clear concept, and strong practicability of the model (Zheng, 2011).

Monte Carlo method, also known as statistical test method or random sampling technique, is based on probability and expected value. When using Monte Carlo method for simulation calculation, the most important thing is to use the computer to randomly sample the fault state of each component, and then accumulate the reliability index of the system (Zhang, 2019). Among them, the sequential Monte Carlo method can accurately simulate the duration of distribution system in different states. Because it does not consider the timing information, compared with sequential Monte Carlo method, its calculation speed is faster and the model is simpler. It is only suitable for short-term field and large-scale circuit system evaluation projects which require higher calculation speed. How to improve the non-sequential Monte Carlo method on the basis of ensuring the convergence speed and storage capacity has become the main research direction of many scholars(Eicha, 2004; Fecci, 2014).

The randomness and volatility of new energy on the power supply side pose a challenge to the reliable power supply of the power grid. On the load side, a large number of data centers will become the typical DC load in the future power grid. The requirements for power supply reliability of the power system are very strict. The scientific research and reasonable planning of distribution network reliability need to be paid enough attention to. At the same time, with the increasing complexity of the urban distribution system, the reliability analysis of the distribution system plays an increasingly important role in the reasonable design and planning of the whole power grid. It is a difficult problem to solve the reliability calculation problem of the AC/DC hybrid distribution system with the multi-port power cluster.

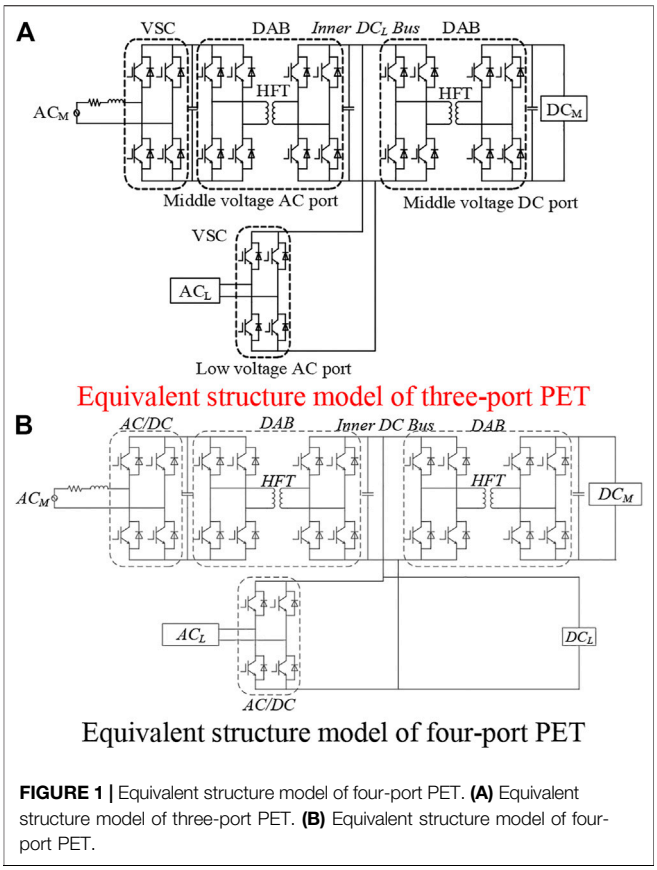


FIGURE 1 | Equivalent structure model of four-port PET. **(A)** Equivalent structure model of three-port PET. **(B)** Equivalent structure model of four-port PET.

AC/DC HYBRID POWER SYSTEM WITH MULTI-PORT PET CLUSTER

AC/DC hybrid system needs enough power supply capacity and power supply radius to meet the demand of rapid load growth and realize high-efficiency access of large capacity AC/DC source and load. The integration of different AC/DC loads and distributed renewable energy makes the power flow direction of the whole system more complex and energy management more challenging. Based on the above reasons, the coordinated control and flexible complementary fault tolerance of PET can be considered to optimize the AC/DC hybrid system.

Multi-Port PET Structure

As shown in **Figures 1A,B**, they are typical structures of three-port PET and four-port PET, respectively. They have medium voltage AC port AC_M, medium voltage DC port DC_M, and low-voltage AC port AC_L, respectively. Four-port PET leads out one low-voltage DC port DC_L more than three port PET. AC_M port is composed of voltage source converter (VSC) and dual active bridge converter (DAB), DC_M is composed of DAB, AC_L is

composed of VSC, and DC_L is led out from PET internal common bus to form low-voltage DC port.

Each port of multi-port PET is connected with the external AC/DC new energy power supply, energy storage, load, and traditional distribution network to form an AC/DC hybrid power system with multi-port PET. The external power grid, new energy, and AC/DC load can be connected to the AC/DC hybrid system through the PET port. The structure has abstracted the internal bus structure; the part from bus to each port is replaced by efficiency module, which shows that multi-port PET is easy to realize modularization and expand ports flexibly, which is convenient for different types and voltage levels of power grid access.

PET Cluster

Cluster Structure

For the AC/DC hybrid system, PET is the core equipment to realize energy conversion. The PET based on cascaded H-bridge (CHB) structure can not only meet the demand of high voltage and large capacity but also provide a high voltage DC port. It has the basic demand of multi-port for power routing and can face the flexible networking of energy Internet. Based on the flexible networking features of cascaded H-bridge power electronic transformers, the concept of "cluster" is introduced on the basis of dual power single bus topology.

Each PET operates autonomously with source and load as a "set," and two or more power electronic transformers are combined with energy ports and interconnected to form a "cluster." PET cluster control is to make the cluster have the function of flexible power routing and efficient energy management through active coordination control. Through the PET cluster networking and cluster control, the reliability of load power supply, system operation flexibility, and redundancy scalability can be improved.

Advantages of Cluster Networking

With PET cluster, the AC/DC hybrid system has the following advantages:

1) Plug and play, increase system power supply capacity and power supply radius

The parallel operation of several power electronic transformers can increase the power supply capacity of the system. After cluster networking, multiple power electronic transformers in different parks are hot standby for each other, and the energy can flow freely in the AC/DC hybrid system, which can increase the power supply radius and reduce the power transmission loss of central power supply, which is in line with the characteristics of plug and play.

2) Enhance capacity scalability and reduce total reserve capacity

The construction of cluster system relies on the combination of energy ports and information interconnection network, and the most basic is the modular design and multi-parallel technology. The power conversion modules of the same type of PET can be combined, which can easily expand or reduce the capacity and reduce the total reserve capacity.

3) Improve the reliability of power supply

N power electronic transformers in different parks are connected by AC/DC bus, with one host and N-1 slaves. If the slave fails, the system can still provide voltage reference by the host. If the total capacity of PET is enough, the whole system can still operate. If the host fails, one of the slaves must change the operation mode to provide voltage reference for the system. When a single PET fails or is overhauled, the power electronic transformers in other parks can provide power support, which can greatly improve the reliability of the power supply.

4) Improve operation economy

The distributed energy management technology can be used to manage the power electronic transformers in different parks, and then the global energy coordination can be realized through the system level controller. The loss and efficiency of a single PET are non-linearly related to its load rate. The power distribution of each PET in the system can be optimized by cluster control to minimize the total loss of n power electronic transformers and make the system run in the optimal condition.

5) Reliable fault tolerance and active mode switching of power electronic transformer

There is direct communication and state feedback between multiple power electronic transformers, and the master-slave mode can be switched online without system level controller.

6) The communication is interrupted and the system is still running

When the system communication is interrupted/failed, the system can turn into non-integrated system operation, and the system operation control is realized by the PET cluster.

AC/DC Hybrid Power System With Multi-Port PET Cluster

Based on the above analysis, a two-stage AC/DC hybrid power distribution system based on PET cluster is proposed, which includes 10 kV AC and 10 kV DC distribution level, and 380 V AC and 380 V DC distribution level ±. The 375 V DC power consumption level is shown in **Figure 2**.

This structure has the following advantages:

1) Through the PET cluster networking mode, improve the operation reliability and economy;
2) According to the capacity of renewable energy, different voltage levels can be flexibly selected to save cost and reduce loss;

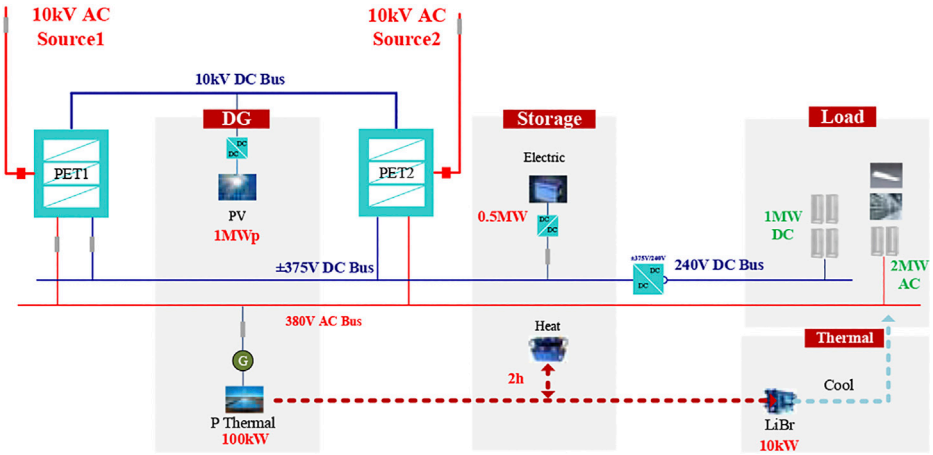


FIGURE 2 | AC/DC hybrid power system with multi-port PET cluster

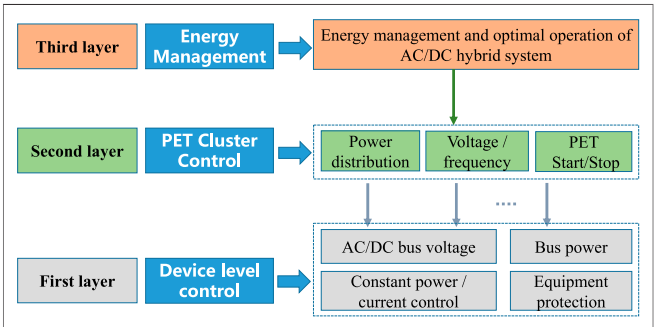


FIGURE 3 | Hierarchical control system of AC/DC hybrid power supply.

3) Through 10 kV DC, the two stations can operate in a closed loop to improve the reliability of the power supply. At the same time, as a power ride through channel, load balancing can be realized.

HIERARCHICAL CONTROL OF AC/DC HYBRID SYSTEM

The multi-port PET cluster AC/DC hybrid power system, based on the idea of hierarchical control, adopts three-layer control mode: integrated automation system, PET cluster controller and PET controller. The integrated automation system is mainly responsible for the overall scheduling of multiple PET cluster controllers, solving the exchange of power, voltage, frequency and other information between the cluster controller and the external power grid, which can realize power optimization control, voltage dynamic control, frequency secondary regulation, system recovery after failure, etc; PET cluster controller is mainly responsible for coordinating and managing each PET in the cluster, formulating operation strategy and distributing it to the PET in the cluster, which can realize fault-tolerant switching, n-1 load transfer, PET re putting into operation, etc; PET controller is mainly responsible for executing the upper control instructions and completing its own optimization operation. The control architecture adopts multi-layer division of labor, which can improve the control robustness of the system, and simplify the direct information interaction and data processing between the integrated automation system and PET.

As shown in **Figure 2**, the operation control objective of the AC/DC hybrid power system is generally applicable to the coordinated control of the simple system. However, for the complex AC/DC hybrid power system with multi-bus, multi-port PET cluster, this structure has certain limitations, which lead to the simple system energy management system and the inability to realize the economic operation of the system.

Therefore, the hierarchical control system as shown in **Figure 3** is introduced into the control of the AC/DC hybrid distributed system with multi-port PET as shown in **Figure 2**. The device level control (corresponding to the first level control) and system level control (corresponding to the second and third level control) strategies are implemented at different levels to realize the standardization and scalability of the AC/DC hybrid power system and improve the overall performance of the system.

First Level Control Strategy

The first layer mainly realizes the device level control, in which the AC/DC bus voltage control is the core. According to the different AC/DC bus voltage control strategies, this layer can be divided into master-slave control and peer-to-peer control. Taking the DC bus voltage control as an example, in the master-slave control strategy, there is usually only one unit in the system to control DC bus voltage. If the unit fails, the DC sub-network will lose the power balance unit, which may cause the DC bus voltage out of control and system collapse. Therefore, the reliability of the master-slave control strategy is poor, which is more suitable for the application of the simple AC/DC hybrid distributed system.

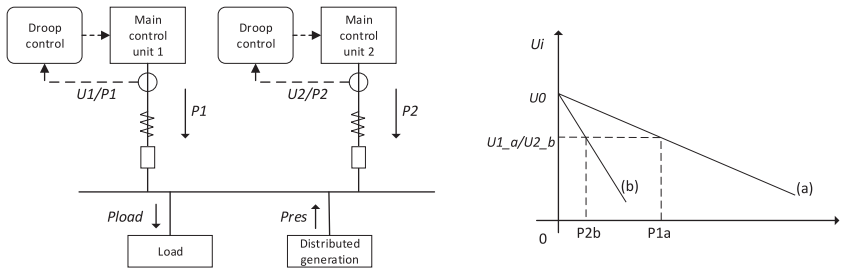


FIGURE 4 | Control schematic diagram of parallel operation of two droop control units.

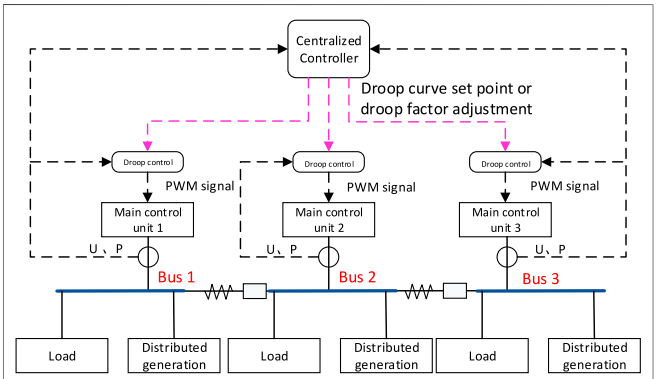


FIGURE 5 | Schematic diagram of secondary centralized control structure.

In order to improve the operation reliability of the bus voltage control system in a complex AC/DC hybrid distributed system, an equivalent control strategy can be adopted for DC bus voltage control. In this control mode, many units or devices are participating in the DC bus voltage control in the system. These units are called the main control unit and have equal status in the control function. The droop control with plug and play characteristics is an effective way to realize the equivalent control strategy. As shown in **Figure 4**, the two distributed generators adopt DC bus voltage output power ($U_{dc\text{-}p}$) droop control mode and droop control characteristic curve of the main control unit. Each main control unit controls DC bus voltage only by injecting local information such as DC bus power and output port DC voltage. In order to cope with the load change in the DC sub-network and the output power fluctuation of the other distributed generation, even if a main control unit in the system is out of operation due to fault, the DC sub-network can still maintain the system stability through the other main control units, so the power supply reliability of the system is improved.

Second Level Control Strategy

Due to the steady-state deviation of DC voltage and the power sharing problem of multiple main control units in the AC/DC hybrid power supply unit, the secondary coordination control strategy suitable for the AC/DC hybrid system is introduced, as shown in **Figure 5**. At present, according to the different communication and control modes, the research on the secondary coordination control strategy of AC/DC hybrid distributed system can be divided into three categories.

Centralized Communication and Control

In this structure, the secondary coordinated control of the AC/DC hybrid power system is realized by a centralized controller. As shown in **Figure 5**, the secondary centralized controller detects the DC bus voltage and the output power of each main control unit participating in the DC bus voltage control, then performs the corresponding DC bus voltage recovery and current sharing control algorithm of each unit output, and adjusts the droop curve set point or droop coefficient and other control parameters of the droop control system of each main control unit to achieve the corresponding control purpose. In the secondary control system, PI regulation is used to compensate for the bus voltage drop caused by droop control and improve the bus voltage to normal level. But the biggest defect of centralized control is that if the secondary centralized controller of AC/DC hybrid distributed system fails, the system will not be able to complete the secondary coordinated control function, so the reliability is low.

Centralized Communication and Distributed Control

In order to improve the reliability of the secondary control system, the secondary coordinated control strategy of centralized communication and distributed control is adopted as shown in **Figure 6**. This method is different from the centralized controller shown in **Figure 5**. The secondary controller is embedded in the local controller of each main control unit, and the information it receives through the communication bus is no longer the droop control parameter reference value adjustment instruction issued by the centralized controller, but the DC voltage and voltage at the outlet of other main control units in the AC/DC hybrid distributed system output power and other primary measurement information. Although the secondary control also needs to obtain the global information of the DC distributed system, the secondary coordinated control algorithm is implemented in the local controller of each main control unit. Therefore, compared with the centralized control system structure, the reliability of this method will be improved. However, the secondary controller of each main control unit needs to obtain the relevant data

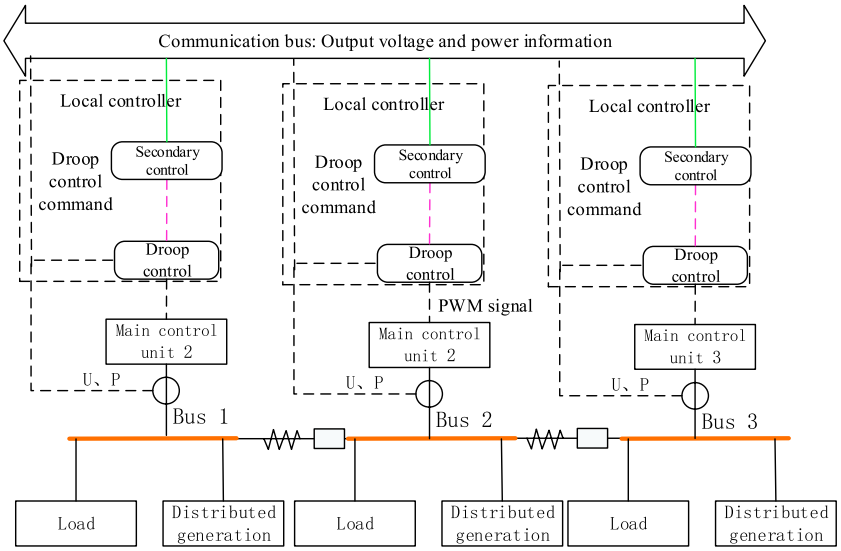


FIGURE 6 | Schematic diagram of centralized communication and distributed control structure.

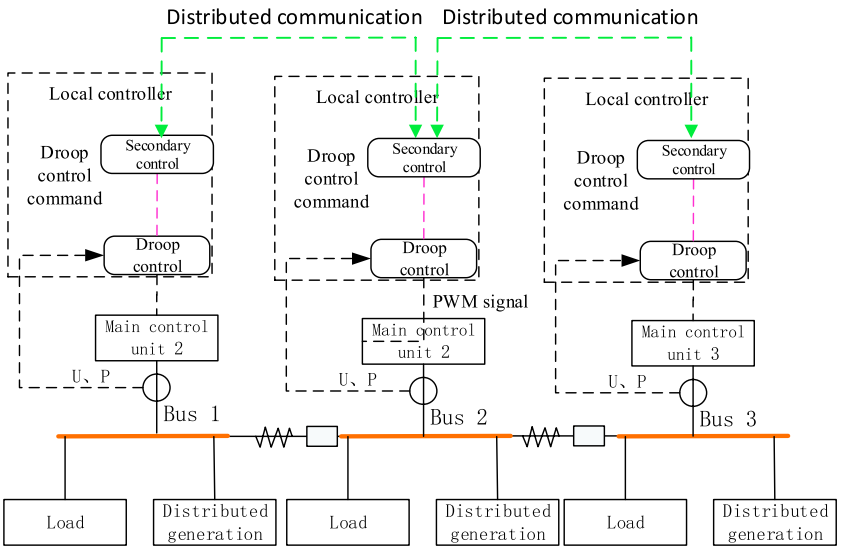


FIGURE 7 | Schematic diagram of distributed cooperative control structure.

information of other main control units in order to realize the secondary control algorithm and provide a reference value for the bottom droop control. Therefore, this method requires high reliability of communication network, and with the increase of the scale of AC/DC hybrid distributed system, the pressure of communication network will increase, which may affect the performance of secondary coordinated control.

Distributed Collaborative Control

Distributed coordination control (DCS) refers to the more complex tasks that each main control unit updates its output state through local control based on its own and neighboring unit data information. Based on the above thought, in order to realize the secondary voltage recovery and current sharing control objectives of the AC-DC hybrid distributed system, each main control unit only communicates with neighboring nodes, and its basic control structure is shown in **Figure 7**.

In the future AC/DC hybrid distributed system, distributed energy storage unit, controllable distributed generation, even wind and other distributed random intermittent generation may be used as the main control unit to actively participate in the DC bus voltage control. If the interface of different types of power supply or converter adopts the equivalent control mode, in order to achieve economic operation, it often needs to accept the

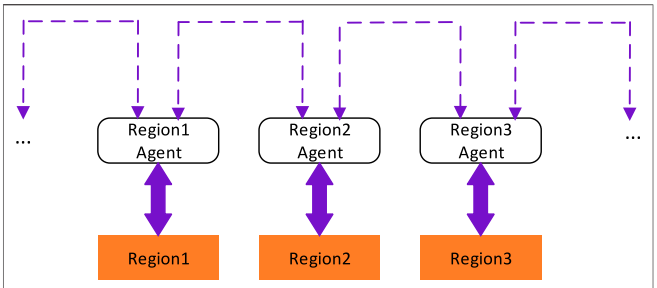


FIGURE 8 | schematic diagram of hybrid hierarchical control combining centralized and distributed control.

scheduling of the upper energy management system. The upper energy management system can often adjust the voltage reference set point or droop coefficient in the droop control curve of each unit in the AC/DC distributed system, Thus, the output level of different distributed generation or power flow controller can be adjusted to ensure the overall optimal operation of AC/DC hybrid power system.

Third Level Control Strategy

The third layer control of AC/DC hybrid distributed system is energy optimization operation and integrated monitoring system. The purpose is to make decisions according to different optimal operation objectives and beam conditions according to the data of distributed power output prediction, load demand, operation status of the energy storage system, and market information and make real-time operation scheduling strategy of AC/DC hybrid distributed system. The flexible dispatching of distributed power supply, energy storage system, load output, and AC/DC system switching power is realized to ensure the safe and economic operation of the system. A reasonable energy management strategy is an important guarantee for the effective utilization of renewable energy and the safe and optimized operation of the system in AC DC hybrid distributed system, as shown in **Figure 8**.

As the top energy management system, its structure mainly includes centralized and distributed. Centralized energy management system is monitored and controlled by a unified central controller, which is simple in structure and easy to realize, but it lacks redundancy and high dependence on central controller and reliability is not high enough; Distributed control is usually controlled by multi-agent, which is easy to implement plug and play, but lack of unified coordination and management, and requires higher requirements for distributed optimization operation algorithm.

MULTI-TIME SCALE CONTROL METHOD

According to different operation control requirements, the control time scales corresponding to different objects are determined, so as to build a multi-scale scheduling system and locate the specific functions of different devices and different levels.

In the third section, the hierarchical control strategy corresponds to the equipment layer, the coordination control layer, and the optimal scheduling layer of the system. Therefore, three levels of time scale control are set.

Considering the operation control requirements of three levels, the corresponding operation control time scales of equipment level, coordination control level, and optimization dispatching level are ≤100 ms, (100 ms, 5s), and (5s, 15 min). Through the organic cooperation of multiple time scales, the

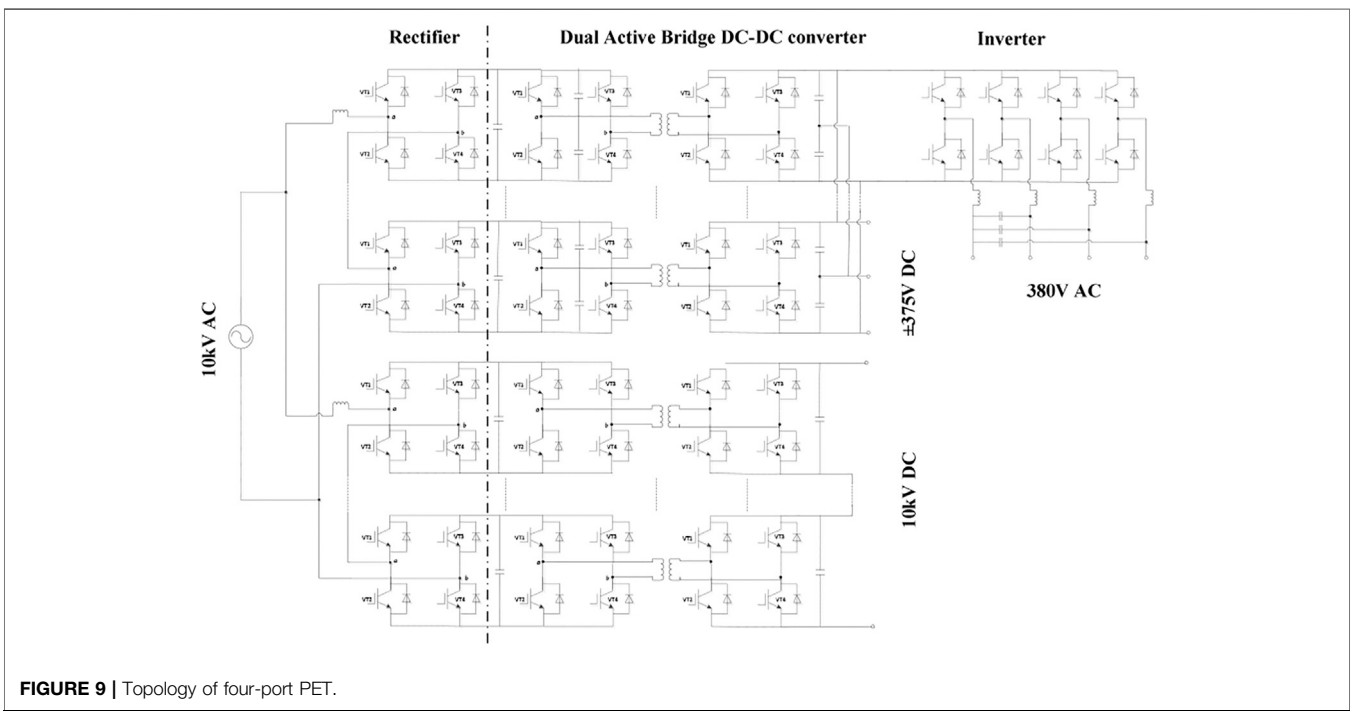


FIGURE 9 | Topology of four-port PET.

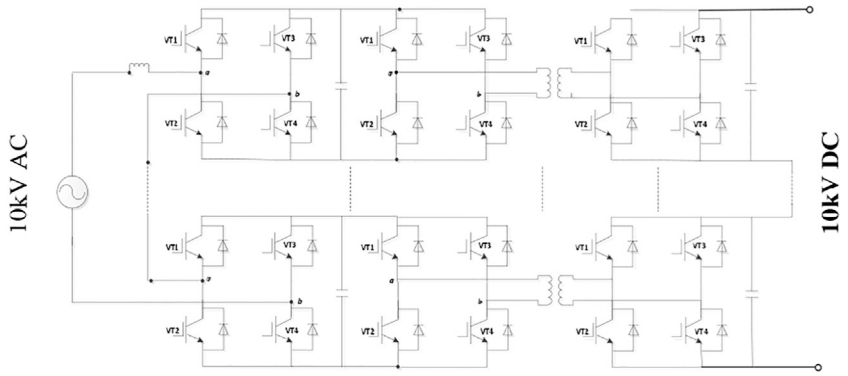


FIGURE 10 | Topology of 10 kV AC-10 kV DC port.

overall operation control efficiency can be effectively improved, and the system operation can be optimized. The main function design involved in each layer of control is described in detail as follows.

Millisecond Level Device Control Layer

The main part of equipment layer ≤ 100 ms level control mainly includes distributed renewable energy, energy storage, load, power electronic voltage regulator, fault current controller and other primary equipment. It mainly involves the autonomous operation of primary equipment ontology, ontology protection and master-slave / peer-to-peer control of PET cluster.

Second Level Coordinated Control Layer

The 100 ms-5 s level control in coordination control layer mainly includes multi-functional coordination control system, regional local controller, AC protection device, DC protection device and other equipment. It mainly involves secondary control of voltage and frequency, smoothing filter control of new energy power below second level, multi pet coordination control, power regulation control, tie line control and system start-up and stop control.

The coordination and control layer is mainly responsible for cooperating with the equipment layer to solve the control requirements within the time range of 100 ms-5 s, and coordinating and controlling layer to help the equipment layer complete the transition of emergency. Taking PET cluster control as an example, when the cluster operates in master-slave mode, if the slave machine fails, the system can still provide voltage reference by the host machine. If the total capacity of PET is enough, the whole system can still operate. If the host machine fails, one of the slave machine must change the operation mode to provide voltage reference for the system. When a single PET fails or is overhauled, the PET in other parks can provide power support, which can greatly improve the reliability of power supply.

Minute Level Optimal Scheduling Layer

The 5 s-15 min level control of optimal dispatching layer is mainly the overall optimal dispatching of "source-network-load-storage" of the whole system, which mainly involves planning curve, peak shaving and valley filling, early warning analysis, prediction, power flow optimization and multi energy complementary control. In this paper, the power flow optimization control is mainly realized by adjusting the power of each port of the multi-functional PET, and the power control is realized by adjusting the output of various distributed generation.

EVALUATION METHOD OF POWER SUPPLY RELIABILITY

The reliable operation of the distribution network is the basic guarantee for the stable supply of power, and it undertakes the important task of transmitting power from the power supply and the grid to the users. How to effectively evaluate the power supply reliability of the AC/DC hybrid distribution network with a multi-port PET cluster is a new problem.

Reliability Modeling of AC/DC Hybrid Power System With Multi-Port PET Cluster

Reliability Modeling of PET

For the reliability modeling of PET, as shown in **Figure 9**, it has 10 kV AC, 10 kV DC ±. It has four ports of 375 V DC and 380 V AC, which can convert medium voltage AC or DC power into low-voltage DC or AC power. In order to calculate the power supply reliability of the structure PET, we can first analyze the failure rate from the 10 kV AC port to the 10 kV DC port and then calculate the power supply reliability of other ports in the same way.

The topology of 10 kV AC-10 kV DC port is shown in **Figure 10**, which is composed of six parts in series (Zhang and Wang, 2004):

1) Single phase bridge full control rectifier and inverter circuit (AC/DC, DC/AC);
2) Transformer primary side series inductance L;
3) High frequency transformer (T);
4) Single phase bridge full control rectifier circuit (AC/DC);
5) Filter capacitor C;



FIGURE 11 | Port reliability evaluation model of 10 kV AC-10 kV DC port.

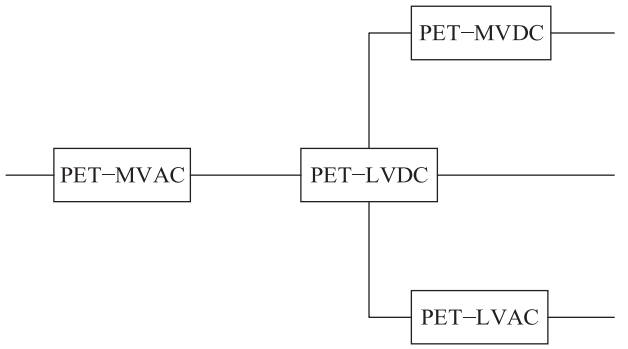


FIGURE 12 | Reliability model of four-port PET.

6) The reliability evaluation model of C and P is shown in **Figure 11**.

By calculating the power supply reliability of each module in **Figure 11**, through series and parallel, the 10 kV AC-10 kV DC port can be calculated. Further, the reliability data of each port can be calculated as shown in **Figure 12**.

Reliability Modeling of AC/DC Hybrid System With Multi-Port PET Cluster

Figure 13 shows a comparison of the calculation of the system reliability for the contained and reliable data.

According to the actual power supply network obtained from the power system of the data center, the use of PET is two PET parallel operations, which form a cluster operation mode and jointly supply power for the load point and energy storage equipment. **Figure 14** shows the reliability block diagram of two PET cluster operation.

In **Figure 14**, L_1 is the 10 kV AC bus, L_2 is the 10 kV DC bus, L_4 is the power supply ±375 DC bus, L_3 is 380 three-phase AC bus, $T_{1\text{-}1}/T_{2\text{-}1}$ is PET 10 kV AC port, $T_{1\text{-}2}/T_{2\text{-}2}$ is PET 10 kV DC port, $T_{1\text{-}3}/T_{2\text{-}3}$ is 380 V AC port, $T_{1\text{-}4}/T_{2\text{-}4}$ is 375 V DC port, Z_1/Z2 is reactor, and DC_1/DC_2 is load step-down converter.

The reliability solution formula of the system can be deduced from the function logic connection relationship of the components shown in **Figure 14**.

$$R = R_{L1}\left[1-(1-R_{T1})^2\right]\left\{1-\left\{1-R_{L4}\left[1-(1-R_{T4}Z)^2\right]\right\}\right\}\left\{1-R_{L3}\left[1-(1-R_{T3})^2\right]\right\}\left\{1-R_{L2}\left[1-(1-R_{T2})^2\right]\right\}.$$

R_x is the power supply reliability of x components in the system, and the reliability data of the original is shown in **Table 1** (Zhang and Wang, 2004; Ye, 2016).

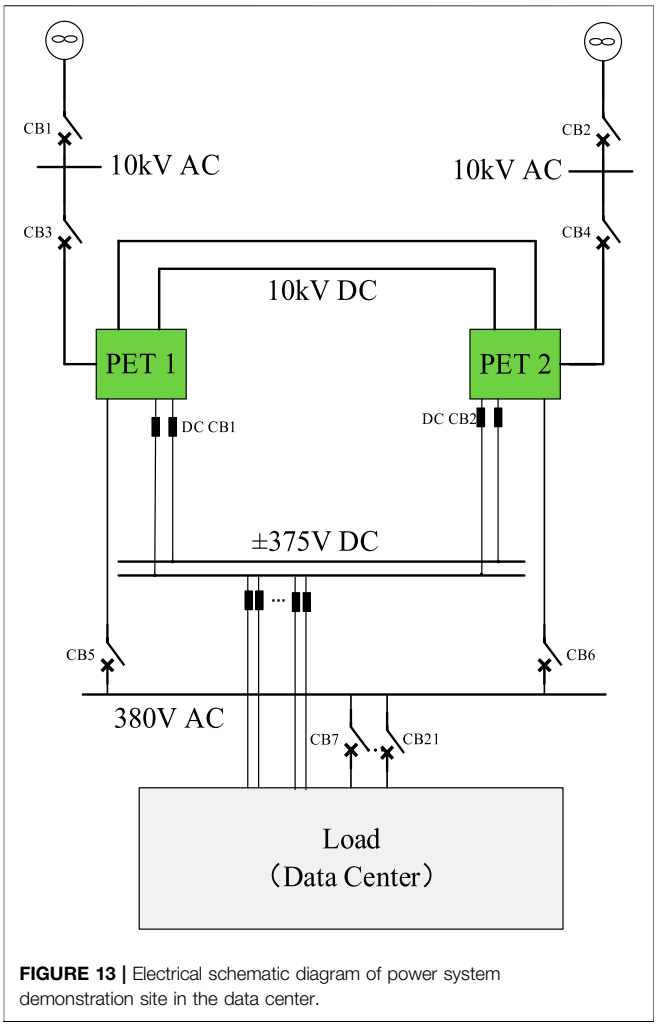


FIGURE 13 | Electrical schematic diagram of power system demonstration site in the data center.

Reliability Analysis and Program Implementation of AC/DC Hybrid System With PET Cluster

The sequential Monte Carlo method is used to calculate the power supply reliability of the multi-port PET AC/DC hybrid system with different structures. Combined with the idea of searching the power supply path of load point, the random number with the same number of system components is generated for random sampling to simulate the operation state of the power system, and the second-order fault and load transfer state of the system are accurately described and calculate the reliability of the power system.

Reliability Evaluation of Distribution System Based on Time Series Monte Carlo Method

According to the main electrical wiring diagram of the demonstration site in the data center, there are n = 26 components in the system. The failure rate and repair time data of all components are obtained, and the failure rate of the ith component is recorded as λ i. The repair rate of the ith component is recorded as μ i, where I = 1, 2, 3, 4, ... ,n.

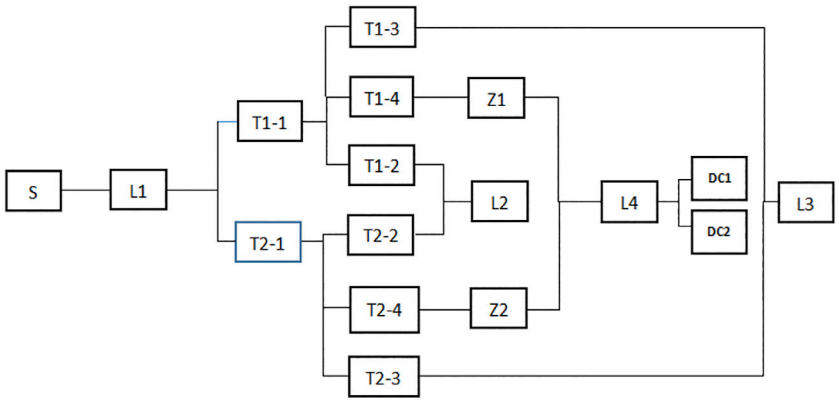


FIGURE 14 | Reliability block diagram of two-station four-port PET clusters unit.

TABLE 1 | Power supply reliability parameter of different modules in PET.

Equipment	Symbol	R_i
PET DC inner bus	T-1	0.998043
	T-2	0.998935
	T-3	0.999740
	T-4	0.9999875
PET DC inner bus	T-1	0.998296
	T-2	0.999094
	T-3	0.999307
	T-4	0.999647
10 kV AC line	L1	0.9999901
10 kV DC line	L2	0.9999938
380 V AC bus	L3	0.999999
375 V DC bus	L4	0.999999
Reactor	Z	0.9999

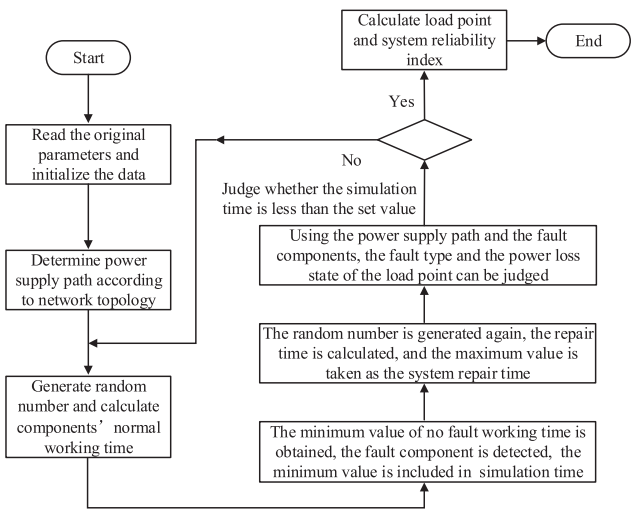


FIGURE 15 | Simulation calculation of power supply reliability based on the sequential Monte Carlo method.

The main process of simulating the actual operation of the distribution network based on the sequential Monte Carlo method is as follows, and the corresponding flow chart is shown in **Figure 15**.

1) Input the original parameter data of each component in the distribution network, and complete the initialization work. In this paper, the number of load points is ntrans = 4 and the number of components is n = 26. **Table 2** shows the failure rate and repair time data for all components.
The simulation time is set as the actual operation time of distribution network. The initialization work is to initialize the simulation time summttf, fault number ftimes, fault time, annual fault rate, fault duration and annual fault time to 0.
2) The quantity of random numbers is the same as the quantity of components. Due to the second-order fault, 226 random numbers are generated, which are recorded as R1 and R2 respectively
3) According to the generated two groups of random numbers, the corresponding MTTF of two groups of 26 components is obtained.
4) The minimum value of each group of data is found by using the calculated no fault working time, so as to determine two faulty components, and the smaller value of the two is included in the simulation time summttf.
5) Two random numbers are generated again to obtain the repair duration MTTR of the two faulty components. The larger value is obtained by comparing the two, which is used to calculate the repair time and related indicators of the load point.
6) By using the transformed power supply path, the fault type is judged, the first-order fault and the second-order fault are judged respectively, and whether the load transfer conditions are met is classified and calculated.
7) Judge whether the simulation time summttf meets the preset running time requirements. If it is less than the set running time, turn to 2; otherwise, proceed to the next step.

TABLE 2 | The original reliability parameters of the power system components.

No.	Components	Failure rate	Repair time
1	Source (S)	0.004795	0.5
2	10 kV AC bus	0.01096	13.65
3	375 V DC bus 1	0.01096	13.65
4	380 V AC bus 1	0.01096	13.65
5	375 V DC bus 2	0.01096	13.65
6	380 V AC bus 2	0.01096	13.65
7	PET port T1-4	0.309048	10
8	Reactor Z1	0.96	10
9	DC/DC1	0.96	10
10	PET port T2-4	0.309048	10
11	Reactor Z2	0.96	10
12	DC/DC2	0.96	10
13	PET port T1-1	0.932563	16
14	PET port T2-1	0.932563	16
15	PET port T1-3	0.379048	26
16	PET port T2-3	0.379048	26

TABLE 3 | PET port capacity and load capacity.

Port	Maximum capacity (MW)	Load (MW)	Load capacity of PET port (MW)
380 V AC	0.7	2	0.5
375 V DC	1	1	0.25

8) The outage indexes of all load points are accumulated, and the reliability indexes of the whole distribution system are calculated.

Example Structure Diagram and Original Data

As shown in **Figure 13**, in the structure diagram of the AC/DC power system, all kinds of components and logic connection modes need to be considered in the process of system reliability analysis. Two four-port power electronic transformers form a cluster group to supply power for a group of DC load and AC load at the same time. Therefore, there are two power supply paths for each load point.

The annual failure rate, repair time, and other reliability data of each power supply module in the AC/DC hybrid system are shown in **Table 2** with reference to the statistical data. PET port capacity and load are given in **Table 3**.

According to the data in the table, in the actual power system, when the load transfer occurs at the low-voltage DC load point due to fault, the capacity of a single PET port can support 100% load normal operation; when the load transfer occurs at the low-voltage AC load point due to fault, the capacity of a single PET port can support 70% load normal operation; then, the power loss percentage is 0.3 of the total load at the load point.

EXAMPLES

Example Analysis of Influence of Different Factors on Power Supply Reliability

Under the condition that the original parameters of all components, port capacity, and load capacity are known,

TABLE 4 | Calculation results of reliability indexes with different port capacities.

Capacity (%) of port	SAIFI	SAIDI	CAIDI	ASAI
100	29.8668	84.4837	2.7548	0.990375
90	30.6086	91.4987	3.0166	0.989553
80	30.6673	94.3294	3.3636	0.989231
70	30.9848	116.7644	3.7639	0.986642
60	31.2168	117.347	3.8148	0.986037
50	31.2703	137.0076	4.4218	0.984384

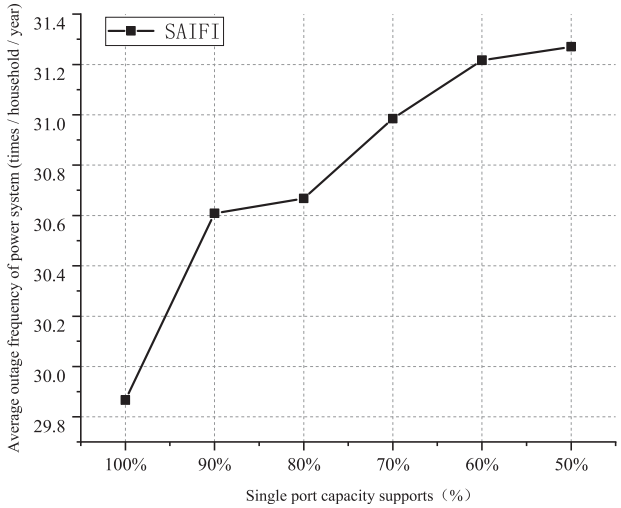


FIGURE 16 | Analysis and comparison of the impact of PET port capacity on SAIFI.

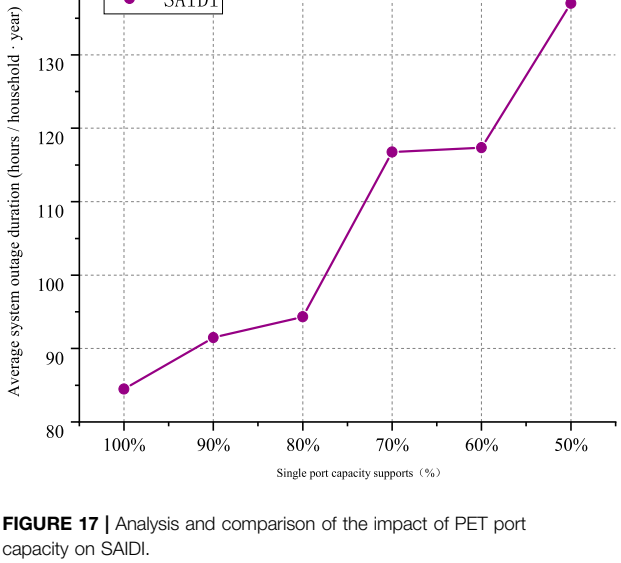


FIGURE 17 | Analysis and comparison of the impact of PET port capacity on SAIDI.

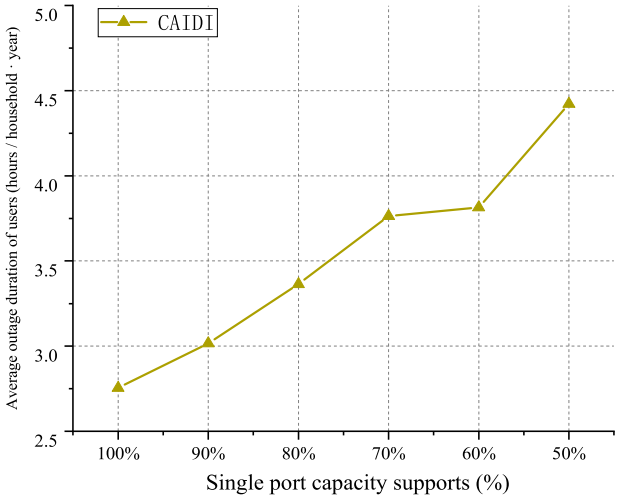


FIGURE 18 | Analysis and comparison of the impact of PET port capacity on CAIDI.

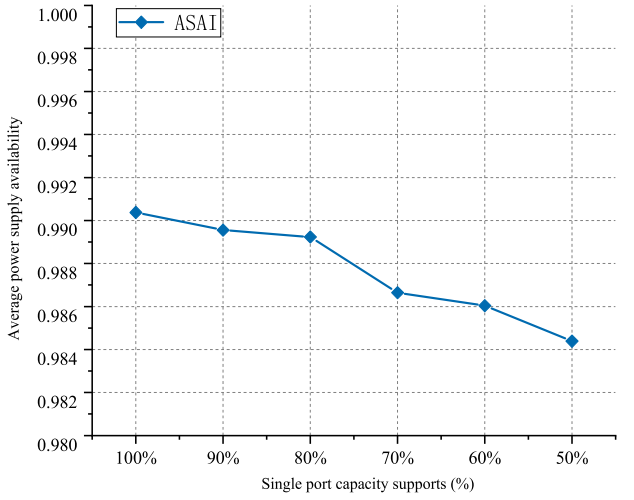


FIGURE 19 | Analysis and comparison of the impact of PET port capacity on ASAI.

simulation of 100000 h operation time of distribution network is conducted.

Analysis of the Influence of Port Capacity on Power Supply Reliability

Since the load amount of load transfer due to fault is determined by the maximum capacity of each port, with the minimum of 50% and the maximum of 100%. A total of six groups of power system outage indicators and reliability related data are generated, as shown in **Table 4** and **Figures 16–19**.

By comparing the chart data, it can be concluded that the port capacity has a positive correlation with the reliability indicators. The larger the port capacity is, the higher the system availability ASAI is, and the lower the SAIFI, SAIDI, CAIDI, and other related indicators are. Compared with the results of qualitative analysis, when the port capacity is larger, the power loss caused by a component failure at each load point will be reduced correspondingly, and the number of users who are not affected by the failure due to load transfer continuing to use electricity normally will increase. Therefore, the reliability of the whole system will be higher, and the relevant outage index of each load point will be lower, but the system investment and operation and maintenance cost will be increased. The economic efficiency is reduced.

Location Optimization of Multi-Port PET AC/DC Hybrid System Connected to Distribution Network

PET is a new power converter which combines the power electronic converter and high frequency transformer. In addition to the functions of voltage conversion and electrical isolation of traditional transformers, it has high-voltage and low-voltage AC/DC interfaces and is suitable for DC source and load access. Multi-port PET is used as an "energy router" in the AC/DC distribution network with a variety of distributed renewable energy sources. Thus, a variety of distributed renewable energy sources can be connected to the distribution network to improve the efficiency and economy of the power system, improve the economy of power grid operation are beneficial.

Therefore, in order to fully study the advantages of multi-port PET applied in the distribution network, in the traditional AC distribution network, how to select the appropriate node to access PET and realize the integration of new energy not only ensures the new energy consumption rate but also ensures the reliability and economy of system operation.

Multi-Port PET AC/DC Hybrid System Connected to IEEE 33 System

IEEE 33 node is a 33-node standard distribution network system consisting of 32 lines. The topology structure of the ieee33 node system with multi-port PET is shown in **Figure 20**. Through the introduction of PET, the access to solar photovoltaic power generation, photothermal, wind power, storage, and heat storage equipment is realized.

In general, the MV AC (10 kV AC) port of PET is connected to the distribution network. This example optimizes the location of PET to IEEE 33 node distribution network and takes the minimum loss of distribution network and the lowest voltage deviation rate of nodes as the target. The constraints include power balance constraint, PET port constraint, and new energy output constraints: two sets of comparison examples are set at the same time: 1) PET medium voltage AC port can send power back to the distribution network, and the upper and lower limit of power transmission are [−2500 kw, 2500 kw]; 2) PET medium voltage AC port cannot send power back to the distribution network, and the upper and lower limit of power transmission are [−2500 kw, 0].

In both cases, the real-time power of PET 10 kV AC port and the optimal access node of 10 kV AC port, PET loss, network loss, voltage deviation rate, waste wind, and light loss are shown in **Table 5**.

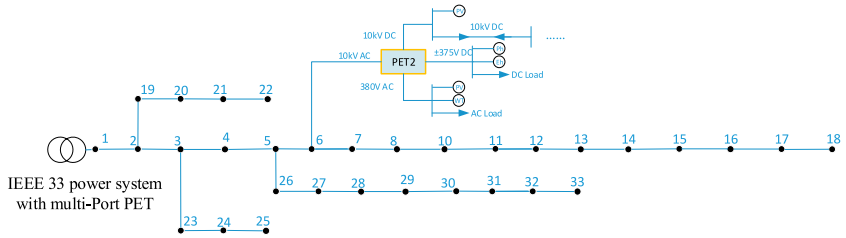


FIGURE 20 | IEEE 33 node distribution network topology with multi-port PET AC/DC hybrid system.

TABLE 5 | Index comparison for whether the 10 kV AC port reverses the power of the power grid or not.

Category	No power can be resent to the main network	Power can be resent to the main network
Node no.	2	8
Active power loss rate of PET converter	0.185	0.232
Rate of abandoned wind and light	0.482	0.258
Active power loss of AC network	0.011	0.020
Voltage deviation rate of AC network	0.018	0.145
Self-balance rate	0.433	0.627
Self-use rate	0.651	0.736
Redundancy rate	0.000	0.022
Utilization rate of renewable energy	0.517	0.741

1) under the condition that PET is prohibited from sending power back to the distribution network, PET is only equivalent to the load compared with the distribution network. The optimization result is that the MV AC port of PET is connected to node 2 of the distribution network. Therefore, it is more favorable for the loss and voltage deviation rate of distribution network to prohibit PET from transmitting power back to the distribution network, and PET is connected to the distribution network near the beginning of feeder;
2) PET can be regarded as a power supply when PET is allowed to send power back to the distribution network. The optimized result is to connect the PET medium voltage port to node 8 of the distribution network. The IEEE 33 node distribution network system is observed in the whole. Node 8 is located in the middle of the longest feeder. When PET is sending power back to the distribution network, it is beneficial to improve the voltage of downstream nodes and the loss of the feeder. From **Table 5**, it can be seen that allowing PET to send back power to the distribution network is beneficial to improve the utilization of renewable energy.

CONCLUSION

In view of the wide access of distributed new energy in the distribution network and the rapid increase of the proportion of generalized DC load in the distribution network, this paper proposes an AC/DC hybrid power system structure based on a multi-port PET cluster. Aiming at the AC/DC hybrid power system, the stable operation and control system are studied, the control objectives of the equipment level and system level of the AC/DC hybrid distributed system are analyzed, the hierarchical operation control architecture of the AC/DC hybrid distributed system is proposed, and the three-layer control mode and multi-time scale control mode of the integrated automation system, PET cluster controller, and PET controller are proposed. A sequential Monte Carlo simulation algorithm is proposed to solve the reliability problem of AC/DC hybrid power system with a multi-port PET cluster. The effectiveness of the reliability calculation model and algorithm is verified by an example. It is concluded that the reliability of the AC/DC hybrid power system can be improved by multi-port PET parallel cluster mode and port capacity increase. The example shows that the AC/DC hybrid power system with a multi-port PET cluster can improve the utilization rate of renewable energy.

DATA AVAILABILITY STATEMENT

The original contributions presented in the study are included in the article/Supplementary Material; further inquiries can be directed to the corresponding author.

AUTHOR CONTRIBUTIONS

XX: wrote the manuscript and overall conception. WH: put forward suggestions on the revision and improvement of the paper. YH: put forward suggestions on the revision and improvement of the paper. NT: put forward suggestions on the revision and improvement of the paper. YJ: put forward the hierarchical control of AC/DC hybrid system. NX: put forward the structure of the AC/DC hybrid power system with the multi-port PET cluster.

FUNDING

This study was supported by: 1) 2017 National Key R and D Program of China, research on key technologies, core equipment and engineering demonstration of AC/DC hybrid distributed renewable energy, Grant No.: 2017YFB0903202, 2) Major Scientific Research and Innovation Project of Shanghai Education Commission in 2019, research on Key Technologies of integrated energy power system based on multi energy flow coupling, Grant No.: 2019-01-07-00-02-E00044.

REFERENCES

Barnes, M., Kondoh, J., Asano, H., Oyarzabal, J., Ventakaramanan, G., Lasseter, R., et al. (2007). Real-world Microgrids[J]. *Proc. Syst. Syst. Eng.* (4), 16–18. doi:10.1109/SYSOSE.2007.4304255

Bie, C. H., and Guan, X. H. (2016). *Basic Theory of Energy Internet Planning, Operation and Trading [R]*. Xi'an: Xi'an Jiaotong University.

Boroyevich, D., Cvetkovic, I., Dong, D., Burgos, R., Wang, F., and Lee, F. (2010). "Future Electronic Power Distribution Systems: A Contemplative view[C]," in 12th International Conference on Optimization of Electrical and Electronic Equipment, OPTIM 2010. Brasov: Transilvania University of Brasov, 1369–1380.

Ding, M., and Li, S. H. (2000). Methods for Accelerating the Convergence Rate of Monte Carlos Simulation in Reliability Calculation [J]. *Power Syst. Automation.*.

Dolatabodi, A., Jadidbonab, M., and Mohammadi, B. (2018). Short-Term Scheduling Strategy for Wind-Based Energy Hub: a Hybrid Stochastic/IGDT Approach[J]. *IEEE Trans. Sust. Energ.* 10 (1), 438–448. doi:10.1109/TSTE.2017.2788086

Dragicevic, T., Guerrero, J. M., and Vasquez, J. C. (2014). A Distributed Control Strategy for Coordination of an Autonomous LVDC Microgrid Based on Power-Line Signaling. *IEEE Trans. Ind. Electron.* 61 (7), 3313–3326. doi:10.1109/tie.2013.2282597

Duan, Q., Sheng, W. X., and Meng, X. L. (2016). Research on New Energy Subnet System for Energy Internet [J]. *Chin. J. Electr. Eng.* 36 (02), 388–398.

Eghtedarpour, N., and Farjah, E. (2014). Power Control and Management in a Hybrid AC/DC Microgrid. *IEEE Trans. Smart Grid.* 5 (3), 1494–1505. doi:10.1109/tsg.2013.2294275

Eicher, S., Rahimo, M., Tsyplakov, E., Schneider, D., Kopta, A., Schlapbach, U., et al. (2004). "4.5kV Press Pack IGBT Designed for Ruggedness and Reliability [C]," in Conference Record of the 2004 IEEE Industry Applications Conference, 2004 3, 1534–1539.

Facci, A. L., Andreassi, L., and Ubertini, S. (2014). Optimization of CHCP (Combined Heat Power and Cooling) Systems Operation Strategy Using Dynamic Programming. *Energy* 66, 387–400. doi:10.1016/j.energy.2013.12.069

Funabashi, T., and Yokoyama, R. (2006). "Microgrid Field Test Experiences in Japan[C]," in Proceedings of the Power Engineering Society General Meeting (Canada: IEEE), 18–22.

Gao, Y., Hu, X., Yang, W., Liang, H., and Li, P. (2017). Multi-Objective Bilevel Coordinated Planning of Distributed Generation and Distribution Network Frame Based on Multiscenario Technique Considering Timing Characteristics. *IEEE Trans. Sustain. Energ.* 8 (4), 1415–1429. doi:10.1109/tste.2017.2680462

Hatziargyriou, N., Asano, H., Iravani, R., and Marnay, C. (2007). Microgrids. *IEEE Power Energ. Mag.* 5 (4), 78–94. doi:10.1109/mpae.2007.376583

He, X., Chu, L., Qiu, R. C., Ai, Q., Ling, Z., and Zhang, J. (2020). Invisible Units Detection and Estimation Based on Random Matrix Theory. *IEEE Trans. Power Syst.* 35 (3), 1846–1855. doi:10.1109/tpwrs.2019.2935739

Huang, A. Q., Crow, M. L., Heydt, G. T., Zheng, J. P., and Dale, S. J. (2011). The Future Renewable Electric Energy Delivery and Management (FREEDM) System: The Energy Internet. *Proc. IEEE.* 99 (1), 133–148.

Liu, Z. R. (2011). *Reliability Evaluation of Distribution Network Based on Non Time Series Monte Carlo Simulation Method [D]*. Changsha: Hunan University.

Ma, Z., Zhou, X. X., Shang, Y. W., and Zhou, L. M. (2015). Future Distribution System Form and Development Trend [J]. *Chin. J. Electr. Eng.* 35 (06), 1289–1298. doi:10.13334/j.0258-8013.pcsee.2015.06.001

Miao, J., Zhang, N., Kang, C., Wang, J., Wang, Y., and Xia, Q. (2018). Steady-State Power Flow Model of Energy Router Embedded AC Network and its Application in Optimizing Power System Operation. *IEEE Trans. Smart Grid.* 9 (5), 4828–4837. doi:10.1109/tsg.2017.2672821

Peng, H. T. (2018). Reliability Analysis Method of Power System[J]. *Sci. Tech. Vision.* (36), 211–212.

Pilo, F., Pisano, G., and Soma, G. G. (2011). Optimal Coordination of Energy Resources with a Two-Stage Online Active Management [J]. *IEEE Trans. Ind. Electron.* 10 (58), 4526–4537. doi:10.1109/tie.2011.2107717

Pu, T. J., Li, Y., Chen, N. S., and Sun, Y. Y. (2018). Key Technologies and Research Framework for Optimal Operation Control of AC/DC Hybrid System Based on PET [J]. *Power Grid Tech.* 42 (09), 2752–2759.

Salonen, P., Kaipia, T., and Nuutinen, P. (2008). "An LVDC Distribution System Concept[C]," in Proceedings of the Nordic Workshop on Power and Industrial Electronics (Espoo, Finland: Helsinki University Department of Electrical Engineering), 1–7.

Sanchez, S., and Molinas, M. (2015). Large Signal Stability Analysis at the Common Coupling Point of a DC Microgrid: A Grid Impedance Estimation Approach Based on a Recursive Method. *IEEE Trans. Energ. Convers.* 30 (1), 122–131. doi:10.1109/tec.2014.2359993

Wan, Q., Xia, C. J., and Guan, L. (2019). Review on Stability of Independent Microgrid with High Penetration Distributed Generation [J]. *Power Grid Tech.* 43 (02), 598–612.

Wang, B. Y. (2014). *Research on the Loss Calculation Method and Temperature Testing of the IGBTs in AC-DC Converters with Chaotic SPWM Control [D]*. Beijing: Beijing Jiaotong University, 21–24.

Wang, P., Jin, C., Zhu, D., Tang, Y., Loh, P. C., and Choo, F. H. (2015). Distributed Control for Autonomous Operation of a Three-Port AC/DC/DS Hybrid Microgrid. *IEEE Trans. Ind. Electron.* 62 (2), 1279–1290. doi:10.1109/tie.2014.2347913

Xiang, Y., Fu, M., Zhang, A. F., and Dou, X. B. (2017). Small Signal Stability Analysis of AC/DC Hybrid Microgrid in Isolated Island Operation [J]. *Electric. pow. construt.* 38 (01), 96–105.

Xiao, H. G. (2015). *Research on Some Key Technologies of AC/DC Hybrid Microgrid [D]*. Changsha: Hunan University.

Xu, S. Y., Ying, Y. L., and Chen, Y. L. (2019). Optimization Method of Integrated Energy System Based on Standardized Matrix Model [J]. *Shanghai energy conservation.* (01), 29–39.

Yan, X., Jiao, Y. J., and Du, Z. (2017). Feasibility Study of a Hybrid AC/DC Distribution Network Based on Flexible DC Technology [J]. *Power Syst. Prot. Control.* 45 (13), 110–116. doi:10.7667/PSPC160985

Ye, C. M. (2016). *Research on Coordinated Planning Method of Transmission Network and Distribution Network in Large Cities [D]*. Shanghai: Shanghai Jiaotong University.

Yin, X. G., Dai, D. Y., Han, Y., and Liao, Z. C. (2012). Research on Key Technologies of AC/DC Hybrid Microgrid [J]. *High voltage apparatus.* 48 (09), 43–46. CNKI:SUN:GYDQ.0.2012-09-010

Zha, Y. B., Zhang, T., Huang, Z., and Zhang, Y. (2014). Analysis of Key Technologies of Energy Internet [J]. *China Sci. Inf. Sci.* 44 (06), 702–713. doi:10.1360/N112014-00008

Zhang, H. T., Xu, T. Q., Yang, J., and Ying, F. F. (2019). Research on Key Technologies of Energy Router in Energy Internet [J]. *Electr. Tech.* (20), 105–107.

Zhang, P., and Wang, S. X. (2004). Interval Algorithm for Reliability Evaluation of Large Scale Distribution System [J]. *Chin. J. Electr. Eng.* 24 (03), 82–89. doi:10.2116/analsci.20.717

Zhang, X., Shahidehpour, M., and Alabdulwahab, A. (2017). Optimal Expansion Planning of Energy Hub with Multiple Energy Infrastructures[J]. *IEEE Trans. Smart Grid.* 6 (5), 2302–2311. doi:10.1109/TSG.2015.2390640

Zheng, X. (2011). *Distribution Network Reliability Evaluation Based on Monte Carlo Method [D]*. Wuhan: Huazhong University of science and technology.

Conflict of Interest: YJ was employed by Beijing Sifang Jibao Automation Co., Ltd., and NX was employed by Electric Power Research Institute of Guangdong Power Grid Co., Ltd.

The remaining authors declare that the research was conducted in the absence of any commercial or financial relationships that could be construed as a potential conflict of interest.

Publisher's Note: All claims expressed in this article are solely those of the authors and do not necessarily represent those of their affiliated organizations, or those of the publisher, the editors, and the reviewers. Any product that may be evaluated in this article, or claim that may be made by its manufacturer, is not guaranteed or endorsed by the publisher.

Copyright © 2021 Xu, Huang, Hu, Tai, Ji and Xie. This is an open-access article distributed under the terms of the Creative Commons Attribution License (CC BY). The use, distribution or reproduction in other forums is permitted, provided the original author(s) and the copyright owner(s) are credited and that the original publication in this journal is cited, in accordance with accepted academic practice. No use, distribution or reproduction is permitted which does not comply with these terms.

frontiers in Energy Research

ORIGINAL RESEARCH
published: 07 September 2021
doi: 10.3389/fenrg.2021.728789

Research on Efficient Soft Switching Based on MPPT of PV Power Generation System

Peng Tao[1,2], *Yan Cui*[1,2]* *and Jiayuan Liang*[1,2]

[1]Department of Electronics and Institute of Technology, Shantou University, Shantou, China, [2]Key Lab of Digital Signal and Image Processing of Guangdong Province, Shantou University, Guangdong, China

In this paper, basic soft-switching technology is proposed based on hard switching, and then the basic soft-switching technology is optimized, and an improved soft-switching technology is proposed to improve the conversion efficiency by reducing the switching loss. The simulation results show that the conversion efficiency of hard and basic soft switching is 94.3 and 96.1%, but the conversion efficiency of improved soft switching optimized on the basis of basic soft switching is only 95.8%. To solve this problem, an innovative soft-switching technology is put forward in this paper, and its conversion efficiency is as high as 96.3%, which is superior to the basic soft-switching technology.

Keywords: soft switching, maximum power point, high conversion efficiency, innovative, multi peak characteristic

OPEN ACCESS

Edited by:
Bo Yang,
Kunming University of Science and Technology, China

Reviewed by:
Fusheng Li,
Southern Power Grid Research Institute. Co., Ltd., China
Kaiping Qu,
China University of Mining and Technology, China

***Correspondence:**
Yan Cui
ycui@stu.edu.cn

Specialty section:
This article was submitted to Smart Grids, a section of the journal Frontiers in Energy Research

Received: *22 June 2021*
Accepted: *20 July 2021*
Published: *07 September 2021*

Citation:
Tao P, Cui Y and Liang J (2021) Research on Efficient Soft Switching Based on MPPT of PV Power Generation System. Front. Energy Res. 9:728789. doi: 10.3389/fenrg.2021.728789

INTRODUCTION

With coal, oil, natural gas, and other fossil fuels increasingly being exhausted, the problem of energy shortage in the world has gradually emerged (Hirsch, 2008; Luo G. et al., 2021; Freeman et al., 2020), and the development of new green energy has become the only way to solve such problems (Hojnik et al., 2021). At present, the newly developed green energy sources include solar, wind, tidal, and geothermal energy and so on (Burnett and Hefner, 2021; Darwesh and Ghoname, 2021; Luo X. et al., 2021; ZOU et al., 2021). The most reliable and convenient energy among these new energy sources is solar energy. This paper includes how to use solar energy efficiently to maximize the conversion efficiency of a photovoltaic (PV) power-generation system. A solar PV power-generation system has the following advantages: pollution-free energy, a flexible application site that is not interfered with by geographical location, high power quality, low loss, and multiple policy support (Qi et al., 2021).

To improve the conversion efficiency of a PV power-generation system, soft-switching technology is proposed in this paper (Aiswariya et al., 2021; Engelkemeir et al., 2019; Genc and Koc, 2017; Yinghua et al., 2012; Pakdel and Jalilzadeh, 2016). As early as the early 1970s, foreign scholars put forward series and parallel resonance (Tkachenko and Baklanov, 2015), and soft-switching technology just uses resonance principles to make the current or voltage in the switching device change sinusoidally and implement a quick soft shutdown and soft open. Soft-switching converters can be divided into four types: ZCS-PWM, ZVS-PWM, ZCT-PWM, and ZVT-PWM. This paper mainly introduces ZVT-PWM. The reason why the ZVT-PWM converter is adopted is that the ZVT converter can avoid the problem of excessive turn-off loss caused by diode reverse recovery and greatly improves conversion efficiency (Ismail and Sebzali, 1998; Jahdi et al., 2011; Kumar et al., 2015).

In the second section, according to the physical equivalent circuit model of PV cells, the output characteristics of PV modules are simulated. The third section introduces the topological structure of basic and improved soft switching. *Simulation and Eexperimental Aanalysis* is based on Multisim to

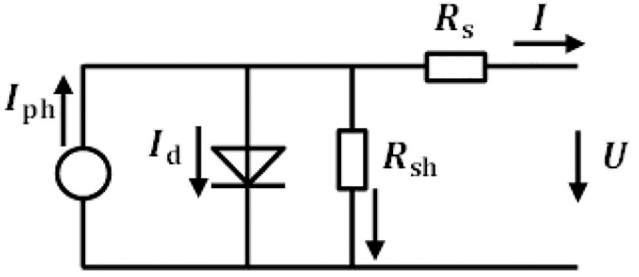


FIGURE 1 | Equivalent circuit of PV cell.

build a DC-DC BOOST circuit (Mirzaei and Rezvanyvardom, 2020; Faraji et al., 2019; Charin et al., 2013; Pahlavandust and Yazdani, 2020; Öztürk et al., 2018). First, IRFZ24N, a power switch tube suitable for a high-frequency circuit environment and a Schottky diode MBR7545 with a moderate forward voltage drop and a large reverse voltage value are selected from Multisim, and the duty ratio in the circuit is analyzed according to the maximum power point (MPP) of the PV module. Then, Proteus is used to reduce the time of tracking the MPP. Finally, to reduce the switching and conduction loss and improve the conversion efficiency, an innovative soft-switching technology is introduced and compared with the basic soft-switching technology, and the improved soft-switching technology shows the superiority and innovation of innovative soft switching in all aspects.

SINGLE- AND MULTIPEAK OUTPUT CHARACTERISTICS OF PHOTOVOLTAIC ARRAY

A PV cell is a kind of nonlinear DC power supply, which cannot be supplied at will. The equivalent circuit of a PV cell is shown in **Figure 1**.

The equivalent circuit model is as follows:

$$I = I_{\mathrm{ph}} - I_{\mathrm{o}}\left(e^{\frac{q(U+IRs)}{AkT}} - 1\right) - \frac{U + IRs}{R_{\mathrm{sh}}}, \tag{1}$$

in which I is the output current of the solar panel, U is the output voltage of the solar panel, I_{o} is the PN junction reverse saturation current, $I_{\mathbf{ph}}$ is the battery photoelectric current, q is the electron charge, A is the coefficient of the diode, k is the Boltzmann constant, T is the temperature, and n is the diode factor. The current flowing through the equivalent shunt resistor R_{sh} is shown as $I_{\mathbf{sh}}$ as follows:

$$I_{\mathbf{sh}} = \frac{U + IR\mathbf{s}}{R_{\mathbf{sh}}}. \tag{2}$$

Because the resistance value of the equivalent series resistance is extremely small, it can be almost ignored, and the resistance value of the equivalent parallel resistance is large, so I_{sh} is very small and can be ignored. Therefore, the electrical performance characteristics of the PV cell can be simplified as follows:

$$I = I_{\mathbf{ph}} - I_{\mathrm{o}}\left(\mathbf{e}^{\frac{q(U+IRs)}{AkT}} - 1\right). \tag{3}$$

The models of the above equivalent circuits are all based on the standard T = 300K ; A≈2.8 ; q = 1.6 × 10–19C ; k = 1.38 × 10^{-23}J/K.

Output Characteristics of Photovoltaic Array Without Shading

Under the condition of no shading, the single-peak characteristic curve is obtained without considering the external environmental factors. In this section, under the standard environmental conditions (1000 W/m, 25°C), the characteristic curves of the unshaded PV cells are simulated experimentally by Simulink **Figures 2**, **3**.

At the same temperature, with the PV cell value changed, the PV array parameters of uniform simulation are as follows **Table 1** and **Table 2**:

Parameters of the PV array simulated uniformly under the same illumination and changing temperature are as follows:

Through the simulation results, it can be seen that the single peak point in the P-U simulation diagram is generally on the right side, and the output power of PV modules first increases and then decreases with the increase of output voltage while the output current remains unchanged and then decreases rapidly with the increase of output voltage.

Output Characteristics of Photovoltaic Array With Shading

This section mainly shows that, in practical engineering applications, PV modules are interfered with by various factors, such as surface dust and dark clouds, which lead to the output power of some PV modules being significantly lower than other parts and accordingly bringing about the phenomenon of multiple peaks or inflection points (Veerapen and Wen, 2016; Mirza et al., 2019; Zhou et al., 2021). Three PV panels are connected in series to form a PV array, and each PV panel is connected in reverse parallel with a bypass diode. However, due to the shunt effect of the bypass diode, the PV arrays do not match, resulting in multiple local extreme points in the P-U characteristic curve, named multipeak characteristics. In this section, the PV array is simulated by Simulink with different illumination intensities at the standard atmospheric temperature to study the condition with shading. The parameters are shown in **Table 3**:

Through the simulation experiment in **Figure 4**, it can be concluded that the P-U characteristic curve of the PV array with different illumination intensities under the shading condition presents multipeaks. Taking Group 2 in **Table 3** as an example, there are three local MPPs in the P-U characteristic curve of the PV array when the open circuit voltage of the PV array is $U_{\mathrm{oc-array}}$ = 10.4 V and the open circuit voltage of the PV cell is $U_{\mathrm{oc-module}}$ = $U_{\mathrm{oc-array}}$/3≈3.47 V. The voltages corresponding to the three local MPPs are U_{mpp1} = 1.97 V≈0.75 × $U_{\mathrm{oc-module}}$, U_{mpp2} = 5.1 V≈2 × 0.75 × $U_{\mathrm{oc-module}}$,U_{mpp3} = 8.4 V≈3 × 0.75 × $U_{\mathbf{oc-module}}$. Thus, it can be drawn that, for an $n \times m$ PV array, there

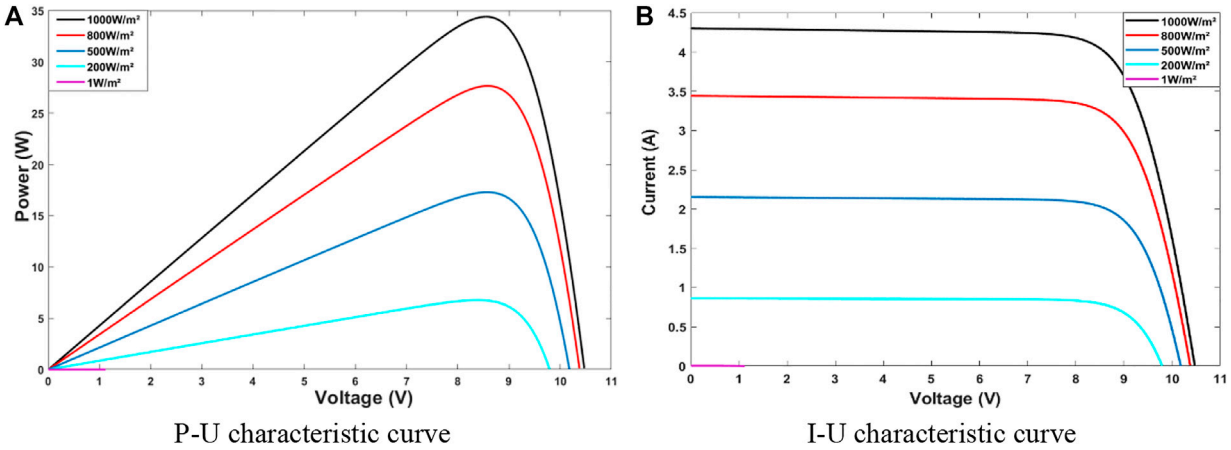


FIGURE 2 | P-U and I-U characteristic curves under the same temperature and different light intensity under uniform conditions.

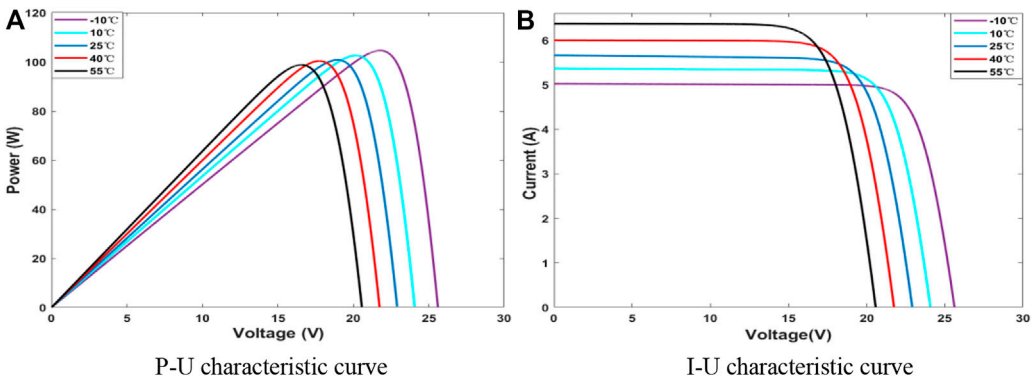


FIGURE 3 | I–U characteristic curve under the same illumination intensity and different temperatures under uniform conditions.

are only local MPPs-n, and the voltage value corresponding to each local MPP is generally $k \times 0.75 \times U_{\mathbf{oc-module}}$.

Through some references and practical research simulation experiments, this paper concludes that, for an $n \times m$ PV array, the total number of cells is m, and the total number of different voltage differences of cells is n. The characteristics of each single cell in the PV array are basically the same, so the output characteristics have nothing to do with which specific cell is shaded and only with the overall parameters in the PV array. If the shielding situation is the same, the output characteristics of the PV array must be basically the same.

RESEARCH ON SEVERAL SOFT-SWITCHING TECHNOLOGIES

Traditional Hard-Switching and Basic Soft-Switching Technology

The switching tubes of traditional Boost circuits generally operate in a hard-switching mode during the switching process. Hard switching began to develop in the 1960s, and it greatly reduced the volume and weight of the device and improved the overall efficiency. However, the power switch tube of the DC-DCPWM converter, which works in a series of hard-switching conditions, is accompanied by the increase of switching frequency and produces serious electromagnetic interference (EMI), which greatly reduces efficiency (Khaled et al., 2020).

According to the power electronics textbook (Society, 1981), the integral of switching on and off loss of the switch tube under the hard-switching technology is expressed as follows.

$$\text{Open}: \quad W_{\mathbf{on}} = \int_0^{t_{\mathbf{on}}} v_{\mathbf{s}} i_{\mathbf{s}} \mathrm{d}t \tag{4}$$

$$\text{Turn off}: \quad W_{\mathbf{off}} = \int_0^{t_{\mathbf{off}}} v_{\mathbf{s}} i_{\mathbf{s}} \mathrm{d}t \tag{5}$$

The total losses of turn on and off in that cycle are

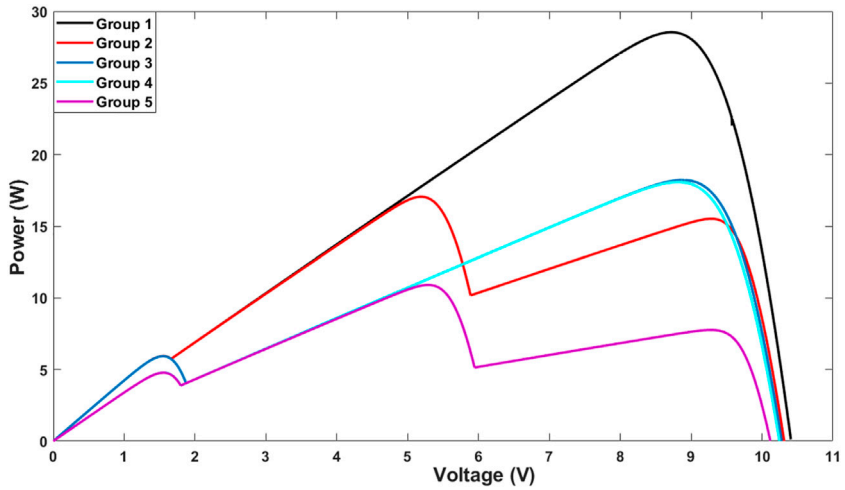


FIGURE 4 | P-U characteristic curve of different illumination intensity under shielding condition.

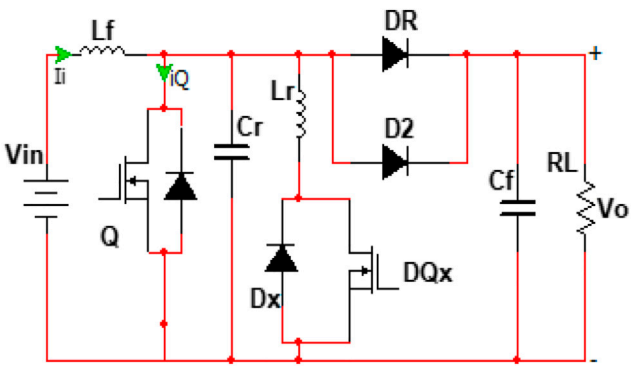


FIGURE 5 | Topology of basic ZVT soft-switching Boost circuit.

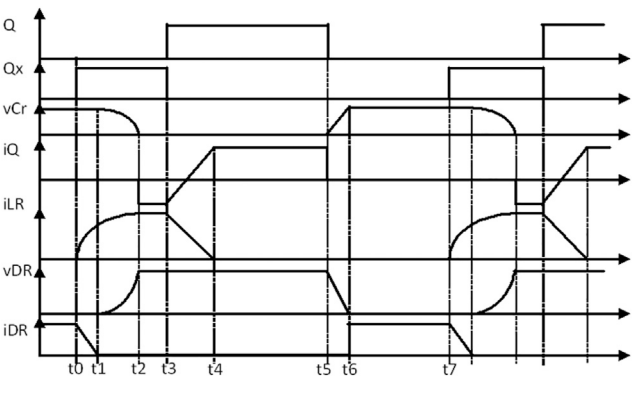


FIGURE 6 | Main working power waveform.

$$\text{Open}: \quad W_{\text{on}} = \int_0^{t_{\text{on}}} v_s i_s \mathrm{d}t \tag{6}$$

$$\text{Turn off}: \quad W_{\text{on}} = \int_0^{t_{\text{on}}} v_s i_s \mathrm{d}t \tag{7}$$

Among them, t_{on} is the opening time and t_{off} is the turn-off time; f_s is the switching frequency, v_s and i_s are the voltages at both ends of the switching tube and the passing current, respectively. There are still many shortcomings of hard switching, such as large switching tube loss (switching loss increases in proportion to switching frequency), poor recovery performance of diodes, capacitive on and inductive off, and serious EMI (Emami et al., 2010). As can be seen, to overcome these existing problems, scholars at home and abroad have implemented improvements on the basis of hard switching and formed soft-switching technology.

Interrupt capability transformation through abrupt switching processes is called hard switching, and the soft-switching process resonates through inductance L and capacitance C. In this paper, to improve the conversion efficiency of the PV power-generation system, basic soft-switching technology is proposed first. **Figures 5**, **6** are the Boost circuit topology and the main power waveform diagrams of basic soft switching, respectively.

As can be seen from **Figure 6**, although basic soft switching has achieved great optimization compared with traditional hard switching, basic soft switching also has many disadvantages. 1) In the case of high-input voltage and light load, the zero voltage condition is almost difficult to meet. 2) Interval and circulation energy need to be dealt with in one switching cycle. 3) Although the basic soft-switching technology improves the efficiency of the main power switch device in the circuit, the auxiliary switch tube is still in the hard-switching state, which results in switching loss

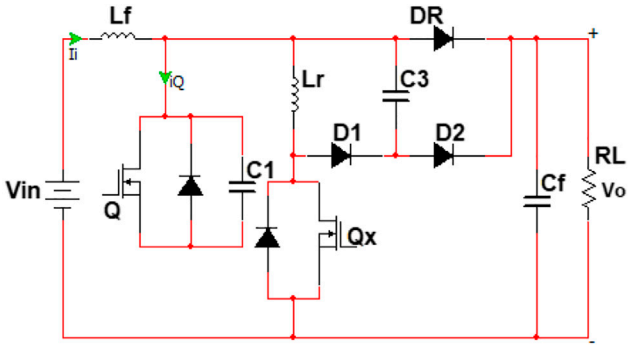


FIGURE 7 | Topology of improved ZVT soft-switching Boost circuit.

that cannot be ignored. Even the switching loss offsets part of the loss that is reduced due to soft switching, which gives rise to the difficulty in improving the efficiency of the whole circuit.

Improved Soft Switching

In 2004, H. Bodur and A.F. Bakan proposed an improved soft-switching topology as is shown in **Figure 7**. Based on the basic ZVT-PWM Boost converter soft-switching topology, only by adding a diode and a capacitor to the auxiliary resonance network can both the main switch and the auxiliary switch complete soft switching and become improved soft switching (Simon and Das, 2014).

Before discussing **Figure 7**, the following assumptions should be made: All components of the circuit are ideal. The capacitance of the output filter is relatively large enough, and the C_f and R_L of one switching period can be replaced by a constant voltage source V_o. The inductance of the input filter is relatively large enough, and V_{in} and L_f of one switching cycle can be replaced by a constant current source I_i. The reverse recovery time of the diode is ignored (Kang et al., 2012; Moshksar and Ghanbari, 2018).

The first four time periods in **Figure 7** are in the resonance process, and at the end of the fourth time period, the following two modes are discussed according to whether the voltage at both ends of C_3 can resonate and rise to V_o. Mode 1 represents the case in which the energy storage of the resonant inductor is small, and the duration of one complete cycle is

$$T_7 = t_7 - t_6 = \frac{I_{\mathrm{Lrm}} Z_3 (C_1 + C_2 + C_3)}{I_i}. \tag{8}$$

It satisfies the initial conditions:

$$\begin{cases} v_{C1} = V_O - I_{\mathbf{Lrm}} Z_3 + \dfrac{I_i}{(C_1 + C_2 + C_3)} (t - t_6) \\ v_{C2} = V_{C3} = I_{\mathbf{Lrm}} Z_3 - \dfrac{I_i}{(C_1 + C_2 + C_3)} (t - t_6), \end{cases} \tag{9}$$

$$\begin{cases} i_{C1} = \dfrac{C_1 I_i}{(C_1 + C_2 + C_3)} \\ i_{C2} = \dfrac{C_2 I_i}{(C_1 + C_2 + C_3)}, \\ i_{C3} = \dfrac{C_3 I_i}{(C_1 + C_2 + C_3)} \end{cases} \tag{10}$$

Mode 2 represents the case in which the resonant inductance is large, and the duration of a complete cycle is

$$T_7 = t_7 - t_6 = \frac{V_o (C_1 + C_2 + C_3)}{I_i}. \tag{11}$$

Initial conditions are

$$\begin{cases} v_{C1} = \dfrac{I_i}{(C_1 + C_2 + C_3)} (t - t_6) \\ v_{C2} = V_{C3} = V_0 - \dfrac{I_i}{(C_1 + C_2 + C_3)} (t - t_6). \end{cases} \tag{12}$$

It can be seen from **Figure 8** that improved soft switching overcomes the fatal defect of basic soft switching; that is, the

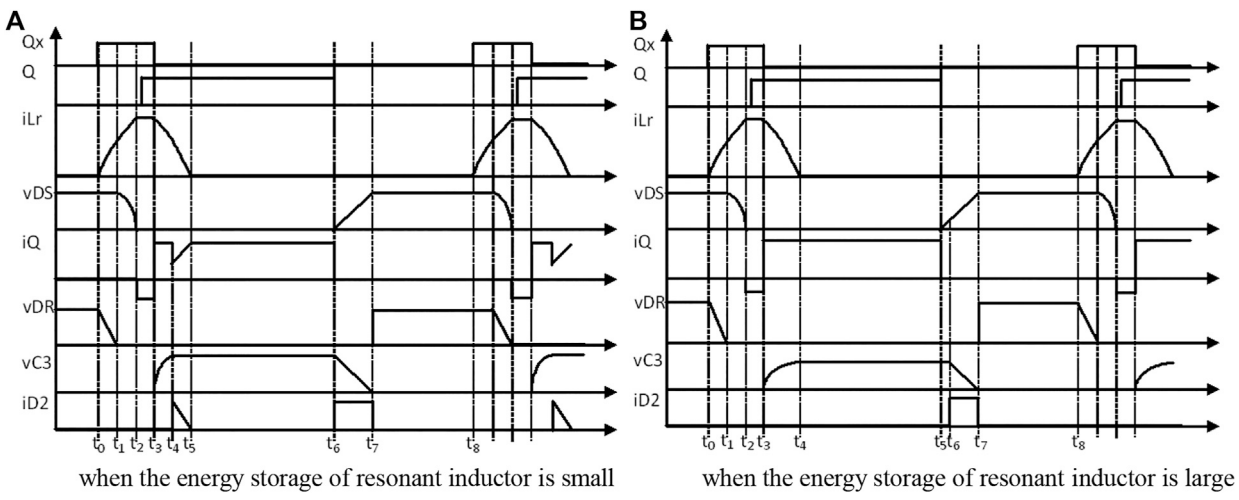


FIGURE 8 | Main power waveform diagram. **(A)** When the energy storage of the resonant inductor is small **(C)** When the energy storage of the resonant inductor is large.

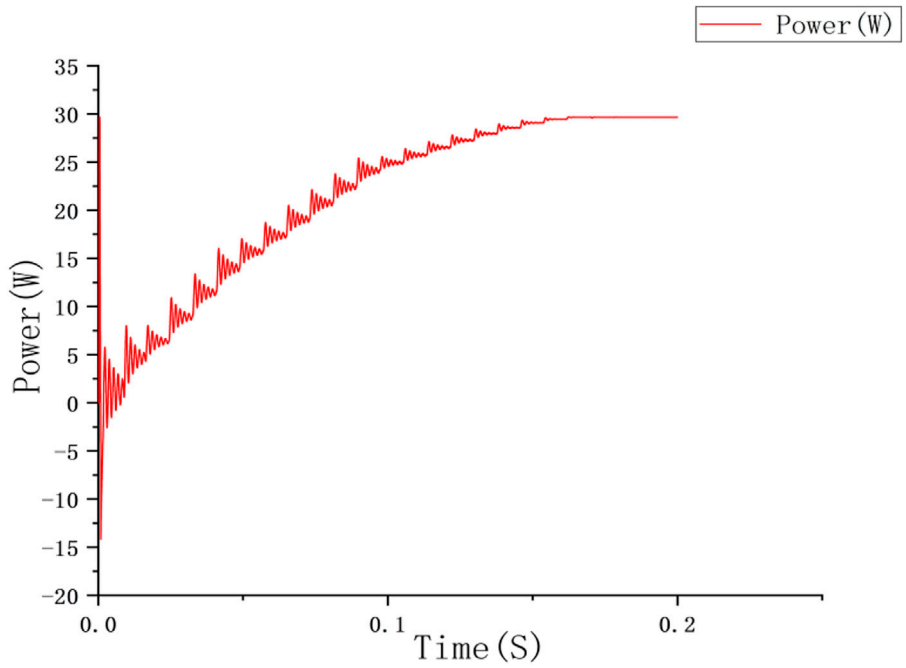


FIGURE 9 | Tracking time of MPP of soft switching.

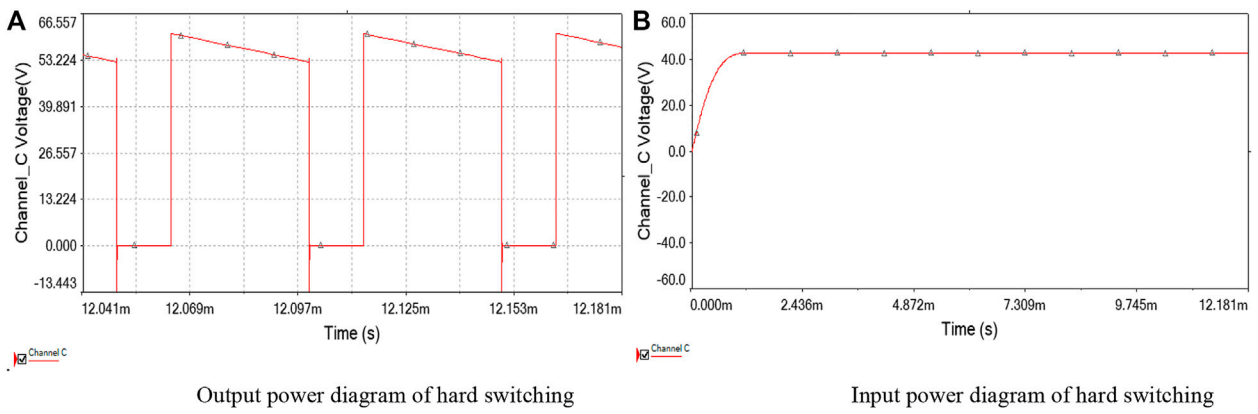


FIGURE 10 | Schematic diagram of hard and soft switching.

switching loss is too large, but improved soft switching increases the conduction loss of the auxiliary switch tube, which makes it difficult to improve the overall conversion efficiency of the circuit.

SIMULATION AND EXPERIMENTAL ANALYSIS

The MPP of PV modules is found based on Multisim, and the duty cycle is adjusted according to the MPP. The advantages and disadvantages of basic and improved soft switches are analyzed. On this basis, an innovative soft-switching technology is proposed to reduce the switching and conduction losses of auxiliary switch tubes. In this section, the MPP is tracked in Proteus first, and then three different methods are adopted to compare and analyze the four technologies in this paper to verify the efficiency and feasibility of the innovative soft-switching technology.

$$tduk = 0.16*(2.45*ek - 0.5*ek1 + 0.7*ek2). \quad (13)$$

Figure 9 uses Proteus to simulate and track the MPP. The experimental results show that the parameters in **Eq. 13** are superior to other parameters that can greatly speed up the tracking speed, there is no oscillation near the MPP, and the average tracking time is only 163 ms.

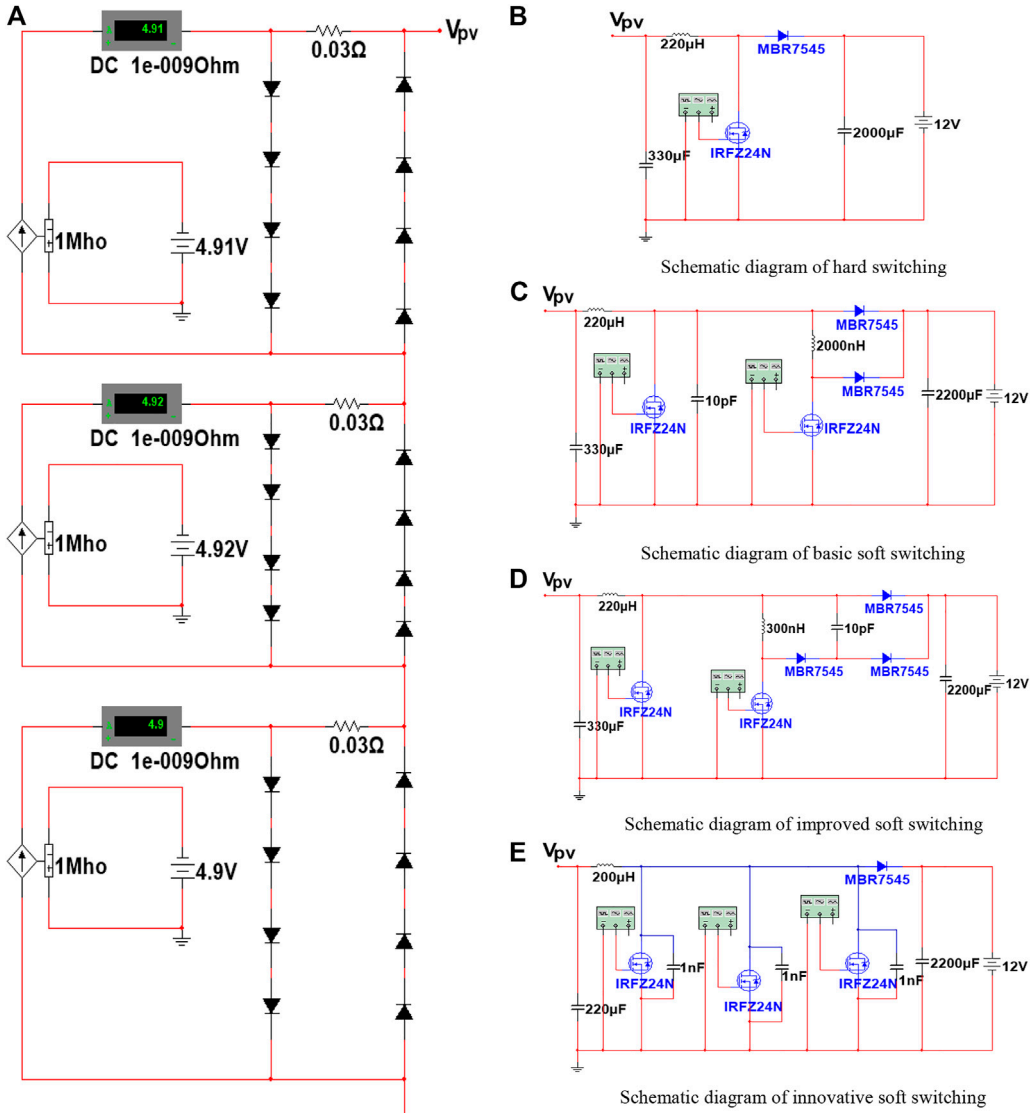


FIGURE 11 | Hard switching input and output power diagram.

Oscilloscope Area Method

Under the frequency of 20 KHZ and standard experimental conditions, the hard switches and various types of soft switches are simulated, respectively, and their areas are calculated. The conversion efficiency is obtained by dividing the output area by the input area. To make the calculation result more accurate, this paper adopts the average value of 30 calculation results.

In a period of 0.00005 s, around the MPP voltage of 9.067 V, adjust the duty cycle of the hard soft switching so that the input voltage of the hard soft switching is close to the MPP voltage. Read at this time. The simulation results in **Figure 10** show that the conversion efficiency of the hard switching is about 94.382%. Similarly, the other three soft-switching technologies are measured with this method. The simulation results show that the conversion efficiency of basic soft switching is about 96.181%, that of improved soft switching is about 95.950%, and that of innovative soft switching is about 96.398%.

The improved soft switching adds a capacitor and a diode based on basic soft switching, and they can improve the conversion efficiency by reducing the switching loss in theory. However, the increased Schottky diode greatly increases the diode conduction loss while reducing the switching loss, so the conduction loss is far greater than the switching loss. Innovative soft switching is improved on the basis of these two types of soft switches. Simulation results show that the conversion efficiency is the highest, which proves the high efficiency of innovative soft switching. To verify the accuracy

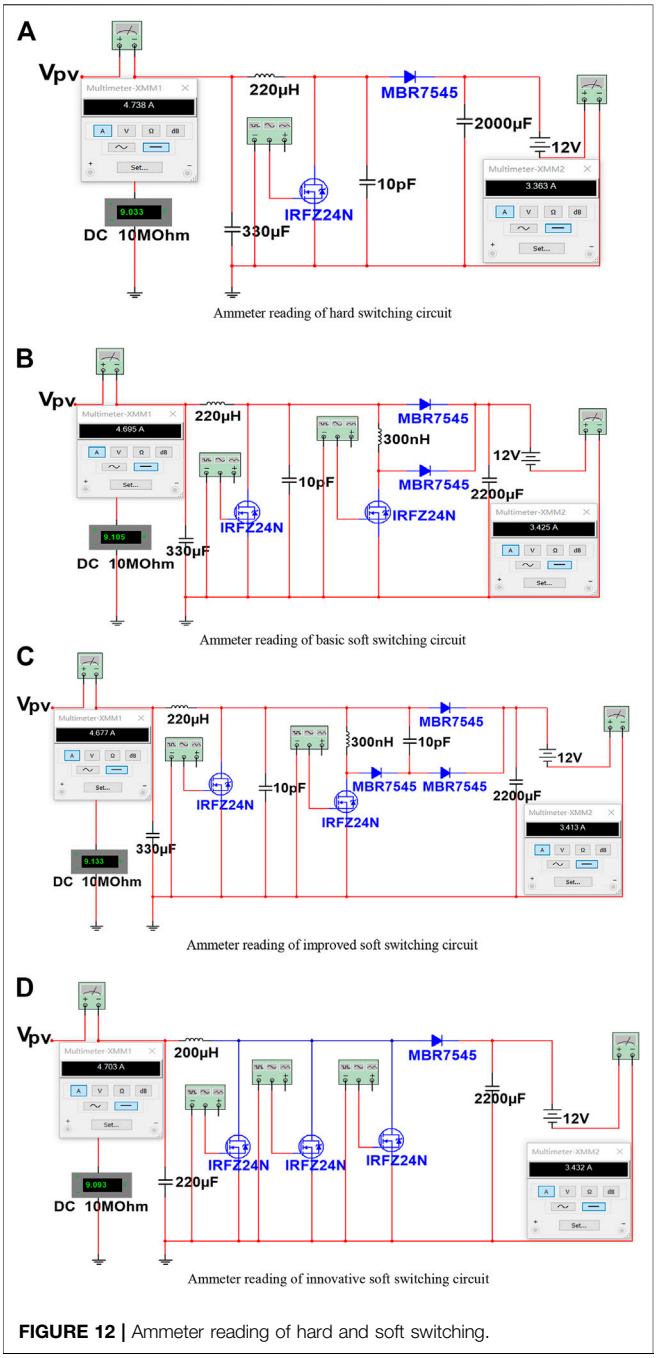


FIGURE 12 | Ammeter reading of hard and soft switching.

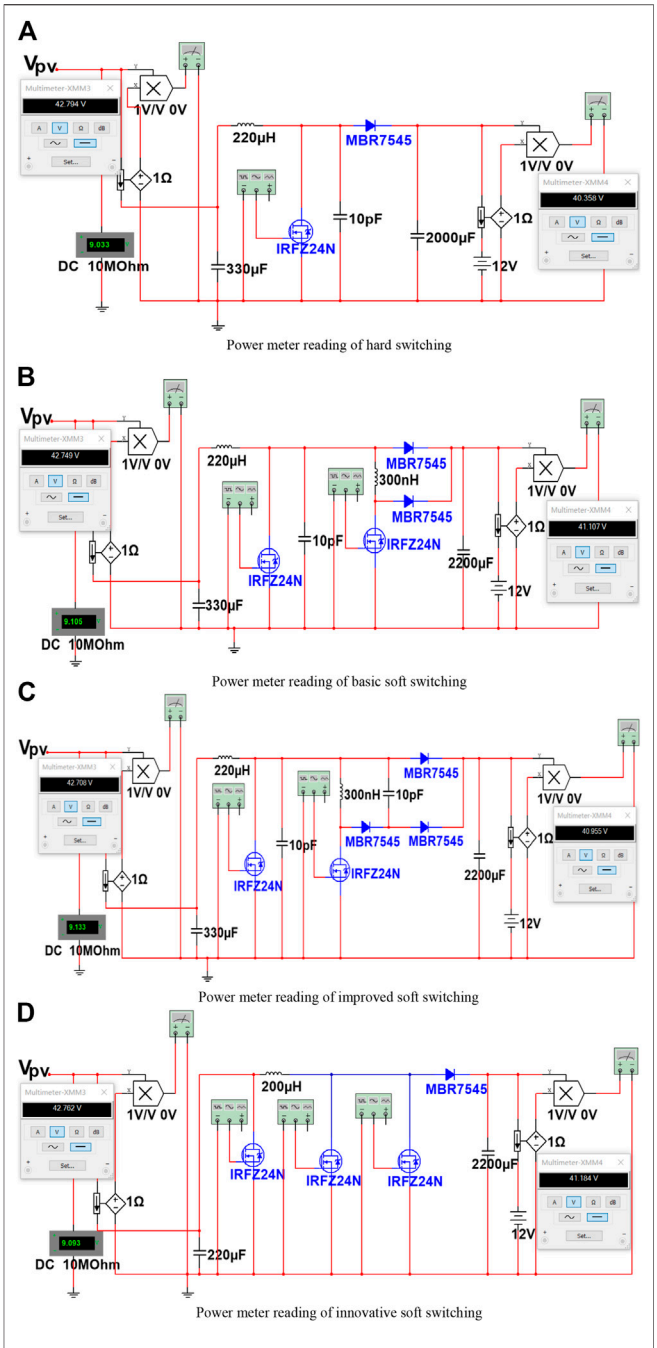


FIGURE 13 | Power meter readings for hard and soft switches.

of this method, two other different methods are applied to calculate the conversion efficiency and compared with this method to obtain accurate values.

Product Method of Ammeter and Voltmeter

In this section, the product methods of ammeter and voltmeter are used to compare with the oscilloscope area method and verify the accuracy of the conversion efficiency. On the basis of the schematic diagram in **Figure 11**, the input and output terminals are connected in series with a multimeter and then adjusted to the current level, and the corresponding power is calculated

TABLE 1 | PV arrays under the same temperature and different voltage values (illumination intensity).

G	S_1W/m^2	S_2W/m^2	S_3W/m^2	Result (Figure 2)
1	1,000	1,000	1,000	Black
2	800	800	800	Red
3	500	500	500	Blue
4	200	200	200	Cyan
5	1	1	1	Purple

TABLE 2 | PV arrays at different temperatures with the same voltage (light intensity).

G	T(°C)	Result (Figure 3)
1	−10	Black
2	10	Red
3	25	Blue
4	40	Cyan
5	55	Purple

TABLE 3 | PV array under shielding condition.

Group	S_1W/m^2	S_2W/m^2	S_3W/m^2	Verification result (Figure 4)
1	1,000	800	800	Black
2	1,000	800	400	Red
3	1,000	500	500	Blue
4	800	500	500	Cyan
5	800	500	200	Purple

TABLE 4 | Statistics on conversion efficiency.

method category	Oscilloscope area (%)	Product method of ammeter and voltmeter (%)	Multimeter direct reading (%)
HS	94.382	94.293	94.308
BSS	96.181	96.145	96.159
ImSS	95.950	95.882	95.895
InSS	96.398	96.305	96.310

according to the values of the input and output current at this time.

According to the method of MPP in *Oscilloscope Area Method*, the simulation results show that the conversion efficiency of hard switching in **Figure 12** is about 94.293%, that of basic soft switching is about 96.145%, that of improved soft switching is about 95.882%, and that of innovative soft switching is about 96.305%.

Multimeter Direct Reading Method

To verify which method, 4.1 or 4.2, is more accurate, this section connects a multimeter to the input and output ends, respectively, based on the schematic diagrams of various types of hard and soft switches. Unlike the second method, there is no specific current source in Multisim, so this method uses a current-controlled voltage source to convert the voltage signal and then connects the multiplier to the multimeter and finally adjusts the multimeter to the voltage level.

Under the experimental conditions in *Oscilloscope Area Method and Product Method of Ammeter and Voltmeter*, the conversion efficiency of hard switching in **Figure 13** is about 94.308%, that of basic soft switching is about 96.159%, that of improved soft switching is about 95.895%, and that of innovative soft switching is about 96.310% **Table 4** is the data summation.

CONCLUSION

The innovative soft switching proposed in this paper can effectively optimize the dynamic and steady-state performance of MPPT and greatly shorten its average tracking time. In addition, this method is simple, convenient, and has little efficiency loss. The fourth section uses Multisim to calculate the conversion efficiency of four kinds of hard and soft switches with three different measuring methods. The experimental results show that the measured results are almost equal, and the error is only within 0.1%. Second, it also verifies that improved soft switching optimizes the shortcomings of basic soft switching, but it also has a more fatal problem. To solve this problem, innovative soft switching is proposed in this paper. Simulation results show that the conversion efficiency of innovative soft switching can reach 96.3%, and its tracking speed is also the most efficient. It can be seen from **Figure 9** that MPP can be tracked in only 162 ms.

To sum up, innovative soft switching technology can greatly improve the conversion efficiency and average tracking time and promote the rapid development of the PV industry (Zhao and Wang, 2020).

DATA AVAILABILITY STATEMENT

The original contributions presented in the study are included in the article/Supplementary Material, further inquiries can be directed to the corresponding author.

AUTHOR CONTRIBUTIONS

PT: As the first author of the paper, I conducted simulation experiments and data modification, and completed the writing of the paper YC: Give guidance and provide literature JL: Check your paper for errors and Modify the format of the paper.

FUNDING

This work was supported by the Key Lab of Digital Signal and Image Processing of Guangdong Province under grant 190827105585418.

REFERENCES

Aiswariya, S., Muthulakshmi, S., Naganathan, G. S., Senthilkumar, M., and Rasheka, B. (2021). Design and Simulation of a Soft Switched Converter for Renewable Energy Systems. *Mater. Today Proc.*, 2214–7853. doi:10.1016/j.matpr.2021.03.321

Burnett, J. W., and Hefner, F. (2021). Solar Energy Adoption: A Case Study of South Carolina. *Electr. J.* 34, 106958. doi:10.1016/j.tej.2021.106958

Charin, C., Iqbal, S., and Taib, S. (2013). A New Soft Switching PWM DC-DC Converter with Auxiliary Circuit and Centre-Tapped Transformer Rectifier. *Proced. Eng.* 53, 241–247. doi:10.1016/j.proeng.2013.02.032

Darwesh, M. R., and Ghoname, M. S. (2021). Experimental Studies on the Contribution of Solar Energy as a Source for Heating Biogas Digestion Units. *Energ. Rep.* 7, 1657–1671. doi:10.1016/j.egyr.2021.03.014

Emami, Z., Farzanefard, H., and Motahari, S. R. (2010). "EMI Evaluation in Hard Switching and Soft Switching PWM Flyback Converters," in 2010 1st Power Electronic & Drive Systems & Technologies Conference (PEDSTC), Tehran, Iran, February 17–18, 2010), 46–51. doi:10.1109/PEDSTC.2010.5471857

Engelkemeir, F., Gattozzi, A., Hallock, G., and Hebner, R. (2019). An Improved Topology for High Power Soft-Switched Power Converters. *Int. J. Electr. Power Energ. Syst.* 104, 575–582. doi:10.1016/j.ijepes.2018.07.049

Faraji, R., Adib, E., and Farzanehfard, H. (2019). Soft-switched Non-isolated High Step-Up Multi-Port DC-DC Converter for Hybrid Energy System with Minimum Number of Switches. *Int. J. Electr. Power Energ. Syst.* 106, 511–519. doi:10.1016/j.ijepes.2018.10.038

Freeman, G. M., Apt, J., and Moura, J. (2020). What Causes Natural Gas Fuel Shortages at U.S. Power Plants? *Energy Policy* 147, 111805. doi:10.1016/j.enpol.2020.111805

Genc, N., and Koc, Y. (2017). Experimental Verification of an Improved Soft-Switching cascade Boost Converter. *Electr. Power Syst. Res.* 149, 1–9. doi:10.1016/j.epsr.2017.04.015

Hirsch, R. L. (2008). Mitigation of Maximum World Oil Production: Shortage Scenarios. *Energy Policy* 36, 881–889. doi:10.1016/j.enpol.2007.11.009

Hojnik, J., Ruzzier, M., Fabri, S., and Klopčič, A. L. (2021). What You Give Is what You Get: Willingness to Pay for green Energy. *Renew. Energ.* 174, 733–746. doi:10.1016/j.renene.2021.04.037

Ismail, E. H., and Sebzali, A. J. (1998). A New Class of Quasi-Square-Wave Resonant Converters with ZCS. *Energ. Convers. Manage.* 39, 1559–1569. doi:10.1016/S0196-8904(98)00028-4

Jahdi, S., Fry, M., and Lai, L. L. (2011). Energy Saving in Drives Using ZCT ZVT DC-DC Converters, PWM Inverters in Variable Speed Compressor Applications. *7th Int. Conf. Compressors their Syst.* 2011, 283–294. doi:10.1533/9780857095350.6.283

Kang, I. H., Kim, S. C., Bahng, W., Joo, S. J., and Kim, N. K. (2012). Accurate Extraction Method of Reverse Recovery Time and Stored Charge for Ultrafast Diodes. *IEEE Trans. Power Electron.* 27, 619–622. doi:10.1109/TPEL.2011.2161889

Khaled, U., Farh, H., Alissa, S., Abanmi, A., and Aldraimli, O. (2020). Efficient Solution of the DC-link Hard Switching Inverter of the PV System. *J. King Saud Univ. - Eng. Sci.* 32, 425–431. doi:10.1016/j.jksues.2018.09.001

Luo, G., Liu, S., Yan, X., and Guo, Y. (2021). Institutional Constraints to China's Low Carbon Transition: A Case Study of China's Coal-To-Gas Program. *Struct. Change Econ. Dyn.* 57, 121–135. doi:10.1016/j.strueco.2021.01.005

Luo, X., Liu, Y., Feng, P., Gao, Y., and Guo, Z. (2021). Optimization of a Solar-Based Integrated Energy System Considering Interaction between Generation, Network, and Demand Side. *Appl. Energ.* 294, 116931. doi:10.1016/j.apenergy.2021.116931

Mirza, A. F., Ling, Q., Javed, M. Y., and Mansoor, M. (2019). Novel MPPT Techniques for Photovoltaic Systems under Uniform Irradiance and Partial Shading. *Solar Energy* 184, 628–648. doi:10.1016/j.solener.2019.04.034

Mirzaei, A., and Rezvanyvardom, M. (2020). High Voltage Gain Soft Switching Full Bridge Interleaved Flyback DC-DC Converter for PV Applications. *Solar Energy* 196, 217–227. doi:10.1016/j.solener.2019.11.032

Moshksar, E., and Ghanbari, T. (2018). A Model-Based Algorithm for Maximum Power point Tracking of PV Systems Using Exact Analytical Solution of Single-Diode Equivalent Model. *Solar Energy* 162, 117–131. doi:10.1016/j.solener.2017.12.054

Öztürk, S., Poşpoş, P., Utalay, V., Koç, A., Ermiş, M., and Çadırcı, I. (2018). Operating Principles and Practical Design Aspects of All SiC DC/AC/DC Converter for MPPT in Grid-Connected PV Supplies. *Solar Energy* 176, 380–394. doi:10.1016/j.solener.2018.10.049

Pahlavandust, M., and Yazdani, M. R. (2020). Single-switch Boost DC-DC Converter with Zero-Current-Switching, High Power Density and Low Electromagnetic Interference. *AEU - Int. J. Electron. Commun.* 121, 153229. doi:10.1016/j.aeue.2020.153229

Pakdel, M., and Jalilzadeh, S. (2016). A Novel Topology and Control Strategy for a Soft-Switched Single-phase Grid Connected Inverter. *J. Electr. Syst. Inf. Technol.* 3, 81–93. doi:10.1016/j.jesit.2015.11.011

Qi, L., Jiang, M., Lv, Y., Zhang, Z., and Yan, J. (2021). Techno-economic Assessment of Photovoltaic Power Generation Mounted on Cooling Towers. *Energ. Convers. Manage.* 235, 113907. doi:10.1016/j.enconman.2021.113907

Shiva Kumar, S., Panda, A. K., and Ramesh, T. (2015). A ZVT-ZCT PWM Synchronous Buck Converter with a Simple Passive Auxiliary Circuit for Reduction of Losses and Efficiency Enhancement. *Ain Shams Eng. J.* 6, 491–500. doi:10.1016/j.asej.2014.10.018

Simon, S., and Das, J. (2014). "PV Powered Soft Switched Boost Converter Using MPPT Control," in 2014 Annual International Conference on Emerging Research Areas: Magnetics, Machines and Drives (Kottayam, India: AICERA/iCMMD)), 1–6. doi:10.1109/AICERA.2014.6908250

Society, P. (1981). Electric Power Systems Textbooks. *IEEE Trans. Power Apparatus Syst.* PAS-100, 4255–4262. doi:10.1109/TPAS.1981.316977

Tkachenko, G. I., and Baklanov, A. N. (2015). A Method of Resonant Series-Parallel Identification. *Proced. Eng.* 129, 690–694. doi:10.1016/j.proeng.2015.12.092

Veerapen, S., and Huiqing Wen, H. (2016). "Shadowing Effect on the Power Output of a Photovoltaic Panel," in 2016 IEEE 8th International Power Electronics and Motion Control Conference (Hefei, China: IPEMC-ECCE Asia), 3508–3513. doi:10.1109/IPEMC.2016.7512858

Xin-gang, Z., and Wei, W. (2020). Driving Force for China's Photovoltaic Industry Output Growth: Factor-Driven or Technological Innovation-Driven? *J. Clean. Prod.* 274, 122848. doi:10.1016/j.jclepro.2020.122848

Yinghua, Y., Honglin, G., Xinhua, W., and Jinfei, T. (2012). Study on Soft Switching Technology to Reduce Electromagnetic Interference of PWM Inverter. *Energ. Proced.* 17, 384–390. doi:10.1016/j.egypro.2012.02.110

Zhou, C.-g., Huang, L., Ling, Z.-x., and Cui, Y.-b. (2021). Research on MPPT Control Strategy of Photovoltaic Cells under Multi-Peak. *Energ. Rep.* 7, 283–292. doi:10.1016/j.egyr.2021.01.068

Zou, C., Xiong, B., Xue, H., Zheng, D., Ge, Z., Wang, Y., et al. (2021). The Role of New Energy in Carbon Neutral. *Pet. Exploration Dev.* 48, 480–491. doi:10.1016/s1876-3804(21)60039-3

Conflict of Interest: The authors declare that the research was conducted in the absence of any commercial or financial relationships that could be construed as a potential conflict of interest.

Publisher's Note: All claims expressed in this article are solely those of the authors and do not necessarily represent those of their affiliated organizations, or those of the publisher, the editors, and the reviewers. Any product that may be evaluated in this article, or claim that may be made by its manufacturer, is not guaranteed or endorsed by the publisher.

Copyright © 2021 Tao, Cui and Jiayuan Liang. This is an open-access article distributed under the terms of the Creative Commons Attribution License (CC BY). The use, distribution or reproduction in other forums is permitted, provided the original author(s) and the copyright owner(s) are credited and that the original publication in this journal is cited, in accordance with accepted academic practice. No use, distribution or reproduction is permitted which does not comply with these terms.

frontiers in Energy Research

BRIEF RESEARCH REPORT
published: 13 September 2021
doi: 10.3389/fenrg.2021.747063

Single-Ended Fast Protection for Transient Power of Multi-Terminal Flexible and Direct Power Grids Containing Renewable Energy

Jieshan Shan, Xincui Tian, Yue Dai, Hongchun Shu, Yong Chang and Jian Song*

Faculty of Electric Power Engineering, Kunming University of Science and Technology, Kunming, China

With the proposal of the carbon peak goal, a multi-terminal flexible DC grid containing various renewable energy becomes the one of main ways of renewable energy power transmission. Thus, it is increasingly important to improve its transmission reliability and stability. This paper proposes a single-ended protection principle based on the analysis method of transient power change for the "mesh structure" ring-shaped flexible direct current (DC) grid. Based on the propagation characteristics of voltage, current, and anti-traveling waves during fault periods, the transient power variation coefficient based on SOD transformation is introduced to distinguish the internal and external faults. Besides, simulation based on the PSCAD/EMTDC platform within the Zhangbei four-port network verifies the effectiveness of the proposed protection principle under various fault conditions. Meanwhile, the protection criterion is designed according to the difference in the change coefficient of the transient power SOD within and outside the fault time zone. Moreover, the setting value of the start of protection is obtained by analyzing the simulation results, thus a set of fast and reliable single-ended protections for the same-side short-time transient power window of an enhanced flexible straight power grid is developed via combining it with the starting criterion of a sudden voltage change.

Keywords: renewable energy power grid, flexible direct current, SOD conversion, transient power, single-ended protection

OPEN ACCESS

Edited by:
Xiaoshun Zhang,
Shantou University, China

Reviewed by:
Guanhua Lu,
South China University of Technology, China
Xuehan Zhang,
Korea University, South Korea

****Correspondence:***
Hongchun Shu
kust_727@163.com

Specialty section:
This article was submitted to Smart Grids, a section of the journal Frontiers in Energy Research

Received: *25 July 2021*
Accepted: *09 August 2021*
Published: *13 September 2021*

Citation:
Shan J, Tian X, Dai Y, Shu H, Chang Y and Song J (2021) Single-Ended Fast Protection for Transient Power of Multi-Terminal Flexible and Direct Power Grids Containing Renewable Energy. Front. Energy Res. 9:747063. doi: 10.3389/fenrg.2021.747063

1 INTRODUCTION

With China's 2060 carbon neutralization target (Tang et al., 2013), the proportion of renewable energy in the energy system will inevitably increase year by year (Li et al., 2016a), and DC load will also continue to rise with the promotion of DC transmission technology (Li et al., 2015). The multi-terminal flexible DC grid containing renewable energy will likely become the main way of renewable energy power transmission (Sun et al., 2020; Bakeer et al., 2021), and improving its transmission reliability is a worthwhile research topic (Liu et al., 2020; Nayak et al., 2021).

In order to improve the protection performance of multi-terminal flexible direct current (DC) grid lines, much related research work has been carried out. Some literature (Li et al., 2016b) has employed the blocking effect of high-frequency components on line boundary elements (Tian et al., 2019; Bakeer et al., 2021) to distinguish the high-frequency transient energy on both sides of the boundary during faults. Though different judgment of internal and external faults effectively reduces the burden of protection setting, an appropriate simulation setting is still required. A wavelet transformation method was devised in reference (ASV et al., 2020) to extract the transient

characteristics of the faults inside and outside the area according to the boundary characteristics of the DC line to construct the best judgment for its protection (Zhao et al., 2011). Further literature (Liu et al., 2017) has been directed at the structure design of two-level VSC converters in the DC system. Based on the boundary element energy storage capacitor and DC reactor, a protection criterion based on the transient voltage ratio method has been proposed. More studies (Tong et al., 2019) measured the attenuation characteristics difference of the same-name traveling wave and the different-name traveling wave on both sides of the fault line and the non-fault line. Meanwhile, the Hausdorff distance was also adopted to form a set of wave-matched longitudinal differential protections (Tong et al., 2019; Wang et al., 2020).

Based on the aforementioned prior studies, this paper proposes a new principle of single-ended protection based on the transient power change analysis method for the "mesh structure" ring-shaped flexible DC grid. Based on the propagation characteristics of the forward wave and anti-traveling wave of voltage and current during a fault period, the transient power variation coefficient based on SOD transformation is introduced to distinguish the internal and external faults. In particular, simulation on PSCAD/EMTDC platform effectively verifies the protection principle under various fault conditions, and the start value of protection is set according to simulation results. Besides, a specific protection criterion is designed based on the difference of transient power SOD variation coefficient within and outside the fault time zone. Thus, a set of fast and reliable single-ended protection is devised through the combination of starting criterion of voltage sudden change.

2 ANALYSIS OF FAULT CHARACTERISTICS OF MULTI-TERMINAL FLEXIBLE DC LINE

The structure of a typical multi-terminal flexible DC system is shown in **Figure 1**, in which f_1 is an internal fault of the line, and f_2, f_3, f_4, f_5, and f_6 are external faults of the line.

There are two problems when considering a protection scheme intended mainly for line pilot protection under the failures of a multi-terminal flexible DC system. Firstly, when a near-end fault occurs, the electrical changes of the fault will be transmitted to the local protection at almost the same time as the fault occurs, and the opposite protection can only transmit acceleration signals to the local protection after the fault traveling wave arrives. The acceleration signal is the post-fault signal in relay protection that unconditionally trips the circuit breaker, but the delay of signal communication can cause damage to the transmission system. Thus, during protection scheme design, it is necessary to consider which fault condition produces the longest delay and set the upper limit of the time constraint according to the length of the line to prevent the converter from blocking before the protection action has occurred. Secondly, in the case of a near-end failure, the opposite side will produce reflected waves after traveling waves are transmitted. According to Peterson's law, it is necessary to strictly ensure that the local side cannot be

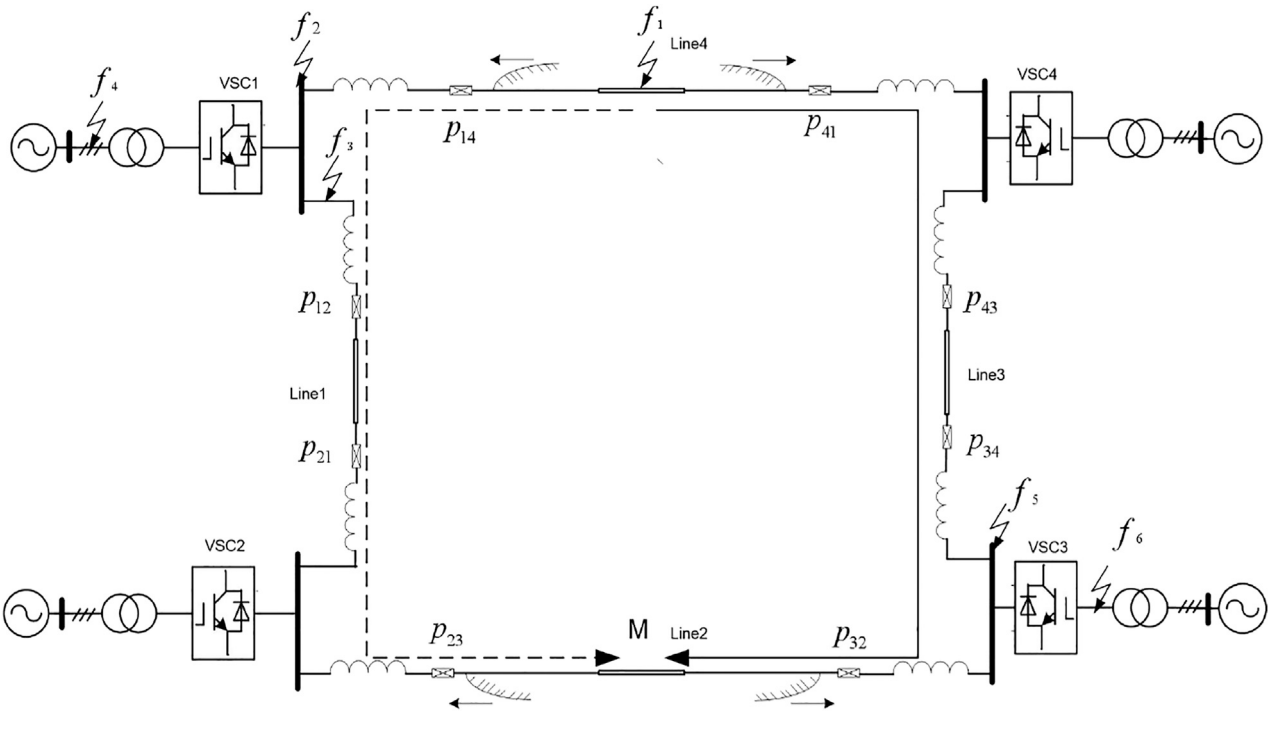


FIGURE 1 | Schematic diagram of structural line failure of four-terminal flexible DC system.

affected by the reflected waves of the opposite side before the fault processing is completed. The lower limit of time must be set according to the line length. The lower limit of time is the time it takes for a faulted traveling wave to propagate over a distance of twice the length of the line, and only an action time of less than this will ensure that the initial wavehead of the faulted traveling wave is not affected by the reflected wave. For practical engineering applications, if the length of each line of a multi-terminal network varies greatly, the difference of action effect of each line will be very obvious, which also brings certain difficulties to the setting of protection time.

As shown in **Figure 1**, when a fault occurs in f_1, the fault traveling wave propagates along the line and converges at the M-point of the four-terminal network system due to the ring characteristics of the multi-terminal flexible DC transmission network. Because the directional characteristics of the traveling wave propagating at the mirror fault point are identical to the initial fault point, but the amplitude is reduced, there is an attenuation effect when propagating on the line. The characteristics of fault on protection p_{34} and p_{43} are similar to those on the M-point, only the magnitude is different. As the traveling wave propagates along the closed four-ended network, the faulty traveling wave from the fault must meet again at another point in the closed four-ended network, this point is the mirror fault point. The appearance of such a "mirror fault point" also brings difficulties to fault identification.

3 LINE PROTECTION BASED ON TRANSIENT POWER CHANGES

3.1 Analysis of Electrical Characteristics

As shown in **Figure 2**, after a short-circuit fault occurs on the DC line, the voltage traveling wave is generated at the short-circuit point and propagates to both sides of the line. f1 is the internal fault of the line and f2 is the external fault of the line.

Let us define the transient power change as the product of the voltage fault component $\Delta u_{\mathrm{M}}$and, the current fault component Δi_{M}, i.e., $\Delta P_{\mathrm{M}} = \Delta u_{\mathrm{M}} \times \Delta i_{\mathrm{M}}$

When a fault occurs in the f_1 area without considering the line attenuation, the fault component of the measured voltage can be expressed by

$$\Delta U_{\mathrm{M1}} = \frac{z_1}{z_1 + 2R_{\mathrm{g}}} (-U_{\mathrm{f}}) \tag{1}$$

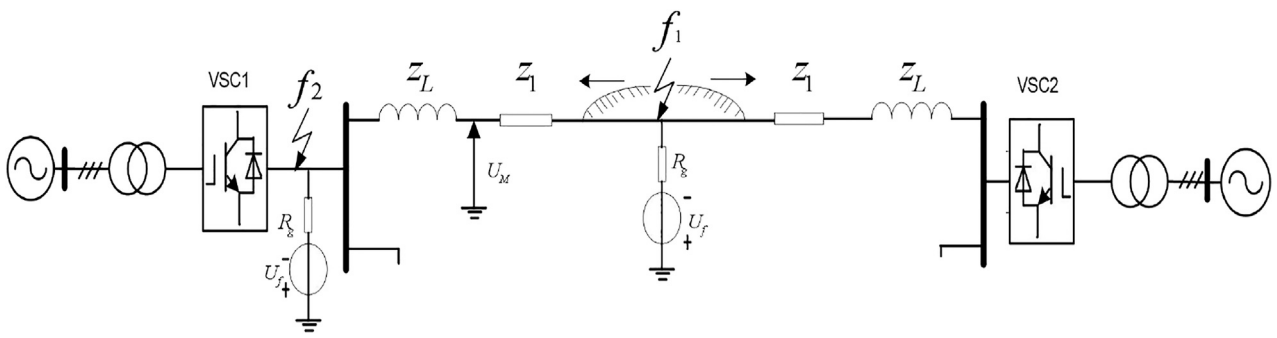


FIGURE 2 | Schematic diagram of line fault voltage traveling wave propagation.

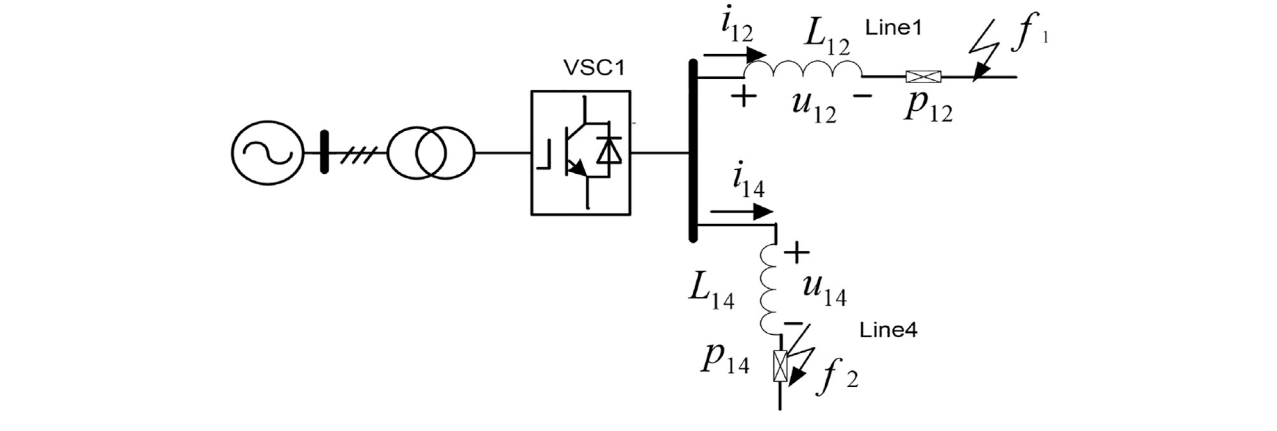


FIGURE 3 | Schematic diagram of fault current propagation in adjacent lines.

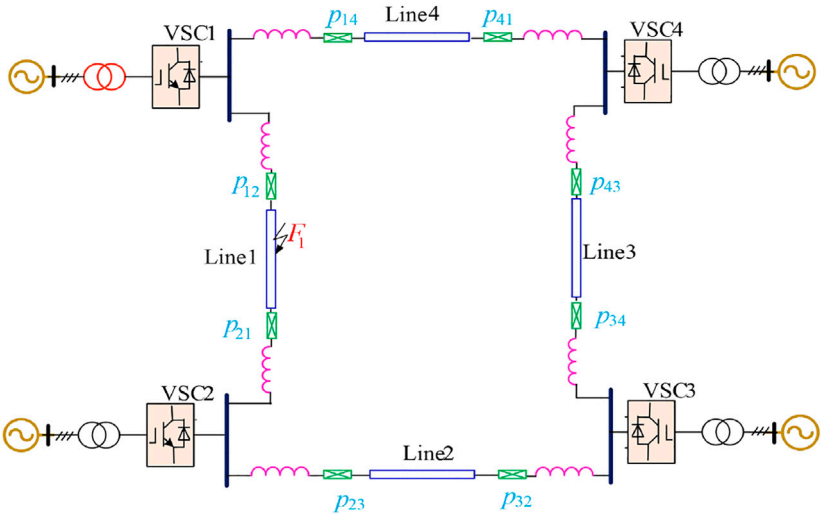


FIGURE 4 | Schematic diagram of line failures of four-terminal flexible DC system.

where z_1 represents the wave impedance of line 1, z_L denotes the inductance of DC reactor, and R_g means the transition resistance, respectively.

When an external f_2 fault occurs, the fault component ΔU_{M2} of the measured voltage U_M can be expressed by

$$\Delta U_{M2} = \frac{z_1}{z_1 + 2R_g}\left(-U_f\right)e^{-t/T_L} \tag{2}$$

where z_1 represents the wave impedance of line 1 and T_L means the time constant, respectively.

When an external fault occurs, due to the existence of attenuation factor in the formula, the voltage component decays with time, that is, the voltage wave head of the fault point becomes gentle under the action of the current limiting reactor. When an internal fault occurs, the fault voltage component changes step by step because there is no attenuation factor in the formula. In the calculation formula of fault voltage component, it can be seen that the sensitivity of response to transition resistance can be improved most obviously through the fault voltage component.

As shown in **Figure 3**, after a short-circuit fault occurs on the DC line, f_1 represents an internal fault of the line, and f_2 denotes an external fault of the line.

The voltage of the smoothing reactor is proportional to the rate of change of current. The current-limiting reactor voltage u_{L12} can be expressed by

$$u_{L12} = L_{12}\frac{\mathrm{d}i_{12}}{\mathrm{d}t} \tag{3}$$

It is noteworthy that the polarity of the fault current is related to the location of the fault. As shown in **Figure 3**, it is assumed that the current reference direction is the positive direction of the bus flow to the line. Taking line protection p_{12} as an example, when the line fault f_1 occurs in the positive direction, its polarity is positive and the value of inductance voltage u_{L12} is greater than zero; when the line has a reverse direction fault f_2, the polarity of i_{12} is negative, and the value of the inductor voltage u_{L12} is less than zero. Therefore, the polarity of the fault current can be used as a directional element to identify forward and reverse faults.

3.2 Analysis of Characteristics of Transient Power Variation

It can be seen from the above analysis that if we define the amount of transient power change as $\Delta P_M = \Delta u_M \times \Delta i_M = \Delta u_M \times \Delta i_M$, compared with Δi_M, the voltage fault component Δi_M is used in ΔP_M to improve the sensitivity of response transition resistance. Compared with Δu_M, the polarity of the current fault component Δi_M is used in ΔP_M to distinguish between forward and reverse faults. Therefore, the difference between internal and external faults can be expanded, and the precision and sensitivity of fault identification can be enhanced. When a fault line wave arrives at the end of the line, a short time series inductance cannot change abruptly, the fault line wave will be completely reflected, and there is almost no refraction wave. After a period of time the inductor current gradually changes, the line end boundary effect weakens, the refraction wave gradually increases, and the reflected wave gradually decreases. According to the analysis of fault boundaries in a multi-terminal flexible DC line, it can be seen that the refraction coefficient transfer effect of the current traveling wave is similar to the refraction coefficient transfer effect of a voltage traveling wave, and the refraction coefficient gradually rises from 0 to 1 within a few milliseconds. The reflection coefficient of the voltage traveling wave gradually decreases from 1 to close to 0 within a few milliseconds, while the transfer effect of the current traveling wave reflection coefficient shows an opposite trend. Thus, during the internal fault of the line, there are multiple reflections of voltage and current traveling waves and multiple sudden changes of the direction of transient power ΔP_M. In engineering practice, the DC outlets of VSC converter stations are often also connected in parallel with filters and series DC reactors, which play a filtering and current limiting role. For DC lines,

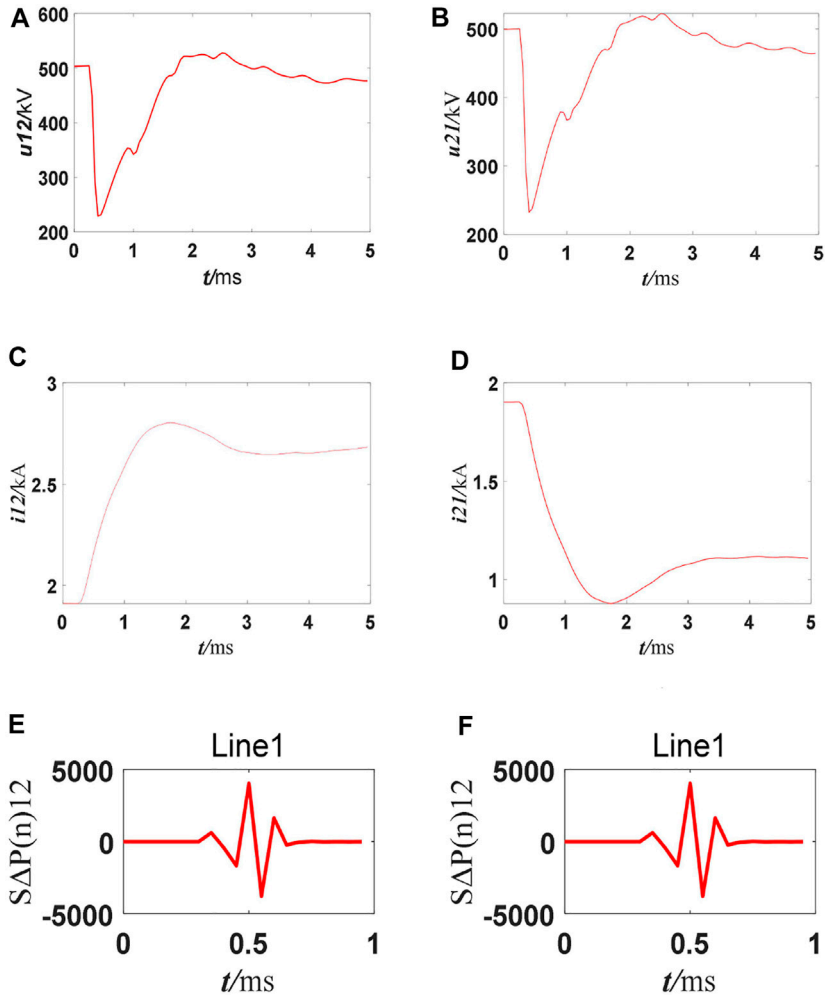


FIGURE 5 | Voltage, current, and SΔP(n) waveform SOD transformation for line1 positive pole fault. **(A)** First-end positive fault voltage waveform; **(B)** Terminal positive fault voltage waveform; **(C)** First-end positive fault current waveform; **(D)** Terminal positive fault current waveform; **(E)** Line 1 head end SΔP(n) K = 4,037; **(F)** End of line 1SΔP(n) K = 4,063.

these primary devices form natural boundaries, and taking into account the absorption and blocking effect of these boundary elements on the high-frequency components, the reactors at both ends of the line form obvious boundaries. Meanwhile, under external fault, due to the influence of the current limiting reactor and the length of the line, the change of the electric quantity tends to be gradual, which leads to the decrease of the direction change of the transient power change, which can be used as the criterion of the fault whether internal or external.

4 SOD-BASED FAULT IDENTIFICATION METHOD

4.1 SOD Transformation Algorithm

In order to further increase the difference between internal faults and external faults, and improve the discrimination, this work makes certain changes on the basis of traveling wave analysis. SOD is the cross overlap difference transform. Besides, a fault identification algorithm based on cross-overlap differential transformation is also employed. The higher the order, the more sufficiently it can reflect the characteristics of high-frequency transients and the direction of their sudden changes, which can be expressed as

$$S_k(n) = \sum_{j=1}^{j=k+1} (-1)^{j+1} \left(c_j\right)_k Q(n-j+1) \tag{4}$$

Based on this transformation, the difference between each sampling point can be enlarged. Moreover, the positive and negative transformation coefficients of each sampling point can also be alternated, which can be regarded as a difference calculation for every two sampling points and then an integral operation, so as to make the fault abrupt change more explicit. According to the subsequent simulation requirements, this work utilizes the seventh-order SOD algorithm for the simulated instantaneous power value.

TABLE 1 | Line 1 combined power SOD conversion coefficient.

Fault type	Transition resistance (Ω)	Line length (km)	K_1	K_2	K_3	K_4	K_5	K_6	K_7	K_8
Positive pole failure	0	10	22,524	11,009	154.4	123.6	172.4	69.7	10.8	21.1
		20	11,130	24,541	14.7	94.6	74.8	34.5	68.3	46.8
		40	12,396	10,766	11.2	56.9	56.1	30.2	95.5	48.7
		80	10,730	25,842	68.3	49.1	35.2	24.8	13.1	92.5
		100	12,005	11,248	74.9	49.2	55.6	33.5	13.2	37.2
		120	25,665	11,575	18.1	60.3	39.7	29.5	144.2	39.5
		140	9,888	28,178	16.7	109.1	36.5	23.4	61.1	20.1
		160	23,713	12,335	130.1	39.6	56.6	29.1	8.8	45.6
		190	11,514	23,974	63.1	16.2	32.2	19.3	24.3	94.9
Positive pole failure	300	10	9,501	4,636	44.3	42.3	80.7	20.2	10.1	25.5
		20	4,043	8,988	12.3	37.9	33.2	27.8	17.1	37.2
		40	4,251	3,857	7.8	17.8	57.7	24.2	95.7	53.8
		80	3,755	9,012	8.2	44.1	27.9	12.3	19.3	38.2
		100	4,037	4,063	26.5	38.6	40.2	27.5	11.8	40.5
		120	8,829	3,909	14.8	12.3	52.2	29.5	49.8	35.1
		140	3,441	9,857	11.4	49.9	38.4	23.4	16.9	20.6
		160	8,163	4,173	14.6	19.7	24.8	22.9	36.8	21.4
		190	4,777	9,734	9.4	32.5	62.6	25.2	18.1	20.2
Negative pole failure	0	10	22,497	10,976	161.8	123.1	171.1	66.1	18.6	49.1
		20	11,064	24,379	11.7	96.9	65.5	22.2	64.3	29.7
		40	12,309	10,734	15.1	41.1	75.1	30.8	91.8	48.4
		80	10,724	25,803	12.8	88.9	38.8	24.2	41.6	23.9
		100	11,912	11,186	11.2	43.9	42.7	22.7	67.8	31.9
		120	25,543	11,553	10.5	42.2	47.1	10.2	149.7	44.9
		140	9,856	28,039	20.8	100.5	150.3	27.3	58.6	36.9
		160	11,236	11,382	5.2	35.1	39.1	22.7	58.4	15.9
		190	11,428	23,790	20.6	95.9	59.7	24.6	58.1	22.9
Negative pole failure	300	10	9,475	4,619	8.3	19.6	27.2	17.8	42.9	26.7
		20	4,022	8,927	9.9	40.8	65.4	22.1	26.3	26.9
		40	4,106	3,850	15.9	22.4	153.4	63.6	38.3	68.6
		80	3,766	9,002	9.9	39.4	32.5	16.7	26.8	39.4
		100	4,009	4,036	10.1	24.1	32.9	27.1	23.2	30.2
		120	8,798	3,906	9.2	14.1	37.5	26.1	57.7	40.4
		140	3,432	9,804	15.6	38.1	150.3	27.3	20.1	39.5
		160	3,786	4,122	9.1	15.5	52.6	28.1	50.1	24.7
		190	4,740	9,662	13.7	37.3	61.9	25.2	20.7	25.8
Bipolar failure	0	10	52,840	25,614	409.9	180.8	64.5	29.7	12.6	99.1
		20	25,665	11,575	18.1	60.3	39.7	29.5	144.2	39.5
		40	33,122	24,461	14.5	110.5	61.8	20.7	152.5	61.7
		80	25,863	62,390	16.4	210.3	67.1	27.6	185.9	78.1
		100	25,863	62,390	16.4	210.3	67.1	27.6	185.9	78.1
		120	63,715	29,828	13.6	98.6	74.2	24.3	359.8	83.5
		140	24,103	67,460	29.6	244.5	26.1	22.7	160.9	39.1
		160	29,430	25,994	6.7	99.1	65.6	16.4	215.1	44.5
		190	29,947	58,363	34.6	223.3	34.9	15.4	154.7	38.3
Bipolar failure	300	10	29,659	13,509	13.5	61.3	86.8	25.5	165.1	57.8
		20	12,774	28,465	12.4	100.6	55.8	27.5	73.4	37.8
		40	14,182	12,152	10.9	44.4	37.4	20.7	102.3	47.1
		80	12,103	29,337	9.8	99.8	45.1	26.4	84.8	56.2
		100	12,497	12,962	12.8	36.8	43.7	22.7	87.1	56.7
		120	29,188	13,231	13.5	40.4	74.2	24.3	166.4	41.3
		140	11,246	31,860	18.6	113.5	106.9	24.8	68.5	21.6
		160	12,917	12,918	10.9	37.5	65.6	25.6	72.4	20.5
		190	15,563	30,425	19.5	114.2	45.2	20.2	73.1	17.2

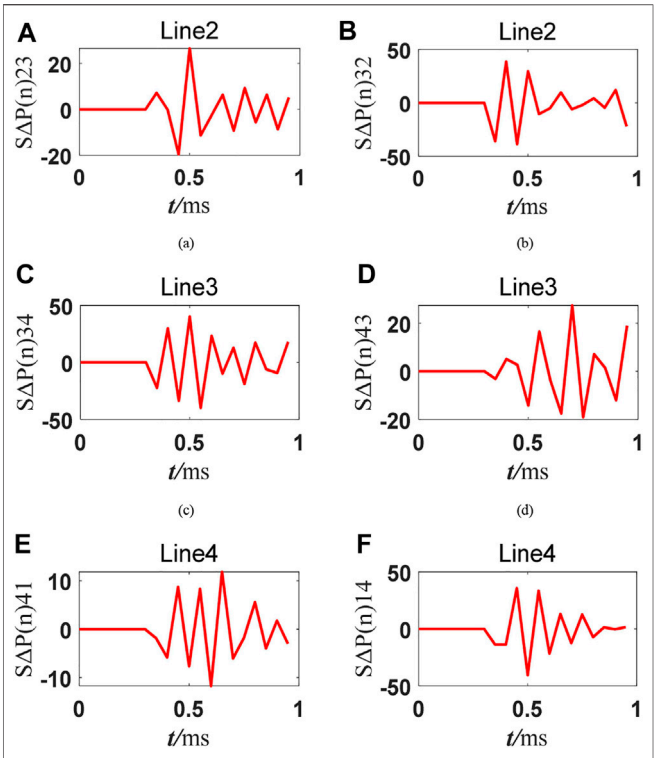


FIGURE 6 | SΔP(n)K value of non-faulty line. **(A)** Line 2 head end *S*ΔP(n) K = 26.5; **(B)** End of line 2 *S*ΔP(n) K = 38.6; **(C)** Line 3 head end *SΔP(n)* K = 40.2; **(D)** End of line 3 *S*ΔP(n) K = 27.5; **(E)** Line 4 head end *S*ΔP(n) K = 11.8; **(F)** End of line 4 *S*ΔP(n) K = 40.5.

4.2 Recognition of Internal and External Faults

As was analyzed in **Section 3**, during an internal line fault, multiple reflections of voltage and current traveling waves and multiple sudden changes in the direction of the transient power occur. Meanwhile, due to the influence of the current limiting reactor and the length of the line, the changes of the electrical quantities tend to be gentler when an external fault occurs, resulting in the direction change of the transient power change being greatly reduced. When ΔP_M is transformed by SOD, the transformation coefficient of SOD increases and the difference between the transformation coefficients of two consecutive sampling points also increases, thus increasing the amplitude of the sudden variable. When the line is in external fault, the change is not obvious, so the transformation coefficient is used to distinguish the internal and external faults, and **Eq. 5** is formed by it. K is defined as the maximum value of the absolute value of SOD transformation coefficient, as shown in **Eq. 6**. Finally, according to the K value, the internal and external faults are divided into zones.

$$S\Delta P(n) = S[\Delta u(n) \times \Delta i(n)] \tag{5}$$

$$K = |S\Delta P|_{\max} \tag{6}$$

Taking the Zhangbei four-terminal flexible DC network as the simulation object, as shown in **Figure 4**, the converter stations in the figure are Zhangbei (vsc1), Beijing (vsc2), Fengning (vsc3), and Kangbao (vsc4), respectively.

Since the line mode component of each electrical quantity is less affected by frequency, and it is suitable for grounding and non-grounding faults, the line mode component is used in the following calculation. Assuming that the line mode components of fault voltage and current measured by P_{12} with 20 K sampling frequency are represented by u_{12} and i_{12}, the higher the differential order is the more obvious the waveform amplitude changes.

The instantaneous power adopts a 7-order SOD transformation to meet the requirements, and the transformed value is expressed by $S\Delta P(n)_{12}$. The expression method of other line protection measurements is the same. According to the analysis results in Section 2.1, the near-end faults of the line and various faults close to the midpoint of the line are analyzed and verified by a large number of simulations.

When a positive fault occurs on line 1 at a length of 100 km and the grounding resistance is 300 Ω, its voltage, current waveform, and transient power SOD transformation are shown in **Figure 5**.

The transient power SOD transformation of non-faulty lines 2, 3, and 4 is shown in **Figure 6**.

In particular, the simulation results of each line are shown in **Table 1**.

It can be seen from **Table 1** that the transient power conversion coefficients of non-faulty lines show an obvious difference compared with that of faulty lines when various faults occur in different positions on the line and under different transition resistances. Based on this, the protection threshold can be set as the basis of distinguishing internal and external faults.

5 CONCLUSION

Fast and reliable DC fault identification is one of the key technologies for a multi-terminal ring flexible DC power grid. Based on the boundary characteristics of multi-terminal flexible DC power grids, a new fast protection method for a single terminal ring flexible DC power grid is proposed in this paper. Firstly, based on the refraction and reflection of the line boundary to the voltage and current traveling waves, the direction change is extracted through the SOD transformation coefficient of the instantaneous power, so as to realize fast and reliable fault identification. Secondly, the reliability of the protection is effectively improved via the over resistance characteristics of the fault voltage component and directional characteristics of the current component, and the difficulty of setting protections is reduced due to the high level of discrimination. It mainly contains the three following advantages, 1) fast operation speed that can respond within 6 ms after a fault occurs, which can effectively prevent the locking of a flexible DC power grid that can greatly improve the reliability of power supply; 2) fault identification is based on local information without communication; and 3) a strong ability to overcome transient resistance.

DATA AVAILABILITY STATEMENT

The original contributions presented in the study are included in the article/Supplementary Material, further inquiries can be directed to the corresponding author.

AUTHOR CONTRIBUTIONS

JS: Conceptualization, Writing—Reviewing and Editing. XT: Writing—Original draft preparation, Investigation. YD: Writing—Reviewing and Editing. HS: Supervision. YC: Supervision. JS: Conceptualization, Resources.

ACKNOWLEDGMENTS

The authors appreciatively acknowledge the support by Key Program of the National Natural Science Foundation of China (52037003); Major Special Project of Yunnan Province of China (202002AF080001).

REFERENCES

Asv, V. L., Manyala, R. R., and Mangipudi, S. K. (2020). Design of a Robust PID-PSS for an Uncertain Power System with Simplified Stability Conditions. *Prot. Control. Mod. Power Syst.* 5 (1), 1–16. doi:10.1186/s41601-020-00165-9

Bakeer, A., Salama, H. S., and Vokony, I. (2021). Integration of PV System with SMES Based on Model Predictive Control for Utility Grid Reliability Improvement. *Prot. Control. Mod. Power Syst.* 6 (1), 1–13. doi:10.1186/s41601-021-00191-1

Li, B., He, J. W., Li, Y., and Ou, Y. (2016). Single-ended protection Scheme Based on Boundary Characteristic for the Multi-Terminal VSC-Based DC Distribution System. *Proc. CSEE.* 36 (21), 5741–5749. doi:10.13336/j.1003-6520.hve.20160926001

Li, X. Y., Zeng, Q., Wang, Y. H., and Zhang, Y. M. (2016). Control Strategies of Voltage Source Converter Based Direct Current Transmission System. *High Voltage Eng.* 42 (10), 3025–3037. doi:10.13648/j.cnki.issn1674-0629.2015.01.002

Li, Y., Luo, Y., Xu, S. H., Zhou, Y. B., and Yuan, Z. C. (2015). VSC-HVDC Transmission Technology: Application, Advancement and Expectation. *South. Power Syst. Tech.* 9 (1), 7–13.

Liu, J., Tai, N., and Fan, C. (2017). Transient-Voltage-Based Protection Scheme for DC Line Faults in the Multiterminal VSC-HVDC System. *IEEE Trans. Power Deliv.* 32 (3), 1483–1494. doi:10.1109/tpwrd.2016.2608986

Liu, J., Yao, W., Wen, J., Fang, J., Jiang, L., He, H., et al. (2020). Impact of Power Grid Strength and PLL Parameters on Stability of Grid-Connected DFIG Wind Farm. *IEEE Trans. Sustain. Energ.* 11 (1), 545–557. doi:10.1109/tste.2019.2897596

Nayak, P. C., Prusty, R. C., and Panda, S. (2021). Grasshopper Optimization Algorithm Optimized Multistage Controller for Automatic Generation Control of a Power System with FACTS Devices. *Prot. Control. Mod. Power Syst.* 6 (1), 1–15. doi:10.1186/s41601-021-00187-x

Sun, K., Yao, W., Fang, J., Ai, X., Wen, J., and Cheng, S. (2020). Impedance Modeling and Stability Analysis of Grid-Connected DFIG-Based Wind Farm with a VSC-HVDC. *IEEE J. Emerg. Sel. Top. Power Electron.* 8 (2), 1375–1390. doi:10.1109/jestpe.2019.2901747

Tang, G. F., He, Z. Y., and Pang, H. (2013). Research, Application and Development of VSC-HVDC Engineering Technology. *Automation Electric Power Syst.* 37 (15), 3–14.

Tian, P. T., Chen, Y., Wu, Q. F., Dai, G., Li, C. X., Lei, Y., et al. (2019). Study on Transient-Based protection Scheme and Cooperation Strategy Based on Flexible DC Grid. *Power Syst. Prot. Control.* 47 (14), 1–8. doi:10.19783/j.cnki.pspc.181046

Tong, N., Fan, L. X., and Lin, X. N. (2019). Waveform Matching Based protection Strategy for VSC-MTDC Independent on Synchronization and Boundary Component. *Proc. CSEE.* 39 (13), 3820–3833. doi:10.13334/j.0258-8013.pcsee.181082

Wang, Q., Yao, W., Fang, J., Ai, X., Wen, J., Yang, X., et al. (2020). Dynamic Modeling and Small Signal Stability Analysis of Distributed Photovoltaic Grid-Connected System with Large Scale of Panel Level DC Optimizers. *Appl. Energ.* 259, 114132. doi:10.1016/j.apenergy.2019.114132

Zhao, C. Y., Chen, X. F., Cao, C. G., and Jing, H. B. (2011). Control and protection Strategies for MMC-HVDC under DC Faults. *Automation Electric Power Syst.* 35 (23), 82–87. doi:10.13334/j.0258-8013.pcsee.160099

Conflict of Interest: The authors declare that the research was conducted in the absence of any commercial or financial relationships that could be construed as a potential conflict of interest.

Publisher's Note: All claims expressed in this article are solely those of the authors and do not necessarily represent those of their affiliated organizations, or those of the publisher, the editors and the reviewers. Any product that may be evaluated in this article, or claim that may be made by its manufacturer, is not guaranteed or endorsed by the publisher.

Copyright © 2021 Shan, Tian, Dai, Shu, Chang and Song. This is an open-access article distributed under the terms of the Creative Commons Attribution License (CC BY). The use, distribution or reproduction in other forums is permitted, provided the original author(s) and the copyright owner(s) are credited and that the original publication in this journal is cited, in accordance with accepted academic practice. No use, distribution or reproduction is permitted which does not comply with these terms.

frontiers in Energy Research

ORIGINAL RESEARCH
published: 23 September 2021
doi: 10.3389/fenrg.2021.739439

Design of Control Strategy and Effect Evaluation for Primary Frequency Regulation of Wind Storage System

Cuiping Li[1], Zheshen Zhang[2], Junhui Li[1], Yunbao Ma[3] and Jiajun Zou[4]*

[1]Key Laboratory of Modern Power System Simulation and Control and Renewable Energy Technology, Ministry of Education (Northeast Electric Power University), Jilin, China, [2]Wenzhou Power Supply Company, State Grid Zhejiang Electric Power Company, Wenzhou, China, [3]Zaozhuang Power Supply Company, State Grid Shandong Electric Power Company, Zaozhuang, China, [4]Jilin Province Electric Power Company of National Grid, Changchun, China

Because of wind sources' volatility and intermittent news, wind power has made a more and more heavy burden on the power system. This paper analyzes in detail the traditional control method, parallel control strategy and serial control strategy of the wind storage system, and combines the advantages of the two to propose an optimal control strategy. A comprehensive performance evaluation method for the primary frequency regulation of the ESS participating in the power grid is proposed based on the power system operation requirements. In the example, the frequency modulation performance of the optimal control strategy is verified by the evaluation method described in this paper in the Chinese frequency adjustment market.

Keywords: wind power, energy storage system, primary frequency regulation, control strategy, effect evaluation

OPEN ACCESS

Edited by:
Bo Yang,
Kunming University of Science and Technology, China

Reviewed by:
Xiaomeng Ai,
Huazhong University of Science and Technology, China
Binyu Xiong,
Wuhan University of Technology, China

****Correspondence:***
Junhui Li
lijunhui@neepu.edu.cn

Specialty section:
This article was submitted to Smart Grids, a section of the journal Frontiers in Energy Research

Received: *10 July 2021*
Accepted: *02 August 2021*
Published: *23 September 2021*

Citation:
Li C, Zhang Z, Li J, Ma Y and Zou J (2021) Design of Control Strategy and Effect Evaluation for Primary Frequency Regulation of Wind Storage System. Front. Energy Res. 9:739439. doi: 10.3389/fenrg.2021.739439

INTRODUCTION

The total installed capacity of wind power in China is rising. As of August 2019, the total installed capacity of wind power in China has reached 198 million kilowatts (Shen et al., 2018; Yan and Zhao, 2018; Wind power grid-connected, 2019). Wind power itself has the unfavorable characteristics of large fluctuation and intermittent power output (Ramtharan et al., 2007; Teninge et al., 2009; Muyeen et al., 2012; Zertek et al., 2012; Dang et al., 2014; Luo et al., 2015; Peng et al., 2015), After wind power is connected to the grid, it will cause a large burden of frequency modulation on the grid. This burden may cause the power system to collapse (Li et al., 2018; Zhang et al., 2018; Annamraju and Nandiraju, 2019; Ayyarao and Ayyarao, 2019; Li et al., 2021). Many studies have been carried out the researches on the influence of wind power on power system frequency.

The following articles mainly solve the problem by improving the frequency regulation capability of wind turbines: In (Sun et al., 2018; Xing et al., 2018), since the wind turbine has no inertia, a control method for reducing the load of the wind turbine is proposed. To increase the reserve capacity of the frequency modulation system, the load capacity of the wind turbines is reduced. In (Wu et al., 2013; Tan et al., 2016), To solve the problem of insufficient capacity of wind turbine frequency modulation reserve, a method for tracking the power curve of sub-optimal wind turbines is proposed. This method guarantees the ability of wind power to participate in frequency modulation by withdrawing from the MPPT mode of the wind turbine. But this method reduces the economy of wind turbines. In summary, the wind turbine's control method for frequency modulation is mainly at the reduced economy or load capacity of wind turbines. Due to its characteristics, the response speed of wind turbines is difficult to meet the needs of power system primary frequency modulation.

The capacity of ESS can be configured as needed, and at the same time, it responds extremely fast to the demand for frequency modulation (Miao et al., 2015; Hu et al., 2016; Li et al., 2017; Tariq et al., 2018; Wu et al., 2018; Pandzic and Bobanac, 2019; Zhao et al., 2019). ESS can assist wind turbines to solve the problem of frequency modulation.

In the related literature of ESS assisting wind turbine to solve the problem of frequency modulation, in (Jing et al., 2005; Sun et al., 2019), the method of adjusting the frequency in stages solves the problem of economic decline caused by using too much energy storage, and uses the ESS to solve the part of the power system where the frequency changes rapidly. In (Hu et al., 2014), the frequency section control method of wind turbine and the ESS is proposed. This method mainly uses Fourier transform to distribute the high frequency components to the ESS and the remaining components to the wind turbine. In (Yan et al., 2016; Zheng et al., 2017), use the ESS to assist the wind turbine to improve the inertial response capability of the wind turbine, thereby improving the overall frequency regulation capability of the wind storage system.

In order to improve the frequency modulation performance, the above literature is mainly to improve the capability of wind turbine's frequency modulation or use energy storage to improve the frequency modulation performance of the wind turbine. But does not consider how to allocate to the wind turbine and ESS when the frequency modulation instruction is issued. Therefore, this paper proposes an optimal control method based on series control and parallel control based on the related issues of ESS auxiliary wind turbines participating in the primary frequency regulation of the power system. This method can take into account both economical and frequency regulation performance. The effectiveness of the above strategy is verified through simulation cases. Finally, a method is proposed for evaluating the performance of the ESS participating in the primary frequency modulation. The results prove that the optimized control method has the best comprehensive performance in the context of the frequency modulation market in China.

ESTABLISHMENT OF MATHEMATICAL MODEL RELATED TO FREQUENCY MODULATION

In this chapter, the models of traditional generating units participating in the power system, such as hydropower units and thermal power units, use commonly used traditional models (Kundur, 2001).

Because the selection of relevant parameters of power system frequency modulation is more complicated, and many parameters are empirical parameters, this paper chooses the parameters in documents (Miao et al., 2015) and (Kundur, 2001) as the main source of this paper.

The specific mathematical model is as follows.

Mathematical Model of Wind Turbine

At present, the mainstream wind turbines have zero inertia characteristics, so it is necessary to adopt certain technical means to make the wind turbines have the ability of conventional primary frequency modulation. And the main control methods of wind turbine are "virtual inertia control" and "pitch control." Both of them simulate the frequency response of traditional units in power system by changing the active output of wind turbines. The transfer function to build the virtual inertia is shown below:

$$G(\mathrm{s}) = \frac{\Delta P_{wind1}}{\Delta f} = -\frac{k_{vd}s}{1 + T_{wind1}s} \tag{1}$$

where k_{vd} is the virtual inertia constant of the wind turbine, which is usually 8; T_{wind1} is the inertial response time constant of the wind turbine, and the value is usually 0.1 s.

The Transfer Function Formula for Pitch Control is as Follows

$$G(\mathrm{s}) = \frac{\Delta P_{wind2}}{\Delta f} = -\frac{k_{change}}{1 + T_{wind2}s} \tag{2}$$

where k_{change} Is the frequency modulation coefficient for pitch control, usually 20; T_{wind2} is the pitch control time constant of the wind turbine, 3 s.

In summary, the overall frequency response transfer function formula of the wind turbine is as follows:

$$G_w(\mathrm{s}) = -\frac{(k_{vd}T_{wind2})\mathrm{s}^2 + \left(k_{change}T_{wind1} + k_{vd}\right)s + k_{change}}{1 + (T_{wind2} + T_{wind1})s + T_{wind2}T_{wind1}s^2} \tag{3}$$

Mathematical Model of the ESS

The advantage of the ESS is that its capacity can be configured according to demand, and at the same time can respond to the fast-changing frequency modulation needs. Configuring the ESSs in wind farms can alleviate the pressure of frequency modulation of power systems. Since the ESS is deployed in the wind farm, the inertial response coefficient and the primary frequency modulation coefficient of the ESS are the same as the wind generator. The mathematical model of the ESS is as follows:

$$G_e(\mathrm{s}) = \frac{\Delta P_{Energy}(\mathrm{s})}{\Delta f(\mathrm{s})} = -\frac{k_{vd}s + k_{change}}{T_{Energy}s + 1} \tag{4}$$

where $\mathrm{T_{Energy}}$ is the frequency response time constant of ESS, generally 0.3 s.

CONTROL STRATEGY DESIGN

After the power system sends down frequency modulation instructions, the traditional unit and wind storage system will allocate frequency modulation tasks according to how many frequency modulation problems are caused. The specific distribution method is as follows:

$$\Delta P_{tra} = (1 - p) * P_{all} \tag{5}$$

$$\Delta P_{w+e} = p * P_{all} \tag{6}$$

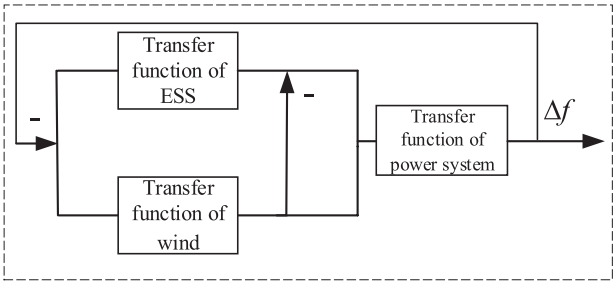


FIGURE 1 | Schematic diagram of wind storage system adopting serial control.

where ΔP_{w+e} is primary frequency regulation command responded by the wind storage system, unit MW; ΔP_{tra} is frequency modulation command that the traditional unit responds to, unit MW; p is the proportion of wind power installed capacity in all units participating in frequency modulation, 0.2; P_{all} is the total frequency modulation command issued by the power system.

In traditional frequency modulation reserve resources, thermal power units and hydropower units are allocated in the following ways.

$$\Delta P_f = k * \Delta P_{tra} \tag{7}$$

$$\Delta P_{wat} = (1-k) * \Delta P_{tra} \tag{8}$$

where ΔP_{wat} and ΔP_f are the regulators of hydroelectric units and thermal power units, respectively. k is the proportion of thermal power units, 0.8.

Control Strategy of Wind-Storage System

The wind turbine and the ESS can be divided into three control modes according to the task assignment when receiving the frequency modulation instruction: serial mode, parallel mode, and optimal operation mode.

Serial Control Mode of Wind-Storage System

Serial control is a classic control strategy of wind/storage system participating in frequency modulation. The schematic diagram is shown in **Figure 1**.

In the serial control mode, the frequency modulation work distribution of the wind turbine and the ESS should be carried out according to the following principles,

$$\Delta P_{w_{chu}} = \Delta P_{vir-ine} + \Delta P_{change-\omega} \tag{9}$$

$$\Delta P_{vir-ine} = \frac{\frac{1}{2}mv^2}{\Delta t_1} \tag{10}$$

$$\Delta P_{change-\beta} = \frac{1}{2}\rho\pi R_1^2 V_m^3 C_p \tag{11}$$

$$C_p = C_p(\beta + \Delta\beta) \tag{12}$$

$$\Delta P_{e_{chu}} = \Delta P_{w+e} - \Delta P_{w_{chu}} \tag{13}$$

where m is the quality of wind turbine, kg; v is the speed of wind turbine, m/s; Δt_1 is the response time for virtual inertia, s; ρ is the air density, the standard value is 1.29 kg/m^3; R_1 is the radius of sweep area, m; V_m is wind speed, m/s; C_p is the percentage of wind energy utilization; β is windward pitch angle of wind turbine; $\Delta\beta$ is the change of upwind pitch angle of wind turbine under serial control; ΔP_{w+e} Is the overall frequency modulation task volume of the wind storage system, MW; $\Delta P_{vir-ine}$ is the virtual inertial power regulation for wind turbines, MW; $\Delta P_{change-\omega}$ is the wind turbine pitch control to regulate the active power, MW; $\Delta P_{e_{chu}}$ and $\Delta P_{w_{chu}}$ are the adjustment of the ESS and the wind turbine, MW.

The frequency modulation flow chart using serial control is shown in **Figure 2**.

When the wind storage combined system responds to the system frequency modulation instruction by serial control mode, the wind turbine first responds to the frequency modulation instruction of the power system. At this time, the wind turbine controls its output power through virtual inertia and pitch control to suppress the frequency modulation of the power system. The unfinished frequency modulation components of wind turbines are allocated to the ESS.

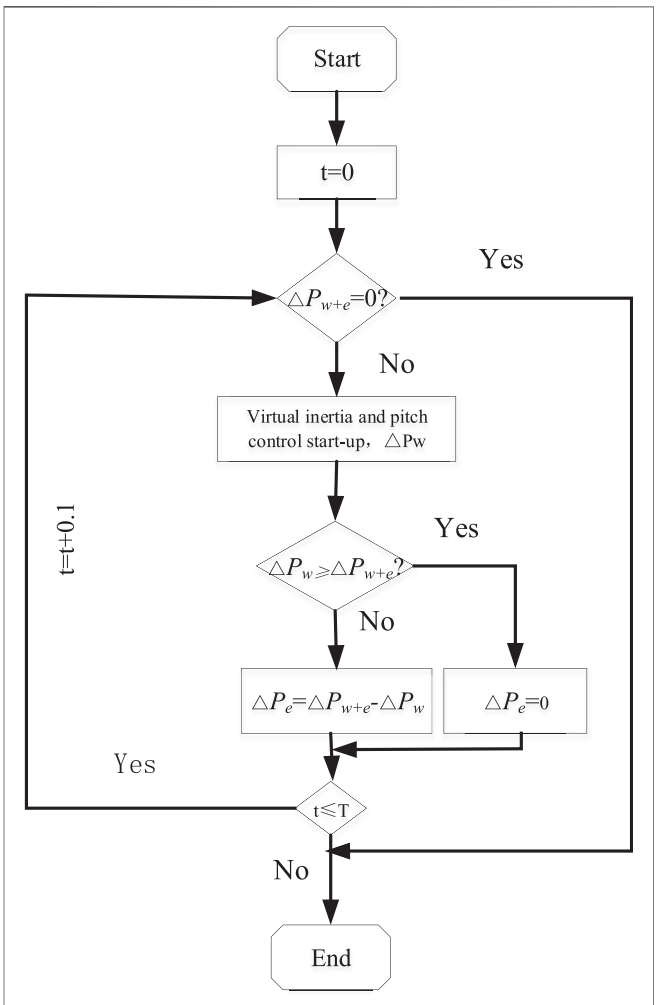


FIGURE 2 | Flow chart of serial frequency modulation for wind storage combined system.

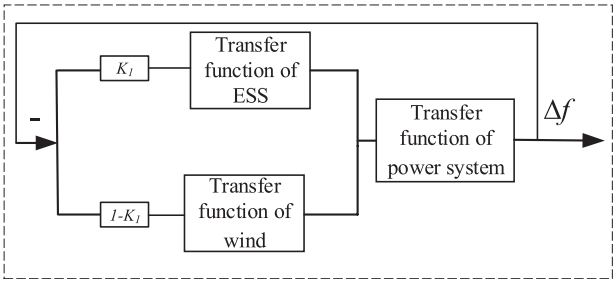


FIGURE 3 | Parallel frequency regulation schematic diagram of wind storage combined system.

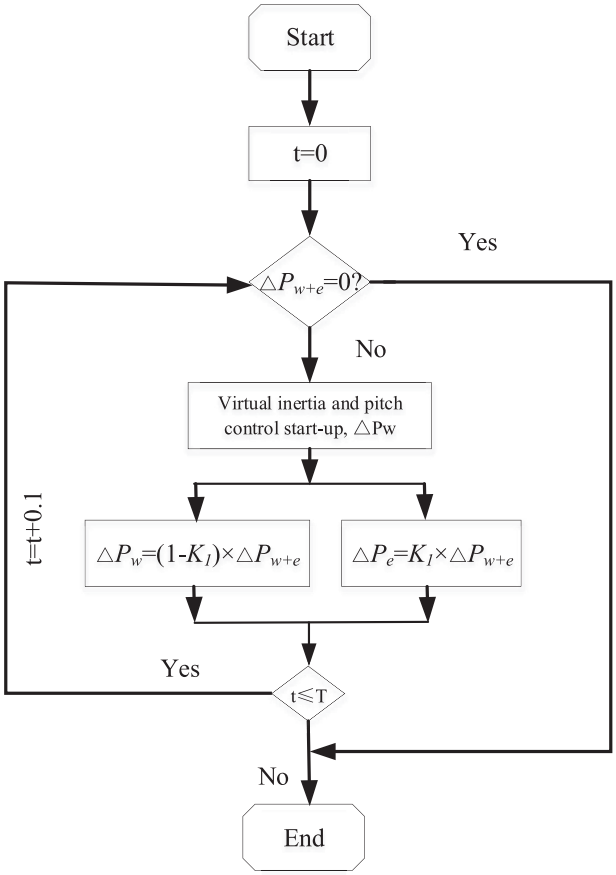


FIGURE 4 | Parallel frequency regulation flow chart of wind storage joint System.

Parallel Control Mode of Wind-Storage System

When a parallel control strategy is adopted to participate in primary frequency modulation of power system, the control strategy sketch is shown in **Figure 3**.

Where K_1 is the control factor that the wind-storage system adopts a parallel control strategy to allocate tasks when receiving a frequency modulation instruction.

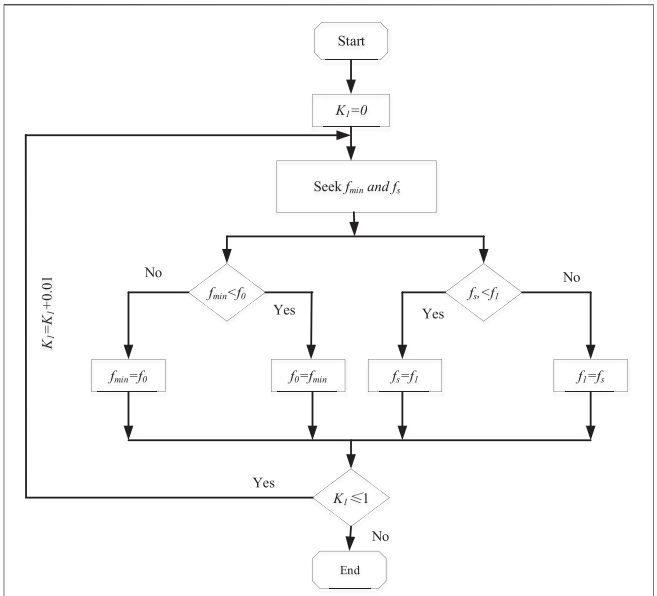


FIGURE 5 | Flow chart of parallel frequency regulation parameters calculation for wind storage combined system.

In the parallel control mode, the frequency modulation work distribution of wind turbine and ESS should be carried out according to the following principles,

$$\Delta P_{e_{bin}} = K_1 * \Delta P_{w+e} \tag{14}$$

$$\Delta P_{w_{\mathrm{bin}}} = (1 - K_1) * \Delta P_{w+e} \tag{15}$$

$$\Delta P_{w_{bin}} = \Delta P'_{vir-ine} + \Delta P'_{change-\omega} \tag{16}$$

$$\Delta P'_{vir-ine} = \frac{\frac{1}{2} m v_1^2}{\Delta t_2} \tag{17}$$

$$\Delta P'_{change-\beta} = \frac{1}{2} \rho \pi R_1^{22} V_m^3 C_p^{'} \tag{18}$$

When adopting parallel control strategy, $\Delta P_{e_{bin}}$ is the energy output of the ESS, MW; v_1 is the speed of wind turbine, m/s; Δt_2 is the virtual inertial response time of wind turbines, s; β_1、$\Delta\beta_1$ are the changes of pitch angle and pitch angle of wind turbine; $\Delta P'_{change-\omega}$、$\Delta P'_{vir-ine}$ are wind turbine pitch control and virtual inertia output, MW.

The schematic diagram of the process of wind storage system adopting parallel control strategy to participate in grid frequency modulation is shown in **Figure 4**.

When wind turbine adopts parallel control, the flow chart of K_1 value determination is shown in **Figure 5**.

Considering the actual operation requirements of the power system, the K_1 value in this paper is taken as 0.5.

When adopting a parallel control strategy, the wind turbine and the ESS will respond to the primary frequency regulation commands of the power system according to their respective frequency modulation task coefficients K_1. Wind turbines change their output through virtual inertia and pitch control. The ESS will respond to frequency modulation instructions quickly within rated power. Wind turbines

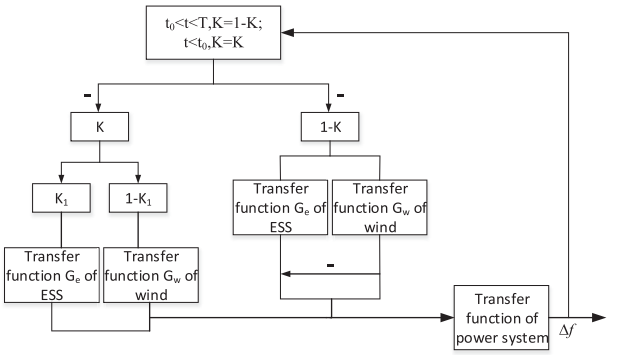


FIGURE 6 | Schematic diagram of optimal control strategy for wind storage system.

and ESS s work together to complete the primary frequency modulation task of the power system.

Optimal Control Mode of Wind-Storage System

The optimized control strategy proposed in this paper mainly considers the capacity allocation of the ESS and satisfies the constraints of serial control and parallel control. At each stage of wind power generation participating in power system frequency regulation, the control method is changed according to the actual situation and the operation status of the ESS to meet the power system frequency regulation needs.

1) Target function construction

Taking into account the actual operation requirements of the power system, the technical indicators of primary frequency modulation mainly include the maximum frequency deviation and the steady-state frequency deviation of the power system, and the economic indicators mainly include the capacity demand and power demand of the ESS. The objective function of the optimized control strategy of the wind storage system is constructed.

$$\min\left[C_1 \times \left(\Delta f_{dev} + \Delta f_{sta}\right) + C_3 \times S\right] \tag{19}$$

where C_1 and C_3 are the frequency modulation performance index penalty factor and energy storage cost penalty factor, both 0.5; Δf_{dev} and Δf_{sta} are the maximum frequency deviation and steady-state frequency deviation of the power system, respectively, HZ. S is the cost coefficient that changes according to different control strategies.

The frequency modulation flow chart of the optimized control strategy is shown in **Figure 6**. Where K and $1\text{-}K$ are the frequency allocation ratio of the ESS using serial control and parallel control, respectively; The system changes the proportion of series control and parallel control at time t_0.

When the wind storage system adopts the optimal control strategy, the total energy output of the wind storage system is as follows.

$$\Delta P_{you} = \Delta P_{t<t_0} + \Delta P_{t_0<t\le T} \tag{20}$$

where $\Delta P_{t<t_0}$ and $\Delta P_{t_0<t\le T}$ are the energy output of the wind-storage combined system at time $0 < t < t_0$ and time $t_0 < t < T$ under the optimized control strategy, respectively, MW; T is the maintenance time of primary frequency modulation, 30 s.

$$t \le t_0 \begin{cases} \Delta P_{t<t_0} = \Delta P_{chu1} + \Delta P_{bin1} \\ \Delta P_{chu1} = \Delta P_{echu1} + \Delta P_{wchu1} \\ \Delta P_{bin1} = \Delta P_{ebin1} + \Delta P_{wbin1} \\ \Delta P_{echu1} = \Delta P_{w+e}(1-K) - \Delta P_{wchu1} \\ \Delta P_{wbin1} = \Delta P_{w+e} \times K \times (1-K_1) \\ \Delta P_{ebin1} = \Delta P_{w+e} \times K \times K_1 \\ \Delta P_{wchu1} = \Delta P_{vir-ine1} + \Delta P_{change-\beta 1} \end{cases} \tag{21}$$

In the period of $0 < t < t_0$, ΔP_{chu1} and ΔP_{bin1} are the total output of the serial control and parallel control of the wind storage system under the optimized control strategy, respectively, MW. ΔP_{wchu1} and ΔP_{wbin1} are the output of the serial control and parallel control of the wind turbine under the optimized control strategy, respectively, MW. ΔP_{echu1} and ΔP_{ebin1} are the output of serial control and parallel control of ESS under optimized control strategy, respectively, MW.

$$t_0 < t \le T \begin{cases} \Delta P_{t_0<t\le T} = \Delta P_{chu2} + \Delta P_{bin2} \\ \Delta P_{chu2} = \Delta P_{echu2} + \Delta P_{wchu2} \\ \Delta P_{bin2} = \Delta P_{ebin2} + \Delta P_{wbin2} \\ \Delta P_{echu2} = \Delta P_{w+e} \times K - \Delta P_{wchu2} \\ \Delta P_{wbin2} = \Delta P_{w+e} \times (1-K) \times (1-K_1) \\ \Delta P_{ebin2} = \Delta P_{w+e} \times (1-K) \times K_1 \\ \Delta P_{wchu2} = \Delta P_{vir-ine2} + \Delta P_{change-\beta 2} \end{cases} \tag{22}$$

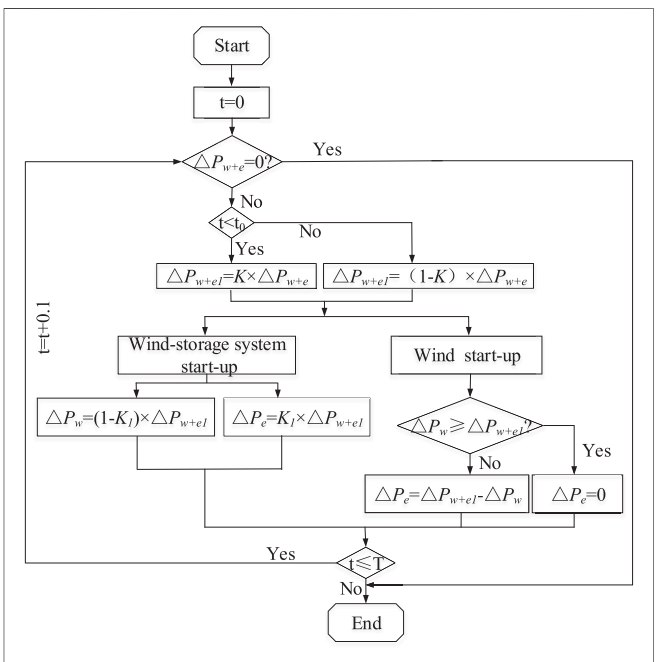


FIGURE 7 | Flow chart of optimal control strategy for wind storage combined system.

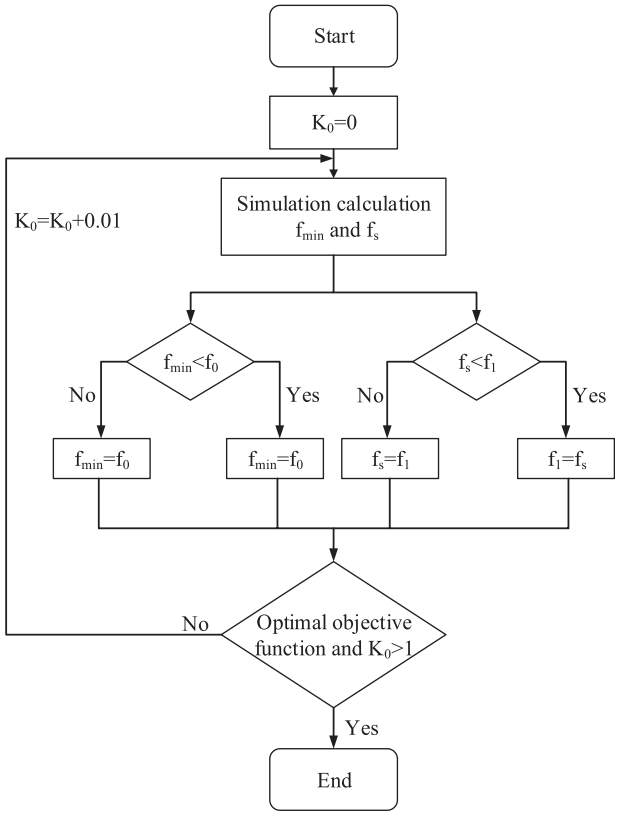


FIGURE 8 | Flow chart for the parameters of the optimizing control strategy.

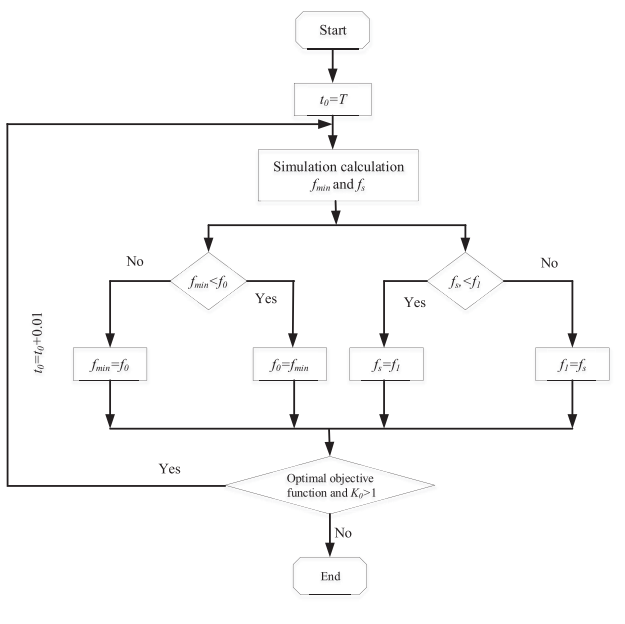


FIGURE 9 | Flow chart of time acquisition in optimal control strategy.

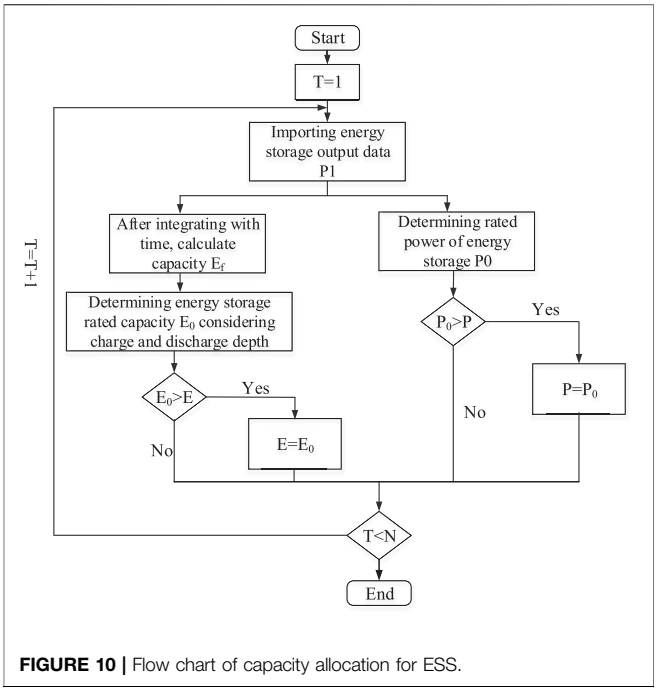


FIGURE 10 | Flow chart of capacity allocation for ESS.

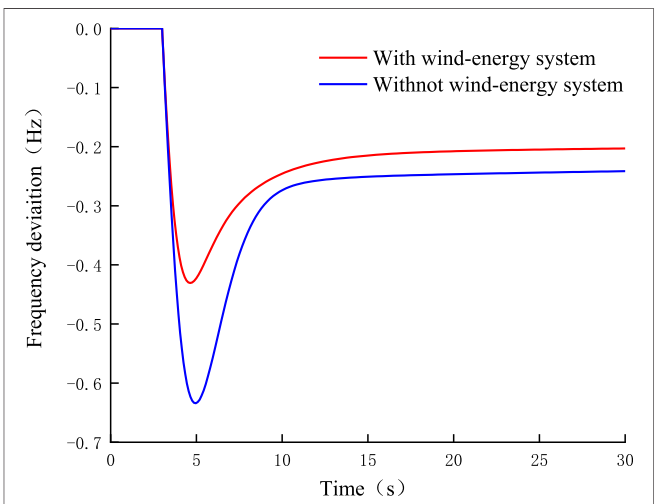


FIGURE 11 | Frequency regulation results with/without wind power and ESS.

In the formula, the number 2 indicates that the time period is $t_0 < t < T$.

The optimized control strategy operation flowchart is shown in **Figure 7**.

The purpose of the optimal control strategy is to reduce the frequency fluctuation of the power system, and reduce the cost of energy storage, and improve the economy.

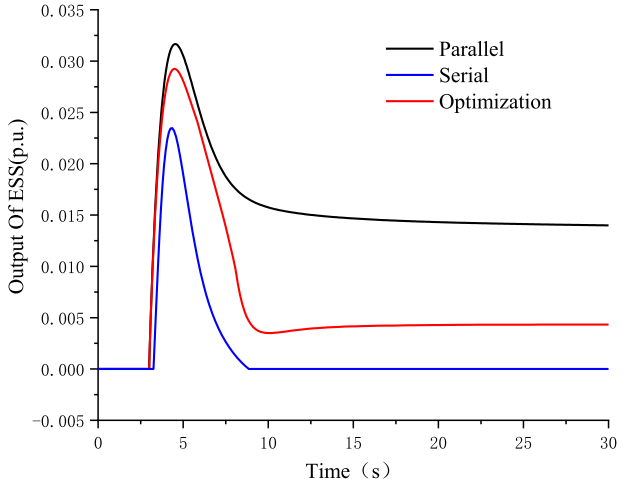


FIGURE 12 | Comparison of energy storage capacity under different control strategies.

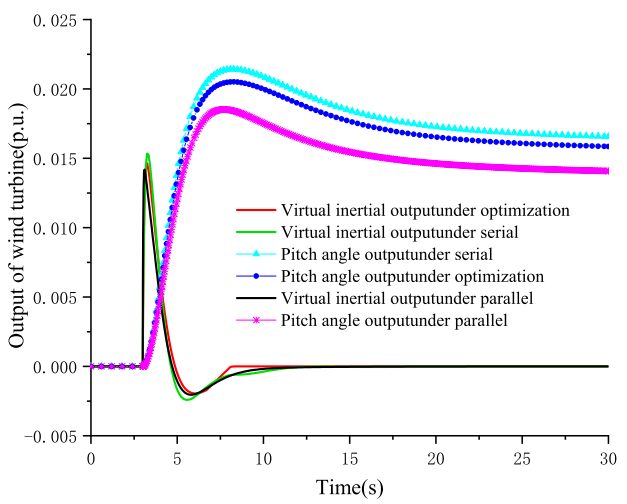


FIGURE 13 | Comparison of wind power under different control strategies.

2) Setting control parameters

Calculate K and t_0 with the control variable method. The calculation method is shown in **Figure 8**. Where K_0 is the initial set value; $f_{\min}$ is the lowest frequency drop point in the simulation process; f_s is the steady-state frequency value. When the value of K is 0.85, the overall frequency modulation effect of the system is the best.

The calculation method of t_0 is shown in **Figure 9**. Where T_n is the initial time set point. Through simulation verification, when t_0 takes 0.45 s, the frequency modulation effect of the system is the best.

Demand Analysis of ESS Capacity

This section mainly solves the problem of capacity allocation of the ESSs, including the determination of the constraints of capacity allocation of the ESSs and the establishment of configuration processes.

Constraints of ESS Configuration

Energy storage systems need to meet the constraints of state of charge (SOC). At a certain time t, SOC is calculated by the following formula:

$$SOC_t = SOC_{t-T} + \frac{\int_{t_0}^{t} P_e dt}{E} \tag{23}$$

where t_1 is the time when the ESS starts to work, s; E is the ESS rated capacity, MWh.

The SOC should meet the constraints of the upper and lower limits:

$$SOC_{\min} \le SOC \le SOC_{\max} \tag{24}$$

$SOC_{\min}$ and $SOC_{\max}$ are the lower and upper limits of charge-discharge of the ESS, respectively, 0.05–0.95.

The ESS should also satisfy the output power P_e constraint, as follows:

$$P_{\min} \le P_e \le P_{\max} \tag{25}$$

Under normal operation, $P_{\min}$ and $P_{\max}$ are the lower limit and upper limit of the output power of the energy storage system, respectively, MW.

ESS Configuration Method

The configuration method of the capacity and power of the ESS is as follows:

1) N = 1, import the first frequency data;
2) The output data P_1 of the ESS is derived and the rated power P of the ESS is obtained;
3) The capacity E_1 of the ESS is calculated according to the energy output during the frequency modulation period;
4) Considering the charging and discharging efficiency of the ESS, the rated capacity E of the ESS can be obtained;
5) N = N + 1.

In summary, the following **Figure 10** configuration flowchart can be obtained.

The energy storage system configuration results of the three control strategies are shown in **Table 1**.

EVALUATION METHOD OF FREQUENCY MODULATION EFFECT

The frequency modulation effect evaluation method proposed in this paper comprehensively analyzes the frequency modulation effect and economy and can be used to compare the comprehensive frequency modulation performance of different control strategies.

Evaluation System

The calculation formula of comprehensive frequency modulation performance evaluation is as follows:

TABLE 1 | Configuration results of three control strategies

Control strategy	Rated power (MW)	Rated capacity (MWh)
Parallel control	6.54	1.062
Serial control	4.84	0.524
Optimize control	5.84	0.636

$$G = \left(\sum_{i=1}^{n} g_i * D_i \right) \Big/ n \tag{26}$$

G is the score of the final frequency modulation effect; g_i is the score of the *i-th* factor affecting the effect of frequency modulation; D_i is the weighting factor of the *i-th* factor that affects the frequency modulation effect; n is the number of factors that affect the frequency modulation effect.

The calculation method of the maximum frequency deviation G_{dev} of the power grid is as follows:

$$G_{dev} = \frac{\Delta f_{dev} - f_{dev-xia}}{f_{dev-sha} - f_{dev-xia}} * (G_{dev-sha} - G_{dev-xia}) + G_{dev-xia} \tag{27}$$

$f_{dev-xia}$ and $f_{dev-sha}$ are the lower limit frequency and upper limit frequency of the frequency change range Δf_{dev}, respectively; $G_{dev-xia}$ and $G_{dev-sha}$ are the lower limit score and upper limit score in the frequency change range Δf_{dev}, respectively.

The calculation method of power system steady-state frequency deviation G_{sta} is as follows:

$$G_{sta} = \frac{\Delta f_{sta} - f_{sta-xia}}{f_{sta-sha} - f_{sta-xia}} * (G_{sta-sha} - G_{sta-xia}) + G_{sta-xia} \tag{28}$$

where $f_{sta-xia}$ and $f_{sta-sha}$ are the lower limit frequency and upper limit frequency of the frequency change range Δf_{sta}, respectively; $G_{sta-xia}$ and $G_{sta-sha}$ are the lower limit score and upper limit score in the frequency change range Δf_{sta}, respectively.

The calculation formula of the power system frequency modulation economy G_{eco} score is as follows:

$$G_{eco} = \frac{P_{fre-cb}}{P_{fre-sy}} * (G_{eco-sha} - G_{eco-xia}) + G_{eco-xia} \tag{29}$$

where P_{fre-cb} and P_{fre-sy} are the cost and revenue of energy storage system participating in frequency modulation, respectively; $G_{eco-xia}$ and $G_{eco-sha}$ are the lower limit and upper limit of the score in the range, respectively.

Evaluation Criterion

Table 2 gives the scoring principles for evaluating the comprehensive performance of frequency modulation:

Considering that the limit value of power system under-frequency load shedding is 0.5Hz, the lowest frequency limit in the table is set to 0.5 Hz; In the case of limit wind power permeability (0.5), the steady frequency of primary frequency modulation is 0.6 Hz under the same disturbance, so 0.6 Hz is set as the upper limit of steady frequency value. Because there is no compensation in the primary frequency modulation market at present in China when the total benefit-cost ratio of primary frequency modulation in power system is greater than or equal to 1, the score is the highest, and vice versa, the score decreases.

SIMULATION ANALYSIS

Simulation Parameters

The method described in this paper is based on the windows10 64bit operating system, and the relevant programs are written using matlab 2018b software, Visio2013 is used for flowchart drawing, and Origin2018 software is used for waveform drawing. with the load set to 1000 MW, the wind farm rated power of 200 MW, and the load fluctuation of 100 MW (0.1p.u).

Simulation Results With Different Control Strategies

First of all, it is necessary to verify whether the configuration of the wind-storage system has a positive effect on power system frequency modulation。When adopting the optimal control strategy, perform the following **Figure 11** simulation analysis:

The results prove that the configuration of wind/storage system is conducive to power system frequency modulation. **Table 3** shows the specific values of the impact of the configuration of the wind storage system on frequency, including steady-state frequency deviation and maximum frequency deviation.

With the addition of wind storage system, the lowest frequency is increased by 0.22 Hz and the steady frequency is increased by 0.044 Hz.

Contribution of Frequency Modulation Resources Under Different Control Strategies

The following is an analysis of two types of frequency modulation resources, including energy storage systems and wind farm.

1) Energy storage system output

The primary frequency modulation output of the energy storage system under the same disturbance is simulated using parallel, serial and optimal control strategies. The simulation results are shown in the following **Figure 12**.

In the process of traditional frequency modulation resource startup, the energy storage system responds quickly to frequency changes after disturbances occur in the power system. The energy storage output rises rapidly from 0 to the maximum in 0.3 s. The maximum energy storage output is 0.03 p.u under parallel control, 0.023 p.u under serial control and 0.03 p.u under optimal control. Therefore, parallel control and optimal control of the energy storage system can provide greater energy support at the early stage of disturbance occurrence and raise the frequency to the lowest point.

The use of energy storage resources in parallel control is stable at 0.015 p.u., the series control is almost 0, and the optimal control is between the two, stable at 0.0047 p.u. The optimized control of the

TABLE 2 | Score table of frequency regulation effect.

Maximum deviation	**≤0.2**	**0.2~0.3**	**0.3~0.4**	**0.4~0.5**	**≥0.5**	
Score	**10**	**8~10**	**6~8**	**4~6**	**≤3**	
Steady deviation	≤0.2	0.2~0.25	0.25~0.3	0.3~0.35	0.35~0.4	0.4
Score	10	8~10	6~8	4~6	2~4	<2
Cost	≤P	P~1.2P	1.2P~1.4P	1.4P~1.6P	1.6P~1.8P	≥1.8P
Score	10	8~10	6~8	4~6	2~4	≤2

TABLE 3 | Frequency deviation with/without wind power and ESS.

Data type	**Maximum deviation (Hz)**	**Steady deviation (Hz)**
With wind-storage system	−0.425	−0.205
Without wind-storage system	−0.647	−0.249

TABLE 4 | Frequency deviation comparison.

Control strategy	**Maximum deviation (Hz)**	**Steady deviation (Hz)**
Parallel control	−0.387	−0.187
Serial control	−0.442	−0.241
Optimize control	−0.401	−0.205

energy storage output power is small, that is, the use of energy storage resources is small, and it can provide backup capacity for the next frequency modulation work.

2) Wind farm output

Wind farms are an important part of the frequency modulation resources of power systems. The control strategy should consider improving the frequency modulation performance of wind farms. The following **Figure 13** is an analysis of the wind farm frequency modulation capabilities of three different control strategies.

In the start-up stage of wind turbine, the virtual inertia response of wind farm under each control strategy releases the kinetic energy of wind turbine rotor within 0.1 s. This will delay the fast frequency drop of power system, and each control strategy has little influence on this process.

In the process of pitch control, because wind power takes on different tasks in different control strategies, the control effect of the control strategy is reflected in the process of pitch output. Serial control mainly uses wind power as the backup energy for ESS, so the maximum output power of wind power is 0.024 p. u. In parallel control, wind power and energy storage work in parallel mode, so the output power of wind power is smaller than 0.017 p. u., and the optimal control strategy is 0.021p.u. between the above two. This proves that the optimized control strategy can reasonably use the capacity of wind power frequency modulation and reduce the amount of energy storage action.

Frequency Modulation Effect Comparison

The following **Supplementary Figure S1** is a simulation analysis of the frequency modulation effects of the three control strategies using Simulink.

Table 4 is the frequency modulation effect data of three control strategies, including maximum frequency deviation and steady-state frequency deviation.

It can be drawn from the table above that the maximum frequency deviation and the steady-state frequency deviation of the optimized control strategy are both between serial control and parallel control, and are superior to serial control.

Generally speaking, the optimal control strategy can provide effective support for the power system by utilizing the fast response characteristics of the energy storage system in the start-up stage of traditional units and wind power. After the start-up of the unit, on the premise of maximizing the frequency modulation capability of the traditional unit, the energy storage capacity is reduced and the economy of frequency modulation is guaranteed.

Cost Analysis Under Different Control Strategies

Taking the lithium batteries which are widely used in frequency modulation of power system as the research object, the economy of lithium batteries under three control strategies is analyzed. The simulation parameters are shown in the following **Table 5**.

There are no compensation measures for battery energy storage participating in primary frequency modulation of power grid (Chen et al., 2016). But battery energy storage can be recycled. For example, lithium batteries can recycle non-ferrous metals for secondary use

TABLE 5 | Economy parameters of frequency regulation.

Parameter name	**Recovery cost**	**Abandoned wind income**	**Unit power price**	**Unit capacity price**	**Time (s)**
Parameter values	4,046 $/t	80 $/MWh	738,462 $/MW	215,385 $/MWh	30

TABLE 6 | Cost comparison under different control strategies.

Control strategy	Profit ($)	Cost ($)
Parallel Control	1,428,154	5,058,277
Serial Control	1,026,262	3,687,015
Optimize Control	1,177,108	4,449,600

TABLE 7 | Scoring table for different control strategies.

Control strategy	Lowest frequency score	Frequency steady score	Cost score	Total score
Parallel control	7.2	10	4.255	6.427
Serial control	5.95	9.35	5.59	6.72
Optimize control	7.05	9.75	5.92	7.122

(Li et al). At the same time, the use of energy storage systems can also reduce wind curtailment. **Table 6** compares the costs and profits of energy storage systems.

From the above data, it can be concluded that the cost of the parallel control strategy under the same interference is the highest. Optimal control reduces the energy storage workload after the traditional frequency modulation resources are started, so the economy is better. Serial control has lower revenue due to less initial power and capacity.

According to the evaluation method proposed in Chapter 4, the three control strategies are scored and compared. The scores are shown in **Table 7**.

According to the results in the above table, the overall score of optimized control is higher than that of serial control and parallel control, which proves that the overall performance of optimized control is higher than that of serial control and parallel control after a comprehensive analysis of the economy and frequency modulation effect.

CONCLUSION

Aiming at the control strategy of large-scale wind storage system participating in power system primary frequency modulation, this paper made the following work:

In this paper, the serial and parallel control modes of ESS and wind turbine are studied based on the traditional frequency modulation mode of power system. Considering the economy and frequency modulation effect, an optimal control strategy based on serial and parallel of wind-storage system is proposed, and the objective function of the optimal control strategy is established. And the control variable method is used to optimize the relevant variables in the optimization strategy.

The comprehensive evaluation method of wind storage combined system participating in primary frequency regulation of power grid is studied. Considering that the current primary frequency modulation evaluation method cannot meet the requirement of paying equal attention to both the effect of frequency modulation and the economy of frequency modulation in the power grid. Considering the effect of frequency modulation under different control strategies and the economic factors of wind storage combined system participating in primary frequency modulation, a comprehensive evaluation method of primary frequency modulation are designed.

In the analysis part of the calculation example, the same interference is added to the three different control strategies, and the frequency modulation effect is analyzed using the simulation system. The results show that the optimized control reduces the maximum frequency deviation by 0.041 Hz and the steady-state frequency deviation by 0.036 Hz than the serial control. Compared with the parallel control strategy, the rated power is reduced by 0.7 MW and the rated capacity is reduced by 0.462 MWh.

According to the proposed evaluation method, the comprehensive frequency modulation effect scores of the three control strategies are evaluated. The results show that the optimal control strategy proposed in this paper scores 7.122 points, which is higher than 6.72 points for serial control and 6.427 points for parallel control. This proves that the overall performance of optimized control is higher than that of serial control and parallel control after a comprehensive analysis of the economy and frequency modulation effect.

OUTLOOK

This paper optimizes the parallel and serial control in the traditional frequency modulation method of wind storage system, and puts forward the optimal control strategy of this paper, and finally achieved certain results. At the same time, this paper still has some areas that can be improved. For example, the effect of the optimal control strategy proposed in this paper may not be better than the serial control strategy and the parallel control strategy under certain conditions. The optimal control strategy is the optimal method proposed after comprehensively considering the cost of energy storage and the effect of frequency modulation. It may not be applicable in some occasions where the accuracy of frequency modulation needs to be improved (while the cost of frequency modulation is allowed to be ignored). In fact, the cost of the current energy storage system is still high, so its economy is still a very important indicator in the power system. If the cost of the energy storage system can be significantly reduced in the

future, then this strategy still has room for continuous improvement.

DATA AVAILABILITY STATEMENT

The original contributions presented in the study are included in the article/**Supplementary Material**, further inquiries can be directed to the corresponding author.

AUTHOR CONTRIBUTIONS

CL: Conceptualization, Methodology, Writing- Original draft preparation. ZZ: Writing- Original draft preparation. JL: Methodology. YM: Data curation. JZ: Translation and Validation.

FUNDING

This work was supported in part by Joint Foundation of Natural Science Foundation of Jilin Province (No. 2020122352JC) and the National Natural Science Foundation of China (No. U1766204).

SUPPLEMENTARY MATERIAL

The Supplementary Material for this article can be found online at: https://www.frontiersin.org/articles/10.3389/fenrg.2021.739439/full#supplementary-material

SUPPLEMENTARY FIGURE S1 | Comparison chart of frequency modulation effect.

REFERENCES

Annamraju, A., and Nandiraju, S. (2019). Robust Frequency Control in a Renewable Penetrated Power System: an Adaptive Fractional Order-Fuzzy Approach. *Prot. Control. Mod. Power Syst.* 4 (4), 181–195. doi:10.1186/s41601-019-0130-8

Ayyarao, T. S. L. V., and Ayyarao, V. (2019). Modified Vector Controlled DFIG Wind Energy System Based on Barrier Function Adaptive Sliding Mode Control. *Prot. Control. Mod. Power Syst.* 4 (4), 34–41. doi:10.1186/s41601-019-0119-3

Chen, Dayu., Zhang, Lizi., and Wang, Liguo. (2016). Control Strategy of Energy System for Frequency Regulation and Evaluation of Investment Income. *Mod. Electric Power* 33 (1), 80–86. doi:10.19725/j.cnki.1007-2322.2016.01.013

Dang, J., Seuss, J., Suneja, L., and Harley, R. G. (2014). SoC Feedback Control for Wind and ESS Hybrid Power System Frequency Regulation. *IEEE J. Emerg. Sel. Top. Power Electron.* 2 (1), 79–86. doi:10.1109/jestpe.2013.2289991

Hu, Zechun., Xia, Rui., and Wu, Linlin. (2016). Joint Operation Optimization of Wind-Storage Union with Energy Storage Participating Frequency Regulation. *Power Syst. Tech.* 40 (08), 2251–2257. doi:10.13335/j.1000-3673.pst.2016.08.001

Hu, Zechun., Xu, X. I. E., and Zhang, Fang. (2014). Research on Automatic Generation Control Strategy Incorporating Energy Storage Resources. *Proc. CSEE* 34 (29), 5080–5087. doi:10.13334/j.0258-8013.pcsee.2014.29.009

Jing, L. I., Fang, Yong., and Song, Jiahua. (2005). Research on Subsection and Layer Control Strategy of Doublyfed Variable Speed Wind Turbine. *Power Syst. Tech.* 29 (9), 15–21. doi:10.13335/j.1000-3673.pst.2005.09.004

Kundur, Prabha. (2001). *Power System Stability and Control*. Beijing: China Electric Power Press.

Li, J., Fu, Y., Li, C., Li, J., Xing, Z., and Ma, T. (2021). Improving Wind Power Integration by Regenerative Electric Boiler and Battery Energy Storage Device. *Int. J. Electr. Power Energ. Syst.* 131 (131), 107039. doi:10.1016/j.ijepes.2021.107039

Li, Jianbo., Zheng, X. U., and Ji, Zhongguang. An Overview on the Current Technologies of Recycling Spent Lithium-Ion Bat-Teries. *Chin. J. Rare Met.* 43 (02), 201–212. doi:10.13373/j.cnki.cjrm.xy17060021

Li, Jianlin., Ma, Huimeng., and Yuan, Xiaodong. (2017). Overview on Key Applied Technologies of Large-Scale Distributed Energy Storage. *Power Syst. Tech.* 41 (10), 3365–3375. doi:10.13335/j.1000-3673.pst.2017.1101

Li, Junhui., Feng, Xichao., Yan, Gangui., Ge, Y., Li, D., and Fu, Y. (2018). Survey on Frequency Regulation Technology in High Wind Penetration Power System. *Power Syst. Prot. Control.* 46, 163–170. doi:10.7667/PSPC170002

Luo, F., Meng, K., Dong, Z. Y., Zheng, Y., Chen, Y., and Wong, K. P. (2015). Coordinated Operational Planning for Wind Farm with Battery Energy Storage System. *IEEE Trans. Sustain. Energ.* 6 (1), 253–262. doi:10.1109/tste.2014.2367550

Miao, Fufeng., Tang, Xisheng., and Qi, Zhiping. (2015). Analysis of Frequency Characteristics of Power System Based on Wind Farm-Energy Storage Combined Frequency Regulation. *High Voltage Eng.* 41 (07), 2209–2216.

Muyeen, S. M., Hasanien, H. M., and Tamura, J. (2012). Reduction of Frequency Fluctuation for Wind Farm Connected Power Systems by an Adaptive Artificial Neural Network Controlled Energy Capacitor System. *IET Renew. Power Gener.* 6 (4), 226. doi:10.1049/iet-rpg.2010.0126

Pandzic, H., and Bobanac, V. (2019). An Accurate Charging Model of Battery Energy Storage. *IEEE Trans. Power Syst.* 34 (2), 1416–1426. doi:10.1109/TPWRS.2018.2876466

Peng, L. I., Dou, Pengchong., Li, Yuwei., and Fengquan, Z. (2015). Application of Microgrid Technology in Active Distribution Network. *Electric Power Automation Equipment* 35 (4), 8–16. doi:10.16081/j.issn.1006-6047.2015.04.002

Ramtharan, G., Jenkins, N., and Ekanayake, J. B. (2007). Frequency Support from Doubly Fed Induction Generator Wind Turbines. *IET Renew. Power Gener.* 1 (1), 3–0. doi:10.1049/iet-rpg:20060019

Shen, Guanye., Chen, L. I., and Xu, Bingliang. (2018). Economic Allocation for Energy Storage System Considering Wind Power. *J. Northeast Electric Power Univ.* 38 (04), 27–34.

Sun, Bohao., Tang, Yong., and Lin, Y. E. (2019). Integrated Frequency Control Strategy for Wind Power Cluster with Mul-Tiple Temporal-Spatial Scale Coordination Based on H-DMPC. *Proc. CSEE* 39 (1), 155–167. doi:10.1109/tec.2015.2476827

Sun, Yi., Li, Zekun., and Liu, Di. (2018). An Optimization Control Strategy for Intelligent UFLS Using Dynamically Aggregated Controllable Loads. *Proc. CSEE* 38 (7), 1913–1921+2207. doi:10.13334/j.0258-8013.pcsee.1707407

Tan, Y., Meegahapola, L., and Muttaqi, K. M. (2016). A Suboptimal Power-Point-Tracking-Based Primary Frequency Response Strategy for DFIGs in Hybrid Remote Area Power Supply Systems. *IEEE Trans. Energ. Convers.* 31 (1), 93–105. doi:10.1109/tec.2015.2476827

Tariq, M., Maswood, A. I., Gajanayake, C. J., and Gupta, A. K. (2018). Modeling and Integration of a Lithium-Ion Battery Energy Storage System with the More Electric Aircraft 270 V DC Power Distribution Architecture. *IEEE Access* 6, 41785–41802. doi:10.1109/ACCESS.2018.2860679

Teninge, A., Jecu, C., Roye, D., Bacha, S., Duval, J., and Belhomme, R. (2009). Contribution to Frequency Control through Wind Turbine Inertial Energy Storage. *IET Renew. Power Gener.* 3 (3), 358 doi:10.1049/iet-rpg.2008.0078

Wind power grid-connected operation in the first three quarters (2019). *Wind Power Grid-Connected Operation in the First Three Quarters of 2019*. Beijing: National Energy Administration.

Wu, Jun., Lu, Zongxiang., Qiao, Ying., et al. (2018). Optimal Operation of Wind Farm with Hybrid Storage Devices Considering Efficiency Characteristics of Dynamic Charging and Discharging. *Automation Electric Power Syst.* 42 (11), 41–47. doi:10.7500/AEPS20180326002

Wu, Zishuang., Yu, Jilai., and Peng, Xiyun. (2013). DFIG's Frequency Regulation Method Only for High Wind Speed with Subop-Timal Power Tracking. *Trans. China Electrotechnical Soc.* 28 (05), 112–119.

Xing, Pengxiang., Shi, Qiaoming., Wang, Gang., Fu, L., Wang, Y., and Wu, Y. (2018). Response Characteristics and Mechanism Analysis about Virtual Inertia

Control of Wind Generators. *High Voltage Eng.* 44 (04), 1302–1310. doi:10.13336/j.1003-6520.hve.20180329033

Yan, Gangui., Wang, Yibo., and Cheng, Z. H. O. N. G. (2016). Frequency Control Strategy for Wind Storage Combined System. *Electric Power Construction* 37 (12), 55–60. doi:10.3969/j.issn.1000-7229.2016.12.007

Yan, Gangui., and Zhao, Weizhe. (2018). ZHANG Liyu Research on Integrated Control of Deloading Frequency Regulation for Variable Speed and Variable Pitch Angle Wind Turbines. *J. Northeast Electric Power Univ.* 38 (05), 1–8.

Zertek, A., Verbic, G., and Pantos, M. (2012). A Novel Strategy for Variable-Speed Wind Turbines' Participation in Primary Frequency Control. *IEEE Trans. Sustain. Energ.* 3 (4), 791–799. doi:10.1109/tste.2012.2199773

Zhang, Xu., Chen, Yunlong., Yue, Shuai., Zha, X., and Zhang, D. (2018). Retrospect and Prospect of Research on Frequency Regulation Technol-Ogy of Power System by Wind Power. *Power Syst. Tech.* 42 (06), 1793–1803. doi:10.13335/j.1000-3673.pst.2018.0359

Zhao, Jingjing., Min, L. I., and He, Xinqin. (2019). Coordinated Control Strategy of Wind Power and Energy Storage in Frequency Regulation Based on Torque Limit Control. *Trans. China Electrotechnical Soc.* 34 (23), 4982–4990.

Zheng, Zhong., Yang, Zhenyong., and Li, Weihua. (2017). Analysis and Comparison of Primary Frequency Control Technology for Wind Power and thermal Power Unit. *Electric Power Automation Equipment* 37 (12), 92–101. doi:10.16081/j.issn.1006-6047.2017.12.013

Conflict of Interest: Author ZZ was employed by the company Wenzhou Power Supply Company, State Grid Zhejiang Electric Power Company. Author YM was employed by the company Zaozhuang Power Supply Company, State Grid Shandong Electric Power Company. Author JZ was employed by the company Jilin Province Electric Power Company of National Grid.

The remaining authors declare that the research was conducted in the absence of any commercial or financial relationships that could be construed as a potential conflict of interest.

Publisher's Note: All claims expressed in this article are solely those of the authors and do not necessarily represent those of their affiliated organizations, or those of the publisher, the editors and the reviewers. Any product that may be evaluated in this article, or claim that may be made by its manufacturer, is not guaranteed or endorsed by the publisher.

Copyright © 2021 Li, Zhang, Li, Ma and Zou. This is an open-access article distributed under the terms of the Creative Commons Attribution License (CC BY). The use, distribution or reproduction in other forums is permitted, provided the original author(s) and the copyright owner(s) are credited and that the original publication in this journal is cited, in accordance with accepted academic practice. No use, distribution or reproduction is permitted which does not comply with these terms.

frontiers in Energy Research

BRIEF RESEARCH REPORT
published: 28 September 2021
doi: 10.3389/fenrg.2021.753718

Nonlinear Maximum Power Point Tracking Control of Wind Turbine Based on Two-Mass Model Without Anemometer

*Jian Chen *, Qun Lu, Libing Chen, Xiaohui Duan, Boping Yang, Wenyong Duan and Lanhong Zhang*

School of Electrical Engineering, Yancheng Institute of Technology, Yancheng, China

A nonlinear control without using anemometer is proposed to achieve the maximum power of the wind turbine (WT) based on two-mass model in this paper. To track the maximum power points, the optimal tip speed ratio control strategy requiring to know the optimal rotor speed of the WT (ORS) is employed. To achieve the ORS, a torque observer is designed to estimate the aerodynamic torque, then the ORS can be obtained by the corresponding calculations based on the estimated torque. Due to the high nonlinearities of the WT and time-varying wind speed, a nonlinear control based on feedback linearization control (FLC) is adopted to track the ORS. In the FLC, the WT is linearized firstly, then the rotor speed controller is designed via linear control technique. The effectiveness of the proposed control strategy is verified by simulation studies. The simulation results show that, compared with the traditional PI control based on torque estimation and FLC based on wind speed estimation, the proposed control strategy provides better dynamic performances and higher power conversion efficiency.

Keywords: maximum power point tracking, torque estimation, feedback linearization control, two-mass model wind turbine, high-gain observer

OPEN ACCESS

Edited by:
Bo Yang,
Kunming University of Science and Technology, China

Reviewed by:
Wang Yao-Wei,
China University of Geosciences Wuhan, China
Xiang Wu,
Zhejiang University of Technology, China
Yang Li,
Northeast Electric Power University, China

****Correspondence:***
Jian Chen
cjycit@163.com

Specialty section:
This article was submitted to Smart Grids, a section of the journal Frontiers in Energy Research

Received: *05 August 2021*
Accepted: *13 September 2021*
Published: *28 September 2021*

Citation:
Chen J, Lu Q, Chen L, Duan X, Yang B, Duan W and Zhang L (2021) Nonlinear Maximum Power Point Tracking Control of Wind Turbine Based on Two-Mass Model Without Anemometer. Front. Energy Res. 9:753718. doi: 10.3389/fenrg.2021.753718

1 INTRODUCTION

With the increasingly serious energy crisis and environmental problems, renewable clean energy such as wind energy, solar energy and hydrogen energy have attracted more and more attention (Liu et al., 2020; Peng et al., 2020; Sun et al., 2020; Li et al., 2021). Among them, due to large reserves and high conversion efficiency, the total installed capacity of wind turbine (WT) is much higher than that of other renewable energy sources (Wang et al., 2020; Xiong et al., 2021). In order to reduce the relatively high operation cost, it is necessary to improve the conversion efficiency of wind power system. More than 50% energy of a typical wind turbine is captured in the operation area below the rated wind speed (Huang et al., 2015). Therefore, it is necessary to effectively improve the efficiency of wind energy conversion through the maximum power point tracking (MPPT) control strategy in this operation area (Yang et al., 2016).

The essence of the MPPT control strategy is to make the WT always operate under the optimal tip speed ratio (OTSR) (Yang et al., 2018). The traditional MPPT control strategies mainly include hill climb searching (HCS) (Youssef et al., 2019), power signal feedback (PSF) (also known as optimal torque method) (Zhang et al., 2019) and OTSR (Chen et al., 2019b). However, the general MPPT control method using HCS is mainly suitable for small and medium-sized WTs, not for large inertia

WTs. The PSF control method usually needs offline training, real-time wind speed information statistics and so on. Compared with the MPPT control strategy of HCS and PSF, the MPPT control strategy based on OTSR directly adjusts the speed according to the speed error, which can obtain faster response speed (Mousa et al., 2021). The traditional OTSR needs to obtain the optimal rotor speed (ORS) through the real-time wind speed. However, in practical application, the wind speed measured by an anemometer cannot accurately represent the effective wind speed acting on the WT. Therefore, the acquisition of accurate optimal rotor speed is one of the important factors for the efficient implementation of MPPT control based on OTSR. In order to achieve the ORS, a Newton-Rafson iteration method (Mérida et al., 2014), a method based on adaptive neuro fuzzy inference system (Golnary and Moradi, 2018), and a non-standard extended Kalman filter-based estimator (Song et al., 2017) are adopted to obtain the estimated wind speed. In this paper, in order to obtain the accurate ORS, a high-gain observer investigated in Chen et al. (2014), Chen et al. (2019b), and Lu et al. (2020) is employed to estimate the aerodynamic torque accurately. Then, the accurate ORS can be obtained based on the estimated aerodynamic torque. The high-gain observer has been successfully used in power system (Chen et al., 2014) and permanent magnet synchronous motor (Chen et al., 2019a), and provides satisfactory estimation ability and strong robustness.

In order to obtain the maximum wind energy from time-varying wind speed, effective control methods need to be adopted after obtaining the accurate ORS. The traditional PI control is widely used in industry because of its simple design and high reliability. However, due to the high nonlinearities of WT and time-varying wind speed, the traditional PI control designed based on a certain operating point cannot provide satisfactory dynamic performance, which reduces the wind energy conversion efficiency. To overcome the shortcomings of traditional PI control and improve wind energy conversion efficiency, a feedback linearization control (FLC) has successfully realized the maximum wind energy capture of permanent magnet synchronous generator (Chen et al., 2019b). Meanwhile, FLC techniques have been widely used in power system, permanent magnet synchronous motor and power electronics. In this paper, in order to obtain the maximum wind energy capture of WT based on two-mass model and avoid using anemometer, the FLC based MPPT control strategy and aerodynamic torque observer will be proposed. Firstly, the aerodynamic torque observer based on the high-gain observer is designed to obtain the accurate aerodynamic torque, so as to obtain the accurate ORS. Then, the WT with two-mass model is transformed into an equivalent linear system. Finally, the ORS is tracked by the designed linear speed controller. In the simulation studies, in order to verify the effectiveness of the proposed control strategy, it will compare with the traditional PI control and FLC based on wind speed estimation (FLC-WE).

The rest of this paper is organized as follows. In **Section 2**, the model of WT and problem formulation are briefly recalled. Meanwhile, the design of aerodynamic torque observer and wind speed estimation technique are presented in this section. The design of the proposed MPPT control scheme is presented in **Section 3**. In **Section 4**, simulation studies are conducted to verify the performances of the proposed FLC based on torque estimation (FLC-TE), and compared with the traditional PI control and FLC-WE. Finally, conclusions are drawn in **Section 5**.

2 TWO-MASS MODEL OF WIND TURBINE AND PROBLEM FORMULATION

2.1 Two-Mass Model of Wind Turbine

The state-space model of the WT (Boukhezzar and Siguerdidjane, 2011) can be obtained as

$$\dot{x} = f(x) + g(x)u = \begin{bmatrix} f_1(x) \\ f_2(x) \\ f_3(x) \end{bmatrix} + \begin{bmatrix} g_{11} \\ g_{21} \\ g_{31} \end{bmatrix} u \tag{1}$$

where

$$f(x) = \begin{bmatrix} f_1(x) \\ f_2(x) \\ f_3(x) \end{bmatrix} = \begin{bmatrix} a_{11} & a_{12} & a_{13} & a_{14} \\ a_{21} & a_{22} & a_{23} & a_{24} \\ a_{31} & a_{32} & a_{33} & a_{34} \end{bmatrix},$$

$$g_{11} = 0, \quad g_{21} = -\frac{1}{J_g}, \quad g_{31} = \frac{D_s}{N_g J_g},$$

$$a_{11} = -\frac{K_r}{J_r}, \quad a_{21} = 0, \quad a_{31} = K_s - \frac{D_s K_r}{J_r},$$

$$a_{12} = 0, \quad a_{22} = -\frac{K_g}{J_g}, \quad a_{32} = -\frac{1}{N_g}\left(K_s - \frac{D_s K_g}{J_g}\right),$$

$$a_{13} = -\frac{1}{J_r}, \qquad a_{23} = \frac{1}{N_g J_g}, \qquad a_{33} = -D_s\left(\frac{J_r + N_g^2 J_g}{N_g^2 J_g J_r}\right),$$

$$a_{14} = \frac{1}{J_r}, \quad a_{24} = 0, \quad a_{34} = \frac{D_s}{J_r},$$

$$x = [\omega_r \quad \omega_g \quad T_{ls}]^T, \quad u = T_g, \quad y = h(x) = \omega_r,$$

where, $x \in R^3$, $u \in R^1$ and $y \in R^1$ are state vector, input vector and output vector, respectively; $f(x)$, $g(x)$ and $h(x)$ are smooth vector fields. J_g is the generator inertia, D_s is the low-speed shaft stiffness, N_g is the gearbox ratio, K_r is the rotor eternal damping, K_g is the generator eternal damping, K_s is the low-speed shaft damping, J_r is the rotor inertia, ω_r is the rotor speed, ω_g is the generator speed, T_{ls} is the low-speed shaft torque, and T_g is the generator torque. It comes then that

$$J_t \omega_r = T_a - K_t \omega_r - T_g \tag{2}$$

where $J_t = J_r + N_g^2 J_g$ and $K_t = K_r + N_g^2 K_g$.

2.2 MPPT Control Strategy Based on OTSR and Aerodynamic Torque Estimation Technique

In this paper, an MPPT controller based on OTSR is used to capture the maximum wind power. To achieve this objective, the maximum power coefficient $C_p$max should be achieved. It is

obtained when the TSR λ keeps at its optimal value λ_{opt}. λ_{opt} can be achieved if the rotor speed ω_r can track its optimal reference ω_{ref} (ORS), which can be calculated as

$$\omega_{ref} = \frac{\lambda_{opt} V}{R} \tag{3}$$

In **Eq. 3**, the ω_{ref} (ORS) has a linear relationship with wind speed when the λ_{opt} is constant. However, in practical application, the effective wind speed acting on the WT cannot accurately obtained (Ren et al., 2016). To obtain the wind speed, it can be estimated by using the Newton-Raphson method (Ren et al., 2016). In this paper, to achieve the ORS, the aerodynamic torque is estimated by a designed torque observer firstly. The aerodynamic torque observer is designed based on the high-gain observer theory mentioned in Chen et al. (2014), Chen et al. (2019a), and Chen et al. (2019b). In Chen et al. (2014), Chen et al. (2019a), and Chen et al. (2019b), the high-gain observer theory has successfully applied in power system, permanent magnet synchronous generator and permanent magnet synchronous motor, which provides satisfactory performance for perturbation estimation. The detailed design process of the observer can refer to the literature mentioned above. According to **Eq. 2** and high-gain observer theory, the aerodynamic torque observer is designed as follows. Carry out the input/output linearization of system (2)

$$\dot{y} = F_1(x) + B_1(x)u \tag{4}$$

where

$$F_1(x) = \frac{1}{J_t}(T_a - K_t \omega_r) \tag{5}$$

$$B_1(x) = -\frac{1}{J_t} \tag{6}$$

and the relative degree is $r_i = [1]$.

The following observer is designed to estimate the perturbation $\hat{F}_1(x)$:

$$S: \begin{cases} \dot{\hat{y}} = \hat{F}_1(x) + l_{11}(\omega_r - \hat{y}) + B_1(x)T_g \\ \dot{\hat{F}}_1(x) = l_{12}(\omega_r - \hat{y}) \end{cases} \tag{7}$$

where the gains are designed as $l_{ij} = \frac{\alpha_{ij}}{\epsilon_i^j}, i = 1, j = 1, r_i + 1$. ϵ_i is a scalar chosen to be within (0,1) for representing times of the time-dynamics between the observer and the real system, and parameters α_{ij}, $j = 1, \ldots, r_i + 1$, are chosen so that the roots of

$$s^{r_i+1} + \alpha_{i1} s^{r_i} + \cdots + \alpha_{ir_i} s + \alpha_{i(r_i+1)} = 0 \tag{8}$$

are in the open left-half complex plane.

According **Eq. 5** and the estimation of $F_1(x)$ obtained from designed observer (7), the aerodynamic torque can be estimated as

$$\hat{T}_a = J_t \hat{F}_1(x) + K_t \omega_r \tag{9}$$

The aerodynamic torque is expressed as

$$T_a = K_{opt} \omega_r^2,\ K_{opt} = \frac{1}{2}\rho\pi R^5 \frac{C_{pmax}}{\lambda_{opt}^3} \tag{10}$$

According to **Eq. 10**, the estimation of the ORS can be obtained as

$$\hat{\omega}_r = \left(\frac{\hat{T}_a}{K_{opt}}\right)^{\frac{1}{2}} \tag{11}$$

2.3 MPPT Control Strategy Based on OTSR and Wind Speed Estimation Technique

To achieve the effective wind speed and avoid using anemometer, the wind speed is estimated by using the Newton-Raphson method (Mérida et al., 2014; Ren et al., 2016).

The wind speed estimator is realized by minimizing the cost function $J(t, V)$

$$J(t,V) = (T_a(t) - f_a(V))^2 \tag{12}$$

$$f_a(V) = 0.5\rho\pi R^2 V^3 \frac{C_p(\beta,\lambda)}{\omega_r} \tag{13}$$

where $T_a(t)$ is the aerodynamic torque at time t, and $f_a(V)$ is the aerodynamic torque function of wind speed V.

The problem is equivalent to find the solution of

$$I(t,V) = J(t,V) = T_a(t) - 0.5\rho\pi R^2 V^3 \frac{C_p(\beta,\lambda)}{\omega_r} = 0 \tag{14}$$

From the partial derivative equation

$$\Delta T_a = \frac{\partial T_a}{\partial V} \Delta V \tag{15}$$

The iteration form of the estimator can be written as

$$\hat{V} = \Delta T_a \left(\frac{\partial T_a}{\partial V}\right)^{-1} \tag{16}$$

where

$$\frac{\partial T_a}{\partial V} = -\frac{3}{2}\rho\pi R^2 V^2 \frac{C_p(\beta,\lambda)}{\omega_r} - \frac{1}{2}\frac{\rho\pi R^2 V^3}{\omega_r}\frac{\partial C_p}{\partial V}$$

$$\frac{\partial C_p}{\partial V} = -\frac{0.22(178.5 - 1450\lambda_t + 5\beta)}{\omega_r R(\lambda + 0.08\beta)^2} e^{-12.5\lambda_t}$$

At time t, the iteration will be performed until

$$I(t,\hat{V}) = T_a(t) - f_a(\hat{V}) < \varepsilon \tag{17}$$

where ε is a small value. The estimation of wind speed at time t is then $\hat{V}$.

3 NONLINEAR MPPT CONTROLLER BASED ON FEEDBACK LINEARIZATION CONTROL TECHNIQUE

For system (1), choose the output of the system as $y = h(x) = \omega_r$ and control input $u = T_g$, we have

$$y^{(2)} = F_2(x) + B_2(x)u \tag{18}$$

where

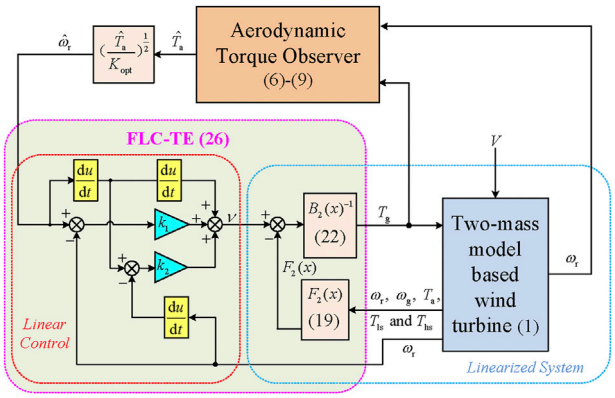


FIGURE 1 | The overall control block diagram of the proposed FLC-TE.

$$F_2(x) = \frac{\dot{T}_a}{J_r} - \frac{(K_r + a34J_r)}{J_r^2}T_a + \frac{(K_r^2 - a31J_r)}{J_r^2}\omega_r - \frac{a_{32}}{J_r}\omega_g + \frac{(K_r - a33J_r)}{J_r^2}T_{ls} \tag{19}$$

$$B_2(x) = -\frac{g_{31}}{J_r} \tag{20}$$

where $B_2(x) \neq 0$ for all nominal operation points.

The feedback linearization control of system (1) is obtained as

$$u = B_2(x)^{-1}(-F_2(x) + v) \tag{21}$$

$$B_2(x)^{-1} = -\frac{J_r}{g_{31}} \tag{22}$$

And the original system is linearized as

$$\ddot{y} = v \tag{23}$$

$$v = \ddot{y}_r + k_1(y_r - y) + k_2(\dot{y}_r - \dot{y}) \tag{24}$$

where, v is input of linear system, k_1 and k_2 are gains of linear controller, and $y_r = \hat{\omega}_r$ is the desired output reference. Define $e = y_r - y$ as track error, the error dynamic is

$$\ddot{e} + k_2\dot{e} + k_1 e = 0 \tag{25}$$

The final control law represented by physical variables is given as follows:

$$u = -\frac{J_r N_g J_g}{D_s}[-F_2(x) + k_1(y_r - y) + k_2(\dot{y}_r - \dot{y}) + \ddot{y}_r] \tag{26}$$

To clearly illustrate the principle of the proposed control strategy for the WT system, a overall control block diagram is shown in **Figure 1**.

4 SIMULATION RESULTS

In simulation studies, to verify the performance of the proposed FLC-TE, it compares with the traditional PI control and FLC-WE. The detailed parameters of the WT are given in Boukhezzar and Siguerdidjane (2011). The parameters of the designed observer are $\alpha_{11} = 3.2 \times 10^2$, $\alpha_{12} = 2.56 \times 10^4$, $\epsilon_1 = 0.02$. The controller parameters are $k_1 = 25$, $k_2 = 10$.

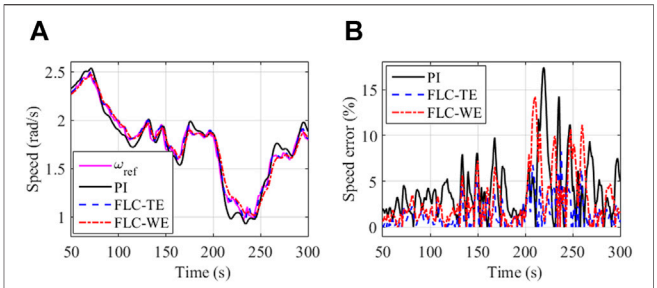


FIGURE 2 | Rotor speed response to random wind speed. **(A)** Rotor speed; **(B)** relative error of the rotor speed.

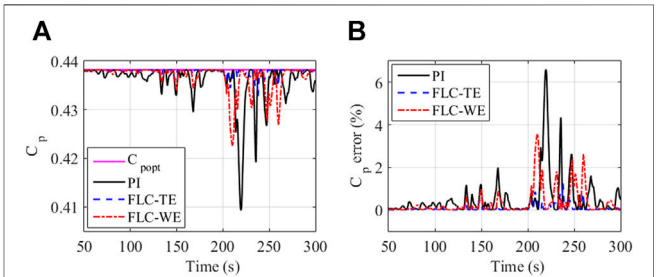


FIGURE 3 | Power coefficient response to random wind speed. **(A)** Power coefficient; **(B)** relative error of power coefficient.

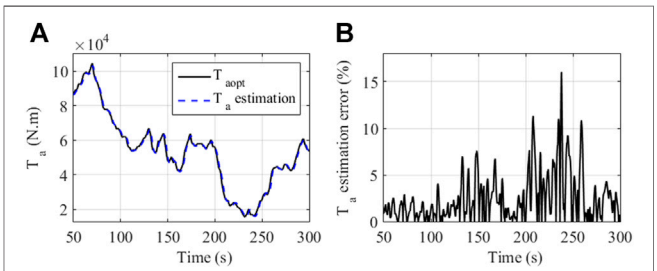


FIGURE 4 | Aerodynamic torque response to random wind speed. **(A)** Aerodynamic torque estimation; **(B)** relative error of aerodynamic torque estimation.

It can be seen from **Figure 2** that, the FLC-TE achieves the best tracking performance among these three controllers. The worst performance is obtained by the traditional PI control. It is because that the PI control designed based one operation point cannot provide optimal performance during time-varying operation points. The FLC-WE achieve a worse tracking performance than the FLC-TE. Although the Newton-Raphson method can be used to estimate wind speed, it requires accurate system model. The inaccurate system model may result in large estimation error. The C_p cannot maintain around its maximum value C_{pmax} when

the rotor cannot be well tracked. **Figure 3** shows that the FLC-TE and PI achieve the highest and lowest efficiency, respectively. In **Figure 4**, the aerodynamic torque T_a is well estimated by the designed observer in most of the time, which is always around its optimal value $T_{aopt} = K_{opt}\omega_{ref}^2$. When the wind speed varies rapidly, it exists the estimation error of T_a. This is mainly due to the WT has large inertia, which cannot immediately respond to the variation of wind speed.

5 CONCLUSION

In this paper, a FLC-TE has been proposed to relaize the MPPT control of the WT. In the proposed control strategy, a high-gain observer is designed to estimate aerodynamic torque, then the ORS can be obtained through the estimated aerodynamic torque. The FLC technique is employed to linearize the WT system, then a linear speed controller is designed for rotor speed regulation. Among the traditional PI, FLC-WE and FLC-TE controllers, the proposed FLC-TE achieves the best dynamic performance and highest efficiency. In the future work, a nonlinear adaptive control based on perturbation estimation technique will be investigated to improve the robustness of the FLC-TE against parameter uncertainties and disturbances.

DATA AVAILABILITY STATEMENT

The raw data supporting the conclusions of this article will be made available by the authors, without undue reservation.

AUTHOR CONTRIBUTIONS

JC, QL, LC, and XD contributed to conception and controller design of the study and wrote sections of the manuscript. JC performed the analysis of the simulation results and wrote the first draft of the manuscript. LZ provides guidance. BY and WD proof reading. All authors contributed to manuscript revision, read, and approved the submitted version.

FUNDING

This research was supported by the Natural Science Foundation of the Jiangsu Higher Education Institutions of China (Grant NO.19KJB470036) and National Natural Science Foundation of China under Grant NO.62003292.

REFERENCES

Boukhezzar, B., and Siguerdidjane, H. (2011). Nonlinear Control of a Variable-Speed Wind Turbine Using a Two-Mass Model. *IEEE Trans. Energ. Convers.* 26, 149–162. doi:10.1109/TEC.2010.2090155

Chen, J., Jiang, L., Yao, W., and Wu, Q. H. (2014). Perturbation Estimation Based Nonlinear Adaptive Control of a Full-Rated Converter Wind Turbine for Fault Ride-Through Capability Enhancement. *IEEE Trans. Power Syst.* 29, 2733–2743. doi:10.1109/TPWRS.2014.2313813

Chen, J., Yao, W., Ren, Y., Wang, R., Zhang, L., and Jiang, L. (2019a). Nonlinear Adaptive Speed Control of a Permanent Magnet Synchronous Motor: A Perturbation Estimation Approach. *Control. Eng. Pract.* 85, 163–175. doi:10.1016/j.conengprac.2019.01.019

Chen, J., Yao, W., Zhang, C.-K., Ren, Y., and Jiang, L. (2019b). Design of Robust Mppt Controller for Grid-Connected Pmsg-Based Wind Turbine via Perturbation Observation Based Nonlinear Adaptive Control. *Renew. Energ.* 134, 478–495. doi:10.1016/j.renene.2018.11.048

Golnary, F., and Moradi, H. (2018). Design and Comparison of Quasi Continuous Sliding Mode Control with Feedback Linearization for a Large Scale Wind Turbine with Wind Speed Estimation. *Renew. Energ.* 127, 495–508. doi:10.1016/j.renene.2018.04.081

Huang, C., Li, F., and Jin, Z. (2015). Maximum Power point Tracking Strategy for Large-Scale Wind Generation Systems Considering Wind Turbine Dynamics. *IEEE Trans. Ind. Electron.* 62, 2530–2539. doi:10.1109/TIE.2015.2395384

Li, Y., Wang, C., Li, G., and Chen, C. (2021). Optimal Scheduling of Integrated Demand Response-Enabled Integrated Energy Systems with Uncertain Renewable Generations: A Stackelberg Game Approach. *Energ. Convers. Manag.* 235, 113996. doi:10.1016/j.enconman.2021.113996

Liu, J., Yao, W., Wen, J., Fang, J., Jiang, L., He, H., et al. (2020). Impact of Power Grid Strength and Pll Parameters on Stability of Grid-Connected Dfig Wind Farm. *IEEE Trans. Sustain. Energ.* 11, 545–557. doi:10.1109/TSTE.2019.2897596

Lu, Q., Zhang, D., Ye, W., Fan, J., Liu, S., and Su, C.-Y. (2020). Targeting Posture Control with Dynamic Obstacle Avoidance of Constrained Uncertain Wheeled mobile Robots Including Unknown Skidding and Slipping. *IEEE Trans. Syst. Man, Cybernetics: Syst. (Early Access)* , 1–10. doi:10.1109/tsmc.2019.2962732

Mérida, J., Aguilar, L. T., and Dávila, J. (2014). Analysis and Synthesis of Sliding Mode Control for Large Scale Variable Speed Wind Turbine for Power Optimization. *Renew. Energ.* 71, 715–728. doi:10.1016/j.renene.2014.06.030

Mousa, H. H. H., Youssef, A.-R., and Mohamed, E. E. M. (2021). State of the Art Perturb and Observe Mppt Algorithms Based Wind Energy Conversion Systems: A Technology Review. *Int. J. Electr. Power Energ. Syst.* 126, 106598. doi:10.1016/j.ijepes.2020.106598

Peng, X., Yao, W., Yan, C., Wen, J., and Cheng, S. (2020). Two-stage Variable Proportion Coefficient Based Frequency Support of Grid-Connected Dfig-Wts. *IEEE Trans. Power Syst.* 35, 962–974. doi:10.1109/TPWRS.2019.2943520

Ren, Y., Li, L., Brindley, J., and Jiang, L. (2016). Nonlinear Pi Control for Variable Pitch Wind Turbine. *Control. Eng. Pract.* 50, 84–94. doi:10.1016/j.conengprac.2016.02.004

Song, D., Yang, J., Cai, Z., Dong, M., Su, M., and Wang, Y. (2017). Wind Estimation with a Non-standard Extended Kalman Filter and its Application on Maximum Power Extraction for Variable Speed Wind Turbines. *Appl. Energ.* 190, 670–685. doi:10.1016/j.apenergy.2016.12.132

Sun, K., Yao, W., Fang, J., Ai, X., Wen, J., and Cheng, S. (2020). Impedance Modeling and Stability Analysis of Grid-Connected Dfig-Based Wind Farm with a Vsc-Hvdc. *IEEE J. Emerg. Sel. Top. Power Electron.* 8, 1375–1390. doi:10.1109/JESTPE.2019.2901747

Wang, Q., Yao, W., Fang, J., Ai, X., Wen, J., Yang, X., et al. (2020). Dynamic Modeling and Small Signal Stability Analysis of Distributed Photovoltaic Grid-Connected System with Large Scale of Panel Level Dc Optimizers. *Appl. Energ.* 259, 114132. doi:10.1016/j.apenergy.2019.114132

Xiong, Y., Yao, W., Wen, J., Lin, S., Ai, X., Fang, J., et al. (2020). Two-level Combined Control Scheme of Vsc-Mtdc Integrated Offshore Wind Farms for Onshore System Frequency Support. *IEEE Trans. Power Syst.* 36, 1. doi:10.1109/TPWRS.2020.2998579

Yang, B., Jiang, L., Wang, L., Yao, W., and Wu, Q. H. (2016). Nonlinear Maximum Power point Tracking Control and Modal Analysis of Dfig Based Wind Turbine. *Int. J. Electr. Power Energ. Syst.* 74, 429–436. doi:10.1016/j.ijepes.2015.07.036

Yang, B., Yu, T., Shu, H., Zhang, Y., Chen, J., Sang, Y., et al. (2018). Passivity-based Sliding-Mode Control Design for Optimal Power Extraction of a Pmsg Based Variable Speed Wind Turbine. *Renew. Energ.* 119, 577–589. doi:10.1016/j.renene.2017.12.047

Youssef, A.-R., Ali, A. I. M., Saeed, M. S. R., and Mohamed, E. E. M. (2019). Advanced Multi-Sector P&O Maximum Power point Tracking Technique for Wind Energy Conversion System. *Int. J. Electr. Power Energ. Syst.* 107, 89–97. doi:10.1016/j.ijepes.2018.10.034

Zhang, X., Zhang, Y., Hao, S., Wu, L., and Wei, W. (2019). An Improved Maximum Power point Tracking Method Based on Decreasing Torque Gain for Large Scale Wind Turbines at Low Wind Sites. *Electric Power Syst. Res.* 176, 105942. doi:10.1016/j.epsr.2019.105942

Conflict of Interest: The authors declare that the research was conducted in the absence of any commercial or financial relationships that could be construed as a potential conflict of interest.

Publisher's Note: All claims expressed in this article are solely those of the authors and do not necessarily represent those of their affiliated organizations, or those of the publisher, the editors and the reviewers. Any product that may be evaluated in this article, or claim that may be made by its manufacturer, is not guaranteed or endorsed by the publisher.

Copyright © 2021 Chen, Lu, Chen, Duan, Yang, Duan and Zhang. This is an open-access article distributed under the terms of the Creative Commons Attribution License (CC BY). The use, distribution or reproduction in other forums is permitted, provided the original author(s) and the copyright owner(s) are credited and that the original publication in this journal is cited, in accordance with accepted academic practice. No use, distribution or reproduction is permitted which does not comply with these terms.

frontiers in Energy Research

BRIEF RESEARCH REPORT
published: 28 September 2021
doi: 10.3389/fenrg.2021.763099

Temperature Control of Proton Exchange Membrane Fuel Cell Based on Machine Learning

Jiawen Li[1], *Yaping Li*[2] *and Tao Yu*[1]*

[1]College of Electric Power, South China University of Technology, Guangzhou, China, [2]China Electric Power Research Institute (Nanjing), Nanjing, China

In order to improve the proton exchange membrane fuel cell (PEMFC) working efficiency, we propose a deep-reinforcement-learning based PID controller for realizing optimal PEMFC stack temperature. For this purpose, we propose the Improved Twin Delayed Deep Deterministic Policy Gradient (TD3) algorithm, a tuner of the PID controller, which can adjust the coefficients of the controller in real time. This algorithm accelerates the learning speed of an agent by continuously changing the soft update parameters during the training process, thereby improving the training efficiency of the agent, and further reducing training costs and obtaining a robust strategy. The effectiveness of the control algorithm is verified through a simulation in which it is compared against a group of existing algorithms.

Keywords: proton exchange membrane fuel cell, twin delayed deep deterministic policy gradient algorithm, stack temperature, PID controller, robustness

OPEN ACCESS

Edited by:
Yaxing Ren,
University of Warwick,
United Kingdom

Reviewed by:
Du Gang,
North China Electric Power University, China
Yunzheng Zhao,
The University of Hong Kong, Hong Kong, SAR China
Chenhao Ren,
The University of Hong Kong, Hong Kong, SAR China

***Correspondence:**
Tao Yu
taoyu1@scut.edu.cn
eptaoyu1@163.com

Specialty section:
This article was submitted to Smart Grids, a section of the journal Frontiers in Energy Research

Received: *23 August 2021*
Accepted: *13 September 2021*
Published: *28 September 2021*

Citation:
Li J, Li Y and Yu T (2021) Temperature Control of Proton Exchange Membrane Fuel Cell Based on Machine Learning. Front. Energy Res. 9:763099. doi: 10.3389/fenrg.2021.763099

INTRODUCTION

The proton exchange membrane fuel cell (PEMFC) (Cheng and Yu, 2019a), as a high-efficiency energy conversion device, has a high hydrogen energy utilization rate, and is expected to become a widely used electric power source in the future (Cheng et al., 2018).

The PEMFC converts chemical energy into electrical energy. During this process, the remaining energy is dissipated as heat due to the limited conversion efficiency of the fuel cell (Cheng et al., 2020). In order to maintain the necessary temperature required for sustaining the reaction inside the fuel cell, two heat dissipation inputs are usually used: cooling water, and air. These inputs differ in terms of the increase in power generation with increasing heat load. If the heat is not dissipated timeously, the heat will accumulate in the stack and the temperature will become excessive, which in turn will have an adverse effect on the working performance of the stack, even endangering operational safety (Cheng and Yu, 2019b).

Low-power stacks require air-injecting cooling equipment such as cooling fans, while high-power stacks require cooling water circulation systems with larger specific heat capacity (Ai et al., 2013).

However, the inclusion of auxiliary equipment in the thermal management system complicates the water-cooled fuel cell arrangement.

Control methods for fuel cell stack temperature control systems proposed by domestic and foreign scholars in recent years include proportional integral (PI) and state feedback control (Ahn et al., 2020; Liso et al., 2014; Zhiyu et al., 2014; Cheng et al., 2015a), Model Predictive Control (MPC) (Pohjoranta et al., 2015; Chatrattanawet et al., 2017), Fuzzy control (Wang et al., 2016; Hu et al., 2010; Cheng et al., 2015a; Ou et al., 2017), and Neural Network Control (NNC) (Li et al., 2006; Li and Li, 2006). However, the inherent nonlinearity of the PEMFC system and the uncertainty of model

parameters greatly limit the effectiveness of these control methods (Li and Yu, 2021b). Since these algorithms cannot adapt easily to the nonlinearity of the PEMFC environment, and in many cases possess an overly complex architecture, the scope for their application in practice is greatly restricted (Li et al., 2015; Sun et al., 2020; Li and Yu, 2021a). For these reasons, the PEMFC requires a model-free algorithm that can perform parameter tracking independent of the PEMFC, which is guided by simple control principles (Li et al., 2021; Yang et al., 2021a; Yang et al., 2021b; Yang et al., 2021c). The Deep Deterministic Policy Gradient (DDPG) algorithm in deep reinforcement learning (Lillicrap et al., 2015) is a model-free method (Yang et al., 2018; Yang et al., 2019a; Yang et al., 2019b; Yang et al., 2021). Due to its strong adaptive ability, the DDPG algorithm can adapt to the uncertainty inherent in nonlinear control systems, and it is applied in various control fields (Zhang et al., 2019; Zhao et al., 2020; Zhang et al., 2021). However, due to its low robustness, DDPG is rarely used in the PEMFC control field.

In recognition of the low robustness of the DDPG algorithm, in this paper we propose an enhancement of the DDPG algorithm which can be used for PEMFC stack temperature control. We can improve the DDPG algorithm by combining it with the PID algorithm-based deep-reinforcement-learning based PID controller in order to realize more accurate stack temperature control in the PEMFC environment. For this purpose, an improved Twin Delayed Deep Deterministic Policy Gradient algorithm operates as a tuner of the PID controller, thereby adjusting the coefficients of the controller in real time. The algorithm accelerates the learning speed of an agent by continuously changing the soft update parameters during the training process, thereby improving the training efficiency of the agent, and further reducing training costs and thus obtaining a robust strategy.

The innovations detailed in this paper are as follows:

1) A deep-reinforcement-learning based PID controller for realizing optimal stack temperature control in the PEMFC is proposed.
2) The Improved Twin Delayed Deep Deterministic Policy Gradient (ITD3) algorithm is proposed as a tuner of the PID controller as it can adjust the coefficients of the controller in real time.

PEMFC HEAT MANAGEMENT SYSTEM

Heat Management System

To maintain the operation of the fuel cell stack in a safe, stable and efficient state, it is necessary to sustain a suitable temperature range. This is the core principle of the PEMFC heat management system. We propose a heat management system model for a water-cooled PEMFC, the design parameters of which reflect the law on the conservation of energy.

The principle of the heat management system in the water-cooled PEMFC stack is to adjust the internal temperature of the fuel cell by controlling the temperature and flow rate of the cooling water entering and leaving the stack, thus determining the heat taken away by the cooling water. It comprises a cooling water circulating pump, radiator fan, controller and sensor. The cooling water pump drives the cooling water into circulating in the stack at a certain flow rate. When it passes through the stack, the cooling water absorbs and removes heat, and so its temperature will increase. Then, when the cooling water from the stack flows through the radiator, the radiator fan rotates in order to create a convection flow between the air and the cooling water, so that excess heat can be eliminated, and the inlet temperature of the cooling water is restored to an acceptable level. In the method proposed in this paper, the cooling water flow rate is treated as the control quantity, the stack temperature is controlled by adjusting the cooling water flow rate, and the radiator is set to run at a fixed speed to meet the heat dissipation requirements.

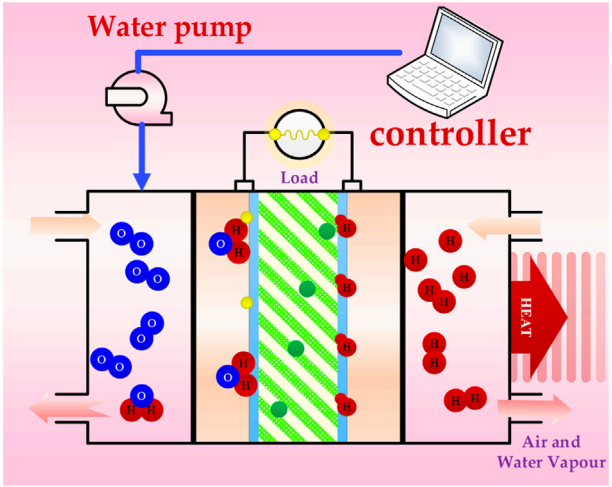


FIGURE 1 | PEMFC control framework.

PEMFC Stack Temperature

According to the law of the conservation of energy, when the hydrogen in the PEMFC reacts with oxygen, all the chemical energy released is converted into electric energy and heat. Then, according to the heat balance equation $Q = CM\Delta T$, excluding the effective power generation and heat from various channels, the remaining energy of the generated chemical energy will affect the internal temperature of the reactor, and so the temperature change of the reactor per unit of time is closely related to the heat generation and heat dissipation of the reactor [44]:

$$C_{st}M_{st}\Delta T = Q_{che} - P_{st} - Q_{gas} - Q_{water} - Q_{rad} \tag{1}$$

Chemical Energy

According to **Figure 1**, The chemical energy converted by hydrogen per unit time is:

$$Q_{che} = \Delta H \times N_{H_2}^{wedd} = \Delta H \frac{NI_{st}}{2F} \tag{2}$$

Electric Power

The output electric power of the PEMFC stack is:

$$P_{st} = NV_{cell}I_{st} \tag{3}$$

Gas Cooling

The stack gas cooling system is designed in accordance with the laws of conservation of energy and matter. The gas and water are consumed and generated in the stack. Based on the energy difference between the intake and the exhaust, the heat caused by the exhaust can be calculated as follows:

$$Q_{gas} = T_{out} \sum_{i=H_2,N_2,O_2,H_2O} C_i^{out} W_i^{out} - T_{in} \sum_{i=H_2,\ N_2,O_2,H_2O} C_i^{in} W_i^{in} \tag{4}$$

Circulating Cooling Water for Heat Dissipation

Circulating cooling water is the main method for dissipating heat in the PEMFC stack. The circulating water pump provides pressure, which drives the cooling water through the stack at a certain flow rate, thus removing excess heat, so that the stack can operate at a safe and efficient temperature. The heat dissipation is calculated as follows:

$$Q_{water} = C_{water}W_{water}\left(T_{out} - T_{in}\right) \tag{5}$$

The cooling water absorbs heat when it flows through the stack, and so the outlet temperature is much higher than the inlet temperature. In order to ensure that the inlet temperature remains at 339.15K, a cooling fan supplies air flow sufficient for transferring heat from the cooling water to the air. The relationship is as follows:

$$Q_{water} = C_{water}W_{mater}\left(T_{st} - T_{in}\right) = C_{air}W_{air}\left(T_{fan,out} - T_{atm}\right) \tag{6}$$

Heat Radiator

Any material of a sufficient temperature will radiate heat in the form of electromagnetic radiation, and the same is true for the PEMFC stack. The heat radiated by it is related to the temperature of the stack:

$$Q_{rad} = \delta\sigma_b A_{rad}\left(T_{st}^4 - T_{atm}^4\right) \tag{7}$$

INTELLIGENT CONTROL OF STACK TEMPERATURE BASED ON ITD3 ALGORITHM

DDPG

The Deep Deterministic Policy Gradient (DDPG) is an improved algorithm based on Deep Q-learning (DQN), which effectively solves the problem of multi-dimensional continuous action output. In addition, similar to other model-free reinforcement learning algorithms, the DDPG algorithm is capable of black-box learning. It only needs to pay attention to the state, action, and reward value at runtime, rather than rely on a detailed mathematical model of the system.

The loss function of the current value network is calculated as follows:

$$J\left(\theta^{\ell}\right) = \frac{1}{m}\sum_{j=1}^{m}\omega^j\left(y^j - Q\left(S_t^j, A_i^j/\theta^Q\right)\right)^2 \tag{8}$$

Wherein,

$$y^j = \begin{cases} R_{t+1}^j & \text{end } j \text{ is true} \\ R_{t+1}^j + \gamma Q'\left(S_{t+1}^j, A_{t+1}^j/\theta^g\right) & \textit{end } j \text{ is false} \end{cases} \tag{9}$$

The loss function of the real value network is calculated as follows:

$$J\left(\theta^*\right) = -\frac{1}{m}\sum_{j=1}^{m}Q\left(S_t^j, A_t^j/\theta^s\right) \tag{10}$$

Among them, by using the gradient descent method to find the minimum value of the loss function $J(\theta^*)$, the maximum action value $Q(S_t^j, A_t^j/\theta^Q)$ can be determined.

The target value network and target strategy network are updated in the following ways:

$$\begin{aligned} \theta^{Q,} &\leftarrow \tau\theta^{\ell} + (1-\tau)\theta^{\ell,} \\ \theta^{n,} &\leftarrow \tau\theta^{\pi} + (1-\tau)\theta^{n,} \end{aligned} \tag{11}$$

T is the soft update coefficient, and thus the update speed of the neural network can be controlled by adjusting τ. In order to avoid excessive updating of the neural network, τ usually ranges between 0.01 and 0.1. The update frequency of the target value network and the target strategy network is specified by the parameter f. Therefore, every time step t reaches an integer multiple of f, the target network is updated once.

ITD3

Clipped Double Q-Learning

According to **Figure 2**, In ITD3, the Clipped Double Q-learning method is used to calculate the target value:

$$y_t^1 = r\left(s_t, a_t\right) + \gamma\min_{i=1,2}Q_{\phi_i}\left(s_{t+1}, \pi_{\phi_1}\left(s_{t+1}\right)\right) \tag{13}$$

Policy Delay Update

After every d times of the critic network update, the actor network is updated once to ensure that the actor network can be updated with a low Q error, so as to improve the update efficiency of the actor network.

Smooth Regularization of Target Strategy

The ITD3 algorithm introduces a regularization method for reducing the variance of the target value, and smoothes the Q value estimation by bootstrapping the estimated value of the similar state action pair:

$$y_t = r\left(s_t, a_t\right) + E_{\varepsilon}\left[Q_{\theta'}\left(s_{t+1}, \pi_{\phi'}\left(s_{t+1}\right) + \varepsilon\right)\right] \tag{14}$$

Smooth regularization is achieved by adding a random noise to the target strategy and averaging on the mini-batch:

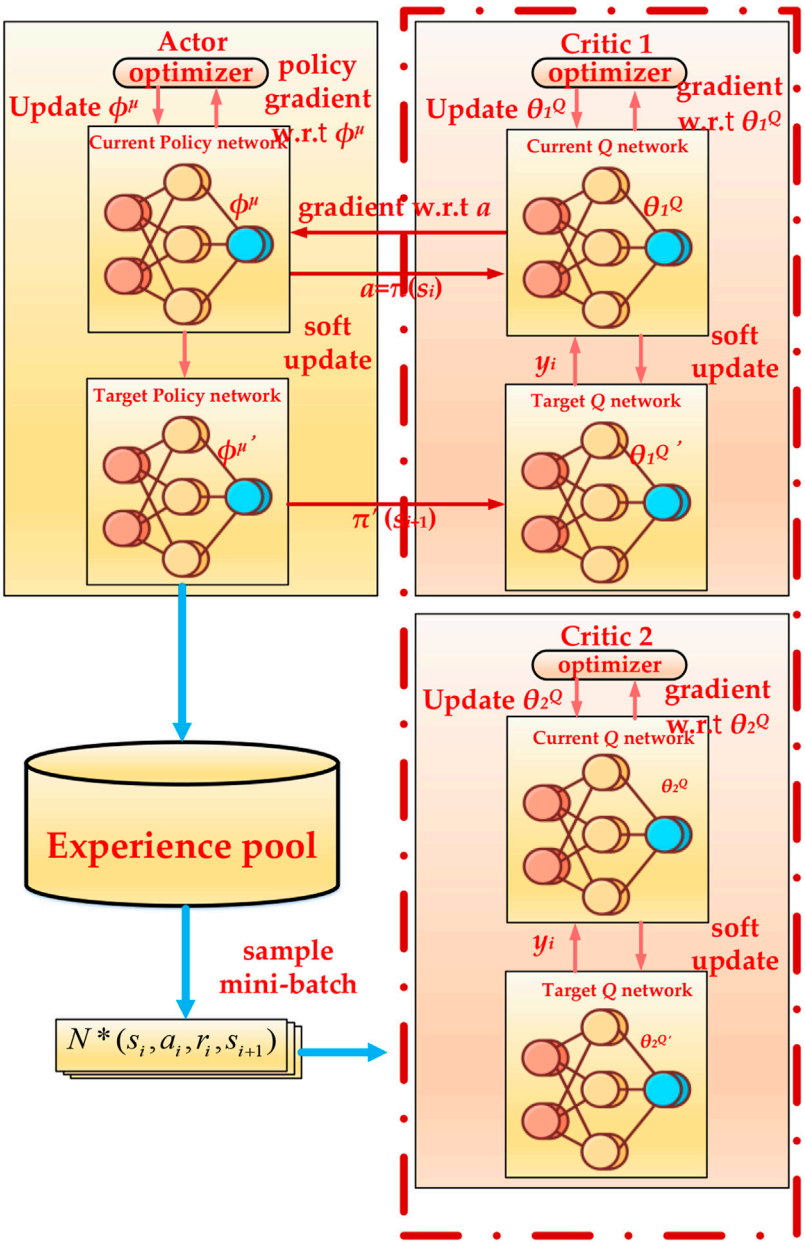


FIGURE 2 | ITD3 algorithm.

$$y_t = r(s_t, a_t) + \gamma \min_{i=1,2} Q_{\theta_t}\left(s_{t+1}, \pi_{\phi'}(s_{t+1}) + \varepsilon\right) \quad (15)$$

$$\varepsilon \sim \text{clip}\left(N(0, \sigma), -c, c\right) \quad (16)$$

$$\tau = \begin{cases} 0.05 & episodes < 1000 \\ 0.1 & 1000 < episodes < 2000 \\ 0.15 & 2000 < episodes < 3000 \\ 0.2 & episodes > 3000 \end{cases} \quad (17)$$

Changeable Soft Update Coefficient

The DDPG algorithm uses a soft update method to update the target deep neural network parameters; however, this method undermines the training efficiency of the DDPG algorithm and increases the training cost. In order to overcome this problem, the soft update coefficient increases with the increase in episodes, as detailed below:

CASE STUDIES

The effectiveness of the proposed method is demonstrated in a simulation in which the proposed algorithm is compared against the following: Apex-DDPG, TD3 controller [6], DDPG controller

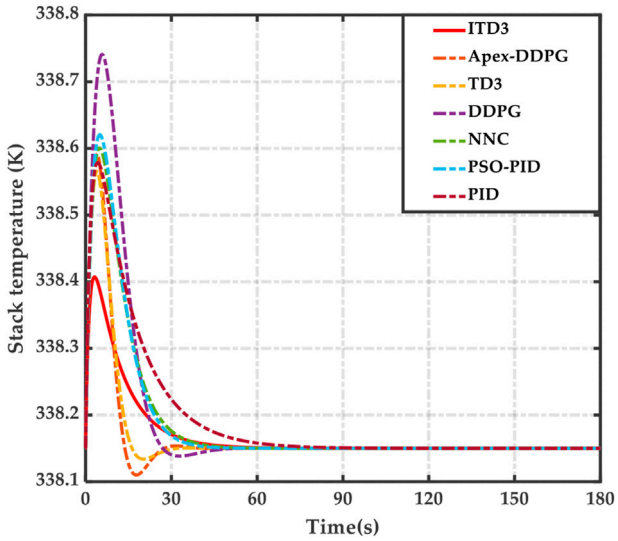


FIGURE 3 | Stack temperature.

[2], PSO tuned PID controller (PSO-PID) [8], PID controller and NNC controller [3].

In the experiment, the operating time in the working condition is 120s.

It is demonstrated in **Figure 3** that when the load current changes step by step, the ITD3 controller can more effectively realize the stack temperature control and effectively control the output characteristics of the PEMFC, compared with the other algorithms. The overshoot of the output voltage is small, with quick response. The ITD3 controller has better adaptive ability and robustness, which makes it possible to obtain a faster response speed for restoring the temperature at the midpoint prior to the early stage of the disturbance, and thus obtain better stability at the later stage of the disturbance, which leads to less overshoot of the stack temperature, and no static error when the system is stable. In addition, because the proposed method can learn a large number of samples under different load conditions during offline training, it has extremely high adaptive ability and robustness, so it is able to automatically arrive at the best decision in the current state according to the collected PEMFC state. Therefore, the proposed method can smoothly control the stack temperature and obtain better control performance under variable load disturbances. By comparison, the TD3 algorithm, DDPG algorithm and NNC algorithm are less robust due to their low exploration ability and excessive reliance on samples. The other conventional algorithms in the simulation lack the capacity for adapting to the time-varying characteristics and nonlinearity of the PEMFC environment.

The ITD3 algorithm has better static and dynamic performance and is able to control the output voltage more effectively than the existing algorithms involved in the simulation.

CONCLUSION

In this paper, we have proposed a deep reinforcement learning-based PID controller for optimal stack temperature of the PEMFC. To this end, we have devised and tested what we term the ITD3 algorithm. This serves as the tuner of the PID controller by adjusting the coefficients of the controller in real time. The algorithm introduces Clipped Double Q-learning, strategy delay update, smooth and smooth regularization of target strategy, and changeable soft update coefficients in the training process, in order to speed up agent learning, thereby improving agent training efficiency, reducing training costs, and obtaining a robust strategy.

The simulation results indicate that the proposed control algorithm can achieve effective control of the temperature of the PEMFC stack. In addition, it has been compared with other RL control methods, including adaptive FOPID algorithm, adaptive PID algorithm and PID algorithm with optimized parameters, and the neural network control algorithm. In summary, the results demonstrate that the proposed control method achieves better control performance and robustness.

DATA AVAILABILITY STATEMENT

The original contributions presented in the study are included in the article/Supplementary Material, further inquiries can be directed to the corresponding author.

AUTHOR CONTRIBUTIONS

JL: Conceptualization, Methodology, Software. YL: Data curation, Writing-Original draft preparation. TY: Supervision.

FUNDING

This work was jointly supported by the National Natural Science Foundation of China (U2066212).

REFERENCES

Ahn, J.-W., and Choe, S.-Y. (2008). Coolant Controls of a PEM Fuel Cell System. *J. Power Sourc.* 179, 252–264. doi:10.1016/j.jpowsour.2007.12.066

Ai, G., Chen, W., Liu, Z., Qi, L., and Zhang, J. (2013). "Tempreture Model and Predictive Control for Fuel Cells in Switcher Locomotive," in Proceedings of the 2016 35th Chinese Control Conference (CCC), Chengdu, China, 27-29 July 2016 (IEEE).

Chatrattanawet, N., Hakhen, T., Kheawhom, S., and Arpornwichanop, A. (2017). Control Structure Design and Robust Model Predictive Control for Controlling a Proton Exchange Membrane Fuel Cell. *J. Clean. Prod.* 148, 934–947. doi:10.1016/j.jclepro.2017.02.033

Cheng, L., Liu, G., Huang, H., Wang, X., Chen, Y., Zhang, J., et al. (2020). Equilibrium Analysis of General N-Population Multi-Strategy Games for Generation-Side Long-Term Bidding: An Evolutionary Game Perspective. *J. Clean. Prod.* 276, 124123. doi:10.1016/j.jclepro.2020.124123

Cheng, L., and Yu, T. (2019). A New Generation of AI: A Review and Perspective on Machine Learning Technologies Applied to Smart Energy and Electric Power Systems. *Int. J. Energ. Res.* 43, 1928–1973. doi:10.1002/er.4333

Cheng, L., and Yu, T. (2019). Smart Dispatching for Energy Internet with Complex Cyber-physical-social Systems: A Parallel Dispatch Perspective. *Int. J. Energ. Res.* 43, 3080–3133. doi:10.1002/er.4384

Cheng, L., Yu, T., Zhang, X., and Yang, B. (2019). Parallel Cyber-Physical-Social Systems Based Smart Energy Robotic Dispatcher and Knowledge Automation: Concepts, Architectures, and Challenges. *IEEE Intell. Syst.* 34, 54–64. doi:10.1109/MIS.2018.2882360

Cheng, S., Fang, C., Xu, L., Li, J., and Ouyang, M. (2015). Model-based Temperature Regulation of a PEM Fuel Cell System on a City Bus. *Int. J. Hydrogen Energ.* 40, 13566–13575. doi:10.1016/j.ijhydene.2015.08.042

Hu, P., Cao, G.-Y., Zhu, X.-J., and Hu, M. (2010). Coolant Circuit Modeling and Temperature Fuzzy Control of Proton Exchange Membrane Fuel Cells. *Int. J. Hydrogen Energ.* 35, 9110–9123. doi:10.1016/j.ijhydene.2010.06.046

Li, D., Li, C., Gao, Z., and Jin, Q. (2015). On Active Disturbance Rejection in Temperature Regulation of the Proton Exchange Membrane Fuel Cells. *J. Power Sourc.* 283, 452–463. doi:10.1016/j.jpowsour.2015.02.106

Li, G., and Li, Y. (2016). "Temperature Control of PEMFC Stack Based on BP Neural Network," in Proceedings of the 2016 4th International Conference on Machinery, Materials and Computing Technology, March-2016 (Atlantis: Atlantis Press), 1372–1376. doi:10.2991/icmmct-16.2016.270

Li, J., Li, Y., and Yu, T. (2021a). Distributed Deep Reinforcement Learning-Based Multi-Objective Integrated Heat Management Method for Water-Cooling Proton Exchange Membrane Fuel Cell. *Case Stud. Therm. Eng.* 27, 101284. doi:10.1016/j.csite.2021.101284

Li, J., and Yu, T. (2021a). A New Adaptive Controller Based on Distributed Deep Reinforcement Learning for PEMFC Air Supply System. *Energ. Rep.* 7, 1267–1279. doi:10.1016/j.egyr.2021.02.043

Li, J., and Yu, T. (2021b). Distributed Deep Reinforcement Learning for Optimal Voltage Control of PEMFC. *IET Renew. Power Generation* 15, 2778–2798. doi:10.1049/rpg2.12202

Li, J., Yu, T., Zhang, X., Li, F., Lin, D., and Zhu, H. (2021b). Efficient Experience Replay Based Deep Deterministic Policy Gradient for AGC Dispatch in Integrated Energy System. *Appl. Energ.* 285, 116386. doi:10.1016/j.apenergy.2020.116386

Li, Y., Wang, H., and Dai, Z. (2006). "Using Artificial Neural Network to Control the Temperature of Fuel Cell," in Proceedings of the 2006 International Conference on Communications, Circuits and Systems, 25-28 june-2006 (IEEE), 2159–2162. doi:10.1109/icccas.2006.284926

Lillicrap, T. P., Hunt, J. J., Pritzel, A., Heess, N., Erez, T., Tassa, Y., et al. (2015). *Continuous Control with Deep Reinforcement Learning*. arXiv preprint arXiv: 1509.02971. doi:10.1016/S1098-3015(10)67722-4

Liso, V., Nielsen, M. P., Kær, S. K., and Mortensen, H. H. (2014). Thermal Modeling and Temperature Control of a PEM Fuel Cell System for Forklift Applications. *Int. J. Hydrogen Energ.* 39, 8410–8420. doi:10.1016/j.ijhydene.2014.03.175

Ou, K., Yuan, W.-W., Choi, M., Yang, S., and Kim, Y.-B. (2017). Performance Increase for an Open-Cathode PEM Fuel Cell with Humidity and Temperature Control. *Int. J. Hydrogen Energ.* 42, 29852–29862. doi:10.1016/j.ijhydene.2017.10.087

Pohjoranta, A., Halinen, M., Pennanen, J., and Kiviaho, J. (2015). Model Predictive Control of the Solid Oxide Fuel Cell Stack Temperature with Models Based on Experimental Data. *J. Power Sourc.* 277, 239–250. doi:10.1016/j.jpowsour.2014.11.126

Sun, L., Li, G., Hua, Q. S., and Jin, Y. (2020). A Hybrid Paradigm Combining Model-Based and Data-Driven Methods for Fuel Cell Stack Cooling Control. *Renew. Energ.* 147, 1642–1652. doi:10.1016/j.renene.2019.09.048

Wang, Y.-X., Qin, F.-F., Ou, K., and Kim, Y.-B. (2016). Temperature Control for a Polymer Electrolyte Membrane Fuel Cell by Using Fuzzy Rule. *IEEE Trans. Energ. Convers.* 31, 667–675. doi:10.1109/TEC.2015.2511155

Yang, B., Li, D., Zeng, C., Chen, Y., Guo, Z., Wang, J., et al. (2021). Parameter Extraction of PEMFC via Bayesian Regularization Neural Network Based Meta-Heuristic Algorithms. *Energy* 228, 120592. doi:10.1016/j.energy.2021.120592

Yang, B., Swe, T., Chen, Y., Zeng, C., Shu, H., Li, X., et al. (2021). Energy Cooperation between Myanmar and China under One Belt One Road: Current State, Challenges and Perspectives. *Energy* 215, 119130. doi:10.1016/j.energy.2020.119130

Yang, B., Wang, J., Zhang, X., Yu, T., Yao, W., Shu, H., et al. (2020). Comprehensive Overview of Meta-Heuristic Algorithm Applications on PV Cell Parameter Identification. *Energ. Convers. Manag.* 208, 112595. doi:10.1016/j.enconman.2020.112595

Yang, B., Yu, T., Shu, H., Dong, J., and Jiang, L. (2018). Robust Sliding-Mode Control of Wind Energy Conversion Systems for Optimal Power Extraction via Nonlinear Perturbation Observers. *Appl. Energ.* 210, 711–723. doi:10.1016/j.apenergy.2017.08.027

Yang, B., Yu, T., Zhang, X., Li, H., Shu, H., Sang, Y., et al. (2019). Dynamic Leader Based Collective Intelligence for Maximum Power point Tracking of PV Systems Affected by Partial Shading Condition. *Energ. Convers. Manag.* 179, 286–303. doi:10.1016/j.enconman.2018.10.074

Yang, B., Zeng, C., Wang, L., Guo, Y., Chen, G., Guo, Z., et al. (2021). Parameter Identification of Proton Exchange Membrane Fuel Cell via Levenberg-Marquardt Backpropagation Algorithm. *Int. J. Hydrogen Energ.* 46, 22998–23012. doi:10.1016/j.ijhydene.2021.04.130

Yang, B., Zhong, L., Zhang, X., Shu, H., Yu, T., Li, H., et al. (2019). Novel Bio-Inspired Memetic Salp Swarm Algorithm and Application to MPPT for PV Systems Considering Partial Shading Condition. *J. Clean. Prod.* 215, 1203–1222. doi:10.1016/j.jclepro.2019.01.150

Zhang, X., Li, S., He, T., Yang, B., Yu, T., Li, H., et al. (2019). Memetic Reinforcement Learning Based Maximum Power point Tracking Design for PV Systems under Partial Shading Condition. *Energy* 174, 1079–1090. doi:10.1016/j.energy.2019.03.053

Zhang, X., Tan, T., Zhou, B., Yu, T., Yang, B., and Huang, X. (2021). Adaptive Distributed Auction-Based Algorithm for Optimal Mileage Based AGC Dispatch with High Participation of Renewable Energy. *Int. J. Electr. Power Energ. Syst.* 124, 106371. doi:10.1016/j.ijepes.2020.106371

Zhao, D., Li, F., Ma, R., Zhao, G., and Huangfu, Y. (2020). An Unknown Input Nonlinear Observer Based Fractional Order PID Control of Fuel Cell Air Supply System. *IEEE Trans. Ind. Applicat.* 56, 5523–5532. doi:10.1109/TIA.2020.2999037

Zhiyu, Y., Tao, X., Zhixiang, L., Yun, P., and Weirong, C. (2014). Study on Air-Cooled Self-Humidifying PEMFC Control Method Based on Segmented Predict Negative Feedback Control. *Electrochimica Acta* 132, 389–396. doi:10.1016/j.electacta.2014.04.003

Conflict of Interest: The authors declare that the research was conducted in the absence of any commercial or financial relationships that could be construed as a potential conflict of interest.

Publisher's Note: All claims expressed in this article are solely those of the authors and do not necessarily represent those of their affiliated organizations, or those of the publisher, the editors and the reviewers. Any product that may be evaluated in this article, or claim that may be made by its manufacturer, is not guaranteed or endorsed by the publisher.

Copyright © 2021 Li, Li and Yu. This is an open-access article distributed under the terms of the Creative Commons Attribution License (CC BY). The use, distribution or reproduction in other forums is permitted, provided the original author(s) and the copyright owner(s) are credited and that the original publication in this journal is cited, in accordance with accepted academic practice. No use, distribution or reproduction is permitted which does not comply with these terms.

frontiers in Energy Research

BRIEF RESEARCH REPORT
published: 29 September 2021
doi: 10.3389/fenrg.2021.754057

Coordinated Frequency Regulation of Smart Grid by Demand Side Response and Variable Speed Wind Turbines

Qi Zhu[1], *Yingjie Wang*[2], *Jiuxu Song*[1], *L. Jiang*[2]* *and Yingliang Li*[1]

[1]School of Electronic Engineering, Xi'an Shiyou University, Xi'an, China, [2]Department of Electrical Engineering and Electronics, The University of Liverpool, Liverpool, United Kingdom

Frequency stability of the power system is impacted by the increasing penetration of wind power because the wind power is intermittent. Meanwhile, sometimes the demand side loads increase quickly to require more power than total power produced. So balancing the active power in the power system to maintain the frequency is the main challenge of the high penetration of wind power to the smart grid. This paper proposes coordination rotor speed control (RSC), pitch angle control (PAC) and inertial control (IC) to control wind turbines, together with demand side response (DSR) participating in frequency regulation to balance active power in the power system. Firstly, the model of a single area load frequency control (LFC) system is obtained, which includes variable-speed wind turbines (VSWT) and DSR containing aggregated air conditioners and plug-in electric vehicles (PEVs). Then the RSC, PAC and IC, which controls wind turbines participating in frequency regulation in the power system, are introduced, respectively. Finally, the coordination of these three methods for wind turbines in different wind speeds is proposed. Case studies are carried out for the single area LFC system with a wind farm and DSR supported grid frequency. Coordination RSC and PAC combined IC are used to control wind turbines with DSR to balance active power in the power system. The proposed method used in the power system with high penetration of wind power and fluctuation of demand load is tested, respectively. Coordinated RSC or PAC with DSR can increase penetration of wind power and reduce peak load.

Keywords: wind turbine, demand side response, frequency regulation, smart grid, plug-in electric vehicle

OPEN ACCESS

Edited by:
Xiaoshun Zhang,
Shantou University, China

Reviewed by:
Chuan-Ke Zhang,
China University of Geosciences Wuhan, China
Yuefang Du,
University of Electronic Science and Technology of China, China

***Correspondence:**
L. Jiang
ljiang@liv.ac.uk

Specialty section:
This article was submitted to Smart Grids, a section of the journal Frontiers in Energy Research

Received: *05 August 2021*
Accepted: *13 September 2021*
Published: *29 September 2021*

Citation:
Zhu Q, Wang Y, Song J, Jiang L and Li Y (2021) Coordinated Frequency Regulation of Smart Grid by Demand Side Response and Variable Speed Wind Turbines. Front. Energy Res. 9:754057. doi: 10.3389/fenrg.2021.754057

1 INTRODUCTION

Due to environmental pressures and increasing fossil fuel prices, intermittent renewable energy has been developed rapidly in recent years, especially wind energy. With the low penetration of wind power in the power system, i.e., less than 20% of the total power system capacity, thermal plants with abundant regulating capability can balance the active power of the power system. However, when the penetration of wind power is increased, the frequency stability will be progressively influenced due to the uncertainty of wind power and insufficient thermal power reserves (Zhang et al., 2011; Khoo et al., 2020; Yang et al., 2020). Moreover, it may even cause one situation that the total power produced by the power system is less than the demand load required. Therefore, balancing the active power in the power system is a challenging problem when the high penetration of wind power level increases to a certain level.

Many methods can be used to solve this imbalance problem caused by intermittent wind power. Traditionally, the spinning generation reserves with enough capacity and the grid-scale energy storage

system can be used to meet this task. However, these solutions require expensive auxiliary equipment and high installation and operation cost. Thus it will increase the operation cost and reduces the advantages of wind power (Dui et al., 2018; Oshnoei et al., 2020; Paul et al., 2020). The advance load frequency control (LFC) scheme is an alternative way to provide the robustness against to the disturbances caused by the intermittent wind power (Zhang et al., 2016; Soliman et al., 2019). However, an advanced LFC scheme usually makes the power system a little complex and can not maintain the power system balance if the high penetration of wind power participates in the power system.

With the increasing penetration of wind power in the power system, variable-speed wind turbines (VSWTs) are required to participate in frequency regulation *via* augmented additional controllers, such as inertial control (IC), pitch angle control (PAC) and rotor speed control (RSC) (Margaris et al., 2012; Ravanji et al., 2020). When the grid frequency changes, not only the synchronous generators will respond to this change, but also wind turbines will quickly change their output active power to follow this disturbance change (Ma and Chowdhury, 2010). The IC method used for frequency regulation can transiently release the large kinetic energy stored in the rotating mass to emulate inertia of wind generators for providing frequency regulation (Ma and Chowdhury, 2010; Ravanji et al., 2020; Prasad and Padhy, 2020). The PAC and RSC used in the VSWT to participate in the frequency control for an extended period are investigated (Ma and Chowdhury, 2010; Zhang et al., 2011; Chau et al., 2018). In this paper, the VSWTs participate in frequency regulation *via* coordination of IC, RSC and PAC control methods under different wind speeds in the LFC system.

Because the wind power and demand side load are all uncertain, sometimes the total produced power is less than the demand loads required. In this situation, the demand side response (DSR), which can control or shift the controllable loads, has become a promising smart grid technology for accommodating intermittent renewable generations (Zhu et al., 2014; Esther and Kumar, 2016; Zhu et al., 2016a; Hosseini et al., 2020). In recent years, the PEVs have drawn increasing attention to the transportation electrification and suppressed the fluctuation in renewable energy sources have been investigated in lots of literature (Kariminejad et al., 2018; Nunna et al., 2018; Liu et al., 2020; Wang et al., 2020). The dynamic demand control (DDC) method, which controls the thermostatically controlled appliances (TCAs), such as electric water heaters (Vivekananthan and Mishra, 2015), refrigerators (Algarni et al., 2021) and air conditioners (Jay and Swarup, 2011), can self-adjust the usage of appliances based on frequency deviation of the power system (Hosseini et al., 2020). In this paper, DSR which includes aggregated air conditioners and PEVs participates in frequency regulation to reduce peak loads and to help the power system in stable.

This paper investigates combination wind turbines and DSR participating in frequency regulation in the power system to solve the imbalance problem caused by high penetration of wind power. Combination wind turbines and DSR participates in frequency regulation to deal with high wind power penetration and the DSR can remit frequency fluctuation when the total produced power is not enough for demand load required. Finally, wind turbines with different capacity of DSR supporting grid frequency are tested. This combination method has several advantages over other resources used for energy balancing and ancillary services, including providing enough capacity to adopt the high penetration of wind power and fluctuation of demand load problems.

2 DYNAMIC MODEL OF SMART GRID FOR FREQUENCY REGULATION

The model of a signal area LFC system is proposed. A wind farm which contains several VSWTs participates in frequency regulation. The DSR which includes several PEVs and air conditioners is used to reduce the peak load and compensate for imbalance problem caused by wind power. **Figure 1** shows the structure of the frequency regulation of the smart grid.

From **Figure 1**, the relationship between the energy imbalance and the corresponding frequency deviation can be given as follows:

$$\begin{aligned}&\Delta P_m(s) + \Delta P_{wind}(s) - \Delta P_L(s) - \Delta P_{DDC}(s) - \Delta P_{V2G}(s)\\&= 2Hs\Delta f(s) + D\Delta f(s)\end{aligned} \tag{1}$$

where ΔP_m is the generator mechanical output, ΔP_{wind} is the deviation of the wind power from the wind farm, ΔP_{DDC} is the power deviation from the DDC based on air conditioners, ΔP_{V2G} is the power deviation from the PEVs, ΔP_L is the load change, $2H$ is the equivalent inertia constant, D is the equivalent load-damping coefficient, and Δf is the frequency deviation of smart grid. $K(s)$ is usually a PID controller.

2.1 The Model of a Variable Speed Wind Turbine

Wind power is developing very fast in recent years and its intermittent characteristic may cause energy imbalance for the smart grid. The details of VSWT model is introduced in (Thomsen and Poulsen, 2007; Boukhezzar and Siguerdidjane, 2011; Zhu et al., 2016b). The VSWT model is a complex nonlinear system, which consists of aerodynamics model, turbine mechanics model, generator model, and pitch actuator model.

The aerodynamic blades on the rotor convert the kinetic energy of the wind into mechanical energy, effectively providing the torque, T_r, on the rotor:

$$T_r = \frac{P_r}{\omega_r} \tag{2}$$

where ω_r is the rotor speed, and the mechanical power absorbed from the wind P_r is shown as:

$$P_r = \frac{1}{2}\rho\pi R_{wind}^2 v^3 C_p \tag{3}$$

where ρ is the air density, R_{wind} is the wind radius, v is the effective wind speed, and C_p is the power coefficient.

The blade pitch angle, θ, is changed by a hydraulic/mechanical actuator. A simplified model of the dynamics in this paper is presented by the following first order linear model:

$$\dot{\theta} = -\frac{1}{\tau_\theta}\theta + \frac{1}{\tau_\theta}\theta_r \tag{4}$$

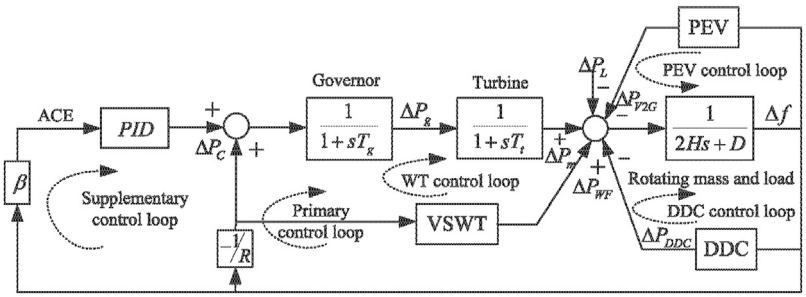


FIGURE 1 | The structure of the frequency regulation of the power system.

where θ_r is the reference and the one control input for the wind turbine.

The generator power, P_e, is given by:

$$P_e = T_g \omega_g \tag{5}$$

where T_g is controlled, however, it cannot be changed instantaneously.

A wind farm represents a number of aggregated individual wind turbines. It assumes the wind speed for each wind turbine is same at the same time. Considering the clustering effect of wind turbines, the deviation of the active power from the wind farm is expressed as:

$$\Delta P_{wind} = \sum_{j=1}^{N_{wind}} (P_{e,j} - P_{wind,desired}) \tag{6}$$

where $P_{wind,\ desired}$ is the desired active power output of the wind farm, ΔP_{wind} is the deviation of the actual power out from the desired value, $P_{e,j}$ is active power output of the jth wind turbines and N_{wind} is the total number of wind turbines in the wind farm (Chang-Chien et al., 2014).

2.2 Plug-In Electric Vehicles Model

The PEVs participating in frequency regulation contain several small capacity batteries. Therefore, large scale PEVs have potential to provide frequency support to the grid. The battery of the PEV comprising parallel/series connected battery cells is connected to the distribution grid through the DC/AC inverter (Hajizadeh and Golkar, 2007). The PEV model is introduced in (Zhu et al., 2016b).

In this paper, the active power losses in the inverter and the transformer are ignored, thus the active V2G power injected into the grid, P_{V2G}, can be given as

$$P_{V2G,i} = I_{dc,i} V_{dc,i} \tag{7}$$

Linearizing (**Eq. 7**) yields the incremental active power as follows

$$\Delta P_{V2G,i} = V^o_{dc,i} \Delta I_{dc,i} + I^o_{dc,i} \Delta V_{dc,i} s \tag{8}$$

where $V^o_{dc,i}$ and $I^o_{dc,i}$ represent for the DC voltage and current of the battery at the initial time, respectively.

Similar to the BESS, the partial adjustment of battery voltage is used to compensate the power change resulting from current deviation (Xia et al., 2018). Thus, the V2G power of PEV_i responding to frequency regulation is

$$\Delta P_{V2G,i} = \frac{k_{b,i}}{1 + sT_{b,i}} \Delta f \tag{9}$$

where $k_{b,i} = -k_{v,i} I^o_{dc,i}$ is the battery gain, which represents the sensitivity of V2G power with respect to frequency deviation.

Assume that there are N PEVs in the smart grid discussed in this paper can be used to provide frequency support, and consider that the $T_{b,i}$ in (**Eq. 9**) is not very sensitive to frequency deviation, then the aggregated V2G power can be approximately presented as following:

$$\Delta P_{V2G} = \sum_{i=1}^{N} \Delta P_{V2G,i} = \frac{k_{ev}}{1 + sT_{ev}} \Delta f \tag{10}$$

where the aggregated PEVs gain $k_{ev} = \sum_{i=1}^{N} k_{b,i}$, and the aggregated time constant $T_{ev} = \sum_{i=1}^{N} \frac{T_{b,i}}{N}$.

2.3 Controllable Air-Conditioner Based Dynamic Demand Control Model

Domestic electric appliances of the user can be classified into five different groups based on their characteristics (Trovato et al., 2017), in which the TCAs can be used as a controllable load for frequency regulation, since they are relevant directly to the frequency derivation. In this paper, a typical TCA, air conditioner, is considered as the DDC loads. The detail of this model is introduced in (Zhu et al., 2016b). The frequency dependent characteristic of air conditioner can be shown as:

$$\Delta P_{\mathrm{DDC}} = \Delta P_{LC} + D_{ac} \Delta\omega = \frac{mc_p}{EER} \Delta T_{st} + D_{ac} \Delta\omega \tag{11}$$

where m is the mass of air flow, c_p is the specific heat capacity of air, EER is the energy efficient ratio (EER) (Ruelens et al., 2017), D_{ac} is the reheat coefficient of the air conditioner, $\Delta\omega = 2\pi\Delta f$ is the deviation of the speed, and ΔP_{LC} is the controllable change in power consumed, which depends on the characteristic of the air conditioner and the set point of a smart thermostat (ΔT_{st}). ΔT_{st} can be expressed as follows:

$$\Delta T_{st} = \frac{\bar{K}}{s} \alpha \Delta f \tag{12}$$

where $\bar{K}$ is integral gain and α is a coefficient (given as 0.5 R/Hz in this paper). The temperature set-point is bounded and varies based on the weather condition and different time interval in a day.

From the aforementioned discussion, the load model with respect to frequency deviation of air conditioner is given as:

$$\Delta P_{\mathrm{ddc,\,i}} = \left(\frac{0.5K_{ddc,i}}{s} + 2\pi D_{ac,i}\right)\Delta f \tag{13}$$

where $K_{ddc} = \frac{mc_p\bar{K}}{EER}$ is the combined integral gain.

Due to the small capacity of an individual air conditioner, it is necessary to aggregate several small domestic loads into a relatively large and lumped DDC load to participate the LFC scheme. Assume that there are M air conditioners in the smart homes of the grid, then the aggregated power of the DDC can be presented as follows:

$$\Delta P_{DDC} = \sum_{i=1}^{M} \Delta P_{ddc,i} = \left(\frac{0.5K_{DDC}}{s} + 2\pi D_{ac}\right)\Delta f \tag{14}$$

where $K_{DDC} = \sum_{i=1}^{M} K_{ddc,i}$, and $D_{ac} = \sum_{i=1}^{M} D_{ac,i}$.

3 CONTROL DESIGN OF THE WIND TURBINE SUPPORTED IN FREQUENCY REGULATION

The wind turbines can be controlled by IC, RSC and PAC control methods to participate in frequency regulation in the smart grid. The IC is used for short-time grid frequency restoration. Meanwhile, RSC and PAC are used for grid frequency restoration.

3.1 Inertial Control for Short-Time Grid Frequency Restoration

For a synchronous generator, the kinetic energy is released automatically from the rotating mass when the frequency drops. In the VSWT, the IC utilizes the kinetic energy of wind turbine's rotor during grid frequency excursion (Ma and Chowdhury, 2010). The kinetic energy is stored in the wind generator as shown in (**Eq. 15**).

$$E_k = \frac{1}{2}J\omega_r^2 \tag{15}$$

where J is the equivalent moment of inertia.

The power from the rotating mass is expressed as follows:

$$\Delta P_{ic} = \frac{dE_k}{dt} = J\omega_r\frac{d\omega_r}{dt} \tag{16}$$

To couple the grid frequency change, $d\omega_r/dt$ is replaced by the grid frequency change df_{sys}/dt for the inertial control loop. So extracted power from the inertial controller is described as:

$$\Delta P_{ic} = K_{ic}\frac{df_{sys}}{dt} \tag{17}$$

where control coefficient K_{ic} has replaced the coefficient $J\omega_r$.

3.2 Rotor Speed Control for Grid-Frequency Regulation

The wind turbine is controlled by RSC based on the frequency drop characteristic. The controller adjusts the active power output in proportion to the frequency deviation with the ratio of $-\frac{1}{R}$ (Parizy et al., 2019) as following:

$$\Delta P_{wind} = -\frac{1}{R}\left(f_{sys} - f_{ref}\right) = -\frac{1}{R}\Delta f \tag{18}$$

where f_{ref} is the nominal frequency and f_{sys} is the measured system frequency.

The wind power $P_{e,ref}$ is the initial wind plant output power and it is held constant during the grid frequency restoration period.

3.3 Pitch Angle Control for Grid-Frequency Regulation

PAC of the wind turbine is designed much like the governor control of the synchronous machine. The PAC is used for preventing the rotor speed from exceeding the nominal value (Zhang et al., 2011).

The input signal is Δf. The ΔP_{wind} can achieve according (**Eq. 17**) and output is the pitch angle. By using the PAC method, the wind farm provides either higher or lower power to share in the frequency restoration strategy in the long term. This method achieves the coordinated control strategies which will be discussed in **Section 3.4**.

3.4 Coordinated Control Strategies

Figure 2 shows the wind turbine power output curve at different wind speeds. In region 1, the wind turbine blades cannot rotate in very low wind speeds. While the wind turbine will start to rotate and generate the maximum electrical power from the wind when the wind speed rises in region 2. In region 3, as the power generated by the wind turbine is higher than its rated output power, the wind turbine starts to regulate the pitch angle to limit the electrical power to its rated value. Finally, at the cut-out wind speed, a braking system is used to stop the wind turbine for the sake of protecting the wind turbine in region 4. In this paper, it presents a novel frequency regulation by VSWT to coordinate IC, RSC and PAC under low or high wind speed.

When the wind speed is in the range [5 m/s, 12 m/s] (in region 2), the output power can be achieved following the trajectory of the 90% sub-optimal operation curve. The PAC does not need to be activated to down-regulate the wind turbine (Zhang et al., 2011). So the RSC is used to control wind turbine and the pitch angle is equal to 0. When the frequency drops, the RSC will control the wind turbine to produce more active output power. On the contrary, the RSC will control the wind turbine to produce less active output power.

When the wind speed is in the range [12 m/s, 25 m/s] (in region 3), the RSC is impossible to control the wind turbines because the MPPT speed has been over maximum rotor speed. Therefore PAC is the only way to down-regulate the wind turbine. When the wind speed is above the rated, the pitch angle is increased to limit the mechanical power of a wind turbine to output its rated value (Ma and Chowdhury, 2010). However, if the power grid requires less power than the rate power, the pitch angle is further increased to satisfy the grid side power demand in order to minimise the frequency deviation of the power system.

The IC can support frequency control in transient. So the IC combined RSC or PAC controls wind turbines to participate in frequency regulation to maintain grid frequency in stable more quickly with smaller fluctuation. When wind turbines produce the

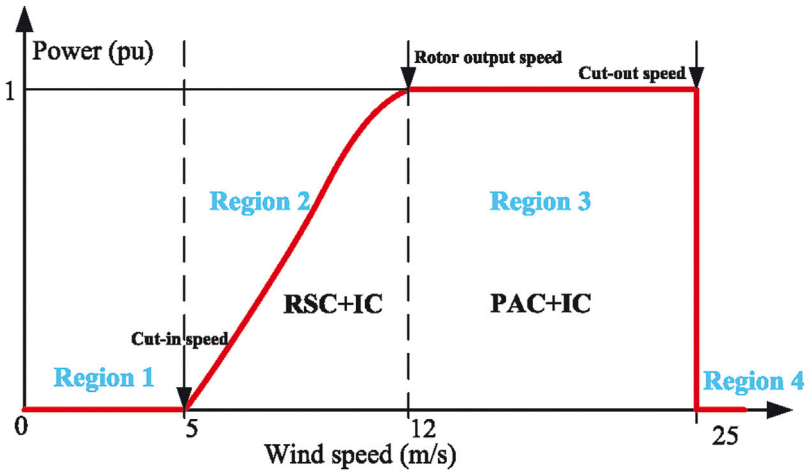


FIGURE 2 | The wind turbine power output curve with different wind speed.

rated power but the total power is less than the demand load need, the DSR will shift controllable load to other time used or reduce controllable load using to solve these imbalance problems. On the contrary, the DSR will move the controllable load to use in this time or add controllable load using to solve these imbalance problems. Coordinated frequency regulation of smart grid by DSR and variable speed wind turbines will increase the stability of the power system and allow more wind turbines to connect to the power system.

4 CASE STUDY

The proposed frequency regulation methods are tested on a single area LFC scheme which includes a wind farm, aggregated DDC based on air conditioners and PEVs. The micro generation equips with a non-heat turbine with a capacity of 800 MW. The wind turbine's capacity is around 2.25 MW. Assume that all wind turbines are identical and the cut-in wind speed, the rated wind speed, and the cut-out speed are 5, 12, and 25 m/s, respectively (Algarni et al., 2021). The related parameters are recalled from literatures (Jay and Swarup, 2011; Xia et al., 2018). The following three cases are studied.

4.1 The High Penetration of Wind Power in the Smart Grid

In this section, the LFC scheme with the high penetration of wind power and DSR is tested. The wind farm consists 400 wind turbines and the total wind farm output power is 900 MW (about 52.94% of the total output power). The DSR and a part of wind turbines joining in frequency regulation. Three scenarios shown in below are tested.

Scenario 1: 40 wind turbines participate in frequency regulation and 360 wind turbines directly connect to the power system.

Scenario 2: 200 wind turbines participate in frequency regulation and 200 wind turbines directly connect to the power system.

Scenario 3: 360 wind turbines participate in frequency regulation and 40 wind turbines directly connect to the power system.

Frequency deviation from three scenarios in the variable low and high wind speed is shown in **Figure 3**. When the wind speed is low (7 m/s-10 m/s), the wind turbines participating in frequency regulation based on the RSC method (shown in subfigures **Figures 3A–C**), in which the dash-dot line, the dashed line and the solid line represent three different control methods to control wind turbine participating in frequency regulation, respectively. Frequency deviation is the fastest convergent to schedule values with the smallest fluctuation by combined RSC and DSR approach. While fluctuation of frequency deviation is the biggest and recovering time is longest by RSC method. Compared to the same control method used in these three scenarios, the Scenario 3 can be obtained the best performance in these three scenarios. When the wind speed is high (16 m/s-20 m/s), the wind turbines participating in frequency regulation based on the PAC method. Subfigures **Figures 3D–F** show frequency deviation in three scenarios in variable high wind speed, in which dash-dot line, dash line and solid line represent for PAC method, PAC combined IC method and combined PAC and DSR method, respectively. Similar results can be obtained from the simulation study. The combined PAC and DSR method is the best method to maintain frequency deviation in desired value with the smallest fluctuation and fastest response time in variable wind speed.

4.2 The Demand Load Required Power Exceeds Produced Power

When the high penetration of wind power connects in the power system, it will cause the total produced power insufficient to demand load required because the wind power is intermittent and time-varying. On the other hand, the demand load change may suddenly increase

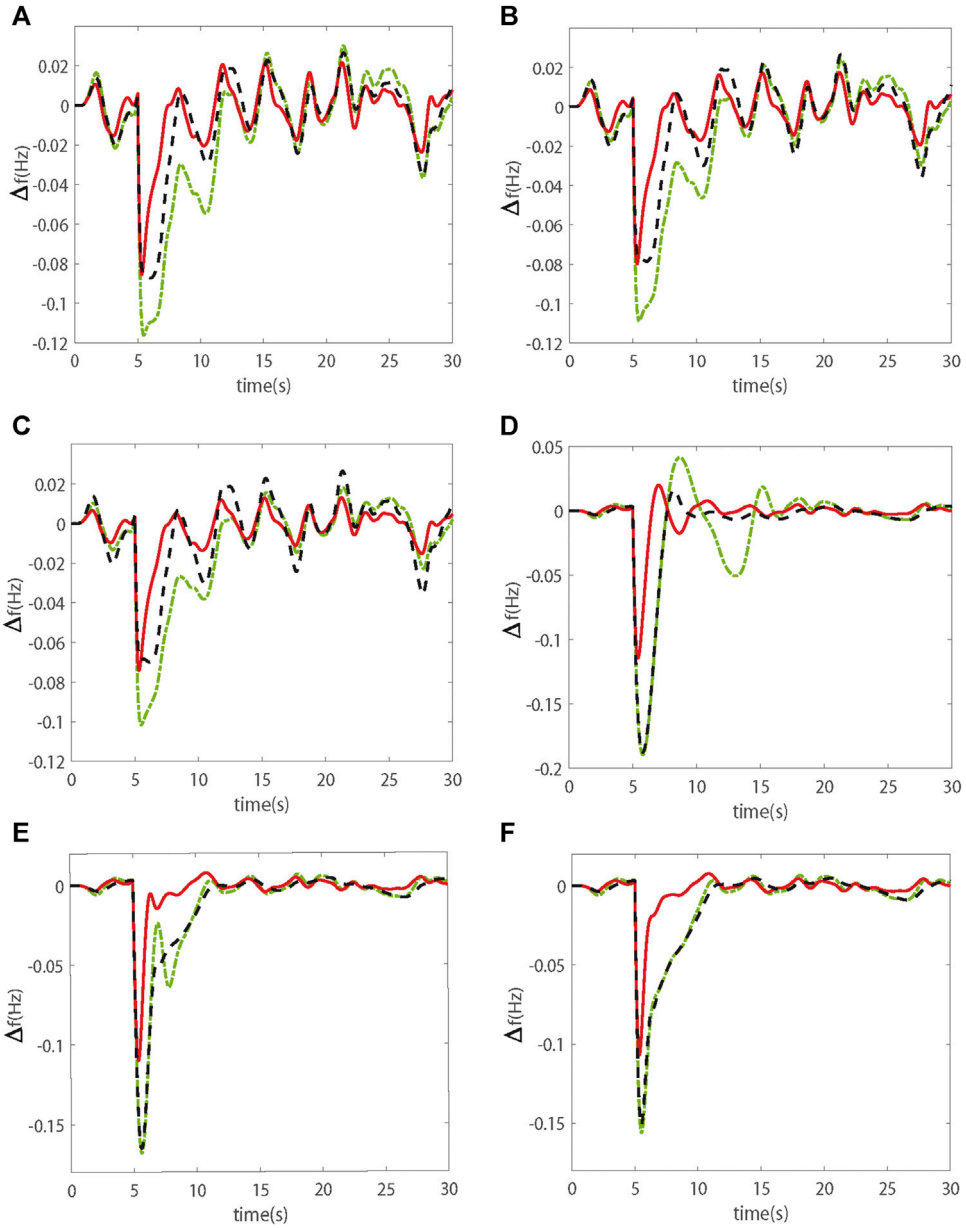


FIGURE 3 | Frequency deviation from different control methods under three scenarios in variable low and high wind speed, **(A)** is Scenario 1 in low wind speed, **(B)** is Scenario 2 in low wind speed, **(C)** is Scenario 3 in low wind speed, **(D)** is Scenario 1 in high wind speed, **(E)** is Scenario 2 in high wind speed, **(F)** is Scenario 3 in high wind speed.

sometimes in a year. Due to these two reasons, the demand side load may need more power than total produced power during some periods. In this section, three scenarios are introduced in the above are simulates with significant demand load change in variable low and high wind speed. The power system required grid frequency in the range 50 ± 0.5 HZ.

A step demand load change is $0.56pu$ at $t = 5$ s in the power system. When wind speed is in [7 m/s, 10 m/s], frequency deviation from three scenarios is shown in **Figure 4**. In these three scenarios, the combined RSC and DSR method can recover the frequency deviation in desired range with the smallest fluctuation and the fastest response time. The fluctuation of frequency deviation from wind turbines controlled by the RSC is the biggest. When more wind turbines participate in frequency regulation, the fluctuation of frequency deviation is smaller. When wind speed is in [16 m/s, 20 m/s], results are similar as above. Wind turbines together with DSR participating in frequency regulation can improve the power system stability and can balance the power system when the demand load change suddenly change. Meanwhile, the more wind turbines participating in the

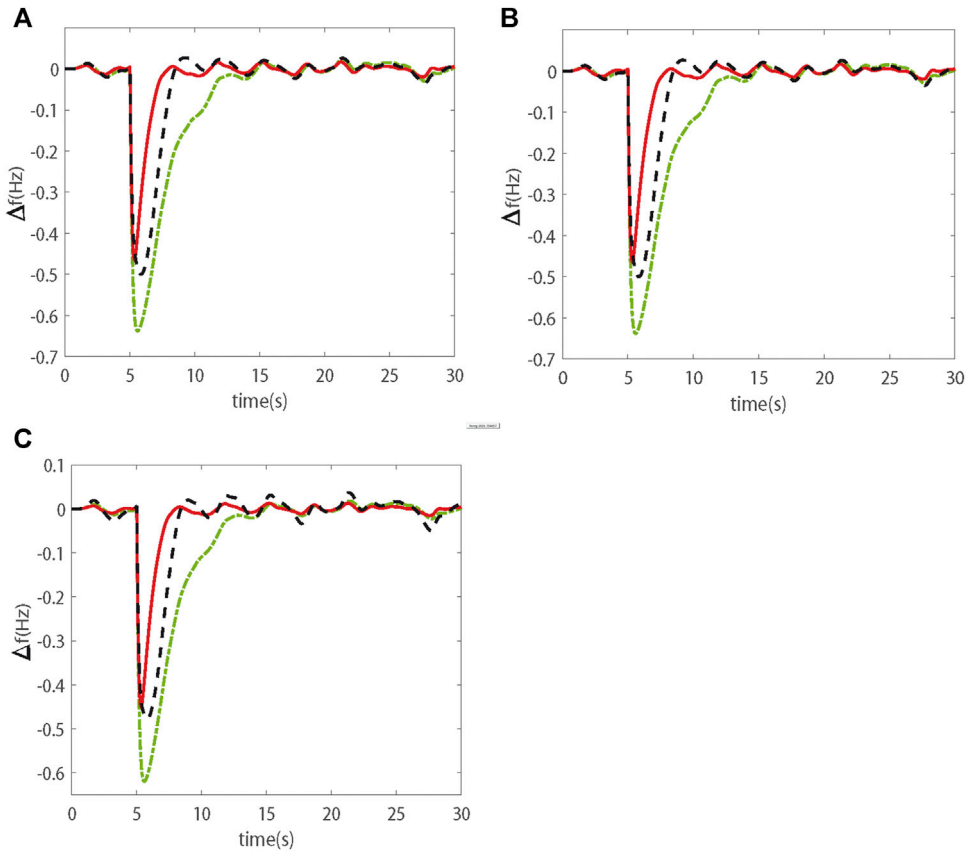


FIGURE 4 | Frequency deviation from different control methods in three scenarios with big load change in variable high wind speed, **(A)** is Scenario 1, **(B)** is Scenario 2 and **(C)** is Scenario 3: dash-dot (RSC), dashed (RSC with IC), solid (RSC with DSR).

frequency regulation can reduce the fluctuation of the frequency deviation.

5 CONCLUSION

With the increasing penetration of wind power, wind turbines are required to participate in frequency regulation. This paper discusses coordination frequency regulation *via* VSWTs and DSR in different wind speeds. The VSWTs participating in frequency regulation are controlled by coordinated RSC, PAC and IC in different wind speeds, together with DSR for the LFC of the power system under intermittent wind power and demand load suddenly increasing. Combined RSC or PAC with DSR can contribute to increase penetration of wind power and also slash peak load.

DATA AVAILABILITY STATEMENT

The original contributions presented in the study are included in the article/**Supplementary Material**, further inquiries can be directed to the corresponding author.

AUTHOR CONTRIBUTIONS

QZ and LJ was responsible for the design and revision of the thesis proposal, YW and JS was responsible for writing the introduction and dynamic model of smart grid for frequency regulation, and YL was responsible for writing the case study and conclusion.

FUNDING

This work was jointly supported by the Scientific Research Program Funded by Shaanxi Provincial Education Department (Program No. 21JK0843) and Natural Science Basic Research Program of Shaanxi (Program No. 2020JM-542).

SUPPLEMENTARY MATERIAL

The Supplementary Material for this article can be found online at: https://www.frontiersin.org/articles/10.3389/fenrg.2021.754057/full#supplementary-material

REFERENCES

Algarni, A. S., Suryanarayanan, S., Siegel, H. J., and Maciejewski, A. A. (2021). Combined Impact of Demand Response Aggregators and Carbon Taxation on Emissions Reduction in Electric Power Systems. *IEEE Trans. Smart Grid* 2 (12), 1825–1827. doi:10.1109/TSG.2020.3023586

Boukhezzar, B., and Siguerdidjane, H. (2011). Nonlinear Control of a Variable-Speed Wind Turbine Using a Two Mass Model. *IEEE Trans. Energ. Convers.* 1 (2), 149–162. doi:10.1109/TEC.2010.2090155

Chang-Chien, L., Sun, C., and Yeh, Y. (2014). Modeling of Wind Farm Participation in AGC. *IEEE Trans. Power Syst.* 3 (29), 1204–1211. doi:10.1109/TPWRS.2013.2291397

Chau, T. K., Yu, S. S., Fernando, T. L., Iu, H. H., and Small, M. (2018). A Novel Control Strategy of DFIG Wind Turbines in Complex Power Systems for Enhancement of Primary Frequency Response and LFOD. *IEEE Trans. Power Syst.* 2 (33), 1811–1823. doi:10.1109/TPWRS.2017.2726160

Dui, X. W., Zhu, G. P., and Yao, L. Z. (2018). Two-Stage Optimization of Battery Energy Storage Capacity to Decrease Wind Power Curtailment in Grid-Connected Wind Farms. *IEEE Trans. Power Syst.* 3 (33), 3296–3305. doi:10.1109/TPWRS.2017.2779134

Esther, B. P., and Kumar, K. S. (2016). A Survay on Residential Demand Side Management Architercture, Approaches, Optimization Models and Methods. *ENTSO-E* 59, 342–351. doi:10.1016/j.rser.2015.12.282

Hajizadeh, A., and Golkar, M. A. (2007). Intelligent Power Management Strategy of Hybrid Distributed Generation System. *Int. J. Electr. Power Energ. Syst.* 10 (29), 783–795. doi:10.1016/j.ijepes.2007.06.025

Hosseini, S. A., Toulabi, M., Dobakhshari, A. S., Ashouri-Zadeh, A., and Ranjbar, A. M. (2020). Delay Compensation of Demand Response and Adaptive Disturbance Rejection Applied to Power System Frequency Control. *IEEE Trans. Power Syst.* 3 (35), 2037–2046. doi:10.1109/TPWRS.2019.2957125

Jay, D., and Swarup, K. S. (2011). "Frequency Restoration Using Dynamic Demand Control under Smart Grid Environment," in Proc. IEEE PES ISGT, Kollam, India, 1–3 December 2011, 311–315. doi:10.1109/ISET-India.2011.6145408

Kariminejad, N., Taher, S. A., Shahidehpour, M., and Khateri, K. (2018). A Hierarchical Governor/Turbine and Electric Vehicles Optimal Control Framework for Primary Frequency Support in Power Systems. *IEEE Trans. Smart Grid.* 6 (9), 6702–6712. doi:10.1109/TSG.2017.2718557

Khoo, W. C., Teh, J. S., and Lai, C. (2020). Integration of Wind and Demand Response for Optimum Generation Reliability, Cost and Carbon Emission. *IEEE Access* 8, 183606–183618. doi:10.1109/ACCESS.2020.3029273

Liu, P., Wang, C. Y., Hu, J., Fu, T. T., Cheng, N., Zhang, N., et al. (2020). Joint Route Selection and Charging Discharging Scheduling of EVs in V2G Energy Network. *IEEE Trans. Veh. Technol.* 10 (69), 10630–10641. doi:10.1109/TVT.2020.3018114

Ma, H. T., and Chowdhury, B. H. (2010). Working towards Frequency Regulation with Wind Plants: Combined Control Approaches. *IET Renew. Power Gener.* 4 (4), 308–316. doi:10.1049/iet-rpg.2009.0100

Margaris, I. D., Papathanassious, S. A., Hatziargyriou, N. D., Hansen, A. D., and Sorensen, P. (2012). Frequency Control in Autonomous Power Systems with High Wind Power Penetration. *IEEE Trans. Sustain. Energ.* 2 (3), 189–199. doi:10.1109/TSTE.2011.2174660

Nunna, H. S. V. S. K., Battula, S., Doolla, S., and Srinivasan, D. (2018). Energy Management in Smart Distribution Systems with Vehicle-To-Grid Integrated Microgrids. *IEEE Trans. Smart Grid.* 5 (9), 4004–4016. doi:10.1109/TSG.2016.2646779

Oshnoei, A., Kheradmandi, M., and Muyeen, S. M. (2020). Robust Control Scheme for Distributed Battery Energy Storage Systems in Load Frequency Control. *IEEE Trans. Power Syst.* 6 (35), 4781–4791. doi:10.1109/TPWRS.2020.2997950

Parizy, E. S., Bahrami, H. R., and Choi, S. (2019). A Low Complexity and Secure Demand Response Technique for Peak Load Reduction. *IEEE Trans. Smart Grid.* 3 (10), 259–265. doi:10.1109/TSG.2018.2822729

Paul, S., Nath, A. P., and Rather, Z. H. (2020). A Multi-Objective Planning Framework for Coordinated Generation from Offshore Wind Farm and Battery Energy Storage System. *IEEE Trans. Sustain. Energ.* 4 (11), 2087–2097. doi:10.1109/TSTE.2019.2950310

Prasad, R., and Padhy, N. P. (2020). Synergistic Frequency Regulation Control Mechanism for DFIG Wind Turbines with Optimal Pitch Dynamics. *IEEE Trans. Power Syst.* 4 (35), 3181–3191. doi:10.1109/TPWRS.2020.2967468

Ravanji, M. H., Canizares, C. A., and Parniani, M. (2020). Modeling and Control of Variable Speed Wind Turbine Generators for Frequency Regulation. *IEEE Trans. Sustain. Energ.* 2 (11), 916–927. doi:10.1109/TSTE.2019.2912830

Ruelens, F., Claessens, B. J., Vandael, S., Schutter, B. D., Babuka, R., and Belmans, R. (2017). Residential Demand Response of Thermostatically Controlled Loads Using Batch Reinforcement Learning. *IEEE Trans. Smart Grid.* 5 (8), 2149–2159. doi:10.1109/TSG.2016.2517211

Soliman, M. A., Hasanien, H. M., Azazi, H. Z., El-Kholy, E. E., and Mahmoud, S. A. (2019). An Adaptive Fuzzy Logic Control Strategy for Performance Enhancement of a Grid-Connected PMSG-Based Wind Turbine. *IEEE Trans. Ind. Informat.* 6 (15), 3163–3173. doi:10.1109/TII.2018.2875922

Thomsen, S. C., and Poulsen, N. K. (2007). "A Disturbance Decoupling Nonlinear Control Law for Variable Speed Wind Turbines," in TProc.15th Mediterreanean Confernece, Athens, Greece, 27–29 June 2007, 1–6. doi:10.1109/MED.2007.4433869

Trovato, V., Sanz, I. M., Chaudhuri, B., and Strbac, G. (2017). Advanced Control of Thermostatic Loads for Rapid Frequency Response in Great Britain. *IEEE Trans. Power Syst.* 3 (32), 2106–2117. doi:10.1109/TPWRS.2016.2604044

Vivekananthan, C., and Mishra, Y. (2015). Stochastic Ranking Method for Thermostatically Controllable Appliances to Provide Regulation Services. *IEEE Trans. Power Syst.* 4 (30), 1987–1996. doi:10.1109/TPWRS.2014.2353655

Wang, M. S., Mu, Y. F., Shi, Q. X., Jia, H. J., and Li, F. X. (2020). Electric Vehicle Aggregator Modeling and Control for Frequency Regulation Considering Progressive State Recovery. *IEEE Trans. Smart Grid* 5 (11), 4176–4189. doi:10.1109/TSG.2020.2981843

Xia, S. W., Bu, S. Q., Luo, X., Chan, K. W., and Lu, X. (2018). An Autonomous Real-Time Charging Strategy for Plug-In Electric Vehicles to Regulate Frequency of Distribution System with Fluctuating Wind Generation. *IEEE Trans. Sustain. Energ.* 2 (9), 511–524. doi:10.1109/TSTE.2017.2746097

Yang, Z., Xia, L., and Guan, X. H. (2020). Fluctuation Reduction of Wind Power and Sizing of Battery Energy Storage Systems in Microgrids. *IEEE Trans. Autom. Sci. Eng.* 3 (17), 1195–1207. doi:10.1109/TASE.2020.2977944

Zhang, S. Q., Mishra, Y., and Shahidehpour, M. (2016). Fuzzy-Logic Based Frequency Controller for Wind Farms Augmented with Energy Storage Systems. *IEEE Trans. Power Syst.* 2 (31), 1595–1603. doi:10.1109/TPWRS.2015.2432113

Zhang, Z. S., Sun, Y. Z., and Li, G. J. (2011). Coordinated Frequency Regulation by Doubly Fed Induction Generator-Based Wind Power Plants. *IET Renew. Power Gener.* 1 (6), 38–47. doi:10.1049/iet-rpg.2010.0208

Zhu, Q., Jiang, L., Yao, W., Zhang, C. K., and Luo, C. (2016b). Robust Load Frequency Control with Dynamic Demand Response for Deregulated Power Systems Considering Communication Delays. *ELECTR. POW COMPO SYS* 1 (45), 75–87. doi:10.1080/15325008.2016.1233300

Zhu, Q., Yao, W., Jiang, L., Luo, C., and Wu, Q. H. (2014). "Load Frequency Control with Dynamic Demand Control for Deregulated Power System," in 2014 IEEE Power Energy Soc. Gen. Meet, Washington, U.S., 27-31 July 2014, 1–5. doi:10.1109/PESGM.2014.6939313

Zhu, Q., Zhang, C. K., Yao, W., and Jiang, L. (2016a). "Chapter 8: Frequency Regulation of Smart Grid via Dynamic Demand Control and Battery Energy Storage System," in *Smarter Energy: From Smart Metering to the Smart Grid*. Editors H. Sun, N. Hatziargyriou, H. V. Poor, L. Carpanini, and M. A. S. Fornie (London: The institution of engineering and technology), 209–243.

Conflict of Interest: The authors declare that the research was conducted in the absence of any commercial or financial relationships that could be construed as a potential conflict of interest.

Publisher's Note: All claims expressed in this article are solely those of the authors and do not necessarily represent those of their affiliated organizations, or those of the publisher, the editors and the reviewers. Any product that may be evaluated in this article, or claim that may be made by its manufacturer, is not guaranteed or endorsed by the publisher.

Copyright © 2021 Zhu, Wang, Song, Jiang and Li. This is an open-access article distributed under the terms of the Creative Commons Attribution License (CC BY). The use, distribution or reproduction in other forums is permitted, provided the original author(s) and the copyright owner(s) are credited and that the original publication in this journal is cited, in accordance with accepted academic practice. No use, distribution or reproduction is permitted which does not comply with these terms.

frontiers in Energy Research

BRIEF RESEARCH REPORT
published: 30 September 2021
doi: 10.3389/fenrg.2021.753064

Control Method for PEMFC Using Improved Deep Deterministic Policy Gradient Algorithm

Jiawen Li[1]*, *Yaping Li*[2] and *Tao Yu*[1]*

[1]College of Electric Power, South China University of Technology, Guangzhou, China, [2]China Electric Power Research Institute, Nanjing, China

A data-driven PEMFC output voltage control method is proposed. Moreover, an Improved deep deterministic policy gradient algorithm is proposed for this method. The algorithm introduces three techniques: Clipped multiple Q-learning, policy delay update, and policy smoothing to improve the robustness of the control policy. In this algorithm, the hydrogen controller is treated as an agent, which is pre-trained to fully interact with the environment and obtain the optimal control policy. The effectiveness of the proposed algorithm is demonstrated experimentally.

Keywords: output voltage, proton exchange membrane fuel cell, deep deterministic policy gradient algorithm, robustness, PEMFC

OPEN ACCESS

Edited by:
Yaxing Ren,
University of Warwick,
United Kingdom

Reviewed by:
Du Gang,
North China Electric Power University, China
Yunzheng Zhao,
The University of Hong Kong, Hong Kong, SAR China

***Correspondence:**
Jiawen Li
eplijiawen@mail.scut.edu.cn
Tao Yu
taoyu1@scut.edu.cn
eptaoyu1@163.com

Specialty section:
This article was submitted to Smart Grids, a section of the journal Frontiers in Energy Research

Received: *04 August 2021*
Accepted: *13 September 2021*
Published: *30 September 2021*

Citation:
Li J, Li Y and Yu T (2021) Control Method for PEMFC Using Improved Deep Deterministic Policy Gradient Algorithm. Front. Energy Res. 9:753064. doi: 10.3389/fenrg.2021.753064

INTRODUCTION

Fuel Cell is the fourth type of power generation technology after hydroelectric, thermal and nuclear power generation. It converts chemical energy stored in fuel and oxidizer directly into electricity through electrode reactions in an isothermal environment (Yang et al., 2021a; Yang et al., 2021b). As a new type of chemical power source, the fuel cell generation process is not a direct combustion of fuel compared to thermal power generation, the power generation efficiency is not limited by the Carnot cycle and the emission of harmful substances is extremely low(Yang et al., 2020; Yang et al., 2018). Its energy conversion rate is as high as 80 %, and its actual efficiency is double that of an ordinary internal combustion engine (Bougrine et al., 2013) The fuel cell is therefore a new power source with high efficiency and clean features, combining new technologies in energy, chemicals, materials and automatic control (Yang et al., 2019a; Yang et al., 2021c).

However, as the PEMFC system is a complex system with multiple inputs and outputs, nonlinear, approximately east, with random disturbances, time-varying and high order (Yang et al., 2019b; Li and Yu, 2021a), it is difficult to achieve satisfactory control results with traditional PID control (Li et al., 2021). In order to obtain accurate and fast response results, various advanced control strategies have been applied in the research of PEMFC output control strategies. (Zhang et al., 2019; Li and Yu, 2021b; Zhang et al., 2021).

In recent years, scholars at home and abroad have done a lot of research on the control of PEMFC, which is mainly divided into the following categories:

1) Model-based control methods (Wang and Kim, 2014): including internal model control (IMC) (Danzer et al., 2008), model predictive control (MPC) (Kim, 2010), model-based adaptive control (Zhang et al., 2008), nonlinear model predictive control (NMPC) (Park and Gajic, 2014), model multivariable control (nonlinear multivariable control) (Talj et al., 2009), time delay control (Liu et al., 2016), generalized model control (Damour et al., 2014), etc.

2) Sliding mode control. Some higher order sliding mode control methods have also been applied to PEMFC, (Ou et al., 2015) such as first order sliding mode control, higher order super twisted sliding mode control and (Chen et al., 2018) higher order sliding mode control with an observer.
3) PID and its improvement algorithms. Some improved algorithms on the PID algorithm have also been used extensively, for example, neural PID controller (Zhao et al., 2020), fuzzy PID control (Sun et al., 2018), and algorithm combining PID and fuzzy controller (Ou et al., 2017), feedback linearization controller, and reference fractional order PID (FOPID) controller.
4) Adaptive control. Some adaptive control has also been applied to PEMFC control, such as data-driven adaptive controller, an adaptive control based on parameter identification, and adaptive pole search controller.
5) Compound control. There are also some compound controllers, for example, PID-neural network control, interval type II fuzzy (Fuzzy)-PID control, fuzzy adaptive PID control.

The existing research problems are:

1) There is no model -free control algorithm that can effectively adapt to the non-linear characteristics of PEMFC.
2) No optimal algorithm with adaptive capabilities and low computational effort.

For this reason, model-free controllers with strong adaptive capabilities are more suitable for such systems.

A data-driven PEMFC output voltage control method is proposed. Moreover, an Improved deep deterministic policy gradient algorithm is proposed for this method. The algorithm introduces three techniques: double Q learning, policy delay update, and policy smoothing to improve the robustness of the control policy. In this algorithm, the hydrogen controller is treated as an agent, which is pre-trained to fully interact with the environment and obtain the optimal control policy. The effectiveness of the proposed algorithm is demonstrated experimentally.

The innovations in this paper are.

1) A data-driven PEMFC output voltage control method is proposed.
2) An Improved deep deterministic policy gradient algorithm is proposed.

The remainder of this paper comprises the following sections: the PEMFC model is demonstrated in *PEMFC Model*, and the proposed algorithm is described in *Proposed Method*; the experimental results are analysed and discussed in *Case Studies*, and the findings in this paper are summarised in *Conclusion*.

PEMFC MODEL

PEMFC Output Voltage

The dynamic model of the PEMFC has been refined from the electrochemical model. Ideally, the voltage released at full reaction is 1.229 V. The actual potential decreases due to irreversible losses, which in practice are also known as polarization overvoltage. In the power generation process of a PEMFC, polarization overvoltage is mainly manifested as activation overvoltage, ohmic overvoltage and concentration overvoltage. Therefore, in the actual power generation process, the individual voltage is inevitably less than the ideal standard electric potential due to the polarization overvoltage. In addition to the factors such as temperature, pressure and current density, chemical and material factors such as electrode material and electrolyte can also influence the polarization or overvoltage of the electrodes.

$$V_{\text{cell}} = E - \eta_{\text{act}} - \eta_{\text{ohm}} - \eta_{\text{con}} \tag{1}$$

For a fuel cell stack consisting of N single cells connected in series, the output voltage V can be expressed as

$$V = NV_{\text{cell}} \tag{2}$$

Ohmic Voltage Overvoltage

The ohmic polarization overvoltage is mainly caused by the equivalent membrane impedance of the proton exchange membrane to the transfer of protons and the impedance of the electrodes and current collectors to the transfer of electrons. Based on the Amphlett model, the PEMFC ohmic overvoltage mainly includes the voltage drop caused by the impedance of the two parts of the PEMFC. These two parts of impedance, one part is the equivalent membrane impedance of the proton membrane, The other part is the resistance that prevents protons from passing through the proton membrane which is usually a constant. According to the resistivity theorem, the equivalent membrane impedance R_m can be obtained by the following formula:

$$R_M = \frac{\rho_M B}{A} \tag{3}$$

In the formula, $\rho_{(M)}$ is the resistivity of the proton membrane to the electron flow $(\Omega \cdot (\text{cm}))$, B is the thickness of the proton exchange membrane. ρ_M can be obtained by the following formula.

$$\rho_M = \frac{181.6\left[1 + 0.03\left(\frac{I}{A}\right) + 0.062\left(\frac{T}{303}\right)(fracIA)^{25}\right]}{\left[\lambda - 0.634 - 3\left(\frac{I}{A}\right)\right]\exp\left[4.18\left(\frac{T-303}{T}\right)\right]} \tag{4}$$

Empirically, the internal resistance of the battery is

$$R_{\text{int}} = 0.01605 - 3.5 \times 10^{-5}T + 8 \times 10^{-5}i \tag{5}$$

Ohmic polarization overvoltage can be expressed as:

$$\eta_{\text{ohm}} = IR_{\text{int}} = I(R_{\text{m}} + R_{\text{c}}) \tag{6}$$

Activation Overvoltage

Activation overvoltage is the deviation of an electrode's potential from its equilibrium potential due to a delay in its electrochemical reaction. The activation polarization overvoltage of the cathode can be obtained

$$V_{\text{ux }t,c} = \frac{RT}{\alpha_c Fn}\left(\ln\left[nFK_c^0 \exp\left(-\frac{\Delta G}{RT}\right) \times \left(C_{i_2}\right)^{(1-\alpha_i)}\left(C_{H_2}\right)^{(1-\alpha_c)}\left(C_{H_2o}\right)^{\alpha_i}\right] - \ln I\right) \tag{7}$$

Anode activation polarization overvoltage:

$$V_{at,a} = -\frac{\Delta G}{2F} + \frac{RT}{2F}\ln\left(4FAK_a^0 C_{H_2}\right) - \frac{RT}{2F}\ln I \tag{8}$$

The total activation polarization overvoltage is the sum of the anode activation overvoltage and the cathode activation overvoltage, expressed as:

$$\eta_{\text{act}} = \xi_1 + \xi_2 T + \xi_3 T \ln c(\mathrm{O}_2) + \xi_4 T \ln I \tag{9}$$

$c(\mathrm{O}_2)$is the concentration of dissolved oxygen at the cathode catalyst interface which is calculated as follows:

$$c(\mathrm{O}_2) = P_{\mathrm{O}_2}/5.08 \times 10^6 \exp(-498/T) \tag{10}$$

Thermodynamic Electric Potential

According to the empirical formula for the PEMFC, the thermodynamic electric potential can be obtained as follows:

$$E = \frac{\Delta G}{2F} + \frac{\Delta S}{2F}(T - T_{\text{ref}}) + \frac{RT}{2F}\left(\ln p_{\mathrm{H}_2} + \frac{1}{2}\ln p_{0_2}\right) \tag{11}$$

PEMFC can directly convert chemical energy into electrical energy. The chemical energy release of a fuel cell can be calculated by the change of the Gibbs self-burning energy $(\Delta g_{(f)})$. The Gibbs self-burning energy is usually used to calculate the externally available energy, for basic chemical reaction formula of hydrogen/oxygen reaction PEMFC is:

$$H_2 + \frac{1}{2}O_2 - H_2O \tag{12}$$

The corresponding change in Gibbs' self-reliance is:

$$\Delta g_f = g_{f,\ products} - g_{f,\ reactan\ is} = \left(g_f\right)_{H_2O} - \left(g_f\right)_{H_2} - \left(g_f\right)_{O_2} \tag{13}$$

The changed Gibbs self-burning energy is a function of temperature and pressure:

$$\Delta g_f = \Delta g_f^0 - \overline{R}T_{fc}\ln\left[\frac{p_{H_2}p_{O_2}^{\frac{1}{2}}}{p_{H_2O}}\right] \tag{14}$$

We can deduce the voltage of the fuel cell:

$$E = \frac{-\Delta g_f}{2F} = \frac{-\Delta g_f^0}{2F} + \frac{RT_{fc}}{2F}\ln\left[\frac{p_{H_2}p_{O_2}^{\frac{1}{2}}}{p_{H_2O}}\right] \tag{15}$$

When specific values are brought in, the equation can be transformed into

$$E = 1.229 - 0.85 \times 10^{-3}(T - 298.15) + 4.3085 \times 10^{-5}T\left(\ln p_{\mathrm{H}_2} + \ln p_{0_2}/2\right) \tag{16}$$

Dense Differential Polarization Overvoltage

Concentration overvoltage is a phenomenon caused by the deviation of the electrode potential from the equilibrium potential due to the difference between the concentration of ions in the solution at the electrode interface layer and the concentration of the body solution in the electrolytic bath, which can be expressed as:

$$\eta_{\text{con}} = -\beta\ln(J/J_{\max}) \tag{17}$$

Dynamic and Capacitive Characteristics of the Double Layer Charge

The phenomenon of a "double layer of charge" in a proton exchange membrane fuel cell is particularly important for the dynamics of the PEMFC. On the surface of the electrode electrons are collected and on the surface of the electrolyte hydrogen ions are collected. Between them there is a potential difference in which charge and energy are stored, which acts as an equivalent capacitance. This "smoothest out" the voltage loss across the equivalent resistance and results in a very realistic dynamic model of the PEMFC. Therefore, when modelling the dynamics of the PEMFC, a capacitance is added to the electrochemical model. This "equivalent capacitance" is able to better represent this effect by smoothing the output voltage response of the fuel cell as the current changes, with a transition time.

In **Figure 1**, the polarization voltage across $_{\text{Rd}}$ isV_{d}, given by the differential equation for the voltage change of a single cell as

$$\mathrm{d}V_{\text{d}}/\mathrm{d}t = I/C - V_{\text{d}}/R_{\text{d}}C \tag{18}$$

$$V_d = iR_d = \eta_{act} + \eta_{con} \tag{19}$$

Thus, the voltage of the stack can be expressed as:

$$V_{st} = nV_{\text{cell}} = n[E - I(R_{act} + R_{\text{con}} + R_{\text{ohm}})] = n\left(E - IR_{\text{equ}}\right) \tag{20}$$

The output power and efficiency of the stack can therefore be expressed as:

$$P_{st} = I \cdot V_{st}\eta = V_{\text{cell}} \cdot I/E \cdot I = V_{\text{cell}}/E \tag{21}$$

PROPOSED METHOD

DDPG

The DDPG method fuses deep neural networks with Deterministic Policy Gradients (DPG) algorithms and uses actor -critic a framework as the basic architecture for the algorithm. The actor network is used to update the policy and the critic network is used to approximate the state action value function. The use a non-linear neural network as an approximator. Inspired by the algorithm, DQN solve this problem by setting up a target actor network and a target critic network, as well as an experience replay mechanism. Instead of DQN directly copying the current network to the target network, DDPG updates the target network in a "soft" way, ensuring that each parameter update is small, thus achieving a stable training effect.

$$\begin{aligned}\theta^{Q_{'}} &\leftarrow \tau\theta^{Q} + (1-\tau)\theta^{Q_{'}} \\ \theta^{\mu_{'}} &\leftarrow \tau\theta^{\mu} + (1-\tau)\theta^{\mu_{'}}\end{aligned} \tag{22}$$

In DDPG, the objective function is defined as a sum with discounted rewards

$$J(\theta^{\mu}) = \mathrm{E}_{\theta^{\mu}}\left[r_1 + \gamma r_2 + \gamma r_3 + \cdots\right] \tag{23}$$

$$L\left(\theta^{Q}\right) = \frac{1}{N}\sum_i\left(y_i - Q\left(s_i, a_i|\theta^{Q}\right)\right)^2 \tag{24}$$

Of which

$$y_i = r_i + \gamma Q'\left(s_{i+1}, \mu\left(s_{i+1}\middle|\theta^{\mu'}\right)|\theta^{\alpha}\right) \tag{25}$$

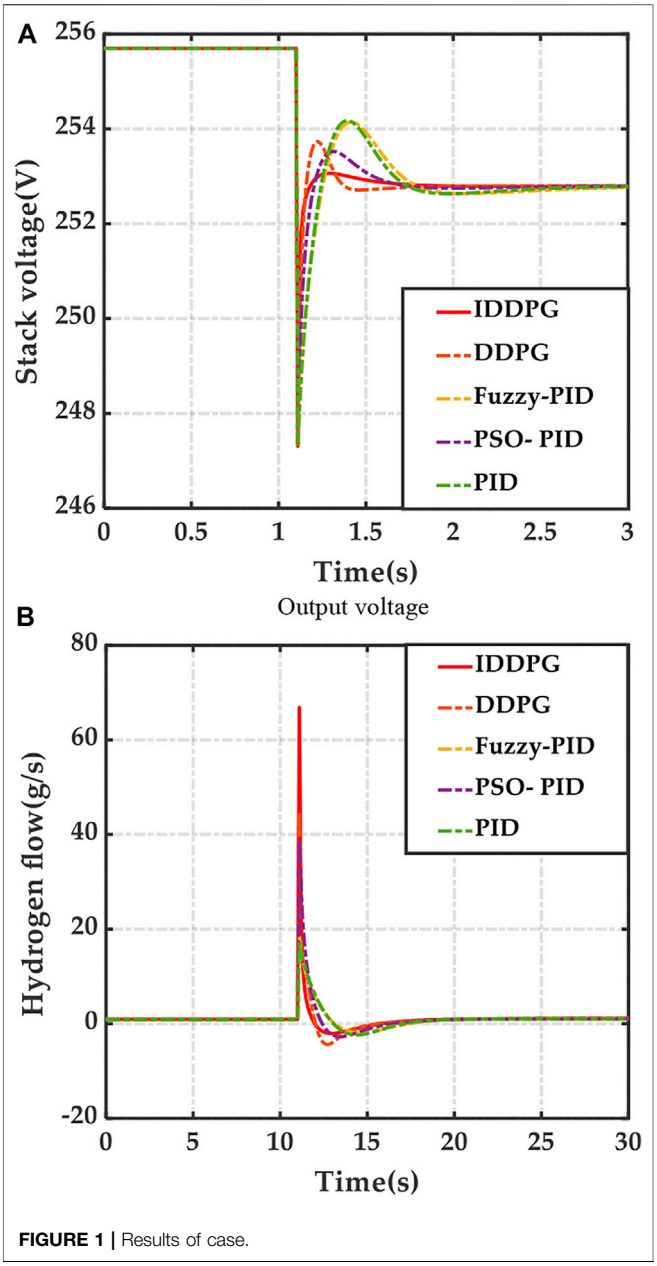


FIGURE 1 | Results of case.

The actor network parameters are updated by means of a chain derivative rule for the objective function:

$$\nabla_{\theta^\mu} J(\theta^\mu) \approx \frac{1}{N}\sum_i \nabla_a Q(s,a|\theta^Q)\Big|_{s=s,a=\mu(x)} \nabla_{\theta^\mu}\mu(s|\theta^\mu)\Big|_{s_j} \quad (26)$$

To address the problem of under-exploration caused by actors mapping states to deterministic actions in the DPG approach, the DDPG algorithm generates temporal correlated noise through the Ornstein-Uhlenbeck (OU) process to improve the exploration capability of the algorithm under deterministic strategies.

DDPG uses an empirical replay mechanism based on random sampling but suffers from Q-value overestimation.

The IDDPG algorithm uses two critics. The target value formula is as follows:

$$y_t = r(s_t, a_t) + \gamma \min_{i=1,2} Q_{\theta_t}\left(s_{t+1}, \pi_{\phi'}(s_{t+1}) + \varepsilon\right) \quad (27)$$

CASE STUDIES

The DDPG control strategy, fuzzy PID controller (Fuzzy-PID), PSO optimized fuzzy PID controller (PSO- PID), and PID are introduced in this paper as comparative examples. The load variation makes the step disturbance at 1 s. The load current magnitude appears from 100 A with load disturbance and rises to 127 A. The results are shown in **Figures 1A,B**.

1 According to **Figures 1A,B**-, the IDDPG algorithm improves the robustness of the algorithm because it uses advanced techniques to solve the Q overestimation problem in conventional deep reinforcement learning algorithms. In contrast, the DDPG algorithm does not use an effective strategy to improve the robustness of the algorithm, so the algorithm tends to fall into local optima, making the final control strategy sub-optimal and not robust. In addition, the other algorithms do not have better optimal control capability and have difficulty in adapting to the non-linear characteristics of the PEMFC, therefore, their output voltage control performance is low.

2 For Fuzzy-based algorithms, their performance is mostly better than Optimized-based algorithms due to their ability to automatically adjust coefficients, but the simplicity of the Fuzzy rule makes them less accurate.

Optimized-based algorithms are not adaptive and robust due to the inability to adjust the coefficients in real time, which ultimately leads to overshooting and instability of the output voltage.

In summary: In Case 1, the IDDPG algorithm has better static and dynamic performance and is able to control the output voltage effectively.

CONCLUSION

A data-driven PEMFC output voltage control method is proposed. An improved deep deterministic policy gradient algorithm is proposed for this method, which introduces three techniques: Clipped multiple Q-learning, policy delay update and policy smoothing to improve the robustness of the control policy. In this algorithm, the hydrogen controller is treated as an agent, which is pre-trained to fully interact with the environment and obtain the optimal control policy. The effectiveness of the proposed algorithm is experimentally demonstrated.

The IDDPG algorithm has a short response time, a fast response time, good dynamic and static performance indicators, enabling timely and effective output voltage control.

DATA AVAILABILITY STATEMENT

The original contributions presented in the study are included in the article/Supplementary Material, further inquiries can be directed to the corresponding authors.

AUTHOR CONTRIBUTIONS

JL: conceptualization, methodology, software, data curation, writing-original draft preparation, visualization, investigation, software, validation. YL: Writing- Reviewing and editing. TY: Supervision.

FUNDING

This work was jointly supported by National Natural Science Foundation of China (U2066212).

REFERENCES

Bougrine, M. D., Benalia, A., and Benbouzid, M. H. (2013). "Nonlinear Adaptive Sliding Mode Control of a Powertrain Supplying Fuel Cell Hybrid Vehicle," in 3rd International Conference on Systems and Control (Algiers, Algeria: IEEE), 714–719. doi:10.1109/icosc.2013.6750938

Chen, J., Liu, Z., Wang, F., Ouyang, Q., and Su, H. (2018). Optimal Oxygen Excess Ratio Control for PEM Fuel Cells. *IEEE Trans. Contr. Syst. Technol.* 26, 1711–1721. doi:10.1109/TCST.2017.2723343

Damour, C., Benne, M., Lebreton, C., Deseure, J., and Grondin-Perez, B. (2014). Real-time Implementation of a Neural Model-Based Self-Tuning PID Strategy for Oxygen Stoichiometry Control in PEM Fuel Cell. *Int. J. Hydrogen Energ.* 39, 12819–12825. doi:10.1016/j.ijhydene.2014.06.039

Danzer, M. A., Wilhelm, J., Aschemann, H., and Hofer, E. P. (2008). Model-based Control of Cathode Pressure and Oxygen Excess Ratio of a PEM Fuel Cell System. *J. Power Sourc.* 176, 515–522. doi:10.1016/j.jpowsour.2007.08.049

Kim, Y.-B. (2010). Improving Dynamic Performance of Proton-Exchange Membrane Fuel Cell System Using Time Delay Control. *J. Power Sourc.* 195, 6329–6341. doi:10.1016/j.jpowsour.2010.04.042

Li, J., and Yu, T. (2021a). A New Adaptive Controller Based on Distributed Deep Reinforcement Learning for PEMFC Air Supply System. *Energ. Rep.* 7, 1267–1279. doi:10.1016/j.egyr.2021.02.043

Li, J., and Yu, T. (2021b). Distributed Deep Reinforcement Learning for Optimal Voltage Control of PEMFC. *IET Renew. Power Generation* 15, 2778–2798. doi:10.1049/rpg2.12202

Li, J., Yu, T., Zhang, X., Li, F., Lin, D., and Zhu, H. (2021). Efficient Experience Replay Based Deep Deterministic Policy Gradient for AGC Dispatch in Integrated Energy System. *Appl. Energ.* 285, 116386. doi:10.1016/j.apenergy.2020.116386

Liu, J., Luo, W., Yang, X., and Wu, L. (2016). Robust Model-Based Fault Diagnosis for PEM Fuel Cell Air-Feed System. *IEEE Trans. Ind. Electron.* 63, 3261–3270. doi:10.1109/TIE.2016.2535118

Ou, K., Wang, Y.-X., and Kim, Y.-B. (2017). Performance Optimization for Open-Cathode Fuel Cell Systems with Overheating Protection and Air Starvation Prevention. *Fuel Cells* 17, 299–307. doi:10.1002/fuce.201600181

Ou, K., Wang, Y.-X., Li, Z.-Z., Shen, Y.-D., and Xuan, D.-J. (2015). Feedforward Fuzzy-PID Control for Air Flow Regulation of PEM Fuel Cell System. *Int. J. Hydrogen Energ.* 40, 11686–11695. doi:10.1016/j.ijhydene.2015.04.080

Park, G., and Gajic, Z. (2014). A Simple Sliding Mode Controller of a Fifth-Order Nonlinear PEM Fuel Cell Model. *IEEE Trans. Energ. Convers.* 29, 65–71. doi:10.1109/TEC.2013.2288064

Sun, L., Shen, J., Hua, Q., and Lee, K. Y. (2018). Data-driven Oxygen Excess Ratio Control for Proton Exchange Membrane Fuel Cell. *Appl. Energ.* 231, 866–875. doi:10.1016/j.apenergy.2018.09.036

Talj, R. J., Hissel, D., Ortega, R., Becherif, M., and Hilairet, M. (2010). Experimental Validation of a PEM Fuel-Cell Reduced-Order Model and a Moto-Compressor Higher Order Sliding-Mode Control. *IEEE Trans. Ind. Electron.* 57, 1906–1913. doi:10.1109/TIE.2009.2029588

Wang, Y.-X., and Kim, Y.-B. (2014). Real-time Control for Air Excess Ratio of a PEM Fuel Cell System. *Ieee/asme Trans. Mechatron.* 19, 852–861. doi:10.1109/TMECH.2013.2262054

Yang, B., Li, D., Zeng, C., Chen, Y., Guo, Z., Wang, J., et al. (2021a). Parameter Extraction of PEMFC via Bayesian Regularization Neural Network Based Meta-Heuristic Algorithms. *Energy* 228, 120592. doi:10.1016/j.energy.2021.120592

Yang, B., Swe, T., Chen, Y., Zeng, C., Shu, H., Li, X., et al. (2021b). Energy Cooperation between Myanmar and China under One Belt One Road: Current State, Challenges and Perspectives. *Energy* 215, 119130. doi:10.1016/j.energy.2020.119130

Yang, B., Wang, J., Zhang, X., Yu, T., Yao, W., Shu, H., et al. (2020). Comprehensive Overview of Meta-Heuristic Algorithm Applications on PV Cell Parameter Identification. *Energ. Convers. Manag.* 208, 112595. doi:10.1016/j.enconman.2020.112595

Yang, B., Yu, T., Shu, H., Dong, J., and Jiang, L. (2018). Robust Sliding-Mode Control of Wind Energy Conversion Systems for Optimal Power Extraction via Nonlinear Perturbation Observers. *Appl. Energ.* 210, 711–723. doi:10.1016/j.apenergy.2017.08.027

Yang, B., Yu, T., Zhang, X., Li, H., Shu, H., Sang, Y., et al. (2019a). Dynamic Leader Based Collective Intelligence for Maximum Power point Tracking of PV Systems Affected by Partial Shading Condition. *Energ. Convers. Manag.* 179, 286–303. doi:10.1016/j.enconman.2018.10.074

Yang, B., Zeng, C., Wang, L., Guo, Y., Chen, G., Guo, Z., et al. (2021c). Parameter Identification of Proton Exchange Membrane Fuel Cell via Levenberg-Marquardt Backpropagation Algorithm. *Int. J. Hydrogen Energ.* 46, 22998–23012. doi:10.1016/j.ijhydene.2021.04.130

Yang, B., Zhong, L., Zhang, X., Shu, H., Yu, T., Li, H., et al. (2019b). Novel Bio-Inspired Memetic Salp Swarm Algorithm and Application to MPPT for PV Systems Considering Partial Shading Condition. *J. Clean. Prod.* 215, 1203–1222. doi:10.1016/j.jclepro.2019.01.150

Zhang, J., Liu, G., Yu, W., and Ouyang, M. (2008). Adaptive Control of the Airflow of a PEM Fuel Cell System. *J. Power Sourc.* 179, 649–659. doi:10.1016/j.jpowsour.2008.01.015

Zhang, X., Li, S., He, T., Yang, B., Yu, T., Li, H., et al. (2019). Memetic Reinforcement Learning Based Maximum Power point Tracking Design for PV Systems under Partial Shading Condition. *Energy* 174, 1079–1090. doi:10.1016/j.energy.2019.03.053

Zhang, X., Tan, T., Zhou, B., Yu, T., Yang, B., and Huang, X. (2021). Adaptive Distributed Auction-Based Algorithm for Optimal Mileage Based AGC Dispatch with High Participation of Renewable Energy. *Int. J. Electr. Power Energ. Syst.* 124, 106371. doi:10.1016/j.ijepes.2020.106371

Zhao, D., Li, F., Ma, R., Zhao, G., and Huangfu, Y. (2020). An Unknown Input Nonlinear Observer Based Fractional Order PID Control of Fuel Cell Air Supply System. *IEEE Trans. Ind. Applicat.* 56, 5523–5532. doi:10.1109/TIA.2020.2999037

Conflict of Interest: Author Y Li was employed by the company China Electric Power Research Institute.

The remaining authors declare that the research was conducted in the absence of any commercial or financial relationships that could be construed as a potential conflict of interest.

Publisher's Note: All claims expressed in this article are solely those of the authors and do not necessarily represent those of their affiliated organizations, or those of the publisher, the editors, and the reviewers. Any product that may be evaluated in this article, or claim that may be made by its manufacturer, is not guaranteed or endorsed by the publisher.

Copyright © 2021 Li, Li and Yu. This is an open-access article distributed under the terms of the Creative Commons Attribution License (CC BY). The use, distribution or reproduction in other forums is permitted, provided the original author(s) and the copyright owner(s) are credited and that the original publication in this journal is cited, in accordance with accepted academic practice. No use, distribution or reproduction is permitted which does not comply with these terms.

frontiers in Energy Research

BRIEF RESEARCH REPORT
published: 30 September 2021
doi: 10.3389/fenrg.2021.748782

Data-Driven Control for Proton Exchange Membrane Fuel Cells: Method and Application

Jiawen Li[1]*, *Kedong Zhu*[2] and *Tao Yu*[1]

[1]College of Electric Power, South China University of Technology, Guangzhou, China, [2]China Electric Power Research Institute (Nanjing), Nanjing, China

A data-driven optimal control method for an air supply system in proton exchange membrane fuel cells (PEMFCs) is proposed with the aim of improving the PEMFC net output power and operational efficiency. Moreover, a marginal utility-based double-delay deep deterministic policy gradient (MU-4DPG) algorithm is proposed as a an offline tuner for the PID controller. The coefficients of the PID controller are rectified and optimized during training in order to enhance the controller's performance. The design of the algorithm draws on the concept of marginal effects in Economics, in that the algorithm continuously switches between different forms of exploration noise during training so as to increase the diversity of samples, improve exploration efficiency and avoid Q-value overfitting, and ultimately improve the robustness of the algorithm. As detailed below, the effectiveness of the control method has been experimentally demonstrated.

Keywords: proton exchange membrane fuel cells, PID controller, data-driven optimal control, double-delay deep deterministic policy gradient, control system

OPEN ACCESS

Edited by:
Yaxing Ren,
University of Warwick,
United Kingdom

Reviewed by:
Chenhao Ren,
The University of Hong Kong, Hong Kong, SAR China
Du Gang,
North China Electric Power University, China

***Correspondence:**
Jiawen Li
eplijiawen@mail.scut.edu.cn

Specialty section:
This article was submitted to Smart Grids, a section of the journal Frontiers in Energy Research

Received: *28 July 2021*
Accepted: *02 August 2021*
Published: *30 September 2021*

Citation:
Li J, Zhu K and Yu T (2021) Data-Driven Control for Proton Exchange Membrane Fuel Cells: Method and Application. Front. Energy Res. 9:748782. doi: 10.3389/fenrg.2021.748782

INTRODUCTION

Proton exchange membrane fuel cells (PEMFCs) convert hydrogen energy into electrical energy, and release heat energy directly via an electrochemical reaction (Sun et al., 2019; Yang et al., 2019). The only by-product of the reaction is water, and the whole reaction process does not involve a heat engine process (Yang et al., 2019; Yang et al., 2019) and so it is not limited by the Carnot cycle; thus, the PEMFC is therefore a more environmentally friendly power generation device (Swain and Jena, 2015; Yang et al., 2016; Yang et al., 2017; Yang et al., 2018).

However, PEMFC systems are not entirely compatible with fluctuating load conditions as they have a time lag factored into the air supply system (Yang et al., 2018), and so the supply of air flow does not respond quickly to changes in load. If the air flow in the system is less than that required for the electrochemical reaction, the system cannot be powered properly, leading to severe damage to the proton membrane and reduced working lifetime of the stack (Yang et al., 2020). If the air flow in the system is much higher than the required flow for the electrochemical reaction, the output power is increased, but the power consumption of the compressor increases significantly, which seriously impairs the electrical efficiency of the system. For high-power PEMFC systems, it is necessary to control the air flow so that the air supply system can respond quickly when the load changes (Li et al., 2021; Li and Yu, 2021).

For the regulation of air systems, a large number of control algorithms have been applied in practice.

To achieve optimum performance, it is necessary to co-ordinate the work of the various systems and design the appropriate algorithms for PEMFC control. The most widely used controller in the

industry is the PID controller, which is simple and easy to design, and which is widely used in the PEMFC field. However, PID controllers have certain shortcomings in their ability to resist interference, and researchers of PEMFC systems have explored the use of complex PID control algorithms as potential replacements for the traditional PID controller.

Rgab et al. (2010) proposed a neural network PID controller for controlling the air flow in a PEMFC. Aliasghary (2018) used an interval type II Fuzzy PID controller to control the air flow in a PEMFC system in order to improve the controller's ability to handle uncertainties within the PEMFC system. Baroud et al. (2017) designed a fuzzy adaptive controller that outperforms the fuzzy logic controller and the transcendental PID controller in terms of key performance indicators such as integration squared error, integration time, overshoot of the closed-loop system, stabilization time, and rise time. The fuzzy controller was used by Beiram et al. (2015) to prevent oxygen starvation and ensure maximum net PEMFC power, reducing steady-state errors.

The above innovations can improve the adaptive ability and anti-interference of PID algorithms to a certain extent, but they also increase the calculation volume and calculation time of the algorithms, which makes it harder to ensure the timeliness of the control. In view of these problems, some algorithms that are optimized for the PID algorithm coefficients are more suitable.

The Deep Deterministic Policy Gradient algorithm (DDPG) in deep reinforcement learning is a model-free control algorithm (Zhang et al., 2019; Zhang and Yu, 2019; Zhang et al., 2021) with a simple structure, small computational effort and high robustness, properties which make DDPG an ideal candidate for optimizing the coefficients of PID control algorithms (Zhang et al., 2018). Since DDPG does not require model identification so as to accommodate the uncertainty inherent in nonlinear control, it has been applied in various control fields (Zhang et al., 2016); nevertheless, the algorithm's weak exploration capability explains its low robustness when the algorithm is applied directly as a controller for the control algorithm.

In order to combine the advantages of the DDPG algorithm and PID algorithm, a data-driven method for the optimal control of air flow in a PEMFC is proposed. A marginal utility-based double-delay deep deterministic policy gradient (MU-4DPG) algorithm is proposed as a tuner for the PID controller, one which is trained offline.

The coefficients of the PID controller are rectified and optimized to obtain a PID controller with better performance. The algorithm operates on the principle of marginal effects, a popular analytical concept in the field of Economics, by continuously switching the form of exploration noise in training in order to increase the diversity of samples, improve exploration efficiency and prevent Q-value overfitting, and ultimately improve the robustness of the algorithm to a better performing PID controller.

The innovations in this paper are as follows:

1) A data-driven method for the optimal control of air flow in a PEMFC with proton exchange membrane fuel cells is presented.
2) For this controller, a MU-4DPG algorithm is proposed as the tuner for the PID controller. The algorithm can rectify and optimize the coefficients of the PID controller during offline training to deliver a PID controller with better performance. As mentioned, the design of the algorithm reflects the principle of marginal effects, in that it can enhance the diversity of samples by continuously switching the form of exploration noise in training to improve the exploration efficiency while preventing Q-value overfitting, ultimately improving the robustness of the algorithm and ensuring a better-performing PID controller.

The remainder of this paper comprises the following sections: the PEMFC model is demonstrated in Section *PEMFC Air Supply System Model*, and the algorithm is described in Section *Proposed Method*; the experimental results are analysed and discussed in Section *Case Studies*, and the findings in this paper are summarised in Section *Conclusion*.

PEMFC AIR SUPPLY SYSTEM MODEL

Theoretical Conditions

1) The gas settings accord with the Ideal Gas Law.
2) The air temperature inside the electrodes is equal to the temperature of the stack.
3) When the relative humidity of the gas exceeds 100%, the water vapour concentrates into liquid form.

Air Compressor Model

The air compressor compresses the air and transfers it at a certain pressure to the supply line, where it is cooled and humidified, and then transferred to the fuel cell cathode. The air compressor is the core component within the PEMFC system. The dynamic characteristics of the air compressor drive motor can be expressed by the following set of equations:

$$J_{cp}\frac{d\omega_{cp}}{dt} = \tau_{cm} - \tau_{cp} \tag{1}$$

The motor driving torque of the compressor can be obtained from the static motor equation :

$$\tau_{cm} = \eta_{cm}\frac{k_t}{R_{cm}}\left(v_{cm} - k_v\omega_{cp}\right) \tag{2}$$

The load torque of the air compressor can be calculated using the following thermal equation:

$$\tau_{cp} = \frac{C_p T_{atm}}{\omega_{cp}\eta_{cp}}\left[\left(\frac{p_{sm}}{p_{atm}}\right)^{\frac{\gamma-1}{\gamma}} - 1\right]F_{cp} \tag{3}$$

The temperature of the air leaving the compressor is

$$T_{cp,\text{out}} = T_{cp,in} + \frac{T_{cp,in}}{\eta_{cp}}\left[\left(\frac{p_{cp,\text{out}}}{p_{cp,in}}\right)^{\gamma-1/\gamma} - 1\right] \tag{4}$$

The supply of air is completed by the compressor, which consumes electric energy when it is working. Taking into account the power consumed by the compressor and ignoring the power consumption of other equipment in the system, the effective power output of the entire PEMFC system can be expressed as:

$$P_{\text{out}} = P_{\text{stack}} - P_{com} \tag{5}$$

Return Pipe Model

The principle of the return line is similar to that of the inlet line, but since the temperature of the gas flowing out of the reactor is much lower than that of the gas flowing into the reactor, the effect of temperature is ignored and the principle of the return line can be expressed as follows:

$$\frac{dp_{rm}}{dt} = \frac{R_a T_{rm}}{V_{rm}} \left(F_{ca,out} - F_{rm,out}\right) \tag{6}$$

In this paper, according to different pressure ratios, a nonlinear mouth equation is used to determine that $F_{\text{rm}.out}$ is

$$F_{rm.\text{out}} = \frac{C_{D.rm} A_{T,rm} p_{rm}}{\sqrt{RT_{rm}}} \left(\frac{p_{atm}}{p_{rm}}\right)^{1/\gamma} \sqrt{\frac{2\gamma}{\gamma - 1}\left[1 - \left(\frac{p_{atm}}{p_{rm}}\right)^{\gamma-1/\gamma}\right]}, \quad \frac{p_{atm}}{p_{rm1}} > \left(\frac{2}{\gamma + 1}\right)^{\gamma/\gamma-1} \tag{7}$$

Cathode Model

This is obtained from the Ideal Gas Law:

$$\frac{V_{ca}}{RT}\frac{dP_{O2}}{dt} = w_{O2,\text{in}} - w_{O2,\text{react}} - w_{O2,\text{out}} \tag{8}$$

$$\frac{V_{ca}}{RT}\frac{dP_{N2}}{dt} = w_{N2,in} - w_{N2,out} \tag{9}$$

$$w_{O2,\text{react}} = \frac{NI}{4F} \tag{10}$$

$$w_{O2,\text{out}} = \frac{P_{O2}}{P_{ca}} w_{ca,out} \tag{11}$$

$$w_{ca,out} = k_{ca}\left(P_{ca} - P_b\right) \tag{12}$$

The oxygen excess ratio (OER) is a key variable that significantly influences the fuel cell system's performance. The OER is expressed as follows:

$$\lambda_{O_2} = \frac{W_{O_2,in}}{W_{O_2,\text{ret}}} \tag{13}$$

Anode Model

The basic principle of proportional valve control can be expressed as follows:

$$\frac{V_{an}}{RT}\frac{dP_{H2}}{dt} = w_{H2,\text{in}} - w_{H2,\text{react}} - w_{H2,\text{out}} \tag{14}$$

$$w_{H2,\text{react}} = \frac{NI}{2F} \tag{15}$$

$$w_{H2,\text{out}} = \frac{P_{H2}}{P_{an}} w_{an,\text{out}} \tag{16}$$

$$w_{an,out} = k_{an}\left(P_{an} - P_b\right) \tag{17}$$

Supply Pipeline Model

In a PEMFC system, the term "gas supply piping" refers usually to the collection of piping for the cathode only, due to the small size of the anode gas supply piping and return piping. The cathode gas supply pipeline connects the air compressor to the fuel cell reactor cathode and, according to the Law of Conservation of Mass, the settings for gas flowing into the pipeline and the gas flowing out of the pipeline satisfy the following equation:

$$\frac{dp_{sm}}{dt} = \frac{\gamma R_a}{V_{sm}}\left(F_{cp} T_{cp,\text{out}} - F_{sm,\text{out}} T_{sm}\right) \tag{18}$$

When the high-temperature gas from the compressor enters the gas supply line, its temperature and pressure change, so, according to the Law of Energy Conservation and the Ideal Gas Equation, the change of pressure in the gas supply line can be expressed as follows:

$$F_{sm,out} = k_{sm,out}\left(p_{sm} - p_{ca}\right) \tag{19}$$

PROPOSED METHOD

Technical Principles

The control model includes the PEMFC reactor, the air compressor and its PID controller. The controller of the PID is equated to an agent undergoing training, which in turn enables the agent to adapt to the non-linear characteristics of the PEMFC and improve the overall control performance of the OER and output voltage. For pre-learning, the proposed algorithm is used to rectify the coefficients k_p, k_i, and k_d of the PID controller.

The tuning methods employ a linear quadratic Gaussian (LQG) objective function.

In order to maintain the water level while minimizing control effort u, the controllers employ the following LQG criterion:

$$J = \lim_{T \Rightarrow \infty} E\left(\frac{1}{T}\int_0^T \left(\left(y_{\text{ref}} - y\right)^2(t) + 0.01u^2(t)\right)\text{dt}\right) \tag{20}$$

When applied online, the agent issues the optimal voltage of the air compressor once it has received data on the status of the PEMFC. The control interval of the agent is 0.01 s.

DDPG

The DDPG algorithm is a policy-based RL method which is based on an empirical replay approach and which uses deep neural networks as nonlinear function approximators to construct $Q(s, a; \theta^Q)$ $\mu(s; \theta^\mu)$ and $\mu'(s; \theta^\mu)$critic network model action and target Q values.

$$\mu'(s_t) = \mu(s|\theta^\mu) + N \tag{21}$$

The critic network is updated by minimizing the loss function. The $L(\theta^Q)$ network parameters are shown as follows:

$$y_t = r(s_t, a_t) + \gamma Q'\left(s_{t+1}, \mu'(s_{t+1}|\theta^\mu)\theta^Q\right) \tag{22}$$

The gradient of the actor network, which depends on which the actor network parameters are updated, is expressed as follows:

$$\nabla_{\theta^\mu} J(\theta^\mu) = \frac{1}{N}\sum_i \nabla_a Q\left(s, a|\theta^Q\right)\Big|_{s=s_i, a=\mu(s_i)} \nabla_{\theta^\mu}\mu(s|\theta^\mu)\Big|_{s_i} \tag{23}$$

DDPG improves the stability of the learning process by slowly updating the weights of the actor target network and the critic target network:

$$\begin{cases} \theta^\mu \leftarrow \tau\theta + (1-\tau)\theta' \\ \theta^{Q'} \leftarrow \tau\theta + (1-\tau)\theta' \end{cases} \tag{24}$$

MU-4DPG Algorithm

MU-4DPG is an extension of the DDPG algorithm, which in turn has low robustness due to its single exploration principle. This problem, similar to the concept of marginal effect in Economics, is due to the fact that the exploration principle is too homogeneous, and so the agent receives only a fixed number of types of actions, and struggles to obtain richer samples. Marginal effects are defined as those in which a successive increase in one input, when other inputs are fixed, results in a gradual decrease in the benefit, that is, the amount of output per unit of input added decreases when the added input exceeds a certain level. Therefore, the diversity of samples obtained by using the same noise model over and over again decreases with an increase of episodes. In order to solve this problem, the method proposed in this paper improves the diversity of samples by continuously switching between different forms of exploration noise during training, improving the exploration efficiency, and adopting a number of strategies in order to prevent Q-value overfitting. The result is an algorithm with higher robustness, and a better-performing PID controller.

The MU-4DPG algorithm includes two critics and one actor, and, in order to solve the Q overestimation problem that occurs in the DDPG algorithm, the proposed algorithm uses three techniques: clipping multiple Q learning, delayed policy update, and smooth regularization of the target policy.

1) Clipped multi-Q learning. The "student" agent in MU-4DPG uses clipped multi-Q learning to calculate the target value:

$$y_t^1 = r(s_t, a_t) + \gamma \min_{i=1,2,3} Q_{\theta i'}\left(s_{t+1}, \pi_{\phi_1}(s_{t+1})\right) \tag{25}$$

2) Policy delayed update. After every d update of the critic network, an update of the actor network is performed so as to ensure that the actor network can be updated with a low Q-value error, in order to improve the update efficiency of the actor network.
3) Target policy smoothing regularization. The algorithm introduces a regularization method to reduce the variance of the target values by smoothing the Q-estimates by bootstrapping estimates of similar state action pairs:

$$y_t = r(s_t, a_t) + \mathrm{E}_\varepsilon\left[Q_{\theta'}\left(s_{t+1}, \pi_{\phi'}(s_{t+1}) + \varepsilon\right)\right] \tag{26}$$

Smooth regularization is also achieved by adding a random noise to the target strategy and averaging over the mini-batch:

$$y_t = r(s_t, a_t) + \gamma \min_{i=1,2} Q_{\theta_t}\left(s_{t+1}, \pi_{\phi'}(s_{t+1}) + \varepsilon\right) \tag{27}$$

$$\varepsilon \sim clip\left(N(0, \sigma), -c, c\right) \tag{28}$$

4) Marginal effect mechanism. The actor network in the agent switches between Gaussian noise and OU noise, depending on the episodes, in order to obtain a more diverse sample.

Episodes are 0–1,000, 2000–3,000, 4,000–5,000, 7,000–8,000, 9,000–10,000 when OU noise is used for exploration:

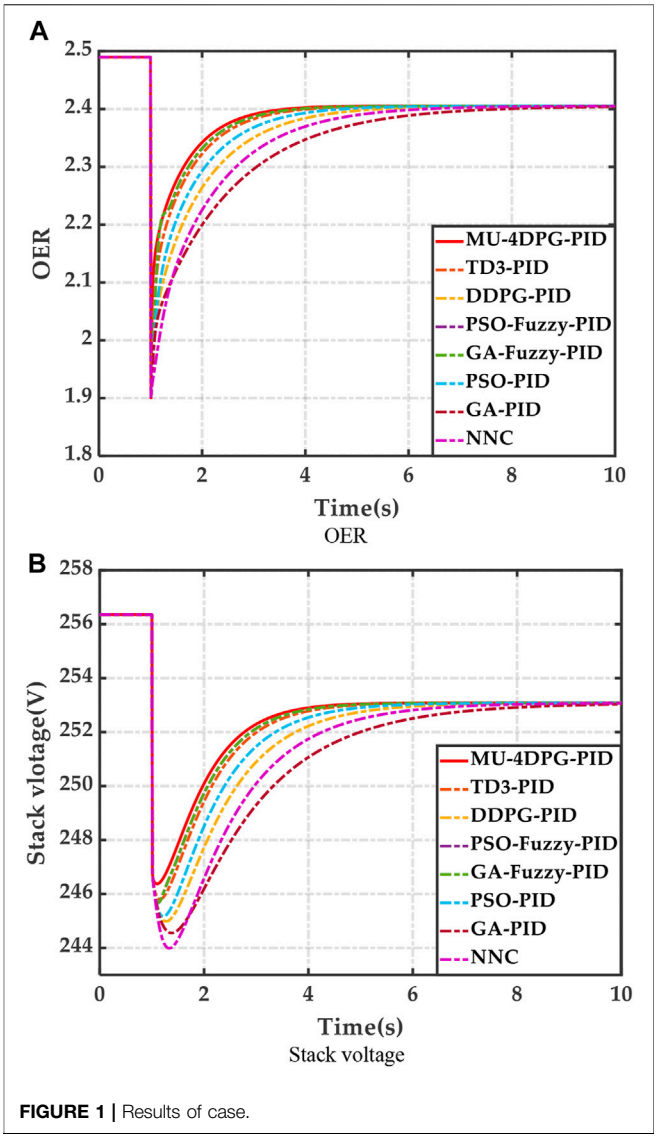


FIGURE 1 | Results of case.

$$a_{OU}^{j} = \pi_{\phi}^{j}(s) + N_{OU}^{j} \tag{29}$$

whereby $\pi_{\theta}^{j}(s)$ is the actor network policy, and N_{OU} is the OU noise.

Episodes are 1,001–1999, 3,001–3,999, 5,001–5,999, 6,001–6,999, 8,001–8,999 when explored using Gaussian noise:

$$a_{\text{Gaussian}}^{m} = \pi_{\theta}^{\text{m}}(s) + \mathcal{N}_{Gaussian}^{m} \tag{30}$$

whereby $\pi_{\theta}^{m}(s)$ is the actor network policy, and $_{NGaussian}$ is Gaussian noise.

CASE STUDIES

In the simulation, the MU-4DPG tuning PID (MU-4DPG-PID) was compared against the TD3 tuning PID (TD3-PID) controller, DDPG tuning PID (DDPG-PID) controller, PSO optimized fuzzy PID controller (PSO-Fuzzy- PID), GA-optimized fuzzy PID controller (GA-Fuzzy-PID), PSO-optimized PID controller (PSO-PID), GA-optimized PID controller (GA-PID), and neural network control (NNC). The results are shown in **Figures 1A,B**.

1) Comparison of the proposed algorithm with other algorithms. According to **Figures 1A,B**, the OER of the MU-4DPG algorithm has a better climbing speed response, a more stable OER, and a smaller overshoot. In addition, the MU-4DPG algorithm has a more rapid response time for the stack voltage and a smaller overshoot, and it does not permit large fluctuations. By contrast, the other algorithms each have a large overshoot in both the OER and output voltage, and a slower response time, resulting in large oscillations in both the OER and the stack voltage, which can lead to large oscillations in the output voltage. Therefore, the MU-4DPG algorithm has the best control performance.
2) The reasons for this phenomenon are: the robustness of the algorithm is reduced compared to other DRL algorithms because more techniques are not used in pre-learning, resulting in a large output voltage overshoot and output voltage fluctuations that affect the output performance of the PEMFC. the Fuzzy-based algorithm is too simple in its rules, resulting in low robustness and adaptive capability of this class of algorithms. The PSO-PID, and GA-PID algorithms inside the conventional control algorithm do not have the adaptive capability to adjust the PID parameters, and therefore have difficulty in adapting to the non-linearity of the PEMFC. The NNC algorithm, on the other hand, relies on the effects of training, resulting in low robustness and therefore the lowest control performance of this class of algorithms.

CONCLUSION

1) This paper presents a large-scale deep reinforcement learning based adaptive optimal PID controller for controlling proton exchange membrane fuel cell (PEMFC) air flow.
2) A marginal utility-based double-delay deep deterministic policy gradient (MU-4DPG) algorithm is proposed as a tuner for the PID controller. The coefficients of the PID controller are rectified and optimized during off-line training to obtain a PID controller with better performance and fixed coefficients. The algorithm operates on the Economics principle of marginal effects, in that it continuously switches between different forms of exploration noise in training in order to increase the diversity of samples, improve exploration efficiency and prevent Q-value overfitting, which altogether lead to an improvement in the robustness of the algorithm and a better-performing PID controller.
3) The results of the simulation involving both the proposed controller and two groups of existing controllers (adaptive PID and conventional control) indicate that the MU-4DPG-PID controller is able to maintain a stable output voltage while effectively avoiding oxygen starvation or oxygen supersaturation in the fuel cell.

DATA AVAILABILITY STATEMENT

The original contributions presented in the study are included in the article/supplementary material, further inquiries can be directed to the corresponding author.

AUTHOR CONTRIBUTIONS

JL: Conceptualization, Methodology, Software. Zhang: Writing-Reviewing and Editing. Data curation, Writing-Original draft preparation. Visualization, Investigation. KZ: Validation. TY: Supervision.

FUNDING

This work was jointly supported by National Natural Science Foundation of China (U2066212).

REFERENCES

Aliasghary, M. (2018). Control of PEM Fuel Cell Systems Using Interval Type-2 Fuzzy PID Approach. *Fuel Cells* 18, 449–456. doi:10.1002/fuce.201700157

Baroud, Z., Benmiloud, M., Benalia, A., and Ocampo-Martinez, C. (2017). Novel Hybrid Fuzzy-PID Control Scheme for Air Supply in PEM Fuel-Cell-Based Systems. *Int. J. Hydrogen Energ.* 42, 10435–10447. doi:10.1016/j.ijhydene.2017.01.014

Beirami, H., Shabestari, A. Z., and Zerafat, M. M. (2015). Optimal PID Plus Fuzzy Controller Design for a PEM Fuel Cell Air Feed System Using the Self-Adaptive

Differential Evolution Algorithm. *Int. J. Hydrogen Energ.* 40, 9422–9434. doi:10.1016/j.ijhydene.2015.05.114

Li, J., and Yu, T. (2021). A New Adaptive Controller Based on Distributed Deep Reinforcement Learning for PEMFC Air Supply System. *Energ. Rep.* 7, 1267–1279. doi:10.1016/j.egyr.2021.02.043

Li, J., Yu, T., Zhang, X., Li, F., Lin, D., and Zhu, H. (2021). Efficient Experience Replay Based Deep Deterministic Policy Gradient for AGC Dispatch in Integrated Energy System. *Appl. Energ.* 285, 116386. doi:10.1016/j.apenergy.2020.116386

Rgab, O., Yu, D. L., and Gomm, J. B. (2010). Polymer Electrolyte Membrane Fuel Cell Control with Feed-Forward and Feedback Strategy. *Int. J. Eng. Sci. Technol.* 2, 80–91. doi:10.4314/ijest.v2i10.64012

Sun, L., Jin, Y., Pan, L., Shen, J., and Lee, K. Y. (2019). Efficiency Analysis and Control of a Grid-Connected PEM Fuel Cell in Distributed Generation. *Energ. Convers. Manage.* 195, 587–596. doi:10.1016/j.enconman.2019.04.041

Swain, P., and Jena, D. (2015). "PID Control Design for the Pressure Regulation of PEM Fuel Cell," in 2015 International Conference on Recent Developments in Control, Automation and Power Engineering (RDCAPE), Noida, India, 12-13 March 2015 (IEEE), 286–291. doi:10.1109/rdcape.2015.7281411

Yang, B., Jiang, L., Wang, L., Yao, W., and Wu, Q. H. (2016). Nonlinear Maximum Power Point Tracking Control and Modal Analysis of DFIG Based Wind Turbine. *Int. J. Electr. Power Energ. Syst.* 74, 429–436. doi:10.1016/j.ijepes.2015.07.036

Yang, B., Zhang, X., Yu, T., Shu, H., and Fang, Z. (2017). Grouped Grey Wolf Optimizer for Maximum Power point Tracking of Doubly-Fed Induction Generator Based Wind Turbine. *Energ. Convers. Manage.* 133, 427–443. doi:10.1016/j.enconman.2016.10.062

Yang, B., Yu, T., Shu, H., Dong, J., and Jiang, L. (2018). Robust Sliding-Mode Control of Wind Energy Conversion Systems for Optimal Power Extraction via Nonlinear Perturbation Observers. *Appl. Energ.* 210, 711–723. doi:10.1016/j.apenergy.2017.08.027

Yang, B., Yu, T., Shu, H., Han, Y., Cao, P., and Jiang, L. (2019a). Adaptive Fractional-Order PID Control of PMSG-Based Wind Energy Conversion System for MPPT Using Linear Observers. *Int. Trans. Electr. Energ Syst.* 29 (9), e2697. doi:10.1002/etep.2697

Yang, B., Zhong, L., Zhang, X., Shu, H., Yu, T., Li, H., et al. (2019b). Novel Bio-Inspired Memetic Salp Swarm Algorithm and Application to MPPT for PV Systems Considering Partial Shading Condition. *J. Clean. Prod.* 215, 1203–1222. doi:10.1016/j.jclepro.2019.01.150

Yang, B., Yu, T., Zhang, X., Li, H., Shu, H., Sang, Y., et al. (2019c). Dynamic Leader Based Collective Intelligence for Maximum Power point Tracking of PV Systems Affected by Partial Shading Condition. *Energ. Convers. Manage.* 179 (18), 286–303. doi:10.1016/j.enconman.2018.10.074

Yang, B., Wang, J., Zhang, X., Yu, T., Yao, W., Shu, H., et al. (2020). Comprehensive Overview of Meta-Heuristic Algorithm Applications on Pv Cell Parameter Identification. *Energ. Convers. Manage.* 208, 112595. doi:10.1016/j.enconman.2020.112595

Zhang, X., and Yu, T. (2019). Fast Stackelberg Equilibrium Learning for Real-Time Coordinated Energy Control of a Multi-Area Integrated Energy System. *Appl. Therm. Eng.* 153, 225–241. doi:10.1016/j.applthermaleng.2019.02.053

Zhang, X., Xu, H., Yu, T., Yang, B., and Xu, M. (2016). Robust Collaborative Consensus Algorithm for Decentralized Economic Dispatch with a Practical Communication Network. *Electric Power Syst. Res.* 140, 597–610. doi:10.1016/j.epsr.2016.05.014

Zhang, X., Yu, T., Xu, Z., and Fan, Z. (2018). A Cyber-Physical-Social System with Parallel Learning for Distributed Energy Management of a Microgrid. *Energy* 165, 205–221. doi:10.1016/j.energy.2018.09.069

Zhang, X., Li, S., He, T., Yang, B., Yu, T., Li, H., et al. (2019). Memetic Reinforcement Learning Based Maximum Power point Tracking Design for PV Systems under Partial Shading Condition. *Energy* 174, 1079–1090. doi:10.1016/j.energy.2019.03.053

Zhang, X., Tan, T., Zhou, B., Yu, T., Yang, B., and Huang, X. (2021). Adaptive Distributed Auction-Based Algorithm for Optimal Mileage Based AGC Dispatch with High Participation of Renewable Energy. *Int. J. Electr. Power Energ. Syst.* 124, 106371. doi:10.1016/j.ijepes.2020.106371

Conflict of Interest: The authors declare that the research was conducted in the absence of any commercial or financial relationships that could be construed as a potential conflict of interest.

Publisher's Note: All claims expressed in this article are solely those of the authors and do not necessarily represent those of their affiliated organizations, or those of the publisher, the editors and the reviewers. Any product that may be evaluated in this article, or claim that may be made by its manufacturer, is not guaranteed or endorsed by the publisher.

Copyright © 2021 Li, Zhu and Yu. This is an open-access article distributed under the terms of the Creative Commons Attribution License (CC BY). The use, distribution or reproduction in other forums is permitted, provided the original author(s) and the copyright owner(s) are credited and that the original publication in this journal is cited, in accordance with accepted academic practice. No use, distribution or reproduction is permitted which does not comply with these terms.

frontiers in Energy Research

ORIGINAL RESEARCH
published: 01 October 2021
doi: 10.3389/fenrg.2021.752422

An Inductor Current Sensorless Control Strategy Based on Modified VSG Method for Single-Phase Microgrid Application With Seamless Transfer Capability

Zhi Zhang[1], Junkai Wu[2], Liupeng Zheng[1], Di Xie[3]* and Xiao Tang[1]*

[1]School of Electrical Engineering and Intelligentization, Dongguan University of Technology, Dongguan, China, [2]Heyuan Power Supply Bureau of Guangdong Power Grid, Heyuan, China, [3]Guangdong HYNN Technologies Co., Ltd., Dongguan, China

This paper proposes an inductor current sensorless control strategy based on modified virtual synchronous generator (VSG) method for single-phase inverter-interfaced microgrid application. Firstly, the outer power loop with Q-U integral term is presented for output reactive power enhancement, and an inner voltage regulation loop based on luenberger state observer is proposed to reduce the inductor current sensor. Meanwhile, in order to improve the response speed of the observer, the luenberger observer is designed based on the optimal pole assignment method. Secondly, a seamless switching strategy based on the modified VSG method is proposed, which can realize the seamless transition between the island mode and grid-connected mode. Finally, a single-phase 3kW VSG prototype is built, and the effectiveness and correctness of the proposed control strategy is verified by the simulation and experimental results.

Keywords: VSG, luenberger state observer, microgrid, seamless switching, single-phase

OPEN ACCESS

Edited by:
Xiaoshun Zhang,
Shantou University, China

Reviewed by:
Bin Liu,
Guangxi University, China
Bin Gu,
Shanghai Institute of Technology, China

****Correspondence:***
Zhi Zhang
zhangz@dgut.edu.cn
Di Xie
xiedi0813@aliyun.com

Specialty section:
This article was submitted to Smart Grids, a section of the journal Frontiers in Energy Research

Received: *03 August 2021*
Accepted: *13 September 2021*
Published: *01 October 2021*

Citation:
Zhang Z, Wu J, Zheng L, Xie D and Tang X (2021) An Inductor Current Sensorless Control Strategy Based on Modified VSG Method for Single-Phase Microgrid Application With Seamless Transfer Capability. Front. Energy Res. 9:752422. doi: 10.3389/fenrg.2021.752422

1 INTRODUCTION

With the increasing popularity of distributed power sources (such as photovoltaic panels, fuel cells, wind turbines etc.) (Valinejad et al., 2020; Canziani et al., 2021), microgrid based on these distributed generations (DGs) has become an effective power supply supplement for the main power grid (Wang et al., 2015; Qazi et al., 2021). Meantime, the inverter-based interfaces which is connected between the DG unit and the power grid are used more and more widely for grid-connected application (Zhu and Fei, 2018; Tran and Kim, 2020), but the traditional inverters exhibit relatively rapid voltage/frequency changes when faced with power changes, which is not conducive to the safe operation of power electronic devices, and it also could lead to the instability of the power grid system (Van, 2010).

In view of the lack of stability of the inverter-based microgrid, the VSG technology which mimics the characteristics of traditional synchronous generator (SG) is proposed (Blaabjerg et al., 2006; Beck and Hesse, 2007; Zhong and Weiss, 2011), it can provide virtual inertia and damping for the inverter to enhance the stability of the microgrid system. At present, the VSG-based inverters are widely implemented for three-phase grid-connected applications and various improved VSG strategies are proposed to obtain better static and dynamic performance of the inverter system. Reference (Li et al., 2017) proposes a self-adaptive inertia and damping combination control method to improve the frequency stability. Reference (Zhong and Weiss, 2011) illustrates a magnitude-reshaping strategy to

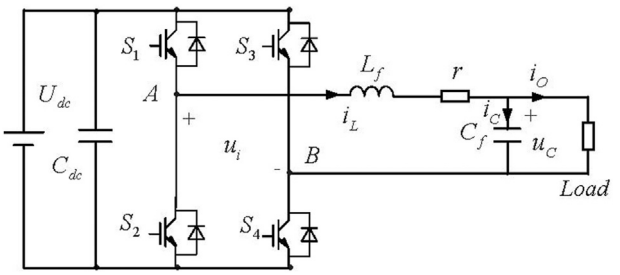


FIGURE 1 | Topology and basic block diagram of the single-phase VSG.

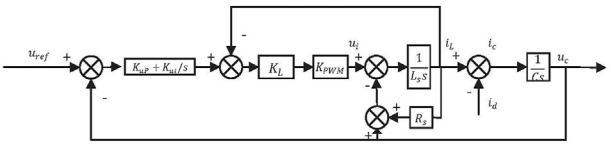


FIGURE 2 | Block diagram of inner voltage regulation loop based on capacitor voltage and inductance current feedback.

TABLE 1 | System parameters.

Parameters	Value
DC link voltage amplitude U_{dc}	400 v
Capacitance capacity of DC link C_{dc}	6500 uF
Filter inductance L_s	2 mH
ESR of inductance R_s	0.01Ω
Filter capacitor C	65 uF
AC line resistance R_g	0.64Ω
AC line inductance L_g	0.26 mH
RMS value of grid voltage U_g	220 V
$P-f$ droop coefficient k_p	2e-5
$Q-U$ droop coefficient k_q	5e-5
$Q-U$ droop integral coefficient k_i	0.1
Reference voltage amplitude E_{ref}	311 V
Virtual inertia J	0.8 $kg \cdot m^2$
Virtual damping D_p	15$N \cdot m \cdot s/rad$
Switching frequency f_s	10 kHz

increase the output impedance and suppress the harmonics when VSG-based system operates under distorted voltage condition, and high quality of grid-connected current can be obtained. In view of the presence of nonlinear loads and distorted grid, a hybrid harmonics suppression method which mainly consists of a local voltage harmonic control loop and an adaptive grid-connected current loop is presented in (Lou et al., 2021), high power quality of local load voltage and grid current are achieved. In (Teng et al., 2021), a composite control method which integrates the integral sliding mode and backstepping control method is proposed to realize the free switch between the island mode and grid-connected mode with high dynamic performance.

With the increasing installation capacity of household DG units, the power interface devices of single phase inverters have gradually received more and more attention (Monfared et al., 2014; Zhang et al., 2021). A flexible inertia optimization method based on hold filter is proposed for single-phase VSG-based inverter (Li et al., 2019), and the inertia can be freely adjusted to meet the actual system requirements without affecting the frequency stability. A robust power regulation controller is presented for single-phase grid-connected VSG-based inverter, the smooth power response characteristics and robustness to parameter variation can be achieved (Shao et al., 2019). A single-phase VSG-based inverter is proposed for vehicle-to-grid (V2G) application (Suul et al., 2016), it can provide primary frequency control, inertia emulation and local voltage or reactive power regulation. Referents (Zhang et al., 2017; Wang et al., 2018) illustrates an adaptive adjustment system damping ratio scheme to suppress the power and frequency oscillations, the dynamic performances of the VSG are enhanced. Reference (Zhao et al., 2017) presents a method based on virtual power calculation to realize the seamless transfer between islanded/grid-connected mode and enhance the stability of single-phase microgrid.

However, most of these control strategies mentioned above require the knowledge of the output voltage, load current and inductor current to achieve power/voltage asymptotic tracking. In order to improve the stability and reduce the sensor counts, some voltage or current sensorless control strategies based on state observer methods are proposed. A robust nonlinear controller based on variable structure observer is proposed for output voltage tracking (Latham et al., 2017), which can improve the steady-state and transient performance of the inverter under nonlinear loads conditions. A full-state feedback current controller with a reduced-order disturbance observer is proposed for single-phase grid-tied inverter systeme (Cheng et al., 2021), it can reduce the influence of uncertain interference factors and improve the robustness of the system. Reference (Hinsui and Sangtungtong, 2019) designed a voltage observer instead of a voltage sensor for the single-phase grid-connected inverter system, and it can achieve the same performance in comparison with the actual solar-array voltage.

In this paper, a modified VSG strategy with the inductor current observer is proposed for single-phase inverter application, and it can be summarized as follows: 1) The improved algorithm for single-phase VSG has the ability to simulate the frequency and voltage characteristics of SG, and it can achieve the zero-steady-error tracking of the reference output reactive power when the VSG operates in grid-connected mode. The small signal model of the modified VSG algorithm for grid-connected application is also established, and the selections for the key parameters of inertia and damping coefficient are analyzed in detail. 2) A luenberger state observer based on the optimal pole assignment method for estimating the inductor current is proposed to reduce the sensor count and improve the dynamic performance of the single-phase inverter. 3) A seamless switching ability between grid-connected mode and island mode based on the proposed modified VSG method can be guaranteed.

This paper is organized as follows. **Section 2** gives the introduction of the basic structure of the modified VSG control strategy, and the influence of the damping coefficient and inertia for the stability of the modified VSG system is analyzed in detail. A luenberger observer-based inductor

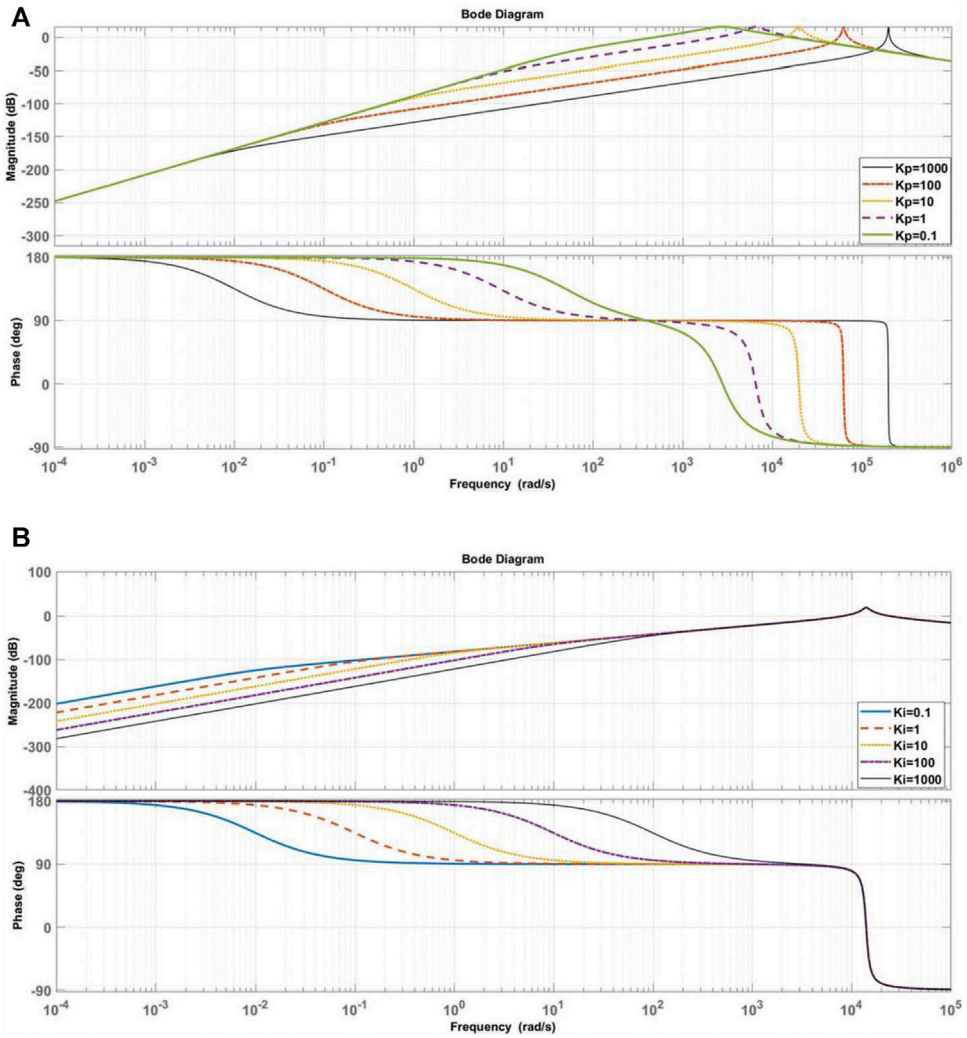


FIGURE 3 | Bode diagram of output impedance $Z_o(s)$. **(A)** Bode diagram of with different parameter K_{up}. **(B)** Bode diagram of with different parameter K_{ui}.

current sensorless control method for inner voltage regulation is presented in **Section 3**, and the optimal pole assignment is also introduced for the luenberger observer. **Section 4** introduces the seamless switching strategy between the island and grid-connected mode. Simulation and experimental results are provided in **Section 5** to verify the validity and feasibility of the proposed modified VSG method. Finally, the conclusion is summarized in **Section 6**.

2 BASIC STRUCTURE OF THE MODIFIED VSG CONTROL STRATEGY

The topology and basic block diagram of the single-phase VSG is shown in **Figure 1**. The main topology consists of a traditional H-bridge circuit with four power switches $V_{T1} \sim V_{T4}$. U_{dc} is the DC side power supply voltage, U_A is the arm-bridge voltage. Inductor L_S and capacitor C are composed of an LC filter circuit. R_s is the equivalent series resistance (ESR) of the filter inductor, and Z_{load} is the load. Z_g represents the line impedance and U_g is the grid voltage. The basic block diagram consists of an outer VSG power loop cascaded with an inner voltage regulation loop. The following are the detailed introduction for the basic block diagram.

2.1 Outer Loop of the Modified VSG

The output active power P_e and reactive power Q_e of single VSG can be calculated in the virtual two-phase system by sampling the output voltage u_C and load current i_d (Suul et al., 2016). The virtual voltage and current will be 90° phase shifted in stationary conditions, and the vector amplitudes of the voltage and current are equal to the amplitude of the measured signals of the voltage and current. Then, the amplitude E_0 and frequency ω of the output voltage reference can be obtained based on the VSG algorithm. The VSG algorithm includes active-frequency ($P - f$) and reactive-

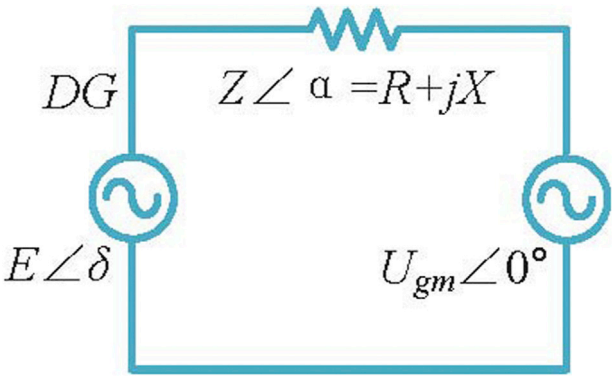


FIGURE 4 | The equivalent circuit when VSG operates in grid-connected mode.

voltage ($Q - U$) control method by mimicing the traditional SG (Zhong and Weiss, 2011). In convenience of practical engineering applications, the second-order model of traditional SG is expressed as

$$\begin{cases} T_m - T_e = \dfrac{P_m}{\omega} - \dfrac{P_e}{\omega} = J\dfrac{d\omega}{dt} + D_p(\omega - \omega_{ref}) \\ \dfrac{d\theta}{dt} = \omega \end{cases} \tag{1}$$

where T_m and T_e are the mechanical and electrical torques respectively, P_m and P_e are the mechanical and electrical power. J is the moment of inertia, D_p is the damping coefficient, ω is the rotor angular velocity, and ω_{ref} is the grid synchronous angular velocity. When the single-phase VSG operates in grid-connected mode, the value of ω_{ref} is the power grid frequency ω_g which can be obtained through a phase-locked loop (PLL). When the VSG works in island mode, its value is equal to the microgrid reference frequency.

In order to mimic the primary frequency function of the SG, the primary frequency controller is substituted into the power frequency **Eq. 1**. The primary frequency controller can be expressed as

$$P_m - P_{ref} = k_p(\omega_{ref} - \omega) \tag{2}$$

where k_p is the $P - f$ droop coefficient, P_{ref} is the active power reference value. By combing **Eqs 1–3** can be deduced as

$$P_{ref} - P_e = \omega J\frac{d\omega}{dt} + \omega D_p(\omega - \omega_{ref}) - k_p(\omega_{ref} - \omega) \tag{3}$$

From the above **Eq. 3**, it can be seen that the $P - f$ controller of the VSG includes the characteristics of the droop control, moment of inertia and damp, which can enhance the stability of the power grid.

The $Q - U$ controller of the VSG mimics the excitation regulation function of the SG to realize the drop characteristics of reactive power and voltage amplitude (Zhong and Weiss, 2011), and the equation can be expressed as:

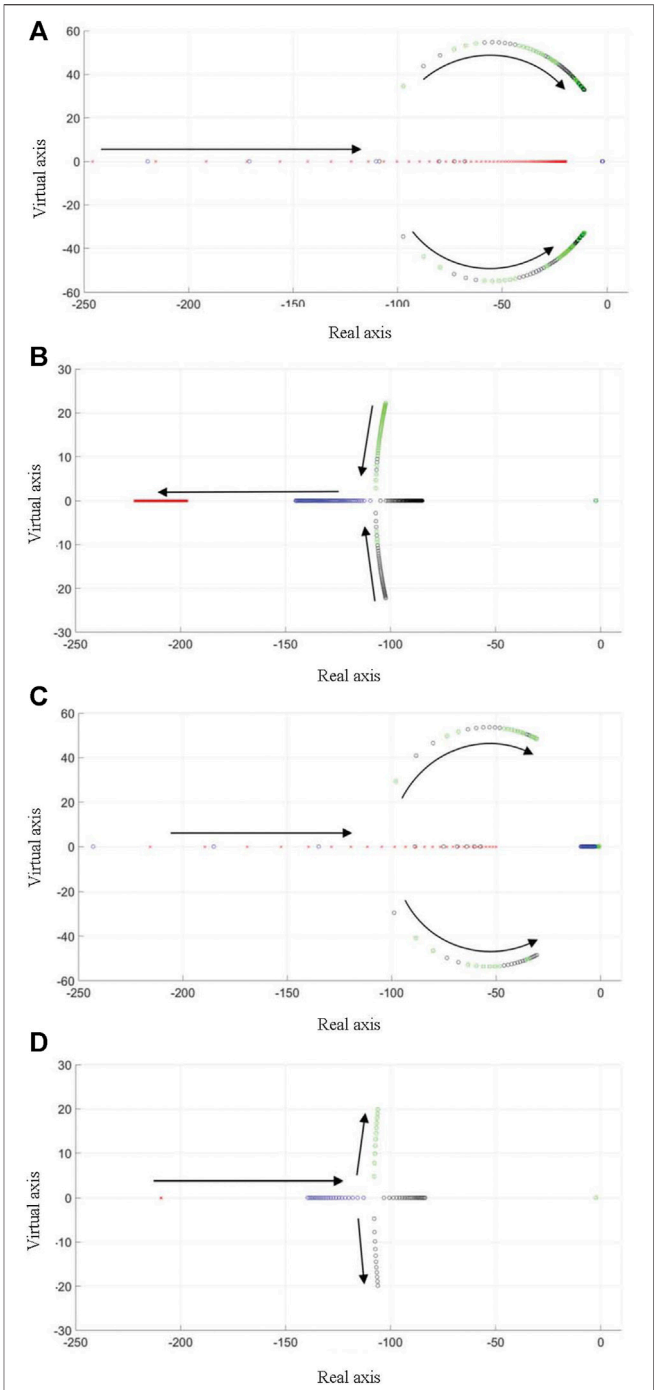


FIGURE 5 | Root locus diagram. **(A)** with different inertia J **(B)** with different damp coefficient D_p. **(C)** with different droop parameter k_p. **(D)** with different droop parameter k_q.

$$E_0 = E_{ref} + k_q(Q_{ref} - Q_e) \tag{4}$$

where E_0 and E_{ref} are the actual output and rated voltage amplitude of the VSG respectively, k_q is the $Q - U$ droop coefficient, Q_{ref} and Q_e are the reference and actual output reactive power respectively.

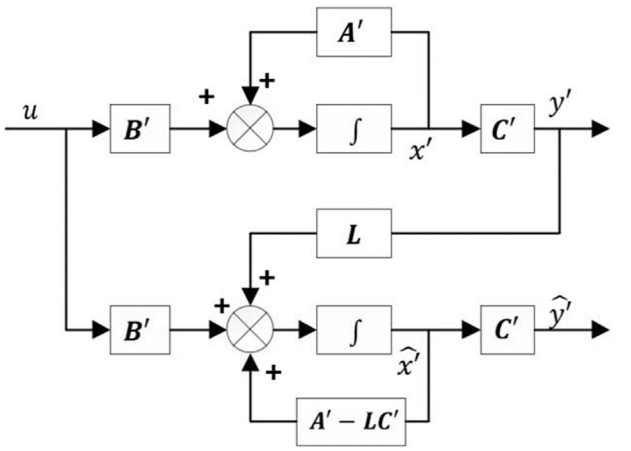


FIGURE 6 | Block diagram of the observer.

However, according to **Eq. 4**, output reactive power Q_e cannot achieve the zero-steady-error tracking of the reference reactive power Q_{ref} based on the proportional gain k_q when the VSG operates in grid-connected mode. Therefore, a modified Q-U controller with integral term is obtained as

$$E_0 = E_{ref} + k_q(Q_{ref} - Q_e) + k_i \int (Q_{ref} - Q_e)dt \tag{5}$$

where k_i is the integral coefficient of the Q-U controller. It should be noted that when the single VSG operates in grid-connected mode, **Eq. 5** is used for achieving the zero-steady-error tracking of the reactive power, and the voltage amplitude E_{ref} is equal to the grid voltage amplitude U_{gm}. When the VSG operates in island mode, **Eq. 4** is used for Q-U controller, the reference reactive power Q_{ref} is equal to zero and the voltage amplitude E_{ref} is equal to rated value.

2.2 Inner Loop of Voltage Regulation

Based on the analysis of the above mentioned section, the amplitude and frequency of the reference voltage E_{ref} can be derived from the outer VSG power loop. In this section, the inner voltage regulation loop based on capacitor voltage and inductor current feedback achieves the tracking of the reference voltage, and the control block diagram is shown in **Figure 2**.

The capacitor voltage transfer function $u_c(s)$ of the closed-loop system can be derived as

$$u_C(s) = G(s)u_{ref}(s) - Z_o(s)i_d(s) \tag{6}$$

For simplicity, the resistance R_s is ignored because the value is small, and the voltage gain $G(s)$ and output impedance $Z_o(s)$ can be respectively expressed as

$$G(s) = \frac{k_{up}k_Lk_{PWM}s + k_{ui}k_Lk_{PWM}}{LCs^3 + k_Lk_{PWM}Cs^2 + (k_{up}k_Lk_{PWM} + 1)s + k_{ui}k_Lk_{PWM}} \tag{7}$$

and

$$Z_o(s) = \frac{Ls^2}{LCs^3 + k_Lk_{PWM}Cs^2 + (k_{up}k_Lk_{PWM} + 1)s + k_{ui}k_Lk_{PWM}} \tag{8}$$

where k_{up} and k_{ui} are the proportional coefficient and integral coefficient of the capacitor voltage feedback loop controller respectively, k_L is the proportional coefficient of the VSG inductor current feedback loop controller. According to **Eq. 6**, the output impedance of the system can be adjusted by changing the proportional and integral (PI) coefficient. Therefore, different output impedance can be obtained by selecting the appropriate PI parameters.

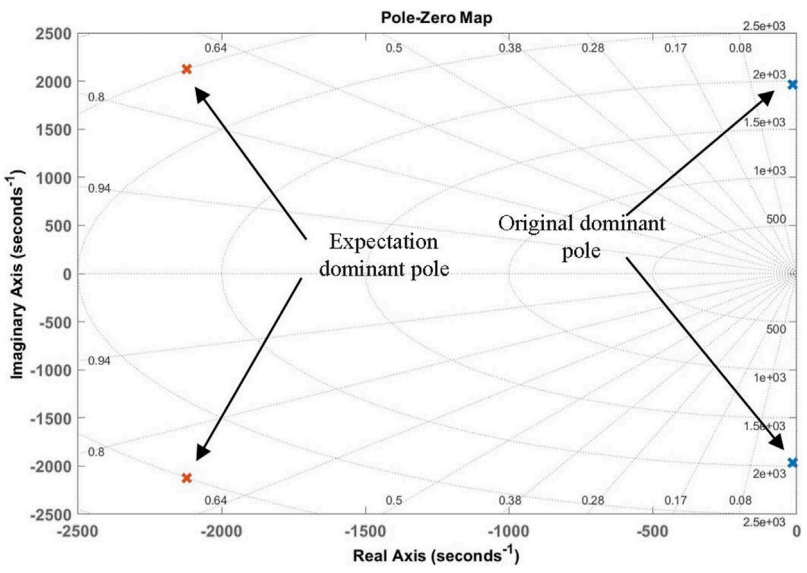


FIGURE 7 | The original dominant pole and the expectation dominant pole.

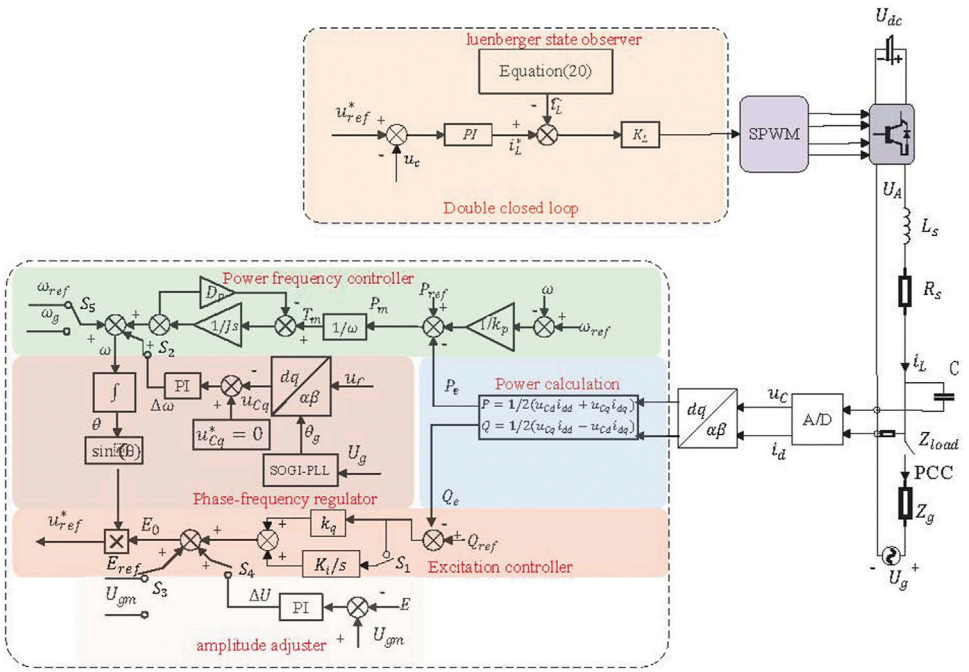


FIGURE 8 | The whole block diagram of the single-phase VSG.

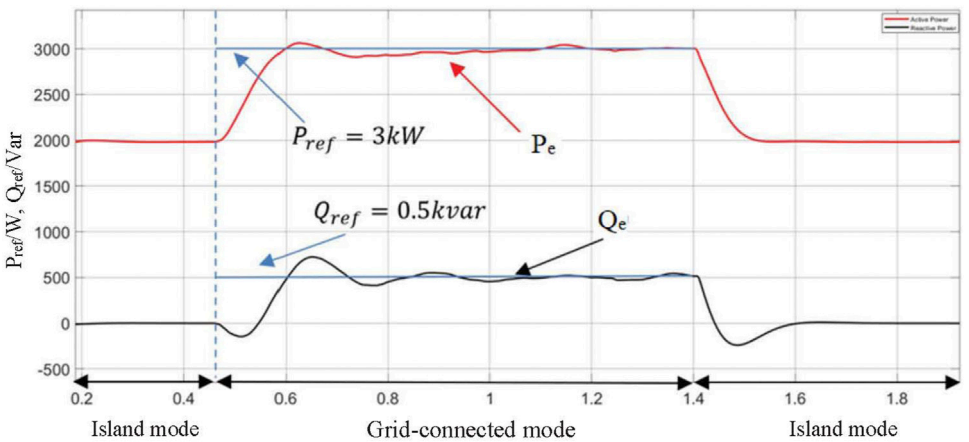


FIGURE 9 | The output active power P_e and reactive power Q_e of the single-phase VSG.

The detailed parameters of the whole system are given in **Table 1** and **Figure 3** shows bode diagram of output impedance $Z_o(s)$ with different PI parameters. As the value of the proportionality coefficient k_{up} increase, it can be seen that the inductive proportion of the output impedance of the system gradually increases at the low frequency as shown in **Figure 3A**. However, large value of parameter k_{up} will cause the instability of the system. Therefore, the parameter k_{up} should be chosen based on the tradeoff the dynamic performance and the stability of the system. **Figure 3B** shows that the inductive proportion of the output impedance of the system gradually increases at the low frequency with the decreasing value of parameter k_{ui}, so a small value of parameter k_{ui} is preferred.

2.3 Small Signal Model and Parameter Analysis

Although the inertia and damping are provided for the single-phase inverter by mimicking the traditional SG, the effects of virtual moment of inertia J, damping coefficient D_p, $P-f$ and $Q-U$

droop coefficients k_p and k_q on the stability of the VSG should be further analyzed. Next, a small signal model of the modified VSG strategy in grid-connected mode is established, and the influence of key parameters on the stability of the system is introduced.

Figure 4 shows the equivalent circuit when VSG operates in grid-connected mode. Where E and U represents the amplitude of the VSG output terminal voltage and the grid voltage respectively. Assuming that the phase angel of the power grid voltage is zero, δ is the phase angle of the VSG output voltage, the total impedance of the line between the VSG and the grid can be equivalent to $Z\angle\alpha = R + jX$, where α is the impedance angle. Therefore, the apparent power output of the VSG can be obtained,

$$\begin{aligned} S &= \dot{U}\dot{I}^{\star} = P_e + jQ_e \\ &= \frac{EUcos(\alpha-\delta) - U^2cos\alpha}{Z} + j\frac{EUsin(\alpha-\delta) - U^2sin\alpha}{Z} \end{aligned} \tag{9}$$

Assuming that the line impedance is mainly inductive and active power P_e and reactive power Q_e can be derived as (Liu et al., 2020b)

$$\begin{cases} P_e = \dfrac{E^2R - EURcos\delta + EUXsin\delta}{R^2+X^2} = \dfrac{EUsin(\delta)}{X} \\ Q_e = \dfrac{E^2X - EUXcos\delta - EURsin\delta}{R^2+X^2} = \dfrac{E^2 - EUcos(\delta)}{X} \end{cases} \tag{10}$$

The small signal model of the modified VSG can be obtained based on **Eq. 8**.

$$\begin{cases} \Delta P_e = \dfrac{\partial P_e}{\partial E}\Delta E(s) + \dfrac{\partial P_e}{\partial \delta}\Delta\delta(s) \\ \quad\quad = K_{PE}\Delta E(s) + K_{P\delta}\Delta\delta(s) \\ \Delta Q_e = \dfrac{\partial Q_e}{\partial E}\Delta Q(s) + \dfrac{\partial P_e}{\partial \delta}\Delta\delta(s) \\ \quad\quad = K_{QE}\Delta E(s) + K_{Q\delta}\Delta\delta(s) \end{cases} \tag{11}$$

where K_{PE} and $K_{P\delta}$ are the partial derivative of active power P_e to voltage amplitude E and power angle δ respectively. K_{QE} and $K_{Q\delta}$ are the partial derivative of reactive power Q_e to voltage amplitude E and power angle δ respectively, and they can be expression as

$$\begin{cases} K_{PE} = \dfrac{Usin\delta}{X} \\ K_{P\delta} = \dfrac{EUcos\delta}{X} \\ K_{QE} = \dfrac{2E - Ucos\delta}{X} \\ K_{Q\delta} = \dfrac{EUsin\delta}{X} \end{cases} \tag{12}$$

As the output power of a single-phase VSG contains secondary power oscillations, a first-order low-pass filter is used to filter the secondary power oscillations contained in the output power. Small signal model of the output voltage amplitude and frequency of the VSG can also be obtained based on **Eqs 1**, **2**, **5**,

$$\begin{cases} \Delta\omega(s) = -\dfrac{\omega_c}{s+\omega_c}\dfrac{k_p}{k_pJ\omega_{erf}s + k_pD_p\omega_{ref} + 1}\cdot \\ \quad\quad (K_{PE}\Delta E(s) + K_{P\delta}\Delta\delta(s)) \\ \Delta E(s) = -\dfrac{\omega_c}{s+\omega_c}\left(k_q + \dfrac{k_i}{s}\right)(K_{QE}\Delta E(s) + K_{Q\delta}\Delta\delta(s)) \end{cases} \tag{13}$$

where, ω_c is the cut-off frequency of the low-pass filter. Since

$$\Delta\omega = s\Delta\delta \tag{14}$$

According to **Eqs 8**, **9**, **12**, it implies that

$$s^4\Delta\delta(s) + as^3\Delta\delta(s) + bs^2\Delta\delta(s) + cs\Delta\delta(s) + d\Delta\delta(s) = 0 \tag{15}$$

where

$$\begin{cases} a = (K_qK_{QE} + 1)J\omega_c\omega_{ref} \\ b = \left(D_p\omega_{ref} + k_qD_p\omega_{ref}K_{QE} + \dfrac{1}{k_p} + k_iK_{QE}J\omega_{ref} + \right. \\ \quad\quad \left.\dfrac{k_q}{k_p}k_{QE}\right)\omega_c \\ c = (k_qK_{QE}K_{P\delta} + K_{P\delta} - k_qK_{PE}K_{Q\delta})\omega_c^2 + \left(D_p\omega_{ref} + \right. \\ \quad\quad \left.\dfrac{1}{k_p}k_iK_{QE}\omega_c\right) \\ d = K_i(K_{QE}K_{P\delta} - K_{PE}K_{Q\delta})\omega_c^2 \end{cases} \tag{16}$$

Eq. 15 describes the characteristics of the system with the small disturbances around the equilibrium point. **Figure 5** shows the root locus diagram with different inertial J, damp coefficient D_p, droop parameters k_p and k_q.

It can be seen that with the increase of inertia J, droop parameters k_p and k_q, oscillation will appear and the system will become unstable. On the contrary, the VSG system will become more stable with the damp coefficient D_p increases.

3 INDUCTOR CURRENT SENSORLESS CONTROL STRATEGY BASED ON LUENBERGER OBSERVER FOR INNER VOLTAGE REGULATION

In this section, an inductor current sensorless control method based on luenberger observer is proposed, and optimal pole assignment of the observer is also analyzed.

3.1 Luenberger State Observer

In order to reduce the sensor counts, a state observer is introduced here to evaluate the actual inductor current i_L value. By the kirchhoff's law of voltage and current, the single VSG system is modeled by

$$\begin{cases} C\dfrac{du_c}{dt} = i_L - i_d \\ L_s\dfrac{di_L}{dt} = U_A - u_C - R_si_L \end{cases} \tag{17}$$

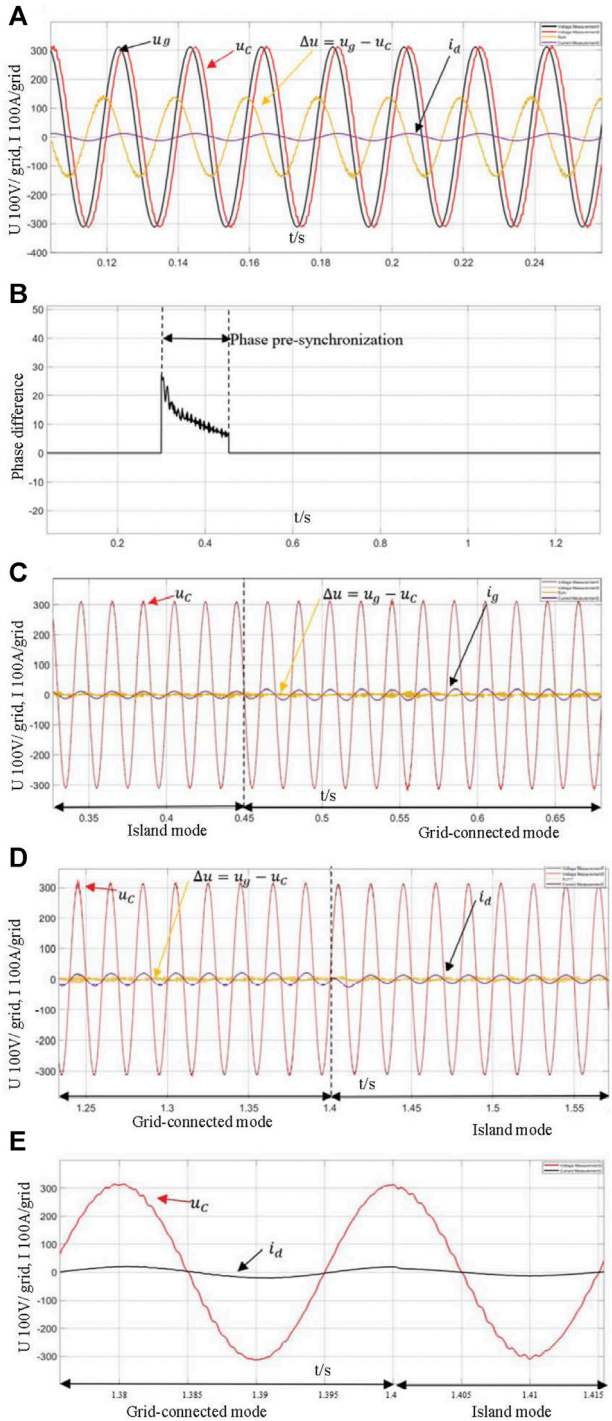


FIGURE 10 | Seamless transfer of the single-phase VSG. **(A)** Simulation waveform of capacitor voltage and load current in island mode. **(B)** Pre-synchronization process. **(C)** Simulation waveforms of capacitor voltage and load current from island mode to grid-connected mode. **(D)** Simulation waveforms of capacitor voltage and load current from grid-connected mode to island mode. **(E)** partial enlarged view of capacitor voltage and load current (grid-connected mode to island mode).

And the state-space mode can be derived by **Eq. 17**

$$\begin{cases} \dot{x} = Ax + Bu + P\omega \\ y = Cx \end{cases} \tag{18}$$

where

$$A = \begin{bmatrix} 0 & 1/C \\ -1/L_s & -R_s/L_s \end{bmatrix}, \quad B = \begin{bmatrix} 0 & 1/L_s \end{bmatrix}^T,$$
$$P = \begin{bmatrix} -1/C & 0 \end{bmatrix}^T, \quad C = \begin{bmatrix} 1 & 0 \end{bmatrix},$$

and state variable x, input variable u, disturbance signal ω, and output variable y can be expressed as

$$x = \begin{bmatrix} u_c & i_L \end{bmatrix}^T, \quad u = U_A, \quad \omega = i_d, \quad y = u_C,$$

As the load current i_d and capacitor voltage u_C must be obtained to calculate the output active power P_e and reactive power Q_e, an observed inductor current $\hat{i}_L$ is used to replace the real inductor current to reduce the sensor counts for the inner voltage regulation. **Eq. 18** can be rewritten as

$$\begin{cases} \dot{x} = A'x + B'\bar{u} \\ y = C'x \end{cases} \tag{19}$$

and matrix $A' = A$, $C' = C$, B' and the input variable $\bar{u}$ can be expressed as

$$B' = \begin{bmatrix} 0 & -1/C \\ 1/L_s & 0 \end{bmatrix}, \quad \bar{u} = \begin{bmatrix} u_c & i_d \end{bmatrix}^T,$$

It is easy to prove that **Eq. 19** satisfies the observability condition, that is

$$rank = \begin{bmatrix} C' \\ C'A' \end{bmatrix} = 2.$$

Therefore, the observed inductor current $\hat{i}_L$ can be obtain based on **Eq. 20**.

$$\begin{cases} \dot{\hat{x}}' = A'\hat{x}' + B'u + L(y' - C'x') \\ \hat{y}' = C'\hat{x}' \end{cases} \tag{20}$$

where L is gain matrix. The block diagram of the observer is shown in **Figure 6**. By subtracting **Eq. 20** from **Eq. 19**, the state error matrix is introduced:

$$\dot{e}_x = (A' - LC')e_x = e^{(A'-LC')}e_x \tag{21}$$

where e_x represents the state error matrix. When the eigenvalue of the matrix $(A' - LC')$ is in the left side of the complex plate, the error of the observer will approach zero. Therefore, it is necessary to adjust the parameters of the state feedback matrix L.

3.2 Pole Assignment

In this section, the optimal pole assignment of the state observer is designed based on the optimal pole assignment principle (Lin, 2007). The distribution of the position of the characteristic root of the system in the complex plane determines the dynamic

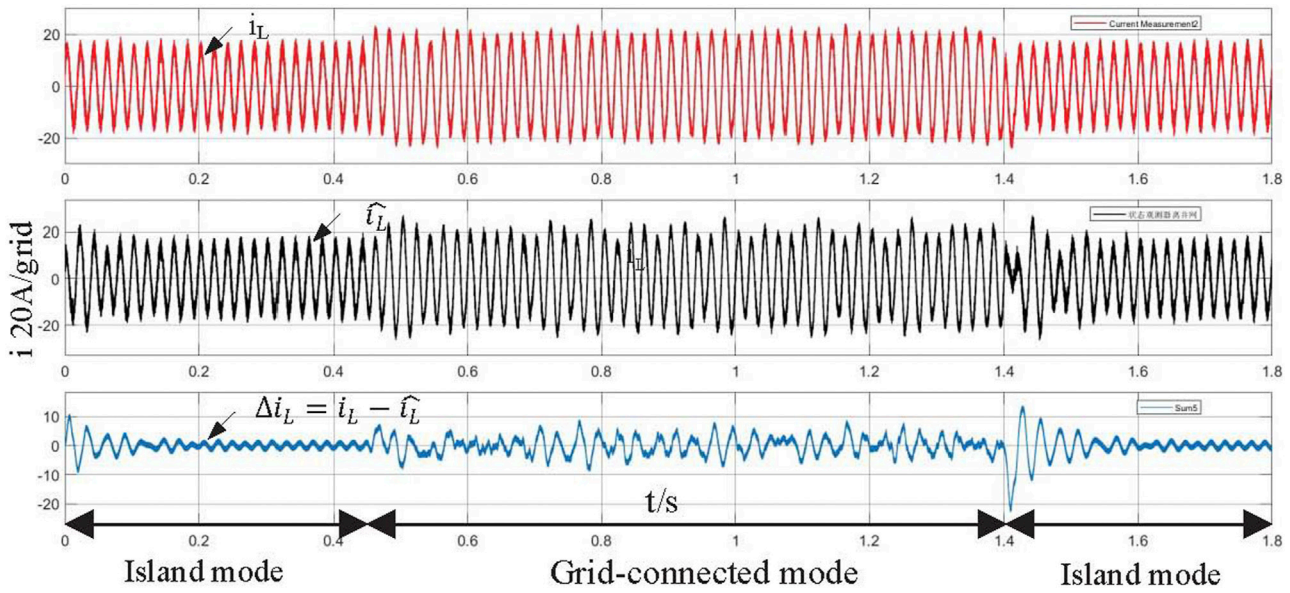


FIGURE 11 | Simulation waveform of real inductor current i_L, observed inductor current $\hat{i}_L$ and error Δi_L.

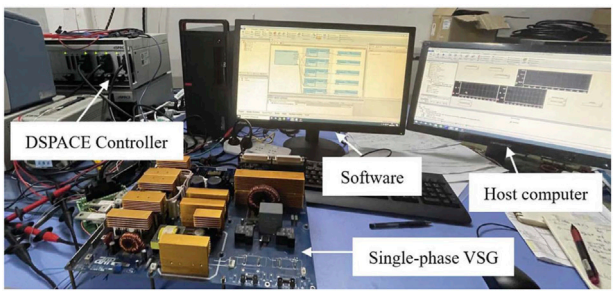


FIGURE 12 | Experimental prototype.

response speed and the degree of oscillation of the system, the farther the pole position of the transfer function is from the imaginary axis, the faster the dynamic response speed of the system.

Based on **Eq. 19**, the state variables of the capacitor voltage u_C and the inductor current i_L have the greatest impact on the system, the poles related to these two state variables are selected as the dominant poles. The original dominant pole and the expectation dominant pole after the optimal pole placement are shown in **Figure 7**. It is found that the original system is relatively close to the imaginary axis, the convergence speed of the system is slow, and it may cause instability of the system. However, the expectation pole is farther from the imaginary axis, which improves the dynamic response speed of the system. As the inductor current must be used for feedback control, the dynamic speed for the state observer should be faster than the controller, that is, its pole is generally 4 to 10 times that of the controller.

4 SEAMLESS SWITCHING

Seamless switching is an important feature for safe operation of the VSG. Due to the deviation between the VSG output voltage and the grid voltage, seamless transfer requires pre-synchronization. As the output voltage and the power grid voltage can be measured, an orthogonal voltage signal must be obtained. In this paper, a phase-locked loop (SOGI-PLL) based on the second-order generalized integral is used to extract the grid voltage information (Matas et al., 2010; Liu et al., 2020a). The whole block diagram of the single-phase VSG is shown in **Figure 8**.

4.1 Island Mode

When VSG operates in island mode, the switch S_2 is disconnected and the VSG works in $P - f$. The switch S_5 is connected to the rated angular frequency ω_{ref}. The switches S_1, S_4 are disconnected and VSG works in $Q - U$, the switch S_3 is connected to the rated voltage amplitude E_{ref}. At this time, the output power of the VSG is the load power.

4.2 Grid-Connected Mode

When the VSG operates in grid-connected mode, the switch S_2 is disconnected and the switch S_5 is connected to the grid and the reference frequency is angular frequency ω_g. The switch S_4 is disconnected, the switch S_1 is connected to make the integration term works, the switch S_3 is connected to the grid voltage amplitude U_{gm}.

4.3 Seamless Switching

When the VSG receives a signal that it needs to switch from grid-connected mode to island mode, since the VSG was previously in grid-connected operation and there is an

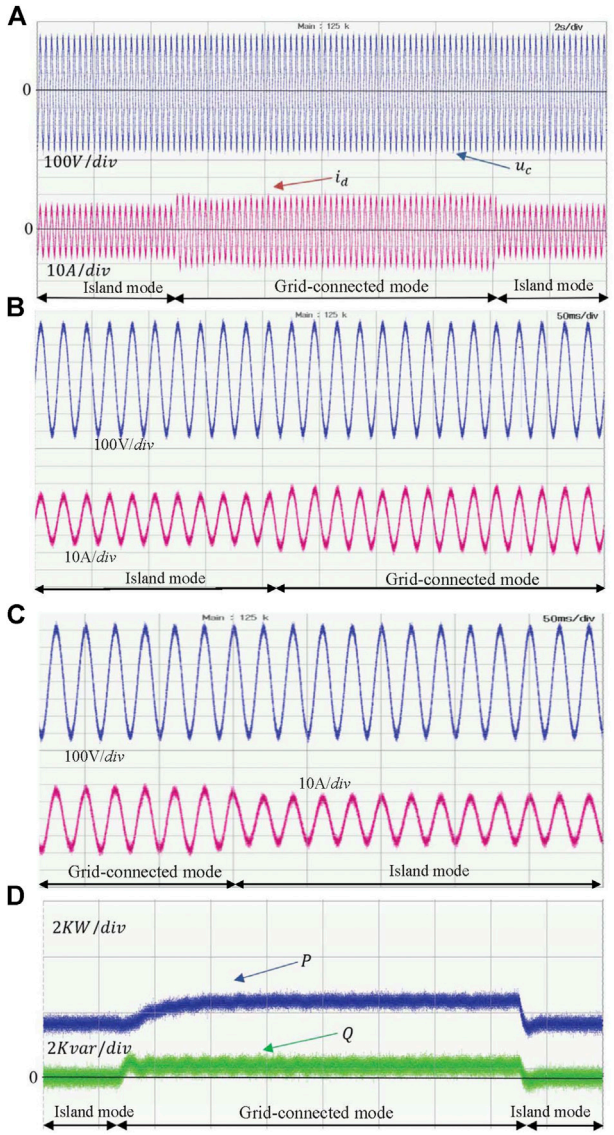


FIGURE 13 | Experimental waveform of seamless transfer. **(A)** Experimental waveforms of single-phase VSG capacitor voltage and load current based on seamless transfer. **(B)** Partial enlarged experimental waveform of the dynamic process from island mode to grid-connected mode. **(C)** Partial enlarged experimental waveform of the dynamic process from grid-connected mode to island mode. **(D)** Experimental waveform of single-phase VSG output power.

inertia link in the VSG, the output voltage of the VSG theoretically will not have a transient sudden change at the moment of switching. At this time, the voltage, angular frequency, power reference value in the VSG control will automatically change to the given amount when the island is isolated, so the switch from grid-connected to island operation of the VSG can be completed without adding a complicated control strategy.

When the VSG switches from grid-connected mode to island mode, it starts the pre-synchronization process. At this time, the switches S_2 and S_4 are closed, the VSG gradually adjusts the phase, frequency and amplitude information of the output voltage in the island operation mode. When the grid-connected standard is reached, the pre-synchronization process finished and the grid-connected switch is closed. The reference power P_{ref} and Q_{ref} in the VSG control loop will be replaced by the grid's active power P_g and reactive power Q_g. Due to the inertia of the VSG, the power output by the VSG will not undergo a step change, the VSG will complete the transfer from island to grid-connected with seamless switching feature.

5 SIMULATION AND EXPERIMENTAL RESULTS

5.1 Simulation Results of Seamless Switching With State Observer

In order to verify the effectiveness of the above-mentioned luenberger observed-based VSG strategy, a 3kVA simulation model based on the single-phase inverter was built. The key parameters are given in **Table 1**. The whole control diagram of the proposed modifier single-phase VSG control strategy is shown in **Figure 8**.

The single VSG operates in island mode initially, and the grid-connected signal is triggered at 0.35s, the island mode signal is triggered at 1.4s. In grid-connected mode, the VSG reference active power and reactive power is 3kW and 500var respectively.

Figure 9 shows the output active power P_e and reactive power Q_e of single-phase VSG when operates in grid-connected mode and island mode. The simulation results demonstrate that when the single-phase VSG switches between the two operating modes, there is no obvious power mutation and the output power of the VSG can reach the reference power in grid-connected mode.

The seamless transfer capability of the single-phase VSG based on the proposed method is also verified by simulation results as shown in **Figure 10**. **Figure 11A** shows the waveform of capacitor voltage u_C, power grid voltage U_g, and the load current i_d when the VSG operates in island mode. As the initial phase difference between the power grid voltage and capacitor voltage u_C is 30°, the voltage deviation Δu between the grid voltage and the inverter output voltage exists.

Figure 10B shows the pre-synchronization process when single-phase VSG switches from island mode to grid-connected mode. At time 0.3s, the trigger signal enables, and the pre-synchronization process starts, the phase angle difference $\Delta\theta$ between the VSG output voltage phase and the grid voltage phase gradually decreases. When the phase difference $\Delta\theta$ is less than the threshold value of 3° at time 0.45s, the pre-synchronization process ends, and the VSG switches to the grid-connected mode.

Figure 10C,D shows the voltage and current waveforms of seamless transfer between the island mode and grid-connected mode at time 0.45 and 1.4 s respectively. Simulation results demonstrate that smooth switching between island mode and grid-connected mode can be achieved, and the inrush current is small. **Figure 10E** shows the partial enlarged view of VSG voltage

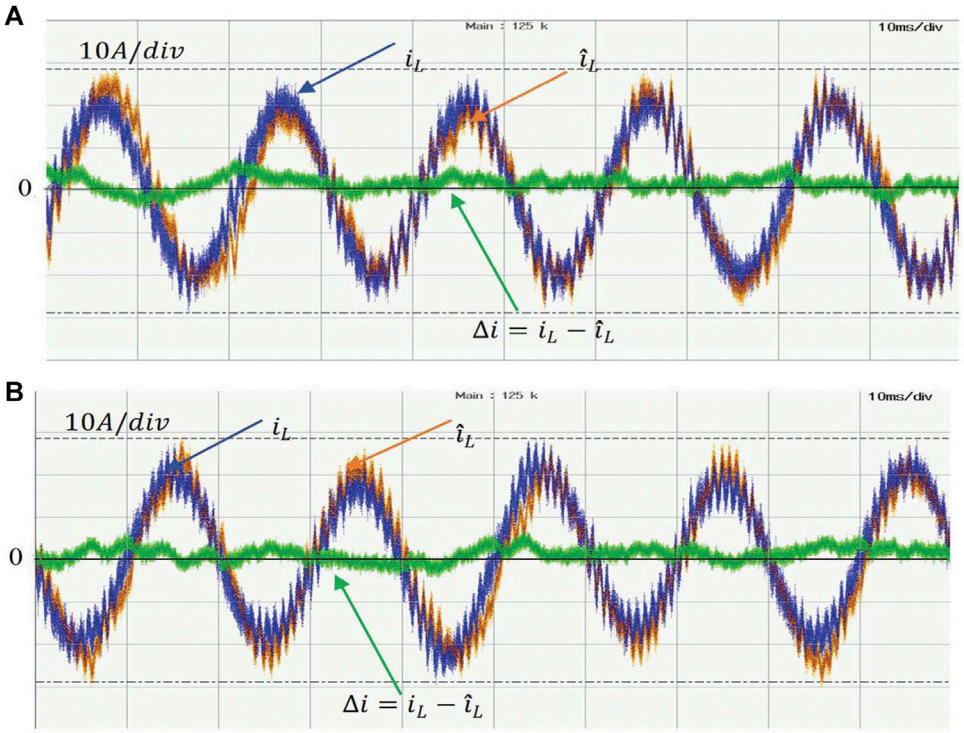


FIGURE 14 | Experimental waveforms of real inductor current i_L, observed inductor current $\hat{i_L}$ and error Δi_L. **(A)** Island model, **(B)** grid-connected model.

u_C and load current i_d, it demonstrates that the voltage sags is small when VSG switches from grid-connected mode to island mode.

Figure 11 shows the simulation waveform of the observed inductor current i_L and the actual inductor current i_L, and Δi_L is the deviation between them. The gain matrix $L = [-500,-500,-500,-500,-500,-500,-500,-500,-500,-500]^T$. It can be seen that the estimation error of the observer is small and the dynamic response speed is fast when the VSG operates in grid-connected mode and island mode.

5.2 Experimental Results of Seamless Switching With State Observer

A 3kW single-phase full-bridge inverter prototype is built to verify the feasibility of the proposed control method. The main parameters of the system use are shown in **Table 1**. The performance of the proposed control strategy is validated by dSPACE SCALEXIO system for real-time implementation, as shown in **Figure 12**. The prototype is mainly composed of single-phase full-bridge inverter main circuit, A/D sampling circuit, DSPACE transfer board, auxiliary switching power supply and host computer. The output voltage and current waveforms are displayed through the oscilloscope YOKOGAWA-DLM2024. The DC side voltage source adopts programmable DC power supply model Chroma62150H-1000s, and the AC power supply adopts the programmable AC power supply model Chroma61845.

Figure 13 shows the experimental results of seamless transfer process between the island and grid-connected based on the proposed control strategy. The output voltage u_C and load current i_d experimental waveform is demonstrated in **Figure 13A** when the VSG is switched between grid-connected and island modes. The output voltage almost unchanged and the grid-connected current fluctuates very little when the operating mode of the single-phase VSG changes. High performance of dynamic waveform can be achieved. **Figure 13B,C** show the partial enlarged experimental waveform of the dynamic process between the island mode and the grid-connected mode, and the voltage waveform changes little throughout the process. **Figure 13D** shows the output active power P_e and reactive power Q_e of the VSG reached 3kW and 500var respectively when connected to the power grid, which is consistent with the reference active and reactive power.

Figure 14 shows the experimental waveforms of the actual inductor current i_L and the observed current $\hat{i_L}$ when the single-phase VSG works in island and grid-connected modes. The blue waveform is the actual value of the inductor current, the brown waveform is the observed value of the inductor current, and the green waveform is the observation error Δi. The experimental results demonstrate that the observed inductor current can track the actual value well based on the proposed luenberger state observer.

6 CONCLUSION

A modifier VSG control strategy for single-phase inverter-interfaced microgrid application is proposed in this paper, and

it can realize the seamless transition between the island mode and grid-connected mode. The effectiveness and feasibility of the proposed control method is verified by the simulation and experimental results. The main contribution of the proposed modifier VSG control strategy can be summarized as follows: 1) It can achieve zero-steady-tracking error of the output reactive power by adding Q-U integral term in grid-connected mode. 2) The proposed control method can reduce the sensor of inductor current based on the luenberger observer. 3) The high performance of the single-phase inverter based on the proposed modifier VSG method can be obtained in island mode, grid-connected mode and the transient process.

DATA AVAILABILITY STATEMENT

The original contributions presented in the study are included in the article/supplementary material, further inquiries can be directed to the corresponding authors.

AUTHOR CONTRIBUTIONS

ZZ is in charge of the method calculation, paper writing and experiment. JW and DX is in charge of literature review, experimental setup, and proofread the manuscript. LZ is in charge of the experimental setup. XT is in charge of the experimental guidance. All authors contributed to the article and approved the submitted version.

FUNDING

This work was supported in part by the Teaching Quality and Teaching Reform Project of Guangdong Province under Grant Nos. PX-3218216 and 201801283006, in part by the Dongguan Social Science and Technology Development Project under Grant Nos. 2019507140826 and Grant 2020507140141, and in part by Enterprise Sci-tech Commssioner of Guangdong province under Grant No. GDKTP2020013700.

REFERENCES

Alcala, J. M., Castilla, M., De Vicuña, L. G., Miret, J., and Vasquez, J. C. (2010). Virtual Impedance Loop for Droop-Controlled Single-phase Parallel Inverters Using a Second-Order General-Integrator Scheme. *IEEE Trans. Power Electron.* 25, 2993–3002. doi:10.1109/TPEL.2010.2082003

Beck, H. P., and Hesse, R. (2007). "Virtual Synchronous Machine," in 2007 9th International Conference on Electrical Power Quality and Utilisation (Barcelona, Spain: IEEE), 1–6. doi:10.1109/epqu.2007.4424220

Blaabjerg, F., Teodorescu, R., Liserre, M., and Timbus, A. V. (2006). Overview of Control and Grid Synchronization for Distributed Power Generation Systems. *IEEE Trans. Ind. Electron.* 53, 1398–1409. doi:10.1109/TIE.2006.881997

Canziani, F., Vargas, R., and Gastelo-Roque, J. A. (2021). Hybrid Photovoltaic-Wind Microgrid with Battery Storage for Rural Electrification: A Case Study in Perú. *Front. Energ. Res.* 8, 1–11. doi:10.3389/fenrg.2020.528571

Cheng, C., Xie, S., Xu, J., and Qian, Q. (2021). State-and-Disturbance-Observer-Based Current Control Scheme for LCL-Filtered Single-phase Grid-Tied Inverters under Non-ideal Conditions. *IEEE J. Emerg. Sel. Top. Power Electron.* 6777, 1. doi:10.1109/JESTPE.2021.3067466

Hinsui, T., and Sangtungtong, W. (2019). "Voltage Observer-Based Control for Single-phase Grid-Connected Pv Inverter," in 2019 7th International Electrical Engineering Congress (iEECON), March 2019. (Hua Hin, Thailand: IEEE), 1–4. doi:10.1109/iEECON45304.2019.8938957

Latham, J., Mohebbi, M., and McIntyre, M. L. (2017). Output Feedback Control of a Single Phase Voltage Source Inverter Utilizing a Variable Structure Observer. *Proc. Am. Control. Conf.* 40292, 4081–4086. doi:10.23919/acc.2017.7963581

Li, D., Zhu, Q., Lin, S., and Bian, X. Y. (2017). A Self-Adaptive Inertia and Damping Combination Control of VSG to Support Frequency Stability. *IEEE Trans. Energ. Convers.* 32, 397–398. doi:10.1109/TEC.2016.2623982

Li, H., Zhang, X., Shao, T., and Zheng, T. Q. (2019). Flexible Inertia Optimization for Single-phase Voltage Source Inverter Based on Hold Filter. *IEEE J. Emerg. Sel. Top. Power Electron.* 7, 1300–1310. doi:10.1109/jestpe.2018.2865214

Lin, F. (2007). *Robust Control Design*. England: Wiley.

Liu, B., An, M., Wang, H., Chen, Y., Zhang, Z., Xu, C., et al. (2020a). A Simple Approach to Reject DC Offset for Single-phase Synchronous Reference Frame PLL in Grid-Tied Converters. *IEEE Access* 8, 112297–112308. doi:10.1109/access.2020.3003009

Liu, B., Wu, T., Liu, Z., and Liu, J. (2020b). A Small-AC-Signal Injection-Based Decentralized Secondary Frequency Control for Droop-Controlled Islanded Microgrids. *IEEE Trans. Power Electron.* 35, 11634–11651. doi:10.1109/tpel.2020.2983878

Lou, G., Yang, Q., Gu, W., Quan, X., Guerrero, J. M., and Li, S. (2021). Analysis and Design of Hybrid Harmonic Suppression Scheme for VSG Considering Nonlinear Loads and Distorted Grid. *IEEE Trans. Energ. Convers.* 8969, 1. doi:10.1109/tec.2021.3063607

Monfared, M., Golestan, S., and Guerrero, J. M. (2014). Analysis, Design, and Experimental Verification of a Synchronous Reference Frame Voltage Control for Single-phase Inverters. *IEEE Trans. Ind. Electron.* 61, 258–269. doi:10.1109/TIE.2013.2238878

Qazi, H. S., Zhao, T., Liu, N., Wang, T., and Ullah, Z. (2021). Optimal Operation of Isolated Micro-grids-cluster via Coalitional Energy Scheduling and Reserve Sharing. *Front. Energ. Res.* 9, 1–14. doi:10.3389/fenrg.2021.629131

Shao, T., Jia, P., Zheng, P., Zheng, T. Q., Wang, J., Li, H., et al. (2019). A Robust Power Regulation Controller to Enhance Dynamic Performance of Voltage Source Converters. *IEEE Trans. Power Electron.* 34, 12407–12422. doi:10.1109/tpel.2019.2906057

Suul, J. A., DArco, S., and Guidi, G. (2016). Virtual Synchronous Machine-Based Control of a Single-phase Bi-directional Battery Charger for Providing Vehicle-To-Grid Services. *IEEE Trans. Ind. Applicat.* 52, 3234–3244. doi:10.1109/TIA.2016.2550588

Teng, Q., Xu, D., Yang, W., Li, J., and Shi, P. (2021). Neural Network-Based Integral Sliding Mode Backstepping Control for Virtual Synchronous Generators. *Energ. Rep.* 7, 1–9. doi:10.1016/j.egyr.2020.11.032

Tran, T. V., and Kim, K.-H. (2020). Frequency Adaptive Grid Voltage Sensorless Control of LCL-Filtered Inverter Based on Extended Model Observer. *IEEE Trans. Ind. Electron.* 67, 7560–7573. doi:10.1109/TIE.2019.2944075

Valinejad, J., Marzband, M., Korkali, M., Xu, Y., and Saad Al-Sumaiti, A. (2020). Coalition Formation of Microgrids with Distributed Energy Resources and Energy Storage in Energy Market. *J. Mod. Power Syst. Clean Energ.* 8, 906–918. doi:10.35833/MPCE.2019.000116

Van, T. V., Visscher, K., Diaz, J., Karapanos, V., Woyte, A., Albu, M., Bozelie, J., Loix, T., and Federenciuc, D. (2010). "Virtual Synchronous Generator: An Element of Future Grids," in IEEE PES Innovative Smart Grid Technologies Conference Europe (Europe: ISGT), 1–7. doi:10.1109/ISGTEUROPE.2010.5638946

Wang, F., Zhang, L., Feng, X., and Guo, H. (2018). An Adaptive Control Strategy for Virtual Synchronous Generator. *IEEE Trans. Ind. Applicat.* 54, 5124–5133. doi:10.1109/TIA.2018.2859384

Wang, T., O'Neill, D., and Kamath, H. (2015). Dynamic Control and Optimization of Distributed Energy Resources in a Microgrid. *IEEE Trans. Smart Grid* 6, 2884–2894. doi:10.1109/TSG.2015.2430286

Zhang, L., Wang, F., Guo, H., Feng, X., Du, Y., and Su, J. (2017). "Perturbation Influences of Parameters on Dynamic Performance of a Virtual Synchronous Generator," in Proceedings IECON 2017 - 43rd Annual Conference of the IEEE

Industrial Electronics Society, October 2017, (Beijing, China: IEEE), 1405–1410. doi:10.1109/IECON.2017.8216239

Zhang, Z., Fan, M., Dai, Z., Zhang, J., Yang, Y., and Chen, X. (2021). Multi-consecutive-samples Based Frequency Estimation for Single-phase Systems under Odd-, Even-Order Harmonics and DC Offsets. *Int. J. Electr. Power Energ. Syst.* 128, 106724. doi:10.1016/j.ijepes.2020.106724

Zhao, Y., Chai, J., Wang, S., and Sun, K. (2017). Instantaneous Power Calculation Based on Intrinsic Frequency of Single-phase Virtual Synchronous Generator. *J. Mod. Power Syst. Clean. Energ.* 5, 970–978. doi:10.1007/s40565-017-0272-5

Zhong, Q.-C., and Weiss, G. (2011). Synchronverters: Inverters that Mimic Synchronous Generators. *IEEE Trans. Ind. Electron.* 58, 1259–1267. doi:10.1109/TIE.2010.2048839

Zhu, Y., and Fei, J. (2018). Disturbance Observer Based Fuzzy Sliding Mode Control of PV Grid Connected Inverter. *IEEE Access* 6, 21202–21211. doi:10.1109/access.2018.2825678

Conflict of Interest: DX was employed by the Guangdong HYNN Technologies Co., Ltd.

The remaining authors declare that the research was conducted in the absence of any commercial or financial relationships that could be construed as a potential conflict of interest.

Publisher's Note: All claims expressed in this article are solely those of the authors and do not necessarily represent those of their affiliated organizations, or those of the publisher, the editors and the reviewers. Any product that may be evaluated in this article, or claim that may be made by its manufacturer, is not guaranteed or endorsed by the publisher.

Copyright © 2021 Zhang, Wu, Zheng, Xie and Tang. This is an open-access article distributed under the terms of the Creative Commons Attribution License (CC BY). The use, distribution or reproduction in other forums is permitted, provided the original author(s) and the copyright owner(s) are credited and that the original publication in this journal is cited, in accordance with accepted academic practice. No use, distribution or reproduction is permitted which does not comply with these terms.

frontiers in Energy Research

BRIEF RESEARCH REPORT
published: 01 October 2021
doi: 10.3389/fenrg.2021.741101

Distributed Imitation-Orientated Deep Reinforcement Learning Method for Optimal PEMFC Output Voltage Control

Jiawen Li[1], *Yaping Li*[2] *and Tao Yu*[1]*

[1]College of Electric Power, South China University of Technology, Guangzhou, China, [2]China Electric Power Research Institute (Nanjing), Beijing, China

In order to improve the stability of proton exchange membrane fuel cell (PEMFC) output voltage, a data-driven output voltage control strategy based on regulation of the duty cycle of the DC-DC converter is proposed in this paper. In detail, an imitation-oriented twin delay deep deterministic (IO-TD3) policy gradient algorithm which offers a more robust voltage control strategy is demonstrated. This proposed output voltage control method is a distributed deep reinforcement learning training framework, the design of which is guided by the pedagogic concept of imitation learning. The effectiveness of the proposed control strategy is experimentally demonstrated.

Keywords: distributed deep reinforcement learning, proton exchange membrane fuel cell, DC-DC converter, output voltage control, robustness

OPEN ACCESS

Edited by:
Yaxing Ren,
University of Warwick,
United Kingdom

Reviewed by:
Lefeng Cheng,
Guangzhou University, China
Si Chen,
University of Glasgow,
United Kingdom

***Correspondence:**
Tao Yu
taoyu1@scut.edu.cn
eptaoyu1@163.com

Specialty section:
This article was submitted to Smart Grids, a section of the journal Frontiers in Energy Research

Received: *14 July 2021*
Accepted: *27 July 2021*
Published: *01 October 2021*

Citation:
Li J, Li Y and Yu T (2021) Distributed Imitation-Orientated Deep Reinforcement Learning Method for Optimal PEMFC Output Voltage Control. Front. Energy Res. 9:741101. doi: 10.3389/fenrg.2021.741101

INTRODUCTION

The voltage of a proton exchange membrane fuel cell (PEMFC) is highly dependent on the temperature, pressure, humidity, and gas flow rate (Yang et al., 2018; Sun et al., 2019). In addition, the output voltage of PEMFC also fluctuates widely with varying load current (Yang et al., 2019a; Yang et al., 2021a). In order to improve the stability of the PEMFC output voltage, the PEMFC DC-DC converters should output a stable bus voltage in the event of fluctuating input voltage and output load so as to normalize the load (Yang et al., 2021b; Yang et al., 2021c).

There are a number of existing PEMFC output voltage control methods based on control of DC-DC converters, including the PID control algorithm (Swain and Jena, 2015), fractional order PID algorithm (Yang et al., 2019a; Yang et al., 2019b; Yang et al., 2020), sliding mode control algorithm (Bougrine et al., 2013; Jiao and Cui, 2013), model predictive control algorithm (Bemporad et al., 2002; Ferrari-Trecate et al., 2002), robust control method (Olalla et al., 2010), and optimal control algorithm (Jaen et al., 2006; Olalla et al., 2009; Montagner et al., 2011; Moreira et al., 2011) methods, and so on. Among them, the PID algorithms are traditional control algorithms whose advantages include simple structure and fast calculation speed. However, these are incompatible with non-linear PEMFC systems. The fractional order PID algorithm is an expanded algorithm based on the PID algorithm, which offers better robustness, but which cannot be adapted for non-linear PEMFC systems. Sliding mode control is an excellent candidate for variable structure systems such as DC-DC converters; however, it is not suitable for PEMFC systems in practice as it is affected by the "jitter" problem. The model prediction algorithm offers higher accuracy and strong robustness; however, the algorithm is heavily reliant on mathematical models, making the control results in reality very different from the theoretical ones. The goal of robust control is to establish feedback control laws

accounting for system uncertainty in order to increase the robustness of closed-loop systems. However, the control performance of a controller employing robust control is compromised it as cannot operate at the optimal point.

Optimal control is one of the more advanced control algorithm designs. By expressing the performance of a system as an objective function of time, state, error, and other combinations, optimal control selects an appropriate control law which enables the objective function to include extreme values in order to obtain the optimal performance of the system. As described by Jaen et al. (2006), the average model of the converter is linearised, and the optimal LQR is obtained by solving the algebraic Riccati equation using the pole configuration, frequency domain metric or integral metric as the optimisation objective function; however, this LQR is not robust enough to cope with large disturbances in the system. Montagner et al. (2011) designed a discrete LQR and determined the existence of the Lyapunov function for the closed-loop system using the LMI method, thus ensuring the stability of the system. Olalla et al. (2009) organised the LQR optimisation problem in the form of an LMI, which was then solved using convex optimisation to obtain a robust linear quadratic regulator. In the study by Moreira et al. (2011), the application of a digital LQR with Kalman state observer for controlling a BUCK converter was tested in a series of simulations. However, the structure of the above optimal algorithm is complex and computationally intensive, leading to a reduction in its control real-time performance in practice (Li and Yu, 2021).

For these reasons, there remains the need for a simple structured model-free PMEFC optimal control algorithm for guiding DC-DC converters (Li et al., 2021).

The DDPG algorithm (Lillicrap et al., 2015) is a data-driven model-free optimal control algorithm, a kind of deep reinforcement learning, which is characterised by strong self-adaptive capability and decision-making ability, and which can arrive at decisions within a few milliseconds. It is used widely in power system control and robot coordination control, and for addressing UAV control problems (Zhang et al., 2016; Qi, 2018; Zhang et al., 2018; Zhang et al., 2019; Zhang and Yu, 2019; Zhang et al., 2020; Zhang et al., 2021; Zhang et al., 2021). However, the poor training efficiency of the DDPG algorithm explains the low robustness of controllers belonging to this class of algorithms, and their ineligibility for PEMFC systems.

In order to stabilise the output characteristics of the PEMFC and improve the stability of its output voltage, a data-driven output voltage control strategy for controlling the duty cycle of the DC-DC converter is proposed in this paper. To this end, an imitation-oriented twin delay deep deterministic policy gradient (IO-TD3) algorithm is proposed, the design of which reflects the idea of imitation learning. In this paper, we propose a distributed deep reinforcement learning training framework for improving the robustness of the PEMFC control policy. The effectiveness of the proposed control policy is experimentally demonstrated by comparing the proposed method with a number of existing algorithms.

This paper makes the following unique contributions to the research field:

1) A 75 kw ninth order output voltage PEMFC dynamic control model that takes into account the DC/DC converter is demonstrated.
2) A PEMFC output voltage control strategy based on an imitation-oriented twin delay deep deterministic policy gradient algorithm for the purpose of increasing robustness is proposed.

The remainder of this paper comprises the following sections: the PEMFC model is demonstrated in *The PEMFC Model*, and the proposed algorithm is described in *Proposed Method*; the experimental results are analysed and discussed in *Experiment*, and the findings in this paper are summarised in *Conclusion*.

THE PEMFC MODEL

PEMFC Modelling and Characterization

A PEMFC is a device that converts chemical energy directly into electrical energy by means of an electrochemical reaction, the individual output voltage of which can be expressed as follows:

$$V_{\text{cell}} = E - \eta_{\text{act}} - \eta_{\text{ohm}} - \eta_{\text{con}} \tag{1}$$

For a fuel cell stack consisting of N single cells connected in series, the output voltage V can be expressed as follows:

$$V = NV_{\text{cell}} \tag{2}$$

Theoretically, the electric potential of the PEMFC varies with temperature and pressure, as expressed in the following equation:

$$E = 1.229 - 0.85 \times 10^{-3}(T - 298.15) + 4.3085 \times 10^{-5} T\left(\ln p_{\text{H}_2} + \ln p_{0_2}/2\right) \tag{3}$$

Thermodynamic Electric Potential

The thermodynamic electric potential of the single cell (i.e., the Nernst electric potential) can be obtained from the mechanism of the electrochemical reaction of the gas inside the PEMFC. This is represented by the following equation:

$$E = \frac{\Delta G}{2F} + \frac{\Delta S}{2F}(T - T_{\text{ref}}) + \frac{RT}{2F}\left(\ln p_{\text{H}_2} + \frac{1}{2}\ln p_{0_2}\right) \tag{4}$$

Activation Overvoltage

The activation overvoltage of the PEMFC is expressed as follows:

$$\eta_{\text{act}} = \xi_1 + \xi_2 T + \xi_3 T \ln c(\text{O}_2) + \xi_4 T \ln I \tag{5}$$

Whereby $c(\text{O}_2)$ is the concentration of dissolved oxygen at the cathode catalyst interface, which can be expressed by Henry's law as follows:

$$c(\text{O}_2) = P_{\text{O}_2}/5.08 \times 10^6 \exp(-498/T) \tag{6}$$

Ohmic Voltage Drop

The ohmic overvoltage is represented by the following equation:

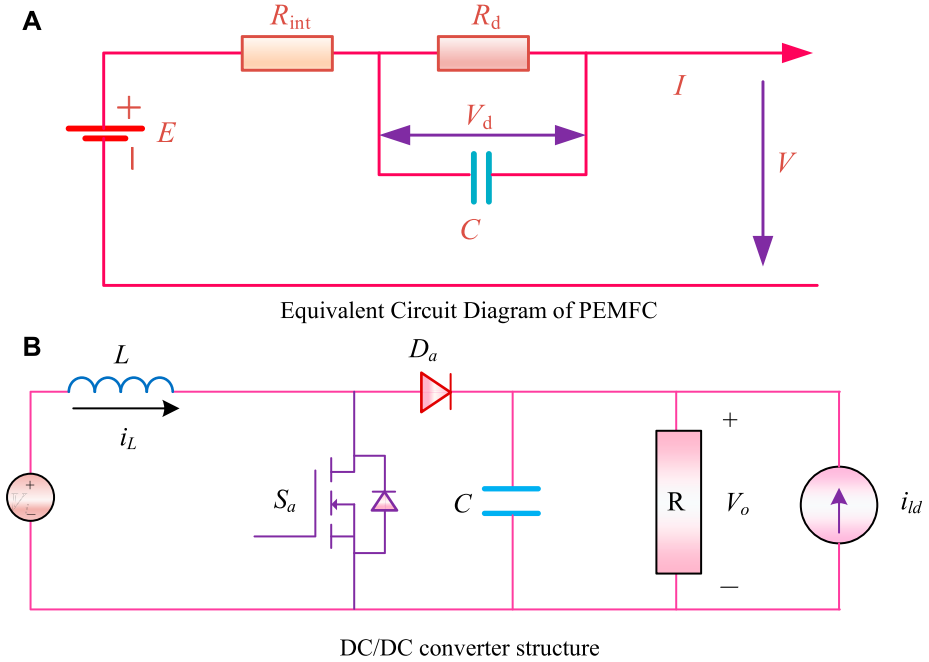


FIGURE 1 | PEMFC equivalent circuit and DC-DC converter. **(A)**Equivalent Circuit Diagram of PEMFC. **(B)**DC/DC converter structure.

$$\eta_{ohm} = IR_{int} = I(R_m + R_c) \tag{7}$$

Empirically, the internal resistance of the PEMFC is expressed as follows:

$$R_{int} = 0.01605 - 3.5 \times 10^{-5} T + 8 \times 10^{-5} i \tag{8}$$

Dense Differential Polarization Overvoltage

The differential overvoltage can be expressed as follows:

$$\eta_{con} = -\beta \ln(J/J_{max}) \tag{9}$$

Dynamic and Capacitive Characteristics of the Double Layer Charge

The dynamic characteristics of the double layer charge of the PEMFC are similar to those of the capacitor, and the equivalent circuit diagram is shown in **Figure 1A**:

As detailed in the figure, the polarization voltage across R_d is V_d and the differential equation for the voltage change of a single cell is expressed as follows:

$$dV_d/dt = I/C - V_d/R_d C \tag{10}$$

PEMFC Stack Voltage

The stack voltage is defined as the value of the voltage at the front end of the PEMFC as it passes through the DC/DC converter. It is assumed that hydrogen is supplied from a hydrogen tank, and is available in sufficient quantities at all times. The air, on the other hand, is controlled by a proportional valve, which allows the air to be controlled efficiently and in time to meet the PEMFC requirements.

Eq. 11 can be obtained from The Law of Conservation of Mass, and the Ideal Gas Law:

$$\frac{V_o}{8.314T} \times \frac{dP_{H2}}{dt} = m_{h2} - K(P_{H2} - P_{EH2}) - \frac{0.5NI}{F} \tag{11}$$

DC-DC Boost Converter Model

The output voltage of the PEMFC is the tap voltage of the DC/DC converter. A boost converter is essentially a step-up power converter, i.e., the voltage is raised and then outputted. An DC/DC boost converter circuit is shown in **Figure 1B**:

Whereby the input and output voltage relationship are controlled output voltage by the switch duty cycle, as expressed in Equation:

$$V_{ou} = \left(\frac{1}{1-u}\right) \times V_{stack} \tag{12}$$

The differential equation for V_{out} is as follows:

$$\begin{cases} \frac{di_L}{dt} = \frac{1}{L} \cdot V_{stack} \\ \frac{dV_{out}}{dt} = \frac{1}{C} \cdot (-i_{ost}) \end{cases} \tag{13}$$

PROPOSED METHOD

Framework of Control Policy

The control model includes a PEMFC stack, a DC/DC converter and its controller. The controller of the DC/DC converter is

equated to an intelligent agent which is trained to adapt to the non-linear characteristics of the PEMFC so as to improve the overall output voltage control performance. When applied online, the intelligent agent outputs the optimal duty cycle according to the state of the DC-DC converter and the state of the output voltage. The control interval of the agent is 0.01 s.

Agent

1) Action space

The action space is set to $u/100$, as follows:

$$\begin{cases} a = [u/100] \\ 0 \le u \le u_{\max} \end{cases} \tag{14}$$

2) State space

The state space is expressed as follows:

$$\left[e \quad \int_0^t e dt \quad U \right] \tag{15}$$

3) Reward function

The reward function is expressed as follows:

$$\mathrm{r}(t) = -\left[\mu_1 e^2(t) + \mu_2 u(t-1)\right] + \beta \tag{16}$$

$$\alpha = \begin{cases} -0.3 & e^2(t) > 0.09 \\ 0 & e_{st}^2(t) \le 0.09 \end{cases} \tag{17}$$

DDPG

The Deterministic Policy Gradient (DDPG) policy determines an action via the policy function $\mu(s)$, which is shown in the following equation:

$$a_i = \mu(s_t|\theta^\mu) \tag{18}$$

This deep reinforcement learning algorithm uses a value network to fit the function Q(s) and the objective function $J(\theta^\mu)$, the latter which is defined as follows:

$$J(\theta^\mu) = E_{\theta,x}\left[r_1 + \gamma r_2 + \gamma^2 r_3 + \cdots\right] \tag{19}$$

In this arrangement, the Q function can be expressed as the expected value of the reward for selecting an action under $\mu(s)$.

In each step, a specific policy is randomly selected for the agent to be executed, and the best policy is selected by maximizing the fusion objective function. The different policy will be executed in different steps, so that an experience replay pool can be obtained for each agent. Finally, the gradient of the fusion objective function $\nabla_{\theta i} J$ is solved for the policy parameters of each agent, as expressed in the following equation:

$$\nabla_{\theta_i} J \approx \frac{1}{S} \sum_j \nabla_{\theta_j} \mu_i\left(O_i^j\right) \nabla_{a_j} Q_i^{\varepsilon} \cdot \left(x^j, a_1^j, \cdots, a_i, \cdots, a_N^j\right)\Big|_{ai=\mu i(O_i)} \tag{20}$$

Nevertheless, the DDPG algorithm suffers from low robustness. The main reasons for this are as follows:

1) The algorithm lacks effective bootstrapping techniques, and so it tends to fall into the local optimum solution, which undermines the robustness of the strategy.
2) Overestimation of the Q-value leads to overfitting of the algorithm's policy, thus making it less robust.

Framework for Offline Training of IO-TD3

In order to address the low robustness of the DDPG algorithm, the IO-TD3 algorithm incorporates the following two innovations:

1) An imitation-oriented distributed training framework for deep reinforcement learning; and,
2) An Integrated anti-Q overestimation policy.

The large-scale deep reinforcement learning training framework for the IO-TD3 algorithm is illustrated.

The algorithm contains three roles, an explorer, an expert and a leader. A total of 36 parallel systems are included in the algorithm, each containing the same PEMFC system and different load disturbances, so as to enhance sample diversity.

Explorer

The Explorer contains only one actor network. The explorers in different parallel systems employ their own different exploration principles. The explorers described in this paper use the following exploration principles: greedy strategy, Gaussian noise, and OU noise.

The explorer in parallel system 1–6 uses an ε-greedy strategy with the following actions:

$$a_\varepsilon^l = \begin{cases} \pi_\phi^l(s) & \text{With } \varepsilon \text{ probability} \\ a_{\text{rand}}^l & \text{With } 1-\varepsilon \text{ probability} \end{cases} \tag{21}$$

The explorer in parallel system 7–12 uses an OU noise exploration strategy with the following actions:

$$a_{OU}^j = \pi_\phi^j(s) + N_{OU}^j \tag{22}$$

The Gaussian noise exploration strategy used in parallel system 13–18 has the following actions:

$$a_{\text{Gaussian}}^m = \pi_\phi^m(s) + N_{\text{Gaussian}}^m \tag{23}$$

Expert

On the basis of imitation learning, the proposed algorithm employs a large number of expert samples, which are used as learning samples, so that the algorithm can be effectively guided to learn correctly during the early stages of training. In this proposed method, the duty cycle of the DC/DC converter is controlled, whereby the parallel systems generate expert samples for the Leader (described below).

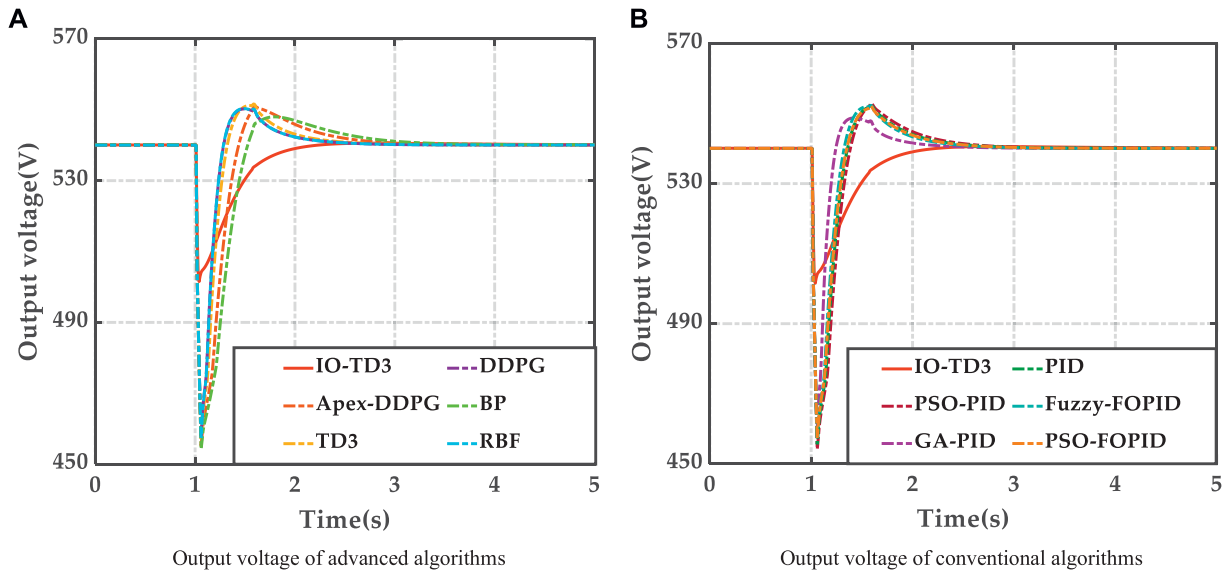


FIGURE 2 | Results of Case 1. **(A)** Output voltage of advanced algorithms **(B)** Output voltage of conventional algorithms

The expert itself uses a variety of controllers based on different principles, including PSO-PID and GA-PID algorithms. The objective function for parameter optimization is as follows:

$$F(t) = \int_0^{\infty} t(e(t))^2 \mathrm{d}t \tag{24}$$

Leader

The leader (termed "Leader") entails a complete agent structure which includes a two-actor network, two critic networks, and an experience pool. It learns samples from the explorer and the critic in order to obtain the optimal control strategy, and periodically sends the latest parameters to the actor network for all the explorers.

The critic in each leader employs an integrated mitigation Q over-estimation technique.

1) The critic in Leader uses the Clipped Double Q-learning technique to calculate the target value:

$$y_t^1 = r(s_t, a_t) + \gamma \min_{i=1,2} Q_{\theta_i}\left(s_{t+1}, \pi_{\phi_1}(s_{t+1})\right) \tag{25}$$

2) The critic network inside Leader uses a policy delay update policy. d updates to the actor network are performed after every d update to the critic.
3) The critic inside Leader uses a goal policy smoothing regularization strategy. The critic introduces a regularization method for reducing the variance of the goal values by bootstrapping the estimates of similar state action pairs.

$$y_t = r(s_t, a_t) + \mathrm{E}_{\varepsilon}\left[Q_{\theta'}\left(s_{t+1}, \pi_{\phi'}(s_{t+1}) + \varepsilon\right)\right] \tag{26}$$

Smooth regularization is also achieved by adding a random noise to the target strategy and averaging over the mini-batch:

$$y_t = r(s_t, a_t) + \gamma \min_{i=1,2} Q_{\theta_t}\left[s_{t+1}, \pi_{\phi'}(s_{t+1}) + \varepsilon\right] \tag{27}$$

$$\varepsilon \sim \mathrm{clip}\left[N(0, \sigma), -c, c\right] \tag{28}$$

EXPERIMENT

In order to verify the superior effectiveness of the proposed method, the IO-TD3 algorithm control strategy was tested against the following methods in case: Ape-x-MADDPG control algorithm (40), MATD3 control algorithm (41), MADDPG coordinated control algorithm (37), BP neural network control algorithm, RBF neural network control algorithm, PSO optimized PID control algorithm (PSO-PID), GA optimized PID control algorithm (GA-PID), PID control algorithm (PID), Fuzzy-FOPID control algorithm (Fuzzy-FOPID), and the PSO-optimized FOPID control algorithm (PSO-FOPID). The first six (including the IO-TD3 algorithm) are referred to as advanced algorithms, and the last five are conventional algorithms.

At 1 s, the load current magnitude appears as a load disturbance which begins at 72.6 A and rises to 250.0 A. The results are shown in **Figure 2A,B**.

1) Comparison between proposed algorithm and advanced algorithms. As shown in **Figure 2A**, the IO-TD3 algorithm has a better response time, smoother output voltage profile and no overshoot. The proposed algorithm's minimum output voltage value is smaller than that of the other advanced algorithms. Conversely, each of the output voltages of the other advanced algorithms is characterized by large overshoot, and these results are affected by varying degrees of overshoot and oscillation, which can lead to unstable output voltages. The IO-TD3 algorithm therefore has the best control performance.

2) Possible reasons for these promising patterns are as follows: firstly, other DRL algorithms tend to fall into local optima; they amount to sub-optimal control strategies as they are not effectively guided in pre-learning, resulting in large output voltage overshoot and output voltage fluctuations, which undermine PEMFC output performance.

The BP and RBF algorithms are too dependent on the trained samples, resulting in limited control performance. A neural network control algorithm which lacks self-exploration will have lower adaptive ability, leading to poorer control performance.

The PSO-PID and GA-PID algorithms within the conventional control algorithm group lack the adaptive capability for adjusting the PID parameters, and therefore struggle to adapt to the non-linearity of the PEMFC environment. The PSO-FOPID algorithm enables greater robustness in the environment, but is impaired by poor adaptive capability due to its fixed coefficients, which ultimately leads to severe output voltage overshoot and oscillation. The Fuzzy-FOPID algorithm, despite its better adaptive capability, is underpinned by overly simple rules, resulting in poor control accuracy and therefore a large overshoot despite the fast response of the algorithm.

In summary, the IO-TD3 controller is a more suitable candidate for practical output voltage control systems, with its short response times, and good dynamic and static performance indicators.

CONCLUSION

In this paper, an imitation-oriented deep reinforcement learning output voltage control strategy for controlling the duty cycle of a DC-DC converter has been proposed. The proposed method is an imitation-oriented twin delay deep deterministic (IO-TD3) policy gradient algorithm, the design of which is structured on the concept of imitation learning. It embodies a distributed deep reinforcement learning training framework designed to improve the robustness of the control policy. The effectiveness of the proposed control policy has been experimentally demonstrated. The simulation results show that the IO-TD3 algorithm has superior control performance compared to other deep reinforcement learning algorithms (e.g., Ape-x-MADDPG, MATD3, MADDPG). Compared to other control algorithms (BP, RBF, PSO-PID, GA-PID, PID, Fuzzy-FOPID, PSO-FOPID), the IO-TD3 algorithm is more adaptable, and, in relation to the output voltage of the PEMFC, has better response speed and stability, and can more effectively track and control the output voltage in a timely and effective manner.

DATA AVAILABILITY STATEMENT

The original contributions presented in the study are included in the article/Supplementary Material, further inquiries can be directed to the corresponding author.

AUTHOR CONTRIBUTIONS

JL: conceptualization, methodology, software, data curation, writing-original draft preparation, visualization, investigation, software, validation. YL: Writing-Reviewing and editing. TY: Supervision.

FUNDING

This work was jointly supported by National Natural Science Foundation of China (U2066212).

REFERENCES

Bemporad, A., Borrelli, F., and Morari, M. (2002). Model Predictive Control Based on Linear Programming - the Explicit Solution. *Ieee Trans. Automat. Contr.* 47, 1974–1985. doi:10.1109/tac.2002.805688

Bougrine, M. D., Benalia, A., and Benbouzid, M. H. (2013). "Nonlinear Adaptive Sliding Mode Control of a Powertrain Supplying Fuel Cell Hybrid Vehicle," in 3rd International Conference on Systems and Control (Algiers, Algeria: IEEE), 714–719.

Ferrari-Trecate, G., Cuzzola, F. A., Mignone, D., and Morari, M. (2002). Analysis of Discrete-Time Piecewise Affine and Hybrid Systems. *Automatica* 38, 2139–2146. doi:10.1016/s0005-1098(02)00142-5

Jaen, C., Pou, J., Pindado, R., Sala, V., and Zaragoza, J. (2006). "A Linear-Quadratic Regulator with Integral Action Applied to PWM DC-DC Converters," in IECON 2006 - 32nd Annual Conference on IEEE Industrial Electronics (Paris, France: IEEE), 2280–2285.

Jiao, J., Cui, X., and Cui, X. (2013). Robustness Analysis of Sliding Mode on DC/DC for Fuel Cell Vehicle. *Jestr* 6, 1–6. doi:10.25103/jestr.065.01

Li, J., and Yu, T. (2021). A New Adaptive Controller Based on Distributed Deep Reinforcement Learning for PEMFC Air Supply System. *Energ. Rep.* 7, 1267–1279. doi:10.1016/j.egyr.2021.02.043

Li, J., Yu, T., Zhang, X., Li, F., Lin, D., and Zhu, H. (2021). Efficient Experience Replay Based Deep Deterministic Policy Gradient for AGC Dispatch in Integrated Energy System. *Appl. Energ.* 285, 116386. doi:10.1016/j.apenergy.2020.116386

Lillicrap, T. P., Hunt, J. J., Pritzel, A., Heess, N., Erez, T., Tassa, Y., et al. (2015). Continuous Control with Deep Reinforcement Learning. arXiv preprint arXiv:1509.02971.

Montagner, V. F., Maccari, L. A., Dupont, F. H., Pinheiro, H., and Oliveira, R. C. L. F. (2011). "A DLQR Applied to Boost Converters with Switched Loads: Design and Analysis," in XI Brazilian Power Electronics Conference (Natal, Brazil: IEEE), 68–73.

Moreira, C. O., Silva, F. A., Pinto, S. F., and Santos, M. B. (2011). "Digital LQR Control with Kalman Estimator for DC-DC Buck Converter," in 2011 IEEE EUROCON - International Conference on Computer as a Tool (Lisbon, Portugal: IEEE), 1–4.

Olalla, C., Leyva, R., El Aroudi, A., and Queinnec, I. (2009). Robust LQR Control for PWM Converters: An LMI Approach. *Ieee Trans. Ind. Electron.* 56, 2548–2558. doi:10.1109/tie.2009.2017556

Olalla, C., Queinnec, I., Leyva, R., and Aroudi, A. E. (2010). "Robust Control Design of Bilinear DC-DC Converters with Guaranteed Region of Stability," in 2010 IEEE International Symposium on Industrial Electronics (Bari, Italy: IEEE), 3005–3010.

Qi, X. (2018). Rotor Resistance and Excitation Inductance Estimation of an Induction Motor Using Deep-Q-Learning Algorithm. *Eng. Appl. Artif. Intelligence* 72, 67–79. doi:10.1016/j.engappai.2018.03.018

Sun, L., Jin, Y., Pan, L., Shen, J., and Lee, K. Y. (2019). Efficiency Analysis and Control of a Grid-Connected PEM Fuel Cell in Distributed Generation. *Energ. Convers. Manage.* 195, 587–596. doi:10.1016/j.enconman.2019.04.041

Swain, P., and Jena, D. (2015). "PID Control Design for the Pressure Regulation of PEM Fuel Cell," in 2015 International Conference on Recent Developments in Control, Automation and Power Engineering (RDCAPE) (Noida, India: IEEE), 286–291.

Yang, B., Li, D., Zeng, C., Chen, Y., Guo, Z., Wang, J., et al. (2021a). Parameter Extraction of PEMFC via Bayesian Regularization Neural Network Based Meta-Heuristic Algorithms. *Energy* 228, 120592. doi:10.1016/j.energy.2021.120592

Yang, B., Swe, T., Chen, Y., Zeng, C., Shu, H., Li, X., et al. (2021b). Energy Cooperation between Myanmar and China under One Belt One Road: Current State, Challenges and Perspectives. *Energy* 215, 119130. doi:10.1016/j.energy.2020.119130

Yang, B., Wang, J., Zhang, X., Yu, T., Yao, W., Shu, H., et al. (2020). Comprehensive Overview of Meta-Heuristic Algorithm Applications on PV Cell Parameter Identification. *Energ. Convers. Manage.* 208, 112595. doi:10.1016/j.enconman.2020.112595

Yang, B., Yu, T., Shu, H., Dong, J., and Jiang, L. (2018). Robust Sliding-Mode Control of Wind Energy Conversion Systems for Optimal Power Extraction via Nonlinear Perturbation Observers. *Appl. Energ.* 210, 711–723. doi:10.1016/j.apenergy.2017.08.027

Yang, B., Yu, T., Zhang, X., Li, H., Shu, H., Sang, Y., et al. (2019a). Dynamic Leader Based Collective Intelligence for Maximum Power point Tracking of PV Systems Affected by Partial Shading Condition. *Energ. Convers. Manage.* 179, 286–303. doi:10.1016/j.enconman.2018.10.074

Yang, B., Zeng, C., Wang, L., Guo, Y., Chen, G., Guo, Z., et al. (2021c). Parameter Identification of Proton Exchange Membrane Fuel Cell via Levenberg-Marquardt Backpropagation Algorithm. *Int. J. Hydrogen Energ.* 46, 22998–23012. doi:10.1016/j.ijhydene.2021.04.130

Yang, B., Zhong, L., Zhang, X., Shu, H., Yu, T., Li, H., et al. (2019b). Novel Bio-Inspired Memetic Salp Swarm Algorithm and Application to MPPT for PV Systems Considering Partial Shading Condition. *J. Clean. Prod.* 215, 1203–1222. doi:10.1016/j.jclepro.2019.01.150

Zhang, X., Li, S., He, T., Yang, B., Yu, T., Li, H., et al. (2019). Memetic Reinforcement Learning Based Maximum Power point Tracking Design for PV Systems under Partial Shading Condition. *Energy* 174, 1079–1090. doi:10.1016/j.energy.2019.03.053

Zhang, X., Tan, T., Zhou, B., Yu, T., Yang, B., and Huang, X. (2021). Adaptive Distributed Auction-Based Algorithm for Optimal Mileage Based AGC Dispatch with High Participation of Renewable Energy. *Int. J. Electr. Power Energ. Syst.* 124, 106371. doi:10.1016/j.ijepes.2020.106371

Zhang, X., Xu, H., Yu, T., Yang, B., and Xu, M. (2016). Robust Collaborative Consensus Algorithm for Decentralized Economic Dispatch with a Practical Communication Network. *Electric Power Syst. Res.* 140, 597–610. doi:10.1016/j.epsr.2016.05.014

Zhang, X., and Yu, T. (2019). Fast Stackelberg Equilibrium Learning for Real-Time Coordinated Energy Control of a Multi-Area Integrated Energy System. *Appl. Therm. Eng.* 153, 225–241. doi:10.1016/j.applthermaleng.2019.02.053

Zhang, X., Yu, T., Xu, Z., and Fan, Z. (2018). A Cyber-Physical-Social System with Parallel Learning for Distributed Energy Management of a Microgrid. *Energy* 165, 205–221. doi:10.1016/j.energy.2018.09.069

Zhang, Y., Mou, Z., Gao, F., Jiang, J., Ding, R., and Han, Z. (2020). UAV-enabled Secure Communications by Multi-Agent Deep Reinforcement Learning. *IEEE Trans. Veh. Technol.* 69, 11599–11611. doi:10.1109/tvt.2020.3014788

Conflict of Interest: The authors declare that the research was conducted in the absence of any commercial or financial relationships that could be construed as a potential conflict of interest.

Publisher's Note: All claims expressed in this article are solely those of the authors and do not necessarily represent those of their affiliated organizations, or those of the publisher, the editors and the reviewers. Any product that may be evaluated in this article, or claim that may be made by its manufacturer, is not guaranteed or endorsed by the publisher.

Copyright © 2021 Li, Li and Yu. This is an open-access article distributed under the terms of the Creative Commons Attribution License (CC BY). The use, distribution or reproduction in other forums is permitted, provided the original author(s) and the copyright owner(s) are credited and that the original publication in this journal is cited, in accordance with accepted academic practice. No use, distribution or reproduction is permitted which does not comply with these terms.

frontiers in Energy Research

BRIEF RESEARCH REPORT
published: 04 October 2021
doi: 10.3389/fenrg.2021.754908

Robust Optimal Dispatching of Wind Fire Energy Storage System Based on Equilibrium Optimization Algorithm

Xiaojiao Chen[1], Liansheng Huang[1,2], Xiuqing Zhang[1], Shiying He[1]*, Zhicai Sheng[1], Zhenshang Wang[1,2], Tao Chen[1,2] and Sheng Dou[1,2]*

[1]Institute of Plasma Physics, Chinese Academy of Sciences, Hefei, China, [2]University of Science and Technology of China, Hefei, China

The uncertainty of wind resources is one of the main reasons for wind abandonment. Considering the uncertainty of wind power prediction, a robust optimal dispatching model is proposed for the wind fire energy storage system with advanced adiabatic compressed air energy storage (AA-CAES) technology. Herein, the operation constraints of the power plant and constraints of the reserved capacity are defined according to the operation characteristics of AA-CAES. Based on the limited scenario method, a solution framework is proposed to achieve the optimal robustness and economical operation of the system, which provides a new way for the application of the intelligent algorithm in the robust optimal dispatching. Specifically, a novel equilibrium optimization algorithm is employed to solve the optimal dispatching problem, which has good global search performance. The proposed solution is validated through simulations based on the IEEE-39 node system. The simulation results verify the effectiveness of the proposed dispatching model and the intelligent solver.

Keywords: robust optimal dispatching, wind fire energy storage, AA-CAES, solution framework, equilibrium optimization algorithm

OPEN ACCESS

Edited by:
Dongran Song,
Central South University, China

Reviewed by:
Bin Liu,
Guangxi University, China
Zhongwei Lin,
North China Electric Power University, China

****Correspondence:***
Xiuqing Zhang
xqzhang@ipp.ac.cn
Shiying He
shyinghe@ipp.ac.cn

Specialty section:
This article was submitted to Smart Grids, a section of the journal Frontiers in Energy Research

Received: *07 August 2021*
Accepted: *13 September 2021*
Published: *04 October 2021*

Citation:
Chen X, Huang L, Zhang X, He S, Sheng Z, Wang Z, Chen T and Dou S (2021) Robust Optimal Dispatching of Wind Fire Energy Storage System Based on Equilibrium Optimization Algorithm. Front. Energy Res. 9:754908. doi: 10.3389/fenrg.2021.754908

INTRODUCTION

Facing the challenge of global warming and energy crisis, wind power generation has been rapidly developed in recent years (Song et al., 2021b). In 2018, a significant growth of 51.3 GW was reached for the global installed capacity (Yang et al., 2021). However, due to the intermittence and uncertainty of wind power, its large-scale grid connection has brought a great challenge to the reliability of power system. Taking China as an example, the average wind abandonment rate in China was 4% in 2019. With the gradual increase of total installed capacity, the problem of wind abandonment has been increasingly prominent (Song et al., 2021a). In order to reduce the wind abandonment rate, the application of multiple energy complementary system and energy storage system has been widely concerned (Chen et al., 2022).

The application of energy storage system is one of the common methods to reduce the wind abandonment rate of wind farm. As a typical energy storage technology, conventional compressed air energy storage (C-CAES) has been widely used in integrated energy system. It was proved that the utilization of C-CAES can increase the flexibility of comprehensive energy system and improve economic benefits (Sedighizadeh et al., 2019). However, the application of C-CAES in the power system is limited, due to its high construction cost, low conversion efficiency and dependence on specific geographical conditions. As an improved energy storage mode of conventional one,

advanced adiabatic compressed air energy storage (AA-CAES) can store compression heat and has the advantages of high efficiency, long service life, low cost, and fast response.

At present, AA-CAES has been applied into the integrated energy system dispatching. The energy system dispatching model based on AA-CAES was studied, and its value was analyzed in monopoly power market, energy market and reserve market (Ding et al., 2019). Based on the heating and power supply characteristics of AA-CAES, it was proposed an optimal dispatching model of zero carbon emission microgrid integrated with AA-CAES (Rui et al., 2016). This series of research verified the effectiveness of AA-CAES system in the integrated energy system, and provided potential dispatching schemes for the integrated energy system with AA-CAES. However, the existing researches only model the combination between the AA-CAES and the traditional energy. Moreover, the uncertainty of reserved capacity and renewable energy is seldom considered.

Generally, the optimal dispatching model of the power system usually presents the characteristics of nonlinearity, high dimension, strong coupling and multi constraints. Most optimal dispatching problems are solved for the whole time series. When using intelligent algorithms, there are problems such as high dimension and difficulty in meeting constraints. Based on these problems, an optimization framework suitable for the utilization of intelligent algorithms is proposed, which has better solution results and shorter solution time. Specifically, to solve the formulated optimal dispatching problem, it is employed a novel equilibrium optimization (EO) algorithm (Faramarzi et al., 2020), which has unique advantages in exploration, exploitation, and local minimum avoidance when solving high-dimensional, nonlinear and multi constraint problems.

Combining AA-CAES with renewable energy, a robust optimal scheduling model is established for the wind fire energy storage system, in which the limited scenario method is used to represent the uncertainty of wind power prediction. In order to solve the dispatching scheme corresponding to minimizing the comprehensive cost in the extreme scenario, an effective framework based on the intelligent algorithm solution is proposed. The novel EO algorithm is used to solve the dispatching scheme corresponding to the minimal comprehensive cost under different prediction error bounds. Finally, the effectiveness of the dispatching model and solution framework is verified under the improved IEEE-39 node.

The remainder of this paper is organized as follows. In section *Robust Optimal Dispatching of Wind Fire Storage System*, the robust optimal dispatching model of the wind fire storage system is established, and a solution framework based on the intelligent algorithm solution is proposed. Experimental validation and result analysis are shown in section *Experimental Validation and Result Analysis*. Finally, section *Conclusion* concludes the paper.

ROBUST OPTIMAL DISPATCHING OF WIND FIRE STORAGE SYSTEM

The limited scenario can represent all error scenarios in the uncertainty set. The robust optimal dispatching model can meet the dispatching of all scenarios only by meeting all limited scenarios. In this section, the limited scenario method is used to establish the robust optimal dispatching model of wind fire energy storage system, and the objective function and related constraints are presented.

Robust Optimal Dispatching Modelling

The limited scenario method is used to quantify the uncertainty of wind power prediction, and the established uncertainty set of wind power prediction is as follows:

$$(1-\beta)P_{Wp,i}^{t} \le P_{Wp,i}^{t} \le (1+\beta)P_{Wp,i}^{t} \tag{1}$$

where $P_{Wp,i}^{t}$ is the predicted power generation of wind farm i at time t, and β is the scaling factor of wind power prediction error limit, which determines the performance of the system.

The integrated energy system studied in this paper includes wind power, thermal power and AA-CAES. Among them, the mechanism model includes operation constraints and reserved capacity constraints. The cost models of these three types of power stations can be expressed in three parts: energy cost, environmental cost and standby market cost. As a part of the comprehensive cost, the production cost of the integrated energy system can be expressed as:

$$C_O = C_F + C_W + C_{CAES} + C_E + \left(C_{Lup} + C_{Ldown}\right) \tag{2}$$

where C_F, C_W , C_{CAES} are the power purchase cost of thermal power, wind power and AA-CAES, respectively. C_E is environmental cost, and C_{Lup} and C_{Ldown} are the positive and negative standby market cost, respectively.

The power purchase cost, environmental cost and power purchase cost of thermal power, wind power and AA-CAES power stations are as follows:

$$C_F = \sum_{t=1}^{T}\sum_{i=1}^{N_G} p_{f,i}P_{F,i}^{t} \tag{3}$$

$$C_W = \sum_{t=1}^{T}\sum_{i=1}^{N_W} p_{w,i}P_{W,i}^{t} \tag{4}$$

$$C_{CAES} = \sum_{t=1}^{T}\sum_{i=1}^{N_C} p_{c,g,i}P_{CAES,i}^{t} \tag{5}$$

$$C_E = \sum_{t=1}^{T}\sum_{i=1}^{N_G}\left(\lambda_s\alpha_i^s P_{F,i}^{t}\Delta t + \lambda_c\alpha_i^c P_{F,i}^{t}\Delta t\right) \tag{6}$$

$$C_{Lup} = \sum_{t=1}^{T}\sum_{i=1}^{N_C} p_{caes,i,Lup}P_{CAES,i,Lup}^{t} + \sum_{t=1}^{T}\sum_{i=1}^{N_G} p_{f,i,Lup}P_{F,i,Lup}^{t} \tag{7}$$

$$C_{Ldown} = \sum_{t=1}^{T}\sum_{i=1}^{N_C} p_{caes,i,Down}P_{CAES,i,Down}^{t} + \sum_{t=1}^{T}\sum_{i=1}^{N_G} p_{f,i,Down}P_{F,i,Down}^{t} \tag{8}$$

where $p_{f,i}$, $p_{w,i}$ and $p_{c,g,i}$ are the unit power purchase cost of wind power, thermal power and AA-CAES, respectively; $p_{c,c,i}$ is the unit cost required to buy electricity under the compression state of the power station. $p_{caes,i,Lup}$, $p_{caes,i,Down}$, $p_{f,i,Lup}$ and $p_{f,i,Down}$ are the unit power purchase cost of wind power and AA-CAES in positive and negative standby Market, respectively; λ_s and λ_c are

the cost factor of gas emission of SO_2 and CO_2 respectively; $P^t_{F,i}$, $P^t_{W,i}$ and $P^t_{CAES,i}$ are the output of the corresponding unit at time t, respectively; $P^t_{F,i,Lup}$ and $P^t_{F,i,Ldown}$ are the positive and negative standby capacity provided by thermal power unit i at time t, respectively. N_G, N_W and N_C are the number of thermal power units, wind power units and AA-CAES units, respectively; T is the dispatching period which is set as 24 in this study.

In order to ensure the effectiveness and accuracy of the established dispatching model, some power system operation constraints need to be considered, including standby constraints, unit climbing constraints, wind power output constraints and wind power prediction uncertainty set constraints. The system operation constraints are set as follows:

- System power balance constraints and positive and negative reserved capacity constraints:

$$\sum_{i=1}^{N_G} P^t_{F,i} + \sum_{i=1}^{N_W} P^t_{W,i} + \sum_{i=1}^{N_C} P^t_{CAES,i} = P^t_{Load} \tag{9}$$

$$\sum_{i=1}^{N_G} P^t_{F,i,Lup} + \sum_{i=1}^{N_C} P^t_{CAES,i,Lup} \geq R^t_{Lup,min} \tag{10}$$

$$\sum_{i=1}^{N_G} P^t_{F,i,Ldown} + \sum_{i=1}^{N_C} P^t_{CAES,i,Ldown} \geq R^t_{Ldown,min} \tag{11}$$

- Thermal power unit output upper and lower limit constraints, positive and negative reserved capacity climbing constraints, start and stop constraints:

$$P^t_{F,i} + P^t_{F,i,Lup} \leq P_{F,i,\max} \tag{12}$$

$$P_{F,i,min} \leq P^t_{F,i} - P^t_{F,i,Ldown} \tag{13}$$

$$0 \leq P^t_{F,i,Lup} \leq r_{F,i,Lup} \tag{14}$$

$$0 \leq P^t_{F,i,Ldown} \leq r_{F,i,Ldown} \tag{15}$$

- Wind power output constraints and wind power prediction uncertainty set constraints:

$$0 \leq P^t_{W,i} \leq P^t_{Wp,i} \tag{16}$$

$$(1-\beta)P^t_{Wp,i} \leq P^t_{Wp,i} \leq (1+\beta)P^t_{Wp,i} \tag{17}$$

where P^t_{Load} is the load value at time t, $R^t_{Lup,min}$ and $R^t_{Ldown,min}$ are the minimum positive and negative reserved capacity required at time t, respectively. $r_{F,i,Lup}$ and $r_{F,i,Ldown}$ are the up and down climbing speed of thermal power unit i, respectively.

Baes on the established robust optimal dispatching model, the risk cost and comprehensive cost can be calculated. Risk cost includes the wind abandonment cost and load shedding cost. In this study, it is assumed that the probability distribution of wind power prediction is a normal distribution with the predicted value as the mean. Therefore, combined with the wind power probability distribution curve, the expected value of the wind power prediction range that fails to be absorbed by the dispatching plan can be obtained, which is the expected value of the abandoned wind power of the dispatching plan in this period. Meanwhile, the cost of wind abandonment also considers the fuel cost and environmental cost of thermal power. The expression of abandoned wind cost is as follows:

$$C_{W,ab} = \sum_{t=1}^{T}\left(a_i Q^2_{W,abandon,t} + b_i Q_{W,abandon,t} + c_i + \lambda_s \alpha^s_i Q_{W,abandon,t} + \lambda_c \alpha^c_i Q_{W,abandon,t}\right) \tag{18}$$

where $Q_{W,abandon,t}$ is the expected value of abandoned wind power corresponding to time t, and a_i, b_i, c_i are the three fuel cost factors.

Meanwhile, the expected value is calculated by integrating the minimum wind power range that the system can dispatch, and then the expected value of abandoned wind power in the dispatching plan in this period can be obtained. Therefore, the load shedding cost can be expressed as:

$$C_{W,cut} = \sum_{t=1}^{T} p_{cut,t} Q_{W,cut,t} \tag{19}$$

where $p_{cut,t}$ is the unit cost required to cut off the load at time t, and $Q_{W,cut,t}$ is the expected value of cut-off load power at time t.

Combined with the abandoned wind cost, load shedding cost and production cost, the comprehensive cost can be finally obtained as follows:

$$C_{Total} = C_O + C_{W,ab} + C_{W,cut} \tag{20}$$

Solution Framework for Solving the Established Dispatching Model

According to the definition of wind power prediction uncertainty set by the limited scenario method, the scaling factor β of the wind power prediction distribution will determine the system performance. The value of scaling factor β depends on the user's estimation of the degree of uncertainty of prediction. In this study, the effective range of scaling factor β is set to be 5–30%. Based on the established robust optimal dispatching model, the robust optimization problem is formulated, and the final objective function is presented in a robust format as follows:

$$\begin{aligned} &\min C_{Total}\left(P_w, P_F, P_{CAES}, P_{F,Lup}, P_{F,Ldown}, P_{CAES,Lup}, P_{CAES,Ldown}, \beta\right) \\ &s.t. \begin{cases} Eq.(9)-(17) \\ P^t_{F,min} \leq P^t_F \leq P^t_{F,max} \\ -P_{CAES,max} \leq P_{CAES} \leq P_{CAES,max} \\ P_{CAES,Lup,min} \leq P_{CAES,Lup} \leq P_{CAES,Lup,max} \\ P_{CAES,Ldown,min} \leq P_{CAES,Ldown} \leq P_{CAES,Ldown,max} \end{cases} \\ &\forall \beta \in [-30\%, 30\%] \end{aligned} \tag{21a}$$

where $P^t_{F,min}$, $P^t_{F,max}$ are the minimum and maximum output of thermal power; $P_{CAES,max}$ is the maximum output of AA-CAES; $P_{CAES,Lup,min}$, $P_{CAES,Lup,max}$ are the minimum and maximum positive standby output of AA-CAES; $P_{CAES,Ldown,min}$, $P_{CAES,Ldown,max}$ are the minimum and maximum negative standby output of AA-CAES.

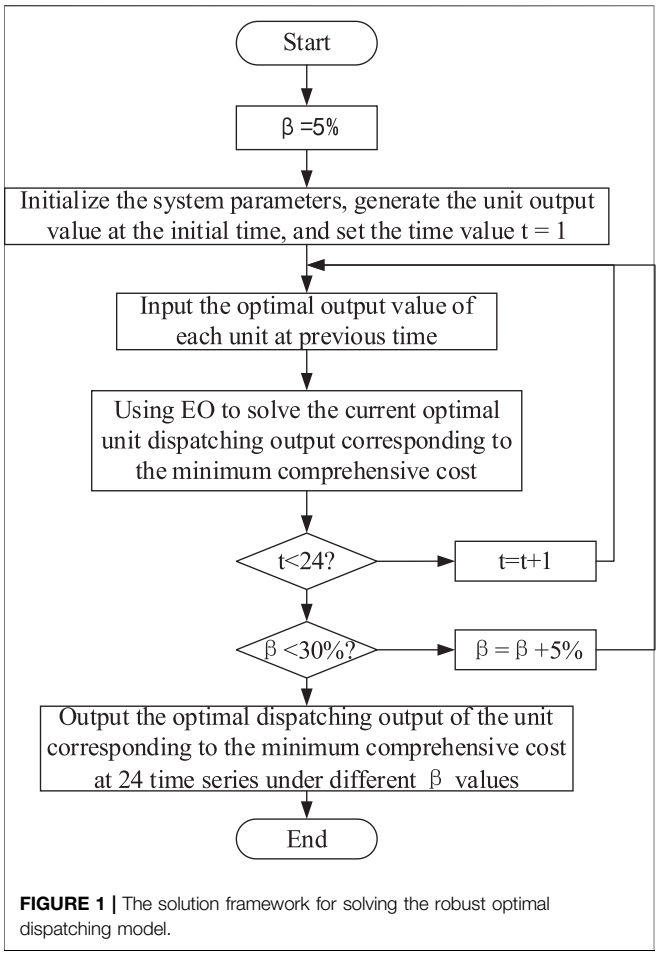


FIGURE 1 | The solution framework for solving the robust optimal dispatching model.

In order to solve the minimum comprehensive cost corresponding to the worst scenario under different β value ranges, an effective solution framework is proposed as show in **Figure 1**. The specific procedure is carried out as follows:

Initialization

Firstly, initialize $\beta = 5\%$, set the current time value $t = 1$, and set input parameters such as unit dispatching output boundary value, cost coefficient and electricity price. Set the initial unit output value as the lower limit of the processing range.

External circulation

Use EO algorithm to solve the optimal scheduling scheme corresponding to the minimum comprehensive cost in the next 24 times when $\beta = 5\%$. When $\beta < 30\%$, then $\beta = \beta + 5\%$, and continue to use EO algorithm to solve the model at all 24 times under the updated β condition. When $\beta > 30\%$, the cycle ends and all the β and its corresponding production cost, risk cost, minimum comprehensive cost and dispatching output are collected.

Internal circulation

First, input the initialized unit output value as the optimal output value at the previous time. Then, use EO algorithm to solve the dispatching model at present time moment, and get the corresponding production cost, risk cost and minimum comprehensive cost. When $t < 24$, $t = t + 1$ and the optimal dispatching output at the current time is used as the system input at the next time. In this way, the optimal dispatching output scheme corresponding to the minimum comprehensive cost under 24 time series at a determined β value is obtained.

The Solver Based on the Equilibrium Optimization Algorithm

According to the established objective function and the relevant constraints, the optimal dispatching model can be transformed into an optimization problem. In order to ensure the solution speed and accuracy, EO algorithm is presented to solve this optimization problem. EO algorithm is inspired by control volume mass balance models used to estimate both dynamic and equilibrium state. Considering the high-dimensional and multi constraint characteristics of this optimization problem, the intelligent algorithm solver proposed in this paper solves a single-step time series and takes the optimal scheduling output at the current time as the input of the next time, which can effectively reduce the solution time while ensuring the solution accuracy. The solver based on EO algorithm is structurally divided into the following parts:

Initialization

Input the optimal dispatching output at the previous time and the system parameters. Determine the user defined parameters, number of design variables and their boundary conditions. Initialize the weight constant coefficient a_1 and a_2 of the global search and the generation probability GP.Based on system constraints and boundary constraints, generate N random points, which are D dimensional.

Individual concentration update

Step 1: When the current iteration number $Iter$ is less than the maximum iteration number, sort the individual concentration according to the fitness function, and put the four individuals with the highest concentration into the equilibrium pool as the optimal candidate solution. Then, save the best point of the previous time and compare it with the current best point. If the best point of the previous time is better than the current best point, the best point of the previous time will replace the current best point.

Step 2: Randomly select a candidate point in the equilibrium pool as $\overrightarrow{C_{eq}}$. Generate random vectors $\vec{\lambda}$ and $\vec{r}$. Update the parameter t and $\vec{F}$ as **Eq. 21a**, **Eq. 21b** and **Eq. 22**. Based on the updated parameters, update the Individual concentration $\vec{C}$ as **Eq. 23**. If the updated Individual concentration $\vec{C}$ cannot meet the system constraints and boundary constraints, repeat step 2 to regenerate the individual concentration until the constraints are met.

$$\mathbf{t} = \left(1 - \frac{\boldsymbol{Iter}}{\boldsymbol{Max_iter}}\right)^{\left(a_2 \frac{Iter}{Max_iter}\right)} \tag{21b}$$

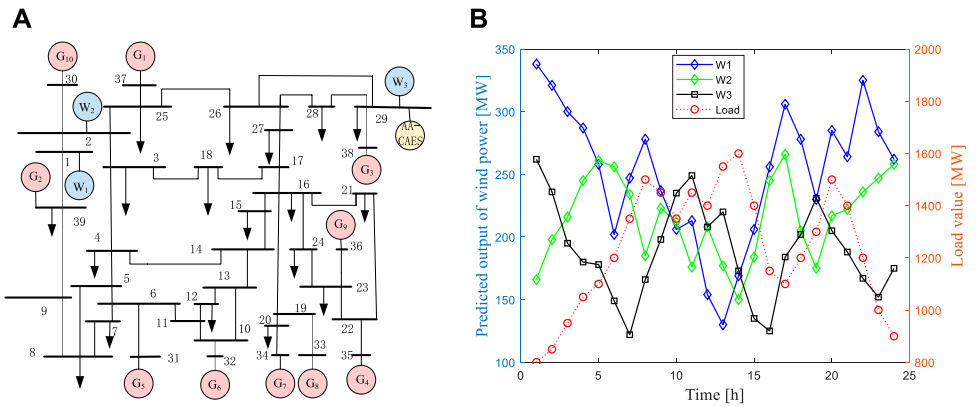


FIGURE 2 | Example node system diagram and wind farm output prediction and load curve: **(A)** node system diagram; **(B)** wind farm output prediction and load curve.

where *Iter* is the current number of iterations, and *Max_iter* is the maximum number of iterations.

$$\vec{F} = a_1 sign\left(\vec{r} - 0.5\right)\left[e^{-\vec{\lambda}t} - 1\right] \tag{22}$$

where $\vec{\lambda}$ and $\vec{r}$ are random vectors, and a_1 is weight constant coefficient.

$$\vec{C} = \overrightarrow{C_{eq}} + \left(\vec{C} - \overrightarrow{C_{eq}}\right)\vec{F} + \frac{\vec{G}}{\vec{\lambda}V}\left(1 - \vec{F}\right) \tag{23}$$

where $\vec{C}$ is the individual concentration, V is the unit set as 1, and $\vec{G}$ is the generation rate.

Full time series solution

The optimal dispatching output at time t is taken as the system input at time $t + 1$. On this basis, the optimal dispatching at time $t + 1$ is solved. In this way, the optimal scheduling output, production cost, risk cost and the corresponding minimum comprehensive cost at each time in the whole time series are obtained. The minimum comprehensive cost under the whole time series is calculated and output as the optimal dispatching scheme of the whole time series under the corresponding β value.

EXPERIMENTAL VALIDATION AND RESULT ANALYSIS

In order to prove the effectiveness of the established robust optimal dispatching model and the proposed solution framework, the improved IEEE-39 node based on a real power grid case is used. The cost changes of the system under different β values are compared. For the optimization problem, EO algorithm is compared with the traditional Grey Wolf Optimizer (GWO) algorithm.

Numerical Example Description

Referring to a regional power grid system in China, the IEEE-39 node system is appropriately modified. Its structure diagram is shown in **Figure 2A**. The wind farms 1 and 2 are connected to the system from nodes 1 and 2, respectively. AA-CAES power station and wind farm 3 are connected to the system from node 29. The predicted power generation curve and load curve of the wind farm are shown in **Figure 2B**, the minimum load is 800 MW, and the maximum load is 1600 MW.

Result Analysis

The production cost, risk cost and minimum comprehensive cost of the whole system under different β values are shown in **Table 1**. It can be seen that with the increase of β value, the minimum comprehensive cost and corresponding production cost of the system tend to decrease. When the β value is 5, 10, 15, 20, 25 and 30%, the minimum comprehensive cost solved by EO algorithm is 23,294,803 ¥, 16,507,080 ¥, 13,997,459 ¥, 13,099,144 ¥, 12,765,750 ¥, and 12,645,801 ¥, respectively. The results show that increasing the uncertainty range can provide an effective way to further reduce the comprehensive cost. When more scenarios are considered, the minimum comprehensive cost decreases with the increase of β value. Meanwhile, with the increase of uncertainty range, the space for comprehensive cost reduction decreases. On the other hand, with the increase of the uncertainty range, the risk cost decreases. At the same time, the production cost and minimum comprehensive cost obtained by EO algorithm under different β values are smaller than GWO, indicating that EO has better global search performance in solving this optimization problem.

When $\beta = 5\%$, the dispatching plan and reserved capacity purchase plan of each power station are shown in **Figure 3**. As can be seen from **Figures 3A–C**, the capacity of thermal power units *No. 1* and *No. 2* is 350 MW, which undertakes the main output of thermal power in the dispatching process because of their large capacity and low production cost coefficient. When the load demand reaches the maximum, the output of *No. 1* and *No. 2* is 344 and 330 MW respectively. Meanwhile, considering the system requirement, the wind turbine output reaches the limit scenario boundary value, which is 95% of the predicted output. For *No. 8*, *No. 9* and *No. 10* thermal power units with small capacity of 50 MW, due to small capacity, high cost and lack of competitive advantage, the output is significantly lower than that of other units.

TABLE 1 | The production cost, risk cost and minimum comprehensive cost under different β values.

(%)β	Algorithm	Production cost [¥]	Risk cost [¥]	Minimum comprehensive cost [¥]
5	EO	12,648,207	10,646,596	23,294,803
	GWO	12,697,791	10,646,596	23,344,387
10	EO	12,627,044	3,880,036	16,507,080
	GWO	12,692,989	3,880,036	16,573,025
15	EO	12,617,752	1,379,707	13,997,459
	GWO	12,697,606	1,379,707	14,077,313
20	EO	12,581,916	517,228	13,099,144
	GWO	12,655,983	517,228	13,173,211
25	EO	12,546,433	219,318	12,765,750
	GWO	12,654,178	219,318	12,873,496
30	EO	12,534,872	110,929	12,645,801
	GWO	12,673,696	110,929	12,784,625

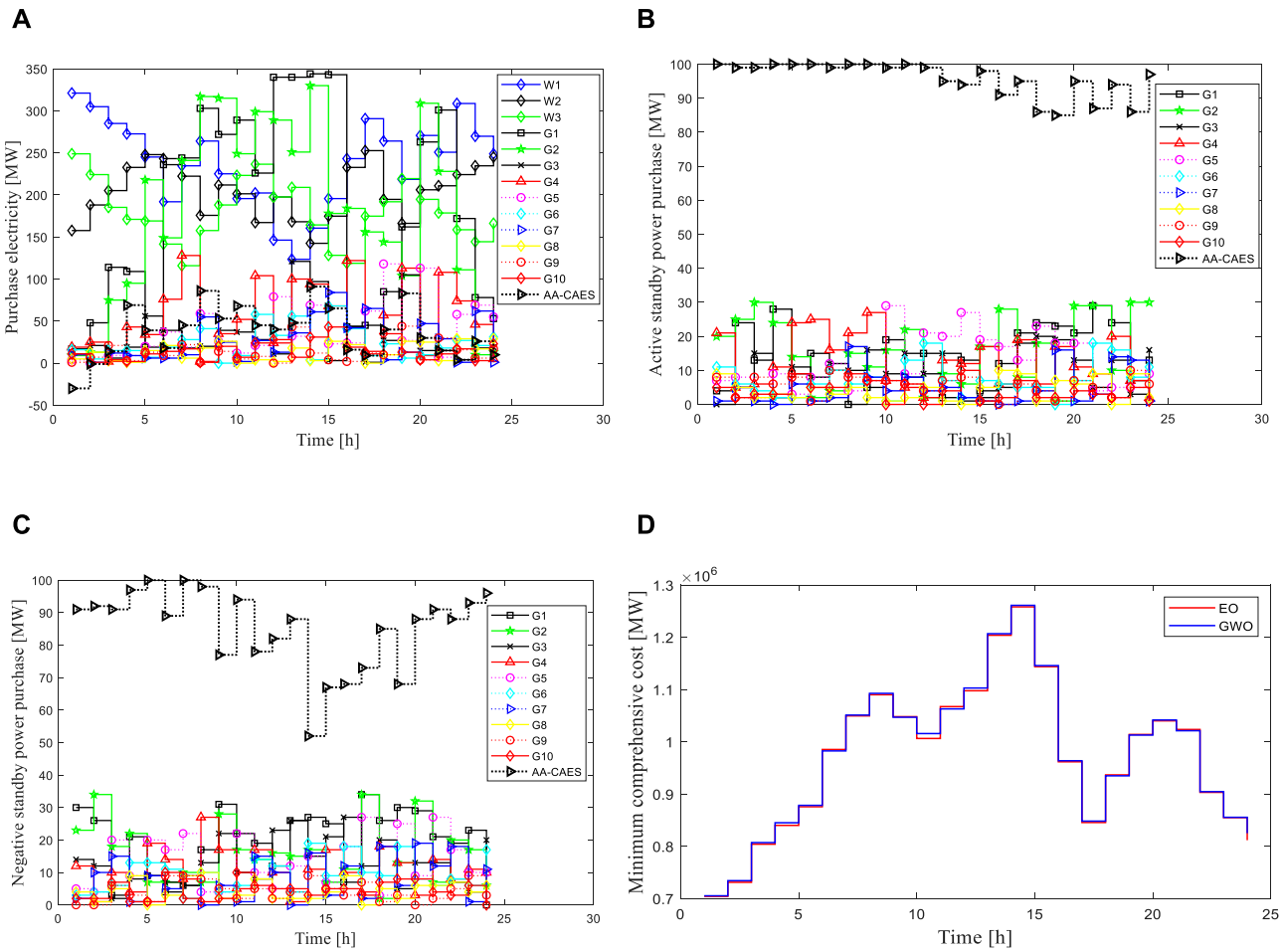


FIGURE 3 | Optimal scheduling scheme and corresponding minimum comprehensive cost: **(A)** Unit output; **(B)** Unit active standby; **(C)** Unit negative standby; **(D)** Minimum comprehensive cost at all times.

AA-CAES undertakes most of the standby capacity due to its low cost and fast response, and its maximum standby capacity is 100 MW. Meanwhile, the output of AA-CAES is low at the peak of wind power output. For example, the output of AA-CAES in time 17 is only 9 MW. It is indicated that AA-CAES has the potential to promote wind power consumption. The minimum comprehensive cost at each time under the optimal scheduling scheme is shown in **Figure 3D**. Among the 24 dispatching times, the minimum comprehensive cost value solved by EO is less than GWO in 17 times. The change trend of minimum comprehensive cost is the same as that of load, which shows that the scheduling scheme tracks the load change well. Meanwhile, the minimum comprehensive cost obtained by EO is lower than GWO at most time, indicating that EO has better search accuracy and local optimal avoidance ability than GWO in solving the optimization problem. Combined with **Figures 3A–C**, it can be explained that the solution framework based on intelligent algorithm can determine an effective unit output scheduling scheme according to load changes, and EO algorithm can effectively solve this optimization problem and has better search ability than GWO.

CONCLUSION

This study has presented an effective intelligent algorithm solution framework for solving the established robust optimal dispatching model of wind fire energy storage which considering the application of AA-CAES and the uncertainty of wind power prediction. The simulation results show that the production cost and comprehensive cost can be further reduced by considering the uncertainty of wind power prediction. Meanwhile, the application of AA-CAES can increase the system flexibility and provide guarantee for system standby. On the other side, the equilibrium optimization algorithm shows better robustness and higher search accuracy than GWO in solving this optimization problem. In the future work, other uncertainties such as operation and maintenance uncertainty and energy storage location uncertainty will be further considered.

DATA AVAILABILITY STATEMENT

The raw data supporting the conclusion of this article will be made available by the authors, without undue reservation.

AUTHOR CONTRIBUTIONS

XC: Ideas; Development of methodology; Writing- Original draft preparation. LH: Methodology; Creation of models, Writing-Reviewing and Editing. XZ: Verification, Conceptualization, Supervision. SH: Validation, Data curation, Conceptualization, Supervision. ZS: Programming, revise grammar and correct expression. ZW: Programming, software development. TC: Specifically performing the experiments. SD: Conducting a research and investigation process.

FUNDING

This work was supported in part by the Plan for Major Provincial Science & Technology Project of Anhui Province under Grant 202003a05020019, and in part by the Comprehensive Research Facility for Fusion Technology under Grant 2018-000052-73-01-001228.

REFERENCES

Chen, X., Huang, L., Liu, J., Song, D., and Yang, S. (2022). Peak Shaving Benefit Assessment Considering the Joint Operation of Nuclear and Battery Energy Storage Power Stations: Hainan Case Study. *Energy* 239, 121897. doi:10.1016/j.energy.2021.121897

Ding, J., Xu, Y., Chen, H., Sun, W., Hu, S., and Sun, S. (2019). Value and Economic Estimation Model for Grid-Scale Energy Storage in Monopoly Power Markets. *Appl. Energ.* 240, 986–1002. doi:10.1016/j.apenergy.2019.02.063

Faramarzi, A., Heidarinejad, M., Stephens, B., and Mirjalili, S. (2020). Equilibrium Optimizer: A Novel Optimization Algorithm. *Knowledge-Based Syst.* 191, 105190. doi:10.1016/j.knosys.2019.105190

Rui, L., Laijun, C., Tiejiang, Y., and Chunlai, L. (2016). Optimal Dispatch of Zero-Carbon-Emission Micro Energy Internet Integrated with Non-Supplementary Fired Compressed Air Energy Storage System. *J. Mod. Power Syst. Clean Energ.* 4 (04), 566–580. doi:10.1007/s40565-016-0241-4

Sedighizadeh, M., Esmaili, M., and Mousavi-Taghiabadi, S. M. (2019). Optimal Joint Energy and reserve Scheduling Considering Frequency Dynamics, Compressed Air Energy Storage, and Wind Turbines in an Electrical Power System. *J. Energ. Storage* 23, 220–233. doi:10.1016/j.est.2019.03.019

Song, D., Zheng, S., Yang, S., Yang, J., Dong, M., Su, M., et al. (2021a). Annual Energy Production Estimation for Variable-Speed Wind Turbine at High-Altitude Site. *J. Mod. Power Syst. Clean. Energ.* 9 (3), 684–687. doi:10.35833/MPCE.2019.000240

Song, D., Chang, Q., Zheng, S., Yang, S., Yang, J., and Joo, Y. (2021b). Adaptive Model Predictive Control for Yaw System of Variable-Speed Wind Turbines. *J. Mod. Power Syst. Clean Energy* 9 (1), 219–224. doi:10.35833/MPCE.2019.000467

Yang, J., Fang, L., Song, D., Su, M., Yang, X., Huang, L., et al. (2021). Review of Control Strategy of Large Horizontal-axis Wind Turbines Yaw System. *Wind Energy* 24 (2), 97–115. doi:10.1002/we.2564

Conflict of Interest: The authors declare that the research was conducted in the absence of any commercial or financial relationships that could be construed as a potential conflict of interest.

Publisher's Note: All claims expressed in this article are solely those of the authors and do not necessarily represent those of their affiliated organizations, or those of the publisher, the editors and the reviewers. Any product that may be evaluated in this article, or claim that may be made by its manufacturer, is not guaranteed or endorsed by the publisher.

Copyright © 2021 Chen, Huang, Zhang, He, Sheng, Wang, Chen and Dou. This is an open-access article distributed under the terms of the Creative Commons Attribution License (CC BY). The use, distribution or reproduction in other forums is permitted, provided the original author(s) and the copyright owner(s) are credited and that the original publication in this journal is cited, in accordance with accepted academic practice. No use, distribution or reproduction is permitted which does not comply with these terms.

frontiers in Energy Research

ORIGINAL RESEARCH
published: 04 October 2021
doi: 10.3389/fenrg.2021.734797

Power Decoupling Control of MMC and Small-Signal Stability Analysis of AC/DC Distribution Network With Renewable Energy

Zhang Xianyong [1,2], Guo Zijuan [1], Huang Yaohong [3], Li Li [1], Peng Weikuan [1] and Cen Jian [1,4]*

[1]The College of Automation, Guangdong Polytechnic Normal University, Guangzhou, China, [2]Anhui Province Key Laboratory of Intelligent Building and Building Energy Saving, Anhui Jianzhu University, Hefei, China, [3]Heyuan Power Supply Bureau of Guangdong Power Grid Co. Ltd., Heyuan, China, [4]Guangzhou Key Laboratory of Intelligent Building Equipment Information Integration and Control, Guangzhou, China

AC/DC hybrid distribution network can realize the high penetration utilization of renewable energy and modular multilevel converter (MMC) is the key equipment to connect AC grid and DC grid. In this paper, the direct modulation based on the virtual resistor and the reference value of dc-bus voltage is adopted, and instantaneous-value model of three-phase half-bridge MMC is derived by introducing differential-mode and common-mode component representation. Then, the decoupling control of AC active power and reactive power is designed based on the linear active disturbance rejection control theory (LADRC). The total disturbances including the coupling term and capacitor voltage fluctuation can be estimated by extended state observer (ESO), and then cancelled exactly. Based on the simplified average-value model of MMC, the small signal stability analysis of three-terminal AC/DC distribution network with 26-level MMCs corresponding to the Tangjiawan-Jishan1-Jishan2 demonstration project is carried out by root locus and bode diagram method, which gives the guidance for the choice of the main circuit component and controller parameters, and shows that the virtual resistor greatly reduces the resonant peak of AC/DC distribution network. Simulation and experiment results verify the effectiveness of the power decoupling control strategy of MMC and the AC/DC distribution network can realize complex multi-directional power flow.

Keywords: MMC, power decoupling control, small signal, stability analysis, virtual resistor

OPEN ACCESS

Edited by:
Yaxing Ren,
University of Warwick,
United Kingdom

Reviewed by:
Weiyu Wang,
Changsha University of Science and Technology, China
Zhi Zhang,
Dongguan University of Technology, China

****Correspondence:***
Li Li
liliarticle@163.com

Specialty section:
This article was submitted to Smart Grids, a section of the journal Frontiers in Energy Research

Received: *01 July 2021*
Accepted: *04 August 2021*
Published: *04 October 2021*

Citation:
Xianyong Z, Zijuan G, Yaohong H, Li L, Weikuan P and Jian C (2021) Power Decoupling Control of MMC and Small-Signal Stability Analysis of AC/DC Distribution Network With Renewable Energy. Front. Energy Res. 9:734797. doi: 10.3389/fenrg.2021.734797

1 INTRODUCTION

In order to realize the plan for peaking carbon dioxide emissions before 2030, it is necessary to build a new power system with renewable energy as the main body. Renewable energy such as wind and solar power is intermittent and varies greatly affected by climate conditions and geographical location. Along with the increasing proportion of renewable energy, high degree of concentration grid-connected renewable energy brings serious challenge to grid stability and power quality (Mithulananthan et al., 2013). Renewable energy access to the distribution network, to achieve local use of power generation, reduce transmission loss, become a new way to improve the utilization rate of renewable energy (Chen et al., 2016a). With the rapid development of DC renewable generation such as PV, and the popularity of DC load such as electric vehicles, DC distribution network gains great attentions because it reduces energy conversion loss and there is no inherent

frequency stability and skin effect of ac system. Since the traditional distribution network is still ac grid, Professor Wang Peng proposed the concept of AC/DC hybrid distribution network (Wang et al., 2011). It can be compatible with the AC grid and DC gird and realize high proportion utilization of renewable energy, improve the reliability of power supply system. Therefore, AC/DC distribution network becomes the latest development trend of the current distribution network.

The converter is the crucial equipment to realize the power exchange among different distribution networks. The voltage-sourced converter has become the most popular because it has the advantages of power supply to island, fast independent control of active and reactive power, and fast response of power flow reversal. With the development of the voltage level and capacity of the transmission system, the converter topology of VSC-HVDC has gradually transited from the two-level or three-level structure to the MMC (Alassi et al., 2019). MMC has cascaded sub-modules (SMs), instead of the power electronic devices to connect in series directly, which has the advantages of low switching frequency, low switching loss, good waveform quality, and easy capacity expansion, etc. (Lesnicar and Marquardt, 2004). There is the half-bridge SM, the full-bridge SM, the clamp double SM, and three-level SM and so on (Marquardt, 2010; Marquardt, 2011). Although the full-bridge SM and the clamp double SM has the ability of DC fault self-cleaning, the half-bridge SM becomes the dominant topology because of its simple control and low cost.

The AC and DC voltages of MMC are obtained simultaneously by switching the SMs. The modulation strategy of MMC mainly includes the nearest level modulation (NLM) and the phase-shifted-carrier PWM (PSC-PWM) (Debnath et al., 2015). The NLM needs to measure the current direction and sort the capacitor voltage of SM, which needs additional control loops. PSC-PWM generates N group of PWM signals when N groups of triangular carriers with phase offsets of $2\pi/N$ angle are compared with the same modulation wave. The PSC-PWM is much simpler and widely used in MMC. The steady state characteristic and open-loop control strategy of MMC are studied in (Antonopoulos et al., 2009; Angquist et al., 2011). The open-loop scheme analysis usually assumes that the modulation indices and the AC current are both sinusoidal, and doesn't consider capacitor voltage ripple, which doesn't reflect the real case. The closed-loop controller design of MMC is similar to that of two-level converters (Guan and Xu, 2012). In order to avoid the instability, the reference value of the dc-bus voltage (Harnefors et al., 2013) or the estimated capacitor voltage (Vasiladiotis et al., 2014) is used to calculate the modulation index, which leads to the strong coupling between active and reactive power (Yang et al., 2018).

A particular average-value model of MMC is presented and the coupled transient response is revealed in (Yang et al., 2017). Reference (Wang and Wang, 2019) identifies four power coupling paths and two power influence factors. The above decoupling strategies usually adopt PI controller and execute the exact cancellation according to the analytical expressions. But the analytical expression can't describe the complex coupling among ac current, circulating current and dc current under different operation conditions precisely. Disturbance-observer-based control instead of precise modeling provides a new idea. A number of widely used linear and nonlinear disturbance estimation techniques such as DUE and DUEA are reviewed in (Chen et al., 2016b). The active disturbance rejection control (ADRC) has obtained excellent control results in motion control (Alonge et al., 2017; Liu et al., 2017; Wang et al., 2019; Liu et al., 2020). The fundamental part of ADRC is the extended state observer (ESO), which estimates the total disturbances including unknown uncertainties and external disturbances. The early MMC based HVDC project is mainly single terminal or two-terminal for wind farm integration (Friedrich, 2010; Bergna Diaz et al., 2015). With the accretion of the grid and renewable energy capacity and the improved requirement of power supply reliability, multi-terminal MMC based HVDC projects becomes the mainstreams (Rao, 2015; Trinh et al., 2016; Zhang et al., 2017). The MMC based multi-terminal HVDC is a complex power electronic system. It is a challenge to investigate the dynamic performance and stability based on appropriate modeling and simulation method to satisfy planning and operational criteria (Adam and Williams, 2014; Wang et al., 2016a; Wang et al., 2016b). Averaged model (Saad et al., 2013), detailed equivalent circuit model (Ahmed et al., 2016), and equivalent circuit model (Xiang et al., 2017) are established to simulate the electromagnetic transient response of HVDC system. When MMC can't provide sufficient damping, the multi-terminal DC grid is easy to resonance and instability. Therefore, virtual impedance damping control is proposed to improve the DC grid's performance (Li et al., 2019; Wan et al., 2018). Small signal stability analyses are used to design the system dynamics and select the controller parameters and DC inductance (Kotb et al., 2016; Li et al., 2018; Lu et al., 2018). On the one hand, above small signal model usually comprises ac current dynamics, phase-locked loop, and MMC dynamics, and DC networks, which is too complex and not easy to identify the key impact factor. On the other hand, above small signal model doesn't consider the effect of the modulation strategy and the virtual impedance simultaneously (Li et al., 2018).

MMC is the key equipment to connect the AC grid and DC grid. MMC based HVDC project usually has unidirectional power flow. But the MMC based DC/AC hybrid distribution network has complex multidirectional power flow. There is seldom theoretical and experimental research about the MMC based medium-voltage DC/AC distribution network. In this paper, the MMC based Tangjiawan-Jishan1-Jishan2 DC/AC distribution network demonstration project is studied. The contribution of this paper is summarized as followings: 1) a novel instantaneous-value model of MMC which introducing the differential-mode and common-mode component representation is derived. The direct modulation strategy is adopted based on the virtual resistor and the reference value of dc-bus voltage, which avoids the direct measurement of SM capacitor voltage and is easy to calculate. 2) AC active and reactive power decoupling control based on LADRC is realized, which doesn't require the precise modeling of coupling factor and uncertainty. 3) a simplified average-value model of MMC is deduced and small signal stability of AC/DC distribution network is analyzed, which identifies the damping effect of the virtual resistor. 4)

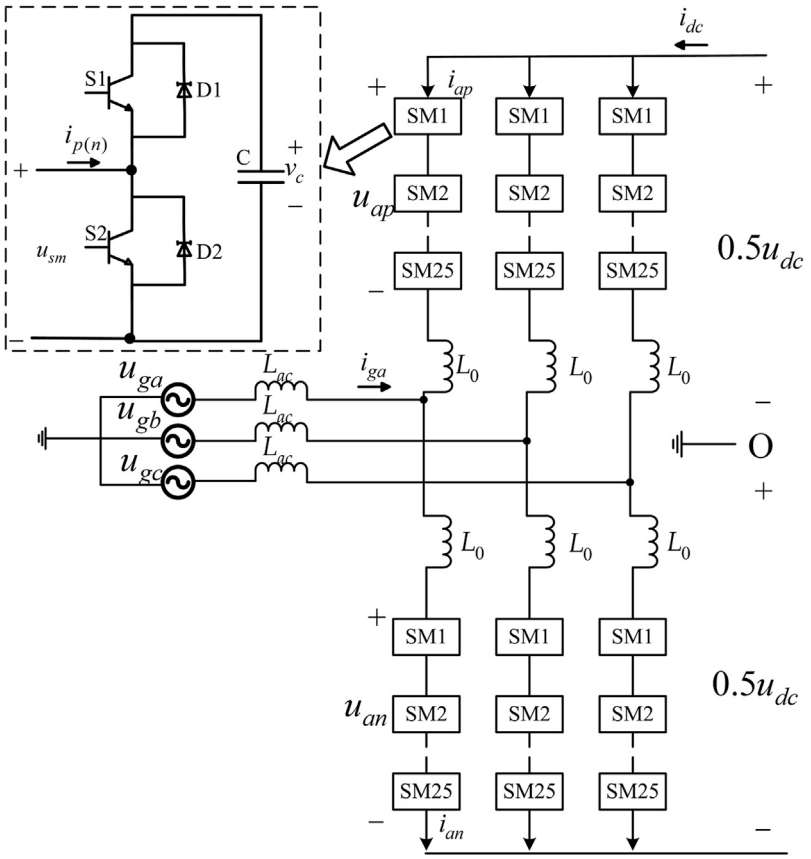


FIGURE 1 | Structure of MMC.

theoretical and empirical research on Tangjiawan-Jishan1-Jishan2 DC/AC distribution network demonstration project are carried out.

The rest of this paper is organized as follows. **Section 2** introduces the common-mode and differential-mode component instantaneous-value model of MMC. **Section 3** presents ac power decoupling control of MMC based on LADRC. **Section 4** is the small signal stability analysis of MMC based three-terminal AC/DC distribution network. **Section 5** is the simulations based on PSCAD. **Section 6** is experiments on the Tangjiawan-Jishan1-Jishan2 AC/DC distribution network. **Section 7** is the conclusions.

2 INSTANTANEOUS-VALUE MODEL OF MODULAR MULTILEVEL CONVERTER

Figure 1 shows the structure of three-phase half-brideg MMC. Each phase consists of the upper and lower arm. Each uppper (lower) arm has N half-bridge submodules and a inductor L_0 in series. L_0 is used to restrain the circulating current and buffer the short circuit. $p(n)$ presents the vairable of upper (lower) arms. u_{jp} (u_{jn}) and i_{jp} (i_{jn}) are the upper (lower) arm voltage and current of phase j ($j = a, b, c$). L_{ac} is the inductor connecting the ac-grid and MMC. C is the submodule capacitor. u_{gj} and i_{gj} are the ac voltage and current respectively. u_{dc} and i_{dc} are the dc voltage and current respectively.

MMC is a complex AC-DC coupling system. The common-mode and differential-mode component representation is introduced to analyze the coupling system.

Defining the common-mode component of variable x is

$$\overline{x_j} = 0.5\left(x_{jp} + x_{jn}\right) \tag{1}$$

The differential-mode component of variable x is

$$\widehat{x_j} = 0.5\left(x_{jp} - x_{jn}\right) \tag{2}$$

where x_{jp} (x_{jn}) is the upper (lower) arm variable of phase j.

The arm current dynamics of phase j are

$$L_0\frac{di_{jp}}{dt} - L_{ac}\frac{di_{gj}}{dt} = \frac{u_{dc}}{2} - u_{jp} - u_{gj} \tag{3}$$

$$L_0\frac{di_{jn}}{dt} + L_{ac}\frac{di_{gj}}{dt} = \frac{u_{dc}}{2} - u_{jn} + u_{gj} \tag{4}$$

Let $\overline{i_j} = 0.5\,(i_{jp} + i_{jn})$, $\widehat{i_j} = 0.5\,(i_{jp} - i_{jn})$, $\overline{u_j} = 0.5\,(u_{jp} + u_{jn})$, $\widehat{u_j} = 0.5\,(u_{jp} - u_{jn})$, Then **Eqs 3**, **4** can be expressed as

$$(2L_{ac} + L_0)\frac{d\hat{i}_j}{dt} = -\hat{u}_j - u_{gj} \tag{5}$$

$$2L_0\frac{d\overline{i_j}}{dt} = u_{dc} - 2\overline{u_j} \tag{6}$$

Eq. 5 shows that the differential-mode current $\hat{i}_j$ can be controlled by the differential-mode voltage $\hat{u}_j$. **Eq. 6** shows that the common-mode current $\overline{i_j}$ can be controlled by the common-mode voltage $\overline{u_j}$. Therefore the independent control of $\hat{i}_j$ and $\overline{i_j}$ can be realized, which greatly simplifies the arm current controller design.

When the switch S1 is on and S2 is off, U_{sm} is equal to the capacitor voltage. When the switch S2 is on and S1 is off, U_{sm} is zero. Arm voltage is obtained from capacitor voltage by PSC-PWM. The relationship between the arm voltage and the capacitor voltage is

$$u_{jp} = m_{jp}v_{jpc} \tag{7}$$

$$u_{jn} = m_{jn}v_{jnc} \tag{8}$$

where v_{jpc} (v_{jnc}) is the sum of upper (lower) arm capacitor voltages, m_{jp} and m_{jn} are the modulation indices.

Let $\overline{m_j} = 0.5(m_{jp} + m_{jn})$, $\hat{m}_j = 0.5(m_{jp} - m_{jn})$, $\overline{v_{jc}} = 0.5(v_{jpc} + v_{jnc})$, $\hat{v}_{jc} = 0.5(v_{jpc} - v_{jnc})$, **Eq. 7** can be expressed as

$$\overline{u_j} = \overline{m_j v_{jc}} + \hat{m}_j\hat{v}_{jc} \tag{9}$$

$$\hat{u}_j = \overline{m_j}\hat{v}_{jc} + \hat{m}_j\overline{v_{jc}} \tag{10}$$

Supposed that the volatge balance control of submodule capacitor is realized for each upper or lower arm, and then the dynamics of capacitor voltages are

$$\frac{C}{N}\frac{dv_{jpc}}{dt} = m_{jp}i_{jp} \tag{11}$$

$$\frac{C}{N}\frac{dv_{jnc}}{dt} = m_{jn}i_{jn} \tag{12}$$

Adopting the common-mode and differential-mode component representation, **Eqs 11** and **12** can be expressed as

$$\frac{C}{N}\frac{d\overline{v_{jc}}}{dt} = \overline{m_j}\overline{i_j} + \hat{m}_j\hat{i}_j \tag{13}$$

$$\frac{C}{N}\frac{d\hat{v}_{jc}}{dt} = \overline{m_j}\hat{i}_j + \hat{m}_j\overline{i_j} \tag{14}$$

It shows that the common-mode component and the differential-mode component of the capacitor voltage have complex nonlinear characteristics.

According to (**Eqs 5**, **6**, **9**, **10**, **13**, **14**), the differential-mode current $\hat{i}_j$ is mainly determined by $\hat{m}_j$. The common-mode current $\overline{i_j}$ is mainly determined by $\overline{m_j}$. Because the capacitor voltage is hard to measure and DC grid is also easy to resonate because of lack of damping, the modulation indices are determined as followings.

$$\overline{m_j} = 0.5 + R_v\overline{i_j}/v^*_{eqc} \tag{15}$$

$$\hat{m}_j = \hat{u}^*_j/v^*_{eqc} \tag{16}$$

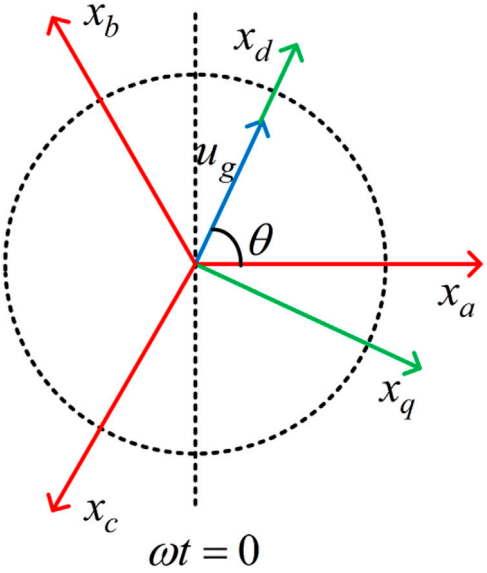


FIGURE 2 | Relationship between stationary coordinates and dq rotating coordinates.

where v^*_{eqc} is the reference value of dc-bus voltage, and it is also the reference value of the sum of the upper (lower) arm capacitor voltage. v^*_{eqc} is used to avoid the measurement of the real capacitor voltage and the virtual resistor R_v is added to increase the damping of DC grid. $\hat{u}^*_j$ is the reference value of the differential-mode component of arm voltage, and it is also the control variable.

3 AC POWER DECOUPLING CONTROL OF MODULAR MULTILEVEL CONVERTER BASED ON LINEAR ACTIVE DISTURBANCE REJECTION CONTROL THEORY

3.1 AC Power Modeling of Modular Multilevel Converter

MMC can exchange active power and reactive power with ac-grid. From **Figure 1**, ac current in the three-phase stationary coordinates is

$$i_{gj} = i_{jn} - i_{jp} = -2\hat{i}_j \tag{17}$$

Power is usually analyze in the *dq* rotating coordinates. The relationship between the three-phase stationary coordinates and dq rotating coordinates is shown in **Figure 2**(Lu et al., 2018). We can get

$$\begin{bmatrix} x_d \\ x_q \\ x_0 \end{bmatrix} = \frac{2}{3}\begin{bmatrix} \cos\theta & \cos\left(\theta - \frac{2\pi}{3}\right) & \cos\left(\theta + \frac{2\pi}{3}\right) \\ \sin\theta & \sin\left(\theta - \frac{2\pi}{3}\right) & \sin\left(\theta + \frac{2\pi}{3}\right) \\ \frac{1}{2} & \frac{1}{2} & \frac{1}{2} \end{bmatrix}\begin{bmatrix} x_a \\ x_b \\ x_c \end{bmatrix} \tag{18}$$

where $\theta = \theta_0 + \int_0^t \omega dt$ is the angle between the coordinates. x_d, x_q, and x_0 are the variables in the dq coordinates. x_a, x_b, and x_c are the variables in the three-phase stationary coordinates.

When the d-axis of the rotating coordinates is aligned with the grid voltage space vector, that is $u_{gq} = 0$, the ac active power and reactive power can be calculated as

$$\begin{cases} P_s = 1.5u_{gd}i_{gd} = -3u_{gd}\widehat{i_d} \\ Q_s = 1.5u_{gd}i_{gq} = -3u_{gd}\widehat{i_q} \end{cases} \tag{19}$$

where active power is determined by $\widehat{i_d}$ and reactive power is determined by $\widehat{i_q}$. The power decoupling control is simplified to the differential-mode arm current decoupling control.

The differential-mode arm current in **eq. 5** can be expressed in dq rotating coordinates as

$$\begin{cases} 2L_s\dfrac{d\widehat{i_d}}{dt} = -2\omega L\widehat{i_q} - \widehat{u_d} - u_{gd} \\ 2L_s\dfrac{d\widehat{i_q}}{dt} = 2\omega L\widehat{i_d} - \widehat{u_q} - u_{gq} \end{cases} \tag{20}$$

Where $L_s = L_0/2 + L_{ac}$.

According to **Eq. 16**, we can get

$$\begin{cases} 2L_s\dfrac{d\widehat{i_d}}{dt} = -2\omega L\widehat{i_q} - \dfrac{v_{eqc}}{v^*_{eqc}}\widehat{u^*_d} - u_{gd} \\ 2L_s\dfrac{d\widehat{i_q}}{dt} = 2\omega L\widehat{i_d} - \dfrac{v_{eqc}}{v^*_{eqc}}\widehat{u^*_q} - u_{gq} \end{cases} \tag{21}$$

where v_{eqc} is the actual value of the sum of the upper (lower) arm capacitor voltages. **Eqs 13** and **14** show that v_{eqc} is nonlinear and hard to measure, so it is difficult to determine the control variables $\widehat{u^*_d}$ and $\widehat{v^*_q}$.

3.2 AC Power Decoupling Controller Design Based on Linear Active Disturbance Rejection Control Theory

The structure of LADRC is shown in **Figure 3**. LADRC is composed of tracking differentiator (TD), linear extended state observer (LESO), and linear state error feedback control law (LSEF). TD can not only overcome the interference noise by obtaining differential signals, but also make reasonable arrangements for the transition process. In other words, TD realizes the fast tracking of reference signal without overshoot and gives the tracking signals of all-order derivatives of reference signal. LESO is based on the development of the traditional observer, which takes the input and output of the control object as one of its inputs. The all-order derivatives of the plant state and the total disturbance variables can be observed through LESO. An obvious advantage of ESO is that it does not rely on the detailed mathematical model for generating disturbances, nor does it need to measure its role directly. LSEF generates the control signal using the output error between the TD and LESO. The mathematical description of one-order LADRC is shown as followings.

One-order TD is

$$\frac{dz_{11}}{dt} = k_0(x_1^{ref} - z_{11}) \tag{22}$$

where z_{11} is the tracking signal of reference input x_1^{ref}.

Two-order LESO is

$$\begin{cases} \dfrac{dz_{21}}{dt} = z_{22} + k_{21}\varepsilon_1 + u \\ \dfrac{dz_{22}}{dt} = k_{22}\varepsilon_1 \\ \varepsilon_1 = x_1 - z_{21} \end{cases} \tag{23}$$

where z_{21} is the estimated value of the plant state x_1. z_{22} is the estimated value of the whole disturbance, which including $w(t)$ and other parameter uncertainties. k_{21} and k_{22} are gain coefficients.

LSEF control law is

$$u = -z_{22} + k(z_{11} - z_{21}) \tag{24}$$

where k are the gain coefficient.

Eq. 21 can be expressed as

$$\begin{cases} 2L_s\dfrac{d\widehat{i_d}}{dt} = f_d - \widehat{u^*_d} \\ 2L_s\dfrac{d\widehat{i_q}}{dt} = f_q - \widehat{u^*_q} \end{cases} \tag{25}$$

Where $f_d = -2\omega L\widehat{i_q} - u_{gd} - \frac{v_{eqc} - v^*_{eqc}}{v^*_{eqc}}\widehat{u^*_d}$, $f_q = 2\omega L\widehat{i_d} - u_{gq} - \frac{v_{eqc} - v^*_{eqc}}{v^*_{eqc}}\widehat{u^*_q}$. f_d and f_q are nonlinear and difficult to measure accurately. According to the LADRC theory, f_d and f_q can be regarded as the total disturbances and estimated by the LESO. So the dynamics of $\widehat{i_d}$ and $\widehat{i_q}$ can be decoupled to two independent subsystems based on LADRC. Then we can design the ac power decoupling control structure as **Figure 4**, which is divided into MMC valve level controller, MMC inner controller and MMC outer controller. The MMC valve level controller contains the modulation strategy and capacitor voltage balancing control,etc. The phase-shifted carrier PWM strategy is adopted, which is calculated based on the virtual resistor and the reference value of DC-bus voltage. The inner controller is core point of decoupling controller, which is designed based on LADRC. The outer controller can receive active power and reactive power commands from power dispatch center.

4 SMALL-SIGNAL STABILITY ANALYSIS OF MODULAR MULTILEVEL CONVERTER BASED THREE-TERMINAL AC/DC DISTRIBUTION NETWORK

Tangjiawan town is located in Zhuhai city, China. With the continuous progress of industrial park, the load of Tangjiawan town has increased too fast. If only Tangjiawan station supplies power, the power supply radius will be too long, the reliability is low, and the line loss is high. In order to improve the power supply quality and reliability, two 10kV buses are introduced

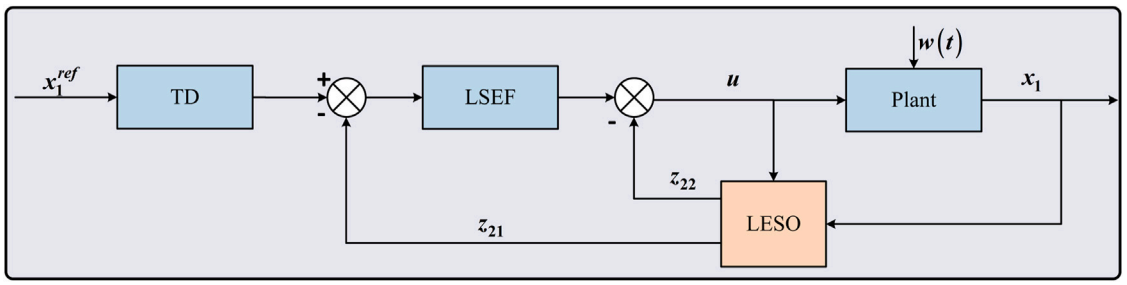


FIGURE 3 | Structure of LADRC.

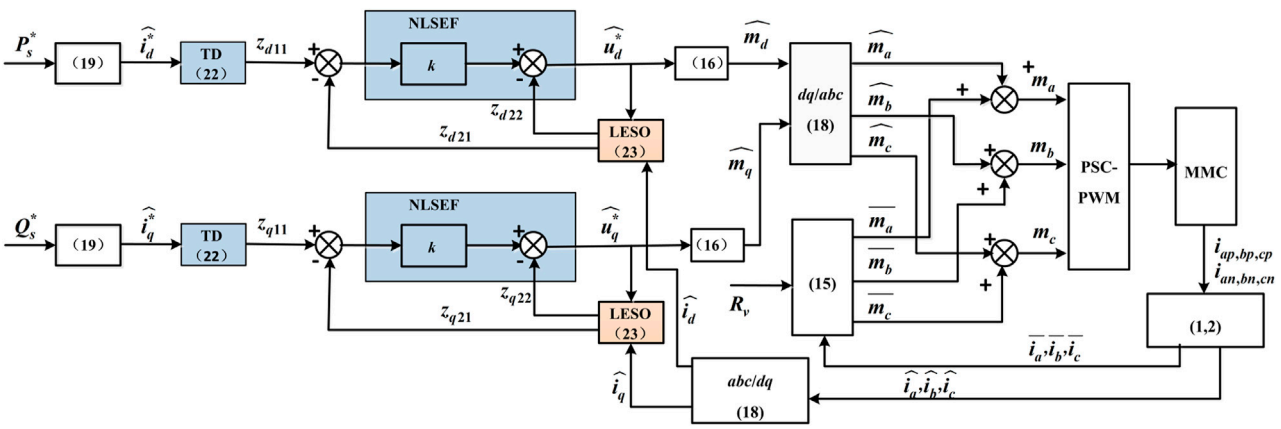


FIGURE 4 | Power decoupling control diagram of MMC.

from Jishan station and connected with the 10 kV bus of Tangjiawan station, so as to increase the load transfer capacity of Tangjiawan station and reserve capacity of grid accident. The topology of Tangjiawan-Jishan1 -Jishan2 AC/DC distribution network demonstration project is shown in **Figure 5**. The rated capacity of Tangjiawan, Jishan1, and Jishan2 station is 20, 10, and 10 MVA individually. The rated DC-bus voltage is ±10 kV and the rated AC voltage is 10.5 kV.

Although MMC has the same hardware topology, it can work as power station or voltage station. So the operation mode of MMC based three-terminal AC/DC distribution network is versatile. In this paper, the master-slave operation mode is studied according to the engineering application, that is, Tangjiawan Station is voltage station and Jishan1 and Jishan two stations are power stations. The instantaneous-value model of MMC is too complicated to the small-signal stability analysis. In order to simplify the analysis, averaged-value model is needed.

4.1 Averaged-Value Model of Modular Multilevel Converter Power Station

According to **Eq. 14**, the differential-mode component of capacitor voltage is ac variables and can be neglected based on the switching period. The common-mode component of capacitor voltage is balanced, that is

$$\overline{v_{apc}} = \overline{v_{anc}} = \overline{v_{bpc}} = \overline{v_{bnc}} = \overline{v_{cpc}} = \overline{v_{cnc}} = v_{eqc} \tag{26}$$

When common-mode component of arm current is balanced, there is

$$\bar{i}_j = \frac{i_{dc}}{3} \tag{27}$$

According to **Eqs 7**, **9**, **12**, **26**, **27** and the law of energy conservation, the state equation of the equivalent capacitance is

$$C_{eq} v_{eqc} \frac{dv_{eqc}}{dt} = i_{dc} v_{eqc} + \frac{2R_v v_{eqc}}{3V_{eqc}^*} i_{dc}^2 + P_g \tag{28}$$

where the equivalent capacitance $C_{eq} = 6C/N$ and P_g is AC active power controlled by LADRC.

According to **Eqs 6**, **9**, **12**, **26**, **27**, the state equation of the DC current

$$2L_0 \frac{di_{dc}}{dt} = 3u_{dc} - 3v_{eqc} - \frac{2R_v v_{eqc}}{v_{eqc}^*} i_{dc} \tag{29}$$

The linearized model of the **Eqs 28** and **29** is

$$\begin{cases} 2L_0 \dfrac{d\Delta i_{dc}}{dt} = 3\Delta u_{dc} - 3\Delta v_{eqc} - \dfrac{2R_v}{v_{eqc}^*} v_{eqc0} \Delta i_{dc} - \dfrac{2R_v}{v_{eqc}^*} i_{dc0} \Delta v_{eqc} \\ C_{eq} v_{eqc0} \dfrac{d\Delta v_{eqc}}{dt} = v_{eqc0} \Delta i_{dc} + i_{dc0} \Delta v_{eqc} + \dfrac{4R_v}{3v_{eqc}^*} i_{dc0} v_{eqc0} \Delta i_{dc} + \dfrac{2R_v}{3v_{eqc}^*} i_{dc0}^2 \Delta v_{eqc} + \Delta P_g \end{cases} \tag{30}$$

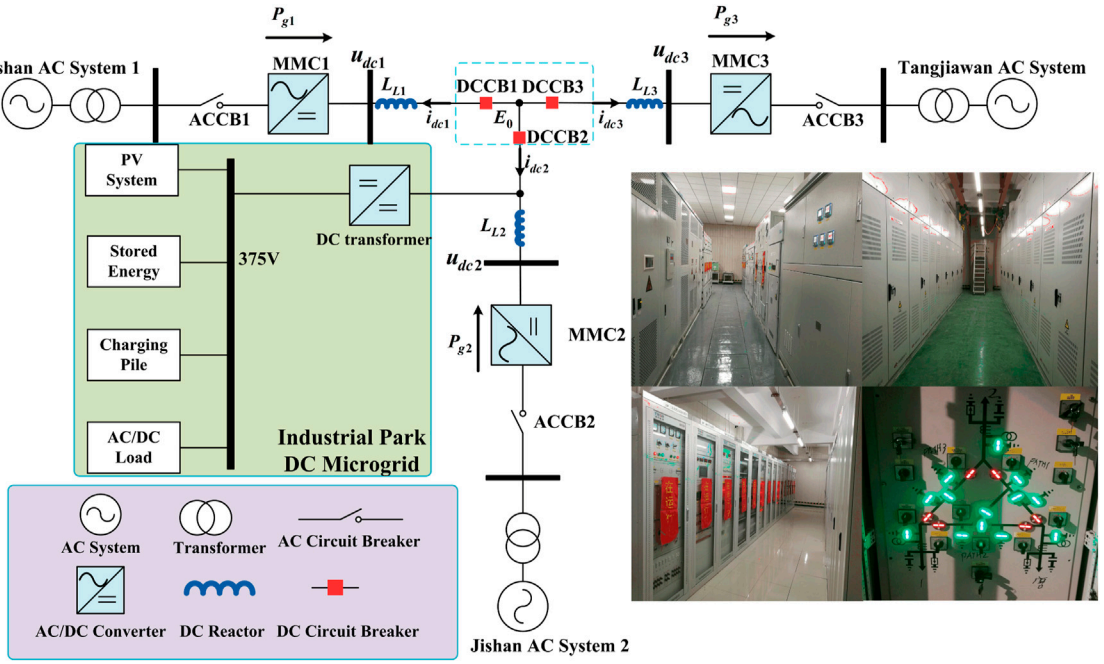


FIGURE 5 | Topology of Tangjiawan-Jishan1-Jishan2 AC/DC distribution network.

where v_{eqc0} and i_{eqc0} are the steady-state operating points satisfying the following equations.

$$\begin{cases} 0 = 3u_{dc0}v^*_{eqc} - 3v_{eqc0}v^*_{eqc} - 2R_v v_{eqc0} i_{dc0} \\ 0 = 3v^*_{eqc} i_{dc0} v_{eqc0} + 2R_v v_{eqc0} i^2_{dc0} + P_{g0} \end{cases} \tag{31}$$

4.1.1 $R_v = 0$

When the virtual resistance is 0, the equilibrium point is

$$\begin{cases} i_{dc0} = \dfrac{P_{g0}}{u_{dc0}} \\ v_{eqc0} = u_{dc0} \end{cases} \tag{32}$$

where v_{eqc0} is determined by the external DC voltage source. i_{eqc0} is determined according to the law of conservation of power. The different choices of v^*_{eqc} don't affect the equilibrium points.

4.1.2 $R_v \neq 0$

When the virtual resistance is nonzero, the equilibrium point is

$$\begin{cases} i_{dc0} = \dfrac{-\left(2R_v P_{g0} + 3u_{dc0}v^*_{eqc}\right) + \sqrt{4R_v^2 P_{g0}^2 + 9u_{dc0}^2 v^*_{eqc} 2 - 12u_{dc0}R_v v^*_{eqc} P_{g0}}}{4u_{dc0}R_v} \\ v_{eqc0} = \dfrac{3u_{dc0}v^*_{eqc}}{3v^*_{eqc} + 2R_v i_{dc0}} \end{cases} \tag{33}$$

where v^*_{eqc} and R_v affect the equilibrium point. The characteristic equations of the system **Eq. 30** is

$$a_2 s^2 + a_1 s + a_0 = 0 \tag{34}$$

where $a_2 = 3L_0 C_{eq} v^*_{eqc} v_{eqc0}$, $a_1 = f(x) = 3v^2_{eqc0} C_{eq} R_v - 2L_0 i^2_{dc0} R_v - 3L_0 i_{dc0} v^*_{eqc}$, $a_0 = v_{eqc0}(3v^*_{eqc} + 2i_{dc0}R_v)^2$. According to the Routh criterion, the MMC power station is stable only when the following equation is satisfied

$$\begin{cases} f(x) > 0 \\ R_v \neq -\dfrac{1.5v^*_{eqc}}{i_{dc0}} \end{cases} \tag{35}$$

So the stable region is that $R_v > 3L_0 i_{dc0} v^*_{eqc} / (3v^2_{eqc0} C_{eq} - 2L_0 i^2_{dc0})$ and $R_v \neq -1.5v^*_{eqc}/i_{dc0}$.

4.2 Small-Signal Stability Analysis of Three-Terminal Modular Multilevel Converter Based DC Grid

The nodal equation of DC network is

$$\begin{cases} L_{L1}\dfrac{di_{dc1}}{dt} = E_0 - u_{dc1} \\ L_{L2}\dfrac{di_{dc2}}{dt} = E_0 - u_{dc2} \\ L_{L3}\dfrac{di_{dc3}}{dt} = E_0 - u_{dc3} \\ i_{dc1} + i_{dc2} + i_{dc3} = 0 \end{cases} \tag{36}$$

where L_{L1}, L_{L2}, L_{L3} are the DC line inductors and E_0 is the nodal voltage at the common connection point.

The relationship between voltage and current of MMC3 is

$$E_0 = L_{L3}\frac{di_{dc3}}{dt} + E \tag{37}$$

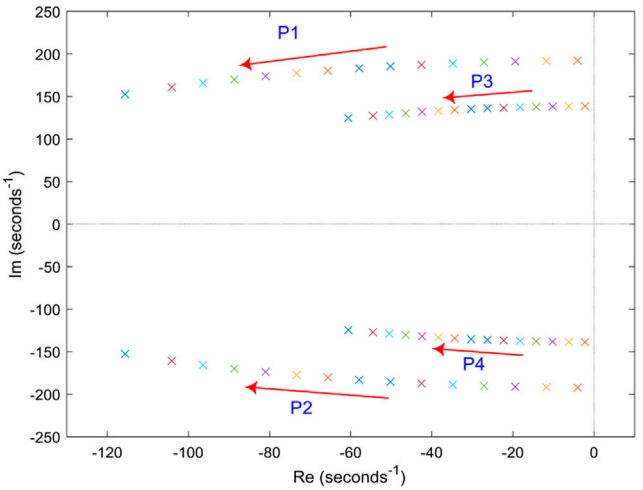


FIGURE 6 | Root locus with increase of R_v.

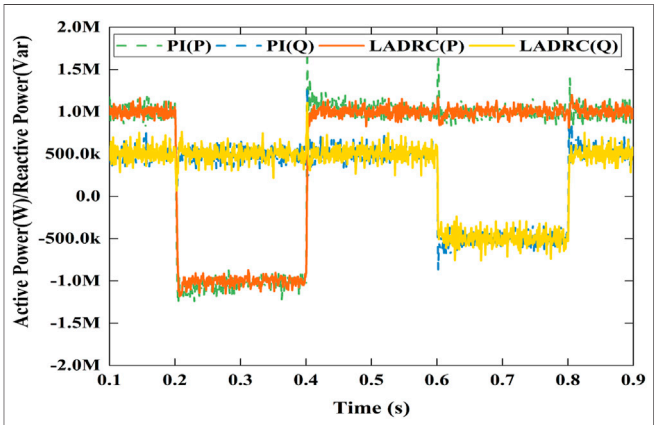


FIGURE 8 | Active power and reactive power.

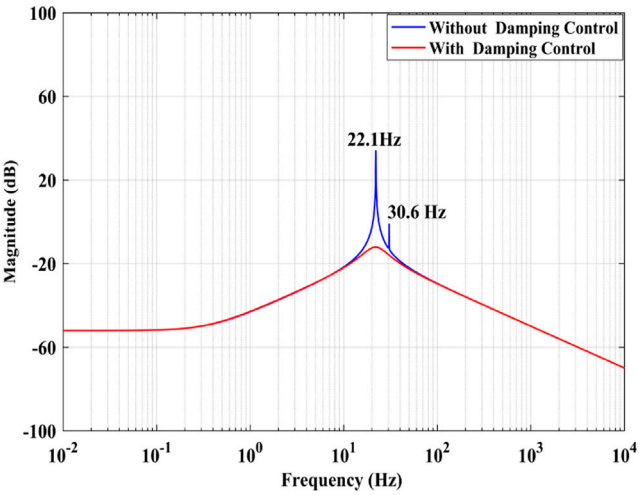


FIGURE 7 | Bode diagram of $\Delta i_{dc3}/\Delta P_{g1}$ (R_v = 1).

where E is the terminal voltage of MM3, the output voltage control can be seen in (Li et al., 2018) and is not discussed in detail in this paper.

According to (**Eq. 30**, **36**, **37**), the linearization model of three-terminal MMC based DC grid is

$$\begin{cases} (2L_0 + 3L_{L1} + 3L_{L1})\dfrac{d\Delta i_{dc1}}{dt} + 3L_{L3}\dfrac{d\Delta i_{dc2}}{dt} = 3\Delta E - \dfrac{2R_{v1}}{v^*_{eqc}}v_{eqc10}\Delta i_{dc1} - \left(\dfrac{2R_{v1}}{v^*_{eqc}}i_{dc10} + 3\right)\Delta v_{eqc1} \\ C_{eq}v_{eqc10}\dfrac{d\Delta v_{eqc1}}{dt} = \left(v_{eqc10} + \dfrac{4R_{v1}}{3v^*_{eqc}}i_{dc10}v_{eqc10}\right)\Delta i_{dc1} + \left(\dfrac{2R_{v1}}{3v^*_{eqc}}i^2_{dc10} + i_{dc10}\right)\Delta v_{eqc1} + \Delta P_{g1} \\ (2L_0 + 3L_{L2} + 3L_{L3})\dfrac{d\Delta i_{dc2}}{dt} + 3L_{L3}\dfrac{d\Delta i_{dc1}}{dt} = 3\Delta E - \dfrac{2R_{v2}}{v^*_{eqc}}v_{eqc20}\Delta i_{dc2} - \left(\dfrac{2R_{v2}}{v^*_{eqc}}i_{dc20} + 3\right)\Delta v_{eqc2} \\ C_{eq}v_{eqc20}\dfrac{d\Delta v_{eqc2}}{dt} = \left(v_{eqc20} + \dfrac{4R_{v2}i_{dc20}v_{eqc20}}{3v^*_{eqc}}\right)\Delta i_{dc2} + \left(i_{dc20} + \dfrac{2R_{v2}i^2_{dc20}}{3v^*_{eqc}}\right)\Delta v_{eqc2} + \Delta P_{g2} \end{cases} \tag{38}$$

The operation condition is that active power of MMC1 is −2 MW and that of MMC2 is 1 MW, the arm inductor is 7 mH and DC inductor is 4 mH. **Figure 6** shows the root locus. there are two pairs of conjugate complex roots in the left half plane. With the increase of R_v, the roots gradually moves away from the virtual axis, which indicates that R_v can enhance the stability of DC grid.

Figure 7 shows the amplitude frequency characteristics of the transfer function $\Delta i_{dc3}/\Delta P_{g1}$. When there is no virtual resistor, there are two low frequency resonance points in bode diagram, which are 22.1 and 30.6 Hz respectively. The resonance peak value at 22.1 Hz is obviously higher than that at 30.6 Hz. So the main resonance frequency of DC grid is about 22.1 Hz. When the virtual resistor is added, the resonance peak value attenuates greatly. Virtual resistor can effectively suppress the system oscillation and improve the transient performance of DC grid.

5 SIMULATIONS OF MODULAR MULTILEVEL CONVERTER BASED THREE-TERMINAL AC/DC DISTRIBUTION NETWORK

The number of sub-modules N = 25. The sub-module capacitance is 13 mF and the switching frequency is 300 Hz. The phase leg reactor is 7 mH and the rated voltage of AC and DC are 10kVac and 20 kVdc individually. PSC-PWM is adopted and the electromagnetic transient model of MMC based three-terminal AC/DC distribution network is established on PSCAD.

Figures 8–13 shows the decoupling power control of MMC under LADRC and PI controller. **Figure 8** shows the simulation results of active power step response. Active power immediately responds step disturbance and changes from 1 MW to −1 MW at 0.2 s and changes from −1 to 1 MW at 0.4 s. Reactive power also instantly responds step disturbance and varies from 0.5 Mvar to −0.5 Mvar at 0.6 s and varies from −0.5 Mvar to 0.5 Mvar at 0.8 s. Obviously, it results in a little

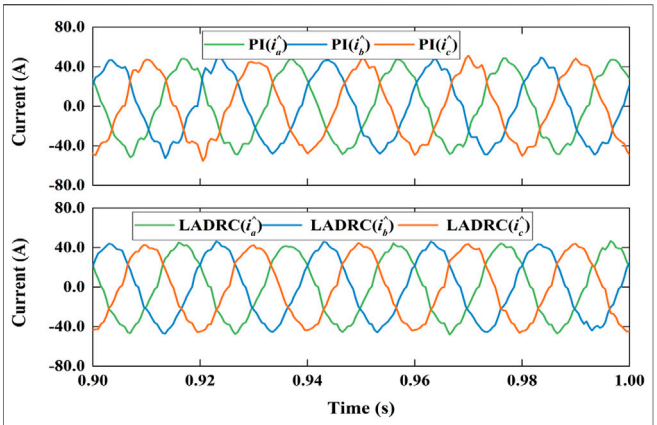


FIGURE 9 | Differential-mode component of arm current.

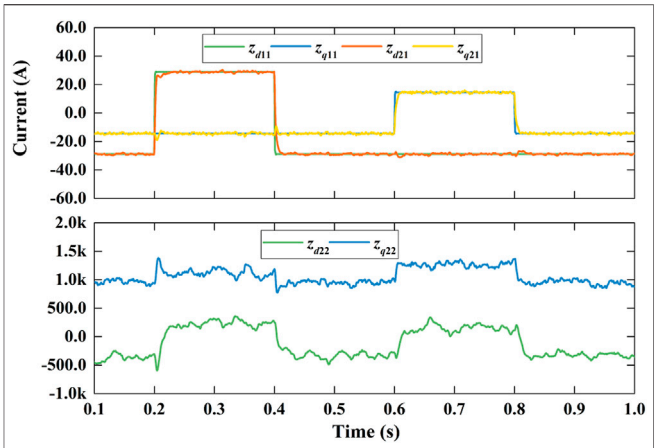


FIGURE 12 | State variables of LADRC.

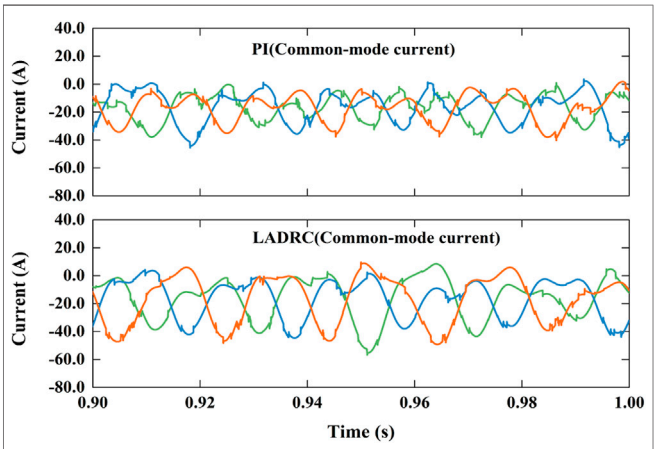


FIGURE 10 | Common-mode component of arm current.

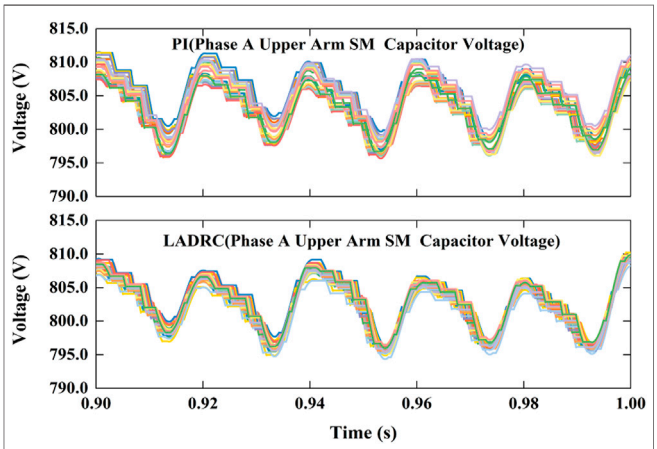


FIGURE 13 | Sub-module capacitor voltage.

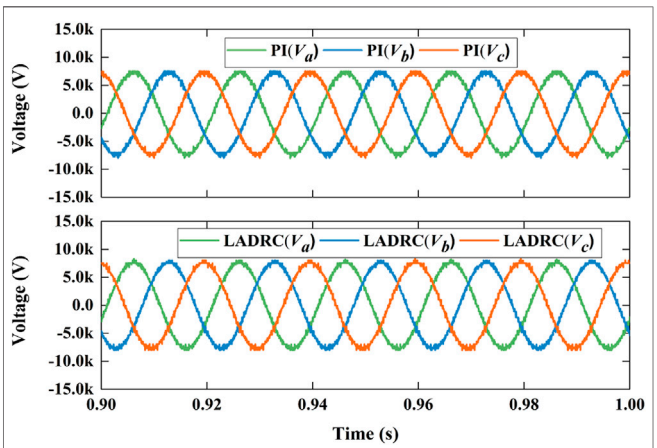


FIGURE 11 | AC voltage of MMC.

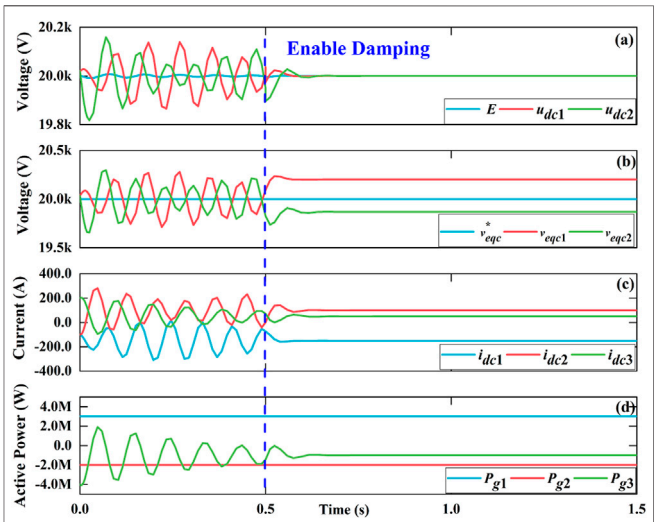


FIGURE 14 | Variables of MMC based three-terminal DC grid (R_v = 1).

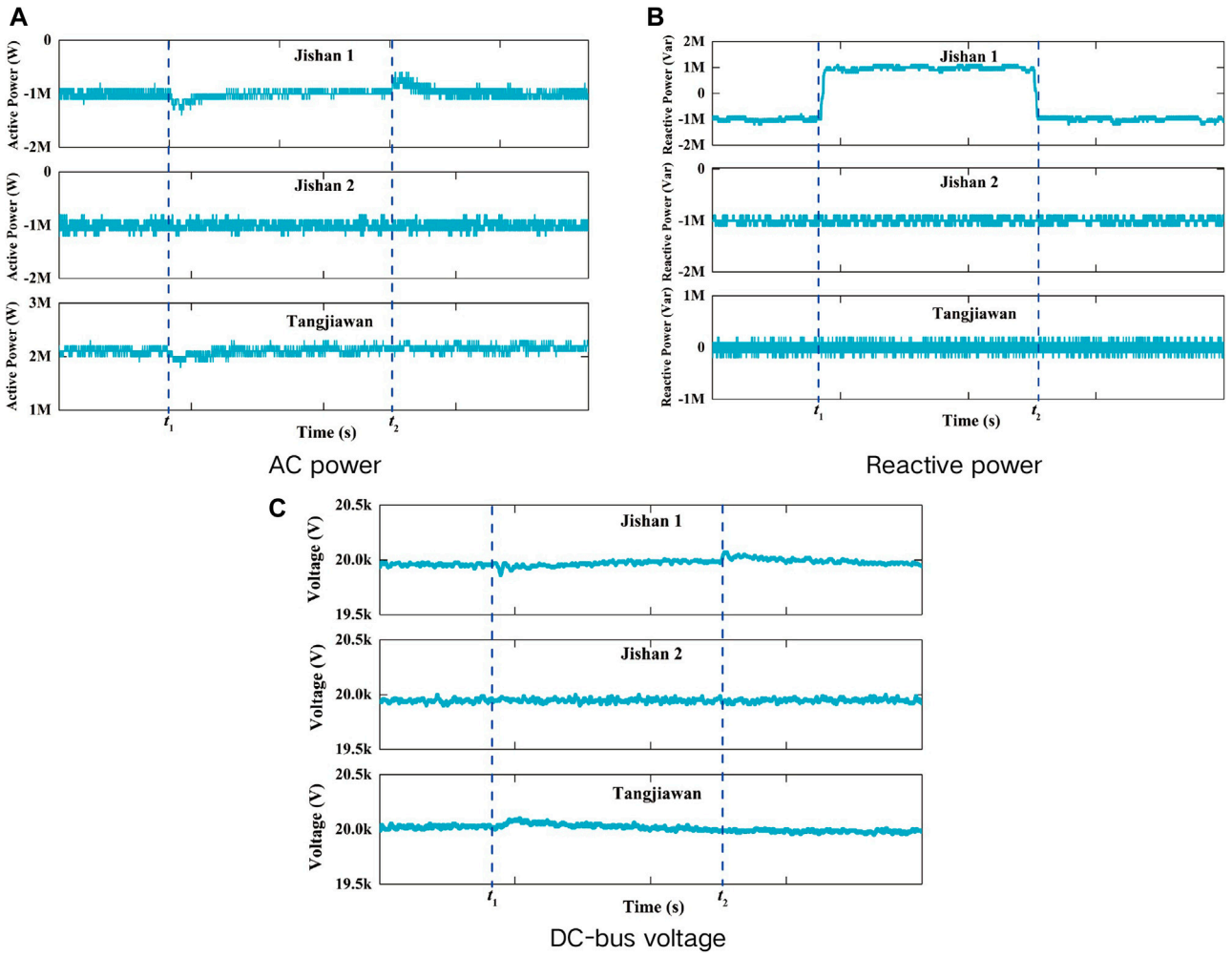


FIGURE 15 | Active power step change in Jishan2 station.

fluctuations when step disturbance occurs momentarily. **Figure 9** is the differential-mode component of arm current which has waveform aberration. **Figure 10** are the common-mode component of arm current with a little more waveform burred. As shown in **Figure 11**, The each phase peak AC voltage output of MMC has reached at about 8.17 kV.**Figure 12** shows the derivatives of LADRC. Z_{d22} and Z_{q22} are estimated of total system disturbances. **Figure 13** is the sub-module capacitor voltages, which is balanced and the capacitor voltage difference is less than 1.2%. In briefly, the simulation results reveal that LADCR can successfully realize the decoupling control of AC active power and reactive power. Compared with PI controller, LADRC has the advantages of smoother power waveform, faster response and lower overshoot, etc.

Figure 14 shows variables of MMC based three-terminal DC grid. When there is no virtual resistor, there exists continuous oscillation in DC-bus voltage, DC current, capacitor voltage and active power because of lack of damping. When virtual resistor is added at $t = 0.5$ s, the oscillation can be suppressed quickly and the DC-bus voltage can be stabilized at 20 kV. When virtual resistor is added, the stable capacitor voltage is determined by the active power.

6 EXPERIMENTS ON TANGJIAWAN-JISHAN1-JISHAN2 AC/DC DISTRIBUTION NETWORK

6.1 Active Power Step Test of Jishan2 Station

Figure 15 shows system waveforms with active power step change in Jishan2 station. As shown in **Figure 15A**, active power of Jishan1 station is constant at −1 MW. Active power of Jishan2 station changes from −1 to 1 MW at t_1, and from 1 MW to −1 MW at t_2. Accordingly, active power of Tangjiawan station changes from 2 to 0 MW at t_1, and from 0 to 2 MW at t_2. Reactive power of Jishan1 remains 1 MVar. There are fluctuations in reactive power of Jishan2 station and Tangjiawan station at the moment of active power

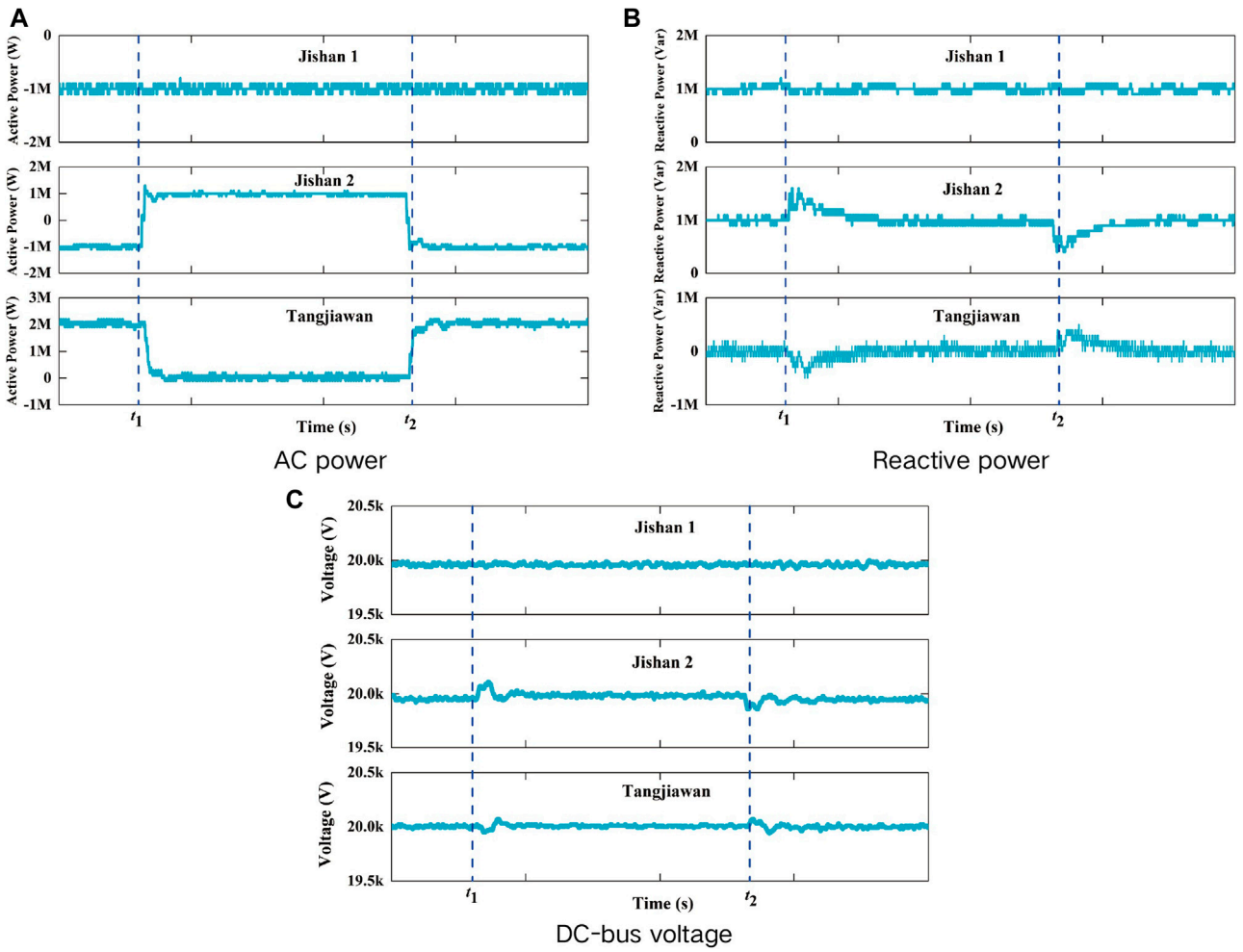


FIGURE 16 | Reactive power step change in Jishan1 station.

change. But reactive power of Jishan2 and Tangjiawan will remain stable at 1Mvar and 0Mvar when active power is stable as shown in **Figure 15B**. **Figure 15C** shows the DC-bus voltage. The DC-bus voltage of Tangjiawan station is constant at 20 kV. There exist slight fluctuations in DC-bus voltages of Jishan1 station and Jishan2 station at the moment of active power change, but the DC-bus voltages still are within the reasonable range.

6.2 Reactive Power Step Test of Jishan1 Station

Figure 16 shows the system waveforms with reactive power step change in Jishan1 station. As shown in **Figure 16A**, active power of Jishan1 station, Jishan2 station, and Tangjiawan station is constant at −1, −1, and 2 MW respectively. **Figure 16B** shows that reactive power of Jishan1 station changes from -1Mvar to 1Mvar at t_1, and changes from 1 to −1 Mvar at t_2. Reactive power of Jishan2 station and Tangjiawan station remains unchanged at -1Mvar and 0Mvar individually. **Figure 16C** shows that the reactive power step change of Jishan1 has influence on the DC-bus voltages of Jishan1 station and Tangjiawan station, but the DC-bus voltage is still within the reasonable range.

6.3 Active Power Flow Reversal Test of Jishan1 Station

Figure 17 is the experiments results of active power reversal test of Jishan1 station. **Figure 17A** shows that Jishan2 station active power still remains 1 MW when Jishan1 station active power flow reversal starts at t_1 and completes at t_2 with active power varies from 1 to −1 MW. However, Tangjiawan station active power responds flow reversal immediately with active power varies from -2 to 0 MW. **Figure 17B** shows that active power flow reversal can influence reactive power of Jishan1 and Tangjiawan station, but the reactive power of Jishan1 station and Tangjiawan station still remains 1 Mvar and 0 Mvar respectively with waveform burr increased.

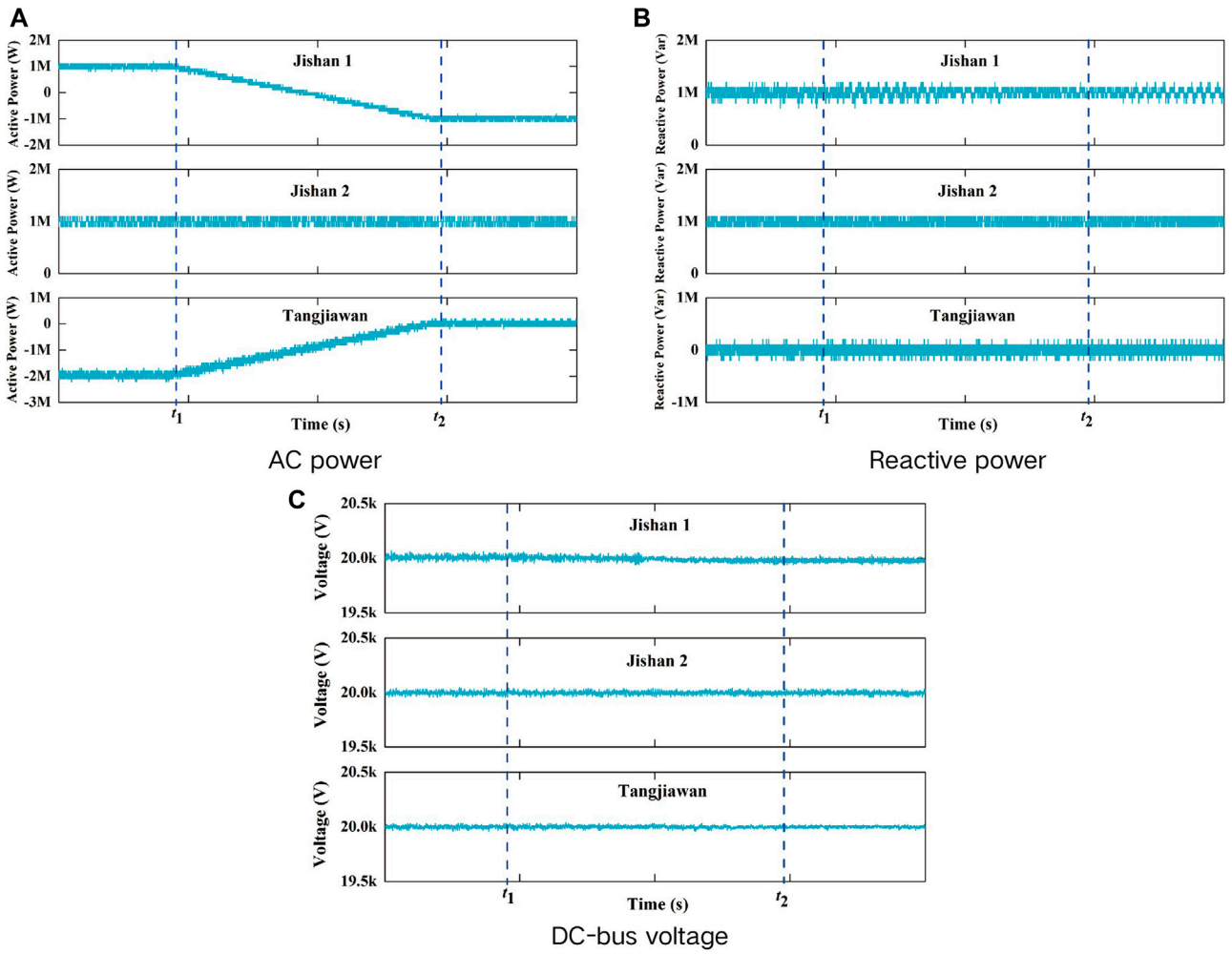


FIGURE 17 | Active power flow reversal in Jishan1 station.

Figure 17C shows that DC bus voltage of three converters station is stable at 20 kV, but Jishan1 station DC bus voltage fluctuates a little bit more than other two stations.

7 CONCLUSION

A novel instantaneous-value model of MMC is derived by introducing the differential-mode and common-mode component representation. Then, ac power modeling of MMC is established based on the PSC-PWM strategy and power decoupling control based on LADRC is realized. Simplified average-value model of MMC power station is deduced and the small signal stability analysis of three-terminal DC grid is carried out. Simulation and experiment results of the Tangjiawan-Jishan1-Jishan2 AC/DC distribution network demonstration project verify that the power decoupling strategy based on LADRC is better than PI controller. The virtual resistor can greatly improve the transient performance and system stability. The modeling and analysis method proposed in this paper is concise and effective. The research of this paper is the expansion of MMC application in the field of distribution network. MMC based multi-terminal AC/DC distribution network can realize the multidirectional power flow among AC-grids, which can greatly improve the power supply reliability.

DATA AVAILABILITY STATEMENT

The raw data supporting the conclusion of this article will be made available by the authors, without undue reservation.

AUTHOR CONTRIBUTIONS

ZX and HY: conceptualization, data curation, methodology and writing. GZ and LL: formal analysis and simulation study. PW and CJ: reagents/materials/analysis.

FUNDING

This journal was supported in part by Natural Science Foundation of Guangdong Province under Grant (2018A0303130111), in part by Open Project of Anhui Key Laboratory of Intelligent Building and Building Energy Saving under Grant (IBES2020KF10), in part by the Guangzhou Science and Technology Planning Project under Grant (201902020003), in part by the Guangdong Special Project in Key Field of Artificial Intelligence for Ordinary University under Grant (2019KZDZX1004), in part by the Guangzhou Key Laboratory Project of Intelligent Building Equipment Information Integration and Control under Grant (202002010003), in part by the Guangzhou Yuexiu District Science and Technology Plan Major Project under Grant (2019-GX-010).

REFERENCES

Adam, G. P., and Williams, B. W. (2014). Half- and Full-Bridge Modular Multilevel Converter Models for Simulations of Full-Scale HVDC Links and Multiterminal DC Grids. *IEEE J. Emerg. Sel. Top. Power Electron.* 2 (4), 1089–1108. doi:10.1109/jestpe.2014.2315833

Ahmed, N., Angquist, L., Mehmood, S., Antonopoulos, A., Harnefors, L., Norrga, S., and Nee, H. (2016). "Efficient Modeling of an Mmc-Based Multiterminal Dc System Employing Hybrid Hvdc Breakers," in 2016 IEEE Power and Energy Society General Meeting (PESGM), Boston, MA, July 17–21, 2016, 1. doi:10.1109/pesgm.2016.7741765

Alassi, A., Bañales, S., Ellabban, O., Adam, G., and MacIver, C. (2019). Hvdc Transmission: Technology Review, Market Trends and Future Outlook. *Renew. Sustain. Energ. Rev.* 112, 530–554. doi:10.1016/j.rser.2019.04.062

Alonge, F., Cirrincione, M., D'Ippolito, F., Pucci, M., and Sferlazza, A. (2017). Active Disturbance Rejection Control of Linear Induction Motor. *IEEE Trans. Ind. Applicat.* 53 (5), 4460–4471. doi:10.1109/tia.2017.2697845

Angquist, L., Antonopoulos, A., Siemaszko, D., Ilves, K., Vasiladiotis, M., and Nee, H.-P. (2011). Open-Loop Control of Modular Multilevel Converters Using Estimation of Stored Energy. *IEEE Trans. Ind. Applicat.* 47 (6), 2516–2524. doi:10.1109/tia.2011.2168593

Antonopoulos, A., Angquist, L., and Nee, H. P. (2009). "On Dynamics and Voltage Control of the Modular Multilevel Converter," in 2009. EPE '09. 13th European Conference on, Barcelona, Spain, September 8–10, 2009 (Power Electronics and Applications).

Bergna Diaz, G., Suul, J. A., and D'Arco, S. (2015). "Small Signal State-Space Modeling of Modular Multilevel Converters for System Stability Analysis," in 2015 IEEE Energy Conversion Congress and Exposition (ECCE), Montreal, Canada, September 20–24, 2015, 5822–5829. doi:10.1109/ecce.2015.7310477

Chen, Y. C., Dhople, S. V., Guggilam, S. S., Dall'Anese, E., and Giannakis, G. B. (2016). Scalable Optimization Methods for Distribution Networks with High Pv Integration. *IEEE Trans. Smart Grid* 7 (4), 2061–2070. doi:10.1109/TSG.2016.2543264

Chen, W.-H., Yang, J., Guo, L., and Li, S. (2016). Disturbance-Observer-Based Control and Related Methods-An Overview. *IEEE Trans. Ind. Electron.* 63 (2), 1083–1095. doi:10.1109/tie.2015.2478397

Debnath, S., Qin, J., Bahrani, B., Saeedifard, M., and Barbosa, P. (2015). Operation, Control, and Applications of the Modular Multilevel Converter: A Review. *IEEE Trans. Power Electron.* 30 (1), 37–53. doi:10.1109/tpel.2014.2309937

Friedrich, K. (2010). "Modern Hvdc Plus Application of Vsc in Modular Multilevel Converter Topology," in 2010 IEEE International Symposium on Industrial Electronics, Bari, Italy, July 4–7, 2010, 3807–3810. doi:10.1109/isie.2010.5637505

Guan, M., and Xu, Z. (2012). Modeling and Control of a Modular Multilevel Converter-Based Hvdc System under Unbalanced Grid Conditions. *IEEE Trans. Power Electron.* 27 (12), 4858–4867. doi:10.1109/tpel.2012.2192752

Harnefors, L., Antonopoulos, A., Norrga, S., Angquist, L., and Nee, H.-P. (2013). Dynamic Analysis of Modular Multilevel Converters. *IEEE Trans. Ind. Electron.* 60 (7), 2526–2537. doi:10.1109/tie.2012.2194974

Kotb, O., Ghandhari, M., Eriksson, R., and Sood, V. K. (2016). On Small Signal Stability of an Ac/dc Power System with a Hybrid Mtdc Network. *Electric Power Syst. Res.* 136, 79–88. doi:10.1016/j.epsr.2016.02.004

Lesnicar, A., and Marquardt, R. (2004). "An Innovative Modular Multilevel Converter Topology Suitable for a Wide Power Range," in Power Tech Conference, Bologna, Italy, June 23–26, 2003.

Li, Y., Tang, G., Ge, J., He, Z., Pang, H., Yang, J., et al. (2018). Modeling and Damping Control of Modular Multilevel Converter Based Dc Grid. *IEEE Trans. Power Syst.* 33 (1), 723–735. doi:10.1109/tpwrs.2017.2691737

Li, Y., Liu, K., Liao, X., Zhu, S., Huai, Q., and Huai, Q. (2019). A Virtual Impedance Control Strategy for Improving the Stability and Dynamic Performance of VSC-HVDC Operation in Bidirectional Power Flow Mode. *Appl. Sci.* 9 (15), 3184. doi:10.3390/app9153184

Liu, C., Luo, G., Wencong, T. U., and Wan, H. (2017). Servo Systems with Double Closed-Loops Based on Active Disturbance Rejection Controllers. *Chin. Soc. Electr. Eng.* 37 (23), 7032–7039. doi:10.13334/j.0258-8013.pcsee.161957

Liu, C., Luo, G., Duan, X., Chen, Z., Zhang, Z., and Qiu, C. (2020). Adaptive LADRC-Based Disturbance Rejection Method for Electromechanical Servo System. *IEEE Trans. Ind. Applicat.* 56 (1), 876–889. doi:10.1109/tia.2019.2955664

Lu, X., Xiang, W., Lin, W., and Wen, J. (2018). Small-Signal Modeling of Mmc Based Dc Grid and Analysis of the Impact of Dc Reactors on the Small-Signal Stability. *Int. J. Electr. Power Energ. Syst.* 101, 25–37. doi:10.1016/j.ijepes.2018.01.046

Marquardt, R. (2010). "Modular Multilevel Converter: An Universal Concept for Hvdc-Networks and Extended Dc-Bus-Applications," in The 2010 International Power Electronics Conference - ECCE ASIA, Sapporo, Japan, June 21–24, 2010, 502–507. doi:10.1109/ipec.2010.5544594

Marquardt, R. (2011). "Modular Multilevel Converter Topologies with Dc-Short Circuit Current Limitation," in IEEE International Conference on Power Electronics & Ecce Asia, Jeju, Korea (South), May 30–June 3, 2011. doi:10.1109/icpe.2011.5944451

Mithulananthan, N., Shah, R., and Bansal, R. C. (2013). Oscillatory Stability Analysis with High Penetrations of Large-Scale Photovoltaic Generation. *Energ. Convers. Manage.* 65, 420–429. doi:10.1016/j.enconman.2012.08.004

Rao, H. (2015). Architecture of Nan'ao Multi-Terminal VSC-HVDC System and its Multi-Functional Control. *CSEE Power Energ. Syst.* 1 (1), 9–18. doi:10.17775/cseejpes.2015.00002

Saad, H., Peralta, J., Dennetiere, S., Mahseredjian, J., Jatskevich, J., Martinez, J. A., et al. (2013). Dynamic Averaged and Simplified Models for Mmc-Based Hvdc Transmission Systems. *IEEE Trans. Power Deliv.* 28 (3), 1723–1730. doi:10.1109/tpwrd.2013.2251912

Trinh, N.-T., Zeller, M., Wuerflinger, K., and Erlich, I. (2016). Generic Model of MMC-VSC-HVDC for Interaction Study with AC Power System. *IEEE Trans. Power Syst.* 31 (1), 27–34. doi:10.1109/tpwrs.2015.2390416

Vasiladiotis, M., Cherix, N., and Rufer, A. (2014). Accurate Capacitor Voltage Ripple Estimation and Current Control Considerations for Grid-Connected Modular Multilevel Converters. *IEEE Trans. Power Electron.* 29 (9), 4568–4579. doi:10.1109/tpel.2013.2286293

Wan, X., Li, Y., and Peng, M. (2018). Modelling, Analysis and Virtual Parallel Resistor Damping Control of VSC-Based DC Grid Using Master-Slave Control Mode. *IET Generation, Transm. Distribution* 12 (9), 2046–2054. doi:10.1049/iet-gtd.2017.1021

Wang, J., and Wang, P. (2019). Decoupled Power Control for Direct-Modulation-Based Modular Multilevel Converter with Improved Stability. *IEEE Trans. Ind. Electron.* 66 (7), 5264–5274. doi:10.1109/tie.2018.2870352

Wang, P., Liu, X., and Loh, P. C. (2011). A Hybrid Ac/dc Microgrid and its Coordination Control. *IEEE Trans. Smart Grid* 2 (2), 278–286. doi:10.1109/TSG.2011.2116162

Wang, P., Zhang, X.-P., Coventry, P. F., and Zhang, R. (2016). Start-Up Control of an Offshore Integrated Mmc Multi-Terminal Hvdc System with Reduced Dc

Voltage. *IEEE Trans. Power Syst.* 31 (4), 2740–2751. doi:10.1109/tpwrs.2015.2466600

Wang, Y., Yuan, Z., and Fu, J. (2016). A Novel Strategy on Smooth Connection of an Offline Mmc Station into Mtdc Systems. *IEEE Trans. Power Deliv.* 31 (2), 568–574. doi:10.1109/tpwrd.2015.2437393

Wang, G., Liu, R., Zhao, N., Ding, D., and Xu, D. (2019). Enhanced Linear Adrc Strategy for Hf Pulse Voltage Signal Injection-Based Sensorless Ipmsm Drives. *IEEE Trans. Power Electron.* 34 (1), 514–525. doi:10.1109/tpel.2018.2814056

Xiang, W., Lin, W., An, T., Wen, J., and Wu, Y. (2017). Equivalent Electromagnetic Transient Simulation Model and Fast Recovery Control of Overhead Vsc-Hvdc Based on Sb-Mmc. *IEEE Trans. Power Deliv.* 32 (2), 778–788. doi:10.1109/tpwrd.2016.2607230

Yang, H., Dong, Y., Li, W., and He, X. (2017). Average-Value Model of Modular Multilevel Converters Considering Capacitor Voltage Ripple. *IEEE Trans. Power Deliv.* 32 (2), 723–732. doi:10.1109/tpwrd.2016.2555983

Yang, H., Li, W., Lin, L., and He, X. (2018). Decoupled Current Control with Synchronous Frequency Damping for Mmc Considering Sub-Module Capacitor Voltage Ripple. *IEEE Trans. Power Deliv.* 33 (1), 419–428. doi:10.1109/tpwrd.2017.2721961

Zhang, L., Zou, Y., Zou, Y., Yu, J., Qin, J., Vijay, V., et al. (2017). Modeling, Control, and protection of Modular Multilevel Converter-Based Multi-Terminal HVDC Systems: A Review. *CSEE J. Power Energ. Syst.* 3 (4), 340–352. doi:10.17775/cseejpes.2017.00440

Conflict of Interest: HY was employed by the company Heyuan Power Supply Bureau of Guangdong Power Grid Co. Ltd.

The remaining authors declare that the research was conducted in the absence of any commercial or financial relationships that could be construed as a potential conflict of interest.

Publisher's Note: All claims expressed in this article are solely those of the authors and do not necessarily represent those of their affiliated organizations, or those of the publisher, the editors and the reviewers. Any product that may be evaluated in this article, or claim that may be made by its manufacturer, is not guaranteed or endorsed by the publisher.

Copyright © 2021 Xianyong, Zijuan, Yaohong, Li, Weikuan and Jian. This is an open-access article distributed under the terms of the Creative Commons Attribution License (CC BY). The use, distribution or reproduction in other forums is permitted, provided the original author(s) and the copyright owner(s) are credited and that the original publication in this journal is cited, in accordance with accepted academic practice. No use, distribution or reproduction is permitted which does not comply with these terms.

frontiers in Energy Research

ORIGINAL RESEARCH
published: 07 October 2021
doi: 10.3389/fenrg.2021.771009

PMSM Wind Farm Aggregation Algorithm Based on Power Equivalence Principle

Haoshu Shao[1], Xu Cai[1], Heming Yan[2], Jiapei Zhou[2], Yao Qin[1] and Zhixiang Zhang[1]*

[1]*Key Laboratory of Control of Power Transmission and Conversion, Shanghai Jiao Tong University, Shanghai, China,* [2]*State Key Laboratory of Advanced Power Transmission Technology, Beijing, China*

With the continuing increase of offshore wind farm power scale, it is urgent to propose a simplified wind farm model, which aggregates the entire wind farm into single or several aggregated wind turbine generators (WTGs), aiming to save computing resources and improve simulation speed. A novel aggregation algorithm that considers the power loss of offshore submarine cable is proposed, which is different from the traditional wind farm modeling method that adopts amplifying transformer as aggregation medium. Moreover, multi machine aggregation (MMA) algorithm is furtherly proposed to improve the aggregation accuracy. Simulation results verify that the proposed aggregation method can present the dynamic characteristics of wind farm with high accuracy, and can be popularized for other types of wind farm.

Keywords: offshore wind farm, PMSM, aggregation modeling algorithm, dynamic characteristics, power loss

OPEN ACCESS

Edited by:
Xing He,
Shanghai Jiao Tong University, China

Reviewed by:
Fujin Deng,
Southeast University, China
Yu Wang,
Guangdong University of Technology, China
Yu Ling,
Shanxi Datong University, China

****Correspondence:***
Xu Cai
xucai@sjtu.edu.cn

Specialty section:
This article was submitted to Smart Grids, a section of the journal Frontiers in Energy Research

Received: *05 September 2021*
Accepted: *21 September 2021*
Published: *07 October 2021*

Citation:
Shao H, Cai X, Yan H, Zhou J, Qin Y and Zhang Z (2021) PMSM Wind Farm Aggregation Algorithm Based on Power Equivalence Principle. Front. Energy Res. 9:771009. doi: 10.3389/fenrg.2021.771009

INTRODUCTION

In recent years, the penetration of wind energy and the scale of wind farm are increasing rapidly (Zou et al., 2014), at the same time, since the energy efficiency for offshore wind energy is relatively higher than onshore wind energy, so there is an obvious trend that the application focus is shifting from offshore to onshore wind farm. On the other hand, wind power is inherently random and intermittent (Sanchez et al., 2012), with the continuing increase of wind power scale, this will impose adverse impact on the stability operation of large scale wind farm, so before the construction of wind farm, it is necessary to conduct a comprehensive feasibility analysis, aiming to analyze the interactive behavior between wind farm and power grid (Xue et al., 2013; Muljadi et al., 2006). Nowadays the modeling of wind farm is usually focused on onshore wind farm with doubly-fed induction generator (DFIG) as the main generator type, but as for offshore wind farm, it usually adopts permanent magnet synchronous motor (PMSM) as the main generator type, so there is also an urgent need to conduct research and analysis on PMSM offshore wind farm and its aggregation application.

For engineering practice, the impact of wind power integrated into power grid is usually analyzed from the perspective of "wind farm" (Ding et al., 2013), if detailed model is adopted for each WTG in one single wind farm, this will lead to an incredible increase in the scale of simulation, one effective solution is to build a simplified wind farm aggregation model to increase the simulation speed while maintaining accuracy. Previous researches have already focused on single machine aggregation (SMA) (Mercado-Vargas et al., 2015) and multi machine aggregation (MMA) (Badr et al., 2015). For SMA aggregation, the entire wind farm will be integrated into one single large WTG, the interface characteristics of single aggregated WTG is the same compared with that of wind farm (L. M. Fernandez et al., 2005). For MMA aggregation, the entire wind farm will be aggregated into several

large WTGs according to certain indexes, normally the wind speed will be the selected as the main grouping index. (H. Dong, 2018). Amplifying transformer is usually adopted to conduct the aggregation work, (Conroy et al., 2009)- (Slootweg et al., 2003), the primary winding is connected to a single WTG, while the output power from the secondary winding is amplified with an artificial constant, this method is easy to conduct and understand, but the most obvious drawback is that the mechanism of adopting amplifying transformer as aggregation medium still needs further verification, and the dynamic characteristics of transmission line or cable is neglected (Yang et al., 2012; Ali et al., 2013), all these shortcomings will severely influence the aggregation accuracy, making aggregation model less convincing. Different from the aggregation method which adopts amplifying transformer, aggregation algorithm is used to calculate the aggregated generator parameter according to the single WTG parameter as well as the number of WTGs in wind farm (Chowdhury et al., 2010; Li et al., 2011).

At present, some results have been achieved in the research of dynamic aggregation modeling of onshore wind farms. However, unlike onshore wind farms, offshore wind turbines have a larger unit capacity and use cable lines as the main collection lines, this is one of the most significant difference from that used on onshore wind farm, besides, the impact brought by the submarine cable cannot be ignored. The modalities of the aggregation model of wind turbines are more abundant (Wang et al., 2018; Badr et al., 2015), and the dynamic characteristics of the collection lines of wind farms have also become a main object of aggregation research, which cannot be ignored.

At the same time, unlike the overhead line collection lines of onshore wind farms, the charging capacity of the cable collection lines of offshore wind farms is very large, generally 20–25 times than that of the overhead line circuits, which is equivalent to the reactive power compensation equipment being connected in parallel, so ignoring the transmission line capacitance in the conventional aggregation method will bring great errors, and the aggregation result will also have a significant difference between the detailed model and the aggregated model. (Teng et al., 2019; Du et al., 2019).

In this paper, a comprehensive aggregation algorithm is proposed considering the power loss of offshore wind farm submarine cable, including the aggregation of WTG electrical parameters, pneumatic parameters as well as the integration of transmission line, the power equivalent principle is also used to calculate all the aggregation parameters of wind farm, simulation results verify that the proposed aggregation algorithm can match well with detailed model, while MMA model is more accurate than SMA to reflect the operation of wind farm in various wind speed environment.

MODELING OF OFFSHORE PMSM WIND FARM

Structure of Offshore PMSM Wind Farm

Offshore wind farm usually adopts permanent magnet synchronous motor (PMSM) as the main generation type due to its relative higher power rating compared with that of tradition doubly-fed induction generator (DFIG). As is shown in **Figure 1**, one single wind farm usually consists of up to 16 feeders which are connected to collection bus, for each feeder in wind farm, up to 12 WTGs are connected in series in each feeder. A typical simplified PMSM wind farm is selected to conduct aggregation simulation research in this paper, six feeders are linked to 35 kV collection bus with three or four WTG connected in series in one single feeder, altogether 34 WTGs are included in this wind farm.

Operation and Control of PMSM Wind Farm

As is shown in **Figure 2**, the working interval within the full wind speed range for PMSM can be divided into four operation modes, which are I-low constant speed mode, II-MPPT mode, III-high constant speed mode and IV-constant power mode respectively, x-axis represents the wind speed v, and y-axis refers to rotor speed ω_r.

When wind speed locates within $[v_{cutin}, v_1]$, the purpose is to control the rotor speed to stabilize at a low constant speed ω_{r_min}. With the increase of wind speed, PMSM then enters the MPPT stage, PMSM will operate at a particular rotor speed so as to catch the maximum power from wind, both tip speed ratio λ and rotor speed will be controlled at their optimal value λ_{opt} and $\omega_{r_opt.}$ When wind speed exceeds v_2, rotor speed reaches the rated value ω_{r_max}, PMSM will then operate at high constant speed ω_{r_max} until exceeding the rated power, afterwards the pitch angle regulator will be activated and PMSM will operate at constant power mode.

Each PMSM WTG in the target research wind farm adopts traditional Vector Control (VC) strategy to decouple the control of WTG active power and reactive power, the control diagram for PMSM rotor side converter (RSC) and grid side converter (GSC) is shown in **Figures 3**, **4** respectively.

PMSM RSC adopts rotor flux linkage oriented vector control strategy, the control purpose of this control strategy is to control RSC active power and reactive power independently. As is shown in **Figure 3**, two cascaded control loops are included in RSC control strategy, the control object of active power control loop is PMSM rotor speed ω_r, so as to track the MPPT point given a specific wind speed. For reactive power control loop, the d-axis reference current i_{sd}^* is set to zero, so that the PMSM electromagnetic torque can only be influenced by q-axis stator current i_{sq}, which is exactly the output of rotor speed closed loop.

The control diagram of PMSM GSC is shown in **Figure 4**, GSC is aimed at controlling dc-link voltage and balancing active power through dc-link capacitor, the GSC d axis reference current is obtained from the output of dc-link voltage regulator and the q axis reference current is get via reactive power regulator.

AGGREGATION PRINCIPLE AND ALGORITHM

Submarine cable is considered as one important aggregation object in this paper, which is less emphasized in traditional amplifying transformer aggregation strategy, the conditions that the aggregation of wind farm must meet are:

1) The amplitude and phase of voltage at PCC of aggregation model is equal to that of wind farm detailed model.

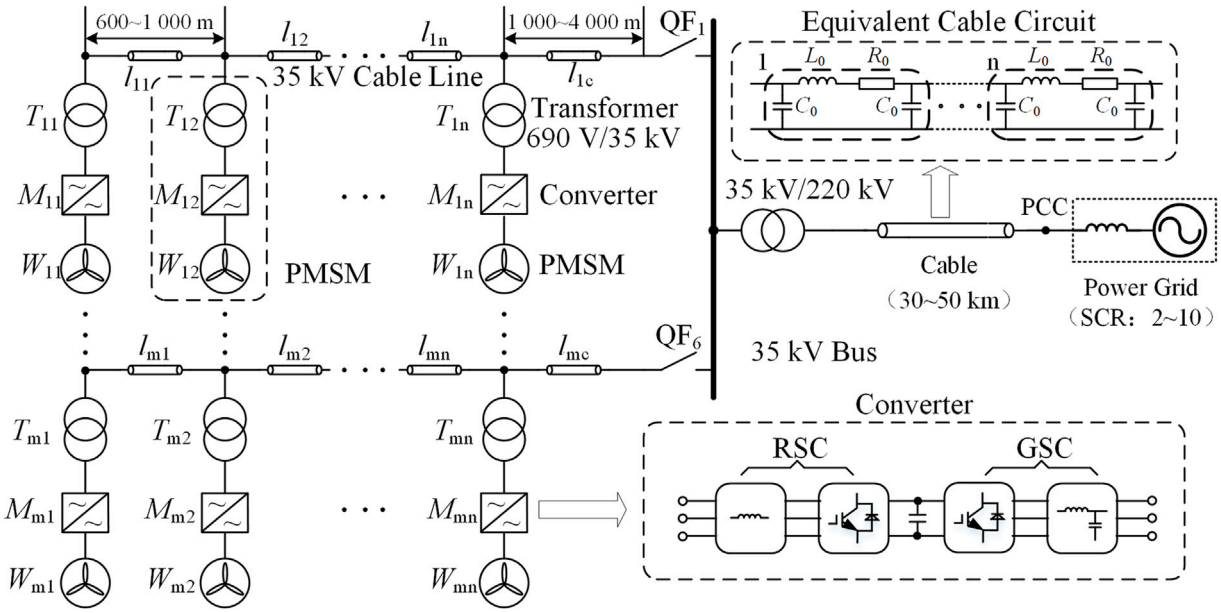


FIGURE 1 | Topological structure of PMSM wind farm.

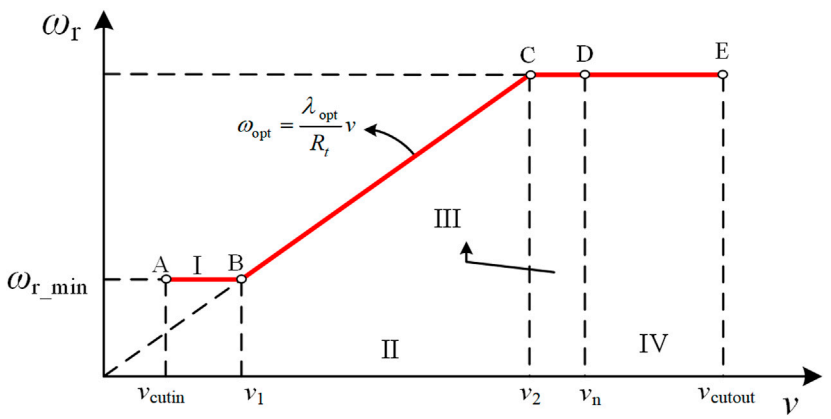


FIGURE 2 | Operation mode division under full wind condition.

2) The total capacity of aggregation model is the sum of the capacities of all WTGs in the detailed model.
3) The consumed active power inside the aggregation model is equal to that of wind farm detailed model.
4) The inductive and capacitive reactive power of aggregation model is equal to that of wind farm detailed model.

PMSM WTG Parameter Aggregation

Based on the principles listed above, the equivalent parameters of aggregated PMSM WTG can be calculated with **Eq. 1**, **2**, where a total of m WTGs with the same generation type are aggregated into one single WTG.

$$\begin{cases} S_{eq} = \sum_{i=1}^{m} S_i = mS_n \\ X_{s-eq} = \dfrac{x_s}{m} \; r_{s-eq} = \dfrac{r_s}{m} \; B_{c_eq} = mB_c \end{cases} \tag{1}$$

$$\begin{cases} H_{t_eq} = H_t \quad H_{g_eq} = H_g \\ K_{s_eq} = K_s \quad D_{s_eq} = D_s \\ S_{T_eq} = mS_T \quad Z_{T_eq} = \dfrac{Z_T}{m} \end{cases} \tag{2}$$

S_n is the rated capacity of one single WTG, x_s, r_s and B_c are the reactance, resistance and admittance of the WTG; m is the total number of WTGs in the same cluster; S_T is the rated

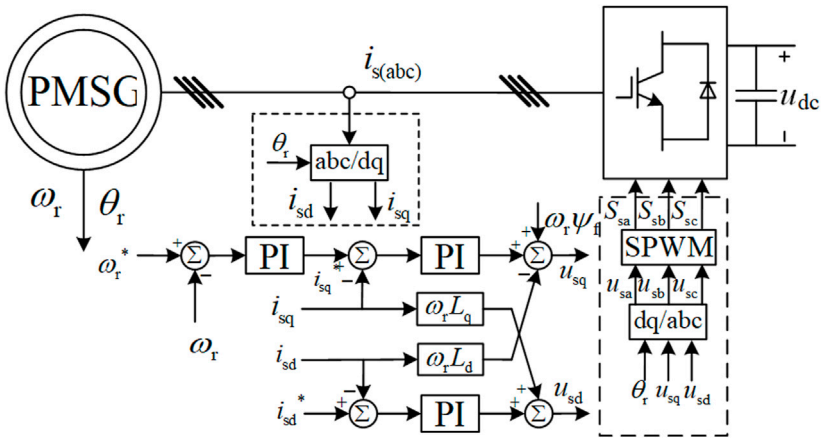


FIGURE 3 | Control diagram of PMSM RSC.

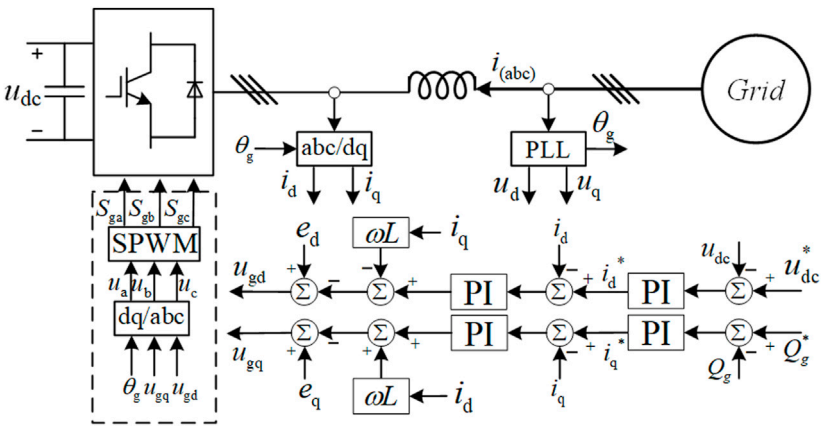


FIGURE 4 | Control diagram of PMSM GSC.

capacity of the transformer; Z_T is the impedance of the transformer; H_t and H_g is the inertia time constant of the wind turbine and generator.

As for the aggregation of wind speed, there are a variety of aggregation methods to calculate the aggregated wind speed for wind farm. When the element of wake effect is not taken in account, then the aggregated wind speed is the same as the speed for single WTG:

$$v_{eq} = v \tag{3}$$

However, when taking wake effect into consideration, then the calculation of aggregated wind speed is based on the power curve of WTG, firstly the power of each WTG in wind farm needs to be calculated and then get the average power, so that the aggregated wind speed can be drawn from the average wind speed as well as the given WTG power curve, assuming that the number of WTGs that will be aggregated is m, then the output power can be calculated as:

$$P_m = f(v_m) \tag{4}$$

Based on the power equation in **Eq. 4**, the aggregated wind speed can be calculated from:

$$v_{eq} = \frac{1}{m}\sum_{i=1}^{m} f^{-1}(v_k) \tag{5}$$

PMSM Wind Farm Aggregation Considering Submarine Cable Power Loss

For offshore PMSM wind farm, the ground capacitance is usually 20–25 times than that of overhead lines. So it cannot be ignored in the SMA analysis. Active power equivalent principle is applied in the aggregation of offshore submarine cable, as is shown in **Figure 5**, S_i and U_i represent the output power and terminal voltage of the ith WTG on the feeder respectively, C_i and Z_i represent the capacitance and impedance of the ith cable line on the feeder respectively, U_{pcc} represents the voltage at the PCC

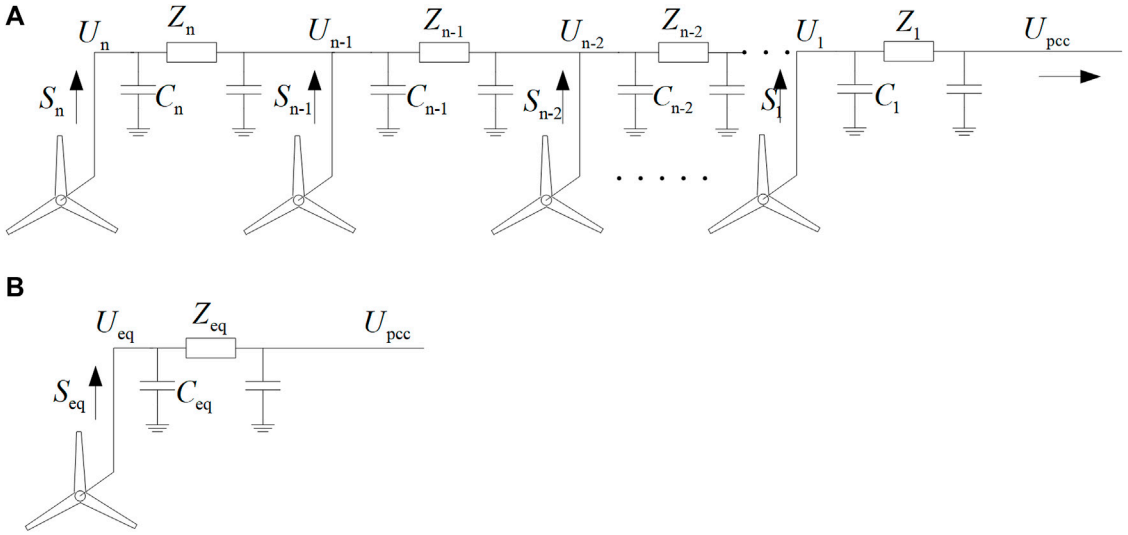


FIGURE 5 | Transmission Line Aggregation process. **(A)** Before Equivalence. **(B)** After Equivalence.

point. And S_{eq} and U_{eq} represent the equivalent output power and terminal voltage of the aggregated WTG separately, C_{eq} and Z_{eq} represent the equivalent capacitance and impedance of the aggregated cable line.

Based on the power equivalent principle, in order to calculate SMA submarine cable parameter, the power loss of the impedance on the *n*th cable at the end of the feeder, and the power loss of the impedance of the *m*th cable on the feeder can be expressed as:

$$\begin{cases} \Delta S_n = \left(S_n - j\frac{1}{2}C_n U_n^2\right)^2 Z_n / U_n^2 \\ \Delta S_m = \dfrac{\left(\sum_{i=m}^{n-1}\left(S_i - j\frac{1}{2}(C_{i+1}+C_i)U_i^2 + \Delta S_{i+1}\right) - j\frac{1}{2}C_n U_n^2\right)^2 Z_m}{U_m^2} \end{cases} \tag{6}$$

Based on **Eq. 6**, the power loss of all submarine cables on one feeder, and the power loss on the equivalent circuit can be expressed as:

$$\begin{cases} \Delta S_{ztotal} = \Delta S_1 + \Delta S_2 + \ldots + \Delta S_n \\ \Delta S_{zeq} = \dfrac{\left(S_{eq} - j\frac{1}{2}C_{eq}U_{eq}^2\right)^2 Z_{eq}}{U_{eq}^2} \end{cases} \tag{7}$$

The expression of equivalence impedance Z_{eq} can be calculated based on the power equivalent principle of $\Delta S_{ztotal} = \Delta S_{zeq}$:

$$Z_{eq} = \frac{\Delta S_{ztotal}}{\left(S_{eq} - j\frac{1}{2}C_{eq}U_{eq}^2\right)^2} U_{eq}^2 \tag{8}$$

Besides, according to the principle that the reactive power consumed on the capacitor before and after the cable line equivalence is the same, the equivalent capacitor can be expressed as:

$$C_{eq} = \frac{\left(C_n U_n^2 + C_n U_{n-1}^2 + C_{n-1}U_{n-1}^2 + \ldots + C_2 U_2^2 + C_1 U_2^2 + C_1 U_1^2\right)}{\left(U_{eq}^2 + U_1^2\right)} \tag{9}$$

Equations 1–9 are the main calculation algorithm for PMSM wind farm single machine aggregation. When referring multi machine aggregation, wind speed for each WTG is selected as the main grouping index, all WTGs in a wind farm are grouped into four groups according to the WTG operation mode so as to minimize the aggregation error, since the operation mode is directly related to the wind speed and wind speed can be well estimated and calculated through various prediction algorithm, so it is easy to group one single wind farm based on wind speed for each WTG.

SIMULATION RESULTS

Simulation Verification of SMA for Grid Fault Situation.

Simulation verification is firstly carried out between detailed model and SMA model under the wind speed of 7, 9, and 11 m/s respectively. A three-phase short circuit fault occurs in simulation and the fault duration is 0.625 s.

Figure 6A shows the comparison between the detailed model and SMA model under the wind speed of 7 m/s. The first panel is the voltage RMS value, indicating that grid voltage drops to 20% of the normal value and lasts for 625 ms, the rest panels are output active power, reactive power and current. **Figure 6B** is the average error

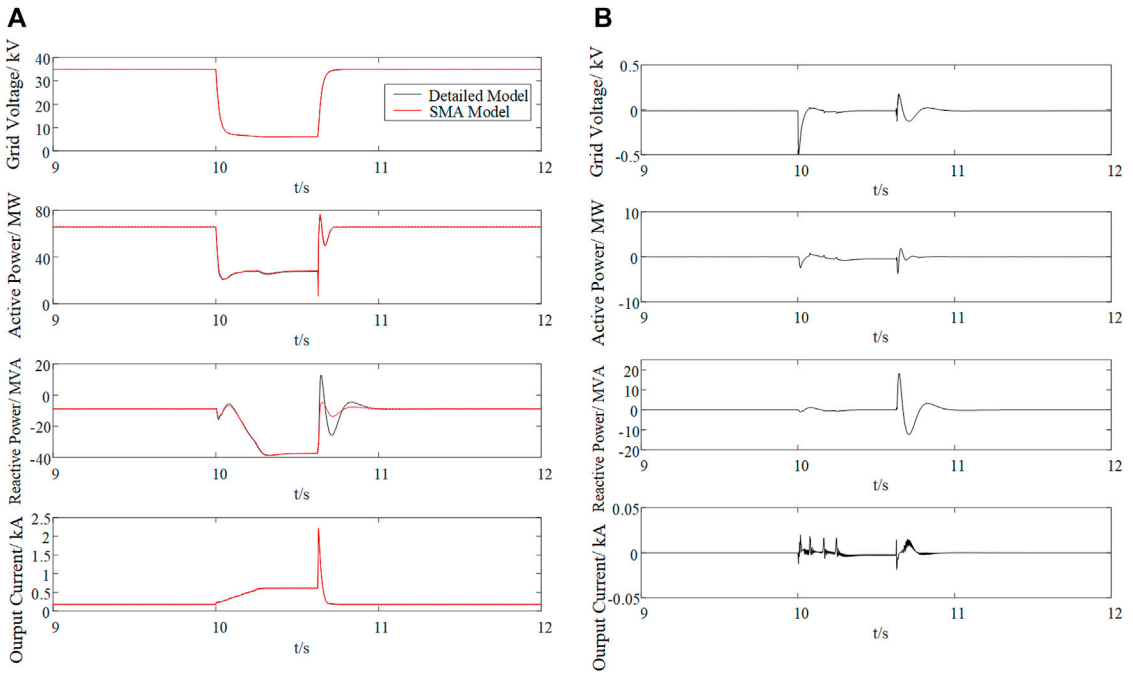


FIGURE 6 | 7 m/s LVRT response comparison. **(A)** Comparison Results **(B)** Error Results.

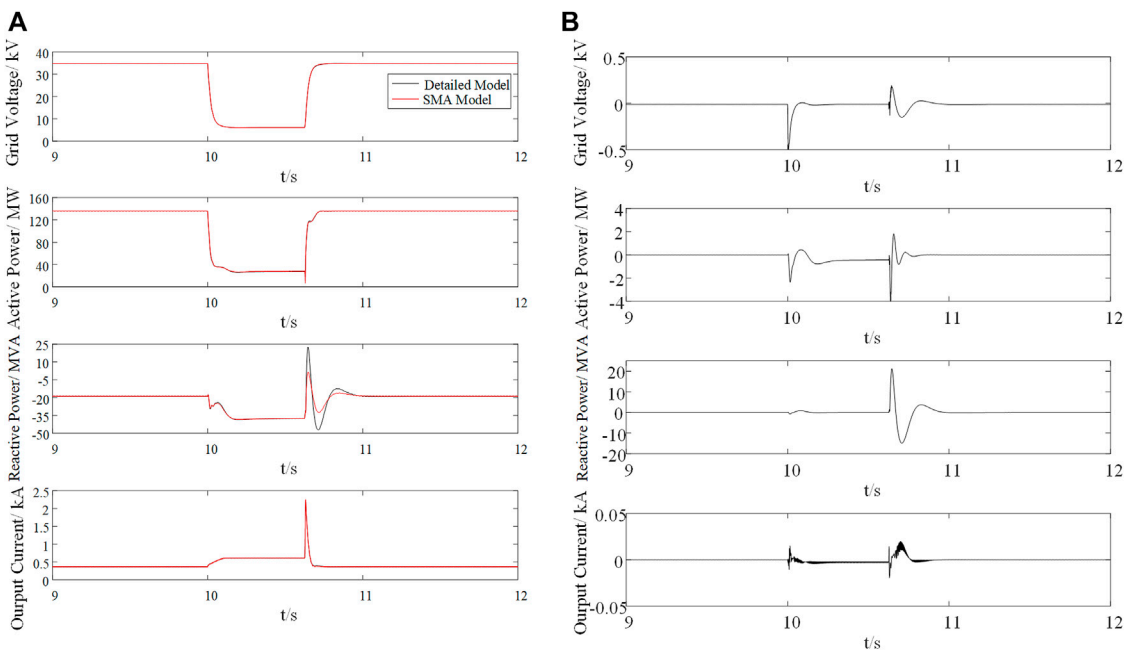


FIGURE 7 | 9 m/s LVRT response comparison. **(A)** Comparison Results **(B)** Error Results.

curve of active power, reactive power and current at the PCC point. Based on **Figure 6A** and **Figure 6B**, it can be seen that the two curves overlap well with each other in steady state. Although there is a deviation in the dynamic process, it is not very large, which means that the SMA model can reflect the dynamic process of the detailed model.

Similar conclusions can also be found in **Figure 7**, **8**, where the wind speed are 9 and 11 m/s respectively.

In order to investigate the aggregation accuracy of SMA model, we define the average error E_x as an important index to quantify the aggregation accuracy, as is shown as:

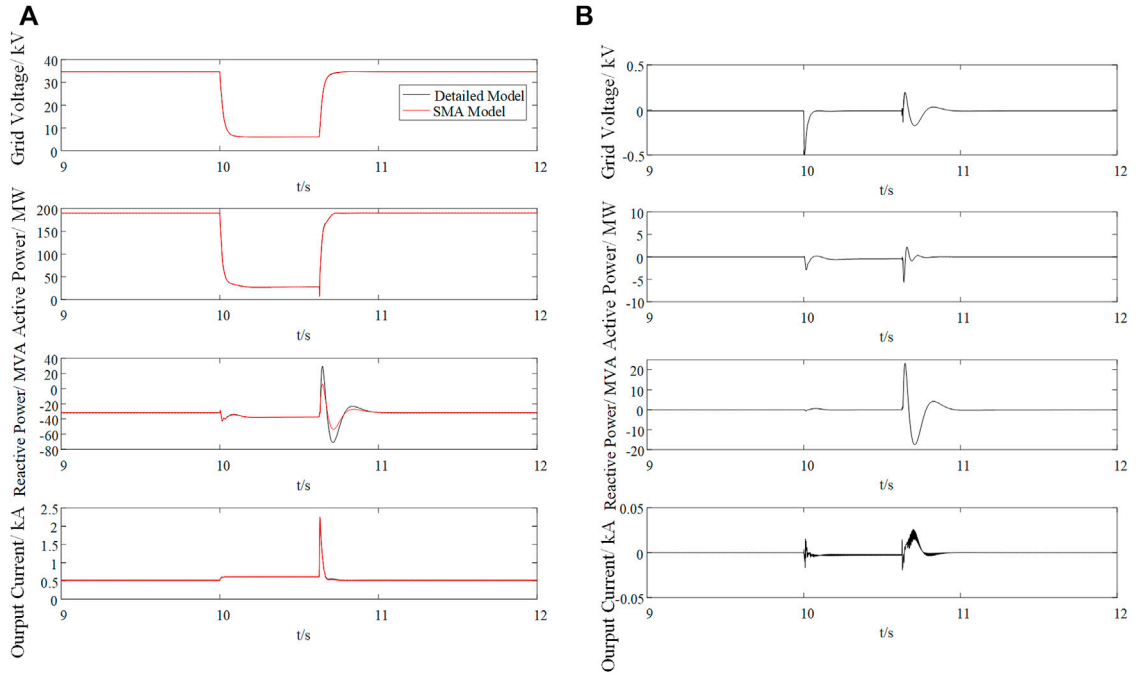


FIGURE 8 | 11 m/s LVRT response comparison. **(A)** Comparison Results **(B)** Error Results.

TABLE 1 | Average error before grid fault between SMA and detailed model.

Wind speed (m/s)	Average error/%			
	Voltage	Active power	Reactive power	Current
7	0.0639	0.0008	0.0192	0.00358
9	0.0656	0.00147	0.0279	0.00475
11	0.0682	0.00143	0.0398	0.0071

TABLE 2 | Average error during grid fault between SMA and detailed model.

Wind speed (m/s)	Average error/%			
	Voltage	Active power	Reactive power	Current
7	0.0446	0.24	0.0444	0.37
9	0.0446	0.23	0.0427	0.37
11	0.0443	0.22	0.0411	0.36

$$E_x = \frac{1}{n}\frac{\sum_{i=1}^{n}\left(X_{eqi} - X_i\right)}{X_N} \times 100\% \tag{10}$$

where x is the parameter to be investigated, n is the number of sampling points, the subscript eq indicates the equivalent parameter of the aggregation model while N indicates the rated value. As is shown from **Tables 1–3**, the average error comparison before, during and after grid fault are listed respectively for further analysis.

It can be seen from **Table 1** that for different wind speeds, when the collection line is a cable line, the results of the wind farm aggregation model match well with the detailed wind model, the average error of voltage, current and active power is within 0.12%, while the error of reactive power is within 0.05%, which can fully prove the correctness of the aggregation method proposed in this paper. As the wind speed increases, it can be seen that the magnitude of the error is also increasing. The reason is that the output parameter is increased with the increase of wind speed, but the base value used in the evaluation method is unchanged, which results in the increase of average error, but the increase is still within the normal range.

TABLE 3 | Average error after grid fault between SMA and detailed model.

Wind speed (m/s)	Average error/%			
	Voltage	Active power	Reactive power	Current
7	0.0642	0.00106	0.0241	0.00436
9	0.066	0.00145	0.0333	0.00542
11	0.0686	0.00138	0.0457	0.00832

Comparing **Table 1**, **Table 2**, and **Table 3**, it can be seen that the average error during grid fault process is larger than that before and after grid fault. The main reason is that the line parameters are calculated at the rated power for the convenience of simulation, during grid fault process, the output active power is less than that in steady state, which causes the loss on the line of the aggregated model to be different from detailed model.

Simulation Verification Between SMA and MMA Algorithm.

Wind speed of each wind turbine generator is randomly set to compare the aggregation accuracy between SMA and MMA

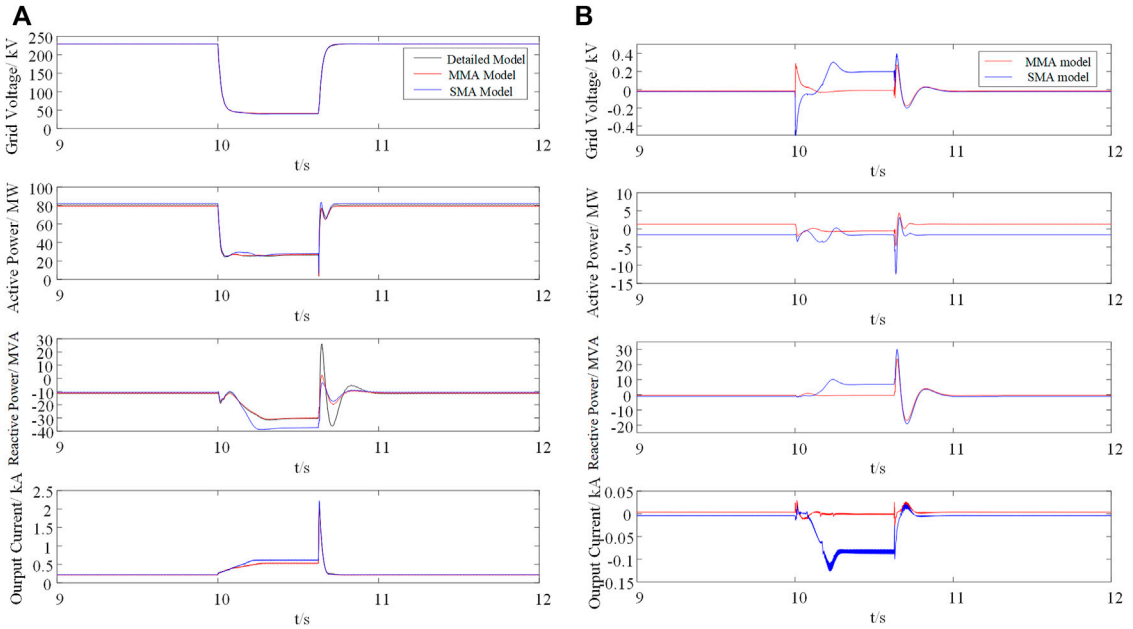


FIGURE 9 | Comparisons between SMA and MMA algorithm. **(A)** Comparison Results **(B)** Error Results.

algorithm. Wind speed for each WTG is selected as the main grouping index, as is shown in **Figure 2**, the wind speed of wind turbine generator determines the operation mode, so all wind turbine generators running in the same operation mode are grouped together to be aggregated into one WTG.

Simulation results are shown in **Figure 9** to compare the aggregation accuracy between detailed model, MMA model and SMA model. A three-phase symmetrical short-circuit fault occurs in the simulation at $t = 10$ s, the amplitude of grid voltage drop is 20% of the rated voltage. The first panel of **Figure 9A** is the grid voltage while the rest panels are output active power, reactive power and current. **Figure 9B** shows the error curve of PCC point voltage RMS, output active power, output reactive power and output current. Combining the two figures, it can be seen that the MMA model has higher accuracy than SMA model, MMA can better reflect the dynamic process of the detailed model in the dynamic process.

From the above simulation results, although the response trend of SMA model, MMA model and detailed model are basically the same, there are still dynamic errors during the whole process, so that a quantitative analysis is still needed to calculate the error before and during grid fault. The results are shown in the following table.

Comparing **Table 4** and **Table 5**, it can be seen that the MMA model has higher accuracy than SMA model. When wind turbines are in different operation modes, the SMA model is not sufficient enough to characterize the entire wind farm, the average error between MMA model and the detailed model are smaller than that between SMA model and the detailed model, showing that grouping wind farm according to wind speed can effectively improve the aggregation accuracy.

TABLE 4 | Average error before grid fault between SMA, MMA and detailed model.

Aggregation type	Average error/%			
	Voltage	Active power	Reactive power	Current
SMA	0.0895	0.74	0.42	0.55
MMA	0.0713	0.62	0.14	0.52

TABLE 5 | Average error during grid fault between SMA, MMA and detailed model.

Aggregation type	Average error/%			
	Voltage	Active power	Reactive power	Current
SMA	0.53	0.66	3.49	12.62
MMA	0.1	0.28	0.21	0.12

CONCLUSION

This paper proposes a comprehensive aggregation algorithm with the consideration of the power loss of offshore wind farm submarine cable. The aggregation algorithm includes the aggregation of WTG electrical parameters, pneumatic parameters as well as the integration of transmission line, the power equivalent principle is used to calculate all the aggregation parameters of wind farm. Detailed conclusions are:

1) The aggregated model can comprehensively reflect the dynamic characteristics of wind farm under different working conditions.
2) Simulation results verify that the proposed aggregation algorithm can match well with detailed model, while MMA model is more accurate than SMA to reflect the operation of

wind farm in various wind speed environment (Sanchez et al., 2012; Mercado-Vargas et al., 2015).

DATA AVAILABILITY STATEMENT

The raw data supporting the conclusions of this article will be made available by the authors, without undue reservation.

AUTHOR CONTRIBUTIONS

HS is responsible for the research on novel aggregation algorithm and analysis. XC is responsible for the research on novel aggregation algorithm and analysis together with HS. HY is responsible for the collection of wind farm parameter and the set-up of simulation platform. JZ is responsible for the collection of wind turbine generator parameter. YQ is responsible for the simulation of wind turbine generator and the novel aggregation algorithm. ZZ is responsible for the simulation of aggregated wind farm and the accuracy analysis of the aggregation algorithm.

FUNDING

Project Supported by the State Key Laboratory of Advanced Power Transmission Technology (SGTYHT/18-JS-206).

REFERENCES

Ali, M., Ilie, I.-S., Milanovic, J. V., and Chicco, G. S. (2013). Wind Farm Model Aggregation Using Probabilistic Clustering. *IEEE Trans. Power Syst.* 28, 309–316. doi:10.1109/TPWRS.2012.2204282

Badr, M. A., Atallah, A. M., and Bayoumi, M. A. S. (2015). Comparison between Aggregation Techniques for PMSG Wind Farm. *Energ. Proced.* 74, 1162–1173. doi:10.1016/j.egypro.2015.07.759

Badr, M. A., Atallah, A. M., and Bayoumi, M. A. (2015). Modifying the Aggregated Wind Farm Model with a Controller. *Adv. Energ. Res.* 3 (3), 133–142. doi:10.12989/eri.2015.3.3.133

Chowdhury, M. A., Hosseinzadeh, N., Billah, M. M., and Haque, S. A. (2010). Dynamic DFIG Wind Farm Model with an Aggregation Technique. *Int. Conf. Electr. Computer Eng. (ICECE 2010)* 2010, 330–333. doi:10.1109/ICELCE.2010.5700695

Conroy, J., and Watson, R. S. (2009). Aggregate Modelling of Wind Farms Containing Full-Converter Wind Turbine Generators with Permanent Magnet Synchronous Machines: Transient Stability Studies. *IET Renew. Power Gener.* 3, 39–52. doi:10.1049/iet-rpg:20070091

Ding, N., Lu, Z., Qiao, Y., and Min, Y. (2013). Simplified Equivalent Models of Large-Scale Wind Power and Their Application on Small-Signal Stability. *J. Mod. Power Syst. Clean. Energ.* 1, 58–64. doi:10.1007/s40565-013-0005-3

Dong, H., Bai, Y., Li, X., Li, H., and Ma, M. Aggregation Modeling of Wind Farms Based on Multi Machine Representation. Proceedings of the 2018 2nd IEEE Conference on Energy Internet and Energy System Integration (EI2), 1–6. October 2018. Beijing, China, doi:10.1109/EI2.2018.8582531

Du, W., Dong, W., Wang, H., and Cao, J. (2019). Dynamic Aggregation of Same Wind Turbine Generators in Parallel Connection for Studying Oscillation Stability of a Wind Farm. *IEEE Trans. Power Syst.* 34 (6), 4694–4705. doi:10.1109/TPWRS.2019.2920413

Feng Xue, F., Xiao-Fang Song, X.-F., Kang Chang, K., Tian-Ci Xu, T.-C., Feng Wu, F., and Yu-Qing Jin, Y.-Q. S. (July 2013). Equivalent Modeling of DFIG Based Wind Farm Using Equivalent Maximum Power Curve. Proceedings of the 2013 IEEE Power & Energy Society General Meeting, 1–5. Vancouver, BC, Canada, doi:10.1109/PESMG.2013.6672848

Fernandez, L. M., Garcia, C. A., Jurado, F., and Saenz, J. R. (June 2005). Aggregation of Doubly Fed Induction Generators Wind Turbines under Different Incoming Wind Speeds. Proceedings of the 2005 IEEE Russia Power Tech., 1–6. St. Petersburg, Russia, doi:10.1109/PTC.2005.4524685

Li, S., Liu, Z., and Jia, Y. Dynamic Aggregation of Doubly-Fed Induction Generators (DFIGs) for Stability Analysis of Wind Power Systems. *Proceedings of the IEEE Power and Energy Society General Meeting*, 1–6. July 2011. Detroit, MI, USA, doi:10.1109/PES.2011.6038990

Mercado-Vargas, M. J., Gómez-Lorente, D., Rabaza, O., and Alameda-Hernandez, E. (2015). Aggregated Models of Permanent Magnet Synchronous Generators Wind Farms. *Renew. Energ.* 83, 1287–1298. doi:10.1016/j.renene.2015.04.040

Muljadi, E., Butterfield, C. P., Ellis, A., Mechenbier, J., Hochheimer, J., Young, R., et al. (June 2006). Equivalencing the Collector System of a Large Wind Power Plant. Proceedings of the2006 IEEE Power Engineering Society General Meeting 1, 9. Montreal, QC, Canada, doi:10.1109/PES.2006.1708945

Sanchez, A. G., Molina, M. G., and Lede, A. M. R. (2012). Dynamic Model of Wind Energy Conversion Systems with PMSG-Based Variable-Speed Wind Turbines for Power System Studies. *Int. J. Hydrogen Energ.* 37, 10064–10069. doi:10.1016/j.ijhydene.2011.12.077

Slootweg, J. G., de Haan, S. W. H., Polinder, H., and Kling, W. L. S. (2003). General Model for Representing Variable Speed Wind Turbines in Power System Dynamics Simulations. *IEEE Trans. Power Syst.* 18, 144–151. doi:10.1109/TPWRS.2002.807113

Teng, W., Wang, X., Wang, X., Meng, Y., and Shi, W. (2019). An Improved Support Vector Clustering Approach to Dynamic Aggregation of Large Wind Farms. *Csee Jpes* 5, 2. doi:10.17775/CSEEJPES.2016.01600

Wang, P., Zhang, Z., Huang, Q., Wang, N., Zhang, X., and Lee, W.-J. (2018). Improved Wind Farm Aggregated Modeling Method for Large-Scale Power System Stability Studies. *IEEE Trans. Power Syst.* 33, 6332–6342. doi:10.1109/TPWRS.2018.2828411

Yang, D., Ban, L., Xiang, Z., Du, N., Zheng, B., and Wu, Z. S. (July 2012). An Aggregation Method of Wind Farm Model for Electromagnetic Transient Simulation Analysis. Proceedings of the 2012 IEEE Power Electronics and Machines in Wind Applications, 1–5. Denver, CO, USA, doi:10.1109/PEMWA.2012.6316356

Zou, J., Peng, C., Yan, Y., Zheng, H., and Li, Y. S. (2014). A Survey of Dynamic Equivalent Modeling for Wind Farm. *Renew. Sustainable Energ. Rev.* 40, 956–963. doi:10.1016/j.rser.2014.07.157

Conflict of Interest: Authors HY and JZ were employed by the State Key Laboratory of Advanced Power Transmission Technology of Global Internet Research Institute Energy Co., Ltd.

The remaining authors declare that the research was conducted in the absence of any commercial or financial relationships that could be construed as a potential conflict of interest.

The handling editor declared a shared affiliation, though no other collaboration, with several of the authors HS, XC, YQ, and ZZ at the time of the review.

Publisher's Note: All claims expressed in this article are solely those of the authors and do not necessarily represent those of their affiliated organizations, or those of the publisher, the editors and the reviewers. Any product that may be evaluated in this article, or claim that may be made by its manufacturer, is not guaranteed or endorsed by the publisher.

Copyright © 2021 Shao, Cai, Yan, Zhou, Qin and Zhang. This is an open-access article distributed under the terms of the Creative Commons Attribution License (CC BY). The use, distribution or reproduction in other forums is permitted, provided the original author(s) and the copyright owner(s) are credited and that the original publication in this journal is cited, in accordance with accepted academic practice. No use, distribution or reproduction is permitted which does not comply with these terms.

frontiers in Energy Research

ORIGINAL RESEARCH
published: 11 October 2021
doi: 10.3389/fenrg.2021.750796

A Learning-Based Bidding Approach for PV-Attached BESS Power Plants

Xiang Gao[1], Haomin Ma[1], Ka Wing Chan[2], Shiwei Xia[3] and Ziqing Zhu[2]*

[1]Industrial Training Centre, Shenzhen Polytechnic, Shenzhen, China, [2]Department of Electrical Engineering, The Hong Kong Polytechnic University, Kowloon, Hong Kong, SAR China, [3]State Key Laboratory of Alternate Electrical Power System with Renewable Energy Sources, School of Electrical and Electronic Engineering, North China Electric Power University, Beijing, China

Large-scale renewable photovoltaic (PV) and battery energy storage system (BESS) units are promising to be significant electricity suppliers in the future electricity market. A bidding model is proposed for PV-integrated BESS power plants in a pool-based day-ahead (DA) electricity market, in which the uncertainty of PV generation output is considered. In the proposed model, we consider the market clearing process as the external environment, while each agent updates the bid price through the communication with the market environment for its revenue maximization. A multiagent reinforcement learning (MARL) called win-or-learn-fast policy-hill-climbing (WoLF-PHC) is used to explore optimal bid prices without any information of opponents. The case study validates the computational performance of WoLF-PHC in the proposed model, while the bidding strategy of each participated agent is thereafter analyzed.

Keywords: BESS, bidding strategy, incomplete information game, multiagent reinforcement learning, PV, WoLF-PHC

OPEN ACCESS

Edited by:
Yaxing Ren,
University of Warwick,
United Kingdom

Reviewed by:
Xueqian Fu,
China Agricultural University, China
Lei Gan,
Hohai University, China

****Correspondence:***
Haomin Ma
mahaomin@szpt.edu.cn

Specialty section:
This article was submitted to Smart Grids, a section of the journal Frontiers in Energy Research

Received: *31 July 2021*
Accepted: *20 August 2021*
Published: *11 October 2021*

Citation:
Gao X, Ma H, Chan KW, Xia S and Zhu Z (2021) A Learning-Based Bidding Approach for PV-Attached BESS Power Plants. Front. Energy Res. 9:750796. doi: 10.3389/fenrg.2021.750796

INTRODUCTION

The share of photovoltaic (PV) installations experiences an exponential growth worldwide and accounts for most of the electricity supply of renewable energy (Zucker and Hinchliffe, 2014). However, the actual output of PV power may be different from the scheduled production, which brings an inevitable challenge in power system real-time balancing. Battery energy storage system (BESS) units can deal with the uncertainty of PV production by the flexible up-and-down regulation capability (Li et al., 2013). Hence, the combination of PV farms and BESS sets will be a promising form of virtual power plant, which will actively participate in the future energy spot market with more deregulated paradigms. Thus, it is necessary to investigate the decision making of such PV–BESS generation as prosumers in the market.

In the work of Shafie-khah and Catalao (2015) and Shafie-khah et al. (2015), bidding strategies of large-scale renewable resources in oligopoly electricity markets were formulated as mathematical programming with equilibrium constraints (MPEC) with the uncertainty of market competitors considered using incomplete information dynamic game theory. However, the equilibrium of such model is often difficult to be obtained because of the computational burden, and the complexity of these models increases with consideration of numerous complicated real-world assumptions and constraints (Ventosa et al., 2005). In this way, this complex set of equations is required to be solved again to find the market equilibrium in the new situation (Salehizadeh and Soltaniyan, 2016/04). With the development of artificial intelligence (AI) techniques in recent years, AI algorithms have been applied in the power system to deal with various problems such as renewable energy forecasting (Zeng et al., 2020), price prediction (Kebriaei et al., 2015), and energy management (Wang et al., 2019). The electricity market can be modeled as an AI-enabled energy platform, where market

participants are regarded as AI agents. Agents make bidding decisions by gradually learning through repetitive communication with the AI-enabled market platform. The common AI learning technologies applied in the electricity market refer to heuristic search, artificial neural network, and reinforcement learning. Market participants make bidding decisions with shuffled frog-leaping algorithm (Jonnalagadda and DullaMallesham, 2013), genetic algorithm (Praça et al., 2003), and fuzzy adaptive gravitational search algorithm (Vijaya Kumar et al., 2013) by performing a heuristic search. Some reinforcement learning methods are used to address bidding problems, for example, the traditional Q-learning algorithms in the work of Najafi et al. (2019) and a deep reinforcement learning-based approach (Ye et al., 2019). However, market players develop the bidding strategy by using the abovementioned methods without consideration of other competitors. In the real-world electricity market, each agent achieves its purpose in response to other agents' bidding behaviors. Considering this, a multiagent multiobjective architecture with reinforcement learning is proposed to minimize energy costs for EV owners, in which agents should communicate with all friendly agents and get their rewards functions (Da Silva et al., 2019). The Markov game approach is utilized to update multiagent competitive bidding strategies in the work of Rashedi et al. (1049), while it is necessary to obtain other agents' previous bidding. However, market participants are not willing to share neither perfect nor part information in practice. The future research is expected to develop a bidding strategy obtained by a fully distributed online training procedure without any information communicated among agents.

Two bidding strategies are formulated considering the uncertainty of PV prediction in the work of Bo et al. (2017). The bidding strategy of battery storage systems in the secondary control reserve market is investigated in the work of Merten et al. (2020). Chen et al. (2021) studied the optimal bidding strategy of a PV-BESS VPP in frequency control ancillary services markets. A two-stage bidding strategy of households PV-BESSs is proposed in peer-to-peer market (Zhang et al., 2019). Niknam et al. (2012) introduced a bidding strategy of combined PV-storage systems in day-ahead (DA) market, in which PV-storage systems are considered as price takers. So far, to the best of the authors' knowledge, there is little research considering PV-attached BESS power plants in a pool-based DA wholesale market as oligopolists to make their bidding decisions without any information of opponents. Furthermore, prior research studies consider aggregated PV-BESSs developing bidding strategy with either complete or part information of other strategic players. In other words, previous work cannot deal with the situation that each strategic participant of PV-BESSs does not share any information with other rivals. This challenging issue is required to be addressed properly. In this study, we propose a DA bidding strategy of PV-attached BESS power plants to maximize their benefits by self-bidding not relied on any information of competitors. A multiagent reinforcement learning win-or-learn-fast policy-hill-climbing (WoLF-PHC) is used to solve the proposed bidding problem. The main contributions of this study are summarized as follows:

1) A stochastic bidding strategy model of PV-attached BESS power plants in a pool-based DA wholesale market is developed, to maximize revenues of PV-attached BESS power plants considering the uncertainty of potential maximum PV power production
2) A multiagent stochastic game framework with incomplete information is used to describe the proposed bidding model, and the proposed model is then solved by a multiagent reinforcement learning *WoLF-PHC* without any opponents' information
3) The validity of the proposed model and the *WoLF-PHC* algorithm is validated by the modified IEEE 6-bus and 118-bus systems

The remaining part of this article is arranged as follows. ***Proposed Bidding Model*** introduces the proposed bilevel stochastic bidding model. In ***Methodology***, the *WoLF-PHC* is used to solve the proposed bidding problem. Simulation results and analysis are conducted in ***Case Study***, while ***Conclusion*** concludes the whole article.

PROPOSED BIDDING MODEL

The DA wholesale pool-based market is considered in this study. Strategic participants PV-attached BESS power plants submit bid prices and power capacities to the market operator (MO) on an hourly basis. The MO runs the market clearing process to confirm the locational marginal pricing (LMP) and scheduled power production of PV-attached BESS power plants. The overall structure figure of the proposed model is presented in **Figure 1**.

The assumptions of the proposed market model are as follows:

1) Uncertainty of potential maximum PV power production is considered in this study, which is dealt with a scenario-based stochastic optimization method. The uncertainty is modeled as a set of scenarios derived from a scenario generation process on account of the roulette wheel mechanism in the work of Niknam et al. (2012) and an efficient scenario-reduction method in the work of Morales et al. (2009). In this way, a stochastic optimization problem can be converted into a deterministic one and solved with many methods.
2) PV-attached BESS power plants are assumed as large-scale strategic players in the wholesale market. Each PV-attached BESS power plant makes a bidding decision to increase its revenue.
3) Loads submit their bid prices to MO but not strategically. The bid prices are their marginal cost prices which are open to strategic PV-attached BESS power plants.
4) The transmission network only considers DC optimal power flow (DC-OPF) without losses.
5) Bertrand model of competition is considered in the proposed work with bidding prices as decision variables. Although the cournot model and the supply function equilibrium (SFE) model, in which a quantity and a pair of bid price and quantity are seperately chosen to bid, can be considered to make bidding decision, the cournot model and SFE model are required to be formulated using mathematical programming approaches, which makes solving difficult (Shafie-khah and

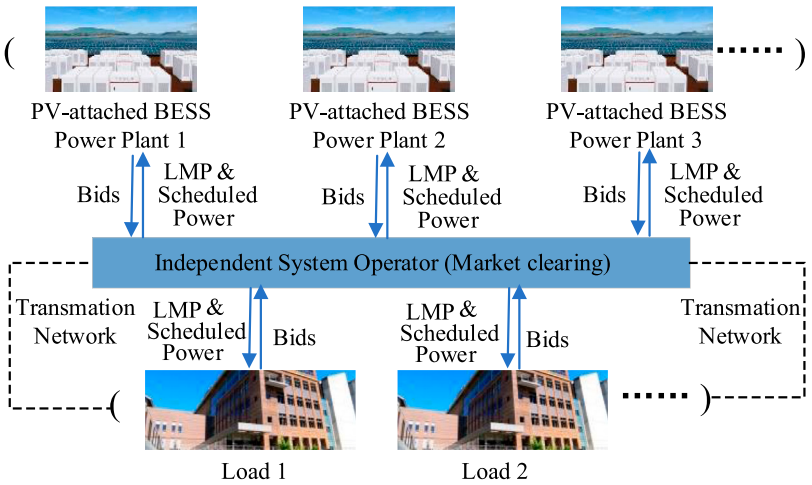


FIGURE 1 | Overall structure figure of the proposed model.

Catalao, 2015; Shafie-khah et al., 2015). There is no such limitation in the Bertrand competition model, and thus, it is selected in this study.

A stochastic bidding model is introduced where the total cost is minimized for the MO completing the market clearing, while respective revenues are maximized for strategic participants PV-attached BESS power plants.

Market Clearing Model

In the market clearing process, suppliers PV-attached BESS power plants and loads first submit their bid prices $\pi^{bid}_{co,t}$ and $\pi^{D}_{d,t}$, respectively, to the MO. The MO then completes market clearing by minimizing the total cost relied on the OPF. At last, the dispatched power production of PV-attached BESS power plants $P^{CO}_{co,\alpha,t}$ and LMP $\lambda_{n,\alpha,t}$ will be returned to maximize revenues of strategic PV-attached BESS power plants.

Minimize

$$\sum_{\alpha\in N_\alpha}\tau_\alpha\cdot\left(\sum_{co\in\Omega^{CO}_n}\pi^{bid}_{co,t}\cdot P^{CO}_{co,\alpha,t}-\sum_{d\in\Omega^{D}_n}\pi^{D}_{d,t}\cdot P^{D}_{d,t}\right) \tag{1}$$

subject to

$$P^{CO}_{co,\alpha,t}-\sum_{m\in\Omega^{N}_n}B_{nm}\cdot\left(\theta_{n,\alpha,t}-\theta_{m,\alpha,t}\right)=P^{D}_{d,t}:\ \lambda_{n,\alpha,t},\forall n,t,\alpha, \tag{1.1}$$

$$P^{PV}_{pv,\alpha,t}+P^{BE}_{be,\alpha,t}=P^{CO}_{co,\alpha,t}, \tag{1.2}$$

$$P^{CO}_{co,\alpha,t}\geq 0. \tag{1.3}$$

$$0\leq P^{PV}_{pv,\alpha,t}\leq P^{PV,\max}_{pv,\alpha,t},\forall pv,t,\alpha, \tag{1.4}$$

$$-P^{BE,\min}_{be}\leq P^{BE}_{be,\alpha,t}\leq P^{BE,\max}_{be},\forall be, \tag{1.5}$$

$$-f^{\max}_{nm}\leq B_{nm}\cdot\left(\theta_{n,\alpha,t}-\theta_{m,\alpha,t}\right)\leq f^{\max}_{nm},\forall n,m\in\Omega^{N}_n,t,\alpha, \tag{1.6}$$

$$\theta_{n,\alpha,t}=0,\forall t,\alpha,n:\ ref, \tag{1.7}$$

$$-\pi\leq\theta_{n,\alpha,t}\leq\pi,\forall t,\alpha,n\backslash n:\ ref, \tag{1.8}$$

$$SOC^{\min}\leq SOC_{be,\alpha,t}\leq SOC^{\max},\forall be,t,\alpha, \tag{1.9}$$

$$SOC_{be,\alpha,t}=SOC_{be,\alpha,t-1}-\left(P^{BE}_{be,\alpha,t}/\eta_{dis}\cdot\Delta t/E^{\max}_{be}\right),\forall be,t,\alpha,P^{BE}_{be,\alpha,t}\geq 0, \tag{1.10.1}$$

$$SOC_{be,\alpha,t}=SOC_{be,\alpha,t-1}-\left(P^{BE}_{be,\alpha,t}\cdot\eta_c\cdot\Delta t/E^{\max}_{be}\right),\forall be,t,\alpha,P^{BE}_{be,\alpha,t}<0. \tag{1.10.2}$$

The objective of **Eq. 1** is to minimize the total cost. The first term is the costs of purchasing electricity from PV-attached BESS power plants $\pi^{bid}_{co,t}\cdot P^{CO}_{co,\alpha,t}$, while the second term represents the revenues of selling electricity to load demands $\pi^{D}_{d,t}\cdot P^{D}_{d,t}$. $P^{CO}_{co,\alpha,t}$ and $P^{D}_{d,t}$ are the power output of the *co*th PV-attached BESS power plant and the *d*th load in each hour. α indexes scenarios of PVs, and τ_α is the corresponding probability. The constraint of **Eq. 1.1** is the power production and consumption balance for node *n* with a dual variable $\lambda_{n,\alpha,t}$ donating the LMP, where B_{nm} is the susceptance of the line connecting nodes n and m, and θ is the voltage angle. **Eq. 1.2** represents the scheduled power of PV-attached BESS power plants $P^{CO}_{co,\alpha,t}$ supplied from PVs $P^{PV}_{pv,\alpha,t}$ and BESS units $P^{BE}_{be,\alpha,t}$. The scheduled power of PV-attached BESS power plants should be nonnegative, as shown in **Eq. 1.3**. Maximum and minimum capacity limitation for PV units and BESS units are considered in **Eq. 1.4** and **Eq. 1.5** respectively. Inequality **Eq. 1.6** limits the thermal capacity of the transmission line f^{max}_{nm}. **Eq. 1.7** and inequality **Eq. 1.8** set voltage angle limits at the slack bus and other buses, respectively. Inequality **Eq. 1.9** represents the SOC range of the BESS at the present hour, while constraints **Eq. 1.10.1** and **Eq. 1.10.2** indicate time-series SOC formulation of the BESS at present and the previous hours. η_c and η_{dis} are the charging and discharging efficiency of the BESS separately. E^{max}_{be} refers to the maximized power capacity of BESS.

The PV-Attached BESS Power Plant Revenue Model

The strategic player revenue for the *co*th PV-attached BESS power plant is maximized and represented by scenarios α with corresponding probabilities τ_α and represented in **Eq. 2**, where

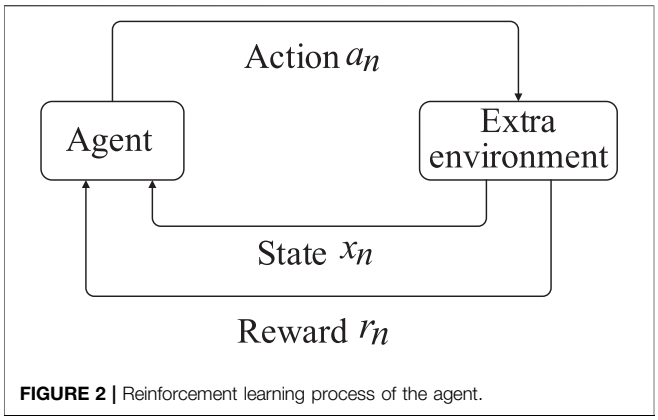


FIGURE 2 | Reinforcement learning process of the agent.

LMP $\lambda_{n,\alpha,t}$ and scheduled power output of PV-attached BESS power plant $P^{CO}_{co,\alpha,t}$ are obtained from the market clearing process. The revenue of a PV-attached BESS power plant in **Eq. 2** includes the income of selling electricity to the electricity market $\lambda_{n,\alpha,t} \cdot P^{CO}_{co,\alpha,t}$ and the battery degradation cost $(\mathrm{K}_b/\varpi_b) \cdot |P^{E}_{be,\alpha,t}|$. K_b and ϖ_b are battery lifetime and battery capital cost, respectively. Absolute-value function in **Eq. 2** can be addressed by a linear programming simplex method in the work of Hill and Ravindran (1975).

Maximize

$$R_{co} = \sum_{\alpha \in N_\alpha} \tau_\alpha \cdot \left(\lambda_{n,\alpha,t} \cdot P^{CO}_{co,\alpha,t} - (\mathrm{K}_b/\varpi_b) \cdot |P^{E}_{be,\alpha,t}|\right). \quad (2)$$

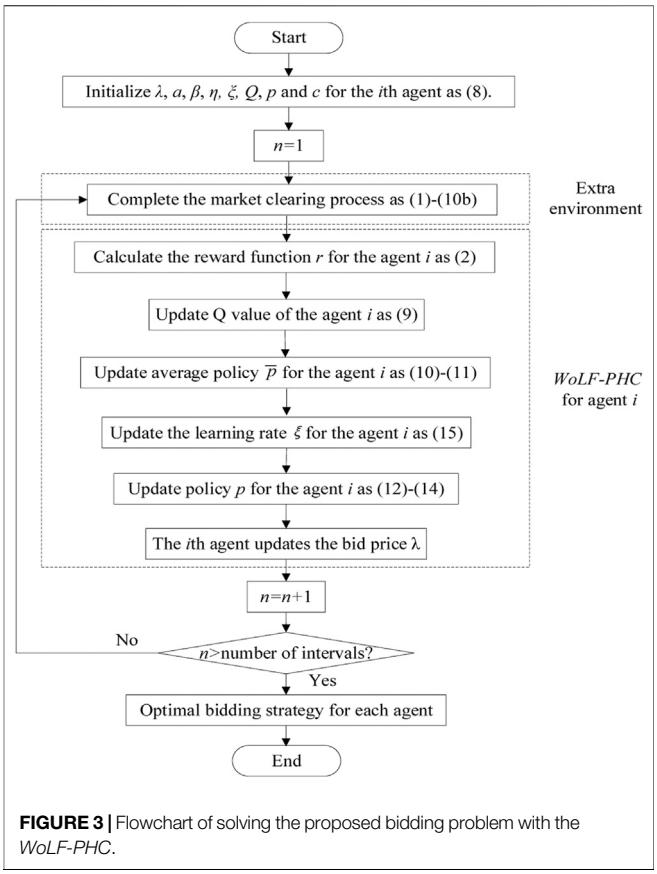


FIGURE 3 | Flowchart of solving the proposed bidding problem with the *WoLF-PHC*.

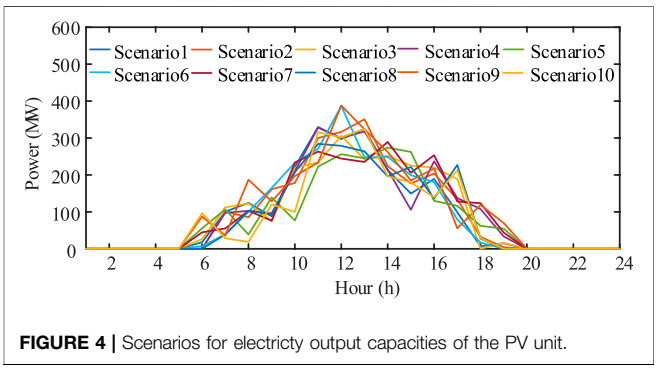


FIGURE 4 | Scenarios for electricty output capacities of the PV unit.

METHODOLOGY

Introduction to Multiagent Reinforcement Learning

The proposed bidding model brings fundamental problems: how the strategic market participants work as AI agents to learn and determine the optimal bid prices? This research implies that, in the electricity market, it is possible to train agents with AI algorithms to better solve the optimization of bidding problems. The common core techniques for AI are classified as the artificial neural network, reinforcement learning, genetic algorithms, and multiagent systems (Xu et al., 2019).

In reinforcement learning (RL), the agent makes its decision in terms of communication with the external environment as in **Figure 2** (Hwang et al., 2017). First, the agent perceives a state x_n and a reward r_n based on its past action a_{n-1} from the environment at each step n. Then, its learning is reinforced by comparing the returned scalar reward signal r_n every time with the one in last round r_{n-1} for evaluating the quality of its environment-based behavior. Specifically, the probability of this potential action p will be increased if the compared result is better and decreased if conversely. Last, the highest probability action a_n would be chosen through the learning by itself. There are three main classes of methods that made use of RL principles, namely, dynamic programming methods, Monte Carlo techniques, and temporal difference learning methods (Tellidou and Bakirtzis, 2006). The premise of using dynamic programming is the complete availability of system information. Although Monte Carlo techniques could cope with unknown environments, the solution process is very time consuming and a long time would be needed to wait for the final outcome of learning. Temporal difference learning methods used to learn from an unknown environment after every step without the final result are more suitable for the problem presented in this study, and Q-learning is one of such most frequently used RL approaches. In Q-learning, sets of states g and actions k of each agent are represented as $\chi = \{x_1, x_2, \ldots, x_g\}$ and $\Lambda = \{a_1, a_2, \ldots, a_k\}$. Then Q values are updated in the nth step Eq. 3,

TABLE 1 | | Parameters of the BESS.

Probability	1	2	3	4	5	6	7	8	9	10
τ_α	0.2340	0.1800	0.1110	0.0480	0.0220	0.0110	0.0100	0.0060	0.2570	0.1210

TABLE 2 | Parameters of the BESS.

Parameter	SOC^{max} (pu)	SOC^{min} (pu)	η_c	η_{disc}	E_{be}^{max} (MWh)
Value	0.9	0.1	0.9	0.85	3000

TABLE 3 | Parameters of the *WoLF-PHC*.

Parameter	α	β	ξ_w	ξ_l
Value	0.1	0.7	0.01	0.02

in which $x_n \in \chi$, $a_n \in \Lambda$, and r_n refers to each pair (x_n, a_n). α and β are the learning rate and discount factor separately, which are both in the range (0,1].

$$Q_{n+1}(x_n, a_n) \leftarrow (1-\alpha)Q_n(x_n, a_n) + \alpha\left(r_n + \beta \max_{a_n'} Q_{n+1}\left(x_n, a_n'\right)\right). \tag{3}$$

Multiagent reinforcement learning (MARL) is developed from the single-agent RL with adding the game relationship between all agents, which are similar to strategic players in the electricity market. Let a tuple (K, χ, Λ, P, r) represent a multiagent game framework, where $K = \{1, 2, \ldots, k\}$ is a set of agents and χ is a set of states $\{x_g\}$. The sects of actions of each agent a_i are described as $a_i = \{aa_{min}, \ldots, aa_{max}\}$ in $\Lambda = \{a_1, \ldots, a_i, \ldots, a_k\}$. P refers to the transition function written as $\chi \times \Lambda \times \chi \rightarrow [0, 1]$. $r = \{r_1, \ldots, r_i \ldots, r_k\}$ is the set of reward functions of all agents, where r_i: $(x_g, a_i) \rightarrow \mathcal{R}$ implies the ith agent's reward function with a pair (x_g, a_i). In each episode, the agent observes the state $x_g \in \chi$ and selects to execute the action a_i relying on an appropriate policy of learning algorithm and then steps into the next state $x_g \in \chi$.

Assumptions and Definitions

The proposed bidding model in ***Proposed Bidding Model*** can be expressed as the multiagent game framework. We consider agents

$$K = \{co \in \Omega_n^{CO}\}, \tag{4}$$

where K is a set of strategic participants PV-attached BESS power plants, states

$$X = \{x_{co}\}_{co \in \Omega_n^{CO}}, \tag{5}$$

where χ is defined as different levels of PV-attached BESS power plants' capacities. $P_{co,\alpha,t}^{CO}$ is obtained from the market clearing, which would show that a state x_{co} is selected after the communication with the extra environment, and actions

$$\Lambda = \{a_i\}. \tag{6}$$

Λ is used to update bid price $\{\pi_{co,t}^{bid}\}_{co \in \{a_j\}}$.

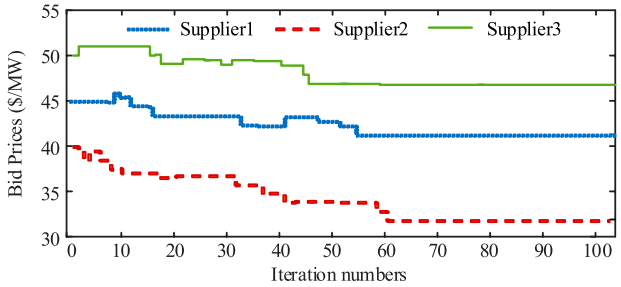


FIGURE 5 | Bid prices of three suppliers PV-attached BESS power plants in the 6-node system.

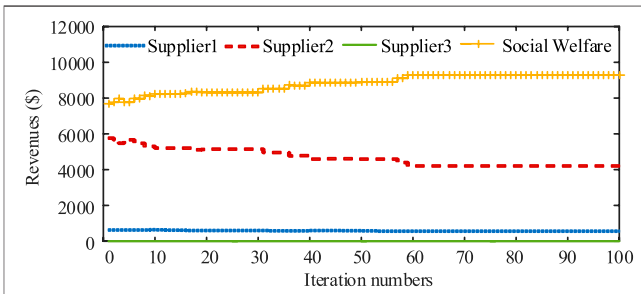


FIGURE 6 | Revenues of three suppliers PV-attached BESS power plants in the 6-node system.

Reward function: r_i $(x_{co}, a_i) \rightarrow \mathcal{R}$ is the revenue of the coth player with the bid price $\pi_{co,t}^{bid}$ in the PV-attached BESS power plant's capacity level x_{co}.

In this way, K, χ, Λ, and r have been defined. The optimal policy p, which is used to choose an action in current state, is required to find. Here, a suitable algorithm win-or-learn-fast policy-hill-climbing (*WoLF-PHC*) would be introduced in this study.

The Step-by-Step Implementation of the Proposed Model With WoLF-PHC

The *WoLF-PHC* is developed from the *Q*-learning, which requires two learning parameters with winning ξ_w and losing ξ_l. The convergence is enhanced with these two learning rates. It is defined that ξ_ω should be smaller than ξ_l. If the agent loses, it will learn faster with ξ_l to update its action. On the contrary, the agent will keep caution with ξ_ω when it wins. The evaluation criterion of winning or losing is comparing the expected revenue and the average profit, in which the average strategy replaces the original equilibrium policy. The *WoLF-PHC* algorithm of agent i is represented as follows.

Algorithm 1. The *WoLF-PHC* for agent *i*.

(1) Let $\alpha \in (0,1]$, $\xi_\omega < \xi_l \in (0,1]$ be learning rate, $\eta \in (0,1]$ be discount factor. Initialize,

$$Q_i(x,a) \leftarrow 0,\ p_i(x,a) \leftarrow 1/|A|,\ c(x_{co}) \leftarrow 0 \tag{8}$$

(2) Repeat, in the nth episode,

(a) According to the policy $p_i(x_{co(n-1)}, a_{in})$, choose the action a_{in} under the past state $x_{co(n-1)}$.

(b) Observing the reward r_{in} and the current state $x_{co(n)}$, and updating Q_i,

$$Q_i(x_{co(n-1)}, a_{in}) \leftarrow (1-\alpha) Q_i(x_{co(n-1)}, a_{in}) + \alpha(r_{in} + \beta \max_{a_{in}'} Q_i(x_{co(n)}, a_{in}')) \tag{9}$$

(c) Updating the average polices $\overline{p}_i(x_{i(n-1)}, a_{in}')$,

$$c(x_{co}) \leftarrow c(x_{co}) + 1 \tag{10}$$

$$\overline{p}_i(x_{co(n-1)}, a_{in}') \leftarrow \overline{p}_i(x_{co(n-1)}, a_{in}') + \frac{1}{c(x_{co})}(p_i(x_{co(n-1)}, a_{in}') - \overline{p}_i(x_{co(n-1)}, a_{in}')), \forall a_{in}' \in A_i \tag{11}$$

(d) Updating the policy $p_i(x_{co(n-1)}, a_{in})$,

$$p_i(x_{co(n-1)}, a_{in}) \leftarrow p_i(x_{co(n-1)}, a_{in}) + \Delta_{x_{co(n-1)} a_{in}} \tag{12}$$

$$\Delta_{x_{co(n-1)} a_{in}} = \begin{cases} -\xi_{x_{co(n-1)} a_{in}}, if a_{in} \neq \arg\max_{a_{in}'} Q_i(x_{co(n-1)}, a_{in}') \\ \sum_{a_{in}' \neq a_{in}} \xi_{x_{co(n-1)} a_{in}'}, otherwise \end{cases} \tag{13}$$

where

$$\xi_{x_{co(n-1)} a_{in}} = \min(p_i(x_{co(n-1)}, a_{in}), \xi_{in}/(|A|-1)) \tag{14}$$

$$\xi_{in} = \begin{cases} \xi_\omega, if \sum_{a_{in}'} p_i(x_{co(n-1)}, a_{in}') Q_i(x_{co(n-1)}, a_{in}') > \sum_{a_{in}'} \overline{p}_i(x_{co(n-1)}, a_{in}') Q_i(x_{co(n-1)}, a_{in}') \\ \xi_l, otherwise \end{cases} \tag{15}$$

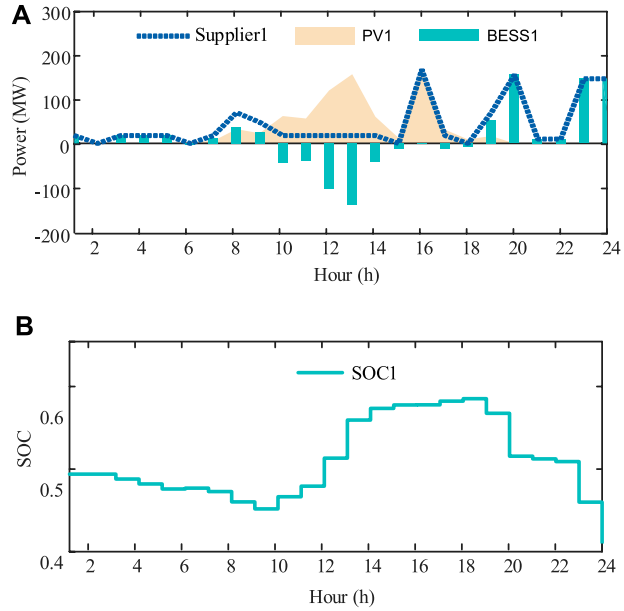


FIGURE 7 | (A) Scheduled power output of PV unit 1, BESS 1, and PV-attached BESS power plant 1 in the 6-node system. **(B)** SOC of PV-attached BESS power plant 1 in the 6-node system.

Specific learning procedures for the *i*th PV-attached BESS power plant strategically bidding with *WoLF-PHC* are described in following steps. 1) Bid price λ_i, parameters α, β, η, ξ_w, and ξ_l, and Q_i, p_i, and $c(x_{co})$ are initialized. 2) In the *n*th episode, market clearing is completed as (1)–(10b). After that, the reward function of the *i*th agent r_{in} can be obtained as (2). Then, Q_i, $\overline{p}_i$, ξ, and p_i are updated in sequence as (9), (10)–(11), (15), and (12)–(14), individually. Last, the bid price of *i*th agent λ_i is updated according to the updated policy p_i. 3) $n = n + 1$ is set, and step 2) is repeated until $n >$ number of intervals. The abovementioned implementation of *WoLF-PHC* for solving PV-attached BESS power plants' bidding problems in ***Proposed Bidding Model*** is shown in **Figure 3**.

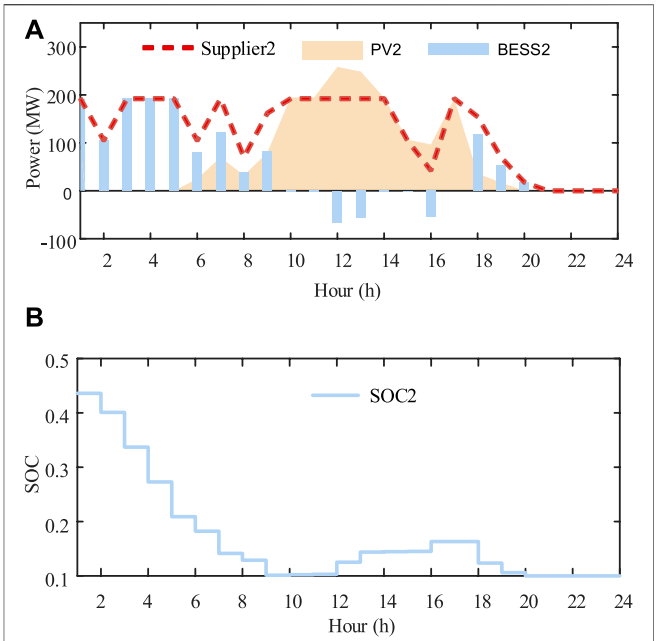


FIGURE 8 | (A) Scheduled power output of PV unit 2, BESS 2, and PV-attached BESS power plant 2 in the 6-node system. **(B)** SOC of PV-attached BESS power plant 2 in the 6-node system.

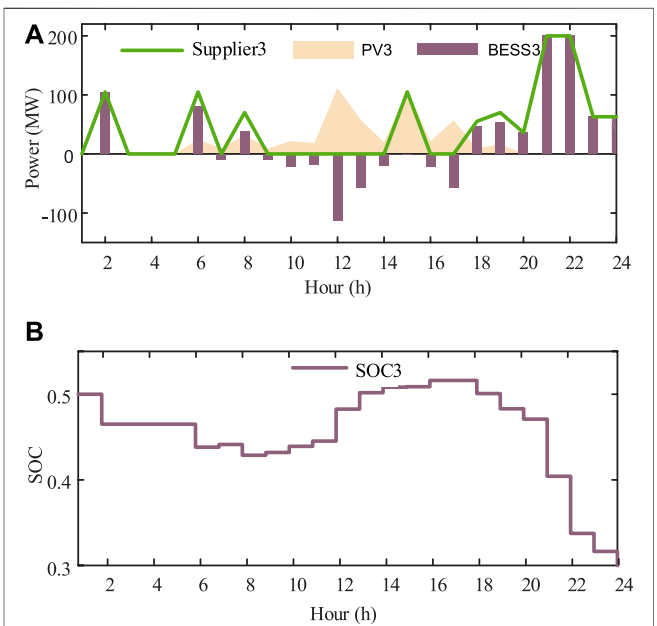


FIGURE 9 | (A) Scheduled power output of PV unit 3, BESS 3, and PV-attached BESS power plant in the 6-node system. **(B)** SOC of PV-attached BESS power plant 3 in the 6-node system.

CASE STUDY

The proposed model is tested on the IEEE 6-node and 118-node systems. Scenarios for electricty output capacities of the

TABLE 4 | Revenues comparison of the proposed model, PV unit, and BESS for 24 h.

Market model		Revenue ($)	Social welfare ($)
Proposed model	PV-attached BESS Power Plant 1	43890.25	79943.1
	PV-attached BESS Power Plant 2	28749.12	
	PV-attached BESS Power Plant 3	8340.97	
Model of PV units as strategic players	PV unit 1	24981.01	3790.25
	PV unit 2	11979.48	
	PV unit 3	3590.6	
Model of BESSs as strategic players	BESS 1	3590.23	4219.76
	BESS 2	1507.43	
	BESS 3	5289.04	

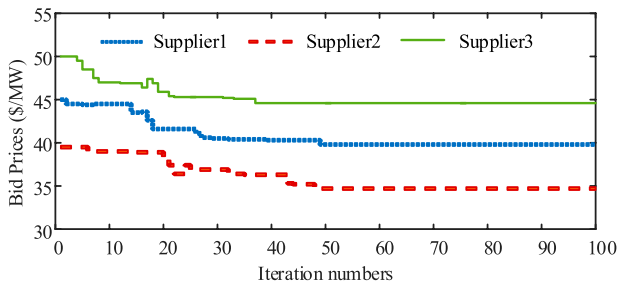


FIGURE 10 | Bid prices of three suppliers PV-attached BESS power plants within increased load in the 6-node system.

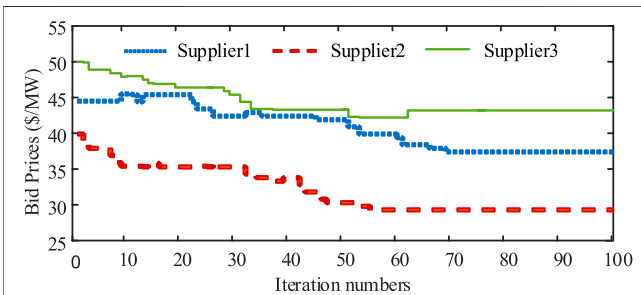


FIGURE 11 | Bid prices of three suppliers PV-attached BESS power plants within reduced load in the 6-node system.

PV unit are derived from historical data from the work of Agathokleous and Steen (2019) and represented in **Figure 4** after scenario generation and deduction (Niknam et al., 2012) (Morales et al., 2009). 10 corresponding probabilities are shown in **Table 1**. Parameters of BESS and *WoLF-PHC* are shown in **Table 2** and **Table 3**, respectively. We run all simulations in MATLAB with a 1.6 GHz Intel Core i5-5250U computer.

Case 1

In the 6-node system, three suppliers PV-attached BESS power plants are located in buses 1–3 separately and three loads are connected to buses 4-6 individually. Bid prices of loads are assumed as constant in 24 h, which are 59.4 $/MWh, 50.8 $/MWh, and 39.7 $/MWh (Zugno et al., 2013).

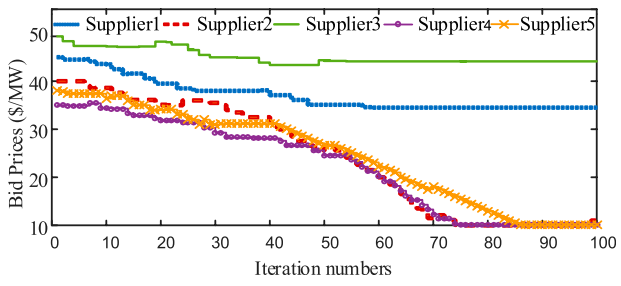


FIGURE 12 | Bid prices of three suppliers PV-attached BESS power plants within increased players in the 6-node system.

Three suppliers PV-attached BESS power plants represent three strategic participants in this case. According to the parameter setting given above, their bid prices and revenues are shown in **Figure 5** and **Figure 6**. It demonstrates that *WoLF-PHC* could be used to, respectively, optimize bid prices for the competitive PV-attached BESS power plants. During this process, each strategic participant obtains optimal bid price only relying on the communication with the extra environment ISO. Rivals' cost functions, bidding information, and historical bidding information are not open to the agent. We protect the personal information of market players with the *WoLF-PHC*. Three PV-attached BESS power plants' power outputs and SOC are, respectively, shown in **Figures 7–9**. There is no solar power output in 1:00-5:00 and 20.00–23:00, and BESSs supply loads by discharging, while PV units satisfy the requirement of load demand and charging of BESSs during 6:00–19.00.

Comparison

The proposed bidding model of the PV-attached BESS power plant is compared with the other two models, which consider only PV units and only BESSs as strategic market participants. Revenue comparison of the proposed model, PV unit, and BESS for 24 h is represented in **Table 4**. Due to the limited light time and the degradation of the battery, revenues of PV unit and BESS separately as the strategic player are both lower than the profit of the proposed model. The social welfare of the proposed model is higher than that of the other two models.

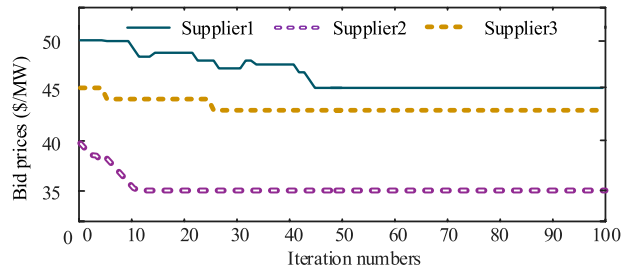


FIGURE 13 | Bid prices of three suppliers PV-attached BESS power plants in the 118-node system.

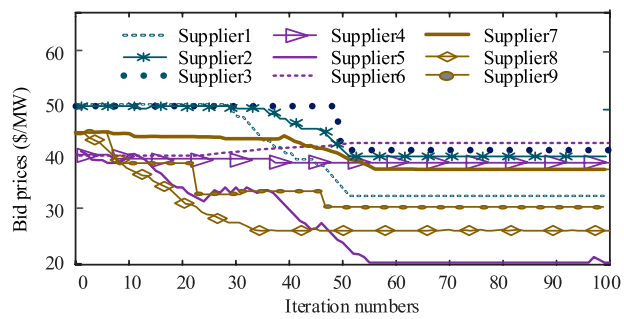


FIGURE 14 | Bid prices of nine suppliers PV-attached BESS power plants in the 118-node system.

Case 2

In this case, results of bidding prices are analyzed with different load levels and different numbers of strategic players. First, the total load demand is set equal to the total capacity of the three strategic players. **Figure 10** represents bid prices of three suppliers in 100 iterations. Compared with bid prices in **Figure 5**, bid prices of three participants are higher in **Figure 10**. The lack of competition among market participants shows that they are not required to lower their bid prices for selling more. On the contrary, each player tries to raise its bid price for earning more profits. Then, total demand is set as half of the load in case 1. Bidding results are shown in **Figure 11**. More competition drives all participants to reduce their bid prices than those in **Figure 5**. Last, the number of strategic players is increased to five and the corresponding curves of bidding prices in 100 iterations are represented in **Figure 12**. Suppliers adopt relatively conservative behaviors so that their price levels are lower than those in **Figure 5**.

Case 3

The proposed model is applied in the IEEE 118-node system with three and nine PV-attached BESS ower plants, respectively, in this case. The three suppliers of PV-attached BESS power plants are located in node 12, 29, and 98, which are then individually duplicated to be three strategic players in the same nodes and then become nine players. The convergences of bidding prices for three suppliers and nine suppliers are shown in **Figure 13** and **Figure 14** separately, which imply that each agent can get its convergent bid price with *WoLF-PHC* in a larger power system with more participants. In this process, any information of opponents is not required. Each supplier communicates just with the ISO in the clearing process, which ensures the privacy of suppliers. Additionally, the overall bid level of nine strategic suppliers in **Figure 14** is lower compared with three suppliers in **Figure 13**,. This is because more competition compels market players to reduce bid prices for selling more.

CONCLUSION

A bidding model with incomplete information for considering the uncertainty of generation output of PV units is proposed. A MARL algorithm *WoLF-PHC* is used to explore optimal bid prices for strategic PV-attached BESS power plants, and it protects personal privacy and respects the autonomy of market players. Three cases are implemented in the modified IEEE 6-node system and a larger IEEE 118-node system, with some conclusions represented as follows: 1) multiple strategic market players can obtain their bid prices individually with the *WoLF-PHC* in the electricity markets; 2) compared with models of PV unit and BESS as strategic participants independently, the revenue of proposed model is higher; and 3) decreased load and increased numbers of market players bring more competition, resulting in strategic suppliers bidding at lower prices.

DATA AVAILABILITY STATEMENT

The original contributions presented in the study are included in the article/supplementary material; further inquiries can be directed to the corresponding author.

AUTHOR CONTRIBUTIONS

All authors listed have made a substantial, direct, and intellectual contribution to the work and approved it for publication.

FUNDING

This work was jointly supported by the Shenzhen Polytechnic, the Hong Kong Polytechnic University, the Natural Science Foundation of Guangdong Province, 2020A1515010461, the National Natural Science Foundation of China (52077075), and the Jiangsu Basic Research Project (BK20180284).

REFERENCES

Agathokleous, C., and Steen, D. (2019).. IEEE Milan PowerTechIEEE, 1–6. doi:10.1109/ptc.2019.8810651 Stochastic Operation Scheduling Model for a Swedish Prosumer with PV and BESS in Nordic Day-Ahead Electricity Market2019.

Bo, T., Ishizaki, T., Koike, M., Yamaguchi, N., and Imura, J.-i. (2017). *56th Annual Conference of the Society of Instrument and Control Engineers of Japan*. SICE) IEEE, 293–298. doi:10.23919/sice.2017.8105613 Optimal Bidding Strategy for Multiperiod Electricity Market with Consideration of PV Prediction Uncertainty 2017.

Chen, W., Qiu, J., Zhao, J. H., Chai, Q., and Dong, Z. Y. (2021). IEEE Transactions on Smart Grid. doi:10.1109/tsg.2021.3053000 Bargaining Game-Based Profit Allocation of Virtual Power Plant in Frequency Regulation Market Considering Battery Cycle Life.

Da Silva, F. L., Nishida, C. E., Roijers, D. M., and Costa, A. H. R. (2019). Coordination of Electric Vehicle Charging through Multiagent Reinforcement Learning. *IEEE Trans. Smart Grid* 11 (3), 2347–2356.

Hill, T. W., and Ravindran, A. (1975). On Programming with Absolute-Value Functions. *J. Optimization Theor. Appl.* 17 (1), 181–183. doi:10.1007/bf00933924

Hwang, K.-S., Jiang, W.-C., and Chen, Y.-J. (2017). Pheromone-Based Planning Strategies in Dyna-Q Learning. *IEEE Trans. Ind. Inf.* 13 (2), 424–435. doi:10.1109/tii.2016.2602180

Jonnalagadda, V. K., and Dulla Mallesham, V. K. (2013). Bidding Strategy of Generation Companies in a Competitive Electricity Market Using the Shuffled Frog Leaping Algorithm. *Turk J. Elec Eng. Comp. Sci.* 21 (6), 1567–1583. doi:10.3906/elk-1109-43

Kebriaei, H., Rahimi-Kian, A., and Ahmadabadi, M. N. (2015). Model-Based and Learning-Based Decision Making in Incomplete Information Cournot Games: A State Estimation Approach. *IEEE Trans. Syst. Man. Cybern, Syst.* 45 (4), 713–718. doi:10.1109/tsmc.2014.2373336

Li, X., Hui, D., and Lai, X. (2013). Battery Energy Storage Station (BESS)-based Smoothing Control of Photovoltaic (PV) and Wind Power Generation Fluctuations. *IEEE Trans. Sustain. Energ.* 4 (2), 464–473. doi:10.1109/tste.2013.2247428

Merten, M., Olk, C., Schoeneberger, I., and Sauer, D. U. (2020). Bidding Strategy for Battery Storage Systems in the Secondary Control reserve Market. *Appl. Energ.* 268, 114951. doi:10.1016/j.apenergy.2020.114951

Morales, J. M., Pineda, S., Conejo, A. J., and Carrion, M. (2009). Scenario Reduction for Futures Market Trading in Electricity Markets. *IEEE Trans. Power Syst.* 24 (2), 878–888. doi:10.1109/tpwrs.2009.2016072

Najafi, S., Shafie-khah, M., Siano, P., Wei, W., and Catalão, J. P. (2019).Reinforcement Learning Method for Plug-In Electric Vehicle Bidding. *IET Smart Grid*.

Niknam, T., Zare, M., and Aghaei, J. (2012). Scenario-based Multiobjective Volt/var Control in Distribution Networks Including Renewable Energy Sources. *IEEE Trans. Power Deliv.* 27 (4), 2004–2019. doi:10.1109/tpwrd.2012.2209900

Praça, I., Ramos, C., Vale, Z., and Cordeiro, M. (2003). MASCEM: a Multiagent System that Simulates Competitive Electricity Markets. *IEEE Intell. Syst.* 18 (6), 54–60. doi:10.1109/mis.2003.1249170

Rashedi, N., Tajeddini, M. A., and Kebriaei, H.. Markov Game Approach for Multi-Agent Competitive Bidding Strategies in Electricity Market. *IET Generation, Transm. Distribution* 10, 3756–3763. Available: https://digital-library.theiet.org/content/journals/10.1049/iet-gtd.2016.0075.

Salehizadeh, M. R., and Soltaniyan, S. (2016/04/01/ 2016). Application of Fuzzy Q-Learning for Electricity Market Modeling by Considering Renewable Power Penetration. *Renew. Sust. Energ. Rev.* 56, 1172–1181. doi:10.1016/j.rser.2015.12.020

Shafie-khah, M., and Catalao, J. P. S. (2015). A Stochastic Multi-Layer Agent-Based Model to Study Electricity Market Participants Behavior. *IEEE Trans. Power Syst.* 30 (2), 867–881. doi:10.1109/tpwrs.2014.2335992

Shafie-khah, M., Heydarian-Forushani, E., Golshan, M. E. H., Moghaddam, M. P., Sheikh-El-Eslami, M. K., and Catalão, J. P. S. (2015). Strategic Offering for a Price-Maker Wind Power Producer in Oligopoly Markets Considering Demand Response Exchange. *IEEE Trans. Ind. Inf.* 11 (6), 1542–1553. doi:10.1109/tii.2015.2472339

Tellidou, A. C., and Bakirtzis, A. G. (20062006).. International IEEE Conference Intelligent Systems, 408–413. doi:10.1109/is.2006.348454 Multi-Agent Reinforcement Learning for Strategic Bidding in Power Markets.

Ventosa, M., Baillo, A., Ramos, A., and Rivier, M. (2005). Electricity Market Modeling Trends. *Energy policy* 33 (7), 897–913. doi:10.1016/j.enpol.2003.10.013

Vijaya Kumar, J., Vinod Kumar, D. M., and Edukondalu, K. (2013). Strategic Bidding Using Fuzzy Adaptive Gravitational Search Algorithm in a Pool Based Electricity Market. *Appl. soft Comput.* 13 (5), 2445–2455. doi:10.1016/j.asoc.2012.12.003

Wang, S., Bi, S., and Zhang, Y. A. (2019). Reinforcement Learning for Real-Time Pricing and Scheduling Control in EV Charging Stations. *IEEE Trans. Ind. Inform.* 17 (2), 849–859.

Xu, Y., Ahokangas, P., Louis, J.-N., and Pongrácz, E. (2019). Electricity Market Empowered by Artificial Intelligence: A Platform Approach. *Energies* 12 (21), 4128. doi:10.3390/en12214128

Ye, Y., Qiu, D., Sun, M., Papadaskalopoulos, D., and Strbac, G. (2019). Deep Reinforcement Learning for Strategic Bidding in Electricity Markets. *IEEE Trans. Smart Grid*, 1.

Zeng, B., Feng, J., Liu, N., and Liu, Y. (2020). Co-optimized Public Parking Lot Allocation and Incentive Design for Efficient PEV Integration Considering Decision-dependent Uncertainties. *IEEE Trans. Ind. Inform.* 20 (1)., p.

Zhang, Z., Tang, H., Huang, Q., and Lee, W.-J. (2019). *IEEE/IAS 55th Industrial and Commercial Power Systems Technical Conference*. I&CPS)IEEE, 1–9. doi:10.1109/icps.2019.8733335 Two-stages Bidding Strategies for Residential Microgrids Based Peer-To-Peer Energy Trading2019

Zucker, A., and Hinchliffe, T. (2014). Optimum Sizing of PV-Attached Electricity Storage According to Power Market Signals - A Case Study for Germany and Italy. *Appl. Energ.* 127, 141–155. doi:10.1016/j.apenergy.2014.04.038

Zugno, M., Morales, J. M., Pinson, P., and Madsen, H. (2013). Pool Strategy of a price-maker Wind Power Producer. *IEEE Trans. Power Syst.* 28 (3), 3440–3450. doi:10.1109/tpwrs.2013.2252633

Conflict of Interest: The authors declare that the research was conducted in the absence of any commercial or financial relationships that could be construed as a potential conflict of interest.

Publisher's Note: All claims expressed in this article are solely those of the authors and do not necessarily represent those of their affiliated organizations, or those of the publisher, the editors, and the reviewers. Any product that may be evaluated in this article, or claim that may be made by its manufacturer, is not guaranteed or endorsed by the publisher.

Copyright © 2021 Gao, Ma, Chan, Xia and Zhu. This is an open-access article distributed under the terms of the Creative Commons Attribution License (CC BY). The use, distribution or reproduction in other forums is permitted, provided the original author(s) and the copyright owner(s) are credited and that the original publication in this journal is cited, in accordance with accepted academic practice. No use, distribution or reproduction is permitted which does not comply with these terms.

frontiers in Energy Research

METHODS
published: 12 October 2021
doi: 10.3389/fenrg.2021.742993

Customer Load Forecasting Method Based on the Industry Electricity Consumption Behavior Portrait

Weiling Guan[1,2], *Daolu Zhang*[1,2], *Huang Yu*[1,2], *Binggang Peng*[1,2], *Yufeng Wu*[1,2], *Tao Yu*[1,2]* *and Keying Wang*[1,2]

[1]School of Electric Power Engineering South China University of Technology, Guangzhou, China, [2]Guangdong Provincial Key Laboratory of Intelligent Measurement and Advanced Metering of Power Grid, Guangzhou, China

With the dramatic increase of energy demand and the continuous increase of power system operation pressure, higher requirements are put forward for the development of power grid planning and optimization operation. It is important for the refinement of distribution network planning to deeply extract the characteristics of user load. First, the process of load characteristic analysis method from the user level to the industry level is proposed, which achieves the division of electricity consumption patterns of various industries, thus building a panoramic portrait of industry electricity consumption behavior. Then, by expanding the information filled in by traditional customers, the feature vector of each user is extracted, and the users' industry electricity consumption patterns are used as the label. Therefore, a method for identifying the electricity consumption pattern of the customer based on the BB-stacking model fusion framework is proposed, which yields the preliminary forecast results of customer load based on the actual load accounting results of the customers. Finally, comparative simulations with different methods verify the effectiveness of the proposed algorithm, which can provide prominent guidance for the actual distribution network planning work.

Keywords: industry electricity consumption behavior portrait, cluster analysis, ensemble learning framework, multidimensional electricity consumption characteristics, customer load forecasting

OPEN ACCESS

Edited by:
Xiaoshun Zhang,
Shantou University, China

Reviewed by:
Guiyuan Zhang,
Shantou University, China
Da Xu,
China University of Geosciences Wuhan, China

****Correspondence:***
Tao Yu
taoyu1@scut.edu.cn

Specialty section:
This article was submitted to Smart Grids, a section of the journal Frontiers in Energy Research

Received: *17 July 2021*
Accepted: *04 August 2021*
Published: *12 October 2021*

Citation:
Guan W, Zhang D, Yu H, Peng B, Wu Y, Yu T and Wang K (2021) Customer Load Forecasting Method Based on the Industry Electricity Consumption Behavior Portrait. Front. Energy Res. 9:742993. doi: 10.3389/fenrg.2021.742993

INTRODUCTION

Development of Customer Portrait

More recently, with the gradual transformation of enterprises from product oriented to user oriented in the production, it is significant for formulating marketing strategies and product design to fully understand customers and their needs (Wu et al., 2020). At present, in-depth mining of user data and research on accurate user portrait are gradually deepening. Accurate user portrait technology has been widely used in the Internet, finance, retail, operators, advertising, and other industries (Liu and Du, 2020; Zhang et al., 2020). In terms of advertising, Google uses big data to locate high-value users, which helps mobile e-commerce app to locate high-value users and push advertisements and adopts flexible data tracking methods for users of different tag categories, so that brands can achieve accurate advertising push for target users (Shan, 2018). In terms of auxiliary business decision-making, eBay carries out business circle customer group analysis, product marketability analysis, store operation analysis, personalized consumption analysis, and customer loss analysis by

integrating online and offline massive data, providing decision support for commercial real estate and comprehensive big data analysis and prediction for project parties and brands (Chen et al., 2021). Obviously, user portrait technology has become an effective method to improve customer service quality and customer experience, which is an important basis for integrating high-quality resources and realizing enterprise and user value (Pitner et al., 2012; Yu et al., 2017).

In the field of electric power research, it has become a rising research direction to build user portraits in different application scenarios according to the actual needs (Qiu et al., 2017). In the early stage of the study, traditional user portraits were mainly used in the marketing portal to build user electricity sensitivity or credit portraits to guide the electricity recovery work (Sanchez et al., 2008; Han et al., 2014; Ampimah et al., 2017). To meet the requirements of demand response, the methods of establishing electricity consumption behavior tag library and realizing the portrait of different types of users' electricity consumption behavior patterns were proposed in (Qiu et al., 2017) and (Zhong et al., 2018). With the gradual popularization of new energy (Yang et al., 2016; Yang et al., 2017; Yang et al., 2018; Yang et al., 2019a; Yang et al., 2019b; Yang et al., 2020), the load change and influence mechanism on the user side are becoming more and more complex. Therefore, the user portrait method is becoming more and more important.

The above pieces of literature are all portraits of the users who have been connected to the power grid, so as to formulate appropriate strategies to guide the corresponding users to change their electricity consumption behavior. However, there is rare research on the reported customers who are not connected to the power grid. In the distribution network planning work, reference (Lian et al., 2014) makes use of the complementarity between user loads to optimize the access decision reasonably, which can effectively improve the load distribution and utilization rate of power supply equipment. Moreover, the multidimensional analysis of user load can also provide effective guidance for the optimal scheduling and control of smart grid (Yang et al., 2015; Zhang et al., 2015; Xi et al., 2016; Zhang et al., 2016; Zhang et al., 2021). However, due to the lack of research on the load of customers who are not connected, it is limited to transfer the user load of the existing distribution network. For the more common scenario of business expansion, the data information support and optimization ability are insufficient.

Research and Contribution of the Paper

In view of the above research results, the contributions of this paper can be summarized as follows:

1) Unlike the traditional single user portrait, this paper digs the power consumption behavior law of massive users, which constructs a more popularized and applied power consumption behavior portrait for industry.
2) A load forecasting method is presented, which is different from the general sense of load forecasting. Aiming at the new customers who are not connected with electricity, this paper extracts the time sequence characteristics of customer load through limited data information, which provides an effective reference for the actual distribution network planning.
3) The software integrating the above functions is developed and has been applied in engineering, which provides an effective tool for the decision-making of distribution network planners.

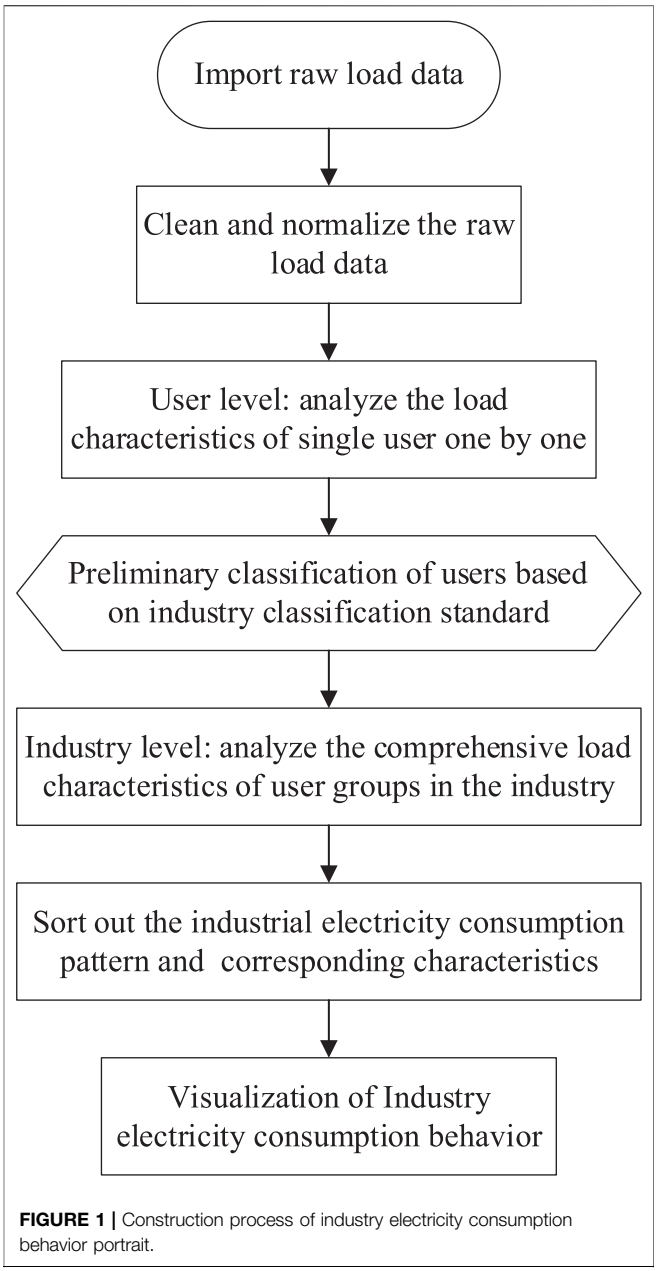


FIGURE 1 | Construction process of industry electricity consumption behavior portrait.

PORTRAIT OF INDUSTRY ELECTRICITY CONSUMPTION BEHAVIOR

In this paper, a load characteristic analysis method from user level to industry level is proposed. First, the massive users of various industries in the region are systematically analyzed and integrated. Therefore, a comprehensive and practical industry

electricity consumption behavior portrait in the region is profiled. The key steps are shown in **Figure 1**.

Load Data Preprocessing

For continuous load data, Lagrange interpolation (Criscuolo et al., 1984) is used to fill the vacancy and bad data, which can play a good repair effect. For the data points that need to be filled, m normal data points adjacent to the point are selected as samples to calculate the Lagrange interpolation formula:

$$L(t) = \sum_{i=1}^{m} x_i \frac{\prod_{j=1, j\neq i}^{m} (t - t_j)}{\prod_{j=1, j\neq i}^{m} (t_i - t_j)}, \tag{1}$$

where t_i and t_j are the sampling time of the i and j data points in a day, x_i means the load value of the i data point, and m is the number of sample points used to construct the polynomial. Finally, the approximate value of the missing value can be obtained by substituting the missing time t into $L(t)$.

To avoid the influence of the actual load value in the follow-up analysis process, the linear proportion normalization method is used to normalize the load data after repair, which can be expressed as

$$\hat{x}_i = \frac{x_i}{x_{max}}, \tag{2}$$

where $\hat{x}_i$ represents the i-th load data point after normalization and x_{max} is the peak load of the user.

Load Analysis of User Level

User Load Curve Analysis

The user load curve has strong randomness, so it is difficult to ensure that the load curve of the day is typical for the user. In this paper, the time series mining method in (Lin et al., 2017) is used to extract the typical daily load curve of the user in a period of time T; the specific process is as follows:

1) Dimensionality reduction of load data: let w be the number of segments of daily load data processed by PAA method, then the daily load time series after dimensionality reduction is $\overline{X} = [\overline{x_1}, \cdots, \overline{x_w}]$, and the calculation formula is as follows:

$$\overline{x_i} = \frac{w}{n} \sum_{j=\frac{n}{w}(i+1)+1}^{\frac{n}{w}} \hat{x}_i, \tag{3}$$

where $\overline{x_i}$ represents the mean value of the time i series segment after dimension reduction.

2) Symbolic representation: the SAX method (Notaristefano et al., 2013) is used to assign symbolic values to each segment of the daily load time series after dimension reduction according to the average value of each segment and then select the optimal value α as the size of symbol set; the discretized symbol sequence can be expressed as $\widehat{Y} = [\widehat{y_1}, \cdots, \widehat{y_w}]$.
3) Frequency of statistical symbol sequence: after the symbolic representation of daily load data is completed, the frequency of various symbol sequences is counted. Then, the most common load curve forms are screened out and the abnormal load is eliminated. Suppose the most symbol sequence appears is s.
4) Extract typical daily load curve: stack the daily load curve corresponding to the symbol sequence with the highest frequency, and calculate the mean value to obtain the final typical load curve $\boldsymbol{L}^d = [l_1^d, \cdots, l_n^d]$, which can be computed by

$$l_i^d = \frac{1}{s} \sum_{r=1}^{s} \overline{x_{r,i}}, \tag{4}$$

where l_i^d stands for the i-th data point of the typical daily load curve $\boldsymbol{L}^d$ and $\overline{x_{r,i}}$ is the i-th data point of the r-th sample daily load curve.

User Load Characteristics Analysis

The user load curve can directly describe the change trend of user load in a day, and the load characteristics can more comprehensively characterize the user's electricity behavior from multiple perspectives. In this paper, user load characteristics are selected and calculated from three aspects, i.e., user load level, typical peak-valley characteristics, and load development law. The names and expression of each index are shown in **Table 1**.

In **Table 1**, the load level indicators represent the volume of user power consumption, which is the key information in the distribution network planning. Indicators of typical peak-valley characteristics can reflect the changing trend of user load in a day with less information granularity. The index of long-term load development reflects the rule that a user's load gradually increases to saturation after access to electricity and the relationship between saturated load and its area occupied. It is an important basis for reasonable estimation of the user's load.

Preliminary Classification of Users Based on Industry Classification Standards

To serve distribution network planning, the results of single user load characteristic analysis lack universality. Thus, it is necessary to explore the general law of massive users' load changes.

Generally, the users are classified into various industries according to the National Economic Industry Classification national standard, forming a user group in each industry, which has similarity in the long-term development law of load. In this way, the summary of the law and subsequent application is facilitated. After the preliminary classification of users is completed, due to the different characteristics of user peaks and valleys, it is necessary to further carry out industry power mode analysis and feature extraction.

Load Analysis of Industry Level

Analysis of Industry Electricity Consumption Pattern

In the same industry, each user's electricity consumption behavior is still different. The gray wolf optimized fuzzy mean clustering algorithm (GWO-FCM) with high clustering accuracy and fast computing speed in (Gao et al., 2019) is used to further subdivide the user groups in the industry. The specific process is as follows:

TABLE 1 | Selected user load characteristics.

Type	User characteristic	Expression
Load level	Contract capacity	P_c
	Final annual maximum load	P_f
Peak-valley characteristics	Daily load rate	$a_1 = P_{av}/P_{max}$
	Daily minimum load rate	$a_2 = P_{min}/P_{max}$
	Peak-valley difference rate	$a_3 = (P_{max} - P_{min})/P_{max}$
	Peak load rate	$a_4 = P_{av.peak}/P_{av}$
	Valley load rate	$a_5 = P_{av.val}/P_{av}$
	Flat load rate	$a_6 = P_{av.sh}/P_{av}$
Long-term load development law	Saturated load density	$D = P_f/S$
	Utility rate	$\epsilon = P_f/P_c$

1) Setting parameters: set the minimum number of clusters as c_{min} and the maximum number of clusters as c_{max} and parameters of GWO-FCM. The number of first clusters is set as c_{min}.
2) Implement clustering algorithm: suppose that there are N users in the industry$\boldsymbol{L}_k^d$; $\boldsymbol{L}_k^d$ denotes the typical daily load curve of user k. GWO-FCM algorithm is used to cluster the typical daily load curves of all users in the industry.
3) Evaluate the clustering effect: use silhouette coefficient (SC) to evaluate the compactness and separability of clusters. $SC(\boldsymbol{L}_k^d)$ represents the SC of $\boldsymbol{L}_k^d$, which can be computed by

$$SC\left(\boldsymbol{L}_k^d\right) = \frac{D_a\left(\boldsymbol{L}_k^d\right) - D_b\left(\boldsymbol{L}_k^d\right)}{max\left(D_a\left(\boldsymbol{L}_k^d\right), D_b\left(\boldsymbol{L}_k^d\right)\right)}, \tag{5}$$

$$D_a\left(\boldsymbol{L}_k^d\right) = \frac{\sum_{k,w\in C_u, k\neq w} d\left(\boldsymbol{L}_k^d, \boldsymbol{L}_w^d\right)}{|C_u| - 1}, \tag{6}$$

$$D_b\left(\boldsymbol{L}_k^d\right) = \min_{1\le v\le c}\left\{\frac{\sum_{k\in C_u, w\in C_v} d\left(\boldsymbol{L}_k^d, \boldsymbol{L}_w^d\right)}{|C_v|}\right\}, \tag{7}$$

where $D_a(\boldsymbol{L}_k^d)$ is the average distance between $\boldsymbol{L}_k^d$ and other samples in C_u cluster; $D_b(\boldsymbol{L}_k^d)$ is the minimum average distance between $\boldsymbol{L}_k^d$ and the samples not in C_u. The closer $SC(\boldsymbol{L}_k^d)$ is to 1, the better the compactness and separability of samples are and the better the clustering effect is.

The mean value of the SC of all samples is calculated to evaluate the effectiveness of the clustering, which can be computed by

$$SCMEAN = \frac{1}{N}\sum_{k=1}^{N} SC\left(\boldsymbol{L}_k^d\right). \tag{8}$$

4) Traverse the optional range of cluster number: if the current cluster number c is greater than c_{max}, go to step 5). Otherwise, if $c = c + 1$, go to step 2).
5) The number of clusters with the maximum mean value of the contour coefficient is selected as the optimal number of clusters c_{best}. After the clustering centers are normalized, the typical curve of the power consumption pattern of the industry is obtained. The typical curve of industry electricity consumption pattern C_u can be expressed as $L_u^c = [l_{u,1}^c, \cdots, l_{u,n}^c]$.

Characteristic Extraction of Industry Electricity Consumption

After completing the division of industry electricity consumption pattern, it is necessary to extract the corresponding characteristics of each electricity consumption pattern in the industry. Considering the nature of the characteristics, it is not significant to summarize and extract the load level and typical peak-valley characteristics at the industry level. Considering the actual needs of the power grid, it is of great significance to extract the long-term load development law of various electricity consumption patterns in the industry.

Nonparametric kernel density estimation (Lambert et al., 1999) is a data sample-driven method, which can fit the probability distribution of features without prior knowledge. In this paper, a nonparametric kernel density estimation method is used to fit the probability density of long-term load development characteristics, and then typical characteristics are extracted.

Taking the saturated load density as an example, suppose that there are N_u users belonging to industry electricity consumption pattern C_u, where the saturated load density of user k is D_k; then the probability density function $f(D)$ of D can be computed by

$$f(D) = \frac{1}{N_u h}\sum_{k=1}^{N_u} K\left(\frac{D - D_k}{h}\right), \tag{9}$$

where k means the kernel function; h denotes the bandwidth.

To ensure the continuity of the probability density function, the kernel function needs to be a smooth probability density function. Generally, Gaussian kernel function is often selected, which can be expressed as follows:

$$K(x) = \frac{1}{\sqrt{2\pi}} e^{-x^2/2}. \tag{10}$$

The point with the largest value of the probability density fitting function $f(D)$ is selected as the typical characteristic value of the electricity consumption pattern C_u, which can be computed by

$$\overline{D_u} = \underset{D}{\operatorname{argmax}}\, f(D), \tag{11}$$

where $\overline{D_u}$ stands for the typical saturated load density value of the electricity consumption pattern C_u.

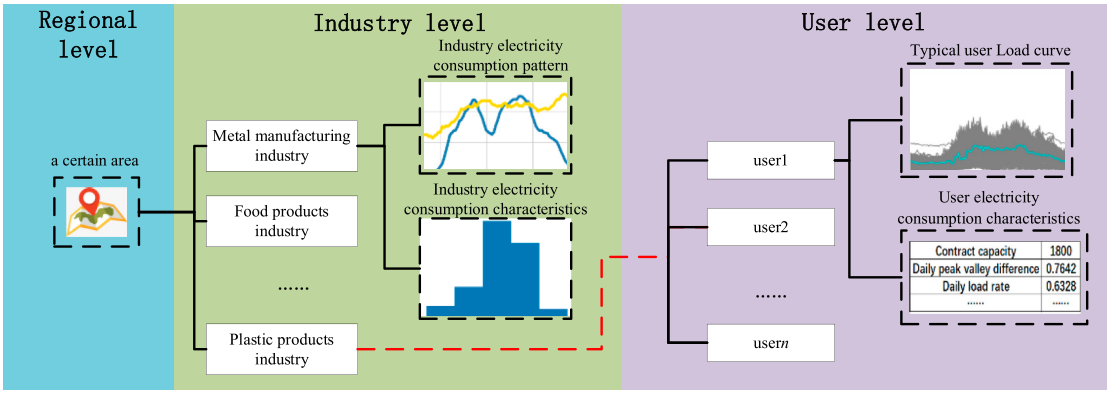


FIGURE 2 | Description process of industry electricity consumption behavior.

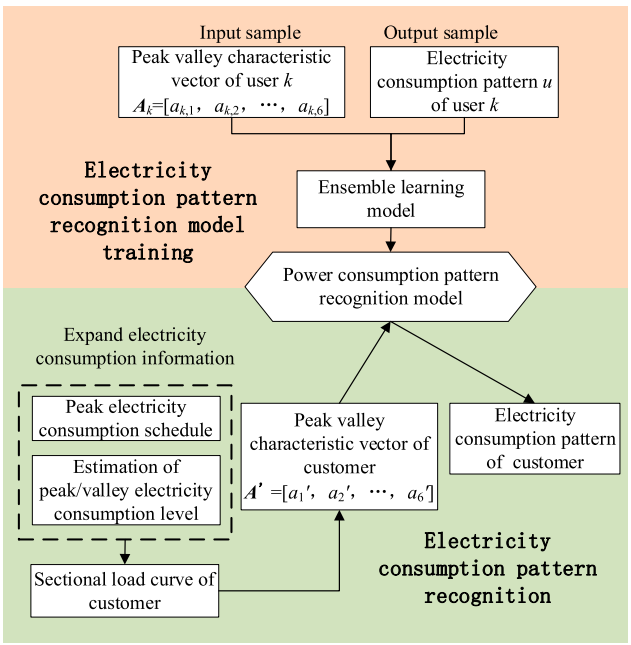


FIGURE 3 | Basic process of electricity consumption pattern classification for customers.

Construction of Industry Electricity Consumption Behavior Portrait

After the load analysis from the user level to the industry level, the load curves and related characteristics of the power users and industry modes are obtained, respectively, at the user level and the industry level, which is the description of the electricity consumption behavior of the industry from different angles and at different levels.

To enable the distribution network planners to grasp the electricity consumption of various industries intuitively, massive analysis results are sorted and visualized. Then, a panoramic portrait of industry electricity consumption behavior in a region is built. The form and content of the portrait are shown in **Figure 2**.

PATTERN CLASSIFICATION OF NEW CUSTOMERS' ELECTRICITY CONSUMPTION

In the traditional business expansion and installation, for the customers who have not been connected to the power grid, the planners are supposed to calculate the customer's load based on the customer's reported capacity and business experience, working out the business expansion and access scheme. The processing flow is extensive and lacks consideration for user load time sequence characteristics.

After the construction of a panoramic portrait of industry electricity consumption behavior in the region, if we can reasonably infer the electricity consumption pattern according to the relevant power consumption information provided by customers, it can provide more effective technical support for business decision-making of planners.

The basic flow of the electricity consumption pattern classification in this paper is shown in **Figure 3**. The training model obtains the electricity pattern classification ability by using the users' characteristics as the training samples. After training the model, the corresponding characteristic vectors are extracted from the electricity consumption information of the customers and input into the classification model to obtain the electricity consumption pattern classification results of the customers.

Customer Classification Algorithm Based on BB-Stacking Model Fusion Framework

In the field of the classification problem, ensemble learning (EL) has gained the attention of a huge number of scholars, because it can make up for each single model's advantages (Wang et al., 2015). Among them, bagging (Hu et al., 2011) and boosting (Lu et al., 2006) are the most classic and widely used integration methods, which have their own characteristics in model generalization and model accuracy. Specifically, bagging builds multiple datasets in bootstrap way and trains multiple single models in parallel, integrating the output by Voting. The advantages of each model are integrated, preventing the overfitting phenomenon effectively. Boosting framework

TABLE 2 | Characteristics and typical algorithms of bagging and boosting.

Integration mode	Training mode	Generalization performance	Accuracy performance	Typical algorithm
Bagging	Parallel	Strong	Weak	RF
Boosting	Serial	Weak	Strong	XGBoost

TABLE 3 | Extended electricity consumption information of a customer.

Peak electricity consumption schedule	Peak electricity consumption level estimation (kW)	Valley electricity consumption level estimation (kW)
8:00–12:00 14:00–18:00	1,000	50

belongs to the mode of serial integration of models. The output of each model is used as the input of the lower model, and the minimum deviation is used as the loss function to continuously improve the accuracy of each model. Generally, the characteristics of the two integration methods are shown in **Table 2**.

To give full play to the advantages of the two integration methods, a model fusion framework of BB-stacking (bagging and boosting in stacking) based on the stacking method is proposed. It combines the two integration methods reasonably to realize the organic trade-off between high-precision and strong generalization performance, yielding the high-precision classification of customers.

Traditional stacking is composed of the base model in the lower layer and the metamodel in the upper layer. Firstly, the initial data is divided into subdatasets by k-fold, and then the subdatasets are input into the base model for training and classification. Then the output of the lower layer is reconstructed and sent to the upper model for training and classification. The BB-stacking model fusion algorithm proposed in this paper changes the lower base model layer into the integration layer on the basis of the two-tier structure of stacking, in which bagging and boosting methods are used to preliminarily integrate the original model and then transferred to the upper metamodel to coordinate the advantages of the two integration modes, obtaining a model with higher accuracy and more stable generalization ability.

Expansion of New Customers' Electricity Consumption Information

In the traditional business process, customers provide limited information in the information filling process. To make the pattern classification of electricity consumption more accurate, this paper proposes an appropriate expansion of the electricity consumption information reported by the customers. In addition to the traditional information of electricity consumption type, electricity consumption location, and electricity consumption capacity, the peak electricity consumption time schedule, peak electricity consumption level estimation, and valley electricity consumption level estimation are added as the customer's electricity consumption information. **Table 3** shows the demonstration of extended power consumption information of a customer.

According to the example of extended electricity consumption information of the reported customer in **Table 3**, the reference load curve of the reported customer is obtained by time simulation. According to the definition of the peak-valley characteristic index in **Table 1**, the peak-valley characteristic vector of the customer can be calculated as the input of the electricity consumption pattern classification model.

CUSTOMER LOAD FORECASTING

Calculation of Customer Load Level

The next step is to calculate the load level of the customers. Based on the regional industry electricity consumption behavior portrait, the corresponding method is adopted to calculate the customers' load according to their type of electricity consumption (Yaoyao et al., 2013). The specific calculation method is as follows:

1) Commercial, nonindustrial, and residential customers

It is recommended to use the load density method to calculate the customers' load because the load level of these customers is closely related to their building area. Assuming that the classification result of the customer is industry electricity consumption pattern C_u, the customer accounting load can be computed by

$$P_{hs} = \overline{D_u} \cdot S_{bz}, \tag{12}$$

where S_{bz} means the building area of the customer.

2) Industrial customers

Generally, the load level of industrial customers often depends on the capacity of production equipment and has weak correlation with the building area. It is recommended to use the utility rate method to calculate the customer load. Similarly, assuming that the classification result of the customer is industry

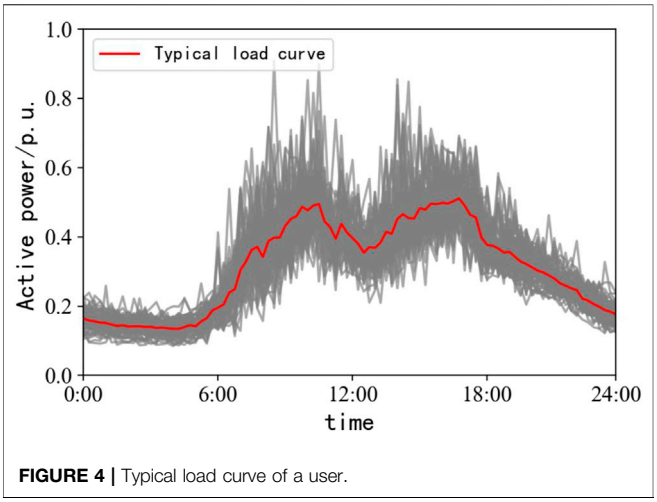


FIGURE 4 | Typical load curve of a user.

electricity consumption pattern C_u, the customer accounting load can be computed by

$$P_{hs} = \overline{\epsilon_u} \cdot P_{bz}, \tag{13}$$

where $\overline{\epsilon_u}$ stands for the typical utility rate value of the electricity consumption pattern C_u; P_{bz} means the building area of the customer.

Forecasting of Customer Load Curve

After the customer load level estimation is completed, the load curve can be forecasted according to the electricity consumption pattern classification results of the customer in the industry. The forecasting load curve of the customer belonging to electricity consumption pattern C_u is $\boldsymbol{L}_{yg}$, and the calculation formula is as follows:

$$\boldsymbol{L}_{yg} = \boldsymbol{L}_u^c \cdot P_{hs}, \tag{14}$$

where $\boldsymbol{L}_u^c$ is the typical load curve of industry electricity consumption pattern C_u.

Evaluation Index of Customer Load Forecasting Results

The customer load forecasting technology is based on the industry electricity consumption behavior portrait of the region. Through the limited electricity consumption information, customer load after access is estimated. To provide guidance for planners to make customer access decisions, the accuracy of the expected results needs to be evaluated. Assuming that the actual load curve of the customer is $\boldsymbol{L}_{sj}$, maximum absolute error ratio (MAER) and Euclidean distance (ED) are used to evaluate the accuracy of the forecasting results.

1) To directly reflect the maximum error level between the forecasting load curve and the actual load curve of customer, MAER is used to measure the error, which can be computed by

$$MAER = \frac{\max_i\left(l_{sj,i} - l_{yg,i}\right)}{max\left(\boldsymbol{L}_{sj}\right)}, \tag{15}$$

where $l_{sj,i}$ means the i-th load point of $\boldsymbol{L}_{sj}$; $l_{yg,i}$ denotes the i-th load point of $\boldsymbol{L}_{yg}$.

2) To ensure that ED is not affected by the actual load level of the customer, the maximum value of the actual load curve $\boldsymbol{L}_{sj}$ is taken as the benchmark, and then the ED between the actual load curve and the estimated load curve can be calculated by

$$\widehat{\boldsymbol{L}_{yg}} = \frac{\boldsymbol{L}_{yg}}{max\left(\boldsymbol{L}_{yg}\right)}, \tag{16}$$

$$\widehat{\boldsymbol{L}_{sj}} = \frac{\boldsymbol{L}_{sj}}{max\left(\boldsymbol{L}_{sj}\right)}, \tag{17}$$

$$d\left(\widehat{\boldsymbol{L}_{yg}}, \widehat{\boldsymbol{L}_{sj}}\right) = \sqrt{\sum_{i=1}^{n}\left(\widehat{l_{sj,i}} - \widehat{l_{yg,i}}\right)}, \tag{18}$$

where $\widehat{l_{sj,i}}$ means the i-th load point of $\widehat{\boldsymbol{L}_{sj}}$; $\widehat{l_{yg,i}}$ denotes the i-th load point of $\widehat{\boldsymbol{L}_{yg}}$.

CASE STUDIES

The dataset used in this paper is the load data of distribution transformer in an economically developed city from 2015 to 2019. One measurement point data is obtained every 15 min, with a total of 96 load data points per day. From the huge dataset, the distribution transformer data with high data quality and load development to saturation are selected. Combined with the corresponding industry information identification of distribution transformer users, the data cleaning and load characteristic analysis from user level to industry level are completed. Finally, the regional industry electricity consumption behavior image of the city is constructed.

In all industries, the metal products industry accounts for the highest proportion of users, which is a typical industry in the region. Taking the metal products industry as an example, this paper analyzes and demonstrates the output results and verifies the effectiveness of the proposed method.

Display of Industry Electricity Consumption Behavior Portrait

Analysis Results of User Level Load Characteristics

1) User load curve analysis

Taking a user in the metal products industry as an example, the typical daily load curve of the user is extracted. Set the PAA segment number as 6 and the number of elements in symbol set as 4. The symbol sequence with the highest number of users is *abdddb*. The typical load curve of the user can be obtained through **Eq. 4**, as shown in **Figure 4**.

2) User load characteristic extraction

TABLE 4 | Examples of user load characteristics.

Type	User characteristic	Index value
Load level	Contract capacity	800 kW
	Final annual maximum load	427.7 kW
Peak-valley characteristics	Daily load rate	0.6316
	Daily minimum load rate	0.2624
	Peak-valley difference rate	0.7376
	Peak load rate	1.1779
	Valley load rate	0.5147
	Flat load rate	1.2931
Long-term load development law	Saturated load density	65.39 W/m^2
	Utility rate	0.5909

Similarly, take the user as an example, collect the user's relevant loading information, and calculate the corresponding user load characteristics, as shown in **Table 4**. It can be found that the user has large-scale production and the daily peak-valley difference is high. From the long-term development point of view, when the user load develops to saturation, the utility rate is low.

Analysis Results of Industry Level Load Characteristics

1) Industry load curve analysis

After extracting the typical load curve of 2,478 users in the metal products industry, the load curve of this user group is clustered. The minimum cluster number c_{min} is set as two and the maximum cluster number c_{max} is set as 8. Finally, the algorithm flow is executed, the average value of SC of each clustering result is calculated through **Eqs 5–8**, and the result is shown in **Figure 5**.

It can be seen that the average value of SC of GWO-FCM clustering algorithm reaches the maximum when $c = 4$, then the optimal clustering number $c_{best} = 4$ is determined, and the corresponding industry typical electricity consumption pattern division results are shown in **Figure 6**. It can be found that the load curves of each electricity consumption pattern are obviously different, and the division effect of electricity consumption pattern is satisfying.

1) Industry load characteristic extraction

After dividing the typical electricity consumption pattern of the industry, the characteristic extraction of the utility rate of 342 users in electricity consumption pattern one is taken as an example. The bandwidth h is set as 0.01. The probability density function of the user utility rate of the group is obtained by fitting **Eq. 9**, and the results are shown in **Figure 7**.

Customers' Electricity Consumption Pattern Classification

To verify the effectiveness of load forecasting technology for new customers, 141 metal products' users with complete electricity consumption data are selected as hypothetical customers. Therefore, the corresponding characteristic vectors are extracted and input into the trained BB-stacking model for electricity consumption pattern classification. In this paper, the traditional decision tree model (Safavian and Landgrebe, 1991), GRNN model (Specht, 1991), and PNN model (Oh and Pedrycz, 2002) are used to compare with the BB-stacking model. The classification accuracy under different training sample sizes is shown in **Figure 8**.

It can be found that, in the training process, the BB-stacking classification model can achieve a better classification effect than other classification models in a small training sample size. When the training sample size increases, the BB-stacking classification model can maintain a more stable generalization ability. It is obvious that the BB-stacking classification model prevents the phenomenon of classification ability decline caused by underfitting, performing better classification effect and stability.

Analysis of Customer Load Forecast Results

After the electricity consumption pattern classification of the customers is completed, the forecasting load curves of 141 customers are obtained through **Eqs 12–14** combined with the typical electricity consumption characteristics of the industry. To compare the effectiveness of various methods, the similarity between the load curve forecast results and the actual load curves is evaluated by EM and MAER, and the comparative analysis is carried out from the following two aspects.

1) Comparative analysis of different clustering numbers

Considering that the different number of clusters selected by the clustering algorithm will lead to different electricity consumption patterns, which may affect the accuracy of the forecasting results of customers, this paper uses the GWO-FCM algorithm to test the case of cluster number c from 2 to 8. The mean value of EM and MAER under each clustering number is compared and shown in **Figure 9**.

2) Comparative analysis of different methods

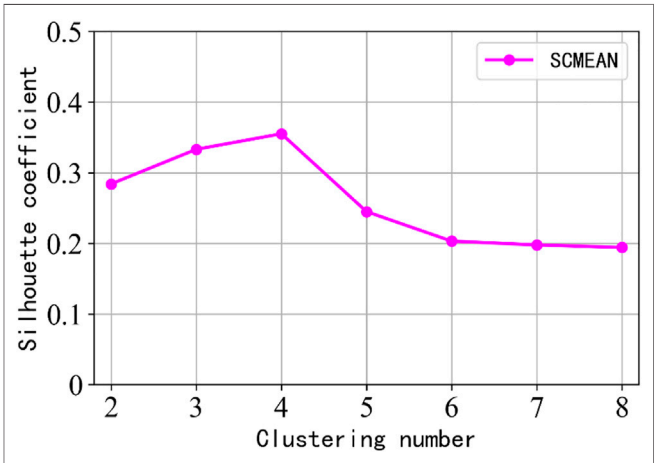


FIGURE 5 | Change trend of clustering effect evaluation index.

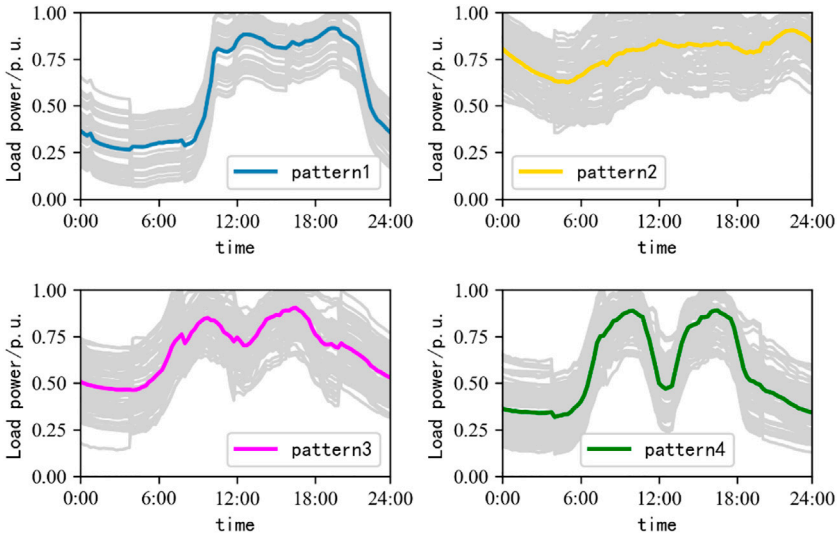


FIGURE 6 | Division result of typical electricity consumption pattern in the industry.

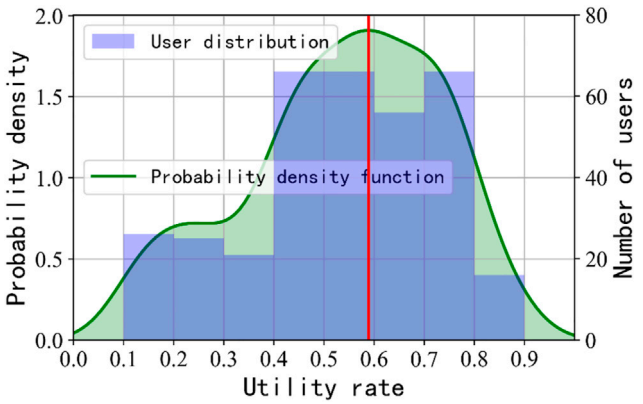


FIGURE 7 | Users' utility rate distribution and probability density function.

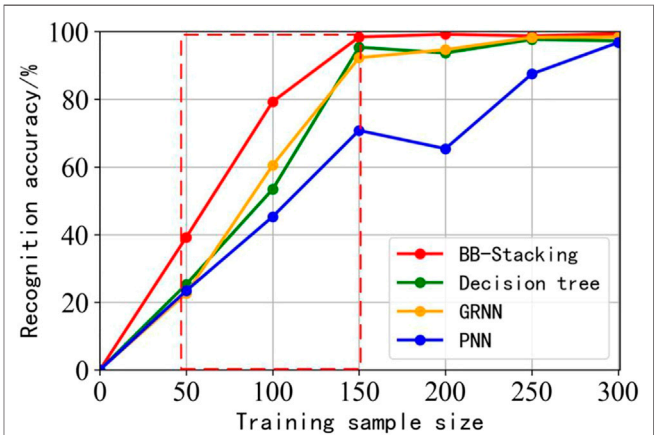


FIGURE 8 | Accuracy rate trend of customer electricity consumption pattern classification.

To further study the effectiveness of the proposed customer load forecasting method, this paper compares the traditional load estimation method with the proposed method. In addition, the sectional load curve obtained by the segment simulation method in the process of electricity consumption pattern classification is compared with the proposed method in this paper.

The comparison between the load curve forecasting result of a certain customer and other methods is shown in **Figure 10**. It can be found that there is little difference between the maximum load level of the estimated load and the actual load curve, but there is no time sequence characteristic. To some extent, the segment simulation method reflects the time sequence characteristics of customers, but the difference is large when the load level changes. The overall trend of the load curve forecasting result is very close to the actual load curve, which can meet the optimal access requirements in the planning field considering the time sequence characteristics of customers' load.

Comparing the error index of actual load curve and load curve forecasting results under different methods, the mean value comparison of test samples is shown in **Table 5**. It can be found that the proposed method performs best in both of the two evaluation indexes. Significantly, the accuracy is greatly improved compared with the traditional load estimation method.

Counting the two evaluation indexes of load estimation results of each hypothetical customer under different methods, two box diagrams are drawn to observe the distribution of sample indexes of each method, which are shown in **Figures 11**, **12**. According to the box diagrams, the sample median level of the two error evaluation indexes of the traditional load estimation method is

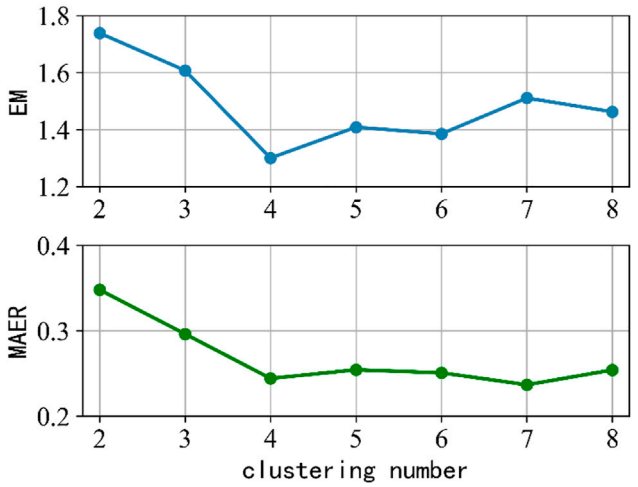


FIGURE 9 | Mean value of evaluation index on different clustering numbers.

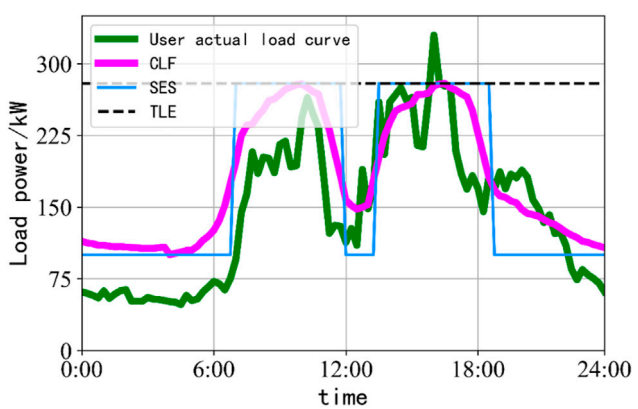


FIGURE 10 | Comparison and analysis of customer load forecasting results.

TABLE 5 | Comparison of the mean value of error indexes of different methods.

Method	ED	MAER
Customer load forecasting	1.3007	0.2444
Segment simulation	1.6246	0.2787
Traditional load estimation	3.3229	0.5886

the highest, and the error fluctuation range is the widest; the results show that the segmented simulation method achieves the suboptimal effect in the two evaluation indexes, and the error fluctuation is also controlled in a small range. It is worth noting that the median of the evaluation index samples of the proposed method is the lowest, the falling range of the error index samples is the narrowest, and the fluctuation range of the algorithm performance is smaller, showing the best stability.

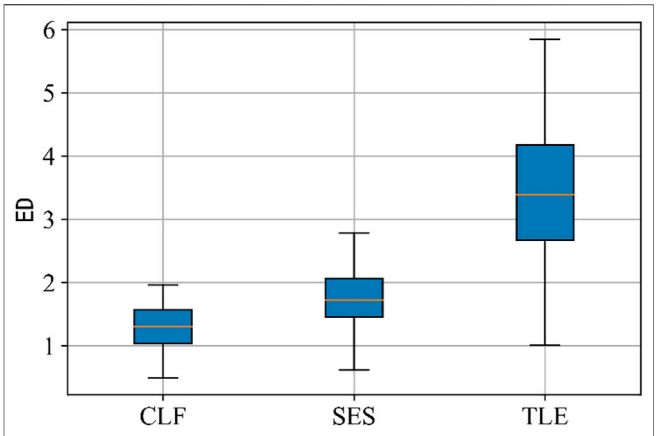


FIGURE 11 | Euclidean distance (ED) of different methods.

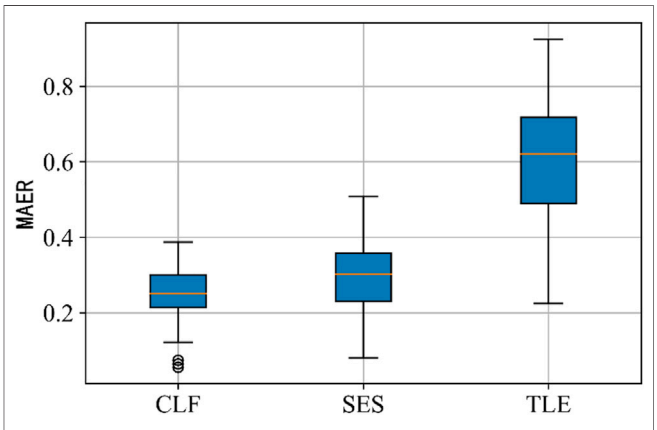


FIGURE 12 | Maximum absolute error ratio (MAER) of different methods.

CONCLUSION

Aiming at the problem of distribution network planning refinement, in this paper, the methods for regional industry electricity consumption behavior portrait construction are proposed. Further, the load forecasting technology of new customers is studied. The main conclusions are as follows:

1) The methods for regional industry electricity consumption behavior portrait construction can fully mine the multidimensional characteristics of users in various industries, providing effective data support for distribution network planning. The division of electricity consumption pattern can comprehensively and accurately reflect the power consumption characteristics and general laws of various industries.
2) The proposed load forecasting method has a good effect on the load forecasting of the customers who are not connected to the power grid, providing effective guidance for the

optimization of the customers' access decision and load scheduling (Li et al., 2021; Li and Yu, 2021). Moreover, the proposed method achieves significant performance in terms of the forecasting effect, algorithm stability, and practical application value.

DATA AVAILABILITY STATEMENT

The datasets presented in this article are not readily available because regional power consumption data are subject to confidentiality requirements. Requests to access the datasets should be directed to 1085283057@qq.com.

AUTHOR CONTRIBUTIONS

Conceptualization, methodology, and writing—original draft, WG; data curation, DZ; investigation, HY; writing—review and editing, BP; formal analysis and visualization, YW; resources and funding acquisition, TY; supervision, KW.

FUNDING

The authors gratefully acknowledge the support of the Science and Technology Project supported by China Southern Power Grid (GDKJXM20172939).

REFERENCES

Ampimah, B. C., Sun, M., Han, D., and Wang, X. (2017). Optimizing Sheddable and Shiftable Residential Electricity Consumption by Incentivized Peak and Off-Peak Credit Function Approach[J]. *Appl. Energ.* 210, S0306261917309716. doi:10.1016/j.apenergy.2017.07.097

Chen, T., Yin, X., Peng, L., Rong, J., and Cong, G. (2021). Monitoring and Recognizing Enterprise Public Opinion from High-Risk Users Based on User Portrait and Random Forest Algorithm[J]. *Axioms* 10 (2), 106. doi:10.3390/axioms10020106

Criscuolo, G., Mastroianni, G., and Occorsio, D. (1984). Uniform Convergence of Derivatives of Extended Lagrange Interpolation[J]. *J. Comput. Appl. Maths.* 282 (1), 669–698.

Gao, C., Wu, Y., Tang, J., Cao, H., and Chen, L. (2019). "Daily Power Load Curves Analysis Based on Grey Wolf Optimization Clustering Algorithm," in International Seminar of Purple Mountain Forum Academic Forum, Beijing, China (Springer).

Han, Y., Shen, B., Hu, H., and Fan, F. (2014). Optimizing the Performance of Ice-Storage Systems in Electricity Load Management through a Credit Mechanism: An Analytical Work for Jiangsu, China. *Energ. Proced.* 61, 2876–2879. doi:10.1016/j.egypro.2014.12.327

Hu, G., Mao, Z., He, D., and Yang, F. (2011). Hybrid Modeling for the Prediction of Leaching Rate in Leaching Process Based on Negative Correlation Learning Bagging Ensemble Algorithm. *Comput. Chem. Eng.* 35 (12), 2611–2617. doi:10.1016/j.compchemeng.2011.02.012

Lambert, C. G., Harrington, S. E., Harvey, C. R., and Glodjo, A. (1999). Efficient On-Line Nonparametric Kernel Density Estimation. *Algorithmica* 25 (1), 37–57. doi:10.1007/pl00009282

Li, J., and Yu, T. (2021). A New Adaptive Controller Based on Distributed Deep Reinforcement Learning for PEMFC Air Supply System. *Energ. Rep.* 7, 1267–1279. doi:10.1016/j.egyr.2021.02.043

Li, J., Yu, T., Zhang, X., Li, F., Lin, D., and Zhu, H. (2021). Efficient Experience Replay Based Deep Deterministic Policy Gradient for AGC Dispatch in Integrated Energy System. *Appl. Energ.* 285, 116386. doi:10.1016/j.apenergy.2020.116386

Lian, H., Di, X., Shen, Z., and Feng, M. (2014). "Detailed Power Distribution Network Planning Based on the Description of Load Characteristics," in China International Conference on Electricity Distribution, Shenzhen, China, September 23–26, 2014 (IEEE), 1759–1762.

Lin, S., Tian, E., Fu, Y., and Tang, X. (2017). Power Load Classification Method Based on Information Entropy Piecewise Aggregate Approximation and Spectral Clustering[J]. *Proc. CSEE* 37 (8), 2242–2252. doi:10.13334/j.0258-8013.pcsee.160279

Liu, C., and Du, J. (2020). "A User Portrait Construction Method for Financial Credit," in Proceedings of 2020 Chinese Intelligent Systems Conference Volume II.

Lu, J., Plataniotis, K. N., Venetsanopoulos, A. N., and Li, S. Z. (2006). Ensemble-based Discriminant Learning with Boosting for Face Recognition. *IEEE Trans. Neural Netw.* 17 (1), 166–178. doi:10.1109/tnn.2005.860853

Notaristefano, A., Chicco, G., and Piglione, F. (2013). Data Size Reduction with Symbolic Aggregate Approximation for Electrical Load Pattern Grouping. *IET Generation, Transm. Distribution* 7 (2), 108–117. doi:10.1049/iet-gtd.2012.0383

Oh, S.-K., and Pedrycz, W. (2002). The Design of Self-Organizing Polynomial Neural Networks. *Inf. Sci.* 141 (3–4), 237–258. doi:10.1016/s0020-0255(02)00175-5

Pitner, T., Kriksciuniene, D., and Sakalauskas, V. (2012). Tracking Customer Portrait by Unsupervised Classification Techniques[J]. *Transformations Business Econ.* 11 (3), 167–189.

Qiu, H., Ying, T. U., and Ding, Q. (2017). Construction of Power Customer Portrait and its Credit Evaluation and Electricity Fee Risk Control Based on Tag Library System[J]. *Telecommunications Sci.* 1, 206–213.

Safavian, S. R., and Landgrebe, D. (1991). A Survey of Decision Tree Classifier Methodology. *IEEE Trans. Syst. Man. Cybern.* 21 (3), 660–674. doi:10.1109/21.97458

Sanchez, J. J., Barquin, J., Centeno, E., and López-Peña, Á. (2008). "A Multidisciplinary Approach to Model Long-Term Investments in Electricity Generation: Combining System Dynamics, Credit Risk Theory and Game Theory," in Power & Energy Society General Meeting-conversion & Delivery of Electrical Energy in the Century (IEEE). doi:10.1109/pes.2008.4596452

Shan, X. (2018). Research on User Portrait Based on Online Review: Taking C-Trip Hotel as an Example[J]. *Inf. Stud. Theor. Appl.*

Specht, D. F. (1991). A General Regression Neural Network. *IEEE Trans. Neural Netw.* 2 (6), 568–576. doi:10.1109/72.97934

Wang, X.-Z., Xing, H.-J., Li, Y., Hua, Q., Dong, C.-R., and Pedrycz, W. (2015). A Study on Relationship Between Generalization Abilities and Fuzziness of Base Classifiers in Ensemble Learning. *IEEE Trans. Fuzzy Syst.* 23 (5), 1638–1654. doi:10.1109/tfuzz.2014.2371479

Wu, T., Yang, F., Zhang, D., Zhu, A., and Wan, F. (2020). "Research on Recommendation System Based on User Portrait," in 2020 IEEE International Conference on Artificial Intelligence and Information Systems (ICAIIS) (IEEE). doi:10.1109/icaiis49377.2020.9194941

Xi, L., Yu, T., Yang, B., Zhang, X., and Qiu, X. (2016). A Wolf Pack Hunting Strategy Based Virtual Tribes Control for Automatic Generation Control of Smart Grid. *Appl. Energ.* 178, 198–211. doi:10.1016/j.apenergy.2016.06.041

Yang, B., Jiang, L., Wang, L., Yao, W., and Wu, Q. H. (2016). Nonlinear Maximum Power point Tracking Control and Modal Analysis of DFIG Based Wind Turbine. *Int. J. Electr. Power Energ. Syst.* 74, 429–436. doi:10.1016/j.ijepes.2015.07.036

Yang, B., Jiang, L., Yao, W., and Wu, Q. H. (2015). Perturbation Estimation Based Coordinated Adaptive Passive Control for Multimachine Power Systems. *Control. Eng. Pract.* 44, 172–192. doi:10.1016/j.conengprac.2015.07.012

Yang, B., Wang, J., Zhang, X., Yu, T., Yao, W., Shu, H., et al. (2020). Comprehensive Overview of Meta-Heuristic Algorithm Applications on Pv Cell Parameter Identification. *Energ. Convers. Manage.* 208, 112595. doi:10.1016/j.enconman.2020.112595

Yang, B., Yu, T., Shu, H., Dong, J., and Jiang, L. (2018). Robust Sliding-Mode Control of Wind Energy Conversion Systems for Optimal Power Extraction via

Nonlinear Perturbation Observers. *Appl. Energ.* 210, 711–723. doi:10.1016/j.apenergy.2017.08.027

Yang, B., Yu, T., Zhang, X., Li, H., Shu, H., Sang, Y., et al. (2019). Dynamic Leader Based Collective Intelligence for Maximum Power Point Tracking of PV Systems Affected by Partial Shading Condition. *Energ. Convers. Manage.* 179, 286–303. doi:10.1016/j.enconman.2018.10.074

Yang, B., Zhang, X., Yu, T., Shu, H., and Fang, Z. (2017). Grouped Grey Wolf Optimizer for Maximum Power point Tracking of Doubly-Fed Induction Generator Based Wind Turbine. *Energ. Convers. Manage.* 133, 427–443. doi:10.1016/j.enconman.2016.10.062

Yang, B., Zhong, L., Zhang, X., Shu, H., Yu, T., Li, H., et al. (2019). Novel Bio-Inspired Memetic Salp Swarm Algorithm and Application to MPPT for PV Systems Considering Partial Shading Condition. *J. Clean. Prod.* 215, 1203–1222. doi:10.1016/j.jclepro.2019.01.150

Yaoyao, H. E., Qifa, X. U., Yang, S., and Yu, B. (2013). A Power Load Probability Density Forecasting Method Based on RBF Neural Network Quantile Regression[J]. *Proc. CSEE* 33 (1), 93–98.

Yu, X., Wang, L., Li, Y., Xin, L., Li, G., and Zhang, Z. (2017). Application Research on the Customer's Portrait of Electric Power Marketing Informatization[J]. *Comput. Technol. Automation*.

Zhang, H., Qin, X., and Zheng, H. (2020). Research on Contextual Recommendation System of Agricultural Science and Technology Resource Based on User Portrait [J]. *J. Phys. Conf. Ser.* 1693 (1), 012186. doi:10.1088/1742-6596/1693/1/012186

Zhang, X., Tan, T., Zhou, B., Yu, T., Yang, B., and Huang, X. (2021). Adaptive Distributed Auction-Based Algorithm for Optimal Mileage Based AGC Dispatch with High Participation of Renewable Energy. *Int. J. Electr. Power Energ. Syst.* 124, 106371. doi:10.1016/j.ijepes.2020.106371

Zhang, X., Yu, T., Yang, B., and Li, L. (2016). Virtual Generation Tribe Based Robust Collaborative Consensus Algorithm for Dynamic Generation Command Dispatch Optimization of Smart Grid. *Energy* 101, 34–51. doi:10.1016/j.energy.2016.02.009

Zhang, X., Yu, T., Yang, B., Zheng, L., and Huang, L. (2015). Approximate Ideal Multi-Objective Solution Q(λ) Learning for Optimal Carbon-Energy Combined-Flow in Multi-Energy Power Systems. *Energ. Convers. Manage.* 106, 543–556. doi:10.1016/j.enconman.2015.09.049

Zhong, C., Shao, J., Zheng, F., Zhang, K., Lv, H., and Li, K. (2018). "Research on Electricity Consumption Behavior of Electric Power Users Based on Tag Technology and Clustering Algorithm," in 2018 5th International Conference on Information Science and Control Engineering (ICISCE). doi:10.1109/icisce.2018.00102

Conflict of Interest: The authors declare that the research was conducted in the absence of any commercial or financial relationships that could be construed as a potential conflict of interest.

Publisher's Note: All claims expressed in this article are solely those of the authors and do not necessarily represent those of their affiliated organizations, or those of the publisher, the editors, and the reviewers. Any product that may be evaluated in this article, or claim that may be made by its manufacturer, is not guaranteed or endorsed by the publisher.

Copyright © 2021 Guan, Zhang, Yu, Peng, Wu, Yu and Wang. This is an open-access article distributed under the terms of the Creative Commons Attribution License (CC BY). The use, distribution or reproduction in other forums is permitted, provided the original author(s) and the copyright owner(s) are credited and that the original publication in this journal is cited, in accordance with accepted academic practice. No use, distribution or reproduction is permitted which does not comply with these terms.

frontiers in Energy Research

ORIGINAL RESEARCH
published: 20 October 2021
doi: 10.3389/fenrg.2021.762480

Optimization and H_∞ Performance Analysis for Load Frequency Control of Power Systems With Time-Varying Delays

Kangyou Su[1], *Yan Li*[2], *Jian Chen*[3] *and Wenyong Duan*[3]*

[1]Electronic and Information Engineering Department, Guangdong Baiyun University, Guangzhou, China, [2]Undergraduate Office, Yancheng Biological Engineering Higher Vocational Technology School, Yancheng, China, [3]School of Electrical Engineering, Yancheng Institute of Technology, Yancheng, China

With the development and expansion of the power grid, the load frequency control (LFC) scheme receives sensor signals and outputs control signals through an open communication network with a mass of data and extensive information exchange, which may introduce constant, and time-varying delays. This paper considers the optimization and H_∞ performance problem for LFC of power systems with time-varying delays. Some improved criteria for guaranteeing the stability and H_∞ performance of the closed-loop system with unknown external load disturbances via the Lyapunov stability theory application. An unique delay-dependent proportional-integral (PI) controller and an optimized PI controller are designed for a specified H_∞ performance index and set, respectively. The criteria proposed in this paper are based on linear matrix inequalities (LMIs), which can be easily solved by the MATLAB LMI-Toolbox. Finally, in case studies, the effectiveness of our method is demonstrated.

Keywords: optimization and control, power system, smart grids, H ∞ control, load frequency control, time delays

OPEN ACCESS

Edited by:
Yaxing Ren,
University of Warwick,
United Kingdom

Reviewed by:
Yan Zhang,
Jinling Institute of Technology, China
Yaping Xia,
Xiangtan University, China

***Correspondence:**
Wenyong Duan
dwy1985@126.com

Specialty section:
This article was submitted to Smart Grids, a section of the journal Frontiers in Energy Research

Received: *22 August 2021*
Accepted: *30 September 2021*
Published: *20 October 2021*

Citation:
Su K, Li Y, Chen J and Duan W (2021) Optimization and H_∞ Performance Analysis for Load Frequency Control of Power Systems With Time-Varying Delays. Front. Energy Res. 9:762480. doi: 10.3389/fenrg.2021.762480

1 INTRODUCTION

LFC strategy is equipped to guarantee the power grid frequency, an important index of power quality, stability (de A. F. Mello et al., 2020). With the development and expansion of the power grid, the dedicated independent communication network has been unable to meet the operation of the power grid (Khalil and Swee Peng, 2018). Recently, LFC scheme transmits sensor and control signals based on an open communication network, where random delays and data packets will be introduced into the LFC scheme (Shen et al., 2021). These network factors may cause the LFC system performance degradation and even instability. Thus, it is necessary to study the influence of time-varying delays on performance of the LFC system in an open communication network.

The network controlled LFC system involves two main cases of time-varying delays: 1) the communication time-varying delay from the control center to the governor (Ramakrishnan and Ray, 2015; Yang et al., 2018; Chen et al., 2020; Manikandan and Kokil, 2020), where delay-dependent stability analysis and controller design are investigated by using single delay to model all time delays; 2) In fact, not only the communication time-varying delay from the control center to the governor but also from the sensor to the control center (Jiang et al., 2012; Xu et al., 2017; Shen et al., 2019a), where general delay-dependent stability analysis is studied by using additive time-varying delays to model two different time delays. In a word, the LFC scheme with communication channels can be treated as a typical delayed system. For the stability analysis of the system, it is significance to seek the

maximum allowable time delay upper bounds to guarantee the stability of the power system based on LFC scheme, which has attracted more and more scholars' attention (Ali et al., 2020; del Giudice et al., 2021; Ladygin et al., 2020; Baykov et al., 2019). The stability conditions and controller design are obtained mainly by the Lyapunov stability theory. For further reducing the conservatism of stability criteria, two updates are in progress. On the one hand, the Lyapunov-Krasovskii functional (LKFs) are improved via some novel approaches. Duan et al. (2019a); Duan et al. (2020a); Hua et al. (2021) constructed new LKFs by using the delay decomposition method. The LKFs were modified in Duan et al. (2016); Duan et al. (2017); Scopus et al. (2020); Gholami (2021) by intruducing some multiple integral items. Duan et al. (2020b) augmented the LKF with some augmented vectors. On the other hand, the upper bounds of the derivatives of the LKFs are estimated using some novel tight inequality techniques. Jensen inequality and B-L inequality were proposed in Gu (2000) and Seuret and Gouaisbaut (2015), respectively, where a tight upper bound of the derivative of the LKFs was obtained. Zhang et al. (2017a); Duan et al. (2018); Duan et al. (2019b); Feng et al. (2020); Kwon and Lee (2021) reduced the conservatism of the stability criterion via some relaxed integral inequality techniques. Recently, a novel negative definite inequality equivalent transformation lemma was proposed in Fúlvia et al. (2020), which improved the degree of freedom for solving the LMI in the main theorem without introducing extra conservatism. Thus, there is still room to further reduce the conservatism of stability criteria for the LFC power system along with the update of stability methods for general time-delayed systems.

Moreover, the growing power system based on network control leads to the complexity and uncertainty. Many important control algorithms, such as robust control (Shayeghi et al., 2008), genetic algorithm (Rerkpreedapong et al., 2003), sliding mode control (Vrdoljak et al., 2010) and H_∞ control (Dey et al., 2012; Shen et al., 2021), are used to ensure the operation stability and disturbance rejection capability of large-scale power systems. However, in many studies, especially in controller design, the influence of time delays, especially time-varying delays, is ignored. Based on the above discussion, the H_∞ LFC problem of power systems with time-varyig delays and load disturbances is studied in this paper. The contributions of this paper can be summarized as follows:

- H_∞ performance problem for the LFC power systems with time-varying delays is considered in this paper, where fixed and optimized controller gains for an given H_∞ performance index γ and an performance index set $[\gamma_1, \gamma_2]$ are respectively proposed;
- An augmented LKF combining delay-dependent non-integral terms with some single-integral terms under different time-varying delay subintervals are constructed, which reduces the conservatism caused by the LKF structure;
- A novel negative definite inequality equivalent transformation lemma proposed in (Fúlvia et al., 2020) is used to transform the nonlinear inequality to the LMI equivalently, which can be easily solved by the MATLAB LMI-Toolbox.

This paper is organized as follows. **Section 2** gives the models of LFC schemes; **Section 3** provides stability assessment and H_∞ controller design for the LFC system. **Section 4** shows cases studies. Conclusions are drawn in **Section 5**.

Notation: Throughout this paper, the notations are standard. $\mathbb{R}^n$ denotes the n-dimensional Euclidean space; $\mathbb{R}^{n\times m}$ is the set of all $n \times m$ real matrices; For $P \in \mathbb{R}^{n\times n}$, $P > 0$ (respectively, $P < 0$) mean that P is a positive (respectively, negative) definite matrix. $\mathrm{diag}\{a_1, a_2, \ldots, a_n\}$ denotes an n-order diagonal matrix with diagonal elements a_1, a_2, …, a_n. e_i ($i = 0, 1, \ldots, m$) are block entry matrices. For example, $e_2 = [0 \quad I \quad \underbrace{0\cdots0}_{m-2}]$. For a real matrix B and two real symmetric matrices A and C of appropriate dimensions, $\begin{bmatrix} A & B \\ \star & C \end{bmatrix}$ denotes a real symmetric matrix, where $\star$ denotes the entries implied by symmetry. $\mathrm{Sym}\{A\} = A + A^T$.

2 SYSTEM DESCRIPTION AND PROBLEM PRELIMINARIES

In this section, the model of one-area power system equipped with PI controllers and taking into account the time-varying communication delays is given. The basic diagram of the simplified LFC of one-area power system is shown in **Figure 1**, where e^{-sd} is time delay, arising during the control signal sent from the control center to the governor.

According the LFC system as shown in (Bevrani, 2014) and **Figure 1**, the common LFC scheme model of one-area can be expressed as follows:

$$\begin{cases} \dot{\bar{x}}(t) = \bar{A}\bar{x}(t) + \bar{B}\Delta P_c(t) + \bar{F}\bar{\omega}(t), \\ \bar{y}(t) = \bar{C}\bar{x}(t), \end{cases} \tag{1}$$

where

$$\bar{x}(t) = \begin{bmatrix} \Delta f(t) \\ \Delta P_m(t) \\ \Delta P_v(t) \end{bmatrix},\ \bar{y}(t) = ACE(t),\ \bar{A} = \begin{bmatrix} -\frac{D}{M} & \frac{1}{M} & 0 \\ 0 & -\frac{1}{T_{ch}} & \frac{1}{T_{ch}} \\ -\frac{1}{RT_g} & 0 & -\frac{1}{T_g} \end{bmatrix},$$

$$\bar{B} = \begin{bmatrix} 0 \\ 0 \\ \frac{1}{T_g} \end{bmatrix},\ \bar{F} = \begin{bmatrix} -\frac{1}{M} \\ 0 \\ 0 \end{bmatrix},\ \bar{C} = [\beta\ 0\ 0]$$

and explanations of some terms are shown in **Table 1**. The following PI controller is used as the LFC scheme:

$$u(t) = -K_P ACE(t) - K_I \int ACE(t)dt. \tag{2}$$

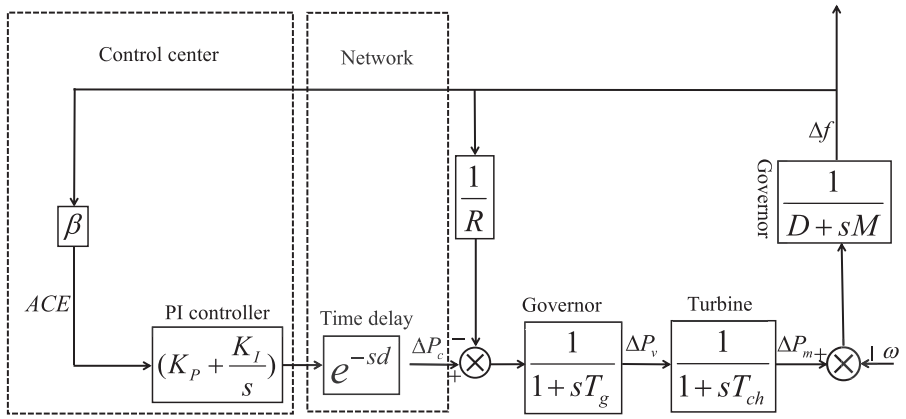


FIGURE 1 | The basic diagram of the simplified LFC of one-area power system.

TABLE 1 | Explanation of terminologies.

Terminology	Meaning
$\Delta f(t)$	frequency deviation
$\Delta P_m(t)$	mechanical output change
$\Delta P_v(t)$	valve position change
$\Delta P_c(t)$	setpoint
$\omega(t)$	load disturbance
$ACE(t)$	area control error
D	generator damping coefficient
M	moment of inertia of the generator
R	speed droop
B	frequency bias factor
T_g	time constant of the governor
T_{ch}	time constant of the turbine
K_P	proportional gain
K_I	integral gain

Due to the existence of the time-varying delay, in the feedback channel, the following is obtained

$$\Delta P_C(t) = u(t - h(t)),\ \ ACE(t) = \beta \Delta f(t), \tag{3}$$

where $h(t)$ represents the time-varying delay, and $0 \le h(t) \le h$, $|\dot{h}(t)| \le \mu$ with h and μ being positive constants.

By defining virtual state and measurement output vector as $y(t) = \mathrm{col}\{ACE(t), \int ACE(t)dt\}$ and $x(t) = \mathrm{col}\{\Delta f(t), \Delta P_m(t), \Delta P_v(t), \int ACE(t)dt\}$, $K = [K_P\ K_I]$, the closed-loop LFC system can be expressed as the following linear system with time-varying delays:

$$\begin{cases} \dot{x}(t) = Ax(t) + BKCx(t - h(t)) + F\omega(t), \\ y(t) = Cx(t), \\ x(t) = \phi(t),\ t \in [-h, 0], \end{cases} \tag{4}$$

where $\phi(t)$ denotes its initial condition which is a vector continuous function of $t \in [-h, 0]$ and the system parameters are listed in the following form

$$A = \begin{bmatrix} -\frac{D}{M} & \frac{1}{M} & 0 & 0 \\ 0 & -\frac{1}{T_{ch}} & \frac{1}{T_{ch}} & 0 \\ -\frac{1}{RT_g} & 0 & -\frac{1}{T_g} & 0 \\ \beta & 0 & 0 & 0 \end{bmatrix},\ B = \begin{bmatrix} 0 \\ 0 \\ -\frac{1}{T_g} \\ 0 \end{bmatrix},\ C = \begin{bmatrix} \beta & 0 & 0 & 0 \\ 0 & 0 & 0 & 1 \end{bmatrix},$$

$$F = \begin{bmatrix} -\frac{1}{M} \\ 0 \\ 0 \\ 0 \end{bmatrix}.$$

A definition and some lemmas need to be displayed here before we proceed with the next step of calculation and discussion.

Definition 1. (Shen et al., 2019b) the system is considered to be asymptotically stable and meets the H_∞ performance index γ if the following conditions are met.

- The system is asymptotically stable when the disturbance input is not taken into account (i.e., $\omega(t) \equiv 0$).
- For any nonzero disturbance, given a positive scalar γ, the following inequality is satisfied under zero initial conditions ($x(t) = 0$, $t \in [-d, 0]$):

$$\Omega = \int_0^\infty [y^T(\alpha)y(\alpha) - \gamma^2 \omega^T(\alpha)\omega(\alpha)]d\alpha \le 0. \tag{5}$$

Lemma 1. (Seuret and Gouaisbaut, 2015). For a positive definite matrix R and differentiable function x in $[a, b] \to \mathbb{R}^n$, the followings hold

$$\int_a^b \dot{x}^T(s)R\dot{x}(s)ds \ge \frac{1}{b-a}\omega^T \mathcal{R}\omega,$$

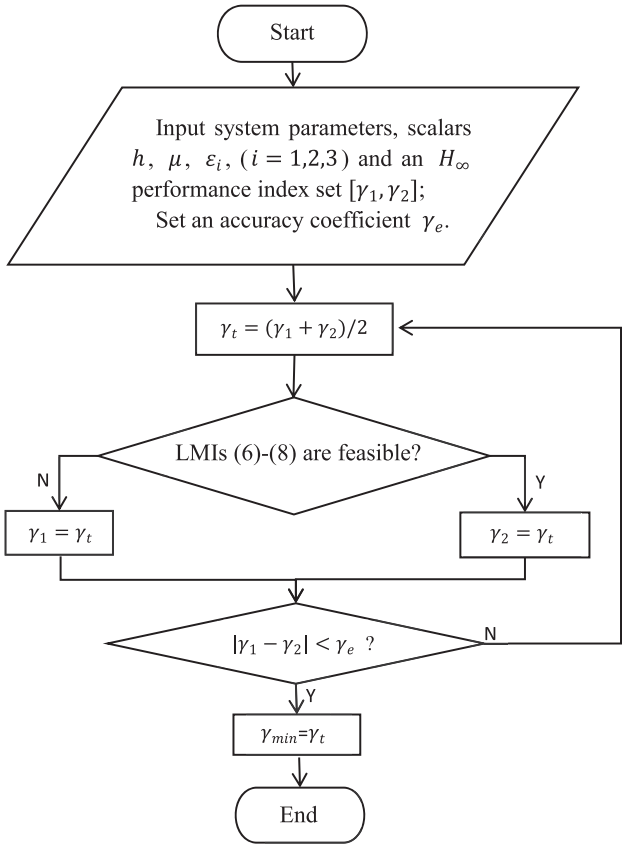


FIGURE 2 | Binary search optimization for solving optimal performance index.

where $\mathcal{R} = \text{diag}\{R, 3R, 5R\}$, $\omega = \text{col}\{\omega_1, \omega_2, \omega_3\}$ with $\omega_1 = x(b) - x(a)$, $\omega_2 = x(b) + x(a) - \frac{2}{b-a}\int_a^b x(s)ds$, $\omega_3 = \omega_1 - \frac{6}{b-a}\int_a^b x(s)ds + \frac{12}{(b-a)^2}\int_a^b (b-s)x(s)ds$.

Lemma 2. (Zhang et al., 2017b). For positive definite matrices R_1, $R_2 \in \mathbb{R}^{n\times n}$, vectors v_1, $v_2 \in \mathbb{R}^n$ and a scalar $\alpha \in [0, 1]$, if there exist symmetric matrices $X_1, X_2 \in \mathbb{R}^{n\times n}$ and any matrices $S_1, S_2 \in \mathbb{R}^{n\times n}$ such that

$$\begin{bmatrix} R_1 - X_1 & S_1 \\ * & R_1 \end{bmatrix} \geq 0, \quad \begin{bmatrix} R_2 - X_2 & S_2 \\ * & R_2 \end{bmatrix} \geq 0,$$

the following inequality holds

$$\frac{1}{\alpha}v_1^T R_1 v_1 + \frac{1}{1-\alpha}v_2^T R_2 v_2 \geq v_1^T[R_1 + (1-\alpha)X_1]v_1 + v_2^T[R_2 + \alpha X_2]v_2 + 2v_1^T[\alpha S_1 + (1-\alpha)S_2]v_2.$$

Lemma 3. (Fúlvia et al., 2020). Let symmetric matrices A_0, A_1, $A_2 \in \mathbb{R}^{m\times m}$ and a vector $\zeta \in \mathbb{R}^m$. Then, the following inequality

$$\zeta^T(h_t^2 A_2 + h_t A_1 + A_0)\zeta < 0$$

TABLE 2 | Parameters of one-area LFC system.

	T_{ch}(s)	β	R	T_g(S)	D	M(s)
Area 1	0.3	21	0.05	0.1	1	10

TABLE 3 | MAUBs h for μ = 0 under one-area LFC system.

K_P	Methods \ K_I	0.2	0.4	0.6
0	Ramakrishnan and Ray, (2015)	6.69	3.12	1.91
	Yang et al. (2017)	7.33	3.38	2.04
	Jiao et al. (2021)	11.70	6.15	4.17
	Corollary 1	7.331	3.382	2.045
0.1	Ramakrishnan and Ray, (2015)	6.94	3.29	2.02
	Yang et al. (2017)	7.79	3.61	2.19
	Jiao et al. (2021)	10.96	5.83	4.05
	Corollary 1	7.790	3.610	2.193

holds for all $h_t \in [0, h]$ if and only if there exist a positive definite matrix $D \in \mathbb{R}^{m\times m}$ and a skew-symmetric matrix $G \in \mathbb{R}^{k\times k}$ such that

$$\begin{bmatrix} A_0 & \frac{1}{2}A_1 \\ * & A_2 \end{bmatrix} < \begin{bmatrix} C \\ J \end{bmatrix}^T \begin{bmatrix} -D & G \\ * & D \end{bmatrix} \begin{bmatrix} C \\ J \end{bmatrix},$$

where $C = [\frac{h}{2}I \quad 0]$ and $J = [\frac{h}{2}I \quad -I]$.

3 MAIN RESULTS

In order to make the calculation process more concise, some expressions are given in advance as below

$$\begin{aligned}
h_t &= h(t),\ \bar{h}_t = h - h(t),\ h_d = 1 - \dot{h}(t),\\
\eta_0(t) &= \text{col}\{x(t), x(t-h_t), x(t-h)\},\\
\eta_1(t) &= \text{col}\left\{x(t), x(t-h_t), \int_{t-h_t}^{t} x(s)ds\right\},\\
\eta_2(t) &= \text{col}\left\{x(t-h_t), x(t-h), \int_{t-h}^{t-h_t} x(s)ds\right\},\\
\eta_3(t,s) &= \text{col}\left\{\dot{x}(s), x(s), \eta_0(t), \int_s^t x(\theta)d\theta, \int_{t-h_t}^{s} x(\theta)d\theta, \int_{t-h}^{t-h_t} x(\theta)d\theta\right\},\\
\eta_4(t,s) &= \text{col}\left\{\dot{x}(s), x(s), \eta_0(t), \int_s^{t-h_t} x(\theta)d\theta, \int_{t-h_t}^{t} x(\theta)d\theta, \int_{t-h}^{s} x(\theta)d\theta\right\},\\
\rho_1(t) &= \int_{t-h}^{t-h_t}\frac{x(s)}{\bar{h}_t}, \rho_2(t) = \int_{t-h}^{t-h_t}\frac{(t-h_t-s)x(s)}{\bar{h}_t^2},\\
\rho_3(t) &= \int_{t-h_t}^{t}\frac{x(s)}{h_t}, \rho_4(t) = \int_{t-h_t}^{t}\frac{(t-s)x(s)}{h_t^2},\\
\xi(t) &= \text{col}\{x(t), x(t-h_t), x(t-h), \dot{x}(t), \dot{x}(t-h_t), \dot{x}(t-h), \rho_1(t), \rho_2(t), \rho_3(t), \rho_4(t), \omega(t)\}.
\end{aligned}$$

3.1 H_∞ Performance Analysis

Theorem 1. Given positive scalars h, μ, ε_j and γ, system (4) is stable and meets the H_∞ performance index γ, if there exist positive definite matrices $S_{i2} \in \mathbb{R}^{3n\times 3n}, Q_i \in \mathbb{R}^{8n\times 8n}$, $R_i \in \mathbb{R}^{n\times n}$, $\mathcal{D}_i \in \mathbb{R}^{(10n+1)\times(10n+1)}$, symmetric matrices $S_{i1}, X_i \in \mathbb{R}^{3n\times 3n}$, skew-symmetric matrices $\mathcal{G}_i \in \mathbb{R}^{(10n+1)\times(10n+1)}$, any matrices $Y_i \in \mathbb{R}^{3n\times 3n}$, $(i = 1, 2;\ j = 1, 2, 3)$, $U \in \mathbb{R}^{n\times n}$, such that the following matrix inequalities hold for $\dot{h}_t \triangleq \mu_i \in \{-\mu, \mu\}$.

TABLE 4 | MAUBs h for $\mu = 0.9$ under one-area LFC system.

K_P	Methods \ K_I	0.2	0.4	0.6
0	Ramakrishnan and Ray, (2015)	6.25	2.85	1.68
	Yang et al. (2017)	6.43	2.91	1.71
	Jiao et al. (2021)	9.98	4.44	2.80
	Corollary 1	7.13	3.21	1.92
0.1	Ramakrishnan and Ray, (2015)	5.93	2.87	1.75
	Yang et al. (2017)	6.59	3.11	1.84
	Jiao et al. (2021)	9.17	4.31	2.83
	Corollary 1	7.14	3.25	1.96

$$hS_{i1} + S_{i2} > 0, \tag{6}$$

$$\begin{bmatrix} \bar{R}_i - X_i & Y_i \\ * & \bar{R}_i \end{bmatrix} > 0, \tag{7}$$

$$\begin{bmatrix} \Omega_0(\mu_i) & \frac{1}{2}\Omega_1(\mu_i) \\ * & \Omega_2(\mu_i) \end{bmatrix} - \begin{bmatrix} \mathcal{C} \\ \mathcal{J} \end{bmatrix}^T \begin{bmatrix} -\mathcal{D}_i & \mathcal{G}_i \\ * & \mathcal{D}_i \end{bmatrix} \begin{bmatrix} \mathcal{C} \\ \mathcal{J} \end{bmatrix} < 0, \tag{8}$$

where the notations of other symbols and matrices can be found in **Appendix A**. Thus, the controller gain matrix calculated by

$$K = (UB)^{+} K_0, \tag{9}$$

where the generalized inverse of (UB) is expressed as $(UB)^{+}$.

Proof. Construct an LKF candidate as

$$V(t) = V_1(t) + V_2(t) + V_3(t) \tag{10}$$

with

$$V_1(t) = \eta_1^T(t) S_1(t) \eta_1(t) + \eta_2^T(t) S_2(t) \eta_2(t),$$
$$V_2(t) = \int_{t-h_t}^{t} \eta_3^T(t,s) Q_1 \eta_3(t,s) ds + \int_{t-h}^{t-h_t} \eta_4^T(t,s) Q_2 \eta_4(t,s) ds$$
$$V_3(t) = h \int_{t-h}^{t-h_t} (h - t + s) \dot{x}^T(s) R_1 \dot{x}(s) ds + h \int_{t-h_t}^{t} (h - t + s) \dot{x}^T(s) R_2 \dot{x}(s) ds,$$

where $S_1(t) = h_t S_{11} + S_{12}$ and $S_2(t) = \bar{h}_t S_{21} + S_{22}$.

Calculating the derivative of $V(t)$, we can obtain the following formulas

$$\begin{aligned} \dot{V}_1(t) = & \; 2\dot{\eta}_1^T(t) S_1(t) \eta_1(t) + \eta_1^T(t) \dot{S}_1(t) \eta_1(t) \\ & + 2\dot{\eta}_2^T(t) S_2(t) \eta_2(t) + \eta_2^T(t) \dot{S}_2(t) \eta_2(t) \\ = & \; 2\xi^T(t) \Delta_{13}^T (h_t S_{11} + S_{12}) (\Delta_{11} + h_t \Delta_{12}) \xi(t) \\ & + \xi^T(t) (\Delta_{11} + h_t \Delta_{12})^T \dot{h}_t S_{11} (\Delta_{11} + h_t \Delta_{12}) \xi(t) \\ & + 2\xi^T(t) \Delta_{23}^T (\bar{h}_t S_{21} + S_{22}) (\Delta_{21} + h_t \Delta_{22}) \xi(t) \\ & - \xi^T(t) (\Delta_{21} + h_t \Delta_{22})^T \dot{h}_t S_{21} (\Delta_{21} + h_t \Delta_{22}) \xi(t), \end{aligned} \tag{11}$$

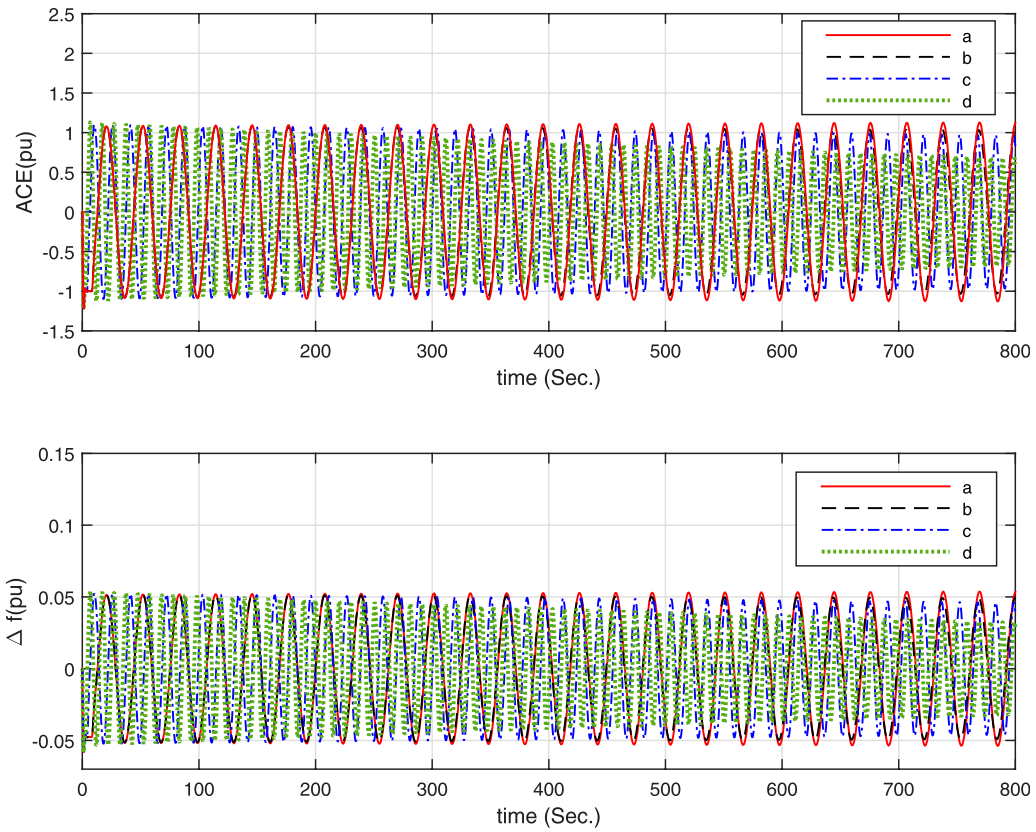


FIGURE 3 | Frequency deviation and control error responses of one-area LFC scheme under $\mu = 0$.

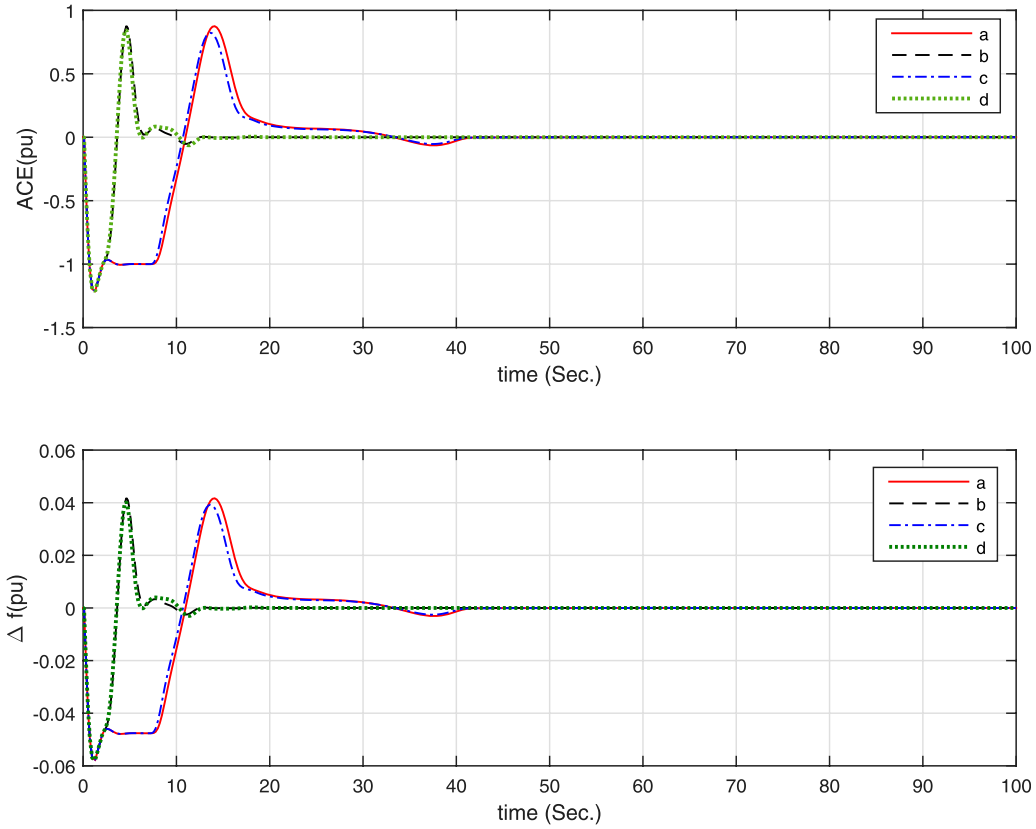


FIGURE 4 | Frequency deviation and control error responses of one-area LFC scheme under $\mu = 0.9$.

$$
\begin{aligned}
\dot{V}_2(t) &= \eta_1^T(t,t)Q_1\eta_1(t,t) - \eta_2^T(t,t-h_1)Q_2\eta_2(t,t-h_1)\\
&\quad - h_{1d}\eta_1^T(t,t-h_t)Q_1\eta_1(t,t-h_t)\\
&\quad + h_{1d}\eta_2^T(t,t-h_t)Q_2\eta_2(t,t-h_t)\\
&\quad + 2\int_{t-h_t}^{t}\eta_1^T(t,s)Q_1\frac{\partial}{\partial t}\eta_1(t,s)ds\\
&\quad + 2\int_{t-h}^{t-h_t}\eta_2^T(t,s)Q_2\frac{\partial}{\partial t}\eta_2(t,s)ds\\
&= \xi^T(t)\Big[(\Delta_{31}+h_t\Delta_{32})^TQ_1(\Delta_{31}+h_t\Delta_{32})\\
&\quad -(\Delta_{41}+h_t\Delta_{42})^TQ_2(\Delta_{41}+h_t\Delta_{42})\Big]\xi(t)\\
&\quad - h_{1d}\xi^T(t)\Big[(\Delta_{33}+h_t\Delta_{34})^TQ_1(\Delta_{33}+h_t\Delta_{34})\\
&\quad -(\Delta_{43}+h_t\Delta_{44})^TQ_2(\Delta_{43}+h_t\Delta_{44})\Big]\xi(t)\\
&\quad + 2\xi^T(t)\Big[(\Delta_{10}+h_t\Delta_{11}+h_t^2\Delta_{12})^TQ_1\Lambda_1\\
&\quad +(\Lambda_{20}+h_t\Lambda_{21}+h_t^2\Lambda_{22})^TQ_2\Lambda_2\Big]\xi(t),
\end{aligned}
\tag{12}
$$

$$
\begin{aligned}
\dot{V}_3(t) &= h^2\dot{x}^T(t)R_2\dot{x}(t) + hh_d\bar{h}_t\dot{x}^T(t-h_t)(R_1-R_2)\dot{x}(t-h_t)\\
&\quad - h\left(\int_{t-h}^{t-h_t}\dot{x}^T(s)R_1\dot{x}(s)ds + \int_{t-h_t}^{t}\dot{x}^T(s)R_2\dot{x}(s)ds\right).
\end{aligned}
\tag{13}
$$

According to $R_i > 0$, $(i = 1, 2)$, letting $\beta = \frac{h_t}{h}$, it follows from Lemmas 1 and 2 that

$$
\begin{aligned}
&-h\left(\int_{t-h}^{t-h_t}\dot{x}^T(s)R_1\dot{x}(s)ds + \int_{t-h_t}^{t}\dot{x}^T(s)R_2\dot{x}(s)ds\right)\\
&\quad \le -\frac{1}{\beta}\xi^T(t)\Gamma_1^T\bar{R}_1\Gamma_1\xi(t) - \frac{1}{1-\beta}\xi^T(t)\Gamma_2^T\bar{R}_2\Gamma_2\xi(t)\\
&\quad \le -\xi^T(t)[\Gamma_1^T(\bar{R}_1+\beta X_1)\Gamma_1 + 2\Gamma_1^T[(1-\beta)Y_1+\beta Y_2]\Gamma_2\\
&\qquad +\Gamma_2^T[\bar{R}_2+(1-\beta)X_2]\Gamma_2]\xi(t).
\end{aligned}
\tag{14}
$$

For an appropriately matrix $U \in \mathbb{R}^{n\times n}$, $\chi = [1\ \cdots\ 1] \in \mathbb{R}^n$, $\varepsilon_i > 0$, $(i = 1, 2, 3)$, we can get

$$
\begin{aligned}
0 &= 2\Big[x^T(t)\,x^T(t-h_t)\,\dot{x}^T(t)\,\omega^T(t)\Big]\mathrm{col}\{U,\varepsilon_1U,\varepsilon_2U,\varepsilon_3\chi U\}\times\\
&\quad [Ax(t)+BKCx(t-h_t)+F\omega(t)-\dot{x}(t)]\\
&= 2\xi^T(t)\Delta_0^T\{U\}\Pi_0\xi(t).
\end{aligned}
\tag{15}
$$

Finally, from the above derivation (11)–(15) and definition 1, we have

$$
\begin{aligned}
\Xi &= V(\dot{t}) + y^T(t)y(t) - \gamma^2\omega^T(t)\omega(t)\\
&\le \xi^T(t)\Big[\Omega_0(\dot{h}_t) + h_t\Omega_1(\dot{h}_t) + h_t^2\Omega_2(\dot{h}_t)\Big]\xi(t).
\end{aligned}
\tag{16}
$$

According to Lemma 3, the LMI (8) implies that $\Xi < 0$. Due to $0 < t < \infty$, associating with **(5)**, it has

$$V(\infty) - V(0) + \int_0^\infty y^T(s)y(s)ds - \gamma^2 \int_0^\infty \omega^T(s)\omega(s)ds < 0. \tag{17}$$

Since $V(\infty) > 0$, $V(0) \equiv 0$, then

$$\int_0^\infty y^T(s)y(s)ds - \gamma^2 \int_0^\infty \omega^T(s)\omega(s)ds \le 0, \tag{18}$$

which can guarantee that system (4) meets the H_∞ performance index. This completes the proof.

3.2 Optimization of the Controller Gain

Obviously, the matrix inequalities in Theorem 3.1 are LMIs, which can be easily solved by the MATLAB LMI-Toolbox. That is, for a given H_∞ performance index γ, the acquisition of the controller gain K can be processed simply by the convex optimization algorithm described as follows:

Algorithm 1: Acquisition of the Controller Gain.	
Input:	System parameters, scalars h, μ, ε_i, $(i = 1, 2, 3)$ and H_∞ performance index γ.
Output:	The controller gain K.
1:	Construct LMIs (6)-(8);
2:	Run the LMI solver to solve the LMIs (6)-(8);
3:	**if** LMIs (6)-(8) are feasible, **then** proceed to the step 6;
4:	**else** reset the Input;
5:	**end if**
6:	Solve the controller gain K by using the formula (9);
7:	**Return** K.

For a given H_∞ performance index set $[\gamma_1, \gamma_2]$, the controller gain K can be optimized via the binary search technique shown in **Figure 2**. Algorithm 2 is used to further illustrate the method.

Algorithm 2: Optimization of the Controller Gain.	
Input:	System parameters, scalars h, μ, ε_i, $(i = 1, 2, 3)$, H_∞ performance index set $[\gamma_1, \gamma_2]$ and an accuracy coefficient γ_e.
Output:	The controller gain K.
1:	Construct LMIs (6)-(8);
2:	Set $\gamma_t = \gamma_2$, $Count = 0$;
3:	Run the LMI solver to solve the LMIs (6)-(8);
4:	**if** LMIs (6)-(8) are feasible, **then** proceed to the step 7;
5:	**else**
6:	**if** $Count = 0$, **then** cannot find a suitable solution, end algorithm; **else** go to step 8; **end if** **end if**
7:	Set $Count = 1$ and solve the controller gain K by using the formula (9); $\gamma_{min} = \gamma_t$;
8:	$\gamma_1 = \gamma_t$;
9:	**if** $\lvert\gamma_1 - \gamma_2\rvert < \gamma_e$, **then** go to step 12;
10:	**else** $\gamma_t = \lvert\gamma_1 + \gamma_2\rvert/2$, and reverse back to step 3;
11:	**end if**
12:	**Return** K.

Optimization of the Controller Gain.

Input: System parameters, scalars h, μ, ε_i, (i = 1, 2, 3), H_∞ performance index set $[\gamma_1, \gamma_2]$ and an accuracy coefficient γ_e.

TABLE 5 | Controller gains for h = 10 under different μ.

$\mu \setminus K$	K_P	K_I
0	−0.0167	0.0824
0.5	−0.0158	0.0889
0.9	−0.0233	0.1027

TABLE 6 | Controller gains for h = 10 under different μ.

$\mu \setminus K$	K_P	K_I	γ_{min}
0	−0.0175	0.0957	0.30
0.5	−0.0194	0.1008	0.37
0.9	−0.0237	0.1191	0.4

Output: The controller gain K.
1: Construct LMIs (6)–(8);
2: Set $\gamma_t = \gamma_2$, $Count = 0$;
3: Run the LMI solver to solve the LMIs (6)–(8);
4: **if** LMIs (6)–8) are feasible, **then** proceed to the step 7;
5: **else**
6: **if** $Count = 0$, **then** cannot find a suitable solution, end algorithm; **else** go to step 8; end if end if
7: Set $Count = 1$ and solve the controller gain K by using
8: $\gamma_1 = \gamma_t$;
9: **if** $|\gamma_1 - \gamma_2| < \gamma_e$, **then** go to step 12;
10: **else** $\gamma_t = |\gamma_1 + \gamma_2|/2$, and reverse back to step 3;
11: **end if**
12: **Return** K.

3.3 Delay-Dependent Stability Criterion for One-Area System

Remark 1. When dealing with unknown external load disturbances in power systems, it can be modeled as a nonlinear perturbation in the current and delayed state vectors (Ramakrishnan and Ray, 2015):

$$Fw(t) = g(x(t), x(t - h(t))) \tag{19}$$

meets the following condition

$$\|g(\cdot)\| \le \varepsilon\|x(t)\| + \theta\|x(t - h(t))\|, \tag{20}$$

where ε and θ are known non-negative scalars. A more generalized form of the condition is adopted, as follows:

$$g^T(\cdot)g(\cdot) \le \varepsilon^2 x^T(t)M^T M x(t) + \theta^2 x^T(t - h(t))N^T N x(t - h(t)), \tag{21}$$

where M and N are known constant matrices with appropriate dimensions. The non-negative scalars ε, θ and matrices M, N can be used to quantify the impact of load disturbances on power systems.

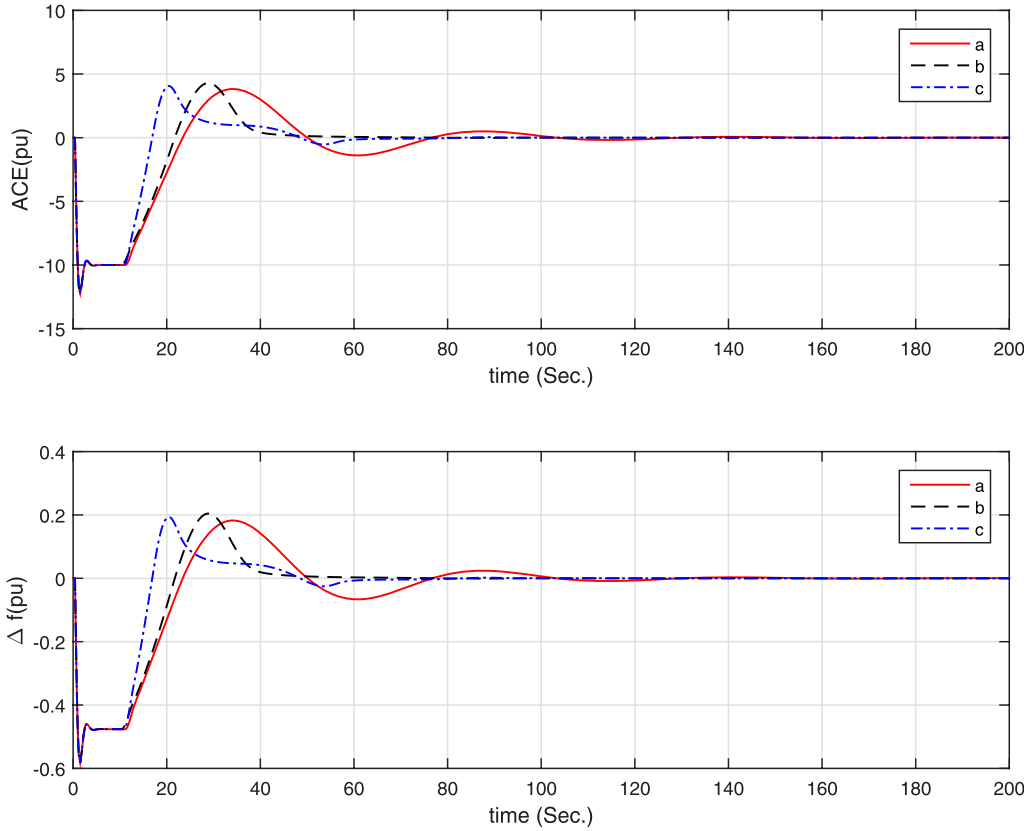


FIGURE 5 | Frequency deviation and control error responses of one-area LFC scheme under $\gamma = 0.4$.

Corollary 1. Given positive scalars h, μ, ε, θ and λ system (4) is asymptotically stable, if there exist positive definite matrices S_{i2}, $Q_i \in \mathbb{R}^{3n\times 3n}$, $R_i \in \mathbb{R}^{n\times n}$, $\mathcal{D}_i$, $\mathcal{G}_i \in \mathbb{R}^{11n\times 11n}$, symmetric matrices S_{i1}, $X_i \in \mathbb{R}^{3n\times 3n}$, any matrices $Y_i \in \mathbb{R}^{3n\times 3n}$, ($i = 1, 2$; $j = 1, 2, 3$), $\tilde{U} \in \mathbb{R}^{4n\times n}$, such that LMIs (6), (7) and the following LMIs hold for $\dot{h}_t \triangleq \mu_i \in \{-\mu, \mu\}$.

$$\begin{bmatrix} \tilde{\Omega}_{10}(\mu_i) & \frac{1}{2}\Omega_{11}(\mu_i) \\ * & \Omega_{21}(\mu_i) \end{bmatrix} - \begin{bmatrix} \mathcal{C} \\ \mathcal{J} \end{bmatrix}^T \begin{bmatrix} -\mathcal{D}_i & \mathcal{G}_i \\ * & \mathcal{D}_i \end{bmatrix} \begin{bmatrix} \mathcal{C} \\ \mathcal{J} \end{bmatrix} < 0 \qquad (22)$$

with

$$\begin{aligned} \tilde{\Omega}_0(\mu_i) = \ & \mathrm{Sym}\{\Delta_{13}^T S_{12}\Delta_{11} + \Delta_{23}^T(hS_{21} + S_{22})\Delta_{21} + \Lambda_{10}^T Q_1 \Lambda_1 + \Lambda_{20}^T Q_2 \Lambda_2\} + \dot{h}_t \Delta_{11}^T S_{11}\Delta_{11} \\ & - \dot{h}_t \Delta_{21}^T S_{21}\Delta_{21} + \Delta_{31}^T Q_1 \Delta_{31} - \Delta_{41}^T Q_2 \Delta_{41} - h_d \Delta_{33}^T Q_1 \Delta_{33} + h_d \Delta_{43}^T Q_2 \Delta_{43} \\ & + e_4^T(\dot{h}^2 R_2)e_4 + h^2 h_d e_5^T(R_1 - R_2)e_5 + \Gamma_1^T \bar{R}_1 \Gamma_1 + \Gamma_2^T(\bar{R}_2 + X_2)\Gamma_2 \\ & + \mathrm{Sym}\{\Gamma_1^T Y_1 \Gamma_2\} + \mathrm{Sym}\{\Delta_0^T \tilde{U}\Pi_0\} + \lambda\theta^2 e_1^T N^T N e_1 + \lambda\varepsilon^2 e_2^T \lambda\varepsilon^2 M^T M e_2 - e_{11}^T \lambda I e_{11} \end{aligned}$$

and other symbols see Theorem 1.

Proof. The proof process of Corollary 1 is similar to Theorem 1, so it is omitted here.

Remark 2. Compared with the literature (Ramakrishnan and Ray, 2015; Yang et al., 2017; Jiao et al., 2021), the results in this paper reduce the conservatism via the augmented LKF application. The LKF proposed in this paper contains more information of the time-varying delay and the coupling information between the state variables and the delay than the literature (Ramakrishnan and Ray, 2015; Yang et al., 2017; Jiao et al., 2021), which reduces the conservatism caused by the LKF structure.

4 CASE STUDIES

In this section, firstly, the effectiveness of the delay-dependent stability criterion for one-area LFC system proposed in this paper is shown. For given different K_P and K_I values, the maximum allowable time-delay upper bound values (MAUB) can be obtained by solving the LMIs in Corollary 1 via Matlab LMI-Toolbox. The LFC system parameters are described as **Table 2** (Jiang et al., 2012), one-area LFC systems will be discussed and comparatively analyzed in the following subsections.

4.1 Conservativeness Comparison

In order to compare with the existing results, **Table 3** and **Table 4** give the MAUB values of the case of given K_P and K_I values, $\varepsilon = 0$, $\theta = 0$, $M = N = 0.1I_4$, $|\dot{h}(t)| \le 0$ or $|\dot{h}(t)| \le 0.9$. From these tables, we can observe the results of Corollary 1 are less conservative

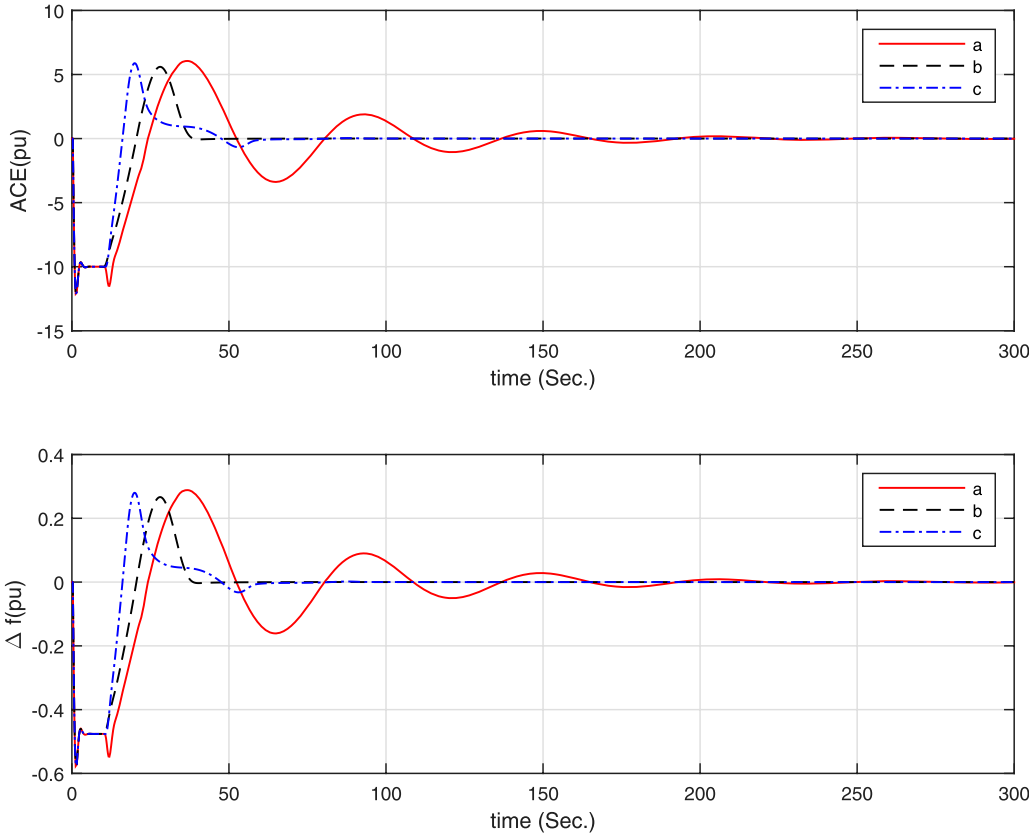


FIGURE 6 | Frequency deviation and control error responses of one-area LFC scheme under $\gamma = 0.37$.

than those of (Ramakrishnan and Ray, 2015; Yang et al., 2017). And the MAUB increases as K_P increases whereas for a fixed K_I value, and the MAUB decreases as K_I increases whereas for a fixed K_P value.

Simple simulations are carried out under an increase step load of 0.1 pu happening at 1s and the following assumptions. The simulation results are shown in **Figures 3**, **4**, in which the LFC has achieve its objective and the control system is stable. In addition, according to the red curve *a* of **Figure 3**, the LFC system closes to critical stability with $h(t) = 7.8$, $K_P = 0.1$ and $K_I = 0.2$, while Corollary 1 in this paper obtains the MAUB $h = 7.790$. Thus, the delay-dependent stability criterion proposed in this paper is effective in estimating the upper bound of the maximum allowable time delay.

- For **Figure 3**, different K_I and fixed $K_P = 0.1$ and $\mu = 0$:
  a. $K_I = 0.2$, $h(t) = 7.8$;
  b. $K_I = 0.2$, $h(t) = 7.79$;
  c. $K_I = 0.4$, $h(t) = 3.61$;
  d. $K_I = 0.6$, $h(t) = 2.193$;
- For **Figure 4**, different K_P, K_I fixed $\mu = 0.9$:
  a. $K_P = 0$, $K_I = 0.2$, $h(t) = \frac{7.13}{2} sin(\frac{1.8}{7.13} t) + \frac{7.13}{2}$;
  b. $K_P = 0$, $K_P = 0.6$, $h(t) = \frac{1.92}{2} sin(\frac{1.8}{1.92} t) + \frac{1.92}{2}$;
  c. $K_P = 0.1$, $K_I = 0.2$, $h(t) = \frac{7.14}{2} sin(\frac{1.8}{7.14} t) + \frac{7.14}{2}$;
  d. $K_P = 0.1$, $K_I = 0.6$, $h(t) = \frac{1.96}{2} sin(\frac{1.8}{1.96} t) + \frac{1.96}{2}$.

4.2 Optimization and H_∞ Performance Discussion

In this subsection, much attention is focused on the following two aspects.

1) Design of the Controller: the **MAUB** is preset as 10 s and $h(t)$ is considered as constant ($\mu = 0$) and time-varying delay ($\mu = 0.9$), respectively. For a given H_∞ performance index $\gamma = 0.4$, the controller gains can be obtained in **Table 5** by referring to the process given in Algorithm 1;
2) Optimization of the Controller: the **MAUB** is preset as 10 s and $h(t)$ is considered as constant ($\mu = 0$) and time-varying delay ($\mu = 0.9$), respectively. For a given H_∞ performance index set [0, 100] and $\gamma_e = 0.5$, the controller gains can be obtained in **Table 6** by referring to the process given in Algorithm 2.

Simple simulations are carried out under an increase step load of 0.1 pu happening at 1s and the following assumptions. The simulation results are shown in **Figures 5**, **6**, in which the LFC has achieve its objective. This scenario suggests that, the use of optimized controller has the merit of improving the performance of the LFC system in terms of its transient response characteristics as well as disturbance rejection capabilities over the tuned local PI controllers acting alone in the system.

- For **Figure 5**, $h = 10$ and $\gamma = 0.4$:
  a. $K_P = -0.0167$, $K_P = 0.0824$, $h(t) = 8$;
  b. $K_P = -0.0158$, $K_P = 0.0889$, $h(t) = \frac{10}{2}sin(\frac{1}{10}t) + \frac{10}{2}$;
  c. $K_P = -0.0233$, $K_P = 0.1027$, $h(t) = \frac{10}{2}sin(\frac{1.8}{10}t) + \frac{10}{2}$;
- For **Figure 6**, $h = 10$:
  a. $K_P = -0.0175$, $K_P = 0.0857$, $h(t) = 8$, $\gamma = 0.3$;
  b. $K_P = -0.0194$, $K_P = 0.1008$, $h(t) = \frac{10}{2}sin(\frac{1}{10}t) + \frac{10}{2}$, $\gamma = 0.37$;
  c. $K_P = -0.0237$, $K_P = 0.1191$, $h(t) = \frac{10}{2}sin(\frac{1.8}{10}t) + \frac{10}{2}$, $\gamma = 0.37$.

5 CONCLUSION

This paper focus on optimization and H_∞ performance problem for LFC of power systems with time-varying delays. For the one-area LFC systems with single communication delays, stability criteria are obtained via Lyapunov stability theory application. Firstly, the one-area LFC system is described as linear systems with time-varying delays and load disturbances; Secondly, a modified LKF is constructed, which contains more coupling information between time-varying delays and state variables than some previous published results to further reduce the conservativeness of the stability criterion; Thirdly, an unique delay-dependent PI controller and an optimized PI controller are designed for a specified H_∞ performance index and set, respectively. Finally, the effectiveness of the proposed method is illustrated by comparison and discussion in numerical examples, which shows that the use of optimized controller has the merit of improving the performance of the LFC system in terms of its transient response characteristics as well as disturbance rejection capabilities over the tuned local PI controllers acting alone in the system. However, the improvement of stability results is in the cost of increasing computational complexity. The derivation method of the stability criterion presented in this paper can be extended to multi-area LFC system, which is one of our further main topics.

DATA AVAILABILITY STATEMENT

The original contributions presented in the study are included in the article/**Supplementary Material**, further inquiries can be directed to the corresponding author.

AUTHOR CONTRIBUTIONS

Conceptualization, methodology, KS and WD; data curation, software, YL; writingoriginal draft, KS; writingreview and editing, JC. All authors have read and agreed to the published version of the manuscript.

FUNDING

This work is supported partly by the Guangdong higher education innovation strong school project under Grant no. 2018KQNCX296, the Technology Research Plan of Guangzhou under Grant no. 202002030230, the Industry University Research Cooperation Project of Jiangsu Province under Grant no. BY2020649, the NSF of Yancheng Biological Engineering Higher Vocational and Technical School under Grant no. x202104 and the Yellow Sea Rookie of Yancheng Institute of Technology.

SUPPLEMENTARY MATERIAL

The Supplementary Material for this article can be found online at: https://www.frontiersin.org/articles/10.3389/fenrg.2021.762480/full#supplementary-material

REFERENCES

Ali, D., Mohammad, M., Zeinolabedin, M., and Lieven, V. (2020). A Novel Technique for Load Frequency Control of Multi-Area Power Systems. *Energies* 13, 2125. doi:10.3390/en13092125

Baykov, D. V., Gulyaev, I. V., Inshakov, A. P., and Teplukhov, D. Y. (2019). Simulation Modeling of an Induction Motor Drive Controlled by an Array Frequency Converter. *Russ. Electr. Engin.* 90, 485–490. doi:10.3103/s1068371219070034

Bevrani, H. (2014). *Robust Power System Frequency Control.* Springer.

Chen, B.-Y., Shangguan, X.-C., Jin, L., and Li, D.-Y. (2020). An Improved Stability Criterion for Load Frequency Control of Power Systems with Time-Varying Delays. *Energies* 13, 2101. doi:10.3390/en13082101

de A. F. Mello, F. R., Apostolopoulou, D., and Alonso, E. (2020). Cost Efficient Distributed Load Frequency Control in Power Systems. *IFAC-PapersOnLine* 53, 8037–8042. doi:10.1016/j.ifacol.2020.12.2236

del Giudice, D., Brambilla, A., Grillo, S., and Bizzarri, F. (2021). Effects of Inertia, Load Damping and Dead-Bands on Frequency Histograms and Frequency Control of Power Systems. *Int. J. Electr. Power Energ. Syst.* 129, 106842. doi:10.1016/j.ijepes.2021.106842

Dey, R., Ghosh, S., Ray, G., and Rakshit, A. (2012). H∞ Load Frequency Control of Interconnected Power Systems with Communication Delays. *Int. J. Electr. Power Energ. Syst.* 42, 672–684. doi:10.1016/j.ijepes.2012.03.035

Duan, W., Du, B., Li, Y., Shen, C., Zhu, X., Li, X., et al. (2018). Improved Sufficient LMI Conditions for the Robust Stability of Time-delayed Neutral-type Lur'e Systems. *Int. J. Control. Autom. Syst.* 16, 2343–2353. doi:10.1007/s12555-018-0138-2

Duan, W., Fu, X., and Liu, Z. (2017). "Improved robust stability criteria for time-delay Lur'e system. *Int. J. Control Automation Syst.* 19, 1–12. doi:10.1002/asjc.1339

Duan, W., Fu, X., and Yang, X. (2016). "Further results on the robust stability for neutral-type Lur'e system with mixed delays and sector-bounded nonlinearities. *Int. J. Control Automation Syst.* 14, 1–9. doi:10.1007/s12555-014-0547-9

Duan, W., Li, Y., and Chen, J. (2020a). An Enhanced Stability Criterion for Linear Time-Delayed Systems *via* New Lyapunov-Krasovskii Functionals. *Adv. Difference Equations* 2020, 37–57. doi:10.1186/s13662-019-2439-z

Duan, W., Li, Y., and Chen, J. (2019). Further Stability Analysis for Time-Delayed Neural Networks Based on an Augmented Lyapunov Functional. *IEEE Access* 7, 104655–104666. doi:10.1109/access.2019.2931714

Duan, W., Li, Y., and Chen, J. (2019). New results on stability analysis of uncertain neutral-type Lur'e systems derived from a modified Lyapunov-Krasovskii functional. *Complexity* 2019, 1–20. doi:10.1155/2019/1706264

Duan, W., Li, Y., Sun, Y., Chen, J., and Yang, X. (2020). Enhanced master-slave synchronization criteria for chaotic Lur'e systems based on time-delayed feedback control. *Mathematics Comput. Simulation* 177, 276–294. doi:10.1016/j.matcom.2020.04.010

Feng, W., Luo, F., Duan, W., Li, Y., and Chen, J. (2020). An Improved Stability Criterion for Linear Time-Varying Delay Systems. *Automatika* 61, 229–237. doi:10.1080/00051144.2019.1706885

Fúlvia, S., de, O., and Fernando, O. (2020). Further Refinements in Stability Conditions for Time-Varying Delay Systems. *Appl. Maths. Comput.* 369, 124866.

Gholami, Y. (2021). Existence and Global Asymptotic Stability Criteria for Nonlinear Neutral-type Neural Networks Involving Multiple Time Delays Using a Quadratic-Integral Lyapunov Functional. *Adv. Differ. Equ* 2021, 112. doi:10.1186/s13662-021-03274-3

Gu, K. (2000). "An Integral Inequality in the Stability Problem of Time-Delay Systems," in Proceedings of the 39th IEEE Conference on Decision and Control, Sydney, NSW, December 12–15, 2000.

Hua, C., Qiu, Y., Wang, Y., and Guan, X. (2021). An Augmented Delays-dependent Region Partitioning Approach for Recurrent Neural Networks with Multiple Time-Varying Delays. *Neurocomputing* 423, 248–254. doi:10.1016/j.neucom.2020.10.047

Jiang, L., Yao, W., Wu, Q. H., Wen, J. Y., and Cheng, S. J. (2012). Delay-dependent Stability for Load Frequency Control with Constant and Time-Varying Delays. *IEEE Trans. Power Syst.* 27, 932–941. doi:10.1109/tpwrs.2011.2172821

Jiao, S., Xia, J., Wang, Z., Chen, X., Wang, J., and Shen, H. (2021). An Improved Result on Stability Analysis of Delayed Load Frequency Control Power Systems. *Int. J. Control. Autom. Syst.* 19, 1633–1639. doi:10.1007/s12555-019-1063-8

Khalil, A., and Swee Peng, A. (2018). An Accurate Method for Delay Margin Computation for Power System Stability. *Energies* 11, 3466. doi:10.3390/en11123466

Kwon, N. K., and Lee, S. Y. (2021). An Affine Integral Inequality of an Arbitrary Degree for Stability Analysis of Linear Systems with Time-Varying Delays. *IEEE Access* 9, 51958–51969. doi:10.1109/access.2021.3070149

Ladygin, A. N., Bogachenko, D. D., and Kholin, V. V. (2020). Efficient Control of Induction Motor Current in a Frequency-Controlled Electric Drive. *Russ. Electr. Engin.* 91, 362–367. doi:10.3103/s106837122006005x

Manikandan, S., and Kokil, P. (2020). Stability Analysis of Load Frequency Control System with Constant Communication Delays. *IFAC-PapersOnLine* 53, 338–343. doi:10.1016/j.ifacol.2020.06.057

Ramakrishnan, K., and Ray, G. (2015). Stability Criteria for Nonlinearly Perturbed Load Frequency Systems with Time-Delay. *IEEE J. Emerg. Sel. Top. Circuits Syst.* 5, 383–392. doi:10.1109/jetcas.2015.2462031

Rerkpreedapong, D., Hasanovic, A., and Feliachi, A. (2003). Robust Load Frequency Control Using Genetic Algorithms and Linear Matrix Inequalities. *IEEE Trans. Power Syst.* 18, 855–861. doi:10.1109/tpwrs.2003.811005

Scopus, P., Tian, Y., and Wang, Z. (2020). Stability Analysis for Delayed Neural Networks Based on the Augmented Lyapunov-Krasovskii Functional with Delay-product-type and Multiple Integral Terms. *Neurocomputing* 410, 295–303.

Seuret, A., and Gouaisbaut, F. (2015). Hierarchy of LMI Conditions for the Stability Analysis of Time-Delay Systems. *Syst. Control. Lett.* 81, 1–7. doi:10.1016/j.sysconle.2015.03.007

Shayeghi, H., Jalili, A., and Shayanfar, H. A. (2008). A Robust Mixed H2/H∞ Based LFC of a Deregulated Power System Including SMES. *Energ. Convers. Manage.* 49, 2656–2668. doi:10.1016/j.enconman.2008.04.006

Shen, C., Li, Y., Zhu, X., and Duan, W. (2019). Improved Stability Criteria for Linear Systems with Two Additive Time-Varying Delays via a Novel Lyapunov Functional. *J. Comput. Appl. Maths.* 363, 312–324.

Shen, H., Jiao, S., Park, J. H., and Sreeram, V. (2021). An Improved Result on $H_{\infty }$ Load Frequency Control for Power Systems with Time Delays. *IEEE Syst. J.* 15, 3238–3248. doi:10.1109/JSYST.2020.3014936

Shen, H., Xing, M., Huo, S., Wu, Z.-G., and Park, J. H. (2019). Finite-time H∞ Asynchronous State Estimation for Discrete-Time Fuzzy Markov Jump Neural Networks with Uncertain Measurements. *Fuzzy Sets Syst.* 356, 113–128. doi:10.1016/j.fss.2018.01.017

Vrdoljak, K., Perić, N., and Petrović, I. (2010). Sliding Mode Based Load-Frequency Control in Power Systems. *Electric Power Syst. Res.* 80, 514–527. doi:10.1016/j.epsr.2009.10.026

Xu, H.-T., Zhang, C.-K., Jiang, L., and Smith, J. (2017). Stability Analysis of Linear Systems with Two Additive Time-Varying Delays via Delay-product-type Lyapunov Functional. *Appl. Math. Model.* 45, 955–964. doi:10.1016/j.apm.2017.01.032

Yang, F., He, J., and Wang, D. (2018). New Stability Criteria of Delayed Load Frequency Control Systems via Infinite-Series-Based Inequality. *IEEE Trans. Ind. Inf.* 14, 231–240. doi:10.1109/tii.2017.2751510

Yang, F., He, J., and Wang, J. (2017). "Novel Stability Analysis of Delayed LFC Power Systems by Infinite-Series-Based Integral Inequality," in Proceedings of the IEEE Conference on Control Technology and Applications (CCTA), Maui, HI, August 27–30, 2017, 1384–1389. doi:10.1109/ccta.2017.8062652

Zhang, C.-K., He, Y., Jiang, L., and Wu, M. (2017). Notes on Stability of Time-Delay Systems: Bounding Inequalities and Augmented Lyapunov-Krasovskii Functionals. *IEEE Trans. Automat. Contr.* 62, 5331–5336. doi:10.1109/tac.2016.2635381

Zhang, X.-M., Han, Q.-L., Seuret, A., and Gouaisbaut, F. (2017). An Improved Reciprocally Convex Inequality and an Augmented Lyapunov-Krasovskii Functional for Stability of Linear Systems with Time-Varying Delay. *Automatica* 84, 221–226. doi:10.1016/j.automatica.2017.04.048

Conflict of Interest: The authors declare that the research was conducted in the absence of any commercial or financial relationships that could be construed as a potential conflict of interest.

Publisher's Note: All claims expressed in this article are solely those of the authors and do not necessarily represent those of their affiliated organizations, or those of the publisher, the editors and the reviewers. Any product that may be evaluated in this article, or claim that may be made by its manufacturer, is not guaranteed or endorsed by the publisher.

Copyright © 2021 Su, Li, Chen and Duan. This is an open-access article distributed under the terms of the Creative Commons Attribution License (CC BY). The use, distribution or reproduction in other forums is permitted, provided the original author(s) and the copyright owner(s) are credited and that the original publication in this journal is cited, in accordance with accepted academic practice. No use, distribution or reproduction is permitted which does not comply with these terms.

APPENDIX A

Notations of other symbols and matrices for Theorem 1:

$$\Delta_0 = \mathrm{col}\{e_1, e_2, e_4, e_{11}\},\ \Pi_0 = Ae_1 + BKCe_2 + Fe_{11} - e_4,$$

$$\bar{U} = \mathrm{col}\{U, \varepsilon_1 U, \varepsilon_2 U, \varepsilon_3 \chi U\},$$

$$\Delta_{11} = \mathrm{col}\{e_1, e_2, e_0\},\ \Delta_{12} = \mathrm{col}\{e_0, e_0, e_9\}, \Delta_{13} = \mathrm{col}\{e_4, h_d e_2, e_1 - h_d e_2\},$$

$$\Delta_{21} = \mathrm{col}\{e_2, e_3, he_7\},\ \Delta_{22} = \mathrm{col}\{e_0, e_0, -e_7\},\ \Delta_{23} = \mathrm{col}\{h_d e_5, e_6, h_d e_2 - e_3\},$$

$$\Delta_{31} = \mathrm{col}\{e_4, e_1, e_1, e_2, e_3, e_0, e_0, he_7\}, \Delta_{32} = \mathrm{col}\{e_0, e_0, e_0, e_0, e_0, e_0, e_9, -e_7\},$$

$$\Delta_{33} = \mathrm{col}\{e_5, e_2, e_1, e_2, e_3, e_0, e_0, he_7\}, \Delta_{34} = \mathrm{col}\{e_0, e_0, e_0, e_0, e_0, e_9, e_0, -e_7\},$$

$$\Delta_{41} = \mathrm{col}\{e_6, e_3, e_1, e_2, e_3, he_7, e_0, e_0\}, \Delta_{42} = \mathrm{col}\{e_0, e_0, e_0, e_0, e_0, -e_7, e_9, e_0\},$$

$$\Delta_{43} = \mathrm{col}\{e_5, e_2, e_1, e_2, e_3, e_0, e_0, he_7\}, \Delta_{44} = \mathrm{col}\{e_0, e_0, e_0, e_0, e_0, e_0, e_9, -e_7\},$$

$$\Lambda_{10} = \mathrm{col}\{e_1 - e_2, e_0, e_0, e_0, e_0, e_0, e_0, e_0\},$$

$$\Lambda_{11} = \mathrm{col}\{e_0, e_9, e_1, e_2, e_3, e_0, e_0, he_7\},$$

$$\Lambda_{12} = \mathrm{col}\{e_0, e_0, e_0, e_0, e_0, e_9 - e_{10}, e_{10}, -e_7\},$$

$$\Lambda_{20} = \mathrm{col}\{e_2 - e_3, he_7, he_1, he_2, he_3, h^2(e_7 - e_8), e_0, h^2 e_8\},$$

$$\Lambda_{21} = \mathrm{col}\{e_0, -e_7, -e_1, -e_2, -e_3, -2h(e_7 - e_8), he_9, -2he_8\},$$

$$\Lambda_{22} = \mathrm{col}\{e_0, e_0, e_0, e_0, e_0, e_8 - e_7, -e_9, e_8\},$$

$$\Lambda_1 = \mathrm{col}\{e_0, e_0, e_4, h_d e_5, e_6, e_1, -h_d e_2, h_d e_2 - e_3\},$$

$$\Lambda_2 = \mathrm{col}\{e_0, e_0, e_4, h_d e_5, e_6, h_d e_2, e_1 - h_d e_2, -e_3\},$$

$$\Gamma_1 = \mathrm{col}\{e_2 - e_3, e_2 + e_3 - 2e_7, e_2 - e_3 + 6e_7 + 12e_8\},$$

$$\Gamma_2 = \mathrm{col}\{e_1 - e_2, e_1 + e_2 - 2e_9, e_1 - e_2 + 6e_9 + 12e_{10}\},$$

$$\mathcal{C} = \left[\frac{h}{2} I\ 0\right],\ \mathcal{J} = \left[\frac{h}{2} I\ -I\right],\ \bar{R}_i = \mathrm{diag}\{R_i, 3R_i, 5R_i\},\ K_0 = UBK,$$

$$\begin{aligned}
\Omega_0(\mu_i) = \mathrm{Sym}\{&\Delta_{13}^T S_{12} \Delta_{11} + \Delta_{23}^T (hS_{21} + S_{22})\Delta_{21} + \Lambda_{10}^T Q_1 \Lambda_1 + \Lambda_{20}^T Q_2 \Lambda_2\} \\
&+ \dot{h}_t \Delta_{11}^T S_{11} \Delta_{11} \quad - \dot{h}_t \Delta_{21}^T S_{21} \Delta_{21} + \Delta_{31}^T Q_1 \Delta_{31} - \Delta_{41}^T Q_2 \Delta_{41} - h_d \Delta_{33}^T Q_1 \Delta_{33} \\
&+ h_d \Delta_{43}^T Q_2 \Delta_{43} \quad + e_4^T (h^2 R_2) e_4 + h^2 h_d e_5^T (R_1 - R_2) e_5 + \Gamma_1^T \bar{R}_1 \Gamma_1 + \Gamma_2^T (\bar{R}_2 \\
&+ X_2)\Gamma_2 \quad + \mathrm{Sym}\{\Gamma_1^T Y_1 \Gamma_2\} + \mathrm{Sym}\{\Delta_0^T \bar{U} \Pi_0\} + e_1^T C^T C e_1 - e_{11}^T \gamma^2 I e_{11}, \Omega_1(\mu_i) \\
= \mathrm{Sym}\Big\{&\Delta_{13}^T S_{11} \Delta_{11} + \Delta_{13}^T S_{12} \Delta_{12} + \dot{h}_t \Delta_{11}^T S_{11} \Delta_{12} + \Delta_{23}^T (hS_{21} + S_{22})\Delta_{22} \quad -\Delta_{23}^T S_{21} \Delta_{21} - \dot{h}_t \Delta_{22}^T S_{21} \Delta_{21} + \Lambda_{11}^T Q_1 \Lambda_1 + \Lambda_{21}^T Q_2 \Lambda_2\Big\} \\
&+ \Delta_{32}^T Q_1 \Delta_{32} \quad - \Delta_{42}^T Q_2 \Delta_{42} - \dot{h}_t \Delta_{34}^T Q_1 \Delta_{34} + h_d \Delta_{44}^T Q_2 \Delta_{44} - h h_d e_5^T (R_1 \\
&- R_2) e_5 \quad - \frac{1}{h}[\Gamma_1^T X_1 \Gamma_1 - \Gamma_2^T X_2 \Gamma_2] + \frac{1}{h}\mathrm{Sym}\{\Gamma_1^T (Y_1 - Y_2)\Gamma_2\}, \Omega_2(\mu_i) \\
= \mathrm{Sym}\{&\Delta_{13}^T S_{11} \Delta_{12} - \Delta_{23}^T S_{21} \Delta_{22} + \Lambda_{12}^T Q_1 \Lambda_1 + \Lambda_{22}^T Q_2 \Lambda_2\} \quad + \dot{h}_t \Delta_{12}^T S_{11} \Delta_{12} \\
&- \dot{h}_t \Delta_{22}^T S_{21} \Delta_{22} + \Delta_{32}^T Q_1 \Delta_{32} \quad - \Delta_{42}^T Q_2 \Delta_{42} - h_d \Delta_{34}^T Q_1 \Delta_{34} + h_d \Delta_{44}^T Q_2 \Delta_{44},
\end{aligned}$$

frontiers in Energy Research

BRIEF RESEARCH REPORT
published: 20 October 2021
doi: 10.3389/fenrg.2021.743465

Coordinated Control Strategy of DC Fault Ride-through for the WF Connected to the Grid Through the MMC-HVDC

Bo Zhu[1], Hongying Li[2], Panteng Xu[1], Shi Jiao[1], Lin Zhang[2] and Yechun Xin[2]*

[1]Guangzhou Bureau of EHV Transmission Company of China Southern Power Grid Co, Ltd, Guangzhou, China, [2]School of Electric Power Engineering, Northeast Electric Power Univer, Jilin, China

Aiming at the problems of DC fault isolation and power surplus in the HVDC system with large-scale wind farm (WF) integration after single-pole grounding fault, this article designs a modified current transfer modular multilevel converter (M-CT-MMC) topology with DC fault isolation and power dissipation functions. The DC fault current can be isolated through the coordination of each branch of the M-CT-MMC. In terms of surplus power consumption, the control mode switching strategy of the M-CT-MMC is designed to improve the power transmission capability of the non-fault pole and enable it to absorb surplus power independently. Furthermore, a coordinated control strategy of wind turbines and dissipation resistors is designed to absorb surplus power. With the advantages of fast response speed of wind turbines and reliable dissipation resistance, DC fault ride-through under different working conditions is realized. Finally, the effectiveness and feasibility of the coordinated control strategy for DC fault ride-through are verified.

Keywords: modular multilevel converter, fault isolating, power dissipation, DC fault ride-through, coordinated control strategy

OPEN ACCESS

Edited by:
Dongran Song,
Central South University, China

Reviewed by:
Rizk Masoud,
University of Menoufia, Egypt
Mehdi Firouzi,
Islamic Azad University, Iran

****Correspondence:***
Hongying Li
732392093@qq.com

Specialty section:
This article was submitted to Smart Grids, a section of the journal Frontiers in Energy Research

Received: *18 July 2021*
Accepted: *13 September 2021*
Published: *20 October 2021*

Citation:
Zhu B, Li H, Xu P, Jiao S, Zhang L and Xin Y (2021) Coordinated Control Strategy of DC Fault Ride-through for the WF Connected to the Grid Through the MMC-HVDC. Front. Energy Res. 9:743465. doi: 10.3389/fenrg.2021.743465

INTRODUCTION

In the HVDC system with large-scale WF integration, when a short-circuit fault occurs at the DC side, the fault current will rise rapidly, and power surplus will occur (Lin et al., 2016; Song et al., 2018; Nian et al., 2020), which will lead to the overload of the converter station. Therefore, how to quickly isolate the fault current and dissipate the surplus power is the key issue to be resolved urgently to realize DC fault ride-through (Xue and Xu, 2014; Moawwad et al., 2016; Rizk-Allah et al., 2021).

At present, AC and DC circuit breakers are mainly used to isolate fault currents. However, the development of a hybrid DC circuit breaker is difficult and expensive (Liu et al., 2017; Xiaoguang et al., 2017). AC circuit breakers have poor speed (Li et al., 2017). Guo et al. (2017) designed asymmetric full-bridge submodules and relied on diode freewheeling to make partial capacitors reversible to achieve fault current suppression. The full-bridge submodules, clamped dual sub-modules, and hybrid sub-modules all can isolate DC fault (Li et al., 2016; Tao et al., 2016; Li et al., 2019; Li et al., 2021), but they have respective problems of high cost or complex control and voltage sharing, or the investment benefit is not clear. In addition, there are combined DC fault current isolating schemes (Song et al., 2017; Ahmed et al., 2018). Wang et al. (2018) proposed a current-transfer MMC topology with DC fault clearing capability. The topology works well in a pseudo bipolar system, but there is a DC bias problem in the bipolar system, which will improve the withstand voltage of the grounding switch and increase the number of devices.

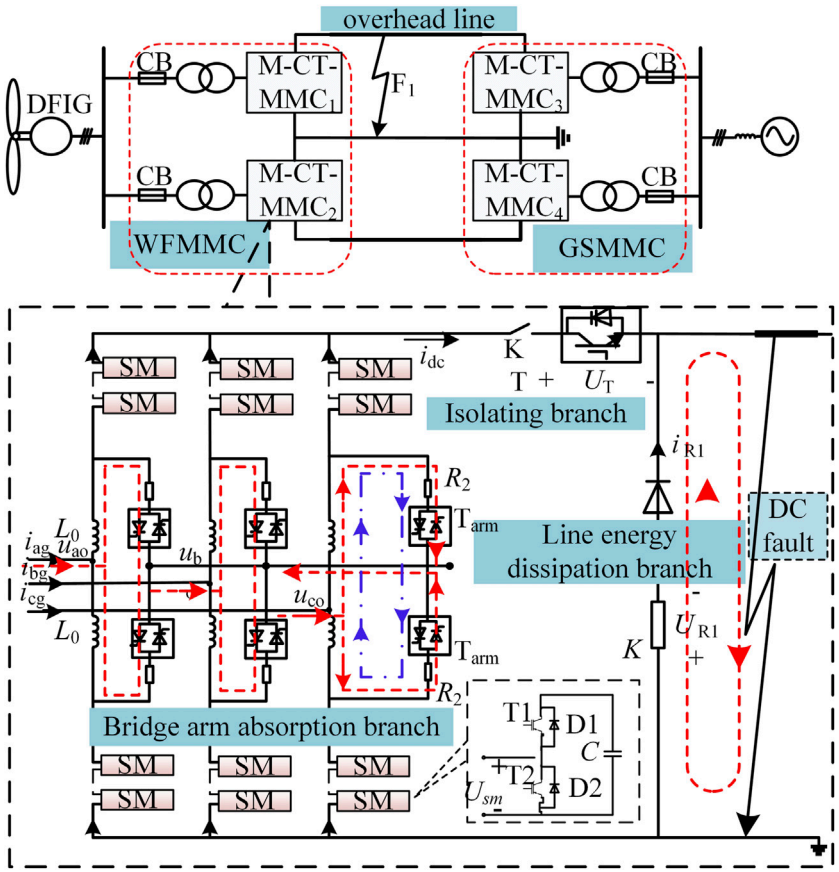


FIGURE 1 | DC system with wind power integration and M-CT-MMC topology.

To deal with the problem of surplus power dissipation after failure, He et al. (2017) proposed a power transfer control strategy for a bipolar connection system, which can balance the surplus power after a fault, but it still needs to cut off the machine and load in the face of extreme conditions. Li et al. (2020) used the coordinated control between the WF and the MMC to actively reduce the output power of the WF by a fast communication method, but the influence of communication delay on response speed should be considered. Cao et al. (2019) designed an accurate switching dissipative resistance control strategy for the multiterminal bipolar system to absorb the surplus power after a fault and effectively improve the fault ride-through capability under the condition of excess power. At present, there is still not enough information to study the cooperative control strategy of wind turbine load-shedding and dissipation resistors absorbing surplus power based on the new topology.

The M-CT-MMC topology is designed for bipolar HVDC connected with the WF to realize DC fault isolation and power dissipation. Under the condition of giving full play to the active load-shedding capacity of wind turbines, a complete coordinated control strategy for DC fault ride-through is designed for self-absorption and non–self-absorption conditions. The bipolar M-CT-MMC control mode switching strategy, wind turbine load-shedding control strategy, and dissipation resistors are used to realize the surplus power consumption, which can meet the needs of different surplus power consumption to realize DC fault ride-through. Finally, the effectiveness and feasibility of the coordinated control strategy for DC fault ride-through are verified.

COORDINATED CONTROL STRATEGY OF DC FAULT RIDE-THROUGH FOR THE WF CONNECTED TO THE GRID THROUGH THE MMC-HVDC

The DC System With WF Integration and M-CT-MMC Topology

The DC System With WF Integration

The system is shown in **Figure 1**. The M-CT-MMC is connected with a symmetrical bipolar metal return line. The DC line is the overhead line. The M-CT-MMC at the WF (WFMMC) side adopts constant frequency/AC voltage control to ensure voltage quality and frequency stability of the WF parallel point. The M-CT-MMC at the grid side adopts constant DC voltage/reactive power control to ensure voltage stability at the

DC side and provide reactive power support for the AC grid at the receiving end.

M-CT-MMC Topology

The M-CT-MMC topology is shown in **Figure 1**. The normal working state of the M-CT-MMC is the same as that of the half-bridge MMC; only three auxiliary branches are added, which can isolate the fault current and dissipate the surplus power. The components of each branch are described below.

1) Isolating branch: It is composed of the isolating switch **T** composed of several diodes and IGBTs in series after an antiparallel connection and an ultrafast mechanical switch **K.**
2) Line power dissipation branch: It is composed of freewheeling diodes **D** and an absorption resistor $\boldsymbol{R_1}$**.**
3) Bridge arm absorption branch: All bridge arm inductors of the MMC are equipped with an absorption branch at both ends, which is composed of the dissipation resistor $\boldsymbol{R_2}$ and bridge arm switch $\mathbf{T_{arm}}$ composed of $\boldsymbol{n}$ antiparallel thyristors in series. The leads between the two switches of each phase are connected to construct the AC flow path.

Fault Current Isolating Control Strategy for the M-CT-MMC Topology

For **Figure 1** system, the isolating process of the M-CT-MMC fault current is introduced by taking mono-pole grounding fault as an example:

1) The fault occurs at $\boldsymbol{t_0}$, the capacitor of the fault pole M-CT-MMC discharges rapidly, and the fault current rises sharply. With a delay of 1 ms, the fault pole M-CT-MMC is locked at $\boldsymbol{t_1}$, and $\mathbf{T_{arm}}$ is triggered. All dissipative resistors are put into operation to reduce the fault current flowing through the converter valve, and the voltage after **T** is disconnected.
2) **T** is turned off at $\boldsymbol{t_2}$, and the fault current is transferred to the line power dissipation branch and the bridge arm absorption branch.
3) After a short delay, the current flowing through submodules of the bridge arm and the isolating branch is reduced to zero, and **K** is turned off. After about 2 ms, at $\boldsymbol{t_3}$, the ultrafast mechanical switch action is completed to achieve physical isolation of the M-CT-MMC and fault point.
4) At $\boldsymbol{t_4}$, $\mathbf{T_{arm}}$ has switched to the dissipation resistor adaptive switching control mode.

The M-CT-MMC can reduce the current stress of the bridge arm converter valve and can also provide breaking conditions for **T** to achieve effective isolation of DC faults. The three-phase neutral point scheme is constructed by the interconnection of bridge arm absorption branch outgoing lines, which saves the grounding investment and does not have the problem of bearing DC bias.

Coordinated Control Strategy of Surplus Power Consumption

After fault isolation, the output power of the WF will be completely borne by the non-fault pole, which may lead to non-fault pole overload. The problem of power surplus must be solved.

Control Mode Switching Strategy of the M-CT-MMC

To improve the power transfer capability of the non-faulty pole M-CT-MMC of the WFMMC, the control mode switching strategy is designed as follows:

1) The faulty pole M-CT-MMC control is switched to constant DC voltage/AC voltage control and put into operation again to maintain the voltage stability of the grid-connected bus of the WF.
2) The non-fault pole M-CT-MMC control is switched to the constant frequency/reactive power—voltage droop control (The reactive power reference value is set to 0 to improve the power transfer capability.)—to absorb the power of the fault pole and maintain the frequency stability of the WF side.

Under the condition that the surplus power can be completely transferred from the non-fault pole M-CT-MMC (self-absorbing condition), the WF and the receiving end system can quickly return to the normal state based on this method.

Control Strategy of Load-Shedding for Wind Turbines

When the non-fault pole M-CT-MMC cannot fully transfer surplus power (the non-self-absorption condition), it should be operated at full capacity. Surplus power is absorbed by wind turbine load-shedding and the dissipation resistors of the bridge arm.

The load shedding control strategy of the wind turbine is a coordinated control strategy between the M-CT-MMC and WF based on the idea of frequency control. Using the frequency control capability of the non-fault pole M-CT-MMC, we improve the frequency of the wind farm side accurately during fault crossing. Then, using the frequency response ability of the wind turbine, the accurate load shedding of the wind turbine is realized. The load-shedding power $\Delta \boldsymbol{P_{WF}}$ of the WF should meet the following equation:

$$\Delta \boldsymbol{P}_{\mathbf{WF}} = \boldsymbol{P}_{\mathbf{WF}} - \boldsymbol{S}_{\mathbf{N}}, \tag{1}$$

where $\boldsymbol{P_{WF}}$ is the output power of WF and $\boldsymbol{S_N}$ is the rated capacity of the non-fault pole M-CT-MMC.

According to the principle of primary frequency regulation of the synchronous generator, the equivalent adjustment coefficient $\boldsymbol{K}$ doubly fed induction generator (DFIG) is defined as follows:

$$\boldsymbol{K} = \frac{\Delta \boldsymbol{f}}{\Delta \boldsymbol{P}_{\mathbf{WF}}}, \tag{2}$$

where $\Delta \boldsymbol{f}$ is the frequency variation of the sending end system.

The expression of the maximum operating power $\boldsymbol{P_1}$ of the WF in the steady state and the output power $\boldsymbol{P_{min}}$ when the rotor speed of the unit reaches the upper limit is shown in **Eq. 3**.

$$\begin{cases} \boldsymbol{P}_1 = \boldsymbol{k}_{\mathbf{mppt}} \boldsymbol{\omega}_1^3 \\ \boldsymbol{P}_{\mathbf{min}} = \boldsymbol{k}_{\mathbf{min}} \boldsymbol{\omega}_2^3 = \boldsymbol{k}_{\mathbf{min}} (1.2 \boldsymbol{\omega}_{\mathbf{N}})^3 \end{cases}, \tag{3}$$

where $\boldsymbol{k_{mppt}}$ and $\boldsymbol{k_{min}}$ are the tracking coefficients of the corresponding power curve, $\boldsymbol{\omega_1}$ is the current rotor speed, $\boldsymbol{\omega_2}$

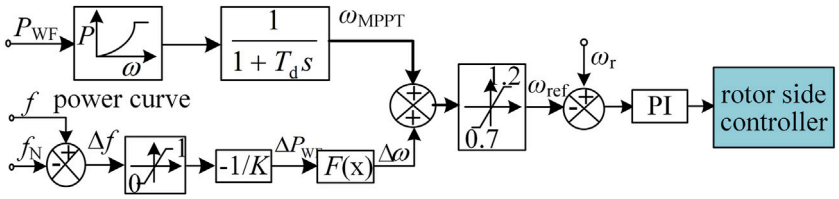


FIGURE 2 | Overspeed load reduction control strategy of the WF.

is the upper limit of rotor speed, and ω_N is the rated rotor speed; usually $\omega_2 = 1.2\omega_N$.

DFIG operates at a maximum power point in the steady state. When the system frequency fluctuates, the output power of the wind turbine meets the following relationship:

$$\begin{aligned} P_1^{'} &= P_1 - \Delta P_e = k_{mppt}(\omega_1 - \Delta\omega)^3 \\ &= k_{mppt}\left(\omega_1^3 - 3\omega_1^2\Delta\omega_1 + 3\omega_1\Delta\omega^2 - \Delta\omega^3\right), \end{aligned} \tag{4}$$

When the speed adjustment range is not large, it can be considered that $\omega_1 >> \Delta\omega$. (4) is simplified:

$$\Delta P_e \approx k_{mppt} 3\omega_1^2 \Delta\omega = \frac{\Delta P_{max}}{f_{max} - f_N}\Delta f, \tag{5}$$

where f_{max} is the peak value of the system's allowable operating frequency, the maximum is 50.5Hz; ΔP_{max} is the limit frequency modulation power at the current wind speed, which can be expressed as the difference between P_1 and P_{min} at the wind speed.

$$\Delta P_{max} = P_1 - P_{min} = k_{mppt}\omega_1^3 - k_{min}(1.2\omega_N)^3, \tag{6}$$

Substituting ΔP_{max} into (6) and sorting it out, we can get

$$\Delta f = K\Delta P_e = K \times k_{mppt} 3\omega_1^2 \Delta\omega, \tag{7}$$

$$K = \frac{f_{max} - f_N}{k_{mppt}\omega_1^3 - k_{min}(1.2\omega_N)^3}. \tag{8}$$

When the system finally runs to a new steady-state point, ΔP_e is the load shedding power of WF ΔP_{WF}, which satisfies $\Delta\omega \propto \Delta P_{WF} \propto \Delta f$ within the frequency adjustment range. The K value of the corresponding wind speed can be determined by using the current speed and relevant tracking coefficient of the wind turbine. Finally, combined with the frequency control of the non-fault pole M-CT-MMC, the precise load shedding of the WF can be realized. The specific implementation methods are as follows:

1) The non-fault pole M-CT-MMC determines Δf according to ΔP_{WF} and K. By adding Δf to the frequency reference value f_N of the non-fault pole M-CT-MMC, the system frequency on the WF side is controlled to reach the new steady-state value $f_N + \Delta f$.
2) The WF monitors the system frequency f in real time. When $f > f_N$, it immediately enters the overspeeding load-shedding control mode. According to **Eq. 1**, the frequency modulation ΔP_{WF} can be calculated. Combined with the functional relationship $F(x)$ between the output power of the WF and the speed of the WF in **Eq. 5**, $\Delta\omega$ is obtained. $\Delta\omega$ is superimposed on ω_1 to obtain a new rotational speed control command ω_{ref} to realize the accurate load-shedding control of the WF. As shown in **Figure 2**, when $f < f_N$, $\Delta\omega = 0$, it does not participate in the system power regulation. The WF continues to work in the maximum power tracking mode to improve the efficiency of wind energy utilization. In this process, the inherent delay of communication between the WF and M-CT-MMC is eliminated, and the load shedding response speed of the WF after the fault is improved.

This method does not require communication, which improves the response speed of the wind turbine load-shedding. And it can achieve accurate load-shedding and maximum power transmission, but the frequency threshold is small and the load-shedding capacity is small, which cannot meet the power dissipation demand of the WF under full-power operation.

Control Strategy of Dissipative Resistors Absorbing Surplus Power

The input capacity P_{hs} (neglecting loss) of dissipation resistors can be expressed as follows:

$$P_{hs} = P_{WF} - S_N = \lambda P_N - S_N. \tag{9}$$

where P_N and λ ($0 \le \lambda \le 1$), respectively, represent the rated power and output coefficient of the WF.

For bipolar HVDC connected by the WF, the rated capacity of the unipolar M-CT-MMC is usually half of the rated capacity of the WF. Therefore, according to **Eq. 9**, if $\lambda \le 0.5$, the non-fault pole is used to transmit surplus power. If $0.5 < \lambda \le 1$, the input capacity of dissipation resistors shall be greater than and close to P_{HS} to eliminate surplus power and reduce the influence on AC voltage and DC transmission power. Input dissipative resistance R_{eq2} can be calculated by **Eq. 10**. When $\lambda = 1$, R_{eq2} is minimum, dissipative resistance R_2 ($R_{eq2|\lambda=1}$) is designed as $M R_{SM2}$ (dissipation resistance of each group) in parallel, as shown in **Eq. 11**.

$$R_{eq2} = \frac{U_L^2}{(\lambda P_N - S_N)} = \frac{U_L^2}{(\lambda - 0.5)P_N}, \tag{10}$$

$$R_{SM2} = 2MR_{eq2}\big|_{\lambda=1}, \tag{11}$$

where U_L is the effective value of line voltage borne by dissipation resistors.

The dissipation resistors of the fault pole M-CT-MMC are cut adaptively according to the actual output coefficient of the WF to maintain power balance, as given in the formula **Eq. 12**.

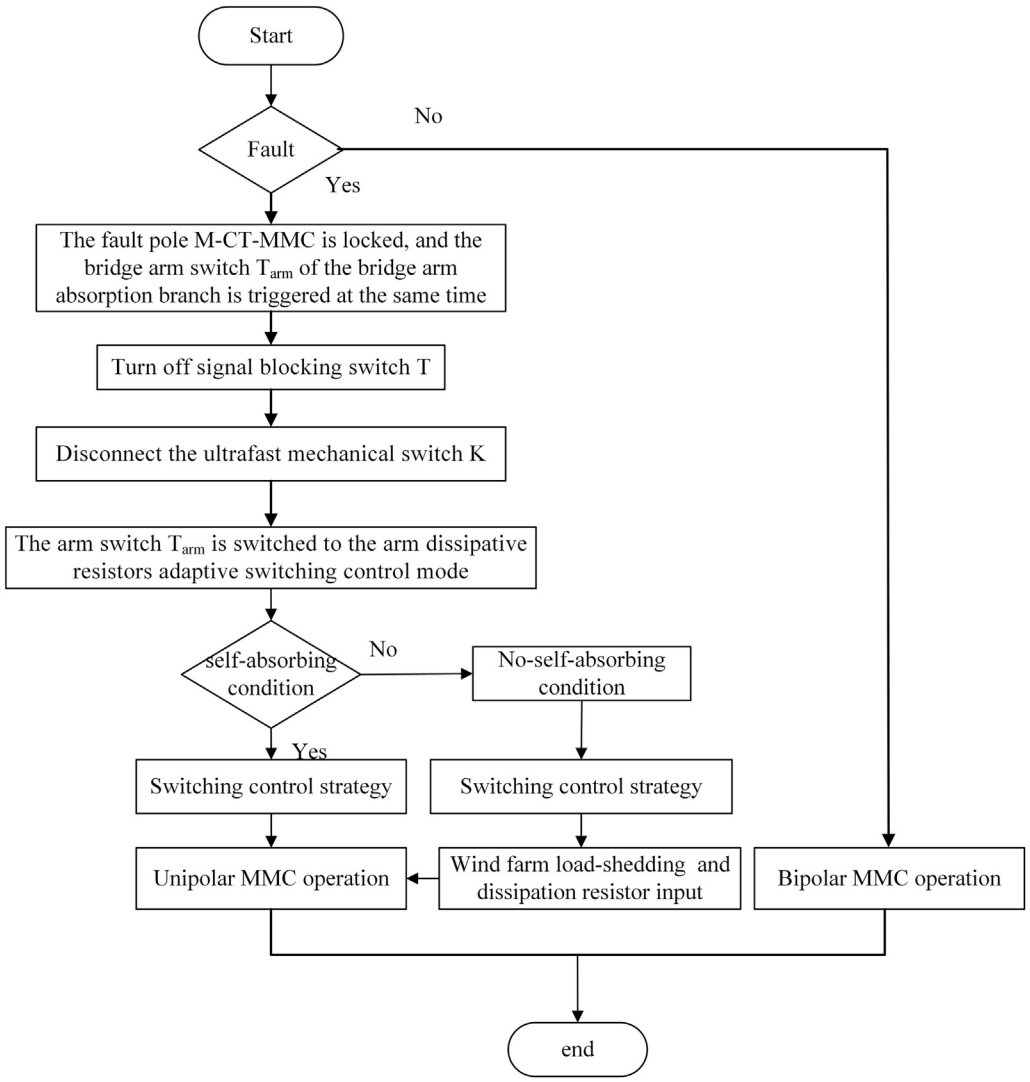


FIGURE 3 | Fault ride-through flow block diagram.

$$\begin{cases} \boldsymbol{M}_{\mathbf{out}} = \boldsymbol{M} & 0 \le \boldsymbol{\lambda} \le 0.5 \\ \boldsymbol{M}_{\mathbf{out}} = \boldsymbol{M} - \left\lceil \dfrac{(\boldsymbol{\lambda} - 0.5)\boldsymbol{P}_{\mathbf{N}}}{\dfrac{0.5\boldsymbol{P}_{\mathbf{N}}}{\boldsymbol{M}}} \right\rceil = \boldsymbol{M} - \left\lceil 2\boldsymbol{M}(\boldsymbol{\lambda} - 0.5) \right\rceil & 0.5 < \boldsymbol{\lambda} \le 1 \end{cases}, \tag{12}$$

where $\boldsymbol{M}_{\mathbf{out}}$ is the number of dissipation resistor groups to be removed after fault isolation; [] represents an upward integer operation.

Coordinated Control Strategy of Load-Shedding for Wind Turbine and Dissipative Resistors Absorbing Surplus Power

The basic idea of the coordinated control strategy based on wind turbine load-shedding and dissipation resistor absorbing surplus power is as follows: first, fault isolation shall be carried out according to the working process of the M-CT-MMC described in *Fault Current Isolating Control Strategy for the M-CT-MMC Topology section*. After the fault is isolated, the M-CT-MMC control strategy is switched, and the bridge arm absorption branch is switched to the adaptive cutoff mode. At the same time, the WF will also operate under load-shedding. The two strategies are carried out at the same time. With the increase of load-shedding power, the number of groups of dissipative resistance is increased to achieve power balance and fault ride-through. The flow block diagram of fault ride-through is shown in **Figure 3**.

SIMULATION VERIFICATION

Based on the Matlab/Simulink simulation platform, the simulation model as shown in **Figure 1** is built. The WF is paralleled by two 500 MV A-rated DFIGs. The main parameters

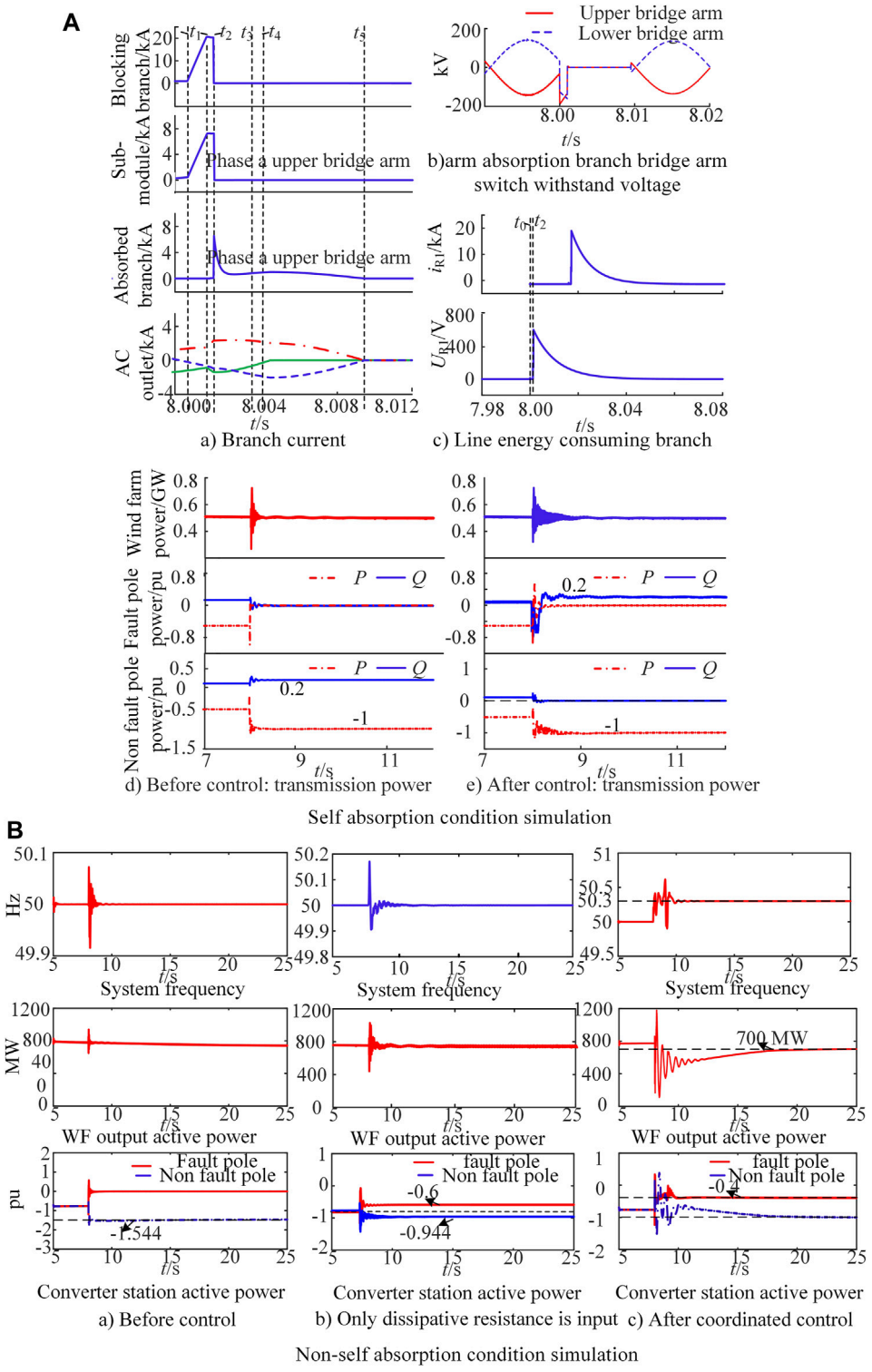


FIGURE 4 | Simulation verification of the DC fault ride-through coordinated control strategy.

of the M-CT-MMC can be found in the study by Li et al. (2021), where R_{SM2} = 550Ω, M = 5. The effectiveness of the abovementioned strategy is verified by simulation. **Figure 4** shows the simulation results of the DC fault ride-through–coordinated control strategy.

Simulation Verification of Self-Absorption Condition

The output power of the WF is set to 500 MW, and the positive and negative pole of the converter station shall bear 250 MW active power and 50MVar reactive power, respectively. At 8.0s, a unipolar metallic short-circuit grounding fault occurred at the DC outlet of the WF side. At t_1, the fault pole M-CT-MMC is isolated and triggers $\mathbf{T_{arm}}$; t_1-t_2 = 0.4 ms; t_2-t_3 = 2 ms; and t_3-t_4 = 0.6 ms. When t = 8.0035s, the control mode of the M-CT-MMC is switched.

After the fault occurs, the submodule current and isolating branch current increase rapidly. After adopting the fault current isolating control, the fault current drops rapidly and transfers to the bridge arm absorption branch and the line energy dissipation branch. The branch current decays to 0 after 1.09 ms and within 50 ms, respectively. As shown in **Figure 4A,a,c**., the M-CT-MMC can effectively isolate the DC side fault. **Figure 4A,b** shows the voltage of $\mathbf{T_{arm}}$ without DC voltage bias, which verifies the effectiveness of the proposed three-phase neutral point scheme.

After the fault is isolated, the power output of the WF remains unchanged. WF output active power (500 MW) and system reactive power (100MVar) can only be borne by the non-faulty pole M-CT-MMC, which leads to its overload operation. After switching the M-CT-MMC control, the faulty pole M-CT-MMC provides 0.2p.u. reactive power support for the system. It can avoid overload operation of the non-fault pole and ensure maximum transmission of active power at the same time, as shown in **Figure 4A,d,e**.

Simulation Verification of the Non–self-absorption Condition

The output power of the WF is 772 MW. Under this condition, the proposed coordinated control strategy is compared with the method of only using dissipative resistance to absorb surplus power, and the simulation results are shown in **Figure 4B**. When the wind turbine load is reduced from 72 to 100 MW (maximum), the input capacity of dissipation resistors is 200 MW. Therefore, to reduce the frequency change of the sending end, the non-fault pole M-CT-MMC frequency reference value adopts 50.3 Hz.

Before control, all output power of the WF is injected into the non-fault pole to enable its active power reach 1.544pu. The non-fault pole overload is shown in **Figure 4B,a**. After control, the system frequency finally stabilizes from 50 to 50.3 Hz; load-shedding of the wind turbine is reduced by 72 MW; 200 MW dissipation resistors are put into operation. The remaining 500 MW power is borne by the non-faulty pole M-CT-MMC to ensure the maximum transmission of active power and reduce the impact of the fault on the receiving end AC system, as shown in **Figure 4B,c**. When only dissipative resistors are put into operation, the output power of the WF is not changed; when three groups of dissipative resistors are put into operation, 300 MW active power is consumed, and the loss increases. The non-fault pole transmits 472 MW power and cannot operate at full load, as shown in **Figure 4B,b**, which increases the probability of load rejection. By comparison, the proposed coordinated control method has obvious advantages.

CONCLUSION

Aiming at the problem of DC fault ride-through in the bipolar DC system with WF integration, the M-CT-MMC with fault isolation and power dissipation is designed, and the coordinated control strategy of surplus power consumption is proposed. The following conclusions are obtained through simulation:

1) In terms of fault isolation, the M-CT-MMC can effectively isolate the fault current and avoid DC voltage bias, which can also dissipate surplus power, transfer fault current, and provide a new discharge path for the bridge arm inductance current.
2) In terms of surplus power consumption, the bipolar M-CT-MMC control mode switching strategy, wind turbine load shedding control strategy, and dissipation resistors are used to absorb the surplus power, which can comprehensively play the rapidity of wind turbine load-shedding and the reliability of dissipation resistors to meet the demand of surplus power dissipation under different conditions, and effectively reduce the fault influence range and improve the ability of safe and stable operation of the system.

DATA AVAILABILITY STATEMENT

The original contributions presented in the study are included in the article/Supplementary Material; further inquiries can be directed to the corresponding author.

AUTHOR CONTRIBUTIONS

BZ: conceptualization. HL: methodology. PX: software. SJ: validation. LZ: formal analysis. YX: data curation. All authors contributed to the article and approved the submitted version.

FUNDING

This research was financially supported by the National Natural Science Foundation of China (Grant No. U2066208).

REFERENCES

Ahmed, K. H., Adam, G. P., Abdelsalam, I. A., and Aboushady, A. A. (2018). Modular Multilevel Converter with Modified Half-Bridge Submodule and Arm Filter for Dc Transmission Systems with Dc Fault Isolating Capability[J]. *IET Power Electron.* 11 (14), 2253–2262. (in Chinese). doi:10.1049/iet-pel.2018.5081

Cao, S., Wang, X., Lin, W., and Win, J. (2019). Fault Ride-Through and Energy Dissipation Control of Bipolar Hybrid MMC-MTDC Integrating Wind Farms [J]. *Power Syst. Prot. Control.* 47 (07), 39–48. (in Chinese).

Guo, X., Cui, X., and Qi, L. (2017). DC Short-Circuit Fault Analysis and protection for the Overhead Line Bipolar MMC-HVDC System[J]. *Proc. CSEE* 37 (8), 2177–2184. (in Chinese). doi:10.13334/j.0258-8013.pcsee.162229

He, Y., Zhou, L., Li, Y., Gu, W., Zhao, B., and Wang, S. (2017). Power Conversion Strategy of VSC-MTDC System Based on Real Bipolar Wiring Mode[J]. *Automation Electric Power Syst.* 41 (19), 95–101. (in Chinese). doi:10.7500/AEPS20170327009

Li, G., Jiang, S., Xin, Y., and Wang, L. (2020). Coordinated Control Strategies for DC Fault Ride-Through of Wind Power Integration via Bipolar MMC-HVDC Overhead Lines[J]. *Proc. CSEE* 40 (11), 3516–3527. (in Chinese). doi:10.13334/j.0258-8013.pcsee.190724

Li, G., Song, Z., and Wang, G. (2019). Asymmetric Full-Bridge Sub-module Topology of MMC with DC Fault Isolation Capability[J]. *High Voltage Eng.* 45 (1), 12–20. (in Chinese). doi:10.13336/j.1003-6520.hve.20181229001

Li, G., Zhang, L., Jiang, S., and Xin, Y. (2021). Coordinated Control Strategies for DC Fault Ride-Through of Wind Power Integration via Bipolar Hybrid MMC-HVDC Overhead Lines [J]. *Power Syst. Prot. Control.* 49 (10), 27–36. (in Chinese). doi:10.19783/j.cnki.pspc.200880

Li, S., Guo, C., Zhao, C., and Xu, J. (2017). Novel MMC Topology with Lower Power Loss and DC Fault Ride-Through Capability[J]. *Proc. CSEE* 37 (23), 6801–6810. (in Chinese). doi:10.13334/j.0258-8013.pcsee.162109

Li, S., Wang, X., Tai, L., and Peng, Z. (2016). Optimal Design for Hybrid MMC and its DC Fault Ride-Through Strategy[J]. *Proc. CSEE* 36 (7), 1849–1858. (in Chinese). doi:10.13334/j.0258-8013.pcsee.162109

Lin, W., Jovcic, D., Nguefeu, S., and Saad, H. (2016). Full-Bridge MMC Converter Optimal Design to HVDC Operational Requirements. *IEEE Trans. Power Deliv.* 31 (3), 1342–1350. doi:10.1109/tpwrd.2015.2475130

Liu, G., Xu, F., Xu, Z., Zhang, Z., and Tang, G. (2017). Assembly HVDC Breaker for HVDC Grids with Modular Multilevel Converters. *IEEE Trans. Power Electron.* 32 (2), 931–941. doi:10.1109/tpel.2016.2540808

Moawwad, A., El Moursi, M. S., and Xiao, W. (2016). Advanced Fault Ride-Through Management Scheme for VSC-HVDC Connecting Offshore Wind Farms. *IEEE Trans. Power Syst.* 31 (6), 4923–4934. doi:10.1109/tpwrs.2016.2535389

Nian, M., Zhou, Y., Tan, L., and Yuan, B. (2020). Energy Consumption Method for Power Surplus in Zhangbei VSC-Based DC Grid[J]. *Power Syst. Technol.* 44 (05), 1991–1999. doi:10.13335/j.1000-3673.pst.2019.1946

Rizk-Allah, R. M., Hassanien, A. E., and Song, D. (2021). Chaos-Opposition-Enhanced Slime Mould Algorithm for Minimizing the Cost of Energy for the Wind Turbines on High-Altitude Sites. *ISA Trans.* (15). doi:10.1016/j.isatra.2021.04.011

Song, Q., Yang, W., Li, X., Li, J., Zeng, W., Huang, Y., et al. (2017). A Modular Multilevel Converter Integrated with DC Circuit Breaker [J]. *Proc. CSEE* 37 (20), 6004–6013. (in Chinese). doi:10.13334/j.0258-8013.pcsee.171497

Song, Q., Zeng, R., Yu, Z., Liu, W., Huang, Y., Yang, W., et al. (2018). A Modular Multilevel Converter Integrated with DC Circuit Breaker. *IEEE Trans. Power Deliv.* 33 (5), 2502–2512. doi:10.1109/tpwrd.2018.2815550

Tao, F., Xie, Z. J., Cheng, J., Li, C., Zhao, L., and Wen, J. (2016). Fast Valve Power Loss Evaluation Method for Modular Multi-Level Converter Operating at High-Frequency. *Prot. Control. Mod. Power Syst.* 1 (1), 2. doi:10.1186/s41601-016-0015-z

Wang, Z., Liu, J., and Zhuang, X. (2018). A Current Transferring MMC Topology with DC Fault Clearance Capability[J]. *Proc. CSEE* 38 (19), 5795–5803. (in Chinese).

Xiaoguang, W., Yang, B., and Tang, G. (2017). Technical Development and Engineering Applications of HVDC Circuit Breaker[J]. *Power Syst. Technol.* 41 (10), 3180–3188. (in Chinese).

Xue, Y., and Xu, Z. (2014). On the Bipolar MMC-HVDC Topology Suitable for Bulk Power Overhead Line Transmission: Configuration, Control, and DC Fault Analysis. *IEEE Trans. Power Deliv.* 29 (6), 2420–2429. doi:10.1109/tpwrd.2014.2352313

Conflict of Interest: BZ, PX, and SJ were employed by Guangzhou Bureau of EHV Transmission Company of China Southern Power Grid Co, Ltd.

The remaining authors declare that the research was conducted in the absence of any commercial or financial relationships that could be construed as a potential conflict of interest.

Publisher's Note: All claims expressed in this article are solely those of the authors and do not necessarily represent those of their affiliated organizations, or those of the publisher, the editors, and the reviewers. Any product that may be evaluated in this article, or claim that may be made by its manufacturer, is not guaranteed or endorsed by the publisher.

Copyright © 2021 Zhu, Li, Xu, Jiao, Zhang and Xin. This is an open-access article distributed under the terms of the Creative Commons Attribution License (CC BY). The use, distribution or reproduction in other forums is permitted, provided the original author(s) and the copyright owner(s) are credited and that the original publication in this journal is cited, in accordance with accepted academic practice. No use, distribution or reproduction is permitted which does not comply with these terms.

frontiers in Energy Research

ORIGINAL RESEARCH
published: 26 October 2021
doi: 10.3389/fenrg.2021.771465

Delay-Dependent Stability Analysis of Load Frequency Control for Power System With EV Aggregator

Zhe-Li Yuan[1,2,3], *Da Xu*[1,2,3]*, *Li Jin*[1,2,3] *and Hong-Zhang Wang*[1,2,3]

[1]School of Automation, China University of Geosciences, Wuhan, China, [2]Hubei Key Laboratory of Advanced Control and Intelligent Automation for Complex Systems, Wuhan, China, [3]Engineering Research Center of Intelligent Technology for Geo-Exploration, Ministry of Education, Wuhan, China

In this paper, the stability of load frequency control (LFC) for delayed power systems with an electric vehicle (EV) aggregator is studied based on Lyapunov theory and linear matrix inequalities (LMIs). Through mechanism analysis, the LFC of power systems with an EV aggregator based on a proportional–integral–differential (PID) controller is modeled. By constructing a delay interval information correlation functional and estimating its derivative using Wirtinger inequality and extended reciprocally convex matrix inequality, a new stability analysis criterion is proposed. Finally, in order to verify its advantage, the proposed method is used to discuss the influence of EV aggregator gains and PID controller gains on the delay margins for LFC of power systems with EV aggregator participation in frequency regulation.

Keywords: power system, load frequency control, electric vehicles, stability analysis, time delay

OPEN ACCESS

Edited by:
Yaxing Ren,
University of Warwick,
United Kingdom

Reviewed by:
Jian Chen,
Yancheng Institute of Technology,
China
Hong-Bing Zeng,
Hunan University of Technology,
China
Wen-Juan Lin,
Qingdao University, China

***Correspondence:**
Da Xu
xuda@cug.edu.cn

Specialty section:
This article was submitted to Smart Grids, a section of the journal Frontiers in Energy Research

Received: *06 September 2021*
Accepted: *23 September 2021*
Published: *26 October 2021*

Citation:
Yuan Z-L, Xu D, Jin L and Wang H-Z (2021) Delay-Dependent Stability Analysis of Load Frequency Control for Power System With EV Aggregator. Front. Energy Res. 9:771465. doi: 10.3389/fenrg.2021.771465

1 INTRODUCTION

Under the guidance of sustainable development concept, the generation of renewable energy sources (RESs) such as wind power, hydropower, and photovoltaic power has developed rapidly in recent years, and part of traditional thermal power generation will be gradually replaced (Zhou et al., 2018). However, the grid connection of these RESs also brings some problems, especially the wind power generation with great intermittency and volatility (Jin et al., 2021b; Shi et al., 2021). These problems aggravate the imbalance between generation and load consumption in the power systems, resulting in obvious frequency fluctuation. Therefore, load frequency control (LFC) is widely used in power systems (Jin et al., 2019; Shangguan et al., 2021b). The frequency deviation caused by an intermittent energy grid connection is difficult to be eliminated by traditional generator sets. With the grid connection of controllable loads such as electric vehicles (EVs) and the rapid response characteristics of batteries, some studies paid attention to vehicle-to-grid technology, which provides frequency regulation services with a large number of converging EVs (Peng et al., 2017; Jia et al., 2018; Pinto et al., 2021; Teng et al., 2021).

In traditional power systems, the time delay phenomenon of the LFC system is not obvious. However, modern power systems tend to use flexible and open communication networks for information exchange (ShangGuan et al., 2021). For power systems with EVs and intermittent wind power connected, the EV aggregator needs to transmit the control command to the EVs through open communication networks (Ko and Sung, 2019; Li et al., 2019). The use of such networks will inevitably bring unreliable factors, such as time delay, packet loss, and potential failure, which may lead to instability of LFC for power systems (Jin et al., 2021a; Shangguan

TABLE 1 | Parameter of the LFC model.

Parameter	Value	Description
M	10	Inertia constant
D	1	Generator damping coefficient
T_g	0.1	Time constant of the governor
T_{ch}	0.3	Time constant of the turbine
T_{WTG}	1.5	Time constant of the wind turbine generator
T_{EV}	0.1	Time constant of the battery
R	0.05	Speed regulation
β	21	Frequency bias factor

et al., 2021a). Therefore, it is very important to analyze the influence of time delays on the LFC of power systems with an EV aggregator. In addition, in order to ensure the stability of power system LFC, it is necessary to calculate the delay margins and determine all parameters of the proportional–integral–differential (PID) controller (Naveed et al., 2019b; Tek et al., 2020).

In recent years, EVs have been widely used in power systems, and there are also some studies on the influence of time delays and EV aggregator on LFC stability. The Rekasius substitution method is used to determine the stability delay margins of LFC with constant communication delays for an EV aggregator (Naveed et al., 2019a). Then, Naveed et al. presented a graphical method to describe the trajectory of the stable boundary and studied the influence of EV aggregators with communication delays on the stability regions and stability delay margins of the LFC system (Naveed et al., 2021). Based on Lyapunov theory and linear matrix inequalities (LMIs), stability criteria for time-varying delays using the Wirtinger-based improved integral inequality are proposed to calculate the delay margins for LFC with EVs, and the relationship between the gains and the delay margins of the PI controller is given in detail (Ko and Sung, 2018). Two stability criteria are derived, respectively, using Bessel–Legendre inequality and model reconstruction technique, and the interregional delay interaction and the effect of EV gain on the delay margins are discussed (Zhou et al., 2020). Khalil et al. proposed a microgrid model of photovoltaic power generation and EVs considering communication delay, and the maximum allowable delay bound for the stable operation of microgrids is calculated by solving the LMIs (Khalil et al., 2017). Dong et al. characterized the asymptotic stability of EV aggregation delays by using the delay distortion matrix structure of infinite operator dimension reduction and proved that convergence delay affects frequency stability in the form of low-frequency oscillation through three unstable modes (Dong et al., 2020). Although there have been some studies on the stability of delayed LFC systems with an EV aggregator, there are few studies on LFC of renewable energy power systems with an EV aggregator. Also, how to obtain more accurate delay margins remains a challenge.

In this paper, the stability of LFC for power systems with EV aggregator participation in frequency regulation is considered, and the influence of EV aggregator and controller gains on the delay margins is studied. Firstly, based on the PID controller, the LFC of power systems with an EV aggregator is modeled. Then, a new delay stability criterion using Wirtinger inequality and extended reciprocally convex matrix inequalities is proposed. Finally, according to the proposed stability criterion, the delay margins of LFC for power systems with an EV aggregator are obtained, and case studies are performed to show the advantage of the proposed method.

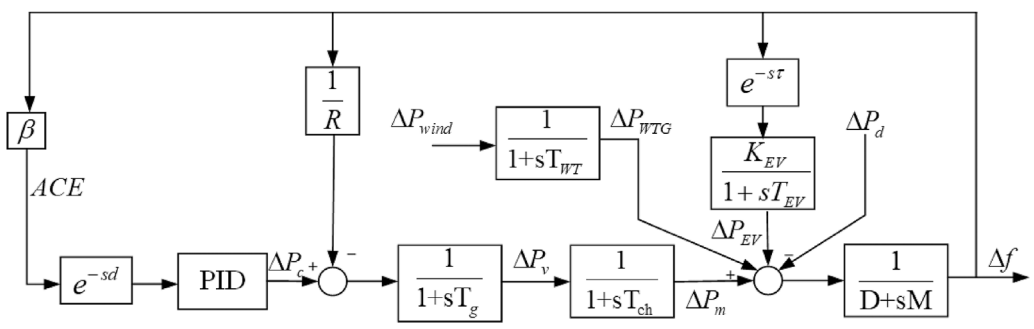


FIGURE 1 | Frequency regulation scheme of the power system with an EV aggregator.

2 MODEL OF LFC FOR POWER SYSTEM WITH EV AGGREGATOR

The block diagram of the LFC for power systems with an EV aggregator is given in **Figure 1**, and the controller is the PID controller. $e^{-s\tau}$ and e^{-sd} denote the time delay of the frequency regulation circuit involved in the EV aggregator and the secondary frequency regulation circuit, respectively; K_{EV} is the gain of the EV aggregator; Δf, ΔP_{EV}, ΔP_{WTG}, ΔP_m, ΔP_v, and ΔP_d are the deviation of frequency, EV aggregator power output, wind turbine generator (WTG) power output, mechanical output of the generator, valve position, and load disturbance, respectively. Definitions of other related symbols in the figure are shown in **Table 1**.

Select the following state variables, output variables, disturbance, and control input:

$$\bar{x}(t) = \left[\, \Delta f \;\; \Delta P_{EV} \;\; \Delta P_{WTG} \;\; \Delta P_m \;\; \Delta P_v \,\right]^T, \tag{1}$$

$$\bar{y}(t) = ACE(t) = \beta \Delta f, \tag{2}$$

$$w(t) = \left[\, \Delta P_d \;\; \Delta P_{\text{wind}} \,\right]^T, \tag{3}$$

$$u(t - \tau(t)) = \Delta P_c(t). \tag{4}$$

Then, the following system state space model can be obtained:

$$\begin{cases} \dot{\bar{x}}(t) = \bar{A}_1 \bar{x}(t) + \bar{A}_2 \bar{x}(t - \tau(t)) + \bar{B} u(t - d(t)) + \bar{F} \omega(t), \\ \bar{y}(t) = \bar{C} \bar{x}(t), \end{cases} \tag{5}$$

where

$$\bar{A}_1 = \begin{bmatrix} -\frac{D}{M} & \frac{1}{M} & \frac{1}{M} & \frac{1}{M} & 0 \\ 0 & -\frac{1}{T_{EV}} & 0 & 0 & 0 \\ 0 & 0 & -\frac{1}{T_{WT}} & 0 & 0 \\ 0 & 0 & 0 & -\frac{1}{T_{ch}} & \frac{1}{T_{ch}} \\ -\frac{1}{RT_g} & 0 & 0 & 0 & -\frac{1}{T_g} \end{bmatrix}, \bar{A}_2 = \begin{bmatrix} 0 & 0 & 0 & 0 & 0 \\ \frac{K_{EV}}{T_{EV}} & 0 & 0 & 0 & 0 \\ 0 & 0 & 0 & 0 & 0 \\ 0 & 0 & 0 & 0 & 0 \\ 0 & 0 & 0 & 0 & 0 \end{bmatrix},$$

$$\bar{B} = \begin{bmatrix} 0 & 0 & 0 & 0 & \frac{1}{T_g} \end{bmatrix}^{\bar{T}} \bar{F} = \begin{bmatrix} -\frac{1}{M} & 0 & 0 & 0 & 0 \\ 0 & 0 & \frac{1}{T_{WT}} & 0 & 0 \end{bmatrix}^T$$

$$\bar{C} = \left[\, \beta \;\; 0 \;\; 0 \;\; 0 \;\; 0 \,\right].$$

The controller is designed as

$$u(t) = -K_{\text{p}} ACE(t) - K_{\text{i}} \int ACE(t)\text{d}t - K_{\text{d}} \frac{\text{d}ACE(t)}{\text{d}t}. \tag{6}$$

Define the new vectors $x(t) = [\bar{x}^T(t) \;\; \int \bar{y}^T(t)dt]^T$, $y(t) = [\bar{y}^T(t) \;\; \int \bar{y}^T(t)dt \;\; \frac{d}{dt}\bar{y}^T(t)]^T$ and $K = [K_p \;\; K_i \;\; K_d]$. The system (**Eq. 5**) is rewritten as

$$\begin{cases} \dot{x}(t) = A_1 x(t) + A_2 x(t - \tau(t)) + B u(t - d(t)) + F w(t), \\ y(t) = C x(t) + D w(t), \\ u(t) = -K y(t), \end{cases} \tag{7}$$

where $A_1 = \begin{bmatrix} \bar{A}_1 & 0 \\ \bar{C} & 0 \end{bmatrix}$, $A_2 = \begin{bmatrix} \bar{A}_2 & 0 \\ 0 & 0 \end{bmatrix}$, $B = \begin{bmatrix} \bar{B} \\ 0 \end{bmatrix}$, $F = \begin{bmatrix} \bar{F} \\ 0 \end{bmatrix}$, $C = \begin{bmatrix} \bar{C} & 0 \\ 0 & 1 \\ \bar{C}\bar{A}_1 & 0 \end{bmatrix}$, and $D = \left[\, 0 \;\; 0 \;\; CF \,\right]^T$.

In order to simplify the analysis, it is assumed that the delay $\tau(t)$ of the frequency regulation circuit involved in the EV aggregator is consistent with the delay $d(t)$ of the secondary frequency regulation circuit. Then, the closed-loop state space equation of LFC for the delayed power system with an EV aggregator can be obtained as follows:

$$\dot{x}(t) = Ax(t) + A_d x(t - d(t)) + F_w w(t), \tag{8}$$

where $A = A_1$, $A_d = A_2 - BKC$, and $F_w = F - BKD$.

3 DELAY-DEPENDENT STABILITY ANALYSIS

When discussing the internal stability of the power system, the influence of external disturbance can be ignored. The model of LFC for the delayed power system with an EV aggregator is obtained as follows:

$$\dot{x}(t) = Ax(t) + A_d x(t - d(t)), \tag{9}$$

where $h_1 \le d(t) \le h_2$ and $\forall t > t_0$.

The following stability criterion for system (**Eq. 9**) is derived by using Wirtinger inequality (Seuret and Gouaisbaut, 2013) and extended reciprocally convex matrix inequality (Zhang et al., 2017).

Theorem 1. For given scalars $\alpha > 0$, $h_2 > h_1 > 0$, the LFC of the closed-loop power system with an EV aggregator (Eq. 9) is exponentially stable, if there exist matrices $P > 0$, $Q_i > 0$, $Z > 0$, $R > 0$, $i = 1, 2$, and any matrix S_1 or S_2 with appropriate dimension, satisfying

$$\Phi_1 = \begin{bmatrix} \Psi_{1,[h_1]} - \Psi_2 - \Psi_4 & E_2^T S_2 \\ \star & -\tilde{R} \end{bmatrix} < 0, \tag{10}$$

$$\Phi_2 = \begin{bmatrix} \Psi_{1,[h_2]} - \Psi_2 - \Psi_5 & E_3^T S_1 \\ \star & -\tilde{R} \end{bmatrix} < 0, \tag{11}$$

where

$$\Psi_{1,[d(t)]} = \Pi_1^T P \Pi_2 + \Pi_2^T P \Pi_1 + e_1^T Q_1 e_1 + e_2^T (Q_2 - Q_1) e_2 - e_4^T Q_2 e_4 + e_s^T \left[h_1^2 Z + h_{12}^2 R \right] e_s$$

$$\Psi_2 = E_1^T [\text{diag}\{Z, 3Z\} e^{-\alpha h_1}] E_1$$

$$\Psi_4 = \begin{bmatrix} E_2 \\ E_3 \end{bmatrix}^T \begin{bmatrix} 2\tilde{R} & S_1 \\ \star & \tilde{R} \end{bmatrix} \begin{bmatrix} E_2 \\ E_3 \end{bmatrix}$$

$$\Psi_5 = \begin{bmatrix} E_2 \\ E_3 \end{bmatrix}^T \begin{bmatrix} \tilde{R} & S_2 \\ \star & 2\tilde{R} \end{bmatrix} \begin{bmatrix} E_2 \\ E_3 \end{bmatrix}$$

$$\Pi_1 = \text{col}\{e_1, h_1 e_5, (d(t) - h_1) e_6 + (h_2 - d(t)) e_7\}$$

$$\Pi_2 = \text{col}\{e_s, e_1 - e_2, e_2 - e_4\}$$

TABLE 2 | Delay margins for different methods.

K_p	Methods	K_i				
		0.2	**0.3**	**0.4**	**0.6**	**1**
0.2	Theorem 1 (Jiang et al., 2012)	3.2831	0.9930	0.7983	0.5286	0.2301
	Theorem 1	5.2094	3.9441	3.0267	1.8634	0.7617
0.3	Theorem 1 (Jiang et al., 2012)	3.4021	0.9833	0.7922	0.5469	0.2600
	Theorem 1	3.6493	3.1177	2.6172	1.7828	0.7617
0.4	Theorem 1 (Jiang et al., 2012)	1.1328	0.8411	0.7214	0.5280	0.2753
	Theorem 1	2.4823	2.2650	2.0142	1.4911	0.7074
0.5	Theorem 1 (Jiang et al., 2012)	0.7916	0.7050	0.6250	0.4840	0.2765
	Theorem 1	1.6492	1.5436	1.4124	1.1115	0.6177
0.6	Theorem 1 (Jiang et al., 2012)	0.6421	0.5859	0.5316	0.4315	0.2679
	Theorem 1	1.1084	1.0474	0.9753	0.8154	0.5249
1	Theorem 1 (Jiang et al., 2012)	0.3253	0.3094	0.2930	0.2600	0.1953
	Theorem 1	0.4144	0.4004	0.3851	0.3540	0.2875

$e_i = [0_{n\times(i-1)n}, I, 0_{n\times(7-i)n}], i = 1, 2, \ldots, 7$
$E_i = \mathrm{col}\{e_i - e_{i+1}, e_i + e_{i+1} - 2e_{i+4}\}, i = 1, 2, 3$
$\tilde{R} = \mathrm{diag}\{R, 3R\} e^{-\alpha h_2} h_{12} = h_2 - h_1$, $e_s = Ae_1 + A_d e_3$.

Proof: Construct the following Lyapunov–Krasovskii functional:

$$\begin{aligned} V(t) = {} & \eta^T(t)P\eta(t) + h_1\int_{-h}^{0}\int_{t+\theta}^{t} e^{\alpha(s-t)}\dot{x}^T(s)Z\dot{x}(s)dsd\theta \\ & + h_{12}\int_{-h_2}^{-h_1}\int_{t+\theta}^{t} e^{\alpha(s-t)}\dot{x}^T(s)R\dot{x}(s)dsd\theta \\ & + \int_{t-h_1}^{t} e^{\alpha(s-t)}x^T(s)Q_1x(s)ds \\ & + \int_{t-h_2}^{t-h} e^{\alpha(s-t)}x^T(s)Q_2x(s)ds, \end{aligned} \tag{12}$$

where $\eta(t) = \mathrm{col}\left\{x(t), \int_{t-h_1}^{t} x(s)ds, \int_{t-h_2}^{t-h_1} x(s)ds\right\}$.

Calculating the derivative of $V(t)$, we get

$$\begin{aligned} \dot{V}(t) + \alpha V(t) \le {} & \eta^T(t)P\dot{\eta}(t) + \dot{\eta}^T(t)P\eta(t) + \alpha\eta^T(t)P\eta(t) \\ & + \dot{x}^T(t)\left(h_1^2Z + h_{12}^2R\right)\dot{x}(t) \\ & - h_1\int_{t-h}^{t} e^{-\alpha h_1}\dot{x}^T(s)Z\dot{x}(s)ds - h_{12}\int_{t-h_2}^{t-h} e^{-\alpha h_2}\dot{x}^T(s)R\dot{x}(s)ds \\ & + x^T(t)Q_1x(t) \\ & + e^{-\alpha h_1}x^T(t-h_1)(Q_2 - Q_1)x(t-h_1) \\ & - e^{-\alpha h_2}x^T(t-h_2)Q_2x(t-h_2) \\ = {} & \zeta^T(t)\psi_{1,[d(t)]}\zeta(t) - h_1\int_{t-h}^{t} e^{-\alpha h_1}\dot{x}^T(s)Z\dot{x}(s)ds \\ & - h_{12}\int_{t-h_2}^{t-h} e^{-\alpha h_2}\dot{x}^T(s)R\dot{x}(s)ds, \end{aligned} \tag{13}$$

where

$$\begin{aligned} \zeta(t) = \mathrm{col}\{ & x(t), x(t-h_1), x(t-d(t)), \\ & x(t-h_2), \int_{t-h_1}^{t}\frac{x(s)}{h_1}ds, \int_{t-d(t)}^{t-h_1}\frac{x(s)}{d(t)-h_1}ds, \int_{t-h_2}^{t-d(t)}\frac{x(s)}{h_2-d(t)}ds\}. \end{aligned}$$

Based on Wirtinger inequality, we have

$$\begin{aligned} h_1\int_{t-h_1}^{t} e^{-\alpha h}\dot{x}^T(s)Z\dot{x}(s)ds \ge \varepsilon_1^T(t)\begin{bmatrix} e^{-\alpha h_1}Z & 0 \\ 0 & 3e^{-\alpha h_1}Z \end{bmatrix} \\ \varepsilon_1(t) = \zeta^T(t)\psi_2\zeta(t), \end{aligned} \tag{14}$$

$$\begin{aligned} h_{12}\int_{t-h_2}^{t-h} e^{-\alpha h_2}\dot{x}^T(s)R\dot{x}(s)ds = {} & h_{12}\left(\int_{t-d(t)}^{t-h_1} e^{-\alpha h_2}\dot{x}^T(s)R\dot{x}(s)ds\right. \\ & \left. + \int_{t-h_2}^{t-d(t)} e^{-\alpha h_2}\dot{x}^T(s)R\dot{x}(s)ds\right) \\ \ge {} & \frac{h_{12}}{d(t)-h_1}\varepsilon_2^T(t)\tilde{R}\varepsilon_2(t) + \frac{h_{12}}{h_2-d(t)}\varepsilon_3^T(t)\tilde{R}\varepsilon_3(t), \end{aligned} \tag{15}$$

where

$$\varepsilon_1(t) = \begin{bmatrix} x(t) - x(t-h_1) \\ x(t) + x(t-h_1) - 2\int_{t-h_1}^{t}\frac{x(s)}{h_1}ds \end{bmatrix},$$

$$\varepsilon_2(t) = \begin{bmatrix} x(t-h_1) - x(t-d(t)) \\ x(t-h_1) + x(t-d(t)) - 2\int_{t-d(t)}^{t-h_1}\frac{x(s)}{d(t)-h_1}ds \end{bmatrix},$$

$$\varepsilon_3(t) = \begin{bmatrix} x(t-d(t)) - x(t-h_2) \\ x(t-d(t)) + x(t-h_2) - 2\int_{t-h_2}^{t-d(t)}\frac{x(s)}{h_2-d(t)}ds \end{bmatrix}.$$

Using extended reciprocally convex matrix inequality to estimate **Eq. 15** yields

$$\begin{aligned} \frac{h_{12}\varepsilon_2^T(t)\tilde{R}\varepsilon_2(t)}{d(t)-h_1} + \frac{h_{12}\varepsilon_3^T(t)\tilde{R}\varepsilon_3(t)}{h_1-d(t)} & \ge \varepsilon_2^T(t)\tilde{R}\varepsilon_2(t) + \varepsilon_3^T(t)\tilde{R}\varepsilon_3(t) \\ & + \frac{h_2-d(t)}{h_{12}}\begin{bmatrix}\varepsilon_2(t)\\ \varepsilon_3(t)\end{bmatrix}^T\begin{bmatrix}\tilde{R}-S_2\tilde{R}^{-1}S_2^T & S_1\\ * & 0\end{bmatrix}\begin{bmatrix}\varepsilon_2(t)\\ \varepsilon_3(t)\end{bmatrix} \\ & + \frac{d(t)-h_1}{h_{12}}\begin{bmatrix}\varepsilon_2(t)\\ \varepsilon_3(t)\end{bmatrix}^T\begin{bmatrix}0 & S_2\\ * & \tilde{R}-S_1^T\tilde{R}^{-1}S_1\end{bmatrix}\begin{bmatrix}\varepsilon_2(t)\\ \varepsilon_3(t)\end{bmatrix} \\ & = \zeta^T(t)\psi_{3,[d(t)]}\zeta(t), \end{aligned} \tag{16}$$

TABLE 3 | Delay margins for K_d = 0.

$K_p - K_i$	0.05	0.1	0.15	0.2	0.3	0.4
0.1	15.8185	11.2262	8.2007	6.2970	4.1388	2.9816
0.2	7.3389	6.7004	5.9119	5.1477	3.9001	2.9550
0.3	4.1736	4.0625	3.8623	3.6151	3.0890	2.5940
0.4	2.6349	2.5977	2.5397	2.4573	2.2430	1.9946
0.6	1.1597	1.1414	1.1194	1.0938	1.0333	0.9625

TABLE 4 | Delay margins for K_d = 0.2.

$K_p - K_i$	0.05	0.1	0.15	0.2	0.3	0.4
0.1	1.5466	1.5955	1.6443	1.6943	1.7902	1.8616
0.2	1.4648	1.5125	1.5607	1.6101	1.7096	1.7920
0.3	1.3391	1.3818	1.4258	1.4722	1.5674	1.6571
0.4	1.1835	1.2177	1.2537	1.2915	1.3721	1.4563
0.6	0.8734	0.8887	0.9039	0.9198	0.9540	0.9900

TABLE 5 | Delay margins for K_d = 0.5.

$K_p - K_i$	0.05	0.1	0.15	0.2	0.3	0.4
0.1	0.4761	0.4785	0.4810	0.4834	0.4889	0.4944
0.2	0.4663	0.4688	0.4712	0.4736	0.4791	0.4840
0.3	0.4559	0.4578	0.4602	0.4626	0.4675	0.4730
0.4	0.4443	0.4462	0.4486	0.4510	0.4553	0.4602
0.6	0.4193	0.4211	0.4230	0.4248	0.4285	0.4327

where

$$\psi_{3,[d(t)]} = E_2^T\tilde{R}E_2 + E_3^T\tilde{R}E_3 + \frac{h_2 - d(t)}{h_{12}}\begin{bmatrix}E_2\\E_3\end{bmatrix}^T\begin{bmatrix}\tilde{R} - S_2\tilde{R}^{-1}S_2^T & S_1\\ * & 0\end{bmatrix}\begin{bmatrix}E_2\\E_3\end{bmatrix}$$
$$+\frac{d(t) - h_1}{h_{12}}\begin{bmatrix}E_2\\E_3\end{bmatrix}^T\begin{bmatrix}0 & S_2\\ * & \tilde{R} - S_1^T\tilde{R}^{-1}S_1\end{bmatrix}\begin{bmatrix}E_2\\E_3\end{bmatrix}.$$

Then, we can get

$$h_{12}\int_{t-h}^{t-h} e^{-\alpha h_2}\dot{x}^T(s)R\dot{x}(s)ds \geq \zeta^T(t)\psi_{3,[d(t)]}\zeta(t). \quad (17)$$

Applying **Eq. 14** and **Eq. 17** to **Eq. 13**, the following holds:

$$\dot{V}(t) + \alpha V(t) \leq \zeta^T(t)\left[\psi_{1,[d(t)]} - \psi_2 - \psi_{3,[d(t)]}\right]\zeta(t). \quad (18)$$

By using the Schur complement, **Eqs 10**, **11** are equal to the following inequalities:

$$\psi_{1,[h_1]} - \psi_2 - \psi_{3,[h_1]} \leq 0, \quad (19)$$
$$\psi_{1,[h_2]} - \psi_2 - \psi_{3,[h_2]} \leq 0, \quad (20)$$

which implies

$$\psi_{1,[d(t)]} - \psi_2 - \psi_{3,[d(t)]} \leq 0. \quad (21)$$

Thus, it follows from **Eq. 21** that $\dot{V}(t) + \alpha V(t) \leq 0$, which further leads to

$$V(t) \leq e^{-\alpha(t-t_0)}V(t_0). \quad (22)$$

Noting that $V(t) \geq \rho\|x(t)\|^2$, $V(t_0) \leq \beta\|\phi\|^2$, $\rho > 0$, and $\beta > 0$, we have

$$\|x(t)\| \leq \sqrt{\frac{\beta}{\rho}}e^{-0.5\alpha(t-t_0)}\|\phi\|, \quad (23)$$

which implies the system (**Eq. 9**) is exponentially stable (Yang et al., 2020).

According to the above, system (**Eq. 9**) is exponentially stable if **Eqs 10**, **11** hold. The proof is completed.

Remark 1. The method proposed in this section establishes the constraint relation between the delay information and the exponential stability of the LFC for power systems with an EV aggregator, which can be used to analyze the influence of delays on the stability of the system and calculate the delay margins. The margins represent the time delay tolerance range of the system to ensure exponential stability, which is composed of the delay lower bound h_1 and delay upper bound h_2.

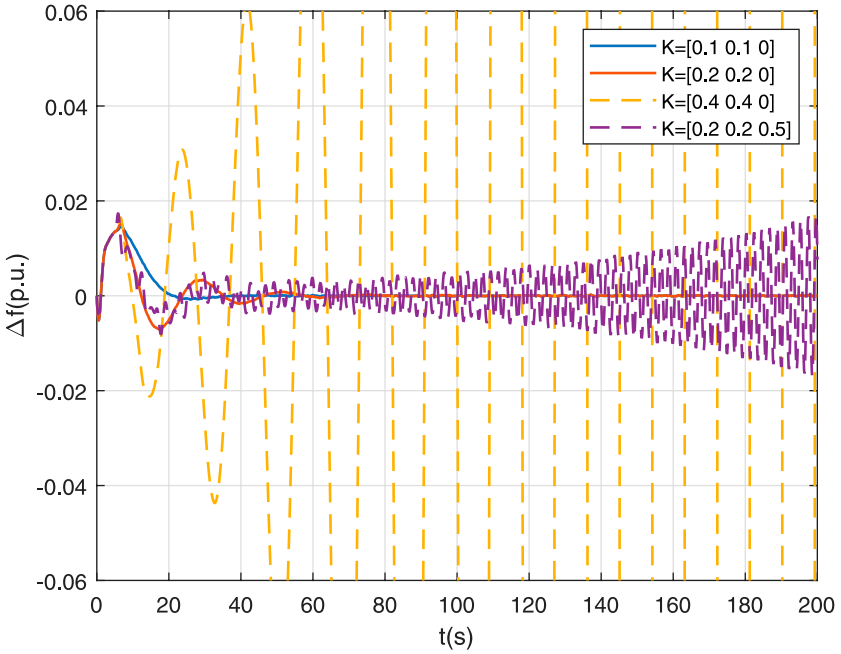


FIGURE 2 | Frequency deviations for different K.

TABLE 6 | Delay margins for different values of K_{EV} and K.

K_{EV} – K	[0.1 0.05 0]	[0.1 0.1 0]	[0.1 0.1 0.2]	[0.2 0.2 0.2]
1	15.8185	11.2262	1.5955	1.6101
2	13.3228	10.4242	1.4941	1.5259
3	8.9191	7.7698	1.3904	1.4270
4	6.3446	5.7806	1.2891	1.3226
5	4.8284	4.5056	1.1969	1.2250

Remark 2. In **Theorem 1**, the LFC for power systems with an EV aggregator is exponentially stable if **Eqs 10**, **11** are satisfied. The calculation steps of the delay margins for the stability of the system can be briefly summarized as follows:

1) Construct the LFC closed-loop model for power systems with an EV aggregator and a PID controller.
2) Choose the values of α, the EV aggregator gain K_{EV}, and the allowable lower bound h_1.
3) Calculate the delay margin h_2 of the power system by using the binary search technique (Zhang et al., 2013) and MATLAB/LMI toolbox to solve the LMIs in **Theorem 1**.

4 CASE STUDIES

Case studies of LFC for power systems with an EV aggregator are presented to verify the advantage of the proposed method and study the influence of PID controller and EV aggregator gains on the delay margins. The related parameters of the system are shown in **Table 1**.

4.1 Comparison With the Existing Research

The method proposed by Jiang et al. (2012) is used to verify the advantage of the proposed method. Set $h_1 = 0$, $\alpha = 0$, $K_d = 0$, and $k_{EV} = 1$, and the system can be considered asymptotically stable if the conditions in **Theorem 1** are true. Then, the delay margins of the method proposed in this paper are compared with the delay margins of time-varying delay ($\mu = 0.9$) in the study of Jiang et al. (2012). It is clear from **Table 2** that the results of the proposed method are less conservative.

4.2 Effect of PID Controller and EV Aggregator Gains

The gains of the PID controller and EV aggregator have an important effect on the delay margins of the LFC for power systems with an EV aggregator. Firstly, let $h_1 = 0$, $\alpha = 0.01$, $k_{EV} =$

1, and PID controller parameters K be different; the delay margins of the system are obtained, and the related results are shown in **Tables 3–5**.

As shown in **Table 3**, when $K_d = 0$ (PI controllers), for fixed K_p, the delay margins decrease gradually with the increase of K_i. For fixed K_i, with the increase of K_p, the delay margins decrease gradually. As can be seen from **Tables 3–5**, when K_d is not 0 (PID controllers), the delay margins gradually become smaller with the gradual increase of K_d. For fixed K_p, the delay margins increase gradually with the increase of K_i; for fixed K_i, the delay margins decrease as K_p increases. To sum up, the delay margins under PI controllers are larger than that under the PID controller. The larger K_p or K_d is, the smaller delay margins are.

Then, the frequency deviations of LFC for power systems with an EV aggregator under the delay of 5.15s and different PID controller gains are simulated. It is assumed that the power deviations of load and WTG fluctuate randomly in the range of 0.19–0.21 p. u. and 0.49–0.51 p. u., respectively. As shown in **Figure 2**, when K = [0.2 0.2 0], the system is stable. When K_p and K_i decrease (K = [0.1 0.1 0]), the frequency deviation also tends to zero. But when K_p and K_i are increased (K = [0.4 0.4 0]), or K_d is increased (K = [0.2 0.2 0.5]), it is clear that the frequency deviations do not converge in these cases. Therefore, **Figure 2** validates the analysis in **Tables 3–5**, and appropriate selection of PID controller gains K is very important for the stability of LFC for power systems with an EV aggregator.

Finally, the gain of the EV aggregator K_{EV} is also an important factor affecting the delay margins of LFC for power systems with an EV aggregator. As shown in **Table 6**, regardless of how the gains of the PID controller change, the delay margins of the delayed LFC system with an EV aggregator and intermittent wind energy decrease with the increase of K_{EV}.

5 CONCLUSION

In this paper, the LFC stability of delayed power systems with an EV aggregator was studied. The LFC of the power system was modeled as a delayed linear system with an EV aggregator. Based on Lyapunov stability theory and the linear matrix inequality approach, a new stability criterion was proposed by using Wirtinger inequality and improved inverse convex matrix inequality. Finally, the influence of EV aggregator gains and PID controller gains on the delay margins was studied, and some case studies have shown the advantage of the results. The research of this paper can solve the delay margins more accurately and guide the design of PID controllers of LFC for power systems with an EV aggregator effectively.

DATA AVAILABILITY STATEMENT

The original contributions presented in the study are included in the article/Supplementary Material, and further inquiries can be directed to the corresponding author.

AUTHOR CONTRIBUTIONS

All authors listed have made a substantial, direct, and intellectual contribution to the work and approved it for publication.

FUNDING

This work was supported by the China Postdoctoral Science Foundation–funded project under Grant No. 2021M692992.

REFERENCES

Dong, C., Xiao, Q., Wang, M., Morstyn, T., McCulloch, M. D., and Jia, H. (2020). Distorted Stability Space and Instability Triggering Mechanism of Ev Aggregation Delays in the Secondary Frequency Regulation of Electrical Grid-Electric Vehicle System. *IEEE Trans. Smart Grid* 11, 5084–5098. doi:10.1109/TSG.2020.3008333

Jia, H., Li, X., Mu, Y., Xu, C., Jiang, Y., Yu, X., et al. (2018). Coordinated Control for Ev Aggregators and Power Plants in Frequency Regulation Considering Time-Varying Delays. *Appl. Energ.* 210, 1363–1376. doi:10.1016/j.apenergy.2017.05.174

Jiang, L., Yao, W., Wu, Q. H., Wen, J. Y., and Cheng, S. J. (2012). Delay-dependent Stability for Load Frequency Control with Constant and Time-Varying Delays. *IEEE Trans. Power Syst.* 27, 932–941. doi:10.1109/TPWRS.2011.2172821

Jin, L., He, Y., Zhang, C.-K., Shangguan, X.-C., Jiang, L., and Wu, M. (2021a). Novel Structure-Exploiting Techniques Based Delay-dependent Stability Analysis of Multi-Area Lfc with Improved Numerical Tractability. *IEEE Trans. Power Syst.* 36, 4194–4211. doi:10.1109/TPWRS.2021.3056594

Jin, L., He, Y., Zhang, C.-K., Shangguan, X.-C., Jiang, L., and Wu, M. (2021b). Robust Delay-dependent Load Frequency Control of Wind Power System Based on a Novel Reconstructed Model. *IEEE Trans. Cybernetics*, 1, 12. doi:10.1109/TCYB.2021.3051160

Jin, L., Zhang, C.-K., He, Y., Jiang, L., and Wu, M. (2019). Delay-dependent Stability Analysis of Multi-Area Load Frequency Control with Enhanced Accuracy and Computation Efficiency. *IEEE Trans. Power Syst.* 34, 3687–3696. doi:10.1109/TPWRS.2019.2902373

Khalil, A., Rajab, Z., Alfergani, A., and Mohamed, O. (2017). The Impact of the Time Delay on the Load Frequency Control System in Microgrid with Plug-In-Electric Vehicles. *Sustain. Cities Soc.* 35, 365–377. doi:10.1016/j.scs.2017.08.012

Ko, K. S., and Sung, D. K. (2019). The Effect of Cellular Network-Based Communication Delays in an Ev Aggregator's Domain on Frequency Regulation Service. *IEEE Trans. Smart Grid* 10, 65–73. doi:10.1109/TSG.2017.2731846

Ko, K. S., and Sung, D. K. (2018). The Effect of Ev Aggregators with Time-Varying Delays on the Stability of a Load Frequency Control System. *IEEE Trans. Power Syst.* 33, 669–680. doi:10.1109/TPWRS.2017.2690915

Li, X., Yu, X., Jia, H., Mu, Y., Wu, J., Wang, M., et al. (2019). Structure Constrained Controller Design for Power Plants and Ev Aggregator in Frequency Regulation Considering Time Delays. *Energ. Proced.* 158, 2966–2971. doi:10.1016/j.egypro.2019.01.961

Naveed, A., Sönmez, Ş., and Ayasun, S. (2019a). Identification of Stability Delay Margin for Load Frequency Control System with Electric Vehicles Aggregator Using Rekasius Substitution. *IEEE Milan PowerTech.* 1, 6. doi:10.1109/PTC.2019.8810662

Naveed, A., Sönmez, Ş., and Ayasun, S. (2021). Impact of Electric Vehicle Aggregator with Communication Time Delay on Stability Regions and Stability Delay Margins in Load Frequency Control System. *J. Mod. Power Syst. Clean Energ.* 9, 595–601. doi:10.35833/MPCE.2019.000244

Naveed, A., Zerdali, E., Sönmez, Ş., and Ayasun, S. (2019b). "Optimization of Pi Controller Gains Using Genetic Algorithm for Time-Delayed Load Frequency Control Systems with Electric Vehicles Aggregator," in 2019 11th International Conference on Electrical and Electronics Engineering (ELECO), 28-30 November, 2019, Bursa, Turkey. doi:10.23919/ELECO47770.2019.8990434

Peng, C., Zou, J., Lian, L., and Li, L. (2017). An Optimal Dispatching Strategy for V2g Aggregator Participating in Supplementary Frequency Regulation Considering Ev Driving Demand and Aggregator's Benefits. *Appl. Energ.* 190, 591–599. doi:10.1016/j.apenergy.2016.12.065

Pinto, J., Carvalho, A., and Morais, V. (2021). Power Sharing in Island Microgrids. *Front. Energ. Res.* 8, 360. doi:10.3389/fenrg.2020.609218

Seuret, A., and Gouaisbaut, F. (2013). Wirtinger-based Integral Inequality: Application to Time-Delay Systems. *Automatica* 49, 2860–2866. doi:10.1016/j.automatica.2013.05.030

ShangGuan, X.-C., He, Y., Zhang, C.-K., Jin, L., Jiang, L., Wu, M., et al. (2021). Switching System-Based Load Frequency Control for Multi-Area Power System Resilient to Denial-Of-Service Attacks. *Control. Eng. Pract.* 107, 104678. doi:10.1016/j.conengprac.2020.104678

Shangguan, X.-C., He, Y., Zhang, C.-K., Jin, L., Yao, W., Jiang, L., et al. (2021a). Control Performance Standards-Oriented Event-Triggered Load Frequency Control for Power Systems under Limited Communication Bandwidth. *IEEE Trans. Control. Syst. Tech.* 1, 9. doi:10.1109/TCST.2021.3070861

Shangguan, X.-C., Zhang, C.-K., He, Y., Jin, L., Jiang, L., Spencer, J. W., et al. (2021b). Robust Load Frequency Control for Power System Considering Transmission Delay and Sampling Period. *IEEE Trans. Ind. Inform.* 17, 5292–5303. doi:10.1109/TII.2020.3026336

Shi, Q., Liu, L., Wang, Y., Lu, Y., Zou, Q., Zhang, Q., et al. (2021). Cooperative Synthetic Inertia Control for Wind Farms Considering Frequency Regulation Capability. *Front. Energ. Res.* 9, 501. doi:10.3389/fenrg.2021.738857

Tek, B., Sönmez, Ş., and Ayasun, S. (2020). "Delay-dependent Stability Analysis of a Two-Area Load Frequency Control System Including Electric Vehicle Aggregator and Dynamic Demand Response," in 2020 12th International Conference on Electrical and Electronics Engineering (ELECO), 26-28 November, 2019, Bursa, Turkey, 178–182. doi:10.1109/ELECO51834.2020.00035

Teng, W., Wang, Y., Sun, S., Cheng, Y., Yu, P., and Wang, S. (2021). Robust Stability Control for Electric Vehicles Connected to Dc Distribution Systems. *Front. Energ. Res.* 9, 423. doi:10.3389/fenrg.2021.740698

Yang, B., Hao, M., Wang, R., Zhao, X., and Zong, G. (2020). Exponential Stability of Delayed Generalized Neural Networks with Intermittent Large-Delay Periods. *IEEE Trans. Syst. Man, Cybernetics: Syst.* 1, 11. doi:10.1109/TSMC.2020.2967506

Zhang, C.-K., He, Y., Jiang, L., Wu, M., and Wang, Q.-G. (2017). An Extended Reciprocally Convex Matrix Inequality for Stability Analysis of Systems with Time-Varying Delay. *Automatica* 85, 481–485. doi:10.1016/j.automatica.2017.07.056

Zhang, C.-K., Jiang, L., Wu, Q. H., He, Y., and Wu, M. (2013). Delay-dependent Robust Load Frequency Control for Time Delay Power Systems. *IEEE Trans. Power Syst.* 28, 2192–2201. doi:10.1109/TPWRS.2012.2228281

Zhou, B., Xu, D., Li, C., Chung, C. Y., Cao, Y., Chan, K. W., et al. (2018). Optimal Scheduling of Biogas–Solar–Wind Renewable Portfolio for Multicarrier Energy Supplies. *IEEE Trans. Power Syst.* 33, 6229–6239. doi:10.1109/TPWRS.2018.2833496

Zhou, S.-J., Zeng, H.-B., and Xiao, H.-Q. (2020). Load Frequency Stability Analysis of Time-Delayed Multi-Area Power Systems with Ev Aggregators Based on Bessel-Legendre Inequality and Model Reconstruction Technique. *IEEE Access* 8, 99948–99955. doi:10.1109/ACCESS.2020.2997002

Conflict of Interest: The authors declare that the research was conducted in the absence of any commercial or financial relationships that could be construed as a potential conflict of interest.

Publisher's Note: All claims expressed in this article are solely those of the authors and do not necessarily represent those of their affiliated organizations, or those of the publisher, the editors, and the reviewers. Any product that may be evaluated in this article, or claim that may be made by its manufacturer, is not guaranteed or endorsed by the publisher.

Copyright © 2021 Yuan, Xu, Jin and Wang. This is an open-access article distributed under the terms of the Creative Commons Attribution License (CC BY). The use, distribution or reproduction in other forums is permitted, provided the original author(s) and the copyright owner(s) are credited and that the original publication in this journal is cited, in accordance with accepted academic practice. No use, distribution or reproduction is permitted which does not comply with these terms.

frontiers in Energy Research

ORIGINAL RESEARCH
published: 28 October 2021
doi: 10.3389/fenrg.2021.759434

Optimal Operation and Control Design of DC Arrester for Renewable Energy Transmission

*Yue Feng[1], Kaiping Li[1], Min Gao[1], Yaozhang Liu[2], Xiaojun Li[3] and Jiawei Zhu[4]**

[1]Yunnan Power Grid Co. Ltd., Wenshan Power Supply Company, Wenshan, China, [2]Guangdong Power Grid Co. Ltd., Chaozhou Power Supply Company, Chaozhou, China, [3]Suzhou Industrial Park Haiwo Science and Technology Co. Ltd., Suzhou, China, [4]School of Information Engineering, Chang'an University, Xi'an, China

The trip probability of transmission line under lightning stroke is rapidly increasing under complex weather conditions when large-scale renewable energy is intergrated with modern power grid. Line arrester plays a critical role in reducing lightning damage and economic losses, in which DC reference voltage is a critical parameter to evaluate line arresters. Hence, a set of on-site DC test system of transmission line arresters is developed to realize the DC reference voltage test in this article. The output DC voltage of the test system is continuously adjustable (0–200 kV), while its rated power and the maximum output current are set to 400 W and 2 mA, respectively. Furthermore, the system is powered by a lithium battery instead of a 220/380 V AC energy source. It employs split design and integrating assembly on-site that reduces the total weight by 36.7%, which considerably decreases the demand for the space of test site. Besides, the weights of control cabinet, multiplying cylinder, and energy source are reduced by 60, 54.55, and 33.33%, respectively. Meanwhile, the Bluetooth remote control module is used to effectively ensure the safety of test personnel. This system accomplishes DC reference voltage tests without removing line arresters on site, which can effectively enhance maintenance efficiency and economic benefits.

Keywords: line arrester, DC reference voltage test, portable, field test, transmission line

OPEN ACCESS

Edited by:
Xiaoshun Zhang,
Shantou University, China

Reviewed by:
Yixuan Chen,
The University of Hong Kong, Hong Kong, SAR China
Liang Chao,
The State Key Laboratory of Scientific and Engineering Computing (LSEC), China
Xuehan Zhang,
Korea University, South Korea

****Correspondence:***
Jiawei Zhu
jiawei.zhu@chd.edu.cn

Specialty section:
This article was submitted to Smart Grids, a section of the journal Frontiers in Energy Research

Received: *16 August 2021*
Accepted: *13 September 2021*
Published: *28 October 2021*

Citation:
Feng Y, Li K, Gao M, Liu Y, Li X and Zhu J (2021) Optimal Operation and Control Design of DC Arrester for Renewable Energy Transmission. Front. Energy Res. 9:759434. doi: 10.3389/fenrg.2021.759434

INTRODUCTION

With the development of technology and economy (Aberoumand et al., 2018; Lei et al., 2020; Tahir et al., 2021), energy demand has further expanded and the crisis of energy shortage has become more severe in recent years (Hori et al., 2020). Therefore, various renewable energies such as wind energy and solar energy (Zhang et al., 2020) have attracted extensive worldwide attention due to their prominent merits of no-pollution and recycling characteristics. For instance, the northeast, north, and northwest regions in China possess a large proportion of renewable energy, which owns high export demand and great development potential. Hence, a series of relevant policies are presented to encourage the development of wind power and solar energy (Zhu et al., 2021). As a result, the installed capacity of wind power and photovoltaic power is rising rapidly in recent years (Guchhait and Banerjee, 2020). However, generated power from the regional power grid far exceeds the consumption capacity of the system. Thus, it is necessary to transmit electric energy outward to improve the consumption capacity. Besides, the intermittence and randomness of renewable energy and the limitation of the consumption capacity of power systems lead to "abandoning wind" and "abandoning light."

To adapt to the profound changes in energy patterns in the future, high-voltage direct current (HVDC) transmission (Muniappan, 2021) has been vigorously developed due to its outstanding performance in long-distance transmission and the optimal allocation of energy resources in a wide area (Liu et al., 2020). In particular, the advantages of HVDC transmission mainly include: 1) Larger transmission capacity, longer transmission distance, and faster adjustment of the size and direction of transmission power; 2) DC transmission makes full use of the line corridor where the width of the line corridor is about half of that of the AC transmission line; 3) For large-sacle power grids, HVDC can realize interconnected power supply between large power grids through DC transmission without interfering and affecting each other.

In addition, HVDC transmission lines play a significant role under the environment with complex geographical conditions, e.g., large and fast temperature changes, as well as rough terrain that are prone to frequent and irregular lightning (Božidar et al., 2016) interference when severe meteorological changes occur (Malcolm and Aggarwal, 2015). Such conditions could bring great safety challenges to the operation of power transmission. Note that more than 40–70% of transmission line flashover accidents are caused by lightning.

To improve the safe operation of transmission lines, a metal-oxide arrester (MOA) (Hoang et al., 2017) is developed to protect the line insulation from over-current based on its superior overvoltage protection performance that has become the standard configuration of over-voltage protection applied in power transmission (Vita and Christodoulou, 2016) and transformation equipment (Seyyedbarzegar and Mirzaie, 2015). In general, the advantages of MOA can be mainly summarized as: 1) fast response, flat volt-ampere characteristics, and high stablility; 2) large flow capacity, low residual pressure, long service life, and simple structure; 3) wide application in power transmission, transformation, and distribution systems; 4) compared with the traditional porcelain sheath arrester, the composite sheath has the advantages of small size, lightweight, solid structure, strong pollution resistance, good explosion-proof performance, and so on.

Besides, another overvoltage protection equipment called line arresters (Christodoulou et al., 2010; Sandrode et al., 2017) that are critical to reliable operation of power system line are mainly installed on transmission lines in mountainous areas, where the operating environment is so complex that some arrester faults or even explosions occur from time to time that poses serious risks to safety operation. Futhermore, with the increasing number of line arresters equipped on transmission lines, it is imperative to carry out sampling tests for line arresters.

According to the power industry standard "guidelines for the implementation of on-site insulation test lightning arrester test," the leakage current tests under DC reference voltage and 0.75 times DC reference voltage are applied to diagnose the defects of line arresters damp and reflect resistor deterioration (Marcel et al., 2015). For a general DC reference voltage test, line arresters are removed from the transmission line (Alberto et al., 2014; Silverio et al., 2020) to test in laboratory condition and then installed back after the test (Hemapala et al., 2018). However, the disassembly and assembly procedure of line arresters are time-consuming, which consumes a lot of manpower and material resources.

To explore a high-altitude test method without dismantling line arresters (Petar et al., 2013; Hemapala et al., 2018), this work presents a novel line arresters DC test system for field tests for 110 and 220 kV sectioned lines. Additionally, the rated power and maximum output voltage of the test system are 400 W and 200 kV, respectively. A thorny obstacle of conventional studies that DC high-voltage tests can only be carried out on the ground is effectively solved through the presented test technique with good economic benefits. Besides, basic working principles and key components of the test system are also described. In general, the main contribution/novelty of this work can be summarized as follows:

1) Compared with traditional devices with the same parameters, the overall portability of the device is significantly improved, e.g., the total weight of this device is decreased by 36.7%;
2) This device is designed to be more suitable for on-site tests, in which multiplying cylinder and control cabinet can be transported separately and lithium battery is applied for power supply;
3) The safety is also considerably enhanced during tests. Wireless transmission and control of the equipment are realized based on the control of infrared measurement circuit and Bluetooth remote control module, which guarantees the safety of testers during the tests under the tower.

The rest of this work is organized as follows: System Modelling is provided in Section *System Modelling*. Design of power driver and control circuit, voltage-double rectifier circuit, and remote control module is shown in Section *System Design of Power Driver and Control Circuit*. The portable DC test system and test results are presented in Section *Portable DC Test System and Test*. Lastly, conclusions are given in Section *Conclusion*.

SYSTEM MODELING

A typical DC test system of line arrester consists of five parts i.e., control cabinet, multiplying cylinder, lithium battery, remote control panel, and line arrester sample, while the overall system framework is represented in **Figure 1A**.

It is extremely difficult to obtain AC 220 V energy source for line arresters on-site. Meanwhile, the volume and weight of conventional 1 kW generators fail to satisfy on-site usage requirements. Thus, lithium battery is employed as an energy source for this test system. Besides, the test system is subject to restrictions with a rated power of 400 W, a continuously adjustable output DC voltage of 0–200 kV, and a maximum output current of 2 mA to meet the DC reference voltage test of 110 and 220 kV sectioned line arresters. Note that energy source power demand is calculated as 450 W according to 90% output efficiency. Mature batteries are lead-acid batteries and lithium batteries, among which lithium batteries perform advantages of large capacity, small size, and small weight.

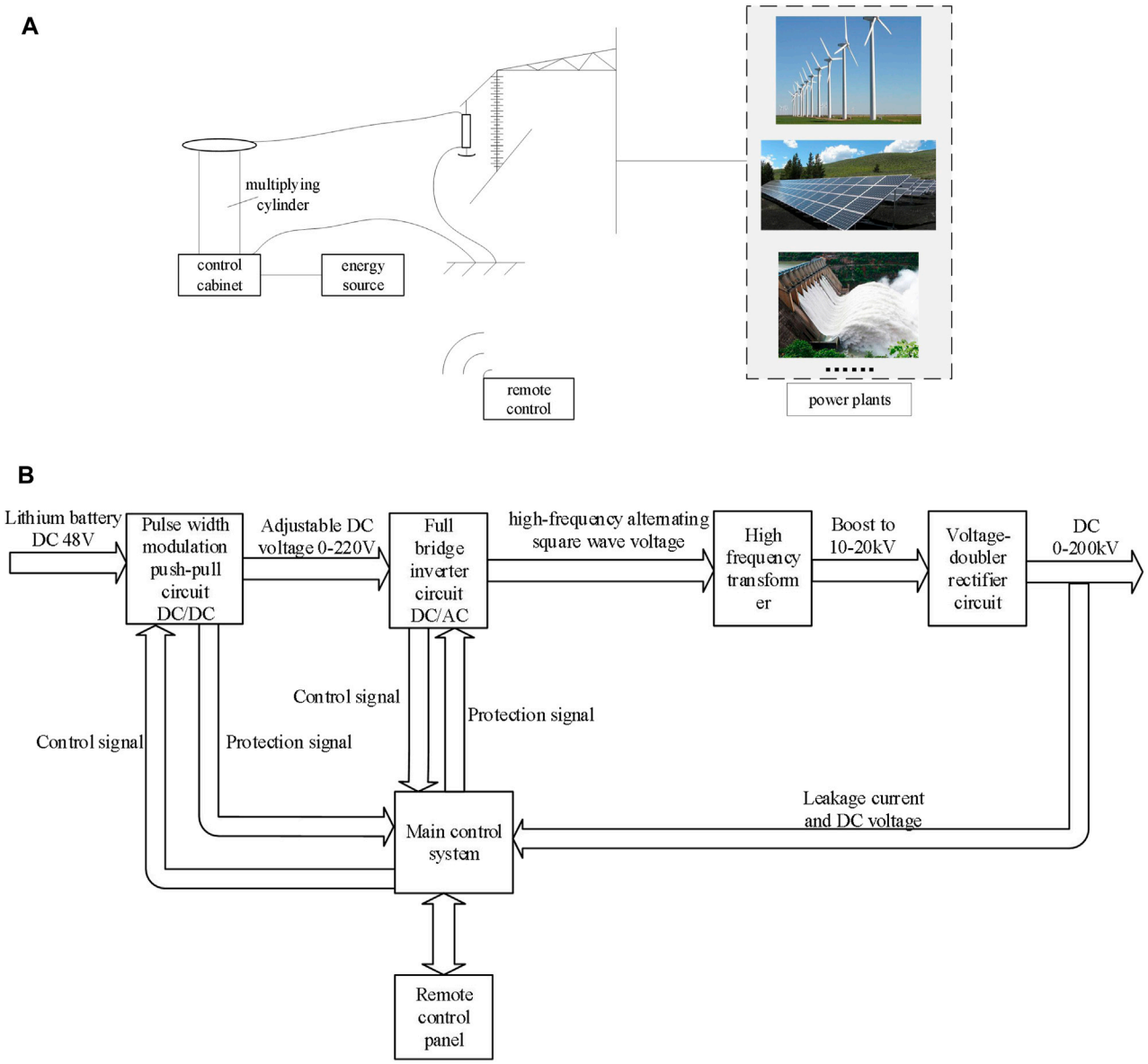


FIGURE 1 | Composition of DC test system. **(A)** Overall system framework; **(B)** Design block diagram of DC test system.

Therefore, 48 V/20 Ah lithium batteries are selected. Meanwhile, the test time of a single arrester generally does not exceed 5 min. A selected lithium battery discharging at 0.5°C can ensure the continuous operation of equipment for 2 h and satisfies continuous test of 24 line arresters.

In addition, the design block diagram of the DC test system is shown in **Figure 1B**. First, 48 V DC voltage of lithium battery pack is transformed to about 220 V continuously adjustable DC voltage (Xue et al., 2020) through pulse width modulation (PWM) push-pull circuit (Shi et al., 2016) and full bridge rectifier circuit in the control cabinet. And then, full bridge inverter circuit inverts DC voltage into a high-frequency alternating square wave voltage of 50–80 kHz (Jing et al., 2018; Zhang et al., 2021). Lastly, the voltage after initial boost is transferred to DC voltage with an amplitude of 200 kV through a voltage doubler rectifier circuit.

SYSTEM DESIGN OF POWER DRIVER AND CONTROL CIRCUIT

Design of Power Driver and Control Circuit

Generally, the voltage-doubler rectifier mode of DC high-voltage generator adopts AC power supply, such as AC 220 or AC 380 V, and bus voltage is often rectified to DC 300 or DC 600 V. In this work, a lithium battery with 48 V DC voltage is adopted as the energy source to reduce its weight. If the voltage cannot be boosted to the rated voltage under the rated current

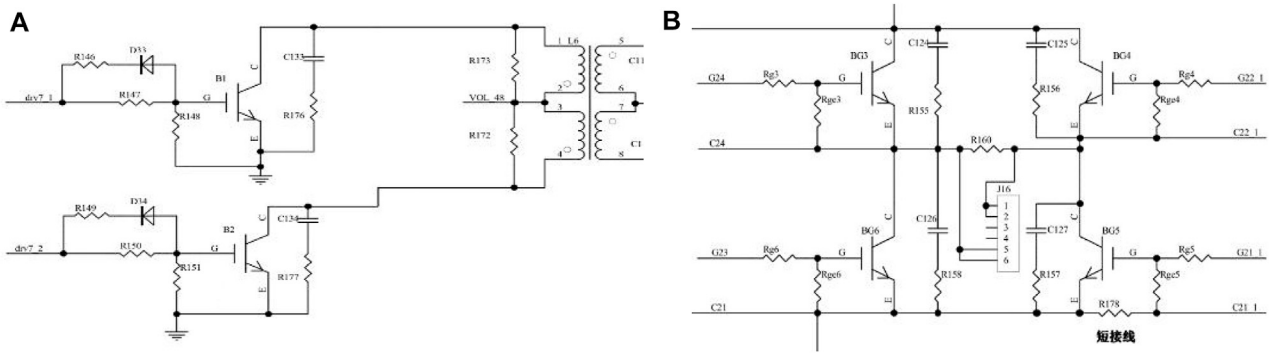


FIGURE 2 | Circuit structure diagram. **(A)** Pulse width modulation push-pull circuit; **(B)** Full bridge inverter circuit.

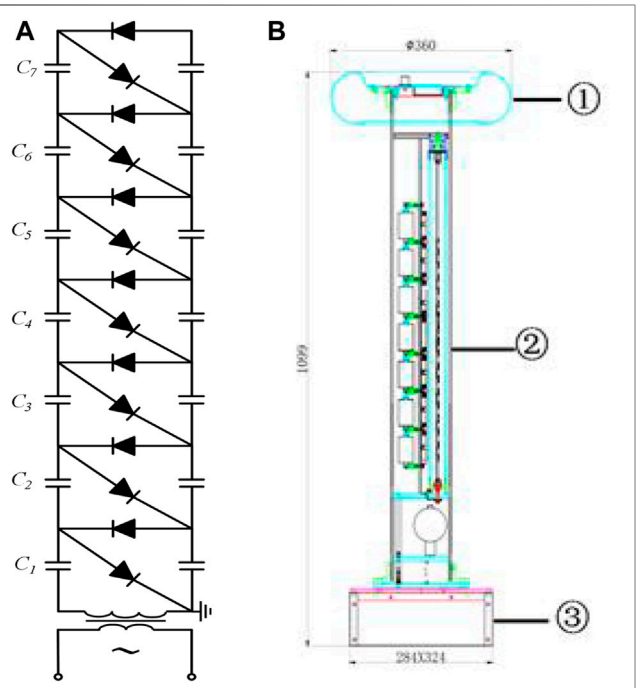


FIGURE 3 | Voltage-doubler rectifier circuit. **(A)** Schematic diagram; **(B)** Design drawing.

via the original mode, the power driver and control circuit shall be redesigned. Considering the power limitation of lithium batteries, internal devices and software design with low power consumption shall be selected. Besides, the internal auxiliary energy source should not only achieve fast boosting speed but also ensure the stability and reliability of output voltage.

The power driver and control circuit of this test system consists of a pulse width modulation push-pull circuit and a full bridge rectifier circuit. Particularly, two power transistors or electronic tubes with the same parameters are adopted in the push-pull circuit to implement amplification in positive and negative half cycle waveforms, respectively. Meanwhile, only one of the two symmetrical power switches is turned on during working time, which effectively contributes to small conduction loss and high transformation efficiency. In addition, the pulse width modulator generates PWM waves to control the on-off state of transistors and adjust voltage and power by regulating the duty cycle of PWM waves.

The pulse width modulation push-pull circuit designed of the test system is shown in **Figure 2A**, where the output voltage of the transformer can be output in a push-pull manner by alternately turning on B 1 and B 2. Furthermore, the later stage is rectified by the full bridge to obtain a relatively smooth DC voltage, which is supplied to the full-bridge inverter. Otherwise, the driving part of the push-pull circuit adopts a chip SG1525, which has a double-ended output pulse width modulator that includes two independent output circuits with opposite phases. Besides, the main control chip of the control circuit adopts MSP430 series 16-bit mixed-signal processor with ultra-low power.

The full-bridge inverter circuit is shown in **Figure 2B**, which is designed to reverse the DC voltage into a high-frequency AC square wave voltage. In particular, when BG 3 and BG 5 are turned on at the same time, BG 4 and BG 6 are turned off. On the contrary, if BG4 and BG 6 are turned on at the same time, BG 3 and BG 5 are turned off.

Design of Voltage-Doubler Rectifier Circuit

For the system design, a typical C-W voltage-doubler rectifier circuit is adopted. As illustrated in **Figure 3A**, the high-frequency AC square wave signal can reach up to 18 kV after passing through the high-frequency transformer, while the maximum output voltage amplitude is 200 kV and the magnification should not be less than 11.11 times. Practically, the output voltage will be reduced after loading. Therefore, the number of voltage doubler stages is finally determined to be seven levels. Besides, multiplying cylinder realizes a compact design via decreasing its size and optimizing the layout of main components, exhibited in **Figure 3B**.

Design of Remote Control Module

Because the majority of towers with line arresters are located in mountainous areas and the test areas under towers are



FIGURE 4 | Compressed loop after assembly.



FIGURE 5 | Laboratory wiring diagram.

seriously narrow, the remote control method is adopted to control the start, stop, and lifting of DC high-voltage generator to ensure the safety of test personnel (Tavakoli and Nafar, 2020). In addition, an infrared measuring circuit is arranged on the top of the multiplying cylinder while the main control chip MSP430 is used to measure the voltage and current signals at the high-voltage end. Furthermore, collected voltage and current signals are converted into infrared signals through protocol coding for transmission. An infrared receiving circuit in the control box is adopted to process the high-voltage end signal. Then, the control box exchanges the high-voltage end signal and other control signals with Bluetooth control box through Bluetooth communication. Note that the main control chip of Bluetooth remote control box adopts STM32f030 with ARM Cortex-M0 core to amplify signal through the front-end RF amplifier. Moreover, the reception and emission of wireless signals can be achieved by the way of controlling the remote equipment *via* a chip nRF24L01.

The main interface of the remote control module is employed to display the output voltage, current, current flowing through MOA of DC high-voltage generator, and the voltage of the lithium battery pack and test results in real time. Note that the on-off control of equipment as well as manual and automatic voltage rise and fall operations can also be achieved on the main interface.

PORTABLE DC TEST SYSTEM AND TEST

The entire DC test system adopts a split design to facilitate transportation, which is divided into five parts i.e., multiplying cylinder, grade ring, control cabinet, energy source, and pressurized wire. Note that multiplying cylinder, grade ring, and control cabinet need to be assembled on site. It is worth noting that the assembled equipment is shown in **Figure 4**.

Furthermore, the total weight of this device is strongly reduced by optimizing voltage-doubler rectifier circuit and energy source, which is also convenient for transportation. **Table 1** depicts the comparison of the weight of each component with traditional high-voltage DC generator. It is easy to see the weight of control cabinet, multiplying cylinder, and energy source part is reduced by 60, 54.55, and 33.33%, respectively, compared with traditional devices with the same parameters. The overall weight of the device is decreased by 36.7% even adding the remote control module.

In addition, the high-voltage voltage and current calibration data are measured in a laboratory to verify the test performance of the device. Consequently, the calibration results are revealed in **Table 2** and **Table 3**, where the high-voltage voltage test accuracy and the high-voltage current test accuracy are less than 0.5 and 1%, respectively. From **Table 4**, it can be seen that under 5 tests, all the indices can be maintained at a relatively stable value, which further verifies its stability and accuracy during voltage tests.

The DC reference voltage test of the arrester (i.e., YH10W-108/281 arrester) is carried out in the laboratory, while the test wiring diagram is shown in **Figure 5**. Moreover, the arrester is tested with DC reference voltage under 1 and 2 mA, respectively, whose test results are presented in **Table 4**.

TABLE 1 | Comparison of the weight of high-voltage DC generator.

Component	This system (kg)	Conventional system (kg)	Variety
Multiplying cylinder	8	12	−4 kg
Grade ring	2	2	0
Control cabinet	2	5	−3 kg
Energy source	5	11	−6 kg
Remote control panel	2	0	+2 kg
Total weight	19	30	−36.7%

TABLE 2 | High-voltage voltage calibration data.

Experiment	20 kV	40 kV	80 kV	160 kV	200 kV
Standard resistance voltage divider (kV)	20.1	39.8	80.4	160.3	200.7
Displayed voltage (kV)	20.0	39.7	80.1	159.8	200.1
Precision (%)	0.5%	0.25%	0.37%	0.3%	0.3%

TABLE 3 | High-voltage current calibration data.

Experiment	10 μA	200 μA	500 μA	1000 μA	2000 μA
Standard high-voltage microammeter (μA)	10.1	203	504	1,003	2007
Displayed current (μA)	10	202	502	999	2003
Precision (%)	1%	0.5%	0.4%	0.4%	0.2%

TABLE 4 | Test results of the arrester.

Number of tests	1	2	3	4	5
DC reference voltage U_{1mA} (kV)	164.8	164.5	164.7	164.9	164.8
Leakage current at $0.75U_{1mA}$ (kV)	22	23	21	21	23
DC reference voltage U_{2mA} (kV)	174.0	174.2	174.1	174.0	174.3
Leakage current at $0.75U_{2mA}$ (kV)	15	14	15	14	16

CONCLUSION

In this article, a DC test system for transmission line arrester is developed, which owns the following novelty/contributions compared with conventional DC high-voltage generator:

1) The portability of the device is considerably improved. Compared with traditional devices with the same parameters, the total weight of this device is decreased by 36.7%. In particular, the weights of control cabinet, multiplying cylinder, and energy source are reduced by 60, 54.55, and 33.33%, respectively;
2) This device is more suitable for on-site tests. The system is powered by lithium battery instead of 220/380 V AC energy source, and adopts multiplying cylinder and control cabinet that can be transported separately, which realize integrated assembly on-site and facilitate line arrester test in the testing field;
3) The proposed device owns high safety during tests.The system accomplishes wireless transmission and control of the equipment through the control of infrared measurement circuit and Bluetooth remote control module, which ensures the personal safety of testers during the tests under the tower.

In future studies, great focus will still be put on the optimization of overall weight and portability of the device *via* more advanced design. Also, with the proper application of 5G technology, the speed of wireless transmission could be considerably improved to help engineers more quickly collect and convey device information.

DATA AVAILABILITY STATEMENT

The original contributions presented in the study are included in the article/Supplementary Material, further inquiries can be directed to the corresponding author.

AUTHOR CONTRIBUTIONS

YF: Conceptualization, Writing- Reviewing and Editing. KL: Writing- Original draft preparation, Investigation. MG: Writing- Reviewing and Editing. YL: Supervision. XL: Supervision. JZ: Conceptualization, Resources.

REFERENCES

Aberoumand, S., Ghamari, S., and Shabani, B. (2018). Energy and Exergy Analysis of a Photovoltaic thermal (PV/T) System Using Nanofluids: An Experimental Study. *Solar Energy* 165, 167–177. doi:10.1016/j.solener.2018.03.028

Alberto, D. C., Fernando, H., and Silveira, S. V. (2014). On the Role of Transformer Grounding and Surge Arresters on Protecting Loads from Lightning-Induced Voltages in Complex Distribution Networks. *Electric Power Syst. Res.* 113, 204–212. doi:10.1016/j.epsr.2014.02.035

Božidar, F., Ivo, U., and Ivica, P. (2016). Application of Line Surge Arresters for Voltage Uprating and Compacting of Overhead Transmission Lines. *Electric Power Syst. Res.* 140, 830–835. doi:10.1016/j.epsr.2016.04.023

Christodoulou, C. A., Ekonomou, L., Mitropoulou, A. D., Vita, V., and Stathopulos, I. A. (2010). Surge Arresters' Circuit Models Review and Their Application to a Hellenic 150kV Transmission Line. *Simulation Model. Pract. Theor.* 18 (6), 836–849. doi:10.1016/j.simpat.2010.01.019

Guchhait, P. K., and Banerjee, A. (2020). Stability Enhancement of Wind Energy Integrated Hybrid System with the Help of Static Synchronous Compensator and Symbiosis Organisms Search Algorithm. *Prot. Control. Mod. Power Syst.* 5 (2), 43–55. doi:10.1186/s41601-020-00158-8

Hemapala, K. T. M. U., Gnana Swathika, O. V., and Dharmadasa, K. P. R. D. S. K. (2018). Techno-economic Feasibility of Lighting protection of Overhead Transmission Line with Multi-Chamber Insulator Arrestors. *Develop. Eng.* 3, 100–116. doi:10.1016/j.deveng.2018.05.003

Hoang, T. T., Cho, M. Y., Alam, M. N., and Vu, Q. T. (2017). A Novel Differential Particle Swarm Optimization for Parameter Selection of Support Vector Machines for Monitoring Metal-Oxide Surge Arrester Conditions. *Swarm Evol. Comput.* 38, 120–126. doi:10.1016/j.swevo.2017.07.006

Hori, K., Kim, J., Kawase, R., Kimura, M., Matsui, T., and Machimura, T. (2020). Local Energy System Design Support Using a Renewable Energy Mix Multi-Objective Optimization Model and a Co-Creative Optimization Process. *Renew. Energ.* 156, 1278–1291. doi:10.1016/j.renene.2019.11.089

Jing, L., Yong, L., Wang, W. Y., Cao, Y. J., Lee, K. Y., and Fang, L. (2018). Fault-Ride through Control Strategy of Multi-Terminal High Voltage DC Systems. *IFAC-PapersOnLine* 51 (28), 540–545. doi:10.1016/j.ifacol.2018.11.759

Lei, Y., Wang, D., Jia, H., Chen, J., Li, J., Song, Y., et al. (2020). Multi-Objective Stochastic Expansion Planning Based on Multi-Dimensional Correlation Scenario Generation Method for Regional Integrated Energy System Integrated Renewable Energy. *Appl. Energ.* 276, 115395. doi:10.1016/j.apenergy.2020.115395

Liu, Z., Gao, H., Luo, S., Luo, S. B., Zhao, L., and Feng, Y. Y. (2020). A Fast Boundary protection for an AC Transmission Line Connected to an LCC-HVDC Inverter Station. *Prot. Control. Mod. Power Syst.* 5 (4), 25–38. doi:10.1186/s41601-020-00175-7

Malcolm, N., and Aggarwal, R. K. (2015). The Impact of Multiple Lightning Strokes on the Energy Absorbed by MOV Surge Arresters in Wind Farms during Direct Lightning Strikes. *Renew. Energ.* 83, 1305–1314. doi:10.1016/j.renene.2015.05.010

Marcel, A., Rogério, A., Ruy, A. C., Oureste, E. B., and Lucas, A. M. (2015). Practical Methodology for Modeling and Simulation of a Lightning protection System Using Metal-Oxide Surge Arresters for Distribution Lines. *Electric Power Syst. Res.* 118, 47–54. doi:10.1016/j.epsr.2014.07.017

Muniappan, M. (2021). A Comprehensive Review of DC Fault protection Methods in HVDC Transmission Systems. *Prot. Control. Mod. Power Syst.* 6, 1–20. doi:10.1186/s41601-020-00173-9

Petar, S., Josip, V., and Ranko, G. (2013). Monte Carlo Analysis of Wind Farm Surge Arresters Risk of Failure Due to Lightning Surges. *Renew. Energ.* 57, 626–634. doi:10.1016/j.renene.2013.03.004

Sandrode, C. A., Wallacedo, C. B., José, S. P., and Rubens, L. M. (2017). Lightning Performance of Transmission Line with and without Surge Arresters: Comparison between a Monte Carlo Method and Field Experience. *Electric Power Syst. Res.* 149, 169–177. doi:10.1016/j.epsr.2017.04.012

Seyyedbarzegar, S. M., and Mirzaie, M. (2015). Application of Finite Element Method for Electro-Thermal Modeling of Metal Oxide Surge Arrester. *Comput. Appl. Eng. Educ.* 23 (6), 910–920. doi:10.1002/cae.21663

Shi, L.-F., Shi, Z.-B., Chen, S., and Xun, J.-H. (2016). Output Voltage Sampling Circuit for Discontinuous Conduction Mode Flyback Pulse-Width Modulation Controller. *J. Circuit Syst. Comp.* 25 (11), 1650140. doi:10.1142/s0218126616501401

Silverio, V., Fernando, H., Silveira, B. P., and Rafael, M. (2020). Constraints on the Use of Surge Arresters for Improving the Back Flashover Rate of Transmission Lines. *Electric Power Syst. Res.* 180, 106064. doi:10.1016/j.epsr.2019.106064

Tahir, M. F., Haoyong, C., and Guangze, H. (2021). A Comprehensive Review of 4E Analysis of thermal Power Plants, Intermittent Renewable Energy and Integrated Energy Systems. *Energ. Rep.* 7, 3517–3534. doi:10.1016/j.egyr.2021.06.006

Tavakoli, M., and Nafar, M. (2020). Human Reliability Analysis in Maintenance Team of Power Transmission System protection. *Prot. Control. Mod. Power Syst.* 5 (1), 1–13. doi:10.1186/s41601-020-00176-6

Vita, V., and Christodoulou, C. A. (2016). Comparison of ANN and Finite Element Analysis Simulation Software for the Calculation of the Electric Field Around Metal Oxide Surge Arresters. *Electric Power Syst. Res.* 133, 87–92. doi:10.1016/j.epsr.2015.11.041

Xue, A., Yue, L., Zhang, J., Cui, J., Li, Z., Li, Y., et al. (2020). A New Quantitative Analysis Method for Overvoltage in Sending End Electric Power System with UHVDC. *IEEE Access* 8, 145898–145908. doi:10.1109/access.2020.3015267

Zhang, B., Hu, W., Li, J., Cao, D., Huang, R., Huang, Q., et al. (2020). Dynamic Energy Conversion and Management Strategy for an Integrated Electricity and Natural Gas System with Renewable Energy: Deep Reinforcement Learning Approach. *Energ. Convers. Manage.* 220, 113063. doi:10.1016/j.enconman.2020.113063

Zhang, Y., Wang, S., Liu, T., Zhang, S., and Lu, Q. (2021). A Traveling-Wave-Based protection Scheme for the Bipolar Voltage Source Converter Based High Voltage Direct Current (VSC-HVDC) Transmission Lines in Renewable Energy Integration. *Energy* 216, 119312. doi:10.1016/j.energy.2020.119312

Zhu, M., Xu, C., Dong, S., Tang, K., and Gu, C. (2021). An Integrated Multi-Energy Flow Calculation Method for Electricity-Gas-Thermal Integrated Energy Systems. *Prot. Control. Mod. Power Syst.* 6 (1), 65–74. doi:10.1186/s41601-021-00182-2

Conflict of Interest: YF, KL, and MG are employed by Yunnan Power Grid Co. Ltd. YL is employed by Guangdong Power Grid Co. Ltd. XL is employed by Suzhou Industrial Park Haiwo Science and Technology Co. Ltd.

The remaining author declares that the research was conducted in the absence of any commercial or financial relationships that could be construed as a potential conflict of interest.

Publisher's Note: All claims expressed in this article are solely those of the authors and do not necessarily represent those of their affiliated organizations, or those of the publisher, the editors and the reviewers. Any product that may be evaluated in this article, or claim that may be made by its manufacturer, is not guaranteed or endorsed by the publisher.

Copyright © 2021 Feng, Li, Gao, Liu, Li and Zhu. This is an open-access article distributed under the terms of the Creative Commons Attribution License (CC BY). The use, distribution or reproduction in other forums is permitted, provided the original author(s) and the copyright owner(s) are credited and that the original publication in this journal is cited, in accordance with accepted academic practice. No use, distribution or reproduction is permitted which does not comply with these terms.

frontiers in Energy Research

ORIGINAL RESEARCH
published: 02 November 2021
doi: 10.3389/fenrg.2021.751884

Feedback Linearization Control Design for Battery/SMES Hybrid Energy Storage Systems Used in Distribution Network

Chengye Tang and Yonghong Huang*

School of Electrical and Information Engineering, Jiangsu University, Zhenjiang, China

A battery/superconducting magnetic energy storage (SMES) hybrid energy storage system (BSM-HESS) is designed for a power system. Meanwhile, a nonlinear feedback control (FLC) is adopted to achieve smooth and fast-tracking performance, and a rule-based strategy (RBS) is applied for power demand allocation. FLC can effectively compensate for the system's nonlinearity to obtain the global consistent control performance; thus, it can properly solve the nonlinearity and modeling uncertainty of BSM-HESS. The effectiveness and advantages of FLC are evaluated *via* three cases, namely, heavy load condition, light load condition, and robustness with uncertain BSM-HESS parameters. Simulation results show that compared with proportional–integral–derivative (PID) control, FLC can achieve the best dynamic performance under various working conditions, which is beneficial for the system to quickly restore stable operation after large disturbance. In addition, the control cost of FLC is lower than that of PID control under both heavy load and light load conditions.

Keywords: battery/SMES hybrid energy storage system, distribution network, feedback linearization control, rule-based strategy, parameter uncertainties

OPEN ACCESS

Edited by:
Bo Yang,
Kunming University of Science and Technology, China

Reviewed by:
Yang Li,
Northeast Electric Power University, China
Jiawei Zhu,
Chang'an University, China

****Correspondence:***
Chengye Tang
chengyetang@outlook.com

Specialty section:
This article was submitted to Smart Grids, a section of the journal Frontiers in Energy Research

Received: *02 August 2021*
Accepted: *13 September 2021*
Published: *02 November 2021*

Citation:
Tang C and Huang Y (2021) Feedback Linearization Control Design for Battery/SMES Hybrid Energy Storage Systems Used in Distribution Network. Front. Energy Res. 9:751884. doi: 10.3389/fenrg.2021.751884

INTRODUCTION

In recent years, withlarge-scale and widespread integration of renewable energy into the power system, energy storage systems (ESSs) have become a hot research topic (Yang et al., 2015; Zhang et al., 2016; Bakeer et al., 2021). The energy storage system used in the power system refers to the device that can store a certain amount of electric energy and can quickly convey or absorb active and reactive power when abnormal events occur to the power system (Xi et al., 2016; ASV et al., 2020). In a transmission system, energy storage equipment is mostly installed on the transmission side of the line to improve the stability of system and rapid response speed (Zhang et al., 2015; Bakeer et al., 2021). In the distribution system, the energy storage device is usually equipped on the load side to protect the important load and balance frequency fluctuation (Nayak et al., 2021).

Electric energy storage has many forms that can mainly be divided into two types: energy storage and power storage (Chaibi et al., 2019; Li et al., 2019). Energy storage represented by leadacid battery, lithium battery, and sodiumsulfur battery has high energy density and long energy storage time but the low power density and short cycle life (Luo et al., 2015; Ruan et al., 2019). Power-type energy storage represented by a super capacitor, flywheel energy storage, and superconducting magnetic energy storage (SMES) has the advantages of high power density, fast response speed, and long cycle life but with deficiencies of low energy density and high self-discharge rate (Adhikari and Li, 2014; Akyurek and Rosing, 2016; Zhang et al., 2021).

It is difficult for a single energy storage technology to have all the aforementioned advantages at the same time to meet the requirements of different application modes (Lalouni et al., 2009; Khalid and Savkin, 2010; Worthmann et al., 2015). However, based on technical complementarity of volumetric energy storage and power-type energy storage, hybrid energy storage can be used to meet the technical requirements of various levels. At present, battery/SMES hybrid energy storage systems (BSM-HESSs) that can effectively improve the stability and reliability of the system have received worldwide research interests (Dali et al., 2010; Malysz et al., 2014; Melo et al., 2019). As the core of the control system, the design of the control strategy plays the most critical role that has both important theoretical and practical significance.

BSM-HESS can effectively improve system stability, the performance of which is closely related to the selected control mode (Bazargan et al., 2018; Serir et al., 2016; Teymour et al., 2014). At present, research on control schemes is mostly focused on proportional–integral–derivative (PID) control (Brenna et al., 2016). However, this method needs to establish an accurate mathematical system model and often focuses on the design of a certain operation point. When the operation point of system changes, the performance will be dramatically affected, and the robustness is poor (Hussain et al., 2017). In order to remedy the existing deficiencies, a large number of academic advanced nonlinear control theories are developed. Magdy et al. (2018) have proposed a coordination of load frequency control (LFC) and SMES technology using a new optimal PID controller–based moth swarm algorithm in the Egyptian power system while considering high wind power penetration. Besides, a new adaptive control strategy based on the particle swarm optimization algorithm is proposed for the optimization of control strategy for a hybrid electric vehicle energy storage system (Ye et al., 2020). Meanwhile, Lin and Lei (2017) have developed a hierarchical control strategy for a hybrid energy storage system. However, the aforementioned studies all have the characteristics of a complex structure, low implementation feasibility, and weak adaptability; thus, their control design needs to be further improved.

Over the last decade, research on the feedback linearization–based nonlinear control theory has achieved great progress, which can successfully transform nonlinear systems into linear systems through state feedback in coordinate transformation domain. Direct feedback linearization is a representative feedback linearization method based on input and output descriptions of the system, which has been utilized to solve many control problems of nonlinear systems. Therefore, a feedback linearization control (FLC) for BSM-HESS is proposed in this article, to realize an efficient and smooth tracking.

The remaining of this article is organized as follows: *Battery/SMES Hybrid Energy Storage Systems Modeling* introduces the BSM-HESS model. In *FLC Design for BSM-HESS*, FLC design is described. Case studies are carried out in *Case Studies section*, along with simulation results analysis. At last, *Conclusion* summarizes the main contributions of the study.

BATTERY/SMES HYBRID ENERGY STORAGE SYSTEMS MODELING

Distributed generation (DG) owns the merits of easy installation, pollution-free, and low costs. As a backup power source of the power system (Huang et al., 2021; Sai et al., 2021), it can ensure the stability and reliability of user's electricity consumption. Although distributed energy has many advantages, there are still many shortcomings; for instance, the control mode of DG is very complex, and the access cost is high (Bizon, 2018; Shi et al., 2018). In addition, since DG is an uncontrollable source, it is imperative to solve the limitations and isolation problems of DG to reduce the influence of DG on large power grid (Murty and Kumar, 2021). In general, DG is a micro-generation unit that can realize energy conversion and independent control. Compared to a distribution network, DG can be regarded as a controlled unit, such that the difficulty of configuring the capacity of DG can be greatly reduced. Microgrids are vulnerable to internal distributed power supply and load fluctuations due to capacity and scale limitations, and ESS provides solutions for these problems. At present, it is difficult for a single energy storage device to simultaneously achieve multiple functions such as power quality improvement and microgrid stability control, so different energy storage devices need to be coupled together for use (Ali et al., 2010; Kasilingam and Pasupuleti, 2015; Olujobi, 2020).

The combination of battery and SMES takes both the instantaneous power supply advantages of SMES and the long-term power supply capacity of battery into account, which specifies the excellent power supply characteristic of BSM-HESS. Besides, BSM-HESS has another advantage compatible with both, such as high energy density and high power density, which surpasses the effect of either (Jae Woong Shim et al., 2013; Kouchachvili et al., 2018). The charging and discharging models of key components of BSM-HESS, that is, battery and SMES, are presented in **Figure 1**.

BSM-HESS generally includes SMES and battery that supply to the common load through a bidirectional buckboost converter with the same structure (Song et al., 2017), respectively. More specifically, the load is typically modeled as motors with an inverter that is equivalent to variable resistance in this model (Montoya et al., 2018). The configuration of BSM-HESS adopted in this study is shown in **Figure 2**. The mathematical equation corresponding to the configuration of BSM-HESS can be described as follows [(Sai et al., 2021), 42]:

$$\begin{bmatrix} \dot{v}_1 \\ \dot{v}_2 \\ \dot{i}_1 \\ \dot{i}_2 \\ \dot{v}_o \end{bmatrix} = \begin{bmatrix} -\frac{v_1}{R_e C_1} - \frac{i_1}{C_1} + \frac{E}{R_e C_1} \\ \frac{I_{sc} - i_2}{C_2} \\ \frac{v_1 - v_o}{L_1} - \left(\frac{R_{L1} + R_{\text{on2}}}{L_1}\right) i_1 \\ \frac{v_2}{L_2} + \left(\frac{R_{\text{on4}} - R_{\text{on3}}}{L_2} D_2 - \frac{R_{L2} + R_{\text{on4}}}{L_2}\right) i_2 + (D_2 - 1)\frac{v_o}{L_2} \\ (1 - D_1)\frac{i_1}{C_o} - \frac{v_o}{RC_o} + \frac{i_2}{C_o} \end{bmatrix} + \begin{bmatrix} 0 & 0 \\ 0 & 0 \\ \frac{R_{\text{on2}} - R_{\text{on1}}}{L_1} i_1 + \frac{v_o}{L_1} & 0 \\ 0 & 0 \\ 0 & -\frac{i_2}{C_o} \end{bmatrix} \begin{bmatrix} D_1 \\ D_2 \end{bmatrix}, \quad (1)$$

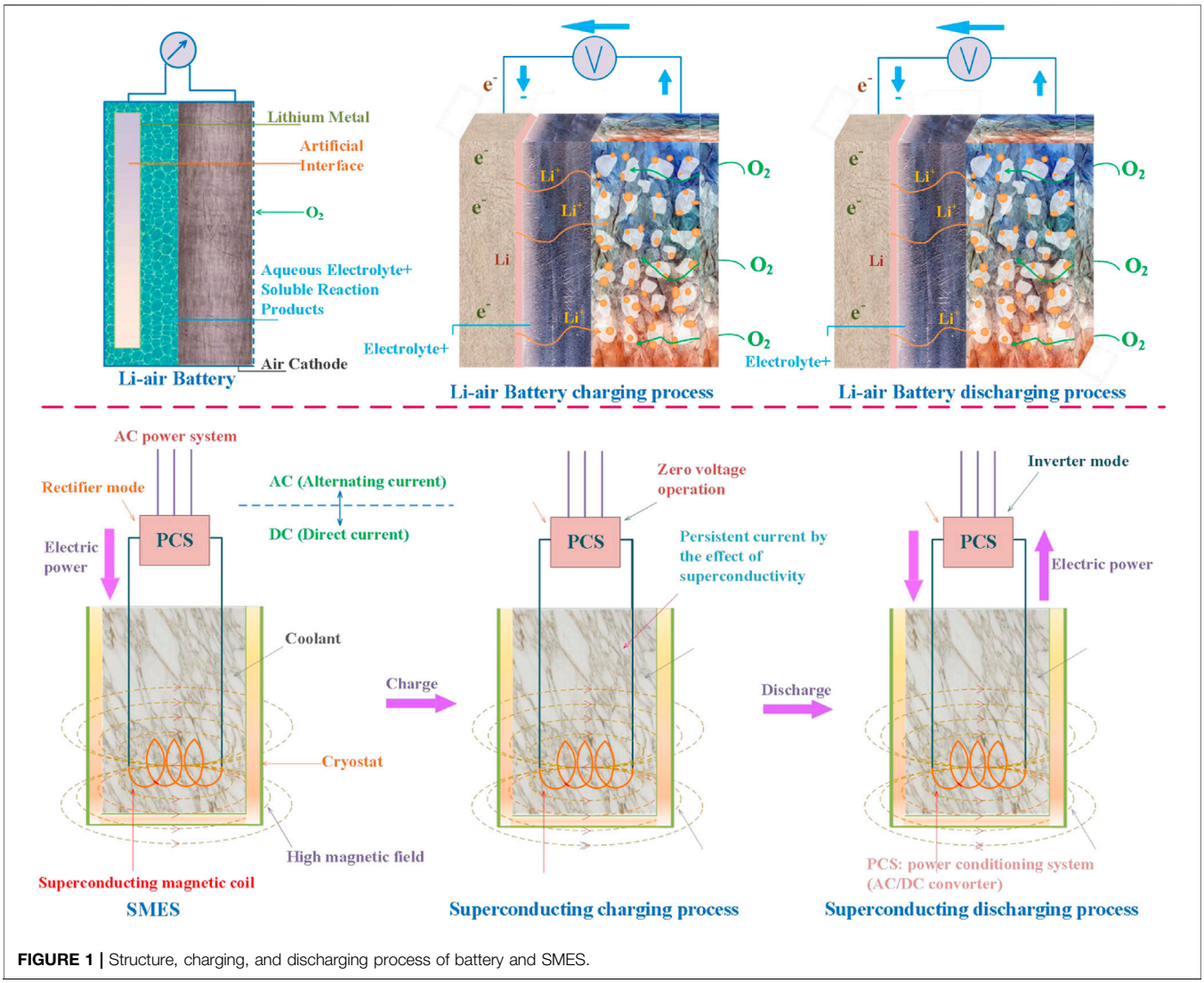


FIGURE 1 | Structure, charging, and discharging process of battery and SMES.

where duty cycles D_1 and D_2 are restricted in a subset of **(0, 1)** for the purpose of ensuring operation safety and efficiency. The meanings of other symbols can be referred to Nomenclature.

FLC DESIGN FOR BSM-HESS

Rule-Based Strategy

The rule-based strategy (RBS), also called logical threshold control strategies, is widely used in engineering practice due to their simplicity and practicality. Heuristic rules or fuzzy logic rules are used to determine the control variable output according to preset conditions. It mainly includes state machine control, threshold control, and power tracking control to ensure the main components work in the most efficient area.

The load power P_{demand} is the prerequisite of the determination of a qualified EMS, where the power distribution between SMES and battery is optimized. The application constraints of BSM-HESS based on RBS are as follows:

(a) State of charge (SOC) of SMES:

$$\frac{i_{sc}}{i_{sc_\max}} \geq \frac{1}{2}, \tag{2}$$

where i_{sc} and $i_{\text{sc_max}}$ denote the current value and maximum allowable current value of the SMES, respectively. When the constraint is not satisfied, SMES will be charged by the battery with a constant power P_{ch}.

(b) SOC of battery:

$$0.2 \leq \frac{Q_c}{Q_I} \leq 0.9, \tag{3}$$

where Q_c and Q_I are the total charge of the battery and the remaining charge of the battery, respectively.

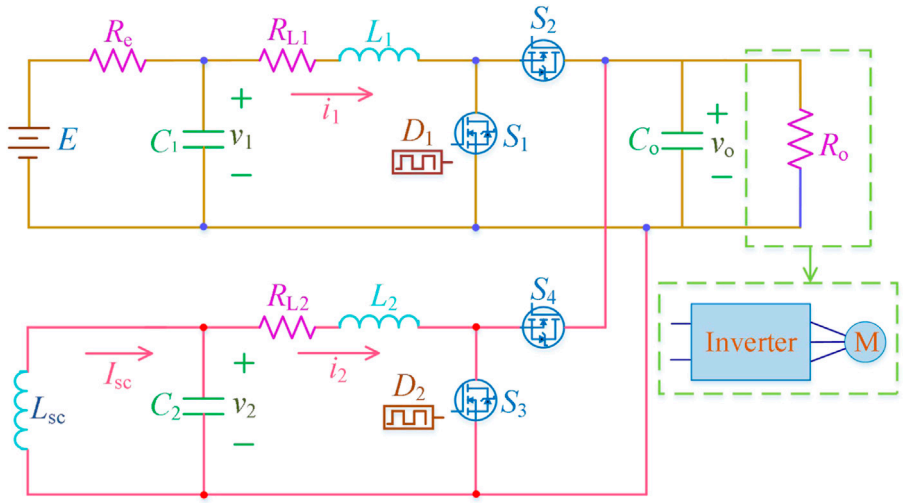


FIGURE 2 | Configuration and equivalent circuit of BSM-HESS.

(c) Constraints of P_{demand}:

When $P_{demand} \geq 0$ is satisfied, the constraints are as follows:

$$\begin{cases} P_{demand} = P_{demand}, P_{SMES} = 0 \, (P_{demand} \leq P_{min}) \\ P_{min} = P_{battery}, P_{SMES} = P_{demand} - P_{min} \, (P_{demand} > P_{min}) \end{cases}. \quad (4)$$

The power threshold P_{min} is set to ensure that once the power demand P_{demand} is lower than the threshold, SMES will not supply power to the load.

When $P_{demand} < 0$ is satisfied, the regenerative energy is absorbed by SMES before the battery is fully charged, and the charging cycle is shortened, thus prolonging the battery life.

Feedback Linearization Control Theory

Feedback linearization is a typical approach in the nonlinear control theory. The idea is to transform a nonlinear system dynamic into an equivalent (fully or partly) linear one through a change of state variables and a suitable nonlinear control input, so that linear control techniques can be then applied to the nonlinear system.

Here, a standard affine multiple-input multiple-output system is considered in a neighborhood around an operation point x_o of the form

$$\begin{cases} \dot{x} = f(x) + g(x)u \\ y = h(x), \end{cases} \quad (5)$$

where $x \in R^n$ is the state vector, $u \in R^m$ is the control input vector, $y \in R^m$ is the output vector, $f(x) \in R^n$, $g(x) \in R^{n \times m}$, and $h(x) \in R^m$ are smooth. The inputoutput linearization of a multiple input multiple output system is obtained *via* differentiating the output y_i of the system until the input u_j appears, assuming that r_i is the smallest integer such that at least one of the inputs explicitly appears in $y_i^{(r_i)}$

$$y_i^{(r_i)} = L_f^{r_i} h_i \sum_{j=1}^{m} L_{g_j} L_f^{r_i - 1} h_i u_j, \quad (6)$$

where $y_i^{(r_i)}$ denotes the ith-order derivative of y_i, if $L_{g_j} L_f^{r_i - 1} h_i(x) \neq 0$ for at least one j. For at least one y_i gives

$$\begin{bmatrix} y_1^{(r_1)} \\ \vdots \\ y_m^{(r_m)} \end{bmatrix} = \begin{bmatrix} L_f^{r_1} h_1 \\ \vdots \\ L_f^{r_m} h_m \end{bmatrix} + B(x) \begin{bmatrix} u_1 \\ \vdots \\ u_m \end{bmatrix}. \quad (7)$$

$$B(x) = \begin{bmatrix} L_{g_1} L_f^{r_1 - 1} h_1 & \cdots & L_{g_m} L_f^{r_1 - 1} h_1 \\ \vdots & \vdots & \vdots \\ L_{g_1} L_f^{r_m - 1} h_m & \cdots & L_{g_m} L_f^{r_m - 1} h_m \end{bmatrix}. \quad (8)$$

Here, $B(x)$ is the $n \times m$ control gain matrix, if $B(x)$ is invertible, the physical control law of the multiple input multiple output nonlinear system can be derived as follows:

$$\begin{aligned} (u) &= B(x)^{-1} \left\{ \begin{bmatrix} -L_f^{r_1} h_1 \\ \vdots \\ -L_f^{r_m} h_m \end{bmatrix} + \begin{bmatrix} v_1 \\ \vdots \\ v_m \end{bmatrix} \right\}, \\ (v_i) &= -\sum_{j=1}^{r_i - 1} \alpha_j y_i^{(j)} \end{aligned} \quad (9)$$

where v_i is the new input of the system and α_j is the linear control gain.

Underlying Controller Design

For BSM-HESS (1), the state vector can be defined as $x = (x_1, x_2, x_3, x_4, x_5)^T = (v_1, v_2, i_1, i_2, v_o)^T$, output $y = (y_1, y_2)^T = (i_1, v_o)^T$, control input $u = (u_1, u_2)^T = (D_1, D_2)^T$, and tracking error $e = [e_1, e_2]^T = [i_1 - i_1^*, v_o - v_o^*]^T$. Then, the tracking error e is differentiated until the control input u explicitly appeared as follows:

$$\begin{cases} \dot{e}_1 = \frac{v_1}{L_1} + \left(\frac{R_{on2} - R_{on1}}{L_1} D_1 - \frac{R_{L1} + R_{on2}}{L_1} \right) i_1 + (D_1 - 1) \frac{v_o}{L_1} - \dot{i}_1^* \\ \dot{e}_2 = (1 - D_1) \frac{i_1}{C_o} + (1 - D_2) \frac{i_2}{C_o} - \frac{v_o}{RC_o} - \dot{v}_o^* \end{cases}. \quad (10)$$

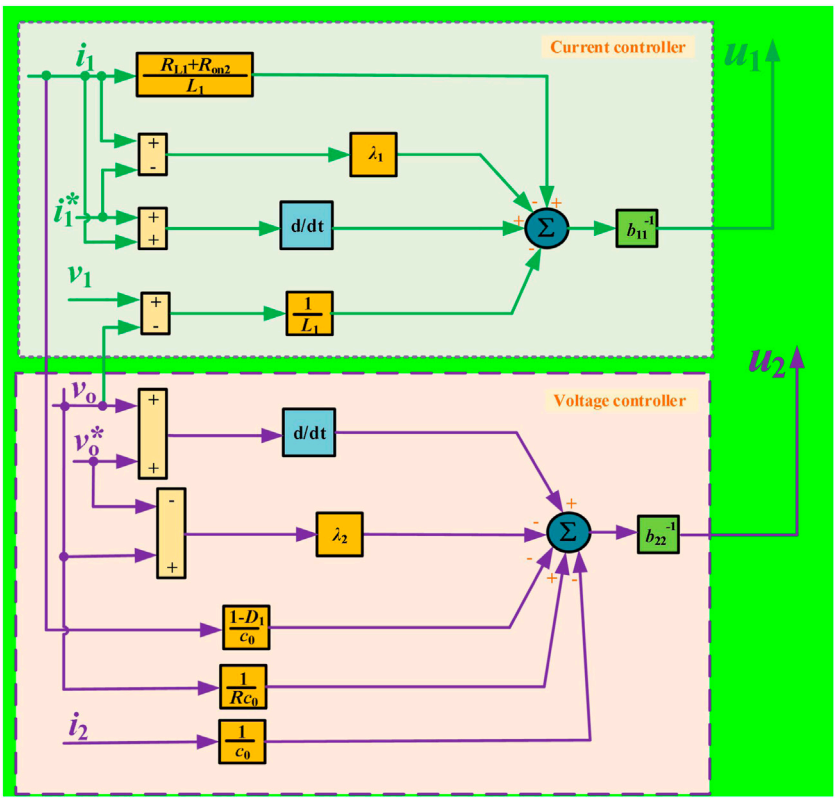


FIGURE 3 | Overall FLC structure for BSM-HESS.

TABLE 1 | BSM-HESS parameters.

Symbol	Parameters	Value	Unit
L_1	Battery side inductance	680	μH
R_e	Battery series resistance	0.04	Ω
R_{L1}	Battery side inductor series resistance	0.25	Ω
C_1	Battery side filter capacitance	1	mF
L_2	SMES side inductance	39	mH
R_{L2}	SMES side inductor series resistance	0.114	Ω
C_2	SMES side filter capacitance	0.22	mH
L_{sc}	Superconducting magnetic coil inductance	25	H
R_{on}	MOSFET on-resistance	0.021	Ω
C_0	Load side capacitance	1	mF

TABLE 2 | Controller parameters.

FLC	λ_1	120
	λ_2	150
PID control	K_{p1}	462
	K_{I1}	328
	K_{D1}	45
	K_{p2}	425
	K_{I2}	287
	K_{D2}	42

In addition, system 2) can be represented in the concise matrix form as follows:

$$\begin{bmatrix} \dot{y}_1 \\ \dot{y}_2 \end{bmatrix} = \begin{bmatrix} g_1(x) \\ g_2(x) \end{bmatrix} + B(x) \begin{bmatrix} u_1 \\ u_2 \end{bmatrix} - \begin{bmatrix} \dot{i}_1^* \\ \dot{v}_o^* \end{bmatrix}, \tag{11}$$

where

$$g_1(x) = \frac{v_1 - v_o}{L_1} - \left(\frac{R_{L1} + R_{on2}}{L_1} \right) i_1 \tag{12}$$

$$g_2(x) = (1 - D_1) \frac{i_1}{C_o} - \frac{v_o}{RC_o} + \frac{i_2}{C_o}, \tag{13}$$

with

$$B(x) = \begin{bmatrix} b_{11} & 0 \\ 0 & b_{22} \end{bmatrix} = \begin{bmatrix} \frac{R_{on2} - R_{on1}}{L_1} i_1 + \frac{v_o}{L_1} & 0 \\ 0 & -\frac{i_2}{C_o} \end{bmatrix}. \tag{14}$$

To ensure the aforementioned inputoutput linearization to be valid, the control gain matrix $B(x)$ must be nonsingular among the whole operation range, that is,

$$\det[B(x)] = -\frac{i_2 [(R_{on2} - R_{on1}) i_1 + v_o]}{C_0 L_1} \neq 0. \tag{15}$$

Since SMES current i_2 is always different from zero, for example, a value of zero means that SMES stops operating;

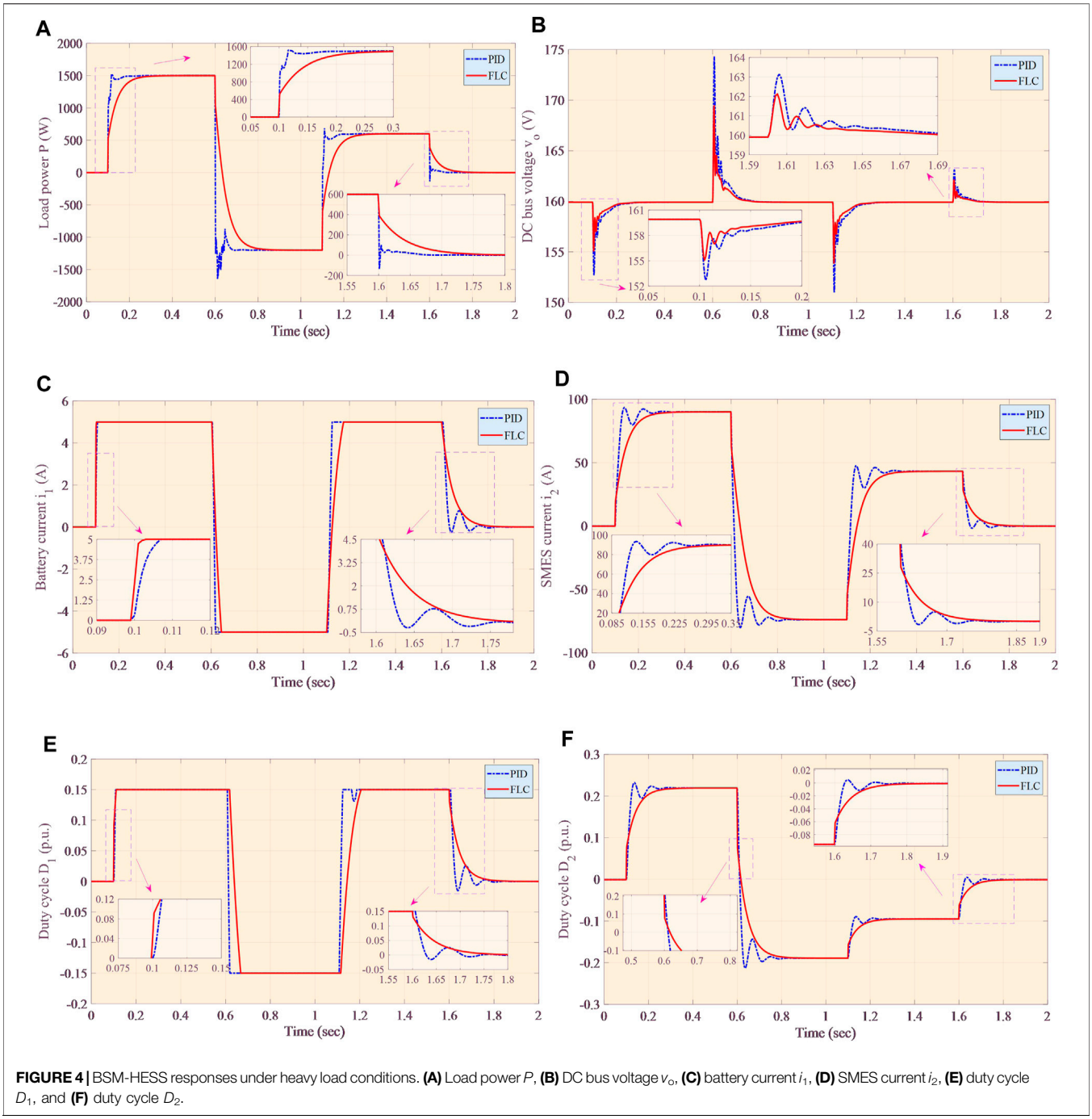


FIGURE 4 | BSM-HESS responses under heavy load conditions. **(A)** Load power P, **(B)** DC bus voltage v_o, **(C)** battery current i_1, **(D)** SMES current i_2, **(E)** duty cycle D_1, and **(F)** duty cycle D_2.

thus, the controllability of SMES is lost. Meanwhile, DC bus voltage $v_o \neq (R_{on1} - R_{on2})i_1$ is always valid among the whole operation range. Therefore, the aforementioned condition is always valid.

The final FLC strategy is designed as follows:

$$\begin{bmatrix} u_1 \\ u_2 \end{bmatrix} = B^{-1} \begin{bmatrix} \dot{y}_1 - \dfrac{v_1 - v_o}{L_1} + \left(\dfrac{R_{L1} + R_{on2}}{L_1}\right) i_1 + \dot{i}_1^* - \lambda_1 e_1 \\ \dot{y}_2 - (1 - D_1)\dfrac{i_1}{C_o} + \dfrac{v_o}{RC_o} - \dfrac{i_2}{C_o} + \dot{v}_o^* - \lambda_2 e_2 \end{bmatrix}, \quad (16)$$

where λ_1 and λ_2 are the control gains. In addition, the overall FLC structure of BSM-HESS is given in **Figure 3**.

CASE STUDIES

The parameters of BSM-HESS and controller are shown in **Table 1** and **Table 2**, respectively. The initial SOC of the battery is set to 90%, the minimum voltage of the battery is 36 V, the maximum voltage is 144 V, and battery pack contains 48 $LiFePO_4$ cells that are connected

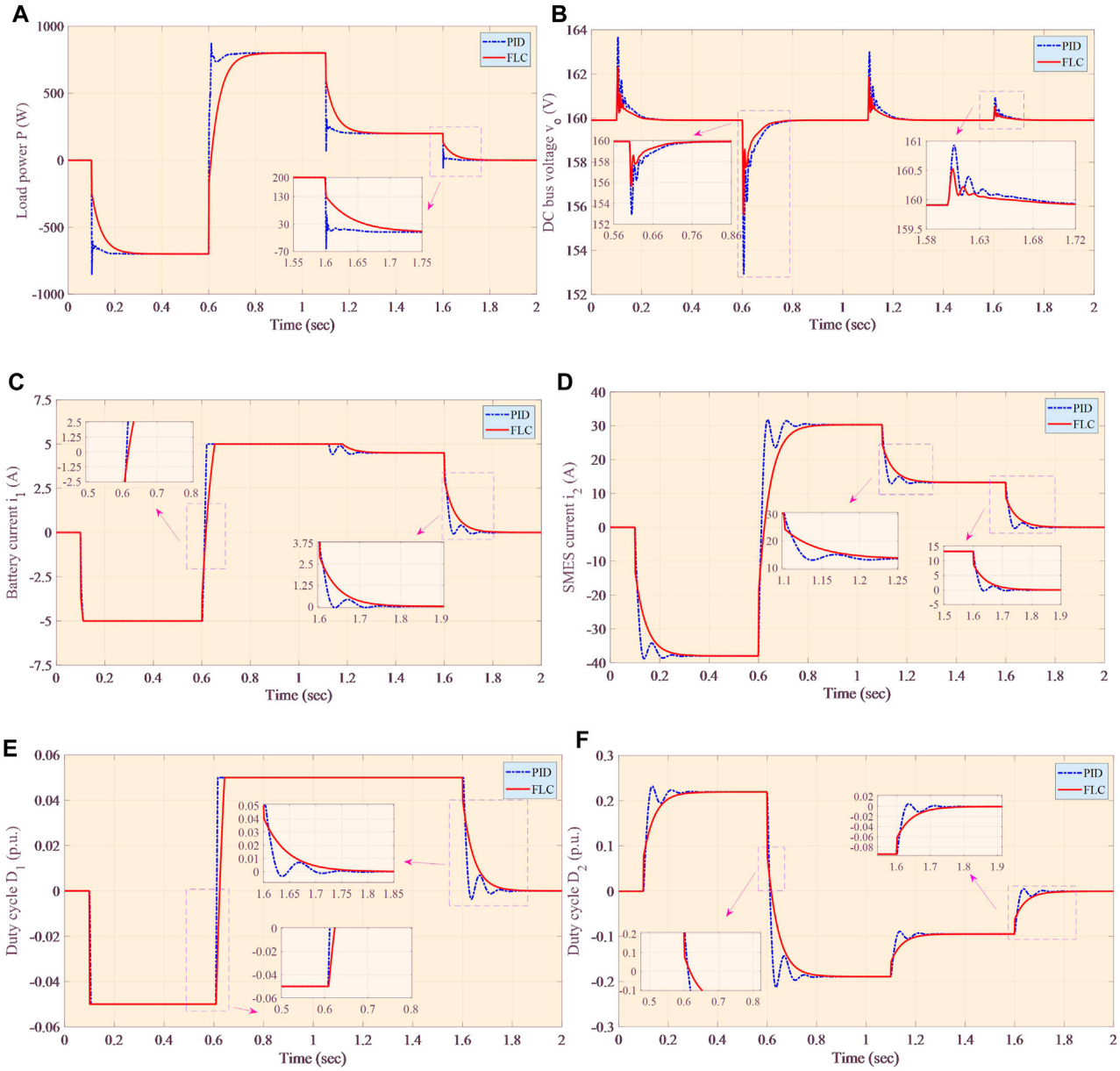


FIGURE 5 | BSM-HESS responses under light load conditions. **(A)** Load power P, **(B)** DC bus voltage v_o, **(C)** battery current i_1, **(D)** SMES current i_2, **(E)** duty cycle D_1, and **(F)** duty cycle D_2.

in series. The rated current of SMES is 100A. In addition, in RBS, P_{min} = 2 kW and P_{ch} = 100 W. Case studies are carried out by Matlab/Simulink 2019b. Besides, the sampling rate was set to 10^{-4} s, and ode23 was selected as the solver.

Heavy Load Condition

Based on the BSM-HESS model, the continuous step change of power demand of the power system under various conditions is studied to validate the specific tracking performance under heavy load conditions. In practical engineering application, heavy load condition usually occurs when the power system is connected with a large load. Here, the regenerative braking is carried out under the condition of corresponding negative load power, while the DC bus voltage reference is maintained at 160 V. The detailed system responses are shown in **Figure 4**, which shows that FLC can smoothly track the change of power demand and stably maintain the DC bus voltage. Compared with PID control, FLC has the smallest tracking error and the highest tracking speed. It is worth noting that such smooth tracking ability is very crucial for economic and reliable power system operation and can considerably prolong the battery service life.

Light Load Condition

The aim of this case is to study the control performance of FLC when the power system is connected with a small load.

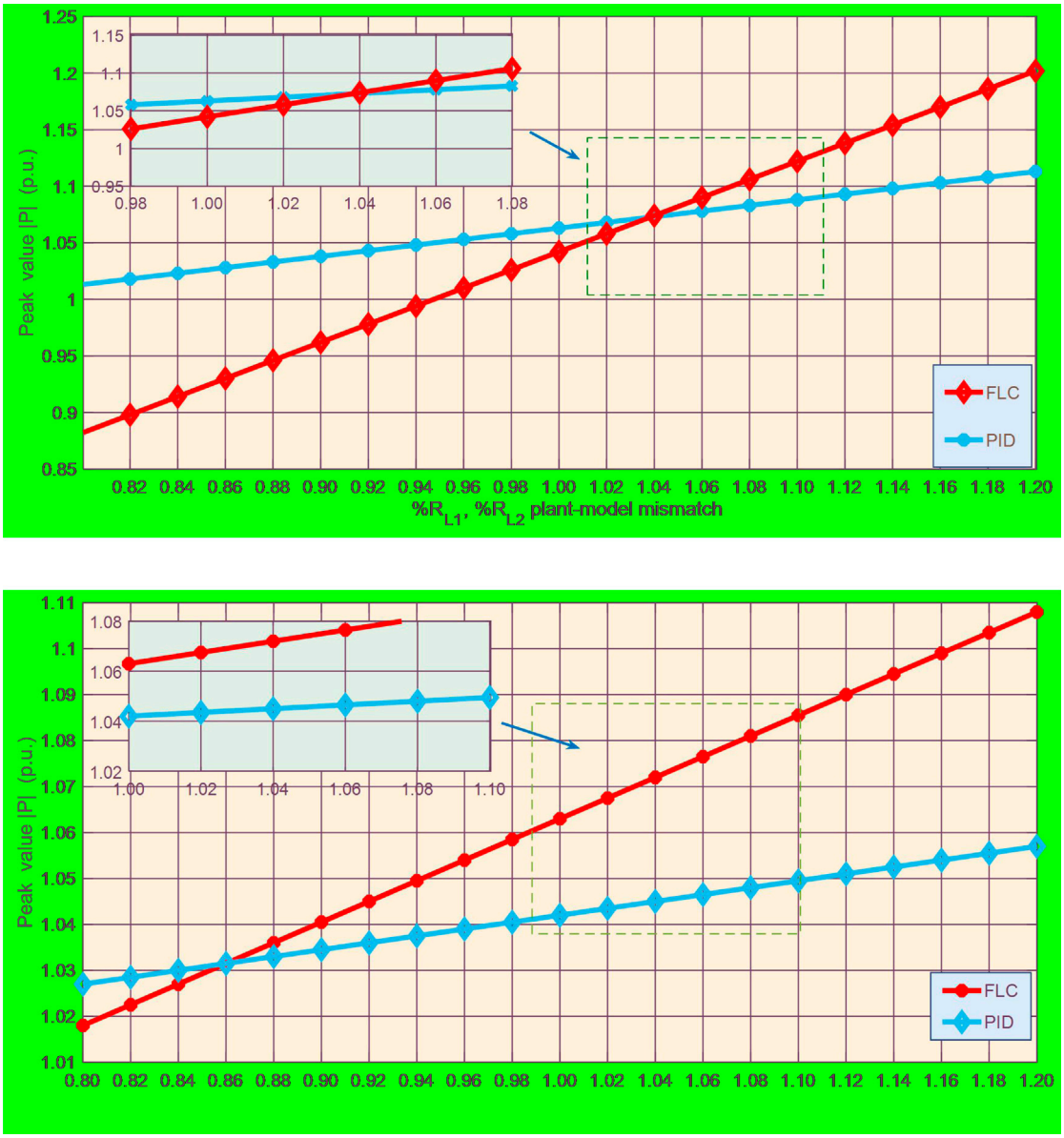


FIGURE 6 | Absolute peak value of active power |*P*| obtained under a 25% load drop lasting 100 ms with 20% variation of the battery/SMES series resistances R_{L1} and R_{L2} as well as inductances L_1 and L_2.

At this time, another power demand step change is used to compare the tracking performance between FLC and PID control. The corresponding responses are shown in **Figure 5**. It can be found that FLC achieves better tracking performance in terms of tracking speed and tracking error than PID control. In addition, FLC has smoother regulation of power *P*, while PID control oscillates severely. Similarly, for DC bus voltage, FLC has a small overshoot and can restore the disturbed power system in a short period of time, while PID control requires much more time for disturbed power system restoration with larger overshoot. Therefore, FLC can effectively decrease the charge and discharge frequency of the hybrid energy storage system, to reduce the wear and tear of the hybrid energy storage system.

Robustness With Uncertain BSM-HESS Parameters

This section is to study the robustness of FLC under the uncertainty of BSM-HESS parameters. Particularly, a series of plant–model mismatches of battery/SMES series resistances R_{L1} and R_{L2}, as well as inductances L_1 and L_2 with ±20% variation around their rated value are applied. Then, a 25% load drop occurs and lasts for 100 ms, during

which the absolute peak value of active power |P| is recorded, as shown in **Figure 6**. Note that the changes of PID control and FLC under the uncertainty of series resistance are 11.31 and 31.86%, respectively.

CONCLUSION

In this study, an FLC is designed to realize an efficient and smooth power tracking for BSM-HESS, and its contributions are summarized as follows:

1. FLC can fully compensate the nonlinearity of the system to achieve a globally consistent control performance; thus, the transient performance can be considerably improved;
2. FLC requires an accurate BSM-HESS system model; thus, it lacks robustness against parameter uncertainties compared to PID control;
3. The effectiveness and superiority of FLC are comprehensively verified and compared with PID control based on three case studies. Simulation results show that FLC outperforms PID control in terms of overshoot and tracking rate.

In the future, the effectiveness of FCL will be further validated by a hardware-in-the-loop (HIL) experiment based on the dSpace platform to meet the practical needs of engineering application.

DATA AVAILABILITY STATEMENT

The original contributions presented in the study are included in the article/Supplementary Material; further inquiries can be directed to the corresponding authors.

AUTHOR CONTRIBUTIONS

CT: conceptualization, writing—original draft preparation, and investigation. YH: writing, reviewing and editing, supervision, and conceptualization.

REFERENCES

Adhikari, S., and Li, F. (2014). Coordinated V-F and P-Q Control of Solar Photovoltaic Generators with MPPT and Battery Storage in Microgrids. *IEEE Trans. Smart Grid* 5 (3), 1270–1281. doi:10.1109/tsg.2014.2301157

Akyurek, A. S., and Rosing, T. S. (2016). Optimal Distributed Nonlinear Battery Control. *IEEE J. Emerging Selected Top. Power Electronics* 5 (3), 1045–1054.

Ali, M. H., Wu, B., and Dougal, R. A. (2010). An Overview of SMES Applications in Power and Energy Systems. *IEEE Trans. Sustain. Energ.* 1 (1), 38–47. doi:10.1109/tste.2010.2044901

Asv, V. L., Manyala, R. R., and Mangipudi, S. K. (2020). Design of a Robust PID-PSS for an Uncertain Power System with Simplified Stability Conditions. *Prot. Control. Mod. Power Syst.* 5 (1), 1–16. doi:10.1186/s41601-020-00165-9

Bakeer, A., Salama, H. S., and Vokony, I. (2021). Integration of PV System with SMES Based on Model Predictive Control for Utility Grid Reliability Improvement. *Prot. Control. Mod. Power Syst.* 6 (1), 1–13. doi:10.1186/s41601-021-00191-1

Bazargan, D., Bahrani, B., and Filizadeh, S. (2018). Reduced Capacitance Battery Storage DC-link Voltage Regulation and Dynamic Improvement Using a Feedforward Control Strategy. *IEEE Trans. Energ. Convers.* 33 (4), 1659–1668. doi:10.1109/tec.2018.2837627

Bizon, N. (2018). Effective Mitigation of the Load Pulses by Controlling the Battery/SMES Hybrid Energy Storage System. *Appl. Energ.* 229, 459–473. doi:10.1016/j.apenergy.2018.08.013

Brenna, M., Foiadelli, F., Longo, M., and Zaninelli, D. (2016). Energy Storage Control for Dispatching Photovoltaic Power. *IEEE Trans. Smart Grid* 9 (4), 2419–2428.

Chaibi, Y., Allouhi, A., Salhi, M., and El-jouni, A. (2019). Annual Performance Analysis of Different Maximum Power point Tracking Techniques Used in Photovoltaic Systems. *Prot. Control. Mod. Power Syst.* 4 (4), 171–180. doi:10.1186/s41601-019-0129-1

Dali, M., Belhadj, J., and Roboam, X. (2010). Hybrid Solar-Wind System with Battery Storage Operating in Grid-Connected and Standalone Mode: Control and Energy Management - Experimental Investigation. *Energy* 35 (6), 2587–2595. doi:10.1016/j.energy.2010.03.005

Huang, K., Li, Y., Zhang, X., Liu, L., Zhu, Y., and Meng, X. (2021). Research on Power Control Strategy of Household-Level Electric Power Router Based on Hybrid Energy Storage Droop Control. *Prot. Control. Mod. Power Syst.* 6 (1), 1–13. doi:10.1186/s41601-021-00190-2

Hussain, I., Ranjan, S., Das, D. C., and Sinha, N. (2017). Performance Analysis of Flower Pollination Algorithm Optimized PID Controller for Wind-PV-SMES-BESS-Diesel Autonomous Hybrid Power System. *Int. J. Renew. Energ. Res.* 7 (2), 643–651.

Jae Woong Shim, J. W., Youngho Cho, Y., Seog-Joo Kim, S. J., Sang Won Min, S. W., and Kyeon Hur, K. (2013). Synergistic Control of SMES and Battery Energy Storage for Enabling Dispatchability of Renewable Energy Sources. *IEEE Trans. Appl. Supercond.* 23 (3), 5701205. doi:10.1109/tasc.2013.2241385

Kasilingam, G., and Pasupuleti, J. (2015). Coordination of PSS and PID Controller for Power System Stability Enhancement - Overview. *Indian J. Sci. Technology* 8 (2), 142–151. doi:10.17485/ijst/2015/v8i2/58441

Khalid, M., and Savkin, A. V. (2010). A Model Predictive Control Approach to the Problem of Wind Power Smoothing with Controlled Battery Storage. *Renew. Energ.* 35 (7), 1520–1526. doi:10.1016/j.renene.2009.11.030

Kouchachvili, L., Yaïci, W., and Entchev, E. (2018). Hybrid Battery/supercapacitor Energy Storage System for the Electric Vehicles. *J. Power Sourc.* 374, 237–248. doi:10.1016/j.jpowsour.2017.11.040

Lalouni, S., Rekioua, D., Rekioua, T., and Matagne, E. (2009). Fuzzy Logic Control of Stand-Alone Photovoltaic System with Battery Storage. *J. Power Sourc.* 193 (2), 899–907. doi:10.1016/j.jpowsour.2009.04.016

Li, G. D., Li, G. Y., and Zhou, M. (2019). Model and Application of Renewable Energy Accommodation Capacity Calculation Considering Utilization Level of Interprovincial Tie-Line. *Prot. Control. Mod. Power Syst.* 4 (4), 1–12. doi:10.1186/s41601-019-0115-7

Lin, X., and Lei, Y. (2017). Coordinated Control Strategies for SMES-Battery Hybrid Energy Storage Systems. *IEEE Access* 5, 23452–23465. doi:10.1109/access.2017.2761889

Luo, X., Wang, J., Dooner, M., and Clarke, J. (2015). Overview of Current Development in Electrical Energy Storage Technologies and the Application Potential in Power System Operation. *Appl. Energ.* 137, 511–536. doi:10.1016/j.apenergy.2014.09.081

Magdy, G., Mohamed, E. A., Shabib, G., Elbaset, A. A., and Mitani, Y. (2018). SMES Based a New PID Controller for Frequency Stability of a Real Hybrid Power System Considering High Wind Power Penetration. *IET Renew. Power Generation* 12 (11), 1304–1313. doi:10.1049/iet-rpg.2018.5096

Malysz, P., Sirouspour, S., and Emadi, A. (2014). An Optimal Energy Storage Control Strategy for Grid-Connected Microgrids. *IEEE Trans. Smart Grid* 5 (4), 1785–1796. doi:10.1109/tsg.2014.2302396

Melo, S. P., Brand, U., Vogt, T., Telle, J. S., Schuldt, F., and Maydell, K. v. (2019). Primary Frequency Control provided by Hybrid Battery Storage and Power-To-Heat System. *Appl. Energ.* 233-234, 220–231. doi:10.1016/j.apenergy.2018.09.177

Montoya, O. D., Garcés, A., and Espinosa-Pérez, G. (2018). A Generalized Passivity-Based Control Approach for Power Compensation in Distribution Systems Using Electrical Energy Storage Systems. *J. Energ. Storage* 16, 259–268. doi:10.1016/j.est.2018.01.018

Murty, V. V. S. N., and Kumar, A. (2021). Multi-objective Energy Management in Microgrids with Hybrid Energy Sources and Battery Energy Storage Systems. *Prot. Control. Mod. Power Syst.* 5 (1), 1–20. doi:10.1186/s41601-019-0147-z

Nayak, P. C., Prusty, R. C., and Panda, S. (2021). Grasshopper Optimization Algorithm Optimized Multistage Controller for Automatic Generation Control of a Power System with FACTS Devices. *Prot. Control. Mod. Power Syst.* 6 (1), 1–15. doi:10.1186/s41601-021-00187-x

Olujobi, O. J. (2020). The Legal Sustainability of Energy Substitution in Nigeria's Electric Power Sector: Renewable Energy as Alternative. *Prot. Control. Mod. Power Syst.* 5 (1), 1–12. doi:10.1186/s41601-020-00179-3

Ruan, J., Song, Q., and Yang, W. (2019). The Application of Hybrid Energy Storage System with Electrified Continuously Variable Transmission in Battery Electric Vehicle. *Energy* 183, 315–330. doi:10.1016/j.energy.2019.06.095

Sai, L., Cheng, Z., Haomin, G., Qingxin, S., Tiancheng, T. E., Schomer, I., et al. (2021). Operational Optimization of a Building-Level Integrated Energy System Considering Additional Potential Benefits of Energy Storage. *Prot. Control. Mod. Power Syst.* 6 (1), 55–64. doi:10.1186/s41601-021-00184-0

Serir, C., Rekioua, D., Mezzai, N., and Bacha, S. (2016). Supervisor Control and Optimization of Multi-Sources Pumping System with Battery Storage. *Int. J. Hydrogen Energ.* 41 (45), 20974–20986. doi:10.1016/j.ijhydene.2016.05.096

Shi, Y., Xu, B., Tan, Y., Kirschen, D., and Zhang, B. (2018). Optimal Battery Control under Cycle Aging Mechanisms in Pay for Performance Settings. *IEEE Trans. Automatic Control.* 64 (6), 2324–2339. doi:10.1109/TAC.2018.2867507

Song, Z., Hou, J., Hofmann, H., Li, J., and Ouyang, M. (2017). Sliding-mode and Lyapunov Function-Based Control for Battery/supercapacitor Hybrid Energy Storage System Used in Electric Vehicles. *Energy* 122, 601–612. doi:10.1016/j.energy.2017.01.098

Teymour, H. R., Sutanto, D., Muttaqi, K. M., and Ciufo, P. (2014). Solar PV and Battery Storage Integration Using a New Configuration of a Three-Level NPC Inverter with Advanced Control Strategy. *IEEE Trans. Energ. Convers.* 29 (2), 354–365. doi:10.1109/tec.2014.2309698

Worthmann, K., Kellett, C. M., Braun, P., Grüne, L., and Weller, S. R. (2015). Distributed and Decentralized Control of Residential Energy Systems Incorporating Battery Storage. *IEEE Trans. Smart Grid* 6 (4), 1914–1923. doi:10.1109/tsg.2015.2392081

Xi, L., Yu, T., Yang, B., Zhang, X., and Qiu, X. (2016). A Wolf Pack Hunting Strategy Based Virtual Tribes Control for Automatic Generation Control of Smart Grid. *Appl. Energ.* 178, 198–211. doi:10.1016/j.apenergy.2016.06.041

Yang, B., Jiang, L., Yao, W., and Wu, Q. H. (2015). Perturbation Estimation Based Coordinated Adaptive Passive Control for Multimachine Power Systems. *Control. Eng. Pract.* 44, 172–192. doi:10.1016/j.conengprac.2015.07.012

Ye, K., Li, P., and Li, H. (2020). Optimization of Hybrid Energy Storage System Control Strategy for Pure Electric Vehicle Based on Typical Driving Cycle. *Math. Probl. Eng.* 2020 (9), 1–12. doi:10.1155/2020/1365195

Zhang, X., Tan, T., Zhou, B., Yu, T., Yang, B., and Huang, X. (2021). Adaptive Distributed Auction-Based Algorithm for Optimal Mileage Based AGC Dispatch with High Participation of Renewable Energy. *Int. J. Electr. Power Energ. Syst.* 124, 106371. doi:10.1016/j.ijepes.2020.106371

Zhang, X., Yu, T., Yang, B., and Li, L. (2016). Virtual Generation Tribe Based Robust Collaborative Consensus Algorithm for Dynamic Generation Command Dispatch Optimization of Smart Grid. *Energy* 101, 34–51. doi:10.1016/j.energy.2016.02.009

Zhang, X., Yu, T., Yang, B., Zheng, L., and Huang, L. (2015). Approximate Ideal Multi-Objective Solution Q(λ) Learning for Optimal Carbon-Energy Combined-Flow in Multi-Energy Power Systems. *Energ. Convers. Management* 106, 543–556. doi:10.1016/j.enconman.2015.09.049

Conflict of Interest: The authors declare that the research was conducted in the absence of any commercial or financial relationships that could be construed as a potential conflict of interest.

Publisher's Note: All claims expressed in this article are solely those of the authors and do not necessarily represent those of their affiliated organizations, or those of the publisher, the editors, and the reviewers. Any product that may be evaluated in this article, or claim that may be made by its manufacturer, is not guaranteed or endorsed by the publisher.

Copyright © 2021 Tang and Huang. This is an open-access article distributed under the terms of the Creative Commons Attribution License (CC BY). The use, distribution or reproduction in other forums is permitted, provided the original author(s) and the copyright owner(s) are credited and that the original publication in this journal is cited, in accordance with accepted academic practice. No use, distribution or reproduction is permitted which does not comply with these terms.

NOMENCLATURE

Variables

$\boldsymbol{v_1}$, $\boldsymbol{v_2}$, $\boldsymbol{v_o}$ voltages corresponding to C_1, C_2, and C_o

$\boldsymbol{i_1}$, $\boldsymbol{i_2}$ currents flowing through L_1 and L_2

$\boldsymbol{E}$ open-circuit voltage of battery

$\boldsymbol{I_{sc}}$ SMES current

Abbreviations

BSM-HESS battery/SMES hybrid energy storage system

SMES superconducting magnetic energy storage

RBS rule-based strategy

PID proportional–integral-derivative

FLC feedback linearization control

BSM-HESS parameters

$\boldsymbol{C_1}$, $\boldsymbol{C_2}$, $\boldsymbol{C_o}$ filter capacitances of battery side, SMES side, and load

$\boldsymbol{L_{SC}}$ inductance of superconducting magnetic coil

$\boldsymbol{L_1}$, $\boldsymbol{L_2}$ inductances of battery side and SMES side

$\boldsymbol{R_e}$ inner series resistances of battery

$\boldsymbol{R_{L1}}$, $\boldsymbol{R_{L2}}$ series resistances of battery side and SMES side

$\boldsymbol{R_{on1}}$, $\boldsymbol{R_{on2}}$, $\boldsymbol{R_{on3}}$, $\boldsymbol{R_{on4}}$ MOSFET on-resistances for S_1, S_2, S_3, and S_4

$\boldsymbol{R_o}$ equivalent load

$\boldsymbol{D_1}$, $\boldsymbol{D_2}$ duty cycle for the on-state of S_1 and S_3

FLC parameters

$\boldsymbol{\lambda_1}$, $\boldsymbol{\lambda_2}$ control gains

frontiers in Energy Research

BRIEF RESEARCH REPORT
published: 18 November 2021
doi: 10.3389/fenrg.2021.752571

Practical Method for Data-Driven User Phase Identification in Low-Voltage Distribution Networks

Huang Yu[1,2], *Yufeng Wu*[1,2], *Weiling Guan*[1,2], *Daolu Zhang*[1,2], *Tao Yu*[1,2]* *and Qianjin Liu*[1,2]

[1]School of Electric Power Engineering, South China University of Technology, Guangzhou, China, [2]Guangdong Provincial Key Laboratory of Intelligent Measurement and Advanced Metering of Power Grid, Guangzhou, China

For low-voltage distribution networks (LVDNs), accurate models depicting network and phase connectivity are crucial to the analysis, planning, and operation of these networks. However, phase connectivity data in the LVDN are usually incorrect or missing. Wrong or incomplete phase information collected could lead to unbalanced operation of three-phase distribution systems and increased power loss. Based on the advanced measurement infrastructure (AMI) in the development of smart grids, in this study, a novel data-driven phase identification algorithm is proposed. Firstly, the method involves extracting features from voltage–time matrices using a non-linear dimension reduction algorithm. Secondly, the density-based spatial clustering of applications with noise (DBSCAN) algorithm is used to divide customers into clusters with arbitrary shape. Finally, the algorithms were tested with the IEEE European Low Voltage Test Feeder of the IEEE PES AMPS DSAS Test Feeder working group. The results showed an accuracy of over 90% for the method.

Keywords: phase identification, DBSCAN cluster, smart meter, low-voltage distribution network, non-linear dimensionality reduction algorithm

OPEN ACCESS

Edited by:
Bo Yang,
Kunming University of Science and Technology, China

Reviewed by:
Jiazheng Xie,
China Electric Power Research Institute (CEPRI), China
Xinwei Li,
China Southern Power Grid, China

***Correspondence:**
Tao Yu
taoyu1@scut.edu.cn

Specialty section:
This article was submitted to Smart Grids, a section of the journal Frontiers in Energy Research

Received: *03 August 2021*
Accepted: *13 September 2021*
Published: *18 November 2021*

Citation:
Yu H, Wu Y, Guan W, Zhang D, Yu T and Liu Q (2021) Practical Method for Data-Driven User Phase Identification in Low-Voltage Distribution Networks. Front. Energy Res. 9:752571. doi: 10.3389/fenrg.2021.752571

INTRODUCTION

Since the introduction of the concept of "Digital Power Grid" (Islam, 2016) and the development of measurement technology, how to deal with electrical data in smart grids has become a focus of research. At the same time, distributed energy resources (DERs) are being deployed in the electric power distribution systems at an unprecedented pace (Yang et al., 2016; Yang et al., 2017; Yang et al., 2018; Yang et al., 2019a). To fully exploit the benefits of the DERs, the distribution network must be actively managed (Yang et al., 2019b; Xi et al., 2020; Yang et al., 2020; Li et al., 2021). The low-voltage distribution network is the last link to connect users in the whole power system. Therefore, the network's level of information interaction ability directly affects the user experience. The distribution network must be actively managed.

The introduction of the smart grid and advanced measurement infrastructure (AMI) concepts has brought new opportunities for developing distribution networks. To operate the distribution system in an efficient and reliable manner, distribution system operators typically need to perform a series of tasks, including three-phase optimal power flow, distribution system restoration and reconfiguration, and three-phase unbalance degree. Although network connectivity models are often accurate, phasing errors are common. Therefore, an accurate phase identification method is needed.

Electric utility companies typically do not have accurate information on phase connectivity. Moreover, phase connectivity of a distribution network may change when new distribution lines are constructed and included in the network. Correct phase connectivity data are essential to the efficient and reliable operation of a distribution system, especially when more advanced applications are

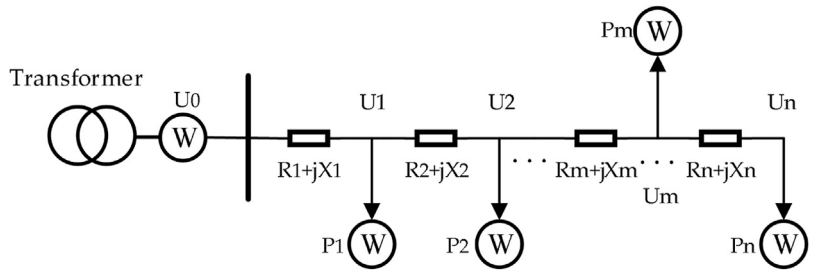


FIGURE 1 | Schematic diagram of single-phase power flow.

connected. A model has been established to identify transformers and user phases based on voltage correlation using linear regression (Short, 2013). The correlation between a circuit and transformers in it can be determined by analyzing the correlation in voltage between buses and user meters from the perspective of power flow (Luan et al., 2013; Tang and Milanovic, 2018). Topology can also be identified by analyzing the correlation in load between lines at upper and lower levels (Pappu et al., 2018; Lisowski et al., 2019). Most of these studies focus on medium-voltage distribution networks, while the identification of topology in LVDNs is yet to be studied. There are two methods to identify the phase in LVDNs. The first method is based on the law of conservation of energy. With all possible user phases listed, the mixed integer programming model is used to find the optimal solution, taking into consideration the degree of three-phase unbalance and line loss (Tian et al., 2016; Tang and Milanovic, 2018; Zhou et al., 2020). The method requires complex calculation, and the electrical features of users in the same phase sequence are not considered. When there are missing user power values, accuracy is not guaranteed. The other method is based on the clustering algorithm in machine learning. User phases in an LVDN are identified by establishing clusters among three-phase users (Wen et al., 2015; Wang et al., 2016; Liu et al., 2020). However, the difference in load fluctuation between phases is not intuitive enough after three-phase treatment in LVDNs.

To address the problem of the existing solutions, the current study proposes a data-driven phase identification algorithm based on the advanced metering infrastructure (AMI) that allows for in-depth exploitation of data features. Then, the LargeVis (Large-scale Visualizing Data) dimensionality reduction algorithm is used to extract data from high-dimensional time–voltage matrices of LVDN users, resulting in low-dimension data which retain only the main features. Finally, the DBSCAN (density-based spatial clustering of application with noise) algorithm is used to analyze the features of users in clusters and identify the specific user phases. The method may improve the efficiency and accuracy of topology identification.

TOPOLOGY OF LOW-VOLTAGE DISTRIBUTION NETWORKS

Through the high-voltage transmission line, the electric energy is transmitted to the distribution network. After the distribution transformer is stepped down to 400 V, the electric energy is transmitted to the clients through the three-phase feeder.

Three-phase gate ammeters are installed at the outlet of the distribution transformer to record voltage, current, active power, reactive power, load, and other values for each of the three-phase electrical data information of the feeder. **Figure 1** shows the relationship between the gate ammeter at the bus and the meter of each user in a singer-phase line.

As low-voltage distribution feeders extend to a shorter distance than high-voltage lines, no more than 500 m in most cases, the influence of line reactance is not considered in this study. Reactive power effects that exist on the lines are not considered neither, as they are negligible in well-managed networks:

$$U_1 = U_0 - \frac{R_1 P_1}{U_0}, \tag{1}$$

$$U_m = U_0 - \frac{R_1 P_1}{U_0} - \frac{R_2 P_2}{U_1} - \cdots \frac{R_m P_m}{U_{m-1}} = U_0 - \sum_{i=1}^{m} \frac{R_i P_i}{U_{i-1}}, \tag{2}$$

$$\triangle U_m = U_m - U_{m-1} = -\frac{R_m P_m}{U_{m-1}} < 0, \tag{3}$$

where U_0 represents the voltage at the bus node; U_1, U_{m-1}, U_m, U_n are the voltage values at the corresponding node; R_1, R_2, R_m, R_n are the impedance values of the corresponding line; and $\triangle U_m$ is the voltage difference between adjacent nodes m and $m-1$.

The voltage of users closest to the bus is related only to the bus voltage and their own load. When positioned with short electrical intervals, adjacent nodes in the same feeder will have similar voltage values and the coefficient of correlation is higher than that when they are in different feeders. By analyzing the changes of user voltage values in time sequences, the phase relationships of users can be identified.

DATA PRE-PROCESSING AND PHASE RECOGNITION ALGORITHM

Time-Series Voltage Data Pre-Processing

The users' smart meter collects voltage data at a given interval and uploads them to the terminal. The time-series variation matrix of voltage amplitude of users in the station area is obtained from the historical data in the terminal. If some data are missing, and the

interpolation method is used to complete the missing values, $U \in R^{N\times M}$ is shown as follows:

$$U = \begin{bmatrix} u_{1,t_1} & u_{1,t_2} & \cdots & u_{1,t_M} \\ u_{2,t_1} & u_{2,t_2} & \cdots & u_{2,t_M} \\ \vdots & \vdots & \vdots & \vdots \\ u_{N,t_1} & u_{N,t_2} & \cdots & u_{N,t_M} \end{bmatrix}, \tag{4}$$

where u_{i,t_j} represents the measured voltage of user i at time t_j, N is the total number of users, and M represents the number of voltage collection times within the analysis period.

For user nodes near the bus, since their voltage is only affected by the bus voltage and their own load, their voltage timing curve will be close to that of the bus if the value of their own load is low. This will cause great disturbance to the subsequent clustering. To avoid this problem, these nodes are distinguished from the rest of the matrix and put into a separate cluster based on their correlation with the bus in terms of voltage and their voltage amplitude. The rest of the data are standardized to eliminate the influence of variation in voltage fluctuation at different phases. The dimensionality of the time–voltage matrix does not change after standardization. The formula used for standardization is as follows:

$$U'_{t_j} = \frac{U_{t_j} - \mu\left(U_{t_j}\right)}{\sigma\left(U_{t_j}\right)}, \tag{5}$$

where U'_{t_j} represents standardization of voltage at t_j; U_{t_j} represents initial values of the voltage at t_j; $\mu(U_{t_j})$ represents the mean value of voltage at all measurement points at t_j; $\sigma(U_{t_j})$ represents the voltage standard deviation at all measurement points at t_j; and U' represents the standardized user voltage dataset.

Feature Dimension Reduction Based on LargeVis

As the time for data collection mounts, the dimensionality of time–voltage matrices also increases. High-dimensional datasets contain excessively redundant information and data noise and require more complex and time-consuming computation.

PCA linear dimension reduction first conducts projection transformation and then finds the low-dimensional space that maximizes its goal. The purpose is to maintain the maximum variance of samples in the low-dimensional space, and the processing speed is fast, but the information loss is serious when the dimension is low. In this study, the LargeVis method is used to reduce the dimensionality of the data, keeping only the main features. It can reduce the high-dimensional dataset of the user voltage matrix to two or three dimensional spaces for visualization and retain the distribution characteristics of the original voltage dataset. The above problems should be improved by means of the feature dimension reduction method.

LargeVis (Tang et al., 2016) is a non-linear reductive dimension algorithm, which can reduce the high-dimensional dataset of the user voltage matrix to two or three dimensional spaces for visualization and retain the distribution characteristics of the original dataset. This algorithm was proposed by Professor Tang Jian in 2016. The dimension reduction process is as follows:

1) In high-dimensional space, LargeVis retains only the weight of KNN edges in the process of mapping. These edges are called positive edges, while nodes that are not directly adjacent are called negative edges. In high-dimensional space, the Euclidean distance between users is transformed into probability similarity, and the formula is as follows:

$$p_{j|i} = \frac{\exp\left(-\left\|X'_i - X'_j\right\|^2/2\sigma_i^2\right)}{\sum_{k\neq i}\exp\left(-\left\|X'_i - X'_k\right\|^2/2\sigma_i^2\right)}, \tag{6}$$

$$w_{ij} = \frac{p_{j|i} + p_{i|j}}{2L}, \tag{7}$$

$$W_i = [w_{i1}, w_{i2}, w_{i3} \ldots, w_{iL}], \tag{8}$$

where w_{ij} is the probability similarity between user i and user j, to avoid the outlier node, getting it by adding conditional probabilities. W_i is the similarity matrix between user i and other users in the same station. W is the Gaussian probability distribution matrix of the normalized voltage dataset. σ_i is the standard deviation of the Gaussian model.

2) In low-dimensional space, the low-dimensional coordinates are determined by the probability of observation, and the probability of an edge connection between two points is set as follows:

$$P\left(e_{ij} = 1\right) = f\left(\left\|y_i - y_j\right\|\right), \tag{9}$$

$$f(x) = \frac{1}{1 + \exp\left(x^2\right)}, \tag{10}$$

$$P\left(e_{ij} = w_{ij}\right) = P\left(e_{ij} = 1\right)^{w_{ij}}, \tag{11}$$

where e_{ij} represents the edge weight between two nodes and $f(x)$ is a probability function, indicating the distance between vertices y_i and y_j. The closer the points are in higher dimensions, the closer the points are in lower dimensions.

3) In the dimension reduction process, the final objective function is as follows:

$$O = \sum_{(i,k)\in E} w_{ij}\log p\left(e_{ij} = 1\right) + \sum_{k=1}^{m} E_{jk} \sim P_n(j)\gamma\log\left(1 - p\left(e_{jk} = 1\right)\right), \tag{12}$$

where E is the set of positive edges, $\bar{E}$ is a complement to E, and γ is the uniform weight assigned to the negative edge.

Using LINE technology (Tang et al., 2015), the weighted edge is regarded as the w_{ij} unit edge. All positive edges are sampled directly, and the weight of the edge is trained to obtain the low-dimensional feature set Y. Y is consistent with the characteristic distribution of the standardized voltage dataset $U_{L\times M'}$.

Phase Identification Based on DBSCAN Algorithm

Clustering of unlabeled voltage–time datasets can be performed with unsupervised learning algorithms. DBSCAN (density-based spatial clustering of applications with noise) as a density-based

clustering algorithm can divide regions with enough density into clusters and identify clusters of arbitrary shape in spatial databases with noise.

After dimension reduction, the Euclidian distance between two points is used as the distance between them. Users at the same phase have relatively shorter distances between them and will form a cluster. Therefore, the DBSCAN method is suitable.

The core point of DBSCAN is determined by setting parameters, including the neighborhood radius (Eps) and the minimum number of sample points (MinPts). To limit the space of density clustering and achieve better visual performance, the maximum and minimum values of the feature set Y after dimension reduction are normalized. The formula is as follows:

$$y'_{ij} = \frac{y_{ij} - \min\left(y_{*j}\right)}{\max\left(y_{*j}\right) - \min\left(y_{*j}\right)}, \tag{13}$$

where y_{ij} is a member of matrix Y, max (y_{*j}) is the maximum value of the j column vector in the Y dataset, min (y_{*j}) is the minimum value of the j column vector in the Y dataset, and y'_{ij} belongs to the normalized dataset Y'.

Based on the dataset Y', the distance between all nodes in the dataset is calculated to form a matrix $D \in R^{L\times L}$. The calculation formulas are as follows:

$$D_i = \left[d\left(Y'_i, Y'_1\right), d\left(Y'_i, Y'_2\right), \ldots, d\left(Y'_i, Y'_L\right)\right]^T, \tag{14}$$

$$D = [D_1, D_2, \ldots, D_L]. \tag{15}$$

Here, $d(Y_i, Y_j)$ indicates the Euclidean distance between Y_i and Y_j.

To establish DBSCAN parameters Eps and MinPts, the calculation formulas are as follows:

$$\text{Eps} = \frac{\min\limits_{i=1}^{L}\left\{\max\limits_{j=1}^{L}\left[D_j\right]\right\}}{Z}, \tag{16}$$

$$MinPts = \frac{\min\left(count\ \left(D_i < Eps\right)\right)}{Z}. \tag{17}$$

Here, Z is the number of predicted clusters and $count\ (D_i < Eps)$ is the number of nodes whose distance between adjacent and surrounding nodes is less than Eps in the distance vector D_j.

After that, set a certain step size, adjust the values of Eps (0.01) and MinPts (1), and determine the most suitable parameter coefficient according to the silhouette coefficient. The formula for calculating the silhouette coefficient is as follows:

$$s(i) = \frac{b(i) - a(i)}{\max\{a(i), b(i)\}}. \tag{18}$$

Here, $a(i)$ represents the average distance between node i and other nodes in the same cluster and $b(i)$ represents the average distance between node i and other cluster nodes. The closer $s(i)$ is to 1, the more reasonable the clustering result is. In other words, the closer $s(i)$ is to -1, the more unreasonable the clustering result is.

After clustering, each cluster group is obtained, and the phase recognition results of users are tested according to the phase tags of clustering results. The specific flow chart is shown in **Figure 2**.

ANALYSIS OF EXAMPLES

The dataset used in this paper is the IEEE European Low Voltage Test Feeder of the IEEE PES AMPS DSAS Test Feeder working group (IEEE and PES, 2019). The low-voltage test feeder is a radial distribution feeder with a base frequency of 50 Hz. The feeder is connected to the medium-voltage power system through the transformer of the substation, which makes the voltage from 11 kV to 416 V. There are 55 users in total, and all of them are single-phase users. There are 21 households with phase A load, 19 households with phase B load, and 15 households with phase C load.

According to the configuration file, the power factor of all loads was set to be 0.95 in the whole simulation range. According to the power load curve of 55 users, the power flow calculation was carried out by OpenDSS software, and the voltage curve lasting 24 h with a resolution of 1 minute was obtained.

Parameter Settings of LargeVis and DBSCAN

In the actual environment, the situation of smart meter measurement may be more complicated, and the error is inevitable. To evaluate the effectiveness of the algorithm in the actual environment, we need to test it in a noisy dataset. Smart meters have a non-negligible uncertainty, and their accuracy levels vary in different countries. According to the measurement, the accuracy can be roughly divided into the following grades: 0.2, 0.5, 1, and 2, which means the uncertainty of 0.2, 0.5, 1, and 2%, respectively.

The number of nodes near the bus caused by error clustering accounted for 5~8% of the total number of nodes. According to the correlation between voltage amplitude and bus, related nodes will be classified separately. The voltage timing matrix composed of other meters has been standardized by the Z-score to obtain the matrix U'. The LargeVis algorithm is used to reduce the dimension of the user timing voltage matrix U'. After dimension reduction, the low-dimensional voltage characteristic matrix Y is obtained. The low-dimensional Y is maximally and minimally normalized to Y'. Calculating the distance matrix between each node of the user, Z is 3 to obtain the initial DBSCAN parameter value ($Eps = 0.126$, $MinPts = 4$). Eps changes with the step size of 0.005, MinPts changes with the step size of 1, and the specific values of cluster parameters are determined by the profile coefficient method.

Analysis of Numerical Example Results

Eps = 0.131, MinPts = 3, as the final cluster input parameter. Three clusters are formed after clustering. After comparing the correlation coefficient between the user voltage in the cluster center and the bus voltage, the phase sequence of the users in the station area can be determined.

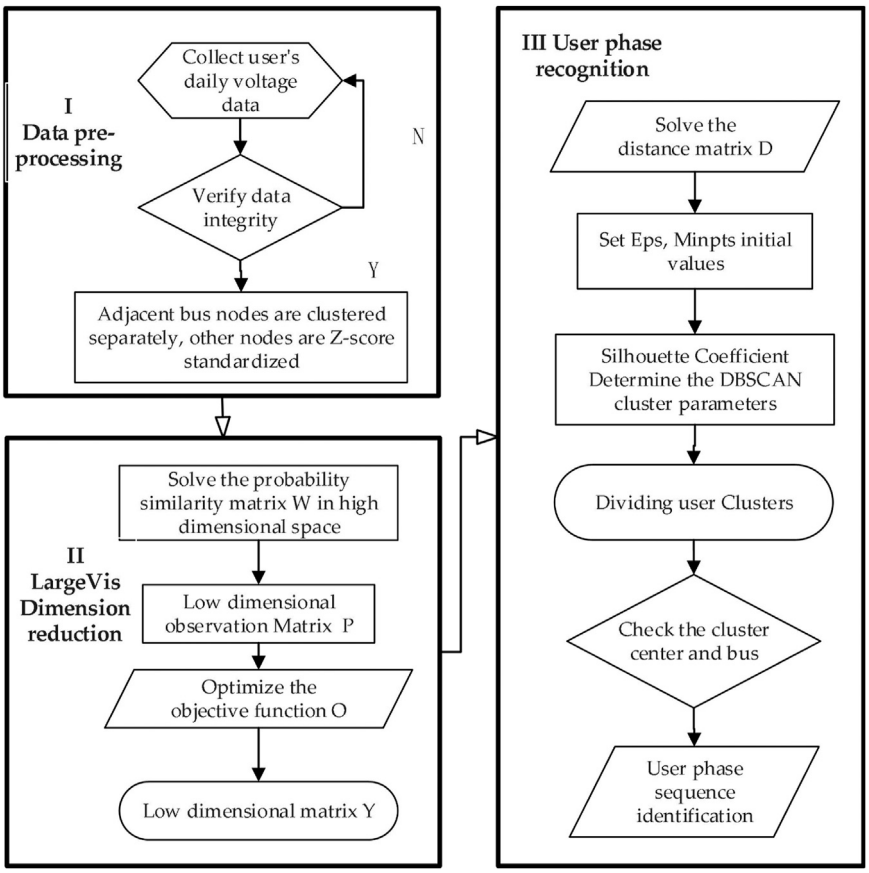


FIGURE 2 | Phase recognition algorithm process.

TABLE 1 | Accuracy comparison of phase recognition methods.

Method	No error	1% error	2% error
k-means	0.927	0.89	0.818
PCA + k-means	0.945	0.927	0.909
Spectral clustering	0.945	0.909	0.892
Method in this paper	1.0	1.0	0.981

TABLE 2 | Evaluation indicators of phase identification in different cases.

Measurement error sampling frequency	0	1%	2%
15 min	1.0	1.0	0.98
30 min	1.0	0.927	0.818
1 h	1.0	0.927	0.6
2 h	0.96	0.854	/

To further prove the accuracy of the proposed method in phase recognition, the proposed method is compared with k-means, PCA, and k-means (Wen et al., 2015) and spectral clustering algorithm (Wang et al., 2016). The cluster number of each method is preset as 3. The recognition accuracy of the results is shown in **Table 1**.

The method proposed in this study showed the highest accuracy compared with the other methods. One of the reasons might be that the users near the bus were put into a separate cluster to avoid interference. Moreover, the LargeVis algorithm is able to retain data features after dimensionality reduction and the DBSCAN algorithm can cluster data points of arbitrary density, making them more suitable for processing datasets. For k-means, errors with ammeters may cause excessively redundant information in the time–voltage matrix, resulting in the instability of clustering results. For PCA, the linear dimensionality reduction approach they use to remove redundant information may lead to loss of data details and thus decreased accuracy. As for spectral clustering, the clustering effect directly depends on the similarity matrix generated in advance, which requires high precision of the original data.

To verify the usability of the proposed algorithms in engineering problems, disturbance errors were set for accuracy analysis under different sampling frequencies. The sampling frequency of the ammeters was set to 15 min, 30 min, 1 h, or 2 h, and the disturbance error was set to no error, 1%, or 2%. The results are shown in **Table 2**.

When the metering error is small, the identification accuracy of the algorithm in this paper decreases. When the metering error increases, the accuracy of phase sequence identification can be guaranteed only on high sampling frequency (15 min). The decrease of acquisition frequency will decrease the accuracy of recognition rate. When the collection frequency is reduced to 2 h, the identification cannot be completed, which indicates that a certain sampling frequency should be guaranteed for phase identification based on users' daily voltage variation characteristics.

CONCLUSION AND DISCUSSION

This paper presents a data-driven method for user phase identification in LVDNs. The LargeVis reductive dimension method is used to extract features from the standardized timing voltage matrix. Then, based on the DBSCAN method, the low-dimensional dataset is clustered as a result of user phase identification. Simulations show that the proposed method is more reliable than other unsupervised learning algorithms for single-phase user identification in LVDNs. The method used in this paper only needs to collect the user's load data for analysis, without additional hardware equipment costs and special personnel to check users one by one, so it can save the cost of user phase verification in the low-voltage distribution network.

DATA AVAILABILITY STATEMENT

The original contributions presented in the study are included in the article/Supplementary Material, and further inquiries can be directed to the corresponding author.

AUTHOR CONTRIBUTIONS

HY involved in conceptualization, performed the methodology, and wrote the article. YW curated the data. WG involved in formal analysis. QL investigated the data. TY obtained the resources and acquired the funding.

ACKNOWLEDGMENTS

The authors gratefully acknowledge the support of science and technology project by China Southern Power Grid (GDKJXM20172939).

REFERENCES

IEEE; PES. (2019). Distribution Test Feeders. Available at: http://sites.ieee.org/pes-testfeeders/resources/. (still can Accessed June 10, 2021)

Islam, S. (2016). "Digital Applications in Implementation of Smart Grid," in International Conference on Accessibility to Digital World (ICADW), Guwahati, India, Dec, 2016, 3–7. doi:10.1109/icadw.2016.7942504

Li, J., Yu, T., Zhang, X., Li, F., Lin, D., and Zhu, H. (2021). Efficient Experience Replay Based Deep Deterministic Policy Gradient for AGC Dispatch in Integrated Energy System. *Appl. Energ.* 285, 116386. doi:10.1016/j.apenergy.2020.116386

Lisowski, M., Masnicki, R., and Mindykowski, J. (2019). PLC-enabled Low Voltage Distribution Network Topology Monitoring. *IEEE Trans. Smart Grid.* 10 (6), 6436–6448. doi:10.1109/tsg.2019.2904681

Liu, S., Jin, R., Qiu, H., Cui, X., Lin, Z., Lian, Z., et al. (2020). Practical Method for Mitigating Three-phase Unbalance Based on Data-Driven User Phase Identification. *IEEE Trans. Power Syst.* 35, 1653–1656. doi:10.1109/tpwrs.2020.2965770

Luan, W., Peng, J., Maras, M., and Lo, J. (2013). "Distribution Network Topology Error Correction Using Smart Meter Data Analytics," in IEEE Power and Energy Society General Meeting, Vancouver, BC, Canada, July, 2013. doi:10.1109/pesmg.2013.6672786

Pappu, S. J., Bhatt, N., and RajeswaranPasumarthy, A. (2018). Identifying Topology of Low Voltage Distribution Networks Based on Smart Meter Data. *IEEE Trans. Smart Grid.* 9, 5113–5122. doi:10.1109/tsg.2017.2680542

Short, T. A. (2013). Advanced Metering for Phase Identification, Transformer Identification, and Secondary Modeling. *IEEE Trans. Smart Grid.* 4 (2), 651–658. doi:10.1109/tsg.2012.2219081

Tang, X., and Milanovic, J. V. (2018). "Phase Identification of LV Distribution Network with Smart Meter Data," in IEEE Power & Energy Society General Meeting, Portland, OR, USA, Aug, 2018.

Tang, J., Liu, J., Zhang, M., and Mei, Q. (2016). "Visualizing Large-Scale and High-Dimensional Data," in Proceedings of the 25th International World Wide Web Conference, WWW, Montreal, Canada, April 11-15, 2016, 287–297. doi:10.1145/2872427.2883041

Tang, J., Qu, M., Wang, M., Zhang, M., Yan, J., and Mei, Q. (2015). "LINE: Large-Scale Information Network Embedding," in Proceedings of the 24th International Conference on world wide web, Montreal, Canada, April 11-15, 2016,1067.

Tian, Z., Wu, W., and Zhang, B. (2016). A Mixed Integer Quadratic Programming Model for Topology Identification in Distribution Network. *IEEE Trans. Power Syst.* 31, 823–824. doi:10.1109/tpwrs.2015.2394454

Wang, W., Yu, N., Foggo, B., Davis, J., and Li, J. (2016). "Phase Identification in Electric Power Distribution Systems by Clustering of Smart Meter Data," in Proceedings. 2016 15th IEEE International Conference on Machine Learning and Applications, ICMLA. Anaheim, CA, USA, Dec, 2016, 259–265. doi:10.1109/icmla.2016.0050

Wen, M., Arghandeh, R., Meier, A., Poolla, K., and Li, V. (2015). "Phase Identification in Distribution Networks with Micro-synchrophasors," in Power and Energy Society General Meeting, Denver, CO, USA, July, 2015.

Xi, L., Wu, J., Xu, Y., and Sun, H. (2020). Automatic Generation Control Based on Multiple Neural Networks with Actor-Critic Strategy. *IEEE Trans. Neural Netw. Learn. Syst.* 32 (6), 2483–2493. doi:10.1109/TNNLS.2020.3006080

Yang, B., Jiang, L., Wang, L., Yao, W., and Wu, Q. H. (2016). Nonlinear Maximum Power point Tracking Control and Modal Analysis of DFIG Based Wind Turbine. *Int. J. Electr. Power Energ. Syst.* 74, 429–436. doi:10.1016/j.ijepes.2015.07.036

Yang, B., Wang, J., Zhang, X., Yu, T., Yao, W., Shu, H., et al. (2020). Comprehensive Overview of Meta-Heuristic Algorithm Applications on Pv Cell Parameter Identification. *Energ. Convers. Manage.* 208, 112595. doi:10.1016/j.enconman.2020.112595

Yang, B., Yu, T., Shu, H., Dong, J., and Jiang, L. (2018). Robust Sliding-Mode Control of Wind Energy Conversion Systems for Optimal Power Extraction via Nonlinear Perturbation Observers. *Appl. Energ.* 210, 711–723. doi:10.1016/j.apenergy.2017.08.027

Yang, B., Yu, T., Zhang, X., Li, H., Shu, H., Sang, Y., et al. (2019). Dynamic Leader Based Collective Intelligence for Maximum Power point Tracking of PV Systems Affected by Partial Shading Condition. *Energ. Convers. Manage.* 179, 286–303. doi:10.1016/j.enconman.2018.10.074

Yang, B., Zhang, X., Yu, T., Shu, H., and Fang, Z. (2017). Grouped Grey Wolf Optimizer for Maximum Power point Tracking of Doubly-Fed Induction

Generator Based Wind Turbine. *Energ. Convers. Manag.* 133, 427–443. doi:10.1016/j.enconman.2016.10.062

Yang, B., Zhong, L., Zhang, X., Shu, H., Yu, T., Li, H., et al. (2019). Novel Bio-Inspired Memetic Salp Swarm Algorithm and Application to MPPT for PV Systems Considering Partial Shading Condition. *J. Clean. Prod.* 215, 1203–1222. doi:10.1016/j.jclepro.2019.01.150

Zhou, L., Zhang, Y., Liu, S., Li, K., Li, C., Yi, Y., et al. (2020). Consumer Phase Identification in Low-Voltage Distribution Network Considering Vacant Users. *Int. J. Electr. Power Energ. Syst.* 121, 106079. doi:10.1016/j.ijepes.2020.106079

Conflict of Interest: The authors declare that the research was conducted in the absence of any commercial or financial relationships that could be construed as a potential conflict of interest.

Publisher's Note: All claims expressed in this article are solely those of the authors and do not necessarily represent those of their affiliated organizations, or those of the publisher, the editors, and the reviewers. Any product that may be evaluated in this article, or claim that may be made by its manufacturer, is not guaranteed or endorsed by the publisher.

Copyright © 2021 Yu, Wu, Guan, Zhang, Yu and Liu. This is an open-access article distributed under the terms of the Creative Commons Attribution License (CC BY). The use, distribution or reproduction in other forums is permitted, provided the original author(s) and the copyright owner(s) are credited and that the original publication in this journal is cited, in accordance with accepted academic practice. No use, distribution or reproduction is permitted which does not comply with these terms.

Advantages of publishing in Frontiers

OPEN ACCESS
Articles are free to read for greatest visibility and readership

FAST PUBLICATION
Around 90 days from submission to decision

HIGH QUALITY PEER-REVIEW
Rigorous, collaborative, and constructive peer-review

TRANSPARENT PEER-REVIEW
Editors and reviewers acknowledged by name on published articles

Frontiers
Avenue du Tribunal-Fédéral 34
1005 Lausanne | Switzerland

Visit us: www.frontiersin.org
Contact us: frontiersin.org/about/contact

REPRODUCIBILITY OF RESEARCH
Support open data and methods to enhance research reproducibility

DIGITAL PUBLISHING
Articles designed for optimal readership across devices

FOLLOW US
@frontiersin

IMPACT METRICS
Advanced article metrics track visibility across digital media

EXTENSIVE PROMOTION
Marketing and promotion of impactful research

LOOP RESEARCH NETWORK
Our network increases your article's readership